SOWE III

Third Asia-Pacific Symposium on Wind Engineering

December 13-15, 1993

Hong Kong

PROCEEDINGS

Volume I

Edited by   K.M. Lam
                Y.K. Cheung

PROCEEDINGS

OF

THE THIRD ASIA-PACIFIC SYMPOSIUM

ON

WIND ENGINEERING

December 13-15, 1993

Hong Kong

Edited by   K.M. Lam and Y.K. Cheung
The University of Hong Kong

VOLUME I

FOREWORD

The Third Asia-Pacific Symposium on Wind Engineering (APSOWE III) is jointly organized by the Department of Civil and Structural Engineering, The University of Hong Kong and The Hong Kong Institution of Engineers from December 13 to 15, 1993 in Hong Kong. The choice of Hong Kong as the location for the Symposium is by no means accidental. As we all know, Hong Kong is one of the great cities in Asia on the Pacific rim, and this region is the only area in the world that is experiencing rapid economic growth and infrastructure development. With her clusters of ultra-tall buildings, her many steep slopes, the frequent onslaught of tropical cyclones or typhoons, her concern for air pollution from factory and vehicle emissions, Hong Kong is definitely the ideal city to hold such a meeting on wind engineering. In addition, Hong Kong is now receiving worldwide attention for her replacement airport at Chek Lap Kok which also includes other core projects such as the Tsing-Ma Bridge which is going to be one of the longest suspension bridges in the world.

Following the objectives of the previous two Symposiums in Roorkee and Beijing, this Symposium aims to bring together scientists and engineers in Asia-Pacific area as well as other parts of the world to discuss and exchange ideas and experience related to the research and practice of wind engineering. In the past decade, there has been rapid development on wind engineering research and practice in the Asia-Pacific region. Learned bodies representing wind engineers and scientists have been formed in many countries. Among which, the Australian Wind Engineering Society, the Chinese Society for Wind Engineering and Industrial Aerodynamics and the Japan Association of Wind Engineering are kindly sponsoring the present Symposium. We are confident that the Asia-Pacific Symposium has become and will remain an important conference for wind engineers and scientists regionally as well as internationally.

This year, the organizing committee has received over 250 abstracts covering all topics of wind engineering from over 20 countries. Based on the submitted abstracts, about 180 papers were selected and authors were invited to submit six-page manuscripts for inclusion in the Proceedings. The present Proceedings in two volumes contain these contributing papers, together with three keynote papers and three invited papers. A noticeable feature is the large number of papers on bridges, probably due to the importance of infrastructure development in the coastal cities in the Asia-Pacific rim. We would like to take this opportunity to thank the authors of all papers as well as those who have submitted abstracts.

In addition, we would like to thank the precious assistance of members of the Scientific Advisory Board and the Organizing Committee. Special appreciation goes to Professor T.F. Sun and the Chinese Society for Wind Engineering and Industrial Aerodynamics who organized the paper submission in China and the participation of the members of his society. We would also like to thank the Hong Kong Institute of Architects for being an honorary sponsor of this Symposium.

Last but not least, the success of the Symposium also depends on the generous support of various organizations. The donations are largely used to subsidize those participants from the developing countries, and we would like to acknowledge their kindness with our deepest gratitude.

Y.K. Cheung
Chairman
Organizing Committee

SCIENTIFIC ADVISORY BOARD

J.E. Cermak	Colorado State University, U.S.A.
C.M. Cheng	Tamkang University, Taipei, China
Y.K. Cheung	The University of Hong Kong, Hong Kong
A.N.L. Chiu	University of Hawaii at Manoa, U.S.A.
E.C.C. Choi	Nanyang Technological University, Singapore
E.J. Cui	Beijing Institute of Aerodynamics, China
A.G. Davenport	The University of Western Ontario, Canada
A.J. Dutt	National University of Singapore, Singapore
J. Gandemer	Centre Scientifique et Technique du Batiment, France
H.J. Gerhardt	Fachhochschule Aachen, Germany
D.X. He	China Aerodynamics Research and Development Centre, China
M. Ito	Saitama University, Japan
P. Krishna	University of Roorkee, India
B.E. Lee	University of Portsmouth, U.K.
W.H. Melbourne	Monash University, Australia
S. Murakami	University of Tokyo, Japan
R.H. Scanlan	John Hopkins University, U.S.A.
N. Shiraishi	Kyoto University, Japan
T.F. Sun	Peking University, China
G.R. Walker	CSIRO Division of Building, Construction and Engineering, Australia
H.F. Xiang	Tongji University, China

ORGANIZING COMMITTEE

Y.K. Cheung (Chairman)	The University of Hong Kong
B.J. Stubbings (Vice-Chairman)	Mitchell, McFarlene, Bretnall and Partners International Limited
K.M. Lam (Secretary)	The University of Hong Kong
K.M. Cheung	Buildings Department, Hong Kong Government
S.C. Kot	Hong Kong University of Science and Technology
A.K.H. Kwan	The University of Hong Kong
P.K.K. Lee	The University of Hong Kong
A.Y.T. Leung	The University of Hong Kong
J. MacArthur	Ove Arup and Partners Hong Kong Limited
H.K. Ng	Buildings Department, Hong Kong Government
H.T. Poon	Royal Observatory, Hong Kong Government
Y.C. So	Housing Department, Hong Kong Government
P.K. Tse	Mott MacDonald Hong Kong Limited
H.S.H. Wu	Leighton Asia Limited

CONTENTS

VOLUME I

Bridge Analysis

Tall Buildings

Towers and Chimneys

Wind Characteristics

VOLUME II

Bluff Body Aerodynamics and Separation

Roofs and Low Rise

Wind Tunnel Techniques

Wind Breaks, Wind Power and Others

Keynote Papers

.

Progress in physical modeling for wind-engineering

Jack E. Cermak

Department of Civil Engineering
Colorado State University, Fort Collins, Colorado USA
and
Cermak Peterka Petersen, Inc.
Fort Collins, Colorado

Abstract: Physical modeling has and continues to be the primary source of information for wind-engineering applications. The capability of boundary-layer wind tunnels to simulate essential features of the atmospheric boundary layer makes this possible. Recent efforts to simulate special aspects of natural winds by modifications to conventional boundary-layer wind tunnels and new types of flow facilities are described. Several instrumentation developments are presented that extend the types of wind-effect information for dispersion of air pollutants and wind loads on buildings and other structures that can be obtained by physical modeling.

1. Introduction

Applications of physical modeling to wind-engineering continue to advance with progress on several fronts [1,2]. Extended capabilities for simulation of natural wind characteristics and development of instrumentation for acquisition of wind-effect data contribute to enhancement of the scope and precision of physical modeling for both research and design. This paper is focused on progress during the last decade in physical modeling of natural wind - - the atmospheric boundary layer (ABL), atmospheric surface layer (ASL), drainage flows, and tornadoes -- and measurement of wind effects. Developments in these areas of primary relevance to wind pressures and loads on buildings and structures and dispersion of air pollutants are emphasized.

2. Simulation of Natural Winds

The paramount requirement for physical modeling of wind-engineering phenomena is proper simulation of natural wind characteristics. Most of the time wind up to a height of about 500 m over flat surroundings can be represented, in the absence of thermal winds, by a boundary layer such as

Fig. 1.   Planetary boundary layer according to model of Lettau [3].

shown in Fig. 1. For wind-engineering applications the gradient wind U_g is taken to be the maximum mean wind speed of the profile and defines height of the ABL z_g.

Basic criteria for kinematic, dynamic and thermic similarity are derived by inspectional analysis of the equations for conservation of mass, momentum and energy. Geometric similarity is retained in this analysis by uniformly scaling horizontal and vertical lengths. The significant global

3

dimensionless parameters which should be equal for model and prototype to achieve "exact" similarity are the following [1]:

1. Reynolds number: $Re = U_oL_o/\nu_o$
2. Richardson number: $Ri = (\Delta T_o/T_o)(L_og/U_o^2)$
3. Rossby number: $Ro = U_o/(L_o\Omega_o)$
4. Prandtl number: $Pr = \nu_o\rho_oC_{po}/k_o$

Additional boundary conditions which must be similar for "exact" similarity are the following: (1) surface roughness and temperature at ground level, (2) flow structure above the atmospheric boundary layer (ABL) or drainage current, (3) zero pressure gradient in direction of mean flow, (4) sufficient upwind fetch to establish equilibrium of the simulated ABL with surface boundary conditions, and (5) height of an inversion layer, if present.

Since the 1960's boundary-layer wind tunnels of the type shown in Fig. 2 [4,5,6] that can satisfy the foregoing requirements, excepting for Rossby number and Reynolds number equality, have been in use. Because $Ro_m >> Ro_p$ (subscripts m and p indicate model and prototype, respectively) turning of the mean wind vector with height in response to Coriolis acceleration as shown in Fig. 1 is not realized in the model. Although $Re_m << Re_p$, the boundary-layer flows become Reynolds number independent

Fig. 2.   Closed-circuit BLWT, Colorado State University [6].

when $u_*k_s/\nu > 70$ where u_* is the surface shear velocity and k_s is equivalent sand roughness [1]. Documentation of characteristics for boundary layers developed by the wind tunnel of Fig. 2 is available in the literature [7,8,9,10].

Developments in physical modeling of wind that extend or supplement capabilities of the BLWT shown in Fig. 2 are described briefly in the following sub-sections. Various flow facilities of recent design for special wind-engineering problems are noted also. Any omissions by the writer are not intentional and are a result of the writer's failure to identify all possible developments.

2.1 Partial modeling of the ABL -- the ASL

Boundary-layer thicknesses at the turntable in Fig. 2 varies from 0.70 to 1.70 m (depending on surface roughness k_s and wind speed U_g); therefore, for a nominal value of 500 m for z_g, the appropriate length scale is in the range of about 1:700 to 1:300. This range of length scale is very good for modeling wind-effects on high-rise buildings and structures. However, the heights H of low-rise buildings are less than z_s and are submerged in the ASL in which the turbulent fluxes, including shear stress, are sensibly constant. The model of a 10-m high building, for a 1:300 scale,

would be only 33 mm high. The building Reynolds number would be too low (about 7,000 for $U_g = 8$ m/s). Considerations of this nature resulted in efforts to simulate a thick "constant" shear-stress layer with only partial simulation of the entire ABL [11]. This has been accomplished by addition of horizontal vanes at the test-section entrance of the BLWT (Fig. 2) as shown in Fig. 3. Figure 4 reveals a "constant" shear stress up to a height of 0.5 m which, for a nominal ASL depth of 50 m, gives a scaling of 1:100. This scale is much more favorable when modeling wind for studies of low-rise buildings than for scales of 1:300 and smaller.
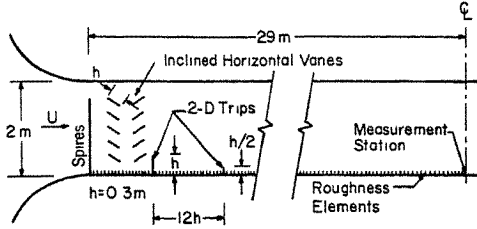
Fig. 3. Test section of BLWT (Fig. 2) with flow-conditioning system for ASL simulation [11].

Fig. 4. Vertical distribution of shear stress with horizontal vanes [11].

The lateral length scale for boundary-layer turbulence in the BLWT is constrained to some degree by the wind-tunnel walls. The system of vertical airfoils shown in Fig. 5 was installed in the BLWT halfway down the test section [11]. Measurements of spectra, autocorrelations and lateral space correlations for the longitudinal turbulence component were made at the turntable location when the amplitude and frequency of the airfoils were varied in a random manner. The lateral integral scale for the longitudinal component was increased from about 0.4 m to 0.6 m. More study of this technique, accompanied by comparisons with atmospheric measurements, is needed for further progress in proper simulation of lateral turbulence characteristics.

2.2 Simulation of convective boundary layers (CBL)

Dispersion of air pollutants in the mixing layer below and elevated inversion over cities is a major concern [12]. Therefore, techniques for physical modeling of convective boundary layers (the mixing layer) have been developed recently [13,14].

Fig. 5. Oscillating airfoil sections to increase lateral length scales.

Elevated inversions are simulated in the wind tunnel shown in Fig. 2 by heated air flowing over the 10-m length of cooled floor followed by flow over a heated length of floor. When large temperature differences must be considered, the inversion persists for only a short distance (1 m or less) because the depth of strong stable stratification is only

5

about 0.1 m at the onset of flow over the heated surface. A cooling system designed to overcome this limitation is shown in Fig. 6 [13]. The arrangement of stacked cooling plates establishes an elevated inversion at an average height of 0.4 m with a local Richardson number of about 2. Temperature profiles at several distances downwind from initiation of heating are shown in Fig. 7. The elevated inversion persists for a distance of about 5.4 m when the surface temperature T_s is maintained at 100°C. With this system a wide variation of meteorological inversion characteristics can be simulated by varying the cooling-plate stacking height, the heated plate temperature, and the temperature of heated air entering the test section. Flows generated in this manner can be used to study a variety of atmospheric dispersion problems, and basic questions on turbulence characteristics for flows with stable and unstable thermal stratification.

A new wind tunnel specifically designed to simulate convective boundary layers has been constructed at the University of Karlsruhe [14]. The wind tunnel has ten channels, as shown in Fig. 8, with independent fans and heaters. The 10-m long working section is 1.5 m high and 1.5 m wide. Maximum operating conditions are as follows: inversion height, 0.5 m; temperature jump, 40°C; temperature gradient, 100°C/m; and surface heat flux, 1.5 kW/m². The minimum wind speed is 0.5 m/s.

Fig. 6. Cooling arrangement for modeling a CBL [13].
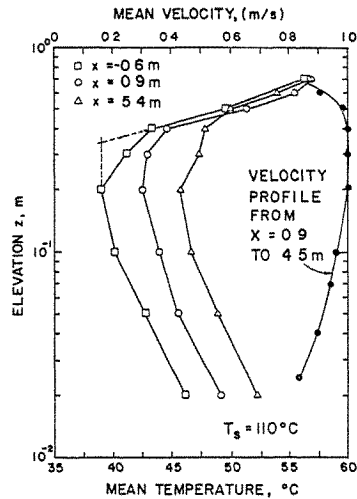
Fig. 7. Mean temperatures and velocity in a CBL [13].

2.3 Simulation of mountain-valley winds

Winds in valleys are induced by synoptic flow over the complex topography and by gravitational effects. The later results in downslope winds during nighttime surface cooling and
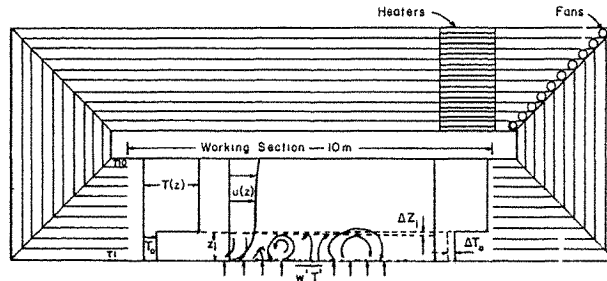
Fig. 8. Stratified BLWT for modeling a CBL, University of Karlsruhe [14].

6

upslope winds during early daylight periods. The synoptic-flow induced winds can and have been studied in BLWTs such as shown in Fig. 2 [10]. Studies of downslope (drainage) winds have resulted in development of special facilities and techniques [15].

Pure natural-convection winds have been modeled by placing a thin aluminum-shell topographic model on a platform in a convection chamber with cooling from below as shown schematically in Fig. 9. A thin aluminum shell model of the topography shown in Fig. 10 was constructed by shaping heavy aluminum foil over a styrofoam model form and placing the aluminum-foil shell on wooden supports over the platform. Cooling of the model to approximately -80°C was accomplished by circulating air (and CO_2) in the space between a bed of solid CO_2 and the model. Vertical profiles of mean velocity and temperature having characteristics shown in Fig. 11 were measured at a set of locations in Coal Creek Valley. It was found that U_m^2 increases linearly with distance from the canyon origin as reported in the literature for full-scale measurements [16]. Exploratory investigations with the cooled shell model placed in a BLWT confirmed that physical modeling of combined natural and forced convection winds is possible.
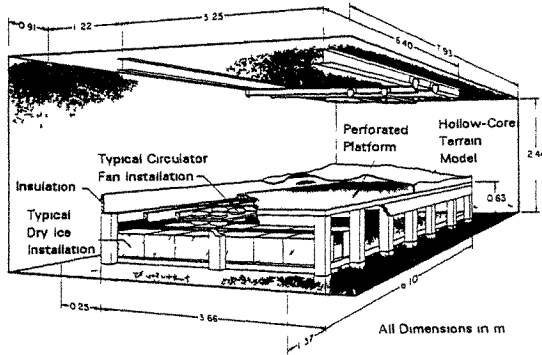
Fig. 9. Natural convection chamber, Colorado State University [15].
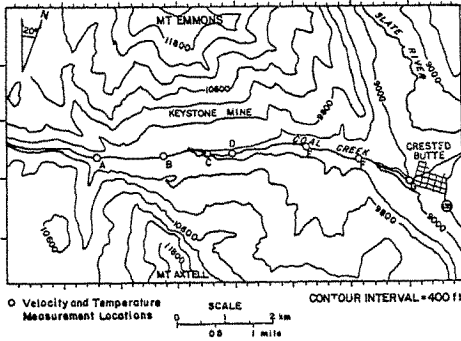
Fig. 10. Topography of Coal Creek Valley, Colorado [15].
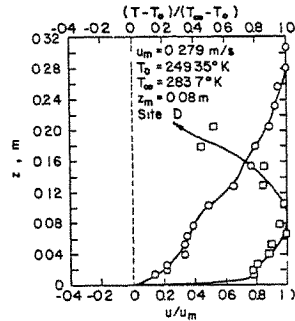
Fig. 11. Mean air temperatures and speeds at Station D, Fig. 10, for 1:1,920 scale model [15].

7

2.4 Progress in other wind simulations

Developments in physical modeling of tornado-like flows, wind over water and wind by flow in water channels are described.

A *"tornado" simulator* comprised of a rotating screen, a ground plane, and entrance contraction of a small wind tunnel is shown in Fig. 12 [17]. In this simulator the vortex is generated with a horizontal axis. Similarity parameters for the flow characteristics are a swirl ratio S, aspect ratio A and a radial Reynolds number Re_r:

$$S = (r_o\Gamma)/(2Qh)$$
$$A = h/r_o$$
$$Re_r = Q/\nu$$

Fig. 12. Schematic view of tornado simulator [17].

where Γ = circulation and Q = volume flow rate per unit depth [18]. A facility of this type is useful for exploring vortex-induced pressures on building models mounted on the ground plane.

Conventional *closed-circuit BLWTs* are designed to have the flow-return section serve as an expanding diffuser, as shown in Fig. 2, to minimize energy losses. The design of a closed-circuit BLWT at the University of Western Ontario (Fig. 13) incorporates a water tank into a constant cross-section flow-return section [19]. This adds the capability for physical modeling of wind characteristics over water and forces on structures caused by wind and waves. When the water tank is not needed it is covered by a floor which is lowered from the roof level. In this configuration, flow over complex topography and wind loads on long-span structures can be modeled.
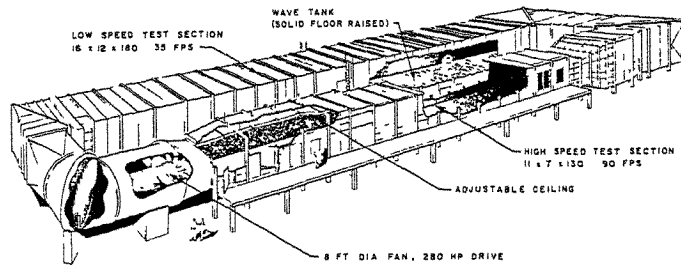
Fig. 13. Combined wind-ground and wind-water BLWT, University of Western Ontario [19].

Research at the Center for Applied Stochastic Research, Florida Atlantic University, has demonstrated capabilities of a *water channel* (Fig. 14) for physical modeling of wind-structure interactions [20]. The test section is 0.6 m wide, 0.4 m deep and 8 m long with an adjustable mean flow speed from 0 to slightly in excess of 0.5 m/s. Flow is generated by a horizontally mounted propeller that moves water from a lower chamber into an upper chamber and on into the test section. The facility has been used to measure torsional flutter derivatives for model bridge sections and flow

(Coanda effects and pulsating jet effect) for two parallel circular cylinders. Modeling with water has two advantages compared to air -- excellent flow visualization with dyes and hydrogen bubbles and a Reynolds number 15 times larger (if flow speed and length scale are the same as for air). Disadvantages arise from difficulties in modeling the ABL and, for dynamic models, preserving equality of the fluid/model mass density ratio.
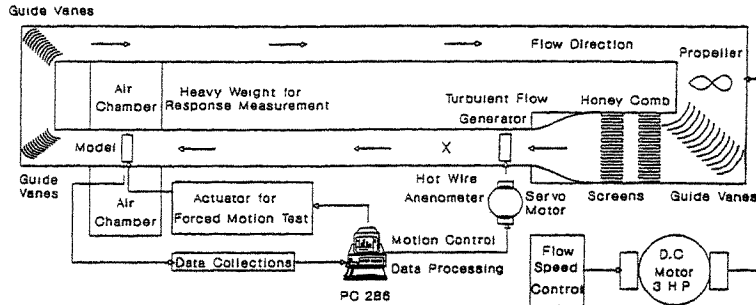
Fig. 14. Water channel, Florida Atlantic University [20].

3. Progress in Instrumentation Development

Measurement of fluctuating quantities in order to determine statistical properties of various wind effects is an ever growing need. Extreme peak concentration fluctuations of toxic and flammable substances are needed for risk and safety analyses. Peak wind loads and pressures are required for design of structural and curtainwall elements as well as analysis of their fatigue life. Several instrumentation developments that have significantly extended information that can be obtained by physical modeling are described.

3.1. Measurements of concentration fluctuations

An infrared-carbon dioxide (IR-CO_2) instrumentation system designed to measure instantaneous integrated concentrations (IC) over a line is illustrated in Fig. 15 [21]. Radiation from a blackbody IR source is pulsed by a light chopper and then transmitted through a 6.35 mm diameter sapphire window into the diffusing CO_2 cloud. The pulsed beam, attenuated according to instantaneous IC of CO_2 along the path line, is sensed by a liquid-nitrogen cooled indium-antimonide photovoltaic IR detector after passing through a narrow-band (4.257 $\pm$ 0.04 μm) optical filter. Following amplification of the AC signal, the signal is fed to a lock-in amplifier, tuned to the chopper frequency, to obtain a DC signal proportional to the transmitted IR beam intensity. Frequency response of the system can be as high as 1000 Hz.

Figure 16 show dimensionless instantaneous line-integrated concentrations $IC^* = (\overline{IC^*} + ic'^*)$ over an interval of dimensionless time T^* measured in the BLWT (Fig. 2) where $IC^* = (IC)$ UM/Q and $T^* = tU/M$. For this example U = 3 m/s, M = 7.82 cm, x_o = 3.39 m, and $y/\sigma = 1.61$ (y is the lateral coordinate and σ the standard deviation from axis of mean plume). Data of this type can be processed to obtain mean values of IC^* ($\overline{IC^*}$), root-mean-square (rms) values of the fluctuations $(ic'^*)_{rms}$, probability density distributions, intermittency, spectra, and other statistics of IC^*. This information can be applied to studies of visibility fluctuations and dosage probabilities for a receptor moving through a concentration field.

9
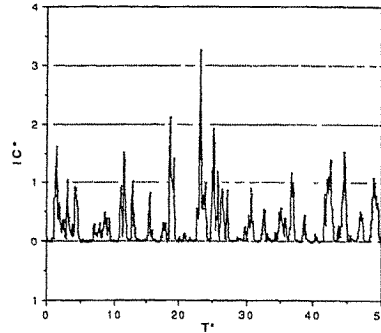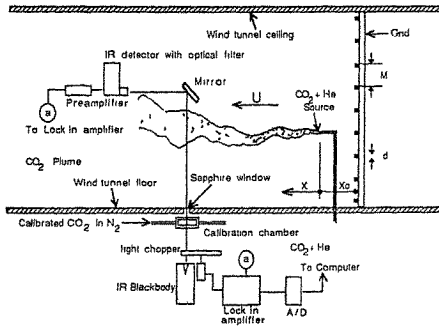
Fig. 15. Schematic of the IR-CO₂ system [21].

Fig. 16. Recorded IC* fluctuations: $x/M = 20$, $y/\sigma = 1.61$, $\overline{IC^*} = 0.30$, $(ic'^*)_{rms} = 0.42$ [21].

3.2. Measurement of wind-load fluctuations

Until about 10 years ago fluctuating wind loads on tall buildings were obtained primarily by physical modeling using aeroelastic models [22]. Aeroelastic modeling has the disadvantage that design changes of mass distribution and/or stiffness requires model modifications and additional data acquisition. During the last decade the high-frequency base balance (H-FBB) test [23,24] that replaces the need for an aeroelastic test for many buildings has been developed and used extensively.

A typical five-component H-FBB is illustrated in Fig. 17. When a low-mass model is mounted on the balance stem, natural frequencies for the three base moments are in excess of 100 Hz. The balance is very stiff; therefore, the model is rigid (static) and does not sway as in an aeroelastic test. Power spectra, peak values and rms values of the fluctuating moments and forces as well as mean moments and forces an measured directly. The power spectra of base moments for an air-traffic control tower where vortex shedding produces the controlling cross-wind loading are presented in Fig. 18 [23]. The measured aerodynamic admittances (power spectra) of moment and force components, for a particular building shape and wind direction, are then combined with the mechanical admittance to calculate dynamic responses. The advantage of this method is that the structural engineer may vary the mechanical admittance by changes in stiffness, mass distribution and damping to achieve an optimum design without additional wind-tunnel tests.

The H-FBB test does not include the effects of aerodynamic damping as does the aeroelastic test. Therefore, predictions of the H-FBB test may be unconservative. Progress in development of a criterion to determine when the H-FBB test is adequate, or that an aeroelastic test should be conducted, has been made by performing both tests on the same building (square cross-section with height-to-width ratio of eight) in the same flow [24]. Comparison of results is made by means of an aeroelastic magnification factor (AMF) -- the ratio of rms cross-wind base moment from the aeroelastic test to that for the H-FBB test. Figure 19 gives values of AMF as a function of reduced velocity for a damping ratio of 0.012. The AMF values in Fig. 19 are in the range 0.9 to 1.1 for values of reduced velocity less than the value for which vortex excitation occurs. Therefore, a H-FBB test will predict loads and dynamic responses within ±10% of aeroelastic test results when the reduced velocity for expected wind speeds does not exceed a value of about 10. This criterion is

10

Fig. 18. Power spectral densities of base moments [23].
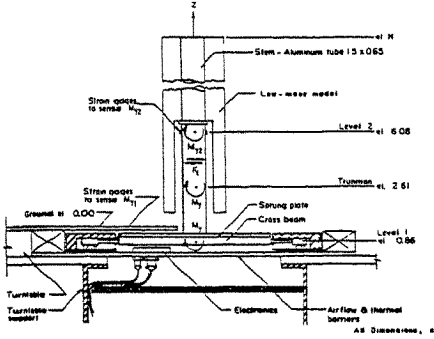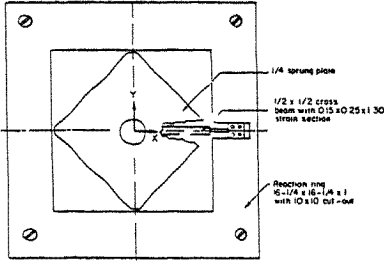
Fig. 17. High-frequency base balance [23].
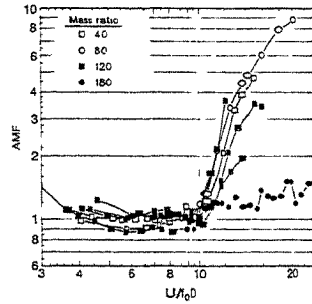
Fig. 19. Aeroelastic magnification factor: damping ratio = 0.012 [24].

strictly valid for the building of uniform cross-section with proportions 1:1:8 and the damping ratio 0.012; however, it provides useful guidance for determining the type of test required.

3.3. High-speed pressure scanning systems

During the last five years economical high-speed, high-capacity computer components have become available and have made design of high-speed pressure scanning systems possible [25]. Sampling rates now vary from about 200,000 to 500,000 samples per second and are increasing at a rapid rate. This enables all pressures at many locations, say 500, to be sampled from 400 to 1000 times a second. This capability permits peak pressure distributions for curtainwall design to be obtained very rapidly. During this process channels can be assigned to give pressure differences between window locations or other possible facade openings for determination of internal pressures.

The high-speed scanning of pressures at a set of several hundred points gives for all practical purposes the instantaneous pressures at all points of the set. By weighting (electronically) each pressure point according to its representative area and influence function, instantaneous forces and moments and their fluctuation statistics can be measured. Particularly useful applications are determination of wind loads on modal areas of large span roofs, on free-standing walls, on canopies, and on various structural components. These high-speed scanning systems, now available in the major wind-engineering laboratories, greatly extend information that can be derived from physical modeling for structural engineers and architects.

11

4. Concluding Remarks

Significant advancements in physical modeling of the ABL and ASL and measurement of wind effects on concentration, pressure and load fluctuations have been achieved during the last decade. These advancements have increased the scope and reliability of wind-effect data available for design and evaluation. Further progress is needed to advance modeling of severe winds associated with hurricanes (typhoons or cyclones), downslope winds, downbursts and tornadoes and to develop efficient data processing systems that are compatible with the high-speed pressure scanning systems.

References

1. J. E. Cermak, "Applications of Fluid Mechanics to Wind Engineering -- A Freeman Scholar Lecture," Transactions of the ASME, J. of Fluid Engineering, 97(Ser 1, No. 1) (1975) 9-38.
2. J. E. Cermak, "Advances in Physical Modeling for Wind Engineering," J. of Engineering Mechanics, ASCE, 113(No. 5) (1987) 737-756.
3. H. H. Lettau, "Theoretical Wind Spirals in the Boundary Layer of a Baratropic Atmosphere," Beitr. Phys. Atmos., 35 (1962) 195-212.
4. J. E. Cermak, "Wind Tunnel for the Study of Turbulence in the Atmospheric Surface Layer," Fluid Dynamics and Diffusion Laboratory, Technical Report, CER58JEC42, Colorado State University, Fort Collins, CO (1958) 31 pp.
5. E. J. Plate and J. E. Cermak, "Micrometeorological Wind Tunnel Facility," Fluid Dynamics and Diffusion Laboratory, Technical Report, CER63EJP-JEC9, Colorado State University, Fort Collins, CO, (1963) 65 pp.
6. J. E. Cermak, "Wind Tunnel Design for Physical Modeling of Atmospheric Boundary Layers," J. of Engineering Mechanics, ASCE, 107(No. 3) (1981) 523-642.
7. H. Chuang and J. E. Cermak, "Similarity of Thermally Stratified Shear Flows in the Laboratory and Atmosphere," Physics of Fluids Supplement, 10 (Part II, No. 9) (1966) S255-S258.
8. S. P. S. Arya and E. J. Plate, "Modeling of the Stably Stratified Atmospheric Boundary Layer, J. of the Atmospheric Sciences, 26 (1969) 656-665.
9. J. E. Cermak, "Physical Modeling of the Atmospheric Boundary Layer (ABL) in Long Boundary-Layer Wind Tunnels (BLWT)," Proc. of the International Workshop on Wind Tunnel Modeling Criteria and Techniques in Civil Engineering Applications, Gaithersburg, MD, Cambridge University Press, (1982) 97-125.
10. J. E. Cermak, "Physical Modeling of Flow and Dispersion over Complex Terrain," Boundary-Layer Met., 30 (1984) 261-292.
11. J. E. Cermak, L. S. Cochran and R. D. Leffler, "Wind-tunnel Modeling of the Atmospheric Surface Layer," Proc. Third Asia-Pacific Symposium on Wind Engineering, Hong Kong, Dec. (1993).
12. J. E. Cermak, "Physical Modeling of Thermal Effects on Flow and Dispersion over Urban Areas," Proc. on Urban and Thermal Environment, Tohwa University, Fukuoka, Japan, September (1992) (to be published in Atmospheric Environment, Part B: Urban Environment).
13. M. Poreh and J. E. Cermak, "Study of Neutrally Buoyant Plumes in a Convective Boundary Layer with Mean Velocity and Shear," Preprints Seventh Symposium on Turbulence and Diffusion, American Meteorological Society, Boulder, CO, (1985) 119-122.
14. M. Rau and E. J. Plate, "Wind Tunnel Modeling of Convective Boundary Layers," Proc. of NATO Advanced Study Institute on Wind Climate and Wind Engineering in Cities, Karlsruhe, Germany, July (1993) (to be published by Kluwer Academic Publishers in 1994).

15. J. E. Cermak and R. L. Petersen, "Physical Modeling of Downslope Mountain Wind and Atmospheric Dispersion," Proc. of the Fourth U. S. National Conf. on Wind Engineering Research, University of Washington, Seattle, WA, July (1981) 371-381.
16. B. Davidson and P. Krishna Rao, "Experimental Studies of the Valley-Plain Wind," Air and Water Pollution, 7(No. 9/10) (1963) 907-923.
17. B. Bienkiewicz and P. Dudhia, "Physical Modeling of Tornado-like Flow and Tornado Effects on Building Loading," Proc. Seventh U. S. National Conf. on Wind Engineering, University of California, Los Angeles, June (1993) 95-104.
18. C. R. Church, J. T. Snow, G. L. Baker and E. M. Agee, "Characteristics of Tornado-like Vortices as a Function of Swirl Ratio: A Laboratory Investigation," J. Atmospheric Science, 36 (1979) 1755-1776.
19. A. G. Davenport, N. Isyumov, J. P. C. King, M. Novak, D. Surry and B. J. Vickery, "BLWT II: The Design and Performance of a New Boundary Layer Wind Tunnel," Proc. of the Fifth U. S. National Conf. on Wind Engineering, Texas Tech University, Lubbock, TX, Nov. (1985) 2A35-2A39.
20. T. C. Su and Q. C. Li, "Water Channel Modeling for Wind Engineering Applications," Proc. Seventh U.S. National Conference on Wind Engineering, University of California, Los Angeles, June (1993) 773-782.
21. M. Poreh and J. E. Cermak, "Fluctuations of Line Integrated Concentrations Across a CO_2 Plume," in Progress in Wind Engineering, Proc. of the 8th International Conf. on Wind Engineering, University of Western Ontario, Elsevier Science Publishers (A. G. Davenport, et al., eds.), also J. of Wind Engineering and Industrial Aerodynamics, 44 (1992) 2745-2755.
22. R. E. Whitbread, "Model Simulation of Wind Effects on Structures," Proc. of Conf. on Wind Effects on Buildings and Structures, Vol. 1, National Physical Laboratory, Teddington, England, June (1963) 284-301.
23. Cermak/Peterka and Associates, Inc., "Wind-Tunnel Tests for Air Traffic Control Tower," Technical Report C/PA 85-0280, Fort Collins, CO, (1985).
24. D. W. Boggs, "Validation of the Aerodynamics Model Method," in Progress in Wind Engineering, Proc. of the 8th International Conf. on Wind Engineering, University of Western Ontario, Elsevier Science Publishers (A. G. Davenport, et al., eds.), also J. of Wind Engineering and Industrial Aerodynamics, 42 (1992) 1011-1022.
25. A. Steckley, S. L. Gamble, M. Accardo, P. A. Irwin and G. D. Schuyler, "The Synchronous Pressure Acquisition Network (SPAN)," Proc. ASCE Structures Congress '91, Indianapolis, IN, ASCE, New York, NY, (1991) 556-559.

HOW CAN WE SIMPLIFY AND GENERALIZE WIND LOADS?

By A. G. Davenport

Boundary Layer Wind Tunnel Laboratory
The University of Western Ontario
Faculty of Engineering Science
London, Ontario, Canada   N6A 5B9

Abstract: The complexity of wind loading arises from their variations in space and time   The paper discusses three key spatial functions which control the magnitude of responses   the influence lines, the mode shapes and pressure distributions   The last can be efficiently described in terms of orthonormal expansions   The paper describes how the different time dependent loadings - the mean the background and resonant responses - are related to the spatial functions

These tools provide a promising route for generalization and simplification of wind loading

1.0 Introduction

Notwithstanding its enormous fascination, wind loading is in fact a parasitic effect, and mostly an obstacle in the way of designing structures for their primary intended use   Without wind, structures - particularly large ones - would probably be a lot easier to design and cheaper

With this in mind, something we should try to do is to make sure that wind loading wherever possible is <u>simple</u> to use (so that errors are reduced) and <u>general</u> (so that there is a universal and consistent coverage). The aim of this paper is to describe several tools which can systematically lead to simplification and generalization

2.0 Orthogonal and Orthonormal Functions

Let us first consider the use of orthogonal and orthonormal functions   By way of an example, let us first consider the description of the mean wind speed with height on a tall mast (McNamara -1975). Measurements of 10 minute average speed made on a 400m mast over a period of several weeks are shown in Figure 1a. For clarity, only the 100 ft and 1200 ft. measurements are shown, in fact the measurements were made at ten levels   Normally we assume that the average wind speed follow a power law or logarithmic velocity profile, this may be a satisfactory assumption for the lowest layers, but in considering a very tall mast or building this may be modified by thermal stability or storm systems passing by. How do we describe a wind speed profile which is constantly varying without getting overwhelmed by numbers and details?

One approach is the use of orthonormal or orthogonal functions - a rather indigestible name for a very useful idea. We proceed as follows: first we form the covariance matrix between the wind speed at every height with the wind speed at every other height, as shown in Figure 1b (The covariance is the average sum of the cross product of the windspeeds at each time step). The rows and columns correspond to the ten heights on the masts.

15

If we invert this covariance matrix - as we do in finding modes of vibration for example - we end up with the eigen functions like mode shapes), which are in fact orthogonal to one another If their mean square amplitude is scaled to unity they are known as "orthonormal shape functions or expansions - ONE's" The first four of these functions are shown in Figure 1c

These functions have the useful property that we can express the wind speed at time t and height z as

$$V(z, t) = a_1(t) \cdot \phi_1(z) + a_2(t) \cdot \phi_2(z) + \tag{1}$$

The great advantage of the orthogonality is that the statistics of the functions are in "the mean square sense" independent of one another This is exactly true if the process follows a normal distribution Knowing these functions, the original record can be reconstructed in terms of the shape functions The amplitudes at each time step are found by multiplying through by each of the shape functions in turn and integrating over the height of the mast

$$a_i(t) = \int_0^1 V(z, t) \cdot \phi_i(z) \cdot dz \tag{2}$$

With a finite number of velocity readings we replace the integral with a summation over the ten instrumented heights This gives us a continuous series of amplitudes $a_i(t)$ which when multiplied by the shape functions reconstruct the complete velocity history This is already a more compact, simpler representation. What makes it even simpler is that the higher order shape functions have progressively smaller amplitudes and after two or three terms they are no longer significant The statistics of the amplitudes of the first two shape functions are given in Figure 1d This indicates that the lowest orthonormal function for wind speed has a Rayleigh distribution (as might be expected), and the second (and higher) orthonormal functions are Gaussian The relative amplitudes indicate the rapid decrease in importance The first term captures roughly 95% of the "energy" of the fluctuations

These orthonormal functions in fact have the property that the first extracts the maximum amount of "energy" in the original velocity record The second is the maximum energy in the remainder and so on. There are other orthonormal functions but these are the most "efficient" in extracting energy.

These descriptions can also be applied to the pressure fields One example of this is in the description of peak local pressure coefficients on an ensemble (population) of tall buildings - about 100 building facades overall. Here the covariance matrix of the pressure coefficients is assembled over a grid of points projected onto each facade and the orthonormal functions defining the pressure coefficients extracted. The lowest order terms then yield the approximations to the pressure field

A further application is to describing the instantaneous pressure patterns over a structure or portions of it. This has been applied by Ho, Surry and Davenport to roof pressures on low buildings, (see Figure 2), by King on suspension bridge design, by Vickery to the roof of a large stadium and Inculet to building facades.

16

This latter is ideally suited to the solid-state pressure sensing systems involving several hundred simultaneous measurements of pressure This system replaces previous techniques using pneumatic averaging and porous surfaces for determining spatial effects of dynamic pressure fluctuations used by Surry, Stathopoulos and Davenport, by Rosales and Sato, and Davenport

3.0 Influence Functions

The second tool I would like to refer to is the use of influence functions These functions are well known but in practice are only used in specific applications They deserve wider usage since they provide a direct link between the load pattern and the response A variety of influence lines are shown in Figures 3a, b and c Several of these have sign reversals which strongly suggest the susceptibility to "patch" loading due to gusts (The following discussion indicates how the magnitude of these unbalanced loads can be determined)

The structural engineer is interested in a wide variety of structural responses ranging from member stress to bending moments and shears, as well as deflections We will designate all of these responses as r They can be related to the wind force through the appropriate influence line or surface denoted $i_r(z)$, defining the magnitude of the response r due to a wind load at point z Referring to Figure 3, the mean response, $\bar{r}$, can then be written

$$\bar{r} = q \int_A \left\{ \bar{C}_p \cdot i_r(z) \right\} dA \qquad (3)$$

In the latter A represents the reference area over which the pressures act, and z is a point in it. The integral reflects the interaction of the force distribution with the influence function for the response This quite general, straight-forward procedure for finding the mean response using the notion of influence lines is also useful for finding the associated dynamic responses

4.0 Dynamic Response and Mode Shapes

The third tool are mode shapes of vibration These are indicated for some of the structures in Figure 3 Some structures such as guyed towers have closely spaced complex modes The inertia loads on the structures are proportional to $\varpi_j^2 \cdot m(z) \cdot \mu_j(z)$ where ϖ_j^2 is the jth circular natural frequency, $m(z)$ the mass and $\mu_j(z)$ the jth mode shape Thus the "convolution" of the mode shape and the influence function determines how much energy feeds into the mode response.

Basically there are three sources of aerodynamic excitation causing dynamic response

- forces induced by turbulent fluctuations in the oncoming flow causing both background and resonant responses in the along-wind and cross-wind directions,

- forces induced by vortices shed in the wake of the structure, these affect primarily the resonant responses and occur primarily in the cross-wind direction;

- forces induced by motion of the structure, the most significant of these are aerodynamic damping forces which control the resonant response amplitude These can add to or subtract from the available structural damping Negative aerodynamic damping is primarily associated

17

with the cross-wind motion and can cause large amplitude oscillation and in the extreme case lead to aerodynamic instability.

The movements of the structure recorded in Figure 4 are influenced by all three sources of excitation. The fluctuations consists of both an irregular, slowly varying component, termed here the "background response", and an oscillatory component, with a well defined frequency (or frequencies) termed the "resonant response", and occurring in bursts of several cycles. The mean response is predominantly in the along-wind direction, but the fluctuating responses occur both along-wind and cross-wind. The large cross-wind oscillations are of critical design importance both from the viewpoint of excessive motion as well as fatigue.

The peak response, $\hat{r}$, can be represented in the form

$$\hat{r} = \bar{r} + \hat{g} \cdot \tilde{r} \tag{4}$$

in which $\bar{r}$ is the mean (time average) response, $\tilde{r}$ is the rms of the fluctuating response and $\hat{g}$ is a statistical peak factor, generally in the range 3 to 4.

The manner in which the energy in the fluctuating response of Figure 4a is distributed with frequency is displayed by the spectrum shown in Figure 4b. The concentration of energy of the r resonant response in the several resonant peaks is in contrast to that of the background response which is spread over a broad frequency range below the resonant peaks. The areas of the spectrum are proportional to the mean square of the response components in the frequency range and the overall mean square fluctuating response, $\tilde{r}^2$, is equal to their sum. Hence

$$\tilde{r} = \sqrt{\tilde{r}_B^2 + \sum_j \tilde{r}_{R_j}^2} \tag{5}$$

Here $\tilde{r}_B$ denotes the rms background response and $\tilde{r}_{R_j}$ the rms of the resonant response peak in the jth mode of vibration.

In design our final objective would be to define the response $\bar{r}, \tilde{r}$ in terms of the aerodynamic forces. The mean responses have already been defined by equation (3).

There are generally speaking three main approaches available to the structural engineer to evaluate the dynamic response. All involve wind tunnel and mathematical models and differ only in where the division is made. The approaches are:

1) Aeroelastic modelling: in this all of the significant dynamic and aerodynamic properties of the natural wind and the structure are modelled. The response of the full scale structure is directly inferred from measurements of the model.

2) Force measurements: In this direct measurements of the steady and dynamic forces are measured on rigid models in a correctly scaled flow. A mathematical model of the structure is used to infer the responses.

3) Analytical model: in this the dynamic response are inferred from general information on the turbulence properties and elementary aerodynamic characteristics.

The first of these approaches requires an understanding of the scaling laws (relating to mass, length and time) but only a rough understanding of the precise aerodynamic mechanism. Both the latter approaches require some understanding of the causes of aerodynamic excitation.

5.0 Background Response

The background response at frequencies below the natural frequency are essentially quasi-static and the structure's response is unaffected by its dynamic behaviour. If the fluctuating component of force at position z is $F'(z)$ the mean square background response can be written

$$\bar{r}_B^2 = \iint_A \overline{p'(z_1) \cdot p'(z_1)} \cdot i_r(z_1) \cdot i_r(z_2) \cdot dA_1 \, dA_2 \tag{6}$$

If we express the rms force at z in the coefficient form as $p(z) = q \cdot C_p(z)$ and if $R(z, z + \Delta z)$ is the correlation coefficient of the forces at position z and $z + \Delta z$ then we can write

$$\bar{r}_B^2 = q^2 \iint_A R(z, z + \Delta z)\{C_p \cdot i_r(z)\}\{C_p \cdot i_r(z + \Delta z)\} \, dA(z) \cdot dA(z + \Delta z) \tag{7}$$

With slender structures useful simplifications can be made. For example it is often reasonable with drag forces to "scale" the force coefficients by $C_p \approx 2 I_u \bar{C}_p$ and to treat the cross correlation as a function of a turbulence scale λ. We then can write

$$\bar{r}_B = q\{2 I_u\}\left[J_r\left(\frac{L}{\lambda}\right) \right]^{\frac{1}{2}} \int_A \{\bar{C}_p i_r(z)\} dA \tag{8}$$

$$= \bar{r}\{2 I_u\}\left[J_r\left(\frac{L}{\lambda}\right) \right]^{\frac{1}{2}} \tag{9}$$

Here $J(L/\lambda)$ is a "joint acceptance factor" and depends on the relative size of the "span" to the "scale of turbulence" in the spanwise direction. It is an important function and its connection to the spatial correlation of turbulence is illustrated in Figure 5. As is indicated the span refers roughly to the length of structure with the deformation of similar sign. The scale of turbulence across the wind is roughly of the order of 50-60m. The magnitude of the joint acceptance function also depends on whether the response is symmetrical or anti-symmetrical. The difference lies at values when the "span" is small compared to the turbulence scale $(L/\lambda < 1)$. When the deflections are anti-symmetrical the gust action on the two span cancels out the response is small. When the turbulence scale is less and approaches the span length there is an opportunity for the gust to envelope one span of the structure and not the other. This produces the maximum response. When the span is larger than the scale the disorganization again reduces the response. When the response has the same sign throughout the scale of turbulence is large compared to the span, the response (λ/L) reaches its full value. For structures which are broad as well as high (high aspect ratio) the joint acceptance falls of more closely as $(\lambda/L)^2$.

19

The background response in the cross-wind direction is generally less than half the response along-wind

Values of the joint acceptance for structures such as guyed towers and chimneys can be calculated quite accurately and account for the patch loading effects needed on these structures

6.0 Resonant Response to Turbulence and Vortex Shedding

Both turbulence in the oncoming flow as well as vortex shedding in the wake can cause significant resonant response The latter can be particularly important for lighter structures for which the aerodynamic damping can be large and negative

The general expression for the resonant response parallels certain features of the background response

$$\widetilde{r}_{Rj} = \sqrt{\frac{\pi f_j^* S_{GFj}(f_j^*)}{4\ (\zeta_s + \zeta_{aj})}} \frac{\int_A \{\phi_m\, \mu_j\, I_r(z)\} dz}{\int_A \{\phi_m\, \mu_j^2(z)\} dz} \tag{10}$$

In this $f_j^* S_{GF}(f_j^*)$ represents the spectrum of the generalized force of the jth mode of the structure at the jth natural frequency f_j ζ_s and ζ_a are the structural and aerodynamic critical damping factors, the latter is explained below   The distribution of mass is defined by $m(z) = \phi_m(z)\, m_o$

The spectrum of generalized force at the natural frequency can usually be estimated on the correlation (λ_f) at the resonant frequency is small compared to the height H or span L The result for slender structures then takes on the form

$$\sqrt{f_j^* S_{GF}(f_j^*)} = [\ J\!\left(\tfrac{L}{\lambda_f}\right) \int_A f_j^* S_F(f_j^*)\, \mu^2(z)\, dA]^{\frac{1}{2}} \tag{11}$$

Here $\{f_j\, S_F(f_j)/\widetilde{F}^2\}$ represents the spectrum of force - a measure of the concentration of the excitation - at the natural frequency

The general form of the spectra for the turbulence excitation is shown in Figure 6   This shows that the intensity of the spectrum is greater for structures operating at lower reduced frequencies $(f_j\, L/U)$. This implies an increase in the spectrum at increasing windspeed   When the increase in the joint acceptance with windspeed is taken into account (increase in $\{\lambda_f/L\}$ the excitation at the natural frequency, $\{f_j^* S_{GF}(f_j^*)\}^{\frac{1}{2}}$ tends to increase with the reduced windspeed $U^* = U/(f_j\, H)$ raised to some power β where theoretically $5/6 < \beta < 4\,3$ depending largely on aspect ratio   The cross-wind resonant response to turbulence is generally less than half the longitudinal.

The wakes behind buildings, bridges, chimneys and other structures contain vortices shed at regular intervals   These produce fluctuations concentrated over a fairly narrow range of

20

frequencies with a centre frequency f_c related through the diameter, D (or B), and windspeed, U, to a characteristic Strouhal number $S = f_c D/U$

7.0 Aerodynamic Damping

The aerodynamic damping ζ_a generally takes on the form

$$\zeta_a = \left(\frac{\rho_{air}}{\rho_{str}}\right) C_a \ (U^*) \tag{12}$$

where C_a is a function of the reduce velocity $U^* = U/(f D)$ If ζ_a is small or positive its role is simply to augment the available structural damping, if negative it reduces the available damping and can lead to instability if it is less than the structural damping Details are not described but relative magnitudes of aerodynamic drag damping are given in Table 1 below

For vertical structures there are significant modifying influences by vertical variations in the mean velocity, the cross section and the turbulence intensity. Changes in mean wind speed and diameter frequency run counter to one another - as in tapered chimneys. This diffuses the peak excitation over a range of frequencies, lowers the spectral amplitude at any given frequency and it also reduces the effective (negative) aerodynamic damping averaged over the height of the structure

TABLE 1

Aerodynamic Drag Damping for Typical Structures (U = 100 ft/sec)

Structure	(ρ_{air}/ρ_{str})	f_o Hz	B	U*	$(\rho_{air}/\rho_{str})U^*$	$\lvert\zeta_a\rvert$ for $\lvert C_a\rvert=1$
Tall building	1/100	0 2	1000	5	0 05	1%
Long span bridge	1/20	0 2	100	5	0 25	5%
Transmission line cable	1/3000	0 2	0 1	5000	1 7	30%
Air supported roof	4	0 2	100	5	20	>100%

8.0 Conclusions

The paper has discussed some powerful tools which enable the wind loading to be defined in general terms and where necessary simplifed Three kinds of shape function can be of paramount importance: the influence functions relating the responses to the load distribution, the mode shapes describing the distribution of inertia loading and finally, the description of the loading patterns. The last are most efficiently described in terms of orthogonal functions Although unfamiliar they represent a promising avenue for systematically simplifying and generalizing wind pressures

In considering the other side of the loading - the time dependencies the paper outlines how the mean, background and resonant responses can be expressed in terms of these shape functions

21
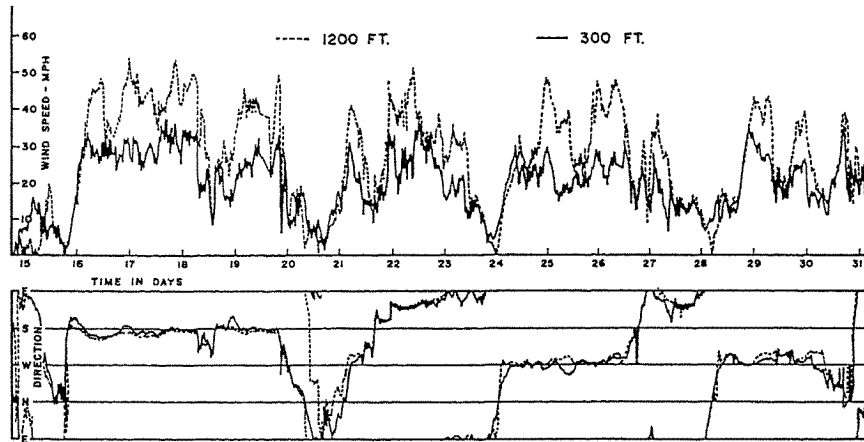
FIGURE 1A   RECORD OF 10 MIN. AVERAGE WIND SPEEDS AND DIRECTIONS -CEDAR HILL

COVARIANCE MATRIX, R(z_m,z_j) FOR PROFILES OF WIND SPEED

126.0	132.8	163.3	201.4	222.3	230.7	242.9	241.1	249.4	246.8
132.8	159.7	196.6	243.3	270.2	280.2	294.8	292.4	302.3	299.1
163.3	196.6	252.1	309.9	347.2	359.8	378.0	374.6	387.0	382.5
201.4	243.3	309.9	410.0	444.2	460.4	483.4	478.8	494.5	488.8
222.3	270.2	347.2	444.2	522.1	541.1	568.5	562.9	581.5	574.4
230.7	280.2	359.8	460.4	541.1	565.9	595.2	590.0	609.7	602.7
242.9	294.8	378.0	483.4	568.5	595.2	632.7	625.1	647.1	640.1
241.1	292.4	374.6	478.8	562.9	590.0	625.1	626.6	645.7	639.0
249.4	302.3	387.0	494.5	581.5	609.7	647.1	645.7	676.2	665.0
246.8	299.1	382.5	488.8	574.4	602.7	640.1	639.0	665.0	660.8

FIGURE 1B   COVARIANCE MATRIX FOR PROFILES OF WIND SPEED (UNITS-MPH^2)
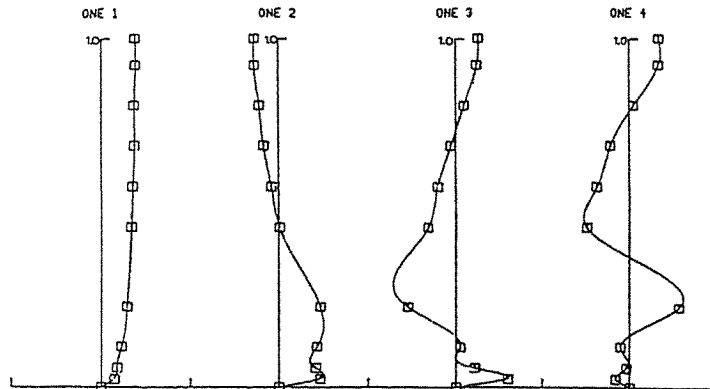
FIGURE 1C   ORTHONORMAL EXPANSIONS FOR WIND SPEED

22
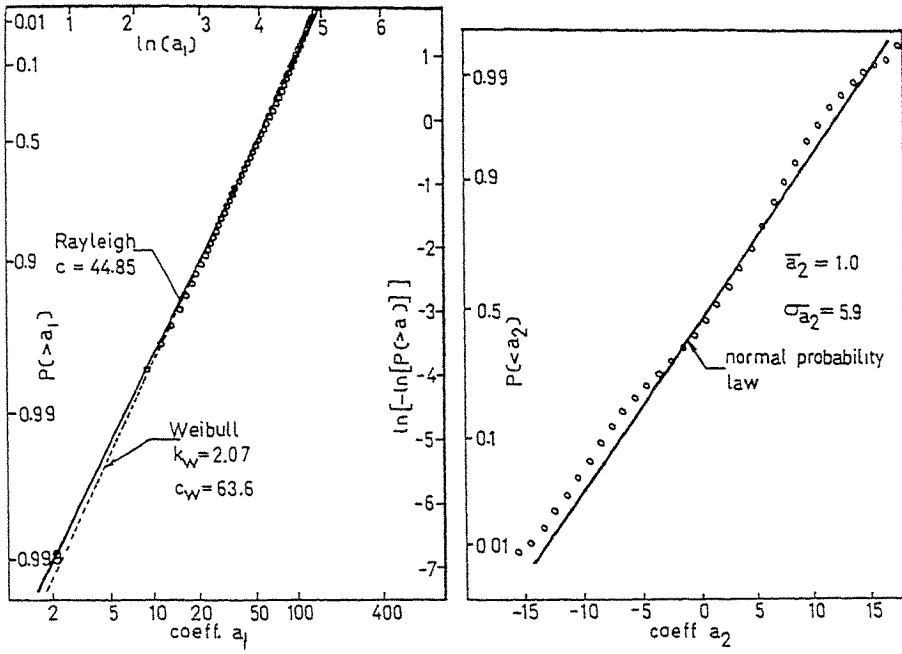
FIGURE 1D PROBABILITY DISTRIBUTION OF WINDSPEED AMPLITUDE OF
FIRST TWO ORTHONORMAL FUNCTIONS
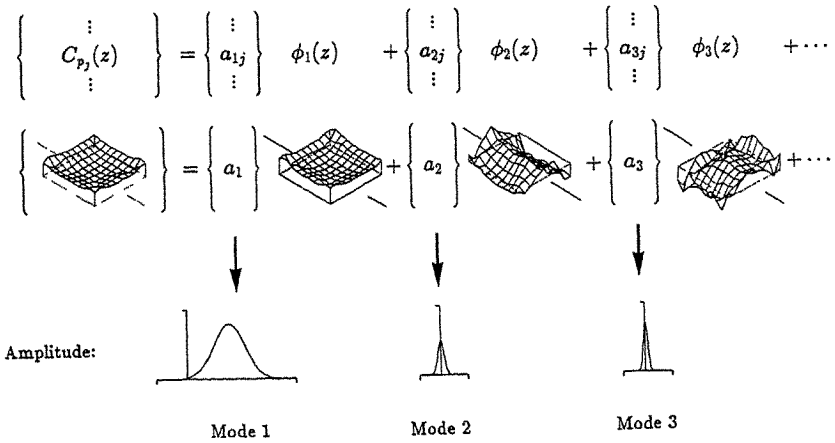
FIGURE 2 ORTHONORMAL SHAPE FUNCTIONS FOR PRESSURE OF A ROOF
OF A LOW BUILDING

23
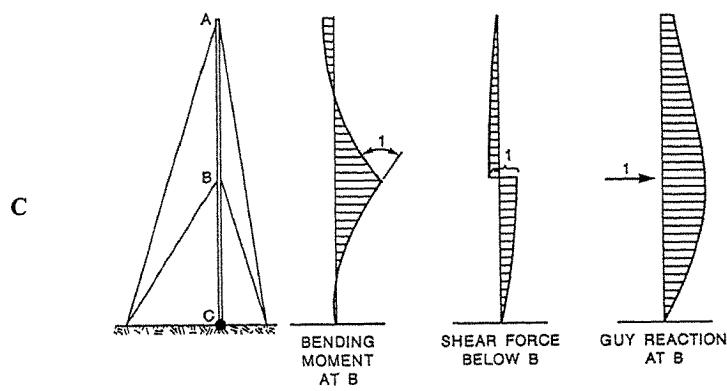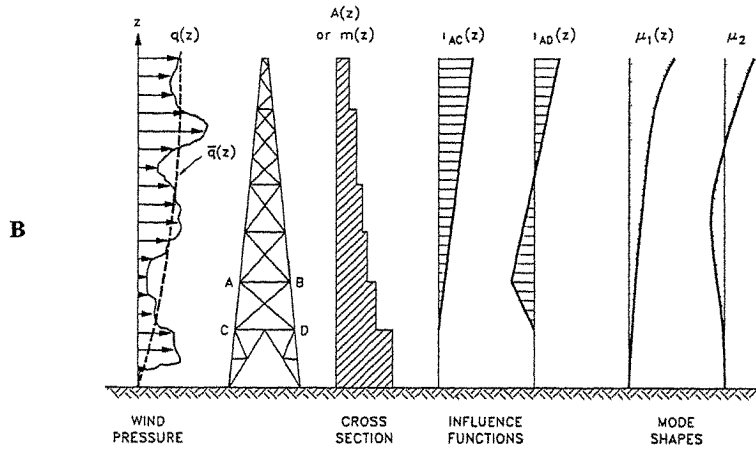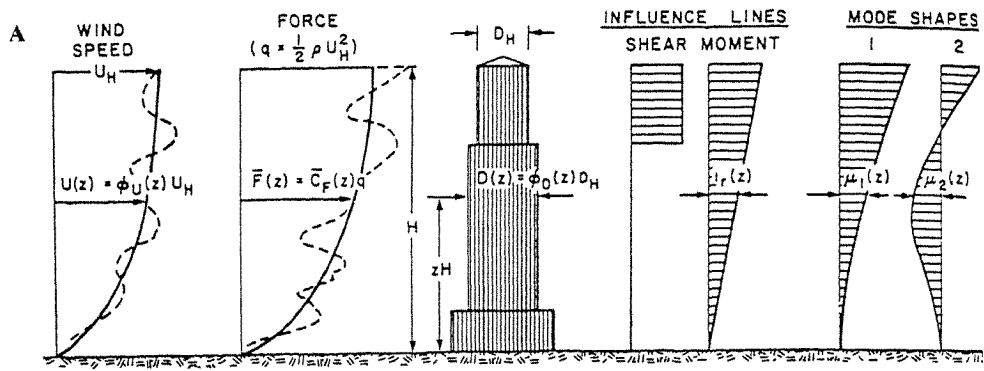
FIGURE 3 A,B,C   INFLUENCE LINES AND MODE SHAPES FOR FREESTANDING
AND GUYED STRUCTURES

24

NORMANDIE
(856 m)

D

LILLEBAELT
(600 m)

NORMANDIE

LILLEBAELT

$\eta \times 10^3$
METER/T

THRUST IN MAIN STAY

avg C_I

1 80
1 40
1 00
0 60
0 30
0 10
−0 10
−0 30
−0 60

E

TENSION IN LOWER STAY
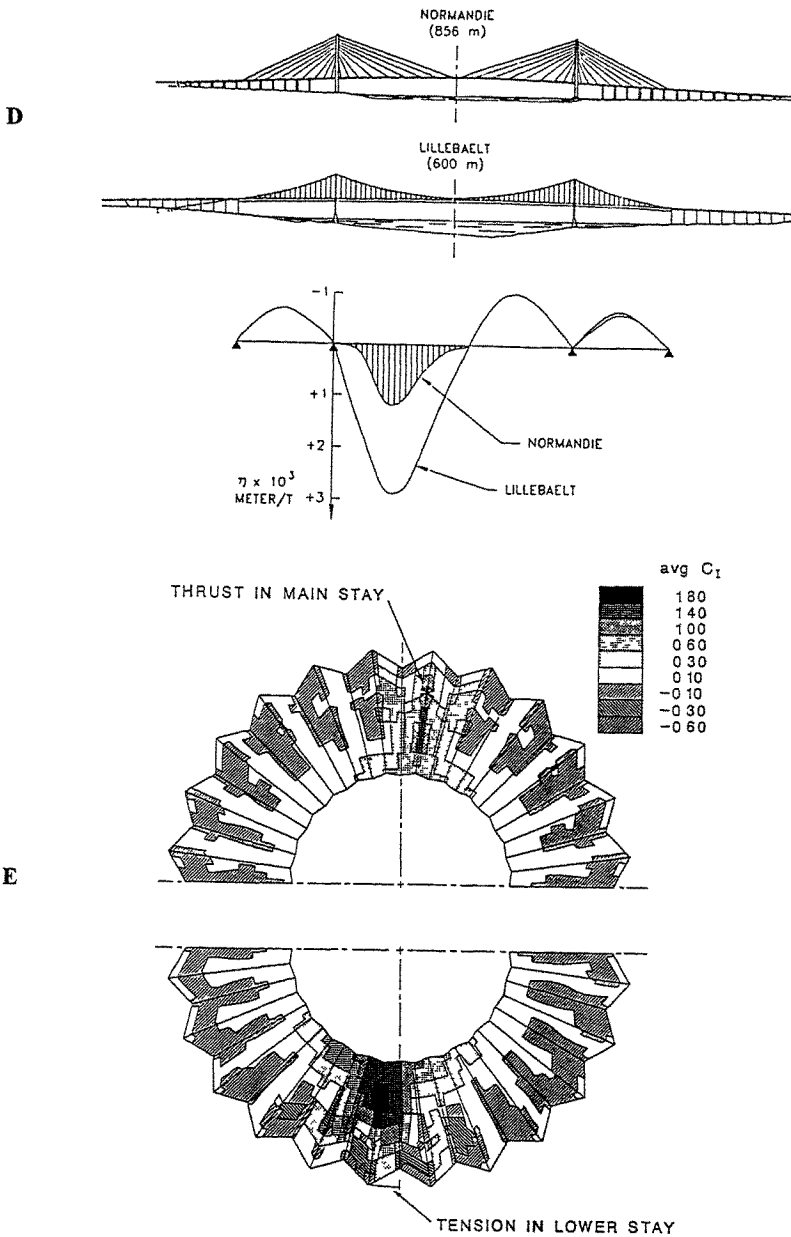
FIGURE 3 D,E INFLUENCE LINES AND SURFACES FOR (D) QUARTER POINT DEFLECTION IN LONG SPAN BRIDGES AND (E) TENSION IN A STAY OF TENSIONED FABRIC ROOF

25

A) RESPONSE

B) SPECTRUM

LOG FREQUENCY f
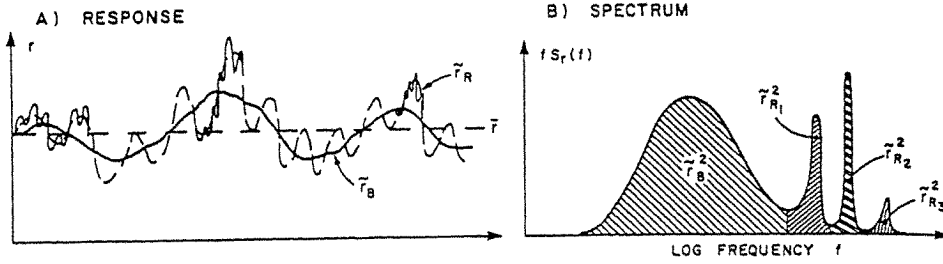
FIGURE 4   CHARACTERISTICS OF DYNAMIC RESPONSE TO WIND

SINGLE CURVATURE

REVERSE

CORRELATION

Δz - SEPARATION

SEPARATION

CORRELATION

JOINT ACCEPTANCE

$J(L/\lambda)$

$\alpha \dfrac{\lambda}{L}$

L / λ
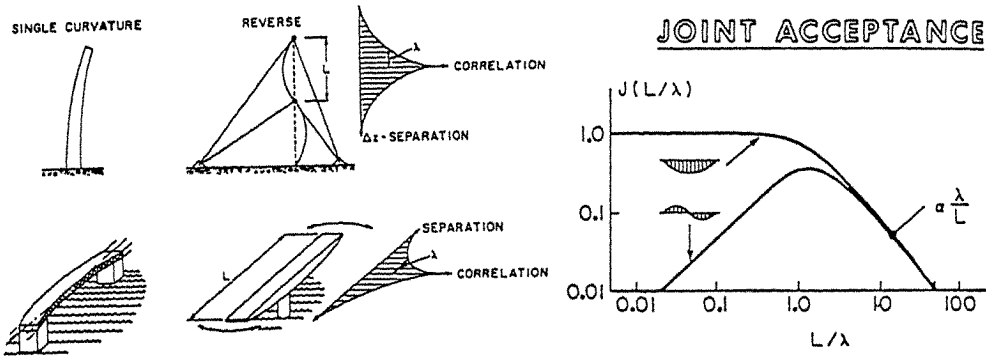
FIGURE 5   THE SPATIAL CORRELATION OF GUSTS AND THE JOINT
ACCEPTANCE

A) TURBULENCE FORCES F_T

$f S_F(f)/\widetilde{F}^2$

RANGE OF
STRUCTURAL
FREQUENCIES

fL/U

B) WAKE FORCES F_W

$f S_{F_W}(f)/\widetilde{F}^2$

TURBULENCE
INTENSITY:

LOW

HIGH

(fB/U)/S
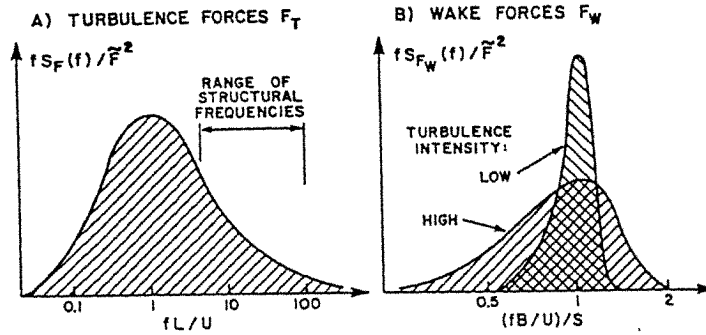
FIGURE 6   FORCE SPECTRA DUE TO ATMOSPHERIC TURBULENCE AND
WAKE VORTEX SHEDDING

26

The response of large roofs to wind action

W. H. Melbourne

Department of Mechanical Engineering
Monash University, Clayton, Vic 3168, Australia

Abstract: The response of very large roof systems has been reviewed through a number of aeroelastic model studies. The review covers cantilevered, enclosed, free edged, arched and suspended roof systems. Comparisons had been made with the equivalent response implied by design loads from the Australian Wind Loading Code. For relatively conventional configurations the comparison between code and peak dynamic response was good. However non-conservative exceptions occurred where interference effects increased response, in particular downward going response, and for arched roof systems where under some conditions very large and complex asymmetric response was found to occur.

1. Introduction

Aeroelastic model studies of a variety of large roof systems, mostly cantilevered but including suspended and arched systems, at Monash University, has resulted in the accumulation of a considerable amount of data. In particular an equation to account for the dynamic response of cantilevered roof systems was developed for the Australian Wind Loading Code AS1170.2-1989 (Ref.1). This paper will review a number of these studies with a view to obtaining generalised design data and in the case of the cantilevered roofs to test the above mentioned design equation in the light of other work.

2. Cantilevered Roofs

A description of the wind loading process on cantilevered roofs is given by Melbourne and Cheung 1988 (Ref.2) which presents the background to the equation for an equivalent static design load distribution given in Ref.1. The response of a cantilevered roof to wind action is a combination of random low frequency response, primarily driven by the fluctuating pressure distribution under the re-attaching shear layer shed from the leading edge, onto which is superimposed a resonant response at the beam (roof) first mode frequency, as illustrated in Figure 1. It was suggested in Ref.2 that a triangular load distribution could be used as a reasonable approximation for an effective peak design load to reproduce a peak deflection equivalent to that which would be caused by the combination of pressure and resonant driven dynamic response.
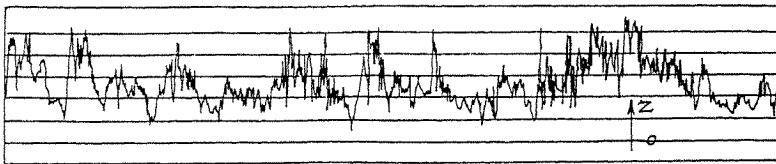
Fig. 1   Trace of vertical displacement of the leading edge of a cantilevered roof showing the skewed distribution and the effect of the low frequency pressure fluctuation under the reattaching shear layer and the high frequency first mode beam resonance component.

27

The peak design triangular load distribution defined by $\hat{Q}$, the pressure at the leading edge, is expressed in Ref.1 in non-dimensional form as $C_{\hat{Q}}$ versus $\frac{\overline{V}_h}{nl}$, where

$$C_{\hat{Q}} \quad = \quad \frac{\hat{Q}}{\frac{1}{2}\rho\overline{V}_h^2}$$

b	=	length of leading edge of roof
h	=	height of leading edge of roof
l	=	length of cantilever beam
n	=	first mode frequency
$\overline{V}_h$	=	mean wind speed at the top of the roof
ρ	=	air density

$C_{\hat{Q}}$ for inboard areas of a cantilevered roof, fully sealed at the rear in typical suburban-urban terrain roughness with turbulence intensity about 0.25 at height h, $l/h \approx 1$ and $b/h > 4$ is given by

$$C_{\hat{Q}} \quad = \quad 5.0 \quad \text{for} \quad \frac{\overline{V}_h}{nl} \quad \leq \quad 0.4$$

$$= \quad 5.0 \quad + \quad 2.5 \quad \frac{\overline{V}_h}{nl} - 0.4] \quad \text{for} \quad \frac{\overline{V}_h}{nl} \quad > \quad 0.4 \qquad (1)$$

This is shown graphically in Figure 2.
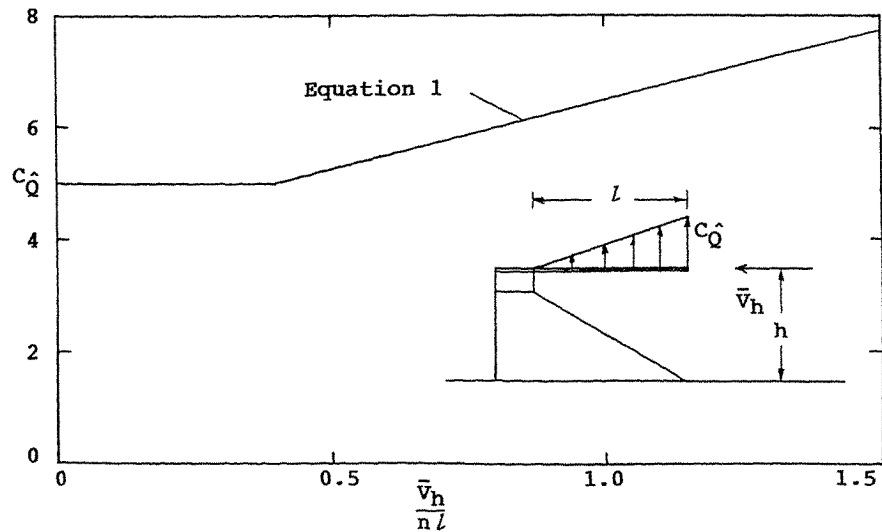
Fig. 2 Peak design pressure coefficient, $C_{\hat{Q}}$, as a function of reduced velocity for cantilevered roofs for turbulence intensity at roof leading edge of $\frac{\sigma_v}{\overline{V}} \approx 0.25$ and $\frac{l}{h} \approx 1$, with rear face fully sealed.

Aeroelastic model measurements on four cantilevered roof configurations which surround the configuration for the design equation are given in Figure 3. The Configuration 1 was the one on which the equation was originally based. It can be seen that for a range of $0.75 < l/h < 1.4$ and turbulence intensity of around 0.25 there is good agreement. This is encouraging because the four configurations, whilst sharing similarity of the above parameters were in fact very different. Configuration 1 had a straight leading edge, Configuration 2 was similar, but with a bluffer leading edge and a small embankment on the far side of the oval, and Configuration 3 was curved and relatively high above ground level with mostly low grandstands on the other side of the oval.

However the problem with a simplified approach, which whilst covering many practical configurations, may not adequately cover, or could be too conservative, for variations such as could be caused by

(i)   upstream interference from a grandstand on the other side of the oval,

(ii)   significant change of turbulence,

(iii)   significant change in ratio of l/h,

(iv)   venting at the rear,

(v)   slotting or venting the leading edge.

Some information on the effects of these variations has been obtained and guidance which can be given will be summarised.

The interference effect from a grandstand on the other side of the oval is potentially the most serious. In some cases there is a shielding effect, which reduces the upgoing response, but the real problem is that the interference effect can create a fluctuating downwash which in turn can introduce a significant downgoing response of the cantilever roof. For the cantilever roof in isolation the increasing mean upward response with wind speed normally produces the situation where the downgoing response rarely goes below the no-wind position. However as can be seen in Figure 3 for a Configuration 4 which has a similar grandstand opposite and for Configuration 3 for winds not normal to the leading edge there can occur some significant downgoing response. Hence it must be concluded that if there is any upstream structure capable of shedding wake vortices of length scales of the order of the cantilever length then some allowance must be made for a downward acting design load along the lines of that shown in Figure 3.

The effect of change in turbulence intensity has only been studied parametrically for Configuration 2 where a very clear dependence of response on turbulence intensity can be seen in Figure 3. This is expected because of the dependence of pressures under the re-attaching shear layer on turbulence intensity as discussed by Melbourne 1979 (Ref.3). However this does highlight the need to consider possible future upstream structures which may increase turbulence levels, if not specific interference effects, as per Figure 3.

The change of the ratio l/h does not seem to be too sensitive for the range about unity as shown in Figure 3. However with most of the low frequency pressure fluctuations occurring near the leading edge it would not be surprising to find that for large values of l/h the Equation 1 overestimates the equivalent design load. The limited study which has been done on this indicates that as l/h approaches 3 the equivalent design loads could approach half the value given by Equation 1.

29
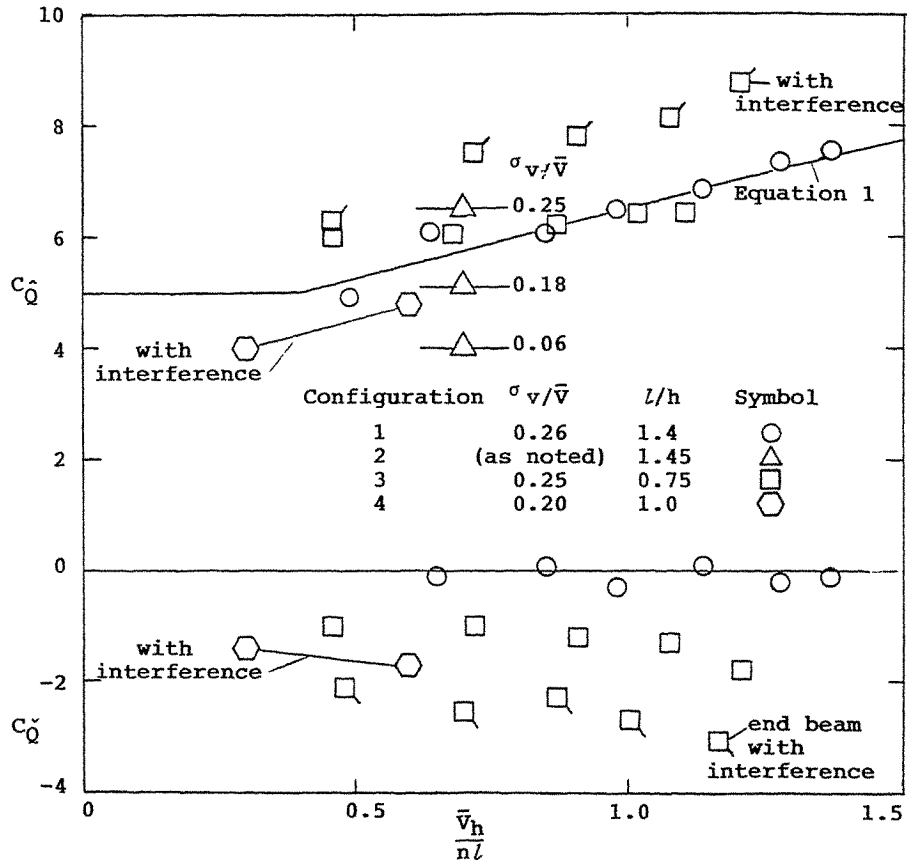
Fig. 3　Peak design pressure coefficients, $C_{\hat{Q}}$, for four cantilevered roofs. (All central beams with wind direction near normal to leading edge, with no interference except where noted.)

The reductions in response and hence design load by venting at the leading edge have been covered in some detail in Ref.2, and it is sufficient here to note that a 25% reduction in response can be achieved with a suitably configured slot width about $0.05l$. The reductions due to venting at the rear, or leeward side of the roof support, has not been so well studied. Evidence from work on Configuration 4 indicates that venting through the type of area typically available at the top level of a grandstand would reduce response by no more than 10%.

30

None of the discussion so far has dealt with the end areas of a cantilevered roof. The reason why this is normally not such a problem is because the end beam normally has a tributary area which is a half that for the inner beams. However it should be noted that wind loads on the ends of a cantilevered roof can be relatively higher than for the inner areas, particularly for end on wind directions and interference. Typically the end beam has design pressures ($\hat{Q}$) similar to or just a little higher than that for the inner beams, but acting on half the tributary area. However under interference there have been cases where downgoing values of C_Q have been as high as 4 which results in a downgoing end beam load the same as for an inner beam for a value of 2 (as shown in Figure 3).

In conclusion it has been shown that the upgoing design pressure given by Equation 1 is reasonable, and generally on the conservative side for typical cantilever roof configurations in suburban/urban locations. However the implication that whilst a zero downgoing design load is reasonable for isolated cantilevered roofs a significant downgoing design load is required to cover interference from other structures such as nearby grandstands.

3. Large roof systems on enclosed buildings

In recent years two aeroelastic model studies have been conducted on very large roof systems ($\approx 7,000 m^2$) on enclosed buildings. In one case the structural system was a cable suspension, and in the other an arch system. The quasi-steady approach to the determination of design wind loads from Ref.1 is as follows:

(i)　A 3 second mean maximum design wind speed at roof height is used which takes into account the effects of surface roughness and hence turbulence intensity.

(ii)　The average external pressure coefficient varies with distance from the windward leading edge, and for a flat roof, with height over streamwise depth less than 0.5 is as follows:

Horizontal distance from windward edge $\dfrac{x}{h}$	Average external pressure coefficient C_p based on $\hat{V}$	Equivalent peak pressure coefficients based on $\overline{V}$ for $\frac{\sigma_v}{\overline{V}} = 0.23$ with area reduction
0 - 1	-0.9	2.5
1 - 2	-0.5	1.4
2 - 3	-0.3	0.8
>3	-0.2	0.6

For an effectively fully sealed building the internal pressure coefficient is zero with the above external pressure coefficients. There are local pressure factors (up to 3 times) for local cladding and fixings design, but which are not relevant to the overall loads on the structure.

(iii)　For large roofs an area reduction factor (with interpolation) is allowed as follows:

Roof Area (m^2)	Reduction factor (multiplier)
≤10	1.0
25	0.9
≥100	0.8

31

The Roof Configuration 1 is set back about h from the windward edge for half the wind directions and set to the windward edge for the other half. It is first interesting to note that the peak response is made up of the low frequency, quasi steady, response to pressure fluctuations and the resonant response in the ratio of about 2:1. The damping ratio of the resonant component in this case was $\zeta = 0.05$.

The Roof Configuration 1 was tested for a turbulence intensity of 0.23 at roof level. Using the relationship between peak 3 second mean maximum gust wind speed, $\hat{V}$, and mean hourly wind speed, $\bar{V}$, of

$$\hat{V} = \bar{V} \left(1 + 3.7\frac{\sigma_u}{\bar{V}} \right)$$
$$= 1.85 \ \bar{V} \tag{2}$$

allows conversion of the Ref.1 pressure coefficients, for use with $\hat{V}$, to equivalent peak pressure coefficients based on $\bar{V}$, which, with a 0.8 reduction for a large area, is given above in (ii) in the last column.

For the Roof Configuration 1 the experimental technique was to measure the mean, standard deviation and peak displacements of four segments of the roof and via a stiffness calibration to convert these to forces and to area averaged pressure coefficients normalised by $\frac{1}{2}\rho\bar{V}_h^2$ and the relevant roof tributary area. It was found that the response coefficients were constant with wind speed, i.e. the response varied exactly as $\bar{V}^2$. For the two types of edge configuration the highest area averaged pressure coefficients were as follows:

Pressure Coefficients		Roof edge set-back h from windward edge		Roof edge at windward edge	
		windward half	leeward half	windward half	leeward half
mean	$C_{\bar{p}}$	0.6	0.4	0.9	0.4
standard deviation	C_{σ_p}	0.07	0.06	0.10	0.06
peak upgoing	$C_{\hat{p}}$	0.85 (g = 3.6)	0.6 (g = 3.3)	1.3 (g = 4.0)	0.6 (g = 3.3)
peak downgoing (+ve up above zero)	C_p	0.3	0	0.5	-0.2

By comparison with the equivalent Ref.1 design pressure coefficients given in the last column of (ii) above it can be seen that the Ref.1 coefficients are conservative for the windward half, but very similar for the leeward half. This comparison is shown graphically in Figure 4.

32
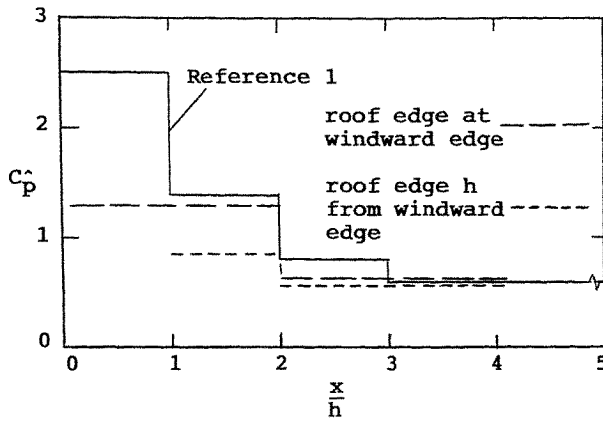
Fig. 4   Comparison of measured C_p from Roof Configuration 1 with design coefficients based on Reference 1.

Roof Configuration 2 is quite different. It is a one-dimensional arched roof, i.e. for the wind blowing along the axis of the arch the roof pitch is 0° and for the wind blowing across the arch the edge roof pitch is effectively about 20°. However it is with the wind blowing generally along the axis, with roof pitch 0°, that the greatest response occurs. The problem is that this type of roof has a very different response to that of a roof supported on beams. Being an arch, one of the natural modes of deformation is a sway or antisymmetric mode where one side goes up as the other goes down. The arched roof displacement is still predominantly driven at relatively low frequencies by the fluctuating pressure fields, with the maximum displacements occurring at around the quarter span points (not the centre) due to pressure driven displacement in something like the first antisymmetric mode (i.e. there was very little resonant response at the natural frequency of this mode). This mode of deformation cannot be simulated by a simple equivalent pressure distribution because one half is acting upwards and the other half downwards, and the true bending moments in the arch can only be reproduced by a load distribution which causes the same peak antisymmetric deformation. However to give some guidance for a designer faced with this complex situation the pressure coefficient, if applied to one half side only of the arch, to give the measured peak dynamic displacement at about quarter span has been determined. These half side pressure coefficients are -

C_p = 0.5   i.e. *upgoing*

C_p = −0.4   i.e. *downgoing*

This Roof Configuration 2 had a further configuration which will be called Roof Configuration 3 in which one side of the arch was supported by a large beam (over 100m in length) and on the other side of which was a more conventional beam supported roof. The deflection of the centre of the large beam was calibrated against a uniform pressure distribution over the whole roof and this gave design pressure coefficients of -

C_p = 1.5   i.e. *upgoing*

C_p = −0.9   i.e. *downgoing*

33

The displacement is still too complex to say that it could be reasonably achieved for design purposes by a simple code based distribution. However it can be noted in very approximate comparison with Ref.1 pressure coefficients given in (ii) that the upgoing displacement would have been reasonably covered, but the very significant downgoing displacement would have been missed altogether.

4. Large suspended free roof

A third type of large roof, beginning to be used a little, is a grandstand roof supported by cables, and which has at least one free edge. Some of these are very similar, in structural action, to a conventional cantilever roof except that the upgoing loads are opposed by dead weight. There is a class of suspended free roof which is cable supported from above and below, and the one which was the subject of a particular aeroelastic study at Monash University had lightweight beams supported at the rear on columns and at about two thirds length by a cable suspension system running the full length of the roof (laterally across the beams) one cable providing upwards support action and the other hold-down action. The roof edge profile was in the form of an arch as illustrated in Figure 5.
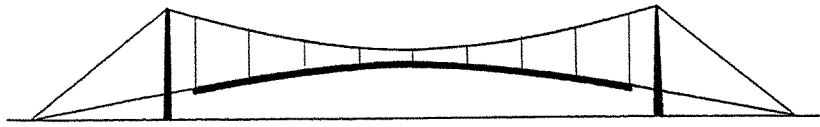
Fig. 5   Cable suspension arrangement for a grandstand roof

Most grandstand roof systems have little need to provide significant moment connection between roof panels, such as through an edge beam, and consequently the motion of each beam and its roof panel is relatively independent of the next (influence coefficients around 20% or less between adjacent beams are typical). However in the suspended type of roof described above, and illustrated in Figure 5, large areas of the roof move together by virtue of the cable suspension system, and in fact the mode shapes look very like that for an arched system.

The aeroelastic model study of this cable suspended grandstand roof system revealed a number of novel characteristics as follows:

(i)   Up to reduced velocities of about 0.7 the response of the canopy was for the leading edge to move as a whole in the first symmetric mode with a broad range of frequencies including those driven by the wake/vortex shedding (pressure field under the re-attaching shear layer) and the first resonant frequency and then some higher resonant frequencies.

(ii)   As the reduced velocity increased the first antisymmetric mode became significant.

(iii)   Initially as the antisymmetric mode became significant the response occurred over a broad range of frequencies as for the symmetric mode. Then as the reduced velocity increased further the wake/vortex shedding driven frequencies began to dominate. Then with further increased reduced velocity to about 1.0 the antisymmetric response, still dominated by the wake/vortex

34

shedding frequencies, became predominantly single sided in the upwards direction with intermittent single high amplitude excursions. The effective resonant response at this stage was very small and the correlation between the two sides of the canopy similarly small. Examples of the displacement traces at quarter span are given in Figure 6.

(iv)   It was found that the very high upward displacements were pressure driven (by the pressure field under the re-attaching shear layer) to produce a dynamic overshoot for one oscillation (predominantly) and that the peak response is, more often than not, quite asymmetric in some mode akin to the first antisymmetric mode.

$$\frac{\bar{v}_h}{nL}$$

0.6

1.0
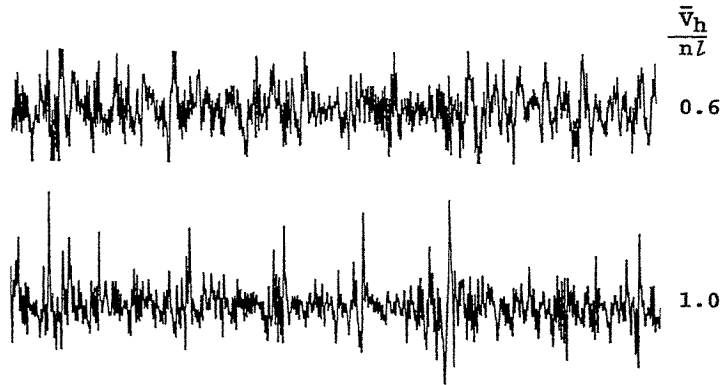
Fig. 6   Traces of displacement at the quarter span leading edge for two values of reduced velocity.

Peak pressure coefficients, C_Q, to define a triangular load distribution which would, under static application, give the same peak displacement as occurred under the dynamic action have been evaluated from the aeroelastic studies and, as can be seen in Figure 7, the values of C_Q for the antisymmetric dynamic overshoot are extremely high relative to that for the more conventional cantilever roof as given by Equation 1. To explain what is occurring in these exteme conditions an analytical simulation of the dynamic overshoot showed that for an applied triangular pressure distribution which would give a static displacement of z at the leaaing edge, if started from $-z$, would produce a total dynamic overshoot (in half a cycle) of $2z$ for a damping ratio of $\zeta = 0.03$. It can clearly be concluded that the provision of Equation 1, whilst reasonable for the centre span area, would grossly underpredict the antisymmetric behaviour of this type of suspended free roof at high reduced velocities.

5. Conclusions

A review of about ten aeroelastic model studies of the response of very large roof systems has been presented. The peak response has been reduced in terms of an equivalent pressure distribution (in coefficient form) which would produce the same peak deflection as would occur in the true dynamic process. These results have been compared with a codified approach to design as given by the Australian Wind Loading Code. For relatively conventional configurations of cantilevered, enclosed and free edged roofs the code approach leads to reasonable design loads. However non-conservative exceptions occurred for cantilevered roofs where interference effects introduced very significant downward going

response and for arched roofs where asymmetric response could be very high. Both of these situations required particular, and sometimes very complex, static design loads to achieve an equivalent diplacement.
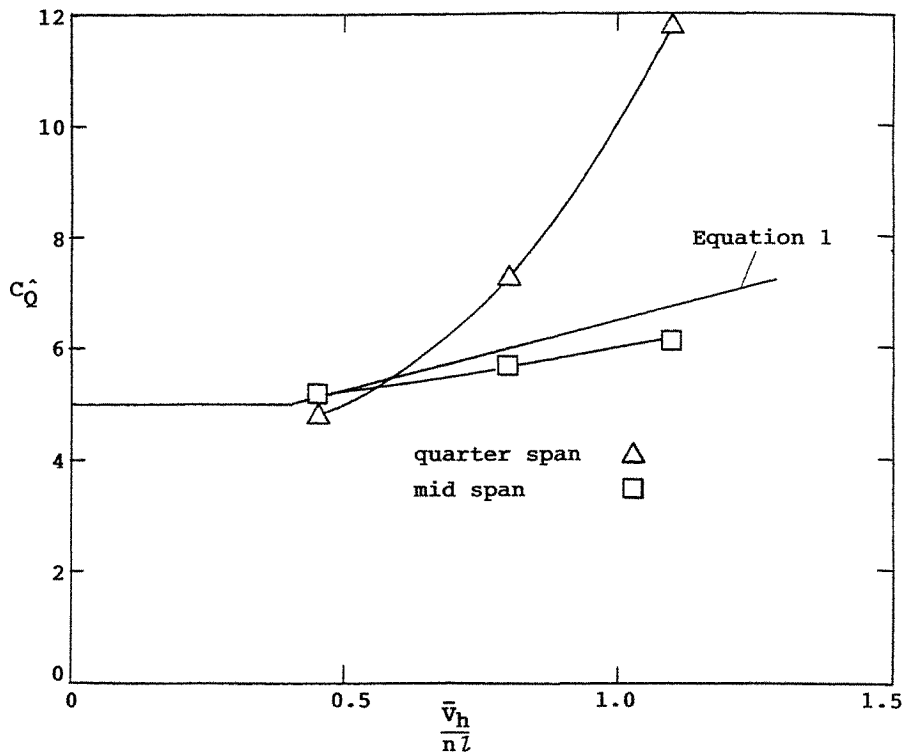
Fig. 7   Peak design pressure coefficients, $C_{\hat{Q}}$, for a suspended arch roof with one free edge.

References:

1.   Australian Wind Loading Code, AS1170.2-1989, Publ. Standards Australia.

2.   W. H. Melbourne & J.C.K. Cheung (1988), "Reducing the wind loading on large cantilevered roofs", Jnl. Wind Engineering & Industrial Aerodynamics, Vol.28, pp 401-410.

3.   W. H. Melbourne (1979), "Turbulence effects on maximum surface pressures - a mechanism and possibility of reduction", Proc. 5th Int. Conf. on Wind Engineering, Fort Collins, USA, pp 541-552.

Invited Papers

Wind Loads on Low Rise Building - A Review

Prem Krishna

Department of Civil Engineering
University of Roorkee, Roorkee, India

Abstract

Determination of wind loading and its effects on low rise building structures has been a subject of many extensive research programmes the world over. Information gathered over the last few decades has found its way into the codal provisions for the design of structures for wind effects. It is noteworthy that even for the simplest of cases there is a scatter amongst the pressure coefficients specified in the various codes. Further, the information does not by any means make a comprehensive coverage of the variables involved. Under the circumstances, that most such engineered buildings survive even in high risk zones is due to a combination of factors, such as the inbuilt factors of safety.

Understandably therefore, this continues to be a live area of enquiry. One of the prime reasons for this, as indeed in most problems of Wind Engineering, is the variability involved in the flow, which is responsible for creating the force, the parameters related to building structures and their situations, as well as the procedures of making measurements. Considerations such as this, led to the Aylesbury International Experiment wherein pressure measurements have been made on a building model of a simple building with sloping roofs in a large number of wind tunnels in different countries. Futhermore, in situations where strong economies and adequate resources permit well engineered constructions, the interest is to know more, so as to minimise or eliminate whatever damage is caused to low rise structures in strong winds. On the other hand, for the teeming millions who do not live in engineered buildings, the most accurate information possible is needed to do the best within the limited resources.

The parameters that are important include, the geometry and size of building, permeability, special features of the building, interference from neighbouring structures, angle of wind incidence and characteristics of wind, as well as the issues related with the measurement of wind loads, which affect the correctness of the obtained results. This paper has attemped to describe the state-of-the-information available, and its limitations, influence of the parameters listed above; the understanding that exists on the subject, the grey areas and future scope.

(Copies of the full paper will be distributed at the Symposium.)

ON TURBULENT VORTEX SHEDDING FLOW
PAST 2D SQUARE CYLINDER PREDICTED BY CFD

S. Murakami
A. Mochida

Institute of Industrial Science
University of Tokyo, Japan

ABSTRACT

Analyses by CFD on unsteady flowfields past a two-dimensional (2D) square cylinder are presented. The accuracy of the predicted results by CFD is examined from various view points. At the first part of the paper, the comparison of the results of Large Eddy Simulation (LES) for 2D and 3D computations are described [13, 30]. The LES results given from 3D computation correspond with the experimental results very well, but the results based on 2D computation are different from those given from 3D computation as well as from those given from experiments. The second part of the paper concerns detailed testing of 3D LES computations for the analysis of periodic and stochastic fluctuations, for which detailed experimental data are available. Results of LES computations are compared with those from turbulence models based on Reynolds-averaged Navier-Stokes equations (RANS models) as well as with those from experiments [2, 26]. Lastly, results of 3D LES of unsteady pressure field and wind force acting on an oscillating square cylinder are presented [28].

1. INTRODUCTION

Distributions of the fluctuating surface pressure and the wind forces acting on bluff-shaped bodies are of great practical interest in the field of structural design in wind engineering. In this paper, turbulent vortex shedding flow past a long square cylinder, which is 2D in the mean, is considered. At high Reynolds numbers, stochastic 3D turbulent fluctuations, which exist even in flow past 2D cylinders, are superimposed onto the 2D periodic vortex-shedding motion. This is illustrated in Fig.1 [1, 2], where f is the instantaneous value of a quantity, $\tilde{f}$ the periodic fluctuation, f'' the stochastic turbulent fluctuation, $<f>_t$ the time averaged value and $<f>_p$ the phase averaged value.

In the first part of the paper, LES predictions of an unsteady flowfield past a 2D square cylinder at Re $= 1.0 \times 10^5$ are presented. Results of 2D and 3D computations are compared with previous experimental data recorded by Ohtsuki [3] and Vickery [4]. This comparison shows that the results based on 2D computation, which cannot reproduce stochastic 3D turbulent fluctuations, are different from those based on the 3D computation as well as from those given from the experiments.

The second part of the paper describes 3D LES computations for a case with a lower Reynolds number (2.2×10^4), for which detailed experimental data are available. Here, the characteristics of periodic and stochastic fluctuations of turbulent vortex shedding flow given by 3D LES are compared with the results of the detailed water channel experiments of Lyn [5]. Furthermore, results of 3D LES are also compared with results of the standard and modified k-ε models, and Reynolds stress equation (RSE) model, which were given by the computations of Franke and Rodi [1, 2], Launder and Kato [6, 7], and Przulj and Younis [8]. Thus, the relative performance of various turbulence models is clarified concerned with the analysis of turbulent vortex shedding flow.

In the last part of the paper, results of 3D LES predictions of unsteady pressure field and wind force acting on an oscillating square cylinder at Re=2.2×10^4 are presented. A very simple procedure to incorporate the influence of the body motion on the flow field is used. The accuracy of the computations by this procedure is made clear by comparing them with the experimental results of Bearman et al. [9].

$\tilde{f}$: periodic fluctuation
f'' : stochastic turbulent fluctuation
f' : total fluctuation (periodic+stochastic)
$<f>_p$: phase averaged value
$<f>_t$: time averaged value
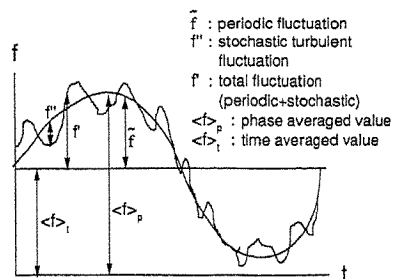
Fig.1 Periodic and stochastic fluctuations in turbulent vortex shedding flow [1, 2]

41

2. COMPARISON BETWEEN 2D AND 3D LES COMPUTATIONS

When the flow is 2D in the mean, it is common for engineering problems to be solved by an unsteady 2D computation because CPU time is reduced greatly in comparison with 3D computations. Here, 2D and 3D LES computations are compared, and the accuracy of 2D LES computation is examined. The outline of LES computation is described in Note 1.

2.1 Mean surface pressure (Fig.2)

Fig.2 shows distributions of mean surface pressure coefficients $<\overline{C}_p>_t$. Here $<\,>_t$ means time averaging and $\overline{}$ indicate filtering (cf. Nomenclature). The distribution of the 3D computation is similar to that of the experiment by Ohtsuki et al. [3] except for the leeward face, while in the case of the 2D computation, the negative value of $<\overline{C}_p>_t$ becomes too large at the center of the side faces.

2.2 RMS value of fluctuating pressure (Fig.3)

Distributions of the rms pressure coefficients C_{prms} given by the two computations are compared with the results of experiments by Bearman et al. [9] and Lee [14] in Fig.3. It can be concluded that the 3D computation reproduces the pattern of C_{prms} distributions in the experiments very well. In the 2D computation, the values of C_{prms} differ greatly at both the side face and the leeward face. This lack of agreement between the results of the 2D computation and the experiment is not acceptable.

2.3 Power spectrum of fluctuating lift and drag forces (Fig.4)

Fig.4 shows the computed and measured spectra of the fluctuating lift force F_L and the drag force F_D acting on the cylinder. As is shown here, the spectrum curves of F_L have a sharp peak in the results of both computations as well as in that of the experiment. The frequency of each peak corresponds to the fluctuation caused by the corresponding Karman vortex shedding. The spectrum shapes of F_L and F_D given by the 3D computation correspond very well with those given by the experiments. On the other hand, the peak frequencies of the fluctuations of F_L and F_D in the 2D computation do not correspond with those in the experiments, but are located at higher frequencies for both F_L and F_D. As is shown here, the 2D computation cannot reproduce accurately the surface pressure field and the resulting lift and drag forces.

2.4 Difference in the flowfield structures near the side face (Fig.5)

Fig.5 compares the power spectra of $u_i{}'$ based on computations near the side face. This figure reveals significant differences in the flow structures predicted by the 2D and the 3D computations. The
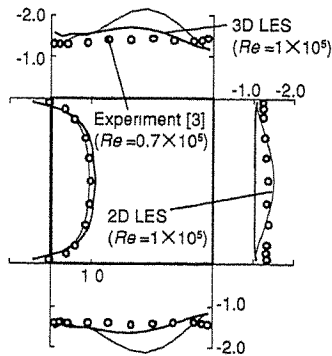
Fig 2 Distribution of $<\overline{C}_p>_t$ [13, 30]
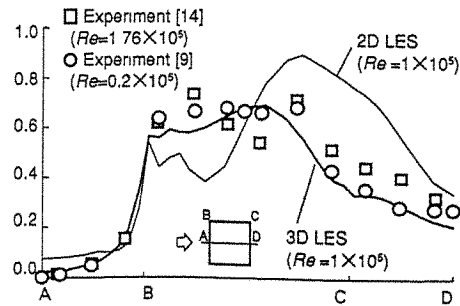
Fig.3 Distribution of C_{prms} [13, 30]
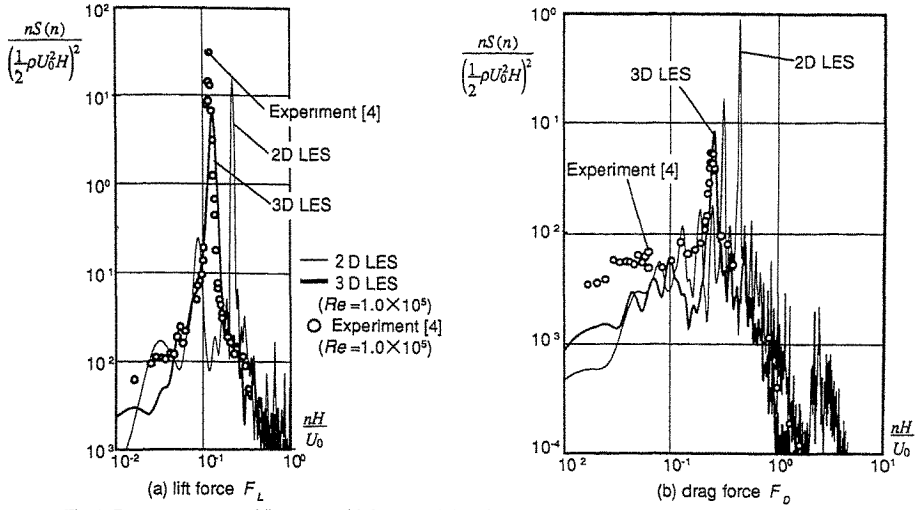
Fig.4 Power spectrum of fluctuating lift force and drag force [13, 30]

(a) lift force F_L

(b) drag force F_D
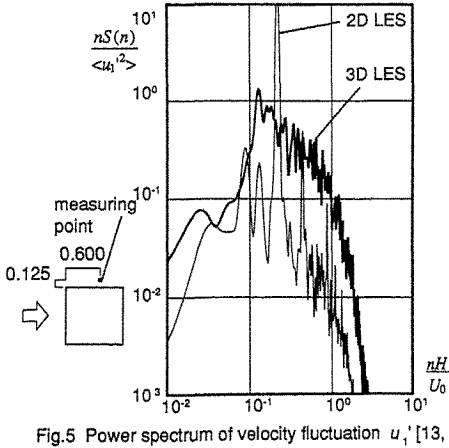
Fig.5 Power spectrum of velocity fluctuation u_1' [13, 30]

spectrum of the 2D computation is confined to a narrow band, and has a sharp peak at the same frequency as that of F_L. On the other hand, the spectrum of the 3D computation extends over a wide band. From this figure, it becomes clear that the energy transfer mechanism throughout a wide spectrum range cannot be reproduced by the 2D computation. This is hardly surprising when we recall that the vortex stretching mechanism, which is essentially three-dimensional and is not reproduced at all in the 2D computation, plays an important role in the energy cascade around this point [15].

In the following section, distributions of mean vorticity, vorticity fluctuations and turbulence terms in vorticity transport equation are discussed in order to examine the structural difference between the results of 2D and 3D computations.

2.5 Structural difference in vorticity fields between 2D and 3D computations (Figs.6-10) [13]

In the flow treated in the present study, which is two dimensional in the mean, the only non-zero component of mean vorticity $\langle\overline{\omega_i}\rangle$ is $\langle\overline{\omega_3}\rangle_t$. Distributions of $\langle\overline{\omega_3}\rangle_t$ and $\langle\omega_3'^2\rangle_t$ given by the two computations are compared in Figs.6 and 7. The value of $\langle\overline{\omega_3}\rangle_t$ in the 2D computation is larger than that in the 3D computation in the area near the side face of the cylinder. On the other hand, the value of $\langle\omega_3'^2\rangle_t$ in the 2D computation is smaller than that in the 3D computation, especially near the frontal and leeward corners of the cylinder. Here, Table 3 shows the transport equation of $\langle\overline{\omega_3}\rangle_t$ for two-dimensional mean flow. The major turbulence terms in the equation are the first and the second ones of the right side of eqn.(3.1), i.e.,

$-\partial\langle u_j' \omega_3'\rangle/\partial x_j$ and $\partial\langle\omega_j' u_3'\rangle/\partial x_j$. The first term is clearly analogous to the Reynolds stress term in the equation for $\langle u_j \rangle$; it is mean transport of ω_3' through its interaction with fluctuating velocities u_j' in the direction of the gradients $\partial/\partial x_j$ (turbulent transport term of ω_3') [15] (cf. Note 2). The second term is

the gain (or loss) of mean vorticity $\langle\overline{\omega_3}\rangle_t$ caused by the stretching and rotation of fluctuating vorticity

43
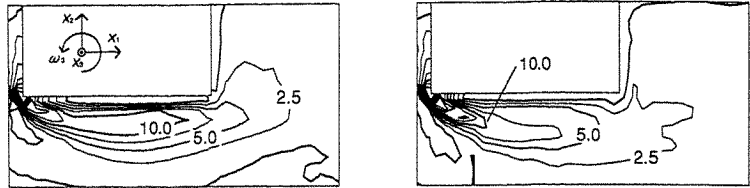
(a) 2D computation   (b) 3D computation

Fig.6   Distribution of mean vorticity $\langle\overline{\omega_3}\rangle_t$ [13]
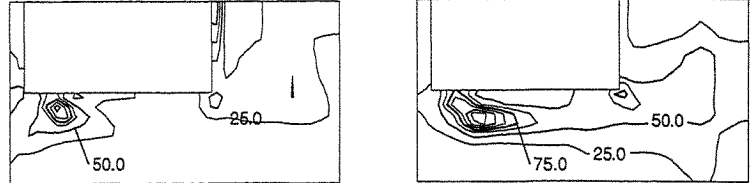
(a) 2D computation   (b) 3D computation

Fig.7   Distribution of vorticity fluctuation $\langle\omega_3'^2\rangle_t$ [13]

Table 3 Vorticity equation

Transport equation of $\langle\overline{\omega_3}\rangle$

$$\langle\overline{u}_j\rangle_t\frac{\partial\langle\overline{\omega}_j\rangle_t}{\partial x_j}=\frac{\partial\langle u_j'\omega_3'\rangle_t}{\partial x_j}+\frac{\partial\langle\omega_j'u_3'\rangle_t}{\partial x_j}+\langle\overline{\omega}_j\rangle_t\langle\overline{s}_{3j}\rangle_t+\nu\frac{\partial^2\langle\overline{\omega}_3\rangle}{\partial x_j\partial x_j} \qquad (3.1)$$

the first term of the right side of eqn.(3.1)=turbulent transport term of w3' (Fig.8) :

$$-\frac{\partial\langle u_j'\omega_3'\rangle_t}{\partial x_j}=-\frac{\partial\langle u_1'\omega_3'\rangle_t}{\partial x_1}-\frac{\partial\langle u_2'\omega_3'\rangle_t}{\partial x_2} \qquad (3.2)$$

the second term of the right side of eqn.(3.1)=vortex-shedding term (Fig.9):

$$\frac{\partial\langle\omega_j'u_3'\rangle_t}{\partial x_j}=\frac{\partial\langle\omega_1'u_3'\rangle_t}{\partial x_1}+\frac{\partial\langle\omega_2'u_3'\rangle_t}{\partial x_2} \qquad (3.3)$$
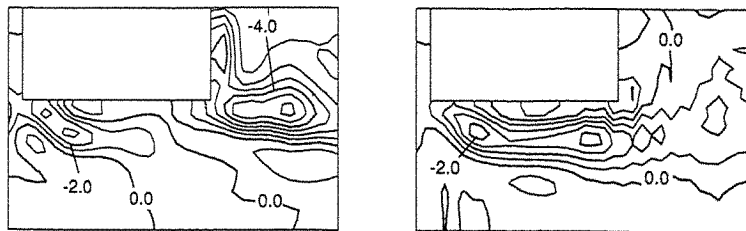
(a) 2D computation   (b) 3D computation

Fig.8   Distribution of $-\partial\langle u_j'\omega_3'\rangle/\partial x_j$ (the first term of the right side of the eqn.(3.1)) [13]

44
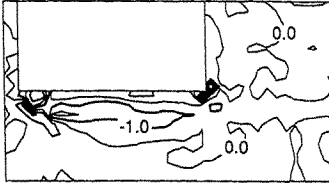
(the second term of the right side of the eqn.(3.1), which becomes automatically zero in 2D computation)

Fig.9 Distribution of $\partial <\omega_j' u_3'>/\partial x_j$ [13]
(3D computation)
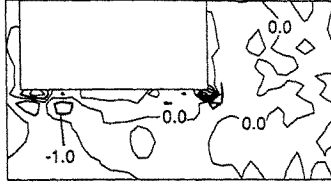
(a) $\partial <\omega_1' u_3'>/\partial x_1$
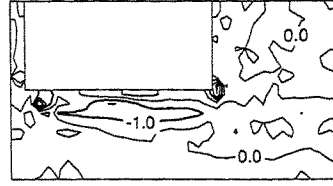
(b) $\partial <\omega_2' u_3'>/\partial x_2$

Fig.10 Distribution of $\partial <\omega_1' u_3'>/\partial x_1$ and $\partial <\omega_2' u_3'>/\partial x_2$ (3D computation) [13]
(components of the second term of the right side of the eqn.(3.1))

components by fluctuating strain rates (vortex stretching term). Distributions of these terms given by computations are shown in Figs.8 and 9. Fig.8 shows the distributions of the first term of the right side of the eqn.(3.1) in Table 3, given by the 2D and 3D computations. Fig.9 shows the distribution of the second term given by 3D computation, which is 0 in the 2D computation. To compare the distributions of these two terms given by 3D computation (Figs.8 (b) and 9), it is found that the first and the second terms show the same order of magnitudes near the side face. It is clarified that the effect of vortex stretching, which is related to the second term and is absent in the 2D computation, has almost the same magnitude of importance to the flow structure compared with the effect of the turbulent transport term. Therefore, it can be concluded that the difference observed in the distributions of $<\overline{\omega_3}>_t$ is mainly caused by the fact that the second term, which is related to vortex stretching and has a significant role, is 0 in the 2D computation. The difference of the distribution of $<\omega_3'^2>_t$ between 2D and 3D can be clarified also by examining the transport equation of $<\omega_3'^2>_t$ with the same manner.

The second term of the right side of eqn.(3.1) in Table 3 can be divided into two terms, i.e., $\partial <\omega_1' u_3'>/\partial x_1$ and $\partial <\omega_2' u_3'>/\partial x_2$. Fig.10 compares values of $\partial <\omega_1' u_3'>/\partial x_1$ and $\partial <\omega_2' u_3'>/\partial x_2$ in order to clarify the contributions by each component in the second term $\partial <\omega_j' u_3'>/\partial x_j$. As is shown in the figure, the component $\partial <\omega_2' u_3'>/\partial x_2$ plays a more significant role than $\partial <\omega_1' u_3'>/\partial x_1$ does since the gradient in the x_2 direction is more steep than that in the x_1 direction in this area. Therefore, it is suggested that the vortex which has its axis along the lateral (x_2) direction has primary importance in the flow structure near the side face of the cylinder.

3. COMPARISON OF 3D LES WITH k-ε/RSE COMPUTATIONS AND MEASUREMENTS[2, 26]

In the case of unsteady vortex shedding flows, proper testing of the accuracy of a numerical simulation is possible only when time-resolved measurements are available. These measurements give information on the temporal variation of the ensemble-averaged quantities and separate the fluctuations into periodic and stochastic turbulent ones. Lyn [5] carried out this kind of measurements on the flow past a square cylinder at $Re = 2.2 \times 10^4$. Here, we analyzed the same flowfield by 3D LES computations. Franke and Rodi [1, 2] also calculated the flow past a square cylinder at $Re = 2.2 \times 10^4$. They used the standard k-ε model and the standard Reynolds-stress-equation (RSE) model of Launder, Reece and Rodi [16], with wall corrections to the pressure-strain terms due to Gibson and Launder [17]. For both models, two types of near-wall treatments are applied ; wall function and the two-layer approach in which the near-wall region is resolved with a one-equation model due to Norris and Reynolds [18]. The results given by LES are compared with those given by

45

the computations of Franke and Rodi as well as with the experimental results [5, 19]. The outline of LES computations for this case is summarized in Note 3.

3.1 Comparison of LES with k-ε/RSE computations and experiments

1) Integral parameters S_t, $<C_D>_t$

Values of various integral parameters (e.g., Strouhal number, drag coefficient, etc.) predicted with the various computational methods are compared in Table 4 with experimental values. In the computations by Franke and Rodi, results with the standard k-ε model using wall functions yielded a steady solution and no vortex shedding(this case is not included in Table 4). The two-layer k-ε model yielded too low shedding frequency and drag coefficient $<C_D>_t$. The two-layer RSE predicted too high Strouhal number and drag, while the RSE with wall functions predicted these parameters in good agreement with the measurements. The LES computation reproduced slightly lower values, which, however, still agree fairly well with the measurements.

Recently some effort has been made to develop the more refined k-ε models which can be applied to the vortex shedding flows such as the flowfield analyzed here [6, 7, 8]. The results of the modified k-ε models, which are also shown in Table 4, are discussed later in section 3.2.

2) Time averaged velocity $<\overline{u}_1>_t$ (Fig.11 (a))

Experimental data of Lyn [5] and Durao et al. [19] are also included in Fig.11. In front of the cylinder, the results are not much influenced by the computation method used, but there are fairly large differences in the wake region. The k-ε model overestimates the length of the reverse flow zone considerably. Both RSE variants predict too short separation, and there is little difference between the results obtained with the two versions of near wall treatment. The LES shows better agreement with the experiments than the RSE computations, although LES still underestimates the length of the separation region.

3) Kinetic energy of fluctuations $< k_{to}>_t$, $< k_s >_t$ (Fig.11 (b), (c))

As shown in Fig.11 (b), the two-layer k-ε model underestimates severely the total fluctuation level behind the cylinder, while the RSE computations give approximately the correct level and distribution of total fluctuations. In front of the cylinder, the standard k-ε model yields an unrealistically high fluctuation level (here, only turbulent fluctuations exist) due to excessive turbulence production by this model in stagnation regions, as pointed out by Murakami et al. [22-26]. The RSE does not have this problem. But, Franke

Table 4 Computed cases of LES and RANS models and comparison of Integral Parameters

cases		$L_1 \times L_2 \times L_3$	$N_1 \times N_2 \times N_3$	S_t	$<C_D>_t$	$\tilde{C}_D$	$\tilde{C}_L$
Present LES computation		20×14×2	104×69×10	0.132	2 09	0.13	1.60
Franke and Rodi [1]	standard k-ε two layer	20×14	186×156	0.124	1.79	0.0	0.32
	RSE wall funct.	20×14	70×64	0.136	2.15	0.38	2.11
	RSE two layer	20×14	186×156	0.159	2.43	0.08	1.84
Launder and Kato [6, 7]	standard k-ε wall funct.	20×14	104×70	0.127	1.66		0.1
	modified k-ε wall funct. (eqn.(8) in Note5)	20×14	104×70	0.145	2.05	0.03	1.16
Przulj and Younis [8]	modified k-ε wall funct. (eqn.(10) in Note6)	35×12	114×92	0.132	2.33	0.92	4.72
Lyn [5]	experiment (Re=22,000)			0.135	2.05-2.23		
Durao [19]	experiment (Re=14,000)			0.139			

$\tilde{C}_D, \tilde{C}_L$: Amplitude of phase averaged drag and lift coefficient,
No velocity fluctuation is imposed at the inflow boundary for the LES computation.

46

and Rodi have shown that all turbulence models tested by them produce too low turbulent fluctuations, $< k_s >_t$, in the wake of the cylinder, as shown in Fig.11 (c) (cf.Note 4). This means that the periodic fluctuations are greatly overestimated by the RSE model. As for the LES computation, it predicts the correct distribution of the fluctuations, but the level is too low in general for both $< k_{to} >_t$ and $< k_s >_t$. LES produces a higher turbulent fluctuation level, $< k_s >_t$, in downstream region, which would be nearly correct, but is too low by about a factor of 2 in the peak region around $x_1/H = 2$. Hence, both total and stochastic turbulent fluctuations are underestimated in the LES simulation. Individually, the LES results are both closer to the measured level than those predicted by the RSE models.

4) Phase averaged velocity $< \overline{u}_2 >_p$ (Fig.12)

The agreement of wall function RSE and LES computations with the measurements is fairly good in general. On the other hand, the result of two-layer RSE slightly overestimates the value of $< \overline{u}_2 >_p$, in comparison with the results of LES and wall function RSE.

5) Phase averaged turbulent kinetic energy $< k_s >_p$ (Fig.13)

Here, the LES computation appears to reproduce the observed behavior better than the computations with the RSE model. The asymmetry in the contour lines predicted by the RSE model is basically the same as in the experiments, but the maxima of $< k_s >_p$ in the experimental data are located much closer to the centerline than in the computations. This points to a weakness in the RSE model, which appears to predict the centers of the shed vortices considerably farther from the centerline than the experiments indicate. The LES computation appears to predict the maxima of $< k_s >_p$ closer to the centerline.

3.2 Performance of the modified k-ε models

Recently, two different types of modified k-ε models were proposed by Launder and Kato [6, 7] (hereafter LK model), and Przulj and Younis [8] (PY model). Details of these models are given in Notes 5 and 6 respectively.

The results of these models are also included in Table 4. The consequence of the modi-

(a) Time averaged velocity $< \overline{u}_1 >_t$ along centerline

(b) Total kinetic energy of fluctuations $< k_{to} >_t$ along centerline
(periodic+stochastic, time averaged value)

(c) Time averaged kinetic energy of stochastic turbulent fluctuation $< k_s >_t$ along centerline (cf.Note 4)
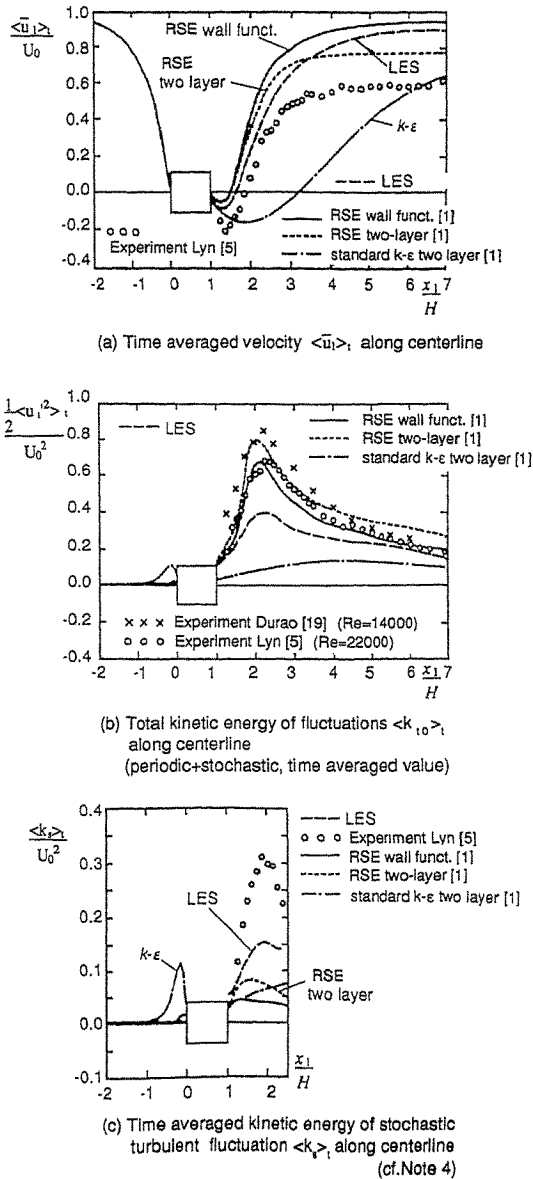
Fig.11 Comparison of LES with k - ε / RSE and experiments [2]
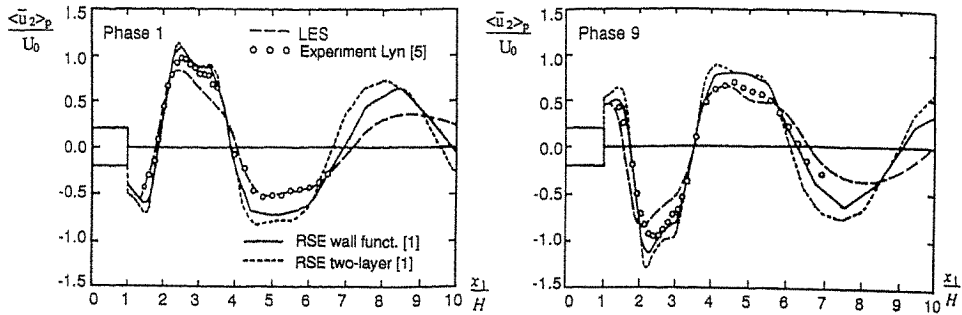
Fig.12 Phase averaged lateral velocity $<\bar{u}_2>_p$ along centerline at 2 phases [2]
(phase 1=1/20T, phase 9=9/20T)

experiment [5]   LES   two layer RSE [1]
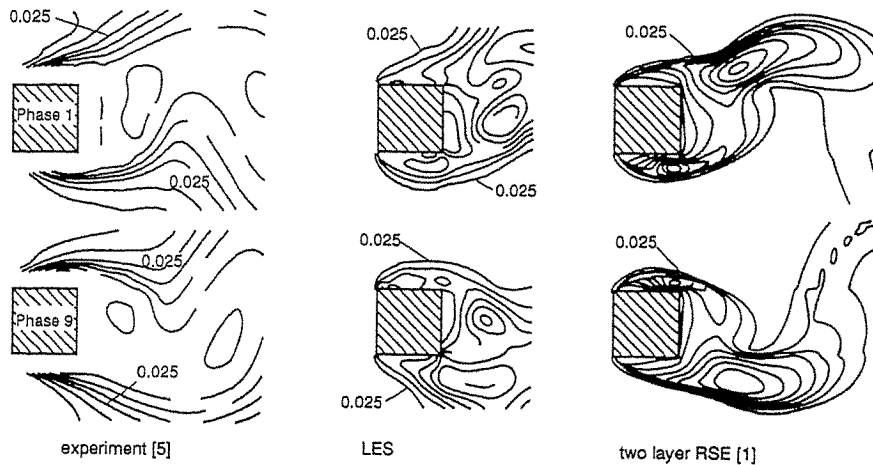
Fig.13 Contours of phase averaged stochastic turbulent kinetic energy $<k_s>_p$ at 2 phases [2]

fication for P_k in the case of LK model is clear in the values of $\widetilde{C_L}$. There is an order of magnitude increase in $\widetilde{C_L}$ resulting from the use of modified production as is shown in Table 4. The use of eqn.(8) in Note 5 in place of eqn.(7) gives remarkably closer agreement with the LES. On the other hand, $\widetilde{C_L}$ given from PY model becomes too high in comparison with that of LES.

Fig.14 (a) compares the time-averaged velocity $<u_1>_t$ along the centerline. LK model (with $C_\mu(<S>_p)$) reproduces the size of the reverse flow zone rather well in comparison with the result of the RSE computation of Franke and Rodi [1] which underestimates it by about a factor of 2.

The total kinetic energy of fluctuations $<k_{t_0}>_t$ is illustrated in Fig.14 (b). $<k_{t_0}>_t$ given from the standard k-ε model computation conducted by Launder and Kato [6, 7] shows excessively large production of turbulent fluctuations in the stagnation region as well as in the result with the standard k-ε model by Franke and Rodi [1] (Fig.11 (b)). Unfortunately this problem still exists in the result of PY model as is indicated in Fig.15, while the accuracy for the prediction of $<k_{t_0}>_t$ is improved remarkably in the stagnation region by LK model (Fig.14 (b)). On the other hand, $<k_{t_0}>_t$ is somewhat underestimated in the wake region by LK model when C_μ is treated as constant. Significant improvement is attained by varying the value of C_μ in space using eqn.(9) in Note 5 (Fig.14 (b)). It is rather surprising that distribution of $<k_{t_0}>_t$ given by PY model shows very close agreement with the experiment in the wake region although $<k_{t_0}>_t$ is severely overestimated in the stagnation region by this model (Fig.15).

48

4. 3D LES COMPUTATION OF UNSTEADY PRESSURE FIELD AROUND AN OSCILLATING SQUARE CYLINDER

4.1 Outline of numerical simulation

Fig.16 illustrates the flow conditions for simulation treated here. The square cylinder is forced to oscillate in a sinusoidal motion in the x_2 (lateral) direction. Table 5 lists the fifteen cases that are considered: two different values for the amplitude (A/H), and nine different values for the oscillation frequency($N_p H/U_0$); case 0 refers to the case of fixed cylinder. In the experiment, the lock-in phenomena occur for all the cases considered herein.

The governing equations are given in Table 6. Reynolds number based on H and U_0 is 2.2×10^4, which corresponds approximately to that in the experiment by Bearman et al.[9].

In the present computation, the whole grid layout (i.e., the coordinates) is treated to move together with the body motion. In order to incorporate the influence of the body motion, some technique is applied to simplify the computation [28]. Instead of moving the body, here the inertia force term, $\dot{V}_p$, whose magnitude is equal to the acceleration of the body, but with the opposite sign, is added to the transport equation of $\overline{u}_2$ as an external force at every grid point of the fluid, including points at the inflow boundary (cf. Table 6). Equivalent form is easily obtained, using ALE (Arbitrary Lagrangian-Eulerian) method proposed by Hirt et al.[29], by letting the spatial derivative of V_p be 0. Numerical methods and boundary conditions are summarized in Note 7.

4.2 Results and discussion
(1) Frequency of Lift Force (Fig.17)

Fig.17 compares the lift force acting on the fixed cylinder (case 0) and the oscillating cylinder (case 23), wherein the imposed body frequency is 0.12(1/8.5= $N_p H/U_0$). The Strouhal number for the case of the fixed cylinder, $(S_p)_F$, is 0.14 (1/7.3) , while it decreases to 0.12, the value of the imposed body frequency for the case of the oscillating cylinder. This change in the vortex shedding frequency by the body motion is known as the lock-in phenomena, which is reproduced successfully in the present computation. The lock-in phenomena is also observed in all other cases conducted here.

(a) time averaged velocity <u₁>, along centerline

(b) total kinetic energy of fluctuations<k₁₀>,along centerline

.... RSE wall funct. [1]
——— standard k-ε wall funct. [7]
—·—— modified k-ε (LK model) wall funct. [7]
—··—·· as above with C_μ(<S>_p) from eq.(9) in Note 5 [7]
· · Experiment Lyn [5]
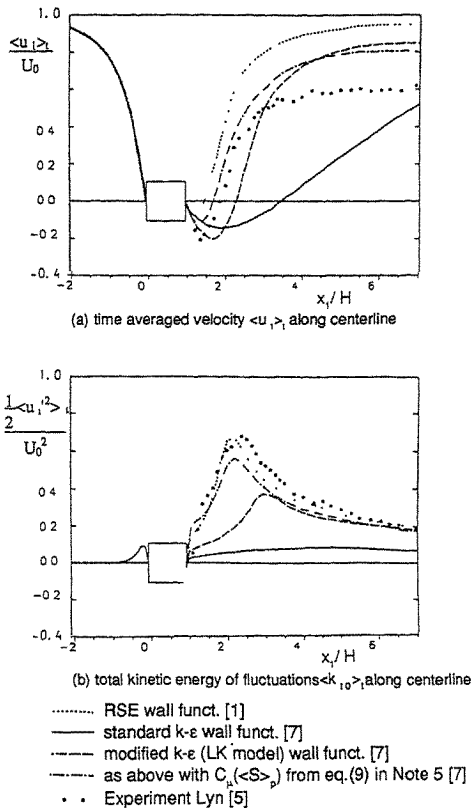
Fig.14 Comparison of LK model with standard k-ε model [7]

□ Experiment Lyn [5]
△ Experiment Durao [19]
——— modified k-ε model (PY model) wall funct. [8]
—·— RSE wall funct. [1]
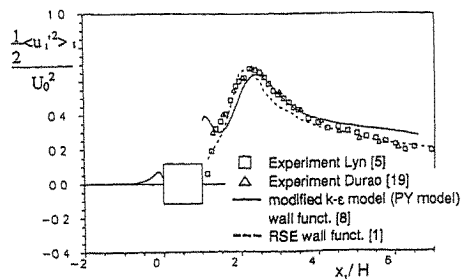
Fig.15 Comparison of PY model with experiment (total kinetic energy of fluctuations <k₁₀>, along centerline) [8]

Table 5 Computed cases

Frequency (non-dimension) (N$_p$H/U$_0$)	Amplitude (A/H)			Frequency (non-dimension) (N$_p$H/U$_0$)	Amplitude (A/H)	
	0 0	0 10	0 25		0 10	0 25
---	case0			1/9 0	case14	---
1/7 0		case10	case20	1/9 5	case15	---
1/7 5		case11	case21	1/10 0	case16	case24
1/8 0		case12	case22	1/11 0	---	case25
1/8 5		case13	case23	1/12 0	---	case26

N$_p$ cylinder oscillation frequency

Table 6   Model equations for LES
(modified for including the effect of ocsillation) [28]

$$\frac{\partial \overline{u_i}}{\partial t} + \frac{\partial \overline{u_i}\ \overline{u_j}}{\partial x_j} = -\frac{\partial}{\partial x_i}\left(\frac{\overline{p}}{\rho} + \frac{2}{3}k_{sas}\right) + \frac{\partial}{\partial x_j}\ (\nu + \nu_{SGS})\cdot \overline{s_{ij}} - \dot{V}_p \delta_{i2}$$

$$\frac{\partial \overline{u_i}}{\partial x_i} = 0$$

$$\nu_{SGS} = \left(C_s\cdot h\right)^2\ \left(\frac{(\overline{s_{ij}})^2}{2}\right)^{\frac{1}{2}} \quad \overline{s_{ij}} = \frac{\partial \overline{u_i}}{\partial x_j} + \frac{\partial \overline{u_j}}{\partial x_i} \quad k_{sas} = \frac{\nu_{SGS}^2}{\left(C_K\cdot h\right)^2}$$

$$h = (h_1 h_2 h_3)^{1/3}\times(1-\exp(y^+/25)),\ C_s=0.10,\ C_K=0.094$$
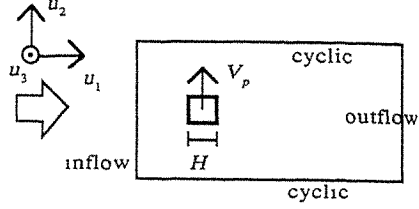
Fig.16 Flow conditions for simulation

$(V_p=2\pi N_p A\cos(2\pi N_p t))$

(2) Phase Angle between Body Motion and Fluid Force (Figs. 18 and 19)

Fig.18 shows the time histories of the displacement of the oscillating square cylinder and the negative pressure acting at the center of the side face of the cylinder for the case 23. The phase angle between the two is about -30° which corresponds well with the experimental value as shown in Fig.19. In Fig.19, the phase angles for the other thirteen cases at A/H=0.1 and 0.25 are also plotted. The predicted phase angles for these cases correspond rather well with the experimental values.

(3) Correlation between Pressures on the Side Face (Fig.20)

Fig.20 compares the distributions of correlation values for the pressures across the side faces. Fig. 20 (1) compares the case of fixed cylinder (case 0) and Fig.20 (2) compares the case of oscillating cylinder (case 11: N$_p$H/U$_0$=1/7.5). As for the oscillating cylinder, the experimental data corresponds to the case of N$_p$H/U$_0$=1/7.9. The values of the imposed body frequency (N$_p$H/U$_0$) locate in the lock-in range both in the computation and in the experiment, although the conditions for the computation and the experiment are not exactly the same. Thus, it is possible to compare the tendency of correlation distribution influenced by the body motion. The computational results show that the correlations decrease rapidly according to the distance from the reference points in the case of oscillating cylinder, in comparison with the case of fixed cylinder. This tendency agrees well with the results of the experiment.

50
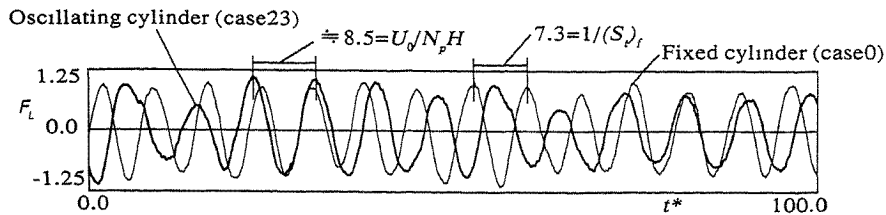
Fig.17　Time history of lift force [28]
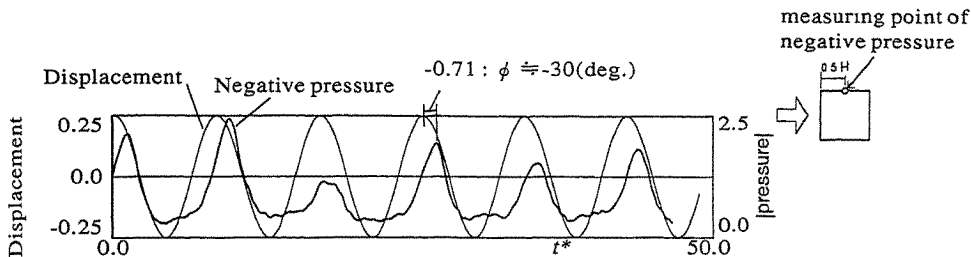
Fig.18　Time history of negative pressure on side and body displacement [28]
(Computation . case 23; A/H=0 25, N_pH/U_o = 1/8 5)

phase angle

X : Experiment [9]　0.10
△ : Experiment [9],　0 25
● : Computation,　0 10
□ : Computation,　0 25
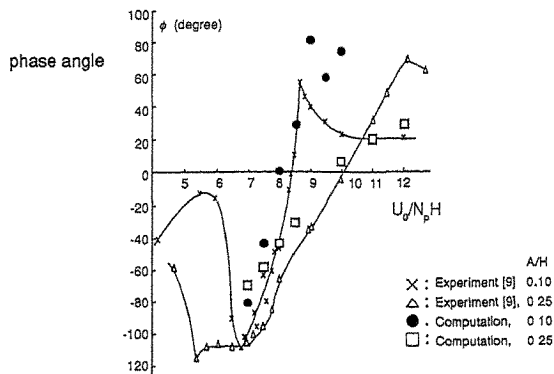
Fig.19　Phase angle of negative pressure
on the side and body displacement [28]

—□— : Experiment [9]
(N_pH/U_o=1/7.9)
——— : Computation
(N_pH/U_o=1/7.5)

(1) Fixed cylinder　　(2) Oscillating cylinder (A/H=0 1)
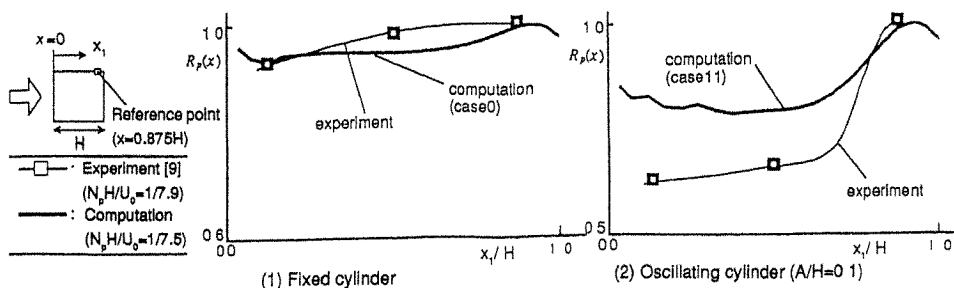
Fig.20　Distribution of correlation Rp(x) between pressures on the side face [28]

51

5. CONCLUSION

The numerical prediction of turbulent flowfield around a square cylinder is one of the most difficult problems in the field of CFD at this stage, since the flowfield is very complicated, characterized by the impinging, the separation at the frontal corner with steep streamline curvature , the recirculation behind the model and the vortex shedding, etc.

The numerical analyses of vortex shedding flow with various turbulence models are presented here. The standard k-ε model did not succeed in reproducing the vortex shedding at all. However, the modified k-ε model succeeded in reproducing it well, with an accurate prediction of some integral parameters. Reynolds stress model reproduced the vortex shedding rather well, but the results show many discrepancies between the experiments, e.g., the overestimation of periodic fluctuation. In general, LES shows best agreement with the experimental results in many respects. However LES results still have some points to be improved. CFD technique makes it possible to analyze the velocity and pressure fields around an oscillating cylinder with certain accuracy.

The improvement of accuracy usually requires the increase of CPU resources. LES needs a great deal of CPU time. Further efforts are expected to be made to develop more reliable turbulence models and more simple and less time-consuming CFD methods.

Note 1 Outline of 2D and 3D LES computations of flow past fixed square cylinder at Re=1.0×10⁵

Model equations are shown in Table 1. The standard Smagorinsky type subgrid scale model was used. The value of the Smagorinsky constant Cs for 2D computation is increased by 50 % in comparison with that for 3D computation in order to compensate for the limited diffusion in the spanwise direction. Specifications for 2D and 3D computations are summarized in Table 2. The Reynolds number based on the cylinder width, H, and the velocity at the inflow boundary, U_0, is 1.0×10^5. No velocity fluctuation is imposed at the inflow boundary. The turbulence levels are 0.04 % in the experiment of Bearman [9] and 0.2 % in the experiment of Ohtsuki [3], respectively. A staggered grid was adopted and a second-order centered difference scheme was applied for the calculation of spatial derivatives. For time advancement, the Adams-Bashforth scheme was used for both convection and diffusion terms. For boundary conditions at solid walls, the generalized logarithmic law (Launder and Spalding [10]) expressed by

$$\frac{<\overline{u}_w>_t}{<\tau_w/\rho>_t}(C_\mu^{1/2}k_w)^{1/2}=\frac{1}{\kappa}\ln\left(\frac{E \cdot \frac{1}{2}h_w(C_\mu^{1/2}k_w)^{1/2}}{\nu}\right) \quad , \qquad (1)$$

was employed in order to estimate the time-averaged wall shear stress, $<\tau_w>_t$. Furthermore, the following relation was used to specify the instantaneous wall shear stress τ_w [11, 12].

$$\tau_w=<\tau_w>_t\times\frac{(\overline{u})_w}{<(\overline{u})_w>_t} \quad . \qquad (2)$$

In the 3D computation, the computational domain covers $32.85 \, H \times 11.0 \, H \times 2.0 \, H$ in the streamwise (x_1), lateral (x_2) and spanwise (x_3) directions, respectively. $99 \times 63 \times 10$ grid points are placed in each direction. For the 2D computation, the computational domain covers the same length of streamwise and lateral directions, and the same number of grid points are placed in both directions, but the computation has no dimension in the spanwise direction.

The interval of time advancement is 2×10^{-4} in non-dimensional time scale, which is the scale based on H and U_0. Starting from the initial conditions, the computations required 5.0×10^5 time steps (100 in non-dimensional time scale) to reach stable periodic conditions. The computations were then continued further for 2.05×10^6 steps (410 in non-dimensional time scale). Thus statistically reliable averaged values were obtained.

Table 1 Model equations for LES

$$\frac{\partial \bar{u_i}}{\partial t} + \frac{\partial \bar{u_i}\,\bar{u_j}}{\partial x_j} = -\frac{\partial}{\partial x_i}\left(\frac{\bar{p}}{\rho} + \frac{2}{3}\,k_{SGS}\right) + \frac{\partial}{\partial x_j}(\nu + \nu_{SGS})\bar{s}_{ij}$$

$$\frac{\partial \bar{u_i}}{\partial x_i} = 0$$

$$\nu_{SGS} = (C_s\ h)^2\left(\frac{(\overline{s}_{ij})^2}{2}\right)^{\frac{1}{2}} \qquad \bar{s}_{ij} = \frac{\partial \bar{u_i}}{\partial x_j} + \frac{\partial \bar{u_j}}{\partial x_i} \qquad k_{SGS} = \frac{\nu_{SGS}^2}{(C_K\ h)^2}$$

2D computation : $h = (h_1 h_2)^{1/2}$, $C_s = 0\ 15$, $C_K = 0\ 094$
3D computation : $h = (h_1 h_2 h_3)^{1/3}$, $C_s = 0\ 10$, $C_K = 0\ 094$

Table 2 Specifications for LES computations

| case | $L_1 \times L_2 \times L_3$ | $N_1 \times N_2 \times N_3$ | boundary conditions | | x_2 | x_3 |
			inflow	outflow		
2D LES	32.85×11 0	99×63	$\bar{u}_1$=1 0, $\bar{u}_2$=0 0	$\bar{u}_1, \bar{u}_2$. $\partial/\partial x_1$=0	periodic	------
3D LES	32.85×11 0×2.0	99×63×10	$\bar{u}_1$=1 0, $\bar{u}_2$=$\bar{u}_3$=0.0	$\bar{u}_1, \bar{u}_2, \bar{u}_3$ $\partial/\partial x_1$=0	periodic	periodic

L_i . computational domain for x_i direction (normalized by H) N_i : number of grid points in the x_i direction
Δt . interval for time advancement = 0.0002 h_w : mesh interval adjacent to the solid wall = 0 05
No velocity fluctuation is imposed at the inflow boundary

Note 2 This term is usually referred to as "turbulent transport term" in many papers. In section 2.5, we also call this term "turbulent transport term", following the previous papers. But it should be mentioned here that the this term includes not only the transport of ω_3' by the turbulent velocity fluctuations but also the transport by the periodic velocity fluctuations. The exact definition of turbulent velocity fluctuation is described in section 3.1.

Note 3 Outline of LES computations of flow past fixed square cylinder at Re=2.2×10⁴

The standard Smagorinsky type subgrid model, shown in Table 1, was applied, as well as for the computations presented in the previous sections. The value of the Smagorinsky constant C_s was 0.13 for this case. Because the Reynolds number, which is 2.2×10^4, is lower than that in the previous section, the grid scales are multiplied by the Van Driest type wall damping function, $1-\exp(-y^+/25)$, in order to account for the near wall effect. For the computations conducted here, a second-order centered difference scheme proposed by Piacsek and Williams [20], which insures spatial conservation of quadratic values, was adopted for the spatial derivatives. For time advancement, the Adams-Bashforth scheme was used for the convection terms and the Crank-Nicolson scheme for the diffusion terms. The interval for time advancement is 1.0×10^{-3} in non-dimensional time scale based on U_0 and H.

The computational domain covers 4.5H upstream of the cylinder, 14.5H downstream and 6.5H on either side of the cylinder. The size of the domain in the plane perpendicular to the cylinder is exactly the same as that in Franke and Rodi's computation [1, 2]. 104×69 grid points were placed in the streamwise and lateral directions, respectively. The grid interval h_w adjacent to the cylinder wall is 0.022. This value is the same as that for Franke and Rodi's wall function case. Franke and Rodi set $h_w = 0.00125$ in the two-layer approach. At the inflow boundary, the approach flow was set to be constant and uniform and no velocity fluctuations were prescribed in the LES computations, while the turbulence level of the approach flow was 2% in Lyn's experiments and Franke and Rodi's computations. At the outflow boundary, zero gradient conditions were imposed. Symmetry conditions were employed for the lateral boundaries, and periodicity conditions were imposed for the boundary planes perpendicular to the cylinder axis. For the boundary condition at the solid walls, Werner and Wengle's approach [21] assuming a linear or 1/7 power law distribution

of the instantaneous velocity is adopted :

$$\frac{\overline{u}}{u_*} = y^+ \quad (y^+ \leq 11.81) \;, \tag{3}$$

$$\frac{\overline{u}}{u_*} = 8.3 \, y^{+1/7} \quad (y^+ > 11.81) \;. \tag{4}$$

This approach was chosen because the Reynolds number, which is 2.2×10^4, is lower than that for the previous case.

The computations required 1.5×10^5 time steps (150 in non-dimensional time scale) to reach stable periodic conditions. The computations were continued further for 1.0×10^5 steps (100 in non-dimensional time scale) covering 13 shedding periods. The time averaged values were determined by time averaging over these 13 periods as well as by averaging over the spanwise direction.

Note 4 We could sample data necessary for the $<k_s>_t$ computation only in the area close to the cylinder. This was due to the limitation of the computer memory.

Note 5 Modified k-ε model proposed by Launder and Kato [6, 7] (LK model)

Launder and Kato defined dimensionless strain and vorticity parameters:

$$<S>_p = k_s/\varepsilon \{1/2(\partial <u_i>_p/\partial x_j + \partial <u_j>_p/\partial x_i)^2\}^{1/2} \;, \tag{5}$$

$$<\Omega>_p = k_s/\varepsilon \{1/2(\partial <u_i>_p/\partial x_j - \partial <u_j>_p/\partial x_i)^2\}^{1/2} \;. \tag{6}$$

The production term of turbulent kinetic energy can be written as follows using the definition of $<S>_p$ in eqn.(5).

$$P_k = C_\mu \varepsilon <S>_p^2 \;. \tag{7}$$

In LK model eqn.(7) is replaced by the following equation.

$$P_k = C_\mu \varepsilon <S>_p <\Omega>_p \;. \tag{8}$$

The values of $<S>_p$ become very large in the stagnation region and the very large values of $<S>_p$ lead to the excessive level of P_k when the original form of eqn.(7) is used. However, the deformation near a stagnation point is nearly irrotational, i.e. $<\Omega>_p = 0$. Thus the replacement $P_k = C_\mu \varepsilon <S>_p <\Omega>_p$ leads to a marked reduction in turbulence production P_k near the stagnation point while having no effect in a simple shear flow.

Further modifications have been proposed by Craft et al.[27] involving a dependence of C_μ on $<S>_p$. Kato and Launder [7] carried out a computation using the model by Craft et al.[27] in which C_μ is treated as a function of $<S>_p$:

$$C_\mu = \min [0.09, 0.3/(1+0.35 \times S^{*1.5})] \;; \; S^* = \min [20, <S>_p] \;. \tag{9}$$

Note 6 Modified k-ε model proposed by Przulj and Younis [8] (PY model)

Przulj and Younis [8] added the time-dependent source term to the ε equation as follows.

$$C_{\varepsilon 1} P_k \frac{\varepsilon}{k_s} (1 + C_t \frac{k_s}{\varepsilon} \frac{|\partial q/\partial t|}{q}) \;, \tag{10}$$

where q is the mean kinetic energy $1/2 <u_i>_p <u_i>_p$. A new coefficient C_t was introduced ; its value was set as 0.26, assigned by computer optimization [8].

Note 7 Numerical methods and boundary conditions for LES computations of flow past oscillating square cylinder at Re=2.2×10⁴

The Van Driest type wall damping function, $1 - \exp(y^+/25)$, is introduced in order to account for the near wall effect. The second order centered difference scheme proposed by Piacsek and Williams [20] was used for the convection terms. For time advancement, the Adams-Bashforth scheme was used for the convection terms and the Crank-Nicolson scheme for the diffusion terms. The size of the computational domain and the boundary conditions are summarized in Table 7. The number of grid points is also indicated in the Table. The minimum grid interval adjacent to the solid wall was set at 0.025. For the boundary conditions at the solid wall, Werner and Wengle's approach [21] is adopted, as well as in the computations in the previous section.

54

Table 7 Computational domain and boundary conditions

$L_1 \times L_2 \times L_3$ $N_1 \times N_2 \times N_3$	boundary conditions		x_2	x_3
	inflow	outflow		
$20 \times 12 \times 2$ $104 \times 69 \times 10$	$\overline{u}_1 = 1.0$, $\overline{u}_2 = -V_p$, $\overline{u}_3 = 0.0$	$\overline{u}_1, \overline{u}_2, \overline{u}_3 : \partial / \partial x_1 = 0$	cyclic	cyclic

Δt : time interval for time marching = 0.001
h_w : grid interval adjacent to solid wall = 0.025
Wall boundary conditions:power law type two layer model[cf.eqns.(3) and (4) in Note3]
No velocity fluctuation is imposed at inflow boundary.

Nomenclature

x_i : three components of the spatial coordinate,
    ($i = 1, 2, 3$: streamwise, lateral, spanwise),
u_i : three components of the velocity vector,
ω_i : three components of vorticity vector
f : instantaneous value of a quantity,
$\overline{f}$: filtered value of f,
$<f>_t$: time averaged value of f,
$<f>_p$: phase averaged value of f,
$\tilde{f}$: $\tilde{f} = <f>_p - <f>_t$, periodic fluctuations,
f'' : $f'' = f - <f>_p$, stochastic turbulent fluctuations,
f' : $f' = f - <f>_t$, total fluctuations (periodic + stochastic),
H : width of the square cylinder,
U_0 : u_1 value at inflow of computational domain,
p : pressure, $<p_0>_t$: reference static pressure,
C_p : instantaneous pressure coefficient,
    $C_p = (p - <p_0>_t)/(1/2 \rho U_0^2)$,
C_{prms} : rms pressure coefficient, $C_{prms} = \{<p'^2>_t\}^{1/2}/ (1/2 \rho U_0^2)$,
$<k_{to}>_t$: total kinetic energy of fluctuation,
    (periodic+stochastic, time averaged value),

k_s : kinetic energy of stochastic turbulent fluctuation,
    $<k_{to}>_t = 1/2<u_i' u_i'>_t$, $k_s = 1/2<u_i'' u_i''>_p$,
C_s : Smagorinsky constant (cf. Table 1),
ν_{SGS} : subgrid scale eddy viscosity,
k_{SGS} : subgrid component of k, ·
h_w : grid interval adjacent to the solid wall,
$(u_t)_w$: tangential velocity component at the near wall node,
k_w : total kinetic energy of fluctuations at the near wall node,
$y+$: $u_* y / \nu$, u_* : friction velocity,
n : frequency, $S(n)$: power spectrum,
F_L : instantaneous lift force, F_D : instantaneous drag force,
S_t : Strouhal number, T : one shedding period (=1/S_t)
$(S_t)_f$: S_t of the fixed cylinder,
V_p : velocity of the forced oscillation of the square cylinder,
    $V_p = 2\pi N_p A \cos(2\pi N_p t)$
A : displacement of the oscillating cylinder
N_p : frequency of the oscillating of the cylinder

When values are made dimensionless, the representative length scale H, velocity scale U_0 and air density ρ are used.

REFERENCES
[1]Franke, R. and Rodi, W. ; Calculation of vortex shedding past a square cylinder with various turbulence models, Proc. 8th Symp. on Turbulent Shear Flows, p.189, 1991.
[2]Rodi, W. ; On the Simulation of Turbulent Flow Past Bluff Bodies, Preprints. 1st Int. Symp. on Computational Wind Eng., Tokyo, 1992.
[3]Y.Ohtsuki et al. ; Wind tunnel experiments on aerodynamic Forces and pressure distributions of rectangular cylinders in a uniform flow, Proc. the 5th Symposium on Wind Effects on Structures, pp.169-175, Tokyo Japan, 1978.
[4]B.J.Vickery ; Fluctuating lift and drag on a long cylinder of square cross-section in a smooth and in a turbulent stream, J.Fluid Mech., vol.25, pp.481-494, 1966.
[5]Lyn, D.A. ; Ensemble-averaged measurements in the turbulent near wake of a square cylinder : Private communication, 1992.
[6]Launder, B.E. and Kato, M.;Modelling Flow-induced Oscillations in Turbulent Flow around Square Cylinder, Proceedings of Forum on Unsteady Flows (FED-vol.157) , ASME 1993, pp.189, 1993
[7] Kato,M. and Launder,B.E.; The Modelling of Turbulent Flow around Stationary and Vibrating Square Cylinders, 9th Symp. on Turbulent Shear Flow, Kyoto, 1993
[8]Przulj, V. and Younis,B.A., Some Aspects of the Prediction of Turbulent Vortex Shedding from Bluff Bodies [FED-vol.149], ASME 1993, pp.75, 1993
[9]P.W.Bearman and E.D.Obasaju ; An experimental study of pressure fluctuations on fixed and oscillating square-section cylinders, J.Fluid Mech., vol.119, pp.297-321, 1982.
[10]Launder, B.E. and D.B.Spalding ; The numerical computations of turbulent flows, Comput. Methods Appl. Mech.Eng., 3, pp.269-289, 1974.
[11] G. Grötzach ; Direct numerical and large eddy simulation of turbulent channel flows, Encyclopedia of Fluid Mechanics, Vol.6, Complex Flow Phenomena and Modeling, pp.1337-1391, 1987.

[12] U. Piomelli, J. Ferziger and P. Moin , New Approximate Boundary Conditions for Large Eddy Simulations of Wall-Bounded Flows, Phys. Fluids, A1 (6), 1061, 1989.

[13]Sakamoto,S., Murakami,S. and Mochida,A.:Numerical Study on Flow past 2D Square Cylinder by Large Eddy Simulation-Comparison between 2D and 3D Computations, Second International Colloquium on Bluff Body Aerodynamics and Applications, Melbourne, Australia, 1992

[14]B.E.Lee ; The effect of turbulence on the surface pressure field of a square prism, J.Fluid Mech., vol.69, pp.263-282, 1975.

[15]H.Tennekes and J.L.Lumley, A First Course in Turbulence, the MIT Press, 1972

[16]Launder, B.E., Reece,G.J. and Rodi,W.;Progress in the development of a Reynolds-stress Turbulence Closure, J. Fluid Mech., Vol.68, pp.537-566, 1975

[17] Gibson, M.M. and Launder, B.E.; Ground Effects on Pressure Fluctuations in the Atmospheric Boundary Layer, J.Fluid Mech., Vol.86, p.491, 1987

[18]Norris,H.L. and Reynolds,W.C. ; Turbulent Channel Flow with Moving Wavy Boundary, Department Mech. Eng. Rept. FM-10, Stanford University, 1975.

[19]Durao, D.F.G., Heitor, M.V. and Pereira, J.C.F. ; Measurements of turbulent and periodic flows around a square cross-section cylinder, Experiments in Fluids, Vol.6, pp.298-304, 1988.

[20]S.A.Piacsek et al. ; Conservation Properties of Convection Difference Schemes, J. Computational Physics 6, pp.392-405, 1970.

[21]Werner, H. and Wengle, H. ; Large-eddy simulation of turbulent flow over and around a cube in plate channel, Proc. 8th Symp. on Turbulent Shear Flows, pp.155, 1991.

[22] S. Murakami et al. ; Scrutinizing k-ε EVM and ASM by means of LES and wind tunnel for flowfield around cube, 8th symp. on Turbulent Shear Flows, Munich, pp.17-1, 1991.

[23]Murakami,S., Mochida,A. and Hayashi,Y.:Examining the k-ε Model by means of a Wind Tunnel Test and Large-Eddy Simulation of the Turbulence Structure around a Cube, J.of Wind Eng. and Ind. Aerodyn.,Vol.35, pp.87-100, 1990

[24]Murakami,S.:Comparison of Various Turbulence Models applied to a Bluff Body, 1st Int. Sym. on Comp. Wind Eng., Tokyo, Japan, 1992

[25]Mochida,A. Murakami,S. Shoji,I and Ishida,Y:Numerical Simulation of Flowfield around Texas Tech Building by Large Eddy Simulation, 1st Int. Sym. on Comp. Wind Eng., Tokyo, Japan, 1992

[26]Murakami,S., Rodi,W., Mochida,A. and Sakamoto,S.;Large Eddy Simulation of Turbulent Vortex Shedding Flow past 2D Square Cylinders, Proceedings of Symposium on Engineering Applications of Large Eddy Simulations (FED-vol. 162), ASME 1993, pp.113, 1993

[27]Craft, T.J., Launder, B.E. and Suga, K.;Extending the Applicability of Eddy Viscosity Models through the Use of Deformation Invariants ", Proc. of 5th IAHR Conference on Refined Flow Modelling and Measurements, 1993

[28]Sakamoto, S. Murakami,S. and Mochida,A.:Unsteady Pressure Field around Oscillating Prism predicted by LES, 1st Int. Sym. on Comp. Wind Eng., Tokyo, Japan, 1992

[29]Hirt, C.W. et al.;An Arbitrary Lagrangian-Eulerian Computing Method for All Flow Speeds, J.Computational Physics 14, pp.227-253, 1974

[30]Murakami,S., Mochida,A., Hayashi,Y. and Sakamoto,S : Numerical Study on Velocity-pressure Field and Wind Forces for Bluff Bodies by k-ε, ASM and LES, J. of Wind Eng. and Ind. Aerodyn., Vol.41-44, pp.2841-2852, 1992

Interference between wind loading on group of structures*

T. F. Sun and Z. F. Gu

Department of Mechanics, Peking University

Beijing 100871, CHINA

Abstract: This paper presents a brief review of research on group effect done in Peking University in past several years. The aerodynamic characteristics of two circular cylinders in various arrangements at high subcritical and supercritical Reynolds numbers, two rectangular cylinders of different slenderness ratios as well as several kinds of group of cooling towers have been treated.

1. Introduction

In engineering practice, structures often appears in group, such as the buildings in congregated large cities, cooling towers in electricity generating stations, reaction towers in chemical industry, group of chimney stacks and many others. Even for a single structure, its components may appear in group, such as legs of offshore platforms, tube-arrays in heat exchangers etc. Due to mutual interference, the mean as well as fluctuating loading on one of the members of the group may be quite different from that of an isolated member. Catastrophic incident may result if group-effect on loading has not been considered in design. On the other hand, unexpected flow phenomena may happen due to interference [3]. For example, though two parallel identical circular cylinders in side-by-side arrangement, separated in certain gap ratio, are symmetric in geometry, the relevant flow may be flip-flopping randomly between two asymmetric status.

In last three decades or so, many researchers have devoted to studying the group-effect. A recent review is given by Ohya et al. [1]. The present paper intends to give a brief review of the work done in Peking University. It has the objectives of understanding the aerodynamic characteristics and thus the fundamental mechanism of the group-effect and,in certain cases, of industry application. The studies were usually conducted to measure and analyze the pressure distributions (mean and/or fluctuating) and to give drag and lift by integrating pressure. Measurements of vortex shedding and flow fields such as wakes as well as visualization of flow pattern by available experimental apparatus and instrumentations were also carried out in certain cases.

In the following, the interference between loading on two circular cylinders at high Reynolds numbers are treated in Section 2. Section 3 devotes to two rectangular cylinders and Section 4 to groups of hyperbolic cooling towers.

2. Group of Circular Cylinders

Group of two equal and parallel circular cylinders is the simplest case of group. Study

---

* This paper is dedicated to Professor William R. Sears for his eightieth birthday anniversary.

of this simplest one gives not only many interesting features of the group-effect and but may also give indications to that of more cylinders [2]. Thus it drew attentions of many researchers and work has been reviewed by Zdravkovich[3] and Ohya, et al[1]. But most of these work is limited to subcritical Reynolds numbers, usually of order of 10^4. In Peking University, it has been studied more or less systematically at high subcritical Reynolds numbers and at supercritical ones too. In this section, some of our results will be given, with emphasis on that of the staggered arrangement, though the results are preliminary.

Schematic diagram showing the two-cylinder configuration and the definitions of symbols is given in Fig. 1. The azimuth angle θ is measured from the direction of wind and varies from -180 to 180°. According to the common practice, the instantaneous pressure p (θ, t), varying with θ and time t, is decomposed into mean pressure $p(\theta)$ and fluctuating pressure $p'(\theta, t)$. $p'(\theta, t)$ should be described by means of statistical quantities and its root-mean-square value $\sigma_p(\theta)$ is the most important one. We define the mean and fluctuating pressure coefficients as $C_p = [p(\theta)-p_\infty]/0.5\rho V_\infty^2$ and $C_p' = \sigma_p(\theta)/0.5\rho V_\infty^2$, respectively. By appropriate integration, we have the drag coefficient C_D and lift coefficient C_L. Reynolds number Re is defined as $V_\infty d/\upsilon$. All these symbols have the usual meanings.

2.1 In staggered arrangement

Fig. 2 gives variation of pressure distributions on Cyl. A (front) and Cyl. B (rear) with wind direction β for N/d=1.7 and Re=3.3x10^5. Broadly speaking, there are three different pressure patterns I_B, II_B, III_B for Cyl. B and two patterns I_A, II_A for Cyl. A as described below:

[I_B] For 0°<β<9.75°, most of the C_p's is negative and C_p vs. θ curve has only one peak whose position θ_m is located on the outer side of cylinder, say about 40° or larger. The peak value C_{pmax} increases from negative to positive as β increases. From θ_m to around 130°, C_p curve concaves downward and attains minimum value C_{pmin} around 90°. On the inner side, pressure changes gradually and is rather flat but it is higher than the back pressure C_{pw} of Cyl. A.

[II_B] At β=9.75° (denoted by Γ_1, say) C_{pmax} on outer side jumps to 1 suddenly, located around θ_m=30°. It means that the oncoming velocity from infinity decreases to stagnation point θ_m on Cyl. B. C_p distribution on outer side is similar to the laminar-separated one. On the inner side, a large area of suction results, with C_{pmin} less than -2.0. It indicats there is flow of rather high velocity around the inner side. Change of patterns from I_B to II_B is of a discontinuous and random nature. II_B persists for a certain range of β, up to 15° at least in the present case.

[III_B] Between 15°<β<30° (at β=Γ_2, say), large area of suction disappears suddenly and the C_p vs. θ curve looks like laminar-separated on both sides. From Γ_2 on, III_B persists up to β=90° though the C_{pw} may vary and θ_m moves toward 0° and then to the inner side.

[I_A] For 0°<β<9.75°, C_p vs. θ curves looks like that of isolated cylinder, i.e. laminar-separated on both sides. C_p has maximum value of 1 at θ_m which is in the neighborhood of θ=0°. When β varies, C_{pw} and separation points θ_w may change.

[II_A] At β=9.75° (denoted by Γ_1' which may be different from Γ_1 in other cases), the C_p distribution on the inner side of Cyl. A suddenly becomes turbulent-separated, with C_{pmin} attaining a value as low as -3.5 near β=90°. On the outer side, the flow keeps lami-

58

nar-separated and C_{pmax} is equal to 1 at $\theta_m < 0°$. Pattern I_A persists much longer than I_B and disappears at β somewhere between 45° and 60° (at Γ_2', say). Then I_A returns back and persists up to $\beta = 90°$, with θ_m turning toward the inner side gradually.

The discontinuous and random change of flow patterns between I_B and II_B was pointed out by Zdravkovich [3,4]. The persistence of II_B for certain range of β was quite clear in paper by Suzuki et al. [5] who gave C_p vs. θ up to $\beta = 15°$. To present author's knowledge, no one has mentioned the sudden disappearance of II_B and the sudden change of I_A for Cyl. A. It should be mentioned that I_A occurs only for cases of smaller N/d and relatively higher Re. For example, no I_A appears at Re = 2.2x10⁵ for N/d = 1.7. On the other hand, the appearance of II_B during $\Gamma_1 \leqslant \beta \leqslant \Gamma_2$ is rather popular, though values of Γ_1 etc. may be different for different combinations of N/d and Re's. At Re = 3.3x10⁵, Γ_2 is generally larger than that at Re = 2.2x10⁵ for same N/d, i.e. the large area of suction on Cyl. B stays longer. We have studied N/d's from 1.05 to 5 for Reynolds numbers from 2.2x10⁵ to 6.5x10⁵. Pressure distribution patterns for small N/d, say smaller than 1.2, may be quite different from the general features mentioned above. We also have not found discontinuous change of pressure patterns at supercritical Re. Values of Γ's obtained at subcritical Re are given in Fig. 3.

C_D and C_L are shown in Fig. 4. The minimum C_D for each N/d is located generally between $\beta = 5°$ to 10° which is rather near to but does not coincide with the value of Γ_1. The line of Γ_1's represents a line of step-jump in C_L but not the inner C_{Lmax} line in general. For N/d $\geqslant$ 3.0, there are also the outer C_{Lmax} as pointed out in [3].

The discontinues change of pressure pattern at Γ_1 was attributed to gap flow by Zdravkovich[3,4]. Flow visualization at low Reynolds number of order of 10² to 10³[6] showed that there was a strong concentrated vortex rolling up in front of rear cylinder and shedding downstream through gap around the inner side of rear cylinder intermittently. Measurement of velocity across the gap by hot-wire anemometer in certain cases indicated there was a flow of high velocity, for $\beta > \Gamma_1$, which was 2 to 3 times large of oncoming velocity V_∞. More detailed and careful study of the flow mechanism should be conducted in order to have an appropriate and satisfactory explanation.

At supercritical Reynolds number, the interference between two cylinders is somewhat weaker than at subcritical Re in general. Fig. 5 gives the pressure distribution on Cyl. A and B at different β's for N/d = 1.7 and Re = 6.5x10⁵. For Cyl. A, C_p's on inner and outer sides keep the pattern of turbulent-separated. During 15° $\leqslant \beta \leqslant$ 45°, C_{pmin} on inner sides is higher than that on outer side but during 60° $\leqslant \beta \leqslant$ 90°, C_{pmin} on inner side is lower, attaining -3.5 approximately. Stagnation point θ_m moves to the inner side too. For Cyl. B, the variation of C_p is somewhat larger. Except $\beta = 0°$ and 5°, C_p vs. θ at outside has the pattern of turbulente-separated. There is also large area of suction on inner side, but it is developed gradually. For 60° $\leqslant \beta \leqslant$ 90°, C_{pmin} on inner side is also lower than that at outer side. It is the result of accelerated flow through the gap. At $\beta = 90°$, back pressures at both cylinders are equal and no biased flow does happen. The appropriate C_D and C_L are given in Fig. 4.

Fluctuating pressures for several cases were measured and analyzed[7]. For instance, at Γ_1 of staggered arrangement N/d = 2.2, Re = 3.3x10⁵, C_p' of as high as 0.45 has been observed on the inner side of rear cylinder while on outer side, C_p' has the value of 0.1 only. Fluctuating pressures are also weaker at supercritical Re. For N/d = 2.2 and Re = 6.

5×10^5, peak value of C_p' is about 0.26 only.

Interference effect between two cylinders in high-turbulent uniform flow has been studied (turbulence intensity Iu equal to 10%)[8,9,10]. It is interesting to note that for staggered arrangement in high-turbulent stream, the effect of rear cylinder on front one is, in general, larger than that of front cylinder on rear one.

2.2 In side-by-side arrangement ($\beta = 90°$)

The variation of C_D and C_L of Cyl. A and B in side-by-side arrangement, with gap ratio N/d, is given in Fig. 6 for Re=2.2x10^5. Similar to lower Re, there is biased flow for $1.1 \leqslant N/d \leqslant 2.0$. When $N/d \geqslant 2.2$, back pressures C_{pw} of Cyl. A and B are equal and their C_D's are equal too.

For certain N/d's, we did measurement at closer intervals of β near 90°. For example, at N/d=1.5, we found C_{pw} on Cyl. B is higher than that on Cyl. A for $\beta=75°$, 78°,79° and for $\beta=82°$, 85° C_{pw} on Cyl. B is lower. For $\beta=80°$ and 90°, both patterns of pressure distributions were recorded at same β. It means that the switching process appears not only at $\beta = 90°$ but also within a certain region in the neighborhood of $\beta = 90°$

For Supercritical Reynolds number Re=6.5x10^5, Cyl. A and B are equal for $N/d \geqslant 1.5$ and therefore both cylinders have same C_D's. No biased flow exits. But for $N/d \leqslant 1.2$, there are larger difference in C_{pw} and hence in C_D's. Biased flow seems to occur at rather small N/d's.

2.3 In tandem arrangement ($\beta = 0°$)

From the C_p distribution on Cyl. B (rear) for various N/d's at Re = 2.2x10^5, we find that, for $N/d \leqslant 2.8$, there are two peaks on both sides of front part of Cyl. B where the pressure is lowest and equal to C_{pw} on Cyl. A. It indicates that the shear layers separating from front cylinder reattach on rear cylinder and the flow within the gap is more or less stagnant. When $N/d \geqslant 3.0$, C_{pw} on Cyl. A and C_p on Cyl. B are rather unstable. In general C_p on front part of Cyl. B becomes higher than that on the rest part of Cyl. B and is larger than C_{pw} on Cyl. A. Nevertheless, we have recorded two different pressure patterns at N/d=3.4 and 3.5. One of them is what just mentioned above and the other is the stable one similar to that for $N/d \leqslant 2.8$. It may conclude that under the condition of the present test, the switching process occurs not at one single N/d but within a certain range, $3.0 \leqslant N/d \leqslant 3.8$, say. C_D of Cyl. A and B are given in Fig. 7. For supercritical Reynolds number Re=6.5x10^5, C_D of rear cylinder is higher than that of the front one and both of them vary not much for all N/d's tested (Fig. 7).

3. Group of Two-Rectangular Cylinders

The interesting aerodynamic characteristics of a single rectangular cylinder by effect of slenderness ratios is well-known. For group of two identical rectangular cylinders(Fig. 1), the effect of slenderness ratio b/h of rectangular cylinders should be considered in addition to N/h and β. In mid-eighties, without knowing the work of other authors (e.g. Okajima [13]), we did wind-tunnel test of the pressure distributions of two identical rectangular cylinders in various arrangements for a number of b/h's at Re=$V_\infty h/\upsilon$ equal to 1.03x10^5.

3.1 Two rectangular cylinders in side-by-side (L/h=0)

Fig. 8 gives the variation of C_D with gap-ratio T/h for five b/h's[11]. It may be seen that when T/h<1. 1, pressure distribution of cylinder I & II (not shown) are almost same and equal to that of isolated cylinder of 0. 5b/h. That is, the two cylinders behaves like a single body. When 1. 1<T/h<(T/h)$_c$, similar to two-circular cylinders, bistable biased flow appears. At Re=1. 03×10^5, values of (T/h)$_c$ are equal to 3. 1 for b/h=0. 3 and 0. 5, 2. 5 for b/h=1 and 2. 2 for b/h=2. For b/h=2, difference of two branches is rather small and for b/h=5. 0, C_D's of two cylinders for all T/h are essentially equal and are larger than that of isolated one. Thus biased flow is suppressed at larger b/h and practically does not appear for b/h=5.

3. 2 Two rectangular cylinders in tandem (T/h=0)

Variation of drag coefficients of C_D of cylinder I (front) and II (rear) with gap ratio (L-b)/h are given in Fig. 8 for six slender ratios b/h. When b/h≤1, C_D's of rear cylinder jump from negative to positive at [(L-b)/h]$_c$ but for b/h=2, C_D changes gradually from negative to positive. At b/h=5, C_D of both cylinders are positive for all L/h and, as L/h increases, C_D of front cylinder keeps constant and that of rear one increases slightly.

3. 3 Two Square cylinders in staggered arrangement

The C_D and C_L varying with β at a fixed N/h are given in Fig. 9 for four N/h's and that varying with N/h along a radial line of fixed β are given in Fig. 10. It is shown that switching process between flow patterns does occur in the neighborhood of 90°, same as that for circular cylinder mentioned above. Step change in C_D does happen too.

4. Group of Cooling Towers

Since the collapse of three cooling towers at Ferrybridge Power Station, much attention has been paid to investigate the wind loading of large hyperbolic cooling towers. We have conducted measurement of surface pressures on cooling towers of different kinds of groups in wind tunnels and participated in in-situ full-scale measurement[14-17].

Cooling tower is a typical three-dimensional structure of circular cross-section and is located in the so called atmospheric boundary layer stream. Its surface pressure varies not only with the azimuth angle θ (measured from wind direction) but also with the elevation Z (from base of tower) of the measurement points. In engineering design practice as well as for easy comparison for different test conditions, a "representative" C_p vs θ curve is usually used. By past experience, we think the average value of C_p from Z/H=0. 4 to Z/H=0. 8 (throat, H being the height of tower) along meridian line is an appropriate choice. This average value, in fact, nearly coincides with the C_p distributions at Z/H=0. 5 or 0. 55. In the following, we use this representative curve for discussion of interference effect of tower group.

Reynolds number of full-scale tower at design wind speed is of order of 10^8 and in wind tunnel model test, of order of 10^5 only. In order to obtain the pressure distribution on ribless tower at Re≈10^8 in model test at Re≈10^5, a number (say n) of equally distributed concentrated roughness of the scotch tape (or others) of width m and height k, was glued along meridian line of the model tower shell. m ,k, and n were chosen such that the C_p vs. θ of full-scale isolated tower at Re of order 10^8 has been simulated, (e. g. C_{pmin} nearly equal to -1. 5 was achieved at Re=1. 42x10^5, comparable to -1. 47 obtained on full-scale ribless

Maomin tower at $Re = 7.5 \times 10^7$[15]). Every towers of the tower-group tested was provided with the relevant roughness.

Atmospheric boundary layer (ABL) stream was simulated in wind-tunnel by means of vortex generators (e. g. spires) and roughness elements on tunnel floor such that the required wind velocity profile and turbulence structure were simulated at the model station.

For convenience, d_o, the diameter of base circle of tower, is used to nondimensionize the gap-ratio. d_o is about 1.5 times of the mean diameter d of tower.

4.1 Two-tower group

The variation of mean pressure distributions on Tower II (rear) of a simple two-tower group at different angle of wind β (not shown) is quite similar to that of circular cylinder and the fluctuating pressure distribution is given in Fig. 11. It is the result of wind tunnel test for the two-tower group built at Shi-Jing-Shan Power Station in the suburb of Beijing, China. Full-scale measurement of surface pressure on these towers was made during 1988-1990, first on Tower I (isolated) and then on Tower I & II. Comparison of full-scale measurement with wind-tunnel result with the effect of terrains and factory buildings etc. is given in Fig. 12. They agreed moderately well. For details, please see [15].

Flow visualization of towers showed that π-type vortex filaments shed from the tower surface, together with the horse-shoe vortices at the tower base.

4.2 Four towers in rhomboid arrangement

Fig. 13 shows the pressure distribution of four towers arranged in rhomboid for $\beta = 90°$. We find the peak suction C_{pmin} and C'_p on Tower C and D are larger than that of isolated tower.

4.3 Four towers arranged nearly in a longitudinal row

Four neighboring cooling towers of Sha-Lin-Zi Power Station are arranged nearly in line. Pressure distribution of the group were measured under different wind directions by wind tunnel test in uniform low-turbulent stream [16]. C_p' vs. θ curves on four towers under directions of prevailing wind ($\beta = 15°$) and of peak speed ($\beta = 37.5°$) as well as on isolated one are given in Fig. 14. C_p' on Tower C and D are much different from that on isolated one.

5. Concluding Remarks

From what presented above, it is evident that the study of interference effect of aerodynamic characteristics of flow around group of structures, or simply the group-effect, is important and essential both from view points of fundamental research in fluid dynamics and of engineering applications. It is also evident that more detailed study needs to be done.

Acknowledgment

References

1. Ohya, Y., A. Okajima and, M. Hayashi, Chap. 10 in Encyclopedia of Fluid Mechanics, Gulf Publishing, 1989
2. Price, S. J. and M. P. Paidoussis, J. Wind Engg. & Indus. Aerodyn., 17 (1984) 329-347
3. Zdravkovick, M. M., Trans. ASME, J. of Fluids Engg, 99(1977) 618-633
4. Zdravkovich, M. M., J. Wind Engg. & Indus. Aerodyn., 28(1988) 183-200
5. Suzuki, N., H. Sato and M. Iuchi, Proc. 3rd Inter. Symp. on Wind Effects on Buildings and Structures, Tokyo, (1971) 377-387
6. Yan, Dachun and Li, Chenxin, Acta Mechanica Sinica, 3(1987) 36-43
7. Sun, T. F., Z. F. Gu, D. X. He and L. L. Zhang, J. Wind Engg. & Indus. Aerodyn., 41-44(1992) 577-588
8. Gu, Z. F., T. F. Sun, D. X. He and L. L. Zhang, Acta Mechanica Sinica, 24(1992) 522-528 (in Chinese)
9. Gu, Z. F., T. F. Sun, D. X. He and L. L. Zhang, Proc. 5th Asian Congress of Fluid Mechanics, Aug. 10-14, 1992, Taejon, Korea, 53-56
10. Gu, Z. F., T. F. Sun, D. X. He and L. L. Zhang, Proc. Bluff Body Aerodynamics and Applications, Dec. 7-11, 1992, Melbourne, Australia.
11. Sun, T. F., S. T. Lin and Z. F. Gu, Preprint 7th Inter. Conf. on Wind Engineering, July 1987, Aachen, Germany.
12. Sun, T. F., S. T. Lin and Z. F. Gu, Proc. 4th Asian Congress of Fluid Mechanics, Aug. 1989, Hong Kong.
13. Okajima, A., R. Sugitani and T. Mizota, Trans. JSME, vol. 51 No. 472 (1985) 3877-3886 (in Japanese)
14. Sun, T. F. and L. M. Zhou, J. Wind Engg. & Indus. Aerodyn., 14(1983) 181-192
15. Sun, T. F., Z. F. Gu, L. M. Zhou, P. H. Li and G. L. Cai, J. Wind Engg. & Indus. Aerodyn. 41-44(1992) 2213-2224
16. Gu, Z. F., T. F. Sun and S. D. Ji, Acta Mechanica Sinica, 24(1992), 129-135 (in Chinese)
17. Wei, Q. D. et al., Electric Power Construction, vol. 12 No. 13 (1991) 44-50 (in Chinese)

(a)Circular　　　　(b)Rectangular
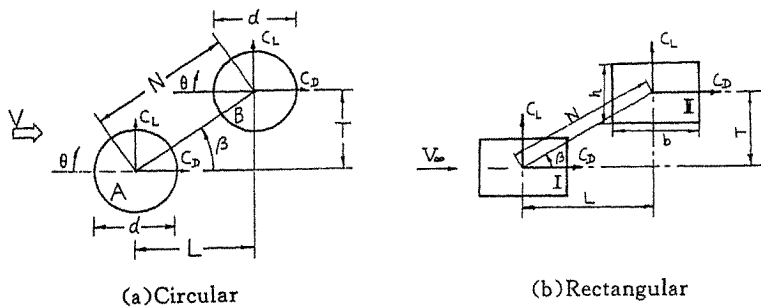
Fig. 1　Schematic diagram of two-cylinder group and notations defined
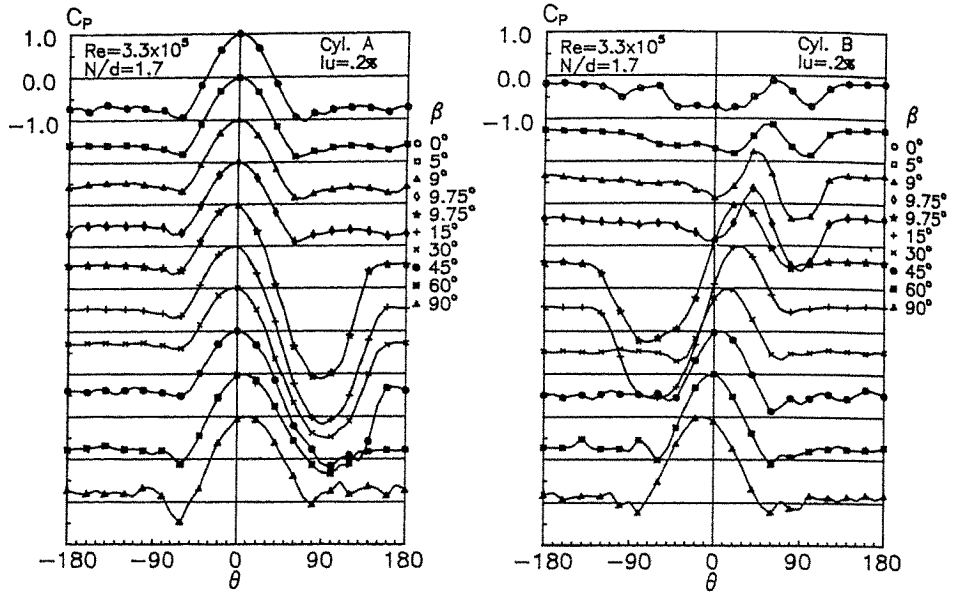
Fig. 2　Mean pressure distribution on two circular cylinders in staggered
arrangement (N/d=1.7, Re=3.3×10⁵)
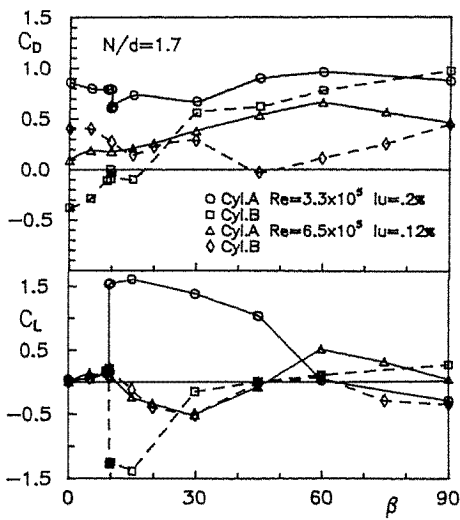
Fig. 4　Variation of C_D, C_L with β for
two circular cylinders in staggered
arrangement
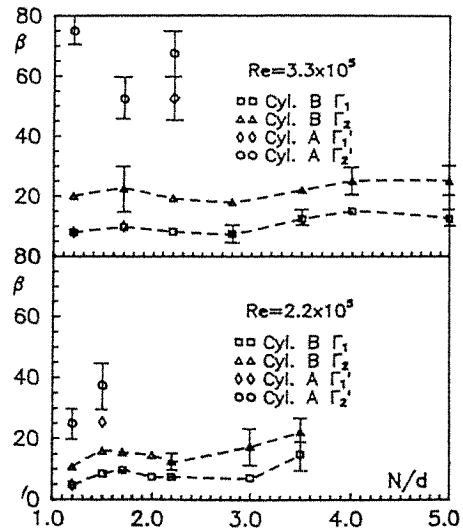
Fig. 3　Values of Γ's for different pressure
patterns on two circular cylinders
in staggered arrangement

64
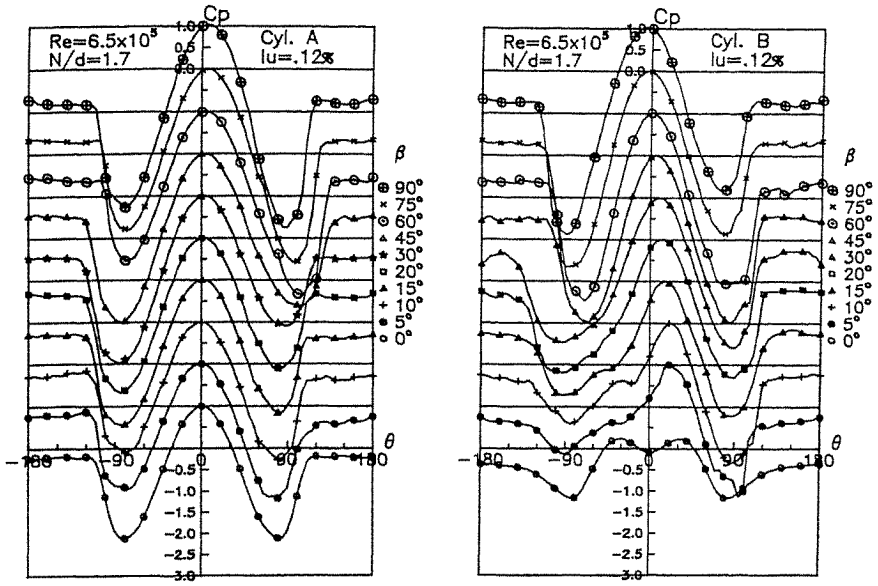
Fig. 5 Mean pressure distribution on two circular cylinders in staggered arrangement (N/d=1.7, Re=6.5×10⁵)
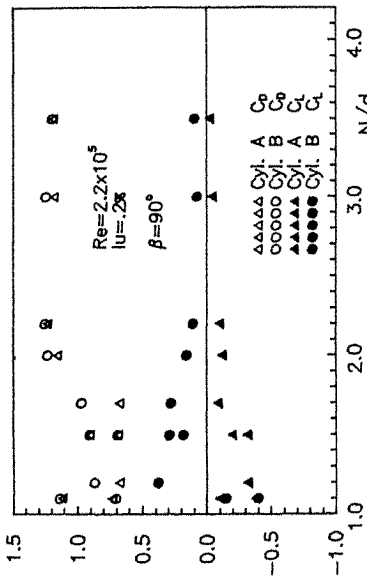
Fig. 6 Variation of C_D and C_L with N/d for two circular cylinders in side-by-side arrangement
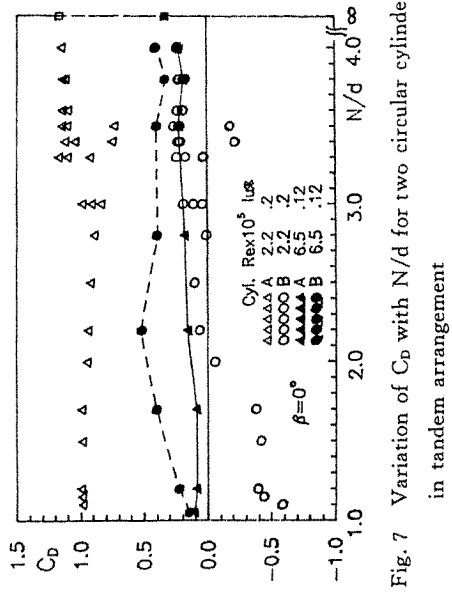
Fig. 7 Variation of C_D with N/d for two circular cylinders in tandem arrangement

65

Fig. 11 C_p' vs. θ on Tower Ⅱ at $N/D_o=1.44$

(b) in tandem
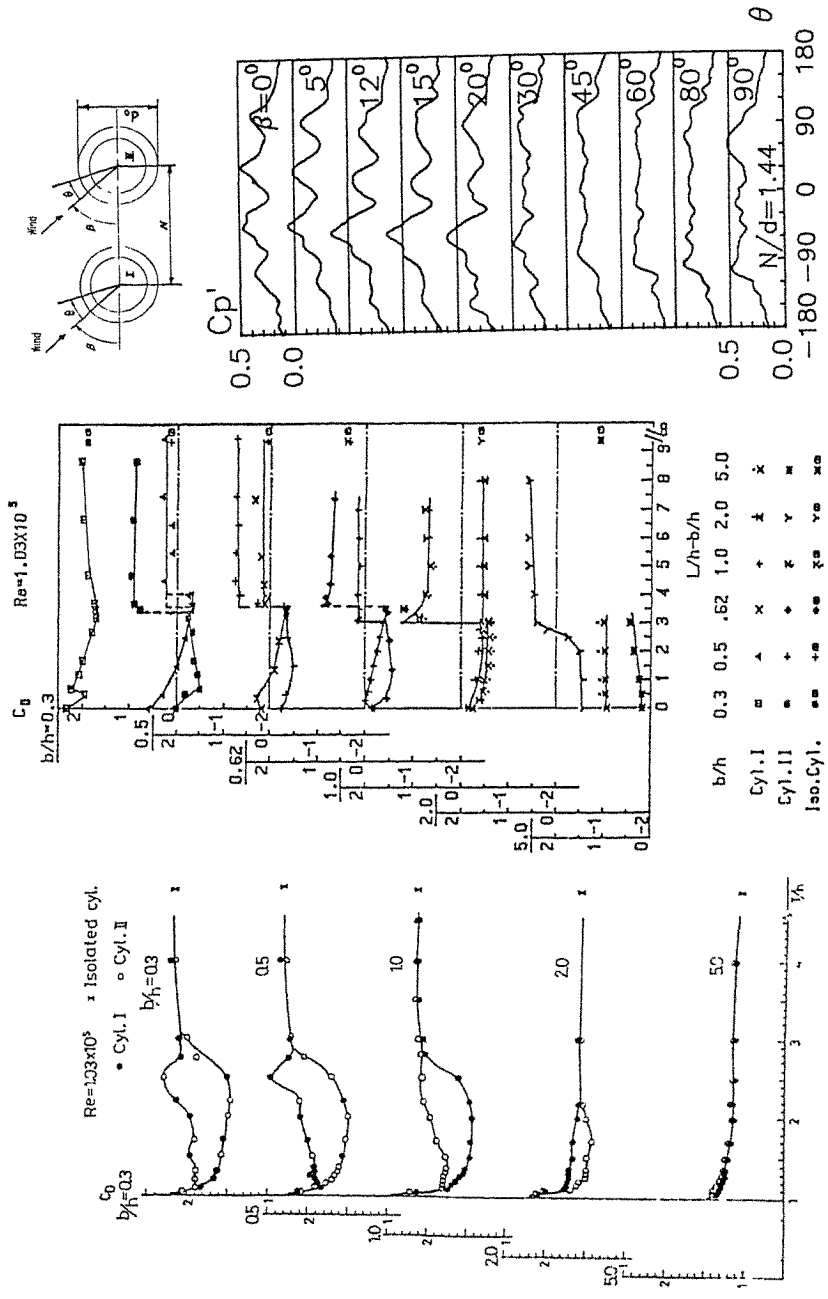
(a) in side-by-side

Fig. 8 Variation of C_D and C_L with N/h for two rectangular cylinders of different slenderness ratio b/h

66

(a) C_D vs. β

(b) C_L vs. β
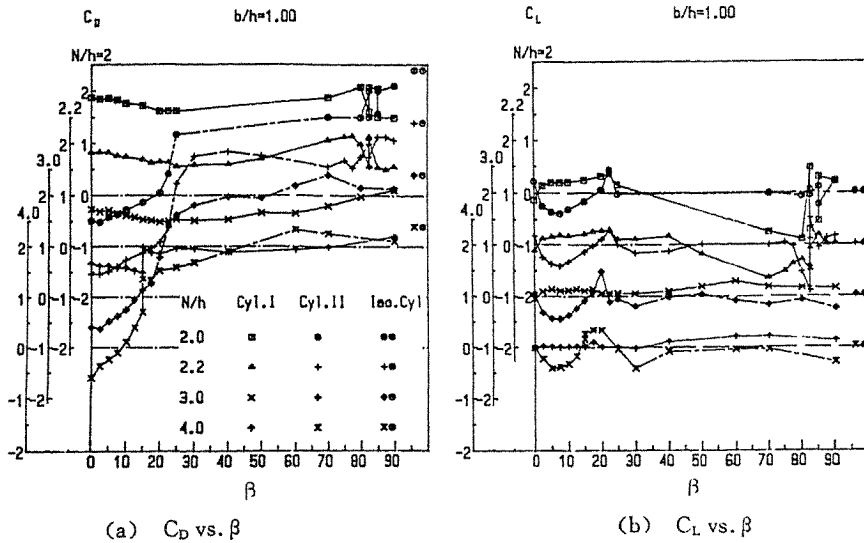
Fig. 9   Variation of C_D and C_L with β at different N/h for two square cylinders in staggered arrangement

(a) C_D vs. N/h

(b) C_L vs. N/h
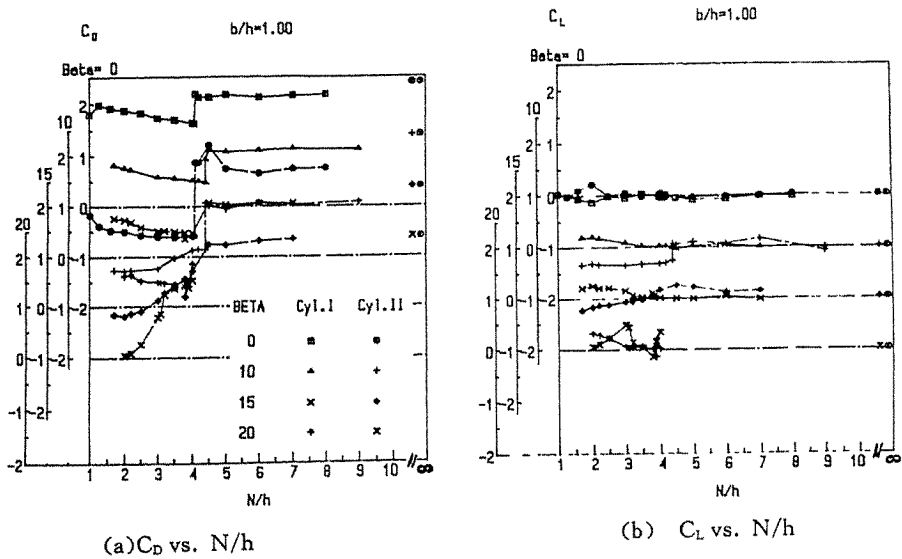
Fig. 10   Variation of C_D and C_L with N/h at different β for two square cylinders in staggered arrangement

67
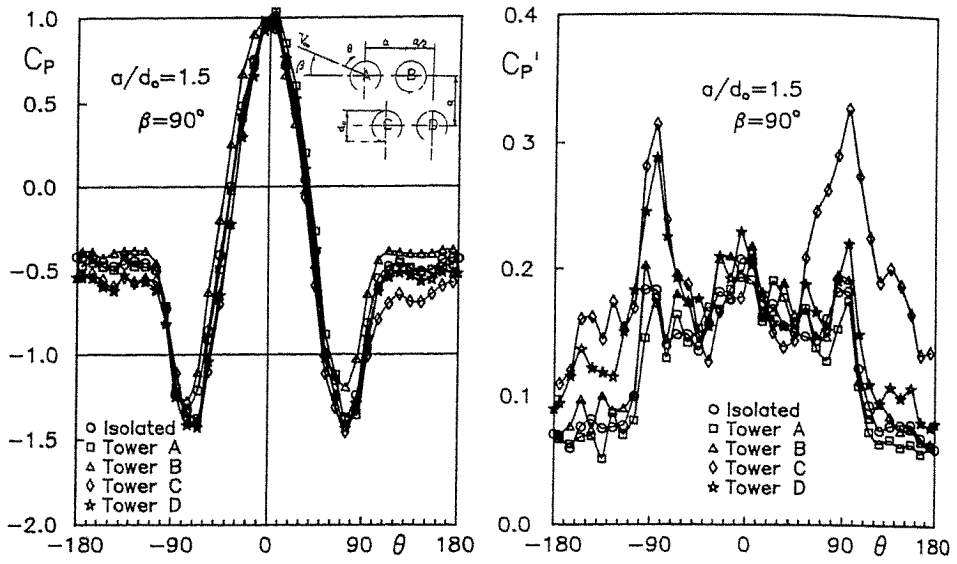
Fig. 13   Pressure distributions on four towers in rhomboid arrangement
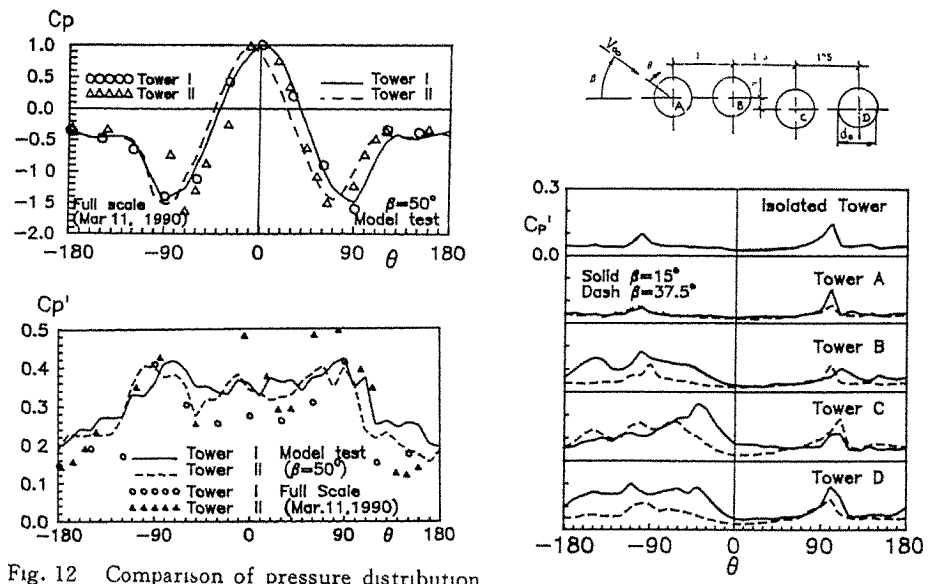
Fig. 12   Comparison of pressure distribution between full-scale measurement and wind-tunnel test

Fig. 14 C_p' vs. θ on four towers of Sha-lin-Zi Power Station

Bridges

The Effect of Section Model Details on Aeroelastic Parameters

N. P. Jones, R. H. Scanlan, P.P. Sarkar[+], and L. Singh

Department of Civil Engineering
The Johns Hopkins University
Baltimore, MD 21218-2686, USA.
[+]Department of Civil Engineering
Texas Tech University
Box 41023, Lubbock, TX 79409-1023, USA.

Abstract: In the five decades since the flutter-induced failure of the Tacoma Narrows bridge, engineers have significantly advanced their understanding of the physical mechanisms at work in this complex aeroelastic phenomenon. Advances in numerical modeling capability, most notably through the finite element method, and developments in the theory of random vibration have contributed dramatically to this development. However, the wind tunnel remains a central component of wind engineering research related to long-span bridges, and modeling a critical element. The results presented herein indicate the dependence of the aeroelastic behavior on a detail even as seemingly minor as the railing. These observations have important implications for both 2-D and 3-D modeling, which are discussed in the paper.

1. Introduction

Despite recent advances in numerical and analytical techniques in recent decades [1], one essential component of the aerodynamic modeling of bridges remains strongly experimental in nature: estimation of the pertinent aeroelastic and aerodynamic parameters through the use of wind tunnel testing. Developments in computational fluid dynamics have yet to enable engineers successfully to predict, quantitatively or qualitatively, the forces on oscillating bluff bodies (specifically, bridge decks in the current context).

An critical component of the wind tunnel modeling process pertains to the modeling of the section, in particular its details. Using a new system identification procedure [2], a series of tests were conducted to measure the flutter derivatives associated with variants of the cross section of the Tsurumi cable-stayed bridge in Japan. The variants were: With railings modeled to maintain reasonable similitude; with railings made impermeable to flow; and without railings.

The primary Tsurumi Fairway Bridge is a three-span continuous cable-stayed bridge, which will connect the Daikoku-Foto Wharf and Ogishima Island (Japan). An additional similar bridge is planned to be constructed alongside the primary Tsurumi Fairway Bridge.

The cross section of the bridge is a trapezoidal, steel box girder of 38 m width and 4 m depth. The streamlined shape of the deck has been selected mainly for wind resistant design considerations. The deck cross section details are shown in Figure 1.

There are six railings: Two on each side of the deck and two at the center which will act as a traffic divide (three lanes on each side). The railings are made of steel beams of rectangular cross section supported on steel columns placed at regular intervals (Fig. 2).

71

Minor modifications in the design have been implemented since initial design, but have not been considered in the modeling described herein.

2. Section Modeling

The primary purpose of the section model is to establish that the proposed contour of the bridge deck has aerodynamically stable characteristics. Acceptance of a deck is based upon considerations of flutter stability and the impact of vortex-induced oscillations. Thus, a rapid check is first made on the preliminary design of the deck configuration. After establishing that the deck is aerodynamically acceptable, usually small modifications or any other added requirements are made to the deck for aesthetic reasons or other constraints that the bridge might need to satisfy. The section model also serves this intermediate design process by providing feedback as to whether or not these local changes render the deck aerodynamically unstable. The section model, in effect, is an analog simulator that reveals aerodynamic mechanisms affecting bridge stability and general response. After the final design of the deck is fixed, the section model serves as a means to investigate the static and dynamic forces expected on the prototype deck.

A section model represents a typical section of the bridge, including its proper degrees of freedom. It must duplicate faithfully, to scale, the local geometric forms and details of the prototype deck. In fact, it is in principle intended to represent the prototype *aerodynamically*, not simply geometrically. The model is suspended from a set of springs configured so as to give the proper degrees of freedom, usually one (vertical or torsional) or at most two (vertical and torsional).

The frequencies of oscillation of the model, determined by selecting the proper stiffness and spacing of the springs, should be decided very carefully and are chosen as discussed below. It is known from the principles of similitude [3], that the reduced velocities of the prototype (U_R^p) and the model (U_R^m) should match, which means

$$U_R^m = \left(\frac{U}{nB}\right)_m = \left(\frac{U}{nB}\right)_p = U_R^p \tag{1}$$

where n is the frequency (Hz). The non-dimensional flutter derivatives, the aerodynamic admittance functions and the normalized spectra of the buffeting forces are functions of the reduced velocity or reduced frequency $(=nB/U)$.

The purpose of the section model is to reliably duplicate the static or dynamic forces according to the velocity scaling and the geometric scaling. Since the static coefficients depend strongly on Reynolds Number – particularly in the lower range – it should be ensured that the scaled forces acting on the small details of the model are not too different from what they would be in the prototype. It can be shown that

$$F_{L,D}^p = F_{L,D}^m \times \frac{1}{\lambda_{C_{L,D}} \lambda_l^2 \lambda_U^2} \tag{2}$$

where $C_{L,D}$ are the static lift, drag coefficients, $F_{L,D}$ are the corresponding static forces, $\lambda_l = B^m/B^p$ is the geometric scale, $\lambda_U = U^m/U^p$ is the velocity scale and $\lambda_{C_{L,D}} = C_{L,D}^m/C_{L,D}^p$ where the superscripts p and m denote prototype and model, respectively. Thus, depending upon the Reynolds numbers holding in the field and in the wind tunnel, the $\lambda_{C_{L,D}}$ may be much different from unity (usually > 1). To overcome this difficulty, a cross section of

72

modified shape and scaled area of its details relative to the prototype may be used. This procedure was used in the design of the railings of the Tsurumi Fairway Bridge section model and is discussed in the next section.

Tsurumi Fairway Bridge Section Model

A 1:200 geometrically scaled section model of the Tsurumi Fairway Bridge was constructed of wood. The width and the maximum depth of the model are 190 mm and 20 mm, respectively.

However, it is difficult to make a geometrically scaled model of the railing because of the small dimensions involved: The smallest scaled dimension was 0.4 mm. Further, since the Reynolds number in the wind tunnel corresponding to this dimension was very small, the coefficient of drag would have changed significantly if a geometrically-faithful rectangular cross section of the railing had been used. The alternative was to use a replacement which was readily available and yet duplicated the aerodynamic and aeroelastic forces scaled according to the velocity and length scales only. It was decided to use a portion of a wire mesh for the railings. The Reynolds number effect on the drag coefficient for the wire circular section is not as high as the rectangular section for the range of Reynolds number associated with the railing dimension. The method for selecting a particular wire mesh size is demonstrated below:

$$F_D^p = F_D^m (\frac{U_p}{U_m})^2 (\frac{A_p}{A_m}) \times FD; \quad \frac{1}{2}\rho U_p^2 C_D^p A_p = \frac{1}{2}\rho U_m^2 A_m' C_D^m (\frac{U_p}{U_m})^2 (\frac{A_p}{A_m}) \times FD \qquad (3)$$

where C_D^p and C_D^m are the static coefficients of drag as function of Reynolds number corresponding to prototype and model, respectively, U_p and U_m are the mean wind velocities acting on the prototype and model, respectively, A_p is the area of unit length of the prototype railing, A_m is the area according to geometric scale and A_m' is the area actually provided for the railing of unit length on the model, and FD is a factor (Eq. 4) which indicates how well the drag forces match (it should be ideally equal to 1.0). FM is similarly defined for base moment (Eq. 4).

$$FD = \frac{\lambda_l^2}{\lambda_{C_D}} \frac{A_p}{A_m'}; \quad FM = \frac{\lambda_l^3}{\lambda_{C_D}} \frac{\sum_i A_i^P X_i^P}{\sum_i A_i^m X_i^m} \qquad (4)$$

where A_i^P and X_i^P are the individual areas and corresponding lever arms contributing to the base moment for the prototype railing, A_i^m and X_i^m are the individual areas and corresponding lever arms contributing to the base moment for the model railing such that $\sum_i A_i^P = A_p$ and $\sum_i A_i^m = A_m'$.

The selection process for the wire mesh for railing A is outlined below. An analogous process was used for railing B. Figure 3 shows the modelled railings.

3. Design of Railing A

The Reynolds Number for the prototype, $\Re_p$, is $2.3 \times 10^4 < \Re_p < 3.4 \times 10^5$ for a typical railing dimension of 75 mm and wind velocity ranging between 2 m/s and 30 m/s. For this range of $\Re_p$ the static drag coefficient (C_D^p) is 1.98. The wire mesh selected has a wire diameter of 0.8 mm. If the velocity for the wind tunnel testing varies between 1 m/s to 10 m/s (typically) then the Reynolds number for the model $\Re_m$ varies between 54 to 540. The drag coefficient for a circular cylinder C_D^m varies in the range 1.2 and 2.0 i.e., $0.61 < \lambda_{C_D} < 1.01$. Since $A_p = 0.53$ m² per 2 m length of prototype railing, $A_m' = 21.4$ mm² per 10 mm length

of model railing and $\lambda_l = 1/200$, then by using Eqn. 3 it can be shown that FD varies between 0.61 and 1.02 where 1.02 corresponds to the highest velocity of the section-model tests. Similarly, by taking $\sum_i A_i^p X_i^p = 0.325$ m³ per 2 m length and $\sum_i A_i^m X_i^m = 84.8$ mm³ per 10 mm length and using Eqn. 4 it can be shown that FM varies in the range 0.47 to 0.79 where 0.79 corresponds to the highest velocity of the section-model tests. Thus, the values of FD and FM are close to one, as desired, for the higher velocities.

4. Tests Results And Discussions

Three tests were conducted with the following variations in railing details. First, section model with railings modeled to maintain reasonable similitude (Case I) was tested and was found to be aerodynamically stable. The maximum wind speed used in the testing was approximately 14.0 m/s. Then, the railings were made impermeable by covering the outermost railings with electric tape (Case II). With this slight modification, aeroelastic behavior of the section model was completely altered. The section turns out to be highly unstable aerodynamically. The torsional motion starts diverging at a much earlier stage (effective damping becomes negative). In fact, so unstable is the section that getting any useful time history at wind speed of 5.0 m/s (and over) was not possible. Lastly, the section was tested without railings (Case III) and was found to be aerodynamically very stable. All the experiments were performed in smooth flow.

All the eight flutter derivatives (for the three cases) $H_i^*, i = 1, ..., 4$ and $A_i^*, i = 1, ..., 4$, as obtained from the coupled motion tests are plotted in Figures 4-5. $H_1^*, H_4^*, A_1^*, A_4^*$ associated with vertical motion were calculated using the frequency n_1 (lower) and $H_2^*, H_3^*, A_2^*, A_3^*$ associated with torsional motion were calculated using the frequency n_2 (higher) at any wind speeds. This was done because in the corresponding single-degree-of-freedom motions, the natural frequencies of vibration for vertical and torsional motions were close to n_1 and n_2 respectively.

The occurrence of torsional flutter in the Case II at such low wind speed can be explained in terms of aerodynamic parameters obtained from the experiments. Typically for bridges (as also in this case), $H_1^*(K) < 0$, but A_2^* may change sign as $(1/K)$ increases. While H_1^* remained almost same for all the three cases, it is interesting to observe the trend of A_2^*. The curve for Case I and III almost match. But for Case II, A_2^* becomes strongly positive at very low value of $(1/K)$. These two parameters are known to influence most the single-mode flutter. Clearly in this case torsion "drove" the overall system to flutter.

The match among the H_3^* and A_3^* in all the three cases is striking. The curves of H_4^* in Case I and III almost match. But in Case II, it clearly deviates and has a much more negative trend.

H_2^* and A_4^* seem to be very sensitive to the small details of the deck. For both these parameters, trend of curves are distinctly different in all the three cases.

The change in one of the natural frequencies due to the aeroelastic effect from which H_4^* and A_4^* were calculated was found to be very small. Further, at higher reduced velocities since the vertical motion was damped faster than the torsional motion, the length of the useful time history of the coupled motion was smaller. Both of these factors made the extraction of H_4^* and A_4^* difficult. Therefore, variations in these two parameters cannot be attributed to a physical effect with any confidence.

74

5. Conclusions

These experiments confirm how changes made even in railing details can influence the characteristics of the flow around the deck and strongly modify the aeroelastic behavior. From the overall comparison, the section models in Case I and III are found to be similar in aeroelastic behavior and both are stable. But just by making the outermost railings impermeable (if done for serviceability reasons etc.), the section is rendered highly unstable. Since the railings are required mainly as guard rails for traffic, it can be concluded that they should be made permeable for better stability.

It is evident that modifications to deck structure, if desired, should be done very judiciously. The two dimensional wind-tunnel modelling is extremely useful in this process. Since the effects produced by small changes in the deck geometry can be so significant, further study is needed to assess the detailed extent of modifications needed for individual prototype structures.

References

1. Scanlan, R. H., Jones N. P. (1990). "Aeroelastic analysis of cable-stayed bridges," *Journal of Structural Engineering*, vol. 116, No. 2.

2. Sarkar, P. P. (1992). "New identification methods applied to the response of flexible bridges to wind," PhD thesis, Johns Hopkins University, Baltimore, Md.

3. Simiu, E. and Scanlan, R.H. (1986). *Wind Effects on Structures*, (2nd Ed.). Wiley, NY.
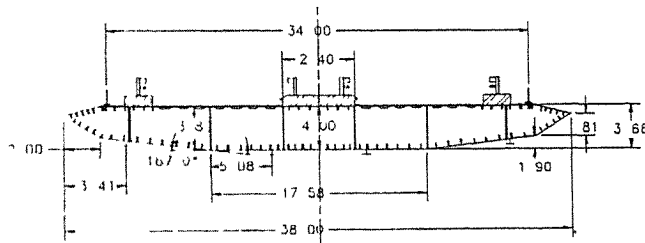
Figure 1. Tsurumi Deck Cross Section (Dimensions in meters, not to scale)
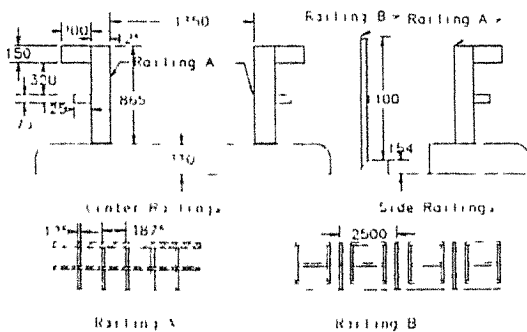
Dimensions in mm (Not to scale)

Figure 2: Tsurumi Fairway Bridge Railings
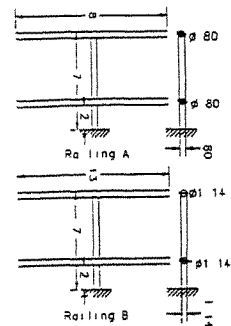
Dimensions in mm (Not to scale)

Figure 3: Model Railings
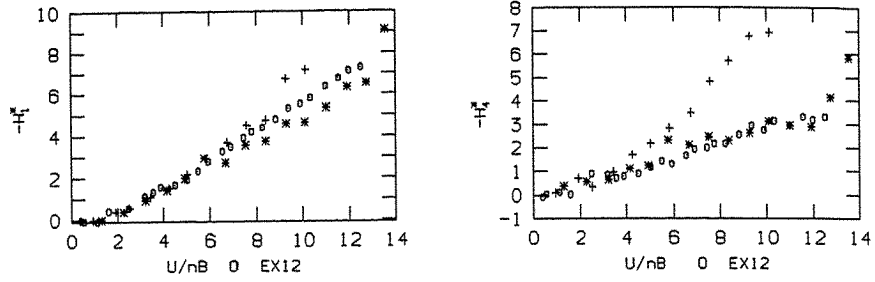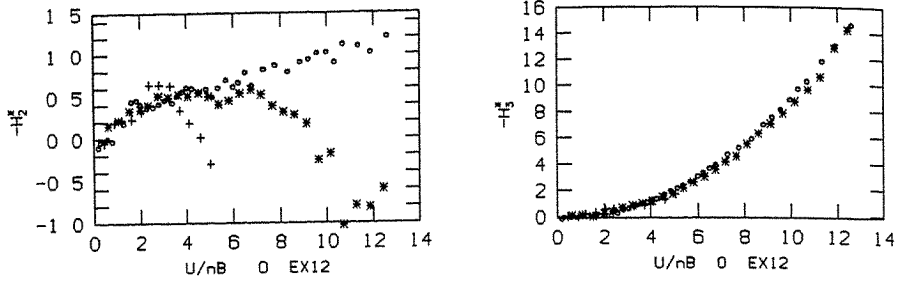
***** Rigs removed, 00000 Permeable rigs ; +++++ Impermeable rigs

Figure 4 Flutter Derivatives $(H_i^*, i = 1, \ldots, 4)$
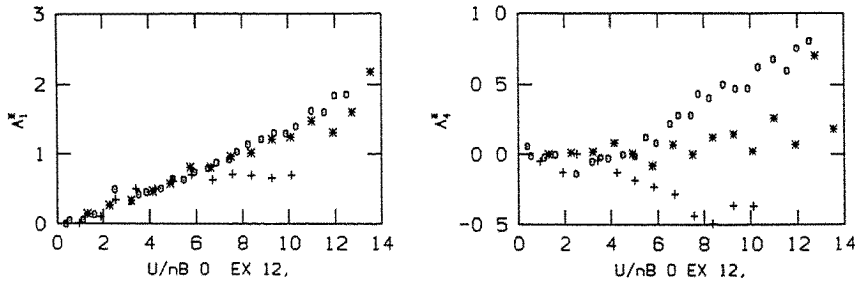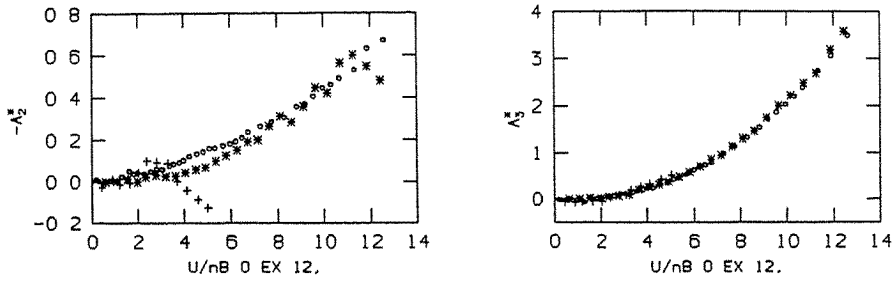
***** Rigs removed, 00000 Permeable rigs ; +++++ Impermeable rigs

Figure 5· Flutter Derivatives $(A_i^*, i = 1, \ldots, 4)$

Improvements of Aerodynamic Behaviors for Box Girder Bridges with Triangular Fairings

F. Nagao, H. Utsunomiya, S. Manabe[*] and A. Kawase

Department of Civil Engineering
The University of Tokushima

[*]Hitachi Zosen Corporation

Abstract: The effects of the triangular edge fairing on bridge aerodynamic stabilities and the mechanism of the improvements of aerodynamic behaviors for box girder bridges with triangular fairings are investigated by the wind tunnel experiments for aerodynamic responses, unsteady pressure distribution and flow visualizations in forced oscillation conditions.

1. Introduction

It is well known that the triangular edge fairing for box girder bridges and plate girder bridges has an effect to stabilize aerodynamic oscillation phenomena such as torsional flutter, galloping and vortex induced oscillation as shown in Longs Creek Bridge [1].   However, it is difficult to determine the effective fairing shape for individual bridge sections because of complex flow properties around those sections.   For example, even if a certain fairing shape for a particular bridge deck showed a satisfactory aerodynamic stability, we had experiences that the same fairing produced unstable aerodynamic phenomenon for another bridge deck sections.

In our recent investigation [2], following results were given. The effective fairing shapes for individual deck sections could be determined by the flow properties around the decks.   The upper side angle of the triangular fairing should be almost the same as the inclination of the streamline for the original bridge deck section in order to minimize the separation from the leading edge. However, the efficiency of fairing depends on the original deck section. If the deck section is too bluff, the fairing shows little effect on the aerodynamic stability of the deck, because it introduces only a minor change in separated flow properties in comparison with those of the original deck section.

In this paper, the results of wind tunnel experiments such as the unsteady pressure properties measured around box girder bridge sections, the aerodynamic responses and the flow visualizations are represented and the effects of the triangular edge fairing on bridge aerodynamic stabilities and the mechanism of the improvements of aerodynamic behaviors for box girder bridges with triangular fairings are discussed.

2. Experimental Procedure

Cross sections of models used here are given in Table 1, where the slenderness ratio of models is $B/d=300mm/35mm \doteqdot 8.57$.   The effects of three types of fairings given in Table 2 are investigated with the hand rail shown in Fig. 1.

The aerodynamic responses of vertical and torsional mode were carried out under the angle of attack $\alpha=+3°$ to increase the aerodynamic instabilities in uniform flow. The structural damping was provided with oil dashpot, and Scruton Numbers (Sc) for both modes were coincident with each experiment ($Sc=2m\delta/\rho dB=6\text{–}8$ in vertical mode, for torsion $Sc=2I\delta/\rho d^2B^2=8\text{–}10$).

In force oscillation method, the measurements of unsteady surface pressure distribution around decks and flow visualization by using the oil mist method were also carried out.

Table 1 Cross sections for Models S1~S12 (B/d=8.57)

Model	shape	Model Parameter B/BU	B/BL	θ
S1		1.00	1.29	45°
S2		1.10	1.29	60°
S3		1.20	1.29	75°
S4		1.29	1.29	90°
S5		1.26	1.79	45°
S6		1.44	1.79	60°
S7		1.70	1.79	75°
S8		1.79	1.79	90°
S9		1.76	3.00	45°
S10		2.14	3.00	60°
S11		2.53	3.00	75°
S12		3.00	3.00	90°

Table 2 Shapes of fairings
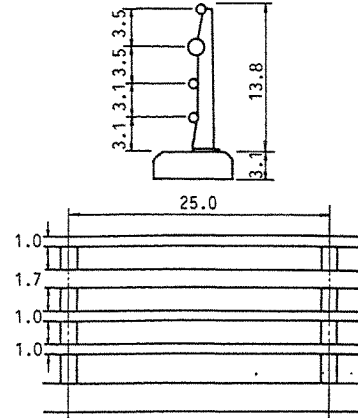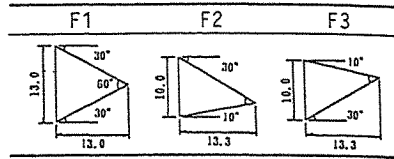
Fig. 1 Detail of hand rail

3. Aerodynamic Properties of Original Cross Sections

The aerodynamic responses of Models S2–S8 under the angle of attack α=3° are shown in Fig. 2, where the torsional responses are given in figure (a) and the vertical responses are indicated in figure (b). The torsional flutter and the vortex induced oscillations of both modes occurred.

Fig. 3 shows the maximum amplitudes of vortex induced oscillations of both modes and the critical flutter velocities for Models S1~S12 under the angle of attack α=3°. The aerodynamic stability is deeply dependent on the shape of the deck cross sections. Cross sections with B/BL=3 (S9~S12) are completely stable for both modes.

Fig. 4 and 5 indicate the relationships between the maximum amplitudes of vertical vortex induced oscillation and cross section parameters, in Fig. 4, the ratio of upper deck length to lower deck length, B/BL, and the slope angle of edge plate, θ, in Fig. 5, respectively. Slender cross sections show more stable aerodynamic stability. However, there are no apparent correlations between responses and cross sectional parameters.

The vertical vortex induced oscillation is focussed in following sections.

4. Effects of Fairing on Vertical Vortex Induced Oscillation

The effectiveness of fairing for vertical vortex induced oscillation for Models S2–S8 is shown in Fig. 6, where the vertical axis indicates the improvement ratio of response amplitude defined following equation.

$$R = (\eta_0 - \eta_F) / \eta_0 * 100 \tag{1}$$

78

(a) Torsional Mode   (b) Vertical Mode

Fig. 2 Aerodynamic responses of Models S2–S8 (α=3°)

Fig. 3 Aerodynamic properties of Models S1–S12 (α=3°)

Fig. 4 2η/d v.s. B/BL

Fig. 5 2η/d v.s. θ

Fig. 6 Effects of fairings on vertical vortex induced oscillation for Models S2–S8 (α=3°)
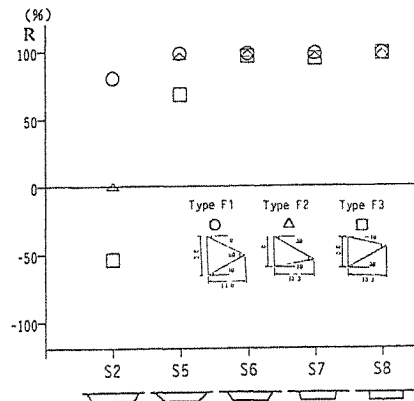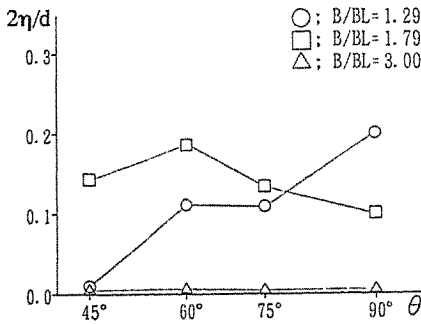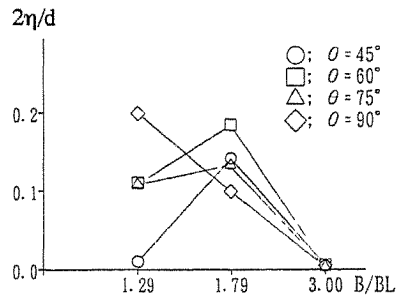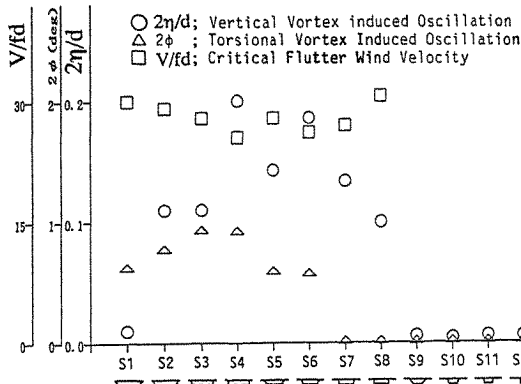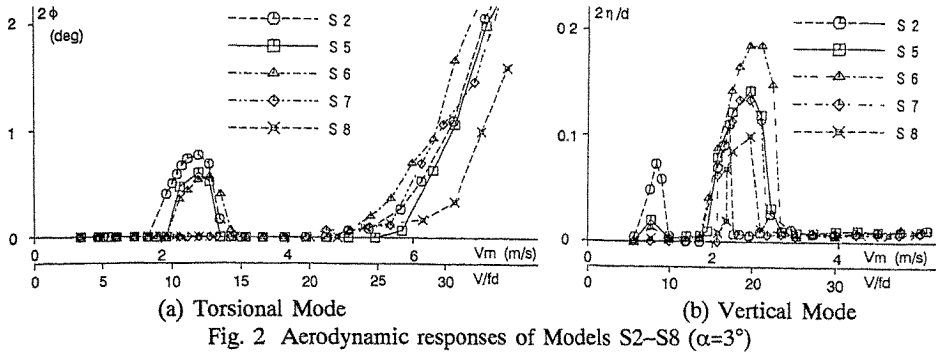
where, η_0 ; the maximum amplitude of original cross section, η_F ; the maximum amplitude with fairing. Therefore, $R=100\%$ means a perfect reduction in response by using the fairing ($\eta_F=0$), in the case of $R<0\%$, the response with fairing (η_F) is larger than the response of the original deck section (η_0).

In exception with Model S2, Fairings F1,F2 and F3 give almost perfect reduction of vortex induced oscillation.

The mechanism of reduction of the responses is investigated by the measurements of unsteady surface pressures.

5. Properties of Unsteady Surface Pressures

The measurements of unsteady surface pressures are carried out by forced oscillation procedure. The surface pressures are referred to the static pressure of a Pitot tube in the wind tunnel and are normalized by dynamic pressure as the mean pressure coefficient Cp. The unsteady pressure is given in terms of the magnitude $|Cp|$ and the phase lag to the motion, β. The component of unsteady pressure in proportion to the speed of motion, C_{pi} is determined by $C_{pi} = |Cp| \sin \beta$, which governs the aerodynamic stability of motion. In upper surface of deck, positive C_{pi} means the exciting force, inversely, negative C_{pi} implies the damping force.

Fig. 7 shows pressure properties of Model S6 with and without fairings during forced oscillation where the experimental condition is correspond to the maximum response of basic section under the angle of attack $\alpha=3°$, that is, the oscillating amplitude $2\eta/d=0.18$ and the reduced wind velocity V/fd=20.

In lower side deck, pressure distributions are almost the same in all sections, on the contrary, pressure properties in upper deck with fairings are greatly different from those for original section. Following reasons for the different effect of fairings on pressure distributions in upper and lower deck are expected. Flow patterns around lower deck mainly depend on not the fairing but the upstream edge plate, conversely, in upper deck, the shape of leading edge does a very important roll, therefore flow patterns change drastically by using the fairings. So the vortex induced oscillation of this cross section (Model S6) is mainly controlled by the upper side flow

(a) Cp

(b) $|Cp|$

(c) β

(d) C_{pi}

Fig. 7 Pressure distributions around Model S6
($2\eta/d=0.18$, V/fd=20, O ; Original section,
□ ; Fairing F1, ▵ ; F2, ◇ ; F3)

properties, that the unsteady pressure properties in upper deck are discussed, hereafter.

In Fig. 7(a), the distributions of the mean pressure, Cp are shown, in which Cp with Fairing F1, where the flow around leading edge is separated evenly to upward and downward, and F2, for which, to lead the flow around leading edge toward the upper deck is intended, recovers near leading edge. So that the reattachment of separated shear flow is promoted by the Fairings F1 and F2.

From Fig. 7(b), the amplitudes of unsteady pressure, $|Cp|$, with Fairing F3, which is designed to lead the flow around leading edge toward the lower deck, are greater than those for original section. On the other hand, $|Cp|$, with Fairings F1 and F2, are smaller than those for the original section. Therefore, it is clear that the vortex induced by the motion with Fairing F3 is stronger than that of original section, oppositely, Fairings F1 and F2 reduce the vortex.

Furthermore, from Fig. 7(c), the phase lag of unsteady pressure from motion, β, indicates different distributions each other. In the original section, the β gradually delays from $0°$ at leading edge to $360°$ at trailing edge, in other word, the vortex induced by the motion reaches at trailing edge in one oscillation period as reported by Shiraishi and Matsumoto [3]. The β with Fairing F3 shows almost the same distribution of the original section, however, the phase lag at the trailing edge is greater than $360°$ because the speed of the vortex is slower than that of the original section. The β with Fairings F1 and F2 distributed around $0°$ is apparently different from those for the original section and Fairing F3. It means that the vortex does not induced by the motion any more.

Finally, the imaginary part of unsteady pressure, C_{pi}, illustrated in Fig. 7(d), explains the aerodynamic forces with and without fairings. For the original section, exciting force acts in the region of downstream half deck, damping force acts in the upstream half deck. In comparison with the original section, the region of exciting force for cross section with Fairing F3 is reduced, on the contrary, the region of damping force is increased because of the change of distribution of phase lag, β. Therefore, Fairing F3 reduces the response of vortex induced oscillation, nevertheless the increase of the unsteady pressure amplitudes, due to the change of the speed of the vortex induced by the motion. On the other hand, Fairings F1 and F2 reduce the vortex induced by the motion and they achieve the aerodynamic stable cross sections.

These phenomena are confirmed by the flow visualizations and the sketches of the flow patterns around Model S2 with Fairings F1 and F3 are illustrated in Fig. 8. The Fairing F1 almost perfectly suppresses the separation from the leading edge. On the other hand, the upward separation from the edge of Fairing F3 is detected as well as the original deck section.

Fig. 9 shows the responses of Model S2 with and without Fairing F3 at the angle of attack $\alpha=3°$. Comparing the both response properties, the amplitude of response with Fairing F3 increased and the wind velocity region of response with Fairing F3 also increases.

The reason for the difference of the wind velocity of response with Fairing F3 is investigated and the result is given in Fig. 10, where the phase lags, β, measured in some different wind speeds under the same oscillating amplitude, $2\eta/d=0.1$ are shown. The values of β at the trailing edge are reduced with increase in the wind speed. When the value of the β equals to $360°$, the vortex induced oscillation occurs as same as the original section.

(a) with Fairing F1   (b) with Fairing F3
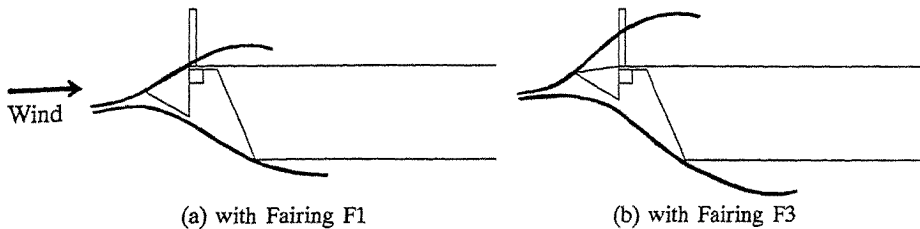
Fig. 8 Sketches of flow patterns for Model S2 with Fairings F1 and F3
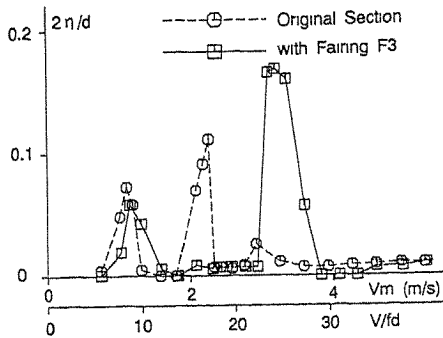
Fig. 9 Aerodynamic responses of Model S2 with and without Fairing F3 ($\alpha=3°$)
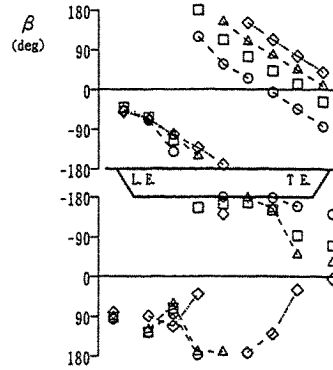
Fig. 10 Phase lag of Model S2 with Fairing F3 ($2\eta/d=0.1$, $\alpha=3°$, O ; V/fd=14, □ ; V/fd=17, ▲ ; V/fd=20, ◇ ; V/fd=24)

6. Conclusions

The unsteady pressure properties around the deck sections with and without fairing are investigated and it is clear that the vertical vortex induced oscillation of these cross sections used here is mainly controlled by the upper side flow properties. The results are summarized as follows:

1) The mean pressure coefficients for decks with the effective fairing recover near the leading edge, therefore, the reattachment of separated shear flow is promoted by it.

2) The phase lag between the unsteady pressure and the motion is greatly changed for using the fairing. For the original deck section, the phase lag at the trailing edge is close to 2π in the region of the vortex induced oscillation. It means that the vortex induced by the movement of deck at the leading edge arrives to trailing edge for one period of oscillation. On the other hand, the phase lag at the trailing edge for the deck with Fairing F3 is larger than 2π. In the case of Fairings F1 and F2, the phase lag of upper deck has almost the same value around $0°$, because the movement of model does not induce the vortex.

3) The amplitudes of unsteady pressure on the deck section with the fairly chosen fairing (Fairings F1 and F2) are reduced in comparison with those for the original deck section, however, it is noted that a wrong shape fairing will make up larger vortex and response.

4) Due to the change of distribution of the phase lag (Fairing F3) and the reduction of unsteady pressure amplitude (Fairings F1 and F2), the improvements of aerodynamic behaviors for box girder bridges with the fairing are performed.

5) The results of pressure measurements are confirmed by the flow visualizations. The flow properties around the deck sections with and without the fairings show good coincidence with the results of the pressure measurements.

References:
1. R. L. Wardlaw, "Some Approaches for Improving the Aerodynamic Stability of Bridge Road Decks", Proc. 3rd Int. Conf. on Wind Effects on Building and Structures, Tokyo, Japan, (1971) 931-940.
2. F. Nagao, H. Utsunomiya, T. Oryu and S. Manabe, "Aerodynamic Efficiency of Triangular Fairing on Box Girder Bridge", Proc. 2nd Int. Colloq. on B.B.A.A., Melbourne, Australia, (1992) vol.2.
3. N. Shiraishi and M. Matsumoto, "On Classification of Vortex-Induced Oscillation and Its Application for Bridge Structures", Proc. 6th Int. Conf. on Wind Engineering, Gold Coast, Australia, (1983).

Effects of Turbulence on Torsional Flutter of A Bridge Deck

H. Kobayashi[1], A. Hatanaka[2], T. Ueda[3]

1 Dept. of Civil Engineering, Ritsumeikan Univ., Japan
2 Technology Headquarters, Nichizo Tech Inc., Japan
3 Steel Structures & Construction Machinery Headquarters
  Hitachi Zosen Corp., Japan

Abstract:
This paper describes the effects of turbulence on torsional flutter of a bluff-structure. Responses of the model in torsional flutter were investigated in some turbulent flows. The effects by turbulence intensity, frequency component of random gust and frequency of sinusoidal flow were discussed. It was recognized that turbulence in high frequency ranges suppressed torsional flutter of a shallow plate girder model.

1. Introduction

Aerodynamic responses are affected by an upstream gust. The upstream gust suppresses vortex-induced oscillations of bridge deck section models except for specific section models (ex. hexagonal section model[1]). Bridge deck flutter is also affected by an upstream gust[2]. Reference 3 reported that an upstream gust reduced a tendency toward flutter and causes buffeting phenomena[3]. Another report said that bridge deck flutter was destabilized in a large scale turbulence[2]. Effects of the upstream gust on the bridge deck flutter are not yet sufficiently investigated.

In this paper, effects of turbulence on torsional flutter are studied. In this experiment, an upstream gust is generated by an active gust generator[4]. Effects of turbulence in lower and higher frequency ranges are focused. Effects of turbulence scale on torsional flutter are also discussed.

2. Experimental procedure

A section model of a plate girder with aspect ratio (width/depth) of 10 is used. Fig.1 shows the cross section of plate girder model and the dynamic properties. The model is allowed to oscillate only in torsional degree of freedom (Fig.2). The center of rotation is

Steel plate (1mm)

Center of rotation

B=350
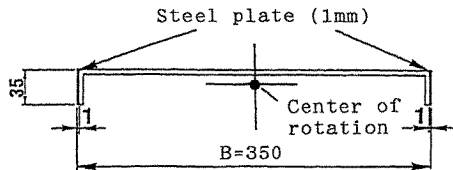
Dynamic properties

Inertia moment (kgf·m·s²/m)	9.0167×10^{-3}
Natural frequency (Hz)	3.19
Logarithmic decrement	0.02
Width × Length (B × L)	350×1800

Fig.1 Cross section of plate girder model

gravitational center. Logarithmic decrement of the model is adjusted by oil dampers. Aerodynamic response of the model is measured by force gauges with coil springs.

Turbulent flows are generated by an active gust generator, which consist of arrays of plates and airfoils [4]. The gust generator is actuated by AC servo motor and controlled by personal computer.
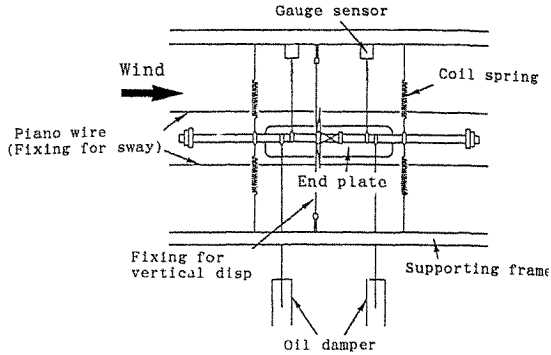
Fig.2 Spring mounting of model

3.Simulation of turbulent flows

Two kinds of turbulence with different turbulence intensity (I_u=10.0% and 5.0%, I_w=I_u/2, L_u=200cm, L_w=50cm) were generated by the active gust generator. I_u and I_w respectively denote turbulence intensity of horizontal and vertical component of wind velocity. L_u and L_u respectively denote turbulence scale of horizontal and vertical component of wind velocity. Kármán type spectra was selected as target power spectra for the simulation. The measured power spectral densities of horizontal and vertical wind velocities are shown in Fig.3. The measured spectra agree well with the target ones.

In order to set off the effects of turbulence in lower frequency ranges,

(a)Horizontal   (b)Vertical
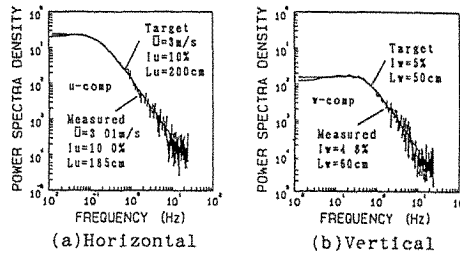
Fig.3 The target and the measured power spectra

(a)Horizontal   (b)Vertical
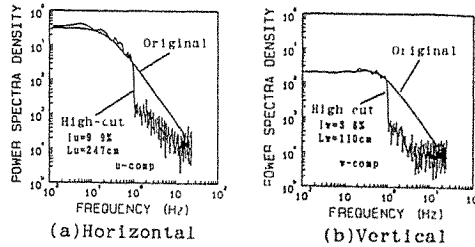
Fig.4 Power spectra of 1.0 Hz high-cut flow

(a)Horizontal   (b)Vertical
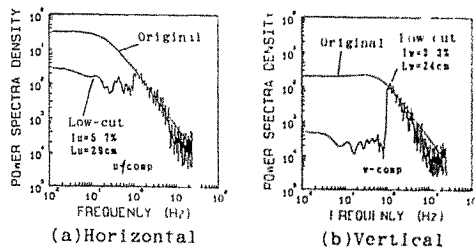
Fig.5 Power spectra of 1.0 Hz low-cut flow

84

the gust flow, in which higher frequency component was eliminated (high-cut flows), were generated. The cut-off frequencies were 0.5,1.0,3.5 Hz. Turbulence intensity is 10% and wind speed is $\bar{U}$=4.0m/s. Low-cut flows was also generated in the same manner. The power spectra of the generated 1.0 Hz high- and low-cut flows are respectively shown in Fig.4 and Fig.5. The power spectra changes discontinuously at 1.0 Hz.

Table 1 shows the turbulence characteristics of high- and low-cut flows. The high-cut flows have about 10% turbulence intensity and have larger turbulence scale than the original flows. The low-cut flows have about 5% turbulence intensity and have smaller turbulence scale than the original flow.

Table 1 Turbulent characteristics of original, high- and low-cut flows

Cut-off frequency (Hz)	No.	Measured			
		Iu(%)	Iw(%)	Lu(%)	Lw(%)
Original	T1	5 1	2 7	171	51
	T2	10 0	4 8	185	60
Low-cut	T2-LC 0 5	6 8	4 1	43	35
	T2-LC-1 0	5 7	3 3	29	24
	T2-LC-3 5	3 2	1 7	12	8
High-cut	T2-HC-0 5	9 0	3 2	316	183
	T2-HC-1 0	9.9	3 8	247	110
	T2-HC-3 5	10 2	4 6	198	66

Table 2 shows the ratio of turbulence scale to the model width L_u/B. The high-cut flows have turbulence scales several or more times greater than the model width. The low-cut flows have nearly the same or smaller turbulence scales than the model width.

Table 2 Ratio of turbulence scale Lu to model width

Cut-off frequency(Hz)		Lu/B
Low-cut	0. 5	1. 2
	1. 0	0. 8
	3. 5	0. 3
High-cut	0. 5	9. 0
	1. 0	7. 1
	3. 5	5. 7

The low turbulence flows, which were given by arrays of plates and airfoils kept at the steady position of 0 degree, were used as semi-smooth flows. The turbulence intensity of these flows are I_u=2.0-0.5%, which vary with wind velocity ranged $\bar{U}$=2-7m/s.

4.Experimental results
(1)flutter responses in turbulent flows

Flutter responses were investigated in the semi-smooth flow and two kinds of turbulences (I_u=10.0% and 5.0 %). Response curves are shown in Fig.6. It is found that turbulence reduce the

tendency toward flutter.

Fig.7 shows the time series of responses when $\bar{U}$=4.0 m/s. The
response in the I_u=5% is almost steady sinusoidal vibration and
is similar to the response in
semi-smooth flow. The response
in the I_u=10.0% is random like
as gust response.
(2)flutter responses in
sinusoidal fluctuating flows

In order to examine
fundamental properties of
effects of turbulence on a
torsional flutter, flutter
responses in a sinusoidal
fluctuating flows of
horizontal component were
investigated. The vertical
component of the flow was not
controlled. The turbulence
intensities of vertical
component was about 2-3 %.
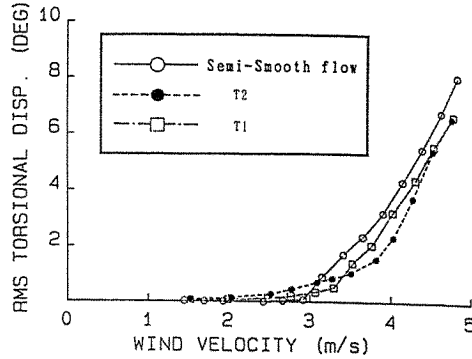
Fig.6 Response amplitude
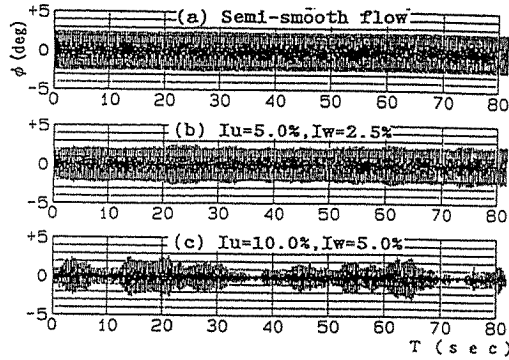
Fig.7 Time series of responses
in semi-smooth and turbulent flows
($\bar{U}$=4.0m/s)

Fig.8 shows standard deviation of torsional response and
turbulence intensity Iu of sinusoidal fluctuating flow for each
frequency. Mean wind velocity was $\bar{U}$=3.5 m/s. The three plots in
group T_A in Fig.8 (a) mean the three different sinusoidal flows
with equal intensity. The correspondent responses are shown by
the three plots in group R_A in Fig.8 (b). The groups T_B-R_B, T_C-R_C
and T_D-R_D have the same relations as above.
These figures show that the increasing frequency has the
tendency to reduces response. The response is also reduced by
increasing intensity of sinusoidal gust.

86

(a)intensity of sinusoidal flow

(b)response amplitude
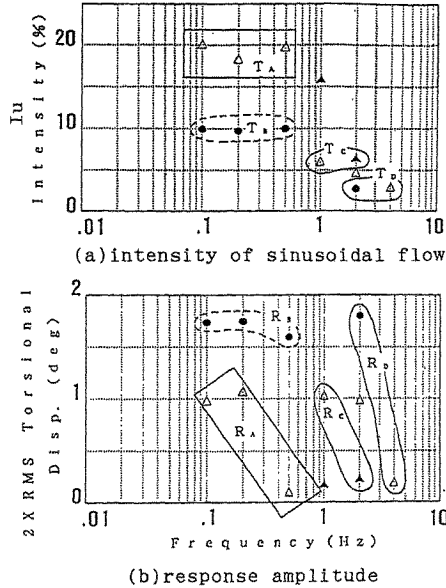
Fig.8 Turbulence intensity of sinusoidal fluctuating flows and standard deviation of response amplitude ($\overline{U}$=3.5m/s)

(3)flutter response in low- and high-cut flow

In order to set off the effects of turbulence on lower and higher frequency ranges, flutter responses in low- and high-cut flows were investigated. Fig.9 shows the responses against turbulence intensity. In the original turbulence flow, torsional response tend to reduce its amplitude with the increase of turbulence intensity.

In high-cut flow, the response amplitudes are larger than those in the original turbulence flow as shown with the black marks. In low-cut flow, the response amplitudes are smaller than those in the original turbulence flow. It is found that turbulence in higher frequency ranges contributes greatly to stabilize the flutter in the turbulence.

Nakamura et.al.[5] reported that small scale turbulence, which have smaller turbulence scales than a model width, caused the earlier reattachment of the shear layer and the effects of turbulence on mean-flow around the bluff structure was vanishingly small with increase of turbulence scale beyond the model width.

Low-cut flows have nearly the same or smaller turbulence scales than the model width. The low-cut flows may cause the earlier reattachment of separation bubble and may lead to the stabilization of torsional flutter. This tendency was observed in the responses due to the sinusoidal fluctuating flows of higher frequencies. The high-cut flows, which have several times larger turbulence scale than the model width, have few influence for torsional flutter.

87

(a)U=3.5m/s

(b)U=4.0m/s
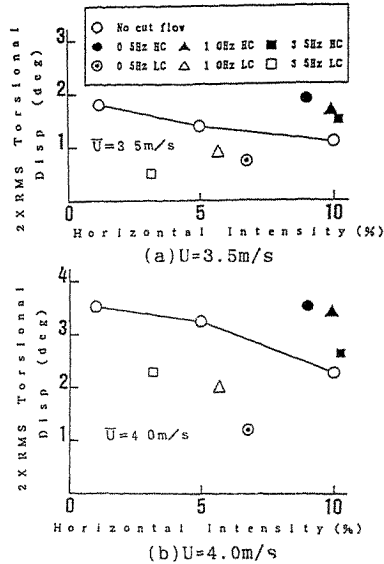
Fig.9 Response amplitude for
band eliminated turbulent flows

6.Concluding remarks

In this study, effects of turbulence on torsional flutter
were investigated. The following results are summarized.
1) Torsional response of shallow plate girder model is reduced by
an upstream gust.
2) Responses of the model in torsional flutter were investigated
in some turbulent flows (sinusoidal flows, original, high- and
low-cut turbulent flows). It is recognized that turbulence in
higher frequency ranges suppresses torsional flutter of a shallow
plate girder model.

References:

1.   H. Kim : Wind-Induced Vibration with Limited-Amplitude of
Bridge Girder Section in Turbulent Flows, Doctoral Dissertation,
Dept. of Civil Eng., Osaka Univ., 1992.
2.   D.R. Huston : The effect of Upstream Gusting on the
Aeroelastic Behavior of Long Suspended-span Bridges, Doctoral
Dissertation, Dept. of Civil Eng., Princeton Univ., 1986.
3.   H. Tanaka and A.G. Davenport : Response of Taut Strip
Models to Turbulence Wind, Proc. of ASCE, Vol. 108,
No.EM1, pp.33-49, 1982.
4.   H. Kobayashi and A. Hatanaka : Active Generation of Wind
Gusts in Two-Dimensional Wind Tunnel, 8th Int. Conf. on Wind
Eng., Canada, 1992.
5.   Y. Nakamura, Y. Ohya and S. Ozono : The Effects of
Turbulence on Bluff-Body Mean Flows, J. of Wind Eng. and
Industrial Aerodynamics, 1988.

TSING MA BRIDGE - SUPERSTRUCTURE EVOLUTION

A.S.Beard, A.G.Simpson and S.A.Coleman[*]

Mott MacDonald Group
[*]BMT Fluid Mechanics Limited

Abstract: The Tsing Ma suspension bridge has a long span, high capacity, deck which will carry both an express highway and the high speed mass transit Airport Railway. It will be subjected to very high winds. This paper traces the evolution of the unique hybrid deck which has been developed to satisfy these conditions. In particular the aerodynamic investigations are described from the initial studies, begun in 1978, through the first design, completed in 1982, to the final design, which is currently under construction.

1. Introduction

The Tsing Ma Bridge forms a major part of the Lantau Fixed Crossing and when completed its 1377 m main span will be the longest in the world to carry both highway and railway traffic. Since it will be an essential part of the only link to Hong Kong's new port and airport it is of paramount importance that it performs satisfactorily in the high wind conditions encountered in the area.

It was initially intended that the bridge should accommodate four lanes of highway traffic with the possibility of future expansion to six or eight lanes. However, the required capacity was increased for the final design. It must now accommodate a dual three lane highway and two tracks for the Airport Railway. In addition two sheltered single lane carriageways are located within the deck. These will allow access to Lantau in all but the most extreme weather conditions.

During the initial phase of the project, beginning in 1978, investigations were undertaken to establish appropriate wind speed criteria for the design of this long span structure. The most extreme winds are experienced in typhoon conditions. Records kept by the Hong Kong Royal Observatory and the University of Hong Kong, at its experimental station at Cape D'Aguilar, were used as a basis. The data most relevant to the Tsing Ma Bridge were those obtained from Waglan island where the 'open sea' exposure of the recording anemometers closely matches that of the bridge site, and meteorological observations have been made over a significant period. Analysis of the data resulted in the basic wind speeds given in Table 1 which apply at deck level, approximately +70m PD.

	120 year return period	200 year return period
Hourly mean wind speed	50 m/s	53 m/s
One minute mean wind speed	58 m/s	62 m/s
Three second gust speed	80 m/s	85 m/s

Table 1. Basic Wind Speeds at Bridge Deck Level

No measurements exist of inclined winds at comparable sites in Hong Kong. The occurrence of such winds in typhoons is little understood. Measurements taken for the Severn Bridge in UK and a number of bridges in Japan have indicated the occasional occurrence of low speed inclined winds. Based on experience at the Severn, and the derived critical wind speed at 0°, criteria were developed for wind inclinations of ±2½° and ±5°.

During periods of extreme wind conditions surface transport ceases to function and hence the bridge was designed as untrafficked in maximum wind speeds. However, the design criteria for the bridge in normal operation were set as three second gust speeds of 44 m/s and 50 m/s for highway and railway operations respectively.

2. Development of Basic Concept

The superstructure of the Tsing Ma Bridge required a deck with low drag which would be aerodynamically stable in winds of typhoon intensity. Research work which followed the Tacoma Narrows Bridge collapse in 1940 demonstrated the beneficial effect of open vents between adjacent carriageway and footpath surfaces on conventional truss stiffened suspended structures. This became American practice and was adopted for the Forth Road Bridge in the UK (designed 1958). However, for the Severn Bridge (designed 1960) a closed box section with faired edges was developed which had a low drag factor. This was found to be stable in winds of up to 65 m/s.

During the initial investigations for the Tsing Ma Bridge it was recognised that potential existed for exploiting the advantages of both deck forms by using a double-deck box construction with truss stiffening and non-structural edge fairings. Longitudinal air vents could be provided in the upper and lower surfaces to enhance its stability.

Two series of aerodynamic tests were carried out on section models to investigate the effects of air vents as well as the need for edge stabilisers. The first tests established that the best performance was obtained by combining air vents in the upper and lower surfaces of the deck with air gaps at the roots of the edge cantilever stabilisers. Subsequently it was found that although the stabilisers reduced vortex shedding amplitudes at low speeds and raised the critical wind speed, satisfactory performance could be obtained without them. As a result stabilisers were eventually omitted from the detailed designs.

The second series of tests investigated the effects of varying the position and width of the air vents themselves. A total of eighteen configurations were tested, examples of which are shown in Figure 1.
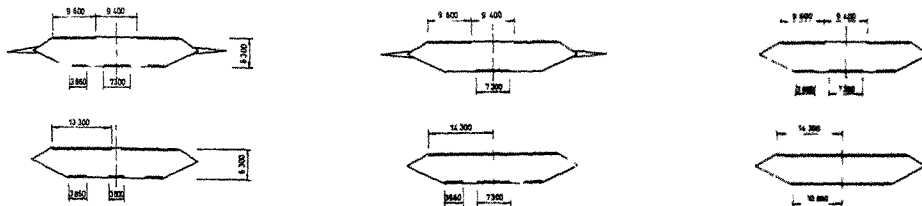
Figure 1. Examples of Deck Configurations Tested in Initial Investigations

For a given arrangement of lower surface vents, it was found that vortex shedding amplitudes were reduced, while maintaining satisfactory critical wind speeds, as the width of the upper vent was decreased from 9.4 m to 2.0 m. However, when the upper vent was closed completely, the critical speed dropped below the required value. When the upper vents were kept constant and the lower ones were altered it was found beneficial to maintain a short closed length adjacent to the lower corners in order to control vortex shedding amplitudes. Again, a low critical wind speed resulted when the lower vents were completely closed.

The deck cross-section developed during this stage of the investigations is shown in Figure 2.
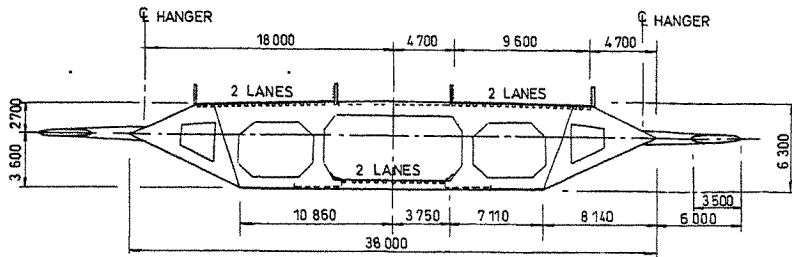
Figure 2. Deck Cross-section Developed During Initial Investigations.

3. The 1982 Design

Following the initial investigations, detailed design was completed for a deck configuration providing dual two lane carriageways on the upper surface plus a single two lane carriageway and two rail tracks within the deck structure. This met the ultimate requirement for the bridge to accommodate the equivalent of eight traffic lanes.

The structural arrangement consisted of Vierendeel cross-frames at 4.5 m centres which allowed rectangular spaces to be provided within the whole length of the suspended structure. The cross-frames were supported on longitudinal, diagonally braced, trusses acting compositely with the stiffened plate carriageway members. Non-structural 1.5 mm thick stainless steel sheeting formed the edge fairing surfaces. The resultant deck cross-section is illustrated in Figure 3.

During the initial investigations, precise values of sectional properties and frequencies could not be applied to every case. When the final form of the suspended structure was decided, in 1981, a new model was constructed which was correctly scaled and had appropriate values of mass, inertia and frequency. Although this model did not include rail tracks, it incorporated the provisions required for their subsequent installation.

In the final design the criteria for critical wind speeds have been set as 93 m/s for 0° inclination, 50 m/s for ±2½° and 31 m/s for ±5°. Test results together with values of vortex shedding amplitudes at the edge of the deck (half peak to peak) are given in Table 2. All values are for a structural damping coefficient of 0.03 and positive angles indicate upward wind inclinations.

91
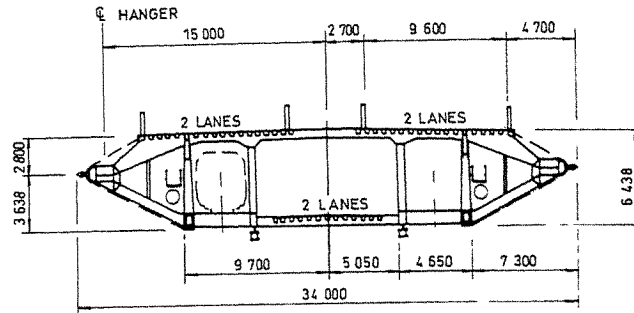
Figure 3. 1982 Deck Cross-section.

	Critical Wind Speed	Vortex Shedding Amplitude	
		Bending	Torsion
- 5°	> 40 m/s	Stable	650 mm
- 2½°	> 65 m/s	Stable	600 mm
0°	104 m/s	Stable	310 mm
+2½°	> 65 m/s	90 mm	Stable
+5°	> 40 m/s	420 mm	Stable

Table 2. Results of Aerodynamic Testing of 1982 Deck

Satisfactory information on the transverse drag coefficients had been obtained from the initial investigations. However, the unusual hybrid form of construction meant that no data was available from other sources for the longitudinal wind forces on the structure. This might be particularly critical during erection. A final series of tests were therefore undertaken to measure drag forces at various horizontal and vertical wind inclinations.

4. 1992 Design

The final design of the Tsing Ma Bridge, completed in 1992, adopted the same basic deck concept as had been previously developed. However, the bridge was now required to carry a dual three lane express highway on its upper deck together with twin tracks for the Airport Railway and two single lane sheltered carriageways on a lower deck. This requirement for increased capacity resulted in a reappraisal of the layout of the deck cross-section. In particular the position and size of the air vents and the degree to which the overall deck presents an aerodynamic profile were changed.

In the final arrangement, which is illustrated in Figure 4, the overall width has been increased to accommodate the required dual three lanes. The Airport Railway has now been moved to the centre of the lower deck and the two sheltered lower carriageways accommodated on either side of it. This rearrangement has resulted in a single lower vent running along the centre line of the deck, immediately under the railway, in place of the previous two side vents. Examination of the results of the original aerodynamic investigations
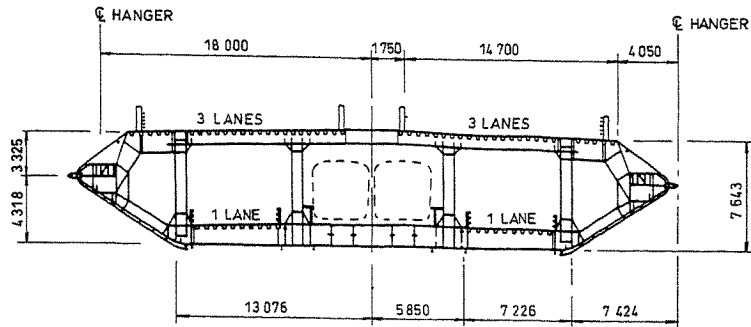
Figure 4. Final Deck Cross-section

suggested that this would be satisfactory. However, a further testing programme was undertaken to confirm its performance.

Tests were carried out to confirm the absence of divergent oscillations. These also examined vortex shedding oscillations, which were found to occur at relatively low wind speeds and to be acceptable both in magnitude and frequency. The tests also confirmed that air movements within the deck were of low speed, thus complying with the operational requirements.

In the final design the performance of the deck was also tested at wind inclinations of up to $\pm 7\frac{1}{2}°$. Test results together with values of vortex shedding amplitudes are given in Table 3. Again all values are given for a structural damping coefficient of 0.03.

	Critical Wind Speed	Vortex Shedding Amplitude	
		Bending	Torsion
- 7½°	> 80 m/s	190 mm	326 mm
- 5°	> 80 m/s	35 mm	468 mm
- 2½°	> 80 m/s	Stable	229 mm
0°	99 m/s	Stable	Stable
+ 2½°	96 m/s	Stable	Stable
+ 5°	54 m/s	Stable	Stable
+ 7½°	26 m/s	393 mm	51 mm

Table 3. Results of Aerodynamic Testing of Final Deck

5. Sensitivity of Critical Wind Speeds to Leading Edge Detail

The aerodynamic tests carried out during the development of the final design also investigated the effects of leading edge details on the critical wind speeds for divergent instability. These tests focused on small geometric changes in the vicinity of the splitter rail at the leading edge of the side fairings. A number of edge detail configurations were tested which included: a triangular splitter rail, sealing the gaps between the splitter rail and the edge fairing, displacing the outboard lip of the splitter rail up (corresponding to the final design),

93

removing the splitter rail, removing the splitter rail and fitting a full triangular edge fairing and the effects of slightly displacing the leading edge of this triangular fairing. The resulting measured critical wind speeds for instability at 0° and +5° are given in Table 4. These values again correspond to a damping coefficient of 0.03.

Edge Detail	Critical Wind Speed for Instability	
	0°	+5°
Triangular Splitter Rail	95 m/s	36 m/s
Splitter Rail - Fairing Gaps Sealed	-	49 m/s
Outboard Lip of Splitter Rail Displaced Up	99 m/s	54 m/s
Splitter Rail Removed	96 m/s	38 m/s
Triangular Edge Fairing	95 m/s	40 m/s
Triangular Edge Fairing - Leading Edge Displaced Up - 300mm	-	> 78 m/s
Triangular Edge Fairing - Leading Edge Displaced Down - 300mm	-	42 m/s

Table 4: Critical Wind Speeds for Various Configurations of Edge Detail

The investigations showed that the critical wind speed was extremely sensitive to very slight changes in edge detail with winds at an inclination of +5°. However, the critical wind speed was found to be relatively insensitive to these changes with winds at 0°. The sensitivity of the critical wind speed at +5° is an indication of the effect that slight changes in edge detail have at this angle on the airflow around the deck and in particular the edge fairing.

A further series of tests with the upper vent sealed, preventing airflow through the deck, demonstrated a large reduction in the sensitivity to variation of leading edge details at +5°. This result highlights the importance of the interaction of the airflow through the deck and the flow around the leading edge on its aerodynamic stability in high winds.

6. Conclusions

The hybrid deck developed for the Tsing Ma Bridge has been shown to be extremely stable in the high winds experienced in Hong Kong. It has also been demonstrated that the performance of this deck is sensitive to the interaction of airflows through and around the deck, in particular as affected by leading edge details.

7. Acknowledgements

Methods of Wind Response Investigation
Employed for the Kap Shui Mun Bridge

R.H. Scanlan[+], S.L. Stroh[++] and J.D. Raggett[+++]

[+]Dept. of Civil Engineering, Johns Hopkins Univ., Baltimore, MD
[++]Greiner, Inc., Tampa, Florida
[+++]West Wind Laboratory, Carmel, California

Abstract: The Kap Shui Mun Bridge, one of the key links of the Lantau Fixed Crossing, Hong Kong, is of cable-stayed type, providing for both rail and road traffic. The wind response analysis, in view of the exposure of the bridge to high typhoon winds, required detailed review of oscillatory stability and buffeting. Specially designed section model wind tunnel studies, coupled with advanced three-dimensional analytical methods, provided a framework in which a comprehensive design envelope could be realized. The process employed was aimed at reducing to minimal necessary proportions both experimental testing and study costs.

1. Introduction. General Approach

The Kap Shui Mun cable-stayed bridge, an on-going project that is part of the Lantau Fixed Crossing, has a requirement of resistance and stability under the very highest predictable typhoon winds (for example, $95\,m/s$ at deck level.)

The bridge is depicted in Fig.1. The main span of this bridge is $430\,m$, with side spans of $160\,m$ each. A cross section of the composite center span is presented in Fig.2.

In selecting the methods by which the wind resistance of this important design was to be demonstrated, several alternative approaches were first considered. Retained were the following key elements: a) basic 2D wind tunnel section model; b) knowledge of the first several dozen bridge vibration modes as provided by a computer model of the full prototype; and c) advanced 3D analytical procedures notably employing standard force coefficients and measured flutter derivatives as obtained by exploitation of the section model.

These choices are supported by the fact that the section model can be constructed and tested at the largest feasible geometric scale available to low-speed atmospheric wind tunnels, thus obviating a potential number of Reynolds number dependencies. Since section model dynamics cannot duplicate full-bridge dynamics however, interpretation is required. This is supplied through employment of a basic analytic description using *force coefficients* and *flutter derivatives*, both of which represent fundamental information extractable from the section model. The model itself is required only to be *aerodynamically* (i.e. geometrically) faithful to the prototype.

95
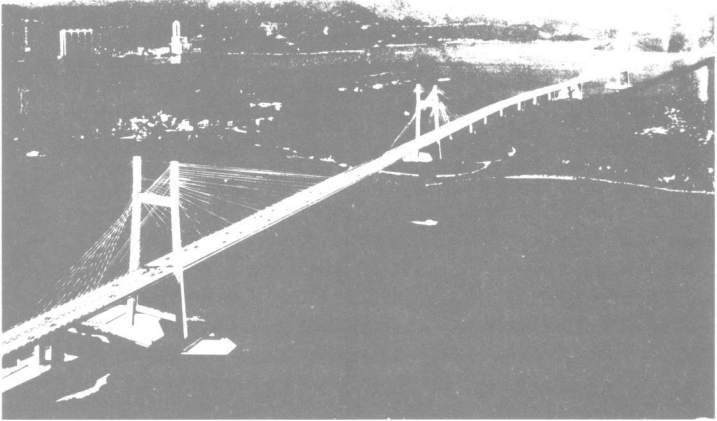
Fig. 1 Kap Shui Mun Bridge
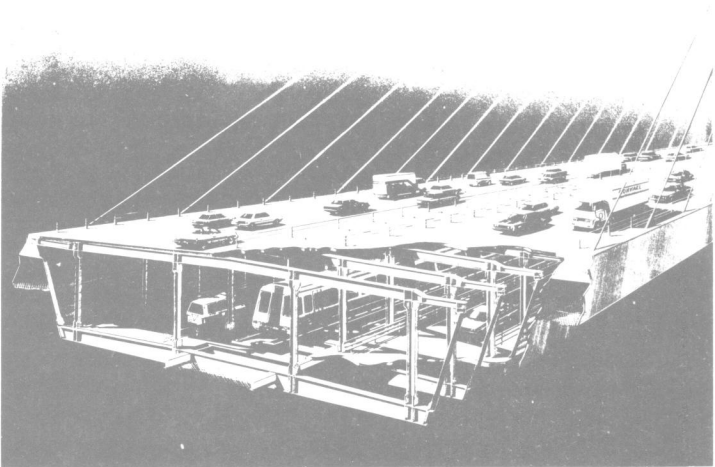
Fig. 2 K.S.M. Deck Box Section

The entire prototype bridge, on the other hand, is accurately modeled mechanically by an appropriate superposition of its fundamental modes. The present state of the art permits comprehensive 3D modeling of the aerodynamics as well. A few basic, cleanly-measured aerodynamic data are incorporated into analytical methods that affectively describe the aeroelastic response of the bridge. This offers the possibility of exploiting a wide range of scenarios that, in total, provide a 'design envelope' of cases that can completely encompass anticipated design conditions.

2. Exploitation of the Section Model

Figure 3 depicts the section model used for this study. It was exploited for static force coefficients and flutter derivatives, under laminar approach flow, a conservative practice. While the extraction of static force coefficients is more routine, the method employed to obtain the flutter derivatives consists of identifying them from decaying oscillations of the spring-supported section model. In recent years identification methods for accomplishing this have become very efficient. (see Refs. 1, 2) These processes yield the information through which, using the natural bridge modes, equations of motion for both flutter and buffeting in 3D can be written. An important incidental use of the flutter derivative information from the section model was as a guide to, and verification of, deck contour changes conducive to enhanced stability.
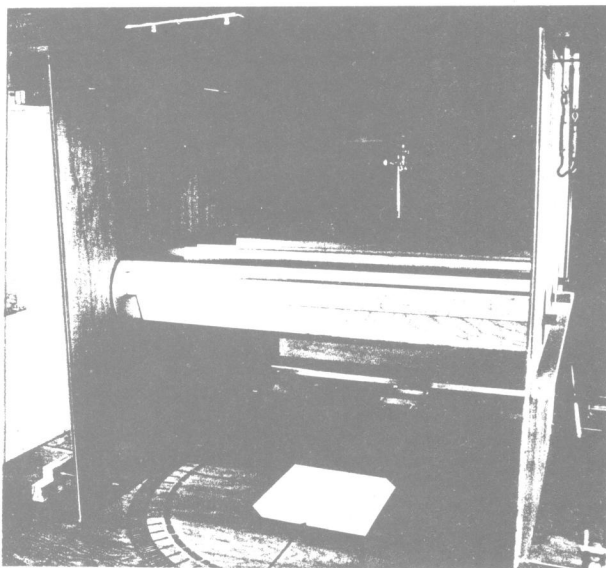
Fig. 3 K.S.M. Wind Tunnel Section Model

3. Full-Bridge Equations of Motion

Space does not permit presentation of all mathematical details. (see Ref. 3) Some basic elements will, however, be given. Vertical, twist and sway components h, p, α of bridge deck motion are characterized respectively for each mode $\imath$ by

$$
\begin{aligned}
h(x,t) &= h_\imath(x)B\xi_\imath(t) \\
p(x,t) &= p_\imath(x)B\xi_\imath(t) \\
\alpha(x,t) &= \alpha_\imath(x)\xi_\imath(t)
\end{aligned}
\tag{1}
$$

where $h_\imath$, $p_\imath$, $\alpha_\imath$ are modal forms; B is deck width; and $\xi_\imath$ is the generalized coordinate of the mode $\imath$. The equation of motion of mode $\imath$ is

$$
I_\imath \left[\ddot{\xi}_\imath + 2\zeta_\imath\omega_\imath\dot{\xi}_\imath + \omega_\imath^2\xi_\imath \right] = Q_\imath
\tag{2}
$$

where $I_\imath$ is the generalized mass of the whole bridge, $\zeta_\imath$ and $\omega_\imath$ are modal damping and circular frequency, respectively. For a cross-wind velocity U, and air density ρ the generalized force takes the form

$$
\begin{aligned}
Q_\imath = \frac{1}{2}\rho U^2 B^2 \ell \Bigg\{ &\frac{KB}{U} \left[H_1^* G_{h_\imath h_\imath} + P_1^* G_{p_\imath p_\imath} + A_2^* G_{\alpha_\imath\alpha_\imath} \right] \dot{\xi}_\imath \\
&+ K^2 A_3^* G_{\alpha_\imath\alpha_\imath} + \int_{deck} \left[\mathcal{L}h_\imath + \mathcal{D}p_\imath + \mathcal{M}\alpha_\imath \right] \frac{dx}{\ell} \Bigg\}
\end{aligned}
\tag{3}
$$

where ℓ is bridge length, and certain modal integrals

$$
G_{q_\imath q_\imath} = \int_{deck} q_\imath^2(x)\frac{dx}{\ell} \quad [q_\imath = h_\imath,\ p_\imath \text{ or } \alpha_\imath]
\tag{4}
$$

are employed. In (3) $H_\imath^*$, $A_\imath^*$, $P_\imath^*$ are flutter derivatives (Ref. 4) and $\mathcal{L}$, $\mathcal{D}$, $\mathcal{M}$ are combinations of force elements due to gust velocities u and w. The terms in $G_{q_\imath q_\imath}$ conservatively incorporate the assumption of complete flutter derivative coherence along the span.

From the equations shown it is possible to derive a single-degree-of-freedom (less than zero damping) flutter criterion, which takes the form

$$
H_1^* G_{h_\imath h_\imath} + P_1^* G_{p_\imath p_\imath} + A_2^* G_{\alpha_\imath\alpha_\imath} \geq \frac{4\zeta_\imath I_\imath}{\rho B^4 \ell} \left[1 + \frac{\rho B^4 \ell}{2I_\imath} A_3^* G_{\alpha_\imath\alpha_\imath} \right]^{\frac{1}{2}}
\tag{5}
$$

where the 'threshold' term on the right is seen to be an aerodynamically influenced Scruton number.

This s.d.o.f. criterion governs all flutter for the subject bridge, as coupled flutter is demonstrated not to occur. The structure is found to be free from any oscillatory instability for all design wind conditions.

The cases of random buffeting by wind turbulence are shown by further development of equation (2) (see Ref. 3) to be governed by

$$\sigma_{\xi_i}^2 = \left[\frac{\rho B^4 \ell}{2I_i K_{i0}^2}\right]^2 \left\{ R_\varphi \left[\frac{\pi n_{i0} S_u(n_{i0})}{4\gamma_i} + 6u_*^2\right] \right.$$

$$\left. + R_\psi \left[\frac{\pi n_{i0} S_w(n_{i0})}{4\gamma_i} + 1.7u_*^2\right]\right\} \frac{1}{U^2} \tag{6}$$

where $\omega_{i0} = 2\pi n_{i0}$ is the principal aerodynamically-influenced response frequency and in which σ_{ξ_i} is the standard deviation of dimensionless coordinate ξ_i, $K_{i0} = \frac{B\omega_{i0}}{U}$, S_u and S_w are along-wind and vertical wind spectra (Ref. 5), u_* is wind friction velocity, γ_i is net aerodynamically-influenced system damping, and R_ρ, R_ϕ are aerodynamic coherence attenuation factors. Eqs.(1) are then employed to obtain the actual bridge desplacements. The parameters in (6) are varied over a wide range, mode by mode, to establish a multiply-documented, overall view.

The bridge proves to be exceptionally resistant to deflection in all modes under these buffeting forces.

The net viewpoint taken for the Kap Shui Mun study has been to reduce aerodynamic data-taking to its cleanest essentials and well-understood mechanisms and to combine the results into dynamic aeroelastic theory to define a comprehensive and conservative envelope of conditions ensuring design safety.

4. References

1. P.P. Sarkar, N.P. Jones and R.H. Scanlan, "System Identification for Estimation of Flutter Derivatives", **Progress in Wind Engineering**, *Proc. 8th Int'l. Conf. on Wind Engineering*, Elsevier 1992, pp.1243–1254

2. J.D. Raggett and R.H. Scanlan, "A Least-Squares Identification Procedure for the Eight Aeroelastic Flutter Coefficients for a 2-Dimensional Section Model", *Proc. 7th U.S. Nat'l. Conf. on Wind Engineering*, UCLA, June 27–30, 1993

3. R.H. Scanlan and N.P. Jones, "Aeroelastic Analysis of Cable-Stayed Bridges", ASCE *Jnl. Struct. Engrg.* Vol.116, No.2, Feb. 1990. pp.279–297

4. R.H. Scanlan and J.J. Tomko, "Airfoil and Bridge Deck Flutter Derivatives". ASCE *Engrg. Mech. Div.* Vol.97, No.EM6, Dec. 1971, pp.1717–1737

5. E. Simiu and R.H. Scanlan, **Wind Effects on Structures**, Wiley, N.Y., 1986

Study on aerodynamic selection of cross section for suspension bridges in China

H. F. Xiang, Z. X. Lin and J. Z. Song

Department of Bridge Engineering
Tongji University, Shanghai, China

Abstract: In this paper the aerodynamic selection of box deck cross section for Humen Bridge(L=888 m) and Jiangyin Bridge(L=1385 m) is made according to the assessment of aerodynamic stability by the aerodynamic derivatives and critical wind speed measured from section model test, as well as the relative comparison of buffeting response.

1. Introduction

While entering into 1990's, China has a tidal surge in building long-span suspension bridges on the basis of outstanding achievement in the successful construction of many cable-stayed bridges, especially two composite cable-stayed bridges over Huangpu River in Shanghai, Nanpu Bridge with a main span of 423 m and Yangpu Bridge of 602 m.

Three suspension bridges are being constructed simultaneonsly in China, the Shantou Bay Bridge with a concrete stiffening girder of 452 m, the Humen(Tiger-gate) bridge over Pearl River in Guangdong Province with a main span of 888 m, and the Jiangying Bridge over Yangtse River in Jiangsu Province, which will be a 1385 m suspension bridge ranking 3rd place in the world after completion in 1997.

In the preliminary design stage of those suspension bridges, the aerodynamic selection of cross section was required by the authorities concerned in order to make an optimal choice of shallow box deck configuration.

The aerodynamic selection of cross section is commonly judged by critical wind speed of flutter stability from section model wind tunnel test at 0 degree of attack angle[1, 2]. For a well-designed streamlined flat box deck, the aerodynamic derivative A_2^* at 0 degree of attack angle has a curve similar to airfoil. However, the A_2^* curve at ± 3 degrees for the same cross section appears another picture like the nonstreamlined deck cross section, which means the attack angle will make the cross section blunt. So that the aerodynamic stability can be checked by both critical wind speed and the derivative A_2^*.

In this paper an approximate method for relative comparison of buffeting response is also presented to estimate easily the buffeting behaviour of candidate cross sections in addition to the flutter assessment mentioned above.

2. Selection of Cross Section for Humen Bridge

The Humen bridge is located at the mouth of Pearl River, and a key project of Guangzhou-Shenzhen-Zhuhai expressway. A shallow box deck with height of 3 m is used as the stiffening girder of this 888 m suspension bridge(Fig.1). The design wind speed at the 60 m deck level is about 60 m/s(10 minute average, 100 years of return period). According to the basic cross section provided by the design group, 5 candidate cross section shapes were chosen for considering the variation of edge configuration. Fig.2 shows the model of selected cross sections with scale of 1/80, in which, type C0 is the original alternative, C1

; the same but with anti-collision walls on the deck.
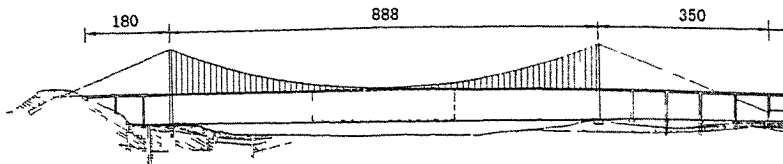
Fig.1. Layout of Humen Bridge
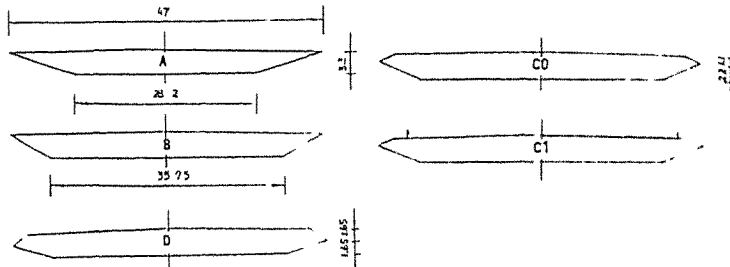
Fig.2. Candidate cross sections of Humen Bridge

The section model tests were conducted in TJ-1 Boundary Layer Wind Tunnel f the State Laboratory for Disaster Reduction in Civil Engineering(SLDRCE) at ongji University. The working section of the wind tunnel has a width of 1.2 m, height of 1.8 m, a length of 18 m and a maximum wind speed of 32 m/s. he stability limit, the aerodynamic derivatives as well as static 3-components nd load coefficients were tested in smooth flow condition.

Fig.3(a) shows the A_2^* curves of original C0 alternative with a omparison of 0 , +3 , -3 degrees of attack angles.
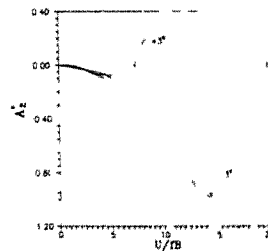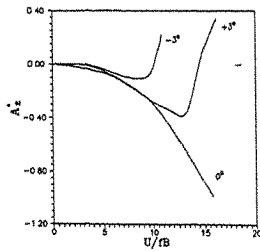
Fig.3(a). A_2^* curve of C0 alternative. Fig.3(b) A_2^* curve of B alternative

102

It can be seen from Fig.3(a) that for such a streamlined shallow box deck, the behaviour of aerodynamic stability become the worst situation at -3 degree incidence between the deck section chord and the wind direction. Oppositely, for B alternative, the A_2 curve at +3 degree becomes worst(Fig.3(b)).

Fig.4 summarizes the most unfavourable A_2^* cuvers for all selected cross section, from which we can judge that C1 and D are better than A and B with a poor behaviour at +3 degree.
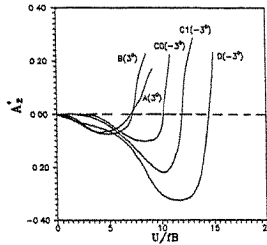
Fig.4. The most unfavourable A_2^* curves of all candidates

The critical wind speed tested for all selected cross sections at -3, 0, +3 degrees of attack angles are listed in Table 1.

selected cross sections	angle of attack		
	+3°	0°	-3°
A	48.6	77.4	93.6
B	52.8	75.6	91.8
C0	87.0	88.2	66.6
C1	79.2	91.2	77.4
D	78.0	88.2	73.8

Table 1. Critical wind speed tested.

The results indicated that C1 and D alternatives are better choice in the point of view from aerodynamic stability, which is compatible with that from aerodynamic derivative A_2^* .

3. Selection of Cross Section for Jiangyin Bridge

Jiangyin Bridge over Yangtze River is a suspension bridge with a longest main span of 1385 m in China, which has started construction in Oct. 1993, and planned to be completed in 1997(Fig.5).

In the feasibility study, the British type deck cross section used in Severn, Bosporus and Humber bridges was taken as a sample(A in Fig.6). Some experts of the reviewing committee gave the comment that the side walk level may be raised appropriately in order to avoid the influences of exhausting from vehicles on the passengers. So that the aerodynamic selection of cross section was required, and 5 candidate were chosen(Fig.6), in which B and C are similar

103

to Great Belt Bridge and Lille Belt Bridge respectively, D and E are the original alternative with modified side walk.
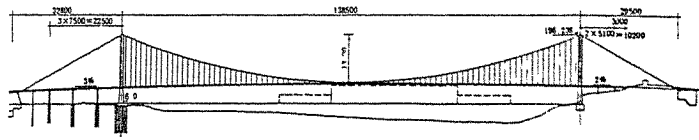
Fig.5. Layout of Jiangyin Bridge
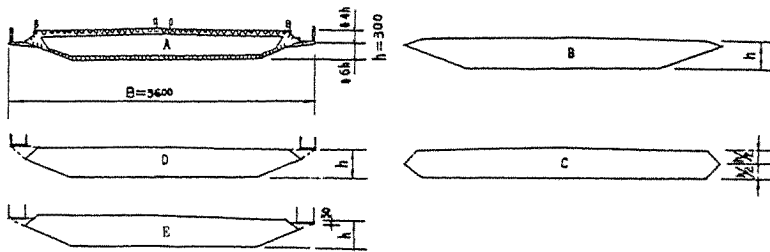
Fig. 6. Candidate cross sections of Jiangyin Bridge

Fig.7 summarizes the most unfavourable A_2^* curves for all alternatives among +3, 0, -3 degrees of attack angle. It can be seen that type A(original cross section) has the best behaviour of aerodynamic stability, type E ranks second, then D, C and B in order.
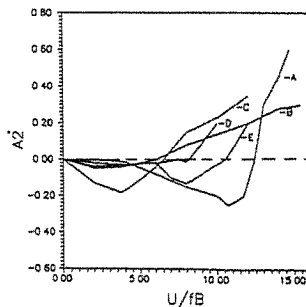
Fig.7. The most unfavourable A_2^* curves of Jiangyin Bridge

4. Relative Comparison in Buffeting-based Selection

In the wind-induced vibration problems of long-span bridges, buffeting response and vortex-excited resonance should also be considered in addition to the flutter instability. For the well-designed streamlined deck, the

104

vortex-excitation is hard to be observed even under smooth flow condition, and the presence of turbulence in the real bridge will suppress the vortex shedding. Therefore, the final choice of cross section should be further made in accordance with the buffeting estimation among the candidate cross sections, which meet the requirement of aerodynamic stability.

The RMS of the first mode vertical buffeting response can be expressed as follows[5]:

$$\sigma^2_{h1}(x,h) = \frac{H_1^2(x)(\rho UB)^2}{\omega_{h1}^3 M_{h1}^2} \frac{\pi}{4z_{h1}} |J_{h1}(\frac{\omega_{h1}}{U})|^2 S_h(\omega_{h1}) \tag{1}$$

in which:

$H_1(x)$=1st vertical bending mode shape,

ω_{h1}=vertical bending frequency of the 1st mode,

M_{h1}=generalized mass of the 1st mode,

$z_{h1} = \zeta_{h1} - \dfrac{\rho B^2 H_1^*}{2M_{h1}}$, total damping ratio,

$|J_{h1}|^2 = \int_0^L \int_0^L H_1(x_1) H_1(X_2) e^{-c|\frac{x_1-x_2}{L}|} dx_1 dx_2$, joint acceptance function

of the 1st mode, and

$$S_h(\omega_{h1}) = [C_L^2 \frac{S_u(\omega)}{S_w(\omega)} + \frac{1}{4}(C_L' + \frac{A}{B} C_D)^2] S_w(u) \tag{2}$$

where $S_u(\omega)$, $S_w(\omega)$ are horizontal and vertical wind speed spectrum respectively.

For different cross sections of a bridge, all terms in Eq.(1) except $S_h(\omega_{h1})$ may be regarded as basically the same. The parameteric analysis shows that the lift slope C_L' value in Eq.(2) plays a predominant role in all factors concerned. So the comparison of buffeting response can be approximately made through C_L' value obtained from the static 3-components test.

Table-2 shows the C_L' value for 5 candidate cross section of Jiangyin Bridge and their relative comparison.

	A	B	C	D	E
C_L'	4.75	4.08	6.18	4.51	4.66
$C_L'/C_L'(A)$	1	0.86	1.30	0.95	0.98

Table 2. Buffeting-based relative comparison for Jiangyin Bridge.

It can be seen that the buffeting-based order is B, D, E, A, C; and the E alternative with side walks 0.5 m below deck level is finally recommended as the cross section of tender design.

Similarly, the results for Humen Bridge are listed in Table 3. It is

obvious that, C1 alternative(the original cross section with anti-collision wall) should be confirmed as an optimal choice according to both flutter and buffeting behaviours.

	CO	C1	B	D
C_L'	3.78	3.04	5.11	3.96
$C_L'/C_L'(CO)$	1.00	0.82	1.35	1.06

Table 3. Buffeting-based relative comparison
for Humen Bridge.

5. Concluding Remarks

1. For long-span suspension bridges, the aerodynamic selection of deck cross section is an important process in the stage of feasibility study for checking the wind-resistant safety of the conceptional design of bridge structure.

2. The effect of attack angle on streamlined cross section may change its aerodynamic derivative A_2^* curve to that like a nonstreamlined one with a critical point on the $\frac{U}{fB}$ coordinate, which can also be used to assess the aerodynamic stability together with the critical wind speed measured directly from the wind tunnel test.

3. The buffeting-based selection can be considered approximately through the relative comparison of lift slope coefficient C_L' measured from static 3-components test in wind tunnel.

4. The final deck cross section recommended for the tender design of Humen Bridge and Jiangyin Bridge in China was decided after the assessment of both aerodynamic stability and buffeting behaviour.

References

1. T. A. Reinhold, M. Brinch and A. Damsgarrd, Aerodynamic of bridge, Balkema,(1992)255
2. T. Miyata, K. Yokoyama, M. Yasuda and Y. Hikami, aerodynamic of bridges, balkema,(1992)217
3. H. F. Xiang, et al, Research Report, SLDRCE at Tongji University, (1993)
4. H. F. Xiang, et al, Research Report, SLDRCE at Tongji University, (1992)
5. M. Gu, W. Chen and H. F. Xiang, Proc. EASEC-3, Shanghai, (1991)

Wind Tunnel Testing for the Second Severn Bridge

P.A. Irwin and J. Xie

Rowan Williams Davies and Irwin, Inc. (RWDI)
650 Woodlawn road West, Guelph, Ontario, Canada N1K 1B8

Abstract: In this paper, wind tunnel studies on the Second Severn Bridge are described, which included 1:50 scale sectional model tests and 1:125 scale aeroelastic model tests. The effects of deck configurations, i.e. wind barrier, built-up ice, traffic, etc. on the wind induced response were investigated. The comparisons between the aeroelastic model, sectional model and the buffeting theory are presented and discussed.

1. Introduction

The Second Severn Bridge is a composite cable stayed bridge with a main span of 456m long over the River Severn in England. A novel feature of the bridge is that it has a 3m high 50% solid wind screen (wind barrier) on each side of the deck to shelter traffic from the wind. This altered the aerodynamic stability characteristics and increased wind loading.

To ensure aerodynamic stability and establish wind loads, wind tunnel tests were undertaken by RWDI during design[1],[2],[3]. The wind tunnel testing examined both the completed bridge and the bridge in construction stages. Initial tests in RWDI's 2.4m x 1.8m wind tunnel utilized sectional models at 1:50 scale. The effects of variations in deck cross section on aerodynamic stability and vortex excitation were explored as well as the influences of turbulence and traffic. Following the sectional model tests, a full aeroelastic model at 1:125 scale was designed and tested in RWDI's 4.9m x 3.0m wind tunnel, Figure 1. The modelling principles used were generally as described by Irwin[4] . Again the effects of deck configurations, turbulence and traffic were examined. A number of different construction stages, which represent the worst cases for wind effects, were examined using the aeroelastic model, including the case of a free-standing tower.

This paper summarizes some results of the wind tunnel tests, which include:
1.   effects of wind barrier;
2.   effects of built-up ice on wind barrier;
3.   effects of traffic;
4.   comparison of open deck cross-section with enclosed cross-section;
5.   comparison of aeroelastic model results with sectional model results; and
6.   comparison of wind tunnel test results with buffeting theory.

2. Effects of Deck Configurations on Wind Response

In the design stage, numerous sectional model tests were carried out on the initial bridge
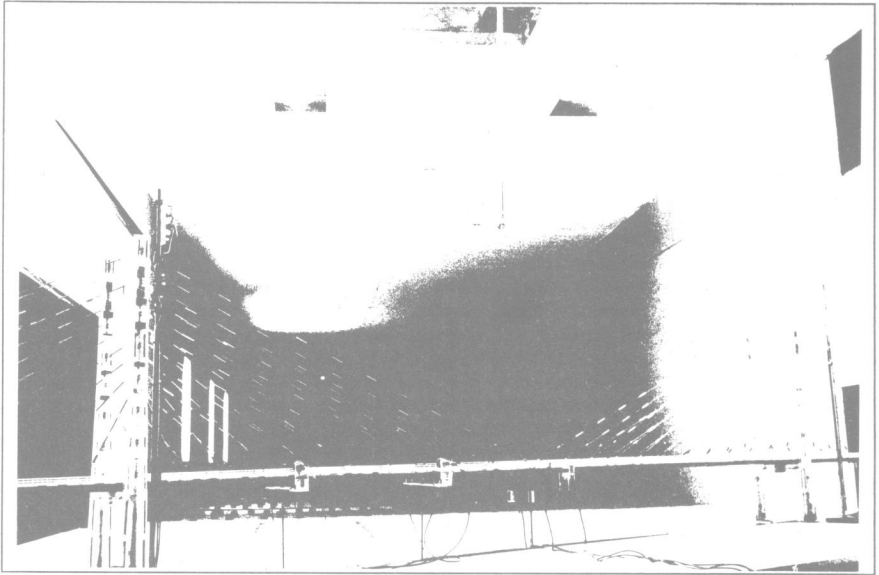
Figure 1: Aeroelastic Model of The Second Severn Bridge

deck design and variations of it. The intent was to arrive at a cross-section with sufficient aerodynamic stability to meet the criteria for the bridge set by the Department of Transport. These included a 60 m/s requirement for the flutter speed at zero angle of attack and a requirement that vortex oscillations cause rms accelerations less than $0.14/\sqrt{N}$ in winds below 20 m/s, where N is frequency in Hz. Through appropriate edge detailing a satisfactory response was achieved.

As the deck in construction stages has no wind barrier, tests were undertaken with and without wind barrier which allowed its effect to be examined in the sectional model tests. Figure 2 shows the static force and moment coefficients for these two configurations. The drag coefficient was based on vertical height of the deck without wind barrier. It can be seen that the wind barrier increased the drag forces by about 67% at zero degree angle of attack, which is quite close to the increase in overall projected area of the deck. On the other hand, the wind barrier will tend to reduce the static lift force and pitching moment for most of the angles of attack. The aeroelastic model tests showed that the completed bridge with this wind barrier achieved a flutter speed of 62 m/s at deck level at zero angle of attack. Vortex excitation was not noticeable even in smooth flow at zero angle of attack, where the structural damping ratio was about 0.65%. Some vortex excitation which occurred at positive 2.5 degrees of angle of attack in smooth flow disappeared in the simulated turbulent boundary layer.

In the early sectional model tests, an enclosed deck version was also investigated, as indicated in Figure 3. The comparison tests with and without enclosure showed that the enclosed

108

version had significant effects on suppressing vortex excitation, but on the other hand the flutter speed was reduced. Figure 3 shows the flutter speed found with sectional model tests for different angles of attack.

In winter time, accumulated ice on the wind barrier may affect the aerodynamic stability and thus in the wind tunnel tests this kind of case was examined. The ice was simulated by modifying the three horizontal rails of the wind barrier with the gap between rails reduced by 75 mm. Figure 4 is the predicted vertical displacement at mid-span at positive 2.5 degrees of wind angle of attack, obtained from the aeroelastic model tests. The ice significantly increase vortex excitation at 2.5 degree angle but the response was considered acceptable at zero degrees. With iced-up barrier, the flutter speed was reduced by 14%. However, the ice does not seem to have much impact on buffeting response.

Figure 2: Static Force and Moment Coefficients for The Deck with and without wind Barrier
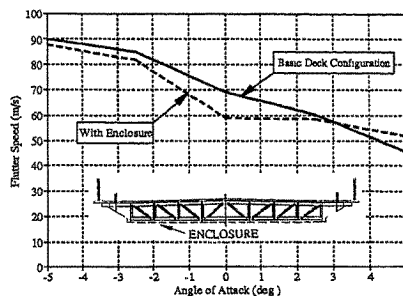
Figure 3: Comparison of Flutter Speed for Open and Enclosed Deck Configuration (Based on Section Model Tests)

Figure 4: Effects of Built-up Ice on Wind-Induced Vortex Excitation (Based on Aeroelastic Tests)

Also, of the static force coefficients only the drag coefficient was significantly affected by the iced-up barrier.

The traffic effects on wind responses were considered by simulating three typical traffic cases, i.e. roughly uniformly distributed traffic (Case 1), an unbalanced traffic case with vehicles on the upwind side only (Case 2) and an unbalanced traffic case with vehicles on the downwind side. Figure 5 presents the measured static force and moment coefficients for these cases. All these traffic cases gave similar results. This is mainly because of the wind barrier and its shielding effect. Based on the sectional model results, traffic case 3, which represented a worst case among the traffic patterns, was chosen for aeroelastic

109

tests, in which both the profile and the weight of the vehicles were simulated. The traffic showed little impact on buffeting response, but caused a noticeable increase in flutter stability. The improvement of flutter stability by traffic is somewhat academic since no vehicles would be on the bridge at these speeds, but the results do verify that the wind-induced responses will not become more severe because of traffic.

Figure 5: Effects of Traffic on Static Forces and Moments

3. Comparison of The Aeroelastic Model Results with Sectional Model Results

Figure 6 shows the predicted vortex-induced vertical deflection at mid-span based on the aeroelastic model tests and the sectional model tests. All these results are for 2.5 degrees angle of attack under varies turbulence intensities, this angle being chosen rather than zero degrees since there was little vortex shedding to be observed at zero degrees even on the sectional model. The amplitude measured on the aeroelastic model was lower than that directly measured from the corresponding sectional model.

The flutter speed obtained directly from a sectional model is often lower than that from an aeroelastic model for cable stayed bridges, especially when the similarity between the vertical mode shape and the torsional mode shape is poor. The flutter instability for cable stayed bridges may occur in higher modes or for multi-mode combinations[5]. An analytic approach is sometimes needed to predict the flutter speed based on sectional model tests[6]. However this seems not the case for the Second Severn Bridge. Both the computed modes and the modes measured on the aeroelastic model showed a close similarity between the vertical

Figure 6: Comparison of Aeroelastic Model Results with Sectional Model Results for Vortex Excitation (2.5° Angle of Attack)

mode and the torsional mode shapes, so good agreement between the aeroelastic model and the sectional model was expected. The measured flutter speed from the aeroelastic model was actually a little lower, by about 10%, than that from the sectional model, but still acceptable, and this was thought to be possibly due to Reynolds number effects, particularly on the flow near the edge which was found in the sectional model tests to be very sensitive to the edge details.

4. Comparison of Buffeting Theory with Aeroelastic Model Tests

The buffeting theory applied to the Second Severn Bridge was quasi-static theory which uses the static force and moment coefficients obtained from sectional model tests and gives a first order approximation of bridge response to wind loading, including both resonant and background contributions[7],[8]. Since the static force and moment coefficients vary with angle of attack, α, weighted average values were used in the buffeting analysis. Let $C(\alpha)$ be any one of these coefficients and $C'(\alpha)$ be the corresponding derivative with respect to the angle of attack, then the weighted averages $\bar{C}$ and $\bar{C}'$ were determined from

$$\bar{C} = \int_{-\infty}^{\infty} C(\alpha) \, p(\alpha) \, d\alpha \qquad ; \qquad \bar{C}' = \int_{-\infty}^{\infty} \frac{dC(\alpha)}{d\alpha} \, p(\alpha) \, d\alpha$$

where $p(\alpha)$ is the probability density of the angle of attack. It was assumed that this probability density could be expressed by a Gaussian distribution, and the angle of attack was mainly due to the vertical component of turbulence velocity. Thus the probability density of the angle of attack was written as

$$p(\alpha) = \frac{1}{\sqrt{2\pi} \, I_w} \exp\left[-\frac{1}{2} \frac{\alpha^2}{I_w^2}\right]$$

where I_w is the vertical turbulence intensity.

The following table gives examples of the mid-span peak amplitudes at 40 m/s wind speed, quoted from Ref.[2] and [3] for the completed bridge. While the buffeting theory provides results of the right magnitude, it does involve a number of assumptions and it is preferable to obtain response information from an aeroelastic model.

Location	Direction	Aeroelastic Model	Buffeting Theory
Deck Centre	Vertical	0.215 m	0.2595 m
Deck Centre	Lateral	0.044 m	0.0556 m
Deck Centre	Torsional	0.592 deg.	0.3962 deg.
Deck Edge	-	0.283 m	0.2917 m

5. Conclusion

Comprehensive wind tunnel studies were undertaken by RWDI for the Second Severn Bridge for both the completed structure and for various construction stages. The testing indicated that satisfactory aerodynamic stability could be achieved even in the presence of substantial barriers near the edge of the deck to shield traffic from wind. The aeroelastic model results gave

111

a slightly lower flutter speed, but less vortex excitation than the sectional model. Comparison of the aeroelastic model with buffeting theory showed the theoretical estimates were of the right order but for best accuracy an aeroelastic model is to be preferred.

Acknowledgements

References:

1. A. Steckley and P.A. Irwin, Sectional Model Studies for The Second Severn Crossing, RWDI Report 91-141F-5-2, December, 1991

2. J. Xie and P.A. Irwin, Prediction of Buffeting Response Based on Steady State Sectional Model Tests for Second Severn Crossing, RWDI Report 91-141F-5-3, March, 1992

3. J. Xie and P.A. Irwin, Full Aeroelastic Model Studies for Second Severn Crossing, RWDI Report 91-141F-5-ARO, February, 1993

4. P.A. Irwin, Full Aeroelastic Model Tests, Proceedings of The 1st International Symposium on Aerodynamics of Large Bridges, Copenhagen, February, 1992

5. J. Xie and H. Xiang, New Concepts on Wind Resistant Design of Bridges - Multi-Mode Coupled Flutter, China Civil Engineering Journal, Vol.23, No.2, 1987

6. J. Xie, State-space Method for 3-D Flutter Analysis of Bridge Structures, Proc. of Asia Pacific Symposium on Wind Engineering, India, 1986

7. P.A. Irwin, Wind Tunnel and Analytical Investigations of The Response of Lions' Gate Bridge to A Turbulent Wind, NRC Tech. Report LTR-LA-210, 1977

8. J. Xie, H. Tanaka, etc., Buffeting Analysis of Long Span Bridges to Turbulent wind with Yaw Angle, J.Wind Eng.Ind.Aerodyn., Vol.37, No.1, 1991

Aerodynamic Stability of Self-anchored
Double Deck Suspension Bridge

S.D. Kwon[+], S.P. Chang[+], Y.S. Kim[++] and S.Y. Park[+++]

[+]Department of Civil Engineering
Seoul National University, Korea
[++]Hyundai Construction Co.
formerly KAIST, Korea
[+++]Yooshin Engineering Co., Korea

Abstract : Aerodynamic stability of Young-Jong bridge was evaluated by section model test, tower model test and full elastic model test. The bridge girder was modified to improve aerodynamic stability through section model test and adopted section was useful to suppress vibration within design wind velocity. Stability of final section was verified by full elastic model test. Bending and torsional vibration was observed at free standing stage and completion stage of tower. The problem could be solved by providing corner cut with tower column or increasing structural damping alternatively.

1. Introduction

Young-Jong bridge (provisional name) is planned to build at western seaside of Korea and it will connect the new international airport at Young-Jong island to Inchun city with total length of 4420m. Most of span consist of steel truss or orthotropic deck but main span of Young-Jong bridge is designed to suspension bridge with center span of 300m and side span of 125m each.

The suspension bridge has some distinctive features. Double deck whose top deck has 6 lanes and bottom deck has 4 lanes with double track railroad is adopted for girder to satisfy the traffic volumes. Main cable is anchored at top steel deck directly without anchorage block and horizontal tension force of cable is resisted by axial stiffness of girder. Ordinary suspension bridge has only vertical cable sag but Young-Jong bridge has both vertical and horizontal sag.

A series of wind tunnel test were carried out to investigate aerodynamic stability, serviceability of girder under various wind condition for design consideration. This paper shows the results of wind tunnel tests and some aerodynamic and/or mechanical remedy for girder and tower to suppress vibration are presented.

2. Test Models

Section model of 1/100 in scale was distinguished three types to edge shape of top deck. Original section consist of bluff top deck and truss members but aerodynamic device such as fairing and spoiler were attached at edge of top deck for modified section.

Elastic tower model scaled 1/150 was manufactured for free standing stage and complete stage. After finishing test for free standing stage, coil spring which was carefully scaled by similarity law was attached at the top of tower instead of cable to simulate structural characteristics of completion stage. But coupling effect of two towers and constraint of connection between girder and tower could not simulated.

Full elastic model of 5.5m long was constructed using steel frame and wooden form. Each steel frame and wooden cover took a role of stiffness and geometric shape. Scale of 1/100 was decided considering convenience of transportation and safety of model. Piano wire was used for cable and mass of cable was adjusted by lumped lead ingot with proper spacing. Measured

frequency of model in Table 2 are good agreement with calculated frequency and damping ratio is luckily similar to design damping ratio.

3. Experimental Procedure

Section model test and tower model test was conducted at Göttingen type wind tunnel of Seoul National University where the test section is 1.37m(W) × 0.95m(H). Wind tunnel of University of Tokyo was used for full elastic model test and test section of the wind tunnel is 16m(W) × 1.9m(H).

Vibration response were measured using pair of non contact optical displacement transducer. Vertical and torsional response were separated by adding and difference of each signal. Two kinds of turbulent flow were generated by wooden grid and oil damper was used to adjust damping ratio of section model.

Static wind force of girder under smooth flow was measured by force balance. Changing angle of attack from -7 deg to +7 deg, spring mounted section model was tested for low damping and design damping ratio to directly watch the aerodynamic instability phenomena. Flutter derivative H_1^*, A_1^*, A_2^* were also derived from free oscillation test. Tower model was exposed to smooth and turbulent flow with various horizontal wind angle.

Full elastic model was tested both smooth and turbulent flow. Response of vertical, torsional and lateral vibration at half and quarter point of center span and at mid point of tower were measured.

4. Response of Girder

Measured aerostatic coefficients are shown in Fig.7. Drag coefficient 2.05 is similar to same type of girder, but gradient of lift coefficient is somewhat large value about 5.432.

From the results of spring mounted model test, catastrophic instability phenomena do not occur, while vertical and torsional vortex-induced vibration occurred at original section within design velocity. Fairing and spoiler are attached at upper deck in order to stabilize vortex-induced vibration. Consequently, only torsional vortex-induced vibration was seen near the design velocity at high attack angle. Fig. 8 shows relation between attack angle and wind velocity of vortex-induced vibration.

No vibration occurred at full model test under smooth flow within 70m/s. Because of sharp gradient of lift coefficient, excessive vertical oscillation under turbulent flow was worried, but experimental results show that changing of attack angle do not affect the magnitude of response greatly. Horizontal RMS response of center span under turbulent flow was just only 5cm at design wind speed and it seems to be the contribution of horizontal cable sag to restrain horizontal movement. Buffeting response are allowable from engineering point of view.

5. Response of Tower

For free standing stage, out-of-plane bending vibration was occurred at low velocity of 11m/s and torsional vibration was observed at near the design velocity. Fig. 9 shows that 1.0% of structural damping ratio is enough to suppress bending vibration, but no remedy was adopted for torsional vibration. Fig. 10 shows the relation between horizontal wind angle and vibration amplitude. When wind blow perpendicular to bridge axis, torsional amplitude of tower became peak but the peak of out-of-bending vibration would observed at 5°. Increasing wind angle, response decrease gradually except for torsional response at 10°.

For full elastic model test, two kinds of vibration were measured under smooth flow. First, out-of-plane bending vibration occurred at 40m/s - 47m/s. Second, torsional vibration started at 51m/s and it would continue until 60m/s. But only a bending vibration was seen under turbulent flow. Furious vertical vibration of girder might be one of the cause of preventing out-of-phase torsional vibration of tower.

The experimental results of full model test and tower model test for completion stage are somewhat different. Velocity of full model which peak amplitude occurred at is lower than that of tower model test. It is not verified but interaction between two tower, model imperfection may effect the discrepancy.

Some aerodynamic devices such as deflector were attached to the column of tower to suppress vibration, but there was just little reduction of amplitude. Finally, corner cut was tried and Fig. 11 shows the results. When width of column to cutting size ratio became about 1/10, amplitude reduced about 50% for bending vibration and 60% for torsional vibration. But large cutting size aggravate bending vibration.

Fig. 12 shows relation between structural damping and peak amplitude. As can be seen, it need high damping ratio to suppress the response especially for torsional response.

6. Concluding Remarks

Aerodynamic stability of Young-Jong bridge was evaluated at various view points by a series of wind tunnel tests. The bridge girder was modified to improve stability through section model test and adquateness of adopted section was verified by full elastic model test. Bending and torsional vibration was observed at tower and not only providing corner cut with tower column but also increasing structural damping would effectively reduce the vibration.

Acknowledgment

Reference

1. Honshu-Shikoku Bridge Authority, Wind Tunnel Testing for Akashi Straits Bridge, 1990
2. Japan High Way Association, Wind Resistant Design for High Way Bridge, 1991
3. K. Okawa, M. Matsumoto, M. Kitazawa and T. Yamasaki, Proc. International Colloquium on Bluff Body Aerodynamics and Its Applications, Kyoto, (1988)501
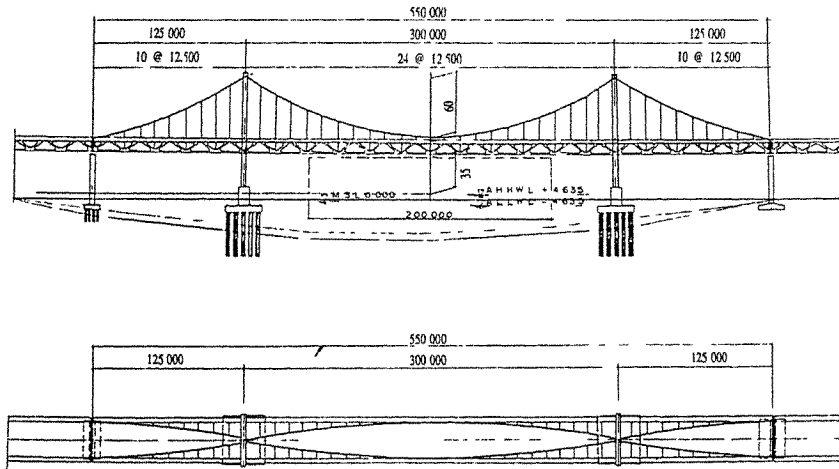
Fig. 1 General views of Young-Jong Bridge

Fig. 2 Tower of Young-Jong Bridge

mode	calculated freq. [Hz]	measured freq.[Hz]	damping ratio(%)
out-of-plane 1	4.206	4.291	0.22
in-plane 1	11.135	11.061	0.45
torsional	21.674	20.404	0.17
out-of-plane 2	26.256	-	-
in-plane 2	46.376	42.375	-

Table 1. Natural frequency and damping ratio of tower model

mode	calculated freq. [Hz]	measured freq.[Hz]	damping ratio (%)
VS1	4.535	4.785	0.493
VS2	11.329	10.938	-
VAS1	7.499	7.813	0.212
VAS2	21.972	24.512	-
TS1	12.228	12.207	0.468
TS2	15.700	15.713	-

Table 2. Natural frequency and damping ratio of full elastic model

Fig. 3 Cross section of Young-Jong Bridge

Fig. 4 Elastic tower model

116

Fig. 5 Section model of girder

Fig. 6 Full elastic model
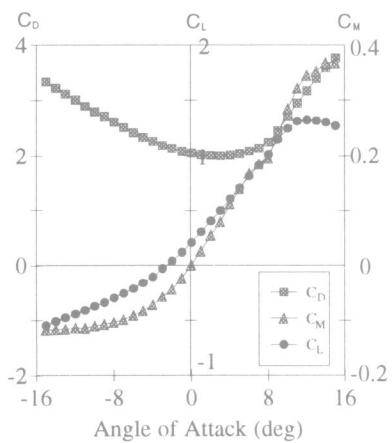
Fig. 7 Aerostatic coefficients of girder
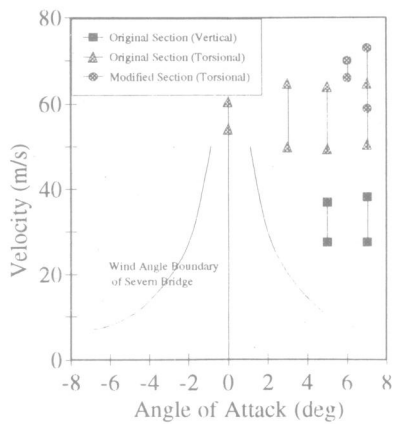
Fig. 8 vortex-induced vibration of
girder (section model test)

117
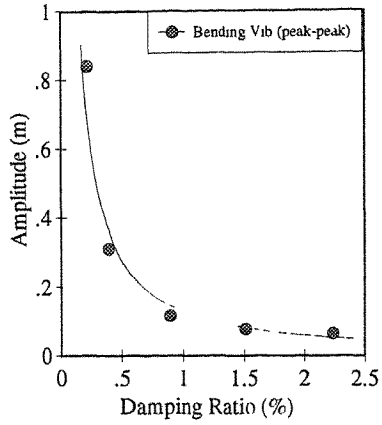
Fig. 9 Relation between amplitude and
damping ratio of free standing tower
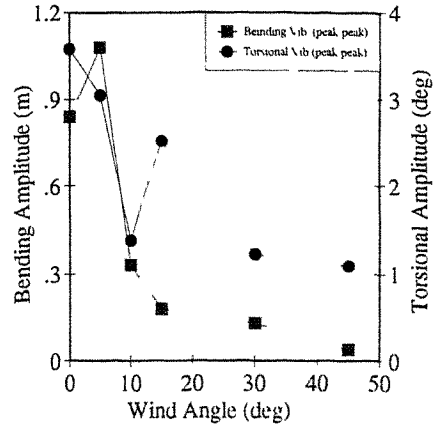
Fig. 10 Relation between wind angle and
amplitude (free standing tower)
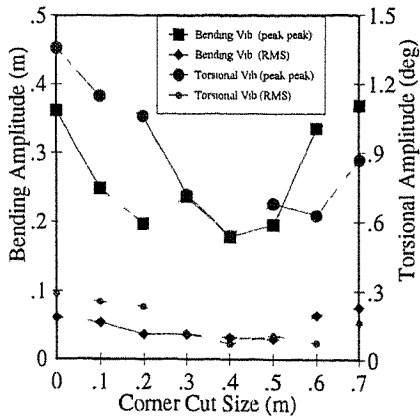
Fig 11 Relation between corner cut size
and amplitude (full model test)
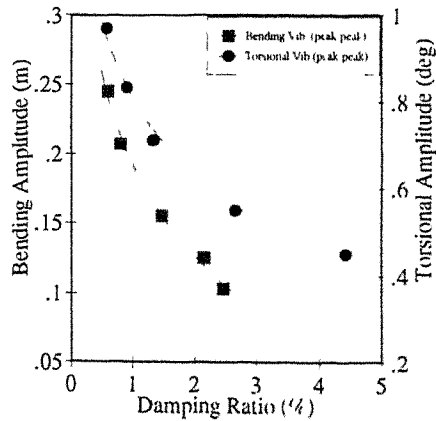
Fig 12 Effect of structural damping and
amplitude (full model test)

118

Analysis of experimental data from wind-induced response of a long span bridge

J. M. W. Brownjohn, A. Zasso[+], G. A. Stephen[++] and R. T. Severn[+++]

Nanyang Technological University, Singapore
[+]Politecnico di Milano, Italy
[++]University College of North Wales, UK
[+++]University of Bristol, UK

Abstract: The movement of the deck of a long span suspension bridge is the result of several different effects. Isolating the individual load-response relationships requires careful measurement of a range of loading and response parameters over a very long period. This paper examines some of the problems and solutions in this procedure and presents a few results.

1. Introduction

Two series of measurements [1] on the Humber Suspension Bridge (Fig. 1) in the first halves of 1990 and 1991 provided a large database of recorded data representing static and dynamic response for vertical, lateral, torsional and longitudinal motion of the main span and a tower under a range of loading conditions.
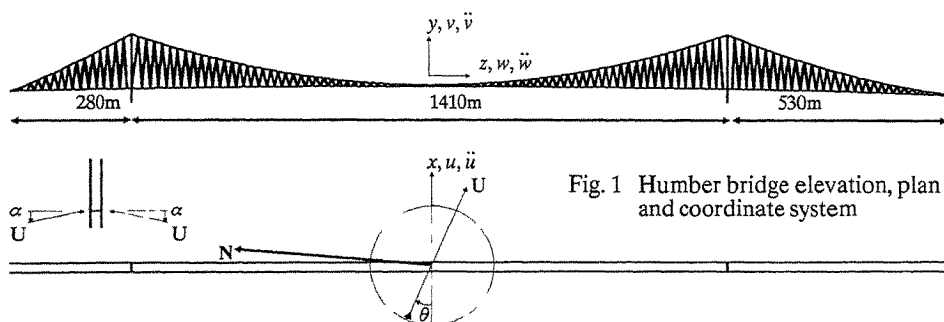
Fig. 1 Humber bridge elevation, plan and coordinate system

The measurements were conducted by Politecnico di Milano, together with the University of Bristol, Humber Bridge Board and ISMES. The main objective of the exercise was to calibrate mathematical modelling [2] of bridge aerodynamic behaviour. A second objective was to quantify relationships between the various loading and response phenomena.

2. Loading and response

Load parameters include:

Traffic   (number, speed and weight of vehicles)
Solar heating   (average and differential temperature T)
Wind   (mean speed U, bearing θ, angle of attack α, turbulence intensity I).

These lead to vertical, lateral, torsional and longitudinal displacement and acceleration of the suspended structure and more limited movements of the towers.

The term 'static' implies an averaging time greater than period of lowest vibration mode (20seconds). The static response is characterised by a deflected shape and an amplitude.

119

'Dynamic' implies vibrations at all frequencies, although for wind induced response deck modes below 1Hz are of greatest interest. The dynamic response is characterised by an amplitude, a deflected (mode) shape φ_n, a resonant frequency f_n and a damping factor ζ_n.

3. Acquired data

Data acquired by Bristol University totalled 4400 hours monitoring of 8 or 16 channels at 8Hz, stored in 3.2GByte of data files. The data channels were selected from up to 70 available wind, temperature and response sensors. Full details of the measurements are given in [1]. To aid identifying relationships between loading and response the data were 'compressed' to manageable quantities by computing parameters over representative averaging periods.

3.1 Choice of averaging period

A 512 second period was chosen for analysis, being longer than any period of oscillation or the time taken for a vehicle to cross the bridge. Data were thus divided into 512 second segments.

For correlations of dynamic loading and response longer segments would have the advantage of improving resolution of frequency and damping estimates while shorter segments would provide more segments to average hence lower variance errors.

Where a load or response measurement is corrupted by noise or instrumentation effects there may be some advantage in using shorter segments, since a smaller proportion of the shorter data segments may not be affected.

3.2 Data reduction

The Bristol data were reduced to 31096 data segments each with values μ, σ for the measured channels and combinations of channels (e.g difference of accelerometer signals to give torsional response or product of wind speed U and $\cos\theta$ to give normal wind vector). Processed dynamic response data were reduced by storing modulus values of Fast Fourier Transform (FFT) for each segment for the 0-1Hz range.

4. Static correlations

In analysing the data most of the possible combinations of static load and response were initially investigated via scatter diagrams of μ and σ for the displacement parameters vs μ for U, U $\cos\theta$ and T. Except for isolated cases of very heavy vehicles, no usable information on traffic loading was available other than number of vehicles per hour.

In 1990 main span lateral and vertical deflection were measured by two optical systems [3,4]. Fig. 2a is a scatter diagram of lateral deck deflection and east main cable midspan temperature for a period of 24 days. The relationship is not clear because of the variable wind. Fig. 2b shows only those data points for Fig. 2a and other monitoring periods for which the wind speed lay in a low, narrow range (3-5m/sec), more clearly showing a linear relationship which probably arises from unequal solar heating.
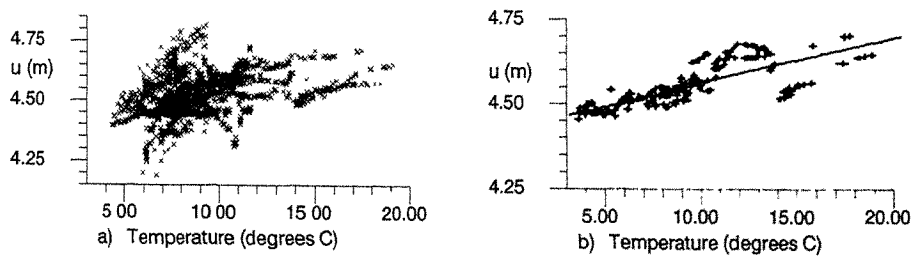
Fig. 2 Main span lateral deflection a) all wind speeds b) for low winds only

Fig. 3a shows lateral deflection and normal wind component U $\cos\theta$ for the same 24 day period. The effects of temperature can be compensated for, given the established relationship of Fig. 2b, and Fig. 3b shows the 'cleaned up' correlation.

a) Normal wind (m/sec)   b) Normal wind (m/sec)
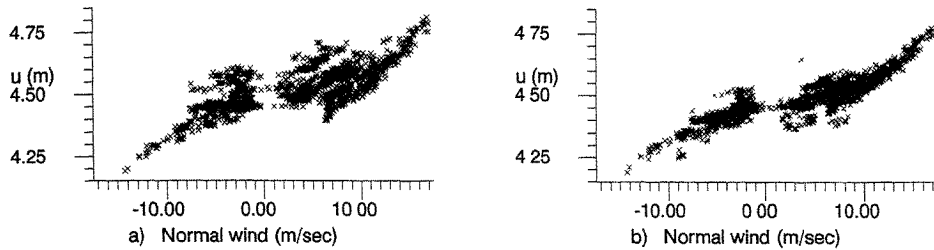
Fig. 3   Main span lateral deflection a) without and b) with compensation for temperature effect

Other possible correlations were investigated, Table 1 gives a summary of the results.

As demonstrated in Figs. 2,3 correlations can be defined clearly if only one load function varies and the response parameter measured is unambiguous.

There is no obvious means of compensating for traffic effects, the best that can be done is to reject data corresponding to periods having high RMS values of longitudinal deck displacement, since this appears be more sensitive to traffic than anything else. Traffic also affects dynamic measurements (of vertical and torsional acceleration response).

	Vertical Displacement	Rotational Displacement	Lateral Displacement	Longitudinal Displacement
(a) Temperature	✓	✗	✓	✓
(b) Mean wind speed	✓	✓	✓	✗
(c) Traffic	✓	✓	✗	✓
(d) Wind turbulence	✓	✓	✓	✗
Main causes	(a) and (c)	(b)	(a) and (b)	(a) and (c)

Table 1   Correlations with displacement; 'tick' is strong, 'x' is weak or nil.

5. Dynamic and directional correlations

For dynamic response the correlations are derived from the FFT of acceleration response. The RMS of acceleration in a particular mode of vibration is taken by summing the squared FFT ordinates around that mode while the damping ζ and resonant frequency f_n are estimated by attempting to fit a single degree of freedom (SDOF) oscillator response curve to the data, Fig. 4. Data storage space could be reduced by storing only these relevant data points rather than the whole spectrum.

Fig. 5a shows variation of RMS for symmetric vertical mode (f_n = 0.125Hz) during part of the monitoring. The values show a daily pattern consistent with variation of traffic volume, and latterly a two day period of high winds. Fig. 5b relates the response during this period to the wind speed U.

$$\ddot{v} = \frac{A_n(2\pi f)^2}{\left| 1 - (f/f_n)^2 + 2i\zeta_n f/f_n \right|}$$

$$RMS = \left[\sum_{i=1}^{n} a_i^2/2 \right]^{1/2}$$
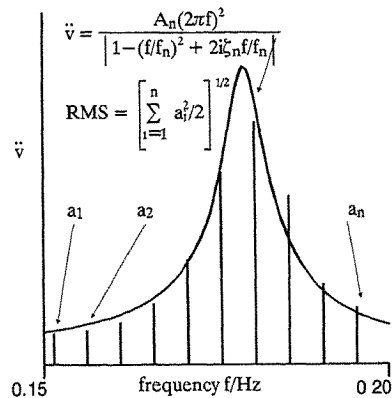
Fig. 4   Evaluation of RMS and modal parameters

121
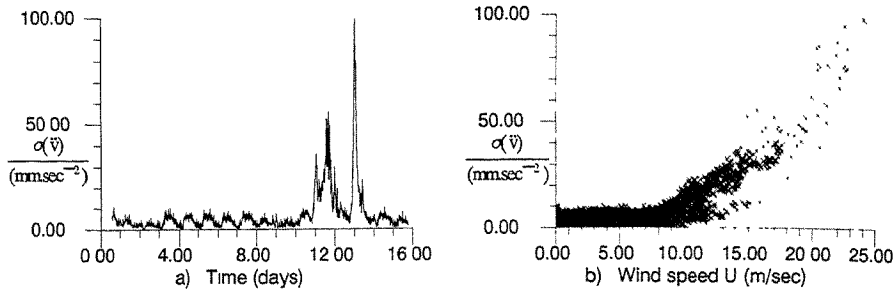
Fig. 5 RMS acceleration, vertical mode 1 a) showing daily cycle b) relationship with wind speed

Data such as in Fig. 5b were obtained corresponding to narrow ranges of θ. Parabolas of the form RMS $= c_1 + c_2(\theta) \cdot U^2$ were fitted to these data [5]. Fig. 6 shows values of c_2 together with the best fit of the expected $c_2 \propto |cos\theta|$ relationship. The goodness of fit for the c_2 values are indicated by size of '×' symbol. Most of the wind and the strongest winds were from the southwest quadrant $(-85.5° < \theta < 4.5°)$.
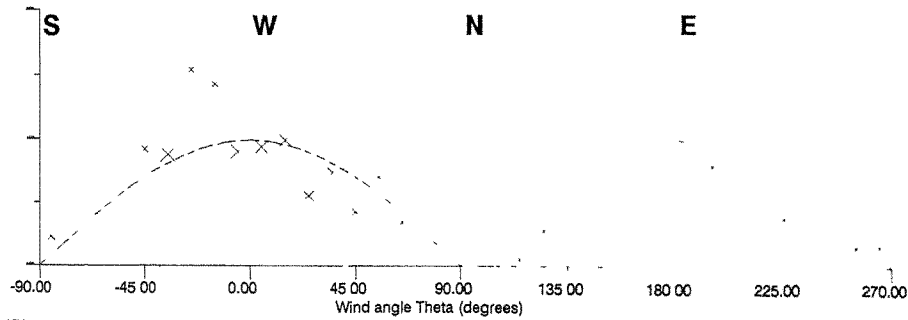
Fig. 6 Variation of parabolic coefficient for RMS response with wind bearing θ

Traffic effects constitute a high level of background noise which can drown the true modal response so the most reliable correlations would be obtained for high winds; RMS values of vertical acceleration response due to vehicles are similar to those due to winds up to about 5m/sec. Periods of heavy traffic (weekdays from 6AM to 8PM) were generally excluded in establishing the relationship of Fig. 6 and c_1 takes some account of traffic background in what is left.

Probably the assumptions of parabolic relationship RMS $= c_2 \cdot U^2$ is not quite realistic [6], and the $|cos\theta|$ relationship is questionable [1]. Also, among other effects, the variation of turbulent intensity I and spectral distribution of wind energy have been ignored. Generally $I < 10\%$ except for northerly winds for which I approaches 20% [7]. A description of local wind characteristics is given in [8]. The scatter in Fig 6 shows that even for the large body of data collected, the data remaining after filtering out noisy data are far from adequate to clarify this type of relationship. Concentrating on the more reliable data i.e. for more frequent higher winds only removes the data points in Fig. 6 for winds close to the south and north directions. Fitting a relationship of the form RMS $= c_3 \cdot U^{c_4}$ to these 'good' data gives values of c_4 between 1.8 and 3, more consistently $c_3 \approx 0.04$ and $c_4 \approx 2.4$ for southwest winds with U in m/sec and RMS in mm/sec^2.

A further directional effect appears in the 'angle of attack' α (+ve is rising, Fig. 1). Fig. 7 shows variation of α during periods including a) very strong south-westerly (SW) winds from landward and b) strong north-easterly (NE) winds coming from flat land and open sea. Care was taken to ensure accuracy of the wind vane, leaving this as a possible factor for some differences between modal characteristics for different wind directions.
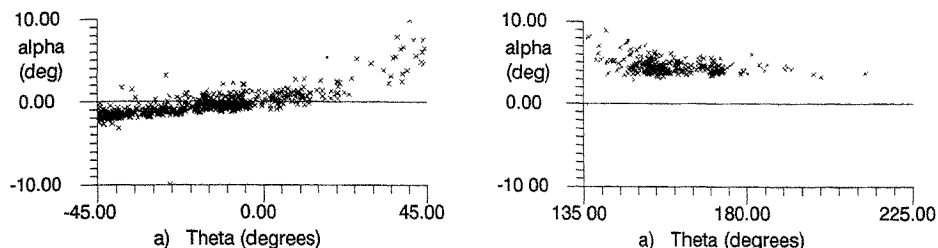
Fig. 7   Wind elevation (angle of attack) α for a) strong westerly and b) strong easterly winds

6. Instrumentation and correlation problems

Dynamic response monitoring equipment presented few problems, only the accelerometers used to measure lateral acceleration sensed static rotation of the deck equally well [4].

The more interesting data were obtained from the optical deflection measuring systems for which this was the first application of this type, requiring measurements of dynamic displacements as small as 1mm and as large as 2m from a distance of 705m in all visual conditions. The prototype Bristol system [4] with sophisticated tracking algorithms was only operable manually, limiting the quantity of data to 60 hours, for some of which the structural tracking system could not operate due to the atmospheric haze blurring the target. The physically more complex ISMES system [3] functioned automatically with occasional realignment to maintain the target in the field of view.

The effect of traffic (particularly heavy goods vehicles) was once again the most significant problem in analysing the displacement data. Vehicles have three significant effects 1) they generate a static deflection whose time history resembles an influence line, 2) they generate vibrations mainly at frequencies above 2Hz but also to a lesser extent at lower frequencies and 3) they modify the dynamic characteristics of the structure.

Effect 1) leads to time histories such as Fig. 8a in which at least five heavy lorries and many cars generate the displacement response, effectively limited to the range 0-0.5Hz. Data of the type shown in Fig. 8b are more reliable for establishing wind-response correlations.
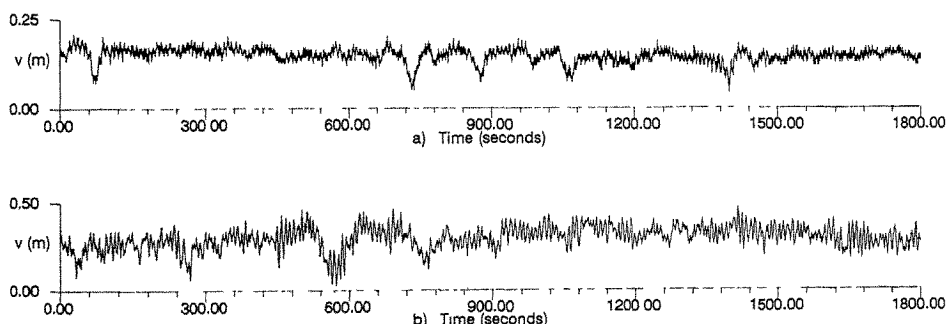
Fig. 7   Main span vertical deflection for a) low wind, high traffic b) high wind, low traffic

For response above ≈ 0.5Hz accelerometers need to be used and effect 2) means that their ranges have to be to at least an order of magnitude more than would be required for wind induced response alone. This reduces signal to noise ratios. Effect 3) can in extremes [9] complicate identification of modal parameters.

7. Conclusions

A number of correlations have been established, with variable clarity. The ranges of loading parameters for which the correlations are valid are strictly limited to those of the measurements.

While the monitoring achieved its main objective (model validation) and also demonstrated the strong effects on response, even with the large body of data there are ranges of loads and load combinations for which the data are sparse and some correlations which are not clear.

If the aim is to produce clear correlations for a large range of loading an intelligent monitoring system should be used over a period of several years to record during low traffic and strong wind and (if necessary to identify temperature effects) during low traffic and minimal winds. Simultaneous data reduction could be used.

8. Acknowledgements

References:
1. J. M. W. Brownjohn, M. Bocciolone, A. Curami, M. Falco, A. Zasso, Humber Bridge full scale measure campaigns 1990-1991. Proceedings, Wind Engineering Society Inaugural Conference, Cambridge, Sep. (1992).
2. F. Cheli, A. Collina, G. Diana, A. Zasso, J. M. W. Brownjohn, Suspension bridge parameter identification in full-scale test. Proceedings, Part 1, 8th International Conference on Wind Engineering, London Ontario, July (1991).
3. A. Zasso, M. Vergani, M. Bocciolone R. Evans, 'Use of a newly designed optometric instrument for long-term, long distance monitoring of structures, with an example of its application on the Humber Bridge.' Proceedings, 2nd International Conference on Bridge Management, April 18-21, University of Surrey, UK (1993).
4. G. A. Stephen, J. M. W. Brownjohn, C. A. Taylor, 'Measurements of static and dynamic displacement from visual monitoring of the Humber Bridge'. Engineering Structures (1993).
5. J. F. Mitchinson, S. F. Sarma, Wind induced response of suspension bridges. BSc thesis, University of Bristol Department of Civil Engineering (1992).
6. A. G. Davenport, G. Larose, The structural damping of long span bridges: an interpretation of observations. Canada-Japan Workshop on Aerodynamics, Ottawa, Sep. (1989).
7. Humber Bridge monitoring: Digital measurements March-May 1990 and preliminary analysis. Report UBCE-EE-90-10, University of Bristol Dept. of Civil Engineering (1990).
8. M. Bocciolone, F. Cheli, A. curami, A. Zasso, Wind measurements on the Humber Bridge and numerical simulations. Proceedings, Part 2, 8th International Conference on Wind Engineering, London Ontario, July (1991)
9. J. M. W. Brownjohn, Damping in suspension bridges: sources, measurements and errors. Proceedings, Third Asia Pacific Symposium on Wind Engineering, Hong Kong, Dec. (1993).

Identification of Flutter Derivatives of Bridge Deck from Free Vibration Data

M. Iwamoto and Y. Fujino+

Department of Architectural and Civil Engineering
Nagoya Institute of Technology, Japan
+Department of Civil Engineering
University of Tokyo, Japan

Abstract: Flutter derivatives of a bridge deck were identified from free vibration motion using a sectional model. Two problems in this method were discussed. First, it is difficult to reduce the identified quantities to non-dimensional parameters because two mode frequencies exist. Parameters can be reasonably obtained using the proposed aerodynamic force model, whose applicability was examined through numerical simulations. Second, at high wind speed the parameters cannot be identified accurately because aerodynamic damping of vertical-dominant mode is too high to last in free vibration. The results of wind tunnel test show that by increasing mass and inertial moment of the experimental model, accurate identification becomes possible at higher wind speed.

1. Introduction

Flutter derivatives of bridge decks are essential parameters necessary to the flutter analysis of flexible bridges such as long-span suspension bridges. There are two kinds of methods to obtain the parameters through wind tunnel tests with the sectional model of bridge decks; the forced vibration technique and free vibration technique, the latter of which is discussed in this paper.

In a theoretical and experimental study of Scanlan [1], a method of extracting flutter derivatives of bridge decks from free vibration data were discussed in detail. This method consists of two stages: first, uncoupled terms are obtained separately from pure vertical and torsional free oscillations; and secondly, coupled terms are obtained from coupled oscillation data.

Yamada et al. [2] proposed a method of simultaneously identifying all eight derivatives from coupled oscillation data using the extended Kalman Filter (EK-WGI method) [3]. This method can simplify the experimental procedure. In their work, wind tunnel tests were made at so high wind speed that the flutter phenomenon occurred in order to obtain the strongly coupled oscillation data. However, it is difficult to obtain the parameters uniquely from such data because the flutter oscillations consist of almost only one mode and have one degree of freedom.

The method proposed in this paper as well as in Ref. 4 is based on the same concept as Ref. 2. All eight flutter derivatives are identified with the extended Kalman Filter from free vibration data. The difference is that the data consisting of two modes i.e. vertical- and torsional-dominant modes at the lower wind speed are used in order to develop the stability of the identification. This method is applied to a thin box girder section.

Two difficulties involved in the proposed method are also discussed. First, it is difficult to reduce the identified quantities to flutter derivatives as non-dimensional parameters because two mode frequencies exist. An approximate model of the aerodynamic forces is proposed to obtain the unique parameter values, whose applicability is examined through numerical simulations. Second, at high wind velocity the flutter derivatives cannot be identified accurately because aerodynamic damping of vertical-dominant mode is too high to obtain vibration data enough for the identification. In order to obtain the flutter derivatives at higher wind speeds, wind tunnel tests are made with experimental models whose mass and inertial moment are increased and the results are used for the identification.

2. Wind Tunnel Experiment

Wind tunnel tests were made with a box girder section model as shown in Fig. 1, whose flutter derivatives had already been measured with the forced oscillation technique. The mass and inertial moment of the experimental model were varied as shown in Table 1 with additional mass. For easiness of comparison, supporting springs were adjusted so that the natural frequencies of each case might be almost constant. The experiment was made at an angle of attack of $0°$ in smooth flow. Table 1 also shows the flutter onset velocities which were measured in the preparatory tests. It is found that flutter onset velocity raises as mass and inertial moment increase. Identification was done with the extended Kalman filter (EK-WGI method) from free vibration data as shown in Fig.2 which ware observed after 2DOF (vertical and torsional) excitation.

292.7   (mm)
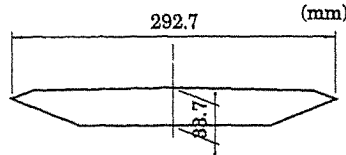
Fig. 1   Cross section of model

Table 1.   Experimental cases and flutter onset velocities

		case 1	case 2	case 3	case 4
mass m (kg/m)		3.35	4.19	4.82	4.19
inertial moment I (kgm²/m)		0.0338	0.0423	0.0486	0.0612
natural frequencies (Hz)	vertical f_z	2.58	2.57	2.82	2.55
	torsional f_θ	5.22	5.13	5.23	5.06
log. structural damping ratios	vertical f_z	0.0217	0.0306	0.0100	0.0172
	torsional f_θ	0.0235	0.0303	0.0187	0.0182
flutter onset velocity U_{cr} (m/s)		15.5	17.6	18.9	19.5
$U_{cr} / (B f_{cr})$		13	14	15	16

a) vertical motion   b) torsional motion
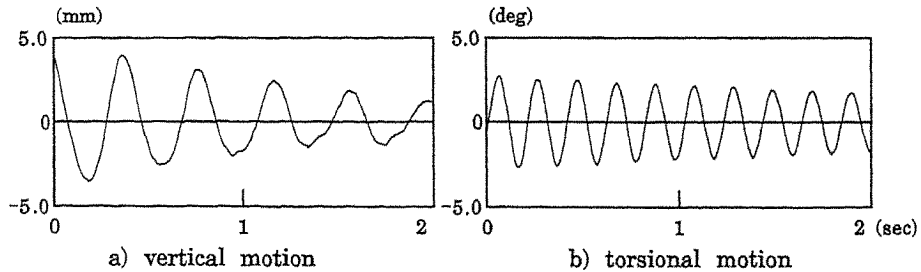
Fig. 2   Time histories at wind speed of 8 m/s, case4

3. Formulation of Aerodynamic Forces

The aerodynamic lift force L and moment M which act on a bridge deck oscillating sinusoidally are written as

$$L = \pi \rho B^3 \omega^2 \left(L_{zR} \frac{z}{B} + L_{zI} \frac{\dot{z}}{B\omega} + L_{\theta R}\theta + L_{\theta I} \frac{\dot{\theta}}{\omega} \right)$$

$$M = \pi \rho B^4 \omega^2 \left(M_{zR} \frac{z}{B} + M_{zI} \frac{\dot{z}}{B\omega} + M_{\theta R}\theta + M_{\theta I} \frac{\dot{\theta}}{\omega} \right)$$

(1)

126

in which z and θ = vertical and torsional motion, respectively; ρ = air density; B = deck width; ω = circular frequency; and L_{zR}, L_{zI}, $L_{\theta R}$, $L_{\theta I}$, M_{zR}, M_{zI}, $M_{\theta R}$ and $M_{\theta I}$ = the non-dimensional flutter derivatives which are functions of the non-dimensional reduced frequency $K = B\omega / U$ in which U = wind speed. According to Eqs. 1, the equations of motion used for the identification are determined as follows

$$m\left(\ddot{z}+2\xi_z\omega_z\dot{z}+\omega_z^2 z\right)=\overline{L}_{zR}z+\overline{L}_{zI}\dot{z}+\overline{L}_{\theta R}\theta+\overline{L}_{\theta I}\dot{\theta}$$

$$I\left(\ddot{\theta}+2\xi_\theta\omega_\theta\dot{\theta}+\omega_\theta^2\theta\right)=\overline{M}_{zR}z+\overline{M}_{zI}\dot{z}+\overline{M}_{\theta R}\theta+\overline{M}_{\theta I}\dot{\theta}$$

(2)

in which m and I = model mass and inertial moment per unit length, respectively; ξ_z and ξ_θ = mechanical damping ratios of bending and torsion, respectively; ω_z and ω_θ = the corresponding natural mechanical circular frequencies; and $\overline{L}_{zR}$, $\overline{L}_{zI}$, $\overline{L}_{\theta R}$, $\overline{L}_{\theta I}$, $\overline{M}_{zR}$, $\overline{M}_{zI}$, $\overline{M}_{\theta R}$ and $\overline{M}_{\theta I}$ = dimensional aerodynamic parameters. These eight parameters are identified as unknown parameters from free vibration data. And then non-dimensional flutter derivatives are given from the identified parameters and known quantities: ρ, B and ω.

Suppose the situation that a bridge deck is oscillating in two modes i.e. vertical- and torsional-dominant modes whose circular frequencies are ω_{q1} and ω_{q2}, respectively, and whose components are (z_{q1}, θ_{q1}) and (z_{q2}, θ_{q2}), respectively. There exist two modal frequencies and the problem is which frequency is to be used for determining the flutter derivatives and the corresponding K values.

In fact, the aerodynamic forces which act on a bridge deck oscillating in the two modes are given form Eqs. 1 as follows

$$L = \pi\rho B^3\omega_{q1}^2\left(L_{zR}\frac{z_{q1}}{B}+L_{zI}\frac{\dot{z}_{q1}}{B\omega_{q1}}+L_{\theta R}\theta_{q1}+L_{\theta I}\frac{\dot{\theta}_{q1}}{\omega_{q1}}\right)+\pi\rho B^3\omega_{q2}^2\left(L_{zR}\frac{z_{q2}}{B}+L_{zI}\frac{\dot{z}_{q2}}{B\omega_{q2}}+L_{\theta R}\theta_{q2}+L_{\theta I}\frac{\dot{\theta}_{q2}}{\omega_{q2}}\right)$$

$$M = \pi\rho B^4\omega_{q1}^2\left(M_{zR}\frac{z_{q1}}{B}+M_{zI}\frac{\dot{z}_{q1}}{B\omega_{q1}}+M_{\theta R}\theta_{q1}+L_{\theta I}\frac{\dot{\theta}_{q1}}{\omega_{q1}}\right)+\pi\rho B^4\omega_{q2}^2\left(M_{zR}\frac{z_{q2}}{B}+M_{zI}\frac{\dot{z}_{q2}}{B\omega_{q2}}+M_{\theta R}\theta_{q2}+M_{\theta I}\frac{\dot{\theta}_{q2}}{\omega_{q2}}\right)$$

(3)

There exist sixteen flutter derivatives in Eqs. 3 and it is impossible to identify all of them uniquely. But Fig. 2 shows that at low and middle wind speed the coupling between vertical and torsional oscillations is weak i.e θ_{q1} and z_{q2} are very small. Therefore, omitting the terms related to θ_{q1} and z_{q2}, we derive an approximate model of aerodynamic forces, with which the flutter derivatives can be identified uniquely:

$$L = \pi\rho B^3\omega_{q1}^2\left(L_{zR}\frac{z_{q1}}{B}+L_{zI}\frac{\dot{z}_{q1}}{B\omega_{q1}}\right)+\pi\rho B^3\omega_{q2}^2\left(L_{\theta R}\theta_{q2}+L_{\theta I}\frac{\dot{\theta}_{q2}}{\omega_{q2}}\right)$$

$$M = \pi\rho B^4\omega_{q1}^2\left(M_{zR}\frac{z_{q1}}{B}+M_{zI}\frac{\dot{z}_{q1}}{B\omega_{q1}}\right)+\pi\rho B^4\omega_{q2}^2\left(M_{\theta R}\theta_{q2}+M_{\theta I}\frac{\dot{\theta}_{q2}}{\omega_{q2}}\right)$$

(4)

Eqs. 4 suggest an answer to the previous problem that ω_{q1} should be used for L_{zR}, L_{zI}, M_{zR}, and M_{zI} related to the vertical motion and ω_{q2} should be used for the others related to the torsion.

4. Numerical Simulations

We examine the applicability of the approximate model of aerodynamic forces through numerical simulations. The actual oscillation waves consisting of two modes in the wind are simulated as shown in Fig. 3 on the supposition that:

127

. The vertical-dominant mode oscillations are caused by eight ω_{q1} components of aerodynamic forces.
. The torsional-dominant mode oscillations are caused by eight ω_{q2} components.
he oscillation waves simulated on these conditions involve the influence of all sixteen derivatives ι Eqs. 3. In these simulations, the structural quantities of case 1 in Table 1 and the flutter erivatives measured with the forced oscillation technique are used. For easiness of calculation, the utter derivatives are calculated with the natural mechanical frequencies f_z and f_θ. These imulated waves are compared with the waves calculated from Eqs.4 on the same initial conditions. ig. 3 shows that the difference is very small.

Next, we identify the flutter derivatives according to Eqs. 4 from the waves simulated with Eqs. and compare the identified values with the assumed values. Fig. 4 shows the results of the omparison. The results shows that the agreement between the identified values and the assumed alues is very good even at high wind speed except for relatively large errors in L_{zR} and M_{zR}, which
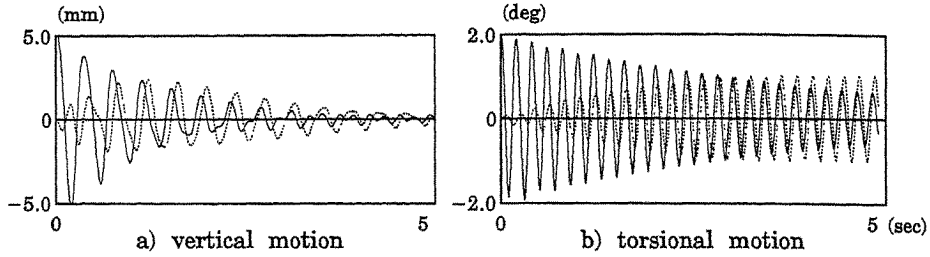
Fig. 3 Comparison between free vibration waves simulaterd from Eqs. 3
and the ones calculated from Eqs.4 (case 1; wind speed: 8 m/s)
———— : simulaterd waves from Eqs.3 ············· : difference (x 50)
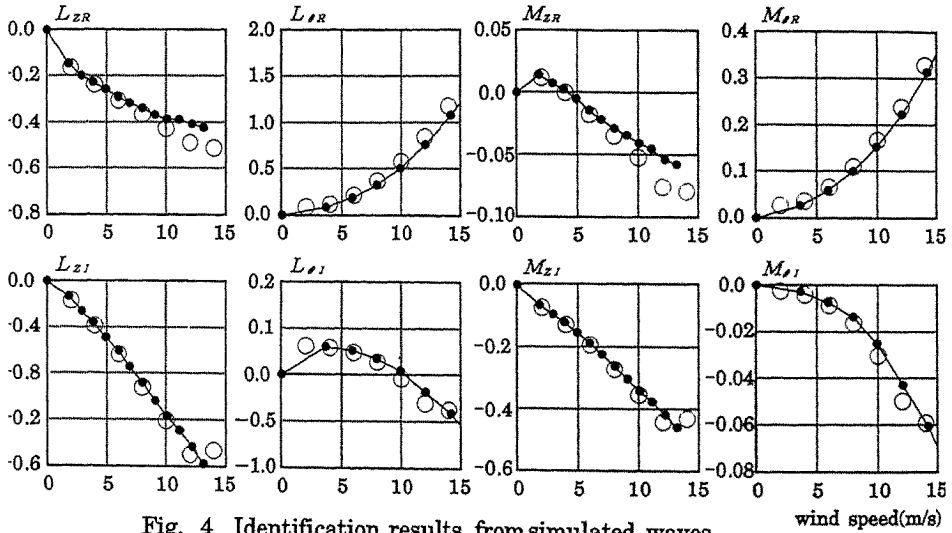
Fig. 4 Identification results from simulated waves
○ : identified values ● : assumed values

128

influence the flutter properties very little.

The proposed approximate model of aerodynamic forces given by Eqs. 4 is therefore very similar to the aerodynamic forces given by Eqs. 3 and is applicable for the identification of the flutter derivatives.

5. Results of Identification from Experimental Data

The sampling time interval and the duration time of the free vibration used for the identification are 0.001 s and 1.0 s, respectively. The corresponding wave numbers of vertical and torsional motions are 2-3 and 5-6, respectively. Fig. 5 shows the identification results of $L_{\theta R}$, M_{zI}, $M_{\theta R}$ and M_{α} for case 1, 3 and 4 in Table 1. It has been proved through the sensitivity tests that these parameters have large influence on the flutter onset velocity. The non-dimensional flutter derivatives are plotted as functions of non-dimensional wind speed $U/(Bf_{q1})$ and $U/(Bf_{q2})$ in which $\omega_{q1} = 2\pi f_{q1}$ and $\omega_{q2} = 2\pi f_{q2}$.

When structural parameters of the experimental model such as mass, inertial moment and natural frequencies are varied, the aerodynamic and modal properties of the system also vary. Additionally, as mass and inertial moment of the model increase, aerodynamic forces decrease relatively to structural terms in the equations of motion (Eqs. 2). These may affect the accuracy of the identification. However, it is found that the tendency of results of all the cases shown in Table 1 agree, and this suggests that even if mass, inertial moment and the ratio between them are varied, constant flutter derivatives can be obtained.

The results of the proposed method and the forced oscillation technique are comparable except two parameters: L_{zR} and M_{zR}. Note that their influence on the flutter properties is very small. By comparison between the cases in Fig. 5, it is found that increasing mass and inertial moment of the experimental model makes stable identification possible at higher wind speed. One of the factors is that increase of mass and inertial moment of the model raises the flutter onset velocity, which is the actual upper limit for the identification of parameters. On the other hand, as is mentioned above, high aerodynamic damping of vertical-dominant mode at high wind speed disturbs accurate identification of the parameters. The increase of mass makes the aerodynamic damping of vertical-dominant mode decrease relatively and makes the oscillations remain for longer time. This is another factor.

In this experiment, the restriction of the supporting springs made large increase of mass and inertial moment of the model impossible. So, we could not obtain the flutter derivatives only until the non-dimensional wind speed of about 15. But, the results of this experiment suggest that if an experiment is made with a heavier model, the flutter derivatives can be obtained at higher wind speed enough for the flutter analysis.

6. Conclusion

This paper proposed an identification method to obtain all eight flutter derivatives simultaneously from free vibration data consisting of two modes i.e. bending- and torsional-dominant modes. As identification technique, the extended Kalman filter (EK-WGI method) was employed. The proposed method was applied to a thin box girder section whose flutter derivatives were measured by the forced oscillation technique. The results of the two methods were comparable except two parameters whose influence on the flutter properties was very small.

Two difficulties involved in the proposed method were also discussed. First, it is difficult to reduce the identified quantities to flutter derivatives as non-dimensional parameters because two mode frequencies exist. An approximate model of the aerodynamic forces was proposed to obtain the unique parameter values. The results of numerical simulations suggested that the proposed model was applicable. Second, at high wind velocity the flutter derivatives cannot be identified accurately because aerodynamic damping of vertical-dominant mode is too high to obtain vibration data enough for the identification. It is shown by wind tunnel test that the increase of mass and inertial moment of the experimental model makes stable identification possible at higher wind speed.

129

a) case 1

b) case 3

c) case 4
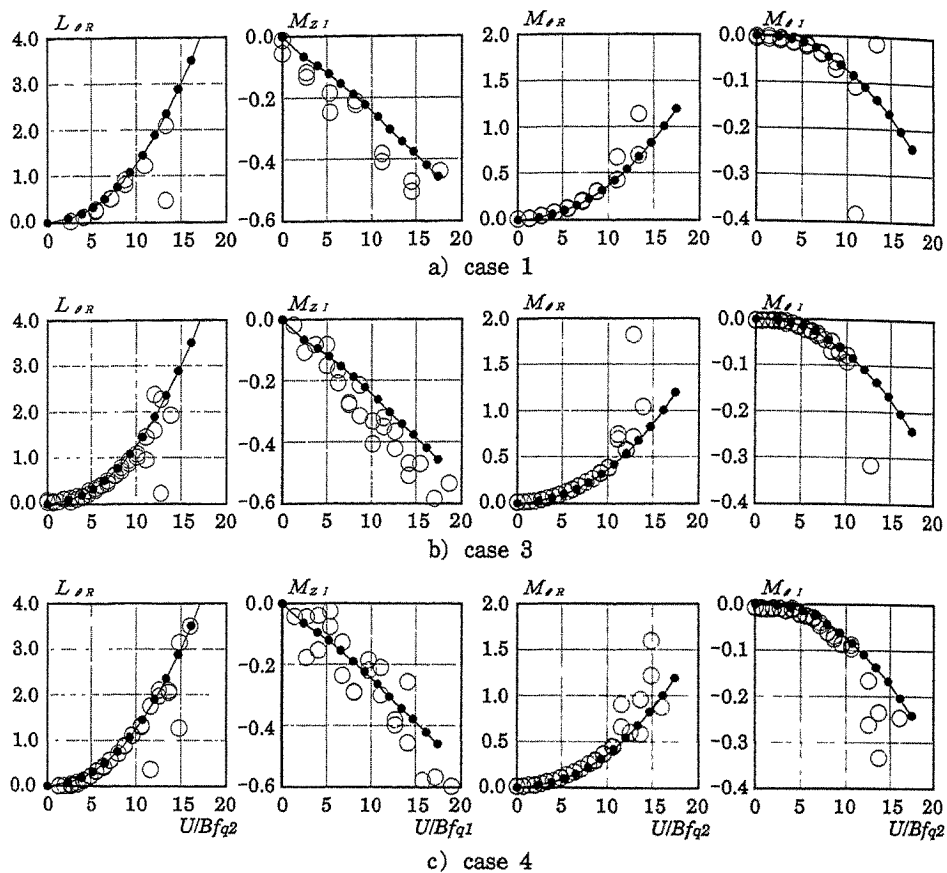
Fig. 5 Flutter derivatives

O: proposed method, ●: forced oscillation technique

References:

1. Scanlan R. H. and Tomko J. J., "Airfoil and Bridge Deck Flutter Derivatives," *Journal of the Engineering Mechanics Division*, ASCE, Vol.97, No.EM6, 1971, pp.1717-1737.
2. Yamada H., Miyata T. and Ichikawa H., "Identification of Aerodynamic Parameters of a Bridge Deck," *Proceedings of the 11th National Symposium on Wind Engineering*, pp.55-60, Tokyo Japan, 1990. (in Japanese)
3. Hoshiya M. and Saitoh E., "Structural Identification by Extended Kalman Filter," *Journal of Engineering Mechanics*, ASCE, Vol.110, No.12, 1983, pp.1757-1779.
4. Iwamoto M., Fujino Y., Isobe S. and Hasebe N., "Identification of Aerodynamic Parameters of Bridge Deck from Free Vibration Data consisting of Two Modes," *Proceedings of the 12th National Symposium on Wind Engineering*, pp.363-368, Tokyo Japan, 1992. (in Japanese)

Comparisons Between Wind Tunnel Tests on a Full Aeroelastic Model of the Proposed Bridge over Stretto di Messina and Numerical Results (Part I)

G. L. Larose, A. Damsgaard, M. Falco[+], A. Cigada[+]

Danish Maritime Institute (DMI), Hjortekæsvej 99, 2800 Lyngby, Denmark
[+]Politecnico di Milano, Dipartimento di Meccanica, Milano, Italy

Abstract: The Final Draft of the proposed bridge over Stretto di Messina was concluded by a 1:250 scale full bridge aeroelastic model study, initiated by Stretto di Messina S.p.A. The 13.6m long model, including the main span of the bridge and the two pylons, was constructed and tested at DMI in the 'Martin Jensen' Wind Tunnel. The objectives of the tests were to investigate the aerodynamic behaviour of the bridge under smooth and turbulent flow, for flow perpendicular to the bridge axis and at yaw angles, and to verify the threshold of the flutter instability. The same aspects have also been investigated by means of an analytical approach in the time domain, carried out by Politecnico di Milano, based on a 3-D finite element schematisation of the bridge with the aerodynamic forces calculated using quasi-steady theory corrected for non-linearities. The experimental results are presented in this Part I of the paper, while Part II compares the experiments to the analitycal predictions.

1. Introduction

Stretto di Messina S.p.A submitted the Final Draft for a fixed link between Sicily and the Italian mainland at the end of 1992. The link is composed of an extraordinary 3300m span suspension bridge, with 376m high pylons, a 60m wide stiffening girder (see Fig. 1) suspended by 4 main cables, 1.2m each in diameter and weighing more than 30 t/m. The bridge is to be built in a region of high winds over sudden topographical changes, defining a 1000 year return period design wind speed of 62m/s at 65m above the Straits. The prediction of the aeroelastic behaviour of the structure is of great importance and all the tools available to wind engineers have been used for this purpose.

Part I of this two part paper presents the results of the best experimental method to predict the aeroelastic response, the full bridge aeroelastic model study. The experimental results are then compared in Part II to analytical predictions in the time domain, using results of section model tests combined with corrected quasi-steady theory [1,2] specifically developed for this bridge.
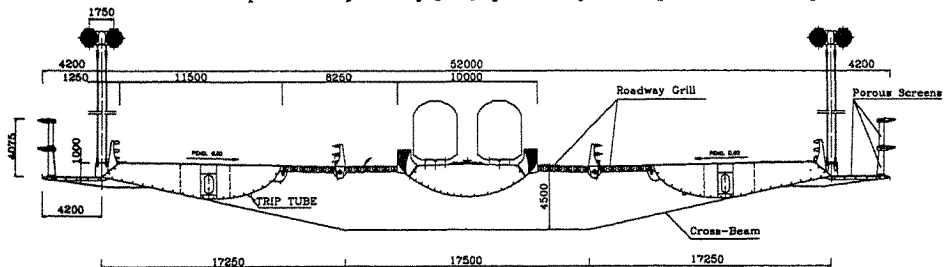
Fig. 1. Cross-section of the Deck For the Proposed Bridge Over Stretto di Messina

131

2. Full Bridge Aeroelastic Model of Stretto di Messina Bridge

2.1 General

A geometrical scale of 1:250 was chosen for the aeroelastic model to allow reproduction of the significant details of the deck and aeroelastic modelling of the main span and the pylons. The relatively short side spans were not included in this 13.6m aeroelastic model but were elastically represented outside the wind tunnel. Respecting Froude Number similitude, tests could be carried out up to an equivalent full scale wind speed of 90m/s.

2.2 Section Model Tests

The first task in the design of the aeroelastic model was to ascertain whether or not the aerodynamic properties of the deck at a 1:250 scale represented the aerodynamics of the prototype. The static aerodynamic force coefficients and the aerodynamic derivatives determined on section models at scales of 1:30 and 1:87 were used as target values. A complete series of section model tests at a scale of 1:250 were carried out, aimed at calibrating the coefficients of the target values for Reynold's numbers two orders of magnitude smaller.

From the results of the static tests, an iterative process took place to define the adequate porosity of the screens and grills, covering approx. 30% of the surface of the deck and to define the size and position of a circular trip, attached to the round surface of the outside box girder, to reduce Re dependency. At low Re, changing the porosity of the screens considerably affected the variations of lift and moment coefficients with angle of attack. Having defined a satisfactory configuration on the basis of the static tests (see Fig. 2), dynamic tests were conducted to obtain the aerodynamic derivatives at 1:250 from the forced oscillation method in Milano, and the initial displacement method at DMI. Both methods gave satisfactory and consistent results. Minor modifications had to be made to fine-tune the deck shape, the largest deviation being for large angles of attack (e.g. +6°) where the aerodynamic damping of the small scale model was smaller than the target values.

The results of the section model tests are presented elsewhere [3]. There is no doubt that the deck cross-section for this bridge was optimized to an unprecedented level to minimize the changes of aerodynamic stiffness at high wind speed, to minimize the drag, lift and torsional forces and to maximize the aerodynamic damping via flaps integrated in the wind screens at the edges of the deck.
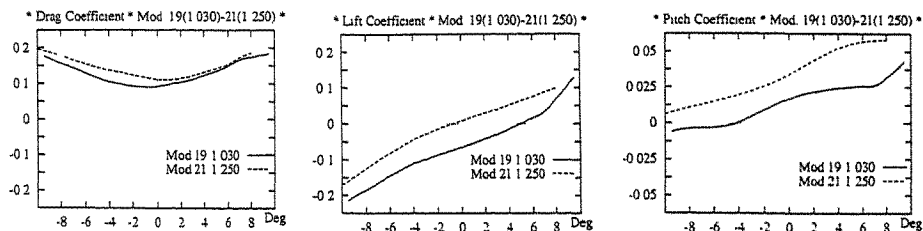
Fig. 2. Static Aerodynamic Force Coefficients for Stretto di Messina Bridge vs Angle of Attack

2.3 Aeroelastic Modelling

The aeroelastic model was constructed respecting Froude number similitude and the appropriate scaling parameters given the 1:250 geometrical scale [4]. The model simplifications were limited to a minimum and their effects on the dynamic behaviour were verified through finite element analyses. The two pairs of main suspension cables were modelled by two steel wires with equivalent axial stiffness and fitted with lead circular cylinders to provide the necessary mass and aerodynamic drag. The vertical hangers were also lumped, two sets in one, and their stiffnesses modelled by springs near the pylons, a region where the displacements of the main cables differ from

the displacements of the deck.

The pylons were also aeroelastically modelled. Their structural damping was adjusted to 1% of critical. They were fitted with screens to mitigate vortex-shedding excitation as described in [5].

2.4 Dynamic Characteristics

A thorough investigation of the eigen frequencies of the model and corresponding mode shapes and damping in still air was conducted for the first 25 modes or so. The results were compared to a 3-D f.e.m. dynamic analysis. An error margin in the range of 2 to 10% was observed between the physical and the numerical model. The structural damping was of the order of 1% of critical for the fundamental modes and gradually reducing to 0.2% for the higher modes. The methods of identification of the dynamic charactersitics are described in Section 4.1.

2.5 Test Programme

The aerodynamic response of the bridge model to smooth and turbulent flow was measured via non-contacting Optical Displacement Sensors (ODS, Dantec), accelerometers (Entran) and strain gauges to determine the main cable tension and pylon base bending moments. Mean and RMS values were calculated from recorded time histories and the consistency of the experimental results was verified through cross-examination of the redundant information such as displacement versus acceleration, cable tension versus pylon base bending moments, etc.

The tests were carried out for wind perpendicular to the bridge axis and for two horizontal yaw angle cases, 30° and 60°. The effect of the turbulence on the vortex shedding phenomena was investigated as well as its influence on the aerodynamic damping and aerodynamic stiffness.

3. Experimental Results

3.1 Response to Smooth and Turbulent Flow

The effect of the turbulence of the oncoming flow on the bridge response is illustrated by Figs. 3 and 4. Vortex shedding oscillations in the vertical and torsional d.o.f. were observed in smooth flow with a turbulence intensity at deck level of 2%. The vortex shedding peaks were attributed to the higher modes of vibration of the deck that have low structural damping (0.2% of critical against the predicted 1% for the prototype structure). Vortex shedding excitation was mitigated by turbulence, 6% at deck level, as clearly seen on Fig. 3.
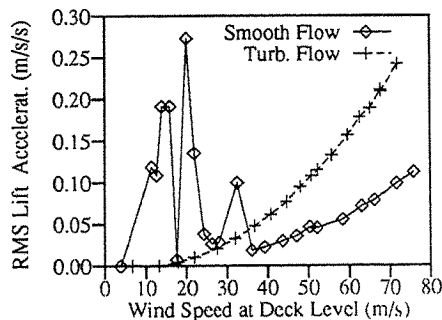
Fig. 3. RMS Vertical Response at Midspan   Fig. 4. RMS Torsional Response at Midspan
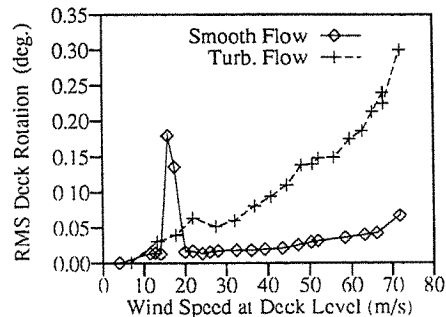
For reduced velocity beyond the vortex-shedding range, the turbulence of the flow had the effect of increasing the buffeting response in direct proportion to the increase in turbulence intensity. The turbulence was generated by an array of 21 spires, 8m upstream of the model. Such a configuration provided a turbulence intensity near the ground that decreased with increasing wind

speed, as for the natural wind. This effect had to be taken into account in the analysis of the buffeting response and the variations of aerodynamic damping with wind speed.

3.2 Effect of Wind at Yaw Angles

The variations of the mean and dynamic responses with reduced velocity for wind at yaw angles are presented in Figs. 5 and 6. The yaw angles are defined as the angle deviation from the wind normal to the bridge axis case. The mean response appeared to reduce following a cosine law for the 30° and 60° cases. The dynamic response however did not follow a cosine law for the 30° case and was at the same level as for the 0° conditions as seen on Fig. 6.
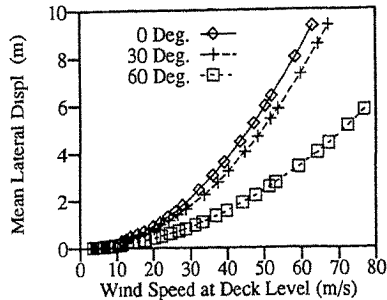
Fig. 5. Mean Lateral Response at Midspan
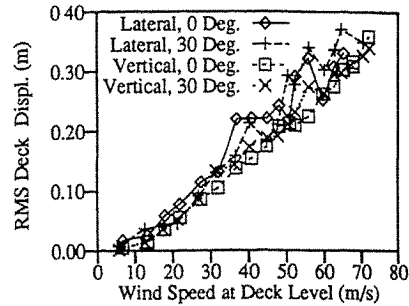
Fig. 6. RMS Response at Midspan, Turb. Flow

3.3 Stabilty Limits

Wind tunnel tests have been conducted in smooth and turbulent flow for equivalent full scale wind speeds at deck level in excess of 80m/s for 0°, 30° and 60° yaw angles. A manual attempt to induce flutter instability at 85m/s in smooth flow was unsuccessful. At this wind speed the vertical aerodynamic damping appeared very strong while the torsional aerodynamic damping appeared to weaken. For higher wind speeds, the deck gradually rotated "nose-up" to a maximum of 1.0-1.5° but reached a limit due to the apparent lateral deformation of the main cables, thus preventing instability.

4. Parametric Identification on Full Aeroelastic Model

4.1 Methods

Tests have been carried out to estimate two among the most important parameters in the definition of the dynamic behaviour of the bridge. These parameters are the damping ratio (as a fraction of critical) and the natural frequencies of the first vertical and torsional modes (additional data was also collected for the higher modes), i.e. the modes eventually involved in the flutter condition. The aim of the tests, repeated in both smooth and turbulent flow, was to provide the data needed for comparisons with numerical simulations and section model tests, and to investigate the influence of the turbulence on the results.

Two methods have been used: the first one consisted of analysis of the free motion of the deck subjected to an impulse and was used mainly for preliminary identification of the modes in still air; the second method relied on a more involved experimental setup (Fig. 7.), consisting of an electrodynamic vibration exciter, two dynamometers and optical displacement sensors.

The forcing mechanism was placed to excite mainly the first vertical and torsional modes; it was possible to control both the amplitude and the frequency of the exciter by means of a synthetiser and a computer. The elastic link between the model and the exciter was carefully chosen to minimize the structural modification (changes within 10%). The value of the vertical force or torque applied to the model were measured by the two piezo-dynamometers connected to the springs. The

134

calibration of this device was periodically repeated. The interval of uncertainties was found to be less than 5% and the phase lag was found to be less than 2°. Inspection of the analog signals prevented aliasing errors. To account for small random errors and negligible systematic errors, the data was fit with a Gaussian distribution to define the measured errors.
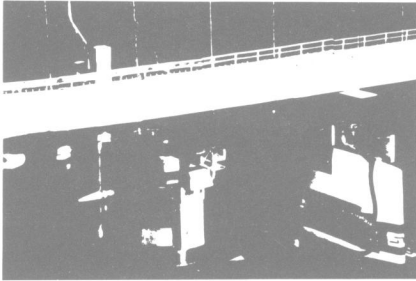
Fig. 7. Experimental Setup, Forced Excitation
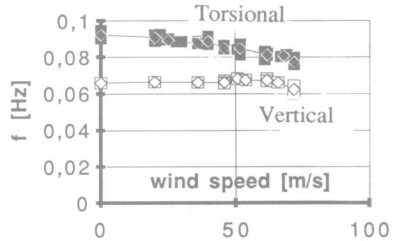
Fig. 8. Variations of Natural Frequency with Wind Speed, Smooth Flow

Several modal techniques were employed to extract the damping ratios; only a summary of these methods is given here whereas a complete description will be part of a future work. One method consisted of using the decay traces by filtering the displacement or torsion signal with a central frequency and performing a Hilbert transform to provide directly a measurement of damping as a function of amplitude [6]. Another technique, known here as the energy technique, utilizes the data collected from the forcing mechanism exciting the bridge with frequencies close to to the natural frequencies of the structure. As the inertial and elastic forces are conservative in steady state conditions, the energy introduced to the structure by the exciter is equal to that dissipated by the aeroelastic force field, so that by measuring the force and displacement, it is possible to extract the damping ratio. Other common methods using the transfer function between the force and displacement have been employed, including a technique of evaluating the derivative of the transfer function phase plot to determine the damping ratio, known as the phase derivative technique [7].

4.2 Changes of Frequency with Wind Speed

The results regarding the variation of the natural frequencies with full-scale wind speed for smooth flow are shown in Fig. 8. Even at high wind speeds (72 *m/s*), there is no coupling of the vertical and torsional modes which could lead to flutter. In the case of turbulent wind, no appreciable changes were observed with respect to the smooth flow case.

4.3 Changes of Damping with Wind Speed

Figs. 9-10 and Figs. 11-12 show the variation of the damping ratio with wind speed and flow conditions, respectively for the first torsional mode and the first vertical mode, obtained by the energy method. In each figure, the average values have been plotted along with the $+2\sigma$ and -2σ points, where σ is the standard deviation, assuming a Gaussian distribution of the random errors. The values obtained with the phase derivative method are in the range of uncertainty of those obtained by the energy method. The increase in σ observed in Fig. 10 for windspeeds in the range 45-52m/s in turbulent flow is possibly due to interference from the second vertical mode that has a natural frequency 1.35 *Hz*, while the first torsional mode has a frequency of 1.45 *Hz* in still air. The two modes involved are orthogonal but coupling terms due to wind turbulence can transfer energy from one mode to another. The vertical aerodynamic damping appeared to reduce slightly with turbulence of the flow. Further investigations of the effect of turbulence on the aerodynamic damping is ongoing.

135
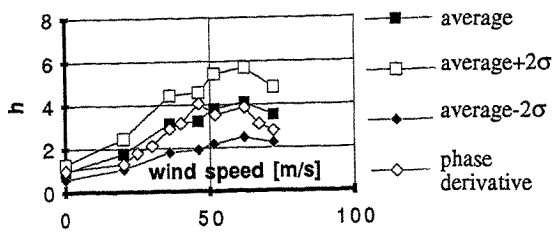
Fig. 9. Variations of Torsional Damping Ratio with Wind Speed, Smooth Flow
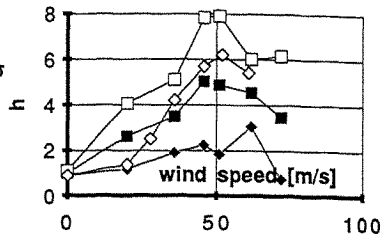
Fig. 10. Variations of Torsional Damping Ratio with Wind Speed, Turbulent Flow
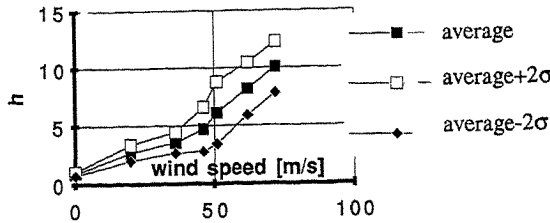
Fig. 11. Variations of Vertical Damping Ratio with Wind Speed, Smooth Flow
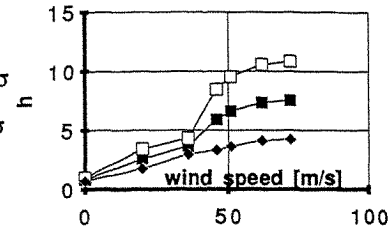
Fig. 12. Variations of Vertical Damping Ratio with Wind Speed, Turbulent Flow

5. Conclusions

The tests carried out on the 1:250 full-bridge aeroelastic model of the proposed bridge over Stretto di Messina have shown that:

1. flutter instability is well beyond the 1000 year return period design wind speed of $62m/s$ as predicted by numerical calculations;
2. the turbulence of the flow appeared to play a minor role in the determination of the critical wind speed for flutter instability;
3. the turbulence of the flow has a strong influence on the vortex-shedding excitation and the buffeting response even for a highly optimized deck cross-sectional profile.

Some further aspects of these problems will be discussed in Part II of this paper.

Acknowledgments

References

1. M.Falco, A. Curami, A. Zasso, "Non-linear Effects in Sectional Model Aeroelastic Parameter Identification " in *JWEIA 42 (1992)* 1321-1332.
2. G. Diana, M. Falco, R.T. Severn, M.L. Stockwell, "Wind Effects on a Long-span Suspension Bridge", in *Proc. ASCE Structure Congress '91*, Indianapolis, 1991.
3. A. Curami, A. Zasso, "Extensive Identification of Bridge Deck Aeroelastic Coefficients: Average, Angle of Attacks, Reynolds Number and Other Parameter Effects", in *Proc. of APSOWE III*, Hong Kong, Dec. 1993.
4. A.G. Davenport, N. Isyumov, D. Fader, C. Bowen, "*A Study of Wind Action on a Suspension Bridge During Erection and Completion*", UWO Research Report BLWTL-3-1969.
5. G.L. Larose, A. Damsgaard and G. Diana, M. Falco, "Wind Investigations of the Tower for the Stretto di Messina Birdge", in *Proc. of IN-VENTO '92*, Capri, Oct. 1992.
6. J.S.Bendat, A.G. Piersol, *Random Data*, John Wiley and Sons, 1986.
7. D.J.Ewins, *Modal Testing: Theory and Practice*, Research Studies Press, 1984.

136

Comparison Between Wind Tunnel Test on a full Aeroelastic Model of the Proposed Messina Bridge and Numerical Results (part II)

G. Diana, F. Cheli, S. Bruni, A. Collina, G. Larose[+]

Diparimento di Meccanica Politecnico di Milano, Italy
[+] Danish Maritime Institute, Copenhagen, Denmark

Abstract: A full aeroelastic model of the proposed Messina bridge has been tested at DMI, in Copenhagen. A comparison between experimental and numerical results is presented in the paper, focussing upon two main topics: influence of turbulence on aerodynamic parameters and response to turbulent wind.

1. Introduction

In the design stage of the Messina straits bridge project, it was decided to test a complete aeroelastic model in the Martin Jensens' DMI wind tunnel in Copenhagen. The model, already described in Part I, was tested in order to define the bridge response under smooth and turbulent flow.

This experimental test gave the opportunity for a convalidation of the mathematical models used for the prediction of the aeroelastic behaviour of the proposed bridge and the response of the structure to turbulent wind. The same topics have been treated in previous papers, concerning the results of an experimental campaign carried out on the Humber Bridge (GB) in 1989-90 [1].

One of the aims of the present test was to establish the influence of turbulence on aerodynamic parameters and then on flutter instability. A second aim of the work was to compare experimental and numerical results concerning bridge response to turbulent wind. In this paper, mean and R.M.S. values as a function of wind speed, and spectra of displacements and accelerations will be shown.

The comparison between numerical and experimental results show to what extent the analitycal model is able to reproduce bridge dynamic behaviour, focussing upon the method for the calculation of aerodynamic forces as a function of reduced velocity and angle of attack.

2. Influence of turbulence upon aeroelastic parameters

Several identification techniques have been adopteted for the measurements performed on the 1:250 aeroelastic model, in order to obtain the modal parameters (damping factor and frequency as a function of mean wind speed U), both under smooth and turbulent flow; this topic is treated in Part I of the paper. The experimental results are compared in Fig.1 with numerical ones obtained by means of a modal approach, taking into account the first torsional mode, and linearizing the aerodynamic forces around the static position due to mean wind.

First of all it can be seen that there is little influence of turbulence on the aeroelastic behaviour of the model. Moreover, it is shown that a satisfactory accordance was achieved between experimental data and the numerical results obtained with the aerodynamic parameters measured in wind tunnel tests on a sectional model, in smooth flow. It can be concluded that there is no strong evidence of a turbulence effect on the aeroelastic parameters, at least for the tested model, presenting at given reduced velocity a relatively small variation of aerodynamic derivatives with the angle of attack ([2], [3]). This is in accordance with the measurements reported by Scanlan ([4]) and with the results obtained from full scale measurements on the Humber bridge [1]. Anyway, this topic is worthy of further investigation.
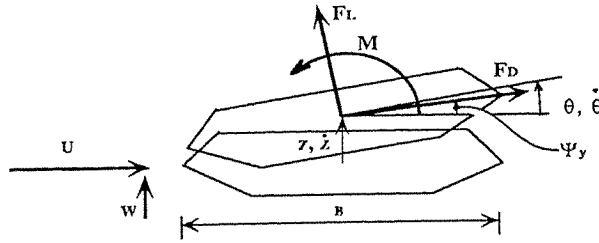
Fig.2: relative velocity of wind and forces acting on the deck.

A more complete explaination of the q.s.c.t. is reported in [1]. Finally, the aerodynamic forces (1) are converted in a generalized force vector $\underline{F}$ on the nodes of the FEM scheme. The resulting equations of motion are written in the following form:

$$[M_s] \, \underline{\ddot{x}} + [R_s] \, \underline{\dot{x}} + [K_s] \, \underline{x} = \underline{F} \, (\underline{V}(t), \underline{x}, \underline{\dot{x}}, V^*) \tag{5}$$

where $[M_s]$, $[R_s]$ e $[K_s]$ are mass, damping and stiffness structural matrices. In this way, the exact dependence of the aerodynamic coefficients on the reduced velocity cannot be taken into account, but the nonlinearities due to the variation of the angle of attack induced by turbulent wind are considered.

The aerodynamic parameters for the wind force calculation (obtained from wind tunnel test in smooth flow, on a sectional model [2]), refer then to a unique reduced velocity, the one corresponding to the band of frequency associated with the lower modes of vibration of the structure, which mainly contribute to the response of the bridge. Such an approach was demonstrated to be suitable for instance in the case of the Humber bridge [1], in which the response, also the acceleration, is mainly due to the lower modes, since the highest modes are structurally more damped. The 1:250 model, on the contrary, showed a low structural damping for the higher modes: as a consequence the spectra of acceleration is not limited to the lower frequencies only.

Being the numerical analysis performed in full scale, for better comparison the experimental results are also presented reported to full scale. First, the mean values are compared: Fig.3 shows the comparison between lateral and torsional mean values at midspan; the agreement can be considered satisfactory.

Fig.4 shows the comparison between numerical and experimental R.M.S., as a function of mean wind speed. As an example vertical displacement at quarter span and torsional rotation at mid span are reported. The numerical results are calculated with two levels of turbulence: the best accordance is obtained at low wind speeds with the higher turbulence (I.T.=7%) and with low turbulence (I.T.=4%) at higher wind speeds. This is in accordance with the circumstance that turbulence intensity of wind generated in the wind tunnel decreases as mean wind spead increases (see part I of the same paper).
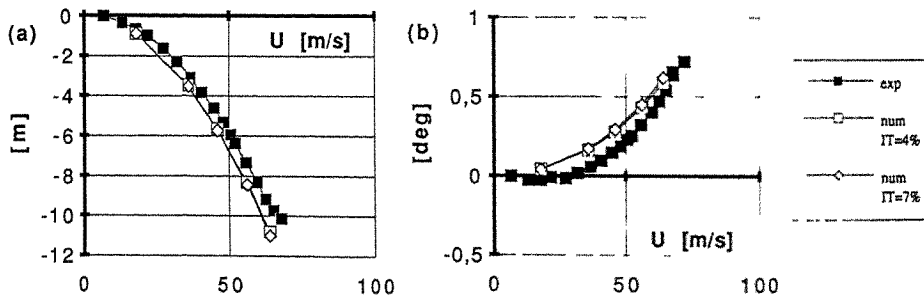
Fig.3: mean values: (a) horizontal displacement at midspan, (b) torsion at midspan.
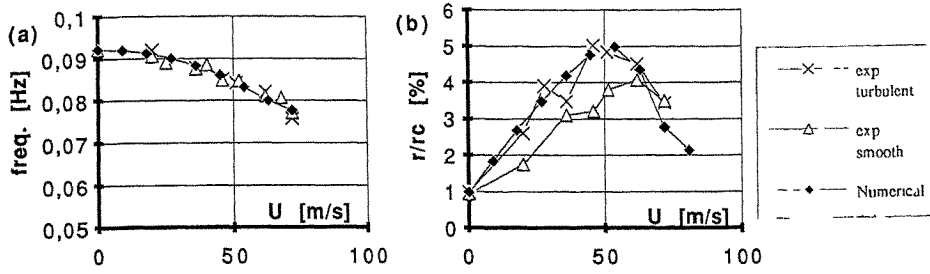
Fig.1: damping factor (a) and frequency variation (b) of first torsional mode.

3. Response to turbulent wind

The second aim of the paper is to determine the dynamic behaviour of the bridge under turbulent flow. Bridge response to turbulent wind has been simulated, by means of a numerical model, already described in [1]. The model is based on a non linear approach; the equations of motion are integrated in the time domain. The structure is modelled with FEM; the aerodynamic forces acting on the bridge are evaluated according to the quasi-static corrected theory (q.s.c.t., [1]).

More precisely, the time history of the horizontal u and the vertical v components of the wind velocity $V = V(t, \xi)$ are numerically generated in some sections along the span, taking into account the along-span coherence of the wind [6]. At each time step the displacement z, y and θ and velocities $\dot{y}$, $\dot{\theta}$ and $\dot{z}$ of each section are calculated from nodal displacements $\underline{x}$ and velocities $\dot{\underline{x}}$ of the FEM scheme. The aerodynamic forces in each section are then calculated as a non-linear function of instantaneous angle of attack $\alpha_{y,\theta}$ between the deck and the turbulent flow (see Fig.2), according to the following formulas [1]:

$$F_z = F_L \cos \psi_y - F_D \sin \psi_y = a B V^2_{ry} \left(C^*_L(\alpha_y) \cos \psi_y - C^*_D(\alpha_y) \sin \psi_y \right)$$
$$F_y = F_L \sin \psi_y + F_D \cos \psi_y = a B V^2_{ry} \left(C^*_L(\alpha_y) \sin \psi_y + C^*_D(\alpha_y) \cos \psi_y \right) \quad (1)$$
$$M = a B^2 V^2_{r\theta} C^*_M(\alpha_\theta)$$

where $a = 0.5 \rho$, B is the deck width, $V^2_{ry,\theta}$ the relative wind velocity, $\alpha_{y,\theta}$ the angle of attack:

$$V^2_{ry,\theta} = (u - \dot{y})^2 + (w - b_{1y,\theta} \dot{\theta} + \dot{z})^2 \qquad \alpha_{y,\theta} = \theta - \psi_{y,\theta} \quad (2)$$

with: $\quad \psi_{y,\theta} = \text{arctg} (w - b_{1y,\theta} \dot{\theta} + \dot{z}) / (u - \dot{y}) \quad (3)$

In (1) C^*_L, C^*_D and C^*_M are corrected aerodynamic coefficients and are obtained integrating the dynamic derivatives:

$$C^*_L = C_{Ls}(\alpha_o) + \int_{\alpha o}^{\alpha} K^*_L \, d\bar{\alpha} \qquad C^*_M = C_{Ms}(\alpha_o) + \int_{\alpha o}^{\alpha} K^*_M \, d\bar{\alpha} \qquad C^*_D = C_{Ds}(\alpha) \quad (4)$$

where K^*_L, K^*_M, b_{1y} and $b_{1\theta}$ are the parameters of the q.s.c.t., related to Scanlan's coefficients [2], and C_{Ls}, C_{Ds} and C_{Ms} the static coefficients of the deck section, α_o the angle of attack in the equilibrium position due to mean wind U conditions. Aerodynamic derivatives and $b_{1y,\theta}$ coefficients are evaluated as a function of the instantaneous angle of attack α using a fixed value of reduced velocity: $V^* = V_o^* = U/(f_oB)$, f_o being the dominant bridge frequency.
The aerodynamic parameters to be introduced in (4) are the ones calculated in wind tunnel tests on a sectional model in smooth flow.

139
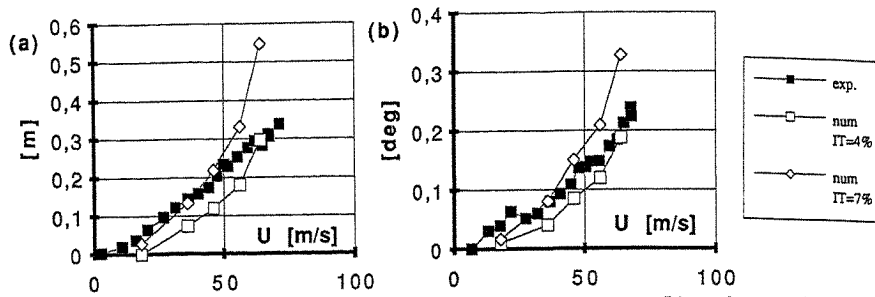
Fig.4: RMS values: (a) vertical displacement at quarter span, (b) torsion at midspan.

In Fig.5 the spectra of vertical displacements and torsional rotations at mid span are plotted, comparing experimental and numerical (high turbulence) results for the mean wind speed $U = 36$ m/s in full scale. A good accordance is shown, especially for lower frequencies.

The same agreement is not found for numerical and experimental accelerations, as shown in Fig.6a, referring to torsional acceleration at mid span. This is probably due to the neglected influence of the reduced velocity on the aerodynamic coefficients: lower modes and higher modes fall in different fields of reduced velocity, to which correspond significantly different values of aerodynamic coefficients, as shown in [3]. This problem was not evident in the comparison with full scale tests on the Humber bridge [1], because the structural damping of higher modes was large enough to mitigate high-frequency vibrations.

On the contrary, for the 1:250 Messina Bridge model the higher modes are very lightly damped: this circumstance is quite unusual for real structures, but, it gave the opportunity to further investigate the problem of the simulation of buffeting response.

The comparison between analytical and experimental results show a good agreement in terms of displacements and rotations because the contribution of the higher modes to the displacements is neglegible. Vice-versa the accelerations, highlighting the contribution of the higher modes, magnify the poorness of the numerical model to reproduce the high frequency behaviour of the structure.
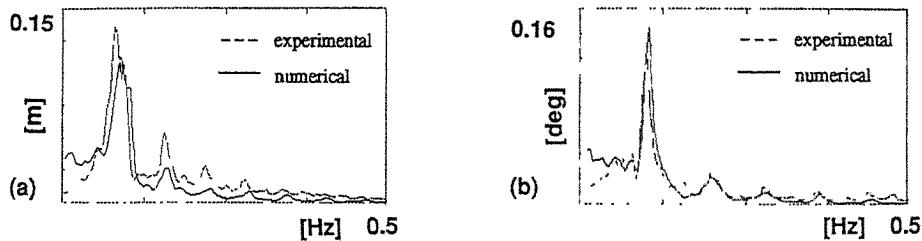
Fig.5: spectra of vertical (a) and torsional (b) displacements at mid span (U=36 m/s).

In order to overcome the discrepancy between experimental and numerical results, the numerical approach has been modified introducing a new procedure for the calculation of the aerodynamic forces in order to take into account the dependence of the aerodynamic coefficients on reduced velocity as well as the variation of the coefficients with the angle of attack.

The modified approach takes advantage from the fact that aerodynamic coefficients, for a given angle og attack, tend to become constant beyond a particular value of reduced velocity. For Messina Bridge deck, this happens for $7<V^*<\infty$, that is in the range of frequencies $0 < f_n \leq f_{max} = 0.085$ Hz (for U=36 m/s) or $0< f_n \leq f_{max} = 0.15$ Hz (for U=64 m/s).

140

It is then possible to first generate a space-time history of the wind $V_1(t,\xi)$, considering only the range of frequencies of turbulent wind corresponding to the those reduced velocities for which aerodynamic coefficients are constant, for this time history V_1 the dynamic response of the bridge can be correctly evaluated using the already mentioned methodology, integrating the non linear equations:

$$[M_s]\,\ddot{x}_1 + [R_s]\,\dot{x}_1 + [K_s]\,x_1 = \underline{F}\,(\underline{V}_1(t),\,\underline{x}_1,\,\dot{\underline{x}}_1) \tag{6}$$

In this way it is possible to take into account the non linear dependance of aerodynamic coefficients on the angle of attack, being the same coefficients constant in respect to the reduced velocity for the considered range of frequencies.

A linearization of the complete equations (1) in the neighborhood of the first solution $\ddot{x}_1(t)$, $\dot{x}_1(t)$, $\underline{x}_1(t)$ can now be performed:

$$[M_s]\,\ddot{\underline{x}}_v + [R_s]\,\dot{\underline{x}}_v + [K_s]\,\underline{x}_v = -[K_1(t)]\,\underline{x}_v - [R_1(t)]\,\dot{\underline{x}}_v + [K_{v1}(t)]\,\underline{\Delta V} \tag{7}$$

$\underline{x}_v(t) = \underline{x}(t) - \underline{x}_1(t)$ being the response of the bridge in the higher frequency range (mainly due to higher modes). In (7) $[K_1(t)]$, $[R_1(t)]$ and $[K_{v1}(t)]$ are the Jacobian matrices:

$$[K_1(t)] = -\left[\frac{\partial \underline{F}}{\partial \underline{x}}\right]_{\underline{x}=\underline{x}_1(t),\,\underline{V}=\underline{V}_1(t)} \quad ; \quad [R_1(t)] = -\left[\frac{\partial \underline{F}}{\partial \dot{\underline{x}}}\right]_{\underline{x}=\underline{x}_1(t),\,\underline{V}=\underline{V}_1(t)} \quad ; \quad [K_{v1}(t)] = \left[\frac{\partial \underline{F}}{\partial \underline{V}}\right]_{\underline{x}=\underline{x}_1(t),\,\underline{V}=\underline{V}_1(t)} \tag{7a}$$

a function of both the instantaneous angle of attack and reduced velocity. Based on the assumption that the main contribution to the angle of attack is due to the lower frequencies of wind spectra, the istantaneous angle of attack can be evaluated from the first analysis (eq.6). Equation (7) is then linear with time dependant coefficients.

The vector $\underline{\Delta V} = \underline{V}(t) - \underline{V}_1(t)$ contains the differences of horizontal and vertical wind velocity components between the complete time-space wind history $\underline{V}(t)$ (taking into account all the frequencies of the spectrum) and the contribution $\underline{V}_1(t)$ due to the first range of frequencies already considered in (6). The order of vector $\underline{\Delta V}$ is $2 \cdot n_s$, where n_s is the number of sections in which a time history of wind velocities is generated.

The range of the higher frequencies (corresponding for the considered case to $V^* < 7$) can be further divided into (p-1) different sub-ranges: $\underline{\Delta V}$ wind variation can be thought as the superposition of different time space histories $\underline{\Delta V}_k(t)$ for each k-th sub-range.

$$\underline{\Delta V} = \underline{\Delta V}_2 + \dots + \underline{\Delta V}_k + \dots + \underline{\Delta V}_p \tag{8}$$

A modal approach is then used, introducing n_q modal coordinates, defined by:

$$\underline{x}_v(t) = [\phi]\,\underline{q} \tag{9}$$

where $[\phi]$ is the modal matrix obtained from the eigenvectors of the matrix $[M_s]^{-1} * [K_s]$ of equation (6). Equation (7) then becomes:

$$[\phi]^T[M_s][\phi]\ddot{\underline{q}} + [\phi]^T[R_s][\phi]\dot{\underline{q}} + [\phi]^T[K_s][\phi]\underline{q} = -[\phi]^T[K_1(t)][\phi]\underline{q} - [\phi]^T[R_1(t)][\phi]\dot{\underline{q}} + [\phi]^T[K_{v1}(t)]\underline{\Delta V} \tag{10}$$

The modes of vibration included in $[\phi]$ can be divided into p subranges, according with the previous subdivision performed for wind velocities. Consequently eq. (9) becomes:

$$\underline{x}_v(t) = [[\phi_1]\dots[\phi_k]\dots[\phi_p]]\,\underline{q}_v = [\phi_1]\underline{q}_1 + \dots + [\phi_k]\underline{q}_k + \dots + [\phi_p]\underline{q}_p \tag{11}$$

being $[\phi_k]$ and $\underline{q}_k$ submatrices and subvectors of $[\phi]$ and $\underline{q}$.

Substituting eq. (10) and (11) into (7) and neglecting the coupling terms of the type $[\phi_j]^T [A] [\phi_k]$ (where $[A]$ is the generic matrix appearing in eq. (10)) and also the coupling terms of wind forces of the type $[\phi_j]^T [K_{v1}(t)] \underline{\Delta V}_k$ for $k \neq j$, for each range of frequency a linear equation can be written as:

$$[m_{sk}]\,\ddot{\underline{q}}_k + [r_{sk}]\,\dot{\underline{q}}_k + [k_{sk}]\,\underline{q}_k + [R_{k1}(t)]\,\dot{\underline{q}}_k + [K_{k1}(t)]\,\underline{q}_k = [K_{v1k}(t)]\,\underline{\Delta V}_k(t) \tag{12}$$

where $[m_{sk}]$, $[r_{sk}]$ and $[k_{sk}]$ are mass, damping and stiffness structural modal diagonal matrices and:

141

$$[R_{k1}(t)] = [\phi_k]^T[R_1(t)][\phi_k] \; ; \quad [K_{k1}(t)] = [\phi_k]^T[K_1(t)][\phi_k] \; ; \quad [K_{v1k}(t)] = [\phi_k]^T[K_{v1}(t)] \qquad (13)$$

are aerodynamic modal matrices (full matrices) depending on instantaneous angle of attack due to V_1 velocity and on the reduced velocity $V_k^* = U /(f_k B)$ different in each sub-range.

Finally, the response of the bridge is calculated superposing the low-frequency response $\underline{x}_1$ with the variations (10) due to high frequencies. As a preliminary result, the spectra of torsional acceleration calculated with the modified approach with p=2 is shown. It can be noticed that some of the higher frequencies reach higher values of vibration, due to the decrease of aerodynamic damping.
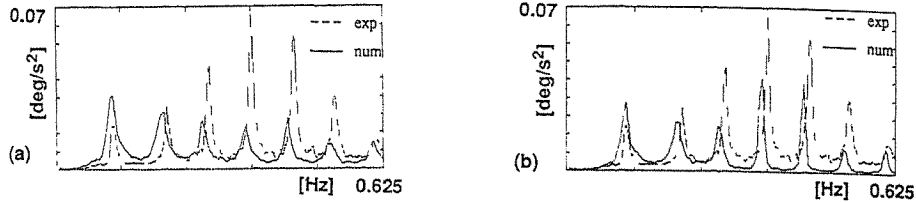
Fig.6: spectra of torsional acceleration at midspan (U=36m/s): (a) one-band, (b) two-band model

4. Conclusions

Experimental and numerical results have been compared for 1:250 model of the proposed Messina Bridge: aeroelastic behaviour of the structure and buffeting response have been analyzed. Concerning aeroelastic behaviour, no strong influence of turbulence is found by examining the damping factors and frequency variations, confirming the validity of adopting for buffeting analysis the coefficients obtained from a sectional model in laminar flow. Concerning the buffeting response, the accordance of numerical and experimental data is good at low frequencies but not at high frequencies. This led to a modified approach to take advantage from measurements of aerodynamic parameters as a function of both the angle of attack and the reduced velocity.

References:
1. G. Diana, F. Cheli, A. Collina, A. Zasso, J.M. Brownjohn, "Suspension Bridge Parameter Identification in Full Scale Test", 8th ICWE Conference, London, Ontario, 1991
2. M. Falco, A. Curami, A. Zasso, "Non-linear Effects in Sectional Model Aeroelastic Parameters Identification", 8th ICWE Conference, London, Ontario, 1991.
3. A. Curami, A. Zasso, "Extensive Identification of Bridge Deck Aeroelastic Coefficients...", 3rd APSOWE Symposium, Hong Kong, December 1993
4. R. H. Scanlan, E. Simiu, "Wind Effects on Structures", Wiley & Sons., 1986, pp 409-413.
5. R. Scanlan, On Flutter and Buffeting Mechanism in long-span bridges, Probabilistic Eng. Mech. Vol.3, No.1,1988
6. M. Bocciolone, F. Cheli, A. Curami, A. Zasso, Wind measurements on the Humber Bridge andNumerical Simulations, 8th ICWE Conference, London, Ontario, 1991
7. R.H. Scanlan, Wind Dynamics of Long-span Bridges, Proc. of the first Int. Symp. on Aerodynamics of Larges Bridges, Copenhagen, Denmark, 91-21 Feb, 1992

Extensive identification of bridge deck aeroelastic coefficients: average angle of attack, Reynolds number and other parameter effects.

A. Curami, A. Zasso

Politecnico di Milano, Dipartimento di Meccanica
P.zza L. Da Vinci 32, 20133 Milano, Italy

Abstract: The aeroelastic coefficient identification technique for bridge sections presented in [1], using controlled displacements and wind forces measurements has been extensively used on different scale three box girder section models. The peculiar features of the measure and analysis method clearly have shown the intrinsic nonlinearities of the phenomenon, allowing to outline, on the least square average identified coefficients, the effects of several parameters besides the reduced velocity: average angle of attack, Reynolds number, vertical-torsional motion phase lag and others.

1. Introduction

The identification of static and aeroelastic characteristics of bridge deck sections through scaled section model tests has a fundamental role in two phases of long span flexible bridge design: the deck aerodynamic optimisation and the definition of the most reliable static and aeroelastic coefficients to be used in the numerical simulations of the real structure behaviour in laminar and turbulent flow [2], [3]. Two approaches are generally used for defining such coefficients: the traditional approach uses system identification techniques on freely oscillating model tests [4]. Alternatively, the direct measure of the aeroelastic forces or dynamic pressures on harmonically driven models can be used, as shown in the past [5], and recently object of new applications and developments [1], [6], [7]. As a prosecution of these latter researches and using the experimental identification method described in [1], this paper presents the results of an extensive application of this technique on different scale models. Besides the coefficients dependence on the reduced velocity, the effects of mean and dynamic incidence angle, vertical-torsional motion phase lag, dynamic amplitudes and Reynolds number are investigated too. Being this study part of a wider research program on the Messina Crossing Project, developed at the Mechanical Department of "Politecnico di Milano" in co-operation with "Società Stretto di Messina S.p.A.", the results of Messina three box girder deck final design are shown.

2. Identification technique

Being the harmonic forced oscillation method fully referenced in [1] as well as the related identification technique, only the essential analytical definitions are given, to interpret the aerodynamic and aeroelastic coefficients identified. In Figs. 2.1, 2.2 the measurements positive conventions are shown, together with the dynamometric (1:30 scale, 2m chord, 3m length) section model. Being $p = 1/2\ \rho V^2$ the wind pressure, ρ the air density, V the approach wind speed, B and L the section chord and length, the aerodynamic drag, lift and moment coefficients are defined as:

$$F_{xs} = pBL\,C_D(\alpha_s) \qquad F_{ys} = pBL\,C_L(\alpha_s) \qquad F_{\vartheta s} = pB^2L\,C_M(\alpha_s) \qquad (2.1)$$

where α_s, F_{xs}, F_{ys}, $F_{\vartheta s}$ are the stationary angle of attack and forces on the section. Being the aeroelastic tests carried out in harmonic motion, the complex notation is used, considering the displacements and forces y, ϑ, F_y, F_ϑ as complex quantities and writing the time derivatives in the form $\dot{y} = i\omega y$ and $\dot{\vartheta} = i\omega\vartheta$, where ω is the motion frequency. Having defined the reduced wind speed as $V^* = (V/\omega B)$, the wind forces for harmonic isofrequent vertical and torsional motion are written as:

$$F_y = pBL\left\{-h_1(C_{D0}+K_{L0})\frac{i\omega y}{V} + h_4\frac{\pi}{2V^{*2}}\frac{y}{B} - h_2(C_{D0}+K_{L0})\frac{i\omega B\vartheta}{V} + h_3 K_{L0}\vartheta\right\} \qquad (2.2)$$

$$F_\vartheta = pB^2L\left\{-a_1 K_{M0}\frac{i\omega y}{V} + a_4\frac{\pi}{2V^{*2}}\frac{y}{B} - a_2 K_{M0}\frac{i\omega B\vartheta}{V} + a_3 K_{M0}\vartheta\right\} \qquad (2.3)$$

$$C_{D0} = C_D(\alpha)\big|_{\alpha=0} \qquad K_{L0} = \frac{\partial C_L}{\partial\alpha}\bigg|_{\alpha=0} \qquad K_{M0} = \frac{\partial C_M}{\partial\alpha}\bigg|_{\alpha=0} \qquad (2.4)$$

143
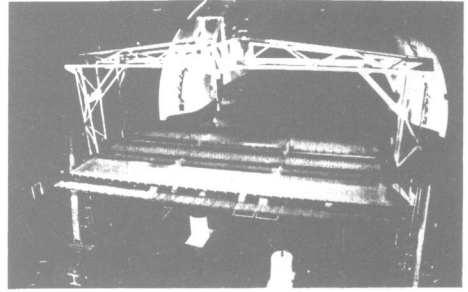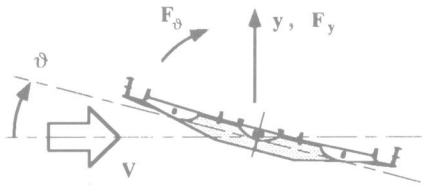
Figs. 2.1, 2.2: measure sign conventions, 1:30 dynamometric section model.

The $\{h_i, \ a_i\}$ coefficients, normalised using the over defined C_{D0}, K_{L0}, K_{M0} values, are function of the equivalent $\{H_i^*, \ A_i^*\}$ coefficients of the Scanlan notation by means of easy algebraic expressions:

$$F_y = \rho BL \left\{ \frac{H_1^*}{V^*} \frac{i\omega y}{V} + \frac{H_4^*}{V^{*2}} \frac{y}{B} + \frac{H_2^*}{V^*} \frac{i\omega B\vartheta}{V} + \frac{H_3^*}{V^{*2}} \vartheta \right\} \tag{2.5}$$

$$F_\vartheta = \rho B^2 L \left\{ \frac{A_1^*}{V^*} \frac{i\omega y}{V} + \frac{A_4^*}{V^{*2}} \frac{y}{B} + \frac{A_2^*}{V^*} \frac{i\omega B\vartheta}{V} + \frac{A_3^*}{V^{*2}} \vartheta \right\} \tag{2.6}$$

Representing the {h_i, a_i, i=1,3} coefficients the % shift from a quasi steady description of the aeroelastic forces, their values range around 1 at high reduced velocities. For this reason the $\{h_i, \ a_i\}$ notation is preferred, leading to an understanding of the phenomenon closer to a physical description and giving a more natural representation of the aeroelastic coefficients.

3. Messina 3 box section: angle of attack effects

A schematic view of the Messina deck is shown in Fig. 3.1. Peculiar feature of the section are the three separate box girders, the central one for railway, connected by grid paved service lanes. Specific design details have been studied to enhance the aerodynamic and aeroelastic performances.
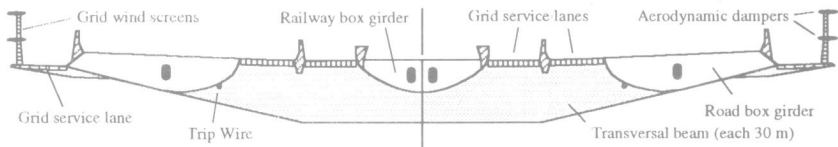
Fig. 3.1: Messina three box girder deck section.
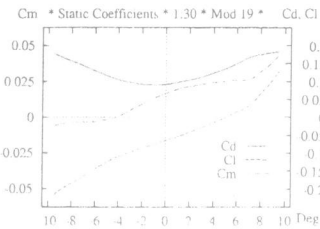
Fig. 3.2: 1:30 static coefficients.

The external and inter-box service lanes grid surface allows direct connection between the upper and lower side of the deck reducing its lifting characteristics. Optimised transparency wind screens including horizontal ailerons are fixed at the leading and trailing edges, with the purposes of both sheltering the vehicles and add aerodynamic damping. Finally, the flow separation and reattachment at the lower road boxes surface have been controlled through trip wires. Fig. 3.2 represents the aerodynamic coefficients of the final section, showing quite satisfactory results of low drag, regular lift and pitch curves with low and always positive derivatives. All the $\{h_i, \ a_i\}$ coefficients quoted in this paper refer through (2.2) and (2.3) to the standard values $C_{D0} = 0.119$, $K_{L0} = 0.65$, $K_{M0} = 0.16$. Two models, 1:30 and 1:250 scale, have been used for investigating scale effects and reaching lower reduced velocity ranges with the 1:30 one. Fig. 2.2 shows the 1:30 model in Pininfarina wind tunnel actuated in 2 D.o.F. (vertical and torsional) through an external truss

144

girder frame by two hydraulic electronically controlled shakers. Figs. 3.3 through 3.10 show the the 1:30 model $\{h_i, a_i\}$ coefficients obtained from 1&2 D.o.F. tests and least square identification [1], represented as functions of V^* with the mean angle of attack α_{av} as parameter. The strong effect of this parameter, ascribable to the static lift and torque derivatives variation with the angle of attack, is highlighted by all the coefficients and especially by the a_i ones, and can't be neglected in estimating the flutter velocity of long span suspension bridges, due to the deck static rotation at high wind speeds. Similarly, the effects of low frequency turbulence, causing angle of attack ranging $\pm 10°$, should also be evaluated, considering the dependence of the aeroelastic behaviour of the section on the instantaneous low pass filtered angle of attack [2]. The $\{h_i, a_i\}$ coefficients asymptotic trend, mainly for the {i=1; i=3} ones confirm, as expected, the consistence of the quasi steady assumptions for $V^* > 10\div15$. On the other hand the peaks shown by some coefficients as a_1 or a_3 at low V^* can be attributed to vortex shedding excitations, typically affecting box girder decks around $V^*=1\div3$. The lower sensitivity of a_2 to the α_{av} parameter can be finally justified by the prevailing ailerons aerodynamic damping.
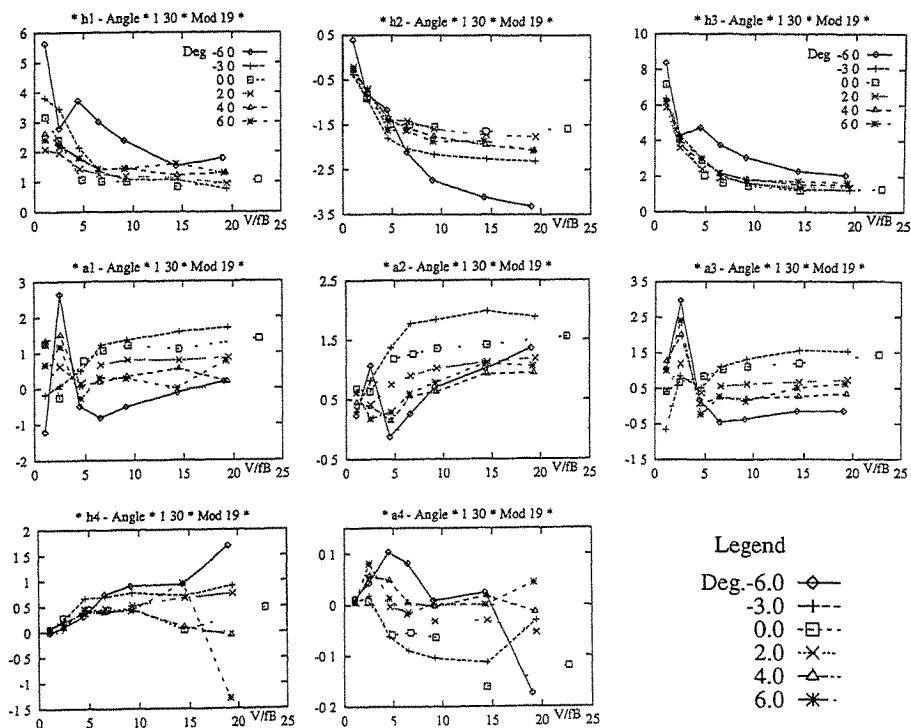
Figs. 3.3 through 3.10: $\{h_i, a_i\}$ coefficients of the 1:30 model.

4. Trip wire and wind screens effects

During the section optimisation phase, relevant importance has the possibility of comparing the aerodynamic and aeroelastic performances of different solutions by means of quick tests: the section model approach and the quasi-steady interpretation of the static C_D, C_L, and C_M curves is in this phase a really effective tool. Fig. 4.1 shows the trip wire regularisation effects on the C_L coefficient (continuous / dashed curve: opt. position / no trip wire). The optimal position has been found just comparing the C_D, C_L, and C_M curves and then verifying the aeroelastic coefficients of the final solution. Figs. 4.2, 4.3 show the section static characteristics without wind screens and the a_3 coefficient with (Y) and without

them (N). Comparing Figs. 3.2, 4.2, 4.3, clearly appears the effect of the negative pitch derivative at $3° < \alpha_{av} < 8°$ giving negative a_3 coefficient, as predictable by the quasi steady assumptions at high V^*. A good compromise in the choice of the grid transparency, damping ailerons orientation and trip wire position allowed to identify the optimal section design in terms of wind loads and aeroelastic stability.
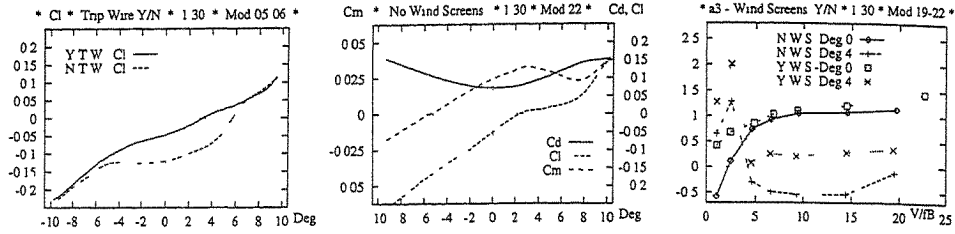
Fig. 4.1, 4.2, 4.3: trip wire, no wind screens static coefficients, a_3 with / without wind screens.

5. Superposition of effects: vertical-torsional phase and dynamic amplitudes

Equations (2.2) (2.3) and (2.5) (2.6) implicitly assume that superposition of effects is verified for the phenomenon studied. The linearity with the displacements was also always considered verified. However, higher harmonics were measured in the forces with pure harmonic displacements [1], especially when complex geometry sections were tested. Confining the analysis to the first harmonic effects, 2 D.o.F. tests with different vertical-torsional phase φ_{v-t} have been separately analysed to verify at which extent the superposition of effects is a valid assumption. Although in some circumstances the least square identified $\{h_i, a_i\}$ coefficients show systematic dependence on the φ_{v-t} phase, as appears in Fig. 5.3 (a_3 coefficient of 1:250 model), a global survey of the 1:30 and 1:250 results (e.g. Figs. 5.1, 5.2) allows to conclude that, concerning the first harmonic, the effect of the φ_{v-t} parameter is weak and the superposition of effects is a good assumption.
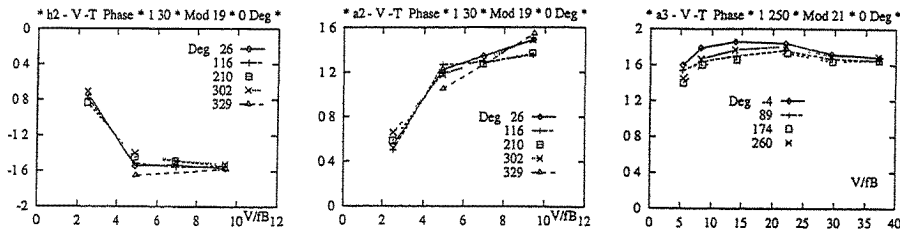
Fig. 5.1, 5.2, 5.3: Superposition of effects: dependence on the vertical-torsional phase φ_{v-t}.
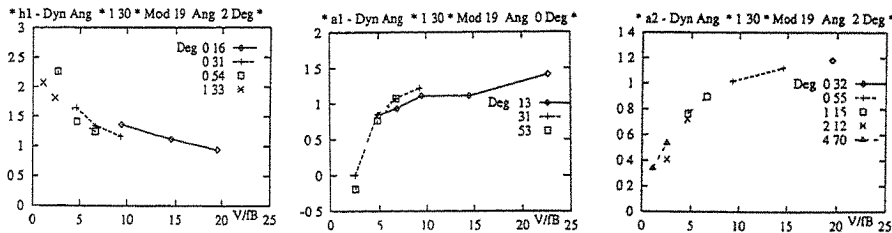
Fig. 5.4, 5.5, 5.6: α^*_{Dy} effects on h_1 and a_1, $\alpha^*_{D\vartheta}$ effects on a_2.

The motion amplitude effects have been studied in terms of dynamic angles of attack α^*_{Dy} $\alpha^*_{D\vartheta}$. As shown in [1], α^*_{Dy} $\alpha^*_{D\vartheta}$ are proportional to the upwash disturbance, being $|y|$, $|\vartheta|$, ω_y, ω_ϑ

146

the vertical and torsional motion amplitudes and circular frequencies:

$$\alpha^*_{Dy} = \frac{\omega_y |y|}{V} \qquad\qquad \alpha^*_{D\vartheta} = \frac{\omega_\vartheta B |\vartheta|}{V} \qquad\qquad (2.7)$$

Although the available tests didn't allow to cover wide V^* ranges, the linearity hypothesis is confirmed in the α^*_{Dy} $\alpha^*_{D\vartheta}$ ranges tested ($0.16°\div1.33°$ α^*_{Dy}, $0.32°\div4.70°$ $\alpha^*_{D\vartheta}$), well above the dynamic angle of attack due to the full scale deck motion (e.g. Figs. 5.4, 5.5, 5.6).

6. Scale ratio and reynolds number effects
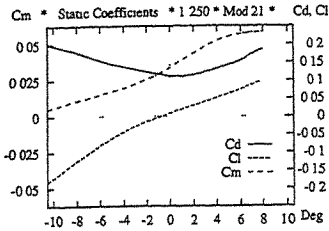
Fig. 6.1: 1:250 static coefficients.

Figs. 6.2 through 6.9 show the aeroelastic coefficients of the 1:250 model as functions of V^* and α_{av}, being the section's static characteristics represented in Fig. 6.1. The 1:250 scale tests had the main purpose of investigating the extent to which section models can give reliable results if complex sections are tested in small scale, being a difficult task the correct reproduction of the design details and being uncertain the effectiveness of scaling section details particularly sensitive to the Reynolds number as semipermeable surfaces and grids. The comparison of 1:30 and 1:250 results highlighted remarkable differences mainly at big α_{av} values. In particular is not negligible, for the direct implications in the torsional stability assessment, the drop of the 1:250 a_2 coefficient at $\alpha_{av}=6°$, not revealed in the 1:30 tests. Further analysis on the 1:250 data
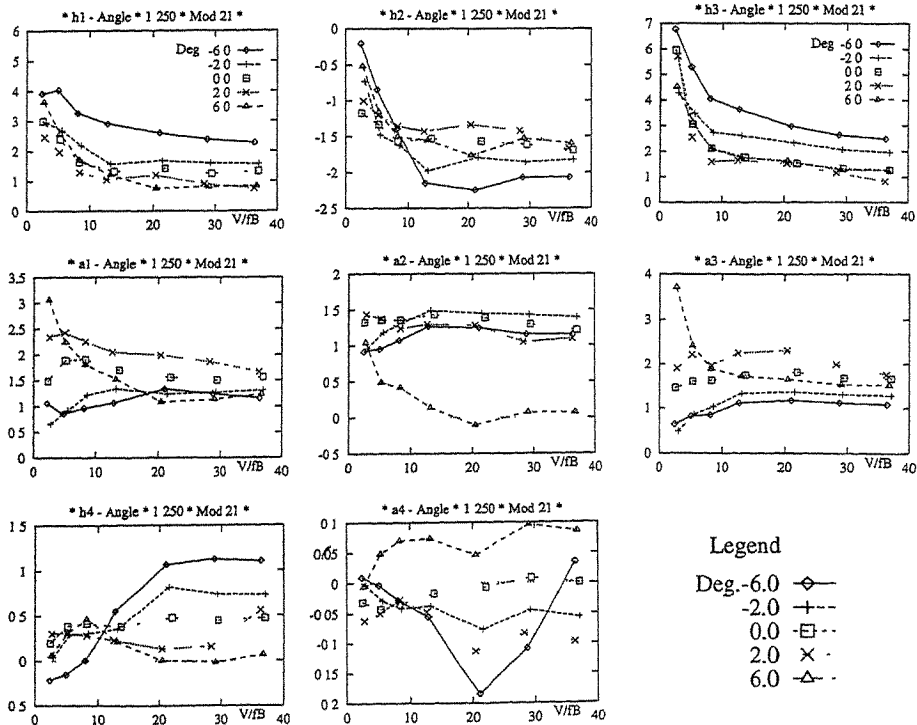
Figs. 6.2 through 6.9: $\{h_i,\ a_i\}$ coefficients of the 1:250 model.

147
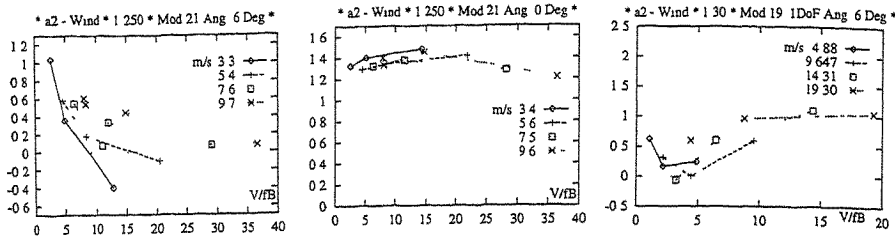
Fig. 6.10, 6.11, 6.12: Reynolds effects on a_2 1:250 $\alpha_{av}=6°$, 1:250 $\alpha_{av}=0°$, 1:30 $\alpha_{av}=6°$.
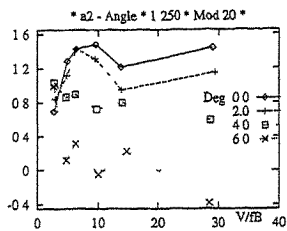
Fig. 6.13: ground distance effect.

performed grouping the tests with the same Reynolds number (using the approach wind speed V as parameter) showed a systematic dependence of a_2 on this parameter, with lower damping effects at lower wind speeds (Fig. 6.10). The same dependence is quite absent at $\alpha_{av}=0°$ (Fig. 6.11), and still present but weak in the 1:30 model at $\alpha_{av}=6°$ (Fig. 6.12). A qualitative justification of the results could rely on the relevant weight of the leading edge wind screen and ailerons, at high α_{av} values, in determining the wake characteristics and the global torsional aerodynamic damping of the section. The grids local Reynolds number ranges 200÷1000 for the 1:250 model and 350÷7000 for the 1:30, so that the 1:250 grid is working in the laminar÷turbulent transition region with relevant changes in the equivalent transparency. All the results quoted were obtained with models-ground distance H_D in scale with the real deck-sea level design value. This parameter, generally neglected, showed remarkable effects especially connected with $\alpha_{av} \neq 0$ values. As an example, the a_2 coefficient of the 1:250 model shows a faster drop in the damping, increasing α_{av} (Fig. 6.13), at ground level distance $H_D/B=0.6$ lower than at the usual $H_D/B=1.2$ (Fig. 6.6).

7. Conclusions and acknowledgements

Section model testing allowed to identify the optimal configuration of wind screens, ailerons, trip wires and semipermeable surfaces controlling the aerodynamics of the complex three box girder Messina section. Extensive testing on different scale models together with the peculiar facilities of the identification technique showed the strong effects of the average angle of attack, to be considered in the incipient instability wind speed assessment and suggesting also possible nonlinearities in the turbulence effects. While superposition of effects in 2 D.o.F. motion and linearity with the upwash disturbance have been verified, the actual deck-ground distance showed remarkable effects on the coefficients. Comparison of different scale ratios results (1:30 and 1:250) suggested that, due to local Reynolds number effects, great care should be taken using the small scale (1:250) data, especially if the aeroelastic behaviour is strongly influenced by small dimension components as grids and ailerons.

References

1 Falco M Curami A Zasso A 'Nonlinear effects in sectional model aeroelastic parameters identification', Journal of Wind Engineering and Industrial Aerodynamics, 41-44 (1992) 1321-1332
2 Diana G., Falco M , Damsgaard A. 'Comparison between wind tunnel test on a full aeroelastic model of the proposed Messina Bridge and numerical results (part I and II)', APSOWE III 1993
3 Scanlan R.H 'Wind dynamics of long-span bridges', Proc. of the First International Symposium on Aerodynamics of Large Bridges, Copenhagen, 19-21 February 1992
4 P. Sarkar, N Jones, R Scanlan 'System identification for estimation of flutter derivatives', Journal of Wind Engineering and Industrial Aerodynamics, 41-44 (1992) 1243-1254.
5 Ukeguchi N et al , 'An Investigation of Aeroelastic Instability of Suspension Bridges', International Symposium on Suspension Bridges, pp 273-284, Proc , Lisbon, November 1966.
6 Széchényi, E , 'Pont de Normandie: effets du vent; étude aéroélastique-essais', ONERA, Rapport N° 10/3588 RY070 R370G % Aug 1987
7 Larose G 'The response of a suspension bridge deck to turbulent wind: the taut strip model approach', Master Dissertation, The University of Western Ontario, London Ontario, March 1992

Consideration of the Typhoon Behaviour of the
Kao Ping Hsi Bridge in Taiwan

Dr Helmut WENZEL

Managing Director
VCE - Vienna Consulting Engineers, Austria

Abstract: The Kao Ping Hsi Bridge is a record-breaking cable stayed bridge in Taiwan Because the probability of a typhoon occurrence, even during construction, is high, special attention had to be given to safety considerations and to realistic wind loading To determine the design wind, a Monte Carlo Simulation was carried out, a sophisticated computer model to calculate the expected wind speed in a defined location for a given return period from available typhoon records The results are then compared with those received from conventional statistical methods To confirm the safety of the structure, wind tunnel tests have been carried out with a portion of the results presented here The design wind speed was determined to be 52m/s Under the worse conditions, none of the numerous tests conducted exhibited a critical wind speed less than 75m/s

1. Introduction

The Kao Ping Hsi is a cable stayed bridge spanning the Kao Ping River located in the south of the island of Taiwan It displays a single pylon, a free span of 330 meters, and an unsupported side span of 190 meters, making it one of the biggest bridges of its type in the world The pylon design is a reversed-Y, and the deck width of 34 5 meters is supported by cables arranged along its center axis The main design task concerned the 330 meter cantilever together with the 190 meter concrete free side span A condition which occurs during construction, making balancing particularly difficult
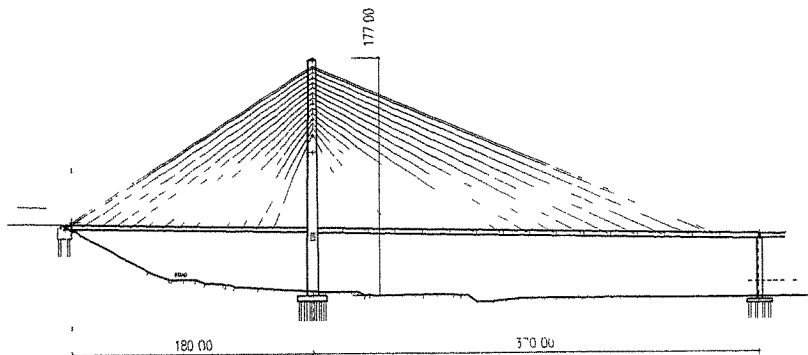
Fig 1. Longitudinal section of the bridge

149

The cross section is a closed box which, in order to balance the structure, is of steel construction in the main span and of concrete in the side span. Particular attention was paid to the expected behaviour under high wind loads, which led to an airfoil-like structure.
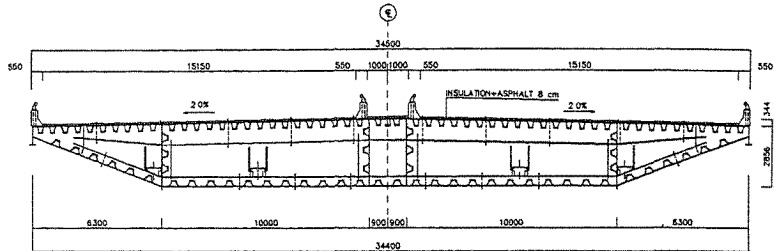
Fig. 2. Steel cross section of the main span

The side span is governed by the considerable mass required to balance the system. Difficulty was had in covering all live load cases within reasonable displacement and stress levels.
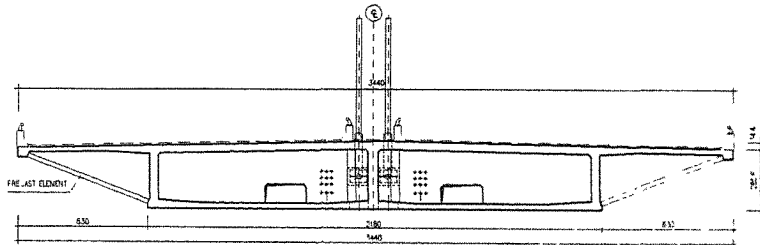
Fig. 3. Concrete cross section of the side span

The cables are designed to be of the strand type, consisting of several 0.6 inch strands, which are individually encased in PVC tubes, inserted into coloured HDPE pipes, grouted with a corrosion protection compound and then lifted into position. The cables are anchored at both ends, in the pylon and in the deck. Stressing will be performed from the top.

The bearing concept of the bridge consists in a rigid support at the abutment, a hinge at the pylon with free movement in longitudinal direction at the dividing pier. This eliminates huge displacements due to seismic activity.

150

2. The Wind in Taiwan

In order to determine the governing load cases, the following activities have been executed:

- Statistical evaluation of existing wind records using Gumbel, Logpearson, and other traditional statistical means so to determine a reliable wind speed for design purposes.

  The result is a design wind speed of 57m/s and a critical wind speed which should not be less than 75m/s.

- A typhoon risk study was performed for the exact location of the bridge. Information on tropical cyclone tracks in the Taiwan area was obtained from two independent data sources. The simulation of typhoon winds at the site was performed using the HURSIM methodology, which is a more advanced Monte Carlo Simulation. Sensitivity studies examining the effects of changes in the modelling of storm size, central pressure distribution, geographic region and rate of storm decay after landfall were performed.

  The result of the simulation yields a 100 year return period wind speed (mean hourly) of approximately 52 m/s at deck height.
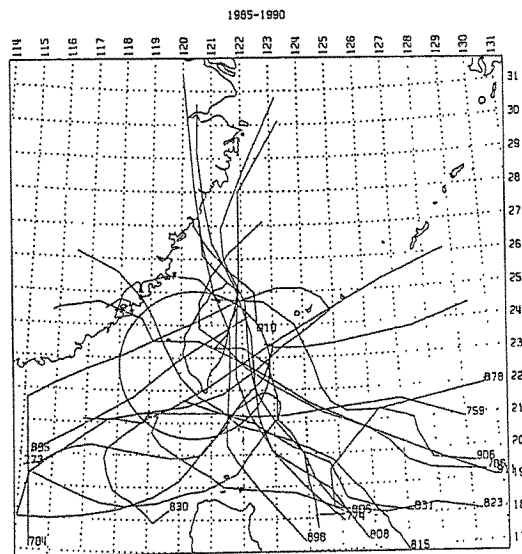
Fig. 4. Tracks of tropical cyclones in the Taiwan area 1985 - 1990 (HKRO Data Base)

3. The Partial Model Wind Tunnel Test

A partial model of the bridge, scale 1:80, was built and tested to determine the suitability of the cross section design. A variety of tests were carried out to find the optimum cross section and to determine the behaviour of the structure under changing conditions, such as wind attacking from different angles. Vortex shedding, buffering and stability were tested on four different arrangements:

151

1) Angle of wind attack at -3°; 2) basic arrangement at horizontal; 3) angle of wind attack at +3°; and, 4) alternate rail position for maintenance car. The results are summarised in the following graph. Generally it was found that the bridge cross section is very stable under any condition.

Measured Wind Speeds
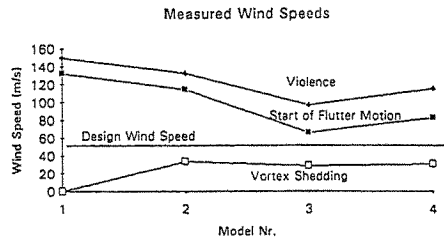
Fig. 5. Partial model test results for the four arrangements

In addition, and to get a clear understanding of the stability limits, the aerodynamic derivatives were determined for the bridge under traffic loading and during construction. Distinct trends can be read from these comparative tests.

KAO PING HSI Section Model Tests
Aerodynamic Derivatives, In-Service Condition, Smooth Flow
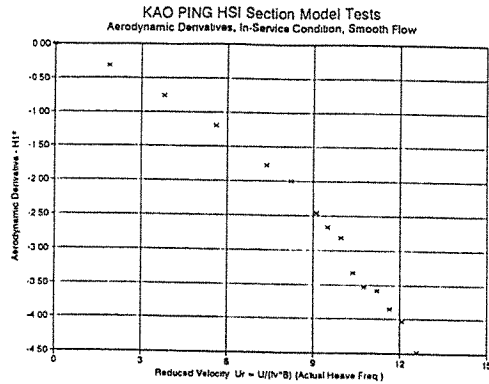
The presented graphs show H1 and A2 - following the definitions of Scanlan - which represent the change of the damping upon the change of wind speed. There is a sign of decreased damping with high wind speeds, but never coming close a definite problem with stability.

KAO PING HSI Section Model Tests
Aerodynamic Derivatives, In-Service Condition, Smooth Flow
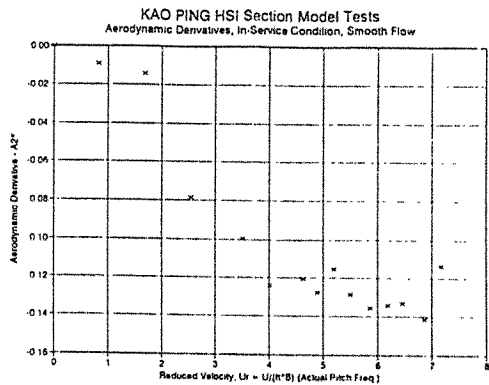
Fig. 6. Aerodynamic Derivatives H1 and A2 for the Kao Ping Hsi Bridge

152

4. Comparison with an Empirical Formula

The most current Austrian Wind Code, ÖNORM B4014, Teil 2 (not yet published), presents the formula to estimate critical wind speed as follows:

$$V_K = k.\pi.f_{e,b}.b\left[1+\left(\frac{f_{e,t}}{f_{e,b}}-0,5\right)\sqrt{\frac{1,5\,mi}{\rho b^3}}\right]$$

$f_{e,t}$	1. Vertical natural frequency	[Hz]	i	polar radius of inertia	[m]
$f_{e,b}$	1. Torsional natural frequency	[Hz]	b	width of the deck structure	[m]
m	mass of the deck structure	[kg/m]	ρ	density of air (1.25 kg/m^3)	[kg/m^3]
k	factor dependent upon shape of deck	[-] (0.70)			

Using the properties of the designed Kao Ping Hsi Bridge, a critical wind speed of 148 m/s is calculated. This coincides well with the test results, and is far beyond the required values.

5. Full Model Tests

A complete model of the bridge was constructed at a scale of 1:150, in order to study the behaviour of the entire structure. The tests included vortex shedding activity in smooth flow, as well as buffering in high or low intensity turbulent flow. To compare these results with the most critical case of the partial model test, a ramp with an angle of +3° was installed to simulate updraft. Wind directions perpendicular to the bridge, as well as a number of other directions, were considered in studying the behaviour of the structure under skewed angles of attack.

Data was collected at a total of 16 channels, which provides ample representation of the structural behaviour. The data includes not only displacement in various locations, but also the acceleration of the pylon top, the bending moment in the deck at the pylon, the cable forces in the longest cable and the longitudinal force in the rigid support of the abutment.
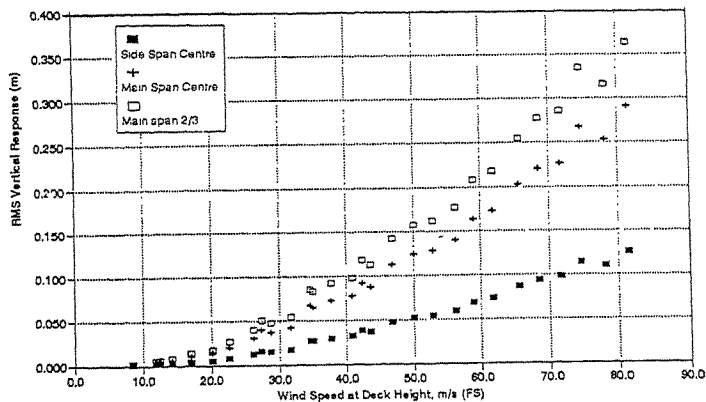
Fig. 7. Vertical response to 6% turbulence and perpendicular wind attack

153

A comparison of the full model date to the partial model test results was performed which produced a favourable correlation, with the partial model test results being conservative and on the safer side.

Special attention was paid to the construction stages, which are far more critical than the condition of the bridge during normal service. The stability limits drop by almost 45% and critical wind speeds are within the range of probability. To cope with this temporary condition, measures to stabilise the bridge during construction have been implemented.
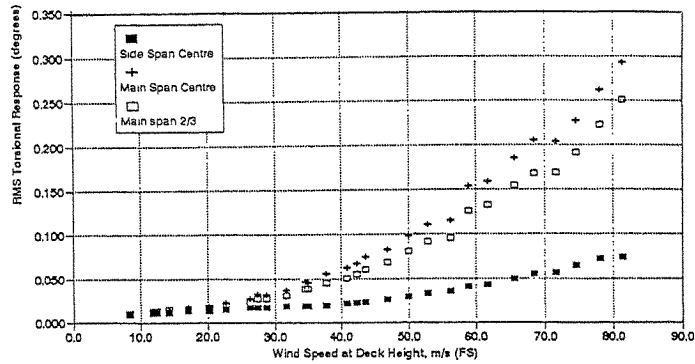
Fig. 8. Torsional response to 6% turbulence and perpendicular wind attack
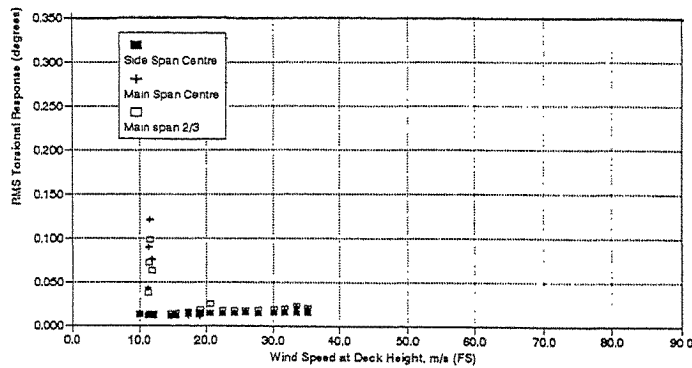
Fig. 9. Vortex shedding in smooth flow

6. Summary

The design and test procedures for an extraordinarily large structure is approached with emphasis on the wind problem presented in this part of the world. It is possible to prove that with careful design, problems of stability in large cable stayed structures can be avoided. It shall be pointed out that a comprehensive site supervision is necessary to ensure that all design intentions are properly observed and safety is not sacrificed through lack of information or poor quality of execution.

154

Damping Effects of Cable Cross Ties
in Cable-Stayed Bridges

H. Yamaguchi and H. D. Nagahawatta[+]

Department of Civil & Environmental Engineering
Saitama University, Urawa, Japan
[+]Formerly Division of Structural Engineering and Construction
Asian Institute of Technology, Bangkok, Thailand

Abstract: The damping effects of cable cross ties connecting several stay cables together, which is one of the typical control measures for suppressing wind-induced cable vibrations in cable-stayed bridges, are investigated experimentally and analytically. A cable system, which consists of two main cables with two cross ties, is studied as a fundamental example. Free vibration testing with scaled model of the cable system as well as its natural frequency and mode shape analysis are conducted. It is concluded in the present paper that there exists more or less damping effect in the vibration control measure of cable cross ties and that the damping effect can be increased by using more flexible and more dissipative ties compared with the stay cables. It also becomes clear that the energy-based method is very effective for evaluating the modal damping of cable systems analytically.

1. Introduction

Various types of wind-induced oscillation such as vortex-induced oscillation, wake-galloping and so-called rain vibration have been frequently evidenced in arrays of support cables of long spanned cable-stayed bridges [1]. One of the typical control measures for suppressing these wind-induced cable vibrations is cable cross tie which connects several stay cables together. It is well known that this control measure is effective but the mechanism of suppression in the cable cross ties has not been fully understood. The main objective of the present study is to investigate the damping effects of cable cross ties, while there can be several functions in cable cross ties such as the energy redistribution [2].

A cable-tie system consisting of two cables with two cross ties, which is considered as a simplest model of the cable arrays with cross ties in cable-stayed bridges, is studied as a fundamental example both experimentally and analytically. Free vibration testing with scaled models is first conducted to measure the modal damping of the cable-tie system as well as the single cable damping, and is followed by the natural frequency and mode shape analysis of the experimental models based on finite element method. The damping increment induced by connecting the cables is mainly discussed for different cross ties: stiff and soft ties with different magnitudes of prestress. An analytical method based on energy concept is also proposed in this paper for the evaluation of modal damping of cable systems.

2. Damping Experiment with Cable-Tie-System Model

The model considered in the experiment is composed of two horizontally-supported cables of different lengths and two vertical cross-ties of same lengths, as depicted in Fig. 1. 12-wire strand rope of diameter 1.3 mm, commercially available, was used for the main cables as well as for the 'stiff' cross-ties. Several pieces of lead weight (10.0 g/piece) were attached only to the main cables at interval of 7.0 cm distances in order to adjust the weight of the cable models. The 'soft' tie which is more flexible and more energy-dissipative than the wire strand rope of the stiff-tie model, was also prepared for comparative study. The specifications of the model cables and ties are given in Table 1.
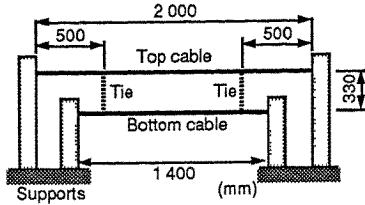
Fig. 1 Schematic diagram of experimental setup for cable-tie system.

Table 1 Specification of model cables and tie.

Cable & tie	Span (m)	Sag ratio (%)	Unit mass (g/m)	Tensile rigidity (kN)
Top cable	2 00	0.55	148.0	14.6
Bottom cable	1.40	0 43	148.0	14.6
Stiff cross tie	0 33	0	7 6	14.6
Soft cross tie	0 33	0	10 8	1.24×10^{-3}

The first in-plane mode of the top longer cable was assumed to be the target of vibration control and the first modal damping of the top cable alone as well as that of the cable-tie system were measured experimentally. The static disturbance was initially given to the top cable alone or cable-tie system by pulling the two points of the cable vertically, which could induce the free vibration purely in the first in-plane mode. The subsequent decay of free vibration of the cable or the cable system due to the initial disturbance was recorded and the natural frequency as well as the modal damping were computed by using the recorded response data. A gap sensor was used for the measurement of the dynamic displacement at the center point of the top cable. In the experiments, the prestress in the cable cross ties was changed step by step. The modal damping of the top cable without tie were re-measured at each step in order to make the comparison of the modal damping values of the cable and the cable-tie system more precisely.

3. Experimental Results

Fig. 2 shows the first natural frequency of the cable-tie-system model. The abscissa is the prestress parameter which is defined as the ratio of the reduction of the tie span-length to the original span length without prestress. As can be seen from Fig. 2, the first natural frequency increases with the increase of the prestress in the cross ties and the experimentally measured values fairly coincide with the analytically calculated values. The analysis was based on the finite element method [3]. The nonlinear static-configuration analysis was first conducted with the experimentally measured displacements of the tie nodes induced by prestressing the ties, and the eigenvalue analysis was then done to obtain the first natural frequency and the corresponding mode of the cable-tie system.
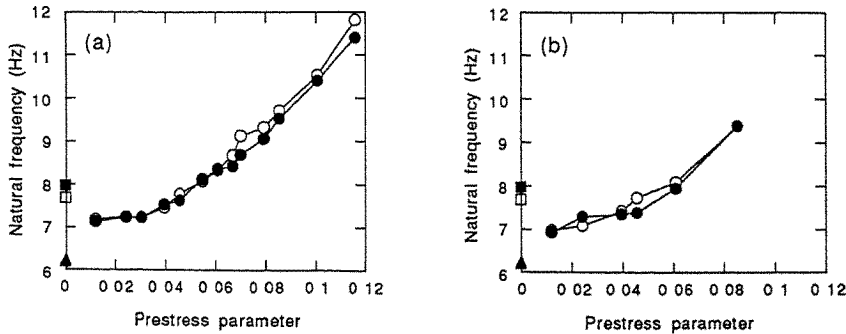
Fig. 2 First natural frequency of cable-tie system versus prestress in tie. (a) Stiff tie; (b) Soft tie. ● ▲ ■ Experimentally measured values, O △ □ analytically calculated values. ● O Cable-tie system, ▲ △ top cable, ■ □ bottom cable.

156
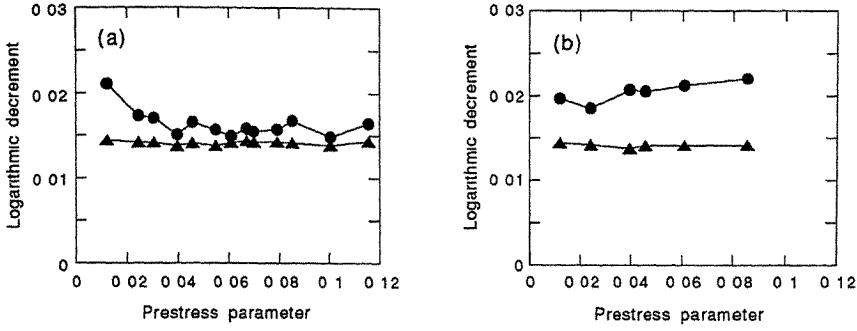
Fig. 3 Experimentally measured modal damping in logarithmic decrement versus pre-
stress in tie. (a) Stiff tie; (b) Soft tie. ● Cable-tie system, ▲ top cable without tie.

Fig. 3 depicts the relation between the experimentally measured modal damping of the cable-tie
system in logarithmic decrement and the prestress parameter. The first modal damping of the top
cable alone is also shown in comparison. The logarithmic decrement measured was dependent on the
vibration amplitude but not much. The averaged value of logarithmic decrement is, therefore, used as
a representative value of the modal damping and plotted in Fig. 3. As shown in the figure, the modal
damping of the cable-tie system is always larger than the damping of the single cable and the damping
increment caused by connecting two cables with the cross ties is more significant in the case of the
soft tie in Fig. 3 (b). It can be also seen from Fig. 3 that the damping increment is almost independent
of the magnitude of the prestress in ties except for the small prestress cases.

4. Theoretical Evaluation of Cable-System Damping

The damping ratio, which is directly related to the logarithmic decrement, is generally defined
for a single degree-of-freedom system as the ratio of the dissipated energy per a cycle to the potential
energy [4]. The n-th modal damping ratio ξ_n of the cable system can be defined in the same manner:

$$\xi_n = \frac{D_n}{4\pi U_n} \tag{1}$$

where D_n and U_n are the modal dissipating energy and the modal potential energy of the cable system.

The n-th modal potential energy of the cable system, U_n, consists of the modal potential energy
due to the initial cable tension, U_{tn}, and the strain energy caused by the modal vibration, V_n [5].

$$U_n = U_{tn} + V_n = \int_0^l \frac{1}{2} A \sigma_0 \frac{\partial u_j}{\partial s} \frac{\partial u_j}{\partial s} ds + \int_0^l \frac{1}{2} EA\varepsilon^2 ds \tag{2}$$

where σ_0 is the prestress in the cable, A is the cross sectional area, E is Young's modulus, u_j is the j-
th component of the dynamic displacement, and s is the coordinate defined along the cable axis. ε in
Eq. (2) is the dynamic strain associated with the modal vibration and is defined as

$$\varepsilon = \frac{dx_j}{ds} \frac{dx_j}{ds} + \frac{1}{2} \frac{\partial u_j}{\partial s} \frac{\partial u_j}{\partial s} \tag{3}$$

where x_j is the initial configuration of the cable.

157

On the other hand, the modal energy dissipation, D_n, in Eq. (1) can be represented in terms of the modal strain energy, V_n, by introducing the loss factor η. This is because it has been experimentally investigated that the source of damping in the cable is mainly the internal damping which is in proportion to the square of the dynamic strain [6-8]. That is,

$$D_n = 2\pi\eta V_n \tag{4}$$

The loss factor is a damping parameter of materials which is defined as the ratio of the damping energy to the strain energy per unit cycle. The dimensionless parameter η in Eq. (4) is, therefore, an equivalent loss factor for the cable which can be estimated as 0.06 for real structural cables [8].

Substituting Eqs. (2) and (4) into Eq. (1) leads to the modal damping as

$$\xi_n = \frac{1}{2}\eta\frac{V_n}{U_{tn} + V_n} \tag{5}$$

It can be understood here that the modal damping of the cable becomes very small compared with other structural members because of the large potential energy due to the large prestress in the denominator of Eq. (5). In the case that the damping characteristics or the loss factor of each cable member which composes the cable system is different, the expression in Eq. (5) is generalized as

$$\xi_n = \frac{1}{2}\sum_i \eta_i \frac{V_{ni}}{U_{tn} + V_n} \tag{6}$$

5. Damping Effects of Cable Cross Ties

The damping effects of cable cross ties are now discussed by using the energy-based damping theory described in the previous section. In order to do so, the modal potential energy due to the initial cable tension and the modal strain energy were evaluated from the first mode-shape obtained by the eigenvalue analysis. The results are given in Figs. 4 and 5 in which the energies in each member of the cable system, i.e., the top cable, the bottom cable and the tie, are shown in comparison. As seen from both figures, the contribution of the top cable to the total modal energy is largest but comparable to that of bottom cable when the prestress in the ties becomes small. The energy in the ties is generally very small especially when the stiff tie is used.
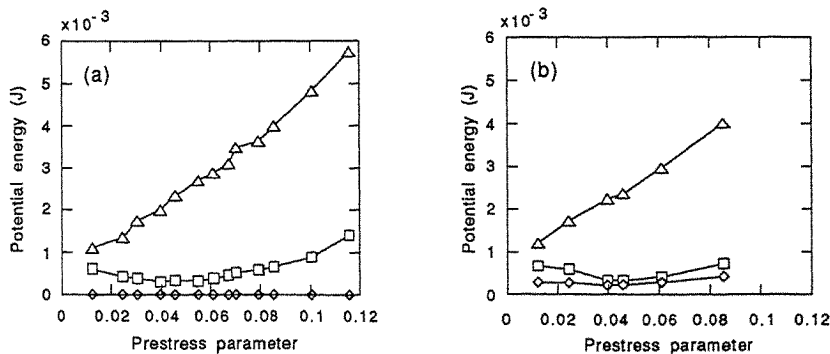
Fig. 4 Analytically computed value of modal potential energy due to initial cable tension in each member of cable-tie system. (a) Stiff tie; (b) Soft tie. △ Top cable, □ bottom cable, ◇ tie.

158
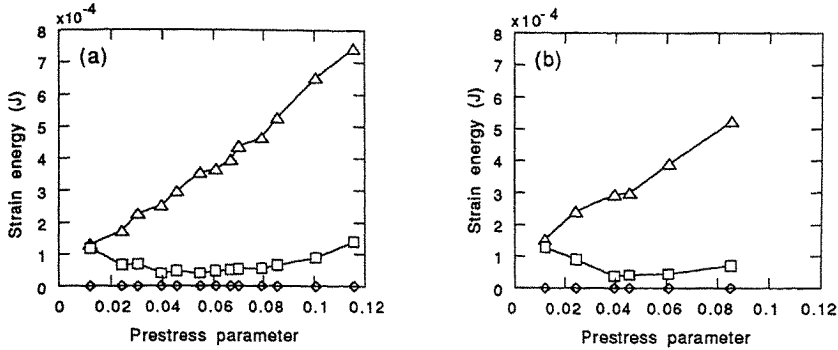
Fig. 5 Analytically computed value of modal strain energy in each member of cable-tie system. (a) Stiff tie; (b) Soft tie. △ Top cable, □ bottom cable, ◇ tie.

In order to evaluate the modal damping of the cable-tie system based on Eq. (6), it is necessary to know the loss factor for each member. The loss factor of the main cable can be estimated by the experimentally measured modal damping of the top cable without the tie. That is, the eigenvalue analysis is conducted only for the top cable to calculate the energy ratio in Eq. (5) and the loss factor of the single cable is calculated by using the experimentally measured damping ratio and analytically calculated energy ratio. Thus obtained value of loss factor for the single cable is averagely 0.052.

Using the modal energies shown in Figs. 4 and 5 as well as the loss factor of the main cable thus estimated, one can easily derive the contributions of the top and bottom cables to the modal damping of the cable-tie system. Fig. 6 depicts the analytically computed damping-contributions of the top cable (△) and the bottom cable (□), along with the experimentally measured modal damping given in Fig. 3. The symbol O in the figure indicates the summation of the damping contributions
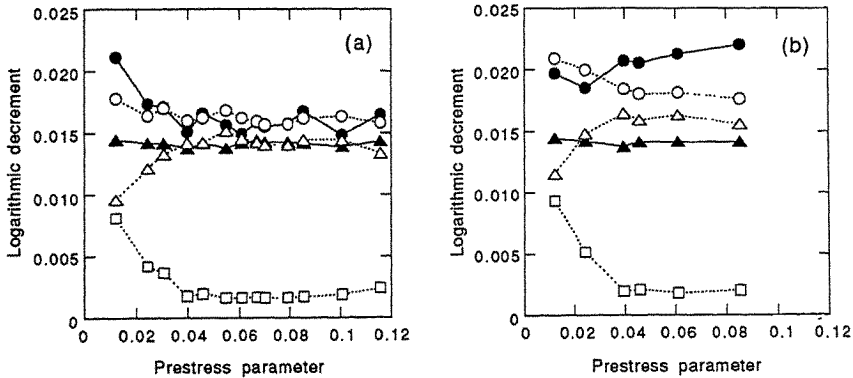
Fig. 6 Comparison between analytically estimated modal damping and experimentally measured one. (a) Stiff tie; (b) Soft tie. △ Analytically estimated contribution of top cable to the modal damping of cable-tie system, □ that of bottom cable, O that of top and bottom cables. ● Experimentally measured modal damping of cable-tie system, ▲ that of top cable without tie.

159

from both the top and bottom cables, which is considered as analytical value of the modal damping of the cable-tie system excluding the damping contribution of the cross ties. The difference between the experimentally measured modal damping of the cable-tie system (●) and the damping contribution of the two cables (O) is, therefore, the damping caused by the energy dissipated in the cross ties. As can be seen from Fig. 6, some amount of vibration energy is dissipated in the soft ties, while there is almost no energy dissipation in the stiff ties. The loss factor of the soft tie was estimated by obtaining the difference between the modal damping of the system (●) and the damping contributions form the two cables (O) in Fig. 6 (b) and the modal energy ratio from Figs. 4 (b) and 5 (b), for different values of the prestress parameter. Thus calculated value of the loss factor of the soft tie was 0.073, 0.078, 0.076, 0.075 for large values of the prestress parameter. That is, the loss factor of the soft tie was obtained as an constant value and this means that the energy-based evaluation of the modal damping by Eq. (6) is valid enough. It should be noted, however, that the energy dissipation in the soft ties is negative for small tie-prestress in Fig. 6 (b). We consider this as an experimental error which might be large especially for the flexible cable system.

As for the damping-increase function in connecting cable-arrays with cross ties, there are several possibilities. If the stiff tie is used with enough prestress, only the damping of other cables is added to the damping of the cable controlled, as shown in Fig. 6 (a) where the damping contribution from the top cable (△) almost coincides with the modal damping of the single top cable (▲). As a result, the modal damping is increased a little in the case of the stiff tie. If the softer tie is used with enough prestress, on the contrary, we can expect not only the additional damping from other cables but also the damping increment in the cable which is to be controlled as well as the additional damping from the soft cross-ties.

6. Conclusions

The damping effects of the cable cross ties which are used for the suppression of wind-induced vibrations of stay cables in cable-stayed bridges, have been discussed both experimentally and analytically. The brief conclusions obtained through the present investigation are summarized as follows:

(1) There is more or less a damping-increase function in crossing stay cables with ties.

(2) The damping effect in the control measure of cable cross ties can be significant if more flexible and more energy-dissipative cross ties are used.

(3) The damping increment in cable-tie system can be caused not only by the additional damping from other cables but also by the damping increment in the cable controlled as well as the energy dissipation in cross ties .

(4) The energy-based method of damping evaluation is very effective and the modal damping of cable systems can be estimated analytically by evaluating modal strain energy and modal potential energy of initial cable tension.

References:
1. Matsumoto, M., Yokoyama, K., Miyata, T., Fujino, Y. and Yamaguchi, H., Proc. Canada-Japan Workshop on Bridge Aerodynamics, (1989) 101.
2. Ehsan, F. and Scanlan, R.H., Proc. 5th US-Japan Bridge Workshop, (1990) 203.
3. Jayawardena, L., Master of Eng. Thesis, Asian Inst. of Tech., Thailand, (1991).
4. Clough, R. W. and Penzien, J., Dynamics of Structures, 2nd Ed., McGraw-Hill, (1993) 56.
5. Washizu, K., Variational Methods in Elasticity and Plasticity, 2nd Ed., Pergamon Press, (1974).
6. Yamaguchi, H. and Fujino, Y., Structural Eng./Earthquake Eng., Vol. 5, No. 2(1988) 303.
7. Yamaguchi, H. and Jayawardena, L., J. Wind Eng. Industrial Aerodyn., 41-44(1992) 1961.
8. Tsuji, M. and Kanou, I., Proc. 13th annual Conf. Japan Construction Consultants Assoc., (1980) 73 (in Japanese).

Aeroelastic Characteristics of a Stressed Ribbon Pedestrian Bridge Spanning 252 m

M. Pirner
Academy of Sciences of Czech Republic
Institute of Theoretical and Applied Mechanics
Prague, Czech Republic

Abstract:The paper describes the experiments with an aeroelastic model of a suspended footbridge. Its sensitivity to the effect of vortex separation at wind velocities from 15 to 17,5 m.s^{-1} was ascertained; the instability of the flutter type was not observed. To reduce the amplitude of flexural vibrations dampers were designed to be installed in the railing posts and in the deck.

1. Description of Footbridge Structure and Wind Tunnel

To connect a holiday resort with an adjacent community in South Moravia the designer used the well-proven system of stressed ribbon foot bridge. The described footbridge has a system of two suspension cables from which the bridge deck is suspended, consisting of precast R. C. components and prestressed longitudinally by two tendons (Fig. 1).

With regard to the expected footbridge sensitivity to wind its aeroelastic model was studied in a wind tunnel.

The aeroelastic model was tested in the dia. 3 m wind tunnel of the Aircraft Research and Testing Institute in Prague, with

MODEL 1:130

1932 mm
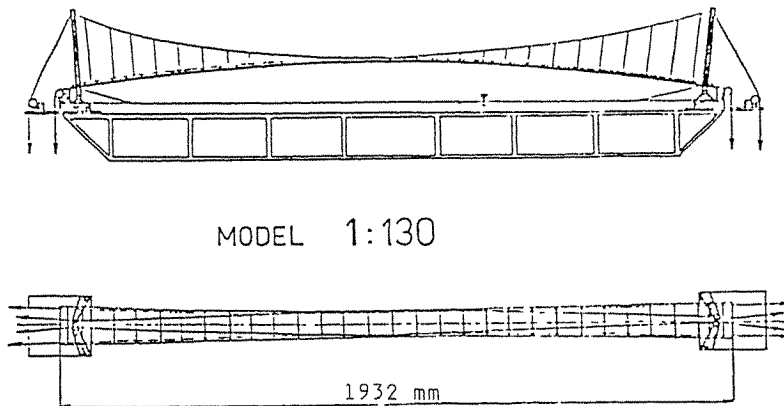
Fig. 1

161

open measuring space and closed air circulation. The longitudinal turbulence intensity for the free air flow velocity of 50 m.s^{-1} was 10 %, for the height of the footbridge centre above the base plate amounting to 90 mm.

2. Theoretical Natural Modes and Frequencies of Vibrations
First method.
Natural modes and natural frequencies were determined on the basis of FEM [5].
Second method.
With regard to the function and form of the couple of suspension ropes and the bridge deck with a couple of prestressing tendons, the theoretical values of natural frequencies and natural modes of vibrations were determined on the basis of the theory of prestressed networks, based on the integro-differential equation of equilibrium in vertical direction.
This 2. method makes it possible to determine the above mentioned quantities of bending vibrations only.

3. Description of the Aeroelastic Model and its Measurements
The footbridge model has been designed in accordance with the model laws. The dimensional scale of 1 : 130 has been determined by the transverse dimension of the turbulence generator in wind tunnel. The two systems of ropes and, consequently, the effect that prestressing force is grater than of gravity force resulted in the neglect of the model law expressed by the Froud number.
The damping was not modelled, as usual. For the vibrations of the mode with the lowest natural bending frequency it was ascertained at ν = 0,04.
The reinforced concrete parts of the actual work were modelled with microconcrete, the free suspension ropes by dia. 1,4 mm piano wires, the prestressing ropes (passing through the bridge deck) by dia. 0,7 mm steel ropes. The bridge deck was assembled of precast components and their joints were filled by plaster.
The aerodynamic stability of the model was assessed by means of the dynamic response of the selected points of the bridge deck, pylon and supports in dependence on the air flow velocity. The dynamic response was measured by a laser VPI sensor connected to a single-channel type 2202 Brüel-Kjaer analyzer.
Table 1 gives a survey of theoretical value of natural frequencies and the respective vibration modes according to first [3] and second method [5] and the values obtained on the model.
Table 1 shows a good accordance of both theories with experimental results; it is proved generally by Columns 2, 4 and 6. There is a disagreement between the theoretical value of the 1st mode according to [3] and according to [5], because the first method assumes that the end points of the suspension ropes will be fixed. Column 7 gives the ratio of the natural frequency of the model to the theoretical frequency of the actual structure, according to [3]; important is the ratio of the frequencies corresponding with the first antimetric vibration mode, because it dominates the overall dynamic response.

Table 1.

1	2	3	4	5	6	7
Theory after [3] (Hz)	Rel. $\dfrac{f_{(j)}}{f_{(2)[3]}}$	Theory after [5] (Hz)	Rel. $\dfrac{f_{(j)}}{f_{(1)[5]}}$	Frequency on model (Hz)	Rel. $\dfrac{f_{(j)M}*}{f_{(2)M}}$	Rel. $\dfrac{f_M*}{f_{SK} 5/1}$
0,572 1st mode	2,07	0,374 2nd mode	1,26	43,20 1st mode	1,20	115,51 (5/3)
0,276 2nd mode	1	0,298 1st mode	1	36,00 2nd mode	1	130,43
0,414 3rd mode	1,50	0,456 4th mode	1,76	60,48 3rd mode	1,68	146,09
0,552 4th mode	2,00	0,547 7th mode	1,84	74,52 4th mode	2,07	135,00
0,690 5th mode	2,50	0,704 9th mode	2,36	92,52 5th mode	2,57	134,09

*) subscripts: M - model
            SK - full-scale

4. Results of Model Measurements and Transfer to the Actual Structure

Fig. 2 as an example gives the results of the measurements of the vertical response of the bridge deck. The measured movement consists of the 2nd, 3rd 4th and 5th natural vibration modes (after [3]). The by-passing of the bridge deck cross section produces its random excitation the frequency range of which is not specifies; the by-passing can be characterized by the Reynolds number of the actual work: Re $= 0.83.10^7$ for wind velocity of $17,85$ m.s^{-1}.

A distinct increase of thy dynamic response in vertical direction can be observed for the air flow velocity of $V_M = 30$ m.s^{-1}. With the further increase of the air flow velocity the response diminishes.

The peaks of the dynamic response curves in Fig. 2 correspond, consequently, with the actual velocity of $15 \div 17,5$ m.s^{-1}

Fig. 2

Fig. 3

Fig. 4

165
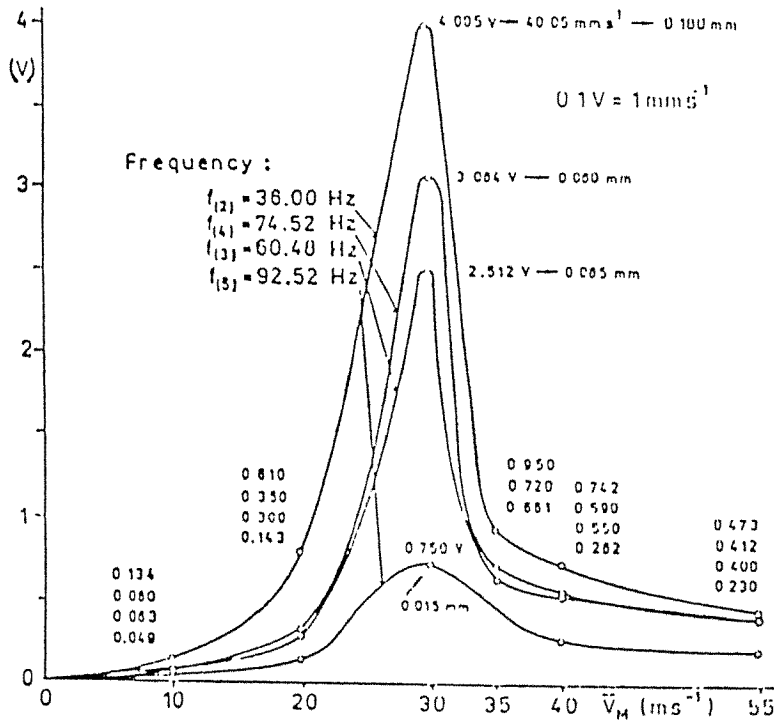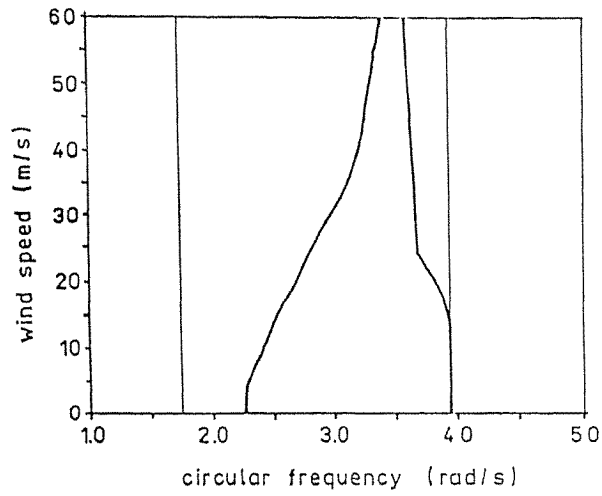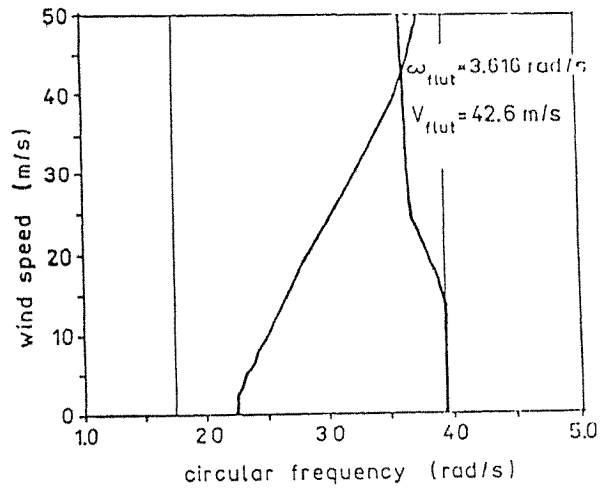
The increase of dynamic response at the air flow velocity of $15 \div 17,5$ m.s^{-1} is the manifestation of the response of the structure to vortex separation beyond the deck cross section, the frequency of which is near $f_{(2)}$, i. e. $f_{Str} = 0,276$. The Strouhal number is then determined by the ratio

$$Str = 0,12 .$$

That means that on the actual work the damping, which will equal only one quarter of the model damping , will produce an amplitude of vertical movement

$$v_{oSk} = 111 \text{ mm} .$$

5. The loss of aerodynamic stability

The model verification of the footbridge response to the air flow within the velocity range of 0 - 30 m.s^{-1} has not revealed any loss of aerodynamic stability due to the bending torsional flutter. This corresponds also with the theoretical solution of Scanlan equations [6] shown in Fig. 3, 4 with logarithmic damping decrements $\vartheta = 0,04$ and with $\vartheta = 0$ below.

6. Proposed Eliminating Excessive Vibration Amplitudes

Although the amplitudes of the vibrations due to the air flow do not threaten the bridge structure, the designer was recommended to include in the design the application of dampers situated in the railings. The author of the paper has used this method for the first time in the Redding in California footbridge [1]. It is obvious that the damper is intended for the damping of the basic antimetric vibrations dominating the response. The number of posts on both sides of one footbridge half-span is 2 x 89. Let us consider the installation of the dampers in 178 the posts; each has 20 kg. The weight of the one half of footbridge, vibrating within the basic antimetric modes, is M = 255310 kg. The amplitudes of the horizontal vibrations could be reduced due to systems of dampers, which consist of spheres (weight 24 kg) on curved bearing plates.

References:
1. Ch. Redfield, T. Kompfner and J. Stráský, Stressed ribbon pedestrian bridge across the Sacramento River in Redding, California, USA, FIP - XIth International Congress on Prestressed Concrete, Hamburg, (1990) 63-66.
2. J. Mazur, Report of turbulence measurements in wind tunnel ø 3 m, VZLU, Prague, (1991).
3. V. Koloušek, M. Pirner, O. Fischer and J. Náprstek, Vind effects on Civil Engineering Structures, Academia-Elsevier, Prague, (1983).
4. V. Koloušek and others, Dynamics of Civil Engineering Structures (in Slovac), SVTL, Bratislava, (1967).
5. P. Krysl and R Chudoba, Nonlinear analysis of hanging footbridge (in Czech), Technical University Prague, Report HS 690/90.
6. R. H. Scanlan, Aeroelastic simulation of bridges, Journal of Structural Engineering, Vol. 109, No 12, (1983).

Bridge Analysis

Wind Resistant Design for Long Span Suspension Bridges

K. Kazama, H. Yamada and T. Miyata

Department of Civil Engineering
Yokohama National University, Japan.

Abstract : Considering the trend of longer bridges in the future, the aerodynamic instability plays a major role in their design. In this paper, the aerodynamic characteristics and the efficiency of the structural countermeasures for aerodynamic instability of long span suspension bridges are discussed using newly developed Direct Flutter Analysis Method for longer dimension than the Akashi Kaikyo Bridge (main span 1990m). As a result, for suspension bridges longer than 2000m-class the aerodynamic characteristics become worse as shown by the drop in flutter wind speed and the coupled torsional-vertical flutter response. The efficiency of the structural countermeasures for long span suspension bridges decrease for spans longer than 2000m. Finally the mode-control countermeasure (partly strengthening of deck rigidity along bridge axis considering flutter mode) was proved to be efficient in gaining stability against flutter.

1. Introduction

The Akashi Kaikyo Bridge (span: 960+1990+960 m) will be the world's longest suspension bridge when it will be completed in 1998. In the design of this bridge, considerable amount of wind tunnel tests and numerical analysis from various points of view has improved its aerodynamic instability [1]. Finally, the truss stiffened girder which pass the aerodynamic requirement of the design code was adopted to the final configuration. And from the point of view of aeroelasticity, long span bridges exhibit high reduced wind speed due to the decrease in their natural frequencies which leads to the coupled flutter phenomenon [2]. In this region, the characteristics of aerodynamic response are similar to the wing in same size.

On the other hand, at the present, some bridge projects of spanning more than 2000m are in consideration in Japan and other countries. With these backgrounds, feasibility studies have been proposed using Selberg's formula [3] or modal technique [4] assuming that the flutter mode is same as the combined one of some modes under no wind to check its stability against wind

However, more attention should be given to the behavior of flutter instability behavior of longer span bridges, since as the span becomes longer the structural rigidity decreases and the coupling of modes under wind that affects the self excited wind force becomes more complicated as compared with ordinary span bridges.

In this paper, we discuss the aerodynamic feature of very long span suspension bridge (case study model with truss girder) using the Direct Flutter Analysis Method [5] that can consider the change in mode shape due to wind load. With this method, the self-exciting wind load will be evaluated correctly.

Next, also the efficiency of some countermeasures for wind resistant design will be discussed. In the long span suspension bridge, the design should be based not only on the static analysis but also on the aerodynamic instability analysis.

2. The Case Studies of Very Long Span Suspension Bridges

There are many conceptions for the design of super-long span bridges. In this paper, we designed a 2,500m span and a 4,000m span suspension bridges as the case study models by simply extending the design procedure applied to the Akashi Kaikyo Bridge, as follows.

1) assume the configuration (allowable stress on the cable was assumed to be 200kgf/mm^2)
2) check the static resistance to dead load and wind load
3) revise the design, if necessary

As for the girder, we preferred truss stiffening girder by its stability against wind and its degree of freedom for realizing certain stiffness. The general configuration of the 2,500m bridge is shown in Fig. 2-1. The geometry of the structure is assumed as follows.
1) Distance between cables: 38.5m, 2) Weight of the girder: 29tf/m,
3) Weight of the cables: 18.5tf/m,   4) Mass moment of inertia of the girder: 13000tfm²/m

For the case of 4,000m span, the design procedure described above was followed.
For long span bridges, the lowest natural frequency is one of the measure of its aerodynamic characteristics. Fig. 2-2 shows the decrease of natural frequency with the span length.
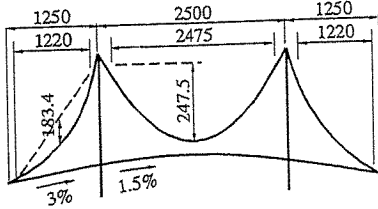
Fig.2-1 General Arrangement of 2,500m Bridge
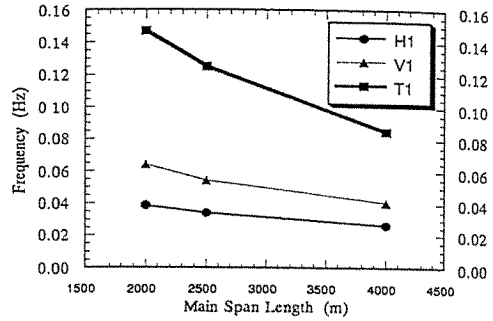
Fig.2-2 Natural Frequency of Long Span Bridges

3. Numerical Method of Flutter Analysis

There is some ordinary methods to analyze flutter instability of bridges includes Serberg's formula and modal flutter analysis method.

In applying these methods to wind instability of long span bridges, some problems relating to the accuracy are encountered: (1) normal modes of vibrations are required to be selected among the natural modes without considering wind effects. 2) for very long span suspension bridges, some modes will be coupled when flutter occurs which make it difficult to prescribe which mode to select.

With these reasons, the aerodynamic characteristics were analyzed using the Direct Flutter Analysis Method (complex eigen value analysis)with three dimensional frame model, as follows.

Fig. 3-1 Schematic Figure of 3-D Frame Model

First, the suspension bridge is modeled as a three dimensional frame shown in Fig. 3-1.
The equations of motion of this system under wind action can be written as

$$M\ddot{u} + C\dot{u} + Ku = F(\ddot{u}, \dot{u}, u) \qquad (1)$$

where M, C, K and F are the mass-matrix, damping-matrix, stiffness-matrix and aerodynamic-force matrix, respectively. And $u, \dot{u}, \ddot{u}$ are displacement-vector, velocity-vector and acceleration vector, respectively. Assuming the harmonic vibration, next relationships between displacement, velocity and acceleration holds as

170

$$u = -\frac{1}{\omega^2}\ddot{u}, \quad \dot{u} = \frac{i}{\omega}\ddot{u}, \quad k = \frac{fb}{U} \tag{2}$$

where ω, b, U and k are natural circular frequency, normal length (deck width), wind speed and reduced frequency, respectively. Substituting eq.(2) to eq.(1), the equations of motion become a complex eigen value problem as

$$(M - F')\ddot{u} + Ku = 0 \tag{3}$$

where F' is the velocity proportional expression of aerodynamic force.

Solving eq.(3), we can get n-sets of complex frequencies and complex vibration modes under wind action for each assumed reduced frequency k. Then we can see the stability of the system, by δ_m which indicates the logarithmic damping of the m-th mode as,

$$\delta_m = \frac{2\pi\omega_{mi}}{\sqrt{\omega_{mr}^2 + \omega_{mi}^2}} \tag{4}$$

where ω_{mr} and ω_{mi} are real-part and imaginary-part of the m-th complex circular frequency under wind action, respectively.

To apply this method to the case study model, we assume the aerodynamic force of the deck girder as the same as that of a flat plate with the same size. According to the flat plate wing theory, the unsteady lift force and unsteady moment are given by

$$L = -\pi\rho b^2(\ddot{u} + U\dot{\phi}) - 2\pi\rho U b C_{(k)}\left(\dot{u} + U\phi + \frac{b}{2}\dot{\phi}\right) \tag{5}$$

$$M = \pi\rho b^3\left(-\frac{U}{2}\dot{\phi} - \frac{b}{8}\ddot{\phi}\right) + 2\pi\rho U b^2\frac{1}{2}C_{(k)}\left(\dot{u} + U\phi + \frac{b}{2}\dot{\phi}\right) \tag{6}$$

where, b is half chord length, C(k) is the Theodorsen function, k(=ω_rb/U) is the reduced frequency, U is wind velocity and ρ is the density of the air.

In the above formulation, assuming one reduced frequency 'k', we can get n-sets of complex eigen values and modes.('n' is the degree of freedom of the structure.) The result of eigen value analysis shows the damping of the system from eq.(4) in wind speed at U (=ω_rb/k) for each mode. Then assume next 'k' we get next n-sets of complex eigen values and modes. In this way, the relationship between the wind speed to logarithmic damping can be obtained.

4. Aerodynamic Characteristics of Very Long Span Suspension Bridges
In the design of long span suspension bridge, considering aerodynamic characteristics, the static analysis with mean wind force and dynamic analysis with aerodynamic force (Direct Flutter Analysis) is done as follows.

4.1 Aerostatic Characteristics
The deformation and the internal force (horizontal bending moment) due to static wind load of the 2,500m span bridge are shown in Figs.4-1 and 4-2.

Considering the stiffness of the truss girder, the horizontal moment governs the design of member sizes. The maximum value of the moment appears at the quarter point of the center span due to the transmission of aerostatic force to the main cables. This is the one of the peculiar feature of long span suspension bridges. For the 4,000m span model, this feature becomes more distinct. The

171

equired stiffness of the girder does not increase so much according to the span length due to this ransmission of the force to the main cables.

For the static design approach, this feature is favorable in economical. On the other hand, for the erodynamic design, this feature cause a reduction in the lowest frequency and flutter wind speed.

Therefore, in the design of very long span bridges, a different approach is necessary for the erodynamic stability.
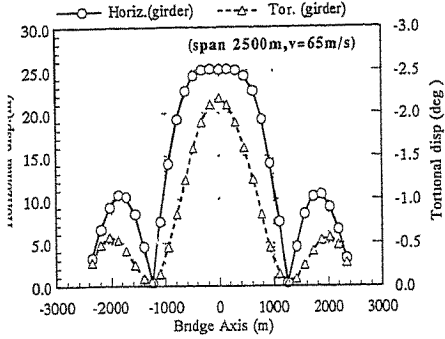
Fig. 4-1 Deformation due to Wind Load   Fig. 4-2 Horizontal Moment of The Girder
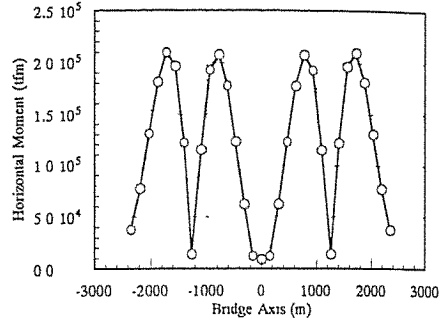
4.2 Aerodynamic Characteristics

To determine the aerodynamic characteristics, the stability under dynamic wind load was calculated by Direct Flutter Analysis Method.

Figs. 4-3 and 4-4 show the aerodynamic characteristics of 2,500m span suspension bridge. The lamping of each mode for each wind speed is shown in Fig.4-3. The aerodynamic damping is positive up to 52.6m/s for every mode. For the torsion-vertical coupled mode (flutter mode), the lamping change from positive to negative at U=52.6m/s. Hereafter the damping of this mode ncreases (become more unstable) in the negative side in proportion to wind speed.

Fig. 4-4 shows this mode of girder just over the critical wind speed with complex mode expression. In this wind speed, vertical, torsional and horizontal motion is combined, though the irst two modes are dominant under the assumption of flutter derivative of the flat plate
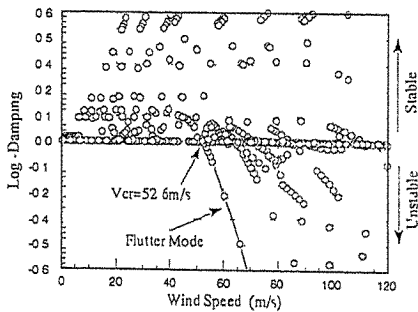
Fig. 4-3 Damping Decrement due to Wind Speed   Fig. 4-4 Flutter Mode (U=52.9m/s)
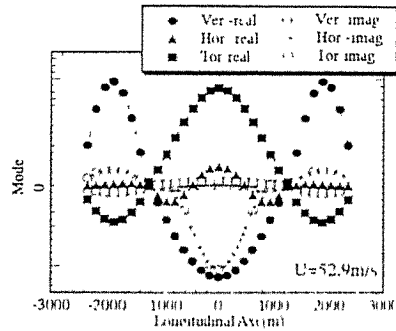
Fig. 4-3 shows the decline of flutter wind speed according to span length by Direct Flutter Analysis and conventional Selberg's formula.

For the case of 4,000m span, the same procedure for the case of 2,500m span bridge was used.

The flutter occurring for the case of 4,000m span bridge is also the coupled flutter (torsional and vertical motion). The wind resistant performance decreases according to its span length. The result of Serberg's formula does not agree well with the Direct Flutter Analysis Method. The dominant cause of this difference may be the assumption of flutter modes.
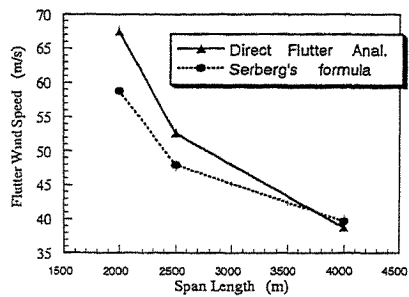
Fig.4-3 Decrease of Flutter Wind Speed

5. Improvements of Aerodynamic Characteristics by Structural Countermeasure

Aerodynamic characteristics deteriorated as the span length increases as shown in previous section. Next, we discuss the Structural Countermeasures to increase the stability against wind of very long span suspension bridges.

When we adopt some countermeasures, its efficiency must be considered. Here we consider first the ordinary method of increasing the stiffness. Then, we propose the structural countermeasure that controls the flutter mode.

5.1 Structural Countermeasure with Increment of Stiffness

To improve the stability against the flutter, some tentative designs were worked out and evaluated its stability using the Direct Flutter Analysis Method. The results of calculations are shown as follows.

1) Increasing The Stiffness of The Girder

Horizontal, Vertical and Torsional Stiffness were increased in truss girder.

The result of the calculation shows that increasing the horizontal and the vertical stiffness of the girder separately does not give any significant effect. On the other hand, increasing the torsional stiffness could increase the flutter speed. When the stiffness of the girder doubled, the flutter wind speed increased 20%.

2) Shallow Cable Sag

When we use High-Tensile-Cable (20% stronger than ordinary one), cable sag ratio of main span can be decreased 1/10 to 1/12 with no increase of mass and mass moment of inertia.

However, this system does not improve the critical wind speed.

3) Increasing of The Stiffness of The Tower

In one of the design, the stiffness of the tower was assumed to be twice as the original, however the flutter wind speed did not increase much (about 6% increase).

As observed from the above, gaining the flutter wind speed of very long span suspension bridge with direct increase of the stiffness is not so efficient.

5.2 Structural Countermeasure to Control The Flutter Mode

To gain the stability in more efficient way, we made some endeavor to control the flutter mode. When the flutter occurs at flutter wind speed, the dominant mode is the coupled torsional and vertical motion. As shown in Fig. 5-1 two methods were used to improve flutter wind speed. One is increasing its stiffness near the supports along the quarter span (Case 1) aiming at increasing torsional stiffness and frequency with minimum increment of the mass and mass moment of inertia. And the other is the ordinary way of increasing the stiffness of the full span (Case 2). The increasing of the stiffness of the girder was realized by changing of the size of the lateral member of stiffening truss.

173

By doubling its lateral member size, the torsional stiffness of the girder became 153% of original with a 5% increment in mass and mass moment of inertia.

Fig. 5-2 shows that increasing the stiffness of the girder leads to higher flutter wind speed. And the effect of Mode Control is proved to be efficient. Comparing the efficiency of two cases, it can be seen from Fig.5-2 that the increase in flutter wind speed for case 1 is 75% of case 2 with only half the weight of countermeasure.
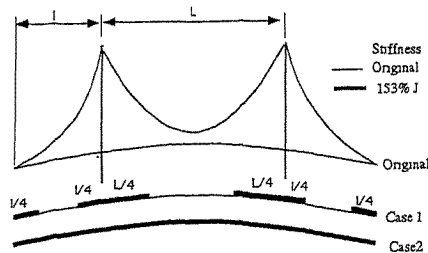
Fig. 5-1 Additionally Stiffened Part for Modal Countermeasure
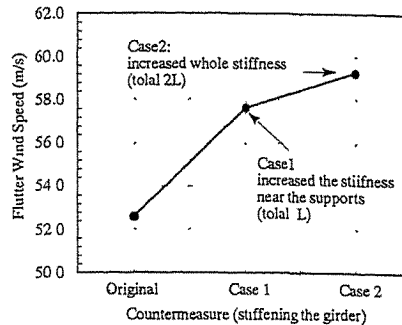
Fig.5-2 Effect of Modal Countermeasure

6. Concluding Remarks

Aerodynamic characteritics and countermeasures for gaining the stability of very long span suspension bridges were discussed based on the suspension bridge case study models with truss girder using the Direct Flutter Analysis Method which can consider the effect of change in mode shape due to wind load.

In static design, since a considerable amount of wind load is transmitted to the main cables, the required stiffness does not increase much as the span increases. This feature becomes more distinctive in longer span models. In this way, based on the static design procedure, the wind resistant characteristics tend to decline. So, not only the static wind load but the dynamic wind load as well must be considered in the wind resistant design for very long span suspension bridges.

The stability against the flutter instability is observed to decrease much according to its span length. The instability occurring at high wind speed for long span suspension bridge up to 4,000m span (as shown in the case studies) was the coupled flutter (torsional and vertical motion) under the assumption of flat plate wing theory.

To gain the stability against the flutter, countermeasure that controls the flutter mode proved to be more efficient compared to increasing the total stiffness of the full span.

References:

[1]   M. Ohashi, T. Miyata, I. Okauchi, N. Shiraishi and N. Narita, "Considerations for wind effects on a 1,990m-main span suspension bridge", Prept. 13th Cong. IABSE(Helsinki), 1988, pp. 911-916

[2]   Y. Yoshida, K. Fujita, M. Miyazaki and K. Kazama, "A Study On The Flutter Instability Of Truss Stiffening Girder In High Wind Speed", Proc. of 11th National Symposium On Wind Engineering, Dec. 1990, pp.43-48.(in Japanese)

[3]   Serberg.A, "Oscillation and Aerodynamic Stability of Suspension Bridges", ACTA Polyteck, 1961.

[4]   H. Tanaka, N.Yamamura, M. Tatshmi, "Similarity Requirements of 2-DOF Aeroelastic Modeling for 3-Dimensional Flutter Behavior of Long-Span Bridges", Journal of Structural Engineering. Vol. 35A,1989.3.(in Japanese)

[5]   T. Miyata, H.Yamada, "Coupled Flutter Estimate of a Suspension Bridge", Journal of Wind Engineering. No.37, 1988.(in Japanese)

System Identification Procedure for Structural Parameters and Wind Characteristics in Ambient Vibration Surveys

Nicholas P. Jones, Tinghui Shi, J. Hugh Ellis[+] and Robert H. Scanlan

Department of Civil Engineering
[+]Department of Geography and Environmental Engineering
The Johns Hopkins University
Baltimore, MD 21218-2686, USA.

Abstract: Over the past several decades, much valuable data pertaining to the structural performance of large civil structures (e.g., bridges) have been obtained through the use of ambient vibration surveys. While there have been significant advances in the technology used to collect the data, processing techniques used in such situations are still unable to routinely and robustly extract "difficult" parameters such as damping. This paper presents an overview of a method designed to overcome these difficulties. Numerical examples are presented.

1. Introduction

Due to the size of many civil engineering structures, full-scale validation of analyses or model studies relative to wind design are expensive and difficult to perform. Wind tunnel modeling is therefore often used to address this task. There exist, however, numerous uncertainties regarding the assumptions made in wind tunnel modeling due to scaling effects. As a result, full-scale testing and measurement of structures is typically the only assured method for verification of analysis and design procedures.

Full-scale, long-term, field measurements of the dynamic performance of bridge structures under wind and vehicular loadings are, for the most part, performed only infrequently. But this practice may be changing, that is, frequent field measurements considered an integral part of ongoing performance monitoring. Notable examples of such trends in the U.S. are those performed on the Deer Isle-Sedgwick Bridge in Maine and the Lulling Bridge in Louisiana. For both of these structures, comprehensive instrumentation (anemometers, accelerometers) was installed and operated for extended time periods.

Short-term ambient vibration studies have been performed on several bridges, but these have been used primarily in the determination of the dynamic characteristics of the structure, rather than for the assessment and measurement of wind effects. Valuable results have been obtained from analysis of the data recorded on these structures, both for future designs and for reliability estimates for existing designs. While much has been learned, the need for field observations has certainly not diminished.

A significant weakness that remains in successfully implementing full-scale measurement experiments has been the inability to analyze and interpret the data fully. With the availability of inexpensive data acquisition systems capable of the efficient collection and processing of large quantities of information, it is appropriate now to reconsider the applicability of existing data analysis techniques.

Past approaches have generally concentrated on analyses using Fourier Transform techniques to estimate power spectra from which estimates of natural frequencies, mode shapes, and modal damping can be made. This process is conceptually simple, but has some significant shortcomings. Of particular concern are the difficulties associated with the estimation of

175

damping, which is a critical parameter for the estimation of structural response to wind loads. Moreover, existing techniques have typically made no attempt to estimate characteristics of ambient excitation forces. Improved techniques which are more automated and informative, yet provide robust and reliable estimates of system parameters (including confidence intervals) and input characteristics are clearly needed.

In this paper, a technique based on the application of a Kalman filter will be presented. The method developed has been tested with numerical simulations and controlled laboratory experiments, and will be applied to the analysis of acceleration data recorded for the Deer-Isle, Sunshine Skyway and Houston Ship Channel (Baytown) Bridges. The controlled experiments enable assessments of the new technique to be made by comparison with more conventional approaches. The Kalman filter-based modelling approach shows significant promise for the extraction of the maximum utility from collected data in its ability to simultaneously estimate both system and input characteristics.

2. Ambient Vibration Surveys (AVS)

Parameter identification for large structures under construction or in service is often carried out through an AVS, that is, the use of accelerometers to record the real acceleration data of the structure under normal conditions. Techniques for this application generally assume that the system is linear, the response is an ergodic random process and the excitation is band-limited locally white noise.

By treating each individual modal response as that of a single-degree-of-freedom (SDOF) oscillator, the transfer function $|H(j\omega)|$ can be determined by:

$$S_0(\omega) = |H(j\omega)|^2 S_{in}(\omega) \tag{1}$$

where S_0 and S_{in} are the power spectral density of the output and input. For ambient vibrations, S_0 can be estimated from recorded response whereas S_{in} is unknown but is often assumed locally constant. The average spectrum of the records can then be used directly as an estimate of $|H(j\omega)|$ in the neighborhood of each modal frequency. Once $|H(j\omega)|$ has been estimated, the frequency can be determined by the resonant-peak technique, and the damping ratios can be estimated by the half-power method [1].

3. Damping Identification

The development of a state-of-the-art bridge analysis for dynamic loads is found in [2]. The damping of a mechanical oscillator may be obtained through the logarithmic-decrement or the half-power method [1]. Since standard forcing procedures (shaker and hammer) are not readily available for large structures, the only economically feasible approach is to use AVS data [1]. Nevertheless, estimations by the approaches mentioned above involve intensive data processing (windowing, smoothing), while biasing, aliasing and leakage are inevitably introduced through such procedures. For deterministic signals, the effects of aliasing and leakage can be predicted and remedied based on some knowledge of the system and sophisticated curve fitting. But when the data are corrupted with significant noise (as is often the case in practice), these ad hoc remedies may fail.

An alternative choice employs System Identification (SID) in the time domain. Frequencies and damping ratios of the structure are estimated directly from time series data. The time domain methods, however, are prone to failure when the random excitation is not known.

176

4. System Identification Techniques

In generl, system identification can be described as the process of deducing the parameters of a model in a real system from its input and output, or solely from its output. Survey articles on identification methods can be found in [3-10], and a review of several system identification methods as applied to structural dynamics problems can be found in [11]. Use of the extended Kalman filter (used herein) applied to earthquake response analysis can be found in [12]. With knowledge of input excitation, it is generally believed that parametric, time-domain SID has advantages over other SID techniques when applied to vibrational problems.

The structural vibration problem can be written

$$M_0\ddot{x} + C_0\dot{x} + K_0 x = L_0 w \tag{2}$$

$$z(k) = x(k) + v(k) \tag{3}$$

where M_0 is the mass matrix; C_0 = damping matrix; K_0 = stiffness matrix; L_0 = transition matrix; x is the displacement vector; w = random excitation force; $z(k)$ = n-dimensional observation vector at $t = k\Delta t$, and $v(k)$ = observation noise vector, generally assumed to be Gaussian white. Conventionally, the state space equation of the problem can be represented as

$$\dot{X} = FX + Gw \tag{4}$$

$$z(k) = MX(k) + v(k) \tag{5}$$

where

$$X = \begin{pmatrix} x \\ \dot{x} \end{pmatrix}, F = \begin{pmatrix} 0 & I \\ -M_0^{-1}K_0 & -M_0^{-1}C_0 \end{pmatrix}, G = \begin{pmatrix} 0 \\ M_0^{-1}L_0 \end{pmatrix}, M = \begin{pmatrix} I & 0 \end{pmatrix}$$

5. Time Domain Formulation

For an SDOF system, the equation may be represented as follows:

$$\ddot{x} + 2\zeta\omega_n\dot{x} + \omega_n^2 x = w(t) \tag{6}$$

where ω_n and ζ represent natural frequency and damping ratio of the system, and $w(t)$ represents measurable random excitation. In the time domain representation, state variables are $x_1 = x; x_2 = \dot{x}; x_3 = \omega_n; x_4 = \zeta$. Denoting $X = (x_1\ x_2\ x_3\ x_4)^T$, (6) can be rewritten in augmented state-space form as:

$$\frac{dX}{dt} = \begin{pmatrix} x_2 \\ -x_3^2 x_1 - 2x_2 x_3 x_4 + w \\ 0 \\ 0 \end{pmatrix} = g(X) \tag{7}$$

where it is assumed that both displacement and velocity components (which can be evaluated from AVS accelerometer data) are measurable, and

$$z = \begin{pmatrix} 1 & 0 & 0 & 0 \\ 0 & 1 & 0 & 0 \end{pmatrix} \begin{pmatrix} x_1 \\ x_2 \\ x_3 \\ x_4 \end{pmatrix} + v = MX + v \tag{8}$$

where v is observation noise, and M is the observation matrix. Application of the Kalman filter the permits simultaneous estimation of the state variables x_3, x_4, the system frequency and mechanical damping components.

For an MDOF system, augmented state variables may be represented by the displacement, velocity, frequency and damping of each DOF, and Kalman filter analysis can similarly be performed.

6. Frequency Domain Formulation for the Single DOF

Alternatively, the problem may be formulated in the frequency domain, taking a frequency point as the "time step" in the Kalman filter. The input PSD can be assumed to be a function of parameters $a_1, a_2, ...$, which are yet to be identified. The observation of Kalman filter can be defined as function of output PSD.

Defining the state variables $X = \{\omega_n, \zeta, a_1, a_2, ...\}^T$, the discrete state equation for the j-th mode is obtained as

$$
\begin{pmatrix} x_{1j}(k+1) \\ x_{2j}(k+1) \\ x_{3j}(k+1) \\ . \end{pmatrix} = \begin{pmatrix} 1 & 0 & 0 & . \\ 0 & 1 & 0 & . \\ 0 & 0 & 1 & . \\ . & . & . & . \end{pmatrix} \begin{pmatrix} x_{1j}(k) \\ x_{2j}(k) \\ x_{3j}(k) \\ . \end{pmatrix} \tag{9}
$$

The advantages of frequency domain formulation over time-domain observation are manyfold: (1)-The PSD of the input function is introduced as a function with parameters $a_1, a_2, ...$; (2)-The number of state variables is halved as compared with time domain; (3)-The system transition matrix is an identity matrix, compared to the nonlinear transition matrix required in the time domain formulation; (4)-Acceleration data can be used directly and the associated integration problems are totally avoided; (5)-Sampling lag in the time domain corresponds to a known phase lag in the frequency domain; therefore complications associated with non-simultaneous sampling problem are readily addressed.

7. Numerical Examples

Numerical examples based on simulated data were conducted to illustrate the application of the algorithm. Given a specified input PSD, Monte-Carlo simulation to random input force was used, and Runge-Kutta integration invoked to obtain displacement, velocity and acceleration.

Table 1: 1-DOF Time-Domain Identification

State variables	Theoretical Value	Initial Value	Final Value
ω	1.000	1.200	1.000
ζ	5.0e-2	4.0e-2	4.990e-2

First, given input knowledge, time domain identification was performed. The sampling interval was $\Delta t = 0.02$ sec; initial error covariances were $P_0 = 0.001I$ for diagonal elements and zero for off-diagonal elements; system and observation uncertainties were assumed as $0.0I$ and $1.0I$, respectively; and 2000 time steps were used. Results are shown in Table 1, and the evolution of the estimation with respect to time step is shown in Fig. 1.

Next, a frequency domain filter was used to analyze the system and input characteristics. Given the same system as used in the previous example: with the input PSD of the form

Table 2: 1-DOF Frequency Domain Identification

State Variables	Theoretical Value	Initial Value (Error Covariance)	First Iteration	Second Iteration	Third Iteration
ω	1.000	1.300 (1.0)	1.001	0.9995	0.9995
ζ	5.0e-2	3.5e-2(1.0)	5.184e-2	4.949e-2	4.949e-2
a_1	0.25	0.20 (1.0)	0.250	0.250	0.250
a_2	0.1	0.08 (1.0)	0.100	0.100	0.100

$a_1 e^{-a_2 \omega}$; step size of filter $= \Delta \omega = 0.004794$; and, frequency points used from $k = 100$ to $k = 2620$. Again $Q = 0.0I$ and $R = 1.0I$ for state variables and observation variables, respectively. Three iterations were performed, each with the initial value taken to be the values from the previous estimation, and the error covariance matrix taken to be value at the end of the preceeding iteration. Results are shown in Table 2, and the evolution of the estimation with respect to frequency step is shown in Fig. 2.

8. Conclusions

An SID method based on a Kalman filtering approach for assessing the characteristics of bridges and the nature of the wind excitation has been presented. With this method, frequencies, damping ratios and mode shapes of structures can be reliably identified. Knowledge of the stochastic characteristics of the input is possible with the same analysis. The technique will not only serve as a new tool for the identification of system and input characteristics of the bridges under wind and earthquake excitation, but also will contribute significantly to other relevant engineering disciplines.

References:
1. Jones, N.P. and Spartz, C.A., 1990, "Structure Damping Estimates for Long-Span Bridges", *J. of Engrg. Mech.*, ASCE, 166(11)
2. Scanlan, R.H. and Jones, N.P., 1990, "Aeroelastic Analysis of Cable-Stayed Bridges", *J. Str. Engrg.*, ASCE, 116(2)
3. Bekey, G.A., 1970, "System Identification – an Introduction and a Survey", *Simulation*, 15
4. Nieman, R.E., Fischer, D.G. and Seborg, D.E., 1971, "A Review of Process Identification and Parameter Estimation Techniques", *Int. J. Control*, Vol. 13
5. Åström, K.J., and Eykhoff, P., 1971, "System Identification – A Survey", *Automatica*, Vol. 7
6. Bowles, R.L. and Straeter, T.A., 1972, "System Identification Computational Considerations", in System Identification of Vibrating Structures, *W.D. Pilkey and R. Cohen (eds)*, ASME, New York
7. Sage, A.P., 1972, "System Identification History, Methodology, Future Prospects", in System Identification of Vibrating Structures, *W.D. Pilkey and R. Cohen (eds)*, ASME, New York
8. Eykhoff, P., 1974, **System Identification – Parameter and State Estimation**, Johns Wiley & Sons, New York
9. Kozin, F. and Natke, H.G., 1986, "System Identification Techniques", *Structural Safety*, 3
10. Ljung, L., 1987, **System Identification: Theory for the User**, Prentice-Hall

11. Imai, H., Yun, C.B., Maruyama, O. and Shinozuka, M., 1989, "Fundamentals of System Identification in Structural Dynamics", *Prob. Engrg. Mech.*, 4(4)
12. Maruyama, O, Yun, C-B, Hoshiya, M and Shinozuka, M, 1989, " Program EXKAL2 for Identification of Structural Dynamic Systems", Technical Report NCEER-89-0014, National Center for Earthquake Engineering Research
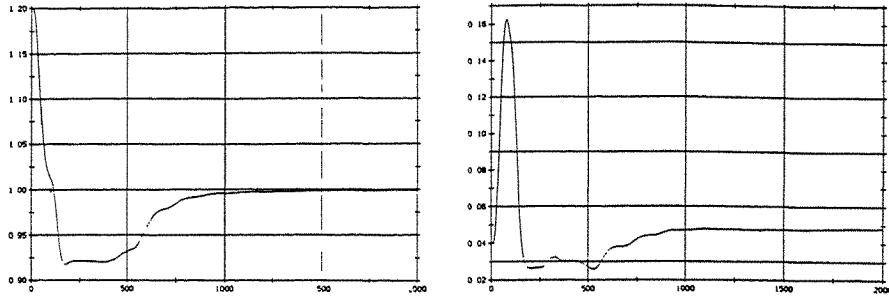
Figure 1: Time-Domain ID (a) Natural Freq. vs. Time Step (2) Damping vs. Time Step
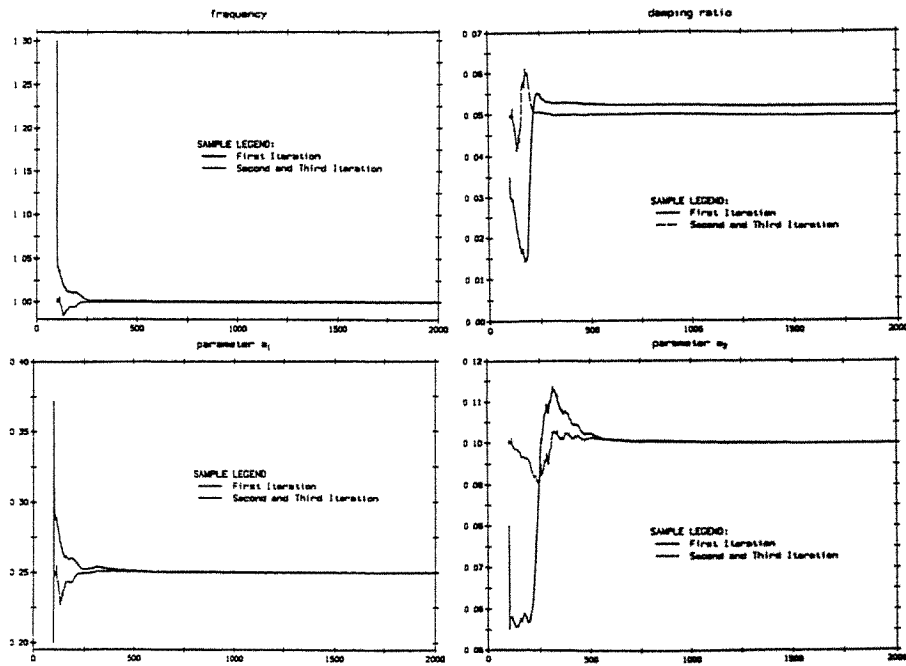
Figure 2: Frequency-Domain Identification (a) Natural Freq. (2) Damping (3) a_1 (4) a_2

180

An Analysis Method for Buffeting Responses of Flexible Bridge with Aerodynamic Coupling Between Modes

W. L. Qu and H. F. Xiang[+]

Department of Building Engineering
Wuhan University of Technology, Wuhan, China
[+]Department of Bridge Engineering
Tongji University, Shanghai, China

Abstract: In the paper, a 3-dimension analysis method for bend and torsion buffeting responses of flexible bridge with aerodynamic coupling between modes is presented. the calculation of engineering example indicate that it is necessary to consider the effect of aerodynamic coupling between modes for the flexible bridge in whose responses effect of high mode shape can not be neglected.

1. Introduction

Cable-suspended bridge is a kind of both long and flexible bridge. Generally, turbulence can cause buffeting responses combined bend with torsion of its deck. Considering that aerodynamic forces can be expressed as the function of the displacement and velocity of bending and torsion vibration of the deck, the generalized coordinate equations of mode shape of structural buffeting responses are coupling. To solve these equations, the approximate method without the aerodynamic coupling between modes is mainly used currently. Although this method is accurate enough for the analysis of buffeting responses of many flexible buidges, it is not accurate for analyzing some flexible bridge in whose responses effects of high mode shape can not be neglected. From this, it is necessary to present a analysis method for buffeting responses of flexible bridge with aerodynamic coupling between mode.

In the paper, a 3-dimension analysis method in frequency domain for buffeting responses of flexible bridge with aerodynamic coupling between modes is provided. On the basis of establishing the discretization model of analysis for 3-dimension buffeting responses of the bridge, the transfer function with aerodynamic coupling in frequency domain is derived. And the calculation formulas of 3-dimension buffeting responses of the bridge with aerodynamic coupling between modes are obtained.

2. Analysis Method for 3-Dimension Buffeting Responses of Flexible Bridge with Aerodynamic Coupling Between Modes

According to the wind vibration theory of flexible bridge, the coupling buffeting responses of vertical and lateral bend and torsion of the deck are caused by the vertical and horizontal fluctuation wind, and the vertical and horizontal vibration responses of cables are induced. Their vibration equations can be expressed as:

$$\begin{aligned}
[M_h]\{\ddot{h}\}+[C_h]\{\dot{h}\}+[K_h]\{h\}+\{L_h\}&=\{F_h\} \\
[I_\alpha]\{\ddot{\alpha}\}+[C_\alpha]\{\dot{\alpha}\}+[K_\alpha]\{\alpha\}+\{M_\alpha\}&=\{T\} \\
[M_p]\{\ddot{p}\}+[C_p]\{\dot{p}\}+[K_p]\{p\}+\{L_p\}&=\{F_p\}
\end{aligned} \right\} \tag{1}$$

and

$$[M_s]\{\ddot{s}\}+[C_s]\{\dot{s}\}+[K_s]\{s\}=\{F_s\} \tag{2}$$

where:

$\{h\},\{p\},\{\alpha\}$ are the vectors for vertical and lateral vibration displacement and the torsion vibration angle of lumped-mass of the deck respectively.

$\{s\}$ is the vector for vertical and horizontal vibration displacement of lumped-mass of the cables.

$\{L_h\}=-\dfrac{1}{2}\rho V^2 2B[\Delta L]\left[\dfrac{KH_1^*(K)}{V}\cdot\{\dot{h}\}+\dfrac{KH_2^*(K)B}{V}\{\dot{\alpha}\}+K^2H_3^*(K)\{\alpha\}\right]$ is the vector

for aerodynamic force of vertical bend vibration of the deck.

$\{M_\alpha\}=-\dfrac{1}{2}\rho V^2(2B^2)[\Delta L]\left[\dfrac{KA_1^*(K)}{V}\{h\}+\dfrac{KA_2^*(K)B}{V}\{\dot{\alpha}\}+K^2A_3^*(K)\{\alpha\}\right]$ is the vector

for aerodynamic force of torsion vibration of the deck.

$\{L_p\}=-\dfrac{1}{2}\rho V^2 2B[\Delta L]\left[\dfrac{KP_1^*(K)}{V}\{\dot{p}\}+\dfrac{KP_2^*(K)B}{V}\{\dot{\alpha}\}+K^2P_3^*(K)\{\alpha\}\right]$ is the vector for

aerodynamic force of lateral bend vibration of the deck.

$\{F_h\},\{T\},\{F_p\}$ are the vectors for lift foree, trosion moment and drag force induced by fluctuation wind acting on lumped-mass of the deck respectively.

$\{F_s\}$ is the vector for drag force induced by fluctuation wind acting on lumped-mass of the cables.

As the aerodynamic forces are there, the three equations of the equation group (1) are coupling. And the equation (1) and (2) are coupling too, since the vibration of the cables and the deck is coupling.

Let $\{Z\}^T=[\{h\}^T|\{p\}^T|\{\alpha\}^T|\{s\}^T]$, the equation (1) with (2) can be combined as:

$$[M]\{\ddot{Z}\}+[C]\{\dot{Z}\}+[K]\{Z\}+\{L\}=\{F\} \tag{3}$$

where:

$$[M]=\begin{bmatrix}[M_h] & & & \\ & [M_p] & & 0 \\ & & [I_\alpha] & \\ 0 & & & [M_s]\end{bmatrix}$$

$$\{L\}=\begin{Bmatrix}\{L_h\}\\\{L_p\}\\\{M_\alpha\}\\\{0\}\end{Bmatrix}; \qquad \{F\}=\begin{Bmatrix}\{F_h\}\\\{F_p\}\\\{T\}\\\{F_s\}\end{Bmatrix}$$

Applying mode superposition method, $\{Z\}$ may be written as:

$$\{Z\} = \sum_{j=1}^{N} \{\Phi\}_j a_j(t) \tag{4}$$

where:

$\{\Phi\}_j^T = [\{\Phi_h\}_j^T | \{\Phi_p\}_j^T | \{\Phi_a\}_j^T | \{\Phi_s\}_j^T]$ is j th mode vector of vibration of the bridge.

$a_j(t)$ is the generalized coordinate of j th mode of vibration of the bridge.

$N = 3(n_d + n_s)$ is number of discretization freedom degree, in which n_d is number of lumped-mass of the deck and n_s is number of lumped-mass of the cables.

Substituting Eq. (4) into Eq. (3), the following equations can be obtained by transformation:

$$\ddot{a}_i(t) + 2\xi_i\omega_i\dot{a}_i(t) + \omega_i^2 a_i(t) + \sum_{j=1}^{N} g_{ij} a_j(t) + \sum_{j=1}^{N} e_{ij}\dot{a}_j(t) = F_i^*(t) \tag{5}$$
$$(i = 1, \cdots, N)$$

where:

$F_i^*(t) = \{\Phi\}_i^T \{F\}/m_i^*$ is the generalized load.

$e_{ij} = b_{2i}\{\Phi_h\}_i^T[\Delta L]\{\Phi_a\}_j + C_{2i}\{\Phi_p\}_i^T[\Delta L]\{\Phi_a\}_j + d_{2i}\{\Phi_a\}_i^T[\Delta L]\{\Phi_a\}_j$.

$g_{ij} = (b_{1i}\{\Phi_h\}_i^T[\Delta L]\{\Phi_h\}_j + b_{3i}\{\Phi_h\}_i^T[\Delta L]\{\Phi_a\}_j) + (c_{1i}\{\Phi_p\}_i^T[\Delta L]\{\Phi_p\}_j + c_{3i}\{\Phi_p\}_i^T[\Delta L]\{\Phi_a\}_j) + (d_{1i}\{\Phi_a\}_i^T[\Delta L]\{\Phi_h\}_j + d_{3i}\{\Phi_a\}_i^T[\Delta L]\{\Phi_a\}_j)$.

$a_{ki}, b_{ki}, c_{ki}, d_{ki}$ are the aerodynumic coefficients.

Obviously, if only the term of i=j for e_{ij} and g_{ij} is there, the equation group (5) expresses the buffeting responses of the bridge without aerodynamic coupling between modes. Let $\{A\}^T = [a_1(t), \cdots, a_r(t)]$, the equation group (5) may be written as matrix form:

$$\{\ddot{A}\} + [B]\{\dot{A}\} + [D]\{A\} = \{F^*(t)\} \tag{6}$$

Where [B] and [D] are the coupling coefficient matrix with aerodynamic coupling between modes. Since the equations in matrix equation (6) are coupling each other, by the common mode superposition method it can not be solved. According to definition of the transfer function in frequency domain of random vibration theory, the frequency response function matrix of Eq. (6) can be derived as:

$$[H(\omega)] = (-\omega^2[I] + i\omega[B] + [D])^{-1} \tag{7}$$

From this, the covariances of generalized coordinate responses of structural mode are:

$$\left. \begin{array}{l} \sigma_{A_j}^2 = \sum_{k=1}^{r} \int_0^\infty |H_{jk}(\omega)|^2 S_{Fk}^*(\omega) d\omega \\[3mm] \sigma_{\dot{A}_j}^2 = \sum_{k=1}^{r} \int_0^\infty \omega^4 |H_{jk}(\omega)|^2 S_{Fk}^*(\omega) d\omega \end{array} \right\} \tag{8}$$

where:

$H_{jk}(\omega)$ is the element on jth row and kth column of $[H(\omega)]$;

$S_{Fk}^*(\omega)$ is the power spectrum density function of kth generalized load.

183

And the covariances of buffeting responses for lumped-mass of the deck and the cables are:

$$
\left.
\begin{aligned}
\sigma_{Z_i}^2 &= \sum_{j=1}^{r} \Phi_{ij}^2 \sigma_{A_j}^2 \\
\sigma_{Z_i}^2 &= \sum_{j=1}^{r} \Phi_{ij}^2 \sigma_{A_j}^2
\end{aligned}
\right\}
$$

$$(i=1,\cdots,N)$$

(9)

3. Spectrum Characteristices of $3-D$ Buffeting Forces of Flexible Bridge

According to previous research, the buffeting forces acting on lumped-mass of the deck may be expressed as

$$
\left.
\begin{aligned}
F_{h_i}(t) &= -\frac{1}{2}\rho v^2 B \Delta L_i \{2C_L \frac{u(x_i,t)}{v} + [C'_L + \frac{A}{B}C_D]\frac{w(x_i,t)}{V}\} \\
F_{p_i}(t) &= -\frac{1}{2}\rho v^2 B \Delta L_i \{C_D \cdot \frac{2u(x_i,t)}{v}\} \\
T_i(t) &= \frac{1}{2}\rho v^2 B^2 \cdot \Delta L_i \{2C_M \frac{u(x_i,t)}{v} + C'_M \frac{w(x_i,t)}{V}\}
\end{aligned}
\right\}
$$

(10)

and the buffeting forces acting on lumped-mass of the cables may be expressed as

$$
F_{s_j}(t) = -\frac{1}{2}\rho v^2 \cdot \Delta S_j \{C_D \cdot \frac{2u(x_j,y_j,t)}{v}\}
$$

(11)

where:

$u(x_i,t)$ and $w(x_i,t)$ are the horizontal and vertical fluctuation wind velocity acting on ith lumped-mass of the deck respectively.

$u(x_j,y_j,t)$ is the horizontal fluctuation wind velocity acting on jth lumped-mass of the cables.

Assuming that the horizontal and vertical fluctuation wind velocity is independent each other, and neglecting the correlativity of horizontal fluctuation wind velocity between lumped-mass of the deck and of the cables, the power spectrum dencity function matrix of 3-D buffeting forces of the bridge can be derived as

$$
[S_F(\omega)] =
\begin{bmatrix}
[S_h(\omega)] & [S_{hp}(\omega)] & [S_{hT}(\omega)] & [o] \\
[S_{ph}(\omega)] & [S_p(\omega)] & [S_{pT}(\omega)] & [o] \\
[S_{Th}(\omega)] & [S_{Tp}(\omega)] & [S_T(\omega)] & [o] \\
[o] & [o] & [o] & [S_s(\omega)]
\end{bmatrix}
$$

(12)

where:

$$
\begin{aligned}
[S_h(\omega)] &= [S]S_{Fh}(\omega); \\
[S_p(\omega)] &= [S]S_{Fp}(\omega); \\
[S_T(\omega)] &= [S]S_T(\omega); \\
[S_{hp}(\omega)] &= [S]S_{Fhp}(\omega);
\end{aligned}
$$

184

$[S_{hT}(\omega)] = [S]S_{FhT}(\omega);$

$[S_{pT}(\omega)] = [S]S_{FpT}(\omega);$

$[S]$ is the cross-correlation coefficient matrix between lumped-mass of the deck.

$S_{Fh}(\omega), S_{Fp}(\omega), S_T(\omega), S_{Fhp}(\omega), S_{FhT}(\omega), S_{FpT}(\omega)$ can be derived from Eq. (10) by the definition of cross-correlation function and cross-spectrum density function.

4. Analysis for Buffeting Responses of Nanjin Suspended Bridge of Gas Piping

Applying the method presented by the paper, an analysis of the 3-dimension buffeting responses of Nanjin suspended bridge of gas piping is completed. Since it is a cable-suspended bridge of steel structure and the span of the bridge is 1066m, it is a very flexible and light suspended bridge. the result of dynamic analysis indicate that the contribution of high mode shape for buffeting responses of the bridge can not be neglected.

From this, the buffeting responses of the deck with (and without) aerodynamic coupling between modes are calculated under v = 48. 21m/s design wind velocity. The result is expressed in Tab. 1. It shows: the practical buffeting responses of the deck with aerodynamic coupling between modes are smaller than the buffeting responses without that by 11%. Therefore, for the calculation of buffeting responses of flexible bridge whose high mode shape influence can not be neglected, to consider aerodynamic coupling between modes is very necessary.

aerodynamic coupling	h_{max} (m)	p_{max} (m)	α_{max} (red)
do not consider	0. 8130	2. 7321	0. 0416
consider	0. 7220	2. 5133	0. 0388

Table 1. Result of calculation

References:

1.   E. Simiu and R. H. Scanlan, Wind Effects on structures, A wiley-Interscience publication, (1977).

2.   R. H. Scanlan, Wind—Induced Dynamic of Bridge, Proceedings of 2nd APSWE, Beijing, (1989)

Comparative Study in Coupled Flutter Analysis methods
of A Long Span Suspension Bridge

Hitoshi Yamada and Toshio Miyata

Department of Civil Engineering
Yokohama National University, Japan

ABSTRACT: The super long span bridges come to be very vulnerable against wind dynamic actions, such as not only ordinal vortex-induced oscillation, torsional instability, but also coupled classical flutter. To analyze the coupled flutter behavior in detail and at good accuracy, there will be two kinds of problems which must be clear. First reliability of the flutter analysis methods must be investigated. Secondly flexible and accurate measurement method of the coupled unsteady aerodynamic coefficients have to be conducted In this paper these two problems are discussed. In the flutter analysis it was concluded that the direct frame analysis and the multiple mode analysis(multimode analysis) can achieve the identical result only when selection of the mode shape combination of the multimode flutter analysis is carefully mode. In the unsteady aerodynamic force measurement newly introduced method is discussed

1. Introduction

The wind resistant design of long span bridges has been based on the sectional model wind tunnel testings against wind actions, not only usual wind resistant design target, such as torsional instability and gust response, but also unusual coupled classical flutter. In these testings two fundamental vibration mode, such as first symmetric bending mode and first symmetric torsional mode, have been picked up as their target. This assumption has been believed to work for the verification of all aerodynamic vibrations including the coupled flutter, because coupled/uncoupled flutter occurrence has been clearly explained in the selection of the natural modes. However according to the recent full bridge wind tunnel test of the Akashi Kaikyo bridge, it was observed that characteristics of its aerodynamic vibration changed from SDOF vibrations at low wind speed region to coupled behavior around the design wind speed gradually. Besides deck bending part of its coupled vibrating mode shape is not similar to its torsional vibrating shape. This fact seems not to be funny, but has meaningful disagreement from the assumption of the sectional model wind tunnel testing. Therefore importance of detailed flutter behavior analysis and the full bridge model testing increase to estimate the flutter behavior with improved accuracy. There are two aspects of this problem. First is the flutter analysis method itself Another is to estimate the coupled unsteady aerodynamic force with reliable accuracy.

In this paper it will be discussed that the numerical flutter analysis methods of three dimensionally framed suspension bridge will be comparatively investigated Secondly a system identification technique will be introduced to estimate the coupled unsteady flutter coefficients.

2. Summary of the flutter analysis

The ordinal coupled flutter analysis of suspension bridge, introduced by Bleich is based on

Theodorsen's flat plate wing unsteady aerodynamic force His research work was one of the starting point of the present two dimensional wind tunnel testing method and also one of flutter analysis methods in which the flutter mode is described by combination of finite number of natural mode shapes(as multimode flutter analysis method [1]) Authors have introduced another flutter analysis without any approximation in description of the flutter mode shape, in which flutter problem is solved directly as complex eigenvalue problem of framed suspension bridge model with unsteady aerodynamic flutter force (as direct flutter analysis method [2]) The former has advantage in the size of numerical analysis depending on number of terms of developing modes, while accuracy of the modal expansion must be verified by the different method The ordinal flutter governing equation of bending-torsion 2DOF system is as follows,

$$
\begin{bmatrix} m & 0 \\ 0 & I \end{bmatrix} \begin{Bmatrix} \ddot{z}/B \\ \ddot{\theta} \end{Bmatrix} + \begin{bmatrix} K_z & 0 \\ 0 & K_\theta \end{bmatrix} \begin{Bmatrix} z/B \\ \theta \end{Bmatrix} = \begin{Bmatrix} \pi\rho B^2\omega^2 & 0 \\ 0 & \pi\rho B^4\omega^2 \end{Bmatrix} \left\{ \begin{bmatrix} L_{zR} & L_{\theta R} \\ M_{zR} & M_{\theta R} \end{bmatrix} \begin{Bmatrix} z/B \\ \theta \end{Bmatrix} + \begin{bmatrix} L_{zI} & L_{\theta I} \\ M_{zI} & M_{\theta I} \end{bmatrix} \begin{Bmatrix} \dot{z}/\omega B \\ \dot{\theta}/\omega \end{Bmatrix} \right\} \tag{1}
$$

,where L and M are unsteady aerodynamic coefficients In this equation, unsteady aerodynamic coefficients of the right hand side depend on only reduced frequency However because of the first matrix one natural frequency must be assumed to describe the unsteady aerodynamic force Only dominant components of the response at one wind speed can be looked at and expressed by equation 1 To solve this problem the aerodynamic force should be rewritten as follows;

$$
\begin{bmatrix} m & 0 \\ 0 & I \end{bmatrix} \begin{Bmatrix} \ddot{z}/B \\ \ddot{\theta} \end{Bmatrix} + \begin{bmatrix} K_z & 0 \\ 0 & K_\theta \end{bmatrix} \begin{Bmatrix} z/B \\ \theta \end{Bmatrix} = -\begin{Bmatrix} \pi\rho B^2 & 0 \\ 0 & \pi\rho B^4 \end{Bmatrix} \begin{bmatrix} L_{zR}+iL_{zI} & L_{\theta R}+iL_{\theta I} \\ M_{zR}+iM_{zI} & M_{\theta R}+iM_{\theta I} \end{bmatrix} \begin{Bmatrix} \ddot{z}/B \\ \ddot{\theta} \end{Bmatrix} \tag{2}
$$

In equation 2 the aerodynamic force depends on only reduced wind speed and this is the basic equation for the flutter analysis In the 3 dimensional flutter analysis unsteady aerodynamic force of the right hand side of equation 2 is applied locally to every bridge deck nodes of the frame bridge model Extending equation 2 the flutter equation can be also obtained as equation 3.

$$
\{[M]-[F]\}\ddot{u}+[K]u=0, \tag{3}
$$

where u, M, F and K are displacement of the whole structure, mass, aerodynamic force and stiffness matrixes respectively In the direct flutter analysis method, equation 3 is solved by complex eigenvalue analysis method, while **u** is expressed by combination of natural mode shapes in the multi-mode flutter analysis as $\mathbf{u} = \left(\sum_j a_j \varphi_j \right) \exp(\omega t).$ \hfill (4)

Outputs of these methods are complex flutter natural modes φ and complex natural frequencies ω, which indicate the flutter frequency as well as the flutter damping of the response
    There is no difference in these methods to solve the flutter equation assuming coupled unsteady aerodynamic force Therefore the point of discussion in the flutter analysis method is whether the assumed flutter mode description is accurate enough to estimate the fluter behavior of the bridge under any situations

3. Unsteady aerodynamic coefficient measurement

There are several methods to measure coupled flutter unsteady aerodynamic coefficients, such as by the forced vibration method, the combination method of the free vibration and recently developed applications of the system identification [3,4,5] However by the ordinal methods it is not easy to expand the measurement from of bending-torsion 2 DOF unsteady aerodynamic force to of bending-torsion-lateral bending 3 DOF flutter derivatives to describe the swing motion of the bridge deck Authors have introduced a force measurement method by a system identification, which is applied to the developing coupled flutter response based on equation 1 as the state equation(Direct method of measurement of the aerodynamic force coefficients[5]) When reverse analysis of the flutter equation(equation 4) is considered, it can be realized that it can be extended to the unsteady aerodynamic force measurement, because enough information of identifying the unsteady aerodynamic force coefficients can be obtained from the set of the natural frequencies and flutter natural modes have as follows

$$[[F]]=[[M]]-[[K]][[\varphi]]\begin{bmatrix} \bullet & 0 & 0 \\ 0 & \omega_j^2 & 0 \\ 0 & 0 & \bullet \end{bmatrix}^{-1}[[\varphi]]^{-1} \tag{5}$$

where $[[\varphi]]$ is array of the measured and required mode shapes as $[[\varphi]]=[\bullet \ \varphi_j \ \bullet]$ Assuming a nDOF system with unsteady aerodynamic force, a set of n natural modes and natural frequencies(in another words, flutter modes and flutter frequencies) at one reduced wind speed must be picked up first, after observed vibrations as wind speed are rearranged as mode shapes, modal dampings and modal frequencies of various reduced wind speeds These information of bending dominant vibration, torsion dominant vibration and so on can be converted to the coupled aerodynamic force coefficients through equation 5(Modal method of measurement of the unsteady aerodynamic force coefficients)

4. Examples of the analysis
1) The flutter analysis

Figure 1 illustrate results of the numerical flutter analysis of a 2000m class suspension bridge, in which the flat plate unsteady aerodynamic force is applied and the static displacement due to the wind load was ignored. Natural modes of this bridge are summarized in Table 1 In ordinal flutter analysis combination of fundamental bending and torsional modes(B1 & TT1 in Table 1) are used as description of the flutter behavior This assumption seems to be effective to estimate the critical wind speed only, while there may be disagreement in estimation of change of its behavior as wind speed. Once 10th mode(TT1) is included in mode combination of the flutter mode description, the estimated critical wind speed seems to become close each other(in Figure 1(a)) Therefore as far as this bridge concern, combination of the fundamental bending mode and torsional mode can describe the flutter mode shape roughly, although actual flutter mode shape is complex[6] When number of natural modes increase or combination of the natural mode shapes are carefully selected, the direct analysis and the multimode analysis results similar estimation

2) The unsteady aerodynamic force measurement

Figure 2 is measured coupled unsteady aerodynamic force coefficient diagrams of a flat plate wing model by the ordinal free vibration method, the direct method and the modal method In these analysis adopted system identification technique of the direct method is the Extended Kalman Filter
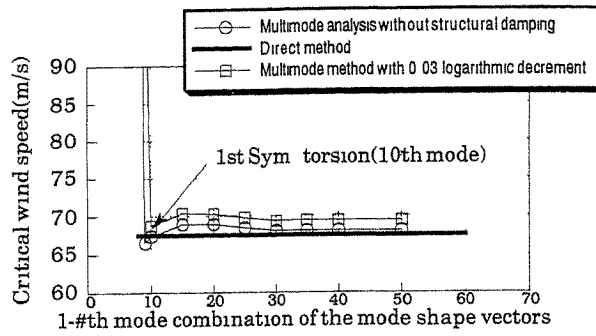
(a)
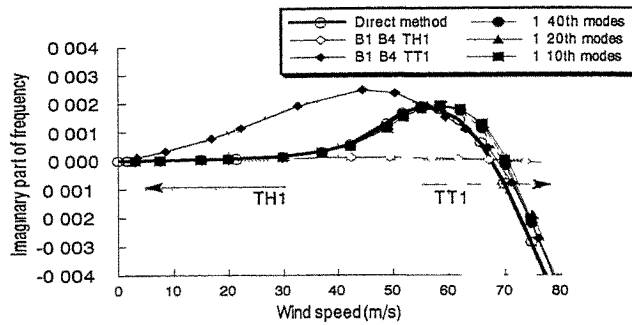
(b)
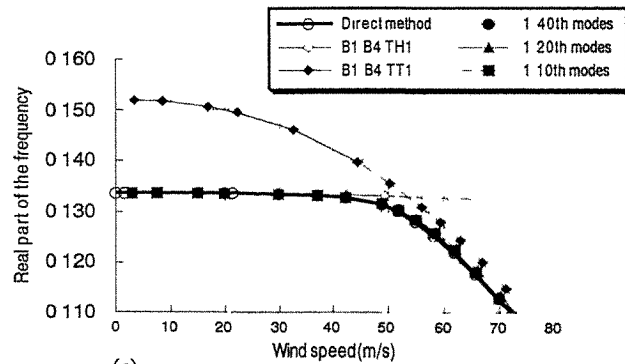
(c)

Figure 1 Coupled Flutter Behavior of a 2000m class Suspension Bridge

190
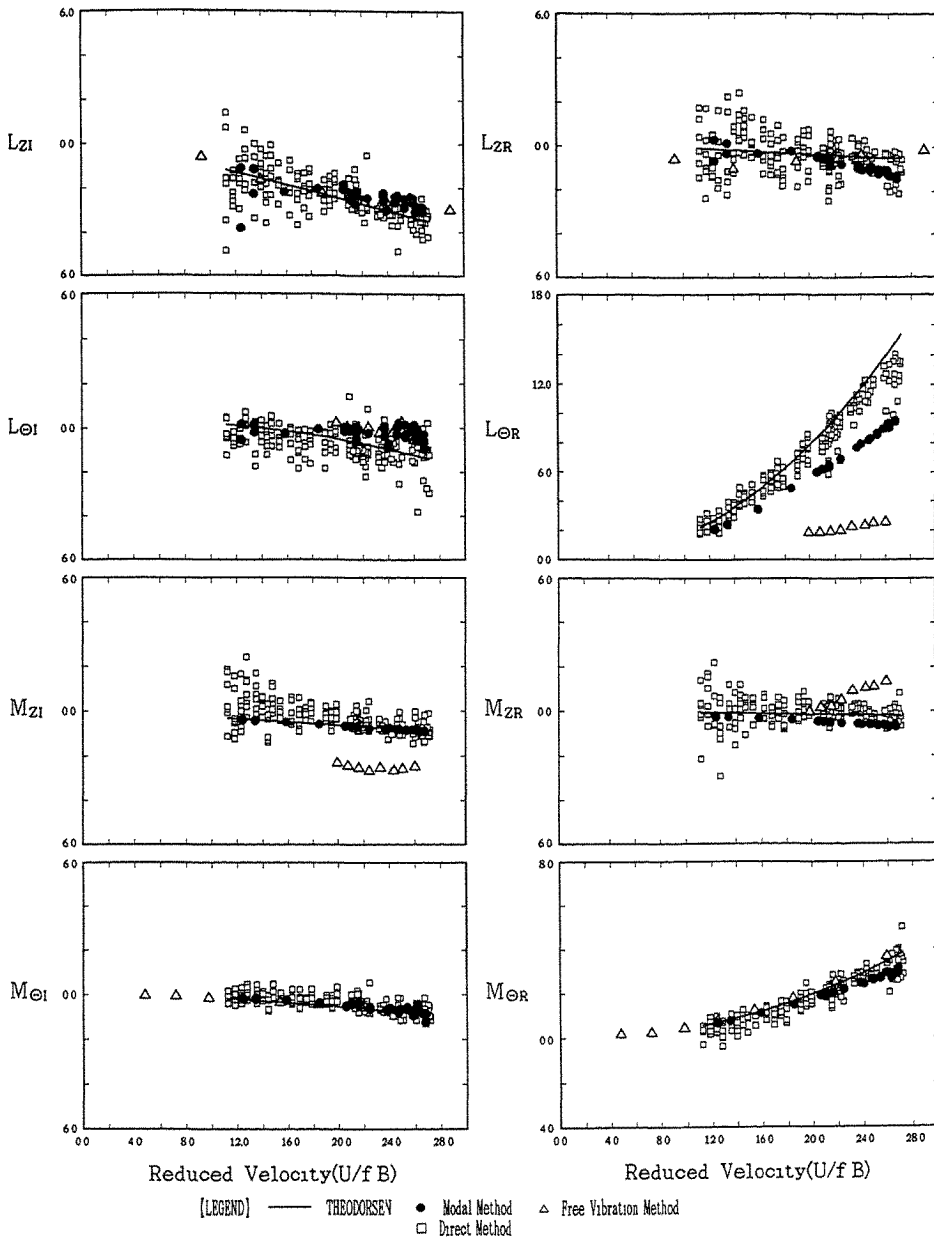
Figure 2 Estimated coupled unsteady aerodynamic force coefficients

191

with global iteration[7]. Although stability of the estimation of the coupled coefficients at high wind speed area by the direct method is apt to be very sensitive to quality of the source signal[5], it can be improved under carefully selected conditions of the identification and noiseproof response measurement. The modal method seems to give more stable and better estimate than the direct method, while identification of the modal vectors and the natural frequencies at same reduced wind speed must be required(equation 5).

Lateral Bending		Torsion	
Symmetrical 1st mode H1	0.041Hz (1st)	Symmetrical 1st mode TH1	0.134Hz(9th)
Asymmetrical 1st mode H2	0.081Hz(3rd)	(Coupled with lateral bending deck motion)	
		Symmetrical 1st mode TT1	0.152Hz(10th)
Vertical Bending		(So called Torsion)	
Symmetrical 1st mode B1	0.065Hz(2nd)	Symmetrical 1st mode TC1	0.174Hz(16th)
Asymmetrical 1st mode B2	0.085Hz(4th)	(Coupled with cable motion)	
Asymmetrical 2nd mode B3	0.094Hz(7th)	Asymmetrical 1st mode TC2	0.177Hz(19th)
Symmetrical 3rd mode B4	0.122Hz(8th)	Symmetrical 2nd mode TC3	0.188Hz(22th)
		Asymmetrical 1st mode TT2	0.191Hz(23th)

Table 1 Natural modes of a 2000m class suspension bridge   ( ) is total order of the natural modes.

5. Concluding remarks

Since the wind resistant design of recent super long span bridges increases its importance, accurate information of their coupled unsteady aerodynamic force and efficient analysis of the flutter response become to have great significance. In this paper methodological discussion in measurement of the unsteady coupled aerodynamic force and in the numerical flutter analysis were made. Conclusions are as follows;

1) In th flutter analysis, the multimode analysis and the direct flutter analysis indicate very close flutter behavior, when the combination of natural mode shapes describe the flutter mode in good accuracy.

2) Under careful tuning, accuracy of the direct estimation of the unsteady aerodynamic force coefficients by EKWGI can be improved.

3) Newly introduced modal flutter coefficient measurement method, which can be extended to MDOF measurements without any large difficulty, seems to output reliable results.

Acknowledgement

References:
1. H.Tanaka et al., J. of Structural Engineering, No.35A(Mar.1989) 827.(in Japanese)
2. T.Miyata et al., J. of Wind Engineering, No.37(Oct. 1988) 485.
3. J.Xie, ADVANCES IN WIND ENGINEERING Part2, Elsevier(1988) 389.
4. P.P.Sarkar et al., PROGRESS IN WIND ENGINEERING Part2, Elsevier(1992) 1243.
5. H.Yamada, PROGRESS IN WIND ENGINEERING part2, Elsevier(1992) 1255.
6. T.Miyata et al., Structural Engineering in Natural Hazards Mitigation vol.1, ASCE(Apr. 1993) 490.
7. M.Hoshiya et a., EM, vol110 no.12, ASCE (Dec.1984) 1757.

PREDICTING AERODYNAMIC RESPONSE OF RETROFITTED DEER ISLE BRIDGE TO TURBULENT WIND

Chun-Sheng Cai*, Pedro Albrecht* and Harold R. Bosch**

*Department of Civil Engineering, University of Maryland
College Park, Maryland 20742, U.S.A.
**Highway Research Center, Federal Highway Administration
6300 Georgetown Pike, Virginia 22101, U.S.A.

Abstract: Previous studies [1,2] investigated flutter behavior of the existing Deer Isle bridge only in the first torsional mode. In the present study both the existing bridge and the bridge as retrofitted with fairings are analyzed, including both torsional and vertical modes, and with both deterministic and indeterministic methods. The critical flutter velocity of the existing bridge predicted in the present study agrees better with field observations than those predicted in previous studies.

1. INTRODUCTION

Wind loading is an important factor that must be considered in designing long-span bridges. Turbulent wind can result in either aerodynamic instability, such as flutter, or aerodynamic random response such as buffeting. The former occurs under self-excited forces that may cause the bridge to collapse. The latter occurs under the combined effects of self-excited and buffeting forces that may lead to fatigue and other damage to structural elements.

The Deer Isle suspension bridge in the state of Maine has a 329 m center span and two 147 m side spans. Like the ill-fated Tacoma Narrows bridge that failed in 1940 under wind-induced flutter, the Deer Isle bridge has a bluff cross section prone to flutter. This bridge was stiffened in the 1940's which makes the existing bridge much more complicated than the original bridges as shown in Fig. 1. Excessive wind-induced vibrations buckled one girder and damaged girder bearings at cable bents even after the bridge was stiffened. The damage has been repaired. As part of an ongoing effort to improve its aerodynamic behavior, the Deer Isle bridge was instrumented, the effect of adding fairings was evaluated experimentally with wind tunnel tests of section models, and fairings will be added along the full length of the bridge.

Previous studies [1,2] investigated flutter behavior of the existing bridge only in the first torsional mode. In the present study both the existing bridge and the bridge as retrofitted with fairings are analyzed, including both torsional and vertical modes, with both deterministic and indeterministic methods.

2. SOLUTION OF AERODYNAMIC MOTION EQUATION

The aerodynamic equation of motion of bridges in turbulent wind was obtained in [3] in terms of the natural mode shapes:

$$[M^*]\{\ddot{\xi}\} + [D^*]\{\dot{\xi}\} + [K^*]\{\xi\} = U^2 \left([AS^*]\{\xi\} + [AD^*]\{\dot{\xi}\}\right) + \bar{U}^2 [f_b^*]\{\eta\} \qquad (1)$$

where $[M^*]$, $[D^*]$, $[K^*]$, $[AS^*]$, $[AD^*]$ and $[f_b^*]$ are the generalized mass, damping, stiffness, aerodynamic stiffness, aerodynamic damping, and buffeting force matrices respectively; $\{\xi\}$ and $\{\eta\}$ are the vectors of generalized coordinates and non-dimensional turbulent wind components respectively. U is the mean wind velocity. U is treated in different ways as in [4, 5, 6] and will be discussed below. The first term on the right-hand side of Eq. 1 is called the self-excited force; the second term is called the buffeting force.

In [4, 5], the wind velocity U is assumed to be the mean (constant) value, and the flutter derivatives needed in [AS*] and [AD*] are those measured in turbulent flow. Physically, the influence of turbulence on the self-excited force (the terms with U in Eq. 1) is included in the flutter derivatives. This makes the self-excited force deterministic and, therefore, Eq.1 is solved by Fourier transformation

$$(-\omega^2[M^*] + [K^*] - \bar{U}^2[AS^*] + \omega([D^*] - \bar{U}^2[AD^*])i)\mathscr{F}(\{\xi\}) = \bar{U}^2\{f^*\}_b\mathscr{F}(\{\eta\}) \qquad (2)$$

The flutter analysis becomes a deterministic instability problem. To obtain a nontrivial solution of Eq. 2, the following condition must be satisfied:

$$|(-\omega^2[M^*] + [K^*] - \bar{U}^2[AS^*] + \omega([D^*] - \bar{U}^2[AD^*])i)| = 0 \qquad (3)$$

from which the flutter velocity $\bar{U}_{cr}$—a wind velocity that makes the bridge unstable--is determined.
The buffeting response in terms of the root-mean-square displacement is obtained with spectral analysis.

In [6], the wind velocity U is decomposed into a mean value $\bar{U}$ plus a turbulent (random) component u(t), and the flutter derivatives are those measured in laminar flow. Physically, the influence of turbulence on the self-excited force is reflected by the turbulent wind component u(t). This makes both the self-excited and buffeting forces time-dependent random (indeterministic) forces. In this case random parametric excitation analysis must be used in both flutter and buffeting analyses. Through a lengthy stochastic operation, the statistical moments are derived and the flutter instability is interpreted as the instability of statistical moments.

Scanlan's method [4, 5] is mathematically much simpler than Lin's method [6] which requires complicated stochastic operations. However, equipment limitations make it difficult to create large turbulence in the wind tunnel. Therefore, the true effect of turbulence on the prototype bridge may not be reflected in the flutter derivatives measured through section model tests. As for Lin's method, different turbulences can be numerically generated by changing the wind component u(t). This is an appealing feature since the influence of different turbulences on the aerodynamic behavior can be investigated numerically. This is an easy task by means of readily available powerful desk-top computers. Meanwhile, in Lin's random parametric excitation analysis, a Markov process and white noise input are assumed.

The Scanlan and Lin methods, each with advantages and disadvantages, provide complementary results. In the present study, Scanlan's method is used because of its simplicity, and Lin's method is used as specified. Both approaches are formulated with finite elements and the numerical effort of Lin's method is reduced significantly. This makes it convenient to conduct flutter and buffeting analyses in terms of many modes. Readers are referred to [3] for more details about these two solutions.

3. FLUTTER ANALYSIS

The design wind velocity for the Deer Isle bridge is 175 km/hr as determined from [7] for the applicable bridge height, importance of structure, and bridge location. The flutter derivatives for the non-streamlined (without fairings) and streamlined (with fairings) sections were taken from [8] and [9] respectively, and the aerodynamic force coefficients from [10].

Existing Bridge: Fig. 2 shows the calculated natural frequencies, mode shapes and corresponding flutter velocities for three different damping ratios. The 20 lowest natural modes were extracted and only those important for flutter analysis were retained. For example, the sway modes and longitudinal modes were discarded. Critical flutter occurs in the first vertical mode at wind velocities of 53, 82 and 120 km/hr for damping ratios of 1, 2 and 3.2% respectively. A value of 1% damping ratio is believed to be reasonable for most long-span bridges. [11] reported a damping ratio of 3.2% in the first vertical mode based on his analysis of the field data from the existing Deer Isle bridge, a value much higher than would normally be expected. In the authors' opinion, the damping ratio is more likely to be about 2%, a value higher than the commonly assumed 1% because the complex stiffening system tends to increase the damping ratio, but not as high as

3.2%. Therefore, the authors believe that the existing bridge has conservatively a critical flutter velocity of 82 km/hr, which is lower than the design wind velocity of 175 km/hr.

In comparison, at a 1% damping ratio, [1] predicted a critical flutter velocity of 470 km/hr and [2] predicted at least 280 km/hr. Continually observed poor aerodynamic performance suggests that these values are much too high. The main reason why previous researchers predicted such high flutter velocities is that they investigated flutter behavior only in the first torsional mode. Actually, the first vertical mode, not the first torsional mode, is critical.

Future Bridge: Because of the observed poor aerodynamic behavior of the existing Deer Isle bridge, the FHWA conducted measurements at the bridge site and tested small scale (1:25) section models with different fairing shapes in the Aerodynamics Laboratory of the Turner-Fairbank Highway Research Center. The "best" fairing shape, shown in Fig. 3, will be added along the full length of the bridge to streamline the cross section and increase the critical flutter velocity.

Since the flutter derivatives of the streamlined section are negative, or have a very small positive value over the full range of reduced velocities, the authors have found that the critical flutter velocity for the future bridge is higher than 400 km/hr when fairings are installed over the full length of the bridge (Fig. 4). This value is much higher than the design wind velocity of 175 km/hr, meaning that the fairing system is very efficient and that full-length fairing may not be needed for structural reasons, although it may be aesthetically more pleasing.

Alternative Fairing Placements: Assuming conservatively a 1% damping ratio, the authors have examined various fairing placements to determine which one is the most economical while still keeping the critical flutter velocity higher than the design wind velocity. The bridge has a total of 72 panels, that is, 17 in each side span and 38 in the center span. The critical flutter velocities were calculated for eight alternative fairing placements.

As Fig. 4 shows, the existing bridge (without fairings) has a critical flutter velocity of 53 km/hr at a 1% damping ratio, while the future bridge (with fairings in all 72 panels) has a critical flutter velocity higher than 400 km/hr.

The eight alternative fairing placements analyzed by the authors are listed in descending order of critical flutter velocity. The findings are as follows:

o   The critical flutter velocity generally increases with the number of streamlined panels.

o   Streamlining the center span is much more effective than streamlining the side spans (alternative 2 versus alternative 8, both with about equal numbers of streamlined panels).

o   Streamlining every other panel is not an effective solution (alternative 6 versus alternatives 1 and 2, all with about equal numbers of streamlined panels).

o   As few as 32 panels (alternative 3) could be streamlined while still keeping the critical flutter velocity of 218 km/hr well above the design wind velocity of 175 km/hr. This is less than one-half of the 72 panels that the Maine Department of Transportation will streamline.

Lin's parametric excitation analysis was also used to check the flutter instability of the bridge under excitation by different turbulences. The flutter is interpreted as the instability of statistic moments. The future bridge with planned full-length fairings and fairing placement 1 was investigated. Fig. 5 shows the relationship between the critical flutter velocity and the spectral density of non-dimensional white noise. The non-dimensional white noise is the white noise turbulence divided by the mean wind velocity. It can be seen that the flutter velocity decreases as the spectral density increases. For Simiu's wind spectrum with a realistic turbulence intensity of 0.15, the equivalent white noise spectral density is less than 0.2 [3]. For this spectral density, the flutter velocity is larger than design wind velocity 175 km/hr.

195

4. CONCLUSION

The analysis was performed in two stages. First, using Scanlan's method, it was found that, at a 1% damping, the critical flutter velocity is 53 km/hr in the first vertical mode for the existing bridge without fairings, 218 km/hr in the vertical mode when fairings are added to 32 of 72 panels, and more than 400 km/hr when fairings are added along the full length of the bridge.

Second, using Lin's method, it was found that the flutter velocity decreases as the spectral density increases. For a realistic turbulence intensity of 0.15, the flutter velocity of the Deer Isle bridge with either full length or partial fairings (alternative 1, 2 and 3) is greater than the design wind velocity of 175 km/hr.

REFERENCES

1. Kumarasena, T., Scanlan, R. H., and Morris, G. R. (1989), J. of Stru. Engrg., ASCE, 115(9), 2297-2312.
2. Ehsan, F., Jones, N. J., and Scanlan, R. H. (1993), J. of Stru. Engrg., ASCE, 119(2), 484-504.
3. Cai, C. S. (1993), Ph.D. Dissertation, Dept. of Civil Engrg., Univ. of Maryland.
4. Scanlan, R. H. (1978), J. of Sound and Vibration, 60(2), 187-199.
5. Scanlan, R. H. (1978), J. of Sound and Vibration, 60(2), 202-211.
6. Lin, Y. K. (979), J. of Engrg. Mechanics Div., ASCE, 105(6), 921-932.
7. American National Standards Institute (1982), ANSI, A58.1-1982.
8. Kumarasena, T. (1989), Ph.D. Dissertation, Dept. of Civil Engrg., Johns Hopkins University.
9. Huston, D. R. (1986), Ph.D. Dissertation, Dept. of Civil Engrg., Princeton University.
10. Bosch, H. R. (1987), Report No. FHWA-RD-87-027, Federal Highway Administration, McLean, Virginia.
11. Spartz, C.A., (1989), Master Essay, Dept. of Civil Engrg, Johns Hopkins University.
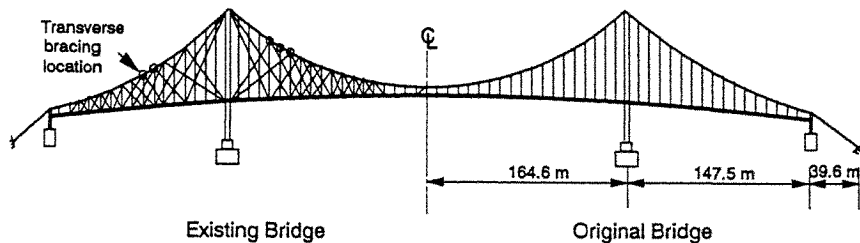
Figure 1 Deer Isle Bridge, Existing and Original
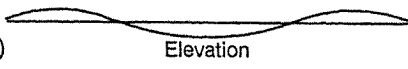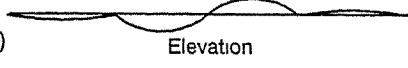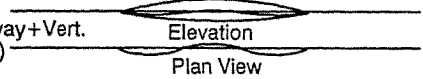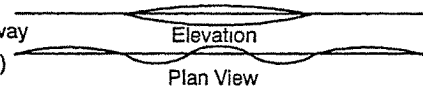
Mode No.	Type				1%	Damping Ratio 2%	3.2%
						Flutter Velocity (km/hr)	
2	Vertical (0.30 Hz)	Elevation			53	82	120
3	Vertical (0.40 Hz)	Elevation			88	154	222
5	Vertical (0.55 Hz)	Elevation			109	196	>225
8	Tors.+Sway+Vert. (1.04 Hz)	Elevation Plan View			125	>225	>225
13	Tors.+Sway (1.43 Hz)	Elevation Plan View			133	156	177

Figure 2 Flutter Velocity of Existing Bridge
(Stiffening System, Towers and Cables not Shown)

Fairing

18.5°

3 m   3 m

115 mm Concrete Slab

W24

45°

2 m

7.2 m
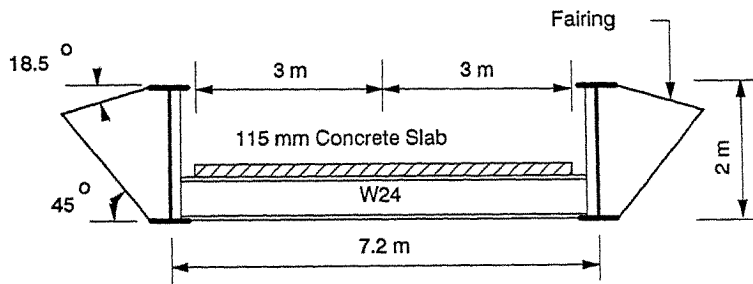
Figure 3 Deck Section and Fairing
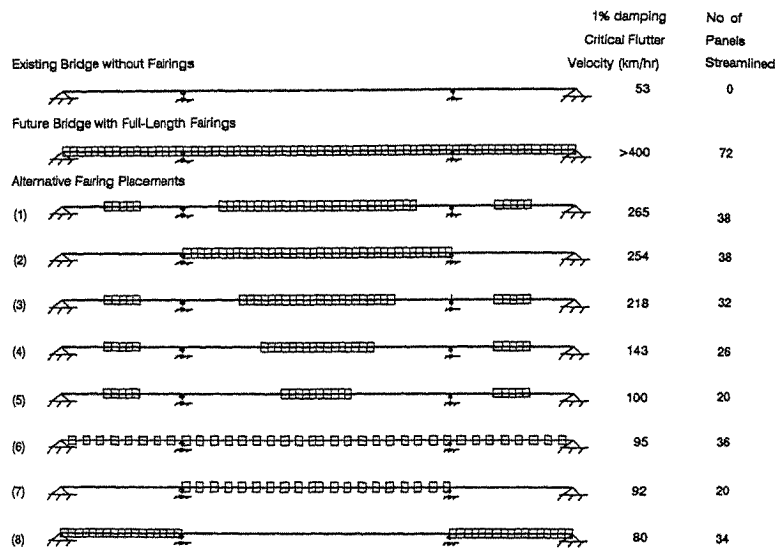
Figure 4 Flutter Velocities for Different Fairing Placements
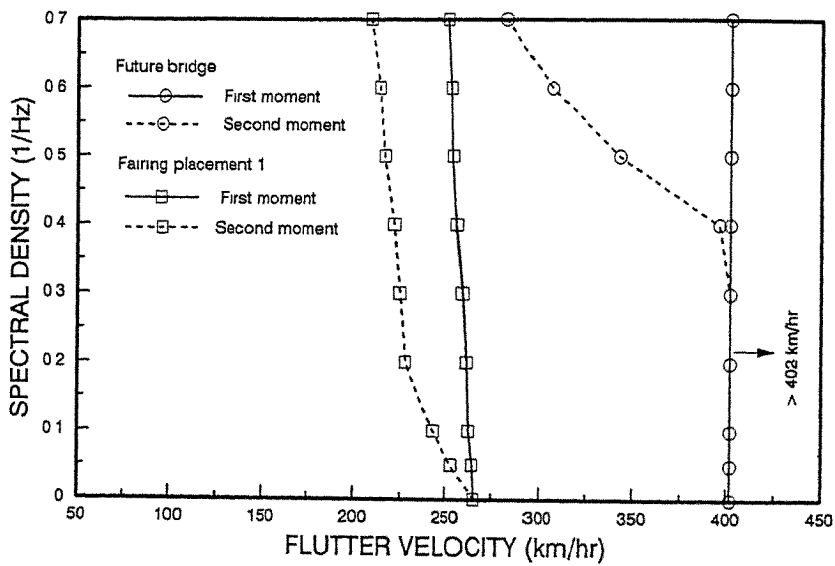
Figure 5 Flutter Velocity vs Spectral Density

Wind-Induced Lateral-Torsional Instability
of Cable-Stayed Bridges during Erection

Virote Boonyapinyo, Toshio Miyata and Hitoshi Yamada

Department of Civil Engineering
Yokohama National University, Japan

Abstract: Wind-induced nonlinear lateral-torsional instability analysis of a long-span cable-stayed bridge with a center span length of 1000 m during erection and on completion is presented. A proposed modeling of lateral-torsional buckling includes the three-component displacement-dependent wind loads as well as the geometric nonlinearity. The results show that the incorporation of the displacement-dependent wind loads as well as the geometric nonlinearity in the modeling results in significant reduction in the critical wind velocity, compared with the linearized buckling modeling. The results also indicate that the partly erected bridge is much more susceptible to the nonlinear lateral-torsional buckling than the completed bridge. Parametric study, such as erection method, support condition, angle of wind incidence, and compressive force contribution to lateral-torsional buckling, are also discussed.

1. Introduction

With the increase in span length of modern cable-stayed bridges, wind-induced lateral-torsion buckling of the whole bridge presents increasingly important problems both in design and construction. These problems result from the large wind loads acting on the flexible bridge as well as the high compressive forces in the towers and deck. These problems are of particular importance for long-span cable-stayed bridges using balanced cantilever erection method where the partly erected bridge has much less stiffness than the completed bridge. Under the wind effects, the long-span bridge is subjected to large, displacement-dependent wind loads of three components, i.e., a drag force, a lift force and a pitching moment. These three-component displacement-dependent wind loads become rapidly large as wind velocity and angle of attack increase, and then may cause lateral-torsion buckling or torsional divergence. Previous research on the wind-induced static instability of this type of bridge has generally been based on the linear method and the separation of three-component wind loads, i.e., the linearized lateral-torsional buckling analysis under the effect of initial drag force, and the torsional divergence analysis under the effect of pitching moment [1]. Boonyapinyo [2] has found that for cable-stayed bridges the lateral-torsion buckling is much more likely to occur than the torsional divergence.

The cable-stayed bridge also exhibits geometric nonlinearity due to beam-column effect, nonlinear behavior of cable, and bridge geometry change. The wind-induced nonlinear lateral-torsional buckling analysis based on an incremental-iterative approach can provide insight into the failure mode behavior and the critical wind velocity of this type of bridge.

In this paper, wind-induced nonlinear lateral-torsional buckling analysis of long-span cable-stayed bridges during erection and on the completion is presented by finite element approach. A three-span-continuous cable-stayed bridge with a center span length of 1000 meters and two side spans of 450 meters, which represents the future trend in design and construction, is considered.

2. Bridge Mathematical Modeling and Nonlinear Stiffness Formulation

A cable-stayed bridge is idealized as a three-dimensional frame-truss structure, in which tower and deck elements are idealized as a beam-column element, and cable element is idealized as a truss element. The nonlinear stiffness and various elastic instabilities, such as bending, torsional, and lateral-torsional bucklings are considered in the nonlinear instability analysis through the use of the geometric stiffness matrix of beam-columns augmenting the elastic stiffness matrix of beams. The geometric stiffness which includes the effects of initial axial force as well as bending and torsional moments of three-dimensional beam-columns is given in references 2 through 4.

The nonlinear behavior of cables due to the cable sag is considered through the use of the equivalent modulus of elasticity (or equivalent elastic stiffness) of the cable as an equivalent straight chord element. In addition, the geometric stiffness matrix of three-dimensional truss elements due to the large nodal displacements of the stay cable is combined with the equivalent elastic stiffness matrix of cables.

3. Modeling of Displacement-Dependent Wind Loads

The three-component displacement-dependent wind loads per unit span acting on the deformed deck can be written in the bridge axes as (Fig. 1)

$$F_X(\alpha) = D(\alpha)\cos(\alpha_0) - L(\alpha)\sin(\alpha_0); \quad F_Y(\alpha) = D(\alpha)\sin(\alpha_0) + L(\alpha)\cos(\alpha_0); \quad M_z(\alpha) = M(\alpha) \quad (1\ a\text{-}c)$$

where

$$D(\alpha) = \tfrac{1}{2}\rho V^2 A_n C_D(\alpha); \quad L(\alpha) = \tfrac{1}{2}\rho V^2 B C_L(\alpha), \quad M(\alpha) = \tfrac{1}{2}\rho V^2 B^2 C_M(\alpha) \quad (2\ a\text{-}c)$$

In Eqs. (1) and (2), F_X, F_Y and M_Z are, respectively, the drag force, lift force, and pitching moment in the bridge axes; D, L, and M are, respectively, the drag force, lift force, and pitching moment in the wind axes; C_D, C_L and C_M are the static aerodynamic coefficients in the wind axes (Fig. 2); V is the mean wind velocity; ρ is the air density; B is the deck width; A_n is the vertical projected area of deck; α is the effective wind angles of attack consisting of the torsional displacement of deck θ and the wind angle of incidence α_0.
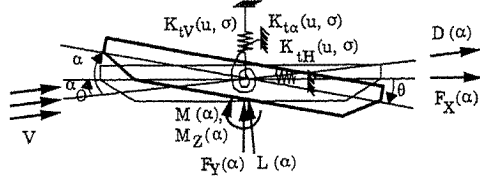
Fig. 1 Motion of a bridge deck and displacement dependent wind loads in wind and bridge axes
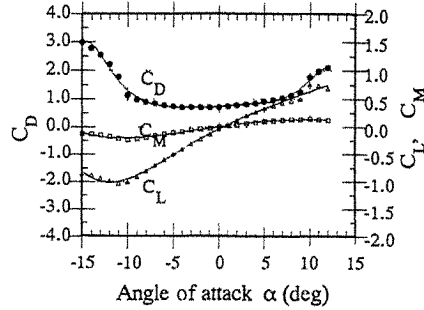
Fig. 2 Static aerodynamic coefficients as a function of angle of attack

The wind forces in Eq. (1) can be written in the alternative forms as

$$F_X(\alpha) = \tfrac{1}{2}\rho V_r^2 A_n C_X(\alpha); \quad F_Y(\alpha) = \tfrac{1}{2}\rho V_r^2 B C_Y(\alpha); \quad M_Z(\alpha) = \tfrac{1}{2}\rho V_r^2 B^2 C_Z(\alpha) \quad (3\ a\text{-}c)$$

where

$$C_X(\alpha) = [C_D(\alpha) - C_L(\alpha)\tan\alpha_0]\sec\alpha_0; \quad C_Y(\alpha) = [C_L(\alpha) + C_D(\alpha)\tan\alpha_0]\sec\alpha_0;$$
$$C_Z(\alpha) = [C_M(\alpha)]\sec^2\alpha_0; \quad V_r = V\cos\alpha_0 \quad (4\ a\text{-}d)$$

It should be noted that if the α_0 is zero, the F_X, F_Y and M_Z are, respectively, equal to D, L and M. Moreover, if the effects of drag and lift forces are neglected in wind load modeling, one obtains the conventional modeling of pitching moment for torsional divergence analysis.

200

4. Modeling of Nonlinear Lateral-Torsional Instability

The modeling of nonlinear buckling under the displacement-dependent wind loads is composed of a two-step process. In the first step process, nonlinear analysis under the initial wind forces of given wind velocity V is performed in one step, utilizing the tangent stiffness of the deformed bridge under dead-load state. In the second step process, nonlinear analysis under the additional wind forces induced by increasing angle of wind attack due to the torsional deformation of the deck is performed. The linearized incremental equilibrium equation of the whole bridge subjected to the additional wind forces for j^{th} iteration is written as

$$\left[\mathbf{K}_e\left(u_{j-1}, \sigma_{j-1}\right) + \mathbf{K}_g^{G+W}\left(u_{j-1}, \sigma_{j-1}\right)\right] \Delta\mathbf{U}_j$$
$$= \mathbf{F}_j\left(F_X(\alpha_j), F_Y(\alpha_j), M_Z(\alpha_j)\right) - \mathbf{F}_{j-1}\left(F_X(\alpha_{j-1}), F_Y(\alpha_{j-1}), M_Z(\alpha_{j-1})\right) \tag{5}$$

where $\mathbf{K}_e$ and $\mathbf{K}_g$ are, respectively, the structural elastic and geometric stiffness matrices based on the displacements u and stresses σ from the preceding iterations; superscripts G and W mean gravity and wind loads, respectively; $\Delta\mathbf{U}_j$ is the incremental displacement vector; $\mathbf{F}_j$ and $\mathbf{F}_{j-1}$ are the displacement-dependent wind load vectors based on the current and preceding wind angles of attack, respectively.

The above process will converge for any given wind velocity less than the critical wind velocity. The convergence criteria for the given wind velocity reaches when the Euclidean norm of static aerodynamic coefficients is less than the prescribed tolerance, i.e.,

$$\left[\sum_{}^{N_a}\left\{C_k(\alpha_j) - C_k(\alpha_{j-1})\right\}^2 / \sum_{}^{N_a}\left\{C_k(\alpha_{j-1})\right\}^2\right]^{1/2} \leq \varepsilon_k, \quad k = X, Y, Z \tag{6}$$

where ε_k represents the prescribed tolerance, N_a = a number of nodes subjected to the displacement-dependent wind loads.

Because the three components of wind loads are a nonlinear function of the angle of wind attack, the procedure for calculation of the critical wind velocity involves the outermost cycle of iteration, in addition to inner cycle of iteration for convergence of each given wind velocity described above. A combination of the eigenvalue analysis with respect to wind forces, i.e., $\left|\left(\mathbf{K}_e + \mathbf{K}_g^G\right) + \lambda\mathbf{K}_g^W\right| = 0$, and the updated wind-velocity bound algorithm is applied to choose the next given wind velocity. This procedure is given in references 2 and 3. The final critical wind velocity reaches when the stable and unstable wind velocities approach to each other.
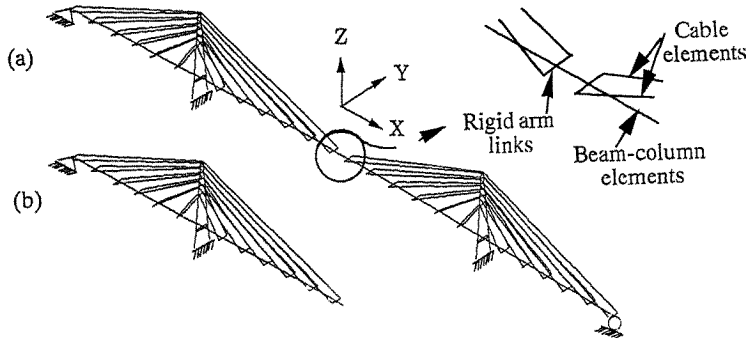
Fig. 3 Three-dimensional finite-element modeling of studied bridges: (a) the completed bridge, (b) the half-span bridge during erection

201

5. Lateral-Torsional Buckling Characteristics

The present method of wind-induced nonlinear lateral-torsional buckling analysis was applied to a three-span-continuous steel cable-stayed bridge with a 1000 m center span and two 450 m side spans. The completed bridge and the half-span bridge just before closer shown in Figs. 3a and 3b were investigated. The bridge consists of A-shape towers with 250 m height, an aerodynamic-shape closed-boxed deck with 3 m depth and 39.8 m width including fairing, and double-plane cables. The static aerodynamic coefficients of the deck are shown in Fig. 2. The fluctuation of wind speed on time and space as well as the dynamic amplification was included in the analysis in an approximate manner through the use of gust response factor given by the Honshu-Shikoku Code [5].

5.1 Displacement-dependent wind loads and geometric nonlinearity:
The effects of the three-component displacement-dependent wind loads as well as the geometric nonlinearity on the lateral-torsional buckling and the critical wind velocity for the half-span bridge is shown in Fig. 4. These effects result in significant reduction in the critical wind velocity as well as change in the buckling mode, compared with the linearized buckling modeling. Such reduction in the critical wind velocity is attributed to: (a) the increase of the three-component displacement-dependent wind loads due to the torsional displacements of the deck (Figs. 5a and 5b), and (b) the geometric nonlinearity effects.

5.2 Instability comparisons between partly erected and completed bridges:
The mid-span torsional and vertical displacement behavior for the completed bridge and the half-span bridge is shown in Figs. 6a and 6b. As expected, the half-span bridge is much more susceptible to the nonlinear lateral-torsional buckling than the completed bridge. The critical wind velocities for the lateral-torsional buckling of both bridges are mainly controlled by the large torsional displacements of the deck (Fig. 6a), which in turn increase the three-component displacement-dependent wind loads (Figs. 5a and 5b). To reduce the three-component displacement-dependent wind loads, the active aerodynamic control means such as active control surfaces with wings or leading edges may be necessary if the cable-stayed and suspension bridges have much longer span in the future.

5.3 Erection method:
The erection method significantly affects the critical wind velocity. In double-side free cantilevering from the tower without temporary supports of bridge deck and tower top, the safety factor against buckling under its own bridge dead load is about to be exhausted. These buckling modes are characterized by one of the following modes: (a) the buckling of the tower having no longitudinal restraint of tower top, and (b) the horizontal buckling of the deck due to the torsional buckling of vertical tower-deck supports. As a result, the critical wind velocity for the lateral-torsional buckling in this erection method is relatively low. However, if the two temporary supports of bridge deck at side span as well as one longitudinal support of the bridge deck are provided in double-side free cantilevering method, the critical wind velocities in all processes of erection are much higher that the design one. Alternatively, in one-sided free cantilevering of center span with one longitudinal support of the bridge deck, the critical wind velocities for lateral-torsiona instability in all processes of erection are much higher that the design one. For the long-span cable-stayed bridge, the intermediate supports at side spans are necessary to increase the stability during erection and on the completion.

5.4 Support condition:
The longitudinal supports of the deck significantly affect the critical wind velocity. The bridges without longitudinal supports of the deck cause significant reduction in the critical wind velocity form 118 m/s to 54 m/s for the half-span bridge and from 135 m/s to 67 m/s for the completed bridge. This reduction results from the buckling of the towers having no longitudinal restraint of tower top. With regards to the elastic stability as well as the earthquake and thermal forces, the longitudinal supports through one hinge support at deck end or through elastic supports at both towers may be appropriate for design of long-span cable-stayed bridges.

5.5 Angle of wind incidence:
The angle of wind incidence considerably affects the critical wind velocities for both the half-span and completed bridges (Fig. 7). The angle of incidence of + 5
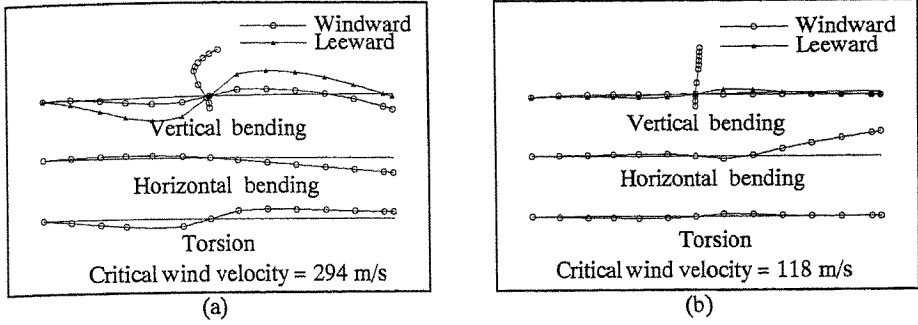
Fig. 4 Effects of displacement-dependent wind loads and geometric nonlinearity on a buckling mode and a critical wind velocity of the half-span bridge: (a) linear, and (b) nonlinear buckling modes
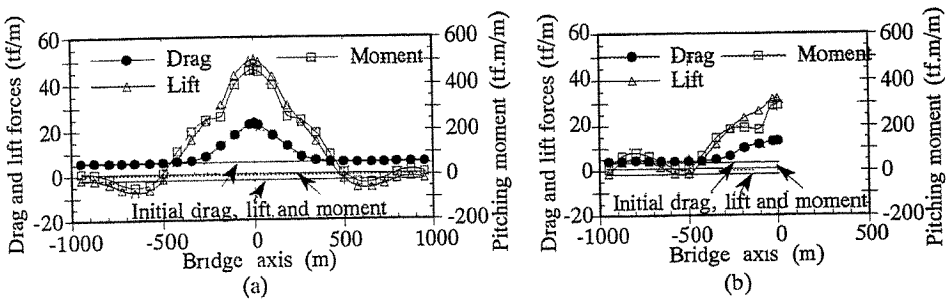
Fig. 5 Three components of displacement-dependent wind loads acting on the deck just before bridge instability: (a) the completed bridge, (b) the half-span bridge
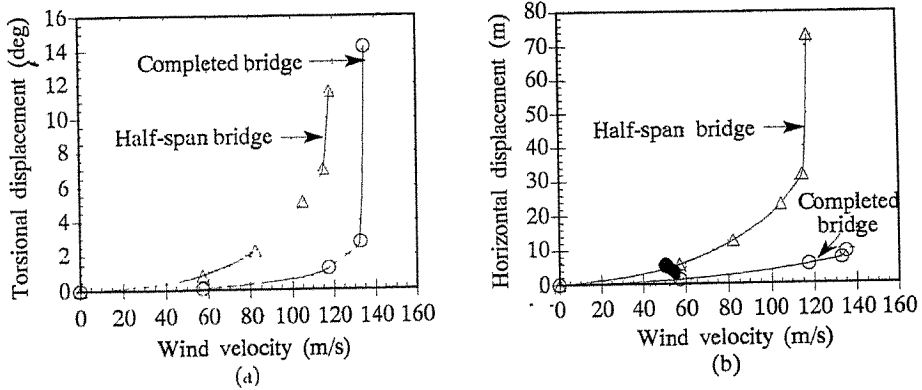
Fig. 6 Comparison of mid-span displacement behavior between the completed and half-span bridges: (a) torsional, (b) horizontal displacements

degree (head up) significantly reduces the critical wind velocity from 118 m/s to 90 m/s for the half-span bridge and from 135 m/s to 113 m/s for the completed bridge.

5.6 Compressive force contribution to lateral-torsional buckling: The contribution of compressive forces in the deck and towers to the lateral-torsional buckling is largely dependent on the bending bucking load factor under its own dead loads [2]. If this buckling load factor is relatively high (e.g., greater than four), this compressive force contribution is not significant. This contribution can be simply demonstrated by using the closed form formula of linear and elastic lateral-torsional buckling for a doubly symmetric beam-column under uniform end moment M and axial force P:

$M_{cr} = M_{cro} \sqrt{(1-1/\lambda_b)(1-1/\lambda_t)}$ where M_{cr} and M_{cro} are the elastic critical moments in the present and absence of initial axial force, respectively; λ_b is the bending buckling load factor for the axis normal to the axis of bending; λ_t is the torsional buckling load factor. For the practical cable-stayed bridges, λ_t is very high compared with λ_b.

Fig. 7 Critical wind velocity of the completed and half-span bridges for various angles of incidence

6. Conclusions

Wind-induced nonlinear lateral-torsional instability analysis of the long-span cable-stayed bridge with the center span length of 1000 m during erection and on the completion is presented. The incorporation of the three-component displacement-dependent wind loads as well as the geometric nonlinearity in the modeling results in significant reduction in the critical wind velocity, compared with the linearized buckling modeling. The partly erected bridge is much more susceptible to the nonlinear lateral-torsional buckling than the completed bridge. The erection method, the longitudinal support of the deck as well as the angle of wind incidence significantly affect the critical wind velocity. The contribution of compressive forces in the deck and towers to the lateral-torsional buckling is largely dependent on the bending bucking load factor under its own dead loads.

With regard to the wind-induced lateral-torsional instability, the long-span cable-stayed bridge with the center span length of 1000 m presents no serious problem both during erection and on the completion, provided that the appropriate erection method is applied. However, it is expected that the wind-induced nonlinear lateral-torsional instability will present a more crucial mode of failure if a cable-stayed bridge has much longer span in the future.

References:
1 Simiu, E., and Scanlan, R.H., *Wind Effects on Structures*, 2nd., John Wiley and Sons, New York, 1986.
2 Boonyapinyo, V., Nonlinear Static Instability Analysis of Long-Span Cable-Stayed Bridges under Gravity and Wind Loads, Doctoral Thesis, Yokohama National University, March, 1993.
3 Boonyapinyo, V., Yamada, H. and Miyata, T., "Nonlinear Buckling Instability Analysis of Long-Span Cable-Stayed Bridges under Displacement-Dependent Wind Load," *J. of Structural Engineering*, JSCE, Vol. 39A, pp. 923-936, March, 1993.
4 Yang, Y. B., and McGuire, W., "Stiffness Matrix for Geometric Nonlinear Analysis, and Joint Rotation and Geometric Nonlinear Analysis," *J. of Structural Engineering*, ASCE, Vol. 112(4), pp. 853-905, 1986.
5 Honshu-Shikoku Bridge Authority, *Wind Resistant Design Code for Honshu-Shikoku Bridge*, Japan, 1976.
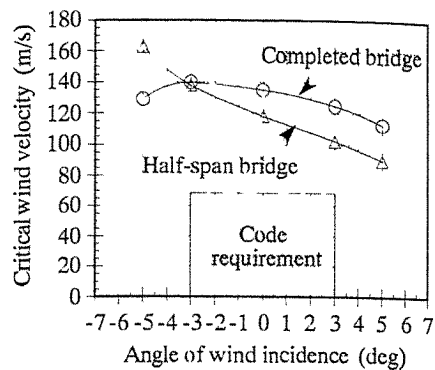
Study on buffeting response spectrum method
for long span bridges

W. Chen, M. Gu and H.F. Xiang

Department of Bridge Engineering
Tongji University, Shanghai, China

Abstract: The measurement technique for swaying aerodynamic derivatives is developed. For buffeting analysis, both the accurate and practical methods for buffeting response spectrum are proposed and comparison between these two methods is carried out through numerical examples of two bridges. It is shown that the practical method is accurate enough for engineering applications.

1. Introduction

Nowadays as the bridge span becomes longer and longer, the buffeting response of swaying motion may be significant. The measurement method for the swaying aerodynamic derivatives using section model test in wind tunnel is established and the experimental result of Yangpu Bridge is given as an example. From engineering requirement, the buffeting response spectrum method, which is rather accurate, is put forward according to R.H. Scanlan's buffeting theory with the consideration of aerodynamic admittance function. More simplified practical method of buffeting response spectrum is also proposed based on the accurate method through detailed parametric analysis. Numerical results of Yangpu Bridge and Shantou Bay Bridge are given as examples. By comparing the practical method with the accurate method, the results of the practical method are accurate enough for engineering applications.

2. Measurement of Swaying Aerodynamic Derivatives

If the section model can only sway horizontally and other motions are restricted, the equation of the section model motion can be expressed as follows

$$\ddot{p} + 2\zeta_p \omega_p \dot{p} + \omega_p^2 p = \frac{\rho \omega B^2}{m} P_1^* \dot{p} \tag{1}$$

In which p is the swaying displacement; ζ_p is the structural damping ratio; B is bridge width; ω_p is the natural circular frequency; m is the mass; ρ is air density; P_1^* is swaying aerodynamic derivative.

Suppose the section model moves sinusoidally with the envelope of exponential decrement

$$p = p_0 e^{-\lambda t} sin\ \omega t \tag{2}$$

We can find $\lambda = \zeta \omega_p$, so that P_1^* is given as below

$$P_1^* = -\frac{2m(\zeta - \zeta_p)}{\rho B^2} \tag{3}$$

where ζ is the total damping ratio including the aerodynamic damping.

Usually, there are two ways of finding damping ratio from testing data, i.e., calculating the logarithmic decrement from time signal curve or finding

damping ratio at the half-power point from frequency signal curve. But these two methods require that the raw testing data must be smooth and undisturbed in time domain or must have highly enough resolution in frequency domain. In order to avoid the shortcomings, we develop another method. By finding the envelope curve from time signal and natural frequency from frequency signal, the ζ value can be calculated with the least square exponential curve fitting technique.

There may be interference on raw data from various noises. By using the least square method the raw data can be preprocessed to remove tendency terms and some noises can be filtered. The data preprocessing and curve fitting are programmed with C computer language. Finally, the section model of Yangpu Bridge is taken as an example to show the measurement method of swaying aerodynamic derivatives mentioned above. The results are given in Fig. 1 in which the solid curve indicates the completed stage of bridge and the dash curve indicates the constructing stage of bridge. The testing results will be used in section 4 for calculation of swaying buffeting response.

3. Accurate Response Spectrum Method

The response spectrum method is widely used in earthquake analysis. Among the buffeting responses of long span bridges, the first mode may be significant and the other higher modes are relatively small. In this case, we take the buffeting theory developed by Scanlan [1] as the main frame and introduce the aerodynamic admittance function for modification to establish the buffeting response spectrum method. In the buffeting response spectrum analysis, several special considerations should be included:

• The wind loading is random in space and time, so that the buffeting response spectrum can only be expressed as a root mean square (RMS) response spectrum or a peak response spectrum by using the random vibration analysis.

• In buffeting analysis, the quasi-steady buffeting forces are used, which is equivalent to suppose that the correlation factor of wind spectrum equals one. This is not suitable for the non-steady turbulent wind. Therefore, the aerodynamic admittance function should be included.

• The self-excited aerodynamic forces is also nonnegligible in buffeting analysis. The Scanlan's formulae in which the self-excited force is expressed with aerodynamic derivatives are used here.

• Both horizontal and vertical wind spectra should be considered. The horizontal and vertical wind spectra are taken from references [2] and [3] respectively.

By ignoring the coupling between different motions and higher modes, the equations of motions in vertical, rotational, and swaying for bridge deck's are

$$\ddot{h}(t) + 2\zeta_h \omega_h \dot{h}(t) + \omega_h^2 \, h(t) = \frac{1}{m_h} L(x,t) \tag{4}$$

$$\ddot{\alpha}(t) + 2\zeta_\alpha \omega_\alpha \dot{\alpha}(t) + \omega_\alpha^2 \, \alpha(t) = \frac{1}{m_\alpha} M(x,t) \tag{5}$$

$$\ddot{p}(t) + 2\zeta_p \omega_p \dot{p}(t) + \omega_p^2 \, p(t) = \frac{1}{m_p} D(x,t) \tag{6}$$

where x is the coordinate along the span; m_h, m_α, m_p are generalized mass; $L(x,t)$, $M(x,t)$, $D(x,t)$ are generalized forces which consist of self-excited aerodynamic forces and buffeting forces; ζ_h, ζ_α, ζ_p are structural damping ratios; ω_h, ω_α, ω_p are natural circular frequencies.

The self-excited forces can be moved from the right side of the equations to the left side and combined with analogous terms. The buffeting forces depend

on turbulent wind speeds of both horizontal and vertical components. Based on random vibration theory, by ignoring the background response part which is very small compared with the resonant response part, the RMS response spectrum of all the three motions can be derived as follows

$$R_h(\omega_h, \zeta_h) = \frac{\rho UB|q(x)|_{max}}{\tilde{\omega}_h^2} \sqrt{\frac{\pi\tilde{\omega}_h}{4\tilde{\zeta}_h} |J_h(\tilde{\omega}_h)|^2 S_L(\tilde{\omega}_h)} \qquad (7)$$

$$R_\alpha(\omega_\alpha, \zeta_\alpha) = \frac{\rho UB^3|r(x)|_{max}}{2\tilde{\omega}_\alpha^2} \sqrt{\frac{\pi\tilde{\omega}_\alpha}{4\tilde{\zeta}_\alpha} |J_\alpha(\tilde{\omega}_\alpha)|^2 S_M(\tilde{\omega}_\alpha)} \qquad (8)$$

$$R_p(\omega_p, \zeta_p) = \frac{\rho UB|s(x)|_{max}}{\tilde{\omega}_p^2} \sqrt{\frac{\pi\tilde{\omega}_p}{4\tilde{\zeta}_p} |J_p(\tilde{\omega}_p)|^2 S_D(\tilde{\omega}_p)} \qquad (9)$$

where

$$|J_n(\omega_n)|^2 = \int_0^L \int_0^L y(x_1)y(x_2) e^{-\frac{\lambda\omega_n}{2\pi U}|x_1 - x_2|} dx_1 dx_2 \qquad (10)$$

$$S_L(\omega) = C_L^2 S_{uu}(\omega) |\gamma_2(\omega)|^2 + \frac{1}{4}(C_L' + \frac{A}{B}C_D)^2 S_{ww}(\omega) |\gamma_3(\omega)|^2 \qquad (11)$$

$$S_M(\omega) = C_M^2 S_{uu}(\omega) |\gamma_4(\omega)|^2 + \frac{1}{4}C_M'^2 S_{ww}(\omega) |\gamma_5(\omega)|^2 \qquad (12)$$

$$S_D(\omega) = (\frac{A}{B}C_D)^2 S_{uu}(\omega) |\gamma_1(\omega)|^2 \qquad (13)$$

$\tilde{\omega}_h$, $\tilde{\omega}_\alpha$, $\tilde{\omega}_p$ and $\tilde{\zeta}_h$, $\tilde{\zeta}_\alpha$, $\tilde{\zeta}_p$ are frequencies and damping ratios concerned with the aerodynamic derivatives; ρ is air density; B is bridge width; U is horizontal mean wind speed; $y(x)$ ($y = q$, r, s) are mode shapes corresponding to each motion; J_n ($n = h$, α, p) are joint acceptance functions defined by Davenport which represent correlations in space; $\lambda = 7$ to 21, small λ value is conservative; C_L, C_M, C_D are static lift, moment, drag coefficients and C_L', C_M' are the slopes of C_L, C_M at the attack angle of α_0 ; L is the span length; A is the projected area per unit span normal to wind speed U; S_L, S_M, S_D are spectra of buffeting forces including the aerodynamic admittance functions; S_{uu} and S_{ww} are horizontal and vertical wind spectra; γ_1 through γ_5 are aerodynamic admittance functions. In this analysis all the admittance functions are simply expressed as Liepmann's formula [4]:

$$|\gamma(\omega)|^2 = \frac{1}{\left(1 + \frac{\pi\omega B}{U}\right)} \qquad (14)$$

According to the above formulae an analytical program has been developed by using the C language for calculating the buffeting response spectra in vertical, rotational, and swaying motions.

4. Practical Buffeting Response Spectrum Method

For practical application, the method mentioned in section 3 is rather complicated, so the method is simplified through detailed parametric analysis which is summarized below:

• Use the reduced frequency $K = \omega B/U$ as the argument so that the wind speed and frequency are combined with one parameter.

• By observing the ratio of horizontal wind spectrum over vertical wind spectrum, we find that the maximum ratio will not exceed 7.5 if $z/(Un)$ ranges from 0.04 to 2.0 (z is bridge height above sea level, n is frequency in Hz), which is suitable for most long span bridges. Hence, the input energy from horizontal wind spectrum is in the same order as that of vertical wind spectrum.

• The coefficients of static wind forces have strong effects on the buffeting responses of vertical and rotational motions. According to the testing data, usually, $C_L' / C_L > 10$, $C_M' / C_M > 8$, and $C_L' \gg C_D A / B$. This means that C_L' and C_M' are important coefficients. For this reason, the horizontal wind spectrum has less effect on the vertical and rotational motions than the vertical wind spectrum (see equations (11) and (12) in section 3).

• If the sine function is used to replace the mode shape which is more suitable for suspension bridges, the joint acceptance function can be simplified by directly integrating equation (10). For symmetric mode shape the half-period of sine function is used and for asymmetric mode shape the one entire period of sine function is used to replace the original mode shapes. In case of cable-stayed bridges, the mode shape of which is more complicated, the effective length can be used instead of the span length in suspension bridges. The effective length can be taken according to a sine curve area roughly equaling the area of mode shape curve under the main span without large errors.

With the above considerations, the practical buffeting response spectrum method can be established in the following equations

$$R_h (K_h) = C_{Oh} \; C_G \; C_{Bh} \; C_{Ah} \; C_{Zh} \; \psi(\tilde{\beta}_h) \; \mu(\tilde{K}_h) \; \phi_{wh}(\tilde{f}_h) \tag{15}$$

$$R_\alpha (K_\alpha) = C_{O\alpha} \; C_G \; C_{B\alpha} \; C_{A\alpha} \; C_{Z\alpha} \; \psi(\tilde{\beta}_\alpha) \; \mu(\tilde{K}_\alpha) \; \phi_{w\alpha}(\tilde{f}_\alpha) \tag{16}$$

$$R_p (K_p) = C_{Op} \; C_G \; C_{Bp} \; C_{Ap} \; C_{Zp} \; \psi(\tilde{\beta}_p) \; \mu(\tilde{K}_p) \; \phi_w(\tilde{f}_p) \tag{17}$$

where $C_{Oh} = 0.866\rho$, $C_{O\alpha} = 0.433\rho$, $C_{Op} = 10.001\rho$ are constants; $C_G = 0.4/\ln(z/z_0)$ depends on geographical situations and bridge height; $C_{Bh} = C_{Bp} = B^2 \sqrt{zB} / m$, $C_{B\alpha} = B^4 \sqrt{zB} / I$ relate to bridge width and height, mass and moment of inertia per unit length; $C_{Ah} = C_L' + \frac{A}{B} C_D \approx C_L'$, $C_{A\alpha} = C_M'$, $C_{Ap} = \frac{A}{B} C_D$ rely on the static air force coefficients and their slopes; $\tilde{K}_h = K_h$, $\tilde{K}_\alpha = \sqrt{1 - \rho B^4 A_3^* / I}$, $\tilde{K}_p = K_p$ are reduced frequencies in which $\tilde{K}_\alpha$ is relative to aerodynamic derivatives; C_{Zh}, $C_{Z\alpha}$, C_{Zp} are mainly relative to the structural damping and aerodynamic damping, and they have the following forms:

$$C_{Zh} = \frac{1}{\sqrt{\zeta_h - \rho B^2 H_1^* / (2m)}} \; , \; C_{Z\alpha} = \frac{1}{\sqrt{\zeta_\alpha - \rho B^4 A_2^* / (2I)}} \; , \; C_{Zp} = \frac{1}{\sqrt{\zeta_p - \rho B^2 P_1^* / (2m)}} \tag{18}$$

$\psi(\beta)$ reflects the joint acceptance function with the sine function replacing the

208

mode shape and $\beta = \lambda L K/(2\pi B)$. It is written as

$$\psi(\beta) = \frac{1}{p^2 + \beta^2}\left[\beta + \frac{2p^2}{p^2 + \beta^2}\right] \qquad (19)$$

in which $p = \pi$ for symmetric mode shape or $p = 2\pi$ for asymmetric mode shape; $\mu(K) = 1\left/\sqrt{K^3(1 + \pi K)}\right.$ includes the modification of aerodynamic admittance function; $\phi_{wh}(f)$, $\phi_{w\alpha}(f)$, $\phi_u(f)$ indicate the influence of wind spectra and static air force coefficients and $f = zK/(2\pi B)$. They take the following forms:

$$\phi_{wh}(f) = \frac{\delta_h(f)}{1 + 4f}, \qquad \phi_{w\alpha}(f) = \frac{\delta_\alpha(f)}{1 + 4f}, \qquad \phi_u(f) = \frac{1}{(1 + 50f)^{5/6}} \qquad (20)$$

in which δ_h and δ_α are modification factors. If $C_L' \gg C_L$, $C_M' \gg C_M$ and $C_L' \gg \frac{A}{B} C_D$, δ_h and δ_α can be taken as 1; otherwise, the following formulae can be used for modification:

$$\delta_h(f) = \sqrt{1 + \left(\frac{2C_L}{C_L' + \frac{A}{B} C_D}\right)^2 \frac{S_{uu}(f)}{S_{ww}(f)}}, \quad \delta_\alpha(f) = \sqrt{1 + \left(\frac{2C_M}{C_M'}\right)^2 \frac{S_{uu}(f)}{S_{ww}(f)}} \qquad (21)$$

All the functions in the above equations can be expressed in data tables or graphic curves. And the buffeting response can be calculated manually by looking up the related data tables or graphic curves.

5. Numerical Examples

The Shanghai Yangpu Cable-stayed Bridge and Shantou Bay Suspension Bridge are taken as examples to illustrate the buffeting response calculations by the practical buffeting response spectrum method in section 4, and the results are compared with the accurate method in section 3. The input data for both bridges are: $\rho = 1.225$ kg/m^3, roughness length $z_0 = 0.45$ m, $\lambda = 7$, and $\zeta = 0.01$ in each motion. For Yangpu Bridge, $L = 602$ m, $B = 32.5$ m, $z = 60$ m, $A = 3.02$ m/m^2, $m = 4.4 \times 10^4$ kg/m, $I = 4.18 \times 10^6$ kg·m^2/m, $C_L = -0.155$, $C_L' = 4.466$, $C_M = 0.047$, $C_M' = 0.546$, $C_D = 1.229$, $n_h = 0.273$ Hz, $n_\alpha = 0.51$ Hz, $n_p = 0.213$ Hz; for Shantou Bay Bridge, $L = 452$ m, $B = 27.4$ m, $z = 49$ m, $A = 2.2$ m/m^2, $m = 3.38 \times 10^4$ kg/m, $I = 1.86 \times 10^6$ kg·m^2/m, $C_L = 0.128$, $C_L' = 5.471$, $C_M = 0.062$, $C_M' = 1.105$, $C_D = 0.908$, $n_h = 0.184$ Hz, $n_\alpha = 0.593$ Hz. The results of buffeting response RMS values are listed in table 1. For the swaying buffeting response calculation of Yangpu Bridge, the swaying aerodynamic derivative of P_1^* is used here. The effective lengths of vertical, rotational, and swaying motions are taken as 355 m, 213 m, and 537 m respectively. In case of Shantou Bay Bridge, the sine curve fits perfectly to its first bending mode shape and fits well with the first rotational mode shape. From table 1, it is shown that the practical method is accurate enough for engineering application.

209

6. Concluding Remarks

The accurate buffeting response spectrum method is developed according to Scanlan's buffeting theory with the modification of aerodynamic admittance function. In order to calculate swaying buffeting response, the measurement method for the swaying aerodynamic derivatives is established and the testing result of Yangpu Bridge is given as an example. For the purpose of engineering application, the practical buffeting response spectrum method is proposed through some parametric analysis in details. The numerical results of two bridges indicate that the practical method is suitable and convenient for engineering applications.
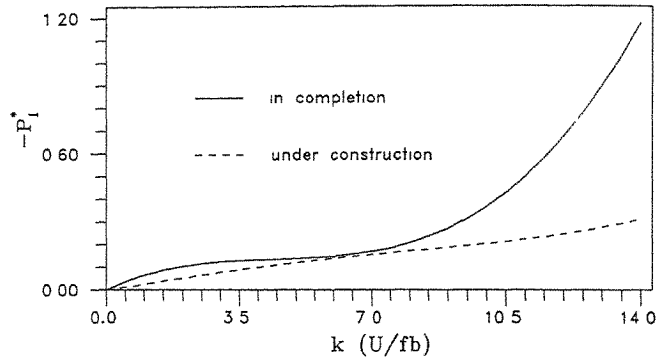
Fig. 1. Swaying Aerodynamic Derivatives of Yangpu Bridge.

U (m/s)	Motion	Yangpu Bridge RMS (m)		Shantou Bay Bridge RMS (m)	
		approx.	accurate	approx.	accurate
20.0	h	0.023	0.0238	0.087	0.0887
	α	0.0025	0.00247	0.0025	0.00253
	p	0.0027	0.00263		
30.0	h	0.070	0.0714	0.250	0.2538
	α	0.0089	0.00896	0.011	0.0105
	p	0.010	0.0096		
40.0	h	0.147	0.1496	0.492	0.4998
	α	0.024	0.0242	0.029	0.0278
	p	0.024	0.0238		

Table 1. The Buffeting Response Results.

References:
1. R.H. Scanlan, J. Sound and Vibration, 60(2) (1978) 719.
2. E. Simiu, ASCE, ST9, 100, Proc. Paper 10851, (1974) 1897.
3. H.A. Panofsky and P.A. McCormick, Coll. of Mineral Industries, Pennsylvania State Univ., (1959).
4. H.W. Liepmann, J. Aeronautical Sciences, 19(12) (1952) 793.

Gust Response of a Long Span Bridge by the Time Domain Approach

Jovito C. Santos, Toshio Miyata and Hitoshi Yamada

Department of Civil Engineering
Yokohama National University, Japan

Abstract : In order to gain insight into the response characteristics of a long span bridge under turbulent wind, the time domain approach was utilized considering the time-space variation of the fluctuating wind velocities. A multidimensional auto regressive-moving average model based on the specified correlation functions was used to generate the fluctuating wind velocities along the bridge axis. Wind forces are modeled using the quasi-steady formulation which considers the instantaneous change in the relative wind velocity and the effective angle of attack. The Akashi Kaikyo Bridge, idealized as a three dimensional frame model, was analyzed in the time domain under turbulent wind. The response of the bridge under gusty wind shows a three-dimensional random oscillation similar to that observed under the full model wind tunnel tests.

1. Introduction

The advancement in construction materials and methods has led to a new breed of tall and long structures never experienced before. These structures exhibit peculiar characteristics like high flexibility, low damping and light in weight, which have made them very susceptible to wind action. The force-response relationship tends to become very complex when the wind-structure interaction is involved. Such complexity is further aggravated if wind turbulence is taken into consideration. In predicting the structural response to wind, it is normal to include (a) the response to mean wind speed and its associated direction, (b) the response to the fluctuating component of the mean wind speed, and (c) the response to the forces generated by the motion of the structure. Since bridge deck section geometry tends to become complicated, wind tunnel tests still play an important role in determining its dynamic characteristics under wind. More so, linearization of the force-response relationship is normally resorted to. For long span cable supported bridges, studies on stability of deck sections have led to expressions for motion-dependent forces in terms of flutter derivatives [1] and indicial aerodynamic functions [2]. Unsteady airfoil forces were also used to determine the flutter characteristics of a very long suspension bridge [3]. Such forces are considered to be functions of the reduced frequency $(B\omega/U)$ and the mean wind speed (U).

Considerations for the fluctuating part of the wind forces due to turbulence are normally done in the frequency domain, making use of an aerodynamic admittance function together with the aerodynamic damping expressions [4,5]. On the other hand, approaches in the time domain made use of the instantaneous relative velocity and the effective angle of attack which combines the wind velocity fluctuations and the structural motion [6,7]. It is the interest of this study to look into the coupled response of a long span suspension bridge under turbulent wind in the time domain.

The Akashi Kaikyo Bridge (Japan) with a main span of 1990 m and two side spans of 960 m is presently under construction. Wind tunnel measurements for the full scale model has been done to verify the stability of this bridge under wind action and results of the tests indicate a three-dimensional random oscillation under turbulent flow [8,9]. In this study, the response of the Akashi Kaikyo Bridge under turbulent wind will be considered in the time domain making use of the instantaneous relative velocity of the oncoming wind.

2. Simulation of fluctuating wind
2.1 ARMA model

In performing the time domain analysis of long span bridge under wind action, the time-space variation of wind velocities along the bridge axis is considered. Simulation of random processes can

be done in several ways but the digital filtering method i.e., the auto regressive-moving average (ARMA) model will be used due to computational efficiency. The multi-dimensional ARMA model is obtained, based on a prescribed correlation function (or the spectral density function), using the two-stage least squares procedure or 2SLS [10] described as follows.

An m - variate ARMA(p,q) process U_r $(r = 1,2, ...)$ of order (p,q) can be expressed in the form

$$\sum_{\iota=0}^{p} A_\iota U_{r-\iota} = \sum_{\iota=0}^{q} B_\iota X_{r-\iota} \qquad (1)$$

where A_i = [m x m] auto regressive (AR) coefficients; B_1 = [m x m] moving-average (MA) coefficients; A_0 = is assumed to be an [m x m] identity matrix, I_m, and X_r = is an m - variate Gaussian white noise series with zero mean. In Equation (1), the multidimensional process U_r can be generated if the A_i and B_i coefficients can be identified accurately. This is done by using an AR model of the form similar to Equation (1) given as

$$\sum_{\iota=0}^{\infty} \overline{A}_\iota U_{r-\iota} = B_0 X_r \qquad (2)$$

Starting with the specified correlation matrix $C_{UU}(k)$ (k = ...,-1,0,1, ...), the AR model is identified and the B_0 matrix and the cross-correlation matrix $C_{UX}(-k)$ (k = 0,1, ...,q) are determined to be used to develop the ARMA model. Equation (1) can be rewritten as

$$U_r = \left[B_1...B_q \ A_1...A_p \right] \left[X_{r-1}...X_{r-q} \ -U_{r-1}...-U_{r-p} \right]^T + B_0 X_r \qquad (3)$$

The above equation is post multiplied by [$X^T_{r-1} ... X^T_{r-q} -U^1_{r-1} ... -U^1_{r-p}$] and the expectations taken to solve the ARMA coefficients A_i and B_i. For a chosen order (p,q), the time histories of wind velocity fluctuations along the bridge can be obtained using Equation (1).

The correlation functions for the ARMA model used to generate the fluctuating velocities are obtained from the given wind spectra and cross-spectra. For the bridge deck, the longitudinal component (u-component) of the velocity fluctuation is based on the Hino spectrum expressed as

$$\frac{nS_u(n)}{\overline{u}^2} = 0.4751 \ \frac{n}{n'} \ \left\{ 1 + \left(\frac{n}{n'} \right)^2 \right\}^{-5/6} \qquad (4)$$

where $n' = 1.718 x 10^{-2} \ \frac{\alpha k_r \overline{U}_{10}}{I_u^3} \ \left(\frac{z}{10} \right)^{(2m-3)\alpha-1}$

k_r = drag coefficient of the ground surface (≈ 0.0025); m = 1; α = 1/8 , power law exponent; $\overline{U}_{10}$ = mean wind speed at 10 m height; I_u = turbulence intensity; n = frequency; and $\overline{u}^2$ = mean square of the fluctuating u-component.

On the other hand, the vertical or w-component of the velocity fluctuation is based on the Bush and Panofsky spectrum expressed as

$$\frac{nS_w(n)}{\overline{w}^2} = \frac{0.632 \ (f / f_{max})}{1 + 1.5(f / f_{max})^{5/3}} \qquad (5)$$

where $f = \dfrac{nz}{U_z}$; reduced frequency

z = height; U_z = mean velocity at height z; $\overline{w}^2$ = mean square of the fluctuating w-component; and f_{max} = spectral peak (≈ 0.3).

The cross-spectra between records at different locations can be expressed by its coherence function. In this study, the coherence function say between points $p_1(x_1, y_1)$ and $p_2(x_2,y_2)$ is assumed to take the form [11]

$$Coh(r,n) = e^{-\hat{f}} \tag{6}$$

where $\hat{f} = \dfrac{n\left[C_x^2(z_1 - z_2)^2 + C_y^2(y_1 - y_2)^2\right]^{1/2}}{\frac{1}{2}\left[\overline{U}_{z_1} + \overline{U}_{z_2}\right]}$

For the present case, the constants C_x and C_y are assumed to take the value 8. Since the height varies along the bridge span, the variation of the mean wind speed with height is assumed to obey the power law.

u-component wind velocities
along the bridge deck axis
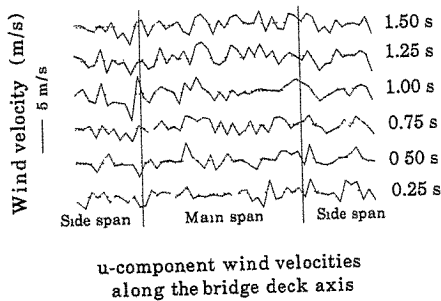
Figure 1 Fluctuating velocities at different
time instants
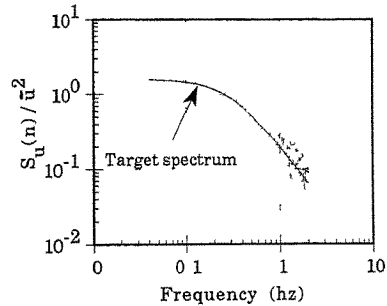
Figure 2 Spectrum of the generated
series

2.2 Wind Simulation

In the analysis, the wind velocity at one point is assumed to compose of a mean part and a fluctuating part for the along wind direction and a fluctuating part for the vertical direction. The fluctuating part, which varies along the span was simulated at different selected nodal points along the bridge axis using an ARMA(6,2) model for the u-component and the w-component of the fluctuating wind velocities. Simulating the correlated wind velocities depend much on the cross-correlation functions at different points. The simple coherence function given by Equation (6) still needs further attention as to the value of the decay coefficient to be used. The variation of mean wind speeds along the bridge is also considered in this study due to the change in elevation at different points in the bridge. Figure 1 shows the fluctuating velocities at each time instant along the bridge axis. Comparison between the target spectra and the spectra obtained from the simulated velocities is shown in Figure 2. It can be seen that velocity fluctuations can be simulated satisfactorily using ARMA models.

3. Wind Forces

The system of external forces consists basically of the wind forces derived from the quasi-steady formulation at an instant of time. At a particular time instant as shown in Figure 3, the wind forces in the global direction is expressed as

213

$$F_z = -D\cos\psi + L\sin\psi$$
$$F_y = D\sin\psi + L\cos\psi \tag{7}$$
$$M_x = -M$$

where

$$D(\alpha_a,t) = \tfrac{1}{2}\,\rho\,V_r^2\,A_n\,C_D(\alpha_a)$$

$$L(\alpha_a,t) = \tfrac{1}{2}\,\rho\,V_r^2\,B\,C_L(\alpha_a) \tag{8}$$

$$M(\alpha_a,t) = \tfrac{1}{2}\,\rho\,V_r^2\,B^2\,C_M(\alpha_a)$$

$$V_r = \sqrt{(U+z)^2 + (w - y + m_l\theta)^2} \tag{9}$$
$$= \text{ relative velocity}$$

Figure 3 Relative velocity and angle of attack

$U = \overline{U} + u(t)$; C_D, C_L, C_M = quasi-static coefficients ; ρ = air density ; B = deck width ; A_n = projected area of the deck ; α_a = effective angle of attack.

This is a simplified quasi-steady model of the forces which directly includes the aerodynamic damping effects of the motion components. Considering rotational motion, m_l is assumed to be equal to B/4 that is, the wind loads on the deck is assumed to be concentrated forces acting at the 1/4 chord point of the deck. This is a gross assumption which may not realistically represent the location of the forces in the bridge section and may lead to an overestimate of the aerodynamic damping since there are indications that m_l may be frequency dependent. In Equation (8), the quasi-static coefficients are functions of the effective angle of attack which depends on the structural motion and wind velocity fluctuations. The quasi-static coefficients for the Akashi Kaikyo Bridge are shown in Figure 4. To consider the dependencies of the quasi-static coefficients with the effective angle of attack, the C_L and C_D coefficients are fitted with a polynomial of order 5 while the C_M coefficient is fitted with a polynomial of order 7.

Figure 4 Quasi-static coefficients

4. Time History Response Analysis

The dynamic model of the Akashi Kaikyo Bridge consists of concentrated masses and stiffness at the elements. A three-dimensional structural idealization of the bridge model is shown in Figure 5.

The equations of motion for the dynamic equilibrium is given as

$$Mu + Cu + Ku = F^{ext} \tag{10}$$

where M = mass matrix; C = damping matrix; K = stiffness matrix; u,u,u = displacements and its derivatives; F^{ext} = external force consisting mainly of wind loads.

In the response analysis, the wind velocity fluctuations along the bridge axis are generated using an ARMA model derived from the given spectra and coherence function. The relative velocities acting at the deck nodes and the effective angle of attack at each time step are then obtained from the previous formulations. At each time increment, the fluctuating drag, lift, and moment forces are

determined based on the relative velocity and effective angle of attack. In the time integration, the Wilson-θ method was used to solve the equations of motion.

Main span · 1990 m

Side spans : 960 m

Deck width : 35 5 m
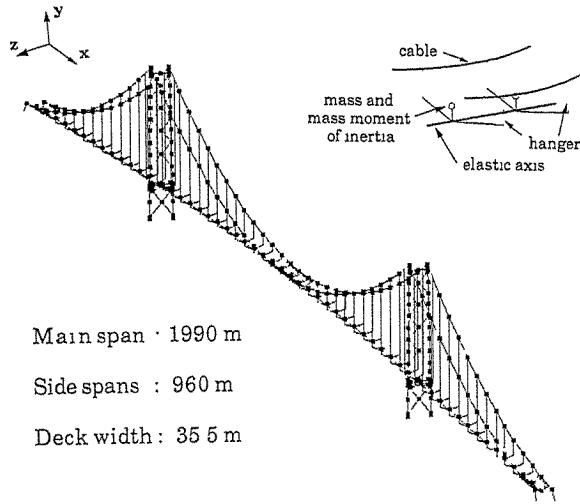
Figure 5 Structural idealization of the bridge model
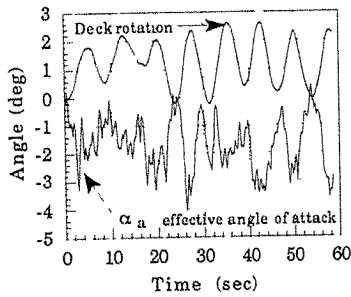
Figure 6   Deck rotation and effective angle of attack
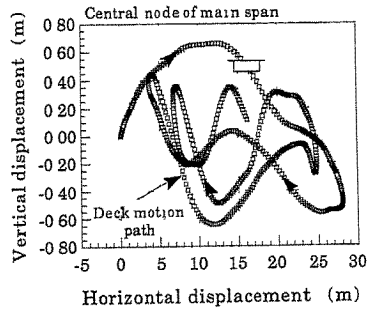
Figure 7   Horizontal - vertical displacement of deck node

During the analysis, the effective angle of attack varies with the fluctuating wind velocities and the structural motion as shown in Figure 6. It can be seen in the figure that the variation of the effective angle of attack depends much on the fluctuating component of the wind velocity. For a mean wind speed of about 60 m/s and turbulence intensity of about 6% at the central node of the main span, a coupled structural motion was observed. The variation of the deck position with time in the horizontal and vertical direction is shown in Figure 7. Similarly observed in the full scale wind tunnel test, the bridge motion under turbulent wind follows that of a coupled random oscillation. Instantaneous displacements of the bridge span was also taken and shown in Figure 8 together with

215

the mean values. Motion in the horizontal, vertical and rotational directions follows that of the fundamental modes with participation of some higher modes in the vertical direction.
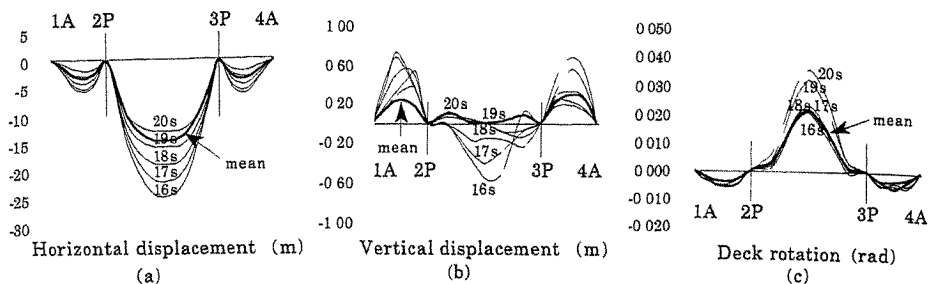
Figure 8   Instantaneous deck displacements

5. Concluding Remarks

The present study dealt with the determination of the dynamic response of a long suspension bridge under turbulent wind.   Considerations for the space-time variation of wind velocity fluctuations was done using an ARMA model based on spectral density and coherence functions. Wind forces followed that of the quasi-steady formulation considering instantaneous change of angle of attack.

Although bridge response can be simulated well using the method described, some comments on the approach seems necessary.   Simulations of correlated wind velocities depends largely on appropriate coherence functions which is presently lacking in the present literature.   Also, a need for proper description of the correlation between the along wind, lateral and vertical velocity fluctuations is indicated.   In the response analysis, the quasi-steady formulation considers directly the aerodynamic damping of the motion at each time instant.   This is a simplification in the time domain approach since self-excited forces are normally frequency dependent.   Also, the aerodynamic admittance was considered to be unity in this study.   Further studies on the frequency dependencies of the buffeting and self-excited forces are being considered at present.

References

[1] R.H. Scanlan and J.J. Tomko, "Airfoil and Bridge Deck Flutter Derivatives", *J. Eng. Mech., ASCE*, Vol. 97, No. EM6, Dec. 1971, pp. 1717 - 1737.
[2] R.H. Scanlan, et. al., "Indicial Aerodynamic Functions for Bridge Decks", *J. Eng. Mech., ASCE*, Vol. 100, No. EM4, Aug. 1974, pp. 657 - 672.
[3] T. Miyata and H. Yamada, "Coupled Flutter Estimates of a Suspension Bridge", *J. Wind Eng.*, No. 37, Oct. 1988, pp. 485 - 492.
[4] A. G. Davenport, "Buffeting of a Suspension Bridge by Storm Winds", *J.Struct, Div., ASCE*, Vol. 88, No.ST3, 1962, pp. 233 - 268
[5] J. D. Holmes, "Prediction of the Response of a Cable stayed Bridge to Turbulence", *Proc. 4th Int'l Conf. on Wind Effects on Buildings and Structures*, Heathrow 1975, Cambridge,pp. 187 - 197.
[6] G Diana, et. al., "Wind Effects on the Dynamic Behaviour of a Suspension Bridge", Politecnico di Milano, Departmento di Meccanica, Jan. 1986.
[7] I. Kovacs, et. al. "Analytical Aerodynamic Investigation of Cable-Stayed Helgeland Bridge", *J. Struct. Eng., ASCE*, Vol. 118., No. 1, Jan. 1992, pp. 147 - 168.
[8] T. Miyata and K. Yamaguchi, "Aerodynamics of Wind Effects on the Akashi Kaikyo Bridge", *Proc. 2nd Italian Nat. Conf. on Wind Eng. (IN-VENTO '92)*, Italy, Oct. 1992.
[9] T. Miyata, et. al., "Akashi Kaikyo Bridge : wind effects and full model wind tunnel tests", *Proc. Int. Symp. on Aerodynamics of Large Bridges*, Denmark, Feb. 1992.
[10] E. Samaras, M Shinozuka and A. Tsurui, "ARMA Representation of Random Processes", *J. Eng. Mech., ASCE*, Vol. 111, March 1985, pp. 449 - 461.
[11] E. Simiu and R. H. Scanlan, *Wind Effects on Structures 2 Ed.*, John Wiley & Sons, 1986.

Damping in suspension bridges: sources, measurements and errors

J. M. W. Brownjohn

Nanyang Technological University, Singapore

Abstract: The appropriate value of damping to be used in determining the dynamic response of a suspension bridge for a particular type of loading derives from effects such as the basic structural damping, non-linearities and aerodynamics. The levels of damping can be assessed from full-scale measurements but these values are subject to a combination of avoidable and unavoidable errors. This paper reviews the problem by considering, structural, external and measurement effects.

1. Introduction

A number of suspension bridges with main spans > 1km are currently under consideration, design or construction. For such bridges the response to sub-critical winds and other loads is heavily dependent on the damping properties of the structure. The basic structural damping also generally contributes a stabilising (delaying) effect against aeroelastic instability.

In all types of simulations with mathematical (and physical) models there is uncertainty in the correct value of damping to use and there is a need to rationalise the choice.

2. Contributions to measured damping

With no sound physical and analytical basis for choosing damping it is necessary to rely on experimental data. The value of equivalent viscous damping (fraction or % of critical) ζ_{me} estimated by physical measurement on a prototype is the sum total of several effects

$$\zeta_{me} = \zeta_{ma} + \zeta_{fc} + \zeta_{hy} + \zeta_{ra} + \zeta_{ae} + \zeta_{nl} + \zeta_{ns} + \cdots + \zeta_{er} \qquad (1)$$

where the components are contributions due to material damping (ζ_{ma}), friction/coulomb damping (ζ_{fc}), hysteretic damping (ζ_{hy}), radiation damping at foundations (ζ_{ra}), aerodynamic damping (ζ_{ae}), geometric nonlinearity (ζ_{nl}), effects of non-stationarity (ζ_{ns}) and measurement error (ζ_{er}). The list is not exhaustive. $\zeta_{ma}, \zeta_{fc}, \zeta_{hy}$ and ζ_{ra} are energy dissipating effects, ζ_{ae} and ζ_{nl} affect response levels in variable ways and ζ_{ns}, ζ_{er} are effects which neither dissipate energy nor control response but erroneously appear as damping when measured.

For welded box-deck structures the contribution ζ_{ma} from material damping probably will not be more than a fraction of a %. For bridges with a stiffening truss there is scope for the large number of joints to contribute more e.g. as friction damping ζ_{fc}. Deck bearings restraining motion at the towers and other bearings e.g. at hanger terminations may contribute friction losses to ζ_{fc}.

The main cables may contribute more than just ζ_{ma} if there is slippage between the strands [1] and certainly a large contribution of hysteretic damping ζ_{hy} is due to friction in the hangers which are usually spiral wound steel ropes. The losses can be increased if the hangers are inclined.

3. Damping estimates from prototype tests

Dynamic characteristics of many suspension bridges have been measured e.g. [2-8]. Most early prototype tests and a few recent tests have used artificially induced vibrations to improve reliability of damping estimates while most recent tests have relied on ambient loading. Attempts have been made [1,8,9] to correlate span or modal frequency with damping. Davenport [9] has shown an inverse relationship. Even so there are variations in measured damping for outwardly similar bridges depending on structural details, type of loading and measurement process.

4. Structural damping

Structural damping ζ_s includes ζ_{ma}, ζ_{fc}, ζ_{hy} and possibly ζ_{ra}. For ζ_{ma} and ζ_{fc} the rate of energy dissipation ΔE per cycle at a given frequency is proportional to strain energy E. The loss factor is defined as $\psi = \Delta E/E$ for which an equivalent viscous damping ratio is $\zeta = \psi/4\pi$. The ability to dissipate energy in part of a structure depends on the proportion of energy stored in that sub-structure as strain energy [10]. For a suspension bridge in which the tangent stiffness at equilibrium is a combination of geometric and elastic stiffness i.e. $\mathbf{K} = \mathbf{K_g} + \mathbf{K_e}$ the energy stored at the stationary point in a vibration cycle is a combination of gravity potential and elastic strain energy (for an inelastic cable all the energy is stored as gravity potential). Taking the (discretised) stiffnesses as constant for small oscillations, for a given mode n with mode shape vector φ_n the proportion of energy stored directly as elastic strain energy in the sub-structure that contributes $\Delta\mathbf{K_e}$ to the total stiffness, is a given by $\nu_n = \varphi_n\Delta\mathbf{K_e}\varphi_n/\varphi_n^t\mathbf{K}\varphi_n$.

Fig. 1 shows the lowest antisymmetric and symmetric modes VA1 and VS1 for Fatih and Bosporus bridges and Fig. 2 shows distribution of stored energy for these and higher order modes of the two bridges. This clearly indicates the scale of contribution to energy dissipation for the various sub-structures. Inclined hangers were introduced primarily to offset the low damping of the welded decks, while for Fatih this was no longer regarded as necessary.

Bosporus bridge   mode VA1   0.127Hz   Fatih bridge mode VA1   0.125Hz

mode VS1   0.165Hz   mode VS1   0.159Hz
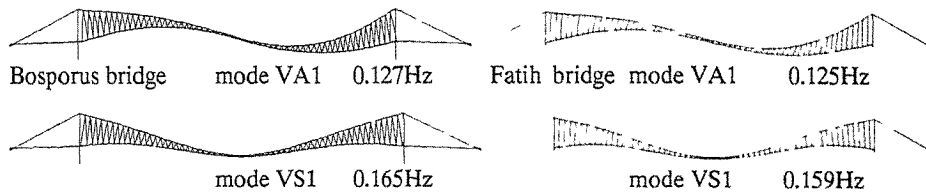
Fig. 1 Lowest vertical plane modes of vibration for Bosporus and Fatih bridges.
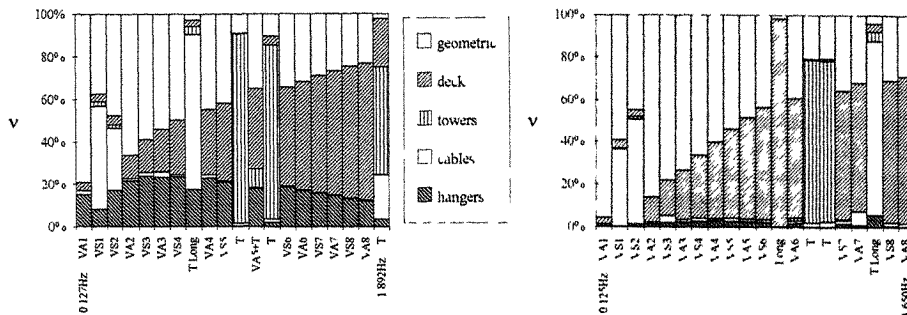
Fig. 2 Distribution of strain energy for sub-structures of Bosporus (left) and Fatih (right) bridges
Key V = vertical   A = antisymmetric   S = symmetric   T = tower   Long = longitudinal

For Bosporus the inclined hangers contribute significantly. Given $\psi \leq 0.4$ [11] and $\nu = 0.2$ leads to $\zeta_{hy} \leq 0.6\%$. In both bridges the contribution of the deck increases with frequency. Taking equilibrium as zero strain energy, significant variations of strain energy in the main cables are found only in the lowest two symmetric modes VS1 and VS2 and higher longitudinal modes.

Measurements at tower foundation levels [2-4] have shown structural response to be several orders of magnitude lower than on the superstructure except in pure tower modes so it is hard to believe that significant energy dissipation ζ_{ra} takes place for moderate response levels.

218

5. Deck bearings

Possibly significant energy losses occur at the deck end bearings due to friction [12], whose contribution to ζ_{fc} decreases with increasing amplitude. For Bosporus in VA1, assuming that the friction force equals the overhung weight of the deck supported at the bearings, at $\pm$ 1cm 1/4 span vertical amplitude friction would contribute approximately $\zeta_{fc} = 0.5\%$

This assumes simple Coulomb friction whereas based on observations it appears that a stiction (stick-slip) type of mechanism operates whose effect cannot be so simply quantified. Fig. 3 shows results of nonlinear analyses [13] for Bosporus in which different levels of antisymmetric random vertical loads were applied to the deck while the bearings were allowed to seize when end of deck velocity dropped below a preset level v_{th} to be released only when the axial force at the bearing exceeded a preset load level f_{th}. The bearings are effectively locked for small loads and VA1 shifts to a significantly higher frequency and in the transition the disruptive effect of the stiction significantly limits response. This effect is consistent with observations at Bosporus where mode VA1 appeared very weakly at two frequencies. In the analyses the damping matrix is given by $\mathbf{C} = \alpha \mathbf{K_e}$, taking $\alpha = 0.01$. The simplifications in the analysis stiffen the higher mode which in fact appears at 0.182Hz on the prototype.
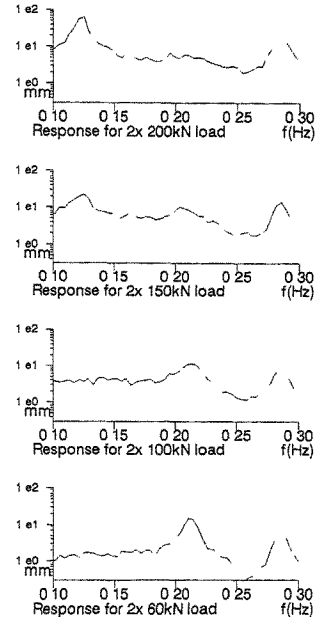
Fig. 3 Frequency shift for VA1, for $v_{th} = 0.5$mm/sec, $f_{th} = 1$MN

6. Geometric non-linearity

Two significant structural non-linearities occur in a suspension bridge. The main cable stiffness changes according to the oscillating sag and tension and hangers cannot sustain compressive loads. While the latter effect is not significant for modest (normal service) conditions both cause changes in natural frequency. Fig. 4 shows auto power spectra of displacement response for Bosporus obtained by non-linear simulations [13] for a) modest and b) very high random vertical loads applied incoherently along the deck. There is a noticeable change in the resonant frequency together with broadening of the resonance, a symptom of increased damping. The effect is marginal for the vertical hanger Fatih bridge even for very large loads and for Bosporus for loads that produce less than 1m RMS vertical deck displacement.
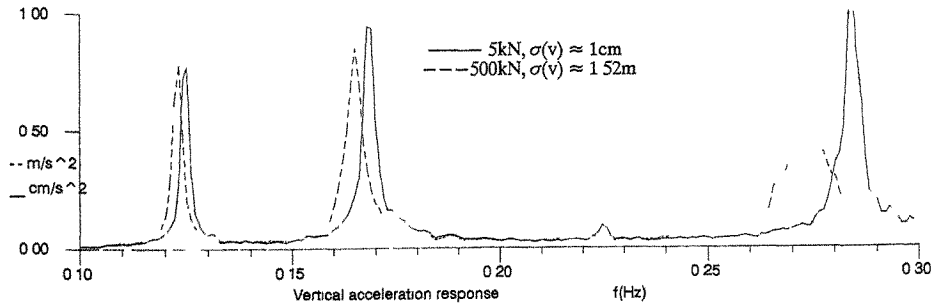
Fig. 4 Auto power spectra of simulated vertical acceleration response $\dot{v}$ at 2/5 span for Bosporus for low (5kN) and high (500kN) deck node loads, for $\alpha = 0.01$.

219

7. Aerodynamic effects

Fig. 5 shows ζ_{me} for Humber modes VS1,2 for a range of mean wind speeds (U). At $U = 0$ $\zeta_{ae} = 0$ and for $U > 0$ the difference should be mainly attributable to aerodynamics. If ζ_{me} for $U > 0$ can be adjusted for measurement error (see below) ζ_s can be obtained by subtracting ζ_{ae}, estimated as $-\rho B^4 l(H_1^* G_{h_i}) / 4I_i$ [5]. Chord, span and air density B, l and ρ are constants and G_{h_i} and I_i for mode i relate to mode shape and mass distribution. The aeroelastic coefficient H_1^* decreases with ratio of wind speed to modal frequency so that for G_{h_i} and I_i constant ζ_{ae} would decrease for higher frequencies. It is tempting to suggest this as a cause of the trend of differing ζ_{me} for different U in Fig. 6 but this would be to ignore the variation of other amplitude effects.

Data for Bosporus and Fatih are included in Fig. 6 to show the similarities for the two inclined hanger box-decks in low winds and the lower values for the vertical hanger Fatih bridge.
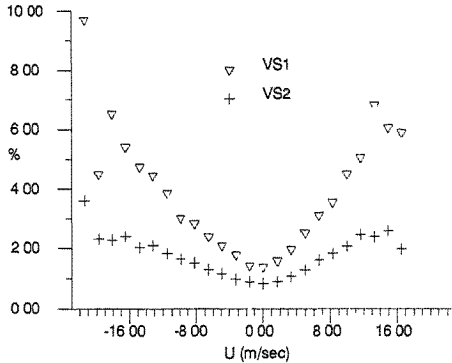
Fig. 5 ζ_{me} for Humber modes VS1,2
U < 0 is Westerly (cyclonic),
U > 0 is Easterly ($\approx$ anit-cyclonic)
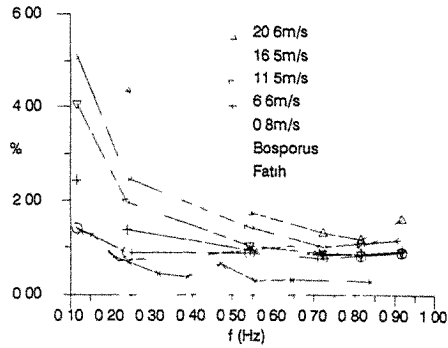
Fig. 6 Humber bridge ζ_{me} vs frequency
for 5 windspeed ranges (U), also for low
wind ranges at Bosporus, Fatih bridges

8. Stationarity and data processing

Full-scale forced vibration testing is uncommon outside Japan[7] and while such tests can provide the most reliable estimates for some modes, ambient vibration response monitoring is cheaper and easier and can provide data for a wide range of natural load conditions. Parameter estimates are often derived from response data via frequency domain techniques such as Fast Fourier Transform (FFT) with averaging of acceleration power spectral ordinates over many response records and finding the parameters for an equivalent single degree of freedom (SDOF) oscillator which best fit the result. A number of assumptions are involved, principally that the 'process' is stationary with constant system parameters (frequency f, damping ζ_s) and that the load is random with a flat power spectrum. The latter assumption is reasonable since the wind speed spectrum varies slowly, but the modal parameters can be affected by wind, traffic or temperature. If these effects shift the frequency during the averaging the resonance can be smoothed. Fig. 7 shows the effect for different f, ζ_s. For high traffic loads the net effect of weight and mass could amount to $\Delta f \approx 1\%$

f increasing, 0.1Hz$\rightarrow$0.5Hz

upper: $\zeta_s = 0.5\%$
middle: $\zeta_s = 1.0\%$
lower: $\zeta_s = 2.0\%$
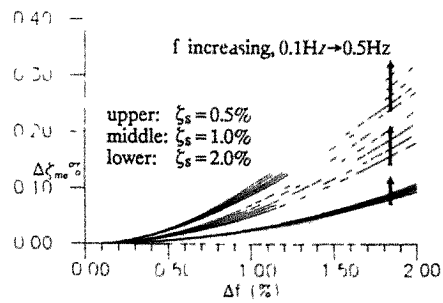
Fig. 7 ζ_{me} increase vs frequency shift

220

increasing ζ_{me} from 0.5% to 0.6% for f = 0.1Hz. Thermal effects are less significant.

Frequency and damping estimates are subject to a) bias and b) variance errors which derive from a) the aperiodicity and limited duration T of the individual response records and b) the random character of the data together with the limited number n of available records. Bias errors in damping estimates (usually) lead to overestimation that decreases with T, likewise variance errors for damping and frequency decrease with n so that with a limited duration nT of 'stationary' data there is a trade-off between T and n. The problems are severe for suspension bridges with very low frequencies so guidelines on choice of n and T would be useful. Error values often quoted for spectral estimates [14] strictly apply to single spectral ordinates.

Fig. 8 shows results of a numerical exercise in which the response of a representative SDOF oscillator with f = 0.1Hz and ζ_s = 1% to white noise was analysed (Hanning window and FFT) to produce, for different combinations of n and T, mean and variance values of ζ_{me} and f.
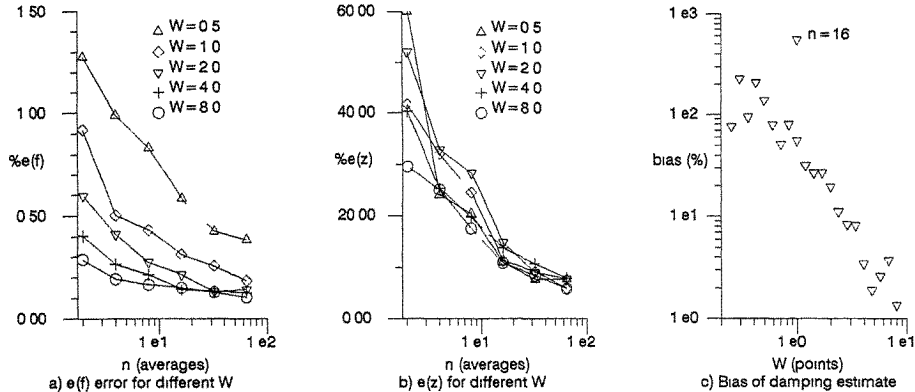
Fig. 8   Statistics of bias and normalised frequency and damping error for 0.1Hz, 1% damped
oscillator, obtained from curve fitting to RMS average of FFT of n T second records

Variances are given as normalised error $e(f) = 100\sigma(f)/\mu(f)$, $e(z) = 100\sigma(\zeta_{me})/\mu(\zeta_{me})$ and bias as $100(\zeta_{me}/\zeta_s - 1)$. $W = 2\zeta_s fT$ is the number of spectral lines spanned by the true half power bandwidth of the oscillator. Fig. 8 shows that variance decreases with n and that while higher W (more data points used in the curve fit) improves the already low frequency error it does little for damping error.

The reductions in variance error for n > 16 probably do not justify sacrificing bias error by increasing n at the expense of T. Although the bias effect is also related to the position of the resonant peak in relation to the sampled frequencies, in general provided W > 1.0 then to a first approximation bias $\propto W^{-1.5}$. Other tests showed that provided W is constant the effect of varying ζ_s, f or T is small, so Fig. 8c would indicate the bias effect for other ζ_s and f.

Fig. 8 can also serve as a guide to actual errors given known f, T, n and ζ_s. Of course ζ_s is not known but an iterative process using Fig. 8 could be used to estimate more realistic values.

9. Recommendations

With the above considerations and data from carefully conducted measurements it should be possible to rationalise the appropriate choice of damping. Some suggestions are:

- In high winds aerodynamic damping could be counted on to reduce amplitude of response to other loading. Wind tunnel studies should be capable of providing a measure of this effect.
- Geometric non-linearity is not significant for the range of vibrations experienced during all but the most severe forms of loading, for which it would be helpfully disruptive.

221

- Deck bearings may provide significant damping but only for low frequency antisymmetric modes at low amplitude levels. Stick-slip behaviour can almost completely inhibit the first antisymmetric bending mode VA1.
- Hangers can provide a significant level of damping via hysteresis if they are inclined.
- Structural damping in the deck has an increasing contribution ν for higher modes, provided the loss factor ψ is significant (generally not the case for welded box decks).
- Main causes of amplitude dependency seem to be friction, nonlinearity and aerodynamics. Frequency effects derive from energy distribution ν, aerodynamics and measurements.
- Measurements of basic structural damping should be obtained during conditions of minimal wind, low traffic and modest temperature variations.
- Where forced vibration testing is not possible and damping is obtained from frequency spectra there are errors which decrease if more and longer response records are used, but with care these can be minimised and even quantified. The decrease of positive bias with increasing frequency can be confused with other effects e.g. aerodynamics.

References:
1.   A. G. Davenport, G. Larose, The structural damping of long span bridges: an interpretation of observations. Canada-Japan Workshop on Aerodynamics, Ottawa, Sep. (1989).
2.   J. M. W. Brownjohn, A. A. Dumanoglu, R. T. Severn, C. A. Taylor, Ambient vibration measurements of the Humber Suspension Bridge and comparison with calculated characteristics. Proceedings, Institution of Civil Engineers, Pt. 2, **83**, 561-600 (1987).
3.   J. M. W. Brownjohn, A. A. Dumanoglu, R. T. Severn, A. Blakeborough, Ambient vibration survey of the Bosporus *(Bogazici)* Suspension Bridge. Earthquake Engineering and Structural Dynamics, **18**, 263-283 (1989).
4.   J. M. W. Brownjohn, A. A. Dumanoglu, R. T. Severn, Ambient vibration survey of the Fatih Sultan Mehmet (second Bosporus) suspension bridge. Earthquake Engineering and Structural Dynamics, **21**, 907-924 (1992).
5.   N. P. Jones, C. A. Spartz, Structural damping estimation for long span bridges. Journal of Engineering Mechanics Division, ASCE **116**, No. EM11, 2414-2433 (1990).
6.   A. Selberg, Dampening effect in suspension bridges. IABSE Publications, **10**, 183- (1950).
7.   K. Yamada, K. Yamamoto, H. Akiyama, Full-scale dynamic testing of very long span bridges. US-Japan Bridge Workshop, San Diego, CA (1988).
8.   Aerodynamic stability of suspension bridges with special reference to the Tacoma Narrows bridge. Bulletin no. 116, University of Washington Engineering Experiment Station, Seattle, Washington (1954).
9.   M. Ito, T. Katayama, T. Nakazono, Some empirical facts on damping of bridges. Symposium on resistance and ultimate deformability of structures, IABSE Publications, Lisbon, 95-100 (1973).
10. S. Nakamura, T. A. Wyatt, Economical computation of stress histories in suspension bridge elements, with special reference to inclined hanger systems. Steel and Aluminium Structures, Cardiff, 8-10 July (1987).
11. M. Raoof, The prediction of axial damping in spiral strands. J. Strain Analysis, **26**, No. 4, 221-229 (1991).
12. T. A. Wyatt, Mechanisms of damping. Symposium on Dynamic Behaviour of Bridges, SR 275, TRRL Crowthorne, May, 10-21 (1977).
13. J. M. W. Brownjohn, Observations on nonlinear dynamic characteristics of suspension bridges. CSE Research Report, Nanyang Technological University, Singapore (1993).
14. J. S. Bendat, A. G. Piersol, Measurement and analysis of random data. John Wiley, (1966).

A practical method of passive TMD for suppressing wind induced vertical buffeting of long-span bridges

M.Gu, H.F.Xiang and A.R.Chen

Department of Bridge Engineering
Tongji University, Shanghai, China

Abstract: Formulas of reduction ratio of TMD for suppressing wind-induced vertical buffeting response of long span bridges and the optimal solutions of parameters of TMD for engineering purpose are derived. An aeroelastic test of full bridge model of Yangpu Bridge with/without TMD was done, the results of reduction ratio being in good agreement with those from the calculation. "TMD design wind speed" and the constraint conditions are further stressed and discussed. At last, Yangpu Bridge is taken as an example to show the application of these formulas.

1. Introduction

For modern bridges tending to be longer and lighter, wind-induced buffeting becomes more and more important. Many engineers and researchers are concerned about how to suppress the buffeting of bridges effectively. TMD(tuned mass damper) device with advantages of reasonable cost and convenience and effectiveness in usage has been mounted in some bridges[1,2]. Its effects on flutter and galloping[3,4] as well as suppressing buffeting[5] of long-span bridges have been theoretically and experimentally studied.

Some measures for inproving flutter characteristics of bridges such as increasing the first torsional eigenfrequency will lead to a phenomenon that the buffeting response is mainly contributed by the vertical bending modes. In view of this fact, the focus of this paper is on suppressing wind-induced vertical buffeting of long-span bridges by using TMD.

2. Fundamental Theory

Assume that the buffeting response takes place in the first vertical bending mode, $\phi_1(x)$, namely, the deck   displacement $y_1(x,t)=\phi_1(x)\xi_1(t)$ and the TMD   displacement relative to the deck $y_2(t)=\phi_1(x_0)\xi_2(t)$.   The equations governing the motions of a bridge deck and TMD are respectively as follows,

$$M_1(\ddot{\xi}_1+2\zeta_1\omega_1\dot{\xi}_1+\omega_1\xi_1^2)=\int_0^L F_{ae}(x,t)\phi_1(x)dx + \int_0^L F_b(x,t)\phi_1(x)dx +$$

$$+M_1(2\mu\zeta_2\omega_2\dot{\xi}_2 + \mu\omega_2^2\xi_2) \tag{1}$$

$$\ddot{\xi}_2 + 2\zeta_2\omega_2\dot{\xi}_2 + \omega_2^2\xi_2=-\ddot{\xi}_1 \tag{2}$$

where ξ_1 and ξ_2 are the first mode time dependent   vertical generalized coordinates of the bridge deck and TMD, respectively; $\phi_1(x_0)$ is the value of $\phi_1(x)$ at the site where TMD is mounted; M_1, ω_1 and ζ_1 are the first mode generalized mass, circular frequency and damping ratio of bridge, respectively;

ζ_2 and ω_2 are the damping ratio and the circular frequency of TMD, respectively; $\mu = m_2 \phi^2(x_0)/M_1$ is the generalized mass ratio of TMD to bridge; m_2 is the mass of TMD; L is the total length of the main bridge; $F_{ae}(x,t)$ and $F_b(x,t)$ are the aeroelastic force and buffeting force acting on the bridge deck proposed by Scanlan(see Ref.[6]).

The total buffeting response equals approximately to the resonant part because the transfer function is highly peaked in the neighborhood of $\omega=\omega_1$. From this point, the equations of mean square displacments of the bridge deck, σ^2_{y1}, and of TMD, σ^2_{y2}, can be approximately given as,

$$\sigma^2_{y1}(U,x,\zeta_t,\mu,\zeta_2,\omega_2)=S_F(\omega_1,U)\ \phi^2_1(x)X_1(\zeta_t,\mu,\zeta_2,\omega_2)/M^2_1 \qquad (3)$$

$$\sigma^2_{y2}(U,\zeta_t,\mu,\zeta_2,\omega_2)=S_F(\omega_1,U)\phi^2_1(x_0)X_2(\zeta_t,\mu,\zeta_2,\omega_2)/M^2_1 \qquad (4)$$

where

$$S_F(\omega_1,U)=(\rho UB)^2\int_0^L\int_0^L\phi_1(x_1)\phi_1(x_2)\ e^{-C|x_1-x_2|/L}dx_1dx_2$$

$$[C^2_L S_u(\omega_1) + (C'_L+\frac{A}{B}C_D)^2 S_w(\omega_1)/4\ ] \qquad (5)$$

$$X_1(\zeta_t,\mu,\zeta_2,\omega_2)=\frac{B^2_0(A_2A_3-A_1A_4)/A_0 + A_3(B^2_1-2B_0B_2) + A_1B^2_2}{A_1(A_2A_3-A_1A_4) - A_0A^2_3}\ \frac{\pi}{2}; \qquad (6)$$

$$X_2(\zeta_t,\mu,\zeta_2,\omega_2)=\frac{A_1B^2_2}{A_1(A_2A_3-A_1A_4)-A_0A^2_3}\ \frac{\pi}{2}; \qquad (7)$$

with $A_4=1$; $A_3=2\zeta_2\mu\omega_2+2\zeta_t\omega_1+2\zeta_2\omega_2$; $A_2=\omega^2_2\mu+\omega^2_1+\omega^2_2+4\zeta_t\zeta_2\omega_1\omega_2$; $A_1=2\zeta_2\omega^2_1\omega_2+2\zeta_t\omega^2_2\omega_1$; $A_0=\omega^2_1\omega^2_2$; B_i in $X_1(\zeta_t,x,\mu,\zeta_2,\omega_2)$ are different from that in $X_2(\zeta_t,\mu,\zeta_2,\omega_2)$:

$$B_2=1,\ B_1=2\zeta_2\omega_2,\ B_0=\omega^2_2,\quad \text{for } X_1; \qquad B_2=-1,\quad \text{for } X_2. \qquad (8)$$

In Eq.5, $S_u(\omega)$ and $S_w(\omega)$ are the power spectra of $u(x,t)$ and $w(x,t)$ respectively. C_L and C_D are the aerodynamic lift and drag coefficients in steady flow respectively; C'_L is the slope of C_L; B is the deck width; A is the deck projected area normal to wind per unit span; C is conservatively estimated as $C=7L\omega/(2U\pi)$. ζ_t is the sum of structural and aerodynamic damping ratios, and can be approximately written as,

$$\zeta_t=\zeta_1+\zeta_a=\zeta_1-\rho B^2H^*_1G_1/(2M_1) \qquad (9)$$

in which $G_1 = \int_0^L \phi_1^2(x)dx$; H_1^* is a aerodynamic derivative.

Calculation results by using Eq. 9 indicate that ζ_t may be much larger than that of structure, ζ_1, for a bridge with a light and wide deck (especially steel deck), and a large value of H_1^* at high wind speed.

Let

$$\eta = \frac{\sigma_y(U,x_0) - \sigma_{y1}(U,x_0)}{\sigma_0(U,x_0)} = 1 - \frac{\sigma_{y1}(U,x_0)}{\sigma_y(U,x_0)} \qquad (10)$$

where η is defined as the reduction ratio; σ_y^2, the mean square resonance displacement of bridge deck without TMD, is given by

$$\sigma_y^2(U,x_0) = \frac{S_F(\omega_1,U)\phi_1^2(x_0)\pi}{4\zeta_t\omega_1^3 M_1^2} \qquad (11)$$

From Eq. 10, the reduction ratio can finally be expressed as,

$$\eta = 1 - \left[\frac{4\zeta_t\omega_1^3}{\pi} X_1(\zeta_t,\mu,\zeta_2,\omega_2) \right]^{1/2} \qquad (12)$$

Eq.12 implicates η depends inversely on ζ_t. This fact means that η may be much smaller at high wind speed than its initial value at zero wind speed.

3. Experimental Study

To verify Eq. 12, an aeroelastic full model test of Yangpu Bridge with/without TMD was done. Yangpu Bridge is a cable stayed bridge with a composite deck in floating system, center span of 602m, two pylons and two sloped cable planes. Model scale and wind speed ratios are 1/225 and 1/15 respectively. The natural frequency ratio and the mass ratio of TMD to the bridge deck are unit and 6/1000 respectively. Damping ratio of TMD is 0.14. Turbulent wind with 10% intensity was generated by a grid.
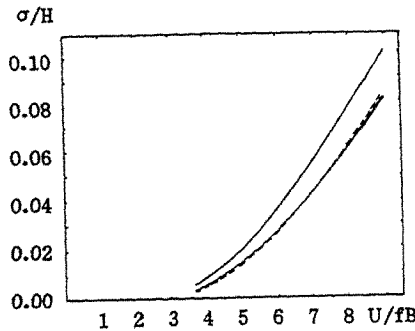
Fig.1 Comparison of the test results with calculation ones

225

The results are shown in Fig.1, in which σ is the total RMS displacement at the center of the bridge span; H is the bridge deck height; the up full line is the value of σ/H of bridge without TMD from the test; the low full line is that with TMD from the test and the dashed line is that with TMD from the calculation by using Eq.12. From Fig.1, it is obvious that the calculation is in good agreement with the test.

4. Optimal Solution and Their Practical Use

By using the computer program made by the authors for seeking the optimal solutions of Eq.12, the relations between the dynamic parameters of TMD and bridges as well as reduction ratio are analyzed in detail. Two equations which describe how the optimal coefficients of TMD, ζ_{2o} and ω_{2o}/ω_1, depend on the mass ratio and ζ_t are given by using the Least Square Method:

$$\zeta_{2o}=0.5\ \mu^{0.5} \tag{13}$$

$$\frac{\omega_{2o}}{\omega_1} = \frac{1}{1+\mu}+3\mu^2-0.2\zeta_t^2 \tag{14}$$

Eq.13 is the same as the classical one[7]. Eq.14 is also the almost same as the formula given in Ref[7] for small ζ_t and μ. But when ζ_t is much larger than ζ_1, it has an effect on the optimal frequency of TMD to a certain extent.

By using the same method as deriving the above two equations, an expression of the optimal reduction ratio as a function of μ and ζ_t is given,

$$\eta_o=\frac{0.0158}{0.1277+\zeta_t}\ln(\mu)+\frac{0.0496}{0.0405+\zeta_t} \tag{15}$$

or

$$\mu= \exp\left[(\eta_o-\frac{0.0496}{0.0405+\zeta_t})\frac{0.1277+\zeta_t}{0.0158}\right] \tag{16}$$

The error ranges of Eq.15 and 16 are found to be less than 2% for $\mu=0.008-0.05$, and $\zeta_t=0.008-0.06$, which are the ranges of μ and ζ in the practical application of bridges.

When engineers design a TMD for a given bridge and a desired reduction ratio, they can determine a value of μ(mass of TMD) at a selected "TMD design wind speed"[5] by using Eq. 16 at first. Then, from Eqs. 13 and 14, they can easily find the optimal coefficients of TMD at the same wind speed.

5. Constraint Conditions

It is important to take the engineering constraint conditions into consideration in the design of TMD. From Eq.4, it can be found how large the vibration amplitude of TMD is, and further how the strength of springs of TMD under the action of static and fatigue loads will be.

It is assumed that the static extension of the spring of TMD caused by the static load of the secondary mass, m_2, equal approximately to its extreme vibration displacement, $Y_{2max}=g\sigma_{y2}$ at "TMD design wind speed", where g is a peak factor. This assumption can be achieved by using special preloded tension coil

226

springs. Based on these, an equation for checking simultaneously the fatigue strength and static strength as well as the allowable space size for motion of the TMD is derived as follows(detailed processes of deriving this equation can be referred from Ref.[5]),

$$\min \left\{ \frac{[\tau]\pi C_0^2 H_0}{2gKG}, \frac{\tau_0 \pi C_0^2 H_0}{(n_F+0.75+n_F g-0.75g)KG}, \frac{H_B-H_0-\Delta}{2g} \right\} - \sigma_{y2} > 0 \qquad (17)$$

where $[\tau]$ and G are the allowable shearing stress and the shear elasticity of the spring material respectively; τ_0 is shearing fatigue limit of the spring material under pulsation shearing stress; n_F is the safety factor for fatigue check; H_0 is the original length of each spring; H_B is height of the bridge deck or the frame; $\Delta = \Delta_1 + \Delta_2 + \Delta_3 + \cdots$ is the sum of the other sizes needed except for H_0(the origonal length of the springs) and $2g\sigma_{y2}$ within the range of H_B; K $=[(C_0-1)/(C_0-4)+0.615/4]$; $C_0=D/d$; D and d are the outside mid-diameter and the diameter of spring wire respectively; σ_{y2} is calculated from Eq.4.

The two former items in the left side in Eq. 17 are both directly proportional to H_0, while the third item is inversely proportional to it. This fact means that when

$$\min \left\{ \frac{[\tau]\pi C_0^2 H_0}{2gKG}, \frac{\tau_0 \pi C_0^2 H_0}{(n_F+0.75+n_F g-0.75g)KG} \right\} = \frac{H_B-H_0-\Delta}{2g}, \qquad (18)$$

$$\min \left\{ \frac{[\tau]\pi C_0^2 H_0}{2gKG}, \frac{\tau_0 \pi C_0 H_0}{(n_F+0.75+n_F g-0.75g)KG}, \frac{H_B-H_0-\Delta}{2g} \right\} \qquad (19)$$

takes the maximum value, which can bring the constraint conditions of Eq.17 into full play. So, H_0 can be appropriately determined from Eq.18.

6. An Example

Yangpu Cable-stayed Bridge in Shanghai during the stage of erection is taken as an example to show the application of the formulas.

Some coefficients of the bridge are given here: the first vertical bending frequency is 0.305, mass per meter of the deck is approximately 32000kg/m, L=544m, n_F=2, g=3, $[\tau]$=5.1e8(N/m^2), τ_0=6.0e8(N/m^2), H_B=3.5m, Δ=0.3m, U_D(TMD design wind speed)=25m/s, desired reduction ratio is at least 0.35 and the structural damping ratiois taken as 0.01. The aerodynamic derivatives and forces are obtained in smooth flow in TJ-1 Wind Tunnel at Tongji University.

A frame, in which TMD set is suggested to be hung, can be removed to the cantilever end of the bridge deck for use. The TMD is so designed for its convenience during the construction of the bridge.

The calculated total mass of TMD is about 40 tons, and the optimal frequency and damping ratio are 0.298 and 0.072 respectively. The optimal η is 39%. Each original length of the springs is 0.82m from Eq. 18. The constraint conditions of Eq.17 are satisfied. It is can be seen from Fig.2 that ζ_t increases with wind speed, such as from 0.012 for 9m/s to 0.028 for 37m/s wind speed, which lead to that the reduction ratio decreases from 49% to 30%.
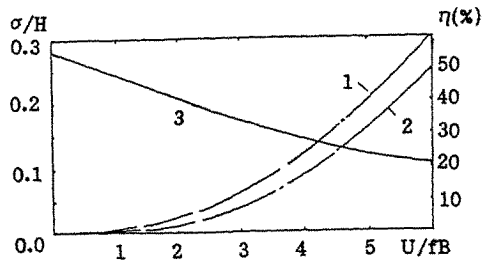
Fig.2 σ/H and η versus U/fB (1— without TMD; 2— with TMD; 3— η)

7. Conclusions

1). An equation of estimating the reduction ratio of TMD for suppressing buffeting of bridges is derived and has been verified by an aeroelastic full model test of Yangpu Bridge;

2). By using the equation of reduction ratio and the computer programe, three simplified equations are given for determining the optimal damping ratio, frequency of TMD and the optimal reduction ratio(or mass ratio). From these, it is obvious that the design of TMD for wind-resistance is different from that for other uses, such as earthquake-resistance, because the reduction ratio depends not only upon the structural characteristics (including the shape of cross section of the bridge deck), but also the wind speed. In view of this, "TMD design wind speed" is further stressed and discussed. In the design of TMD for a given bridge and a selected "TMD wind design speed", engineers can determine the mass of TMD based on the desired reduction ratio at first, then the optimal damping ratio and frequency;

3). Some engineering constraint conditions, including static and fatigue strength of springs and allowable space size for the motion of TMD, etc, should be taken into consideration. A formula for seeking the original length of spring of TMD is recommended based on these conditions;

4). Yangpu Bridge is taken as an example to show the applications of the proposed method.

Acknowledgement

References

1. R. L. Wardlaw, Aerodynamics of Large Bridges, A.Larsen(ed.), Balkema, Rotterdam, (1992)59.
2. G. Huffmann, R. A. Freeman & C. W. Brown, Proc. of Int. Conf. on Cable Stayed Bridges, Bangkok, Nov.,(1987)1485.
3. J. Nobuto, Y. Fujino & M. Ito, J. of JSCE(in Japanese), Oct.,(1988)413.
4. Y. Fujino, P. Warnitchai & M. Ito, J. of the Faculty of Eng., The University of Tokyo(B), Vol.38, No.2, (1985)49.
5. M. Gu & H. Xiang, J. Wind Eng. Ind. Aerodyn., 42(1992)1383.
6. R. H. Scanlan & R. H. Gade, J. of the Struct. Div., ASCE, Vol.103, No.ST9, Sept.,(1977)1867.
7. R. J. Mcnamara, J. of Struct. Div. ASCE, Vol.103, No.ST9, Feb., (1977)1785.
8. T. Ioi, K. Ikeda, Bulletin of the JSME, Vol.21, No.151, January, (1978)64.

228

State-Space Method of Wind-Induced Response Analysis for Suspension Bridge

Sun Bingnan, Zhou Qiang, Tang Jinchun

Dept. of Civil Engineering, Zhejiang University,
Hangzhou, Zhejiang, P. R. China

ABSTRACT: The paper developed a state-space method of the wind-induced response analysis for suspension bridge. Meanwhile, an equivalent Барштейн spectrum of wind velocity was applied instead of conventional wind fluctuating spectrum and a shapping filter also was introduced. The RMSD of stochastic dynamic response including displacement, velocity and acceleration can be solved from state equation. Especially, 3σ edge deflection (maximum edge deflection) of suspension bridge can be obtained in terms of SRSS method.

I . Introduction

It is well known that the main analysis method of wind-induced response for suspension bridge, which was proposed by Prof. R. H. Scanlan[1] several years ago, is spectral density analysis method. But the spectral density analysis method has to treat the complicated calculation of generalized integral which is not easy to design a computer program and costs a large amount of computing time. In present work, a state-space method of analyzing wind-induced dynamic response for large span bridge, such as suspension bridge, was proposed successfully following some ideas of modern control theory. Finally, some numerical examples were calculated by the developed state-space method and were compared with the results obtained by conventional spectral density analysis method. The calculation results reveal that the state-space method is suitable for wind-induced dynamic response analysis of suspension bridge. Also it has high accuracy and good convergency.

I . Equivanlent Барштейн spectrum of wind fluctuating velocity and shapping filter

Based upon the view point of engineering application, the spectrum function of wind fluctuating pressure should adopt the Барштейн spectrum because it has simple form and generalization. The Барштейн spectrum can be expressed as follows :

$$S_w(\omega) = \frac{(\alpha-\mu\beta)\omega^2 + (\alpha + \mu\beta)(\alpha^2 + \beta^2)}{\pi[\omega^4 + 2(\alpha^2-\beta^2)\omega^2 + (\alpha^2 + \beta^2)^2]} \tag{1}$$

in which ω is a circular frequency; α, β and μ are three constants. When ω goes to zero, the spectrum $S_w(\omega)$ will trend to a constant. It means that a component of zero frequency is contained in wind velocity spectrum or pressure spectrum. In order to cancel the component of zero freguency in spectrum $S_w(\omega)$, set:

$$\mu = -\alpha/\beta \tag{2}$$

The spectrum defined by equation (1) is a standard spectrum, which should satisfy:

$$2 \int_0^\infty S_w(\omega)d\omega = 1 \tag{3}$$

according to statistic: by Dr. Davenport[3], the area of wind velocity spectrum should be a constant, i. e.

$$2 \int_0^\infty S_v(\omega)d\omega = b \tag{4}$$

Then, applying the equation (2) and (4), the Барштейн velocity spectrum $S_v(\omega)$ can be derived from the wind pressure spectrum $S_w(\omega)$ as follows:

$$S_v(\omega) = \frac{2ba\omega^2}{\pi[\omega^4 + 2(a^2-\beta^2)\omega^2 + (a^2 + \beta^2)^2]} \tag{5}$$

The wind velocity spectrum expressed by above equation (5) is a generalized spectrum. The paprameters α, β and b can be determined by equality in spectrum area, peak frequency and peak value if comparing the Баршгейн spectrum with other engineering wind velocity spectrum such as Davenport's spectrum. For example, if setting equality of Баршгейн spectrum and Davenport's spectrum, we have $\alpha = 6.0398 \times 10^{-3}\bar{v}_{10}$, $\beta = 4.4755 \times 10^{-3}\bar{v}_{10}i$; $b = 12u_*^2$, in which u_* is a friction velocity, $\bar{v}_{10}$ is the velocity at 10m above ground; i is a imaginary number unit.

Based upon the wind fluctuating velocity spectrum $S_v(\omega)$, the cross-spectral density function matrix of fluctuating wind force vector $\{p\}$ can be expressed as follows:

$$[S_p(\omega)] = [S_0]S_f(\omega) \tag{6}$$

where $[S_0]$ is a constant coefficient matrix and $S_f(\omega)$ can be obtained from equation (5):

$$[S_f(\omega)] = \pi S_v(\omega)/b \tag{7}$$

From above equations, we can find that the fluctuating wind force vector $\{p\}$ is a colored noise vector. Therefore, a shapping filter was introduced for simpling the calculation and the colored noise vector $\{p\}$ can be changed to a white noise output through the shapping filter. If we neglect the correlation between horizontal fluctuating velocity and vertical fluctuating velocity, the fluctuating wind forces—drag force and torson monment can be considered separately. Then introducing a state space vector $\{V\}$, a model of the shapping filter for the fluctuating wind force vector $\{p\}$ can be:

$$\left.\begin{array}{l} \{V\} = [A_s]\{V\} + [D_s]\{\eta\} \\ \{p\} = [C_s]\{V\} \end{array}\right\} \tag{8}$$

in which $\{\eta\}$ is Gauss stationary white noise vector with zero average value which has constant cross-spectral density matrix.

For the flutter and buffeting forces caused by horizontal wind fluctuation :

$$\{V\} = [v_1, \cdots\cdots, v_m, \dot{v}_1, \cdots\cdots, \dot{v}_m]^T$$

$$[A_s] = \begin{bmatrix} 0 & E \\ -[(\alpha^2 + \beta^2)] & -[2\alpha] \end{bmatrix}_{2m \times 2m}$$

$$[D_s] = \begin{bmatrix} 0 \\ E \end{bmatrix}_{2m \times m}, [C_s] = [[0] \quad [(2\alpha)^{1/2}]]_{m \times 2m}$$

where, $[(\alpha^2+\beta^2)]$, $[2\alpha]$, $[(2\alpha)^{1/2}]$ are diagonal matrices; $[E]$ is a unit matrix; z and U are the altitude of bridge deck and average wind velocity at bridge deck. For that caused by vertical wind fluctuation, the similar expresions can be obtained.

II. Expanded State Equation of Wind-Induced Response Analysis

Considering a section of a suspension bridge, as shown in Fig. 1, with two degrees of freedom: vertical vibration and torsional vibration. The governing motion equation of wind-induced response for a single, typical section of the bridge span were obtained by R. H. Scanlan [1]. If the cross-flutter aerodynamic coefficients were neglected, the bending vibration and torsional vibration in the motion equation will be uncoupled. Considering the effect of whole bridge span in section model, the motion equation of wind-induced response of a bridge model can be written as follows:

$$\{\ddot{q}\} + [2\zeta_j\bar{\omega}_j]\{\dot{q}\} + [\bar{\omega}_j^2]\{q\} = \{p^*\} \tag{9}$$

in which, $\{q\}=[q_1,q_2\cdots\cdots q_m]^T$ is generalized coordinate vector. For vertical bending vibration $\bar{\omega}_j^2=\omega_{zj}^2$ is natural circular frequency in bending; $\zeta_j=(2\zeta_{zj}\omega_{zj}-\rho B^2\omega H_1^*/m_0)/(2\bar{\omega}_j)$ is a mechanical and aerodynamic damping in bending; $\{p^*\}=[L]\{p_L\}$ is a generalized buffeting force vector, $[L]=[M^*]^{-1}[\Phi]^T$; $[M^*]=[\Phi]^T[M][\Phi]$ is generalized mass matrix; $[\Phi]$ is mode matrix in which m modes were contained; $\{P_L\}=\{l\}L_z(x,t)$ is buffeting lift force vector, $\{l\}=[l_1,l_2\cdots l_n]^T$, l_k is the length of wind action for kth concentrated mass; $L_z(x,t)$ is wind buffeting force in lift for per unit span. For torsional vibration, $\bar{\omega}_j^2=\omega_{aj}^2-\rho B^4\omega^2 A_3^*/I_0$; $\xi=(2\xi_{aj}\omega_{ai}-\rho B^4\omega A^*2/I_0)/(2\bar{\omega}_j)$; $\{p^*\}=[L]\{p_m\}$ is a generalized torsional moment vector; $[L]=[I^*]^{-1}[\Phi]^T$; $[I^*]=[\Phi]^T[I][\Phi]$ is a generalized torsion matrix of inertia moment; $\{p_m\}=\{l\}M_a(x,t)$ is torsional moment vector due to the wind; $M_a(x,t)$ is sectional torsion buffeting moment per unit bridge span.

$$L_z(x,t)= \frac{1}{2}\rho U^2 B\{2\frac{u(x,t)}{U}C_L(\alpha_0) + \frac{w(x,t)}{U}[C_L'(\alpha_0) + \frac{A}{B}C_D(\alpha_0)]\} \tag{10}$$

$$M_a(x,t)= \frac{1}{2}\rho U^2 B^2\{2u(x,t)C_M(\alpha_0)\frac{1}{U} + C_M'(\alpha_0)\frac{w(x,t)}{U}\} \tag{11}$$

The forces $Lz(x,t)$ and $M_a(x,t)$ are active forces due to the impingement of the gust wind upon the bridge deck section. In the presence of varying wind horizontal velocity and vertical velocity components $u(x,t)$, and $w(x,t)$, respectively, the aerodynamic lift and moment may be defined as above equations (10) and (11). In which, A is deck projected area normal to wind per unit span, B is deck width; α_0 is the attack angle when the bridge is in equilibrium position in steady wind. Generally $\alpha_0\approx 0$; $C_l(\alpha_0)$ is lift coefficient of the deck section in steady flow based on the deck width B; $\frac{dC_L}{d\alpha}\big|_{\alpha=\alpha_0}=C_L'(\alpha_0)$ is slope of lift coefficient curve versus angle of attack; C_D is drag coefficient of the deck section in steady flow (based on the projected frontal area A); C_M is moment coefficient of the deck section (based on the deck width B); $\frac{dC_M}{d\alpha}\big|_{\alpha=0}=C_M'(\alpha_0)$ is slope of moment coefficient curves versus angle of attack; ρ is air density; ω is natural circular frequency of bridge motion; m_0 is mass per unit span and I_0 is mass inertia moment per unit span of bridge; H_i^* and A_i^* are aerodynamic coefficients which are discussed in Ref 4; $\omega_{zj},\omega_{aj},\zeta_{zj},\zeta_{aj}$ are natural circular frequencies and mechanical damping for bending and torsional vibration respectively.

Assuming the state response vector:
$$\{Y\} = [q^T|\dot{q}^T]^T \tag{12}$$

The state equation of the wind-induced response for suspension bridge can be obtained from

equation (9):

$$\{\dot{Y}\} = [A][Y] + [D]\{p^*\} \tag{13}$$

in which, coefficient matrices $[A]$ and $[D]$ are respectively:

$$[A] = \begin{bmatrix} 0 & E \\ -[\overline{\omega}_j^2] & -[2\xi_j\overline{w}_j] \end{bmatrix}_{2m \times 2m}, [D] = \begin{bmatrix} 0 \\ E \end{bmatrix}_{2m \times m}$$

It is obvious that the state equation (11) is a linear system. Therefore, the superposition principle can be applied for solving equation (11). The total wind-induced response of the suspension bridge can be summation of horizontal wind-induced response and vertical response. In following section, the horizontal and vertical wind-induced response would be solved separately.

If we introduced another expanded state response vector $\{Z\}$:

$$\{Z\} = [Y^T|V^T]^T \tag{14}$$

Combining equations (8) and (13), a expanded state equation for wind induced response will be:

$$\{\dot{Z}\} = [\overline{A}]\{Z\} + [\overline{D}]\{\eta^*\} \tag{15}$$

where the coefficient matrices $[\overline{A}]$ and $[\overline{D}]$ will be respectively:

$$[\overline{A}] = \begin{bmatrix} A & DC_s \\ 0 & A_s \end{bmatrix}, [\overline{D}] = \begin{bmatrix} 0 \\ D_s \end{bmatrix}$$

in which cross-spectral function matrix $[S_0^*]$ of the white noise vector $[\eta^*]$ will be:
For the vertical bending wind-induced vibration:

$$[S_0^*] = [M^*]^{-1}[\Phi]^T[S_{L0}][\Phi]([M^*]^{-1})^T \tag{16}$$

For the torsional wind-induced vibration:

$$[S_0^*] = [I^*]^{-1}[\Phi]^T[S_{M0}][\Phi]([I^*]^{-1})^T \tag{17}$$

In above equation, the elements of cross-spectral coefficient matrices $[S_{L0}]$ and $[S_{M0}]$ of lift force and torsional moment can be expressed as follows:

$$[S_0]_{kj} = \rho_x(x_k, x_j)(S_k, S_j)^{1/2} \qquad (k, j = 1, \cdots, n) \tag{18}$$

where $\rho_x(x_k, x_j)$ is space correlative coefficient which is

$$\rho_x(x_k, x_j) = exp(-|x_k - x_j|/L_x), (L_x = 50 \; for \; general)$$

For horizontal fluctuating wind-induced response:

$$\begin{aligned} S_k &= bl_k^2[\rho UBC_L(\alpha_0)]^2/\pi & (for [S_{L0}]) \\ S_k &= bl_k^2[\rho UB^2C_M(\alpha_0)]^2/\pi & (for [S_{M0}]) \end{aligned} \right\} \tag{19}$$

232

For vertical fluctuating wind-induced response:

$$S_k = bl_k^2 \{0.5\rho UB[C_l'(\alpha_0) + \frac{A}{B}C_D(\alpha_0)]\}^2/\pi \quad (for\ [S_{L0}]) \Bigg\}$$
$$S_k = bl_k^2[0.5\rho UB^2C_M'(\alpha_0)]^2/\pi \quad (for[S_{M0}])$$

(20)

Based upon the above equations, the covariance matrix $[D_z]$ of expanded state vector $\{Z\}$ should be the solution of Lyapunov equation, which is:

$$[\overline{A}][D_z] + [D_z][\overline{A}]^T + \pi[\overline{D}][S_0^*][\overline{D}]^T = [0]$$

(21)

By applying the symbol function method for solving equation(21), the matrix $[Dz]$ can be obtained. Then the displacement response vector $\{x\}$ and the response variance σ_s can be calculated.

IV. Numerical Example

After calculating many numerical examples, it is proved that the state-space method is suitable for wind-induced response analysis of suspension bridge. Also it has high accuracy and good convergency. Here, because of limit of paper length, the Golden Gate Bridge over San Francisco bay of US was calculated by state-space method for wind-induced response analysis as a numerical example. The deck data of Golden Gate Bridge are that: The width B $=27.432$m; the average height above mean sea level $Z=65.523$m and $\frac{A}{B}=0.1284$; the main span $L=1280.16$m and side span $Ls=343.01$m; $\rho=1.225$kg/m³, $m_0=34058.63$kg/m, $I_0=3.81005 \times 10^6$kgm²/m; the roughness length $Z_0=0.003048$m. The vibration modes are assumed as follows: 1st torsion is full sine wave over L, $\omega_{a1}=0.41\pi$rad/s; 2nd torsion is half sine wave over L, $\omega_{a2}=0.44\pi$ rad/s; 1st vertical is full sine wave over L, $\omega_{Z1}=0.19\pi$ rad/s; 2nd vertical is half sine wave over L, $\omega_{Z2}=0.268\pi$ rad/s; and the mechanical damping was adopted 2% in all modes. Assumed acrodynamic coefficients are $C_M=1$, $C'_M=-3.67$, $C_L=0$,$C'_L=1.64$ and $C_D=0.3$. The flutter aerodynamic derivatives A_i^* and H_i^* were obtained from Fig. 2 (Bridge 2) of Ref.[1].

The calculation results are shown in Fig. 2 and Fig. 3, which are RMSD responses of bending and torsion wind-induced vibration for Golden Gate Bridge respectively. Also the figures give the comparision of RMSD results calculated by state-space method (SSM) and spectral density method (SDM) respectively at L/4 and L/2 span of bridge . It shows that the results for wind-induced torsion response have very good agreement by these two methods, but the wind-induced bending response has certain error,which does not exceed 5%,and caused from $C_L=0$ assumption. The reason is that the bending vibration of bridge deck is only caused by vertical fluctuating wind action when assuming $C_L=0$ and the fitting of equivalent Бариштейн spectrum and vertical fluctuating wind spectrum is not so excellent.

The Fig. 4 shows the extreme displacement response 3σ(3-RMSD) deck edge deflection. From the figures, it is revealed that the results by state-space method and spectral-density analytical method respectively have very good agreement. Comparing the Fig. 4 with Fig. 2 and Fig. 3,it is important to observe that the torsion response has 80% ratio of total response deflection . This phenomenon also was discovered in experiments. [1]

The Calculation results show that 1. The present state-space method, based upon one-order differential matrix equation, describes the state of a engineering system and offers a effective method of caluclating wind-induced response for large span bridge especially for suspension bridge under gust wind. By introducing the equivalent Бариштейн spectrum of fluctu-

ating and shapping filter of turbulent force, the state-space method avoids a series of complicate generalized intergral calculation and has very high accuracy and good convergence.

References

[1] Scanlan R. H. and Gade, R. H. , J. of structural Division, ASCE, Vol. 103, No. ST9, 1977,pp 1867—1883.

[2] Барцтейн М. Х. , Строителъная Механика II, Раснет Соорунии,1959.

[3] Emil Simiu and R. H. Scanlan," Wind Effects on structures: An Introduction to Wind Engineering ", A Wiley-Insterscience Publication, 1986.

[4] Scanlan, R. H. and Tomko, J. J. , "Airfoil and Bridge Deck Flutter Derivatives", J. of the Engineering Mechanics Division, ASCE, Vol. 97, 1971, pp. 1717—1737.
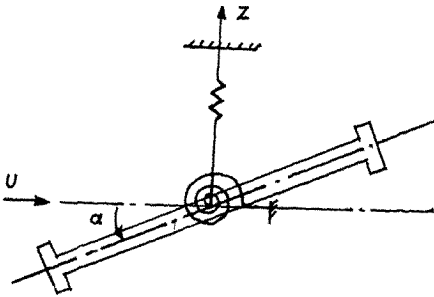
Fig. 1　Degree of Freedom for Deck Section
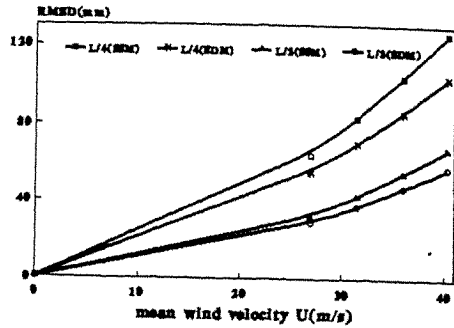
Fig. 2　RMSD Response of Virtical Bending Vibration
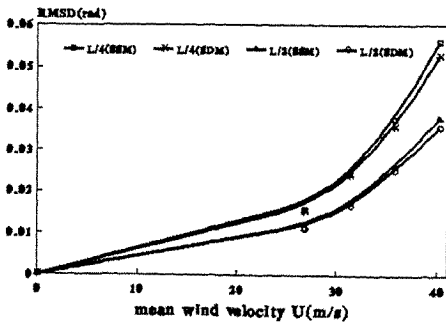
Fig. 3　RMSD Response of Torsional Vibration
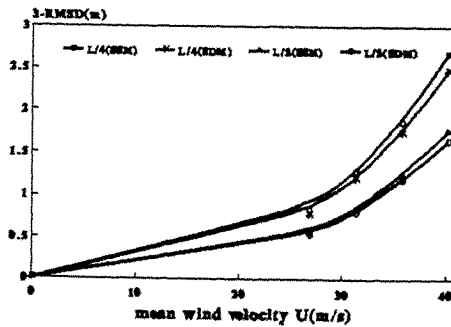
Fig. 4　3σ deck Edge Deflection

Vortex-excited vibration control of bridges using TMD

A. R. Chen, H. F. Xiang and M. Gu

Department of Bridge Engineering
Tongji University, Shanghai, China

Abstract: This paper deals with the suppressing effectiveness of Tuned Mass Damper on vortex-excited vibration of flexible bridges. The nonlinear equations of the deck equipped with TMD is derived. The semi-analytical nonlinear aerodynamic force model at the vortex "lock-in" region is employed, and the approximate solution of the nonlinear equations is given on the quasi-steady motion assumption. The analysis shows that TMD is a very effective mechanical means for suppressing the vortex-excited vibration of bridges. Furthermore, the formulas for optimal "tuning" of TMD are given.

1. Introduction

Vortex shedding is an important aeroelastic phenomenon in wind-induced vibrations of bridges. Some bridge decks, which satisfy the flutter stability requriement, may be set into periodic oscillation by cross wind. Although the wind speed at which vortex-excited vibration occurs is relatively low, the amplitude may be large and the sustained oscillation will cause the fatique of the structure and uncomfort to users. In the vortex "lock-in" region, the response is mainly contributed by self-excited oscillation[1]. So, how to suppress the vortex shedding resonance is one of the main concerns in wind resistant study of bridges.

Recently, passive dampers such as TMD, TLD, TLCD etc have been widely used in vibration reduction of civil structures. As the convenience and effectiveness of passive TMDs, they have been mounted in some existed bridges. Fujino et al examined the damping effect of TMD on galloping of bridge towers[2], Gu et al presented the results of a detailed study on the buffeting suppressing of cable-supported bridge decks with TMD[3]. However. no analysis appears in damping efficiency of passive TMD on vortex-excited vibration of flexible bridges.

In this paper, the study is limited to the case of suppression effectiveness of TMD on vortex-excited vertical vibration of cable-supported bridges. The aeroelastic force model of vortex shedding of the bridge deck at "lock-in" region suggested by Scanlan is adopted[1]. The approximate solution of the nonlinear equations of motion is given by employing the Kroloff-Bogoliuboff averaging method, in which the motion of the system is assumed to be quasi-steady.

2. Equations of Motion

As the vortex lock-in phenomenon selects only one particular mode for "resonance"[1], which might be bending or torsion, the analysis of the suppression effectiveness of TMD on vortex shedding will be discussed with attention to the vertical bending mode. Fig.1 shows the mechanical model of a bridge equipped with TMD at midspan. The vertical displacement X_1 of the deck and the displacement X_2(relative to X_1) of the mass of TMD can be expressed as:

$$X_1 = B\phi(z)\xi_1(t) \tag{1}$$

235

$$X_2 = B\phi(z_0)\xi_2(t) \tag{2}$$
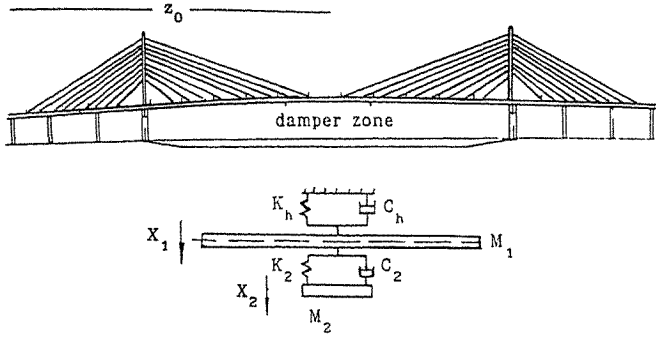
Fig.1. A bridge equipped with TMD.

The motion equations of the system in vertical bending can be written as:

$$\ddot{\xi}_1 + 2\beta_1\omega_1\dot{\xi}_1 + \omega_1^2\xi_1 = -\frac{1}{M_1}\{\rho_a UBL\int_0^L y_1[1-\varepsilon\phi^2(z)\xi_1^2]\phi^2(z)dz\}\dot{\xi}_1 - r\ddot{\xi}_1 - r\ddot{\xi}_2 \tag{3}$$

$$\ddot{\xi}_2 + 2\beta_2\omega_2\dot{\xi}_2 + \omega_2^2\xi_2 = -\ddot{\xi}_1 \tag{4}$$

in which B=bridge deck width, L=lenth of bridge span, $\phi(z)$=vertical bending mode to be controlled, $\phi(z_0)$=mode value of the deck at which TMD mounted; ρ_a=air density, U=vortex "lock-in" wind speed. ξ_1 and ξ_2 are generalized coordinates of bridge deck and TMD mass, respectively. y_1 and ε are aerodynamic coefficients, β_1 and β_2 are damping ratios of the main system and TMD, respectively. ω_1 and ω_2 are circular frequencies of main system and TMD, respectively. $M_1 = \int_0^L m\phi^2(z)dz$, generalized mass of bridge deck, where m is mass per unit span; $M_2 = m_2\phi^2(z_0)$, m_2 is mass of TMD; $r = M_2/M_1$, the generalized mass ratio of TMD to the deck. Let

$$a_1 = \int_0^L \frac{\phi^2(z)}{L} dz \tag{5}$$

$$a_2 = \int_0^L \frac{\phi^4(z)}{L} dz \tag{6}$$

then, Eq.(3) and (4) can be rewritten as:

$$\ddot{\xi}_1 + 2\beta_1\omega_1\dot{\xi}_1 + \omega_1^2\xi_1 = \frac{\rho_a UBL}{M_1} y_1(a_1\dot{\xi}_1 - \varepsilon a_2\xi_1^2\dot{\xi}_1) - r\ddot{\xi}_1 - r\ddot{\xi}_2 \tag{7}$$

$$\ddot{\xi}_2 + 2\beta_2\omega_2\dot{\xi}_2 + \omega_2^2\xi_2 = -\ddot{\xi}_1 \tag{8}$$

Actually, y_1 and ε represent aerodynamic damping and nonlinear aerodynamic response coefficients, which must be evaluated by experiment. According to the identification method developed by Scanlan[1], let $[X_{01},\beta_{01}]$ and $[X_{02},\beta_{02}]$ be the pairs of amplitude and corresponding mechanical damping ratios used in two successive deck model "resonance" experiments at the "lock-in" Strouhal frequency, then

$$y_1 = \frac{R[\beta_{h1}-(X_{01}/X_{02})^2\beta_{h2}]}{1-(X_{01}/X_{02})^2} \tag{9}$$

$$\varepsilon = \frac{4B^2}{X_0^2}(1-R\frac{\beta_h}{y_1}) \tag{10}$$

$$R = \frac{4\pi mS}{\rho_a AB} \tag{11}$$

where A=the cross-flow projected aera of the bridge deck per unit length, S=Strouhal number. In Eq.(10), the data either in (X_{01},β_{h1}) or (X_{02},β_{h2}) can be used as (X_0,β_h).

3. Approximate Solution

As Eq.(7) and (8) are nonlinear coupled differential equations, it is difficulty to get an analytical solution. In the analysis, the approximate solution is given on the quasi-steady motion assumption, namely

$$\xi_1(t)=\Lambda_1 e^{i\omega t} \tag{12}$$

$$\xi_2(t)=\Lambda_2 e^{i\omega t} \tag{13}$$

in which Λ_1 and Λ_2 are complex constants, ω is the circular frequency of the coupled system. From Eq.(8), one obtain

$$\Lambda_2/\Lambda_1=\zeta+i\eta \tag{14}$$

where

$$\zeta=\delta^2(\Omega^2-\delta^2)/\{(\Omega^2-\delta^2)^2+(2\beta_2\Omega\delta)^2\} \tag{15}$$

$$\eta=-\delta^2(2\beta_2\Omega\delta)/\{(\Omega^2-\delta^2)^2+(2\beta_2\Omega\delta)^2\} \tag{16}$$

in which $\delta=\omega/\omega_1$, $\Omega=\omega_2/\omega_1$. Ω is the frequency "tuning" ratio of TMD.

From Eq.(13), we get

$$\ddot{\xi}_2(t)=-\omega\zeta\xi_1(t)-\omega\eta\dot{\xi}_1(t) \tag{17}$$

then, Eq.(7) can be simplfied as:

$$\ddot{\xi}_1 + \omega_1^2 \xi_1 = f(\xi_1, \dot{\xi}_1) \tag{18}$$

in which

$$f(\xi_1, \dot{\xi}_1) = \frac{\rho_a UBL}{M_1} y_1 (a_1 \dot{\xi}_1 - \varepsilon a_2 \xi_1^2 \dot{\xi}_1) + r\omega\eta\dot{\xi}_1 +$$

$$+ r\omega^2 (\zeta + 1)\xi_1 - 2\beta_1 \omega_1 \dot{\xi}_1 \tag{19}$$

The solution is assumed in following forms:

$$\xi_1 = a \cos(\omega t - \psi) \tag{20}$$

$$\dot{\xi}_1 = -\omega a \sin(\omega t - \psi) \tag{21}$$

in which a and ψ are slowly varying functions of time, then,

$$\dot{a} = \frac{1}{2\pi\omega} \int_0^{2\pi} [f(\xi_1, \dot{\xi}_1) + a(\omega^2 - \omega_1^2)\cos\tau]\sin\tau \ d\tau \tag{22}$$

$$\dot{\psi} = \frac{1}{2\pi\omega a} \int_0^{2\pi} [f(\xi_1, \dot{\xi}_1) + a(\omega^2 - \omega_1^2)\cos\tau]\cos\tau \ d\tau \tag{23}$$

The conditions for steady-state vibration are

$$\dot{a} = \frac{da}{dt} = 0 \tag{24}$$

$$\dot{\psi} = \frac{d\psi}{dt} = 0 \tag{25}$$

Eq.(24) yields the amplitude of the vibration as follows

$$a = 2\sqrt{\frac{a_1}{\varepsilon \ a_2}} \ [1 - \frac{4\pi m(\beta_1 - r\delta\eta/2)S}{\rho_a ABy_1}]^{1/2} \tag{26}$$

in which $\omega A/U = 2\pi S$. It can been seen in Eq.(26) that the effect of passive TMD to the main structure is equal to adding an equivalent damping ratio which is given as

$$\beta_e = -r\delta\eta/2 \tag{27}$$

From Eq.(25), we have

$$\delta^2 = 1 - r\delta^2(\zeta + 1) \tag{28}$$

By using an iterative procedure, the value of δ can be determined.

4. Optimization of TMD Parameters

In practical design of TMD, the displacement ratio ρ and the phase lag θ

between TMD and the deck must be taken into consideration. ρ and θ are defined as

$$\rho = |\frac{\xi_2}{\xi_1}|_{\max} = \sqrt{\zeta^2 + \eta^2} \qquad (29)$$

$$\theta = \tan^{-1}(\eta/\zeta) + 180° \qquad (30)$$

From the analysis, the equivalent damping ratio β_e, δ, ρ and θ all are function of TMD "tuning" parameters r, Ω and β_2.

Fig.2 shows that β_e is sensitive to Ω and the peak equivalent damping ratio can be achieved when Ω is close to 1. Fig.3 shows the generalized mass ratio r has no effects on phase lag θ if β_2 is given, furthermore, θ varies with β_2 when r is given. At the peak of β_e, $\theta \approx 90°$. From Fig.4, it can be seen that r has no effect on ρ, but ρ is sensitive to β_2. Fig.5 shows that if r and Ω are given, there is an optimal value of β_2 at which β_e becomes maximum.

Fig.2. β_e — Ω.   Fig.3. θ — Ω.   Fig.4. ρ — Ω.
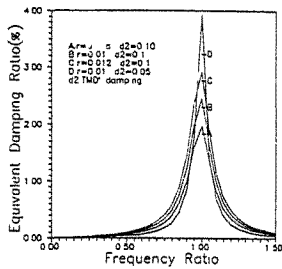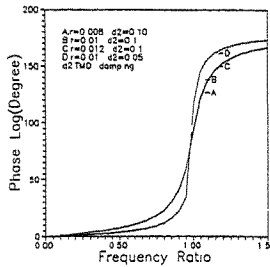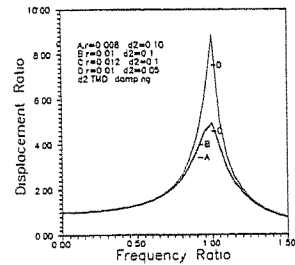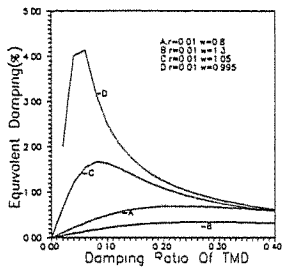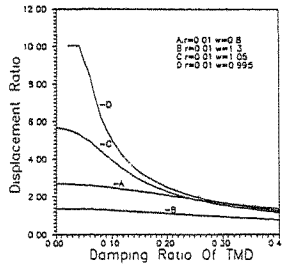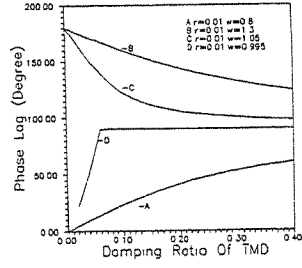
Fig.5. β_e — β_2.   Fig.6. ρ — β_2.   Fig.7. θ — β_2.

It is obvious, when $\theta \approx 90°$, $\zeta = 0$, the peak of β_e is achieved. Hence, the formulas for the best "tuning" of TMD are given below

239

$$(\delta)_{op} = 1 - \frac{r}{2} \tag{29}$$

$$(\beta_e)_{op} = \frac{r}{2} (\rho)_{op} \tag{30}$$

$$(\Omega)_{op} = (\delta)_{op} = \frac{r}{2} (\rho)_{op} \tag{31}$$

$$(\beta_2)_{op} = \frac{1}{2(\rho)_{op}} \tag{32}$$

in which $(-)_{op}$ denotes the optimum parameters.

5. Application

Consider an example(presented in Ref.[1]) of a cable-supported bridge with a main span of L=183 m and a mass per unit span m=6709 kg/m. Assume a Strouhal number of S=0.15 at a frequency f=0.5 Hz, with a corresponding bridge vertical mode that is a half sine wave over the span. Assume a deck width B=9.15 m, a frontal area per unit span of A=1.52 m.

From a 1/30 scale section model, 1.53 m long, of the bridge tested at vortex "lock-in", one get R=742.3, y_1=33.4, ϵ=8075, a_1=0.5, a_2=0.375. Assume the damping ratio of the bridge β_1=0.01, the maximum vortex-excited amplitude at midspan X_1=0.207 m. A TMD with r=0.01, β_2=0.1 and Ω=0.995, is attached at the midspan, then, β_e=2.475%, ρ=5, the displacement at midspan X_1=0.112, the reduction ratio is about 46%.

6. Conclusions

1. Passive TMD is a very effective means for reducing vortex-excited vibration of bridges. The effectiveness is equal to adding an equivalent damping ratio to the bridge.

2. According to the optimal analysis, the peak effectiveness of TMD will be achieved when the phase lag between TMD and the deck θ=90°. The selection of the displacement ratio is important in practical design of TMD.

Acknowledgement

References

1. R.H. Scanlan, Report No. FHWA/RD-80/050,(1981).
2. Y. Fujino, P. Warnitchai, M. Ito, J. of the Faculty of Engrg. the University of Tokyo, Vol.38, No.2,(1985)49.
3. M. Gu, H. Xiang, Journal of Wind Engineering and Industrial Aerodynamics, Vol.42, No.2,(1992)1383.

Numerical Simulation of Flow Around Bridge Deck
by the Penalty—Hybrid/Mixed FEM

B. Zhu and D. P. Chen[+]

Bridge & Underground Engineering Department, Southwest
Jiaotong University, Chengdu, Sichuan 610031, China
[+]Computational Mechanics Department, Southwest Jiaotong
University, Chendu, Sichuan 6100031, china

Abstract: This paper describes a numerical simulation method for analyzing the areo — dynamic characteristics of bridge deck. A pseudo — penalized multi — field variational principle for unsteady incompressible viscous flow is proposed via perturbed—Lagrangian methodology, based on which a penalty — hybrid/mixed finite element formulation is established. As the first trial, the two — dimensional flow around the bridge deck is simulated by the penalty hybrid/mixed FEM.

1. INTRODUCTION

Flow around bluff bodies such as bridges, buildings and so on are offen encountered in wind engineering problems. Studies on such problems are of practically extra — ordinary significance in determining the reasonable wind load for structure designs as well as in establishing the effects on environments due to the flow around structures under consideration.

Basically, interactions between bridge and air is a problem with flow around bridge under very complicated geometrical boundary conditions. Existed investigations mainly involved with wind tunnel model tests. In recent years, in pace with the advent of computers with increasingly enhanced speed and core storage together with that of the noticeably improved computational techniques, investigation on flow around bridge featuring joint efforts of numerical analysis and wind tunnel tests has aroused significant research interests.

A pseudo — penalty hybrid/mixed variational principle for unsteady incompressible Navier-Stokes flow analysis is established by assuming independently velocity field and deviatoric stress field which is related to the hydrostatic pressure via the homogeneous equilibrium equation. In order to overcome the difficulties encountered in dealing with the

241

incompressiblity constraints and the velocity field, in the present paper, the penalty hybrid/ mixed finite element model is incorporated in the perturbed — Lagranean fomulation. As such, the incompressibility constraint is replaced by the slightly compressible condition. A fact that enables the nodal velocities to remain as the sole solution unknowns in the final finite element matrix equations.

2. THE FINITE ELEMENT MODEL

As long as the speed of air flow encountered in wind engineering problems is rather low, usually the flow is considered incompressible. The discussions herein presented are mainly based on the penalty — hybrid/mixed pseudo — variational functional for unsteady Navier — Stokes flow analysis[1].

$$\Pi(\sigma_1, p, u) = \Sigma\{-(1/2)\int_{V_*} \sigma_1^T S \sigma_1 dV + \int_{V_*} \sigma_1^T (Du) dV$$
$$- \int_{V_*} p(div u) dV - (\varepsilon/2)\int_{V_*} p^2 dV$$
$$+ \int_{V_*} \rho \overline{[\frac{\partial u}{\partial t} + (u \cdot \nabla)u]} u dV - W\}$$ (1)

where σ_1 is the deviatoric stress vector, p the hydrostatic pressure, u the velocity vector, S the deviatoric compliance matrix, ∇ the Hamilton operator, and W the external work. Note that $[\; \cdot \;]$ is not subjected to variation.

In finite element formulation[2,3,4], assume individually over each element

$$\sigma_1 = P(x)\beta,$$ (2)

$$u = N(x)q, \qquad \forall \; (x) \in V_*$$ (3)

and, the hydrostatic pressure is available via the homogeneous equilibrium equations

$$\sigma_1 \cdot \nabla - \nabla p = 0$$ (4)

Accordingly, one has

$$p = \alpha_* + P'(x)\beta$$ (5)

where P (x) is the deviatoric stress interpolation matrix, N (x) is the shape function, β represent the unknown parameters, and, α_n is the constant to be determined.

Using eqns(2), (3)(5)and(1), via $\delta\Pi = 0$, the following final finite element matrix equations are available

$$M\frac{dq}{dt} + [K_1 + \frac{1}{\varepsilon}K_2 + K_3(q)]q = Q$$ (6)

where M, K_1, K_2, K_3(q), Q are the global mass, stiffness and consistent load matrices

respectively, The corresponding element mass matrix and element stiffness matrix are

$$\underset{\sim}{m}^{(e)} = \int_{V_e} \rho \underset{\sim}{N}^T \underset{\sim}{N} dV, \qquad \underset{\sim}{k}^{(e)} = \underset{\sim}{k}_1^{(e)} + \frac{1}{\varepsilon}\underset{\sim}{k}_2^{(e)} + \underset{\sim}{k}_3^{(e)},$$

with $\underset{\sim}{k}_1^{(e)} = \underset{\sim}{G}^T \underset{\sim}{H}^{-1} \underset{\sim}{G},$

$\underset{\sim}{k}_2^{(e)} = \underset{\sim}{S}^T \underset{\sim}{S}/V,$

$\underset{\sim}{k}_3^{(e)}(\underset{\sim}{q}) = \int_{V_e} \rho \underset{\sim}{N}^T [(\underset{\sim}{u} \cdot \nabla)\underset{\sim}{N}] dV,$

$V = \int_{V_e} dV .$ (7)

It shoud be pointed out that in eqn. (6) only the nodal velocity $\underset{\sim}{q}$ are involved as

unknowms.

3. NUMERICAL CALCULATION SCHEME

In solving the finite element matrix equation(6), the backword difference scheme is adopted

i. e.

$$\frac{d\underset{\sim}{q}}{dt} = \frac{\underset{\sim}{q}^{(t)} - \underset{\sim}{q}^{t-\Delta t}}{\Delta t} .$$ (8)

Substituting eqn. (8) into (6), one has

$$\frac{\underset{\sim}{M}}{\Delta t}\underset{\sim}{q}^t + [\underset{\sim}{K}_1 + \frac{1}{\varepsilon}\underset{\sim}{K}_2 + \underset{\sim}{K}_3(\underset{\sim}{q}^t)]\underset{\sim}{q}^t = \underset{\sim}{Q} + \frac{\underset{\sim}{M}}{\Delta t}\underset{\sim}{q}^{t-\Delta t}$$ (9)

In the above equation, Δt is the time step which should be appropriately selected; $\underset{\sim}{q}^{t-\Delta t}$ is the initial velocity field or the velocity field of the previous stage, both being known quantites. The velocity field for time t is available via iteration. And, $\underset{\sim}{q}^{t+\Delta t}$ is obtained on the basis of $\underset{\sim}{q}^t$. As such, the velocity field for every time stage can be obtained.

4. NUMERICAL EXAMPLE

(1)Square cylinder

Numerical analysis of the flow around square cylinder is conducted at Re = 4. 8 × 10^5. Fig. 1 demonstrates the finite element mesh and boundary conditions with 238 eight—node elements. In Fig. 2, the areodynamic coefficients are plotted against time. As can be seen, C_L is basiclly zero when C_D is around 2. 0.   Hence, remarkable coincidence with

the experimental results $(C_D = 2.03, C_L = 0)$ is achieved. Fig3. demonstrates the velocity field at $t = 2$ sec.
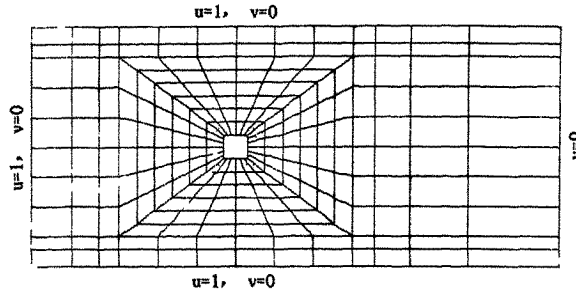
Fig. 1. Mesh Configuration and Boundary Condition
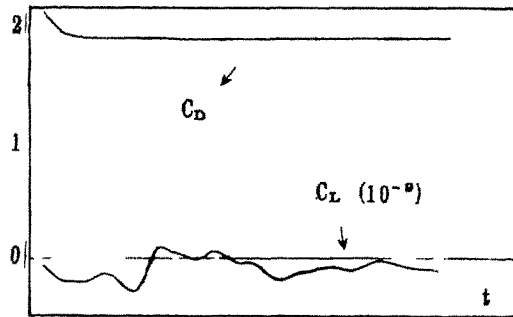
Fig. 2. C_D, C_L of the square cylinder
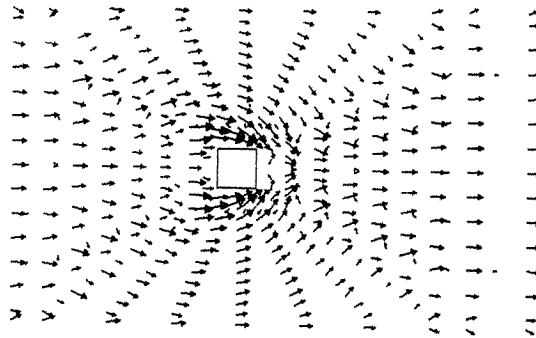
Fig. 3. Velocity Field Around the Square Cylinder

(2) A bridge deck

Numerical analysis of the flow around a bridge deck is conducted at $Re = 2.4 \times 10^6$,

244

Finite element mesh with 232 eight — node elements and boundary conditions are demonstrated in Fig. 4. where zero initial velocity field is used. Fig. 5 gives the velocity field at t = 2 sec. The figures indicate the flow separating at the corner. The pressure contour is available in Fig. 6.
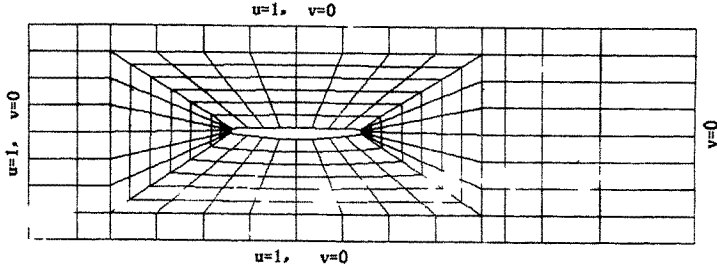
Fig. 4. Mesh Configuration and Boundary Condition
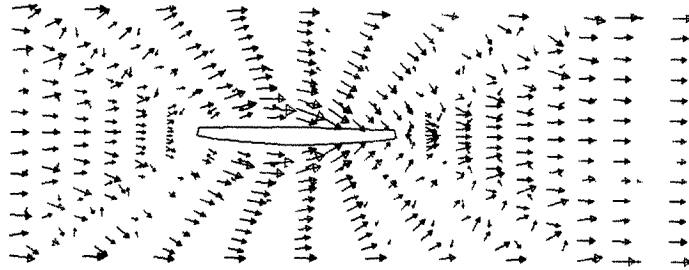
Fig. 5. Velocity Field Around the Bridge Deck

Fig. 6. Pressure Contour Around the Bridge Deck

245

5. CONCLUDING REMARKS

(1)Based on the hybrid/mixed finite element model,numerical calculation results for flow around a bridge deck are presented. Although the two—dimensional flow model does not exactly describe the actual flow, the feasibility of the present H/M FE model for application to bridge deck analysis is apparent.

(2)It is obvious that the analysis of the flow separation is possibly achieved by use of the hybrid/mixed FE model even if relatively high Reynolds number is involved in flow around bridge decks.

Acknowledgement

References:

1. B. Zhu,Numerical solution of flow around bluff body by the penalty hybrid/mixed FEM ,Ph. D Thesis,Southwest Jiaotong University,July,1993.

2. D. P. Chen,Z. Zhao,'Numerical analysis of incompressible flow using a new finite element formulation' ,Proc. 6th Int. Conf. Num. Meth. ,Laminar & Turbulent Flow, eds. C. Taylor,et al,169—177,1989.

3. D. P. Chen,Z. Zhao,'A penalty—hybrid finite element method for the analysis of Stokes flow' ,Compt. meth. ,eds. S. N. Atluri,G. Yagawa,Springer—Verlay,1988.

4. B. Zhu,D. P. Chen,J. S. Shang,'Wind loads on bridge deck by penalty-hybrid/mixed FEM' ,Reprints vol. 1,BBAA2,Melbourne,Australia,Dec. 1992.

A STUDY OF WIND-RESISTANT STABILITY OF LONG-SPAN CABLE-STAYED STEEL BRIDGE

Hou Wen Wei

Associated Researcher
China Academy of Railway Sciences

Of the large span bridges, cable-stayed and suspension bridges are the most popular ones. Over the decades, since the Tacoma cable-stayed bridge in the United States was broken due to its flutter at a wind velocity of 19m/s, the wind-resistant stability of cable-stayed and suspension bridges has become a key research subject and has led to positive results. This paper describes the study on wind-resistant stability of long-span cable-stayed steel bridge.

1. Relationship between Natural vibration Characteristics and Wind-Resistant Stability of the Existing Cable-Stayed Bridge

Wind engineering research on bridges is focussed on the follows:

1) Study of the theory on bridge flutter and the testing methods
2)Study of the limited amplitude excitation of bridge caused by vertex shedding.
3)Study of wind-induced beam buffet and cable gallap.
4) Inspection, through wind-tunnel testing, of the aerodynamic elasticity characteristics of various bridge cross sections and the applicability of the auxiliary facilities for obstacle flow and diversion flow.

The high light of study on wind-resistant stability of cable-stayed bridge is the critical wind velocity of flutter, it is set higher than the designed velocity. The excitation caused by vortex shedding should not take place at an mean velocity and should be limited within the permissible range of amplitude.

To reach this end, the study is focussed on the first bending and torsional frequency of the bridge structure in considering that bridge flutter is typically the mode of torsion-bending coupling vibration or torsional vibration.

According to the information related to the tunnel tests on twenty double-tower cable-stayed steel bridges of various spans in Japan, France, Canada, Argentina, BRD and Yugoslavia, etc., following formulas have been worked out:

The relationship between the first bending frequency and the span of a double-tower cable-stayed steel bridge is expressed by:

$$F_b = 98.0748/L^{0.95} \qquad (1.1)$$

Where, F_b ---the first bending frequency
       L ---the span

The relationship between the first torsional frequency and the span of the double tower cable-stayed steel bridge is:

$$F_t=184/L^{0.90} \qquad (1.2)$$

Where: F_t ---the first torsional frequency.

The torsional frequency is related to the height-width ratio of the bridge, the relationship is shown by:

$$F_t=4.7122/\gamma^{0.72} \qquad (1.3)$$

The formula of Vankaman can be used to calculate the critical wind-velocity for a structure flutter based on (1.1) and (1.2).

2. Three-Dimensional Analysis of Bridge Flutter

Flutter of an elastomer in the fluid suggests a profound physical relationship. In the point of its causes in terms of aerodynamics, flutter can be classified into two types. The first one is featured by a coupling of multi-degree of freedom. Typically taking place in the potential motion of the fluid, it receives less influence from fluid separation and boundary layer effect. The second one, however, is featured by mono-vibration. It is directly related to fluid separation and creation of whirlpool. As the physical phenomenon is concerned, when the motion of elastomer in the fluid is stable, the fluid induces damping force while absorbing the energy created by the motion. But, when the motion accelerates to a certain speed, the force turns to supply the elastomer with energy, leading to a shedding motion.

Two-dimensional analysis theory should be adopted in the primary analysis of the flutter of the suspension bridge. It is based on the view that vertical and torsional vibration of the bridge are coincident with each other, so that the segment flutter characteristics of an independent segment represent that of a suspension bridge, Scanlan summarizes the two-dimensional equation as follows:

$$\ddot{h}+2\,\zeta\,bFb\dot{h}+Fbh=H_1\,h+H_2\,\dot{\phi}+H_3\,\phi$$
$$\ddot{\phi}+2\zeta\,\tau\,F\tau\,\dot{\phi}+F\tau\,\phi=A_1\,h+A_2\,\dot{\phi}+A_3\,\phi \qquad (2.1)$$

By means of wind-tunnel testing on segment models, $H_1(K)$, $H_2(K)$, $H_3(K)$, $A_1(K)$, $A_2(K)$, $A_3(K)$ can be measured at different wind velocities.

Where: h and ϕ are coordinates of vertical and torsional motion respectively.

ζ_b, ζ_T --- Damping ratio of vertical and torsional motion.

F_b, F_T --Self-induced vibration frequency of vertical and torsional motion.

Critical wind velocity of structure flutter could be obtained from the above.

However, the assumption that the flutter characteristic of an independent segment can represent that of a bridge is to be proved for the bending and torsional vibration forms of the cable-stayed bridge, as shown in the figure, are not coincident with each other, though similar. The effects of the coupling of various vibrations on the flutter is to be explored since a bridge demonstrates different vibration forms in the three-dimensional space, and, the complex action of wind to bridge and the changeable longitudinal wind field is to be alerted. Therefore, the issue of three-dimensional analysis is being focussed with the deepening of the study on wind-induced bridge vibration.

For which, a hypothesis of air narrow piece is established, namely, the value of aerodynamic force acting on any cross section of a structure is considered to be the same as that when a cross section is assumed to be a two dimensional one. According to this hypothesis, coefficient of aerodynamic force of the two-dimensional segment model test could be directly adopted in three-dimensional analysis on structure flutter.

Provided that the aerodynamic force of individual joints of a structure are given(derived from the following equation), the flutter equation becomes:

$$[M]\{\ddot{X}\}+[c]\{\dot{X}\}+[K]\{X\}=[L_1 \quad]\{\ddot{X}\}+[L_2 \quad]\{\dot{X}\}+[L_3 \quad]\{X\}+[L_4 \quad] \quad (2.2)$$

In considering that the acceleration and constant terms exert less influence to aerodynamic force and frequency respectively, the first and fourth terms have been omitted and the original coordinate is superseded by a normal one.

Equation(2.2) normalizes to:

$$[M]\{\ddot{g}\}+[w^2 M]\{\dot{g}\}+[c]\{g\}=[L_2]\{\dot{g}\}+[L_3]\{g\} \quad (2.3)$$

It reduces to:

$$[M]\{\ddot{g}\}+([w^2 M]-[L_2])\{\dot{g}\}+([c]-[L_3])\{g\}=0 \quad (2.4)$$

Makes $[k]=[w^2 M]-[L_2]$

$$[D] = [c] - [L_2]$$

Add one equation: $[M]\{\dot{g}\} - [M]\{\dot{g}\} = 0$ (2.5)

Group the two equations:

$$\begin{bmatrix} 0 & [M] \\ [M] & [D] \end{bmatrix} \begin{Bmatrix} \dot{g} \\ g \end{Bmatrix} + \begin{bmatrix} -[M] & 0 \\ 0 & [k]^* \end{bmatrix} \begin{Bmatrix} g \\ \dot{g} \end{Bmatrix} = 0 \quad (2.6)$$

Make $u = \begin{Bmatrix} \dot{g} \\ g \end{Bmatrix}$ $\dot{u} = \begin{Bmatrix} \ddot{g} \\ \dot{g} \end{Bmatrix}$ {

$$A = \begin{bmatrix} -[M] & 0 \\ 0 & [k]^* \end{bmatrix} \qquad B = \begin{bmatrix} 0 & [M] \\ [M] & [D] \end{bmatrix} \quad (2.7)$$

Equation(2.6) reduces to $Bu + A\dot{u} = 0$

Make $u = u_e\, e^{-\lambda t}$ $\dot{u} = -\lambda\, u_e\, e^{-\lambda t} = -\lambda \cdot u$

Fig. 2.1

Then, equation(2.7) has $Au = \lambda Bu$, this is the well known eigenequation, with the difference of   is a complex eigenvalue and u a complex eigenvector.

Here, the aerodynamic coefficient matrices $[L_1]$ and $[L_2]$ in equation(2.3) is considered.

By means of wind tunnel test on segment model, aerodynamic coefficient could be obtained and be reduced to joint aerodynamic force.

Where, lift force $Li = mi(H_1\, Y + H_2\, \phi + H_3\, \phi)$ $i = 1 \ldots\ldots NAN$
    lift force moment $Mi = Ii(A_1\, Y + A_2\, \phi + A_3\, \phi)$

NAN is a element of aerodynamic force. By using the form function expressed in the text book and imaginary principle, aerodynamic coefficients in various directions and further, the elementary aerodynamic force matrices could be obtained.

By grouping together the joint aerodynamic force of each element, matrices $[L_1]$ and $[L_2]$ could be obtained. By solving for the complex eigenvalue of equation(7), flutter reduction frequency could be achieved and the frequency and the relative flutter critical wind velocity could be derived.

Fig.2.1 shows the calculating program.

This program could be used to solve for the three-dimensional characteristic of structure flutter with different element length

250
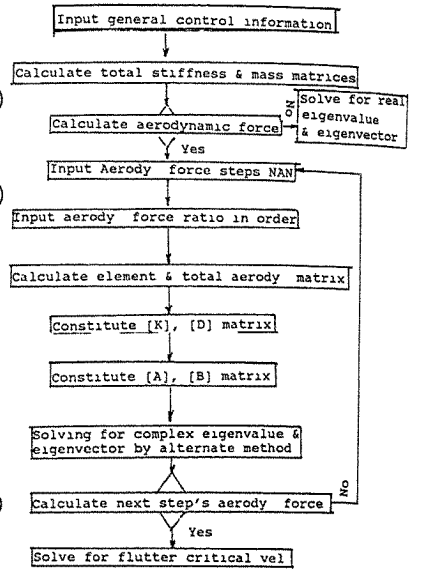
and aerodynamic force, including phase difference between various vibrations. It also can be used to analyze three-dimensional natural vibration characteristic of structure.

3. Wind-Resistant Stability of Railway Long-Span Cable-Stayed Steel Bridge

As compared with highway bridge, railway bridge, due to its large live load, is much stronger in bending rigidity, larger in beam height and smaller in width. In considering of railway's clearance limitation, the width of even a double track railway is limited in over ten meters, which increases the ratio between the beam height and width. In view of the construction cost, however, the width of the bridge should be minimized. Therefore, the improvement of wind-resistant stability of railway long-span cable-stayed steel bridge lies in a rational ratio of bending-torsional frequency.

To study the wind-resistant stability of railway long-span cable-stayed steel bridge, double track railway suspension cable-stayed steel bridge with a mid-span of 336m is taken as an example. Fig.3.1 shows the possible alternative of the bridge and its calculating diagram. It is a steel bridge with reinforced concrete towers. In the calculating mode, thickly spaced cables are converted into thinly spaced one. Two types of cross sections are designed, for the first alternative, cross section of the bridge is of a longitudinal-lateral beam system with steel box beam and reinforced concrete deck, the second alternative is of a system with steel box beam and orthotropy deck. As shown in Figure 3.2, the calculation is based on the conditions that the bridge is free from train load and one track is zhong-22 class loaded. In the Figure, cross beams do not exceed the steel box, in the calculation mode, the cross beam is hinged to the main girder, the calculation results are summarized in table 1.

· Fig. 3.3 shows some vibration modes. Alternative one indicates that when the bridge is loaded by train, the vibration mode of the first bending is not coincident with that of the first torsion, therefore, coupling flutter should not take place.

As expressed in the table, the lowest critical wind velocity for both alternatives has reaches to 3.5m/s, though facilities of diversion flow are not installed and the stream line design is not adopted. This critical value, however, can not meet the demand in case that the bridge is much higher than the water level. In view of the above, the cross section of the bridge is modified, as shown in Fig.3.4, leading the cross beam through the main girder. In the calculating mode, the increase of restraint of the mid-cross beam on rotating angle of the main girder in X direction contributes a great improvement to wind-resistant stability of the bridge. See table 2.

Wind resistant stability of cable-stayed steel bridge can be guaranteed by optimizing the bridge configuration, for example,

251

an up side down trapeze double-box type with minimized beam height.

Lateral vibration of tower imposes influences to beams, either the coincident or criss-cross vibration may induce torsional vibration of beams. Therefore, study on lateral vibration of tower is recommended as a special subject which may include a single tower or the control of lateral natural vibration of tower.

In this alternative, the natural vibration characteristics of beams, cables and towers are separated in calculation, the calculation of cables is based on their primary forces and length, with different frequencies.

Fig.3.1

4. Conclusion
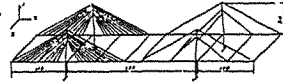
This article, based on aerodynamic characteristics of twenty bridges in the world, summarizes the formulas of the relationship between the first bending frequency and span, the torsional frequency and span, and, the torsional frequency and height-width ratio. The paper derives a calculation method and solving program for three-dimensional flutter directivity characteristics, which may be helpful to the analysis of flutter performance of a segment or a bridge as a whole. Taking a 336m span cable-stayed steel bridge as an example, critical velocity of the flutter of this bridge is calculated and its torsion-resistant mode for railway cable-stayed bridge put forward.

Table 1

	Frequency	Alternation one		Alternation 2	
		unload	loaded	unload	loaded
Vertical	1	0 5059	0.4273	0.6975	0.5469
	2	0 6891	0.6106	0.9308	0.787
Lateral	1	0 202	0 1724	0.2057	0.1503
	2	0.5759	0.5116	0 5957	0.7288
	3	0 774	0.7491	0.8002	0.8936
Torsional	1	0 6839	0.62	0.9458	0.6999
	2	0.8913	0.8137	1.162	0.9168
Tor.-bend fre. ratio		1.36		1.28	1.36
Critical wind vel.of flutter		37.226		46 84	50 64
Flutter mode				Bend, torsion, Longitudinal	

Table 2

	Frequency	Alternation one	Alternation 2
Vertical	1	0 5037	0.6975
	2	0 6888	0 9308
	3	0 9266	1.1936
Torsional	1	1 4507	1 6604
Tor.-bend fre. ratio		2.88	2.38
Critical wind vel.of flutter (m/s)		90	99
Flutter mode		Bend, torsion	Bend, longi. torsion

Fig.3.2

(a) Model, loaded

(b) Model, with calculate mode changed

Fig. 3.3

252
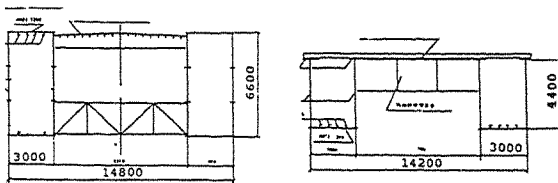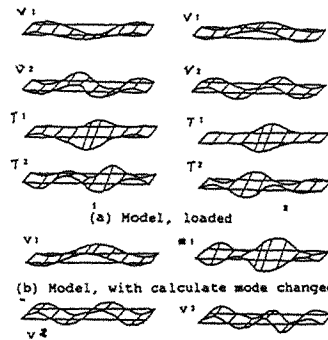
Tall Buildings

A Parametric Study of Dynamic Wind Loads on Buildings

B.E. Lee, S. Lui[*], Q. Wang[*] and C. Xie[*]

School of Civil Engineering
University of Portsmouth, UK
[*]Institute for Low Speed Aerodynamics
China Aerodynamics Research and Development Centre
Sichauan, China

Abstract: This paper presents the current status of a joint UK – China project on the measurement of dynamic wind loads on buildings being carried out at the China Aerodynamic Research and Development Centre. The wind tunnel based project is on-going and currently scheduled to run for a number of years. This paper reports the objectives behind the project and indicates some conclusions based on the results currently available.

1. Introduction

The purpose of the project is to help establish the confidence limits with which dynamic wind loading design data can be used in practice. It has been established previously that a number of simplifying assumptions are required in order to construct either a physical or mathematical model of the relationship between the wind structure and the building response for buildings of given shape in known locations. Since these simplifying assumptions are treated differently by different wind tunnel directors and the authors of different numerical prediction methods, considerable uncertainty may surround the results yielded for any one-off test or calculation. Thus the level of confidence which the structural engineer has when asked to use the results of a single test is low, leading to uncertainties in the safety factor associated with the design, or alternatively, a conservative but costly structural solution. The hypothesis of this project is that the structural engineer using such results, or the wind engineer supplying them, would be in a far better position to exercise judgement in their interpretation if more information were available regarding their potential variability as functions of the parameters which influence the simplifying assumptions referred to earlier.

2. Project Objectives

In order to establish the confidence levels which should be associated with the evaluation of dynamic wind loads determined from physical model studies it is necessary to carry out a parametric test series of wind tunnel experiments to meet the following specific objective.

These are: to determine the effect on the modal loads of

(i)   the effect of different terrain roughness for buildings of a fixed shape and size,
(ii) the effect of changes of terrain roughness at different fetch lengths upstream for a given building,
(iii) the effect of changes of building shape,
(iv) the influence of overall size for given shaped buildings in a given terrain situation,
(v)   the effect of incident wind angle for buildings of simple shape, and
(vi) the effect of increasing incident mean wind speed,

Objective (iv) is important because it has a number of purposes which may be illustrated as follows. If a building of a given height, say 100m, is to be built in a given terrain location it may be modelled at a selected scale ratio, say 1:500, to yield a model size, 200mm high, in a modelled boundary layer whose length scale is also 1:500. Modal forces can then be scaled up from model to full size using conventional equations. If a model scaled at 1:250, 1:200 or even 1:100 were then to be testing in the same boundary layer flow the results could also be scaled up to full size by the same equations and compared with the original test. Any lack of agreement between the results may be considered to be a result of the "scaling mismatch" between the model and the boundary layer if wind tunnel blockage effects are accounted for. Such an exercise yields valuable information on the validity of model tests. However, if an identically shaped building of a different size, say 200m high, were to be built in the same terrain location a true 1:500 scale model would now yield a model size of 400mm, i.e. the same size as the 1:250 scale model of the 100m building - formerly a "scale mismatch" but now the correct scale for the larger building. It will be significant to determine from these tests whether or not the correct scale wind tunnel tests for buildings of different sizes bear the same relationship to each other as that indicated by the results of difference empirical calculation methods applied to buildings of different sizes. This exercise will be a test of the spatial integrity of the turbulence characteristics of the terrain simulation as much as of the turbulence descriptions built into the calculation methods.

The results of Objective (v) will help to clarify the validity of empirical calculation methods in terms of directional sensitivity. If the model studies confirm earlier findings, Ref(1), that modal loads on rectangular plan form buildings are at a maximum when the wind is normal to a face and decrease for oblique wind directions then the finding will lend confidence to the use of calculation methods which are usually only valid for normal wind angles. Hence in these circumstances calculation methods will yield conservative results for most wind directions.

3. Experimental Arrangements
The experiments are being conducted in the CARDC FL-11 low speed open circuit, wind tunnel whose shape has been modified to carry out these experiments, being 1.4 x 1.4m in cross section and having a

256

working section length of 6m. Simulated atmospheric boundary layers are created in the upstream part of the working section by a fence, spires and roughness elements arrangement to yield a range of boundary layers whose length scales vary in the range 1:250 to 1:350 based on spectral scaling. This range of boundary layers have parameters characteristic of flow over rural, suburban or rough rural, and city terrains.

A range of high frequency base balances have been designed and built for the project. The designs include the plate type based on an earlier UWO style, Ref (2), as well as a plate plus stem type. The four balances produced so far have a range of sensitivities which cater for the model sizes used in the experiments, and all have natural frequencies in excess of 100Hz for all fundamental modes with models mounted in place. Further details of the balance design parameter are presented elsewhere in this conference, Ref (3).

In order to contain all the possible variables in the parametric test series envisaged in this project a large number of models is required. For practical purposes the number of models has been restricted to 36, and are grouped into two arrays, a tall slender group which contains the CAARC model, Ref (4), and a cuboid type whose range includes the Sheffield Arts Tower building, Ref (5), where the geometries of both groups are reproduced at 3 scales for the purposes of Objective (iv).

4. Results

The results of one of the series of tests is shown in Figures 1 and 2. The boundary layer flow used here is characteristic of flow over suburban terrain, α = 0.29, which also has appropriate turbulence characteristics.

The results show the mean base moments (Figure 1) and the fluctuating base moments (Figure 2) acting on a series of rectangular block models whose cross sectional dimensions Dx and Dy vary in the ratios indicated on the figures, where Dx is the dimensions in the in-wind direction and Dy is the cross-wind dimension at a wind angle, β = 0. The height, H, of all the models is given by the constant ratio H/Dx = 6. For the mean base moments the variation of in-wind moment with frontal body width, C_{Mx} at β =0°, shows a surprisingly small variation (Fig. 1(b)) due presumably to a similarity of wake structure based on comparable side wall flow structures. The corresponding variations of in-wind moment with afterbody length, C_{My} at β =90°, depicts a significant trend (Fig. 1 (a)) with decreasing moment as the length increases due to side wall flow reattachment and the downstream deflection of the wake formation region. As might be expected, the maximum value of torque occurs for the most slender shape, Dy/Dx = 4, Figure 1(c).

The fluctuating base moments shown in Figure 2 indicate substantially larger values for the square cross section, Dy/Dx =1, than for other geometrics for both in-wind and cross-wind cases. It is worth noting that the values for Dy/Dx = 1.5, the maximum mean drag cross section, Ref (6), indicate smaller values of the in-wind fluctuating moment for the short afterbody position ($C\sigma_{Mx}$ at β =0, the maximum drag position) than for the in-wind fluctuating moment the

257

long afterbody position ($C\sigma_{my}$ at $\beta = 90$). It might have been anticipated that for the maximum drag shape and orientation the wake vortex formation region, which is situated close behind the rear of the body and gives rise to maximum negative base pressures, might also be a case giving cause for high fluctuating base bending moments in the in-wind direction. Finally in view of the comments made earlier it is reassuring to note that for all body shapes, the maximum values of the fluctuating base moments, from which modal forces may be simply derived, occur for flow directions approximately normal to the building faces, thus ensuring a conservative design approach is embodied in empirical calculation methods..

5. Conclusion

This paper describes the objectives of a large parametric study of dynamic wind loads on buildings using wind tunnel methods. Initial results are presented which demonstrate that the experimental techniques employed are capable of yielding data with a resolution amply sufficient for the projects purposes.

References:
1. Lee B.E and Evans R.A., Jnl. Wind Engng. Ind. Aero. 13(1983) 161
2. Tschanz T., Proc Wkshp. Wind Tunnel Modeling for Civil Engineering Applications. C.U.P. (1982) 296
3. Lui S.P., Lee B.E. and others., Asia Pacific Symp. Wind Engng III. (1993).
4. Wardlaw R.L. and Moss G.F., CAARC Memo CC662. (1970)
5. Littler J., Ellis B., Jeary A. and Lee B.E., Proc 4th Conf. Tall Buildings Hong Kong. 1(1988) 259
6. Lee B.E., Jnl. Wind Engng Ind. Aero. 37(1988) 213
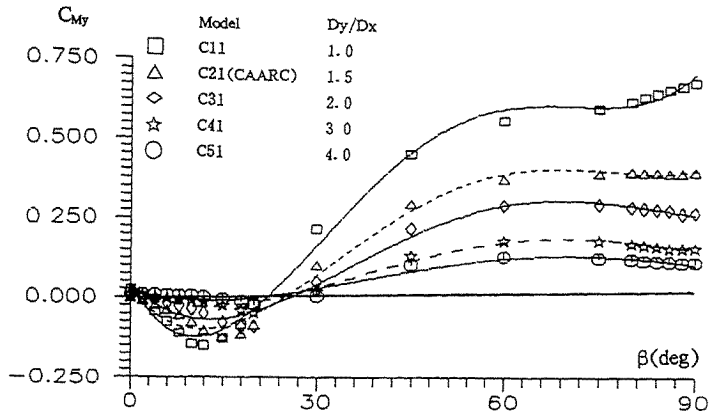
1-(a) C_{My} versus wind angle.
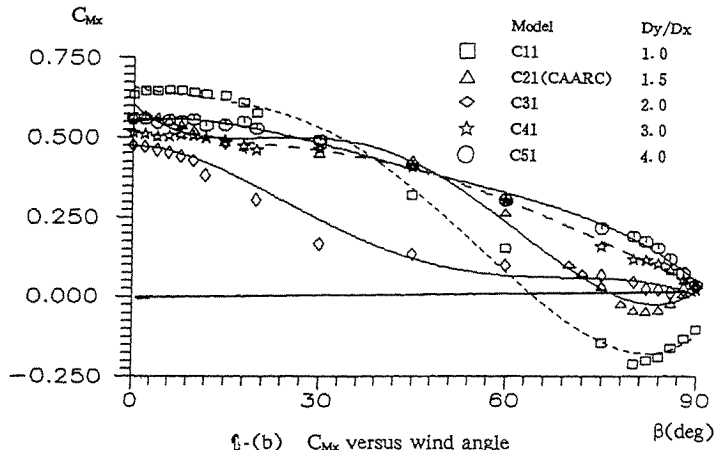
$\mathfrak{f}$-(b) C_{Mx} versus wind angle
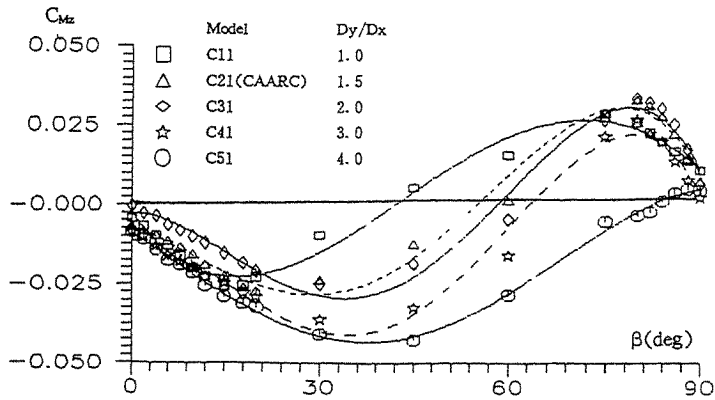
1-(c) C_{Mz} versus wind angle

Fig. 1 The influence of model shape on mean base moments
and torque.

259
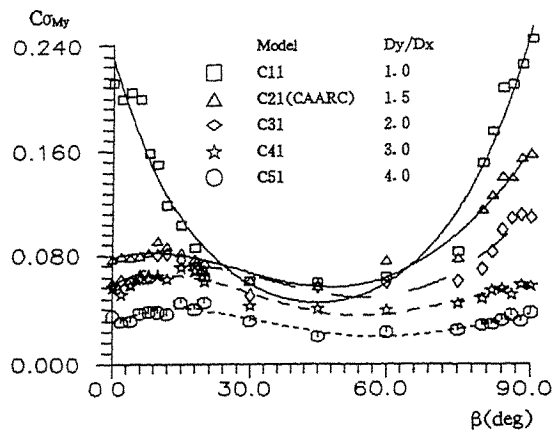
2 (a) Co_{My} versus wind angle
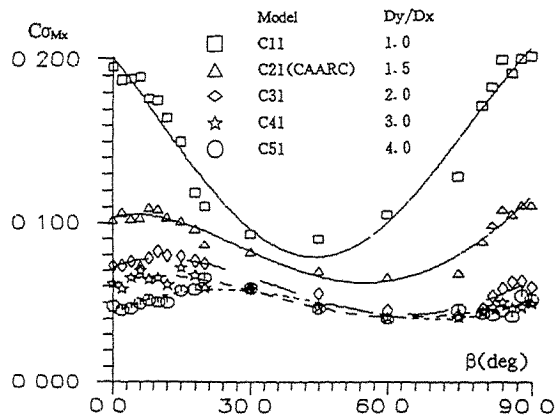
2 (b) Co_{Mx} versus wind angle

Fig. 2 The influence of model shape on fluctuating base moments and torque.

260

An Assessment of Dynamic Wind Loads
on a Series of CAARC-Like Slender Buildings

Liu Shangpei, Wang Qizhi and Lee,B. E. [+]

China Aerodynamics Research & Development Center
+University of Portsmouth, UK

Abstract:The selected results of a China-UK joint project on "Assessment of Dynamic Wind Loads on Buildings" were reported in the paper. Five models evolved from CAARC standard tall building model were tested using high frequency base balance in simulated boundary layer. The effects of building shape on mean and fluctuating wind loads were discussed, which indicated the significant role of flow pattern around model. The agreement of present CAARC data with those from other labs offered a confidence to the data base obtained in this project.

1. Introduction

In last years, a China-Britain joint project on "Assessment of Dynamic Wind Loads on Buildings" has been carried out. [1] The objectives of the project are to establish a data base which will help to determine the confidence limits associated with the wind tunnel assessment of dynamic wind loads. Specific series of tests have been undertaken in CARDC boundary layer wind tunnel test section using high frequency base balances. Three series of building models are tested in an attempt to concern with the influence on dynamic wind loads of, such as, terrain type, building shape, wind angle and mean speed, model scaling, and so on.

Some results available were selected in this paper, dealing with a series of five slender prismatic tall building models. All five have equal full-scale height 180m and narrow side 30m, but varied cross-section shape $Dy/Dx = 1.0, 1.5, 2.0, 3.0$ and 4.0, respectively. It is understood that this model series was evolved from CAARC standard tall building model ($30.5m \times 45.7m \times 182.9m$) which has been tested extensively in many wind tunnel laboratories around world using aeroelastic model, pressure model and also force balance techniques.

2. Apparatus and Test Procedures

2.1 *Atmospheric Boundary Layer Simulation*

The experiments were conducted in $1.4m \times 1.4m$ Low Speed Wind Tunnel, China Aerodynamics Research and Development Center. The modification for wind engineering purpose consists of extending the original aeronautical test section, resulting in a new boundary layer test section, $1.4m \times 1.4m \times 6.0m$. With "fence, spire and roughness element" method, a $0.8m$ high atmospheric boundary layer was generated in model area. A profile of longitudinal mean velocity with power law exponent 0.29 and turbulence shown in Fig. 1 was measured in this phase. Based on spectral scaling, the flow structure scale is $1/270 \sim 1/345$.

2.2 *Base Balance Technique*

The high frequency base balance technique is developed for the measurement of wind loads as a function of only the wind structure and the aerodynamic shape of the building. This would greatly assist our understanding of the nature and origins of fluctuating wind loads, particularly much convinience such

a big parametric test matrix. The balance employed in present test[6] is a high strain output of the balance system with five components, while maintaining a high rigidity. The natural frequencies of the balance are 552Hz for Mx, 552Hz for My and 287.5Hz for Mz, respectively.

2.3 Model Details

The model dimensions and loads were difined in Fig. 2, where wider side is denoted Dy, zero wind angle is normal to wider side, and Mx, My were generated by Fx, Fy respectively. Model C21 was designed as a simplified CAARC standard tall building model. Maintaining the height H and narrow side Dx, the cross-sections were varied with Dy/Dx. A length scale of $1/300$ was chosen to match flow scaling. The models were made of thin, light wooden plate and an aluminum plate on the bottom for connecting with balance.

2.4 Test Procedure

The models were mounted on a turntable to model the wind angle variation. A PC based computer data acquisition system was developed for the measurement of the mean, PSD, variance and co-variance of each component, in a balance coordinate shown in Fig. 2. The data were processed as mean and fluctuating moment coefficients:

$$C_{Mi} = \overline{M_i}/0.5\rho U_H^2 H^2 Dy \qquad i = x,y,z,$$
$$C\sigma_{Mi} = \sigma_{Mi}/0.5\rho U_H^2 H^2 Dy \qquad i = x,y,z,$$

where U_H is reference mean wind speed at model hight H.

3. Results on CAARC Model

The present values of $C_{Mx}, C_{My}, C\sigma_{Mx}$ and $C\sigma_{My}$ are compared with existing data in Fig. 3. The dashed curves were drawn by Melbourne,[3] derived from the measurements of tip deflection made in six wind tunnels. Also shown are two sets of data by Tanaka and Lawen,[2] from pressure measured on a rigid model and from tip displacements measured on an aeroelastic model. The force balance data to compare were latest published by Obasaju, BMT, UK.[4] The size of most models was smaller than the present one, with scale $1/500 \sim 1/1000$.

In general, the comparison on mean overturning moment indicated good agreement particularly between both balance data. The along-wind load when wind was normal to narrow side (C_{My}, at β near 90°) measured by balance was about 20% higher than fitting curve. The negative lobes in the curves of C_{My} near $\alpha=0°$ and C_{Mx} near $\alpha=90°$ in Fig. 3 indicated that galloping could occur when face of the model was normal to flow. The tendency to galloping was suppressed when the narrow face was normal to flow. The other technique overestimated $C\sigma_{Mx}$ and $C\sigma_{My}$ than balance tests because the derivation from deflection didn't include resonance and damping, probably. The joint study has found that the relationship of r.m.s load with mean wind speed was a power law with exponent larger than two, which means that the normalization with U^2 may not result in agreed coefficient values.

4. Effects of Building Shape

4.1 Mean Base Moments and Torque

The mean base moments and torque of models with different Dy/Dx were shown in Fig. 4a~c. The similar analysis as above indicated the galloping tendency was suppressed greatly when $Dy/Dx>1.5$. The shift of values C_{My} near $\beta=90°$ (narrow face normal to flow) indicated that the flow reattachment occured on larger Dy/Dx models reduced along-wind load, though with equal frontal area. Two trends were seen in torque, that the wind angle where torque sign changed and the maximum of torque were increased with Dy/Dx.

262

4. 2 Unsteady Moments and Torque

The unsteady loads versus wind angle were shown in Fig. 5 a～c. Again, the flow pattern occured when narrow face was normal to flow reduced the dynamic along-wind load with Dy/Dx increased, though with equal frontal area. Such trends seems more critical for cross-wind load (Fig. 5b), that $Dy/Dx>1.5$ might classify the flow nature. The stronger variation of dynamic torque with wind angle occured towards $Dy/Dx=1.0$. In Fig. 6 it could be seen again that the higher peak fluctuating wind loads occured toward $Dy/Dx=1.0$.

5. References

1. Lee,B. E. , Liu Shangpei and Wang Qizhi, A Parametric Study of Dynamic Wind Loads on Buildings, Third Asia-Pacific Symposium on Wind Engineering, 13-15 Dec. 1993, Hong Kong.

2. Tanaka,H. and Lawen,N. , Test on the CAARC Standard Tall Building Model with a Length Scale of 1 : 1000, J. Wind Eng. Ind. Aerodyn. , 26(1986)15—29.

3. Melbourne, W. H. , Comparison of Measurements of the CAARC Standard Tall Building Model in Simulated Model Wind Flows, J. Wind. Eng. Ind. Aerodyn. ,6(1980)78—88.

4. Obasaju,E. D. ,Measurement of Forces and Base Overturning Moments on the CAARC Tall Building Model in a Simulated Atmospheric Boundary Layer. J. Wind Eng. Ind. Aerodyn,40(1992)103—126.

5. Liu Shangpei and Wang Qizhi, The Measurement of Dynamic Wind Loads on Tall Building Models Using Force Balance, Part I: Slender Model Series, CARDC Report,Feb. 1993

6. Chen Feng, Hu Guofeng and Lee,B. E. , Desing and Calibration of High Frequency Base Balances Used for Dynamic Wind Load on Building Models, Third Asia-Pacific Symposium on Wind Engineering, 13—15 Dec, Hong Kong.
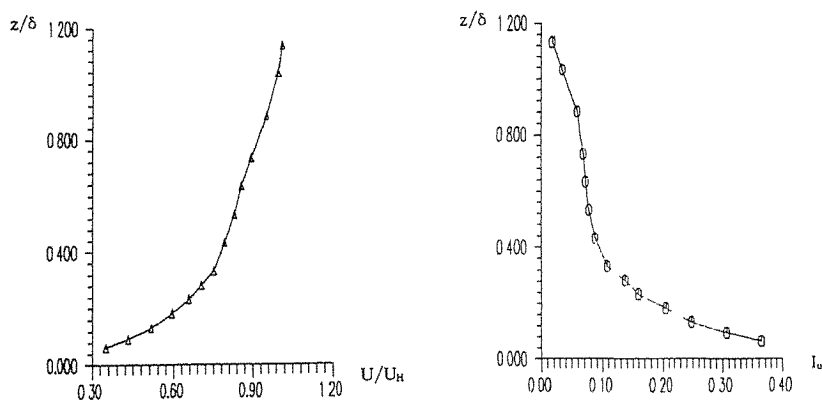
Fig. 1   Profile of longitudinal mean velocity and
turbulence intensity in simulated atmospheric
boundary layer.

Fig 2 Definition of model coordinates and wind loads
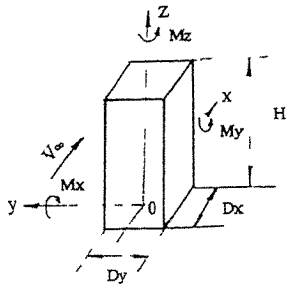
Model	Full-scale Size (m) $H \times Dy \times Dx$	Dy/Dx
C11	$180 \times 30 \times 30$	1 0
C21	$180 \times 45 \times 30$	1 5
C31	$180 \times 60 \times 30$	2 0
C41	$180 \times 90 \times 30$	3 0
C51	$180 \times 120 \times 30$	4 0
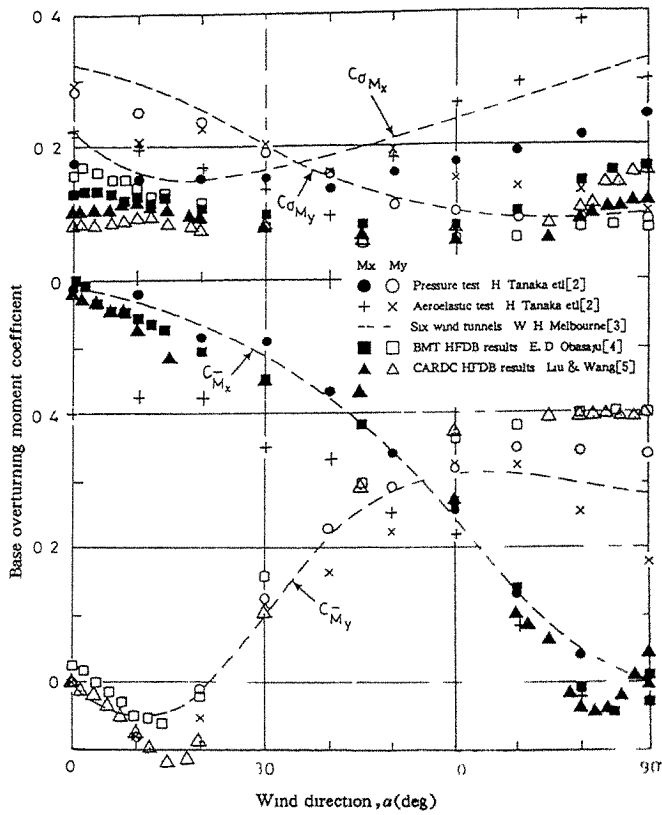
Fig 3 Variation of base overturning moment vorggivirny
on CARDC model with wind angle

264
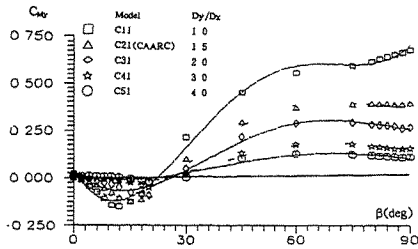
4a $C_{\overline{My}}$ versus wind angle
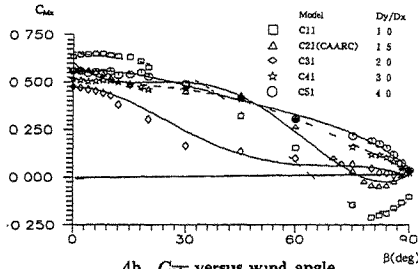
4b $C_{\overline{Mx}}$ versus wind angle
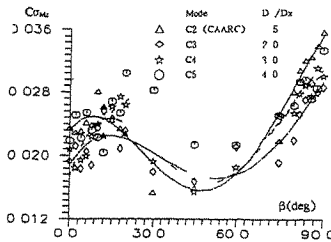
4c $C_{\overline{Mz}}$ versus wind angle

Fig 4 The influence of model shape on mean
base moment and torque
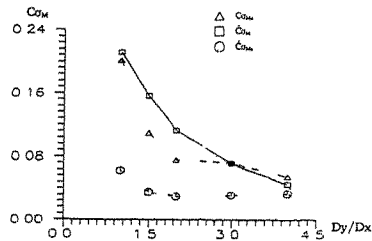
Fig 6 The influence of model shape on
the peak values of fluctuating
base moment and torque

5a $C\sigma_{My}$ versus wind angle

5b $C\sigma_{Mx}$ versus wind angle

5c $C\sigma_{Mz}$ versus wind angle
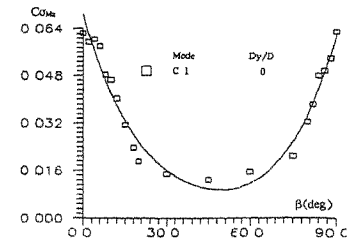
Fig 5 The influence of model shape on
fluctuating base moment and torque

265

Equivalent wind spectrum for torsional response of symmetrical buildings

T.Balendra C.G.Koh and R.Ramanathan

Department of Civil Engineering
National University of Singapore, Singapore

Abstract: For the prediction of torsional response of buildings due to along-wind turbulence, an equivalent wind velocity spectrum is proposed. The equivalent wind velocity spectrum is derived from the rigorous frequency domain solution. The root mean square values of torsional responses are obtained for symmetrical buildings modelled as continuum, by solving the modal equation of motion in frequency domain, using the equivalent wind velocity spectrum technique. The results are compared with those obtained by rigorous method. The proposed equivalent wind velocity spectrum method predicts the torsional responses due to along-wind accurately with tremendous reduction in the computation time.

1. Introduction

Since wind is always oscillatory and random in nature a probabilistic approach has to be employed for analytical method of estimating the along-wind response of buildings. Recently, Solari [1] proposed an equivalent wind spectrum technique for predicting the dynamic along-wind translational responses of structures. This method involves a height independent velocity field and as such response prediction is very much simplified. Using this height independent wind velocity spectra, the four spatial coordinate integrals of the coherence function in the frequency domain, is reduced to a single integral expression, saving a lot of computational effort. This equivalent wind spectrum technique is elegant for time domain analysis and provides reasonably accurate results [2]. Because the gust in the approaching wind lacks spatial correlation in the across wind direction, even a symmetrical building could twist, thus torsional vibration is significant even for symmetrical buildings [3]. In this paper, an equivalent wind velocity spectrum for the prediction of torsional response of symmetrical buildings due to along-wind is developed.

2. Derivation of Equivalent Wind Velocity Spectrum

Assuming the fluctuating wind velocity as a stationary Gaussian process, the actual spectral density of the torsional moment spectrum at the top of the building shown in Fig. 1, is given by

$$S_{TT}(n) = \rho^2 C_D^2 \int_0^H \int_0^H \int_{-B/2}^{B/2} \int_{-B/2}^{B/2} y_1 y_2 \phi_\theta(z_1) \phi_\theta(z_2) \overline{V}(z_1) \overline{V}(z_2) \sqrt{S_v(z_1,n) S_v(z_2,n)}$$

$$\exp \left[\frac{-2n\sqrt{C_y^2(y_1-y_2)^2 + C_z^2(z_1-z_2)^2}}{\overline{V}(z_1) + \overline{V}(z_2)} \right] dy_1 dy_2 dz_1 dz_2 \qquad (1)$$

267

where, ρ is the density of air, C_D is the drag coefficient, $\phi_\theta(z)$ is the mode shape along the building height, $\overline{V}(z)$ is the mean wind velocity at height z, $S_v(z,n)$ is the wind velocity spectrum at z and n is the excitation frequency in Hz and C_y, C_z are the exponential decay constants in Y and Z directions respectively.

The determination of the rms response from Eq. (1) involves the computation of four integrals in spatial coordinates, which will be time consuming. The four integral expressions are successively reduced to a single integral expression as formulated below.

In Eq. (1), introducing the following non-dimensionalised variables with a linear mode shape approximation for the first mode

$$\overline{z_1} = z_1/H; \ \overline{z_2} = z_2/H; \ \overline{y_1} = y_1/B; \ \overline{y_2} = y_2/B;$$

$$\phi_\theta(z_1) = z_1/H = \overline{z_1}; \ \phi_\theta(z_2) = z_2/H = \overline{z_2}$$

we obtain

$$
S_{TT}(n) \ = \ \rho^2 C_D{}^2 H^2 B^4 \int_0^1 \int_0^1 \int_{-\frac{1}{2}}^{\frac{1}{2}} \int_{-\frac{1}{2}}^{\frac{1}{2}} \overline{V}(\overline{z_1})\overline{V}(\overline{z_2})\overline{y_1}\ \overline{y_2}\ \overline{z_1}\ \overline{z_2}\sqrt{S_v(\overline{z_1},n)S_v(\overline{z_2},n)}
$$

$$
\exp\left[\frac{-2n\sqrt{C_y{}^2(\overline{y_1}-\overline{y_2})^2 + C_z{}^2(\overline{z_1}-\overline{z_2})^2}}{\overline{V}(\overline{z_1}) + \overline{V}(\overline{z_2})}\right] d\overline{y_1}d\overline{y_2}d\overline{z_1}d\overline{z_2} \tag{2}
$$

where $\overline{V}(\overline{z_1})$ and $S_v(\overline{z_1},n)$ are respectively the mean wind and spectral density of fluctuating component at the non-dimensional coordinate $\overline{z}_0$.

$$
\overline{V}(\overline{z}) \ = \ 2.5u_*\ln\left[\frac{H\overline{z}}{z_0}\right] \ ; \ \ H\overline{z} \ > \ 10 \text{ m}
$$

$$
= \ 2.5u_*\ln\left[\frac{10}{z_0}\right] \ ; \ \ H\overline{z} \ \leq \ 10 \text{ m} \tag{3}
$$

$$
S_v(\overline{z},n) \ = \ \frac{u_*^2}{n}\frac{200\overline{f}}{[1 + 50\overline{f}]^{5/3}} \tag{4}
$$

$$
\overline{f} \ = \ \frac{n\overline{z}H}{\overline{V}(\overline{z})} \tag{5}
$$

As a *first step* towards the derivation of the equivalent wind spectrum, the variables $\overline{z_1}$ and $\overline{z_2}$ are separated by the geometric mean of the functions involving either $\overline{z_1}$ or $\overline{z_2}$ through the introduction of a coefficient K_y, as follows :

$$
S_{TT}(n) \ = \ \rho^2 C_D^2 H^2 B^4 \int_0^1 \int_0^1 \overline{V}(\overline{z_1})\overline{V}(\overline{z_2})\overline{z_1}\ \overline{z_2}\sqrt{S_v(\overline{z_1},n)S_v(\overline{z_2},n)}
$$

$$
\sqrt{\Psi(D_y)}\exp\left[\frac{-2n\alpha C_z H|\overline{z_1} - \overline{z_2}|}{\overline{V}(\overline{z_1}) + \overline{V}(\overline{z_2})}\right] d\overline{z_1}d\overline{z_2} \tag{6}
$$

where

$$
\Psi(D_y) = \sqrt{\Psi(D_{y1})\Psi(D_{y2})} \tag{7}
$$

in which the functional approximation $\Psi(D_y)$ is defined as

$$\Psi(D_y) = \left[\frac{1}{6D_y} - \frac{1}{2D_y^2} + \frac{2}{D_y^4} - 2\exp(-D_y)\left(\frac{1}{D_y^2} + \frac{1}{2D_y}\right)^2 \right] \qquad (8)$$

Also,

$$D_{y_1} = \left[\frac{K_y n C_y B}{\overline{V}(\bar{z}_1)} \right] \text{ and } D_{y_2} = \left[\frac{K_y n C_y B}{\overline{V}(\bar{z}_2)} \right] \qquad (9)$$

The value of the coefficient K_y appearing in Eq. (6) through $\Psi(D_{y1})$ and $\Psi(D_{y2})$ of Eq. (9) is evaluated numerically for the assumed linear mode shape by comparing Eq. (2) and Eq. (6) for various practical values of (B/H) ratio [0.10 to 0.60] and excitation frequencies (n) of interest [0.05 Hz to 0.60 Hz]. The chosen range for excitation frequency covers the typical range for torsional natural frequency of buildings.

The variation of K_y is approximated as a function of (B/H) ratio only, and independent of frequency, by least squares approximation involving a second degree polynomial. The approximated K_y for the assumed linear mode shape may be expressed as

$$K_y = 0.60 - 1.10(B/H) + 2.0(B/H)^2 \qquad (10)$$

As a *second step* towards the derivation of equivalent spectrum, the remaining exponential term in Eq. (6) involving $\bar{z}_1$ and $\bar{z}_2$ is replaced by a function Υ with a coefficient K_z and due to the interchangeability of the variables $\bar{z}_1$ and $\bar{z}_2$, it can be further modified as a square of the single integral as

$$S_{TT}(n) = \rho^2 C_D^2 H^2 B^4 \left[\int_0^1 \overline{V}(\bar{z}_1)\bar{z}_1 \sqrt{S_v(\bar{z}_1, n)} \Psi[D_{y1}] \Upsilon[\eta_1] \, d\bar{z}_1 \right]^2 \qquad (11)$$

where

$$\Upsilon[\eta_1] = \frac{1}{\eta_1} - \frac{1}{2\eta_1^2}(1 - e^{-2\eta_1}) \qquad (12)$$

$$\eta_1 = \frac{K_z n C_z \bar{z}_1 H}{\overline{V}(\bar{z}_1)} \qquad (13)$$

The coefficient K_z appearing in Eq. (11) through the function $\Upsilon[\eta_1]$ is computed by comparing Eq. (11), either with Eq. (2) or with Eq. (6). This comparison requires K_y for different values of (B/H) and n. Exact values of K_y are used instead of the approximated expression, so that K_z need not account for the error introduced through K_y.

K_z is approximated as a constant value equal to the average 0.485 for a linear mode shape. The value of K_z depends on the type of mode shape used. In Eq. (11), both $[\bar{z}_1 \overline{V}(\bar{z}_1)]$ and $\sqrt{S_v(\bar{z}_1, n)} \Psi[D_{y1}] \Upsilon[\eta_1]$ are
a) Continuous in the interval (0,1) and
b) Integrable in (0,1)
The mean velocity profile defined in Eq. (3) yields a positive value for all values of $H\bar{z}_1$, since z_0 is less than 10m for any possible terrain condition. Hence the quantity $[\bar{z}_1 \overline{V}(\bar{z}_1)]$, in Eq. (11) *does not become negative* in the interval (0,1).

Also, the functions $\Psi[D_{y1}]$ and $\Upsilon[\eta_1]$ do not become negative in the interval (0,1). With these conditions, there exists a nondimensional reference height $\bar{z}_1 = h$,

269

such that the square of the integral in Eq. (11) can be equated as follows [6]:

$$S_v(h,n)\Psi\left[\frac{K_y n C_y B}{\overline{V}(h)}\right]\Upsilon\left[\frac{K_z n C_z h H}{\overline{V}(h)}\right]\left[\int_0^1 \overline{V}(\overline{z_1})\overline{z_1}d\overline{z_1}\right]^2$$

$$= \left[\int_0^1 \overline{V}(\overline{z_1})\overline{z_1}\sqrt{S_v(\overline{z_1},n)\Psi[D_{y1}]\Upsilon[\eta_1]}d\overline{z_1}\right]^2 \qquad (14)$$

The value of h is obtained numerically by solving the above equation. It is found that for linear mode shape, h varries from 0.60 to 0.65 for different velocities and terrain conditions. A value of $h = 0.619$ is recommended as a reasonable approximation for linear mode shape. The values of K_y, K_z, and h for other non-inverting mode shapes are given in Reference [4].

Using Eq. (14) in Eq. (11) the final expression for modal torsional moment spectrum becomes

$$S_{TT}(n) = \rho^2 C_D^2 H^2 B^4 S_v(h,n)\Psi\left[\frac{K_y n C_y B}{\overline{V}(h)}\right]\Upsilon\left[\frac{K_z n C_z h H}{\overline{V}(h)}\right]\left[\int_0^1 \overline{V}(\overline{z_1})\overline{z_1}d\overline{z_1}\right]^2 \qquad (15)$$

Eq. (15) holds good for any type of non-inverting mode shapes and can be written in general form as,

$$S_{TT}(n) = \rho^2 C_D^2 H^2 B^4 S_v(h,n)\Psi\left[\frac{K_y n C_y B}{\overline{V}(h)}\right]\Upsilon\left[\frac{K_z n C_z h H}{\overline{V}(h)}\right]\left[\int_0^1 \overline{V}(\overline{z})\varphi_{\theta_1}(\overline{z})d\overline{z}\right]^2 \qquad (16)$$

Let

$$S_{veq}(n) = S_v(h,n)\Psi\left[\frac{K_y n C_y B}{\overline{V}(h)}\right]\Upsilon\left[\frac{K_z n C_z h H}{\overline{V}(h)}\right] \qquad (17)$$

where $S_{veq}(n)$ is the equivalent wind velocity spectrum for torsional response, and $\overline{V}(h)$ and $S_v(h,n)$ are given by Eqs. (3) and (4) respectively. In view of Eq. (17), Eq. (16) becomes

$$S_{TT}(n) = \rho^2 C_D^2 H^2 B^4 S_{veq}(n)\left[\int_0^1 \overline{V}(\overline{z})\varphi_{\theta_1}(\overline{z})d\overline{z}\right]^2 \qquad (18)$$

Hence, the modal torsional spectra can be computed using a single integral in Eq. (18) instead of four integrals in Eq. (1). It should be noted that the expression for equivalent wind velocity spectrum for torsional response needs to be defined only at the reference height of the building, hH.

3. Numerical Examples

Following numerical examples are considered to determine the efficiency and accuracy of the proposed method. The details of the numerical examples are as follows:
Several rectangular symmetrical buildings possessing wide range of fundamental torsional natural frequencies are selected. The dimensions of the selected buildings are given in Table 1. A damping of 2 % is assumed in all cases. Mass of the buildings per metre height is assumed to be 295 Kg/m. Assumed density of air is 1.25 Kg/m^3 and the drag coefficient adopted is 1.30. A mean wind velocity of 28 m/s is assumed at 10 m height above ground level. The roughness length assumed is 0.3 m. The exponential decay constants C_y and C_z are taken as 16.0 and 10.5 respectively.

Table 1: Rms values of torsional responses of symmetical buildings

| Building | H | B | D | n_θ | $\sigma_{\theta\theta}$ in Rad. | | Ratio |
No.	(m)	(m)	(m)	(Hz)	Actual Spectrum (1)	Equ.Spectrum (2)	(2)/(1)
1	200.0	60.0	25.0	0.20	1.6005E-03	1.6485E-03	1.0299
2	150.0	50.0	25.0	0.30	6.9270E-04	7.2915E-04	1.0526
3	121.9	24.4	24.4	0.40	4.2690E-04	4.4265E-04	1.0368
4	100.0	40.0	25.0	0.50	2.3490E-04	2.5437E-04	1.0828

The root mean square values of the torsional responses $\sigma_{\theta\theta}$ are obtained for the selected symmetrical buildings in the first torsional mode, using linear mode shape from modal torsional spectra given in Eq. (2) and Eq. (18)

The results obtained from the above methods are tabulated in Table 1. It can be seen that the errors incurred in adopting equivalent wind velocity spectrum method do not exceed 8.28 %. The equivalent wind spectrum method gives slightly higher torsional response values than the actual spectrum.

The CPU time required for computing $\sigma_{\theta\theta}$ in each case, using the DEC Unix Workstations based on Ultrix operating system with a F-77 optimising compiler, is 9500 sec. using actual spectrum method, whereas the equivalent wind spectrum method needs 0.032 sec. only.

4. Conclusions

An equivalent wind velocity spectrum method for predicting the torsional response of symmetrical building due to along-wind is presented. The proposed equivalent wind velocity spectrum method for the prediction of along-wind torsional response of buildings provides reasonably accurate results with tremendous reduction in the CPU time.

5. References

1. G.Solari, J. Structural Engg., ASCE, Vol.114, No.6.(1988).

2. G.Solari, J. of Engineering Mech., ASCE, Vol.115, No.9,(1989).

3. E.Safak, Vibration of Buildings under Random Wind Loads, Ph.D Thesis, Dept. of Civil Engg., University of Illinois at Urbana-Champaign,(1980).

4. R.Ramanathan, Equivalent Wind Spectrum for Torsional Response of Buildings, Master of Engineering Thesis, Dept. of Civil Engg., National University of Singapore, Singapore, (1992).

5. G.Solari, J. of the Structural Div., ASCE, Vol.108, No.ST1.(1982)
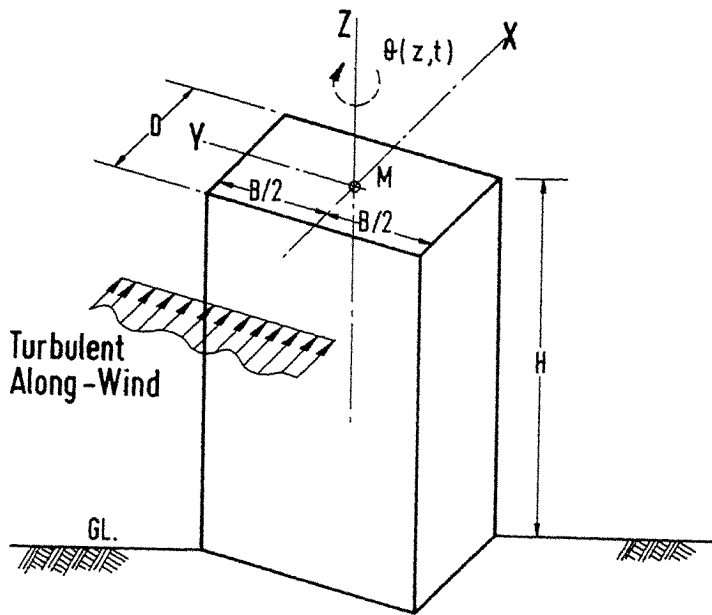
Fig. 1 Building Dimensions

Stochastic Stability of Wind Excited Structures

Y. K. Lin and Q. C. Li

Center for Applied Stochastics Research
Florida Atlantic University, Boca Raton, FL 33431, U.S.A.

Abstract: Concepts of stochastic stability of randomly excited dynamical systems are described and compared. Controversies surrounding their applications to wind-loaded structures are explained. Examples of some analytical results are presented and discussed.

1. Introduction

Motion instability can be a major cause for failure for flexible structures, such as long-span bridges, in strong winds. Since turbulence is always present in a natural wind flow, the effects of turbulence on structural motion stability has become an important topic in wind engineering. If one accepts the notion that wind turbulence can be modeled mathematically as a stochastic process, then the subject belongs to that of stochastic stability.

2. Stability of a Deterministically Excited System

It is useful to review briefly the concept of motion stability of a system under deterministic excitations, in order that the case of random excitation can be properly explained. In general, the state of a dynamic system may be represented by an n-dimensional vector $x(t)$, measured from a reference position, which will be called the trivial solution in what follows. The boundedness and convergence of $x(t)$ can be defined rigorously in terms of a suitable norm of $x(t)$, denoted by $\|x(t)\|$. Examples of such norms are

$$\|x(t)\| = \sum_{i=1}^{n} |x_i(t)|, \ \|x(t)\| = \left[\sum_{i=1}^{n} x_i^2(t)\right]^{1/2}, \ \|x(t)\| = \left[\sum_{i=1}^{n}\sum_{j=1}^{n} a_{ij} x_i(t)x_j(t)\right]^{1/2} \tag{1}$$

where a_{ij} are the elements of a positive definite square matrix, etc. The following concepts, attributable to Lyapunov [1] are fundamental in the investigation of stability of deterministic systems.

(i) *Lyapunov stability*: The trivial solution is said to be stable if, for every $\varepsilon > 0$, there exists a $\delta(\varepsilon, t_0) > 0$ such that

$$\sup_{t \geq t_0} \|x(t; x_0, t_0)\| < \varepsilon \tag{2}$$

provided $\|x_0\| \leq \delta$, where $x_0 = x(t_0)$, and sup (abbreviation for supremum) denotes the least upper bound.

(ii) *Lyapunov asymptotic stability*: The trivial solution is said to be asymptotically stable, if it is stable, and if the right-hand side tends to zero as t increases.

3. Concepts of Stochastic Stability

Let the motion of a structure be represented by $X(t)$, where the capitalized $X(t)$ signifies that the motion is random. Let $\|X(t)\|$ be a suitable norm of $X(t)$. The following definitions for stochastic stability are of particular interest [2].

(i) *Lyapunov stability with probability one*: The trivial solution is said to be stable in the Lyapunov sense with probability one if, for every pair of ε_1, $\varepsilon_2 > 0$, there exists a $\delta(\varepsilon_1, \varepsilon_2, \boldsymbol{x}_0, t_0) > 0$ such that

$$\text{Prob}\left[\bigcup_{\|\boldsymbol{x}_0\| \leq \delta}\left\{\sup_{t \geq t_0}\|X(t;\boldsymbol{x}_0,t_0)\| \geq \varepsilon_1\right\}\right] \leq \varepsilon_2 \qquad (3)$$

where $\boldsymbol{x}_0 = X(t_0)$ is deterministic, and $\cup$ represents the union of multiple events. This mode of stability is also known as sample stability, or almost sure stability.

(ii) *Stability in probability*: The trivial solution is said to be stable in probability if, for every pair of ε_1, $\varepsilon_2 > 0$, there exists a $\delta(\varepsilon_1, \varepsilon_2, \boldsymbol{x}_0, t_0) > 0$ such that

$$\text{Prob}[\|X(t;\boldsymbol{x}_0,t_0)\| \geq \varepsilon_1] \leq \varepsilon_2, \quad t \geq t_0 \qquad (4)$$

provided $\|\boldsymbol{x}_0\| \leq \delta$, where $\boldsymbol{x}_0 = X(t_0)$ is deterministic.

(iii) *Stability in the mth statistical moment*: The trivial solution is said to be stable in the mth statistical moment if, for every $\varepsilon > 0$, there exists a $\delta(\varepsilon, \boldsymbol{x}_0, t_0) > 0$ such that

$$\text{E}[\|X(t;\boldsymbol{x}_0,t_0)\|^m] \leq \varepsilon, \qquad m > 0, \quad t \geq t_0 \qquad (5)$$

provided $\|\boldsymbol{x}_0\| \leq \delta$, where $\boldsymbol{x}_0 = X(t_0)$ is deterministic, and the symbol $\text{E}[\ ]$ denotes an ensemble average.

It is interesting to note that Inequality (3) is concerned with the boundedness of $\|X(t;x_0,t_0)\|$ within the entire time interval $[t_0,t]$, whereas Inequalities (4) and (5) are related only to its value at an arbitrary t. Clearly, (3) implies (4), but comparisons between (3) and (5), and (4) and (5) are not so obvious. However, in the special case of a linear system, (3) and (4) becomes equivalent, and (5) is in fact more stringent than (3). This is an important observation, since stability conditions for various statistical moments are much easier to obtain. A system is said to be asymptotically stable in one of the three modes, if it is stable, and if the right-hand side in Inequality (3), (4) or (5) tends to zero as t increases.

4. Stability of a Long-Span Bridge in a Turbulent Wind

As an example, consider a long-span bridge excited by a horizontal wind flow. Let the bridge motion be represented by a single torsional degree of freedom α. Without taking into account the effects of turbulence, the equation of motion may be written in the following form [3]

$$I(\ddot{\alpha} + 2\zeta_\alpha\omega_\alpha\dot{\alpha} + \omega_\alpha^2\alpha) = \tfrac{1}{2}\rho(2B^2)\left\{u^2[c_1\alpha + c_2\frac{B}{u}\dot{\alpha}] + \int_{-\infty}^{t}u^2[X_{M\alpha}(t-\tau)-1]\dot{\alpha}(\tau)\,d\tau\right\} \qquad (6)$$

where I = modal moment of inertia, ω_α = natural frequency, ζ_α = ratio of structural damping to the critical damping, ρ = air density, B = width of bridge deck,

274

u = horizontal wind velocity, $X_{M\alpha}(t)$ = experimentally determined aerodynamic indicial function, and c_1 and c_2 are experimentally determined aerodynamic constants, supposedly in a non-turbulent flow. In many cases, the $X_{M\alpha}(t)$ function may be fitted in the form of

$$X_{M\alpha}(t) = 1 + c_3 \exp[-d_3(\frac{u}{B})t] + c_4 \exp[-d_4(\frac{u}{B})t] \tag{7}$$

where c_3, c_4, d_3 and d_4 are again constants. As the wind velocity u increases to a critical value u_c, called the flutter velocity, the combined structure-fluid system can sustain a steady-state sinusoidal motion, with a frequency ω_1, called the flutter frequency. The analysis can be carried out most conveniently in the frequency domain.

The question now arises as how the effects of turbulence can be analyzed. In one approach, use is still made of the frequency-domain analysis, with the aerodynamic function $X_{M\alpha}(t)$, and constants c_1 and c_2 determined experimentally in a turbulent flow. This approach suffers the following drawbacks: (i) In a turbulent flow, u in Eq. (6) is changing with time; therefore, the dynamical system is not time-invariant, and the frequency-domain analysis is no longer applicable. (ii) Eq. (6) is no longer a theoretical model in the true sense of the word, since it reproduces what have been measured in a particular turbulence field, but it cannot be used to predict the system behavior in other turbulence fields. (iii) Accurate scaling of an on-site turbulence field in a laboratory setting is difficult. (iv) The effects of vertical turbulence, which results in an additive inhomogeneous term in Eq. (6) (called the buffeting term), cannot be separated from the measurements. Yet, it is well-known in dynamics, that the additive inhomogeneous term has no influence on motion stability of a linear system.

In another approach, it is reasoned that since the scale of turbulence in a natural wind is generally much larger than the typical dimension of a bridge cross-section, the flow pattern around a bridge cross-section should be nearly the same as one without the turbulence. Furthermore, the flutter frequency ω_1 is generally quite low (usually less than 1 Hz); therefore, only those turbulence eddies of larger sizes contribute importantly to the excitation. On this basis, we have proposed [4,5,6] that the main effects of horizontal turbulence can be accounted for by replacing the constant flow velocity u in Eq. (6) by a variable $U(t) = u[1 + F(t)]$, where $F(t)$ is treated as a stochastic process with a zero mean. The "randomized" Eq. (6) can then be solved in the time-domain, using the same aerodynamic constants and function measured in a non-turbulent flow.

We now believe that while the dominant larger eddies in the turbulent flow contribute essentially to the excitation energy in the low frequency range, important to the dynamics of the system, the smaller eddies may provide a different effect even though their energy is contained in the higher frequency range which is far from the flutter frequency. There have been some experimental evidences [7] to suggest that the small eddies may "fill up" the cavities behind a bluff body, and effectively transforming a bluff body into a stream-lined one. If this is indeed true, then experimental measurements to determine the aerodynamic parameters should be conducted in a flow with small eddies. The exact composition of the larger eddies should be unimportant, especially those larger than the cross-section of the structural model.

5. Some Examples

Theoretical results have been obtained for a bridge sectional model of the following characteristics [3]: $\omega_\alpha = 0.74\pi$ rad/s, $\zeta_\alpha = 0.01$, $B = 16.4$ m, $I = 8.95 \times 10^5$ kg m^2, $\rho = 1.226$ kg/m^3, $c_1 = 0.04272$, $c_2 = -0.3329$, $c_3 = 0.2159$, $d_3 = 0.1809$, $c_4 = 0.8391$, $d_4 = 2.1894$. The non-dimensionalized velocity fluctuation $F(t)$ in the turbulence is modeled as

$$F(t) = \varepsilon \sin[\nu t + \sigma B(t) + \chi] \qquad (8)$$

where ε, ν, σ are positive constants, $\varepsilon < 1$, $B(t)$ is a unit Wiener (Brownian motion) process, and χ is a random variable uniformly distributed in the range of $[0, 2\pi)$. This turbulence model is versatile. It is a stationary random process with a bounded mean-square value of $\varepsilon^2/2$. It can be either a wide-band (large σ) or a narrow-band (small σ) process, and its spectral peak can be adjusted by changing the value of ν. Spectral densities computed for several sets of ν and σ values are illustrated in Fig. 1.
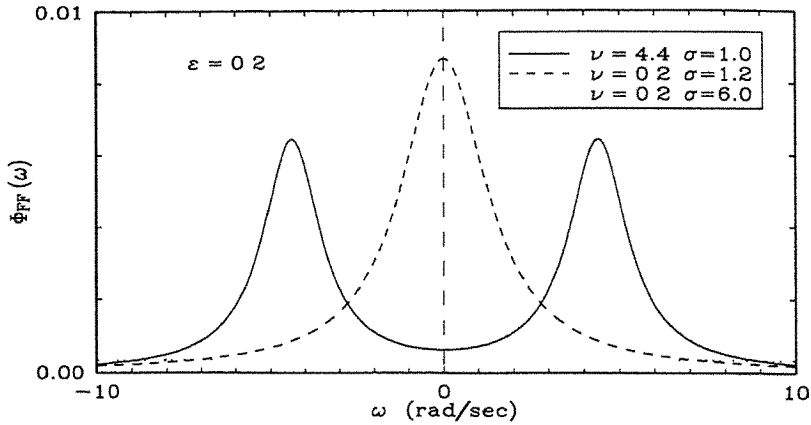
Fig. 1 Spectral shapes of turbulence model

Figs. 2 and 3 show the boundaries for sample stability computed for three different cases: (i) turbulence is narrow-banded, and its peak frequency is nearly tuned to $2\,\omega_1$, (ii) turbulence is narrow-banded, and its peak frequency is far from $2\,\omega_1$, and (iii) turbulence is broad-banded (σ is large). It is seen that turbulence is destabilizing in the first case, it is stabilizing in the second case, and it has smaller stabilizing effect in the third case. The condition for stability in the second statistical moment has also been computed for the broad-band turbulence, and found that the stabilizing effect in the moment stability is slightly smaller than that of sample stability, in agreement with the earlier observation that, conditions for moment stabilities are more stringent than that of sample stability, at least for linear systems.

276
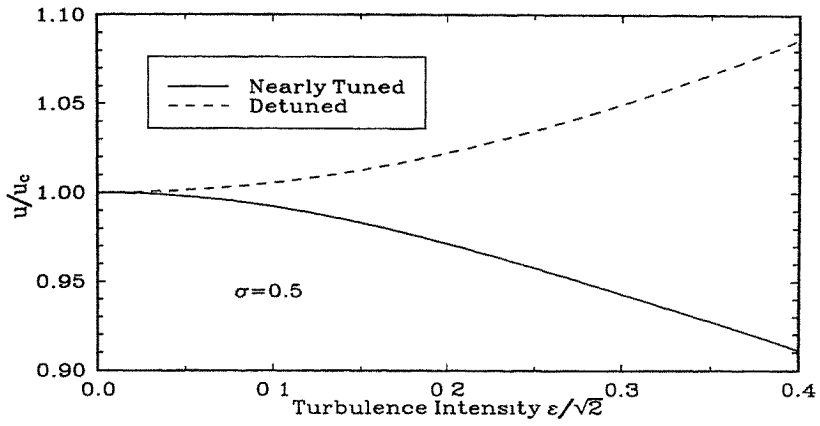
Fig. 2 Sample stability boundary of a bridge in a narrow-band turbulent wind
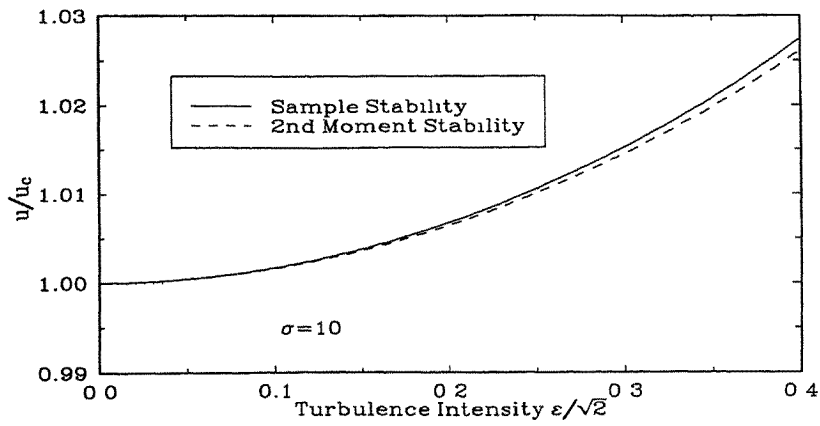
Fig. 3 Stability boundary of a bridge in a broad-band turbulent wind

277

6. Concluding Remarks

Motion stability of structures under turbulent wind excitations must be defined in terms of probability and statistics. Analytical techniques are now available to obtain the stability conditions corresponding to various definitions. The question as how the aerodynamic parameters in a combined structure-fluid model should be measured in a laboratory setting remains open. It is proposed that they be measured in a flow containing small turbulent eddies in order to simulate the cavity-filling effect behind a bluff body.

References:
1. A. M. Lyapunov, *Comm. Soc. Math. Kharkov*, 2 (1892). Reprint: *Ann. of Math. Studies*, Princeton University Press, 17 (1949). .
2. F. Kozin, 1969, *Automatica*, 5 (1969) 95.
3. R. H. Scanlan, J. G. Béliveau and K. S. Budlong, *J Engrg. Mech. Div.*, ASCE, 100 (1974) 657.
4. Y. K. Lin and S. T. Ariaratnam, *J. Struct. Mech.*, 8 (1980) 1.
5. C. G. Bucher and Y. K. Lin, *J. Engrg. Mech.*, ASCE, 114 (1988) 2055.
6. Y. K. Lin and Q. C. Li, *J. Engrg. Mech.*, ASCE, 119 (1993) 113.
7. M. Kawatani, H. Kim, H. Uejima and H. Kobayashi, *Proc. 2nd Int. Colloquium on Bluff Body Aerodyn. and Appl.*, Melbourne, Australia, (1992).

Simulation method of simultaneous time-series of multi-local wind forces on tall buildings by using dynamic balance data

K. Yoshie, T. Ohkuma[+], H. Marukawa[++], H. Niwa[+], T. Teramoto, and H. Kitamura

Tokyo Structural Office, Nikken Sekkei, Tokyo, Japan.
+Department of Architecture and Building Engineering
Kanagawa University, Kanagawa, Japan.
++Research and Development Division
Izumi Sohken Engineering Co., Ltd., Tokyo, Japan.

Abstract: This study discusses the method how to simulate simultaneous time-series of multi-local wind forces on tall buildings based on dynamic balance data, taking into consideration up to the 2nd mode vibrations of the building. Because this method is not needed complicated experiments, it can be easy applied to the structural designing of buildings. Firstly, the method considering the spatial correlation in the vertical direction is proposed. This method divides power of the 1st modal force among local forces based on "referent height" idea. The parameters of the simulation were determined by wind tunnel tests. The simulation of local wind forces on one face reproduces well the results of the wind tunnel tests. Secondly, the above method is developed to 3-component simultaneously.

1.Introduction

Concerning the structural design of tall buildings, as buildings become taller and more slender, the force of the wind has a more severe effect on the buildings. The determination of the design wind load and the investigation of habitability have been carried out through the use of spectral analysis after employing a wind tunnel test[1]. However, time-domain analysis is needed for the verification of the vibration control effect, which is for building with vibration control devices, or the response analysis in consideration of the elasto-plasticity of the structures[2]. Time-domain analysis requires as an input data, simultaneous 3-component multi-local wind force data; for which the equipment arrangement to set up the wind tunnel testing is very extensive and elaborate. This study discusses the method how to simulate simultaneous time-series of multi-local wind forces on tall buildings based on dynamic balance data, taking into
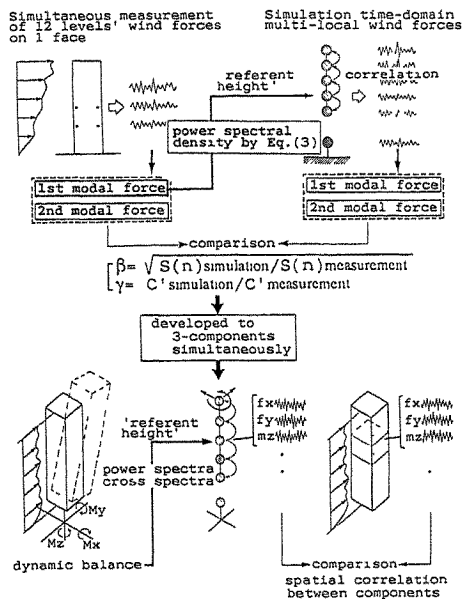
Fig.1 Conceptual flow of this study

279

consideration both the first mode and the second mode vibrations of the building. This study is investigated as shown in Fig.1.

2.Wind tunnel test

The wind tunnel is a boundary layer wind tunnel owned by Kanagawa University. The approaching flow employed corresponds to an urban exposure condition. The shape of the test model selected in this study has a span ratio (D/B, D:depth, B:breadth of building) of 1.0, and an aspect ratio (H/B, H:height of building) of 4.0. The wind direction employed is parallel on one side of the model (See Fig.2). This wind tunnel test were carried out as follows; (1) Local wind forces on at 12 different levels in one face obtained from a manifold system were measured simultaneously. (2) Local wind forces at 2 different levels – " referent height " and an other 11 levels – were measured simultaneously by a manifold system. (3) Base moments (over turning moments and a torsional moment) of the model were measured by a dynamic balance.

The results are shown in Fig.3–9. Fig.3 shows that the wind force coefficients distribute almost equally in the vertical direction. The discrepancy of these coefficients near the top and bottom of the model is due to the turbulence of the flow over the top and on the ground level of the model. Fig.4 and 6 show that the power spectra of local wind forces at the all levels exhibit similar shape except near the top and the bottom. These results show that the local wind force at the height of $2/3 \cdot H$ is the representative, the "referent height". Then, the level 8 is defined the "referent height" in this study.
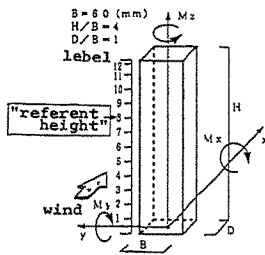
Fig.2 Test model
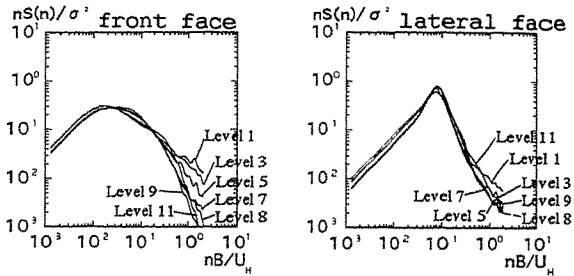
Fig.4 Measured power spectra of local wind forces on face
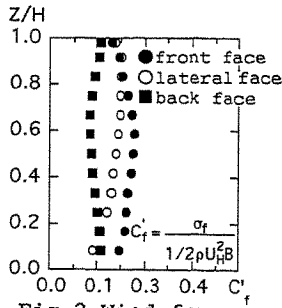
Fig.3 Wind force coefficient
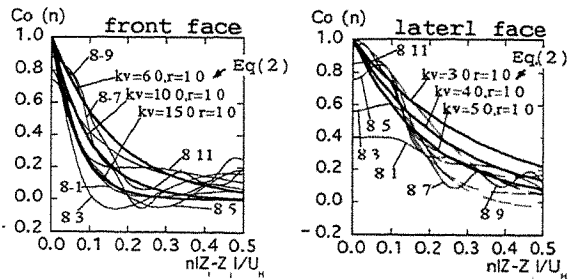
Fig.5 Measured co-cospectra between local wind forces on face
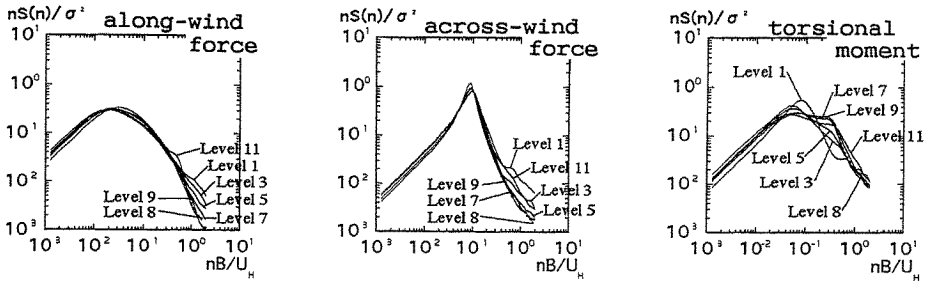
Fig.6 Measured power spectra of local wind forces
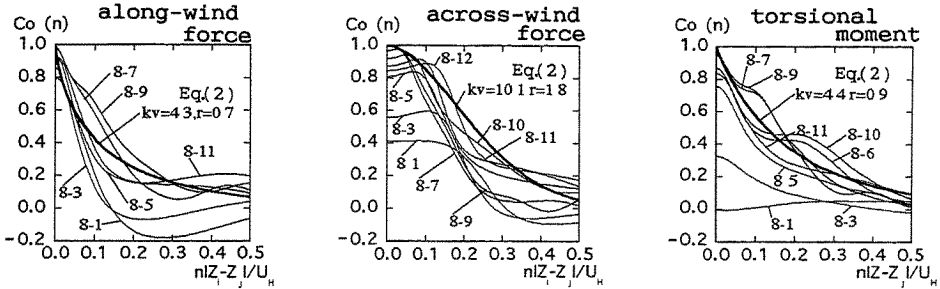
Fig.7 Measured co-cospectra between local wind forces
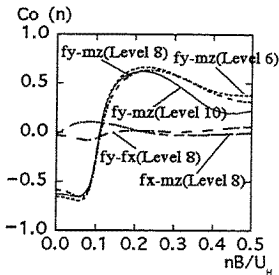
Fig.8 Measured co-cospectra between components
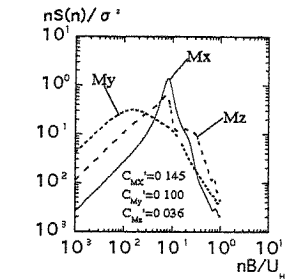
Fig.9 Measured power spectra by dynamic balance
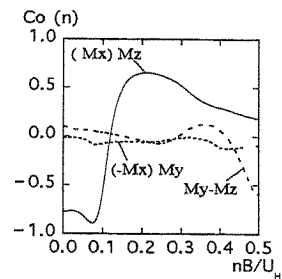
Fig.10 Measured co-cospectra by dynamic balance

3.Simulation of wind forces in one component

3.1 Simulation method

Simultaneous multi-local wind forces in one component are simulated by the Monte Carlo method[3]. The local force at the "referent height" is determined independently. The local forces at the other levels are determined depending on that of the neighboring level. Then, the only correlations between the neighboring 2 levels are considered in the evaluation of the spatial correlation of multi-local forces. Based on the results of the wind tunnel test, the power spectra of the local wind force (S(n;zi)) and the co-cospectra between the local wind forces of height zi and zj (Co(n;zi,zj)) are assumed as follows ;

281

$$nS(n;zi)/\sigma^2(zi)=nS(n;z0)/\sigma^2(z0) \qquad \cdots Eq.(1)$$

; z0 is "referent height"

$$Co(n;zi,zj) = \exp[-kv(n \mid zi-zj \mid /U_H)^r] \qquad \cdots Eq.(2)$$

; U_H = mean wind velocity at the top of the building,

kv =6.0,10.0,15.0 for front face and 3.0,4.0,5.0 for lateral face, and r=1.0

According to Eq.(1) and (2), the power spectra of the "referent height" local wind force $(S(n;z0))$ and of the 1st modal force $(S_{F1}(n))$ and are related in the following equation ;

$$S(n;z0)=S_{F1}(n)/\{\sum_i\sum_j[(C'_{fi}\cdot C'_{fj}/C'_{f0}{}^2)\cdot(ai\cdot aj\cdot \eta i\cdot \eta j\cdot Co(n))]\} \qquad \cdots Eq.(3)$$

where, C'_f ; local wind force coefficient, ai; normalized vertical span of i level,

ηi; value at i level of 1st vibration mode, and suffix 0; "referent height"

3.2 Results of simulation

The ratios (γ) of the 1st and 2nd modal wind force coefficients obtained from the simulation to the ones from the measurement, square root ratios (β) of the modal power spectra from the simulation to the ones from the measurement are shown in Fig.11 and 12. In Fig.12, the hatching part means the frequency equivalent to the 1st and 2nd fundamental frequencies of the building when U_H=20~80m/s.
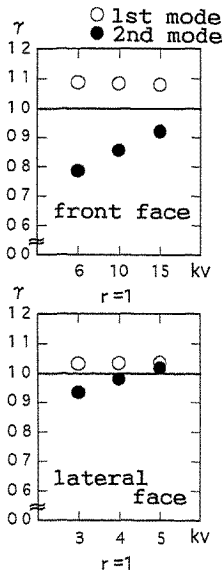
Fig.11 Ratio of modal wind force coefficient γ (simulation vs. measurement)
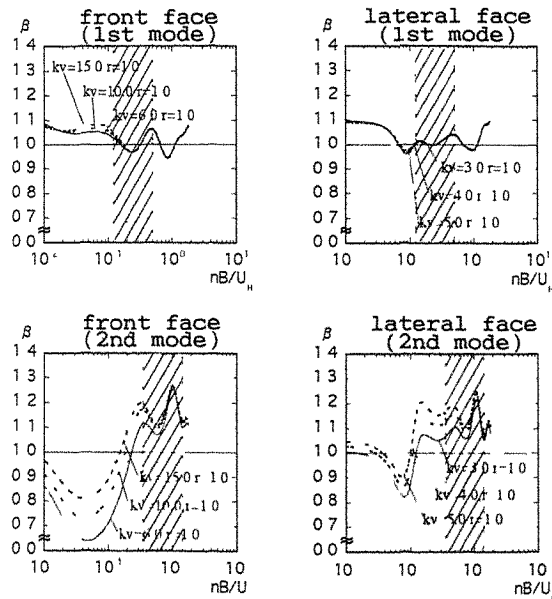
Fig.12 Square root ratio of power spectra of modal wind force β (simulation vs. measurement)

282

The values of γ and β evaluated by the 1st modal forces are hardly influenced by the change of kv. In case of the 2nd modal forces, the values of γ are underestimated a little, and the β's fluctuate more than of the 1st mode. These errors are due to Eq.(2) that ignores the phase difference in the front face and underestimates the spatial correlation at the peak frequency of the power spectra in the lateral face. However, the β in hatching part is within 1.1 – 1.3. These results show that the simulation of time–series of multi–local wind forces can be applied to the 2nd mode vibration of the building by selecting suitable parameter kv and r.

4.Simulation of 3–component multi–local wind forces
4.1 Simulation method

According to the results of section 3, the simulation method of simultaneous multi–local wind forces based on dynamic balance data with correlation among three components, along–wind,across–wind and torsion, is proposed. The correlation among the three components is considered as follows, based on the results of the co–cospectra between two different components of the local wind forces at each level of the model and the ones between the base moments (shown in Fig.13);

1) The correlations between local across–wind force (fy) and local torsional moment (mz) at the same level are equivalent to the correlation between across–wind and torsional base moments (Mx and Mz).

2) The relations between local along–wind force (fx) and the others are independent. (They are assumed no–correlations between each other.)

And, the correlation among components are directly considered at the " referent height " only. So, at the other levels, they are considered through the correlation of the " referent height ".

3) The spatial correlation in vertical direction is accord to the way showed last section.

The concept of this method is shown in Fig.14.
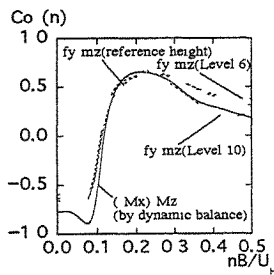
Fig.13 Measured co-cospectra between across-wind and torsional direction
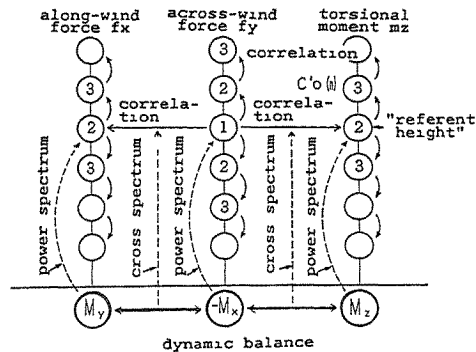
Fig.14 Simulation Method (considering 3-component simultaneity)

283

4.2 Results of simulation

The results of simulation are shown in Fig.15–17, comparing to the measurement. It corresponds to results of the section 3, this simulation reproduces well the base moments' power spectra from the wind tunnel test (See Fig.15). The correlations between components obtained from the simulation are weaker than the ones from the measurement at the part of the nondimensional frequency over 0.2. Although the correlations among components are considered at the "referent height" only, the simulation generally reproduces well the correlations at other than the "referent height" (See Fig.16 and 17).
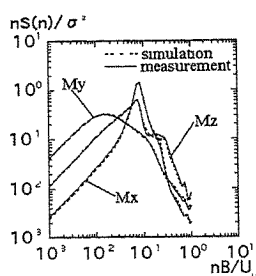
Fig.15 Result of simulation (power spectra of base moments)
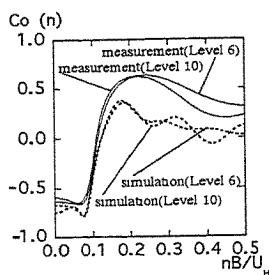
Fig.16 Result of simulation (co-cospectra between fy and mz)
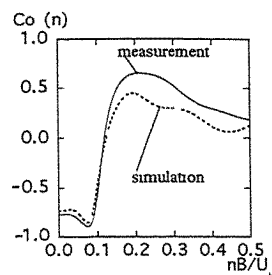
Fig.17 Result of simulation (co-cospectra between −Mx and Mz)

5.Concluding Remark

The simulation method of multi–local wind forces in the time domain and its validity is confirmed. This method can be applied to the case which has to been considered even the 2nd mode vibration of the building. Although this method can be applied on square cylinders of the aspect ratio 4.0 only, storing up data of other shapes can spread the limit of this method. The Eq.(2), approximating the co–cospectra in vertical direction, is considered only the decline depending on the nondimensional frequency. The development of more accurate simulation method, in which the effects of the phase difference and the distance between considering levels are also included, is in progress.

References:

1. T. Ohkuma, H. Marukawa et al., Across–wind and torsional acceleration of prismatic high rise buildings, proc. of the 8th International Conference on Wind Engineering, Canada, 1991
2. H. Kitamura, T. Ohkuma et al., Time history evaluation based on energy balance for wind–induced vibration of tall building, proc. of the 12th National Symposium on Wind Engineering, Tokyo, 1992 (in Japanese)
3. T. Ohkuma, H. Marukawa, Numerical experiment on wind–induced vibration of Chiba port tower, summaries of technical papers of Annual Meeting A.I.J., 1989 (in Japanese)
4. T. Ohkuma, H. Marukawa et al., Time history analysis of tall building using art. wind force based on dynamic balance data, summaries of technical papers of Annual Meeting A.I.J., 1992 (in Japanese)

Random response analysis of multi—story and tall buildings under pulsating wind

M.K.Xiao   M.Lai & Ch.Zhang

Deparment of Civil Engineering
Chongqing Inst. of Arch. and Engg., China

Abstract:In this paper, stochastic process is employed to analyse random response analysis of multi—story and tall buildings under pulsating wind loading. The obtained results are compared with those acquired by the suggested method the Code provides and by the results of time—history analysis through computer simulation. More applicable computation method is set forth to carry random response analysis of pulsating wind loading in practice.

1.Introduction

Wind is one of most destructive disasters human beings face. Wind loading plays an important role, even a dominant part in structural design of multi—story and tall buildings. The wind pressures a structure resists include two parts: average and pulsating wind pressures. The action of average wind pressure on a structure is similar to that of static forces, while the action of pulsating wind pressure, caused by irregularity of the wind itself, is the dynamic part that its strength varies with time at random. So, the pulsating wind is a random load. In this paper , theory and analytical methods of random process is employed to study stochastic response of multi—story and tall buildings under pulsating wind action.

2. Analytical Foundamentals and Parameters' Determination

(1) Probabilistic Characteristics of Pulsating Wind

Wind records show that , wind vibration is nonstationary at the beginning, as time passes, this nonstationary process disappears and it enters into stationary process. If the initial strong nonstationary part of the process is ignored, the wind vibration, as a whole, is closely similar to a stationary process. All the describing probabilistic variables do not change with time. Under this assumption, the pulsating wind can be treated as a stationary random process. At the same time, for the sake of obtaining the probabilistic variables of a random process $X(t)$, all the sample functions of $X(t)$ should be available. But it is impossible in practice. However, if the probability distribution of sample functions is the same as one another, the probability distribution of parental function can be deduced by that of a sample function. Then, the random process $X(t)$ is called an ergodic process. In view of a wind record, the probabilitical distribution of sample functions is almost the same, thus, in this paper, the pulsating wind is treated as an ergodic process in which time average is substituted for sample average.

(2) Power Spectrum of Pulsating Wind

Under pulsating wind, a structure responses in random when time and frequency ω change. The response can be analyzed in frequency dormain. Thus, analyzing random response of a structure under pulsating wind first concern itself with the problem of obtaining the power spectrum function of input pulsating wind.

The power spectrum of pulsating wind should be obtained by observed wind velocity records. Many influencial factors are included in the spectrum. On basis of different point of view and foundamental assumptions, various kinds of forms of the spectrum have been put

forth. One of them is the Davenport spectrum, the most widely used one. In this paper, the Davenport spectrum and another two spectrum, acquired on basis of research on the characteristics of mountain pulsating wind in southern part of Sichuan Province, China, and modified on the specific probabilistical characteristics of the pulsating wind in this area are employed. Here is the form of the spectrum we use,

Davenport spectrum:

$$S_v(n) = 4K\bar{v}_{10}^2 \frac{x^2}{n(1+x^2)^{4/3}} \tag{1}$$

Power spectrum of mountain pulsating wind in southern part of Sichuan:

$$S_v(n) = 6.000 K\bar{v}_{10}^2 \frac{x^2}{n(0.8+x^2)^{1.2936}} \tag{2}$$

$$or \qquad S_v(10) = \frac{2.3312 K\bar{v}_{10}^2}{n} exp\left[-\frac{(lgx - 0.5839)^2}{0.9215} \right] \tag{3}$$

Where, $\bar{V}_{10}$ represents average wind velocity at the height of 10m, and $x = 1200n / \bar{v}_{10}$. In this paper, the roughness coefficient K is 0.0024.

In general, there are three kinds of analytical models that are used, according to their characteristics of deformation, to carry out random response of multi-story and tall building under wind load, they are shear type model, bending type model and shear-bending type model. Thus, a structure is modelled as a multi-degree-of freedom system. The masses of the structure are lumped at the height of each floor. For a shear type model, only one horizontal deflection freedom is considered; as for a bending type or shear-bending type model, one horizontal and one rotational freedoms are considered.

Pulsating wind loading is not only time-variant, but also space-variant. In this discussion, the depth of a building is far more small than that of its horizontal length or its total height H. So, it's backward and forward variance are ignored. As a structure is treated as an MDOF system, it's impossible to account for horizontal variance of pulsating wind loading, in this paper, only up and down variance is considered.

Davenport studied the factors such as frequency n, $(n = \omega / 2\pi)$, distance between two points $(h_i - h_i')$ and average velocity $\bar{V}_z$ and the correlation coefficient is shown as

$$\rho(n, h_i, h_{i'}) = exp\left(-C_z \frac{n|h_i - h_{i'}|}{\bar{v}_z} \right) \tag{4}$$

C_z is relevant with area, distance, height and climate. Its value has not yet received general agreement. Davenpart suggested the C_z is equal to 7, $\bar{V}_z$ is usually the average velocity of point i and i′, $\frac{\bar{V}_z}{n}$ stands for wave length. In pulsation of a gale, the longer the wave length is, the stronger the correlation is.

Many scholars have set forth many other kinds of formula to obtain correlation coefficient ρ_{xy}. Among all of them discussed above, Davenport's formula is the most appropriate one. So, equation (4) of Davenport's is used to study effect of space correlation of pulsating wind on multi-story and tall buildings.

3. Basic Formula of Linear Response of Regular Multi-story and Tall Buildings in the Direction of Wind

(1) Differential Equations of Structures

A multi-story or tall building in linear response is discreted as an MDOF system. Its dynamic differential equation is

$$[M]\{\ddot{y}\} + [c]\{\dot{y}\} + [K]\{y\} = \{P(t)\} \tag{5}$$

The element of right column $\{P(t)\}$, $P_i(t) = A_i W_i(t)$, in which, A_i, $W_i(t)$ represent the facet area and pulsating wind pressure respectively. $\{P(t)\}$ is a column of wind loading. $[M]$, $[c]$ and $[K]$ stand for mass, damping and stiffness matrices. $\{y\}$, $\{\dot{y}\}$ and $\{\ddot{y}\}$ are displacement, velocity and acceleration columns.

(2) Mode Superposition Procedure

Equation (5) can be solved by using mode superposition procedure. Normal coordinates $q_i(t)$ provided by the free-vibration mode shapes are employed to describe the displacement $y_i(t)$, and normal coordinates $q_i(t)$ based on the vibration mode Φ_{ij} are employed to describe the displacement of mass point. That is,

$$y_i(t) = \sum_{i=1}^{n} g_i(t) \cdot \varphi_{i} \quad or \quad \{y(t)\} = [\varphi]\{q(t)\} \tag{6}$$

As the mode shapes constitute N independent displacement patterns, and because of their orthogonality properties, they can be used to decouple equation (5). Thus, N independant generlized SDOF system dynamic equations are obtained.

Using equation (6) to substitute $\{y(t)\}$ in eq.(5), and premultipling $[\varphi]^T$ yields,

$$[\Phi]^T[M][\Phi]\{\ddot{q}(t)\} + [\Phi]^T[c][\Phi]\{\dot{q}(t)\} + [\Phi]^T[k][\Phi]\{q(t)\} = [\Phi]^T\{P(t)\} \tag{7}$$

Because of the orthogonality property of mode shapes and damping matrix $[c]$, equation (7) changes into the form as

$$\ddot{q}_i(t) + 2\xi_i\omega_i\dot{q}_i(t) + \omega_i^2 q_i(t) = F_i(t) \qquad (i = 1,2,\cdots,n) \tag{8}$$

Where, damping coefficient of mode i is represented by the damping ratio ξ_i. Thus, equation (5) is decoupled as N independant equations. $F_i(t)$ stands for the loading term of i mode.

Mode superposition procedure is very efficient both in the solution of determinate and nonderterminate differential equations.

(3) Displacement Response

Power spectrum density function of displacement response of a structure can be availed by eq.(6). That is,

$$S_{Y_i} = \sum_{j=1}^{n} \sum_{i=1}^{n} \Phi_{ij}\Phi_{ik} H_j(-i\omega)H_k(i\omega)S_{F F_k}(\omega) \tag{9}$$

In which,

$$H_j(-i\omega) = \cfrac{1}{\omega_j^2\left[1 - \left(\cfrac{\omega}{\omega_j}\right)^2 - 2i\xi_j\cfrac{\omega}{\omega_j}\right]} \tag{10}$$

$$H_k(i\omega) = \cfrac{1}{\omega_k^2[1 - \left(\cfrac{\omega}{\omega_k}\right)^2 + 2i\xi_j\cfrac{\omega}{\omega_k}]} \tag{11}$$

287

$H_r H_k$ are called frequency dormain response functions.

$$S_{F_r F_k}(\omega) = \frac{\sum\limits_{i=1}^{n}\sum\limits_{i'=1}^{n} \varphi_{Li}\varphi_{ri}A_iA_{i'}S_{\omega}(h_i,h_{i'},\omega)}{\sum\limits_{i=1}^{n}m_i\Phi_{Li}^2 \sum\limits_{k=1}^{n}m_i\Phi_{ki}^2} \tag{12}$$

In the above equation, $S_{\omega}(h_i,h_{i'},\omega)$ is power spectrum of pulsating wind pressure. Considering the relation between auto—spectral density and cross—spectral density functions, the space relevance of pulsating wind and the fact that when the wind velocity is the same, if the shape of a building is different, the distribution of wind pressure is different, assuming that pulsating wind velocity spectrum does not change with the height, we have

$$S_{F_r F_k} = \frac{\sum\limits_{i=1}^{n}\sum\limits_{i'=1}^{n} \rho^2\mu_{Si}\overline{V}_i\mu_{Si'}\overline{V}_{i'}\rho(h_i,h_{i'},\omega)S_v^{(\omega)}\Phi_{Li}\Phi_{rk}}{\sum\limits_{i=1}^{n}m_i\Phi_{Li}^2 \sum\limits_{i=1}^{n}m_i\Phi_{ki}^2} \tag{13}$$

In which ρ is mass density of air, μ_s is shape coefficient of a building under wind load.

Due to the fact that practical structure's damping ratio is small in general, correlative terms are ignored. Variance of the structural displacement response is

$$\sigma_{Y_i}^2 = \sum\limits_{j=1}^{n} \Phi_{Li}^2 g_j \lambda_{oj} \tag{14}$$

In which,

$$g_j = \sum\limits_{j=1}^{\infty}\frac{\Phi_{Li}^2}{M_j^{*2}} \sum\limits_{i=1}^{n}\sum\limits_{i'=1}^{n} \rho^2\mu_{si}\overline{V}_i\mu_{si'}\overline{V}_{i'}\rho(h_i,h_{i'},\omega)\Phi_{Li}\Phi_{ri}A_iA_{i'} \tag{15}$$

$$\lambda_{oj} = \int_o^{\infty} |H_j(i\omega)|^2 S_v(\omega)d\omega \tag{16}$$

(4) Force of Wind Loading and Internal Force Response

If the probabilitic displacement value of $\sigma_{Y_{ij}}$ or the maximum value $\mu\sigma_{Y_{ij}}$ in design of jth mode is acquired, then all other values ,such as moment, shear, can be deduced. That is to say, $\sigma_{Y_{ij}}$ is used to obtain equivalent loading force of corresponding jth mode ,and then internal forces are calculated by structural analysis. The equivalent wind load is,

$$P_{di_j} = \mu\sigma_{di_j} = m_i\omega_j^2\mu\sigma_{Y_j} \tag{17}$$

Then structral response of each mode can be obtained by structral analysis after the loading can be obtained, total response of a structure under pulsating wind loading can be obtained by SRSS method.

As the displacement terms of the first mode are of the same sign, alternative signs occurs to the other modes ,so the first mode plays dominant role in structural response. Influence of higher modes can be ignored. Thus, in the computation of equivalent wind loads and total structural response, it is appropriate only to consider the influence of the first mode.

4. Example

For the three kinds of structures discussed above, various methods, the Code sug-

gested method, random process method and time history analysis in time dormain are used to compare with each other the results obtained. Here is an example.

The height of a R / C chimney is 100m. Slope ratio $L_x(H) / L_x(o) = 0.5$, $\mu_{si} = \mu_s = $ constant, $W_0 = 0.40 KN / m^2$, ground roughness B, its foundamental period $T_1 = 0.6S$.

The results of the above three kinds of methods are shown in the following table.

5. Conclusions

By the comparison shown above, it is concluded that pulsating wind is a kind of dynamic loading that can not be ignored. Response of a structure under pulsating wind loading is about $30 \sim 50\%$, even more, compared with that caused by average wind pressure. The modified Daverport spectrum density based on the records in the mountain area of southern Sichuan, China, is employed to carry out random response of structures and the results are appropriate. Results of the method suggested in this paper are similar to those obtained by time—history analysis on computers and are reasonable. The method suggested in the Code under estimates the effect of pulsating wind. So in this paper, it is suggested to employ random process in frequancy dormain or time—history analysis in time dormain to take this effect into consideration. These two methods have satisfactory accuracy.

References:
1. Emil Simil, Roberth Scanln, Wind Effects on Structure.
2. Z.D.Yu, Random Theory and application.
3. X.T.Zhang, Structure Wind Pressure and Vibration Calculate.

force	method	0	10	20	30	40	50	60	70	80	90	100
Shear (KN)	code method	55.3072	55.3072	55.0723	54.1901	52.2698	49.0074	44.145	37.6407	29.418	19.5709	8.3268
	Random vibration method	71.3871	71.3871	70.8168	68.8265	64.7849	58.5078	50.163	40.162	28.9102	17.085	5.5876
	Time history method	158.6000	158.6000	92.3400	69.9600	62.1700	53.4300	44.0000	34.1500	24.1000	14.1200	4.6300
bending moment (KN·m)	code method	4049.486	3456.414	2945.687	2403.786	1881.088	1391.014	949.564	573.157	278.977	83.268	0.000
	Random vibration method	4762.309	4048.438	3340.27	2652.005	2004.156	1419.078	917.448	515.828	226.726	55.876	0.000
	Time history method	4932.000	3613.000	3066.000	2367.000	1745.000	1210.000	770.300	428.700	187.700	16.370	0.000

Table Comparasion of distribution of internal force along the height
of structure under pulsating wind

290

DAMPING ESTIMATE FROM FULL-SCALE MEASUREMENT OF THE DYNAMIC RESPONSE OF A HIGH-RISE BUILDING UNDER WIND LOADS

J. Jong Lou and Kang-Ning Lou[+]

Weidlinger Associates, Inc., New York, NY, USA
Polytechnic University, Brooklyn, NY, USA
[+]Institute of Mechanical Engineering
National Chung-Cheng University, Chia-Yi, Taiwan, R.O.C.

Abstract: Damping estimates from full-scale measurements of the dynamic response of a high-rise building under wind loads have been attempted for the first translational modes. Inconsistencies in the estimated damping values by the half-power method have led to the investigation of the quantities of data necessary to achieve reasonable statistical estimates. With the availability of a wealth of data, the present study has identified the method of moments as a practicable way to assess the response of wind-excited structures. Damping measurements taken in light winds as well as in strong winds are seen in good agreement with values assumed in design, with quantitative evaluation providing an insight into the structural damping and aerodynamic damping.

1. Introduction

A long term full-scale measurement program for the dynamic response of a high-rise building under wind loads has been instituted. Measurements were made of the acceleration response of the wind-excited structure with the use of horizontal-axis accelerometers near the top of the building. Numerous records of building response under various wind conditions were collected over a period of two years when building activities exceed a preset threshold level.

Data were analyzed to identify the structural parameters of the vibrating building. However, preliminary attempts to estimate the structural damping have yielded "inconsistent" results. An extensive literature survey has revealed that these inconsistencies in the damping estimate from measurements would not have been encountered in most prior published studies due to the quantities of data involved [1]. These previous damping estimates were obtained from relatively short records of building ambient response under light wind conditions. The half-power method, for example, has normally been employed to estimate the damping associated with motion in the fundamental mode of vibration. The shape of the spectral curve at the half-power points is "eyeballed" using adjacent points to some degree. Furthermore, in order to obtain a better estimate of the smooth "true" spectral density, it has been common to modify the "raw" estimate by frequency averaging. However, the statistical errors in the estimated damping values have rarely been discussed. It can be shown that for 10 % confidence interval and 9 % bias error a record length of $200/\varsigma fr$ seconds is necessary, or approximately 5 1/2 hours for a structural with a natural frequency $fr = 1.0$ Hz and

291

damping $\varsigma = 1.0\%$ of critical [2]. It has become clear that the quantities of data necessary to achieve reasonable statistical estimate are much larger than those used in the past. Furthermore, it seems unlikely that a sequence of stationary data can be found for the quantities of data required.

The present study, with a wealth of data available, allows a practicable method to assess the response by using combined ensemble plus frequency averaging techniques, in which data occurring when similar conditions exist are averaged. Various explorations have led to the employment of the method of moments by Vanmarcke to estimate the damping values [3]. The method of moments involves computation of the first three moments of the estimated response power spectral density in a frequency band which includes the fundamental frequency. No prior smoothing of the spectrum is necessary and the record length needed is relatively small. Results from these verification processes have shed light on the record length needed to obtain reasonably stable estimates of spectral moment. Some other earlier studies have used the autocorrelation method in estimating damping ratio. However, it has been shown that, when using an acceleration response, significant inaccuracies will likely occur when damping ratio approaches 0.016 [4]. Although the method may be applied to records of light wind activities, under strong wind conditions, high excitation levels and aerodynamic effects have been confirmed to contribute to the amount of damping in the present study. The aerodynamic characteristics giving rise to the possibility of both positive and negative aerodynamic damping in the along wind and across wind response have been examined. The wind characteristics obtained during the measurement of building movements have permitted quantitative estimates of aerodynamic dampings.

The algebraic sum of the structural damping empirically estimated and the aerodynamic damping theoretically derived and confirmed by wind tunnel tests gives the total damping, which is seen in good agreement with damping values computed from the measurements.

2. Damping Estimates

Damping values are computed by the half-power method with ensemble averaging as shown selectively in Table 1. It can clearly be seen that large fluctuations exist in these estimates. Damping values compiled by using Vanmarcke's method of moments are compared in Table 1. Several cycles of iteration have been carried out to account properly for the contribution of other modes to the partial moment. It is interesting to note that damping values computed by the method of moments are consistent at different reduced bandwidths. It appears that the confidence level is relatively high for damping values estimated by Vanmarcke's method with a reasonable number of ensemble averages.

3. Light Wind Conditions

From measurements, damping values for the tower in the North-South (less stiff) and East-West (stiffer) directions are estimated to be approximately 1.5% and 1.0% respectively under light wind conditions. It should be noted that the damping estimate is usually not known to an accuracy better than ±0.5% of the actual value. The low damping ratios from the measurements are not surprising, at least at the low amplitudes of vibration encountered, since the structural members are rigidly tied together to act as a single tube, and most of the

energy is dissipated by internal friction within the material rather than in joint slippage. The contribution of aerodynamic damping to the total damping is small at low wind speeds, i.e., low amplitude. In fact damping estimates drawn from this study agree favorably with value (1.3%) empirically put forth in the original design of the tower under light wind conditions.

4. Strong Wind Conditions

Under strong wind conditions, damping in the fundamental modes for the tower is estimated, from measurements, to lie between 1.5% and 2.5% (see Table 1). It is apparent that high excitation levels and aerodynamic effects have contributed to the amount of damping present. Damping assumptions put the total damping of the tower under strong winds to be approximately 2.0% of critical, an increase on the order of 0.8% over that assumed for light wind conditions.

The aerodynamic characteristics giving rise to the possibility of both positive and negative damping are present in the tower. The aerodynamic damping is a function of the reduced velocity V(H)/fD, where V(H) is the mean wind speed at height H (top of the tower), D a characteristic length and f the fundamental frequency of vibration. At large values of the reduced velocity, the aerodynamic damping becomes significant. For damping in the along-wind direction, the aerodynamic damping (according to Davenport) can be expressed as [5]:

$$\zeta_{aero} \approx \frac{1}{2\pi} \frac{\rho D^2}{M} \frac{\overline{V}(H)}{fD} \frac{3}{2(3+a)} C_D \tag{1}$$

where a is the exponent of the velocity profile and C_D is the drag coefficient. The factor $\rho D^2/M$ represents the ratio of the air density ρ to the nominal building density M/D^2 where M is the mass per unit length. According to this relationship the aerodynamic damping in the along-wind direction is always positive, i.e., additive to the structural damping, and increases with wind speed.

In the across-wind direction, aerodynamic damping can have either a positive or a negative value, as expressed by [5]:

$$\zeta_{aero} \approx -\rho \frac{D^2}{M} C_a (\overline{V}(H)/fD) \tag{2}$$

293

RESPONSE RECORDS		ς = % CRITICAL DAMPING				
		1/2 POWER METHOD	METHOD OF MOMENTS (1ST TRIAL)	METHOD OF MOMENTS (ITERATED)		
				Wb=100 LINES	Wb=50 LINES	Wb=25 LINES
LIGHT WINDS	E/W, 11 AVERAGES	0.86%	-	-	0.8%	1.0%
	N/S, 100 AVERAGES	1.89%	1.8%	-	1.4%	1.4%
	N/S, 11 AVERAGES	1.09%	3.4%	-	2.0%	1.5%
STRONG WINDS	N/S, 100 AVERAGES	2.77%	7.8%	2.2%	2.1%	2.2%
	E/W, 100 AVERAGES	2.32%	3.5%	1.7%	1.4%	1.4%

Table 1. Computed damping values from measurements

where C_a is an aerodynamic damping derivative, which must be evaluated from experiments. The derivative is a function of the reduced velocity V(H)/fD. Figure 1 depicts the across-wind aerodynamic damping derivative for a prism, calculated from measurements by Otsuki et al [6]. The diagram shows that, at the critical reduced velocity for vortex shedding, the sign of the derivative changes and the damping becomes suddenly negative. Below the
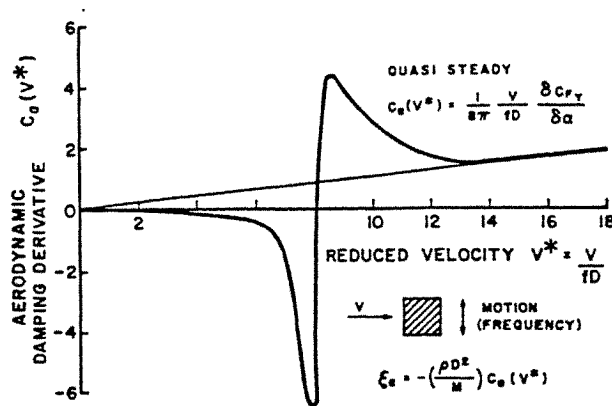
Fig. 1   Measurements of Aeroelastic Damping Derivatives
For Across-Wind Motion by Otsuki et al [6]
(after Davenport and Tschanz [5])

294

critical velocity the across-wind damping is positive (C_x negative). At very high reduced velocities, the damping approaches the quasi-steady value.

The wind information obtained during the measurement of building movements is from the U.S. Weather Bureau data recorded at a nearby airport. Windspeeds and directions were measured at 10 ft above the runway. These surface records would have to be converted, for purposes of the dynamic study, to be representative of the wind at the height of the tower. The use of the power-law formula

$$\overline{V}(H) = \overline{V}(z) \, (H/z)^a \qquad\qquad (3)$$

allows a rough estimate of the wind speed at the top of the tower. The wind direction shift from surface to the building height is thought to be approximately 15 to 25 degrees clockwise. It is seen that, at the time of the experiments, the surface average wind speed was roughly 30 mph and 110 to 140 degrees from Grid North. The wind tunnel test report indicates a power-law exponent of 0.3 for the range of these wind directions. It is estimated, then, that wind speed at the top of the tower were approximately 130 mph and 135 to 165 degrees from Grid North. The reduced velocity V(H)/fD is roughly 10.5 with a base width D = 208 ft and the observed frequency f = 0.086 Hz. The x, y acceleration time traces of the record indicate a dominant across-wind (East/West) response. The aerodynamic damping at V(H)/fD = 10.5 in the across-wind direction was assumed to be approximately -0.5% based on wind tunnel test report as shown in Fig.2. Building movements in the North/South direction are seen to be along-wind in nature and the aerodynamic damping is estimated by Equation (1) to be approximately +0.5%. The algebraic sum of the structural damping (2.0% previously assumed for strong winds) and the aerodynamic damping (± 0.5% theoretically derived for strong winds) gives the total damping, which is seen in good agreement with damping values computed from the measurements (1.5% in the across-wind direction and 2.5% in the along-wind direction).

It should be pointed out, however, that the damping investigation described above represents simply an attempt to provide a knowledge of the range of damping which may be present in the building. The inherent uncertainties of the analytical methods, which are further augmented by the uncertainties in estimating the wind and the building response, prohibit more precise numerical estimates of overall damping.
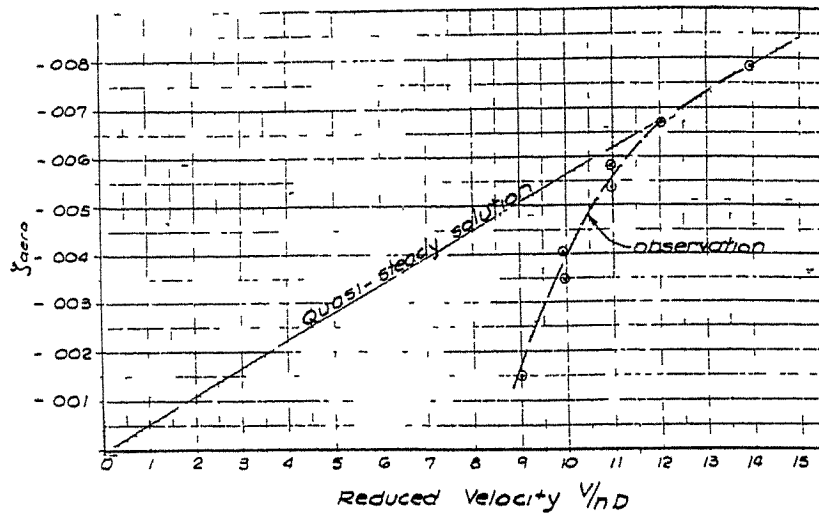
Fig. 2.   Variation of aerodynamic damping with reduced velocity from
wind tunnel test results

Acknowledgements

References:

1.   P.J. Durning and D. Engle, Proc. Specialty Conference ASCE/EMD, Los Angeles,
(1976) 143.

2.   A.P. Jeary and B.R. Ellis, Proc. Wind Engineering 5th International Conference, Fort
Collins, (1979) 1357.

3.   E.H. Vanmarcke, Proc. 3rd Annual Offshore Technology Conference, Houston,
(1971) OTC1407.

4   A P. Jeary, Proc. Inst. Civ. Engle, Part 2, (1973) 321.

5   A G Davenport and T Tschanz, Proc 4th U S. National Conference on Wind
Engineering, Seattle, (1981) 205.

6.   Y. Otsuki, K. Washizu, H Tomizawa, and A. Ohya, Jl. of Sound and Vibration,
(1974) 233

296

A computer program for the evaluation of dynamic response of structures   to wind turbulence

M Attou

Ecole Centrale, Nantes, France
+ Centre Scientifique et Technique du Bâtiment, Nantes, France

Abstract : The paper presents a computer program designed for the evaluation of displacements and accelerations of flexible structures to wind turbulence loads. An up to date model of wind turbulence has been required for the evaluation of wind-induced froces and moments. Dynamic structure response has been calculated by spectral method The structures have been discretized by finite element method. The program named DYCAST has been tested on complex examples. The program can be used in parametric study to provide data of displacements and accelerations of flexible structures. These data are useful to professional engineers for estimations of some variable magnitudes before doing experiences in wind-tunnels and also for preliminary design purposes

1 Introduction

The evaluation of wind effects on particular types of structures often presents difficulties.Because the wind load on structure depends on many factors, some of which are connected with the wind-structure interaction. The present work presents a computer program designed for the evaluation of wind-induced effects, particularly turbulence effects, on a linear elastic structural system The structural dynamic response is characterized by a spectral density function obtained by the stochastic approach preconised by Davenport [1]. The structure has been represented by an equivalent discrete system of N degrees of freedom obtained by the finite element analysis [6] The free vibration analysis is described and natural frequencies are examined with this discrete structure The wind turbulence model near the ground has been considered as a stationary Gaussian process The evaluation of wind-induced forces and moments has been based on a steady experimental lift, drag and moment coefficients C_L C_D, C_M obtained from scaled model test in wind-tunnel The computer program has been tested on   complex examples Normandie Cable Stayed Bridge (free standing pylon and full span completed bridge [8],[9])

2 The DYCAST computer program

2.1 Structure model

The computation of the dynamic structure response can be reduced to the research of an equivalent discrete system The differential equation of motion which can be written using the displacement based on finite element method [13] as

$$M\{D\} + C\{D\} + K\{D\} = \{F\} \tag{1}$$

where M, C and K are the mass damping and stiffness matrices, respectively $\{F\}$ is the external applied load vector and $\{D\}$ $\{D\}$ and $\{D\}$ are the nodal displacement, velocity and acceleration vectors, respectively All vectors are N-dimensional, where N is the total number of degrees of freedom of the discretized structure. The elements used by the program for discretization purposes are beam 2-node with six degrees of freedom per node (three displacements and three rotations) and bar 2-node with three displacements degrees of freedom per node Stresses and strains components are evaluated in local coordinate system using the Hooke generalized strain-displacement relationships [6]. It is supposed that the structural damping matrix C can be written as generalized Rayleigh form

$$C = M \sum_j \alpha_j (M^{-1} K)^j \tag{2}$$

2.2 Turbulence model

With reference to a cartesian system of coordinate X, Y, Z the instantaneous wind velocity $\vec{U}(M,t)$ has been considered to be composed of two vectorial components: the mean velocity component $\vec{U}(M)$ and the fluctuating component $\vec{V}(M,t)$. The first one is only a function of the point height, while the second one is also a function of the time.

It is supposed that the fluid motion is horizontal and homogeneous, and the terrain roughness parameter is constant. Supposing that the X-direction coincides with the mean wind direction (fig. 1), the following equation can be stated
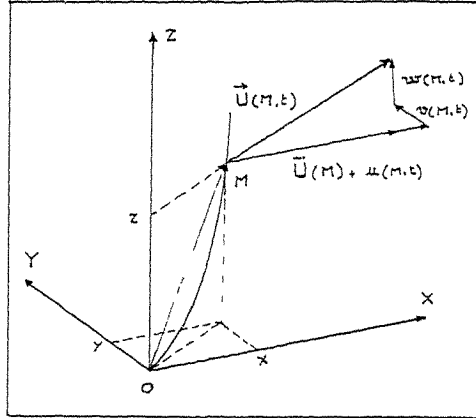
Fig. 1.

$$\vec{U}(M,t) = \vec{U}(Z)\ \vec{X} + \vec{V}(M,t) \tag{3}$$

$$\overrightarrow{OM} = \left\{\begin{matrix} X \\ Y \\ Z \end{matrix}\right\}; \quad \vec{V}(M,t) = \left\{\begin{matrix} u(M,t) \\ v(M,t) \\ w(M,t) \end{matrix}\right\} \tag{4}$$

The mean wind velocity $\vec{U}(Z)$ has been expressed by the logarithmic profile

$$\vec{U}(Z) = \frac{u_*}{k} . \ln\left(\frac{Z}{Z_0}\right) \tag{5}$$

Where u_* is the shear velocity, $k = 0.4$ is the Von Karman constant and Z_0 terrain roughness length.

The fluctuating component of the wind velocity has been considered as a stationary Gaussian process, with zero mean value, stochastically characterized by its auto- and cross-correlation functions. Turbulence intensity which is a global characterization on each point in the space of atmospheric turbulence is defined as the ratio of the standard deviation of the instantaneous fluctuating velocity component to the mean wind speed.

$$\xi = u, v, w, \quad I_\xi(M) = \frac{\sigma_\xi}{\vec{U}(M)} \tag{6}$$

In the frequency domain the characterization is given by the spectral density function for each of the processes u, v and w and the cross-spectral density function between longitudinal component u and vertical component w. The Von Karman formulations have been required in the program (fig. 2)

298
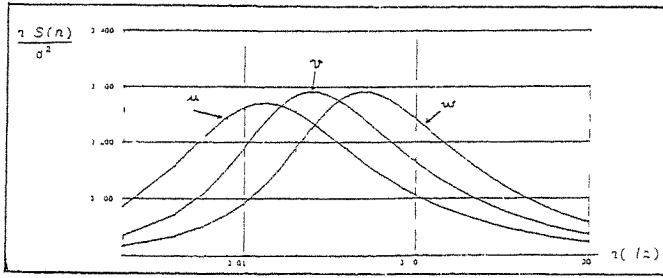
Fig. 2.

$$\xi = u; \quad \frac{n.S_{\xi\xi}(M,n)}{\sigma_\xi^2} = 4\frac{x_\xi}{[1+70.7x_\xi^2]^{5/6}} \tag{7}$$

$$\xi = v,w; \quad \frac{n.S_{\xi\xi}(M,n)}{\sigma_\xi^2} = 4x_\xi\frac{[1+188.4(2x_\xi)^2]}{[1+70.7(2x_\xi)^2]^{11/6}} \tag{8}$$

$$x_\xi = \frac{n\,L_\xi^x(M)}{\overline{U}(M)} \tag{9}$$

where $L_\xi^x(M)$ is longitudinal length scale of fluctuating component ξ. Length scales of turbulence are useful quantities because they are a comparative measurement of the average time size of a gust in approppriate directions.

The cross-spectral density function between two points M and M' in space has been expressed as

$$\xi = u,v,w; \quad S_{\xi\xi}(M,M',n) = \sqrt{S_{\xi\xi}(M,n)S_{\xi\xi}(M',n)}\; \gamma_\xi(M,M',n) \tag{10}$$

where the term $\gamma_\xi(M,M',n)$ called coherence function has been approximated by

$$\gamma_\xi(M,M',n) = \exp\left[-\frac{2n.\sqrt{\tau}}{\overline{U}(Z)+\overline{U}(Z')}\right] \tag{11}$$

$$\tau = [C_\xi^Y(Y-Y')]^2 + [C_\xi^Z(Z-Z')]^2 \tag{12}$$

Values of C_ξ^Y and C_ξ^Z are measured or estimated [5].

Values of cross-spectral density between u and w, $S_{uw}(M,n)$ have been considered for evaluating response of some particular structures as bridges. These are given by the empirical expression [7]

$$S_{uw}(M,n) = \sqrt{S_{uu}(n)S_{ww}(n)}\,.\,\Gamma_{uw}(M,n) \tag{13}$$

$$\Gamma_{uw}(M,n) = \frac{1}{A_z}\frac{-0.3}{\sqrt{1+0.4x_u^2}} \tag{14}$$

$$x_u = \frac{n.L_u^x(M)}{\overline{U}(M)} \tag{15}$$

$$A_z = 0.247 + 0.344\log Z - 0.036(\log Z)^2 \tag{16}$$

where Z is the height of the point M.

2.3 Aerodynamic loads model

Representing structures by beams or bars allows practice evaluation of aerodynamic forces acting on these beams or bars. The aerodynamic forces and moments acting on a beam or a bar (fig. 3) are related to values of instantaneous wind velocity through the use of aerodynamic coefficients C_L, C_D, C_M obtained from scaled model test in wind-tunnel.

299
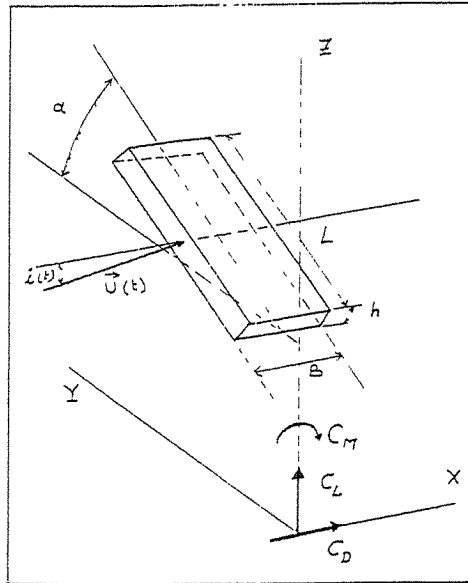
Fig. 3.

Formulations from Scanlan [10] have been required for evaluating aerodynamic forces and moments. The expression of lift aerodynamic force is

$$F_L = 1/2\rho \overline{U}^2 B . L \left[C_L + 2C_L . \frac{u(t)}{\overline{U}} + \frac{dC_L}{dt} . \frac{\zeta(t)}{\overline{U}} - 2C_L \frac{Z(t)}{\overline{U}} \right]$$ (17)

Where ρ is the atmospheric air density and

$$\zeta(t) = w(t)\cos\alpha - v(t)\sin\alpha$$ (18)

The first term represents the action of the mean-wind. The second provides the effect of wind-velocity fluctuating $u(t)$. The third term expresses the effect of transversal components of turbulence $v(t)$ and $w(t)$. And the last one represents the effect of the vertical displacement velocity of structure ,it is the self exitation . Both the third and the last term needs evaluation of slope of the lift coefficient $\frac{dC_L}{dt}$ which is measured in wind-tunnel

In similar way the drag aerodynamic force is expressed by following relation

$$F_D = 1/2\rho \overline{U}^2 B . L \left[C_D + 2C_D . \frac{u(t)}{\overline{U}} + \frac{dC_D}{dt} . \frac{\zeta(t)}{\overline{U}} - 2C_D \frac{X(t)}{\overline{U}} \right]$$ (19)

The aerodynamic moment is expressed as :

$$M = 1/2\rho \overline{U}^2 B^2 . L \left[C_M + 2C_M \frac{u(t)}{\overline{U}} + \frac{dC_M}{dt} \frac{\zeta(t)}{\overline{U}} \right]$$ (20)

This relation is obtained with supposing the same hypothesis which have been required for the forces expressions, but the self exitation resulting from the rotation of the beam or bar about moment axis is neglected here.

2.4 Computation procedure

For a linear elastic structural system, a commonly used technique for solving equation (1) is the modal synthesis. It has the computational advantage that the response of a structure discretized as a large order N degrees of freedom configuration can be effectively reduced to one with P degrees of freedom with $P \ll N$, where P is the number of modes required.

As shown in figure 4, the resulting free vibration eigenvalue problem is solved by an iteration algorithm for a specified number of lowest vibration modes [ϕ].

300

These natural frequency and mode shape characteristics are stored in files for use in subsequent buffeting analysis. The response of each uncoupled mode of vibration to wind turbulence can be studied separately and superimposed at the end. The correlation between the differents modes is neglicted in this approach, but it would be incorporated in the future.

Equation of an uncoupled mode can be expressed as

$$M(\ddot{\phi} + 4\zeta\pi n_0 \dot{\phi} + 4\pi^2 n_0^2 \phi) = F \tag{21}$$

where M is the mode generalized mass, n_0 is the natural frequency of this mode, ζ is the total damping, expressed as fraction of critical damping, ϕ is the mode shape function describing deflected shape of structure in this mode and F is the mode generalized force.

$$\zeta = \zeta_s + \zeta_a \tag{22}$$

where ζ_s is the structural damping and ζ_a is the aerodynamic one which provides the self exitation effect.

The modal response is estimated using spectral approach [3]

$$\sigma_\phi^2 = \int_0^\infty S_\phi(n)dn \tag{23}$$

with :

$$S_\phi(n) = |H(n)|^2 . S_F(n) \tag{24}$$

where $S_F(n)$ is the spectral density function of F, and $|H(n)|$ is the modulus of mechanical transfer function between F and ϕ, given by

$$|H(n)|^2 = \frac{1}{(4\pi^2 n_0^2 M)^2 \left[\left(1 - \frac{n^2}{n_0^2}\right)^2 + 4\zeta^2 \frac{n^2}{n_0^2}\right]} \tag{25}$$

The program evaluate (23) as sum of background and resonant response

$$\sigma_\phi^2 = \sigma_B^2 + \sigma_R^2 \tag{26}$$

with

$$\sigma_B^2 = \int_0^\infty |H(0)|^2 S_F(n)dn \tag{27}$$

$$\sigma_R^2 = \int_{n_0 - \Delta n}^{n_0 + \Delta n} |H(n)|^2 S_F(n)dn \tag{28}$$

σ_R^2 can be estimated by

$$\sigma_R^2 = |H(0)|^2 . \frac{\pi n_0}{4\zeta} . S_F(n_0) \tag{29}$$

The spectral density function $S_F(n)$ of F is related to the spectral density functions of fluctuating wind component processes

$$S_F(n) = \left(1/2\rho \bar{U}^2 B C_F\right)^2 \int_0^L \int_0^L \phi(r_1)\phi(r_2)S(r_1, r_2, n)dr_1 dr_2 \tag{30}$$

$$S(r_1, r_2, n) = S_{uu}(r_1, r_2, n) + S_{vv}(r_1, r_2, n) + S_{ww}(r_1, r_2, n) + S_{uw}(r_1, r_2, n) \tag{31}$$

where C_F is the appropriate aerodynamic coefficient and r_1, r_2 are the coordinates of points 1 and 2.

In this approach, it is supposed that the fluctuating aerodynamic forces are closely related to the gust wind components $u(t), v(t), w(t)$ via the steady aerodynamic coefficients. This assumption is adapted for low frequencies wind fluctuations, aerodynamic admittance effects are neglected for higher frequencies leading to conservative results.

3 Numerical examples

An aeroelastic model of free standing pylon (fig. 5) of Normandie Cable Stayed Bridge has been studied in CSTB wind-tunnel [8]. A comparison between calculated and measured response σ_ϕ of the first two modes is presented on table 1 for see wind ($Z_0 = 0.05cm$) and on table 2 for country wind ($Z_0 = 23.0cm$).
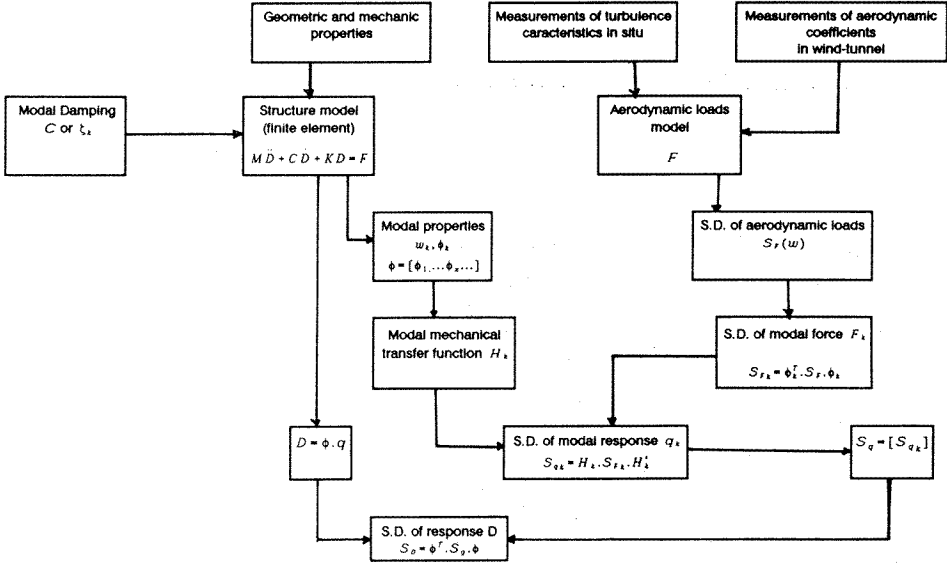
Fig. 4. General flow chart of DYCAST program
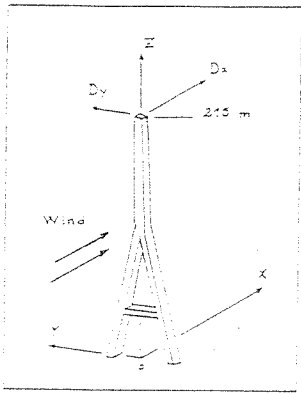
Fig. 5. Pylon of Normandie Cable Stayed Bridge

$\bar{U}$, m/s	Mode 1 $f = 0.21$ Hz ; $\zeta = 0.56$ %		Mode 2 $f = 0.56$ Hz ; $\zeta = 0.53$ %	
	σ measured, cm	σ computed, cm	σ measured, cm	σ computed, cm
6.34	0.08	0.05	0.000	0.008
12.1	0.26	0.22	0.023	0.036
17.6	0.67	0.55	0.136	0.086
23.9	1.67	1.16	0.190	0.173
29.3	2.49	1.86	0.332	0.267
32.9	2.94	2.59	0.478	0.364
38.6	4.23	3.37	0.739	0.531
44.9	7.10	5.71	1.340	0.767
62.6	13.70	13.40	2.930	1.760

Table 1. See turbulence ($Z_0 = 0.05$ cm)

$\bar{U}$, m/s	Mode 1 $f = 0.21$ Hz ; $\zeta = 0.56$ %		Mode 2 $f = 0.56$ Hz ; $\zeta = 0.53$ %	
	σ measured, cm	σ computed, cm	σ measured, cm	σ computed, cm
5.27	0.12	0.07	0.000	0.012
8.32	0.24	0.19	0.005	0.032
11.5	0.45	0.40	0.033	0.066
17.5	1.27	1.09	0.209	0.172
23.7	2.53	2.31	0.373	0.346
26.8	3.31	3.14	0.506	0.460
32.9	5.97	5.29	0.873	0.748
39.2	8.66	8.24	1.390	1.140
45.2	11.50	11.90	2.140	1.160
58.9	18.60	20.40	3.580	3.110

Table 2. Country turbulence ($Z_0 = 20.0$ cm)

302

Table 3 provides the influence of the cross-correlation between longitudinal component of turbulence $u(t)$ and the vertical one $w(t)$ on Normandie Cable Stayed Bridge response.

| Mode n° | f, Hz | σ_s, cm | σ_s, cm | $\frac{\sigma_2 - \sigma_1}{\sigma_1}$, % |
		σ_1, $S_{uw} = 0$	σ_2, $S_{uw} \neq 0$	
1	0.151	89 56	83 58	-6 68
2	0.222	107 09	113.25	+5.75
3	0 269	51 58	63.76	+23.61
4	0.358	9 25	8 50	-8 11
5	0.377	22 67	24 25	+6 97
6	0 384	18 64	19 87	+6.60
7	0.470	12 99	13 59	+4 62
8	0.506	5 45	5 26	-3 48

Table 3 Influence of S_{uw} on Normandie Cable Stayed Bridge response

4 Conclusions

A computer program written in FORTRAN 77 for the evaluation of turbulence-induced response of flexible structures has been presented in this paper. No restrictions are imposed on the geometry of structures to be solved. The program runs with turbulence loads in addition to others types of loading cases, it runs with any boundary conditions.

The program has been tested on complex examples, so it can be used in parametric studies providing turbulence-induced displacements and accelerations which are useful to professional engineers for preliminary design purposes.

References :
1. Bietry, J. 1980. Action d'ensemble REEF, Vol.2, Fascicule Aérodynamique, CSTB
2. Davenport, A.G. 1961. The application of statistical concepts to the wind loading of structures. Proceedings of the institution of Civil Engineers, Vol.19
3. Davenport, A.G. 1962. Buffeting of a suspension bridge by Storm winds. Proc. ASCE, J. of Structural Division, Vol.88
4. Davenport, A.G. 1964. Notes on distribution of the large value of random   function with application to gust loading. Proc. of the Institution of Civil Engineering
5. Delaunay, D. 1983. La turbulence atmosphérique en mer par vents forts. Synthèse bibliographique. CSTB Nantes, EN-CLI 87.120
6. Dhatt, G. and Touzot, G. 1984. Une présentation de la méthode des éléments finis. 2nd edition, Maloine S.A., Paris
7. E.S.D.U. 1975. Characteristics of atmospheric turbulence near the ground. Part. 1, 2 and 3. Engineering Sciences Data Units
8. Grillaud, G. and Barré, C. 1991. Effets du vent sur les pylônes du pont de Normandie en phase de construction. Etude en soufflerie sur modèle aéroélastique à échelle du 1/250. CSTB Nantes, EN-AS 91.1 C
9. Grillaud, G. Flamand, O. and Barré, C. 1991. Comportement au vent du pont de Normandie. Etude en soufflerie sur maquette aéroélastique à échelle 1/200. CSTB Nantes, EN-AS 91.5 C
10. Scanlan, R.H. and Simiu, E. 1978. Wind effects on structures. J. Wiley and Sons publication, N.Y.
11. Scanlan, R.H. 1987. Interpretaging aeroelastic models of Cable Stayed Bridges. J. of Eng. Mech., ASCE, vol. 113, n°4
12. Virlogeux, M. 1992. Wind design and analysis for the Normandie Bridge. Aerodynamics of large bridges, Larsen editor : 183-216
13. Zienkiewicz, O.C. and Taylor, R.L. 1989. The finite element method. Basic formulation and linear problems. Mc Graw Hill Book Company, UK

Equivalent modal damping ratios of a composite tube-type tall building under dynamic wind loading

B.C. Huang[+], K.M. Lam, A.Y.T. Leung and Y.K. Cheung

[+]Department of Engineering Mechanics,
Tongji University, Shanghai, China
Department of Civil and Structural Engineering,
The University of Hong Kong, Hong Kong

Abstract: This paper is concerned with the damping of a composite tube-type tall building under wind-induced vibrations. A detailed method incorporating Rayleigh damping and transfer matrix method and a simplified method for engineering applications are proposed for the computation of equivalent modal damping ratios of the composite building. Results on a forty-storey building are presented showing example of the computation and relationships between the properties of the external and internal tubes.

1. Introduction

In wind-induced vibrations of tall buildings, the first or first two modes are predominant. In engineering applications, modal superposition adopting Rayleigh damping presents itself as a simple method for the analysis of dynamic responses of tall buildings to wind action [1]. When applied to a tall building of composite tube-in-tube structure with different materials for the internal and external tubes, it is necessary to use a single pair of equivalent modal damping ratios of the composite building. However, there have not been quantitative analysis methods to determine these equivalent modal damping ratios, which are related to the different damping characteristics of the internal and external tubes and the distributions of stiffness and masses. In this paper, we shall present two methods for the determination of equivalent damping ratios of a composite tube-in-tube tall building.

2. The Damping Matrix

Composite tube-in-tube structures are not uniform systems. Different damping behaviours and mechanisms work in the internal and external tubes. Assuming that damping in each tube is represented by a damping matrix of its own, the damping matrix [C] of the whole structure can be represented as:

$$[C] = [C]_e + [C]_i \qquad (1)$$

where $[C]_e$ and $[C]_i$ are the damping matrices of external and internal tube respectively. Each matrix is proportional to the mass matrix [M] and stiffness matrix [K] of the corresponding tube as follows:

$$[C]_e = a_e[M]_e + b_e[K]_e \qquad (2a)$$

$$[C]_i = a_i[M]_i + b_i[K]_i \qquad (2b)$$

where a and b are arbitrary proportionality factors, which are related to the frequencies and the modal damping ratios of the internal or external tube:

$$a = 2\omega_1\omega_2 \ (\zeta_2\omega_1 - \zeta_1\omega_2) \ / \ (\omega_1{}^2 - \omega_2{}^2) \qquad (3a)$$

$$b = 2 \ (\zeta_1\omega_1 - \zeta_2\omega_2) \ / \ (\omega_1{}^2 - \omega_2{}^2) \qquad (3b)$$

In this paper throughout, we use subscripts e, i for the external and internal tubes respectively, and subscripts 1, 2 for the first two vibration modes.

It should be noted that we shall consider only structural damping in this analysis. Aerodynamic damping will not be dealt with. There have been a number of proposed models on structural damping [2,3,4]. We choose to use Rayleigh damping here due to its advantages that the damping ratio is a commonly used parameter in engineering applications and that Rayleigh damping allows the damping effect to be related directly to the damping ratio. Our analysis covers the first two vibrating modes.

3. The Equation of motion

A composite type tall building with a steel framed outside tube and a reinforced concrete inside tube is considered. The building is assumed symmetrical about the two horizontal axes so that torsional motion is neglected.

For the external tube, Coull & Bose's equivalent plate method is used [5]. Flexural and shear deformation of the elements are included in the equivalent shear rigidity. The internal tube is modeled as bending and shear bars. The mode in which the internal tube works in coordination with the external tube is shown in Fig. 1.
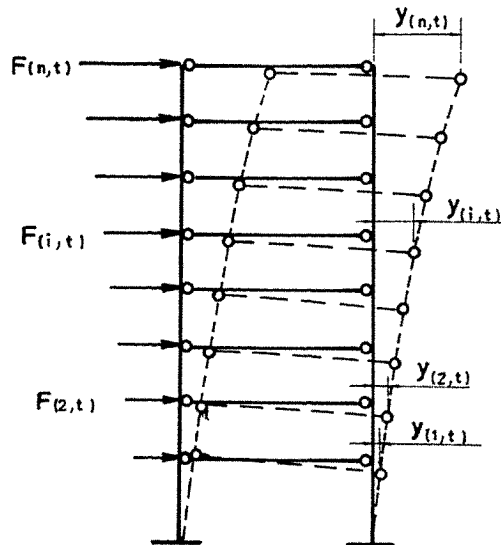
Fig. 1. Analysis mode of the tube-in-tube system.

306

Under dynamic wind loading F(i,t) on the ith storey, the equation of motion in the along-wind direction is:

$$[M]\{\ddot{y}\} + [C]\{\dot{y}\} + [K]\{y\} = \{F\} \qquad (4)$$

in which $\{y\},\{\dot{y}\},\{\ddot{y}\}$ are the along-wind displacement, velocity and acceleration vectors; [M] is the inertia matrix of the tube-in-tube system, a diagonal matrix for the mode shown in Fig. 1. [C] and [K] are the damping matrix and stiffness matrix of the tube type building. The stiffness matrix [K] can be expressed as:

$$[K] = [K]_e + [K]_i \qquad (5)$$

where $[K]_e$ and $[K]_i$ are the stiffness matrices of the internal and external tubes respectively after static condensation. It is shown from the Eq.(4) that mode-coupling is caused by the damping matrix [C] so that the usual mode- superposition method cannot be adopted to solve the equation. The response must be obtained by integrating these equations simultaneously The Newmark ßeta method is employed in this paper.

In our analysis, the stiffness matrices $[K]_e$ and $[K]_i$ are obtained by the transfer matrix method. Essentially, a transfer matrix is constructed to represent the transfer relationships relating the forces at the upper and lower ends of each and every ith storey of the internal or external tube. Horizontal displacements resulting from unit forces applied to each storey in succession are computed from the transfer matrices, giving rise to a flexibility matrix for each of the two tubes. The stiffness matrices are obtained from the inversion of these flexibility matrices.

4. Dynamic Wind Loading

The fluctuating part of the wind forces in the along-wind direction is:

$$F(i,t) = \rho\, C_D(i)\, \bar{U}(i)\, u(t)\, A(i) \qquad (6)$$

in which ρ is the density of air, $C_D(i)$ is the drag coefficient, A(i) is windward area of the building, $\bar{U}(i)$ and u(t) are mean and fluctuating parts of the wind velocity. Wind velocity fluctuations u(t) has been modeled by Davenport [6,7] as

$$u(t) = \sqrt{2} \sum_{k=1}^{n} [2S(\omega_k)\Delta\omega]^{1/2} \cos(\omega_k t + \phi_k) \qquad (7)$$

where $S(\omega_k)$ is the Davenport spectrum of fluctuating wind. In general, $\omega_k = (k-0.5)\,\omega_u\,/\,n$, with n=25 and $\omega_u = 4(1/s)$.

5. Equivalent Damping Ratios

In general, two equivalent principles should be considered in the analytical computation of the equivalent damping ratios. The first is the maximum acceleration at the top storey, and the next is the base overturning moment. The former may ensure human comfort under wind load from the structural stiffness. The latter is important in the design of the structural strength of the whole building. The base overturning moment is calculated from the equivalent static loads. For a particular mode j, the equivalent damping ratio $\zeta_{eq\,j}$ of the entire building is thus the value which

307

will give the same maximum acceleration at the top or the same base overturning moment obtained from the numerical integration described in Section 3.

The Rayleigh damping matrix, which is related to equivalent damping ratios is given by

$$[C] = a [M] + b [K] \qquad (8)$$

where $[M]$ and $[K]$ are the mass and stiffness matrix of the composite tube. The formulae of the proportional factors a and b are similar to Eq.(3), but the equivalent damping ratios $\zeta_{eq,1}$, $\zeta_{eq,2}$ and frequencies ω_1, ω_2 of the composite building are used.

6. The Simplified Method

Consider two single-degree-of-freedom systems shown in Fig.2. The equation of motion of the two tubes working in coordination with each other in the horizontal direction is

$$\ddot{y} + 2\zeta\omega\dot{y} + \omega^2 y = F(t) / (M_1+M_2) \qquad (9)$$

where

$$2\zeta\omega = (C_1+C_2) / (M_1+M_2)$$

$$\omega^2 = (K_1+K_2) / (M_1+M_2)$$

It is assumed that

$$C_1 = 2\zeta_1\omega_1 M_1; \qquad C_2 = 2\zeta_2\omega_2 M_2 \qquad (10)$$

where ζ_1 and ζ_2 are critical damping ratios of the M_1 and M_2 systems.

Substituting Eq.(10) into Eq.(9), we get

$$\zeta = \zeta_1\sqrt{\alpha\beta} + \zeta_2\sqrt{(1-\alpha)(1-\beta)} \qquad (11)$$

where

$$\alpha = K_1/(K_1+K_2); \qquad \beta = M_1/(M_1+M_2)$$
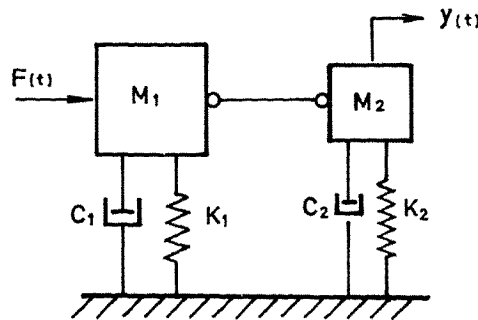
Fig. 2. Model of two-mass system.

308

Our simplified method models the composite tube-in-tube tall building by this two-mass system. Hence the parameters ζ and ζ_1, ζ_2 in Eq.(11) are comprehended as equivalent damping ratio ζ_{eq} and damping ratios ζ_i, ζ_e of the internal and external tube; M_1, M_2 as the generalized masses M_i, M_e; and K_1, K_2 as the generalized stiffness K_i, K_e of the internal and external tube for any mode j. Eq.(11) can thus be rewritten as

$$\zeta_{eq,j} = \zeta_{e,j}\ \alpha_{e,j}\beta_{e,j} + \zeta_{i,j}\ (1-\alpha_{e,j})(1-\beta_{e,j}) \qquad (12)$$

with

$$\alpha_{e,j} = M_{e,j}/M_j; \qquad \beta_{e,j} = K_{e,j}/K_j \qquad (13)$$

where M_j and K_j are the generalized mass and the generalized stiffness of the tube-in-tube building for the jth mode:

$$K_j = M_j\omega_j^2; \qquad K_{e,j} = M_{e,j}\omega_{e,j}^2$$

The computation of the equivalent damping ratio $\zeta_{eq,j}$ of the tube type building by Eq.(12) is simple, once the frequency and vibration mode are obtained for mode j of whole building and the external tube.

7. Results and Discussions with an Illustrative Example

Plan of a composite tube-in-tube building of forty-storey high is shown in Fig.3. The storey height are 4.5 m from storey 1 to 5, and 3.5 m from storey 6 to 40. The total height is 145 m. The cross sections of the beam, columns and internal tube are varied along the height step by step. Their data are omitted here. Results of the equivalent damping ratios computed for the first mode with the detailed method are shown in Table 1.

It can be observed that the equivalent damping ratios obtained with the criterion of equal base overturning moment are very slightly higher than those with the criterion of equal roof acceleration. Due to space limitation, the results for the second vibration mode are not shown here. Generally speaking, the equivalent damping ratios $\zeta_{eq,2}$ for the second mode are slightly higher than $\zeta_{eq,1}$ for the first mode.

$\zeta_{e,1}$	$\zeta_{i,1}$	Detailed Method		Simplified Method $\zeta_{eq,1}$
		$\zeta_{eq,1}$ a)	$\zeta_{eq,1}$ b)	
0.01	0.020	0.0113	0.0132	0.0118
	0.025	0.0130	0.0147	0.0126
	0.030	0.0147	0.0162	0.0135
	0.035	0.0164	0.0177	0.0144
	0.040	0.0182	0.0192	0.0153
	0.045	0.0199	0.0207	0.0161
	0.050	0.0216	0.0224	0.0170

Table 1. Equivalent Modal Damping Ratios for the first mode.
a) criterion of equal acceleration at the top floor;
b) criterion of equal base overturning moment.

309

For the simplified method, when the equivalent damping ratios for the jth mode is analyzed, the frequency and mode shape of the whole structure and the external tube structure for mode j are computed, with the corresponding generalized mass and stiffness obtained. The results for the first mode are shown in Table 1 as well. Most values of equivalent damping ratios are lower than those values from the detailed method by less than 15%. The accuracy of the simplified method is thus considered to be adequate for most engineering applications.

References:

1. W.E. Saul and A.H. Peyrot, "Response to Stochastic Wind of N-Degree Tall Building", J. Str. Div., ASCE, 102(1976), 1059-1075.
2. A.Y.T. Leung, "Damped dynamic substructures", Int. J. Numer. Methods Eng., 26 (1988), 2355-2365.
3. W.T. Thomson et al., "A Numerical Study of Damping", E.E.S.D., 3 (1974).
4. Z. Liang and G.C. Lee, "Representation of Damping Matrix", J. Engrg. Mech. Div., ASCE, 5 (1991), 1005-1020.
5. A. Coull and B. Bose, "Simplified Analysis of Framed-Tube Structures", J. Str. Div., ASCE, 101 (1975), 2223-2240.
6. A.G. Davenport, "The Application of Statistical Concepts to Wind Loading of Structures". Proc. Inst. of Civil Engrg., 19 (1961), 449-472.
7. R. Vaicaitis, M. Shinozuka and M. Takeno, "Response Analysis of Tall Buildings to Wind Loading", J. Str. Div., ASCE, 101 (1975), 585-600.
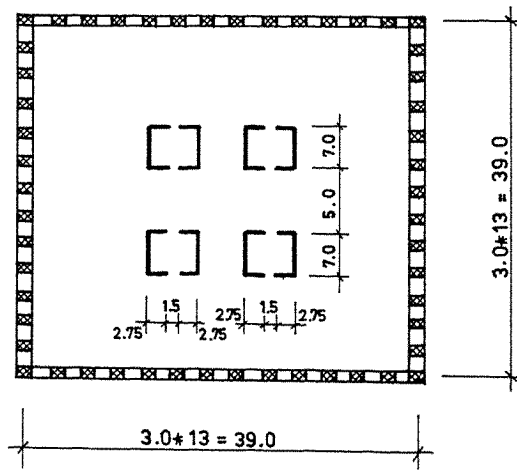
Fig. 3. Plan of the example tall building (dimensions in metres).

Observations and Responses of Occupants in High-rise Buildings During Severe Typhoon

Edmund C. C. Choi

School of Civil and Structural Engineering
Nanyang Technological University, Singapore

Abstract

The observations, experiences, physical and emotional responses of people residing in high-rise buildings during the passage of a severe typhoon is reported in the present paper. Immediately after typhoon Ellen which is one of the strongest typhoons to hit Hong Kong in the past 50 years, a survey was carried out to gather information on the perceptions of residents of high-rise buildings and how they react during the typhoon.

Sixteen high-rise residential buildings spread out all over Hong Kong were studied. These buildings were selected from different locations and different building groups; there were government housings and private developments. There were new buildings and there were old building. The heights of the buildings varied from 14 storeys to 42 storeys. Survey forms were send to the occupants of these buildings. Occupants were asked about their personal details and details of their units, their observations and experiences during the typhoon, any damage to the unit caused by the typhoon and their assessments of the safety of the construction of their buildings and fixtures.

Result of the study indicates that although buildings in Hong Kong are structurally safe in resisting typhoons, as residential buildings their vibrations (dynamic response) during typhoons are far from being satisfactory. For residents of upper storeys, a large percentage indicated that they felt sea sick.

There were also problems with the construction of the windows. There were many cases where the window frames were torn out, the hinges and locks were broken, glass panels shattered. Water seeping (pouring as reported by some occupants) through window units was a serious problem.

1. Introduction

The experience of having a severe typhoon passing immediately over your dwelling can be traumatic and even horrifying. Yet, the average statistics of having a typhoon in Hong Kong is about once every year. It is important to know the experience of residents, their feelings and their responses during the passage of a typhoon. Such information would be very useful for the future design of typhoon resistant buildings.

Immediately after Typhoon Ellen, a survey was carried out to gather information on the observations and experiences of residents of high-rise buildings during the typhoon.

2. Typhoon Ellen

Typhoon Ellen is one of the strongest typhoons to hit Hong Kong in the past 50 years. On 9 September 1983 it passed to the south of Hong Kong moving in a northwest directions. When it was closest to Hong Kong its centre was within a distance of about 40 km from the central business district of Hong Kong Island. As the movement of Ellen was relatively slow, during its passage, the whole

311

of Hong Kong was subjected to very high wind speeds for over 9 hours[1]. The maximum gust recorded at various locations in Hong Kong were : Royal Observatory 100 knots [52m/s], Waglan Island 122 knots [63m/s], Cheung Chau 128 knots [66m/s] and Stanley 134 knots [69m/s].

Using the Waglan data and comparing it with its long term wind statistics[2], the 122 knots corresponds to about a one in 25 year extreme gust. The Highest mean hourly wind speed recorded in Waglan was 86 knots which corresponds to about a one in 50 year wind.

Typhoon Ellen also brought with it a lot of rainfall; the rain was heaviest just after dawn on 9 September and rained continuously throughout the day. The rainfall recorded at Royal Observatory for the day was 172.4mm

2. The Survey

The survey was targeted to obtain information from residential building. Questionnaires were sent to sixteen high-rise residential buildings spread out all over Hong Kong. These buildings were so chosen such that they covered various geographic locations of Hong Kong (from the east end to the west end of Hong Kong Island, different parts of Kowloon peninsula and several areas in the New Territories), different building heights (14 storeys to 42 storeys) and different building groups (new buildings and old buildings, government housings and private developments).

In the survey occupants were asked a number of questions. These questions can broadly be classified into the following groups; (a) personal details and details of the building and the unit, (b) Their observations, experiences and reactions during the typhoon, (c) damage to the unit caused by the typhoon and (d) their assessments of the safety of the construction of their buildings and fixtures. The questionnaire is reproduced as show in Appendix A.

3. Results

Over two thousand questionnaires were sent out, the response is not particularly encouraging; less than twenty percent had sent back the forms. However, for a survey of this nature, the response can be considered reasonable.

Building vibration :

First of all 70% of the population (those who responded) indicated that they noticed movement of their units; 39% with distinct perception, while 31% with faint perception. Most of the people noticed movement of fixtures (e.g. hanging lamp) during vibration of their building. As shown in figure 1 over 50% of those who noticed building movement are in this category. Others detected building movement when they observed the views outside their windows moved, or the surface of water stored in their units moved. There were a few cases where it was reported that water in the toilet bowl was rocking so much that it splashed all over.

As shown in figure 2, majority (87%) of the people experienced horizontal sway of their units. Less than 10 percent detected rotational or vertical motion. As for how much the building was swaying, it seemed that different people had different perception. Figure 3 shows the distribution of the different values observed. On further analysis, it showed that the observations were consistent with the trend that residents staying in upper storeys observed larger sways of their buildings. Although within the same group of storeys, there was still a significant spread of the observations.

312
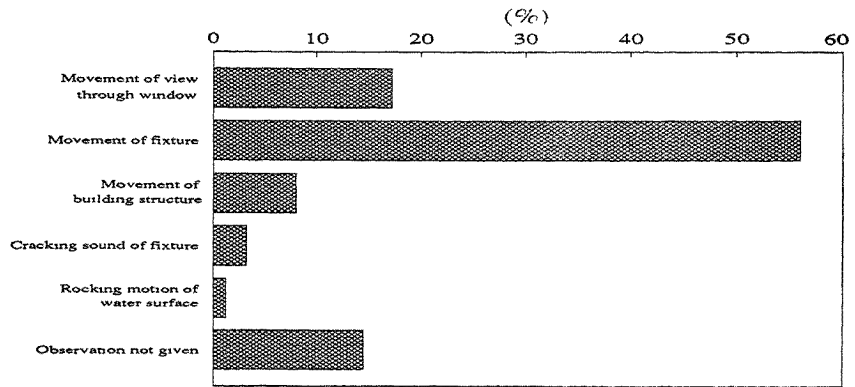
Figure 1 Observations on building movement
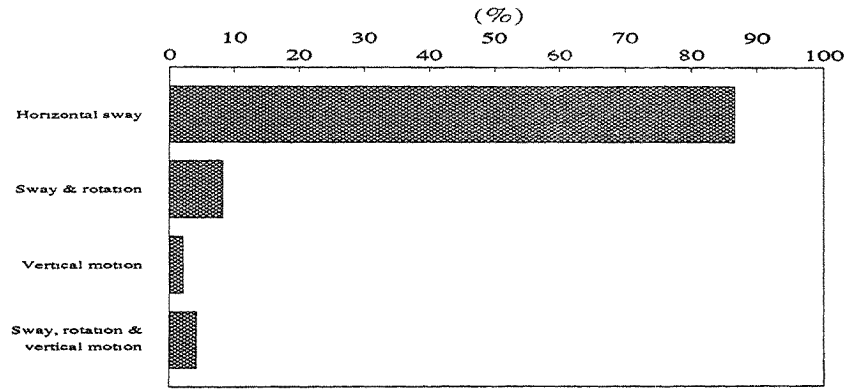
Figure 2 Modes of building movement
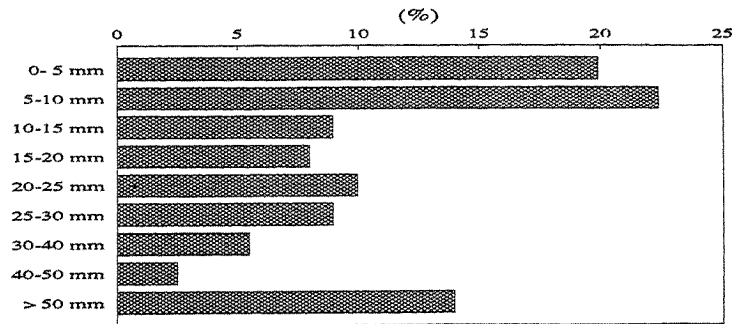
Figure 3 Amount of building sway

313

Human response :

Out of those who perceived building motion, 74% indicated that they were affected physically and/or psychologically by the building motion. This amounted to 52% of the whole population. Figure 4 shows a distribution of how they were affected of those who perceived building motion.
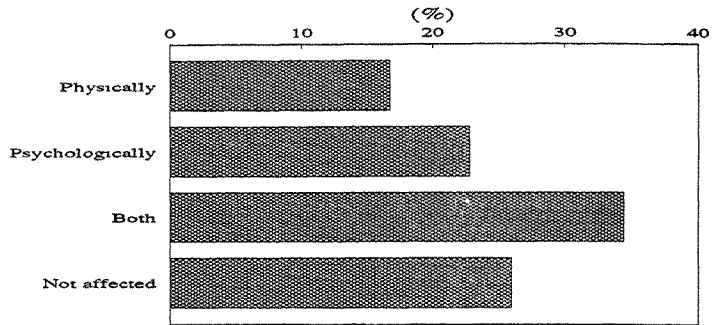
Figure 4 Motion effect on occupants

Of those who indicated that they were affected, 76% felt uneasy and tension while over 30% complained about motion sickness. Figure 5 shows a more detailed break down of their descriptions of how they were affected. There were several cases where occupants were so afraid that they actually left their home and stayed somewhere else.
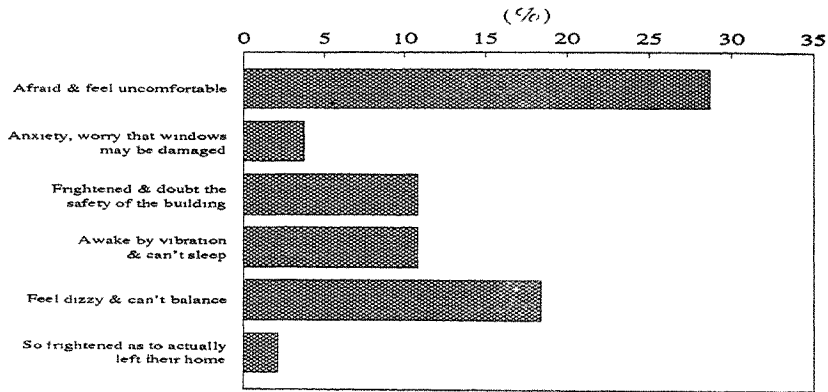
Figure 5 Description of how occupants were affected

Damage by Typhoon Ellen :

In general, occupants of residential high-rise buildings in Hong Kong were moderately satisfied with the performance of their buildings during typhoon Ellen, but were not so satisfied with the performance of their windows. 79% of the population believed their buildings were well designed against typhoons. While only 50% of the population believed that their windows were well designed. The reasons given for doubting the well design of their windows varied. Some were based on observations such as

314

window being broken, strong vibration of their windows and leakage of rain water through their windows. Others were just suspicions, thinking that the window frame too flimsy or the glass panel too large.

Occupants were also asked to report the actual damage suffered by their unit during typhoon Ellen. 52% of the population reported that there were no damage and 5% not giving any answer. All others making up 43% of the population reported some form of damage. Figure 6 shows a break down of the various forms of damage reported. The most often reported damage was damaged window glass (21%) and with damaged window frame and glass at 12%. Complaint of water leakage though windows was another popular item amounting to 10% of the population. There were reports complaining that water was pouring in and gushing through the window in very large quantity. There were several cases where it was reported that the air conditioning unit was completely dislocated and blown into their unit and another case reported that the air conditioning unit was completely suck out and ended up many storeys below.
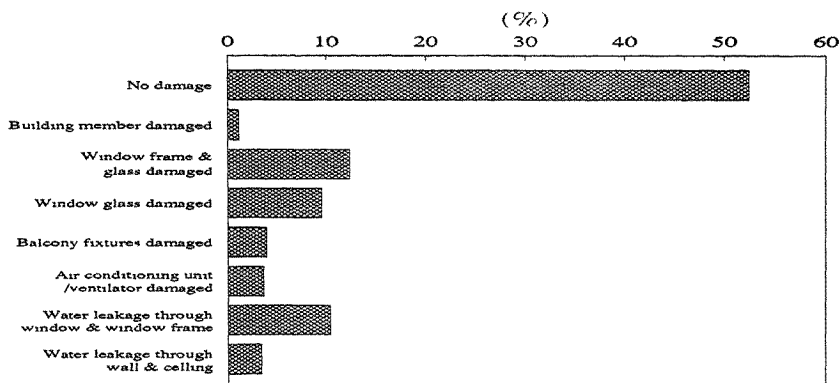
Figure 6 Damage incurred during typhoon Ellen

4. Discussion

Result of the survey gives us a good picture of the experience of residents in high-rise residential buildings during a severe typhoon. Although such surveys tend to be biased where those who responded are those who have positive response (in this case, those affected by the typhoon), one can still draw useful deductions from the survey. As mentioned earlier less than one fifth of all the forms send out were returned. Assuming that all those who did not send back the forms were not affected by typhoon Ellen, the values for the positive response percentage should be divided by five. Even than the survey result gives us quite an alarming picture. About 6% of all those staying in residential high-rise buildings suffered motion sickness during typhoon Ellen. Over 8% of the residential units were damaged one way or the other by the typhoon. And window glasses were damaged in 4% of the units.

It seems buildings in Hong Kong are structurally sound in resisting severe typhoons, some of them seem to be too flexible for human comfort. Although the buildings are strong enough to resists the loading, perhaps more considerations should be given to the dynamic sway characteristics of the structure.

It also indicates that the windows especially the window glasses for residential high-rise buildings did not perform very well. Design and construction should be improved to reduce damages.

315

5. References:

1.   'Typhoon Ellen', Royal Observatory Hong Kong, Hong Kong.

2.   E.C C. Choi 'Wind Loading in Hong Kong', Hong Kong Inst. of Engr., 1983

Appendix A
University of Hong Kong
Department of Civil Engineering

Date

Circle or tick the answers as appropriate

1 Total number of storeys in your building

2 During Typhoon Ellen you are in which floor

3 Your flat is facing N, NE, E, SE, S, SW, W, NW

4 Did you perceive your building moving during Typhoon Ellen?
   a) Distinctly perceptible
   b) Faintly perceptible
   c) Not perceptible
   If your answer is positive in question 4, answer the following questions
   If not, skip to question 14

5. Did you observed the following
   a) Movement of the view from the window
   b) Movement of fixtures e.g hanging lamp
   c) Movement of building members e g column
   d) Cracking sound of fixtures e g. door, beam, column etc

6 How did the building move?
   a) Swaying horizontally from side to side
   b) Swaying and rotating
   c) Vertical motion
   d) Combination of the above

7. By how much do you think the building was moving?
   0-5 mm, 5mm-10mm, 10mm-15mm, 15mm-20mm, 20mm-25mm,
   25mm-30mm, 30mm-40mm, 40mm-50mm, 50mm and above

8 How did you perceive the movement of your building?
   a) Physically   i e   by the body
   b) Visually   i e   by the eyes
   c) Noise   i e   by the ears

9 What were you doing when you perceived the motion?
   Sleeping, sitting, standing, reading, writing,
   doing light labour   others

10 Did you feel you were affected physically and/or psychologically by the
   motion?
   a) Physically
   b) Psychologically
   c) Both
   d) No

If the answer to question 10 is positive, please answer the following questions

11 Describe how you were affected

12 Did you have the following symptoms?
   a) Motion sickness
   b) Headache
   c) feel uneasy and tension
   d) feel excited or refreshed

13 Did you take any measures to overcome the symptom?
   a) stop working
   b) sitting down
   c) lying down
   d) take some form medicine
   e) nothing

14 As a domestic building, do you think your building is well designed against
   typhoon?   YES/NO
   If NO why not?

15 As a domestic building do you think the windows of your building is well
   designed against typhoon?   YES/NO
   If NO why not?

16 As a domestic building, to what extent would you tolerate the recur-
   rence of building motion in a typhoon such as Typhoon Ellen?
   a) Never
   b) Once in 50 years
   c) Once in 10 years
   d) Once in a year or more

17 Did Typhoon Ellen damage your building?
   a) Building member e g. roof
   b) Window frame and glass
   c) Window glass
   d) Others
   e) No

18 Your sex   male/Female

19 Your age   less than 20
                20   to 30
                30   to 40
                40   to 50
                50   to 60
                60   and above

20 Did any member of your family felt differently during the typhoon?
   If they felt differently please ask them to fill in another form

21 Your address

316

The investigation of wind—induced dynamic response on a square—section tall building

Zhang Liangliang and Xie Changtian

China Aerodynamic Research and Development Center

Abstract: In this paper, the dynamic response of Jing Jiang New Hotel in Shanghai has been investigted. Methods of random vibration theory are used to estimate the across—wind dynamic response of the building. The estimation of dynamic response of the building in alongwind direction is still analysis by means of gust factor theory. The predicted and measured response agree within the limits of expected experiment errors. It is shown that the maximum dynamic response of the building is proportional directly to the power of the reduced wind speed regardless of the wind directions. The cross—wind response more significant than those in other directions at the same wind speed, which shoud be taken into account in the building design. From the power spectral density, it is found that the vibration energy is mainly centered around the minimum frequency, and the influence of the higher vibration mode can be ignored.

1. Introduction

The use of high—strength lightweight building materials in modern tall buildings coupled with the use of modern computational tools for design have led to more economical structural design. However, these designs are producing complex structures with less damping and mass than earlier structures. The assurance of structural safety and service performance of the tall buildings during strong winds, based on strength and serviceability criteria is an important design objective. The required stiffness of the structural system of a tall building usualy depends on wind—induced loading, and serviceability is affected by wind induced sway acceleration at the top floors that may cause discomfort to the building occupants. Therefore, a comprehensive dynamic analysis of buildings subjected to high winds is essential for the evaluation of response paramenters to ensure an efficient and economically viable structural system.

In this paper, the dynamic response of Jing Jiang New Hotel in Shanghai has been investigated, which is a 50 story tall building. The plane form of the building is 32m by 32m and height of 155. 94m.

2. Estimation of the dynamic response

The dynamic respones of buildings in the alongwind direction can be predicted with reasonable ac-

curacy by a gust factor approach[1], here, the across—wind response has been discussed.

Considering the dynamic equation of motion in the acrosswind direction is as follows:

$$[M]\{\ddot{y}\} + [c]\{\dot{y}\} + [k]\{y\} = \{f(t)\} \tag{1}$$

in which $[M], [C], [K]$ are real symmetric mass, damping, and stiffness matrices, respectively; $\{y\}$ and $\{f(t)\}$ are the column matrices for the node displacements and the stochastic wind loads applied to the modes, respectively. The stochastic wind loads is given as:

$$f_i(t) = \int_0^H W_i(z,t)\Phi_i(z)dz \tag{2}$$

where: $W_i(z,t)$ is the instantaneous fluctuating wind induced force; $\Phi_i(z)$ is the fundamental mode shape of the ith mode; Z is the height to the point of application of the force; H is the height of the building.

The spectra of the generalized force is given as:

$$S_{F_i}(f) = \int_0^H \int_0^H S_{w_{i_1}w_{i_2}}(z_1,z_2,f)\Phi_i(z_1)\Phi_i(z_2)dZ_1dZ_2 \tag{3}$$

where $S_{w_{i_1}w_{i_2}}(Z_1,Z_2,f)$ is the cross—spectrum of the wind—induced forces per unit height at heights Z_1 and Z_2.

By the properties of the Fourier treansforms and the orthogonality of random Fourier components, the variance of response $\sigma_{y_i}^2$ is given as:

$$\sigma_{y_i}^2 = \int_0^\infty S_{F_i}(f) \cdot |H(i2\pi f)|^2 df \tag{4}$$

$$|H(i2\pi f)| = \frac{1}{(2\pi^2)[(f^2 - f_n^2) + 2i\xi ff_n]} \tag{5}$$

in which: $|H(i2\pi f)|$ is the mechanical admittance function of the structure. In order to compute the response in the fundamental mode, the following simplified expressions are used:

$$\sigma_{y_1}^2 \sim \frac{\sigma_{F_1}^2}{K_1^2} + \frac{1}{K_1^2}\frac{\pi}{4}\frac{f_{01}S_{F1}(f_{01})}{\xi_1} = \frac{\sigma_{F_1}^2}{K_1^2}\Big[1 + \frac{\pi}{4}\frac{f_{01}S_{F1}(f_{01})}{\xi_1\sigma_{F_1}^2}\Big] \tag{6}$$

in which: $K_1 = (2\pi f_{01})^2\int_0^H m(z)\Phi_1^2 dz \tag{7}$

$$\sigma_{F_1}^2 = \int_0^\infty S_{F1}(f_{01})df \tag{8}$$

$$S_{F1}(f_{01}) = \{\Phi_1\}^T[G_F(f_{01})]\{\Phi_1\} \tag{9}$$

Where: $\{\Phi_1\}$ is the fundamental model shape. For many tall buildings are somewhat linear in form and can be approximated by:

$$\{\Phi_1\} = Z/H \tag{10}$$

and $G_F(f_{01})$ is the spectrum of the wind induced base bending moment,. and it is esay to be measured by a high—frequency force—balance.

In any design application, it is usually necessary to have a probabilistic description of peok response of a building subjected to random wind excitation. This can be obtained from theoretical consid-

eration of the probability density of extreme values of a normal stationary random signal. The expected values of largest peak response experienced in the time interval, T, are given by:

$$y_{max} = g\sigma_y \tag{12}$$

in which: g is the peak factor, approximately:

$$g = \sqrt{2ln\upsilon T} + \frac{0.577}{\sqrt{2ln\upsilon T}} \tag{13}$$

Where: υ is the effective cycling rate of the response.

Once the deflection y_{max}, has been determined, the wind — induced acceleration is estimated through:

$$\ddot{Y}_{max} = (2\pi f_{01})^2 Y_{max} \tag{14}$$

The results are plotted in Fig. 1 and Fig. 3.

3. Experimental Response Prediction

3.1 Experimental Apparatus and Data Reduction

The test was conducted in a $1.4 \times 1.4 m^2$ low speed wind tunnel of China Aerodynamic Research Development Center (CARDC). The length of the test section is 6.3m, the maximum wind speed is 45m/s. A 1 : 300 scale—down aeroelastic model was used.

The mean (static) and dynamic along—wind acceleration response $\bar{a}_x$ and $\tilde{a}_x$, and the dynamic cross—wind acceleration response $\tilde{a}_y$ at the top of the model were measured at reduced wind speed $\bar{u}/(f_0 . b)$ ranging from 3 to 12 and at a structural damping value of 1% of critical damping by acceleration transducers. Here, $\bar{u}$ is the mean wind speed at the top of the model, f_0 is the natural frequency of the model, and the b is width of the model.

3.2 Experimental Results and Analysis

Fig. 1 shows ratios of experimentally measured along—wind acceleration response to the corresponding acceleration using the gust facter theory, and Fig. 3 is the comparisons of experimental results and numerical results using random vibration theory. It can be seen that the predicted and measured response agree within the limits of expected experment errers.

Along—Wind Response The mean and dynamic along—wind accerleration at the top of the model were normalized as $\bar{a}_x/g$ and $\tilde{a}_x/g$, respectively, and are presented as a function of reduced wind speed in Fig. 1. In general, both the mean and dynamic response are proportional to the power of reduced wind speed regardless of the wind directions. For V = 30m/s, the peak acceleration at the top of the full—scale building is 2.19%g, and the results gaining from the gust factor is 2.33%g, both agree with the Code of Canada[2] the 2.23%g, less than the "Discomfort Code" 3%g.

319
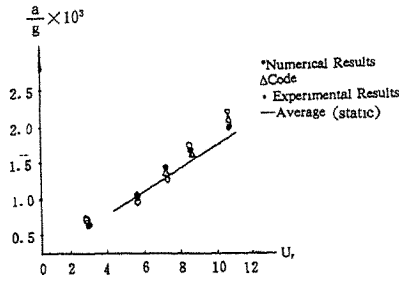
Fig. 1 The Variation of Along—Wind Response with Reduced Wind Speed

From the power spectral density in Fig. 2, it is found that the vibration energy is mainly centered around the minimum frequency, and the influence of the higher vibration mode can be ignored, it can be seen from[3].

Fig. 2 The Spectral Density of Along—Wind Response(logarithmic coordinate)

Cross—Wind Response The mean and dynamic cross—wind acceleration response at the top of the model were normalized as $\bar{a}_y/g$ and $\tilde{a}_y/g$, respectively, and are presented as a function of reduced wind speed in Fig. 3. It is found that the cross—wind acceleration response at the low range of reduced wind speed is essentially wake—excited. There is a signifcant increase in response at reduced wind speed close to a critical value of about 10 which represents the wind condition at which the votex shedding frequency f is very close to the natural frequeney f_0 of the model, for example, the model is operating near the peak of the wake energy spectrum. The large amplitude cross—wind acceleration respose at a reduced wind speed of 12 is beliveed to be caused by galloping excitation.

When $V=30m/s$, the cross—wind peak acceleration at the top of the full—scale building is 2. 68%g, and the numerical results is 2. 57%g, both less than the "Discomfort Code" 3%g, but the peak acceleration from the Code of Canada is 2. 03%g, less than the experimental and numerical results.

320
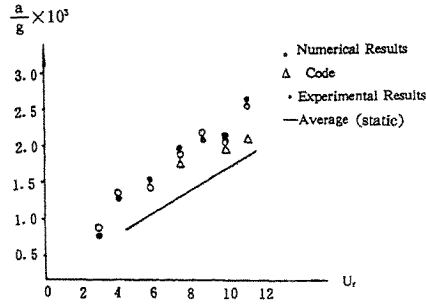
Fig. 3. The Variation of Cross—Wind Response with Reduced Wind Speed

From the power spectral density in Fig. 4, it can be seen that the vibration energy is also mainly centered around the

minimum frequency, the power of higher vibration mode is only a small contribution, and therefore for wind tunnel test about buildings and structures, only the minimum natural frequency needs to be considered, the influence of the higher vibration mode can be ignored.
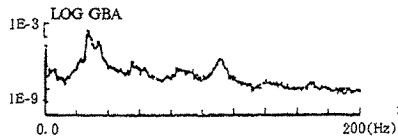
Fig. 4. The Spectral Density of Cress—Wind Response(logarithmic coordinate)

According to Fig. 2 and Fig. 4 (or Fig. 1 and Fig. 3), It can be observed that, for this model, the cross—wind acceleration response are higher than the results of along—wind acceleration response at the same wind speed, which should be taken into account in the building design.

4. Summary of Results and Conclusions

This paper has utilized a aeroelastic scale model and a semi—analysis formula derived from random vibration theory to analyse the dymmic response of Jing Jiang New Hotel. The following conclusions may be made:

(1)The cross—wind acceleration response obtained by numerical analysis are agree with the results of wind tunnel areoelactic model test. both less than the allowable value $3\%g$.

(2)The maximum dynamic response of the building is proportional directly to the power of the reduced wind speed regardless of the wind directions.

(3)The cross—wind response more significant than those in other derections at the same wind

321

speed, which shoud be taken into account in the building design.

(4) From the power spectral density, it is found that the vibration energy is mainly centered around the minimum frequency, and the influence of the higher vibration mode can be ignored.

References:

1. Davenport, A. G. , "Gust Loading Factors," Journal of the StructuralDivision, ASCE, Vol. 93, Njo. ST3, Proc. Paper 5255, June, 1967,pp. 11—34.
2. The National Building Code of Canada, 1980.
3. Kareem, A. ,"Wind—Excited Respense of Building in Higher Models", Journal of the Structural Dwision, ASCE, Vol. 10—7, ST4, Proe. Paper 16155, Apr. , 1981, pp. 701—706.

Effect of Angle of Attack on Vortex Induced Vibration and Galloping of Tall Buildings in Smooth and Turbulent Boundary Layer Flows

H. Kawai

Department of Civil Engineering
Tokyo Denki University,Hatoyama,Saitama 350-03, Japan

Abstract: Effects of angle of attack and free stream turbulence on occurrence of vortex induced vibration and galloping of tall buildings were investigated by wind tunnel experiments. From the investigation, following results are obtained.
1. The vortex induced vibration is strengthen by free stream turbulence when the separated shear flow does not reattach to the side face.
2. The onset velocities of the vortex induced vibration and the galloping are smallest and the amplitude of the vibrations are largest when wind attacks normal to the face or the angle of attack is $0°$

1. Introduction

The onset velocity of the vortex induced vibration and the galloping can be within the design velocity for the tall building of which aspect ratio is greater than 8. Kawai[1] investigated the effect of the free stream turbulence on occurrence of these vibrations for building models which had the rectangular cross section of which side ratio of D/B is from 1/2 to 3 and aspect ratio of $H/\sqrt{BD}$ was 10 where D was the depth in flow direction, B was the breadth and H was the height. He found that the vortex induced vibration still occured in strong turbulent flow over urban area. However, his experiments were limited to the cases when flow attacks normal to the windward face. As wind does not always attack normal to the face in real situations, it is important to investigate the effect of the angle of attack on occurrence of vortex induced vibration and galloping.

Therefore, the other series of wind tunnel experiments were carried out by the same building models in the same flow condition to investigate the effect of angle of attack. From the experiments, the various characteristic of the vortex induced vibration were emerged. In this paper, some interesting points are discussed.

2. Experimental procedure

The wind tunnel experiments were carried out in the boundary layer wind tunnel of Tokyo Denki University with the working section of 1.2m × 1.2m and 10m long. The arrangement of the experiments are as same as those in Kawai[1]. The building models have the rectangular cross section of which height is 50cm, sectional area is $25cm^2$ and density is $120kg/m^3$. The experiments were carried out in three types of flow, that is the smooth flow, the turbulent boundary layer flow over open terrain (T.B.L.(open)) and the turbulent boundary layer flow over urban area (T.B.L.(urban)). The velocity profiles in the turbulent boundary layer flows fitted well with the power law of which exponents were 0.1 for T.B.L.(open) and 0.3 for T.B.L.(urban).

3. Results of wind tunnel experiments
3.1 Effect of angle of attack

Fig.1 and 2 shows r.m.s. responses in y-direction in the smooth flow and T.B.L.(urban) for angles of attack of 0, 15, 30, 45 $°$ where the y-direction means the across-wind
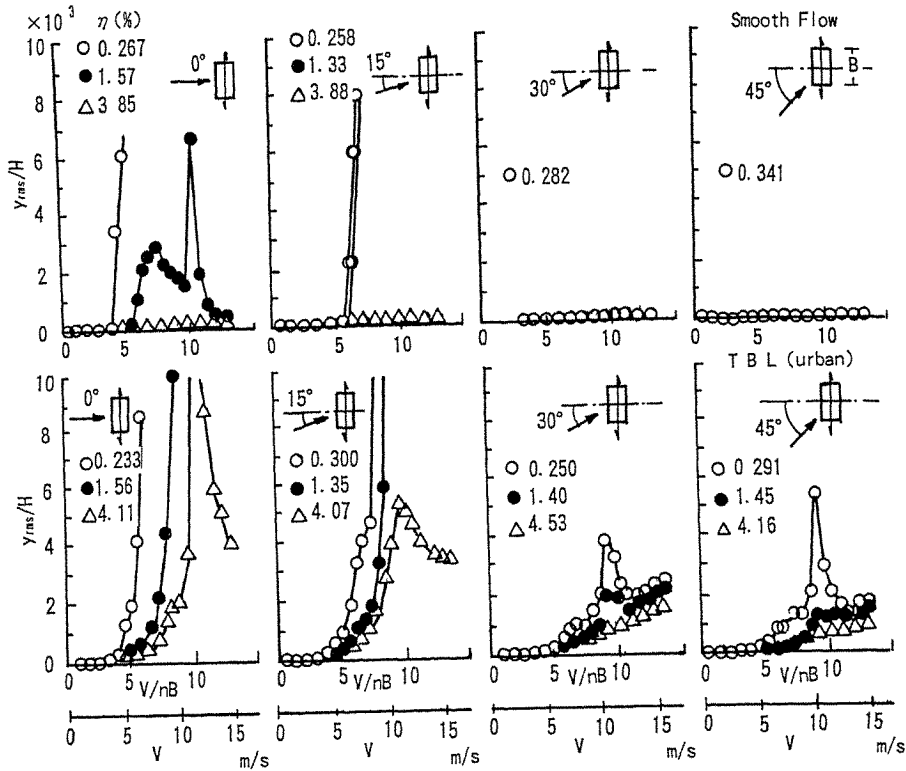
Fig.1 RMS response in y-direction for various angles of attack, D/B=1/2
Top figure: smooth flow, Bottom figure: T.B.L.(urban)
η :critical damping ratio, ○ 0.2%, ● 1.5%, △ 4%

direction when wind attacks normal to the windward face as shown by the arrow in the
section in Fig.1 and 2. In the case of the shallow section or the side ratio of D/B=1/2, the
strong vortex induced vibration occurs from the reduced velocity of V/nB=5 for the angles
of attack of 0 and 15 °. The amplitude of the vibration in T.B.L.(urban) is much larger
than that in the smooth flow. When the angle of attack increases larger than 15 °, the
vortex induced vibration becomes week and the vibration can not be observed in the
smooth flow even for the very low damping ratio. On the other hand, the week vortex
induced vibration can still be observed in T.B.L.(urban) for the angle of attack larger than
15 °.
   In the case of the deep section or the side ratio of D/B=2/1, the motion induced
vibration synchronizing with the rolling up of the separated shear layer occurs around
V/nB=5, and then the galloping type vibration with the vortex sheding starts from
V/nB=10 when the angle of attack is 0 °. The motion induced vibration only occurs in
the case of the very small critical damping ratio of 0.2%. When the angle of attack is
larger than 10 °, the galloping vibration can not be observed but the resonance with
vortex shedding can be observed for the small damping. In the case, the resonance is

324
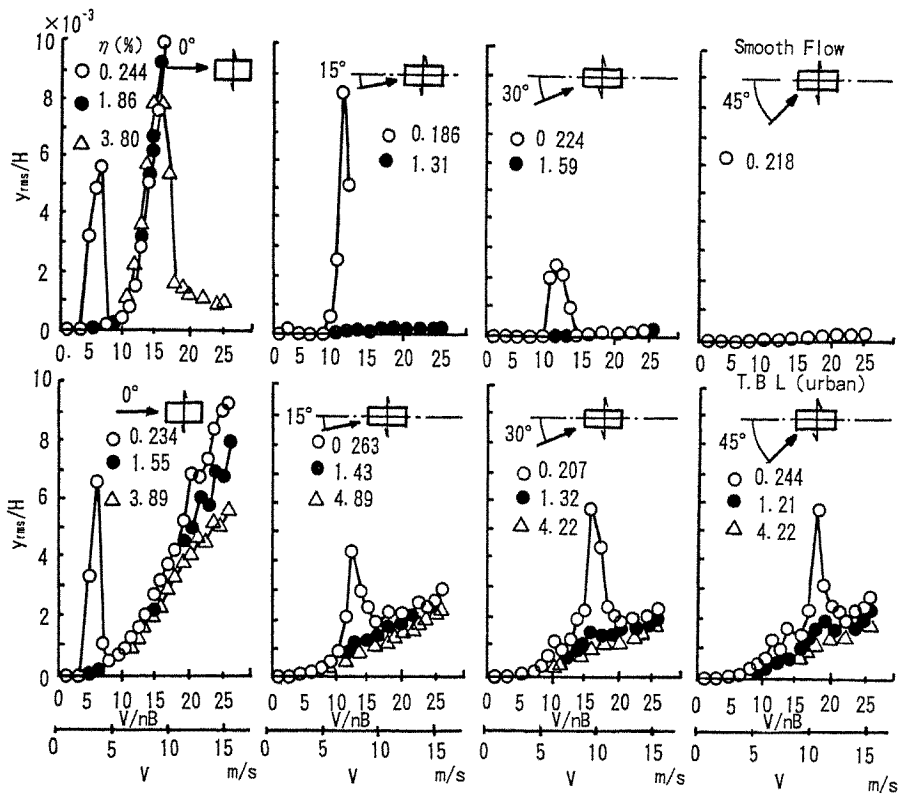
Fig.2 RMS response in y-direction for various angles of attack, D/B=2
Top figure: smooth flow, Bottom figure: T.B.L.(urban)
η :critical damping ratio, $\bigcirc$ 0.2%, $\bullet$ 1.5%, $\triangle$ 4%

strengthen by the free stream turbulence. The onset velocity of the galloping vibration is not effected by the structural damping level. The amplitude of the galloping in the smooth flow is much larger than that in T.B.L.(urban), and is little effected by the structural damping level.

3.2 Spectrum of dynamic response

As described in the previous section, the vortex induced vibration is strengthen by the free stream turbulence. Turbulence promotes the entrainment of flow through the separated shear layer to produce the stronger vortex shedding when the shear layer does not reattach to the side face[2].

Fig.3 shows the power spectra of the dynamic response in the y-direction when the angle of attack are 0 ° and 15 ° in the smooth flow. The critical damping ratio is about 1.5%. The vortex induced vibration with the large amplitude occurs nearly from V/nB=6 in the both cases of the angle of attack. It is rather surprising that there is no spectral peaks corresponded with the vortex shedding before the vortex induced vibration begins. When the vortex induced vibration occurs at V/nB=6, the small spectral peak appears at

325

the frequency about the half of the natural frequency, and the frequency of the peak moves closer to the natural frequency as the velocity increases.

On the other hand, there is the very clear peak caused by the vortex shedding in the spectra of the dynamic response in T.B.L.(urban) when the angle of attack are 0° and 15°. The vortex induced vibration begins when the frequency of the vortex shedding becomes about half of the natural frequency, and then the amplitude of the vibration reaches to the maximum as the shedding frequency equals to the natural
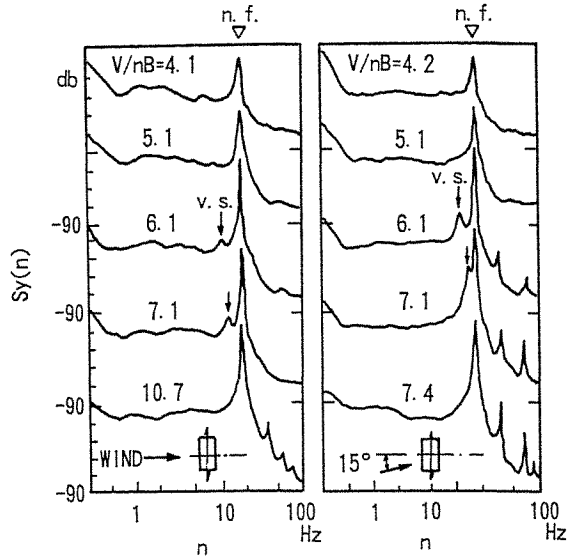
Fig.3 Power spectra of dynamic response in y-direction in smooth flow, D/B=2, η =1.5%
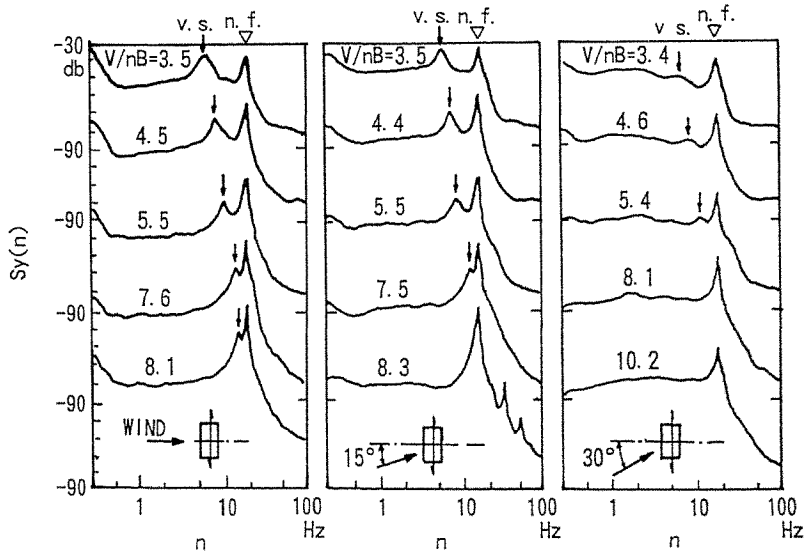
Fig.3 Power spectra of dynamic response in y-direction in smooth flow, D/B=2, η =1.5% v.s.:frequency of vortex shedding,   n.f.:natural frequency of vibration

326

Smooth Flow   T. B. L. (open)   T. B. L. (urban)
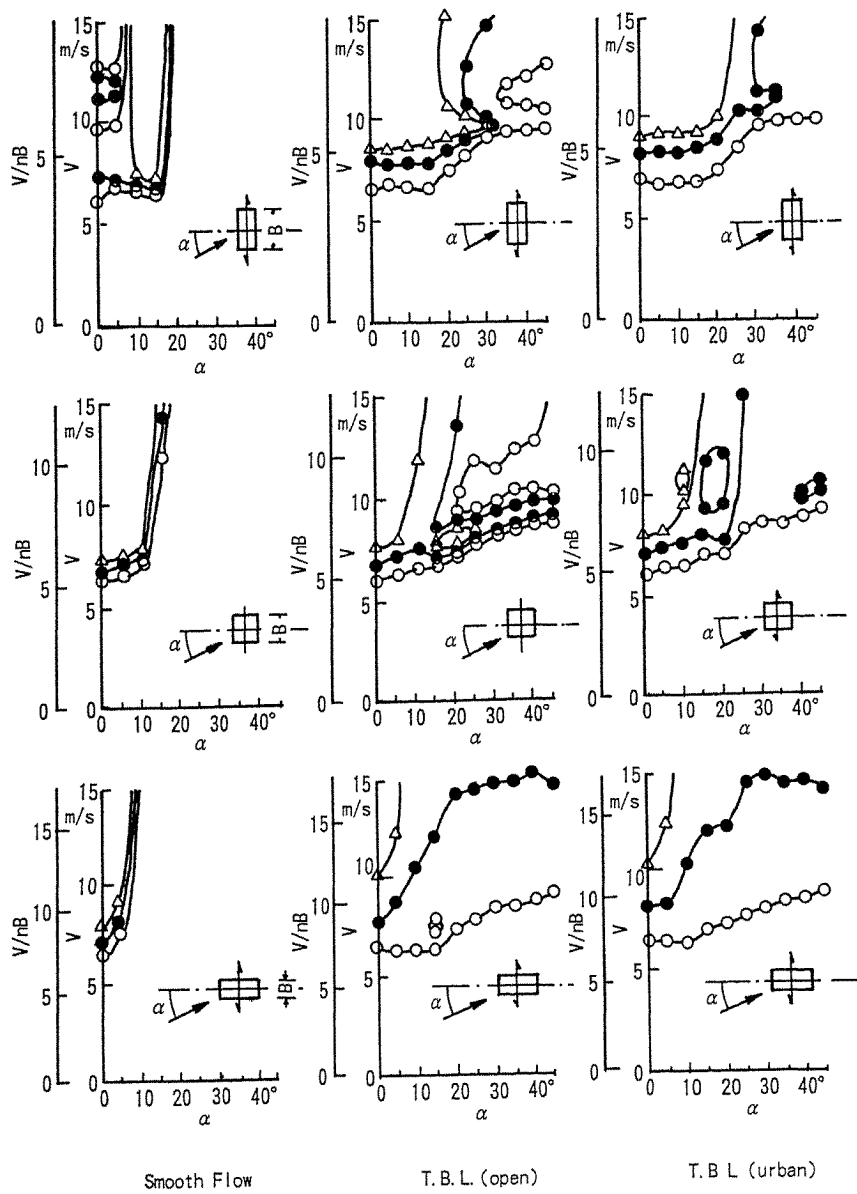
Fig.5 Stability diagram, left:smooth flow, middle:T.B.L.(open), right:T.B.L.(urban)
Critical level of amplitude, $\bigcirc$ $y_{rms}/H=1/1000$, $\bullet$ 1/500, $\angle$ 1/250

frequency. When the angle of attack is greater than 20°, the spectral peak corresponded with the vortex shedding is not clear and the resonance is suppressed considerably.

3.4 Stability diagram
In order to summarize the experimental results and show the range of the flow induced instability, the stability diagram is produced from the response-velocity diagram like as Fig.1 and 2, and is shown as Fig.5. The three levels of the amplitude is checked and is shown in the figure, that is the levels of $y_{rms}/H=1/1000$, $1/500$, $1/250$ when the critical damping ratio is about 1.5%.

In the smooth flow, there is no instability when the angle of attack is greater than 20°. Particularly, the galloping vibration for the deep section of $D/B=2$ occurs only at the angles of attack of 0° and 5°.

On the other hand, the instability zone spreads widely over the angle of attack in T.B.L.(open) and T.B.L.(urban). In the case of the top critical level of $y_{rms}/H=1/250$, the instability zone is limited within the angle of attack of 30°. When the level of instability is the ordinary design critical or $y_{rms}/H=1/1000$, the critical velocity ranges from $V=6 \sim 9m/sec$ or $V/n\sqrt{BD} = 5 \sim 8$. The critical velocity is the smallest when the angle of attack is 0° and is not much effected by the side ratio.

4. Summary
From the experiments, the following conclusions were obtained.
(1) The strong vortex induced vibration occurs in both smooth and turbulent boundary layer flow over urban area for a building with a shallow section of $D/B=1/2$ when the separated shear layer does not reattach to the side face. In this case, the free stream turbulence encourages the vortex induced vibration by shedding the strong vortices into the wake. This is caused by the promotion of the flow entrainment through the separated shear layer by the free stream turbulence.
(2) The galloping type vibration with the vortex shedding occurs for the deep section of $D/B=2/1$ when the separated shear layer partially reattaches to the side face. This type of vibration is limited within the very narrow range of the angle of attack around 0°. In the case, the amplitude of the galloping vibration in the turbulent boundary layer flow is much smaller than that in the smooth flow.
(3) The vortex induced vibration and the galloping vibration are most violent when the flow attacks normal to the front face both in the smooth and turbulent flow. When the angle attack increases, the amplitude of the vibrations rapidly decreases and the vibrations ceases at the ordinary structural damping level. This effect of the angle attack may be brought by the flow over the roof as the conical vortex to break the Karman vortex in the wake.
(4) The critical velocity for the level of $y_{rms}/H=1/1000$ is about $V/n\sqrt{BD} = 5$, and is little affected by the side ratio. Therefore, the critical condition for the aero-elastic instability can be determined whether the reduced velocity $V/n\sqrt{BD}$ is greater than 5 or not.

References:
1. H.Kawai, Vortex induced vibration of tall buildings, J. Wind Engineering and Industrial Aerodynamics, 41-44 (1992) 117-128
2. A.Laneville, I.S.Gartshore, G.V.Parkinson, An explanation of some effects of turbulence on bluff bodies, Proceedings of the Fourth International Conference on Wind Effects on Buildings and Structures, 1975, 333-341

RESPONSE OF MULTISTOREY BUILDINGS SUBJECTED TO WIND LOADING

M. Qamaruddin, A.L.M. Mauroof and H.K.R. Al-Hatimi

Department of Civil Engineering
Sultan Qaboos University
Sultanate of Oman

Abstract: The damage of buildings due to wind forces depends on
the wind environment and also on their dynamic characteristics.
Wind response of multistorey framed buildings, assumed to be
erected in the Sultanate of Oman, has been presented in the paper.
The wind data, appropriate to Khasab, Buraimi and Sur regions of
the Sultanate, have been employed in the response computations.
Two equivalent static methods and modal analysis using response
spectrum method are used in the present study. It turns out from
the present study that the wind response of the building located
at a site in country terrain of a region has more values than the
response obtained for the same building if built in town terrain
of the same region.

1. Introduction

The task of the structural engineer is to ensure that the
performance of structures subjected to the wind force will be
adequate during their anticipated life. This adequacy should be
from standpoints of both the structural safety and serviceability.
To achieve this goal, the designer needs information regarding (i)
the wind environment, (ii) the relation between the wind environ-
ment and forces it induces on the structures, and (iii) the beha-
viour of structures under the action of these forces.

Until recently, drag (along-wind) forces used in structural
design calculations were in all cases specified on the basis of
climatological, meteorological, and aerodynamic considerations
alone. The mechanical properties of the structure, i.e., mass
distribution, flexibility and damping were not considered in the
design [1]. But these parameters must be taken into account in
the design because the natural frequencies of vibration may be in
the same range as the average frequencies of occurrence of power-
ful gusts. Therefore, large resonant motions induced by wind may
occur. The multistorey buildings are bluff bodies that cause the
flow to undergo separation. The wake flow thus created behind the
building exhibits various degrees of periodicity.

Wind response of multistorey framed buildings, assumed to be
constructed in the Sultanate of Oman, has been presented in this
paper. A typical plan of multistorey framed building [2] has been
selected for the wind analysis. The buildings investigated are
assumed to be located in Khasab, Sur, and Buraimi regions of the
Sultanate. The investigation has been made to study the effect of
wind parameters on the buildings depending on their location in
different regions of a country. The wind and other related data
appropriate to these regions have been used in the response compu-
tation.

2. Mathematical Model

The framed building configuration is considered as symmetrical about its principal axes to achieve a simple mathematical model. The building material is assumed to be elastic and lies within limits of proportionality. The frames are assumed to resist the wind force with roof and/or floor acting as a rigid diaphragm. The building is subjected to wind load to generate horizontal action. The multistorey framed building is represented by a multidegree of freedom shear-beam system. The frames, which are located parallel to the direction of wind force, are assumed to provide spring action. The mass of the walls and slabs (lumped at storey levels) are considered to be connected to each other through massless springs and viscous damper. The degree of each mass in horizontal translation is one, ignoring the vertical translation and rotational degrees of freedom.

3. Methods of Analysis

The following three methods have been employed for computation of wind response of the buildings:

(a) Equivalent static method 1 (ESM1) (based on British Code CP: 3 Chapter V Part 2) [3]: In this method, the assessment of wind forces for design and analysis of structures depends on basic wind speed factors and the force coefficient.

(b) Equivalent static method 2 (ESM2) (British Standard BS 6399 Part 2) [4]: This deals with the methods developed to categorise structures according to their sensitivity to dynamic behaviour when subjected to wind load. The wind force on a structure is determined using the modified reference wind speed for the effect of topography, the dynamic magnification factor, and the pressure coefficient. The reference wind speed is determined using the site wind speed and the appropriate gust size dependent on the terrain of the site. The site wind speed depends on the basic maximum hourly wind speed, the altitude, direction of the wind and seasonal exposure of the structure.

(c) Modal analysis using response spectrum method (MRSM) [5]: The dynamic characteristics of the building are obtained by the modal analysis. The along-wind response computation can be performed after modal analysis results have been obtained. The response computation has been made by using DYNA computer program [5]. The mean-maximum response calculated by this program is effectively the summation of the mean response caused by the mean hourly wind speed plus the expected peak dynamic response contained in the fluctuations about the mean response.

4. Parametric Study

The wind response of the multistorey building has been studied for varying parameters concerning the building and the wind environment. A typical building plan [2] is assumed to be invariant for any number of storeys. The analysis has been done for ten, fifteen, twenty and twenty-five storey buildings. Three regions of the Sultanate are selected as locations for construction of such buildings. The wind parameters for design of the structures include the variation of hourly mean wind speed with height above ground, and the dependence of the wind speed and of turbulence upon roughness of terrain.

330

The basic wind speed used in the wind analysis for the build-
ings assumed to be erected in Khasab, Sur, and Buraimi are ob-
tained from the Department of Meteorology, Sultanate of Oman [6].
A set of fetch factors are used for sites in country terrain to
account for the effects of terrain on the wind speed [2]. Also
turbulence factors depend on the same parameters as the fetch
factor. To account for further decelerating effect of the mean
wind speed for sites in town, an adjustment fetch factor is used.
Similarly to account for the increased turbulence over rougher
town terrain, an adjustment turbulence factor is used [2]. The
building sites are located at distances from the sea equal to 0.3
km in Khasab, 10 km in Sur and 100 km in Buraimi. The wind param-
eters which are dependent on the altitude of the site, direction
of the wind and seasonal exposure of the structure are also em-
ployed in the present work [2].

The dynamic magnification factor, gust peak factor and topo-
graphic factor for country and town terrain of each region have
been computed for wind response analysis and reported elsewhere
[2]. The wind response has been obtained by the two equivalent
static methods and the method of modal analysis using response
spectrum. In all these cases, the analysis has been made when the
wind acts in the transverse direction of the building. The analy-
sis of the buildings subjected to wind load acting in their longi-
tudinal direction has not been made. Because, it has been estab-
lished in an earlier study [7] that in such cases, the wind re-
sponse would be less than the corresponding values of the response
when the wind load acts in their transverse direction.

5. Results and Discussion

The results obtained by the analysis of four multistorey
framed buildings with different number of storeys and subjected to
wind load acting in their transverse direction are presented in
this paper through a few representative figures. The discussion
of these results is presented in the following paragraphs.
(a) Comparison of wind response computed by the three methods:
Figures 1 through 12 show that in general there is a good agree-
ment between the response values computed by the British Standard
ESM2, and the response spectrum method MRSM. It is seen from
Figures 1, 2, 5, 6, 9, and 10 that the shear force values obtained
by MRSM are more than the values computed by ESM1 and ESM2 in few
top storeys whereas the shear forces calculated by the former
method lie between their values obtained by the latter two methods
from ten to twenty storeys. Then these values decrease and become
less than the values calculated by ESM1 and ESM2. Figures 3, 4,
7, 8, 11, and 12 show that the variation of bending moment re-
sponse computed by MRSM follows very closely with the correspond-
ing response obtained by ESM2. But the values of the bending
moment obtained by ESM1 are much higher than the corresponding
storey-wise values computed by ESM2 and MRSM.

331
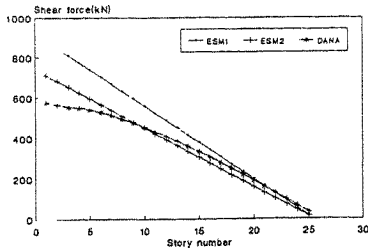
Fig. 1 Comparison of shear force
response for KHAC25
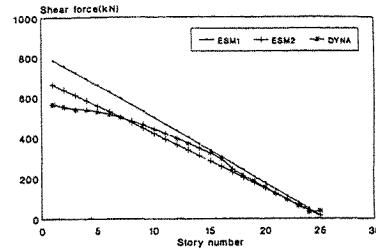
Fig. 2 Comparison of shear force
response for KHAT25
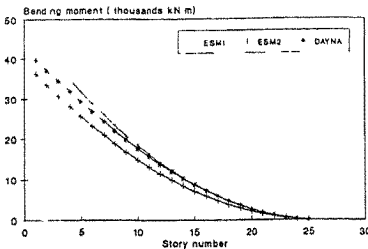
Fig. 3 Comparison of bending moment
response for KHAC25
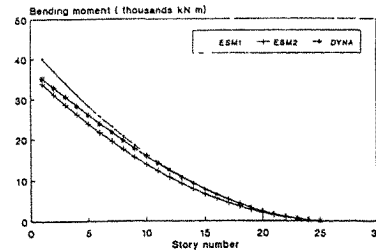
Fig. 4 Comparison of bending moment
response for KHAT25

KHA, SUR and BUR stand for the buildings in the cities of KHASAB, SUR and BURAIMI. C and T
stand for country and town terrains.

(b)   Effect of wind and building site parameters on wind response:
The response computation involves the fetch factor, turbulence
factor, topographic factor and dynamic magnification factor in
addition to gust factor.   Comparison of results through Figures 1
to 12 shows that for a building site in country and town terrains
of a region, the response obtained in the former case has more
values than that in the latter case.   This trend is true for the
shear forces and the bending moments obtained by all the three
methods.
(c)   Comparison of wind response for buildings located in differ-
ent regions:
It is seen from the graphs shown in Figures 1 through 12 that for
the buildings which have been analysed for Khasab region, the wind
develops more shear force and bending moment in them compared to
the similar buildings of Sur and Buraimi regions.   Similar trend
is noted for the buildings situated in country and town terrains
of these regions.   The hourly mean wind speed is the governing
factor for the development of higher response in such situations.
The other factors such as topography and terrain roughness are
also affecting the wind response to give different values in
different regions.

332
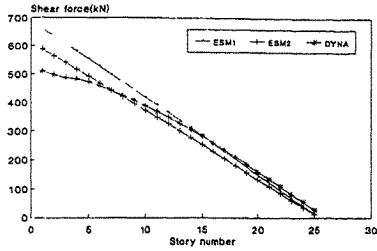
Fig. 5 Comparison of shear force
response for SURC25
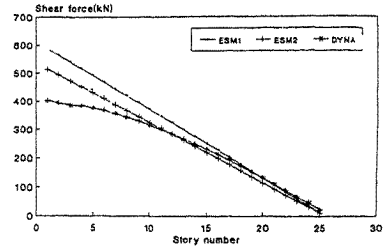
Fig. 6 Comparison of shear force
response for SURT25
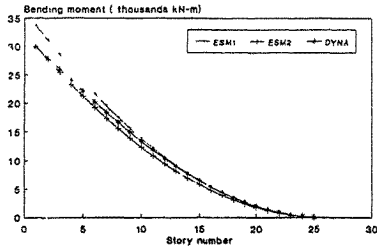
Fig. 7 Comparison of bending moment
response for SURC25
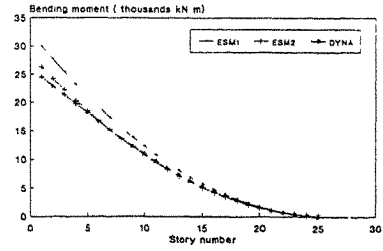
Fig. 8 Comparison of bending moment
response for SURT25
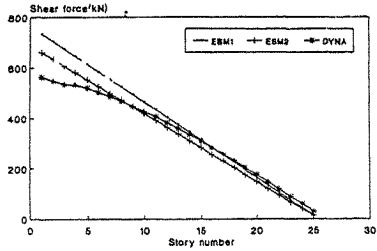
Fig. 9 Comparison of shear force
response for BURC25
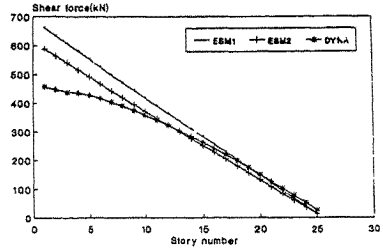
Fig. 10 Comparison of shear force
response for BURT25
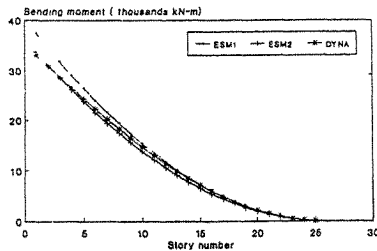
Fig. 11 Comparison of bending moment
response for BURC 25
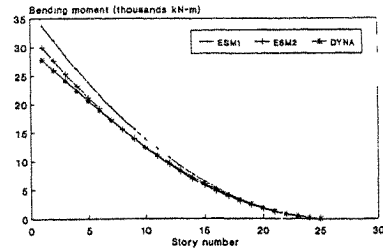
Fig. 12 Comparison of bending moment
response for BURT25

333

6. Conclusions

The following conclusions are drawn from the present study concerning the wind response of multistorey buildings:

(1) For the buildings which have been analysed for Khasab region, the wind develops more shear force and bending moment in them compared to the similar buildings of Sur and Buraimi regions.

(2) The wind response of the building located at a site in country terrain of a region has more values than the response obtained for the same building if constructed in town terrain of the same region.

(3) A study is required to develop all the wind parameters based on the available wind data [6] for different regions of the Sultanate of Oman.

References:

1. S. Scanlan, Wind Effects on Structures, John Wiley and Sons, (1986).
2. H.K.R. Al-Hatimi, Wind Response of Multistorey Buildings, Project Report submitted to the Department of Civil Engineering, Sultan Qaboos University, (1993).
3. BSI PP 7312 3rd Edition July: Extracts from British Standards for Students of Structural Design, (1988).
4. N. J. Cook, The Designer's Guide to Wind Loading of Building Structures, Part 2, Butterworths, London, (1990).
5. Dyna User Manual, Oasys Computer Program Manual, Structural Engineering, Dynamic Analysis, Oasys Limited, London, (1987).
6. Department of Meteorology, Directorate General of Civil Aviation and Meteorology, Ministry of Communication, Sultanate of Oman, Wind Data, (1991).
7. S.H.S. Al-Kaabi, Wind Analysis of Multistorey Masonry Buildings, Project Report submitted to the Department of Civil Engineering, Sultan Qaboos University, (1992).

Reliablity of tall buildings and high-rise structures based on comfortable requirement of residents

Li Guiqing   Cao Hong   Li Qiusheng[+] and   Ou Siyuan

Department of Civil Engineering
Wuhan University of Technology, China
+Department of Mechanical Engineering
Monash University ,Australia

Abstract: The riteria for comfortable requirement of residents to motion in tall buildings and high-rise structures is established. The calculation method for wind-induced vibrations of structures and the reliability analysis of tall buildings and high-rise structures are proposed in this paper.

1.Introduction

It is important to investigate calculating methods of acceleration response of wind-resistant buildings and high-rise structures, because the riteria for comfortable requirement of residents to motion in such buildings and structures is the acceleration reasponse. This problem was investigated by Yamada, Goto [1] and Chang[2] , but the reliability of tall buildings and high-rise structures based on comfortable requirement of residents had not been investigated. The mode-superposition method for wind-induced vibrations and reliability of tall buildings and high-rise structures is proposed in this paper.

2.Acceleration Response of Wind-Resistant Structures

The equation of along-wind vibrations of tall buildings and high-rise structures can be written in matrix form as

$$[M]\{\ddot{y}\} + [C]\{\dot{y}\} + [K]\{y\} = \{f(t)\} \tag{1}$$

where the element of the wind force vector, $\{f(t)\}$, is $\alpha_i A_i W_i \mu_i$, A_i and $W_i(t)$ are the area of windward face and wind pressure of the ith concentrated mass, μ_i is the drag coefficient,α_i is the fluctuating coefficient.

By using mode-superposition method, the fluctuating flection of the structure considered can be written as

$$\{y\} = \sum \{\Phi\}_j q_j(t) \tag{2}$$

where $\{\Phi\}_j$ and $q_j(t)$ are the jth mode shape and the jth generaltion coodinate respectively. On the assumption that the damping is orthogonal , the differential equation of the jth genneration coordinate is

$$\dot{q}_i + 2\xi_j\omega_j\dot{q}_j + \omega_j^2 q_j = Q_j \tag{3}$$

in which ξ_j is the jth ratio of damping, ω_j is the jth natural frequency, and Q_j is the jth generalized force:

$$Q_j = \sum \alpha_i A_i W_i \mu_i \Phi_{ij} / \sum m_i \Phi_{ij}^2 \tag{4}$$

The relation of spectrum between acceleration responses, a_j, a_k, of generalized coordinates and generalized forces can be derived as

$$S_{a_j a_k}(\omega) = H_j^*(i\omega) H_k(i\omega)\omega^4 S_{Q_j Q_k} \tag{5}$$

The acceleration response spectrum of the ith concentrated mass is

$$S_{A_i}(\omega) = \sum_{j=1}^{n} \sum_{k=1}^{n} \Phi_{ij}\Phi_{ik} S_{a_j a_k}(\omega) \tag{6}$$

Neglecting the correlation between the mode shapes. Eq.(6) becomes

$$S_{A_i}(\omega) = \sum_{j=1}^{n} \Phi_{ij} S_{a_j}(\omega) \tag{7}$$

The variance of the acceleration response of the jth concentrated mass is

$$\sigma_{A_i}^2(\omega) = \int_{-\infty}^{\infty} S_{A_i}(\omega)d\omega = \sum_{j=1}^{n} \Phi_{ij}^2 \sigma_{a_j}^2 \tag{8}$$

in which $\sigma_{a_j}^2$ can be written as

$$\sigma_{a_j}^2(\omega) = \int_{-\infty}^{\infty} S_{a_j}(\omega)d\omega = \lambda_{4j}g_j \tag{9}$$

where

$$\lambda_{4j} = \int_{0}^{\infty} \left| H_j(i\omega) \right|^2 S_v(\omega)\omega^4 d\omega \tag{10}$$

$$g_j = \sum_{i=1}^{n} \sum_{k=1}^{n} \Phi_{ij}\Phi_{kj} D_i D_k \rho V_i V_k r(x_i, x_k) \tag{11}$$

in Eq.(10) $S_v(\omega)$ is the wind velocity spectrum, ρ is the air density, $r(x_i, x_k)$ is the coefficient of correlation.

The closed solution of the parameter, λ_{4j}, is obtained by use of the calculation of residues as follows

(1) Davenports Sprectrum

$$S_v(\omega) = \frac{4KV_{10}^2}{\omega} \frac{x^2}{(1+x^2)^{\frac{4}{3}}} \tag{12}$$

Substituting Eq.(11) into Eq.(10) gives

$$\lambda_{4j} = \frac{6KV_{10}^2}{B}\{1 + \Sigma_j[0.5f_j Ln(1 + 2rcos\theta_j + r^2) + \frac{r + 3cos\theta_j f_i}{3sin3\theta_j}(tg^{-1}\frac{1 - rcos\theta_j}{rsin\theta_j}$$

$$+ \frac{\pi}{2} - \theta_j)]\} \tag{13}$$

in which

$$b = (1 + x_j^2)^2 - 4\xi_j^2\chi_j^2, \quad \chi_j = 600\omega_j/(\pi V_0), \quad r = b^{-\frac{1}{3}}$$

$$b_1 = (1 + x_j^2 - \xi_j^2\chi_j^2/6, \quad \theta_j = cos(b_1\sqrt{b}) + 2\pi(j-1)/3$$

$$f_j = 2sin\theta_j/\{3r^5sin3\theta_j[(b_1 - 1)r^3 - 2(1 - r)^6cos\theta_j]\}$$

(2) Author's Spectrum

$$S_V(\omega) = \frac{Ca_0}{\pi}\frac{\omega^2}{\omega^4 + 2a_1\omega^2 + a_2^4} \tag{14}$$

Substituting Eq.(13) into Eq,.(10) gives

$$\lambda_{4j} = C_1 a_0 a - C_1 C_2[2a_1(a_0 b_2^2 + b_0 a_2^2) + (a_0 + b_0)a_4^2] \tag{15}$$

in which

$$C_1 = C/(2a_0 b_0 a)$$

$$C_2 = (a_2^2 - b_2^2)^2 + (a_0 - b_0)(a_0 b_2^2 - b_0 a_2^2)$$

$$a_0 = 2\beta, \quad a_1 = \beta^2 - \gamma^2, \quad a_2^2 = \beta^2 + \gamma, \quad \beta_1 = \xi_j\omega_j$$

$$\gamma_1 = \sqrt{1 - \xi_j^2\omega_j^2}, \quad b_0 = 2\beta_1, \quad b_2 = \omega_j$$

$$a = \Pi[(\gamma \pm \gamma_1)^2 + (\beta \pm \beta_1)^2]$$

β, γ are the parameters of the correlation function:

$$R(\tau) = e^{-\gamma|\tau|}(cos\beta\tau - \frac{\gamma}{\beta}sin\beta|\tau|) \tag{16}$$

It is important to point out that the derivative of the acceleration response of structures is infinite for Davenport's spectrum and the Author's spectrum of this paper, because the variance of the derivation of the acceleration response of jth mode shape is

$$D_{a_j} = \int_0^\infty S_v(\omega)|H_j(i\omega)|^2\omega^6 d\omega \tag{17}$$

Substituting Eq.(12) into Eq.(13) obtains

$$D_{a_j} = \int_0^\infty \frac{2a^2\omega^8}{3\omega(1 + a^2\omega^2)^{4/3} + [(\omega^2 - \omega_j^2)^2 + 4\xi_j^2\omega_j^2\omega^2]} d\omega \tag{18}$$

337

in which

$$a = \frac{V_{10}\pi}{600}$$

It is evident that the integral, D_{a_j} , is infinite, so, this problem needs to be investigated.

3. Dynamic Reliability

The comfortable bound is taken as the curve in Fig.1[3]. The number of extreme points of the wind–induced vibrations is determied by use of Motel Carlo method. A lot of analysis results show that

(1) Displacement response of structures subjected to wind load is a narrow process(Fig.2)

(2) Accelaration response of structures subjected to wind load is a wide process(Fig.3), but the number of extreme points of acceleration response can be estimated by using a narrow process model, for example, using natural frequency or video frequency of velocity response of the structure estimates the number of extreme points of acceleration response, the errors of computational results obtained by the narrow process are small. The compulational resluts are listed in table 1

(3) The reliablity of a structure for various periods determined by use of normal distribution is more close to that determined by Monte Calo method among the results determined by eight distributions, such as Logarithm–Normal, Type I ,Type II and the Scale Transform of Extreme, Possion, Raleigh, Vanmarcke and Normal distribution. The dynamic reliablity of tall buildings and high–rise structures under the action of wind load at one time based on comfortable requirement of residents and determined by use of Normal distribution is given by

$$P_s(V,\lambda) = [1 - erf(\frac{\lambda}{\sqrt{2}\sigma_{a,v}})]^n \tag{19}$$

in which n is the number of extreme points. λ is the boundary value, $\sigma_{a,v}$ is the standard deviation when the wind velocity is V,erf( ) is the error function.

Following the assumption in Ref.[3], the dynamic reliability of structure within N years is

$$P(N) = [\Pi_i P_i(1)]^N$$

where $P_i(1)$ is annual dynamic reliability of the structure at direction i

The first natural frequency	The number of extreme points by Monte Carlo method	The estimation by natural frequency		The estimation by Video frequency of velocity respense of the structure	
		The number of extreme points	Relative error	The number of extreme points	Relative error
0.5	401	400	0.25%	412	2.70%
1.0	417	400	4.25%	408	2.25%
1.5	410	400	2.5%	408	0.5%
2.0	402	400	0.50%	408	1.5%

Table 1 Comparison of the number of extreme points between Monte Carlo and approximate method

4.Conclusion

The exact solution of wind—induced vibrations of structures corresponding Davenport's spectrum and the Author's spectrum have been found in this paper. These exact solutions will have an extensive application in the field of civil engineering, but their derivatives of the acceleration response of structures are infinite, so, the expression of wind spectrum needs to be investigated.
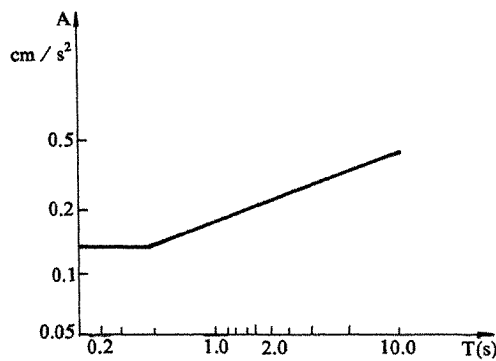
Fig.1 The Riteria Comfortable Requirment of Residents
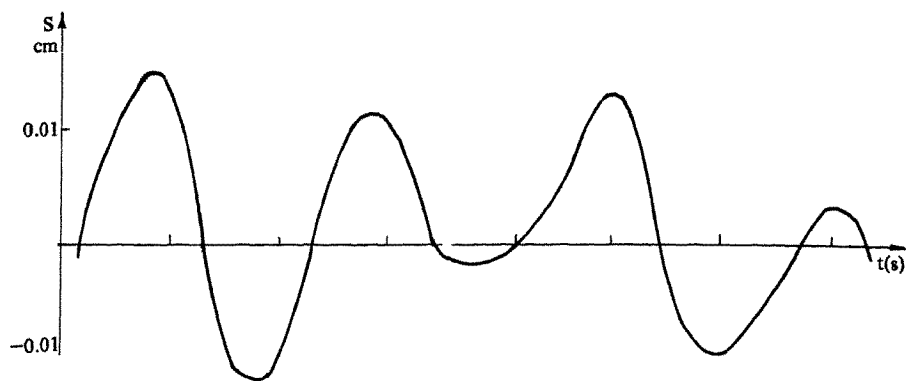
Fig.2 Displacement Response
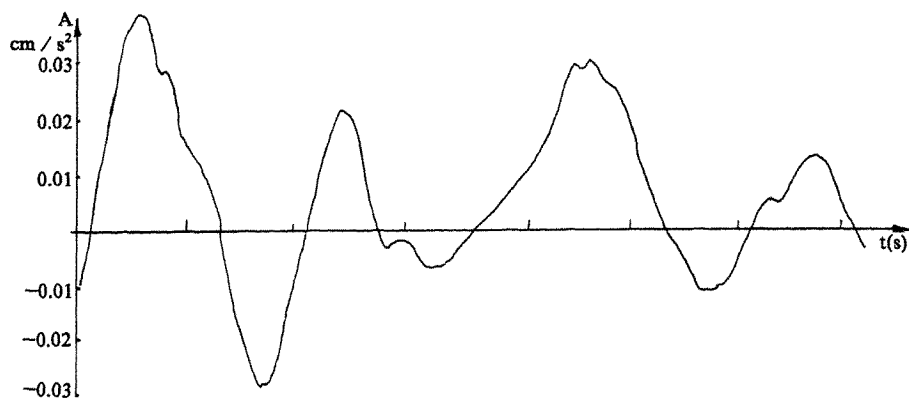
Fig.3 Acceleration Response

References

1.M.Yamada, T.Goto, The riteria to motion in Tall Buildings, Pan Pacific Tall Buildings Conference Preceedings,1975

2. F.K.Chang, Human Response to Motion in Tall Buildings,ASCE(ST),Vol.99,1973

3.Li Guiqing, Cao Hong, Li Qiusheng and Huo Da, Theory and Its Application of Dynamic Reliability of Structures, Seismic Press, China,1993

340

AN ESTIMATION PROCEDURE FOR WIND INDUCED TORSION OF TALL BUILDINGS

D.L. BENEKE[a] AND K.C.S. KWOK[b]

[a]Acer Wargon Chapman Consulting Engineers
51 Bathurst Street, SYDNEY NSW 2000 AUSTRALIA

[b]School of Civil and Mining Engineering
University of Sydney, NSW 2006 AUSTRALIA

Abstract: This paper describes a procedure for estimating the wind induced torsional response of tall buildings. This procedure not only considers strength design criteria, it also considers design criteria associated with tall building serviceability requirements.

1. INTRODUCTION

Most modern wind loading codes provide structural engineers with relatively simple procedures for estimating both crosswind and alongwind base overturning moments of tall buildings for strength design purposes. In addition to this, provision is also made for estimating the associated roof top accelerations to ensure that serviceability design requirements are also satisfied. It is however apparent that most of these codes including the Australian Wind Loading Code AS1170.2 - 1989 [1] do not consider torsional effects.

Previous estimation procedures for torsional response of tall buildings were first devised by Greig [2]. This method was based on wind tunnel tests on 10 buildings of varying cross section within their associated terrain.   A three degree of freedom aeroelastic rig incorporating a linear mode shape was used to determine the torsional moments on each model.   The peak torque was initially estimated using a quasi-steady solution however it did not match the experimental results.   The empirical solution then developed was in the form shown below:

$$T_R = \phi_P \, \phi_R \, (T_{mean} + g_f T_{rms})$$

Equation 1

where T_{mean}, T_{rms} and T_R = mean, dynamic and peak torque respectively, ϕ_P = 0.92 (non coincidence of worst mean and dynamic effects), ϕ_R = 0.78 (wind directionality) and g_f = peak factor.

Isyumov [3] and Isyumov and Poole [4] further refined the work presented by Greig [2] with Lythe and Surry [5] using this information, along with pressure tapping test results, in a data base to verify the empirical method.

2. EXPERIMENTAL DATA BASE

The following torsional estimation procedure is based on the experimental data base presented by Beneke and Kwok [6]. Four buildings were tested in a boundary layer wind tunnel within flow conditions representing Terrain Category 2 and 4 as prescribed by AS1170.2 - 1989 [1]. Each model was mounted on a single degree of freedom aeroelastic torsion rig incorporating a constant mode shape. The cross section of each

model represented a basic shape - Rectangular, Triangular, Diamond and D-shape. The height of each model was 500 mm which represented a 65 storey building in full scale. Building properties such as density and torsional damping were constant for all the models tested and were set at 225 kg/m^3 and 1% of critical damping respectively.

3. STRENGTH DESIGN CRITERIA

The results presented by Beneke and Kwok [6] have indicated that the excitation mechanisms which effected the dynamic torsional response included turbulence buffeting excitation, wake excitation, flow reattachment excitation and displacement dependant excitation. An empirical model was chosen due to the complex nature of wind induced torsion of tall buildings and is similar to that first presented by Greig [2].

The fundamental equation used for the strength criteria for wind induced torsion on tall buildings is shown in equation 2. A peak base twisting moment ($\hat{M}_T$) is derived by adding a peak number of standard deviations of base twisting moment ($\tilde{M}_T$) to the mean base twisting moment ($\bar{M}_T$).

$$\hat{M}_T = [\bar{M}_T + g_f \tilde{M}_T]k_t \qquad \text{Equation 2}$$

The number of standard deviations added is dependent on the peak factor (g_f). A mode shape correction factor (k_t) converts the wind tunnel test results which were derived with a model of constant mode shape to that which approximates the prototype case.

3.1 Mean and Dynamic Base Twisting Moments

Expressions for the mean and dynamic base twisting moments are shown in equations 3 and 4 respectively.

$$\bar{M}_T = \emptyset_{ms} V_r^{\alpha ms} \rho L^4 h n_t^2 \qquad \text{Equation 3}$$

$$\tilde{M}_T = \emptyset_{ds} V_r^{\alpha ds} \rho L^4 h n_t^2 \zeta^{-\frac{1}{2}} \qquad \text{Equation 4}$$

The calculation of V_r for equations 3 and 4 is based on an ultimate limit state mean hourly wind speed. The mean and dynamic power law exponents (α_{ms} and α_{ds}) and torque coefficients ($\emptyset_{ms}$ and $\emptyset_{ds}$) were derived from the wind tunnel test results of the four building shapes of basic cross section. Selection of these parameters was undertaken so as to yield the most conservative result. The selection procedure for these parameters involved the following steps:

(a)   Calculate the maximum reduced velocity which can be expected to be encountered by the prototype, (in this case maximum V_r was approximately 2.5),

(b)   From the results presented by Beneke and Kwok [6], choose the angle of wind incidence which produces the maximum peak base twist for the reduced velocity range under both Terrain Category 2 and 4 flow conditions,

(c)   For both mean and dynamic torque, calculate a power law exponents and torque coefficients which represent the change in mean and dynamic torque with respect to reduced velocity and

(d)   Determine conservative power law exponents and torque coefficients which reflect the general trend of data for both approach flow conditions.

Figure 1 shows graphs of normalised torque versus reduced velocity for the four models tested. Each graph displays the trend of mean and dynamic base twist from the wind tunnel test results in both flow conditions for the angle of wind incidence which

342

produced the maximum peak base twist. Table 1 presents the associated adopted values of the power law exponents and coefficients for the mean and dynamic torsional response for all four models tested. Mean and dynamic torsional response power law exponents and coefficients derived by previous researches, Xu et al [7], Greig [2], Isyumov [3], Isyumov and Poole [4] and Lythe and Surry [5] are presented for comparison in Table 2.

The mean torque coefficients for the Diamond and D-shape models are generally 3-4 times larger than those values presented by Greig [2] and Lythe and Surry [5].
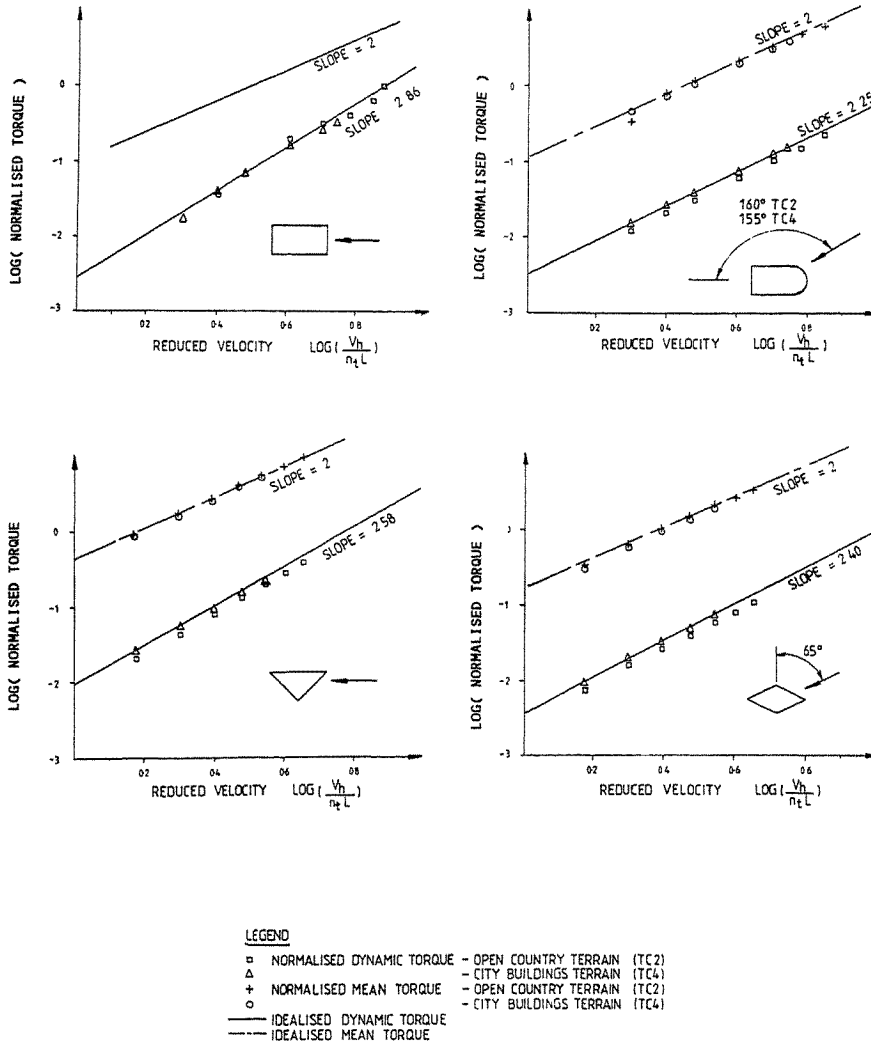
Figure 1. Graphs of normalised mean and dynamic torque versus reduced velocity for all models tested.

343

However, the value for the Triangular model is 10 times larger. The dynamic torque coefficient for the Rectangular model is about twice those values presented by Greig [2], Isyumov [3], Isyumov and Poole [4] and Lythe and Surry [5] and is about 50 % larger than the value derived by Xu et al [7]. The dynamic torque coefficients for the Diamond and D-shape models are generally 2-3 times larger than the values presented in Table 2. The dynamic torque coefficient of the Triangular model is larger than the values in Table 2 by a factor of approximately 6. The mean and dynamic torque power law exponents for all models shown in Table 1 are well matched with those values present in Table 2.

The observed mismatch of the mean and dynamic torque coefficients for the four models tested with those previously presented by Greig [2], Isyumov [3], Isyumov and Poole [4] and Lythe and Surry [5], can be attributed to differences in approach flow, model mode shape and the inherently high variability of the large data base which was used by the latter four authors.

MODEL	$\emptyset_{ms}$	α_{ms}	$\emptyset_{ds}$	α_{ds}
Rectangle	0.000	2	0.0029	2.86
Triangle	0.383	2	0.0093	2.58
Diamond	0.146	2	0.0036	2.40
D-Shape	0.113	2	0.0034	2.25

Table 1   Adopted values of the power law exponents and torque coefficients for each model.

Author	Models	$\emptyset_{ms}$	α_{ms}	$\emptyset_{ds}$	α_{ds}
Xu et al (1991)	Rectangle	-	-	0.00190	2.68
Greig (1981)	All types	0.0353	2	0.00151	2.80
Isyumov (1982) Isyumov & Poole (1983)	All types	-	-	0.00160	2.78
Lythe & Surry (1990)	All types	0.0578	2	0.00134	2.77

Table 2   Adopted values of the power law exponents and torque coefficients from previous research.

3.2 Peak Factor

The peak factor is the ratio of the expected peak value to the standard deviation of the resonant part of the fluctuating response which occurs once per hour (3600 seconds). This peak factor is currently used for the calculations of the along-wind and cross-wind base overturning moments for AS1170.2 - 1989 [1], and is determined by equation 5.

$$g_f = [2\log_e(3600n_t)]^{\frac{1}{2}}$$ Equation 5

3.3 Mode Shape Correction Factor

If the prototype fundamental torsional mode shape departs significantly from a constant magnitude mode shape, it is necessary to adjust the results obtained from torsional aeroelastic tests. The mode shape correction factor adopted is one which has been developed by Xu et al [7] and is shown in equation 6.

$$k_t = [(4\alpha_w+1)/(4\alpha_w+2\beta+1)]^{1/2} \qquad \text{Equation 6}$$

At this stage this type of mode shape correction for torsional vibration is believed to be the most appropriate. If however, a superior mode shape correction is devised in the future it need only be substituted into equation 2 for peak torque.

4. SERVICEABILITY DESIGN CRITERIA

Limiting roof top accelerations induced by the vibration of tall buildings is an integral component of any design process. The apparent rotating horizon created by torsional vibration can be more perceptible to human occupants than the movements induced by translational motion. The fundamental equation used for the serviceability design criteria is presented in equation 7. This equation calculates the planar acceleration at a point r_b away from the elastic centre of the building and is similar to the equation derived by Greig [2].

$$\hat{y}_t = (2r_b/\rho_b A h r_z^2) \tilde{M}_T g_f k_t \qquad \text{Equation 7}$$

The calculation of $\tilde{M}_T$ is based on a reduced velocity (V_{5yr}) corresponding to a five year return period wind. The peak factor g_f is based on an expected peak value which occurs, on average, once every 10 minutes (600 seconds) i.e. $g_f = [2\log_e(600n_t)]^{1/2}$. The mode shape correction factor used in the serviceability design criteria is the same as that used for strength design purposes.

5. CONCLUSION

An estimation procedure for torsional response is presented which determines the wind induced torsional response of tall buildings for strength and serviceability design. Due to the complex nature of the excitation mechanisms inducing torsional response, the procedure adopted was empirical and is based on the results of wind tunnel tests previously presented. When compared with the results of previous research, the empirical model shows reasonable correlation and can be expected to produce conservative estimates. This empirical model was developed to take into consideration reduced velocity ranges which reflect those which can be expected to be encountered in prototype cases based on reasonable assumptions of building geometry and flow conditions. If the expected operating reduced velocity range exceeds the presented range, amplitude dependent excitation may cause large amplitude torsional response and the empirical model presented here will not be applicable.

6. REFERENCES

[1]   The Australian Standard Wind Loading Code AS1170.2 (1989)

[2]   Greig, G.L. (1980). Towards an estimate of wind-induced dynamic torque on tall buildings, *M.E. Thesis, University of Western Ontario, Canada*

[3]   Isyumov, N. (1982).   The aeroelastic modelling of tall buildings, *Proc. Int. Workshop on Wind Tunnel Modelling for Civil Engineering Applications*, Gaithersburg, Maryland, USA, Cambridge Univ. Press, pp. 373-407.

[4]   Isyumov, N., and Poole, M. (1983).   Wind induced torque on square and rectangular building shapes, *J. Wind Eng. Ind. Aerodyn.*, Vol. 13, pp. 183-196.

[5]   Lythe, G.R., and Surry, D. (1990).   Wind-induced torsional loads on tall buildings, *J. Wind. Ind. Aerodyn.*, 36, pp. 225-234.

[6]   Beneke D.L, and Kwok K.C.S. (1992). Aerodynamic effect of wind induced torsion on tall buildings. *2nd International Colloquim on Bluff Body Aerodynamics*, Melbourne, Australia, Volume 1, Session 3B.

[7]   Xu Y.L., Kwok, K.C.S. and Samali, B. (1991) Torsional vibration of wind excited tall building and its suppression by tuned mass dampers. *Research report R641* School of Civil and Mining Engineering, Sydney University.

7. ABBREVIATIONS AND SYMBOLS

A	=	Cross sectional area of model
ds	=	Small section of the perimeter of the model
g_f	=	Peak factor
h	=	Building height
k_t	=	Mode shape correction for first mode torsional vibration
L	=	Model shape factor (refer Greig [2])
	=	$(\oint_s \lvert \acute{r} \times \bar{u} \rvert ds)/A^{\frac{1}{2}}$
$\bar{M}_T$	=	Mean torsional moment
$\tilde{M}_T$	=	Dynamic torsional moment
$\hat{M}_T$	=	Peak torsional moment
n	=	Frequency
n_t	=	Torsional natural frequency of vibration
$\acute{r}$	=	Vector from the elastic centre to the midpoint of the surface ds
r_b	=	Distance from elastic centre to reference point in building section.
r_z	=	Radius of gyration of building
$\bar{u}$	=	Unit vector normal to the surface ds
V_h	=	Incident wind velocity at building height
V_r	=	reduced velocity $= V_h/(n_t L) = V_u/n_t L$ (Strength design criteria)
		$= V_{5yr}/n_t L$ (Serviceability design criteria)
V_u, V_{5yr}	=	Ultimate limit state and 5 year return period mean hourly wind speeds
$\hat{y}_t$	=	Peak torsional acceleration
α_{ms}, α_{ds}	=	Mean and dynamic torque power law exponents
α_w	=	Power law exponent of the mean wind velocity profile
$\varnothing_{ms}, \varnothing_{ds}$	=	Mean and dynamic torque coefficients
β	=	Exponent of prototype torsional mode shape
ς	=	Torsional damping as a fraction of critical damping
ρ	=	Air density
ρ_b	=	Building density

Dynamic behaviour of high−rise structures

Cao Hong,   Li Qiusheng[+],   Ou Siyuan   and Li Guiqing

Department of Civil Engineering
Wuhan University of Technology, China
+Department of Mechanical Engineering
Monash University, Australia

Abstract:The measured results of dynamic behaviour of high−rise structures and tall buildings are given in this paper. In the calculation of free vibrations, high−rise structures and some tall buildings are treated as multi−step bars, each step of which may have varying cross section. All solutions are expressed in the terms of Bessel's functions.

1. Introduction

Most tall buildings in the past two decades in China were designed to be frame, shear wall and frame−shear wall buildings and most of China belongs to strong earthquake zones, strong wind zones, or both. It is important to investigate calculating methods of natural frequencies and mode shapes, especially the first mode of tall buildings and high−rise structures, because the first mode shape component is determinant in wind−induced vibration and earthquake−induced vibration of tall buildings and high−rise structures. This problem was investigated by Wang [1]; buildings considered in Reference [1] were treated as having variably distributed stiffness, but uniform mass. In this paper, an approach to determine natural frequencies and mode shapes of tall buildings and high−rise structures with variably distributed stiffness and variably distributed mass, including uniform stiffness and mass, is studied.

2. Measurement Results of Natural Periods of Tall Buildings

The first natural periods of many tall buildings in China were measured by us. The statistical results of the measured data are as follows:

(1) Frame

$T_t = 0.072N$, C_v is 37%; $T_1 = 0.058N$, C_v is 25%

(2) Shear Wall

$T_t = 0.045N$, C_v is 13%; $T_1 = 0.033N$, C_v is 18%

(3) Frame−Shear Wall

$T_t = 0.051N$, C_v is 17%; $T_1 = 0.049N$, C_v is 19%

in which T_t represents the transverse period, T_1 is the longitudinal period, N is storey number of the building considered, and C_v is the variation coefficient.

As is well known, since the first natural frequencies measured by the environmental method are greater than the true values, it is necessary to note that the measured value is multiplied by a reduced coefficient. Many measurement results show that the measured natural frequencies of frame buildings are too high, while the measured frequencies of shear wall buildings are little greater than the true values. Considering the fact mentioned above, the formulae estimating the first natural period of tall buildings are proposed as follows:

$$T_t = \begin{cases} 0.085N & \text{for frame buildings} \\ 0.045N & \text{for shear wall buildings} \\ 0.060N & \text{for frame}-\text{shear wall buildings} \end{cases} \tag{1}$$

$$T_t = \begin{cases} 0.070N & \text{for frame buildings} \\ 0.045N & \text{for shear wall buildings} \\ 0.055N & \text{for frame}-\text{shear wall buildings} \end{cases} \tag{2}$$

The measured results of dynamic behaviour of high–rise structures and tall shear wall buildings show that the deformation of those structures can be considered as pure bending deformation only [2].

3. Calculation of Free Vibrations

In order to simplify the calculation of free vibrations the high–rise structures and tall shear wall buildings are treated as multi–step bars, each step of which has a varying cross section, and the effect of rotatory, inertia and transverse shear deformation is neglected herein.

It is assumed that the stiffness and mass distribution of the ith step are given by

$$EJ_i(x) = EJ_i(1 + \beta_i x)^{n+2} \quad , \quad \overline{m}_i(x) = \overline{m}_i(1 + \beta_i x)^n \tag{3}$$

If the ith step is a uniform bar, then $\beta_i = 0$.

The mode shape equation of the ith step is given by

$$\frac{d^2}{dx_i^2}[EJ_i(x)\frac{d^2 X_i(x)}{dx_i}] + \overline{m}_i(x)\omega^2 X_i(x) = 0 \tag{4}$$

in which $EJ_i(x), \overline{m}_i(x), X_i(x)$ are the flexural rigidity, mass distribution intensity and mode shape of the ith step, respectively.

Substituting Eq.(3) into Eq.(4) gives the general solution of the mode shape function of the ith step

$$X_i(x) = C_1 A_1(x) + C_2 A_2(x) + C_3 A_3(x) + C_4 A_4(x) \tag{5}$$

in which $A_1(x) - - A_4(x)$ are four special solutions for the differential equation, $C_1 - - C_4$ are four constants. The simplest forms of $A_1(x) - - A_4(x)$ are as follows

348

$$\begin{cases} A_{1i}(x) = (\frac{r}{\lambda})^{-n} J_n(r) \ , \ A_{2i}(x) = (\frac{r}{\lambda})^{-n} Y_n(r) \\ A_{3i}(x) = (\frac{r}{\lambda})^{-n} I_n(r) \ , \ A_{4i}(x) = (\frac{r}{\lambda})^{-n} K_n(r) \\ r_i = \lambda_i (1 + \beta_i x)^{\frac{1}{2}} \ , \ \lambda = \frac{2}{|\beta_i|} \left\{ \frac{\overline{m}_i \omega^2}{EJ_i} \right\}^{\frac{1}{4}} \end{cases} \tag{6}$$

In Eq.(6), J_n, Y_n, I_n and K_n are four kinds of the nth Bessel's functions.

In order to simplify the frequency equation , it is better to write the mode shape function of the ith step as follows

$$X_i(x) = X_{0i} Y_{1i}(x) + X'_{0i} Y_{2i}(x) + M_{0i} Y_{3i}(x) + Q_{0i} Y_{4i}(x) \tag{7}$$

in which X_{0i}, X'_{0i}, M_{0i} and Q_{0i} are the displacement, rotation, bending moment and shear force at end (the lower end) of the ith step, respectively, and $Y_{1i}(x)$, $Y_{2i}(x)$, $Y_{3i}(x)$ and $Y_{4i}(x)$ are a set of fundamental functions which meet the following conditions at end 0 of the ith step [2]

$$\begin{matrix} Y_{1i} = 1 & Y_{2i} = 0 & Y_{3i} = 0 & Y_{4i} = 0 \\ Y'_{1i} = 1 & Y'_{2i} = 0 & Y'_{3i} = 0 & Y'_{4i} = 0 \\ Y''_{1i} = 1 & Y''_{2i} = 0 & Y''_{3i} = \frac{1}{EJ_i} & Y''_{4i} = 0 \\ Y'''_{1i} = 1 & Y'''_{2i} = 0 & Y'''_{3i} = 0 & Y'''_{4i} = \frac{1}{EJ_i} \end{matrix}$$

Using the fundamental functions, the displacements and internal forces at end 1 of the ith step can be written as

$$\begin{Bmatrix} X_{1i}(x) \\ X'_{1i}(x) \\ M_{1i}(x) \\ Q_{1i}(x) \end{Bmatrix} = \begin{bmatrix} B_i(x) \end{bmatrix} \begin{Bmatrix} X_{0i} \\ X'_{0i} \\ M_{0i} \\ Q_{0i} \end{Bmatrix} \tag{8}$$

in which

$$\begin{bmatrix} B_i(x) \end{bmatrix} = \begin{bmatrix} Y_{1i} & Y_{2i} & Y_{3i} & Y_{4i} \\ Y'_{1i} & Y'_{2i} & Y'_{3i} & Y'_{4i} \\ EJ_{i1} Y''_{1i} & EJ_{i1} Y''_{2i} & EJ_{i1} Y''_{3i} & EJ_{i1} Y''_{4i} \\ (EJ_{i1} Y''_{1i})' & (EJ_{i1} Y''_{2i})' & (EJ_{i1} Y''_{3i})' & (EJ_{i1} Y''_{4i})' \end{bmatrix}$$

Because there is a lumped mass m_1 at end 1 (the upper end) of the ith step, the shear force will be changed abruptly at that end, so that:

$$\begin{Bmatrix} X_{0,i+1} \\ X'_{0,i+1} \\ M_{0,i+1} \\ Q_{0,i+1} \end{Bmatrix} = \begin{bmatrix} 1 & 0 & 0 & 0 \\ 0 & 1 & 0 & 0 \\ 0 & 0 & 1 & 0 \\ -m_i\omega^2 & 0 & 0 & 1 \end{bmatrix} \begin{bmatrix} B_i(x) \end{bmatrix} \begin{Bmatrix} X_{0i}(x) \\ X'_{0i}(x) \\ M_{0i}(x) \\ Q_{0i}(x) \end{Bmatrix} = \begin{bmatrix} D(i+1,i) \end{bmatrix} \begin{Bmatrix} X_{0i}(x) \\ X'_{0i}(x) \\ M_{0i}(x) \\ Q_{0i}(x) \end{Bmatrix} \quad (9$$

The relationship for the top step and the bottom step is

$$\begin{Bmatrix} X_{1n}(x) \\ X'_{1n}(x) \\ M_{1n}(x) \\ Q_{1n}(x) \end{Bmatrix} = \begin{bmatrix} D(n,0) \end{bmatrix} \begin{Bmatrix} X_{01}(x) \\ X'_{01}(x) \\ M_{01}(x) \\ Q_{01}(x) \end{Bmatrix} \quad (10$$

in which

$$\begin{bmatrix} D(n,0) \end{bmatrix} = \begin{bmatrix} D(n.n-1) \end{bmatrix} \cdots [D(2,1)][D(1,0)]$$

The frequency equation of a multi−step cantilever can be established from Eq.(10 as

$$D_{33}D_{44} - D_{34}D_{43} = 0 \quad (11$$

where D_{ij} represents the elements of matrix [D(n,0)].

4. Examples

Example 1.   Calculation of Free Vibration of Guangzhou Hotel (A 27−Storey Building)

The analysis procedure consists of the following steps:

(1) Determination of the mass per unit length (Fig.1)

The stiffness and the mass per unit length of Guangzhou Hotel Building vary in echelon. For simplification, the building is treated as a varying cross−section beam. Because the variation of the mass per unit length is small, it is reasonable to assume $\overline{m}$ as a constant, i.e., $\overline{m} = 37611.4 kg / m$; $\overline{m}$ is the average of the mass per unit length.

The lumped mass attached at the top of the building is M = 30612.2 kg.

(2) Evaluation of the Stiffness (Fig.1)

Because the mass is uniformly distributed, the stiffness can be taken as

$$EJ(x) = \alpha(1 + \beta)^2 \quad (a)$$

According to the conditions

$$at \ x = 0, \quad J = 2156.50m^4$$
$$at \ x = l, \quad J = 1099.57m^4$$

the constants α, β are determined as

$$\alpha = EJ_0 = 60.38 \times 10^{10} \quad KN.m.sec^2, \quad \beta = -3.769 \times 10^{-3}$$

350

The distribution of stiffness given by Eq.(a) is shown in Fig.1 (dotted line and the va ues in parentheses)

(3) Evaluation of the Natural Frequencies

Solving the frequency equation (10) (n = 1) gives the fundamental frequency as 6.358 and the fundamental period, T_1, is 0.988 sec. The measured value is 0.970 sec. It is evident that the computed value approaches the measured one

(4) Calculation of the fundamental mode shape

After computing the fundamental frequency, the fundamental mode shape is determined from eq.(6). The results are shown in Fig.2.

Example 2. Calculation of Free Vibrations of Wuhan T.V.Tower

Wuhan T.V.Tower is a reinforced concrete tube structure, its geometric configuration is shown in Fig.3

The mass and stiffness distribution of the ith segment are assumed as

$$EJ_i(x) = EJ_i(1 - \beta_i x)^3, \quad \overline{m}_i(x) = \overline{m}_i(1 - \beta_i x), \quad i = 1, 2, \cdots, 18$$

The 9th–12th, 16th and 18th are uniform segments, so $\beta_i = 0$ (i = 9–12,16 and 18).

The natural frequencies and mode shapes of the Wuhan T.V.Tower obtained by use of the method in the paper are listed in Table 1 and shown in Fig.4, respectively.

In order to check the method proposed in the paper, the lumped mass method is also used to determine the natural frequencies and mode shapes of the Wuhan T.V.Tower. The structural mass is divided into 40 lumped masses and the calculation values of natural frequencies and mode shapes of the Wuhan T.V.Tower are also listed in Table 1 and shown in Fig.4, respectively.

The fundamental frequency and fundamental mode shape were measured by the authors. The measured values are also listed in Table 1 and shown in Fig.4, respectively.

It can be seen from Table1 and Fig.4 that the calculated values and corresponding measured values of natural frequencies are approximately equal, and the fundamental mode shape obtained by the method in the paper is a fair approach to the measured one.

Example 3. The residence building of China Broadcast Affair Bureau is 12 stories. There are 5 shear walls in every story, and its foundation can be treated as firm.

Using Eq.(1) gives the fundamental frequency of the building as 0.54 sec. and the value calculated by the method in the paper is 0.56 sec.

5. Conclusion

The calculation method and its program proposed by the authors can be used to solve natural frequencies and mode shapes of tall buildings and high–rise structures with simple and complicated variation in cross section. The accuracy and storage space

of the program are acceptable.
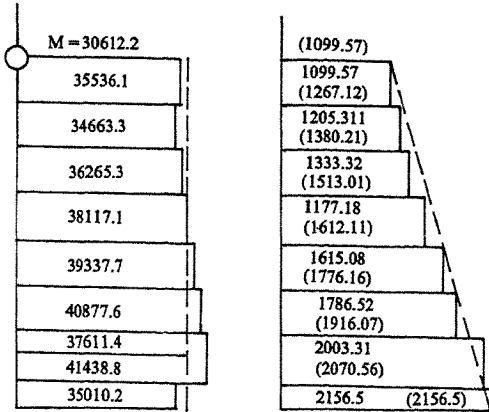
Fig.1 Stiffness and mass distribution of Guangzhou Hotel
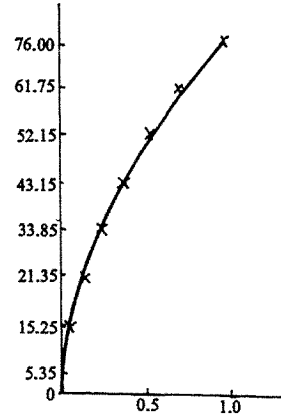
Fig.2 The fundamental mode shape of Guangzhou Hotel
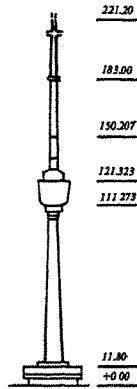
Fig.3 Wuhan T.V. Tower

ω_i	1	2	M
ω_1	2.01	1.99	2.00
ω_2	6.78	7.50	
ω_3	14.97	14.02	

Table 1 Natural frequencies

1——Lumped mass method

2——proposed method

×, M——measured values
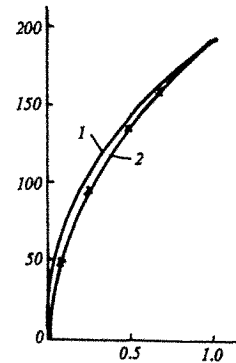
Fig.4 The mode shape of Wuhan T.V. Tower

References

1. Wang Guangyuan, Vibrations of Building Structure, Press of Science and Technology, China, 1978.

2. Li Guiqing, Calculation Theory and Methods of Aseismic Structures, Seismic Press, China,1985.

352

The Wind Tunnel Model Testing of Tall Buildings
of Haijiang Garden at the Chinese Town in Shenzhen

G. H. Cai

Beijing Institute of Aerodynamics

Abstract: This paper report presents the test results of the forces and pressure distributions on the model of a tall building group consisting of four 32-storey structures of Haijing Garden at the Chinese town in Shenzhen on the scale of 1:200. It gives the data of wind loads on a sngle building and the building group with wind flow towards them in different directions in the atmospheric boundary layer. The analysis results indicate that they are relative to the direction of air flow, the configuration of construct, each building's site in a building group and the environment etc. So when we design high structures, we must pay sufficient attention to the points mentioned above.

1. Introduction

Tall buildings and towering structures are developing rapidly in our country in recent years. Buildings are built higher and higher and each has different configuration, further more they always appear in the form of building groups. All these pose new problems to architects and designers. Storms are frequent in Shenzhen, and they always do damage to constructions. So research in the wind load characteristics of tall buildings will directly affect the reasonableness, economy and safety of structure design.

We have made systematic researches on wind loads on structures in two ways since early 1970s. One is scaled model testing in wind tunnel and the other is site measurement. Each has its characteristics but the former has the advantage over the latter because it is economic, convenient and has short period. Most important, the testing is not limited by climate environment, it can simulate different wind field conditions and repeat them. So scaled model testing in low-speed wind tunnel is widely used, and the test data play an important role in construct design and strength calibration.

2. Experiment Details

We had the test done in FD-09 low-speed wind tunnel at Beijing Institute of Aerodynamics (BIA). The test section of the wind tunnel is $3M \times 3M \times 12M$, the wind speed range is from 10 m/s to 100 m/s. In the middle of the section there is a turntable which has a diameter of 1700 mm and can rotate from $o°$ to $360°$. The models were fixed on it. Constructions are in atmospheric boundary layer. Progressive increases in height produce progressive increases in average wind speed and progressive decreases in turbulence [1,2]. Though natural wind is a random phenomenon, it has evident characteristic--perpendicular to the ground, wind speed varies with height in index rule. It's mostly determined by the roughness of wind swept area. We simulated not only the wind speed distribution but also the turbulence distribution of atmospheric boundary layer [3].

We used a six-component strain gauge balance to measure the aerodynamic force and moment, we also used six pressure transducers for measuring the surface pressures on the model. Using computers, we can easily finish data sampling, computation and graphics.

The tall buildings of Haijing Garden consist of 4 single 104.42-meter-high structures with the same configuration, and each has 32 storeies, the maximum face-on-attack area is $3711.44m^2$. Fig.1 shows the cross sections of the four structures. We call them No.1, No.2, No.3 and No.4 in turn. Being asymmetric, No.1 and No.2 were chosen as force-measuring models; No.3 and No.4 were pressure-measuring models as Fig.2 and Fig.3 show. There are 5 pressure-tapped sections up along the structures, 62 taps in each section, so there are 310 taps in total on each structure.

3. Measurement and Treatment

Measurement items: We measured the three forces three moments and pressure distributions on the surfaces on a single body and on a building group separately. Wind azimuth is from $0°$ to $360°$, the interval is $30°$. We also did wind spectrum observation. The wind speeds we chose were 30 m/s and 40 m/s. Forces and pressures were measured separately in case of interference between them.

Mathematic treatment: The aerodynamic forces and moments on the models were measured by a six-component balance. They are drag coefficient F_x, side force coefficient F_y, lift coefficient F_z, pitching moment coefficient M_y, side bending moment coefficient M_x, twisting moment coefficient M_z, so we can yield the total force coefficient F_r and the total moment coefficient M_r and the height $\bar{H}$ between the action point and the bottom. Force axis system and moment axis system are shown in Fig.4. The midpoint of the bottom is chosen as moment reference point.

F_r, M_r and $\bar{H}$ are given by

$$F_r = \sqrt{F_x^2 + F_y^2 + F_z^2} \ , \quad M_r = \sqrt{M_x^2 + M_y^2 + M_z^2} \ , \quad \bar{H} = \frac{M_y}{F_x} \ \%$$

Pressure coefficient is $Cp_i = \dfrac{P_i - P_\infty}{q_\infty (1+\eta)}$. Where P_i is the pressure of each pressure tappings, q_∞ is speed pressure of the approaching flow, P_∞ is static pressure, η is choking correction factor.

4. Experimental Results

Models No.1 and No.2 are force-measuring models. We also measured the forces on a single body of No.2. Analysing the results, we drew some conclusions written concisely as follows:

(1)When B is $180°$, drag coefficient $F_{xmax}=1.085$. With the concavity toward the approaching flow, the drag force is surely maximum.

(2) There are evident differences between the side force on a single body and that on a group. We find side force on a single is higher than that on a group. They are $F_{ymax(s)}=0.825$ (single) and $F_{ymax(g)}=0.563$ (group). The causation is simple: a single structure is directly influenced by natural wind, but a body in a group is also influenced by the other bodies stand nearby.

(3) No matter to a single body or a building group, they both produce a up-lift force through out the wind azimuth range from $0°$ to $360°$. This is caused by the higher speed and lower pressure wind flow over the tops of the structures.

(4) Two wind azimuthes $90°$ and $270°$ give maximum side bending moment on a single structure, and it is $M_{xmax}=0.377$. The wind azimuthes $150°$ and $210°$ give maximum side bending moment on a building group, the maximum is $M_{xmax}=0.262$.

(5)When B is $180°$, there has maximum pitching moment on a single body or a building group. $M_{ymax}=0.401$ (single), $M_{ymax}=0.507$ (group). The curves of pitching moment have the same shape as drag curves have. We know M_y is produced by F_x.

(6)Twisting moment is small throughout the whole wind azimuth range. This is because the total force action point is very near the perpendicular axes.

(7)We can write out the position of the force action point $\bar{H}=46\%$. We can also yield the same result using total force and moment.

(8)The experiment indicates that Reynolds numbers don't influence the results likely. Because to a configuration with sharp edge, the position where flow line break is fixed, we needn't pay much attention to the influence of Reynolds numbers.

(9)Using the widely used programme of Beijing Institute of Civil and Structural Engineering, we can obtain the theoretical results. We chose the average wind pressure W = 2.286 kPa (corresponding wind speed is 60 m/s), shape coefficient $\xi = 1.4$. The wind-induced vibration coefficient and the variation wind pressure coefficient with height are chosen according to the new wind load standard [4]. We can find that theoretical results are greater than experimental results.

Obtaining pressure distribution is to get the wind load shape coefficient of construction. The shape coefficient is a very important parameter in structure design. Because the flow spectrum of construction

Obtaining pressure distribution is to get the wind load shape coefficient of construction. The shape coefficient is a very important parameter in structure design. Because the flow spectrum of construction is complex and turbulent, the pressure distribution is impossibly uniform. Simplifing the calculations, we generally chose the average pressure on a surface as the shape coefficient. Limited by the length of the article, we only discuss the measurement result of 4-structure group (No.3 and No.4 models) when B(wind azimuth) are $o°$, $90°$, $180°$ and $270°$ and only discuss the $3^\#$ section in the middle.

Some conclusions are represented involving [5]:

(1)$B=0°$. As Fig.5 shows the pressures on the walls which towards the approaching flow are positive, the Cp values are 0.672 and 0.565; the pressures on the back walls are negative, the Cp values are -0.538 and -0.620. Δ Cp is about 1.2. There are numerous differences between the pressure on the left wall and that on the right wall. These are caused by the interference of the nearby structures.

(2) $B=90°$. As Fig.6 shows pressures on each wall of No.3 and No.4 model are negative, the shape coefficient varies conspicuously. This is because No.3 and No.4 models are in the wake of No.1 and No.2 models

(3) $B=180°$. As Fig.7 shows the Cp values on the surfaces toward approaching flow are 0.654 and 0.690, and those on the back surfaces are -0.668 and -0.651 separately, the ΔCp value is about 1.33. With concavities toward the approaching flow, the shape coefficient is maximum.

(4) $B=270°$. As Fig.8 shows No.4 model has great influence on No.3 model standing in the down stream; on the contrary, No.3 model has influence on No.4 too. So when we design high building groups, we shouldn't choose the shape coefficient just equal to that of a single body according to the general construction standard.

The experiment indicates that pressure measurement results coincide with force measurement results.

References

1   W.H.MELBOVRNE, The Structure of Wind Near the Ground, a Lecture by MELBOURNE at the Beijing University, 1984.

2   R.L.Wu, Simulation Research of Towering Building Test in Wind Tunnel, Beijing Aeronautical and Astronautical University, 1982.

3   Y.D.Xu, Producing and Adjusting of Atmospheric Boundary Layer Simulator of FD-09 Low Speed Wind Tunnel, Beijing Institute of Aerodynamics, 1985.

4   Structure Load Standard of National Standardized Construction (GBJ 9-87), 1989.

5   G.H.Cai, Wind Tunnel Model Testing Reports of Constructions of Haijing Garden in Shenzhen Beijing Institute of Aerodynamics, 1990.
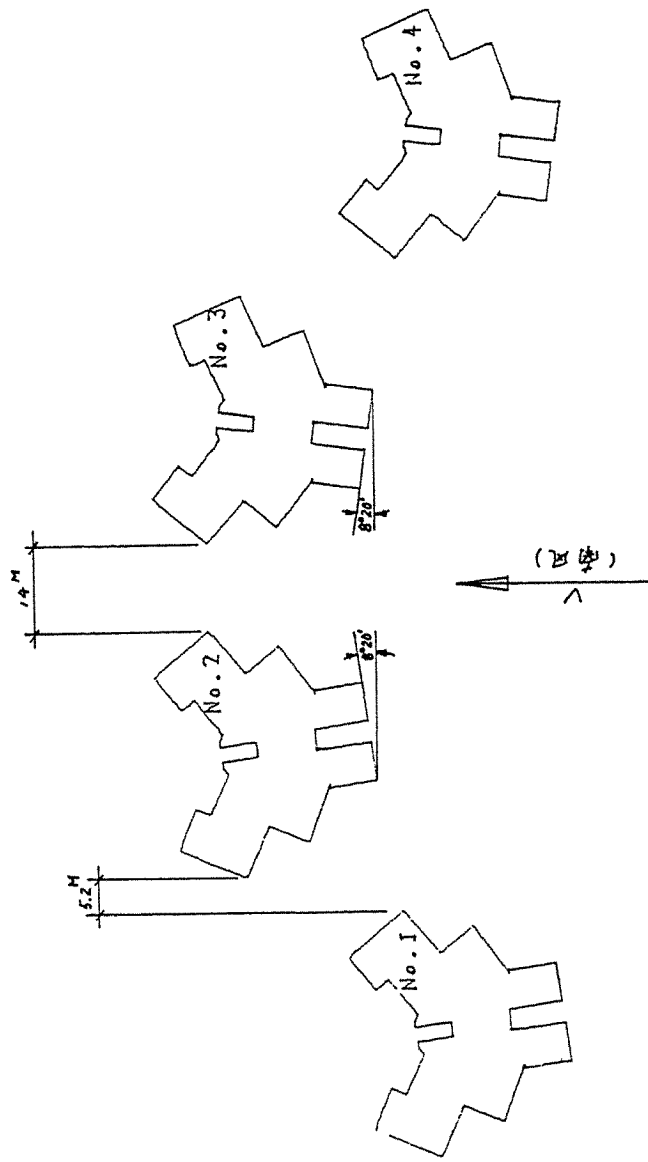
Fig.1 4-Building model section
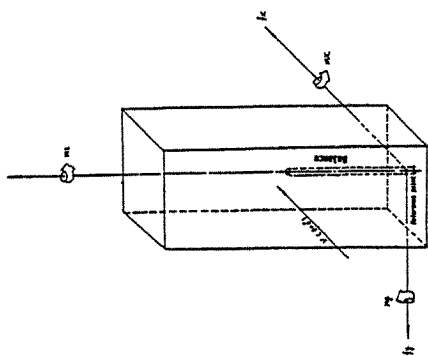
Fig 4 Coordinate axes
of the forces and moments
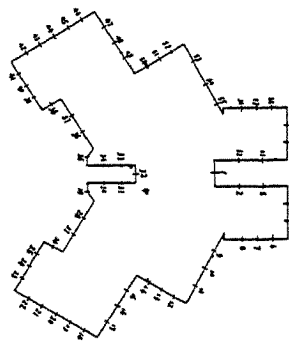
Fig.3 Pressure taps distribution
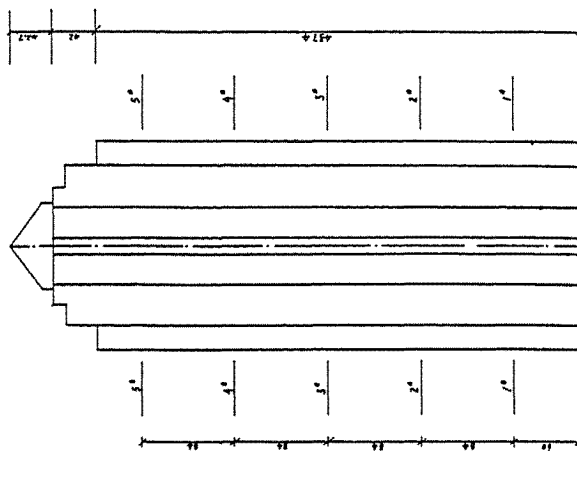
Fig.2 Pressure measuring sections

357
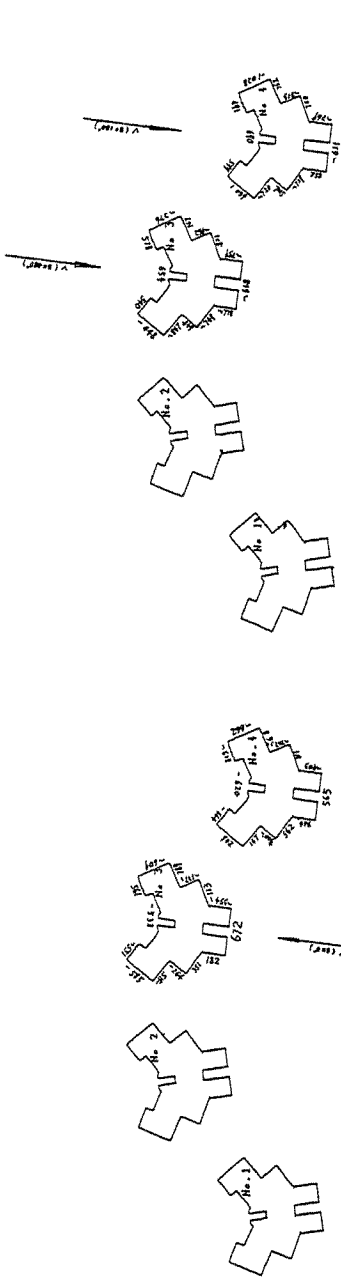
Fig 7 Shape coefficient (β=180)
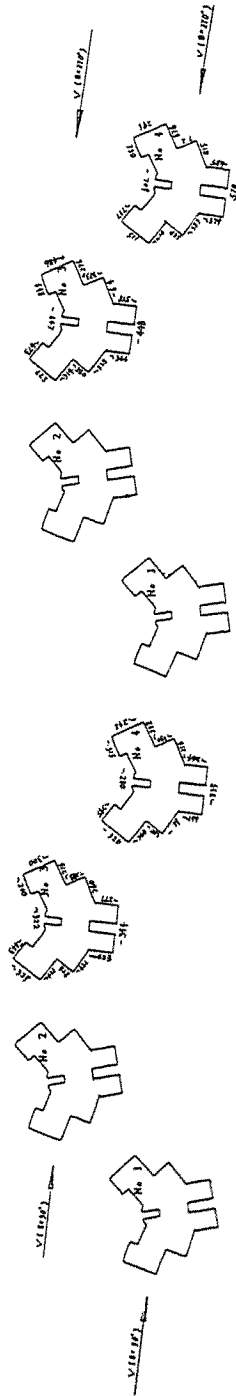
Fig 8 Shape coefficient (β=270)
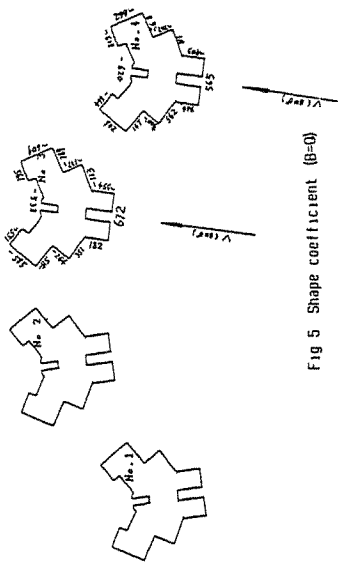
Fig 5 Shape coefficient (β=0)
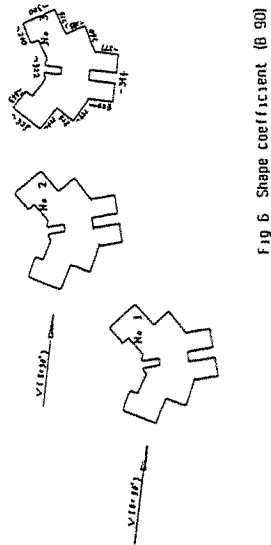
Fig 6 Shape coefficient (β 90)

358

Study on The Exponential Model of The Fluctuating Wind Load

Zhou Bicheng   Tao Qibin

Hefei University of Technology

Abstract: Discussed is the question of analysis and simplification of the fluctuating wind load in nature. Using probability characteristic corresponding value, the random fluctuating wind pressure can be fitted to the exponential wind pressure model with approximate value. Under another discussion in this paper is the error of exponential wind pressure model and the method to obtaining the wind speed spectral which is further fitted with that of Davenport after the model correction. The feasibility of the theory of using exponential wind pressure model instead of the gust fluctuating wind pressure is further verified. The another also made useful discussion on how to use this theory in the practice.

1. Statistical characterisitics of the fluctuating wind load

1.1 The statistical characterisitics of the fluctuating wind load can be expressed by the autocorrelation function and autospectral density function of the fluctuating wind pressure (wind speed). [1] [2] [3]. The autocorrelation function of the fluctuating wind pressure can be expressed as follows:

$$R(\tau) = e^{-\alpha |\tau|}(\cos\beta\tau + \mu\sin\beta|\tau|) \tag{1}$$

And the auto-spectral density function is:

$$S(\omega) = \frac{1}{\pi} \frac{(\alpha-\mu\beta)\omega^2 + (\alpha+\mu\beta)(\alpha^2+\beta^2)}{\omega^4 + 2(\alpha^2-\beta^2)\omega^2 + (\alpha^2+\beta^2)^2} \tag{2}$$

On the basis of the above equations, we can see that the autocorrelation function of fluctuating wind pressure (speed) is related to two parts. One is the exponential factor which plays main role. Another is the triangle function which will produce little modulation .

1.2 On the basis of neglecting triangle function, the eqn (1) can be simplified as follows: (without normalization)

$$R(\tau) = (\sigma_w^2 + \overline{W}^2)e^{-\alpha |\tau|} \tag{3}$$

where: $\overline{W}$ - average wind pressure.

$\sigma_w{}^2$ - variance of the fluctuating wind pressure

1.3 The eqn(3) expresses the simplified autocorrelation function of horizontal fluctuating wind pressure. So its corresponding wind pressure autospectral density function is given by:

$$S(\omega) = \frac{\sigma_u{}^2 + \overline{W}^2}{\pi} \cdot \frac{\alpha}{\alpha^2 + \omega^2} \qquad (4)$$

2. The exponential model of the fluctuating wind pressure

2.1 Owing to the autocorrelation function of different exponential wind pressure is still in terms of the exponential function . So it has similar form with the autocorrelation function of simplified fluctuating wind pressure.

2.2 Now we suggest an exponential wind pressure with uncertain coefficients a and b, expressed as :

$$W(t) = ae^{-bt} \qquad (5)$$

Based on the above equation, the autocorrelation function and autospectral density function can be given by: [7]

$$R_W(\tau) = 0.166a^2 e^{-b|\tau|} \qquad (6)$$

$$S_W(\omega) = \frac{0.166a^2}{\pi} \cdot \frac{b}{b^2 + \omega^2} \qquad (7)$$

Let the corresponding coefficients in the exponential part in the equations(3) and (6) be the same, then the uncertain coefficients must be:

$$a = 2.45\sqrt{\sigma_u{}^2 + \overline{W}^2} \qquad b = \alpha$$

Substituting a, b into eqn(5), we can obtain the exponential wind pressure model as follows:

$$W(t) = 2.45\sqrt{\sigma_w{}^2 + \overline{W}^2} \cdot e^{-\alpha t} \qquad (8)$$

2.3 If the averaged value of fluctuating wind pressure, variance and roughness parameter are definite. It is easy to set up the exponential wind pressure model which is approximate the same with the fluctuating wind pressure.

3. The error and correction of exponential wind pressure model

3.1 In order to make comparison of exponential wind pressure spectrum with Davenport spectrum of horizontal wind velocity, it is neccessery to reduce this spectrum eqn (7) as the corresponding wind speed autospectral density, [4]. which is given by following:

$$S_v(\omega)=\frac{(1+24k)\overline{V_{10}^2}}{4\pi}\cdot\frac{\alpha}{\alpha^2+\omega^2} \tag{9}$$

Where: $\overline{V}_{10}$ is the mean wind speed at 10m above ground.

k is the roughness coefficient.

According to Darenport's expression of the universal wind speed power spectrum, we make coordinate transformation of eqn (9), then following eqn will be obtained

$$\frac{nS_v(n)}{k\overline{V}^2}=\frac{Ax}{B^2+x^2} \qquad S_v(n)=\frac{k\overline{V}^2}{n}\frac{Ax}{B^2+x^2} \tag{10}$$

Where: $x=1\frac{n}{\overline{V}}$, $A=\frac{(24+\frac{1}{k})1}{16\pi^2\overline{V}}\alpha$, $B=\frac{1\cdot\alpha}{2\pi\overline{V}}$. 1: is turbulence length scale

3.2 The empirical formular of Davenport's horizontal gusty spectrum is given follows

$$S_v(n)=4k\overline{V}_{10}^2\frac{x^2}{n(1+x^2)^{\frac{4}{3}}} \tag{11}$$

$$x=\frac{1200n}{\overline{V}_{10}}$$

Based on eqn. (10) and (11), the spectrum of exponential wind pressure model and the spectrum of Davenport wind speed will be obtained, shown in fig. 1. Comparing these two spectrum, we can find that their curves fit very well around the position of the maximum when n/v>0.01, then the error will be increased.

3.3 The neglection of the triangle function in the expression of the fluctuating wind pressure autocorrelation function cause the error of the wind speed spectrum by means of the exponential wind pressure. According to the frequency shift theorem of the Fourier transformation, the triangle function which times the exponential part will modulate to the exponential curve. And just this modulation results in the frequency shift of the frequency spectrum. So the frequency shift must be under consideration in the error correction to the wind speed spectrum of the exponential model. [9] After correcting the equation (9) and (10), we obtain the following:

$$S_v(\omega)=\frac{(1+24k)\overline{V}^2}{4\pi}\cdot\frac{\alpha}{\alpha^2+(\omega+\omega_a)^2} \tag{12}$$

$$S_v(n)=\frac{k\overline{V}^2}{n}\frac{Ax}{B^2+C^2+2Cx+x^2} \tag{13}$$

Where: $C=\frac{1}{\overline{V}}\cdot\frac{\omega_a}{2\pi}$

3.4 Comparing the corrected wind spectrum of exponential wind pressure model with that of Davenport as shown in fig. 2, we obtained that the correction of the frequency shift effectively decreases the error of model spectrum and also increases the fitting precision of model spectrum and the fluctuating wind speed spectrum.

4. Dynamic response to the exponential wind excitation

4.1 As theoretical exame, the elastic structure with single degree of freedom is sele-

cted as the object excited by wind. Its transfer function is expressed as follows:

$$H(\omega) = \frac{1}{k\,[1-(\frac{\omega}{\omega_o})^2 + J2\xi\frac{\omega}{\omega_o}]} \tag{14}$$

Thence, the module of this transfer is given by

$$|H(\omega)| = \frac{1}{k\sqrt{[1-(\frac{\omega}{\omega_o})^2]^2 + (2\xi\frac{\omega}{\omega_o})^2}} \tag{15}$$

4.2 The exponential wind pressure is treated as excitation source and used to excited on the elastic structure with single degree of freedom, the dynamic response which results from this excitation can be expressed by the structure displacement response power spectrum. Based on eqn (4) and (15), the following expression can be obtained:

$$S_y(\omega) = |H(\omega)|^2 S(\omega) = \frac{\frac{\sigma_w^2 + \bar{W}^2}{\pi} \cdot \frac{a}{a^2+\omega^2}}{k^2\left\{[1-(\frac{\omega}{\omega_o})^2]^2 + (2\xi\frac{\omega}{\omega_o})^2\right\}} \tag{16}$$

4.3 Fig. 3.a. indicates the displacement response spectrum of the exponential wind pressure excitation calculated from eqn (16). Fig. 3.b. indicates the displacement response spectrum of tower structure with single degree of freedom excited by the natural fluctuating wind load tested by H.R. Smart. Comparing the response curves in two figs, we can see clearly that they are in the very simular forms.

5.   Model test of exponential wind pressure excitation

5.1 Structure wind vibration model test system include excitation source of the exponential wind pressure container, structure model and test analysis system. The flow chart of structure wind vibration model test equipment is shown in fig. 4.

5.2 As to the model test of structure wind vibration, wind load model must keep the same similarity law with the structure dynamically similar model.

5.3 When the reduced scale of the model is c , then its force scale c , time scale c and frequency scale c also changed. They have the definite relationship with c [8]. According to the similarity scale, the corresponding parameters in eqn (8). and (4) can be rewrited so as to obtain the exponential wind pressure model which is just related to the similarity relation.

$$w^*(t) = 2.45\sqrt{\frac{\sigma_w^2 + \bar{W}^2}{C_F^2}} \cdot e^{-a \cdot t/C_t} \tag{17}$$

$$S^*(\omega) = \frac{\sigma_w^2 + \bar{W}^2}{\pi C_{\rho}^2} \cdot \frac{a}{a^2 + (\frac{\omega}{C_t})^2} \tag{18}$$

5.4 Fig 3.c. indicates the displacement response spectrum tested from the elasticity structure model excitation by means of exponential wind pressure. It has the same response trend with fig. 3. a & b. Therefore, the theory of using the exponential wind pressure model instead of the fluctuating wind pressure has been further verified.

5.5 Fig. 5. show the series of the displacement response spectrums which are obtainii
by increasing the natural frequency of the structure model gradually with the
same exponential wind pressure model excitation. From these figs, it is seen that
the first order resonance amplitude peak value decreases with the increase in tl
natural frequency of structure. So we can see from this test that the exponential
wind pressure excitaton is of better apply value in the optimization design for
resisting wind vibration of the structure.

Reference:

1. М.Ф.Барщтейн, "Строительная Механика И Расчет Сооружений", 1959.1.

2. Choi Cheong Chuen. Correlation and Spectral Functions of Atmospheric Turbulence,
    Proc. Wind E.B.S. 1971

3   Simiu.E and Scanlan.R.H. Wind Effect on Structures: An Introduction to Wind
    Engineering. J.Wiley and Sons. New York 1978

4   Zhang Xiang Ting . Wind Pressure on Structure and Wind Vibration Calculation
    Tongji University Press 1985

5   V.Kolousek, M.Pirner, O.Fischer, J.Naprstek. Wind Effects on Civil Engineering
    Structures, Elsevier New York 1984

6   Tian Pu, Et Al. A Study of Typhoon Spectrum, Proc. APSOWE 1989

7   Deng Sheng Kong, Zhou Bi Cheng. Similar Simulation of Fluctuating Wind Pressure.
    Acta Energiae Solaris sinica. 1989. vol. 10, No. 3.

8   Zhou Bi Cheng and Wang Yong Zhi . Vibration Analysis of Windmill Tower by means
    of Dynamic Similarity Model . ICMD' 87, 8-15 1987

9   E.O.Brigham. The fast fourier transform . Prencice-hall Inc 1974

10 H.R.Smart . The Dynamic reponse of structure to wind loading. University of
    Tormto Press 1968
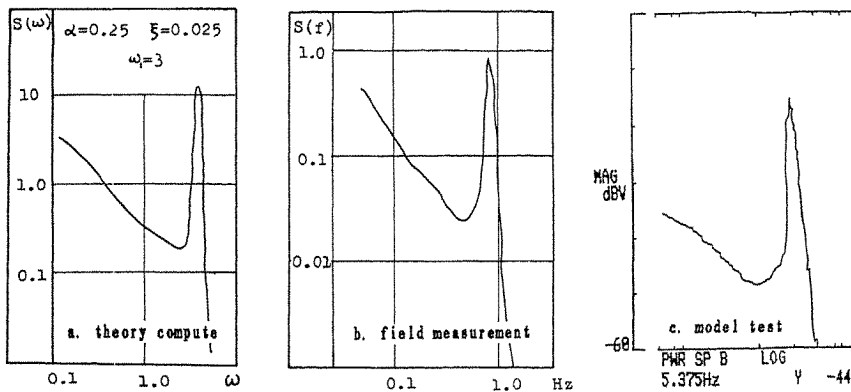
Fig. 3. The displacement response spectrum

363
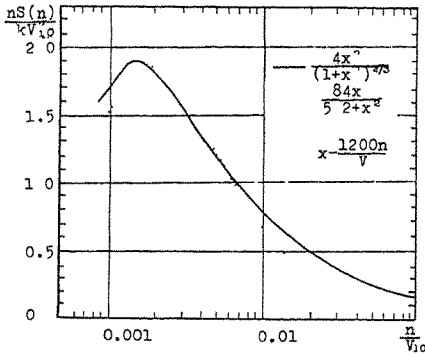
Fig.1. Comparing the spectrum of exponential with that of Davenport

$$\frac{4x^2}{(1+x^2)^{4/3}}$$

$$\frac{84x}{5\ 2+x^2}$$

$$x=\frac{1200n}{V}$$
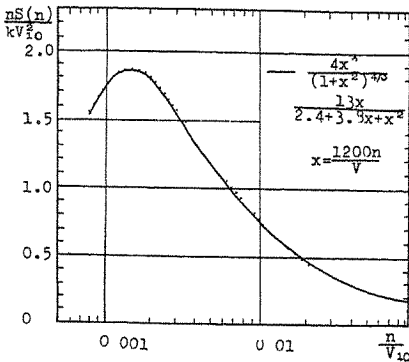
Fig 2 Comparing the corrected spectrum of exponential with that of Davenport

$$\frac{4x^2}{(1+x^2)^{4/3}}$$

$$\frac{13x}{2.4+3.9x+x^2}$$

$$x=\frac{1200n}{V}$$

Fig 4. Model test system

exponential wind pressure model

pressure container

displacement tansducer

pressure tansducer

voltage amplifiel

voltage amplifier
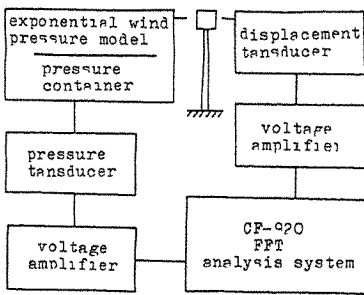
CF-920 FFT analysis system
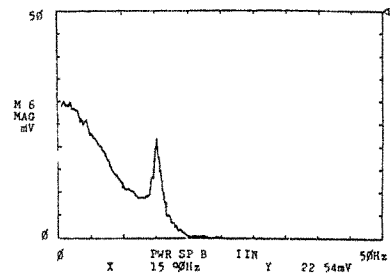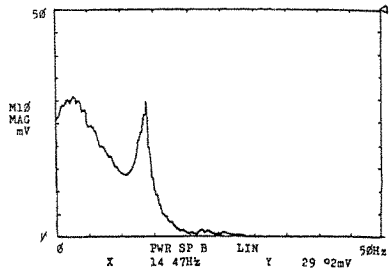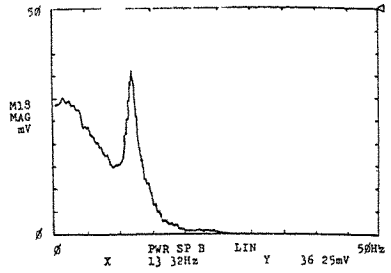
Fig.5. The displacement response spectrum (model test)

364

Towers and Chimneys

DYNAMIC CHARACTERISTICS AND WIND INDUCED RESPONSE
OF A STEEL FRAME TOWER

M.J.Glanville and K.C.S.Kwok

The University of Sydney
School of Civil & Mining Engineering

Abstract: This paper describes a field measurement program being conducted on a steel frame tower. Dynamic characteristics of the tower are measured to determine its frequencies of vibration, mode shapes and damping values.   A STRAND6 computer model is assembled and confirms these findings. Finally the dynamic response of the tower under wind loading is investigated.

1. Introduction

A microwave communications tower was constructed in 1992 at Prospect Electricity in the western suburbs of Sydney. The 67m high tower had to satisfy strict deflection limits for both static and dynamic loads to reduce signal transmission interference and loss. This was achieved using a frame system comprising of four circular column sections rigidly joined to rolled section platforms.

Testing commenced in June 1992 before any microwave dishes were installed on the tower so that the wind induced response and dynamic characteristics of the bare structure could be measured.

2. Measurement Program

Two accelerometers are installed at the 57m level and aligned orthogonally along the major axes of the tower. Wind speed and direction are measured at the same level using a cup anemometer and wind vane respectively. Analogue data is transmitted via co-axial cable to the base of the tower where it is recorded onto magnetic tape and later converted into digital format. Wind with yaw angle between 20° and 100° (see Figure 1) is not recorded to avoid interference from the tower.

Force vibration tests were performed on the tower in order to obtain decay curves for each mode of vibration. The tower was excited into vibration by oscillating a body weight in time with a metronome at each natural frequency of the tower. Forcing ceased once the tower was resonating at which time the tower was allowed to vibrate freely until it came to rest.   Force vibration tests were performed during still atmospheric conditions to eliminate any background excitation.

Tower decay during force excitations was measured using the installed accelerometers and a laser beam. A He-Ne laser was placed at the base of the tower and magnified through a zenith plummet. The beam was projected onto a grid placed at the top of the tower. The relative movement of the grid to the stationary beam was then filmed for later analysis.

Mode shape of the tower was measured using an additional set of accelerometers. After calibration at the 57m level of the tower, one pair of accelerometers was moved step by step to lower levels. Mode shape was determined from the ratio of simultaneously recorded acceleration signals. The presence of any torsional modes was similarly detected using an additional pair of accelerometers eccentrically placed at the 57m level.
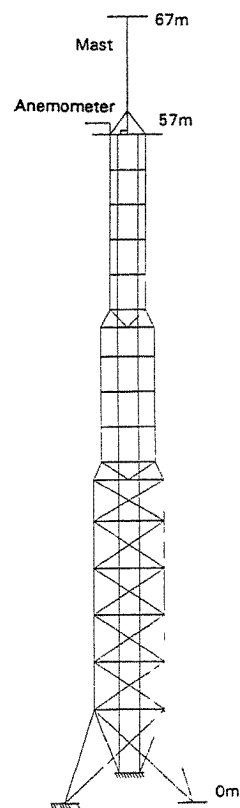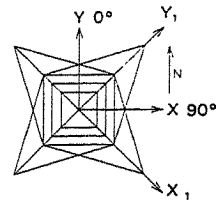
Figure 1   General arrangement of the Prospect tower

3. Computer Model

Natural frequencies and mode shapes for the tower were calculated using STRAND6. STRAND6 is a commercially available suite of full three dimensional finite element programs including a natural frequency solver. The natural frequency solver calculates the natural frequencies (eigenvalues λ) and vibration modes (eigenvectors $\{x\}$) based on a lumped mass assumption and solving the equation:

$$[K]\{x\} = \lambda[M]\{x\}$$

[K] and [M] represent the banded stiffness matrix and the lumped (diagonal) mass matrix respectively.

4. Results
4.1 Dynamic Characteristics

4.1.1 Natural Frequency

Power Spectral Density was computed for the acceleration response of the tower under wind loading (Figure2). Spectral peaks indicate that mode one dominates the tower's response at 1.08Hz. The two smaller peaks represent the second and third modes of tower vibration. The difference in natural frequencies along perpendicular axes are less than 2% producing strong coupling between the X-X and Y-Y axis.

Natural frequency values obtained through full scale measurement are compared to those calculated by STRAND6 in Table1. The computed results agree well with those measured, particularly modes one and two.

X-X AXIS

Figure 2 Power spectra of acceleration

Table 1

NATURAL FREQUENCY	X-X AXIS (Hz)			Y-Y AXIS (Hz)		
	MODE 1	MODE 2	MODE 3	MODE 1	MODE2	MODE3
FULL SCALE	1.08	1.41	3.22	1.07	1.39	3.28
STRAND6	1.10	1.40	3.52	1.10	1.40	3.54
STRAND6-MAST	1.14	3.53	6.06	1.14	3.54	6.07

4.1.2 Mode Shape

The mode shapes measured in full scale are compared to those calculated by STRAND6 in Figure3. Figure4 is a STRAND6 three dimensional representation of mode one vibrating along the Y-Y axis.
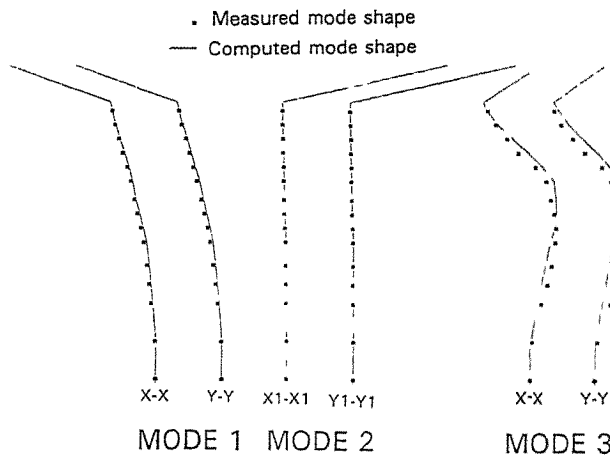
Figure 3 Computed and measured mode shapes
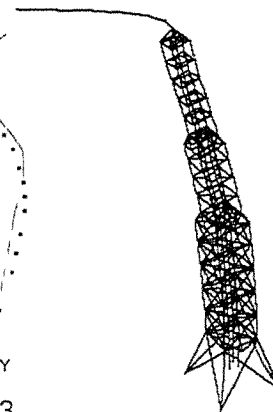
Figure 4 Mode 1 Y-Y axis

368

Mode one displays typical quarter sine wave bending with the top mast dominating the tower's displacement. The ratio of mast displacement to tower displacement is about 2.5:1. The ratio of mast to tower displacement in mode two is about 24:1 suggesting that this mode of vibration is due to the vibration of the top mast alone. Mode three displays the full sine wave shape with a small amount of torsion towards the top of the tower. Some torsion was measured in full scale at mode three only. Two eccentrically placed angle sections running up one side of the top third of the tower are probably responsible for this behaviour. It should be noted that a purely torsional mode was calculated by STRAND6 at 2.7Hz however no evidence of this mode was found during full scale measurement.

STRAND6 was used to simulate removal of the top mast from the tower. Table1 summarises the new frequencies found after the mast was removed. The natural frequency and mode shape of mode two without the mast is almost identical to that of mode three before the mast was removed as shown in Figure3. The natural frequency of the mast removed from the tower was also calculated by STRAND6 at 1.4Hz. This confirms that the second mode of the tower is simply the natural frequency of the top mast. Removing the mast would remove this mode of vibration.

4.1.3 Damping

High amplitude free vibration decay curves obtained from filtered acceleration records for mode one are shown in Figure5. Percentage critical damping along the Y-Y axis is greater than that along the X-X axis. This may be attributed to the higher number of bolted connections which offer additional damping along the Y-Y axis. Alignment of the ladders and cable trays running up the centre of the tower also contribute to the higher value of damping. Damping for modes two and three was similarly determined at 0.25% critical damping and 1.5% critical damping respectively. A low value of damping at mode two is expected since this mode represents vibration of the mast alone.

The decay curves shown in Figure5 are peculiar since they exhibit lower damping at higher amplitudes. This may be explained by the large dependence of mode one upon the vibration of the lightly damped mast which acts as an excitation mechanism during tower decay. It is intended to guy the mast in full scale and repeat the free vibration tests to confirm this.

Figure6 is a plot of the peak tower displacements as mapped from the laser trace during a free vibration decay along the tower's X-X axis. Both methods of decay analysis produce the same damping values as expected.

An autocorrelation analysis was employed to measure tower damping at relatively low amplitudes under wind loading alone (less than 5mg). One of the requirements for an autocorrelation analysis to be stable statistically is
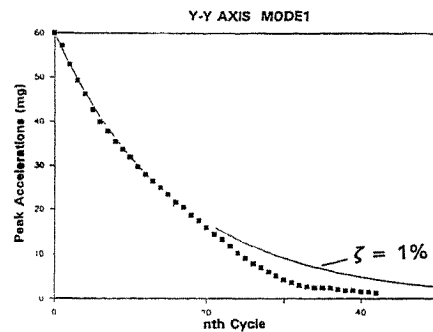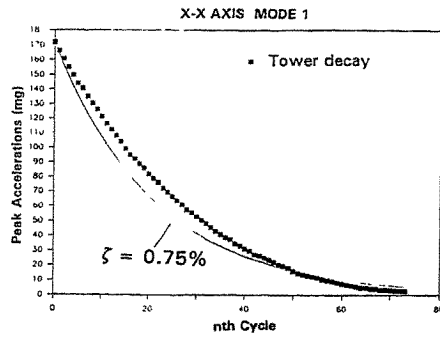
Figure 5 Free vibration decay curves obtained from acceleration records
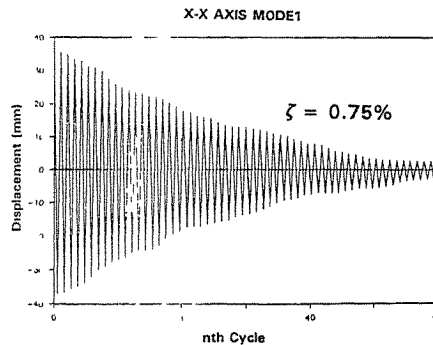
Figure 6 Free vibration decay mapped from laser trace

369

stationarity of the data on which the analysis is based. Jeary (ref 4) describes the run test for stationarity based on the variation of rms response. Figure7 presents the results of such a run test performed on a sample of data obtained from the tower. From 40 samples nineteen runs were found, satisfying the $a = 0.05$ level of significance set down by Bendat and Piersol (ref 1). This 468 second sample was the only data found which exhibited such stationarity in wind excited structural response over a significant time frame. Having effectively removed the forcing (wind) non-stationarity from the data, what remains is the non-linear response of the tower itself.

The stationary set of data was then bandpass filtered at the first mode and an autocorrelation analysis performed. The resulting autocorrelation curves shown in Figure8 indicate that damping along both tower axes is of similar magnitude at low amplitudes. Both levels of damping are typical for a steel structure under serviceability stress levels (ref5).

4.2 Wind Induced Response

A time history of tower acceleration and wind velocity over a 40 second period is shown in Figure9. Mode one is seen to dominate while modes two and three contribute towards the background response of the tower. An increase in along-wind (Y-Y) response can be seen due to wind energy fluctuating near n_1 between 20 and 40 seconds. A locus of dynamic response over 50 seconds is shown in Figure10. Along-wind and cross-wind components are of similar magnitude due to the strong coupling which exists between the two axes.
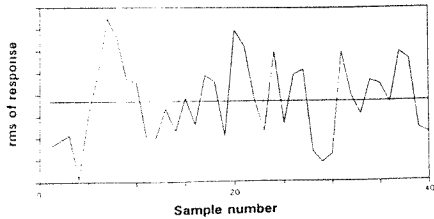
Figure 7 Run test for stationarity using 40 samples
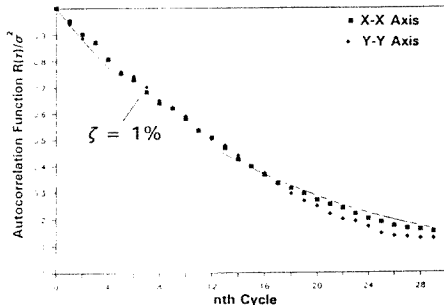
Figure 8 Autocorrelation function of first mode acceleration
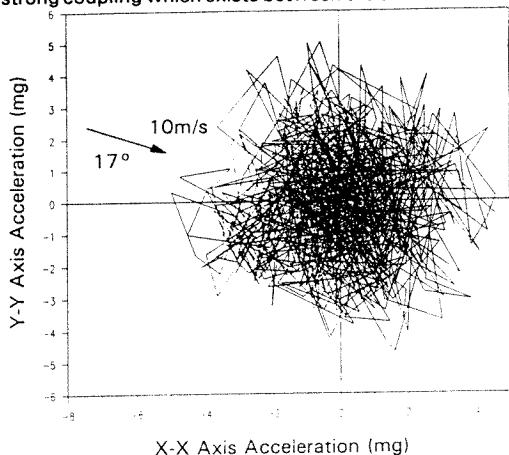
Figure 10 Locus of tower acceleration

Figure 9 Time history of tower acceleration, wind speed and direction

370

Along-wind
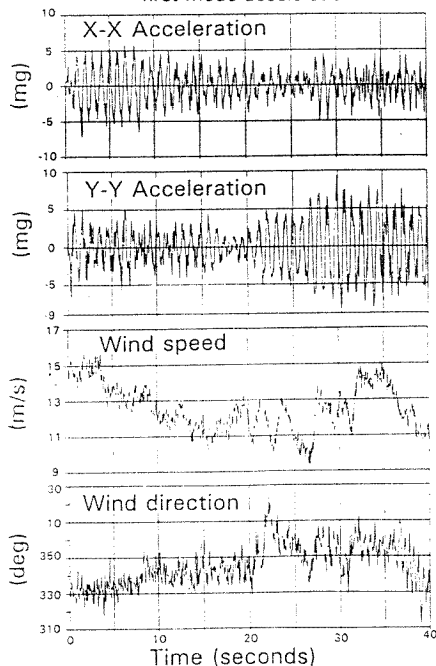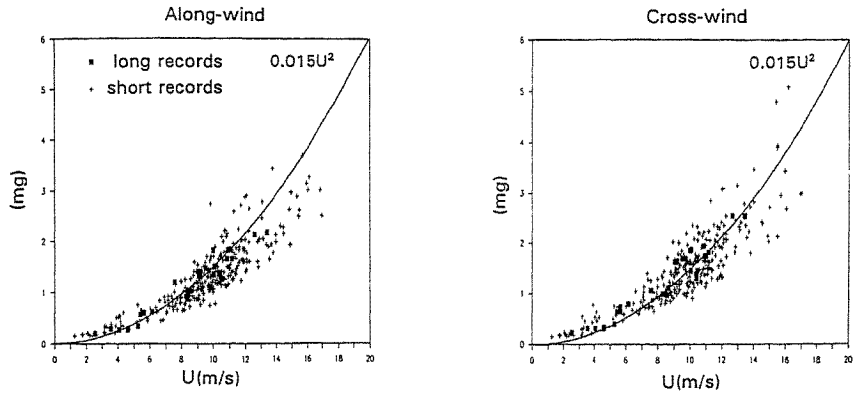
Cross-wind

Figure 11 rms acceleration versus mean wind speed

Figure11 shows that rms acceleration increases in proportion to the square of wind velocity for both along-wind and cross-wind components. This is low compared to full scale measurements completed by Hiramatsu and Akagi (ref2) on more conventional and less rigid angular section towers of similar height to the Prospect tower. They found that tower response increases as a power of 2.5. The long records (819 seconds) in Figure11 exhibit less scatter than the short records (63 seconds) due to smaller statistical errors. Variation in turbulence also contributes to the scatter.

The ratio of along-wind to cross-wind acceleration response remains close to unity for increasing mean wind speed as shown in Figure12. While the short records show some deviation from unity the long records indicate that both components of acceleration response are equivalent.
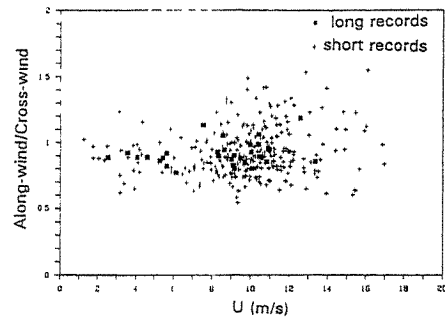
Figure 12 The ratio of along-wind to cross-wind rms acceleration versus mean wind speed

Along-wind
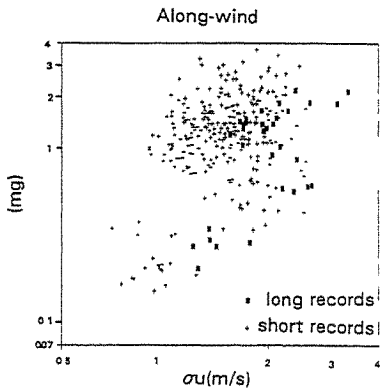
Cross-wind

Figure 13 Along-wind rms acceleration versus wind speed fluctuation
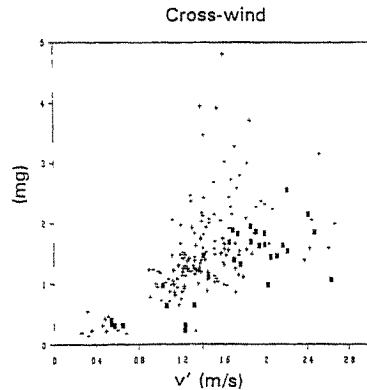
Figure 14 Cross-wind rms acceleration versus lateral turbulence

371

Fluctuation in wind speed is plotted against the dynamic response of the tower in the along-wind direction in Figure13. There is a general increase in tower response with increased buffeting by wind gust. Figure14 illustrates the increase in cross wind response due to lateral turbulence v' (wind direction changes).

Figure15 shows that turbulence ($\sigma u/U$) decreases with increasing mean wind speed up to about 8m/s. At this point $\sigma u/U$ levels off to about 0.151 (the value assumed by AS1170.2 for terrain category 2 at 50m). It is suspected that the high turbulence measured at low wind speeds is partly due to the inertia of the anemometer cups.

Mean wind speed is plotted against peak factor g (ratio of maximum and standard deviation) in Figure16. This measured peak factor represents a single maxima found in the signal over a period T. Peak factor g increases with increasing averaging time T although there is no change with increasing mean wind speed. Davenport has derived an 'average' peak factor g_R for resonant response based on a narrow band Gaussian process according to the equation.

$$g_R = \sqrt{2\log_e(n_1 T)} + \gamma/\sqrt{2\log_e(n_1 T)}$$

γ is Euler's constant equal to 0.5772 whilst n_1 is the first natural frequency of the tower. Expected peak g_R is plotted in Figure16 and is seen to be lower than the absolute peak g measured as would be expected.

Acceleration due to tilting of the tower has not been separated from the resonant response accelerations since its contribution is negligible.

Figure 15 Turbulence intensity versus mean wind speed
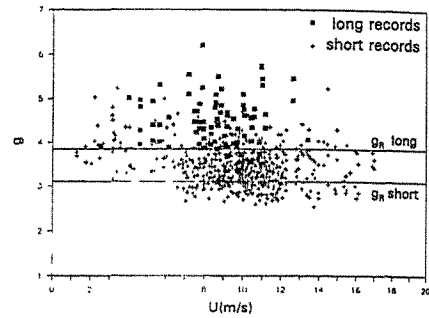
Figure 16 Peak factor versus mean wind speed

5. Conclusions

Natural frequencies and mode shapes of the Prospect tower are measured in full scale and agree well with a STRAND6 computer prediction. Mode one dominates the response of the tower at 1.08Hz whilst mode two represents vibration of the top mast on the tower alone. Damping is determined by large amplitude (5-170mg) free vibration decay and low amplitude (<5mg) autocorrelation analysis. Damping for the tower is around 1% critical damping for mode one. Both the along-wind and cross-wind response of the tower was found to increase in proportion to the square of mean wind speed. This is lower than the response expected from more conventional towers of similar height built from steel angle sections. An increase in tower response was found with increasing wind speed fluctuation and lateral turbulence.

References:
1. Bendat, J Piersol, A "Measurement and analysis of random data", J Wiley,New York,1966.
2 Hiramatsu, K Akagi, H "The response of latticed steel towers due to the action of wind", Journal of Wind Engineering and Industrial Aerodynamics, 30 (1988) 7-16.
3 Holmes, J.D. "Lattice towers-wind loads and dynamic response", Wind Engineering course notes,The Department of Mechanical Engineering Monash University, Ch8,1992.
4 Jeary, A.P. "Establishing non-linear damping characteristics of structures from non-stationary response time histories", The Structural Engineer,Volume 70/No.4/18 February 1992.
5 Standards Australia. AS1170.2-1989 "SAA loading code. Part2: Wind Loads", Standards Australia,North Sydney,1989.

Full-Scale Measurements of Vortex-Induced Vibrations

Hans Ruscheweyh, Thomas Galemann

Windengineering
Institute for Steel Construction
University of Technology Aachen (RWTH), Germany

Abstract: Vortex-induced vibrations have been measured on a full-scale experimental steel chimney, which has been erected on the test field of the Technical University Aachen, Germany. Within a three years test period meteorological data, pressure distribution on the circular cross section and the wind-induced vibrations have been measured. It could be verified that the prediction for the vortex-induced vibration calculated by the "correlation length model" as proposed in the Eurocode is in good agreement with the full-scale response.

1. Introduction

Vortex-induced vibrations are very important for the design of slender structures, like chimneys, TV-Towers, antenna masts, pylons, poles, guyed masts, cables, tubes etc. Many authors have reported about observations of such vibrations, but most of these reports do not present exactly measured values but only subjectively observed amplitudes. In most cases these "observations" overestimate the real amplitudes, sometimes by a factor of 10(!).

Carefully verified full-scale measurement have been reported by Ruscheweyh /1/ including several sources from literature.

These values have been compared with existing prediction methods. The full-scale data are close to the predicted values of the so called "correlation length model", presented by the first author in /2/ (see Fig. 7). Nevertheless most of the measured data belong to a relatively short observation time, i.e. only some days or weeks. Possibly the maximum vortex-induced amplitudes could have been not attained within this time.

Model tests do not satisfy the open question for full-scale response at all, because the full-scale Reynolds number cannot be realized in aeroelastic model tests for chimneys. Therefore long term full-scale measurements have been made by the authors with an experimental steel chimney of 28 m height, which has been erected on the test field of the University of Technology Aachen, Germany. Permanent measurements have been made over 3 years including three extreme wind storm events. Besides this measurements some other objects have been measured and compared with the prediction method.

2. The experimental chimney Aachen
2.1 General

The experimental chimney Aachen has been described by Galemann and Ruscheweyh in /3/ in detail. The main structural parameters and the site details will be repeated here (see Table 1).

The vibration could be measured by two independent measuring systems: First by accelerometers at the top of the chimney and second by strain gauges at the base of the cylindrical shaft. The pressure distribution on the cylinder circumference could be measured, too. The wind data are obtained by anemometers at levels of 10 m, 16 m, 22 m and 26 m

which are placed on a meteorological mast standing close to the chimney (see Fig. 1). All data were recorded by a computer which logges and processes the data.

height	h	28 m
diameter	d	0.91 m
natural frequency	n_e	1.7 Hz
equivalent mass	m	87 kg/m
log. decrement of damping	δ	0.012
critical wind speed	v_{crit}	9.0 m/s
Reynolds number at v_{crit}	Re	$5 \cdot 10^5$
Scruton number	Sc	2.1
Cylinder surface		painted
surrounding:		slightly hilly terrain with a free fetch in the prevailing wind direction (SW)

Table 1: Structural data of the experimental chimney

2.2 Cross-wind vibrations caused by vortex shedding

Since the critical wind speed is relatively low (v_{crit} = 9 m/s), the vortex resonance vibrations did occur very often. From pressure measurements the Strouhal number of the vortex shedding could be analysed, and the vibration amplitude had been taken from the calibrated strain gauge signals.

2.2.1 Strouhal number

By integrating the pressure distribution in lateral direction the time history of the lift coefficient c_L has been analysed. Regular vortex shedding exists only for few periods. These regular shedding is repeated more or less regular depending on the turbulence of wind and the locking-in effect of the vibrating stack. the Strouhal number variates in the range of 0.16 to 0.26 with a frequent value of

$$Str = 0.21$$

Figure 1: The experimental chimney and the site of location

A special situation should be discussed here: If the wind speed is nearly 50 % above the critical wind speed, three peaks in the power spectrum of the lift coefficient c_L are oberserved (see Fig. 2).

The right peak represents the Strouhal number of Str = 0.21, the peak at n = 1.7 Hz is produced by the vibration of the chimney (natural frequency of the first mode) and the left peak results from the interaction effect of the two frequencies described before. The interaction is explained in Fig. 3, where an artificial summation of the two frequencies n_1 = 2.6 Hz and n_2 = 1.72 Hz is generated. The summation produces a "new" frequency of n_3 = 0.87 Hz, which can be found in the spectrum of Fig. 2.

The three peaks in the spectrum of the existing force for the cross-wind vibration increases the band width of the vortex resonance response as shown in Fig. 4. There has been also observed a hysteresis effect depending on increasing or decreasing wind speed.
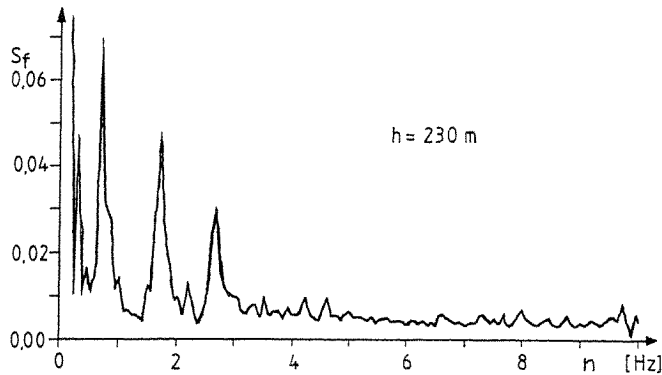
Figure 2: Power spectrum of the lift coefficient c_L

2.2.2. Vortex resonant amplitude

An example of the measured vortex resonant vibration is shown in Fig. 5. Within the observed period, the amplitudes have been rather stable. In most cases the amplitudes had been modulated. The reason for this modulation is the fact, that the regular vortex separation is disturbed by the variation of the wind direction, which shifts the separation line to another position /4/. During this shifting process the vortex shedding is disturbed and the exciting force is reduced respectively. After a short time the regular vortex separation starts again.

Figure 3: Generated time history of lift coefficient

The largest vibration amplitudes could be observed at rainy wether. If the rain stopped, the amplitudes decreased. This surprising observation could be explained with Cheung's diagram

375

/5/ in Fig. 6. He found out that the exciting force depends on the roughness Reynolds number, Re_k, where Re_k is defined with the roughness, k, of the cylinder surface:

$$Re_k = \frac{k \cdot v_{crit}}{v}$$

($v = 15 \cdot 10^{-6}$ m^2/s). At lower and higher values of Re_k the exciting force increases and this increase can be 300%.
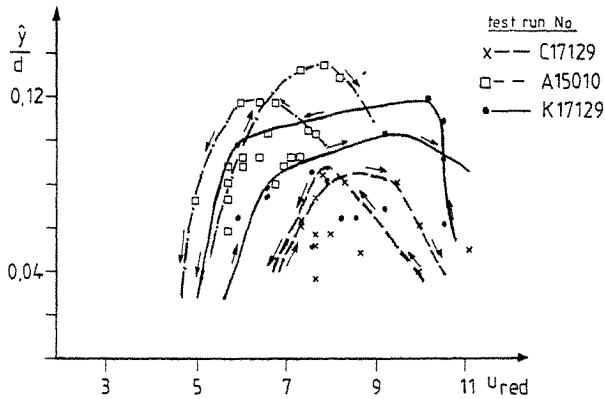
Figure 4: Vortex resonance curves for three measured cases
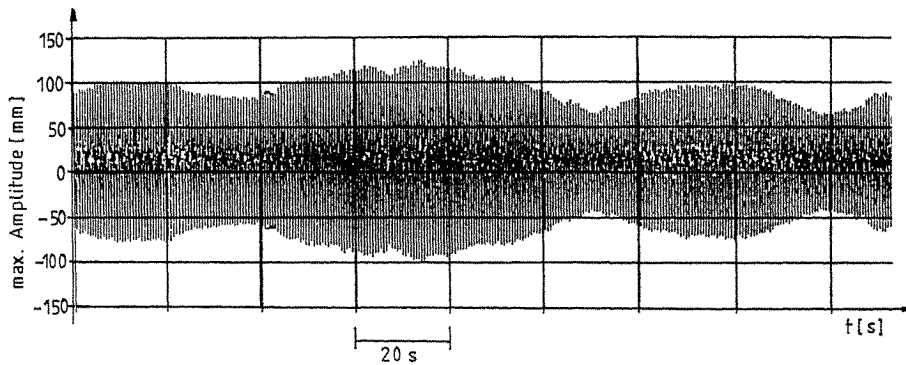
Figure 5: Example of vortex resonant vibration of the experimental chimney at critical wind speed

376
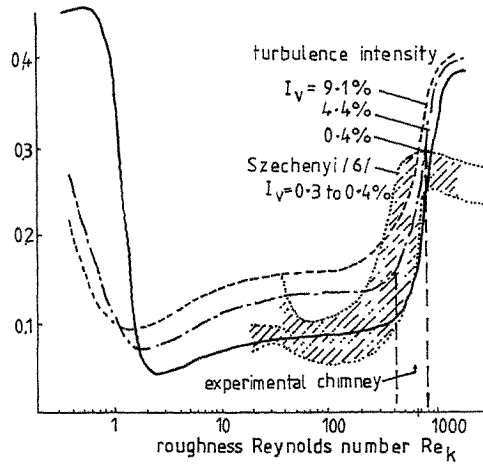
Figure 6: Exciting force coefficient versus roughness Reynolds number, Re_k /5,6/

The experimental chimney Aachen has a roughness Reynolds number of Re_k = 670 and is in the range of the lower level of the exciting force coefficient c_L. With rain many drops are shifted downwards the cylinder surface as could be observed on the chimney. The roughness is increased by this drops and the roughness Reynolds number is shifted into the range of higher exciting force coefficients. This is indicated in Fig. 6.

During a three years period of measurements between 1987 and 1990 the maximum vortex-induced vibration amplitude had been analysed. It is presented in Table 2 together with the predicted amplitude after the "correlation length model" /2/.

3. Comparison of prediction with full-scale measurements

A comparison of the predicted amplitudes for steel chimneys with full-scale measurements based on own measurements and on verified informations from literature and consulting work is shown in Fig. 7. The predicted values are close to the measured values and are always on the safe side.

The "correlation length model" /2/ has been applied to slender structures since more than 15 years and the experience is very good. The procedure has been included in German standards for steel chimneys and antenna masts as well as in the new European wind load code proposal.

	max y/d
measured	0.154
predicted	0.163

Table 2: Measured and predicted vortex resonant amplitude of the experimental chimney

377
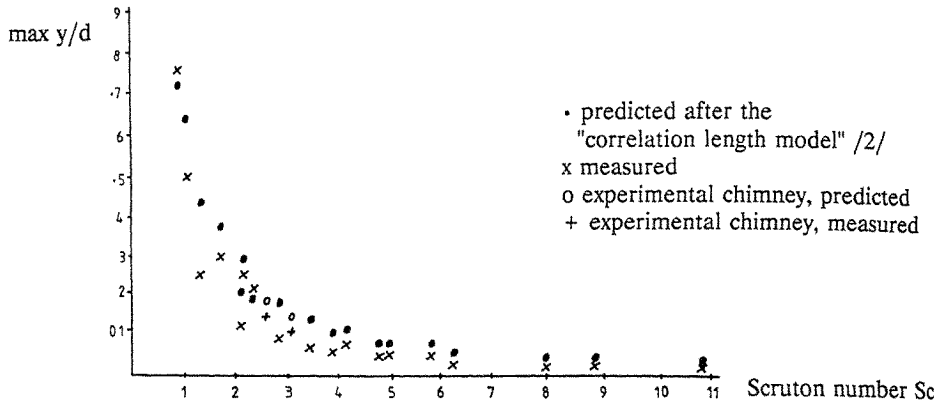
Figure 7: Comparison between predicted and measured cross wind amplitudes of steel stacks

4. References

/1/ Ruscheweyh H., Sedlacek, G.: Crosswind vibrations of steel stacks - Critical comparison between some recently proposed codes -, in: Proc. of the 7th Intern. Conf. on Wind Engineering, Aachen, Germany, J. of Wind Eng. and Industr. Aerodynamics, 30 (1988) 173-183

/2/ Ruscheweyh, H.: Vortex-excited vibrations, CISM-course "Wind-Excited Vibrations of Structures", Undine, Italy, 1992

/3/ Galemann, Th., Ruscheweyh, H:. Measurements of Wind-induced vibrations of full-scale steel chimney, J. of Wind Eng. and Industrial Aerodynamics, 41-44 (1992) 241-252

/4/ Ruscheweyh, H.: Wind Loading on the Television Tower, Hamburg. Symp. on Full-scale Measurements of Wind Effects on Tall Buildings and other Structures, Univ. of Western Ontario, Canada, 1974

/5/ Cheung C. K.: Effect of turbulence on the aerodynamics and response of a circular structure in wind flow, Ph.D. thesis 1983, Depart. of Mech. Eng., Monash University, Victoria, Australia

/6/ Szechenyi E., Loiseau H.: Unsteady lift forces on a vibrating cylinder placed in a supercritical flow. Rech. Aerosp. No. 1975-1, Jan, Febr., pp 45-57

378

ANALYTICAL DETERMINATION OF EQUIVALENT MODAL DAMPING RATIOS
OF A COMPOSITE TOWER IN WIND-INDUCED VIBRATIONS

B.C. Huang[+], A.Y.T. Leung, K.M. Lam and Y.K. Cheung

[+]Department of Engineering Mechanics,
Tongji University, Shanghai, China
Department of Civil and Structural Engineering,
The University of Hong Kong, Hong Kong

Abstract: We present two methods to determine the equivalent modal damping ratio of a composite tower under wind-induced vibrations.   The first method employs a detailed numerical integration procedure assuming Rayleigh damping and using the transfer matrix method.   The second method makes use of a simplified approximatin of two lumped masses. A numerical example is presented for a composite T.V. tower of a total height 459 m.

1. Introduction

Tall and slender towers are highly sensitive to dynamic responses under wind loads. Dynamic behaviors of the towers and their wind-induced responses are strongly influenced by the degree of damping.   Thus, it is important to determine a value of damping to reasonable confidence in the dynamic analysis of the wind-induced responses.   Damping under wind effects is composed of structural damping and aerodynamic damping.   In this paper, we attempt to analyze the structural damping of a composite tower which is made up of two different materials for the upper and lower parts.   A common example is a composite T.V. tower, in which the structure consists of two parts, namely a lower body of reinforced concrete and an upper aerial supporting the steel mast.

In the dynamic analysis of vibrations of tall and slender towers, the modal superposition method is widely used.   However for a composite tower, the damping behaviours of the upper and lower structures are different.   In order to apply the modal superposition method, equivalent modal damping ratios must be determined for the composite tower as a whole.   In this paper, we describe two methods for this determination, namely a detailed method and an approximate method.   The accuracy of the former method is good but numerical computation is required.   The latter method is simple and convenient to use and the accuracy is acceptable for practical engineering analysis.

2. Assumption of the Damping Matrix

A slender structure such as a T.V. tower, is usually modeled as a multi-degree-of-freedom system along the height in a dynamic analysis (Fig.1a). For the damping behaviors of a composite tower, our approach is firstly to build up damping matrices of the upper and the lower structure respectively; and then to assemble them to form the damping matrix of the whole structure. While the lower substructure can be analyzed quite independently, the upper substructure is under an elastic constraining action exerted by the lower substructure.   This can be represented by an elastic horizontal and rotation constraint supporting the upper substructure, as shown in Fig.1b.

Assume that the damping matrices [C] of the upper and the lower independent substructures are represented by Rayleigh's method.   They will be related to both the mass matrices [M] and the stiffness matrices [K] of their

own, as given by

$$[C]_U = a_U[M]_U + b_U[K]_U \qquad (1a)$$

$$[C]_L = a_L[M]_L + b_L[K]_L \qquad (1b)$$

where the subscripts U and L denote the upper and lower structures respectively. The stiffness matrices represent the condensed stiffness corresponding to each of the horizontal displacements. Parameters a_U, a_L, b_U, b_L are proportional factors, which are related to frequencies and the damping ratios of each independent substructure.

For the tower as a whole, the damping effect can thus be represented by a damping matrix which is the combination of the two damping matrices for the two substructures:

$$[C] = [C]_U + [C]_L \qquad (2)$$

It is generally agreed that structural damping is difficult to express and analyze exactly. There have been proposed a number of damping assumptions and expressions [1,2]. We choose to adopt Rayleigh damping in this paper because it is widely applied in engineering with a simple parameter of damping ratio and is convenient for mathematical treatment.

3. The Equation of Motion

For the structural model of the composite tower shown in Fig.1a, the equation of motion can be expressed by

$$[M]\{ \ddot{y} \} + [C]\{ \dot{y} \} + [K]\{ y \} = \{ F \} \qquad (3)$$

where [M] is the mass matrix of the whole structure system; [C] is the damping matrix in Eq (2); and [K] is the stiffness matrix after static condensation corresponding to the vector {y} of horizontal displacements. {F} is the vector of dynamic wind loading. It is obvious from Eq.(3) that the equation is coupled, which is caused by the damping matrix [C].

In our analysis, the stiffness matrices are developed by the transfer matrix principle, in which the structure is divided into connecting elements and each element is subjected to a horizontal and a rotation spring stiffness at its end (Fig.2).

There are many types of wind-induced vibration based on experimental observations and analytical data of T.V. tower structure. In this paper we mainly concentrate on the along-wind responses while the across-wind responses will be dealt with briefly.

4. Equivalent Modal Damping Ratio

The criteria for equivalent modal damping ratios can be either an equivalence of the maximum acceleration at a reference point near the top of the tower or an equivalence of the maximum base overturning moment. Namely the equivalent damping ratios ζ_{ej} can be obtained by equating these dynamic responses of the tower with damping ratios ζ_{ej} and those with practical damping ratios ζ_{Uj}, ζ_{Lj}. The damping matrix expressed by equivalent damping ratio ζ_{ej} is also of the form of Rayleigh damping. For the whole structure, the first two frequencies will be generally employed in the formulae of the proportional factors. The Newmark-βeta numerical integration method is used for computing the dynamic responses in this paper. Due to space limitation, we shall not present the details of computation here.

5. The Approximate Method

Let us imagine a simplified model of two degrees of freedom system shown in Fig.3 for the composite tower. The upper part represents steel and the lower part reinforced concrete structure. Assume that the circular frequency in the jth mode is ω_j, and the modal displacement A_{2j} of mass point 2 is unity.

So the modal displacement of mass point 1 is

$$A_{1j} = 1 - \alpha_{Uj}^2 \qquad (4)$$

where $\alpha_{Uj} = \omega_j / \omega_U$; $\omega_U = \sqrt{K_U / M_U}$

Assume that orthogonality condition applies to the damping matrix in obtaining the modal damping ratio. Therefore for the jth mode, the normal diagonal damping is given by

$$C_j^* = A_{1j}^2 C_L + (A_{1j}^2 - 2 A_{1j} + 1) C_U$$

By setting $2M_j^* \omega_j \zeta_{ej} = C_j^*$, and $C_L = 2M_L \omega_L \zeta_L$, $C_U = 2M_U \omega_U \zeta_U$, one may obtain the following expression:

$$\zeta_{ej} = \frac{1}{\alpha_{Uj} \beta_{Uj}} [A_{1j}^2 \alpha_L \beta_L \zeta_L + (A_{1j}^2 - 2A_{1j} + 1)\zeta_U] \qquad (5)$$

where $\omega_L^2 = K_L / M_L$, $\alpha_L = \omega_L / \omega_U$, $\beta_L = M_L / M_U$ and $\beta_{Uj} = M_j / M_U$. ζ_L and ζ_U represent damping ratios of the lower reinforced concrete part and the upper steel structure respectively.

The first two damping ratios may be obtained from Eq.(5). In practice, however, it is only possible to obtain the ideal first equivalent modal damping ratio in most cases. Fortunately only the first modal damping ratio is mainly used in engineering design. The second modal damping ratio can be confidently set to be equal to or slightly larger than the first. It is important that the parameters M_U and M_L will be comprehended as the generalized mass M_{U1} and M_{L1}. Similarly, K_U and K_L should be comprehended as the generalized stiffness of the first mode when determining damping ratio of the first mode, and calculating them in terms of the mean.

Note that the modal coordinates of the upper and the lower substructure should be decided appropriately when computing generalized mass M_{U1} and M_{L1}.

The top coordinate of the lower substructure and bottom of the upper should be equal to that of the whole structure at the same mass point. The modal shapes of the two substructures remain unaffected by each other.

6. Numerical Example

The example chosen is a composite T.V. tower, with a total height of 459 m (Fig.4a). The T.V. tower may be modeled as a system with 16 mass points, as shown in Fig.4b. The upper spheroid and the cabin are located at the 9th and 10th mass points respectively. The results of equivalent modal damping ratios ζ_{e1} for the first mode are as follows:

(1) Detailed procedure:

For along-wind responses the equivalent modal damping ratios obtained by equating the maximum acceleration at the 9th mass point and the maximum base overturning moment are shown in Table 1. Computation of damping ratios in the

across-wind direction have also been performed   Their values are listed in Table 1.   It is noted that the computation for across-wind responses is more complex.

It is observed that the values of equivalent damping ratios obtained with the criterion of equal accelerations are smaller than the corresponding values obtained with the criterion of equal base overturning moments for along-wind vibrations.   In the across-wind direction, the reverse is true.

ζ_{U1}	ζ_{L1}	Numerical integration procedure				Approximate method
		along-wind		across-wind		
		(a)	(b)	(a)	(b)	
	0.050	0.0308	0.0355	0.0306	0.0295	0.0311
	0.045	0.0263	0.0315	0.0275	0.0266	0.0280
0.01	0.040	0.0228	0.0274	0.0244	0.0236	0.0249
	0.035	0.0183	0.0233	0.0213	0.0206	0.0219
	0 030	0 0144	0.0193	0.0183	0.0177	0.0188

(a)   uses the criterion of equal maximum acceleration at the
      9th mass point,
(b)   uses the criterion of equal base overturning moment.

Table 1.   Equivalent modal damping ratios ζ_{e1}

(2) Approximate method:

From separate analysis, the circular frequencies of the tower and the substructures are $\omega_1=0.9312$, $\omega_2=1.6173$, $\omega_{L1}=0.9966$, $\omega_{L2}=3.9712$, $\omega_{U1}=1.5862$, $\omega_{U2}=3.8231$ rad/sec. The first modal shapes of the tower are sketched in Fig.5. $M_1=125.712$, $M_{L1}=167.695$, $M_{U1}=25.084$.   Substituting these values into Eq.(5) then leads to

$$\zeta_{e1} = 0.6135 \ \zeta_{L1} + 0.0404 \ \zeta_{U1}$$

The equivalent modal damping ratios ζ_{e1} of the first mode are also shown in Table 1.

For along-wind vibrations, values of equivalent damping ratios obtained by the approximate method lie somewhere between the values computed numerically for equal maximum acceleration and those for equal base overturning moment. In across-wind direction, the values from the approximate method are nearer to the computed values for equal acceleration.   The results of Table 1 indicate that the approximate method gives satisfactory estimates of the equivalent damping ratios.

References:
1.   R. W Clough and J. Penzien, "Dynamics of structures", Mcgraw-Hill Book Company(1975)
2.   Z. Liang and G. C. Lee, "Representation of Damping Matrix", J. Engrg. Mech. Div., ASCE, 5 (1991), 1005-1020.
3.   R.Vaicaitis, M. Shinozuka and M. Takeno,   "Response Analysis of Tall Building under wind loading", J. Struc. Div., ASCE, 101 (1975), 585-600.
4.   A. G. Davenport,   "The Application of Statistical Concepts to Wind Loading of Structures", Proc. Inst. of Civil Engrg., 19 (1961), 449-472.
5.   B. J. Vickery and A.W.Clark, "Lift or Across-wind Response of Tapered Stacks", J. Struc. Div., ASCE, 98 (1972), 1-20.
6.   M. B. Ahmad, P. K. Pande and P. Krishna, "Self-Supporting Tower under Wind Loads", J. Struc. Div., ASCE, 110 (1984), 370-384.
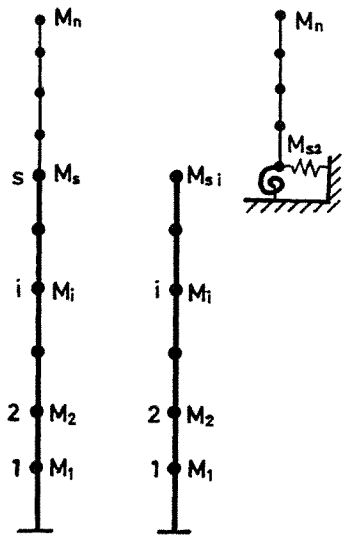
Fig. 1. MDOF model of a
composite tower
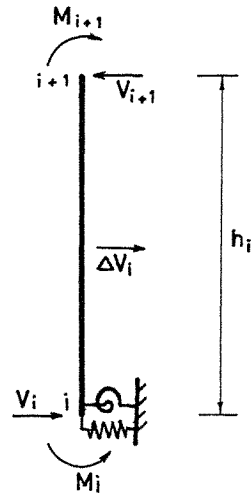
Fig. 2. Transfer matrix model
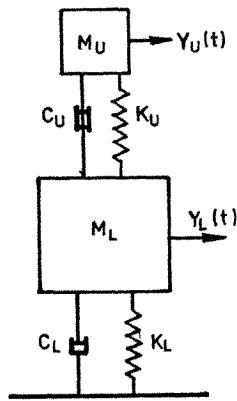
Fig. 3. Two DOF system
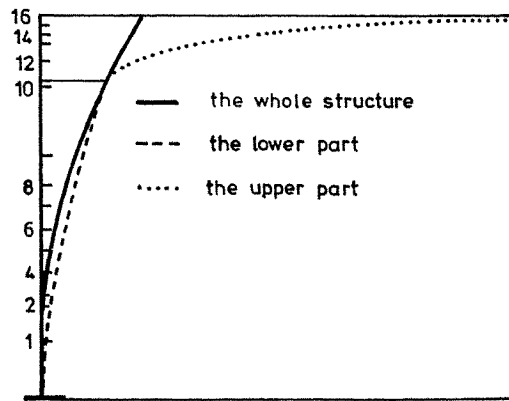
Fig. 5. First mode shape of the T.V. tower

383

459 0 M

848.5 M

272.5 M

93.0 M

16
15
14
13
12

11
10

9

8
7
6
5
4
3
2
1

steel

concrete

(a)   (b)
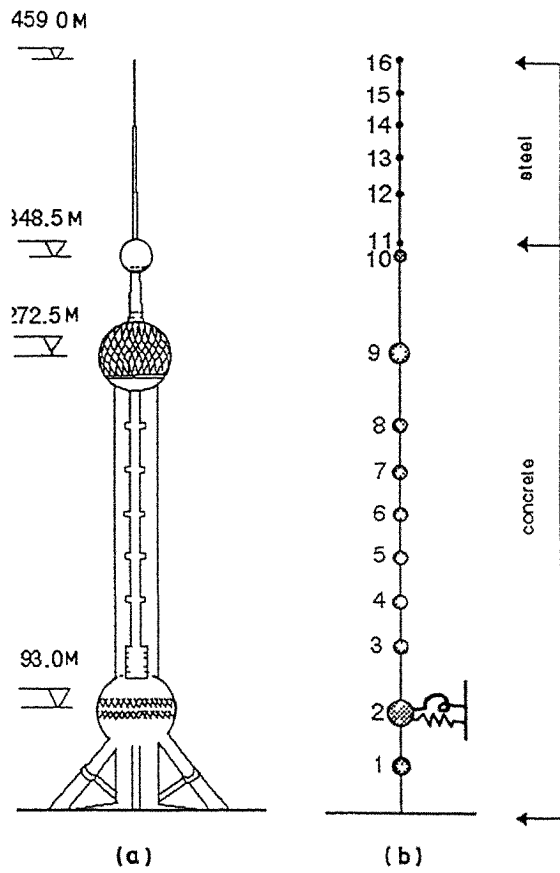
Fig. 4.   Example of a composite T.V. tower

EFFECTS OF SOIL-STRUCTURE INTERACTION AND CRACKING ON GUST FACTOR OF R.C. CHIMNEYS

Lakshmanan, N., Balakrishna Rao, S.V.S., and Venkateswarlu, B.

Structural Engineering Research Centre, Madras, India.

Abstract : A mathematical model for including base flexibility and effect of cracking to realistically estimate the natural frequencies of reinforced concrete chimneys has been proposed. A parametric study has been carried out to bring out the effects of soil-structure interaction, cracking and terrain conditions on the gust response factor of reinforced concrete chimneys. Based on the above study significant conclusions have been drawn on the gust response factor for reinforced concrete chimneys.

1. Introduction

Gust response factor method has been widely accepted by various international codes for predicting the dynamic response of wind sensitive structures. A recent study at the Structural Engineering Research Centre (SERC), Madras, using spectral method of analysis has revealed that (i) the first mode alone contributes significantly to the dynamic response, the second and higher modes providing less than 5% of the total, (ii) the variation of the gust response factor is insignificant with height, while it is considerable with terrain conditions, and (iii) the provisions of Bureau of Indian Standards IS-875 (Part-3) on Wind Loads for Buildings and Structures can be relied upon for evaluation of the gust response factor for chimneys in different terrain conditions [1].

2. Gust Response Factor Method for Chimneys

The along wind force F_z on a strip of area A_e at any height 'z' on the chimney is given by :

$$F_z = C_f A_e p_z G \tag{1}$$

where C_f is the along the wind force coefficient, p_z is the mean design wind pressure at height z, and G is the gust response factor which is the ratio of peak response to mean response under dynamic wind action. The gust response factor depends on the roughness factor r, the background factor B, the size reduction factor S, the gust energy factor E, and the damping factor β. IS:875 (part-3) gives the following expression for the gust response factor :

$$G = 1 + g_f r \left[B (1+\phi)^2 + \frac{SE}{\beta} \right]^{1/2} \tag{2}$$

where g_f is the peak factor and ϕ is a factor for including the secondary effects of turbulence. The values for B, $g_f r$, S and E are given in IS:875 (Part-3) in the form of charts. Based on the turbulence model recommended in ESDU for open country, the height of the chimney, the fundamental frequency of the chimney, the mean hourly wind speed at 10.0 m level, and the structural damping, Vickery has derived expressions for B, S, E and g_f [2]. These have been adopted as such in the CICIND model code. The Indian code on Chimneys IS:4998 has adopted the expressions for the above variables with certain modifications to account for different terrain conditions.

The ACI code (ACI-307) [3] recommends the following simple expression for G :

$$G = 1.30 + 7.0 \left[(u_{10} / f_1)^{0.47} / (H+5)^{0.86} \right] \qquad (3)$$

where u_{10}, f_1 and H are the hourly mean velocity at 10 m height, fundamental natural frequency and height of the structure respectively.

Vickery has shown that the values of G obtained using the above expression are within ± 5% of the values derived by him for open country terrain conditions [2].

3. Dynamic Flexural Rigidity of Reinforced Concrete Elements

Reinforced concrete structures are optimally designed when they are in the post-cracking stage. Based on the thirty two dynamic tests on the reinforced concrete beam type elements at various stages of preloading in the post cracking range, Lakshmanan et al., [4] have suggested the following formulae for the post-cracking stiffness of reinforced concrete beams.

$$EI = \frac{EI_r}{0.975 - (M_r/M)(z/d)(1-x/d)}, \qquad 0 \le \frac{M_r}{M} \le 0.65$$

$$= \frac{EI_r}{0.975 - 0.65(z/d)(1-x/d)}, \qquad 0.65 \le \frac{M_r}{M} \le 1.0$$

$$\le EI_D \qquad (4)$$

where EI is the effective flexural rigidity in the post-cracking stage, M_r is the cracking moment, EI_r is the flexural rigidity at a cracked section, EI_D is the uncracked dynamic flexural rigidity, M_r is the cracking moment, M is the maximum moment to which the section has been subjected to, d is the effective depth, z is the lever arm, and x is the depth to neutral axis. They have also evaluated the damping factor as 2% in the post-cracking stage. The cracked moment of inertia for an annular section

with uniformly distributed vertical steel and subjected to combined axial force and bending moment can be evaluated using the expressions available in standard reference books and codes [5].

4. Soil-Structure Interaction

With the assumption that (i) the chimney and the foundation are rigid, and (ii) the elasticity provided by the soil at the base can be idealised with a horizontal and a rotational spring, the equations of motion about the mass centre can be written as (Fig.1).
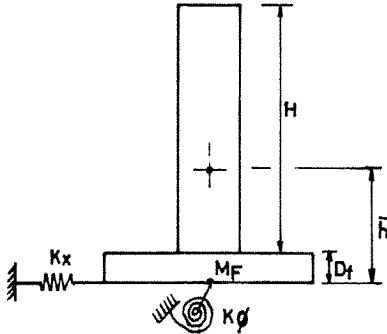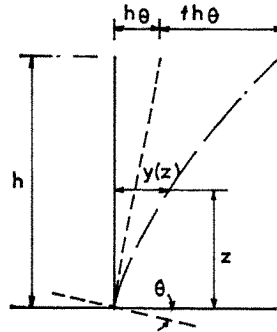
FIG.1 NOTATION FOR A   FIG. 2 DEFORMATION PROFILE OF A
      RIGID CHIMNEY STACK   CHIMNEY STACK

$$
\begin{bmatrix} M & 0 \\ 0 & I_g \end{bmatrix} \begin{Bmatrix} \ddot{x} \\ \ddot{\theta} \end{Bmatrix} + \begin{bmatrix} k_x & -k_x\bar{h} \\ -k_x\bar{h} & k_\phi+k_x\bar{h}^2 \end{bmatrix} \begin{Bmatrix} x \\ \theta \end{Bmatrix} = \begin{Bmatrix} F(t) \\ M(t) \end{Bmatrix} \tag{5}
$$

where M is the total mass of the structure equal to $M_s + M_f$, M_s is the mass of the shell of the chimney stack, M_f is the mass of the foundation, I_g is the mass moment of inertia of the structure about mass centre, k_x is the stiffness of the horizontal spring, k_ϕ is the stiffness of the rotational spring, $\bar{h}$ is the height of centre of mass of the structure above the base and x and ϕ are the horizontal displacement and rotation at the centre of mass, respectively. k_x and k_ϕ can be evaluated based on the elastic half space theory [6]. The fundamental frequency, ω_1 for the dynamic system given in equation (5) can be derived as :

$$
\omega_1^2 \simeq k_\phi \Big/ \left[I_o + M_s (D_f + H/2)^2 \right] \tag{6}
$$

387

where I_o is the sum of mass moments of inertia of the foundation and the shell about their own mass centres, D_f is the depth of the foundation and H is the height of the chimney. Equation (6) leads to the conclusion that for considering the effects of soil structure interaction the chimney can be modelled only with a rotational spring at the centre of elasticity of the base.

With the provision of a rotational spring at the base the translational displacement at any height 'z' can be written as :

$$Y(z) = z\theta + fh\theta [1 - \cos (\pi z/2h)] \qquad (7)$$

where h is equal to $H + D_f$, $fh\theta$ is the deformation at the top of the chimney due to flexure and $h\theta$ is the deformation at the top of the chimney due to base rotation (Fig.2). Using Rayleigh's method and deformation profile given in equation (7), the fundamental frequency of the chimney can be worked out as

$$\omega_n^2 = F_1 / F_2 \qquad (8)$$

where $F_1 = (3EI/h) \left[1 + \left\{ k_\phi h / (3EI f^2) \right\} \right]$

$F_2 = m_s h^3 \left[\left\{ 0.2268 + (0.537/f) \right\} / \left\{ I_B / (m_s h^3 f^2) \right\} \right]$

$m_s = (M_s /H)$, and $f = (k_\phi h/4EI)$.

In equation (8), I_B is the mass moment of inertia of the chimney and its foundation, EI is the effective flexural rigidity of the chimney and the factor 'f' can be termed as relative flexibility factor.

5. Illustrative Examples

Soil-structure interaction and cracking lead to reduced natural frequency for a chimney, which can be evaluated using equations (4) and (8). The reduced natural frequency leads to increased values for size reduction factor S, and gust energy factor E leading to increased values of gust response factors. A number of problems of chimneys have been solved for evaluating gust response factors using a basic wind speed of 50 m/sec and the provisions of IS:875 (Part-3) for two terrain conditions, namely terrain categories 2 and 4. Terrain category-2 corresponds to open country exposure, and hence the derived gust response factors are compared with equation (3) given by ACI 307 for similar terrain conditions. Two chimney geometries as given in Table-1 have been considered.

6. Conclusions

Based on the values of the gust factors tabulated in Table-2 the following conclusions can be derived :

(i) Even a flexurally rigid chimney (EI $\longrightarrow \infty$) can be dynamically sensitive when soil-structure interaction influences are considered as can be seen from problems 1(a), 1(b), 11(a) and 11(b) in Table-2.

(ii) The maximum deviation for the values of G derived using IS:875 (Part-3) provisions and ACI formula for terrain category-2 is less than 4% in all cases. Hence the charts given in IS:875 (Part-3) may be adequate for designing chimneys also.

(iii) The gust response factors for terrain category-4 are significantly higher than for open country exposure, the minimum increase being 20% (problems 12 and 15) and the maximum increase being 40% (problems 5 and 10).

(iv) The omission of soil-structure interaction leads to unsafe estimates of the gust response factor. An increase of 10% is realised for values of flexibility factor 'f' nearly equal to unity for terrain category-2 and 13% for terrain category-4. It appears that soil-structure interaction influences can be neglected if the value of 'f' is greater than 5. If an exact analysis is not carried out for soil-structure interaction the following expression may be used for design purposes.

$$G_f = G_o (1 + F), \text{ for } 1 < f < 5$$

where G_f is the gust response factor corresponding to a given flexibility factor f, G_o is the gust response factor with fixed base, and the value of F being taken as (0.15/f).

(v) Cracking has led to nearly 20% increase in values of G for both terrain categories. When cracking and soil-structure interaction influences are considered an increase of 22% is seen implying reduced role for soil-structure interaction as the value of 'f' is very much greater than 5.

7. Acknowledgement

References:

1. IS:875 (Part-3) - Wind Loads, Bureau of Indian Standards, 1987.

2. Vickery, B.J., National Seminar on Tall Reinforced Concrete Chimneys, New Delhi, 1985.

3. ACI committee 307, Standard Practice for the Design and Construction of cast in-place Reinforced Concrete Chimneys, (ACI-307-88), American Concrete Institute, Detroit, 1988.

4. Lakshmanan, N., etal, Journal of Structural Engineering, SERC, Vol.17, No.4, Jan., 1991.

5. IS:4998(PART-1)-1975, Criteria for Design of Reinforced Concrete Chimneys, part-1 : Design Criteria , Bureau of Indian Standards, 1975.

6. Richart, F.E., etal, Vibrations of Soils and Foundations, Prentice Hall , New Jersey, U.S.A, 1970.

Table 1 : GEOMETRIC PROPERTIES OF CHIMNEYS

Sl. No.	D_o (m)	D_i (m)	H (m)	D_f (m)	r_o (m)	M t sec^2/m	I_B tm sec^2 (x10^5)	Remarks
1.	9.25	8.50	90	1.50	7.0	418.75	10.25	Prob. 1 to 10
2.	18.50	17.50	195	2.00	12.50	2250.00	262	Prob. 11 to 17

Note: D_o – outside diameter of chimney; D_i – internal diameter of chimney; D_f – depth of foundation; r_o – effective radius of foundation; M – total mass of foundation-chimney system; and I_B – mass moment of inertia of foundation chimney system for rotation in "θ" direction (Fig.2).

Table 2 : RESULTS OF THE ANALYSIS FOR GUST RESPONSE FACTORS

Prob. No.	Terrain category	EI tm^2 x10^7	G tm^2 x10^4	f	f_n(Hz)	Gust Factor, G IS:875	ACI
1.a)	2	∞	4.0	0	1.23	–	1.96
b)	2	∞	1.0	0	0.62	–	2.20
2.	2	30.94			0.63	2.12	2.20
3.	2	30.94	4.0	4.2	0.565	2.15	2.24
4.	2	30.94	1.0	1.10	0.430	2.32	2.38
5.	2	7.73	4.0	17.75	0.305	2.53	2.57
6.	2	7.73	1.0	4.44	0.289	2.60	2.60
7.	4	30.94			0.630	2.90	–
8.	4	30.94	4.0	4.20	0.565	2.98	–
9.	4	30.94	1.0	1.10	0.430	3.22	–
10.	4	7.73	4.0	17.75	0.305	3.546	–
11.a)	2	∞	4.0	0	0.58	–	1.58
b)	2	∞	1.0	0	0.29	–	1.98
12.	2	343.8			0.278	1.96	2.00
13.	2	343.8	4.0	4.92	0.250	2.07	2.04
14.	2	343.8	1.0	1.23	0.20	2.14	2.12
15.	4	343.8			0.278	2.40	–
16.	4	343.8	4.0	4.92	0.25	2.53	–
17.	4	343.8	1.0	1.23	0.20	2.72	–

Note : $k_x = \left[32(1-\mu) \, G \, r_o \, / \, (7-8\mu) \right]$; $k_\phi = \left[8 \, G \, r_o^3 \, / \, 3(1-\mu) \right]$

where G = Shear modulus of the soil ,
 μ = Poisson's ratio of the soil = 0.40

Dynamic reliability of Wuhan T.V. Tower
under the action of wind load

Li Qiusheng   Cao Hong[+]   and Li Guiqing[+]

Department of Mechanical Engineering
Monash University, Australia
+Department of Civil Engineering
Wuhan University of Technology, China

Abstract: The scale transform method based on extreme distribution is used in the statitistics of wind pressures or velocities. The calculation method of dynamic reliability of structures and the estimation of dynamic reliabilty of Wuhan T.V. Tower considering the effect of wind direction and based on Poisson and Normal distribution are established in the paper.

1. Introduction

Wuhan T.V. Tower is a high–rise structure, the main load of which is wind load, hence, it is significant to study the dynamic reliability of this structure under the action of wind load. In general, the problems of such structures can be divided into two classes, one of which is the comfort requirement of residents and the other the safety of structures. Although the problem of residental comfort was studied by several authors[1], it has not been treated as dynamic reliability. This paper does not going to study this problem, and only studies structural safety. Although several calculation methods of dynamic reliability of high–rise structures have been proposed[2], comparisons are usually not given. The theoretical analysis and digital comparison of eight common methods for dynamic reliability of structures have been made, and some important conclusions are given in this paper.

2. Dynamic Reliability of Structures Subjected to Wind Load at One Time

As is well known, several calculation methods of dynamic reliability of structures have been proposed, the Poission process method and Vanmarcke's method are better among them. Since structural response under the action of wind load consists of static and dynamic components, so the safety bound is an unsymmetrical double bound. Because Vanmarcke's method is only suitable for a symmetrical double bound or a single bound, the modified Vanmarcke's method is proposed as follows:

$$P_s(\lambda_1, -\lambda_2) = \exp\left\{-\frac{\omega_2 T}{2\pi}\left[\exp(-\frac{\gamma_1^2}{2})\frac{1 - \exp(-\sqrt{\frac{\pi}{2}}q\gamma_1)}{1 - \exp(-\frac{\gamma_1^2}{2})} + \exp(-\frac{\gamma_2^2}{2})\frac{1 - \exp(-\sqrt{\frac{\pi}{2}}q\gamma_2)}{1 - \exp(-\frac{\gamma_2^2}{2})}\right]\right\} \quad (1)$$

in which T is the duration of dynamic response of a structure, and λ_1 and λ_2 are bound values:

$$\gamma_i = \frac{\lambda_i}{\sigma_x} \quad (i = 1,2), \quad \omega_2 = \frac{\sigma_{\dot{x}}}{\sigma_x}, \quad q = \sqrt{1 - \frac{\sigma_x^2}{\sigma_x \cdot \sigma_x}}$$

If it is assumed that the extreme values are independent of each other, and there are n extreme values of structural response in the range (0,T], then the distribution of the maximum value of these n extreme values is given by

$$F_{Z_m}(\lambda) = [F_{x_m}(\lambda)]^n = P\{Z_m \leqslant \lambda, 0 < t \leqslant T\} \quad (2)$$

in which $F_{x_m}(\lambda)$ and $F_{Z_m}(\lambda)$ are the probability distribution functions of the extreme value and the maximum extreme value, respectively.

It should be pointed out that $F_{Z_m}(\lambda)$ has three cases, the probability distribution function of maximum, minimum and absolute maximum value. In this paper, only the probability distribution of the absolute maximum value is discussed, but all formulas for this can be extended to the other cases.

When the probility distribution function of the maximum extreme value is given, the dynamic reliability of structures can be written as

$$F_s(\lambda, -\lambda) = F_{Z_m}(\lambda) = [F_{X_m}(\lambda)]^n \quad (3)$$

When only the absolute maximum values of structural response is considered, n can be determined by

$$n = \int_0^T \int_\lambda^0 \int_{-\infty}^0 x f_x(x,0,x) dx dx \quad (4)$$

The formula for the stationary response is

$$n = \sigma_x T / (\pi \sigma_{\dot{x}}) \quad (5a)$$

The number n determined by Eq.(5a) is the video frequency of velocity response of structures. Using it for determining the number of extreme values of displacement and acceleration response of structures brings some errors, so it is proposed to use the times of zero crossing estimates as the number of extreme values of structural response, that is, the duration, T, is divided by the video frequency, f_2, of structural response

392

$$n = T / f_2 \qquad (5b)$$

in which f_2 is as follows

$$f_2 = \sigma_{\dot{x}} / (\pi \sigma_x) \qquad (5c)$$

for structural displacement. Substituting Eq.(5c) into Eq.(5b) yields

$$n = \sigma_{\dot{x}} T / (\pi \sigma_x) \qquad (5d)$$

The number n determined by Eq.(5d) is the video frequency of displacement response of structures.

Eq.(5a) and Eq.(5d) give the same results for a single degree of freedom system subjected to a white–noise process, but differ for wind–resistant structures.

When $F_{x_m}(\lambda)$ is a Rayleigh distribution, that is

$$F_{x_m}(\lambda) = 1 - \exp(-\frac{\lambda^2}{2\sigma_x^2}) \qquad (6)$$

then

$$F_s(\lambda, -\lambda) = \left[1 - \exp(-\frac{\lambda^2}{2\sigma_x^2}) \right]^n \qquad (7)$$

The method based on Eq.(7) is called the Rayleigh distribution method.

When the probability distribution of extreme value of structures is a modified Gaussian distribution, then

$$F_{x_m}(\lambda) = \mathrm{erf}[\lambda / (\sqrt{2}\sigma_x)] \qquad \lambda > 0 \qquad (8)$$

in which erf( ) is the error function.

The method based on Eq.(8) is called the Normal Distribution Method.

The results of dynamic reliability of wind resistant structures obtained by use of Vanmarcke's method and Poisson process, Rayleigh, Normal, Extreme I distribution, Extreme II distribution method, the scale transform method based on extreme distribution and Monte Carlo method are listed in Table 1 and Table 2. The structural parameters adopted in the calculation are : natural frequency $f = 0.5$HZ, damping ratio $\zeta = 0.02$, mean wind velocity $V_{10} = 30$ m / sec., the gust spectrum is taken as Davenport's spectrum [2], $\sigma_x = 0.098465$, $\sigma_{\dot{x}} = 0.624144$, $\sigma_{\ddot{x}} = 4.077119$.

It can be seen from Table 1 that when the bound value is not high ($\lambda < 1.5$) the results of dynamic reliability determined by Rayleigh method decreased more quickly than those determined by Poisson process method, and the results determined by Vanmarcke's method are close to those obtained by the Monte Carlo method. When the bound value is high ($\lambda > 3$), the results of dynamic reliability found by the Normal distribution method are close to those found by the Monte Carlo method. A lot of cal-

culation for the other parameters of structures are made, which show that the results found by normal distribution method are close to those found by the Monte Carlo method. It can be shown that the results adopting a double bound are almost equal to those adopting a single bound.

3. Dynamic Reliability of Wind Resistant Structures in Lifetime

Following the assumptions in Ref[2], the dynamic reliability of structures within N years is

$$P_s(N) = [P_{si}(1)]^N \tag{9}$$

where $P_{si}(1)$ is annual dynamic reliability of structures at direction i:

$$P_{si}(1) = \int_0^\infty P(S_i < R_i | V_i = V_{i0}) f(V_{i0}) dV_{i0} \tag{10}$$

in which f( ) is the probability density function of the maximum annual mean wind velocity at standard height at direction i.

As is well known, the structural displacement under the action of wind load consists of two parts, static and dynamic displacement, S_s and S_d, so the safety bounds of dynamic response of the structure can be written as

$$\lambda_1 = R - S_s, \quad -\lambda_2 = -R - S_s \tag{11}$$

In order to simplify the calculation, it is assumed that the dynamic response of the structure obeys Normal distribution, and comparing the probability of exceeding the safty bound, λ_1, the probability of exceeding the safety bound, $-\lambda_2$, can be neglected. In this case, the conditional reliability of the structure under the action of mean wind and gust velocity is given by

$$P_s(\lambda_1, -\infty) = [1 - \text{erf}(\lambda_1 / \sigma_x)]^n , \quad n = \sigma_{\dot{x}} T / (\pi \sigma_x) \tag{12}$$

4. Dynamic Reliability of Wuhan T.V. Tower

Wuhan T.V. Tower is the first reinforced concrete tower designed by China, its height is 221.2m, which consists of tower base, tower body, tower building and wireless mast (Fig.1). The main structure of Wuhan T.V. Tower is a reinforced concrete cone shell, with the diameter of the cone varying linearly along the height. Its external base section diameter is 16m, and that of the top section is 3.9m, with terraces at several heights. In analysis of free vibrations of the tower, the terraces are treated as lumped masses, and the whole tower is treated as a varying cross section bar with variably distributed masses and several lumped masses.

It is assumed that the annual maximum mean wind velocity obeys the extreme distribution of a new variable, t, that is, let

394

$$t = a_1 + a_2 V + a_3 \lg(v - b) \tag{13}$$

and

$$F(t) = \exp[-\exp(-t)] \tag{14}$$

in which a_1, a_2, a_3 determined by the least square method. This method is called the scale transform method based on extreme distribution. According to the data of wind velocity in the region of Wuhan, the parameters are found as follows

$$a_1 = 18.5530, \quad a_2 = 1.7040, \quad a_3 = -36.9236.$$

The main wind direction in the region of Wuhan is NNE-NE, its parameters found by the method mentioned above are as follows

$$a_1 = 18.5530, \quad a_2 = 1.7040, \quad a_3 = -36.9236.$$

The wind velocity profile is taken as $V(x) = V_{10}(x / 10)^\alpha$ in which $\alpha = 0.16$, the air mass density is taken as 0.12676, the safety bound is considered as H / 500; H is the height of the Tower, Davenport's gust spectrum is adopted in analysis and the coefficient of ground roughness, K, is 0.003; the calculated results are shown in Fig.2. When N < 10 years, the results obtained by the Normal distribution method are almost equal to that obtained by the Monte Carlo method. When N = 100, the difference between them is less than 10 per cent.

5. Conclusion

The following important conclusions are made by means of theoretical analysis and a lot of calculation:

(1) The results of dynamic reliability of a structure found from a single safety bound are almost the same as those found from a double safety bound;

(2) The application scope of Vanmarke's method is extended by the method of this paper.

(3) The Normal method is the best for analysis of dynamic reliability of wind-resistant structures.

(4) The number of extreme points of displacement response in the analysis of dynamic reliability of wind-resistant structures should be estimated by the video frequency of displacement response.

(5) The dynamic reliability of Wuhan T.V. tower is high enough.

References

1. Melbourne, W.H. and Cheung, J.C.K, Designing for Serviceable Accelerations in Tall Buildings, 4th Int. Conf. on Tall Buildings, Hong Kong and Shanghai, (1988)148.
2. Li Guiqing, Structural Reliability, Press of Wuhan University of Technology, (1989)197

Method 1	2	3	4	5	6	7	8
Bound $\gamma = \lambda / \sigma_x = 1.5$							
.929779	.848057	.913943	.819334	.810641	.796286	.837607	.908725
.864489	.719201	.835292	.671308	.657139	.634071	.701585	.825781
.803783	.609924	.763409	.550025	.532704	.504902	.587653	.750407
.747341	.517250	.697713	.450654	.431382	.402046	.492222	.681913
.694861	.438658	.637670	.369236	.350060	.320144	.412288	.619672
.646067	.372007	.582794	.302528	.283773	.254926	.345336	.563111
.000700	.315483	.532640	.247871	.230038	.202994	.289256	.511713
.558518	.267548	.486803	.203089	.186478	.161641	.242282	.465006
.519298	.226896	.444910	.106398	.151107	.128712	.202937	.422562
.482832	.192421	.406622	.136336	.122542	.102492	.169982	.383993
Bound $\gamma = \lambda / \sigma_x = 3.0$							
.998629	.994876	.996576	.994345	.987621	.989961	.978151	.999018
.997359	.988785	.993163	.988722	.975395	.980022	.950779	.998037
.995891	.983224	.989762	.983131	.963321	.970183	.935875	.997057
.994525	.977695	.986372	.977572	.951396	.960443	.915427	.996079
.993161	.972197	.982995	.972043	.939619	.950801	.805426	.995101
.991799	.966730	.979628	.966547	.927388	.941256	.875862	.994124
.990439	.961293	.976274	.961031	.926500	.931806	.856725	.993147
.989081	.955387	.972930	.955046	.905155	.922451	.838007	.992172
.987724	.950512	.969599	.950242	.893950	.913190	.819697	.991198
.986670	.945167	.966278	.944869	.882884	.904023	.801788	.990225
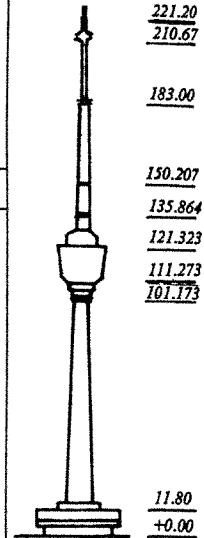
Table 1. Dynamic reliability of structures

Note: 1—Normal, 2—poisson, 3—Vanmarcke, 4—Rayleigh, 5—Scale transform method, 6—Extreme I , 7—Extreme II , 8—Monte Carlo method

Fig. 1. Wuhan T.V. Tower

Method		The Duration of Structural Response			
		1 s.	2 s.	3 s.	4 s.
P	S	0.848057	0.719201	0.609924	0.517250
	D	0.848057	0.719201	0.609923	0.517249
V	S	0.901658	0.812987	0.733037	0.660949
	D	0.901658	0.812987	0.733037	0.660948
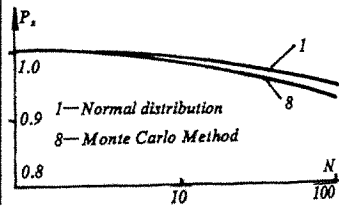
Table 2. Comparison of structural reliability between double and single bound

Note: P—Poisson, V—Vanmarcke, S—Single, D—Double

Fig. 2 The Dynamic Reliability Wuhan T.V. Tower

An analysis of galloping oscillation for the mast
of the central TV transmission tower

Liang Shuguo, Le Junwang[+] and Qu Weilian[++]

Department of Civil Engineering, Wuhan University
of Hydraulic and Electric Engineering, Wuhan, China
[+]The Design Institute, the Ministry
of Broadcast Film and TV, Beijing, China
[++]Department of Civil Engineering, Wuhan
University of Technology, Wuhan, China

Abstract: The critical wind velocities and responses of galloping oscillations are analysed for the mast which is 130m in height at the top of the central TV transmission tower in this paper. The dynamic characters of the tower are calculated by finite element method, and the nonliner differential equation of galloping oscillations are solved by the method of Bogoliubov and krylov. The calculated result shows that the danger of galloping oscillations for the central TV transmission tower is very small.

1. Introduction

The central TV transmission tower which has been built recently is 405m in height. The main part of the tower is of R. C. structure. There is a mast which is 130m high at the top of the tower. The mast is divided into five sections. The lower two sections are made of reinforced concrete, and the upper three sections are made of steel. The sections of the mast are square. Since a mast with square sections may gallop under the actions of strong wind, it is necessary to analyse its onset wind velocity and responses of galloping oscillations. In this paper, the structure of the central TV transmission tower is simplified as a ladderlike cantilever bar whose mass is concentrated on 22 points along its height, and the natural frequencies, mode shapes and reduced damping ratioes of the tower for bending vibration are obtained by the finite-element computer program. In the light of quasi-steady approach, the galloping oscillations of the central TV transmission tower under the actions of perpendicular incident flow to a side face of the mast is considered as a kind of nonliner vibration that a liner structure is excited by liner and nonliner aerodynamic damping force. By solving the non-liner differential equation, the critial wind velocity at which galloping oscillations take place and the critical wind velocities at which the amplitudes of galloping oscillations jump up or down are obtained, and the response curve of galloping oscillations of the tower is described.

2. The Calcaclation of the Structural Dynamic characteres of the Central TV Transmission Tower

(1)The Structural Model of the Tower

The total mass of the central TV transmission tower is about 49633 ton, and 12550 ton of which is on the ground or under the ground. By using a structural model of muti-degrees-of-freedom, the structure of the tower above the ground can be simplified as a ladderlike cantilever bar which is divided into 22 sections with equal stiffness and whose mass is concentrated on 22 points at the top of each section. The mass distribution and structural model of the tower can be seen in Fig. 1 and Fig. 2.

(2)The Calculation of the Bending Natural Frequencies and Mode Shapes of the Tower

The rotational freedoms of the bending vibration of the tower structure can be eliminated by the

process of static condensation[2]. When the loads on every mass lump are only horizontal, the relationship of stiffness matrix, displacement vector and load vecter is as follows

$$\begin{bmatrix} [K_{11}]_{22 \times 22} & [K_{12}]_{22 \times 22} \\ [K_{21}]_{22 \times 22} & [K_{22}]_{22 \times 22} \end{bmatrix} \left\{ \begin{matrix} \{\theta\}_{22 \times 1} \\ \{A\}_{22 \times 1} \end{matrix} \right\}$$
$$= \left\{ \begin{matrix} \{o\}_{22 \times 1} \\ \{P\}_{22 \times 1} \end{matrix} \right\} \qquad (1)$$

in which, $[K_{11}]$ is the stiffness matrix of angular displacement, and $[K_{22}]$ is the stiffness matrix of horizontal displacement. $[K_{12}]$ and $[K_{21}]$ are cross-stiffness matrix of $[K_{11}]$ and $[K_{22}]$. It is obvious that

$$[K_{21}]_{22 \times 22} = [K_{12}]_{22 \times 22}^T \qquad (2)$$

Eq. 1 can be rewritten as following two group of equations

▽ 386.50
▽ 322.00
▽ 256.50
▽ 200.00
▽ 130.00
▽ 60.00
▽ 0.00
△ -21.00

3. R. C. tower body

1. Steel mast
2. R. C. mast

Fig. 1. The mass distribution

Fig. 2. Structural model

$$[K_{11}]\{\theta\} + [K_{12}]\{A\} = \{o\} \qquad (3)$$
$$[K_{21}]\{\theta\} + [K_{22}]\{A\} = \{P\} \qquad (4)$$

The relationship of angular displacement vector and horizontal displacement vector can be obtained by Eq. 3

$$\{\theta\} = -[K_{11}]^{-1}[K_{12}]\{A\} \qquad (5)$$

Substituting Eg. 5 into Eq. 4 provides

$$[S]\{A\} = \{P\} \qquad (6)$$

in which

$$[S] = [K_{22}] - [K_{21}][K_{11}]^{-1}[K_{12}] \qquad (7)$$

When the structure vibrates freely, the horizontal loads are inertial force of every mass lump. Then

$$[S]\{A\} = \omega^2[M]\{A\} \qquad (8)$$

in which ω is natural circular frequency, and $[m]$ is lumped mass matrix. Rewritting Eq. 8 as

$$[D]\{A\} = \lambda\{A\} \qquad (9)$$

In which $[D] = [m]^{-1}[s]$ and $\lambda = \omega^2$. Then, the characteristic value λ_k and vector $\{A\}_k (k = 1, 2, \ldots 22)$ of $[D]$ can be obtained by computer program. The natural period T_k and unitized mode shape vector $\{\overline{A}\}_k$ of kth mode of the tower structure are expressed as

$$\left. \begin{matrix} T_k = 2\pi / \sqrt{\lambda_k} \\ \{\overline{A}\}_k = \{A\}_k / A_{22} \end{matrix} \right\} (10)$$

The natural fretuencies and mode shape curves of the first five modes of the tower for bending vibration are tabulated and described in Table 1 and Fig. 3.

(3) The structural reduced damping ratioes

Table 1. The natural period of the first five modes
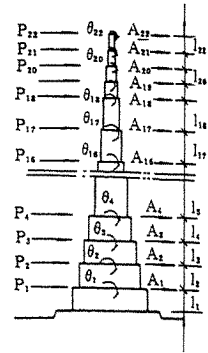
Mode	Period(s)
1	8.1232
2	3.4909
3	2.0361
4	1.0344
5	0.7536

(1)　(2)　(3)　(4)　(5)
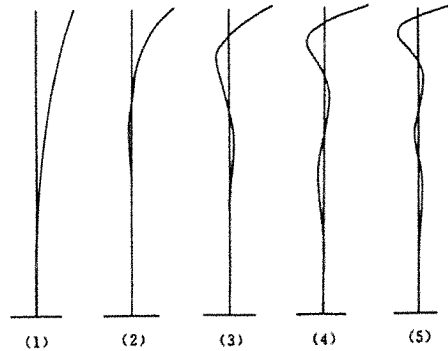
Fig. 3. The first five mode shapes

of lower modes of the tower.

As the upper section and the lower section of the tower are made of different materials, the reduced damping ratioes of the tower structure should be analysed in the light of complex-damping theory. The damping parameter of kth mode can be calculated by following equation

$$\gamma_k = \frac{\gamma_{kL}\{\varphi\}_k^T[K]_L\{\varphi\}_k + \gamma_{kU}\{\varphi\}_k^T[K]_U\{\varphi\}_k}{\{\varphi\}_k^T[K]\{\varphi\}_k} \tag{11}$$

in which $\{\varphi\}_k$ is a unitized mode shape vector which contains angular and horizontal displacements of each joint, and its order is 44×1, i. e.

$$\{\varphi\}_k^T = \{\vartheta_1,\overline{A}_1,\cdots\cdots\vartheta_{22},\overline{A}_{22}\}^T \tag{12}$$

ϑ_i in Eq. 17 can be obtained from

$$\{\vartheta\}_k = -[K_{11}]^{-1}[K_{12}]\{\overline{A}\}_k \tag{13}$$

The order of $[K]$ is 44×44, and its element K_{ij} is the sum of the shear forces or bending moments of the section ends at joint i induced by the unit horizontal or angular displacement at joint j. $[K]_L$ and $[K]_U$ are the stiffness matrixes for the lower R. C. structure and for the upper steel structure respectively

$$[K]_L = \begin{bmatrix} [K]_{ll} & [o] \\ [o] & [o] \end{bmatrix}_{44\times44} \tag{14}$$

$$[K]_U = \begin{bmatrix} [o] & [o] \\ [o] & [K]_{uu} \end{bmatrix}_{44\times44} \tag{15}$$

in which, the order of $[K]_{ll}$ is 32×32, and the order of $[K]_{uu}$ is 14×14. The relationship of $[K]$ and $[K]_L$, $[K]_U$ is

$$[K]_L + [K]_U = [K] \tag{16}$$

In the light of complex-damping theory, the damping parameter γ or damping rato ξ for each mode of a structure made of the same material can be assumed to be the same. For every mode, that provides

$$\gamma_k = \gamma = 2\xi \quad (k = 1,2,\cdots\cdots22) \tag{17}$$

By assuming that the damping ratioes of the upper steel mast and the lower structure equal 0. 01 and 0. 05 respectively, the damping paramenters for every mode of the upper steel mast and the lower structure are as follows respectively

$$\left.\begin{array}{l} \gamma_{kL} = \gamma_L = 0.1 \\ \gamma_{kU} = \gamma_U = 0.02 \end{array}\right\} \tag{18}$$

By Eq. 11 ~ 18, the reduced damping ratioes for the first five modes of the tower are tabulated is Table 2.

Mode	Damping ratio
1	0. 0499
2	0. 0347
3	0. 0390
4	0. 0424
5	0. 0350

Table 2. Reduced damping ratioes of the tower
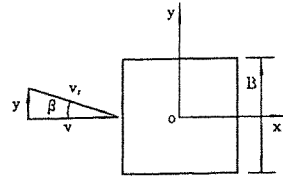
Fig. 4. The galloping oscillations of the mast in wind flow

3. An anslysis of the Critical Wind Velocities and Responses of Galloping Oscillations for the Central TV Transmission Tower

Usually, when wind flow is normal to a side face of a square structure, the probabilhty that the structure gallops in across-wind direction is greater. In the light of quasi-steady approach, the differential equation of galloping oscillations in across-wind direction for the central TV transmission tower is

$$[M]\{\ddot{Y}\} + [C]\{\dot{Y}\} + [S]\{Y\} = \{F\} \tag{19}$$

in thich $[C]$ is the damping matrix of the structure. $\{Y\}$ and $\{F\}$ are horizontal displacement vector and galloping force vector in across wind direction, and their orders are 22×1. The expression of element

399

F_i in $\{F\}$ is

$$F_i = \frac{1}{2}\rho C_y(z_i)B_i\Delta H_i v^2(z_i) \qquad (20)$$

ρ is the density of air mass, $C_y(z_i)$, B_i and $v(z_i)$ are the lateral force coefficient, the width of windward and wind speed at height z_i. H_i is the reduced length of the ith mass lump. Obviously, galloping force $F_1 \sim F_{11}$ for the main part of the tower equal zero as $C_y=0$ for round cross-section. The C_y for the mast can be expressed as a power series of incidence β.

$$C_y(\beta) = \sum_{j=1}^{n} b_j \beta^j \qquad (21)$$

According to the date from wind tunnel test, the C_y for squre section can be expressed as an odd function of β[1]:

$$C_y(\beta) = 2.69\beta - 168\beta^3 + 6270\beta^5 - 59900\beta^7 \qquad (22)$$

Considering that β is a small quantity and the effect of fluctuating wind on galloping oscilltions can be neglected, provides

$$\left. \begin{array}{l} \beta = \dfrac{y}{v} \\[2mm] v(z_i) = S(z_i)\bar{v}_{10} \end{array} \right\} \qquad (23)$$

$S(z_i) = (z_i/10)^\alpha$, α is a parameter corresponding to the surface roughness, $\bar{v}_{10}$ is mean wind speed at 10m height. Then, Eq. 20 can be rewritten as

$$F_i = \frac{1}{2}\rho B_i \Delta H_i \sum_{j=1}^{7} b_j y^j [S(z_i)]^{2-j} \bar{v}_{10}^{2-j} \qquad (j = 1,3,5,7) \qquad (24)$$

According to mode-superposition method, displacement y can be expressed as

$$y_i(z_i,t) = \sum_{k=1}^{22} \bar{A}_k(z_i)q_k(t) \qquad (25)$$

Substitutiong Eq. 25 into Eq. 19 and utilizing the orthogonality relationship of modes, the differential equation of kth mode for galloping oscillation is as follows

$$\ddot{q}_k + 2\xi_k\omega_k q_k + \omega_k^2 q_k = \frac{1}{M_k^*}\sum_{j=1}^{7} R_j q_k^j \qquad (j = 1,3,5,7) \qquad (26)$$

in which,

$$\left. \begin{array}{l} M_k^* = \displaystyle\sum_{i=1}^{22} m_i \bar{A}_k^2(z_i) \\[3mm] R_j = \dfrac{1}{2}\rho \bar{v}_{10}^{2-j} b_j \displaystyle\sum_{i=12}^{22} B_i \Delta H_i [\bar{A}_k(z_i)]^{j+1}[S(z_i)]^{2-j} \end{array} \right\} \qquad (27)$$

By using the method of Bogoliubov and Krylov, the solution of Eq. 26 is assumed to be of the form

$$\left. \begin{array}{l} q_k = a(t)\cos[\omega_k t + \theta(t)] = a\cos\varphi \\[2mm] \dot{q}_k = -a(t)\omega_k\sin[\omega_k t + \theta(t)] = -a\omega_k\sin\varphi \end{array} \right\} \qquad (28)$$

in which a and θ are considered to be a slowly varying function of time, and $\dot{a}$, θ are small quantities. It is convenient to obtain a and θ by calculating their mean values in a period of vibration. This provides

$$\dot{a} \approx \frac{1}{2\pi}\int_0^{2\pi} a d\varphi \qquad (29)$$

$$\theta \approx \frac{1}{2\pi}\int_0^{2\pi} \theta d\varphi \qquad (30)$$

Substituting Eq. 28 into Eq. 26 provides the expressions of $\dot{a}$ and θ, and by Eq. 30 it is obtained that $\theta = 0$. When $\dot{a}=0$, stead response of galloping oscillations exist. Calculating Eq. 29 and letting $\dot{a}=0$ yields

$$\frac{35}{64}R_7 a^6 \omega_k^6 + \frac{5}{8}R_5 a^4 \omega_k^4 + \frac{3}{4}R_3 a^2 \omega_k^2 + (R_1 - 2M_k^*\xi_k\omega_k) = 0 \qquad (31)$$

When galloping oscillations take place, the attack angle $\beta \to 0$. By neglecting the higher order terms of q_k^j in Eq. 26, galloping oscillations occur on condition that the coeffecient of q_k in Eq. 26 is equal to or less

than zero, i. e.

$$2M_k^* \xi_k \omega_k - R_1 \leqslant 0 \tag{32}$$

This gives the expression of onset wind velocity for galloping oscillations of kth mode

$$V_{10k}^c = \frac{4\xi_k \omega_k \sum_{i=1}^{22} m_i \overline{A}_k^2(z_i)}{\rho b_1 \sum_{i=12}^{22} B(z_i)\Delta H_i S(z_i)\overline{A}_k^2(z_i)} \tag{33}$$

Let $\rho = 1.227$ kg/m^3, $b_1 = 2.69$, and $\alpha = 0.16$. The onset wind velocities for the galloping oscillations of the first five modes of the tower are tabulated in Table 3.

Mode	1	2	3	4	5
$\overline{V}_{10}^c$(m/s)	367.57	69.18	307.30	653.70	428.73

Table 3. The onset wind velocities for galloping oscillations of the central TV transmission tower.

Knowing form Table 3, the probability of galloping oscillations for the mast of the central TV transmission tower is very small. The galloping oscillations for each mode can not occur except for the second mode on condition that the tower is under the action of extremely strong wind.

Analysing the response for the second mode of galloping oscillations, when wind relocity $\overline{v}_{10} = 69.18$ m/s, a = 0. When wind velocity exceeds this critical value, the solution for Eq. 31 is

$$\alpha = \frac{\sqrt{2}}{\omega_2}\left\{\sqrt{\sqrt[3]{\frac{4}{35R_7}}\left[2\xi_2 M_2^* \omega_2 - E + \sqrt{(2\xi_2 M_2^* \omega_2 - E)^2 - F^2}\right]^{1/3}} + \right.$$
$$\left. + \left[2\xi_2 M_2^* \omega_2 - E - \sqrt{(2\xi_2 M_2^* \omega_2 - E)^2 - F^2}\right]^{1/3} - \frac{4R_5}{21R_7}\right\}^{1/2} \tag{34}$$

in which

$$\left. \begin{array}{l} E = R_1 + \dfrac{10R_5}{35R_7}\left(\dfrac{40R_5^2}{189R_7} - R_3\right) \\[3mm] F = \sqrt{\dfrac{4}{35R_7}\left(\dfrac{20R_5^2}{63R_7} - R_3\right)^3} \end{array} \right\} \tag{35}$$

Let

$$d = (2\xi_2 M_2^* \omega_2 - E)^2 - F^2 \tag{36}$$

be the discriminant of Eq. 31. When $d = 0$, Eq. 31 has a single and a double real solution, and the amplitude of galloping oscillations abruptly jumps at the critical wind velocties determied by the equation that $d = 0$. This gives

$$V_{10}^{c1} = \frac{4\xi_2 M_2^* \omega_2}{\rho\left[Q + \dfrac{10Q_5}{35Q_7}\left(\dfrac{40Q_5^2}{189Q_7} - Q_3\right) + \sqrt{\dfrac{4}{35Q_7}\left(\dfrac{20Q_5^2}{63Q_7} - Q_3\right)^3}\right]} \tag{37}$$

$$V_{10}^{c2} = \frac{4\xi_2 M_2^* \omega_2}{\rho\left[Q_1 + \dfrac{10Q_5}{35Q_7}\left(\dfrac{40Q_5^2}{189Q_7} - Q_3\right) - \sqrt{\dfrac{4}{35Q_7}\left(\dfrac{20Q_5^2}{63Q_7} - Q_3\right)^3}\right]} \tag{38}$$

in which

$$Q_j = \sum_{i=12}^{22} b_j B_i \Delta H_i [\overline{A}(z_i)]^{j+1}[S(z_i)]^{2-j} \tag{39}$$

When wind velocity $\overline{v}_{10}$ is greater than $\overline{v}_{10}^c$ and less than $\overline{v}_{10}^{c1}$, or greater than $\overline{v}_{10}^{c2}$, the discriminant d > 0. In these cases, Eq. 31 has a single real solution whose expression is Eq. 34. When wind velocity $\overline{v}_{10}$ is greater than $\overline{v}_{10}^{c1}$ and less than $\overline{v}_{10}^{c2}$, the discriminant d < 0. In this case, Eq. 31 has three different real solutions. Their expressions are as follows

$$a_1 = \frac{2\sqrt{2}}{\omega_2}\sqrt{-\frac{1}{21}\frac{R_5}{R_7} - \cos\left(\frac{\alpha}{3}\right)\sqrt{\frac{1}{35R_7}\left(\frac{20}{63}\frac{R_5^2}{R_7} - R_3\right)}} \tag{40}$$

$$a_2 = \frac{2\sqrt{2}}{\omega_2}\sqrt{-\frac{1}{21}\frac{R_5}{R_7} + \cos\left(\frac{\alpha+\pi}{3}\right)\sqrt{\frac{1}{35R_7}\left(\frac{20}{63}\frac{R_5^2}{R_7} - R_3\right)}} \tag{41}$$

$$a_3 = \frac{2\sqrt{2}}{\omega_2}\sqrt{-\frac{1}{21}\frac{R_5}{R_7} + \cos\left(\frac{\alpha-\pi}{3}\right)\sqrt{\frac{1}{35R_7}\left(\frac{20}{63}\frac{R_5^2}{R_7} - R_3\right)}} \tag{42}$$

in which

$$\cos\alpha = \frac{2\xi_2 M_2^* \omega_2 - E}{F} \tag{43}$$

According to above formulas, the critical wind velocities and amplitude of galloping oscillations for the tower are calculated by computer programs. The results are: $\bar{v}_{10}{}^{c1} = 100\text{m/s}$, $\bar{v}_{10}{}^{c2} = 103.51\text{m/s}$, and the amplitude a of galloping oscillations versus wind speed is described in Fig. 5. The amplitude a jumps up and down at $\bar{v}_{10}{}^{c1}$ and $\bar{v}_{10}{}^{c2}$ respectively, and bifurcaitons of the amplitude curve occur between the above two critical values.

Knowing the value of the amplitude a, the horizontal displacement y at height z, for the galloping oscillation of the central TV transmission tower is

$$y(z_i) = \bar{A}_2(z_i)a \tag{44}$$

4. Conclusions

Following conclusions can be obtained by the calculation and analysis in this paper:

(1) The danger of galloping oscillations for the mast of the central TV transmission tower is very small for the extreme wind speed in the return period of 30 year is only 23.7m/s in Beijing.

(2) The influnce of the steel mast at the top of the central TV transmission tower is quite small on the damping ratio of the first mode of the tower, and is greater on that of the higher mode of the tower.

(3) For a structure like the central TV transmission tower, whose mass and aerodynmic stability of lower part are greater and better than those of upper part, the most dangerous mode for galloping oscillations is usually the second one, and not the first one. The danger of galloping oscillations for even higher modes are also smaller than that for the second one.

Fig. 5 The amplitude curve of galloping oscillations

(4) After galloping oscillations occur, the amplitude of galloing oscillations increases relatively gently at wind velocity rang $\bar{v}_{10}{}^c < \bar{v}_{10} < \bar{v}_{10}{}^{c1}$. When $\bar{v}_{10} > \bar{v}_{10}{}^{c1}$, the amplitude a increases dramatically, and abruptly jumps up at $\bar{v}_{10}{}^{c2}$.

References

1. Milos Novak and A. G. Davenport, Jour. of the Engineering Mechanics Division, Feb. 1970, vol. 96, EM1.
2. R. W. Clough J. Penzien Dynamics of Structures, McGraw-Hill Inc. 1975.
3. Milos Novak, Jour of the Engineering Mechanics Division, Feb. 1969, Vol. 95 , EM1.

An Investigation of Aerodynamic Loading
for Huge Luminous Lighthouse

Y. H. Ren
Beijing Institute of Aerodynamics, China

Abstract: The aerodynamic loading of the huge luminous lighthouse under the action of wind was studied in this paper. For the lamp tressel which was huge in shape and complex in construction, the aerodynamic coefficients were measured experimentally in low-speed wind tunnel. For high and large cylinder-like lamp-post, the drag and moment were calculated with the approximate method for flow around a cylinder. Therefore, the drags of the normal and side, the torque and moment for the whole lighthouse can be calculated. The results provided a solid basis for the design on strength and rigidity of the lighthouse.

1. Introduction

Four huge luminous lighthouses are used to lighten the foot-ball play-ground at Feng-Tai Sports Center, which was one of the important competition places of Asian Games. The lighthouse is composed of lamp tressel and lamp-post. The cuboid-like lamp tressel is huge in shape and complex in construction. It is 13.4m tall, 6m wide and 2m thick. The lamps with 12 ranks are installed inside, each rank with 6 lamps, totally 72 lamps. The lamp is shaped like reverse frustum-cylinder with length and maximum diameter of the same size, that is to say, 0.665m. The length of cylindrical section is 0.4m, diameter 0.25m. The lamp tressel is supported by an empty steel post with upper diameter of 1m and down diameter 3.2m. The total height of the luminous lighthouse is 57m from ground to the top.

In nature, the huge luminous lighthouse would be suffered from action of the wind loading and the deformations of torque and deflection would be occurred necessarily. For safety, before designing the lamp-post, the normal force, side force, torque, moment and corresponding stress of lamp-post had to be calculated and checked as a reference for strength and rigidity design.

For such huge luminous lighthouse, there was no present standard to be followed, and there was no any information about design to be referred. The system of the lamp tressel was so complex that there was disability in theoretical calculation. Thus the test in the low-speed wind tunnel was the only useful method for the tressel. And for the lamp-post we could use the results from flow around the infinite cylinder to calculate the aerodynamic loading.

2. The investigation of the lamp tressel in low-speed wind tunnel

2.1 Wind tunnel, model and testing technique

The tests were conducted in FD-09 Low-speed Wind Tunnel in Beijing Institute of Aerodynamics. The FD-09 Low-speed Wind Tunnel was set up in 1966. It is of closed-circuit, single-return type. The test section is 12m long. The cross-section is $3m \times 3m$ square with circular corner fillets of 0.5m in radius. If you were interested in more detail, please see Reference 1.

The model of lamp tressel used was similar to the object geometrically. The scale was 1:10 (Figure 1). There were two functions of the cylindrical sting under the lamp tressel. One was in conjunction with the inner balance which had six components and supported the model. The other was to simulate the effect of the lamp-post on the flow field around the tressel.

The cylindrical sting was fixed on the rotating-floor of the wind tunnel. The wind direction angle B was changed by turning the rotating-floor. The angle B was changed in the range from $0°$ to $180°$. The measurements were made at intervals of 10 degrees.

2.2 The testing results

There were four wind speeds to be used in test. They were V=20, 30, 40 and 50m/s. Reynolds numbers based on the diameter of lamp face were 0.91×10^5, 1.37×10^5, 1.82×10^5, and 2.28×10^5, respectively.

The results were shown in the Cartesian coordinate system oxyz of the lamp tressel body axis. The origin was located at intersecting point of the normal line through the center in the fore face and the axis of the lamp-post (see Figure 1).

The curves of the normal drag coefficient Cy and the the side drag coefficient Cz, which changed with wind direction angle B, were shown in Figure 2 and Figure 3. We can see that four curves of Cy and Cz with respect to B were nearly repeated respectively. It showed that when the wind speeds were changed from V=20m/s to 50m/s, or corresponding Reynolds numbers changed from 0.91×10^5 to 2.28×10^5, there were very little effects of flow speeds, or Reynolds numbers, on the normal drag coefficient Cy and side drag coefficient Cz. The torque and moment coefficients were the same as above mentioned (they were not plotted in the Figures).

Figure 2 showed that the normal drag coefficient Cy of the lamp tressel was decreased with increasing wind direction angle B. It reached maximum in value at $B = 0°$ and approached zero around $B = 85°$. As B increasing much more, it decreased continually, and became negative value. Then it reached maximum negative value at $B = 180°$. But its absolute value was still smaller than the value at $B = 0°$.

From Figure 3, it was observed that the value of the side drag coefficient Cz was always positive. It was increased with increasing wind angle B in enlarging wave mode. There existed several wave crests around $B = 20°$, $65°$, $140°$, and the maximum one was around $B = 140°$. Above $140°$, the varying tendency was in reverse, becoming zero when $B = 180°$. The minimum value was appeared about $B = 0°$ and $180°$.

From Figure 4, it was observed that the torque coefficient Cmx, which was all negative in value, varied with increasing wind direction angle B in similar wave mode as compared to the side drag coefficient. There were a few wave troughs around $B = 20°$, $65°$, and $130°$. When B was greater than $130°$, Cmx was increased with increasing angle B. At $B = 180°$ it approached zero. The minimum value was occurred about $B = 130°$.

By comparing Figure 3 with Figure 4, it could be concluded that the acting point of the side drag of the tressel was at the negative half-axis of y. That is, the acting point of the side drag was close to the lamp face.

The curves of the side moment coefficient Cmz and the normal moment coefficient Cmy varying as wind direction angle B were shown in Figure 5. It could be seen that the absolute values were all very small. They were all in the range of testing error, so be negligible. It indicated that the acting lines of the normal drag and side drag were basically on the symmetric planes of left-right and up-down respectively.

3. The wind loading of the lamp-post of the lighthouse

The flow over the lamp-post can be considered as the flow over the cylinder approximately. The disturbances were presented near the top from the lamp tressel and near the bottom from ground, but as concerns engineering, it can be still treated approximately as a flow around the infinite cylinder. However, the cross-section of lamp-post was variable.

3.1 The drag calculation of lamp-post

From Reference 2, when the Reynolds number based on the diameter of cylinder was 10^6 in order of magnitude, the drag coefficient $C_D = f / \frac{1}{2} \rho V^2 R$ of unit length of cylinder is about from 0.8 to 1.0, where f is the average drag acting on the unit length of cylinder.

Suppose R_b is the radius of lamp-post at the bottom, R_t is the radius at the top, h_t is the height of the lamp-post. At the point where the height is h, radius is R, we have

$$R = R_b - \frac{R_b - R_t}{h_t} h \qquad (1)$$

There is a distribution of wind drag acted on the lamp-post along the axis. The drag on the element dh of lamp-post is

404

$$dF = \frac{1}{2} \rho \ V^2 \ C_D \ R \ dh \tag{2}$$

The total drag F of lamp-post is

$$F = \int_0^{h_t} \frac{1}{2} \ \rho \ V^2 \ C_D \ R \ dh$$

$$= \frac{1}{4} \ \rho \ V^2 \ C_D \ h_t \ (R_b + R_t) \tag{3}$$

Two components F_y and F_z in the body coordinate system of tressel are as follows

$$F_y = F \ \cos B \tag{4}$$

$$F_z = F \ \cos B \tag{5}$$

3.2 The moment calculation at any point P on the lamp-post

Suppose the distance from ground to the point P is h_p. As a result of action on the lamp-post from wind drag, the moment about P is

$$M_p = \int_{h_p}^{h_t} \frac{1}{2} \ \rho \ V^2 \ C_D \ R \ (h-h_p) \ dh \tag{6}$$

Upon the substitution of (1) into (6) and integration, we yield

$$M_p = \frac{1}{2} \rho \ V^2 \ C_D \ \left[-R_b \ h_p \ (h_t - h_p) + \frac{1}{2}(R_b + \frac{R_b - R_t}{h_t} \ h_p) \right.$$

$$\left. (h_t^2 - h_p^2) - \frac{1}{3} \frac{R_b - R_t}{h_t} \ (h_t^3 - h_p^3) \right] \tag{7}$$

The side and normal components of the moment in the body axis coordinate system are as follows

$$M_{zp} = M_p \ \cos B \tag{8}$$

$$M_{yp} = -M_p \ \sin B \tag{9}$$

4. The aerodynamic loading of the luminous lighthouse

The aerodynamic loading of the lighthouse is composed of the aerodynamic loading of the tressel and the one of the lamp-post. The total normal drag F_{y0} and total side drag F_{z0} are given as follows

$$F_{y0} = \frac{1}{2}\rho \ V^2 \ S \ C_y + F_y \tag{10}$$

$$F_{z0} = \frac{1}{2} \rho \ V^2 \ S \ C_z + F_z \tag{11}$$

405

Because the lamp-post does not generate torque, the total torque M_{x0} is given as follow

$$M_{x0} = \frac{1}{2} \rho \ V^2 \ S \ H \ CM_x \qquad (12)$$

where S is fore face area of the tressel, H is the height of the tressel.

Because the side and normal moment coefficients of the tressel are all very small, they are all neglected. At the point P on the lamp-post, the total side moment M_{zp0} and the total normal moment M_{yp0} are as follows

$$M_{zp0} = \frac{1}{2} \rho \ V^2 \ S \ C_y \ (h_t - h_p + \frac{H}{2}) + M_{zp} \qquad (13)$$

$$M_{yp0} = -\frac{1}{2} \rho \ V^2 \ S \ C_z \ (h_t - h_p + \frac{H}{2}) + M_{yp} \qquad (14)$$

The resultant moment M_{p0} is shown as follow

$$M_{p0} = \sqrt{M_{zp0}^2 + M_{yp0}^2} \qquad (15)$$

When wind speed V and wind direction angle B are given, using the formulas from (10) to (15), substituting the geometric parameters, drag coefficient C_D and the results from the test in the wind tunnel, the series of parameters could be calculated at once.

5. Conclusion

For the lamp tressel which was huge in shape and complex in construction, we have studied it experimentally in the low-speed wind tunnel. For the lamp-post, it was studied by using the method of calculation theoretically. Thus the subject about the aerodynamic loading of huge luminous lighthouse is resolved finally. It provided a solid basis for the designing the luminous lighthouse. But it must be pointed here that these are only the static aerodynamic loading on the lighthouse. In fact, in nature there are many dynamic problems followed at the same time, for example, the unsteady flow from changeable speed in magnitude or direction by accident, aeroelastic vibration, stability and so on. They should be considered and treated necessarily in designing for the huge luminous lighthouse. Fortunately, they had been studied successfully in other report (Reference 3) by my colleagues.

References

1. FD-09 Low-Speed Wind Tunnel in Beijing Institute of Aerodynamics (Internal Information)

2 F.M. W" ಜ, Viscous Fluid Flow, McGRAW-HILL BOOK COMPANY (1974)

3. Z. Q. Liu, G. M. Fu and E. J. Cui, The Wind Loading of Luminous Lighthouse of Stadium at Feng-Tai Sports Center, The National Conference on Wind Engineering and Industrial Aerodynamics (1990)

Figure 3. $Cz \sim B$

Figure 5. $CMz, CMy \sim B$

Figure 2. $Cy \sim B$

Figure 4. $CMx \sim B$

Figure 1. Sketch of model and coordinate system
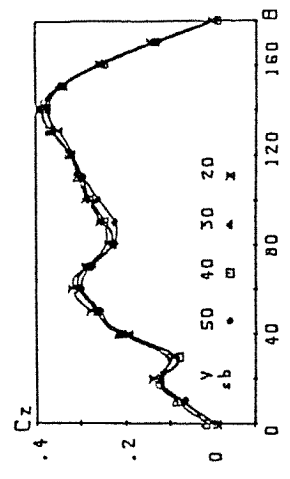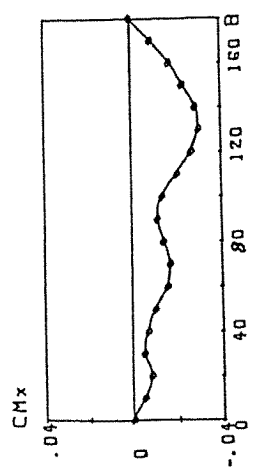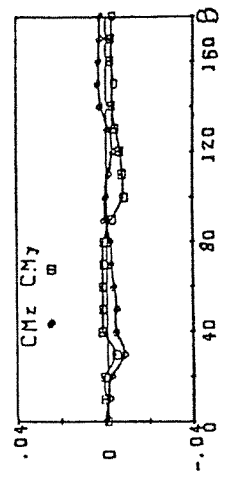
Wind Characteristics

WAS THE HARRIS AND DEAVES VELOCITY PROFILE A STEP IN THE WRONG DIRECTION?

D.A.PATERSON

CSIRO Division of Building, Construction and Engineering,
Gate 2 Delhi Rd., North Ryde, NSW 2113, AUSTRALIA.

Abstract: The Harris and Deaves (HD) velocity profile for strong winds has been incorporated in the Australian and New Zealand wind loading codes but is not as accurate as either log or power law velocity profiles.

1. Introduction

Successful and accurate predictions strong winds and the damage that they cause have great practical importance. This paper is about finding a velocity profile for strong winds generated by upper level pressure gradients.

The Harris and Deaves (HD) mean velocity profile [1] for strong winds is:

$$V = \frac{u_*}{\kappa}\left[\ln\frac{z}{z_0} + 5.75\left(\frac{z}{h}\right) - 1.88\left(\frac{z}{h}\right)^2 - 1.33\left(\frac{z}{h}\right)^3 + .25\left(\frac{z}{h}\right)^4\right] \qquad (1)$$

V is the mean velocity at height z. u_* is the friction velocity. $\kappa = 0.41$ is Von Karman's constant. z_0 is the ground roughness length.

2. Derivation

From similarity theory we have:

$$\kappa V / u_* = \ln z / z_0 \qquad \text{for } z \text{ small} \qquad (2)$$

$$h = u_* / \beta f \qquad (3)$$

$$\kappa G / u_* = \ln(u_* / f z_0) - A = \ln(h / z_0) + \ln \beta - A \qquad (4)$$

A and β are constants to be found from experimental data. As z approaches h, we expect:

$$\kappa(V - G) / u_* = F(z / h) \text{ with } V = G \text{ and } dV / dz = 0 \text{ at } z = h \qquad (5)$$

From the low-level form of $\kappa V/u_*$ given in (2) and the expression for $\kappa G/u_*$ given in (4), the only possible profile law for V throughout the boundary layer which will satisfy (5) is given by the form:

$$\kappa V / u_* = \ln z / z_0 + \phi(z / h) \qquad (6)$$

$$\text{where } \phi(0) = 0 \text{ in order to satisfy (1) for z small} \qquad (7)$$

From (4), (5) and (6):

$$\kappa(V - G) / u_* = F(z / h) = \ln(z / h) + \phi(z / h) - \ln \beta + A \qquad (8)$$

We now introduce the new variable $\eta = 1 - (z / h)$ so that in this new variable the top boundary condition becomes $V = G$ and $dV/d\eta = 0$ at $\eta = 0$ and we have:

$$\kappa(V - G) / u_* = \ln(\eta) + \Phi(\eta) - \ln \beta + A \qquad (9)$$

Measurements suggest a parabolic velocity defect law for about the upper 70% of the boundary layer. As η increases from zero, the series for $\ln(1-\eta)$ converges only slowly, so that we can only obtain a parabolic velocity defect law for values of η up to about 0.7 if the function $\Phi(\eta)$ is such that the terms in its power expansion cancel those in the expansion of $\ln(1-\eta)$, except the term in η^2. We arbitrarily chose to truncate the expansion at the term in η^4, so that the departures from a parabolic velocity law are $O(\eta^5)$ which guarantees about 1% error

411

up to amount $\eta = 0.7$ for the parabolic velocity defect law (clearly higher order terms could be included). Thus HD obtained:

$$\Phi(\eta) \approx -A + \ln\beta + \eta + \alpha\eta^2 + \eta^3/3 + \eta^4/4 \tag{10}$$

where $\alpha = A - \ln\beta - 1 - 1/3 - 1/4$ in order to satisfy the boundary condition (7) which becomes $\Phi = 0$ for $\eta = 1$ in terms of the new variable η.

Using this expression for $\Phi(\eta)$ and restoring the original variable z/h leads to:

$$\frac{\kappa V}{u_*} = \ln\left(\frac{z}{z_0}\right) + \left(\frac{1}{6} + 2\ln\beta - 2A\right)\frac{z}{h} - \left(A - \ln\beta + \frac{11}{12}\right)\frac{z^2}{h^2} - \frac{4}{3}\frac{z^3}{h^3} + \frac{z^4}{4h^4} \tag{11}$$

Experimentally one finds $A = -1$, $\beta = 6$, thus:

$$\frac{\kappa V}{u_*} = \ln\left(\frac{z}{z_0}\right) + 5.75\left(\frac{z}{h}\right) - 1.88\left(\frac{z}{h}\right)^2 - 1.33\left(\frac{z}{h}\right)^3 + 0.25\left(\frac{z}{h}\right)^4 \tag{12}$$

3. Problems Stemming From The Derivation

Eq. 12 is not the only profile that satisfies the boundary conditions in Eqs. 2, 4 and 5 as well as the parabolic velocity defect law in the upper 70% of the boundary layer when $A = -1$ and $\beta = 6$. Two alternative formulae that satisfy all the conditions are plotted along with the HD formula in Figure 1. These alternatives were created using a blending technique that uses the tanh function [2].
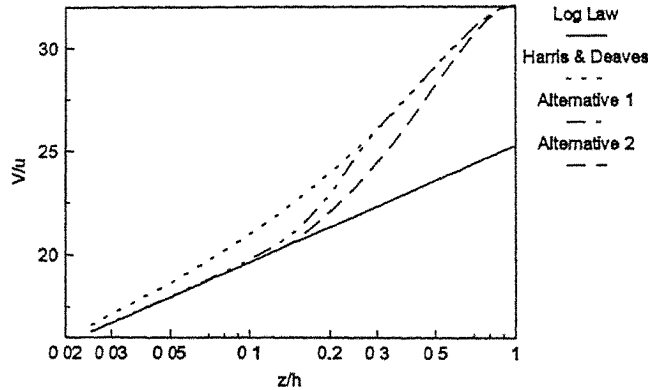
Figure 1. The non-uniqueness of formulae that satisfy the HD boundary conditions.

The one thing that sets the HD formula apart from all others is the use of the power series expansion for $\ln(1-\eta)$ about $\eta = 0$. This ensures good agreement with the parabolic velocity defect law near the top of the atmospheric boundary layer but gives a very poor formula in the bottom 20% of the boundary layer where accuracy is most needed.

The near ground part of the power series is very inaccurate and this is used in conjunction with the ground boundary condition (7) in the evaluation of α. This means that the value of α in the above derivation is inaccurate. The curvature of the parabolic velocity defect law at the top of the boundary layer is directly related to α. Because this curvature is wrong the upper part of the velocity profile is inaccurate. The net result is that the whole of the HD velocity profile is inaccurate.

The values of A and β used by HD are inaccurate. A review by Zilitinkevich [3] suggests

412

$1/\beta = 0.3$. The value of A, calculated from A_0 and B_0 in this review by:

$$(11.56 - B_0)^2 + A_0^2 = (11.56 + A)^2 \qquad A_0 = 4.5 \qquad B_0 = 1.7 \qquad (13)$$

is $A = -0.72$. A typical value for $\ln(h/z_0)$ of 10.36 is used in this derivation.

4. Comparison With Other Boundary Layer Formulae

One of the earliest and best known formulae is the Power law formula:

$$V / u_* = C(z / z_0)^{1/n} \qquad (14)$$

This formula does not satisfy Eq. (2) but has been found to agree fairly well with experimental data. Another early formula is the Log law profile:

$$V = \frac{u_*}{\kappa} \ln \frac{z}{z_0} \qquad (15)$$

Coles' [4] velocity profile was developed in 1956 for laboratory boundary layers and is still widely used. Coles' mean velocity profile is based on Eq. (6) and can be written:

$$V = (u_* / \kappa)(\ln z / z_0 + \Pi w(z / h)) \qquad (16)$$

Π is a profile parameter and w is the wake function. No attempt is made to force this equation to match a parabolic velocity defect law. The wake function w is found from a large amount of experimental data and is published by Coles in tabular form.

The wake function can be approximated by:

$$w(\zeta) = 1 - \cos(\pi\zeta) \qquad (17)$$

The value for profile parameter Π to match A and β derived from the review by Zilitinkevich is $\Pi = 0.96$. The Coles' mean velocity profile need not satisfy Eq. (5) because the experimental data from which the profile has been derived supports the contention that dV/dz is discontinuous at $z = h$.
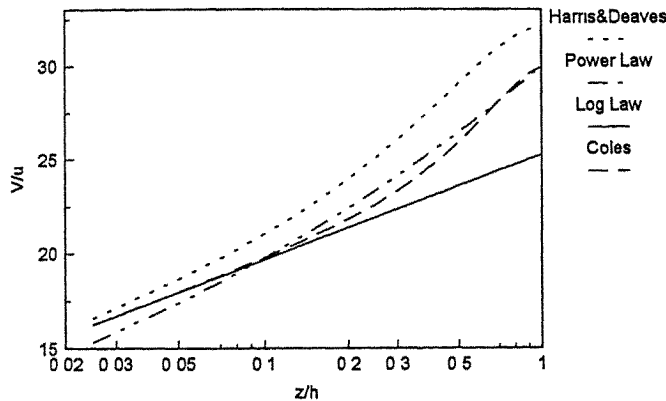
Figure 2. A comparison of velocity profiles.

Eqs (1), (14), (15) and (16) are compared in Fig. 2. The value $\ln(h/z_0)$ is set to a typical value of 10.36 to allow direct comparison.

The HD profile does not satisfy Eq. 2; it does not behave like the logarithmic law of the wall at small values of z. This is because the HD profile has a linear deviation from the Log law near the ground. This linear deviation near the ground is a feature of non-neutral boundary layer velocity profiles.

Practical applications of mean wind flow profiles usually involve the lower 20% of this

413

profile. Profiles are matched to the value and slope of the Log law profile at 5% of the boundary layer height and deviations at 10% and 20% are noted. A typical value for $\ln(h/z_0)$ of 10.36 is used.

Table 1. Deviation from the Log law in the lower 20% of the boundary layer.

	$z/h = 0.05$	$z/h = 0.1$	$z/h = 0.2$
Log Law Profile	0	0	0
Power Law Profile	0	0.08	0.34
Coles Profile	0	0.08	0.41
Harris & Deaves Profile	0	0.15	1.76

The HD profile differs much more from the Log law profile than the Power law profile does in the lower region of the boundary layer. To make the HD profile match the Log law profile at $z/h = 0.05$ requires a massive change of 28% in $u*$ and 484% in z_0.

5. Comparison of Profiles with Data from Harris & Deaves [1]

HD report the agreement between their profile and data from Nantes, Rugby, Cranfield, Leipzig and Farnborough. The Nantes and Cranfield results only extend up to $z/h=0.04$, at which point any deviation from the Log law is negligible. The Rugby, Leipzig and Farnborough results are plotted in Figure 3.
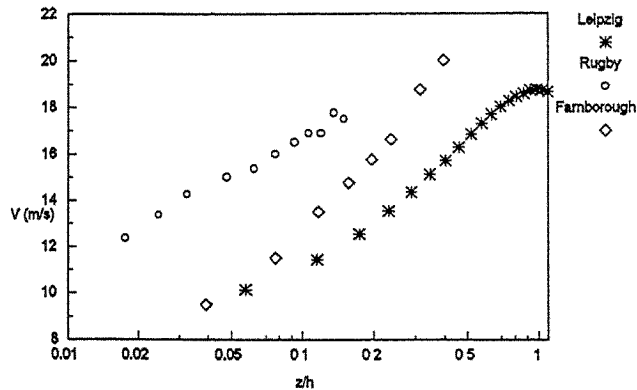
Figure 3. Data from Harris and Deaves.

The reported G value [5] is used for the Leipzig profile and an arbitrary value of $G = 25$ m/s is used for scaling the other data. The Rugby data shows no deviation from the Log law. The Farnborough data shows a deviation from the Log law that is of the same order of magnitude as Coles profile or the Power law profile. This deviation is smaller than could be explained by the HD profile (see Table 1).

The Leipzig data agrees very well with the HD profile and not at all well with the other profiles. It does not match the Log law at all, even at small z/h. The Leipzig profile was derived by Lettau [5]. It is a semi-theoretical profile based on original data reported in 1932 by Mildner [6]. This data is plotted in Figure 4.

The peak velocity in Mildner's data is 20.9 m/s which occurs at an unstated height. Mildner's data shows a much smaller deviation from the Log law than Letau's profile. This deviation is of the same order of magnitude as in the Coles profile or the Power law profile. It

414

is smaller than could be explained by the HD profile.
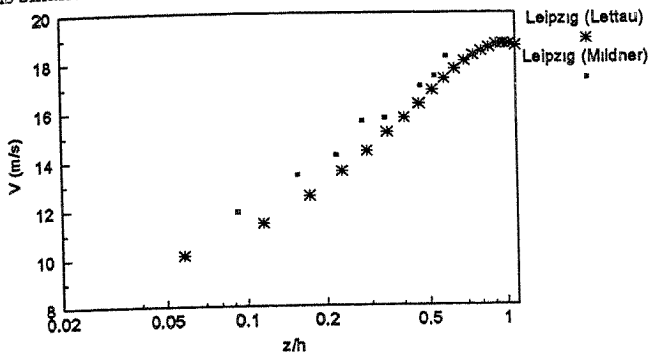
Figure 4. Two interpretations of the velocity data from Leipzig.

6. Comparison of Profiles with Data from Other Sources.

Fig. 5 shows data collected at Rugby (obtained privately). The winds are fairly strong. The profiles were measured by anemometers mounted on a mast surrounded by flat terrain. The highest anemometer was 182m above ground level. This has a z/h value of about 0.153 if the HD estimate of $\beta = 6$ is used. My detailed statistical analysis shows that there is a slight deviation from the Log law. The Power law fits the data better than the Log law for all but two of the 11 profiles (Runs 70 and 87). The HD profile does not fit the data best for any of the 11 runs.
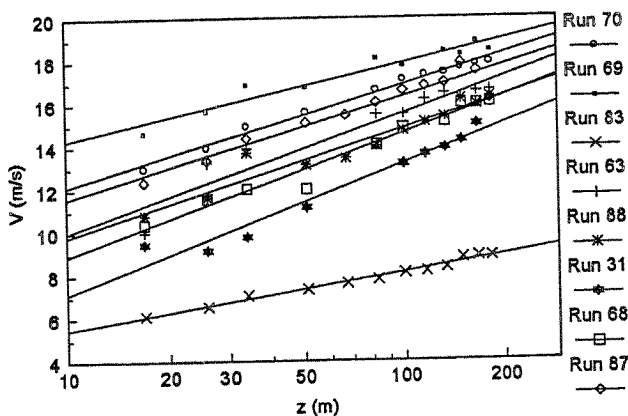
Figure 5. Strong wind data from Rugby.

Soma [7] reported wind profiles to heights of 253 m and velocities to 33.2 m/s measured at Tokyo Tower. This data contains some cyclone winds and some ordinary winds. Nine of these profiles, selected for high wind speeds at the highest and lowest anemometer, are shown in Figure 6. This figure does not include data from the anemometer at 107 m in the six profiles measured on the same day (61.9.16) because it consistently reads low on that day.

These nine profiles show some deviation from the Log law profile. Four profiles most

415

closely match the Log law profile, four most closely match the Power law profile and only one closely matches the HD profile. This is the profile 61.9.16.16.
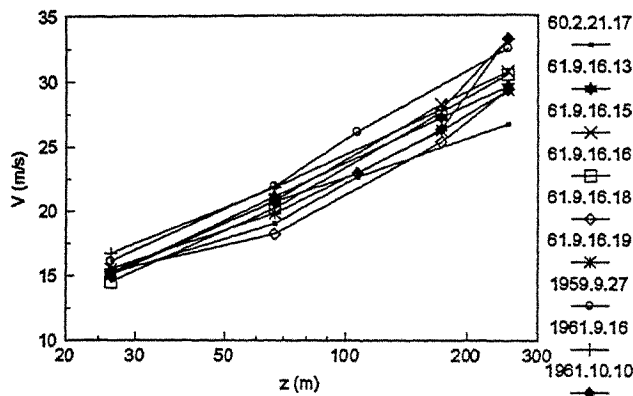
Figure 6. Strong wind data from Tokyo Tower

7. Conclusions.

The HD profile is not the only profile that satisfies the boundary conditions specified in its derivation. There are an infinite number of alternative formulae that satisfy these conditions. The one thing that sets the HD formula apart is the use of the power series expansion for $\ln(1-\eta)$ about $\eta = 0$. This gives a very poor formula in the bottom 20% of the boundary layer where accuracy is most needed.

The HD profile does not behave like the logarithmic law of the wall near the ground because it has a linear deviation from the Log law at small values of z. The difference between the Power law and the Log law near the ground is much less than the difference between the HD formula and the Log law, even allowing for very large changes in u_* and z_0.

The HD profile agrees very poorly with measured data. It has worse agreement with data from Rugby, Tokyo Tower and other data than both Log law and Power law profiles.

References:
1.   R. I. HARRIS and D. M. DEAVES *The structure of strong winds* Wind Engineering in the Eighties, Proceedings of the CIRIA conference held on 12/13 November 1980.
2.   D. A. PATERSON *Making sense of experimental data using tanh blending* CSIRO DBCE Doc. 92/19(S), Nov. 1992.
3.   S. S. ZILITINKEVICH *Velocity profiles, the resistance law and the dissipation rate of mean flow kinetic energy in neutrally and stably stratified planetary boundary layer* Boundary Layer Meteorology, Vol. 46, pp. 367-387, 1989.
4.   D. COLES *The law of the wake in the turbulent boundary layer* J. Fluid Mechanics, Vol. 1, pp. 191-226, 1956.
5.   H. LETTAU *A re-examination of the "Leipzig wind profile" considering some relations between wind and turbulence in the frictional layer* Tellus, Vol. 2, pp. 125-129, 1950.
6.   P. MILDNER *Über Reibung in einer speziellen Luftmasse in den untersten Schichten der Atmosphäre* Beitr. Phys. fr. Atmosph., Vol. 19, p. 151, 1932.
7.   S. SOMA *The properties of atmospheric turbulence in high winds*, Journal of the Meteorological Society Japan, pp. 372-378, 1964 (in Japanese).

416

Wind Tunnel Study Of The Wind Flow Over Auckland City And Comparison With Full-Scale Data

R.G.J. Flay and R.J. Andrews[+]

Senior Lecturer, Mechanical Engineering Department
University of Auckland
[+]Former Postgraduate Student, Mechanical Engineering Department
University of Auckland

Abstract: The purpose of this study was to investigate the wind flow over the City of Auckland using wind tunnel models to provide information for wind loading for future high-rise building design. A new wind tunnel model of the City was constructed to a scale of 1:1000 centred near the major intersection of Queen and Wellesley Streets. The model included two sites where full-scale Meteorological data had been recorded, fairly near to the centre of the modelled area. Appropriate onset flow to the model was developed by use of a trip barrier and roughness blocks by considering the nature of the full-scale surrounding terrain. The ratio of the mean wind speeds at the two full-scale anemometer sites were obtained for six wind directions and compared to the full-scale ratios. Reasonable agreement was obtained once due allowance had been made for the change in Cityscape that had occurred, and for local building effects by using a detailed 1:250 scale model.

1. Introduction

The City of Auckland is located on a narrow hilly isthmus where the terrain can be summarised as complex, and tall buildings are increasingly being located along the tops of ridges which are very exposed to the prevailing winds, which tend to be from the north-easterly and south-westerly quarters. Because of this, wind tunnel testing of buildings is now an established and successful procedure which is a prerequisite for most large proposals in Auckland City. Such tests require detailed wind climate data so that the wind statistics can be used with the wind tunnel data to calculate speeds, pressures etc. The Auckland City wind data which have been used for this purpose were collected over the period 1970 - 1984 at the top of the former NAC building where the Meteorological Service was located at that time. This is called the Auckland City or NAC data.

Auckland City grew rapidly in the 1980's, with many tall buildings going up in the central city area. It was thus felt that a close look should be made of wind flow in this area so that the data could continue to be used with confidence. It was decided to conduct a wind tunnel study, and the Auckland City Council (ACC) was approached and agreed to assist, so the study became a joint venture. The ACC built a 1:1000 scale model of Auckland city, and also provided financial support to a student to carry out the wind tunnel study. A computer controlled traversing rig was developed for the wind tunnel [1] and many measurements taken and analysed as described below.

2. The Models

The centre of the 1:1000 model is at the intersection of Elliot St and Wellesley St West, near the centre of the downtown core of the city. A map of the City and the extent of the modelled area can be seen in Fig 1. The centre circular area was always located in the wind tunnel and upstream sections of the larger incomplete circular area corresponding to the test direction were also used.
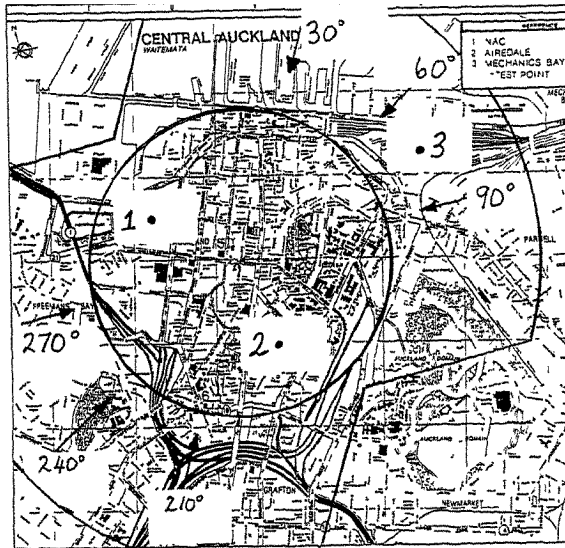
Fig. 1 The modelled area of Auckland City.
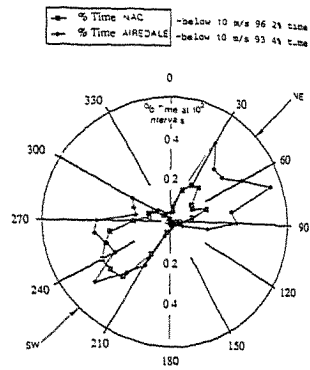
Fig. 2 Percent time wind speeds
greater than 10m/s
(10^0 intervals)

The model was extended in the north-easterly and south-westerly directions only because the prevailing winds in the Auckland area tend to be from these quarters as shown in Fig. 2 which are from full-scale data discussed later. Six test directions of 30, 60, 90, 210, 240, and 270^0 were selected for testing.

The model was built on a base of 10mm customwood. The terrain of Auckland City was contoured using layers of 2.4mm plain gasket cork and corresponded approximately to 3m in full-scale. The contours were not smoothed as this added aerodynamic roughness to the model surface which made some allowance for the small scale detail not modelled. The buildings were modelled with blue insulation Styrofoam. Large areas of trees were modelled from a black open-cell synthetic upholstery foam. A very detailed model of the central area of Auckland had previously been made to a scale of 1:250 primarily for pedestrian level wind studies. This model was also used in the present study for comparative purposes at low levels.

3. Full-scale Wind Data

Meteorological wind and temperature data have been recorded at a variety of sites in the Auckland area for the past several decades. Wind frequency distribution data from 5 sites were fitted by Weibull equations of the form

$$P(> V) = A \exp\left(-(\tfrac{V}{c})^k\right) \qquad (1)$$

at 10^0 intervals. The resulting values of A and c are shown in Fig. 3. A is the percentage of time the wind blows from a particular direction and it can be seen that apart from Whenuapai which is 10km west of the central city, the curves all show good agreement. Fig 3 also shows the variation of c (which is related to mean wind speed), and here it can be seen that the Mechanics Bay site is fairly sheltered except to the NE, compared to the others. In all cases k was around 2 as expected. Only data collected at two sites, Auckland City and Airedale, both located in the central city area were used for comparative purposes. The former data were recorded over the period 1970 - 1984 with a

418
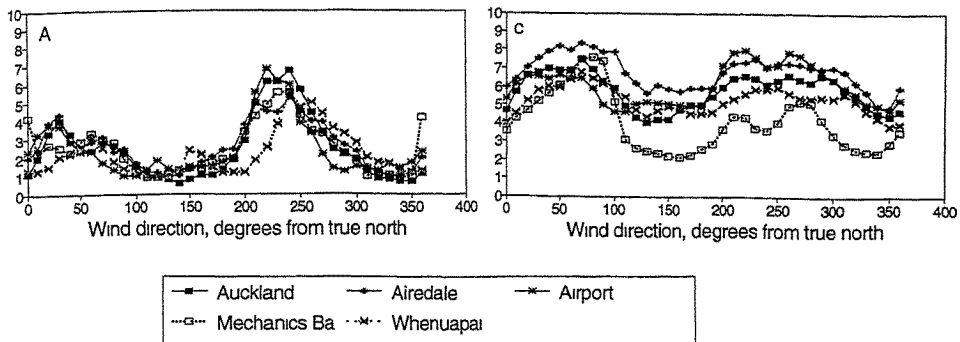
Fig. 3 Variation of Weibull coefficients A and c for 5 sites near Auckland.

Munro Anemograph mounted on a 10m tower above the roof of the former NAC building at the intersection of Hardinge St and Victoria St West. This height corresponds to 31m above local ground level, and 54m above mean sea level. The latter data were recorded over the period 1967 - 1971 by the same kind of instrument mounted on the Post Office tower at the intersection of Lydock and Airedale Streets at a height of 77m above local ground level and 113m above mean sea level. In all cases the data used had been converted into wind speed frequency distribution tables by the NZ Meteorological Service.

4. Wind Tunnel and Associated Equipment

The low speed test section of the de Bray closed circuit wind tunnel has a 2.6.1 contraction ratio. The test section is 9.75m long, 1.83m wide, and nominally 1.06m high. The fetch to the model centre is about 8m, and the roof is adjustable. There is a removable flow conditioning section at the beginning of the test section where an initial flow conditioning device such as a trip barrier can be positioned to accelerate boundary layer growth. Onset flows were measured 6.2m downstream of the flow conditioning section, 1.8m upstream of the model centre

A constant temperature hot-wire anemometer developed in-house, with Dantec probe equipment, was used to obtain the flow measurements. The probe was always mounted with the probe shaft and wire both horizontal. An IBM XT personal computer was used for data acquisition and reduction, and also for controlling the traversing rig to which the probe was attached.

5. Development of the Boundary Layer Flows

Testing was carried out for geometric model scales of 1:250 and 1:1000 so appropriate approach flow had to be developed for each case. This was done using a trial and error basis using a trip barrier, roughness blocks, and carpet [2]. The 1:1000 velocity profile for 3 lateral positions across the wind tunnel can be seen with the corresponding turbulence intensity profiles in Fig 4. Both figures have curves labelled Category 3 corresponding to a roughness length z_0 of 0.2m [3]. These profiles were regarded as being adequate for the onset flow to the detailed model The figures illustrate that the flow in the wind tunnel has some lateral non-uniformity, and this was investigated carefully by performing horizontal traverses across the test section at four heights: 10, 200, 400, and 600mm. To prevent this potential bias, a regression analysis was performed and it was found that

419
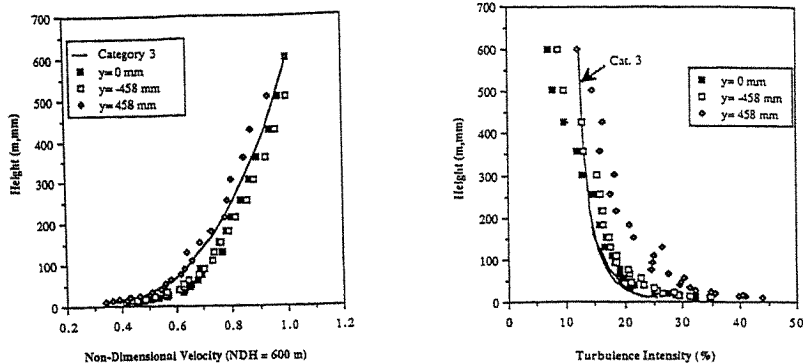
Fig. 4 Vertical velocity and turbulence intensity profiles 1.8m upstream of model centre.

normalised horizontal velocity profiles at all heights could be fitted by a parabola described by:
$$\bar{V}_{ND} = -4.124 * 10^{-7} * (y+95)^2 + 1.0 \qquad (2)$$
which is shown in Fig 5. This systematic error was eliminated from all measured results by noting the distance y from the centreline, and making appropriate corrections to the measured mean velocities.

A suitable 1:250 scale boundary layer was also developed using a trip barrier, bar grid and roughness blocks placed on the floor

6. Comparison of Full-scale and Wind Tunnel measurements

Validation of the wind tunnel flow was done by measuring velocity profiles at sites 1 and 2 (see Fig. 1) for the 6 test wind directions. These measurements were all made at nominally the same wind speed. The velocity profiles at the positions being investigated enabled the velocities at the equivalent heights of the anemometers in full-scale to be obtained by interpolation. Velocity ratios NAC:AIREDALE were then formed from the wind tunnel measurements at these heights.
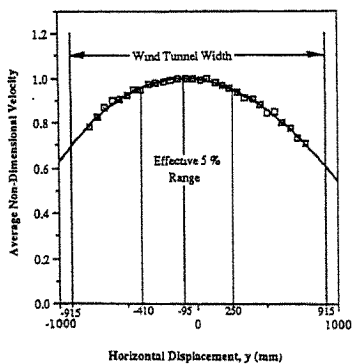
Fig. 5 Non-dimensional lateral velocity profiles 1.8m upstream of model centre.
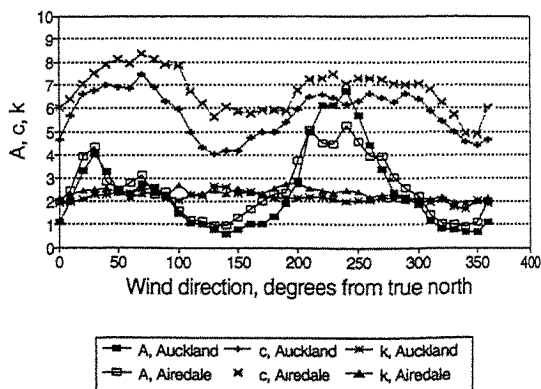
Fig. 6 Weibull coefficients for Auckland and Airedale sites.

420

The Weibull coefficients A, c, and k for the NAC and Airedale data are shown in Fig. 6. There is a fair degree of agreement in the shapes of the curves, and not unexpectedly c is generally higher for the more elevated 77m high anemometer at Airedale St. A and k differ significantly for some wind directions, but it is only the coefficient c which can be adjusted using measured wind tunnel velocity ratios.

When it is desired to transfer Meteorological data to a site which has no data from one for which long term records are available, the procedure is to instrument the new site with an anemometer and to record wind speed and direction data from both sites for as long a period as possible. This enables instantaneous values of $R=V_2/V_1$, $\Delta = \theta_1 - \theta_2$ to be found. These data can then be put into "bins" corresponding to wind direction at the reference site 1 , i.e. $R(\theta_1) = \frac{V_2}{V_1}$; $\Delta(\theta_1) = \theta_2 - \theta_1$. Armed with the functions R and Δ, one can then easily transform tables of data from the Meteorological site to the building site. The same procedure can be carried out in the wind tunnel using topographic models, but generally only the wind speed ratio would be measured. In the present study, wind speed ratios were obtained between sites where historical wind speed data were available so that the data from one site could be transferred from one to the other, and then compared with the real data as a way of validating the procedure.

The measured velocity ratios NAC:AIREDALE were corrected for the lateral velocity profile in the wind tunnel, but the resulting ratios did not agree very well with the full-scale data. There were potentially several reasons for this, such as: (i) the full-scale data were obtained when the surrounding buildings were much shorter, (ii) local building effects, (iii) full-scale data included winds of all speeds including a large proportion at low speeds, possibly under unstable atmospheric conditions. It was expected that the effect of item (iii) would have been mitigated by fitting Weibull curves to all of the data, but items (i) and (ii) required further investigation. The 1:1000 model was fully up to date as at 1989. However, the full-scale data were obtained much earlier when the city buildings were shorter. It was expected that this would affect the NAC data the most, as its height was only 31m, and many of the central city buildings in 1989 were over 100m tall. It was also possible that the 1:1000 model with its rather small models of buildings was unable to capture properly details of the wind flow very close to the tops of buildings. Further wind tunnel testing was therefore scheduled to examine (i) and (ii). This was done by using the very detailed 1:250 model and measuring profiles above the NAC building. Item (i) could be examined because this model was made in small pieces, and the tall recent buildings were simply omitted from it. Item (ii) could be examined by measuring profiles through the anemometer location.

Fig. 7 Comparison of actual and predicted Airedale data for the NE and SW directions.

421

These measurements were carried out, and dimensionless velocity profiles used to obtain the ratios V_{1000}/V_{250} at the NAC anemometer height. The ratios were used to correct the earlier data. The final ratios are applied to the NAC "c" values to predict c's at Airedale. The measured and pre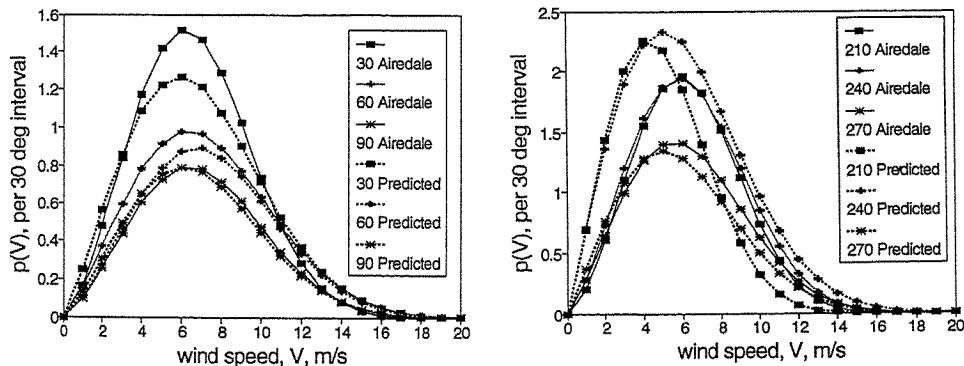dicted Airedale data are compared in Fig. 7 for the NE and SW directions respectively. It can be seen in the figure that the agreement is good for directions 30, 60, 90, and 270°, but that the agreement is only fair for the others. This shows the difficulty of dealing with low level data when the surrounding fetch is altering with time, even with a detailed wind tunnel study using two different model scales. Reference to Fig. 6 shows some reasons for the discrepancies. At 200 to 260° the A's differ somewhat for the two data sets and a simple wind tunnel study such as this cannot alter this parameter except perhaps by reducing the % time of calms in some fashion by arguing that since the Airedale site is more exposed, it should be calm less often

7. Conclusions
1. Full-scale Meteorological data show that the wind climate varies significantly at different locations around the Auckland area.
2. Within the city itself the wind climate varies, and is also changing with time as the city buildings become taller.
3. The wind tunnel had considerable flow lateral non-uniformity which has to be accounted for in wind studies - this problem has been addressed recently with changes made to the wind tunnel circuit
4. Full-scale wind data could not be transferred from one city site to another using the 1 1000 model alone as it did not model the city as it stood when the data were recorded.
5. More detailed investigation of the flow at the anemometer sites using the 1 250 model enabled corrections for local building effects and the effect of new upstream buildings to be made, resulting in velocity ratios which matched the full-scale data quite closely apart from the 210 and 240° direction
6. The disagreement between the 210 and 240° data was also in large part due to the disagreement between the A's and k's, and the wind tunnel study was unable to change these

8. Auckland Wind Data
This study suggests that it would be an improvement for wind tunnel studies to use wind data which better described the situation in Auckland City. It is likely that this would be a composite distribution described by Weibull curves at 10° intervals, made up by combining all of the local historical records in an appropriate fashion. Probably the best way of doing this would be to attempt to extrapolate the data at each location to a greater elevation, say 300m above ground level. There should be a fair amount of agreement of the data at such a height. Appropriate averaging of the data set could be used to obtain the most refined composite data set for subsequent use. High level balloon data (900m) measured at Auckland Airport about 16km south of the city centre could also be extrapolated down to 300m to provide another source of data to build up the best possible description of the local wind climate.

9. References
1. R.J. Andrews, Computer controlled traverse mechanism, Dept of Mech Eng Report No MEG 89-10, Univ of Auckland, Private Bag 92019, Auckland, NZ
2. R. J. Andrews, Modelling the wind flow over Auckland City, ME Thesis, Dept of Mech Eng, Aug 1990, Univ of Auckland, Private Bag 92019, Auckland, NZ.
3. NZ Standard NZS4203, General Structural design and design for buildings, Part 4, Wind Load Provisions, 1993.

Full-Scale Measurements of Windspeeds at a Suburban Area

Koichi Miyashita[a], Yukio Tamura[b], Yutaka Asami[c] and Syunichi Naito[d]

[a]Wind Engineering Institute Co.Ltd.,8-20-4, Nishi-shinjuku, Shinjuku-ku, Tokyo 160 (Japan)
[b]Tokyo Institute of Polytechnics,1583,Iiyama, Atsugi, Kanagawa 243-02(Japan)
[c]Technology Research Center,Taisei Corporation,344-1,Nasemachi,Totsuka-ku,Yokohama 245(Japan)
[d]Taku Stractural Engineering Co.Ltd.,2-6-11,Higashi-nakano,Nakano-ku,Tokyo 164 (Japan)

Abstract: Full-scale measurements of windspeed characteristics in a suburb area northwest of Tokyo have being conducted since 1990. About 5,000 runs of a 10-minute period each collected at four altitudes were analyzed to assess the vertical profiles of mean windspeeds and turbulence intensities with the altitude. Power spectral densities, turbulence scales and spatial correlations of wind fluctuations were evaluated from the records of two strong storms. Some preliminary findings are outlined to be: the power-law distribution could well represent the vertical mean windspeed profile of strong winds; an exponent of 0.2 was found to be appropriate for the exposure at the site; and power spectra of windspeeds at all four altitudes were in good agreement with the Karman type spectrum.

1   Introduction

The construction of buildings and structures is taking a direction of creating still higher ones and, in many circumstances, wind loads are replacing seismic forces to play a decisive role in the design of structural frames in Japan. Accurate determination of design wind loads relies heavily on our knowledge about winds. As an effort to contribute to a better understanding of the characteristics of natural winds, the authors of this paper have been conducting full-scale measurements of windspeeds and wind-induced vibrations on a steel communication tower located in a typical suburban area. Analyses were carried out to obtain the vertical profiles of the mean windspeed and the turbulence intensity based on the whole data. For particularly strong winds of a typhoon and a depression, turbulence scales, power spectra, spatial coherences and so on were also evaluated. Wind-induced vibrations of the communication tower will be presented in another opportunity and is not addressed here.

2   Observation Site and Instrumentation

The site for full-scale observation is located in a suburban area northwest of Tokyo. It is a flat terrain covered mostly by low-rise buildings dotted with farming fields and woods, as shown in Photo 1.

A schematic views of the communication tower on which the measurements were carried out is illustrated in Fig.1. Windspeeds and wind directions at four altitudes, i.e. 45m, 80m, 115m and 150m, were measured. Three-cup anemometers(Model AF860) plus directional vanes(Model VR236) and sonic anemometers(Model WA-200) were employed, and the details of instrumentation are presented in the figure.

3   Results and Discussions

Analyses are made on the records for three directions, NNW, S and SSE, in which the effects of the distortion by the tower itself are thought to be negligible.

An automatic data acquisition system was provided separately for the regular observation and the strong-wind observation. Recordings of mean values, standard deviation, and most

423

Photo 1 South veiw from the tower

Level 1(150m)
1 anemometer(3-cup type)
1 directional vane
3 accelerometers(x, y, θ)

Level 2 (115m)
1 anemometer(3-cup type)

Level 3 (80m)
1 anemometer(3-cup type)
1 directional vane
1 sonic anemometer
2 accelerometers(x, y)

Level 4 (45m)
1 anemometer(3-cup type)

accelerometers(x, y, θ)

N

23°   X

Y

3m

anemometer and
directional vane

(a) Plan view at level 1(150m)

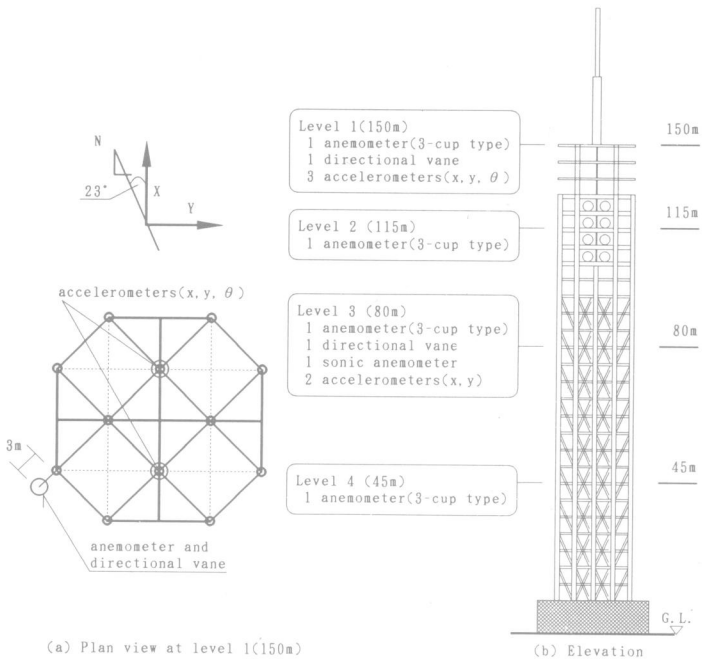150m

115m

80m

45m

G.L.

(b) Elevation

Fig.1 Schematic Views of the Tower and Instrumentations

frequent wind direction every 10 minutes were made for regular observation. For strong wind observation, turbulence scales, power spectral densities and coherence functions were analyzed.

3.1 Regular Observations

Through the use of the selected data obtained from June 15, 1990 through Oct. 11, 1991, mean wind speed and turbulence intensity were evaluated for each level.

About 3000 runs for the 3 azimuths were processed, and some statistics are outlined in Table 1. Results are based on those data with wind speed of 5 m/s or more and those of 10 m/s or more, respectively, at 80m measured with the sonic anemometer. Mean values and the coefficients of variation of both the windspeed ratio to the value at Level 1(150m) and the turbulence intensity at each level are listed in this table. Furthermore, power exponents were estimated utilizing the method of least squares, assuming that vertical profiles are represented by the power low.

Table 1 Windspeed Ratio and Turbulence Intensity

Windspeed Ratio

Height		$U_{80} \geq 5m/s$			$U_{80} \geq 10m/s$		
		NNW	S	SSE	NNW	S	SSE
150m	Mean Value	1.00	1.00	1.00	1.00	1.00	1.00
	C.O.V.(%)	—	—	—	—	—	—
115m	Mean Value	0.92	0.92	0.97	0.94	0.92	0.96
	C.O.V.(%)	7.2	5.8	5.5	4.2	4.2	2.9
80m	Mean Value	0.81	0.84	0.88	0.87	0.85	0.88
	C.O.V.(%)	14.1	10.1	9.2	7.1	6.3	5.5
45m	Mean Value	0.65	0.75	0.78	0.74	0.77	0.78
	C.O.V.(%)	22.8	16.6	15.5	10.3	9.5	8.9
Power Exponent α		0.36	0.24	0.22	0.25	0.21	0.21

Turbulence Intensity

Height		$U_{80} \geq 5m/s$			$U_{80} \geq 10m/s$		
		NNW	S	SSE	NNW	S	SSE
150m	Mean Value	10.8	10.7	10.7	12.9	12.0	11.7
	C.O.V.(%)	43.0	34.2	42.5	29.7	24.3	26.1
115m	Mean Value	12.7	12.4	12.0	14.9	13.5	13.0
	C.O.V.(%)	38.3	33.2	41.6	25.9	22.4	24.0
80m	Mean Value	14.7	14.0	13.7	17.0	15.1	15.0
	C.O.V.(%)	34.7	31.3	36.5	21.8	20.1	20.8
45m	Mean Value	18.5	17.0	16.7	19.9	17.6	17.5
	C.O.V.(%)	39.3	32.7	31.6	17.5	18.2	17.1
Number of Data		678	812	1230	266	349	437

*C.O.V.(%): Coefficient of variation

The variation of the power exponent, α, are plotted in Fig.2 for the three directions. Here, the data with a mean windspeed at 80m, U_{80}, not less than the value indicated by the abscissa were used to evaluate the value of α. It can be seen from this figure that there is only a slight change in α over the whole windspeed range for the S and SSE directions, while a remarkable variation is noticed for NNW at small U_{80}. For $U_{80} \geq 10m/s$, the power exponent for NNW is close to 0.2. This value can be considered appropriate, judging from the surface conditions at the site.

Figure.3 shows the vertical profiles of the mean windspeed ratio for the case $U_{80} \geq 10m/s$ together with $\pm$ one standard deviation. As shown in Table 1, the coefficient of variation becomes large toward lower altitude, for example, about 4% at 115m and 9% at 45m.

425

The vertical profiles of turbulence intensity I_u, for the data of $U_{80} \geq 10m/s$, are given in Fig.4. The turbulence intensity for NNW is larger than those for S and SSE, corresponding to the fact of having a larger value of the power exponent α for NNW.
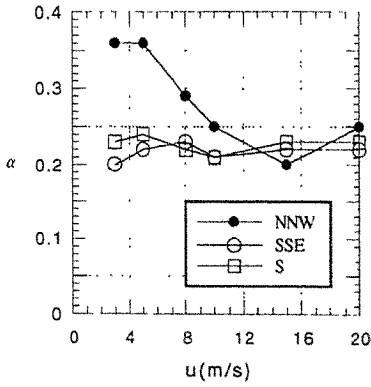

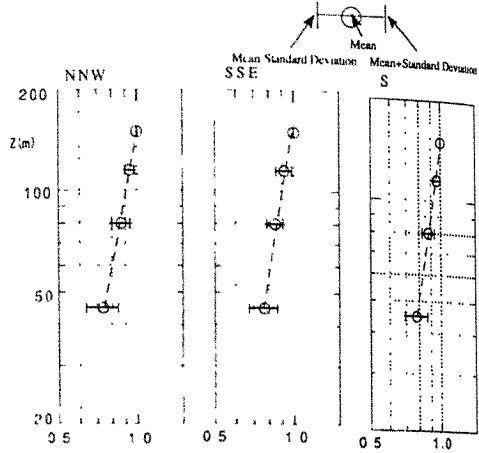Fig.2 Power-law exponent, α, versus lowest mean windspeed of the data used for evaluated of α

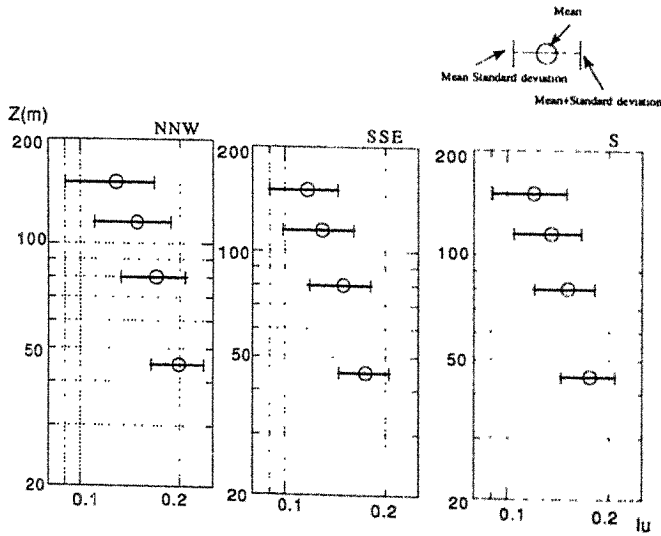Fig.3 Vertical profiles of mean windspeed ratio by regular observations ($U_{80} = 10m/s$)

Fig.4 Vertical profiles of turbulence intensity by regular observations
($U_L = 10m/s$)

426

3.2 Strong Wind Observations

Two storms were selected for the evaluation of turbulence scale, power spectral density and coherence function in addition to other statistics. One was typhoon 9011, on August 8, 1990, and another one was a depression, on Oct. 11, 1991. The SSE winds were recorded during the typhoon with a mean windspeed of 23m/s at 80m, while northerly winds with a mean windspeed of 15m/s were observed during the passage of the depression.

Six runs of 10-minute duration for the typhoon and 11 runs for a depression were analyzed in detail. Spectral analyses were also performed by using the AR method.

Figure 5 shows vertical profiles of the mean windspeed, turbulence intensity and the turbulence scale. The value of the power exponent $\alpha = 0.2$ approximates the observed mean windspeed profile fairly well. The turbulence intensity of the depression wind is smaller than that of the typhoon. Although the turbulence scale shows reasonable tendency of becoming small scale with the decrease of altitude, the variation above 80m is not significant. The turbulence scale of the typhoon is greater than that of the depression. The profile of those terms proposed in the AIJ Reccomendations for Wind Loads[1] corresponding to the terrain category with $\alpha =0.2$ are shown by dotted lives for reference.

Figure 6 shows the power spectra of the fluctuating windspeeds. Spectra at all measuring points for both the typhoon and the depression are represented by the Karman type spectrum model quite well.

Figure 7 shows the root coherence function, $\sqrt{Coh}$, of the fluctuating windspeeds. The abscissa is a non-dimensional frequency $n\Delta z/U$, in which Δz is the vertical distance between any two measuring point of wind speed and U is a reference mean windspeed. In the figure, approximate expression by

$$\sqrt{Coh} = exp(-kn\Delta z/U)$$

are also shown, where the value of decay constant k is set at 8 and 16. Except the cases with large separation, 150m-80m and 150m-45m, the spatial correlations of both the typhoon and the depression can be approximated by the above formula with acceptable accuracy if $k = 16$ is assumed.
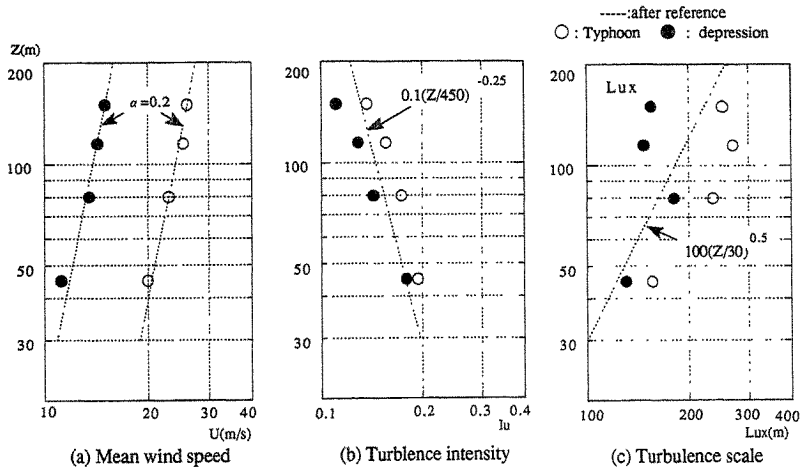
Fig.5 Vertical profiles of mean wind speed, turbulence intensity and turbulence scale by strong wind observations $(U_{80} = 10m/s)$

Fig.6 Power spectra of fluctuating windspeeds

O : 150m-115m , △ : 150m-80m , + : 150m-45m , × : 115m-80m , ◇ : 80m-45m
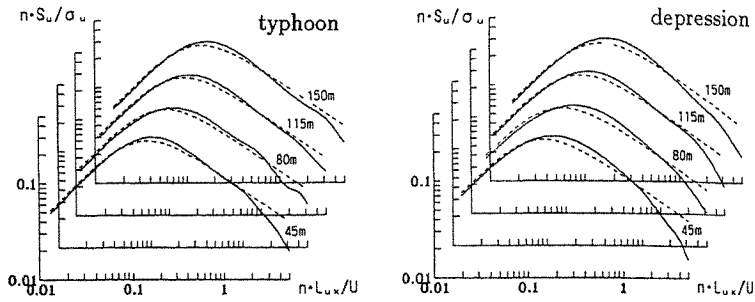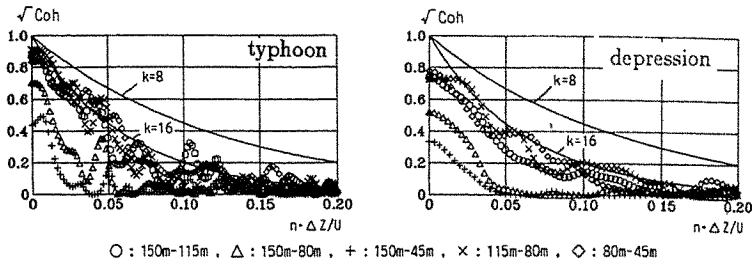
Fig.7 Spatial coherence function

4 Concluding Remarks

The foregoing discussion are summarizied as follows.

(1) The vertical distribution of the mean windspeed can well represented by the power law with an exponent of 0.2.
(2) The turbulence intensity at 80m is about 15%. The absolute turbulence intensity (standard deviation of fluctuating windspeeds) becomes small with the increase of the altitude.
(3) The turbulence scale at the lowest altitude showed the smallest value.
(4) Power spectra of fluctuating windspeeds are expressed by the Karman type spectrum model accurately.
(5) A decay constant of $k = 16$ is found to be proper for the spatial coherence for small Δz. The typhoon and depression have similar characteristics so far as the power spectrum and spatial coherence are concerned.

References

1) Architectural Institute of Japan : RECOMMENDATIONS FOR WIND LOADS ON BUILDINGS(in Japanese), 1993

An æolian geographical informative system for structural engineering: some results

Gianni Bartoli[*], Vittorio Gusella[**], Paolo Spinelli[*]

*Department of Civil Engineering
Università di Firenze, Firenze, Italy
**Institute of Energetic
Università di Perugia, Perugia, Italy

Abstract: The main characteristics and goals of the Æolian Geographical Informative System, ÆGIS, are briefly illustrated: the different modules composing the system, the methods used in data banks construction, the link with different data banks, the procedure to obtain the wind design, the influence of several parameters over this value, are depicted.
The application of the ÆGIS on the Tuscany Region is shown. The obtained results have permitted to estimate the design wind speed for this territory and to propose an "effective" roughness map of the same region. Moreover, a simplified procedure proposed as Italian Addendum to the EuroCode (EC1) recommendations is reported too [1].

1. Introduction

The correct definition of the wind characteristics over a given territory is often a difficult task. Instead of using detailed local analysis, in most of the usual cases a possible solution is represented by the definition of maps allowing to give the values of some of the necessary quantities, by means of automatic procedure capable to take into account several different factors. The utility of an æolian map could then be very large: it could be used for estimating pollutant diffusions as well as to design civil and industrial development plans, avoiding situations in which particular wind conditions could result worrying for some reasons. Moreover, the simplest utilisation is represented by the use of the map as a structural design tool; the designer could have a local information, deriving from a wider analysis, capable to exactly quantify the wind loads on a existing or designing structure.

The use of these maps is very relevant especially in those cases where a complex orographic situation exists, thus making very difficult the exact determination of the local wind characteristics; this situation is very frequent in Italy, often driving to an incorrect estimation of the wind loads to be used.

For this reason, an Informative system has been designed in order to define the correct wind characteristics on a given site, taking into account several factors.

The system (called Æolian Geographical Informative System, ÆGIS, [2]) is essentially a data bank related to territory, the geographical region is subdivided by a constant grid, typically 400×400 m^2, into several cells, thus obtaining a *raster* representation of the territory.

For each cell, several data are known, grouped into other rasters. These rasters mainly collect data about:

- the altitude above sea level (in m), used for the determination of the reference wind speed as a function of the altitude as well as for the estimation of local orographic (topographic) conditions;
- the roughness length, that is the mean "apparent" roughness length, estimated by means of the "soil use" map and the presence of buildings;
- possible directional factors, to take into account local peculiar characteristics modifying the estimated direction of the incoming wind;

reference wind velocity, evaluated over a given period of time (usually 10 minutes), at a given height (10 m above ground level) and for given terrain roughness characteristics (roughness length of about 3÷5 cm).

These data constitute the basis of the procedure for estimating, at pre-fixed heights, the wind properties; usually, both the mean and the gust velocity over a given time period, for each one of the incoming wind direction, are given as output of the procedure.

The ÆGIS has been used over all the Tuscany territory, in order to obtain its æolian map; moreover, the influence of several parameters on the design mean wind speed has been tested, and comparison between obtained and experimental results have been performed.

These results allowed us to propose some modifications to the EuroCode proposal [1], concerning the Italian map: a simplified procedure has then been suggested, based on the effective roughness length evaluated by means of ÆGIS and thus obtaining a subdivision of the territory into several homogenous roughness areas.

2. Utilised procedure

The determination of the wind speed is performed by means of the B.R.E. program StrongBlow [3]. The velocity on a site is given, starting from the reference wind velocity, by means of some multiplying coefficients, each of them taking into account different factors. The procedure mainly consists in the determination of homogeneous roughness areas, examined at different scales, for which the characteristics over a circle area of 200 km radius around the investigated site must be known.

For this reason, three different roughness maps have been built, arranged according three different scales (1:10,000; 1:100,000; 1:1,000,000), using a procedure consisting into the digitalization of such information in a vector form and then converting the obtained data in a raster form that can be utilised by the automatic procedure.

The first two have been obtained utilising the "soil use" map developed by the Tuscany Administration and converted into a raster form, setting an equivalence between soil use and roughness length. The 1:100,000 map has been built by a condensation of the previous one, and a new grid of 4000×4000 m^2 has been obtained. The 1:1,000,000 map has been built identifying homogeneous roughness areas (i.e. singling out flat areas, hills ones, mountain sites, large towns, and so on); the borders of these zones has been digitized and the obtained data has been converted from a vector format into a raster one.

Fig. 1 shows the "apparent" roughness length (i.e. the one derived from the "soil use" map) for Tuscany, with a raster grid of 400×400 m^2; in Fig. 2 the roughness length of the northern and central part of Italy (raster grid of 10×10 km^2). The roughness categories are those proposed by B.R.E. [4] (0 is the lowest one while 5 is the one possessing higher roughness length); the histogram on the left side of the figures reports the relative frequency of each category. The other raster maps utilised by ÆGIS has been obtained by similar procedures, according the same grids as those used before.

The main aspect of the program research has been to obtain a ÆGIS "architecture" that allows the program to be:

- *SPLITTED INTO DIFFERENT MODULES*, that is input data, their management and the elaboration must be performed by different parts of the system,
- *CAPABLE TO BE MODIFIED*, so allowing modifications of a single component (Data Bank, algorithms for wind design estimation, etc.), because of their improvement or natural variation (for example a change in the use of soil implies a change in the site roughness that influences the æolian characteristics of both the considered area and the neighbouring ones),
- *RELIABLE*, by means of comparison with statistical analysis of experimental data

430

EASILY AND PROPERLY USABLE, that is the user can obtain information which must be consistent with the actual load Code.
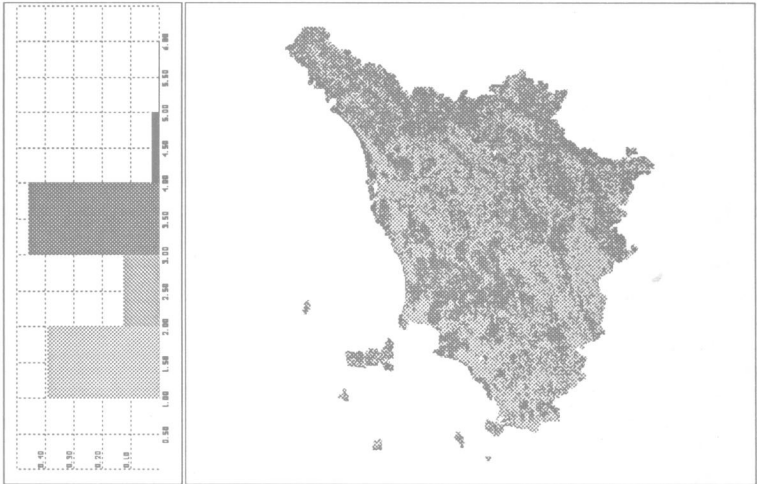

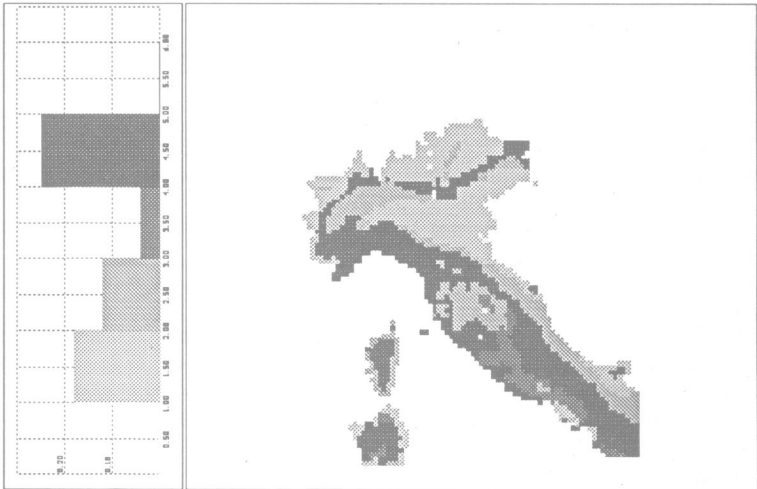Fig. 1: "Apparent" roughness length of Tuscany (B.R.E. roughness categories)

Fig. 2: "Apparent" roughness length of Northern and Central part of Italy
(B.R.E. roughness categories)

3. Comparison with experimental data

The global system reliability has been checked [5] by a comparison with 50-years return wind speed evaluated for four different sites (Firenze-Peretola, Siena, Grosseto and Pisa) and obtained from experimental data [6]. The results achieved from ÆGIS has been evaluated setting the reference wind velocity value equal to 26 m/s and imposing directional coefficients equal to one.

Apart from some differences between the experimental and the evaluated values (probably due to the choice of the reference wind speed), other disagreements have been pointed out referring to the direction from which the maximum wind comes. This fact is due to the presence of very peculiar situations (i.e. Firenze, where the local influence of the "Tramontana" wind, a very strong northern wind, is not predictable only using the adopted parameters); these macro-meteorological aspects, have then been taken into account by the program by means of some changes in the directional co-efficients, letting them play the role of local correction besides their statistic properties [4].

From the performed analyses, two different directional coefficient sets could be pointed out, the first one valid for coastal areas and the second for internal ones, obtained by an averaging procedure between the available data.

Further studies are ongoing in order to better understand and estimate this directional factors, considering more experimental data.

4. Determination of the "effective" roughness length

The results reported in the previous paragraphs (obtained by means of ÆGIS procedure and shown for the particular case of Tuscany Region) have been utilised for the determination of the "effective" roughness length. The map has been built evaluating, for each cell of the grid, the design mean wind speed at 10 m height with a return period of 50 years, using the same reference velocity as the one proposed in EC1 (that is 26 m/s) and neglecting both the topographic and the altitude effects.

An effective roughness length has been assigned to every cell, finding out which should have been the equivalent roughness category to obtain (by means of the EC1 procedures) the same design wind speed. In other words, considering this effective terrain category, the design wind speed value obtained by ÆGIS can be recovered using the EC1 recommendations; topographic as well as altitude effects are not taken into account and so they must be added up Figure 3 shows this map, where the category subdivision is the same as the EC1 proposal.

5. The Italian Addendum to the EC1 proposal

Starting from the results previously described, a procedure to determine roughness category estimation has been proposed. Considering the histogram of the relative frequency of terrain category (see Fig. 3), it can be observed that most part of the territory lies between second and third category, with the exception of sites near to the sea.

The choice of a second category for all the territory can then be considered as a conservative one, thus avoiding the errors related to an incorrect decision about the terrain category, that could lead to strong errors in the evaluation of wind loading. For sites near to the sea, a category one can be assigned if the distance from the coast is lower than 10-15 km, as it can be seen from Fig. 3.

Urban and suburban areas must be considered in a different way and a detailed study has been performed. As a matter of facts, by means of ÆGIS, several conditions has been considered: an "ideal" urban site has been modelled, composed by a central part with higher category (IV), a suburban area possessing roughness characteristics of a third category, external areas having a II category roughness length. In order to avoid directional effects, this model possess a radial symmetry, and the mean wind speed in the centre of the urban areas has been evaluated Several tests have been performed varying the extension of both the urban and the suburban area, and considering possible conditions near to the sea, to which a I roughness category has been referred

432
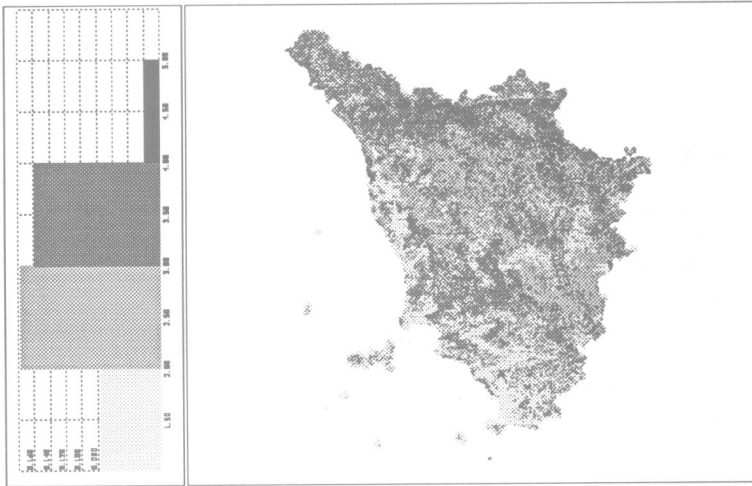
Fig. 3: "Effective" roughness length of Tuscany (EC1 roughness categories)

The results have been plotted and it has been pointed out that the centre of the site could possess IV category characteristics only if it is distant more than 50 km from the sea and the urban plus suburban area is wider than 6 km. On the contrary, for the centre of very small towns (extension of about 1 km^2) near to the sea (less than 15 km), a II roughness category seems to be adequate. All the other urban cases, are covered by the III roughness category.

The obtained results have been checked and then extended to all the Italian territory; finally, the reference category reported in Table 1 has been proposed, unless specific and detailed analyses are performed.

6. Conclusions

The research program developed in these last years allowed us to set an Æolian Geographical Informative System, ÆGIS, that can be easily utilised in order to properly define the design wind speed at a given site, to be used for structural applications. Some comparisons with experimental data have tested the reliability of the system.

The use of ÆGIS permitted to build the effective roughness length map of the Tuscany Region. This map constitutes the base of the Italian proposal for a simplified procedure to be introduced as an addendum to the EC1.

ÆGIS represents a system that can be part of wider territorial systems, and so it can be a very important tool in the correct definition of territorial managing programs.

Site exposure	Minimum distance d (km) of site from sea coast		
	d≤15	15<d≤50	d>50
A Urban areas in which at least 15% of the surface is covered with buildings and their height exceeds 15 m This exposure applies to sites surrounded by the above terrain in every direction for at least 6 km	III	III	IV
B Urban, suburban or industrial areas and permanent forests. This exposure applies to sites surrounded by the above terrain in every direction for at least 1 km	II	II	III
C All other situations	II Along Liguria and Eastern Sardegna coast I In all other sites	II	II

Table 1 - Equivalent terrain categories

References:

1. Eurocode n. 1 , Basic of design and actions on structures, CEN, Brussels, Belgium, 1993 (draft version)

2. Gusella, V., Spinelli, P , Bartoli, G. An Æolian Geographical Informative System for civil engineering, Journal of Wind Engineering and Industrial Aerodynamics, 1992, vol 41-44, 497-506

3. Cook, N.J., The designer's guide to wind loading of building structures, Part 2, Program STRONGBLOW, B R E , Butterworths, London, 1985

4. Cook, N.J , The designer's guide to wind loading of building structures, Part 1, B R E , Butterworths, London, 1985

5. Biagioli, F., Sistema informativo territoriale eolico studio degli aspetti teorici e realizzazione di un codice automatico di calcolo, Thesis, Univ of Florence, Faculty of Engrg , Firenze, Italy, 1993

6. Aminti, P.L., Borri, A , Spinelli, P., Azioni del vento sulle strutture elaborazioni statistiche relative a stazioni anemometriche della Toscana, Dipartimento di Ingegneria Civile, Università di Firenze, UFIST 17/83, 1983

SODAR -A Useful Remote Sounder to Measure
Wind and Turbulence

S. Vogt and P. Thomas

Institut für Meteorologie und Klimaforschung
Kernforschungszentrum/Universität Karlsruhe
Postfach 3640, D-76021 Karlsruhe
Germany

1. Introduction

The SODAR is a ground-based remote sensor for the detection of vertical profiles of wind and turbulence data. The advantages of this technique compared with in-situ measurements at meteorological towers are:
- easy to install,
- mobile,
- commercially available,
- operates unattended for long periods,
- low prime cost and very low running cost,
- maximum range up to 1 km,
- good range resolution 10 - 100 m,
- measurements are spatial averages over volumes (appropriate for modelling).

In 1981 the VGB (German acronym for Association of Operators of Large Power Plants) charged our institute with the testing of Doppler SODAR systems. The systems were to be compared with in-situ sensors mounted on a 200 m high meteorological tower.

Since that time we have tested three different Doppler SODAR:
- DS 108 manufactured by Rosenhagen, operated in 1982.
- A0   manufactured by Remtech, operated since 1983 up to 1990.
- PA2   manufactured by Remtech, operated since 1990.

During this time a tremendous amount of data has been compiled in order to compare wind and turbulence data of SODAR and in-situ instruments, and to study various meteorological phenomena.

2. SODAR technique

An informative survey of this topic can be found in [1].

2.1 Measuring Principle

A SODAR emits short pulses of acoustic waves ($\lambda = 21$ cm) as a collimated beam into the atmosphere. A small fraction of the transmitted energy is backscattered by inhomogenities of the refractive index of the air generated by turbulent fluctuations and by differences in humidity and temperature of the air (clear air turbulence). Due to the Doppler effect the frequency of the backscattered signal is shifted, if the scatterer is in motion. The backscattered signals are received and processed in such a manner that the Doppler spectrum (frequency spectrum) is obtained by means of Fast Fourier Transform. From the Doppler spectrum the component of the wind velocity in the direction of the transmitted energy is determined. The running time of the transmitted and backscattered signal determines the height of measurement at up to 30 levels yielding a vertical profile.

2.2 Types of SODAR

As the wind vector is 3-dimensional, 3 antennas with different orientations are used. In case of the DS 108 and the A0 the three beam directions are achieved by 3 antennas mounted in a fixed position on a trailer (Fig. 1). The big funnel shaped tubes are acting as shielding against environmental noise contaminations and also to suppress side-lobes of the acoustic beam.
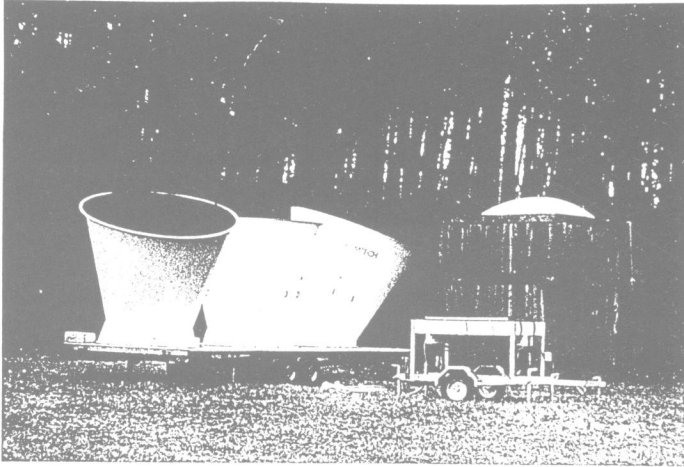
Fig. 1 Phased array SODAR PA2 (right hand side) and the SODAR A0 (left hand side).

The antenna configuration of the PA2-SODAR is much smaller. Here the different beam directions are produced by a phased array antenna field. 196 tweeters (electro acoustic elements) are mounted in 14 rows and 14 columns in a horizontal plane. The beam steering is achieved by applying signals with incremental phase shifts to successive rows or columns.

The major advantages of this new type of antenna are:
- The antenna trailer is small in dimension and weight and therefore suitable in terms of transportation and siting.
- The emitted power is increased significantly, although each tweeter has a relatively low power level.
- No antenna enclosure is needed due to the tapering of the amplitude towards the periphery of the array.

3. Availability of SODAR Data

The availability of SODAR data as a function of height depends on:
- the performance of the SODAR,
- meteorological conditions (availability of inhomogeneities of the refractive index of the air with the appropriate length scale),
- site conditions (ambient noise, fixed echos).

The availability of wind speed measured by the SODAR PA2 and A0 is plotted as a function of the height in Fig. 2.

The height range is most affected by the sampling time: The 50 % values can differ by about 220 m between 10 min and 30 min sampling time. Also the wind speed has a pronounced effect on the availability. But the influence of the power output on the

436

Fig. 2 Height of the two SODAR systems PA2 (---) and A0 (——) as a function of wind speed
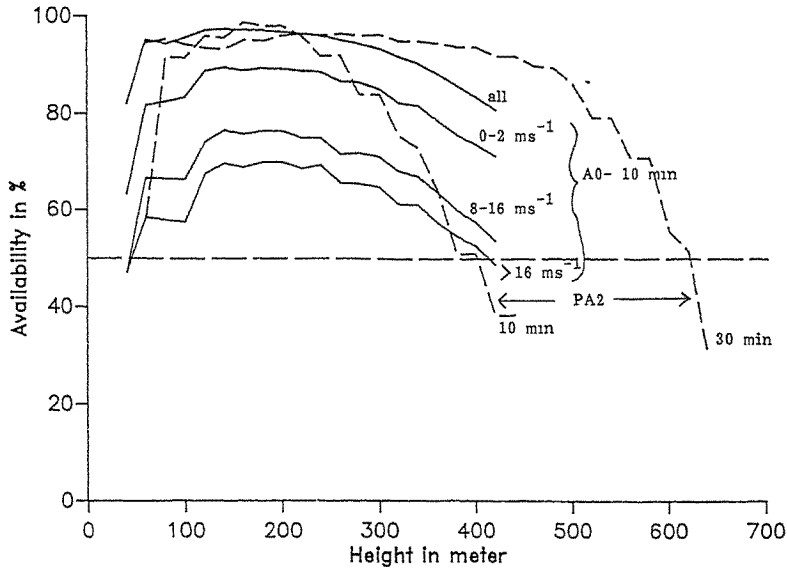and sampling time (10 min, 30 min means sampling time of SODAR; 0-2, 8-16,
> 16 ms^{-1} means: only these wind speeds are taken into account)

availability is small. As a rule of thumb we found a height reduction of only 100 to
150 m for the 50 % value of availability when reducing the power output by at least
12 dB.

4. Intercomparison of SODAR and Tower Instruments

4.1 Tower instruments and site description

The KfK-tower data were used as ground truth to provide reference data. The
200 m tower is equipped with instruments at 10 levels. These instruments are cup-
anemometers, temperature sensors, wind vanes and vector vanes. All tower data are
stored continuously as 10-min mean values on a routine basis. Additionally during the
months from June to September 1990 a sonic anemometer was mounted at the 100 m
level of the tower.

The local topography is roughly flat. All the SODAR were located about 200 m
north of the tower on a meadow. For more information about instrumentation and loca-
tion see /2/.

4.2 Comparison on a statistical basis

The following data measured by the SODAR and at the tower were compared:
- Wind speed u and wind direction θ at 40 m, 60 m, 80 m, 100 m, 160 m and
  200 m above ground level (AGL).
- Standard deviation σ_w of the vertical wind at the levels of 40 m, 100 m and
  160 m AGL. At the tower, σ_w is measured by vector vanes and in 1990 by a son-
  ic anemometer at 100 m AGL.
- Spectra of the vertical wind speed w at 100 m AGL during some intensive mea-
  suring periods.

437

Details of the procedure of the intercomparison can be found in /2/. The most important results are given in Tabs. 1 to 3, where

— N ist the number of used data couples,
— $\bar{Y}$ is the mean value of all SODAR data,
— rel. BIAS is the mean difference between tower and SODAR data normalized to the mean value of all tower data,
— rel. Precision is the root mean square difference of all data couples corrected for the BIAS and normalized to the mean value of all tower data,
— R is the correlation coefficient.

Level in m AGL	40	60	80	100	160	200
N	8541	10005	9889	10048	9984	9597
$\bar{Y}$ in ms^{-1}	2.43	3.38	4.09	4.62	5.17	5.69
rel. BIAS in %	-21.4	-11.8	-4.9	-1.9	-10.4	-11.1
rel. Precision in %	32.5	25.4	21.2	19.7	15.9	15.2
R	0.75	0.86	0.91	0.93	0.96	0.96

Tab. 1 Linear regression of SODAR-A0 vs tower wind speed as a function of different height levels.

Level in m AGL	80	100	160	200
N	1917	1912	2064	2048
$\bar{Y}$ in ms^{-1}	3.26	3.31	3.95	4 34
rel. BIAS in %	-6.9	-14.0	-14.3	-13.4
rel. Precision in %	24.6	19.7	15.0	15.0
R	0.92	0.94	0.97	0.97

Tab. 2 Linear regression of SODAR-PA2 vs tower wind speed as a function of different height levels.

Level in m AGL	A0-vector vane			A0 - sonic
	40	100	160	100
N	9146	8801	9249	1509
$\bar{Y}$ in ms^{-1}	54	42	40	58
rel. BIAS in %	-46.3	-33.3	-30.0	-18.9
rel. Precision in %	59.3	50.0	47.5	31.0
R	0.62	0.83	0.85	0.82

Tab. 3 Standard deviation of vertical wind speed σ_w measured by tower instruments and SODAR A0.

More details and a discussion of the results are given in /2/, /3/ and /4/. In summary the following conclusions can be drawn:

- In case of the wind speed both systems are measuring the horizontal wind speed with an excellent reliability and accuracy.
- The standard deviation σ_w of the vertical component w of the wind vector can be measured by a SODAR. Although the SODAR derived σ_w should be taken at heights not affected by the influence of the surface roughness.

A SODAR is also capable to estimate spectra of the vertical wind speed as our intercomparison of a sonic anemometer and the SODAR A0 showed [2]. This allows more insight in the turbulence of the bounday layer although the SODAR has its special limitations at high frequencies (~ 0.1 Hz). However, because the peak in the spectra moves to lower frequencies at increasing heights and because the SODAR operates at relatively large heights, the derived velocities apparently do reach into the inertial subrange, particularly in instable, convective conditions.

5. Special Applications

Our long-term intercomparisons of SODAR and in-situ instruments showed that the reliability and accuracy of wind vector and special turbulence parameter measured by a SODAR is generally good. Consequently we have used the SODAR in several field campaigns dealing with boundary layer investigations, problems of orographic flow systems or turbulence experiments over complex terrain. Fig. 3 shows as an example of a very pronounced shift in wind direction starting from ground level and moving up to 640 m AGL within 4 h. Here the SODAR was located in complex terrain at a mountain top.
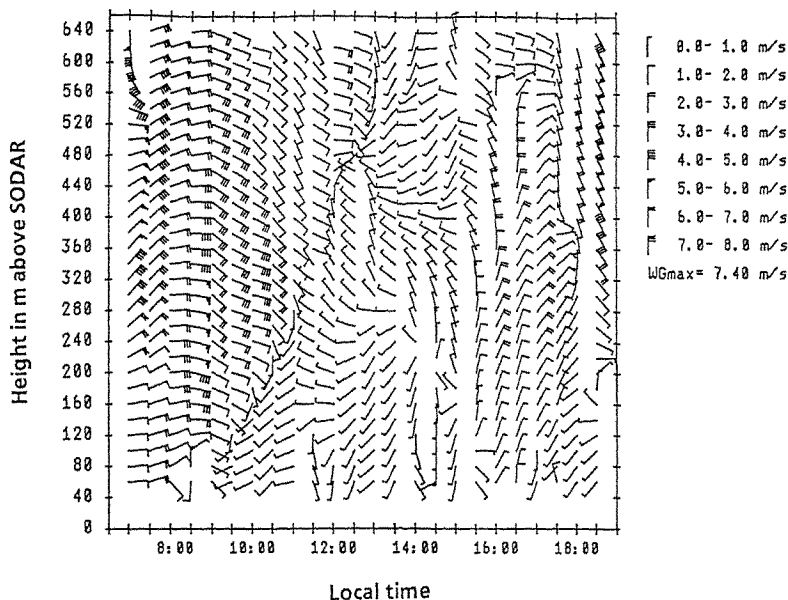
Fig. 3 Time-height cross section of the horizontal wind measured on February 7, 1992 (0.5 h mean values, wind barbs are flying with the wind).

6. Conclusion

From our experience with several SODAR systems and based on the results presented so far we believe the SODAR to be a valuable tool to monitor not only the wind field on a routine base but also to study special meteorological phenomena. Moreover a Doppler SODAR gives unique insights in nonstationary three dimensional processes as for example organized convection or flow patterns in complex terrain, and will be a valuable instrument to investigate wind effects on buildings and other manmade structures and to study problems connected with the use of wind power.

References

1. D. H. Lenschow. Probing the Atmospheric Boundary Layer, A.M.S. Boston (1984).
2. P. Thomas, S. Vogt. Variances of the Vertical and Horizontal Wind Measured by Tower Instruments and SODAR. To be published in Appl. Phys. B56 (1993).
3. P. Thomas, S. Vogt. Measurements of Wind Data by Doppler SODAR and Tower Instruments: An Intercomparison. Met. Rdsch. 42, No. 3-5 (1990).
4. S. Vogt, P. Thomas. Test of a Phased Array SODAR by Intercomparison with Tower Data. To be published in J. of Atmos. and Ocean. Techn. (1994).

Research on the Characters of Land—Sea Breeze
and Environmental Planning

Lin Kongguang

Fujian Provincial Institute for Science of Environmental Protection
Hualin Road Fuzhou, Fujian,   China

Abstract: This paper is based on the climate data around Meizhou Bay both in the past several years and being obtained resently by large scale observations, The study can provide characteristics of wind field and land—sea breeze in atmospheric boundary layer, find no close of the circulation of land—sea breeze and that thermel internal boundary layer in sea breeze would appear. It is an important basis for research on environmental planning and appropriate distribution of industries in local area.

1. Introduction

Lying on the middle of coastal area in Fujian and being opposite to Taiwan province accross the channel, Meizhou Bay is an under—development zone with a fine barbor. Also it is an ideal tourism area with the world— famous Mazu Temple. According to the land—planning, Meizhou Bay will be devoleped as an industrinal base with barbor as well as a tourism area. Research on meterological characters of atmosphere boundary layer and regularities of conveyance and diffusion in atmosphere,which can offer an important basise no the enviromental planning, both economic development and environmental protection is the main objects of the paper

As a result of effects of the mountain of northeast—southwest on the middle of both fujian and Taiwan, thus, great wind speed is available (channel effect), Air current is in the direction of NE or SW in lower atmosphere layer. Direction of System current is by N in winter,and mainly NE in coastal area , because of SW monsoon wind in summer, system current is by S wind, SW wind in this area. As seen, capacity of atmospheric conveyance and dilution are very sthong on coast of Meizhou Bay. As the impact of ocean bringing about process of land—sea breeze, Ability of atmosphere conveyance in coastal areas may be limited. That being so, Research should involve main contents of land—sea breezeof atmosphere boundary layer on coastal area.

2. Research methods

Based on the hourly information about wind direction, wind speed and local cloud situation,Which has been obtained from 4—years obsertation and monitoring by meteorological

station in XiuYu. The number of the days with representative month and characteristics of sea—land breeze within can be counted considesing daily weather situation.Beyond this, 15 observational sites for wind and temperature near ground were also established in local areas during 1988—1989 to gain the hourly data about wind, temperature, cover of cloud and sea water temperature in 4 represeataion months to analyse when land—sea breeze occurs or disppears and changes and characteristics of level wind field, Besides, 6 stations of observation have been set up to measure the low—atomasphere wind and temperature for 15 days in both winter and summer(see fig. 1), three out of six can make up to be a vertical cross—section coordination wind field neer ground and weather situation, We can study the wind field, and temperature field within atomophere boudary layer, stucture and influent range of land— sea breeze and possibility of appearance of thermal internal boundary layer.

Fig 1. disposition of meteorological observing point

★ — sounding point of the atmosphere

• — observing point of surface wind

1 — Meizhoudao	2 — Weijia
3 — Zhongmen	4 — Yiuyu
5 — Hushi	6 — Lingchuan
7 — Fengting	8 — Tuling
9 — Waicuo	10 — Shanyiang
11 — Jingyou	12 — Putian
13 — Xianyou	14 — Chongwu
15 — Jinjiang	

   Statistic methods for land—sea breeze: The days of characteristis of land—sea breeze must meet the following :

   (1) Wind speed near ground is less than 8 (m / s) whole day

   (2) Daily change of wind direction is obvious, that is: Land wind will change into sea wind during day time, contrariwise at night.

   (3) After changing into sea wind during day time, It will last for 3—hours

   (4) Hourly cover of low—cloud less than eight—tenth from 6 o'clock to 18 o'clock.

   (5) Influence of weather systems must be taken out.

   Statistic methods for average direction and velocity of land—sea breeze:

   wind vactor of sea—wind: $Va = (\sum Vai) / Na$

   wind vactor of land—wind: $Vl = (\sum Vli) / Nl$

where: Va, Vl — average vactor of sea—wind and land—wind

        Vai, Vli— vactor of sea—wind and land—wind at certain time

        Na, Nl — vactor number of sea—wind and land—wind

   Research on the characters of land—sea breeze: Analysing through datas of sounding for typical land—sea breeze,refering to wind near ground, weawher situation, and change of wind,

temperature, poteneial temperature by time and space, especially analysing change of land—sea breeze on vertical cross—section. Research on the character of wind field of atmosphere boundary layer and posibility of occurrence of thermal internal bounadry layer in land—sea breeze.

According to meteoyological characters of atmosphere boundary layer, especially the characters of land—sea breeze, we can reveal the capacity for conveyance and diffusing capacity for atmosphere and pave the bases of environmental planning and industrinal distribution on thr zone.

3. The characteristics of land—sea breeze

Emergence freguency of land—sea breeze is hight in this area. According to the analysis of the four representative months data in the past several years, the frequeney is the highest in Junly(summer) in which monthly average wind speed is the fastest, direction of sea wind often is SSE, and direction of land wind often is NW, while the freguency is the lowest in Jannury(winter), (see tab.1). Some of the flow fields caused by the thermal balences between land and sea just show that air current run to in—land in local area after midday, and the remaining time is shorter, but some show that typical land—sea circulations form in regional area and converse in day and night . About 30‰ are typical circulations in summer, and April is sencondly. In autumn and winter , airflow controlled by large scale weather system is strong, so land—sea circulation seldom emerges(see Table 1). But atmospheric circulation topogration may be seriously different in different years.

month	sea wind			land wind		
	frequency (%)	speed (m / s)	direction	frequency (%)	speed (m / s)	direction
一	17.8	2.3	SSE	12.9	1.7	NNW
四	23.3	2.3	SSE	17.9	1.4	NNW
七	59.8	3.8	SSE	27.5	2.1	NW
十	19.4	3.6	SE	17.7	2.0	NNW

Table 1. Mean of the land—sea breeze

Sea breeze often occurs round midday in the area, nine to twelve o'clock in summer, twelve to fourteen o'clock in other seasons, and it is usually the most vigorous round 15 o'clock. Sea wind after vanishes in the period between 17 to 21 o'clock, changing with the different seasons and weather conditions. The remaining time of sea breeze is short in winter. No matter what season it is, sea breeze usually emergences after midday and before dusk.

In the area, sea breeze often comes from E to S, and the most direction is SEE. Directions

of land breeze are W to N, and the most one is NNW. It is calm or genthe in conversion inter-
val of land—sea breeze, and the remaining time is about 1—2 hours and different with the
weather systems. It is unfavorable for atmosphere contaminations to transport in calm or gen-
tle condition. So this makes it easy to occur air pollution in local area.

By analyzing the wind and temperature fields data of low altitude of typical land—sea
breeze, it is found that land and sea breezes do not form a close circulation, and just march in
a spiral circle. when strong sea wind moving to inland, the air mass is heated by ground and a
thermal interval boundary layer will form in the air.

The height of the layer increases with distance into land. Air mass in the thermal interval
boundary layer is extremely unstable, so air contaminations in it will diffuse downto ground,
and a fumigation phenomenon may apperence.

In day of typical land—sea breeze, near gound inversion is not obvious at nightfall.

In summer, land—sea breeze may emergence in the day when weather system is effected by
the east airflow from south of the subtropic high, or in the fine day when hight altitude is ef-
fected by north—west air currence and feeble cold air has just passed in low altitude. In winter
land—sea breeze may occur in the condition controlled by feable weather system.

4. Individual analysis

On July 27,1988, a weak cold air came across the area,and in high altitude was
north—west currence, It was a fine and party cloudy day. Effected by cold air, air temperature
was low. In daytime, heated by sunlight, air temperature up land increase fast while there is
little change of temperature in sea surface as the thermal capacity of seawater is large. The
balences of land. and sea became more severe because of the turbulence transport. Then air in
boundary layer became baroclinic and formed a large scale land—sea circulation. As showed
on cross—section diagram of low alfitude perpendicular to coastline (see figure 2). Fengwei lies
near seabank, Guocuo is 3.5 km far away from seabank, and Tuling is 14 km.
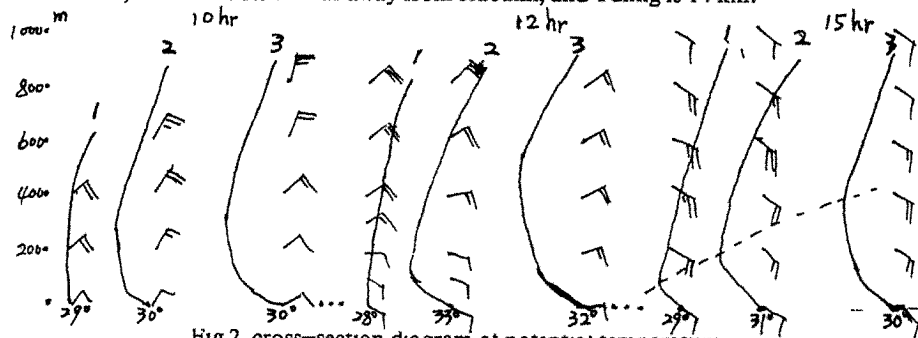

Fig 2. cross—section diagram of potential temperature

1 — Fengwei   2 — Guocuo   3 — Tuling

The potential temperature curve of 10 A.M. indicated that height of over adiabatic layer

444

was about 300 meters at Guocuo. And Tuling (see figure 2). Sea breeze began to run round 11 A.M. Wind direction near ground layer turned to south—east or east—leaning. From chart 2, we knew that, at 12 A.M., greater part of the ground layer under 300 meters turned to sea breeze from fengwei to Tuling. Effected by cold sea breeze, air layer near ground became stable at that time at Fengwei. Also for the reason, a 100 meters high over adiabatic layer reestablished at GuoCuo. But over adiabatic layer at Tuling had not effected still at that moment. Sea breeze was the most vigorous at time about 15 o'clock. Then under 1000 meters in the area was south—east airflow. It indicated that low layer had been obstained by air mass from sea. A mixed layer which was 80 meters thick built at Fengwei, while at Guocuo mixed layer developed from 100 meters at 12 A.M. up to 170 meters that time. But mixed layer at Tuling decreased from 500 meters downto 400 meters.

The mixed layer set up in sea air mass increased at its thickness along into the land. That was just thermal internal boundary layer caused by sea breeze. The contaminations entered it would diffuse down tapidly and produce a fumigation phenomenon.

5. Enivronmental planning and industrinal distribution

It is certaintly and inevitable that economic development should be accompanied with a particular pressure to envoronmental system. Coastal areas of Meizhou Bay is being devoloped. Reseanable environment planning and distribution of industrics is a most important factor for the solution of the contradiction between the economic devolopment and quality of atmospheric environment. Research on the meterrological character of atmosphere boundary layer and ability to air dispersion and self—clearning is an important basis for environmental planning and distribution of industries.

According to the studies above, the wind is strong in the areas of Meizhou Bay. Especially in close to coastal aera, northeast wind prevail in Winter, but in Summer, Southwest wind becomes dominating. To sum up, power of atmosphere conveyance and dilution is strongs in coastal areas. The industries which will release lots of air pollutant can be located in this areas. In addition, a characteristic weather process—Land—Sea Brcege which does exist along coastal areas, and all that probally resultes in a thermal internal boundary layer within the Sea—wind systems. Refering to the enviromental falculties, MeiZhou Island will become a tourism area. To conclude these, following opinious should be proposed on the industrinal distribution and environmental planning of development.

(1) Some kinds of industries which will led to heavies air pollution, such as power plants of flame force. Should be settlea close to coast to make a convenience for dispersion and reduce air pollution.

(2) Big jump of sources of air pollution should not be arranged on the line in accord with the direction of prevailing wind in order to avoid pollutant superimposition.

(3) Considering the Mei Zhou Island being a tourism site, Don't put where should make sources of air pollution in the direction of its windward or the region probably inffuence. Pay attention to environmental scent about.

(4) Because of the existance of little wind and static wind, which occurs during the alteration of Land—Sea Breeze and cause contamination integraty in near by sources, which brings about local pollution easly. Industrinal pollutant sources should be located to avoid the concentration of sources of ground and low emission. Emission amount of pollutant Must be controted strictly .

(5) Although the circulation of Lond—Sea Breege usually isn't enclosed. It is possible for pollutant to come back with the wind. This problem should be seriously taken notice of.

(6) Sea wind can intrude from the southern of this areas into inland and cause a thermal internal boundary layer because the sufficient mixing of pollutant within it could result in superimposition. It must be consider that the sources of air pollution among the south coast of Meizhou Bay would generate pottutant Superimposition to downwind areas.

The suggestions above will take a positive role in protection of atmospheric environmente of Meizhou Bay and the guidences to industrinal distribution in developing region as well as environmental planning.

References:

[1] Slade.D.H.(Ed). Meteorology and Atmic Energy, U.S.Atomic Energy Commission, Div. Tech. Inf. (1968).

[2] Li ZhongKai.Pan Yunxian.Shun Runqiao. Principle and app;ication of Meteorlogy on air pollution. Publishedby Meteorological Society, (1985).

A study on the characteristics of steady mountain wind

Y.M.Li, M.Lai, X.L.Wang and J.H.Wang

Department of Civil Engineering
Chongqing Inst. of Arch. and Engg.,China

Abstract:This paper studies the characteristics of steady mountain wind depending on the wind historical of ten mereorological observation stations in the south of Sichuan Province in China. The results of model identification show that the conversion relations between different wind velocities agree with linear model, so the paper regresses 8 conversion relations using the Least Square Method. The paper establishes and compares Extremum I–type and Pearson I–type distribution of annual maximum wind velocity for 10 groups of data. The results of statistical hypothesis inspection indicate that the Extremum I–type model reflcets the probabilitical construction of steady mountain wind better than other models. Those results provide a foundation for thorough study on the characteristics of steady wind and for the wind resistant structural design in mountainous areas.

1. Introduction

The formation of wind is greatly influenced by geographical features position, landforms and topography. The complicated topographical features and landforms cause that the characteristics of wind in mountainous areas is very distinct from that in coastal areas or in plain areas. Studies of the characteristics of mountain wind have been noticed because of the wind disasters are increasingly more serious. Because of the restrictions of subjective and objective conditions, varied methods are used to record the wind velocity in different meteorological obserbation stations, so it is essential to establish the conversion relations between wind velocities under standard conditions and the others. Calculating the basic wind velocity and pressure by probabilitical method is the basis to determine the wind action on structures, so the probability model of annual maximum wind velocity should also be researched. The results on that two aspects, which have been generally obtained from wind data in coastal and plain areas, do not suit well to the characteristics of wind in mountainous areas. So based on a great number of historical data of wind velocity which were collected from 10 meteorological observation stations in the south of Sichuan Province in China, this paper studies the characteristics of steady mountain wind.

2. Conversion Relations Between Different Velocities of Steady Mountain Wind in Sichuan Province

The south of Sichuan Province has suffered from several times wind disasters in the past few years. The paper collected a great number of historical wind data of 10 meteorological observation stations at some representative cities, such as Luzhou, Zigong and Chongqing of Sichuan Province. Because there are few automatically–recorded wind velocity data before 1980 in most observation stations, the paper studies the conversion between each two different observating times and time–distance, including automatically–recorded 10–minute average velocity $\overline{V}_{(10)}$, automatically–recorded 10–minute maximum average velocity

$\overline{V}_{(10)max}$, 4–time one day 2–minute average velocity $\overline{V}_{(F4)}$, 4–time one day 2–minute maximum average velocity $\overline{V}_{(F4)max}$, 24–time one day 2–minute average velocity $\overline{V}_{(F24)}$ and instantaneous velocity V_s.

The Compound Form Optimization Method of parameter identification technique is used to identify the mathematical models of those relations according to 1582 groups of data. The same conclusion has been reached, as that of other researches in the world, that is, the relations agree with linear models[1]. So the conversions are regressed by the Least Square Method as

$$\overline{V}_{(F24)} = 0.8906\overline{V}_{(F4)} + 0.2864 \tag{1}$$

$$\overline{V}_{(F24)} = 1.0651\overline{V}_{(10)} - 0.0279 \tag{2}$$

$$\overline{V}_{(F24)} = 0.3303\overline{V}_{(10)max} + 0.3712 \tag{3}$$

$$\overline{V}_{(F4)} = 0.9755\overline{V}_{(10)} + 0.1426 \tag{4}$$

$$\overline{V}_{(F4)} = 0.3028\overline{V}_{(10)max} + 0.5069 \tag{5}$$

$$\overline{V}_{(10)max} = 2.0032\overline{V}_{(10)} + 0.6771 \tag{6}$$

$$V_s = 0.9491\overline{V}_{(10)max} - 1.6268 \tag{7}$$

$$V_s = 0.8266\overline{V}_{(F4)max} + 8.4507 \tag{8}$$

Owing to the limitation of paper space, only the comparision between formula (2) and 1318 observational points are given, as shown in Fig.1 .

3. Probabilitical Model of Steady Mountain Wind in the South of Sichuan Province

The basic wind velocity or wind presure, needed in wind resistant structural design, should be obtained from probabilitical distribution of annual maximum wind velocity. Most scholars think that the distribution obeys Extremum I–type distribution, but some have different views. China's Code on Structural Loads GBJ9–87 has changed Pearson III –type to Extremum I–type, and American code selects Extremum II –type as the distribution model of annual maximum wind velocity[1,3]. Scholars have defferent opinions especially with the probabilitical model of steady mountain wind. Based on historical wind data in the past 20 to 30 years from the 10 meteorological observation stations, the paper discusses the

Fig.1 Formula (2) and practical points

probabilitical structure of steady mountain wind in the south of Sichuan Province by using Extremum I–type and Pearson models[2].

Having calculated initial parameters of the 10 groups of datum, it can be determined preliminarily that Extremum I–type can be established for all the 10 groups, furthermore, 5
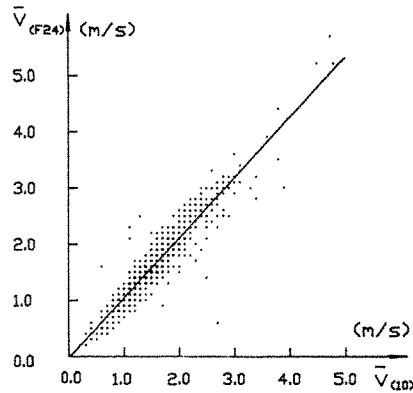
448

groups can be modelled with Pearson I–type models and 4 groups can be simulated with Pearson IV –type models. Considering suitability, only Extremum I–type and Pearson I–type models are established for the 10 groups of datum, as shown in Fig.2 to Fig.11.
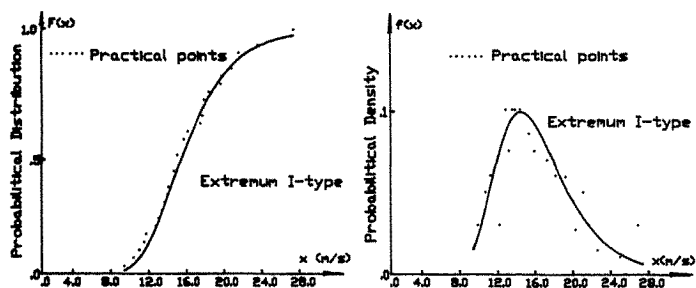

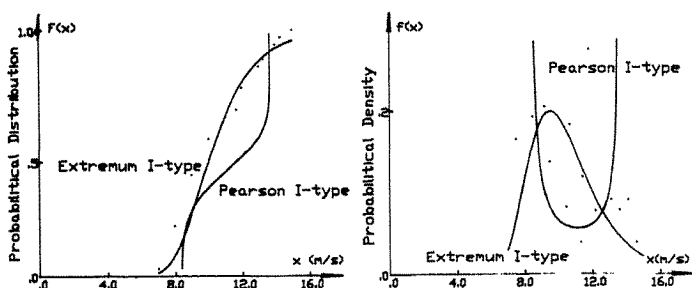Fig.2 Probabilitical Structure of the 1st observation station

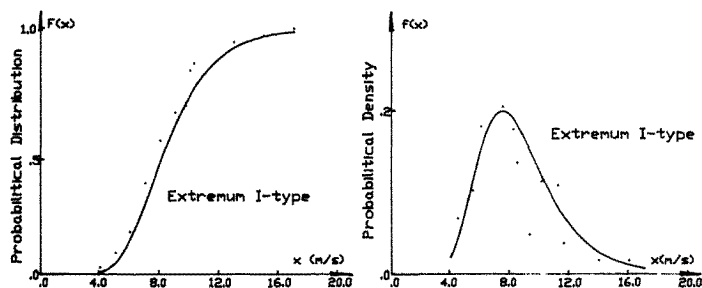Fig.3 Probabilitical Structure of the 2nd observation station

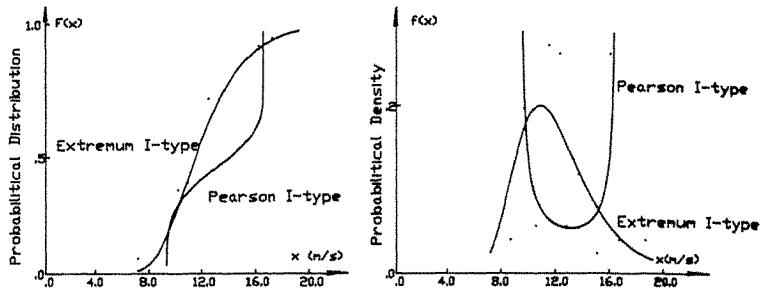Fig.4 Probabilitical Structure of the 3rd observation station

449

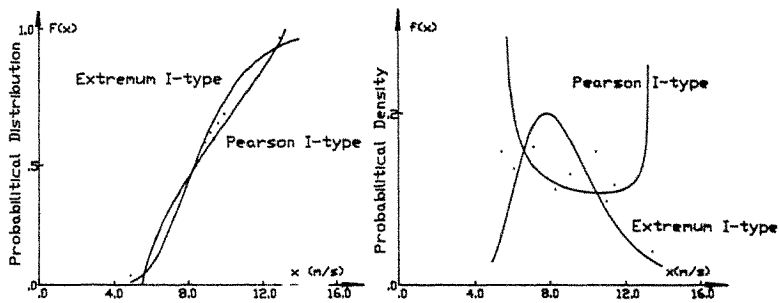Fig.5 Probabilitical Structure of the 4th observation station

Fig.6 Probabilitical Structure of the 5th observation station
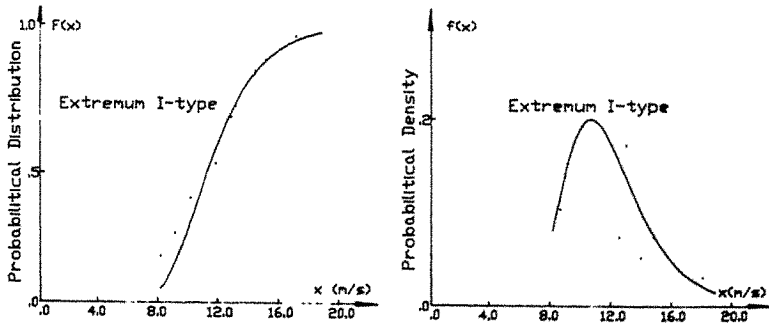

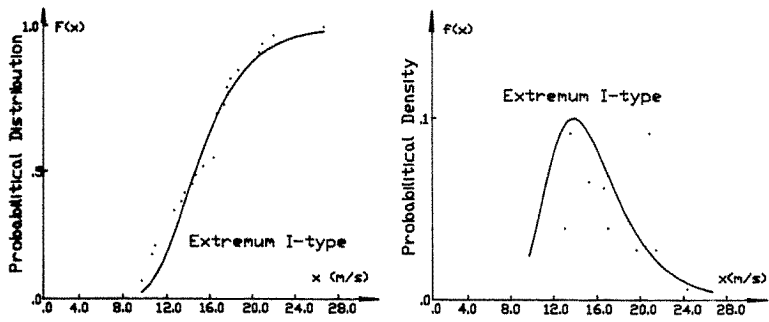Fig.7 Probabilitical Structure of the 6th observation station

450

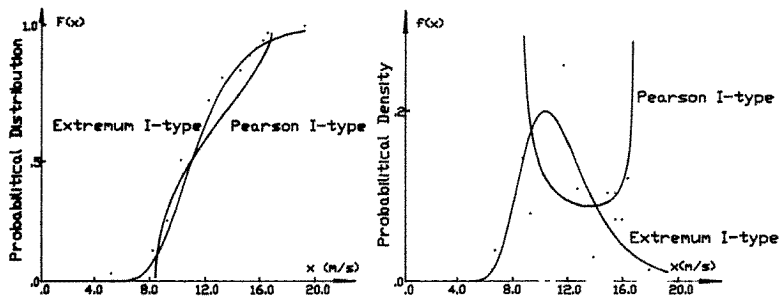Fig.8 Probabilitical Structure of the 7th observation station

Fig.9 Probabilitical Structure of the 8th observation station
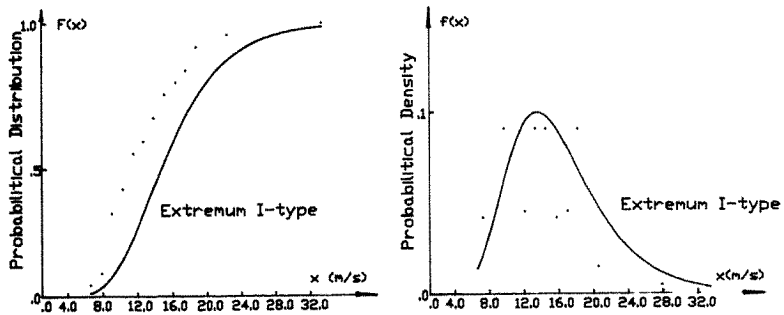

Fig.10 Probabilitical Structure of the 9th observation station
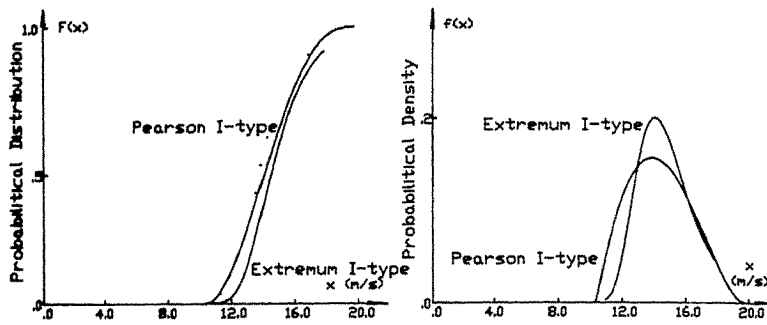
451

Fig.11 Probabilitical Structure of the 10th observation station

And then, distribution hypothesis inspection is done as follows. P(x) and $P_n(x)$ are assumed the theoritical value of probabilitical distribution and practical value respectively, and n the total number of samples. Let $D = |P_n(x) - P(x)|_{max}$, $\lambda = \sqrt{n}\,D$. According to the suitability criterion, when $1-p(\lambda) \to 1$, the theoritical distribution will agree well with practical data[1]. The results indicates that, being described by Extremum I–type model, the average degree of suitability of the 10 groups of data is 0.6724. Except the 4th group and the 9th group, the average degree of suitability can reach 0.8405; and when described by Pearson I–type model, the average degree of suitability of the 5 groups of data is 0.7801. From the viewpoint of applicable range and suitability level, the Extremum I–type model can reflect the probabilitical distribution of steady mountain wind in the south of Sichuan Province better than others.

4.Conclusions

Laying particular stress on wind resistant structural design, this paper studies the characteristics of steady mountain wind in the south of Sichuan Province in China from two aspects, that is, the conversion relations between different wind velocities and the probabilitical distribution of annual maxmium wind velocity. Based on a great deal of observed data, 8 conversions between wind velocities are regressed, which can provide a foundation for the utilization of historical wind data. After the analysis of the 10 groups of historical wind data collected from the south of Sichuan Province, the comparision of some distribution models and the inspection of the distribution hypothesis, the paper formulates the Extremum I–type model of annual maximum wind velocity. The research achivement can be a basis for wind resistant structural design in the related areas.

References:
1. X.T.Zhang, Theory of Structural Load and Handbook of Wind Resistant Calculating, Publishing House of TongJi University, 1990.
2. G.Y.Jin, Principle and Method of Hydrology Statistics, Publishing House of Water Conservancy and Electric Power, 1964.
3. X.T.Zhang, The Current Chinese Code on Wind Loading and Comparative Study of Wind Loading Codes, 7th ICWE, 1987.

Characteristics of Wind Direction Meander
at the Site of Guangdong Nuclear Power Station

Zhou Ruming,Yang Zhongqin,Yu Wenzhuo

Suzhou Thermal Engineering Research Institute
Ministry of Energy, Suzhou, Jiangsu, China

Abstract: 711 obvious cases of wind direction meander which occurred during two years' period from 1 September 1984 to 31 August 1986 were found by identifying the strip chart records of MK4 wind—vane mounted at the site of Guangdong Nuclear Power Station. The accumulated time of these cases was 1274 hours, and accounted for 8% of the hours in which the wind data were identified. The statistics indicated that most of meander cases occurred under low—windspeed conditions. However, the wind direction meander did not always occur under low—windspeed conditions. This paper describes the characteristics of the observed cases of wind direction meander and discusses the effect of wind direction meander on plume dispersion.

1. Introduction

Periodical oscillatory or wave—like motions occurring in the lower atmosphere with periods of minutes or tens of minutes are particularly effective in dispersing airborne gases over short and medium ranges. Such motions are most frequently observed as meander in the horizontal wind direction.

In 1959, Gifford deduced that the total plume dispersion can be separated into the spreading component caused by atmospheric turbulences and the meandering one by wind direction fluctuations[1] . Since then, a number of atmospheric diffusion experiments conducted under low—windspeed conditions have further revealed that the wind direction meander plays an important role in the plume dispersion. In 1976, after having investigated the field data of the atmospheric diffusion experiments under low—windspeed conditions performed in the regions of Idaho, Tennessee, etc., Van der Hoven concluded that, for near—surface source, the plume concentrations measured under such conditions are much lower than those predicted by using ΔT classification scheme and Pasquill—Gifford diffusion curves[2] . In 1978, the atmospheric diffusion experiment sponsored by US Nuclear Regulatory Commission and carried out at the site of Sancho Seco Nuclear Facility was completed, and the results confirmed the existence of obvious plume meander under low—windspeed conditions and neutral and stable stability conditions[3] .

With the progresses in the diffusion experiments under low—windspeed conditions, several agencies have suggested to introduce a meander factor into the atmospheric dispersion calculation. For example, US NRC(1979) recommended that the horizontal plume standard deviation with windspeed less than 6m / s be a meander factor M (with maximum of 6) times σ_y attributed by turbulence diffusion[4]. Similarly, the International Atomic Energy Agency(1980) recommended to introduce a meander factor of 4 into the dispersion calculation for low—windspeed conditions[5] . In contrast, some other experiments indicated that such kind of modification using a meander factor shoud be made cautiously. After having analyzed the

wind data in Long Island of New York, Raynor et al.(1984) from US Brookhaven National Laboratory indicated that the horizontal dispersion of plume during periods of meander was enhanced significantly but the wind direction meander did not always occur under the low-windspeed stable conditions[1] .

In this study, the occurrence and characteristics of wind direction meander at the site of GNPS (north latitude $22^0 36'$, east longitude $112^0 32'$) were analyzed, and the results similar to those given by Raynor et al. were obtained. This paper introduces the method used in identifying wind direction meander cases, describes the occurrence and characteristics of meander cases, and discusses the effect of wind direction meander on plume dispersion. Finally, a recommendation for the consideration of meander effect in the atmospheric dispersion calculation for nuclear power stations is presented.

2. Method

The strip chart records of MK4 wind-vane mounted at 10m above the ground on the 102m tower were used as well as other meteorological data obtained by the tower data acquisition system. Figure 1 gives several typical meander cases recorded in the strip chart of MK4 wind-vane. As shown in Figure 1, the strip chart records were carefully identified by the periodic wave-like nature of the wind direction trace so that the obvious meander cases were distinguished from higher frequency turbulence, wind direction shifts and the random motions occurring during variable winds. Only the meander cases with two or more full waves were taken into account.

For each meander case, the following data were recorded as shown in Figure 2: the date and time of beginning and end, the number of half-waves, the time of the peak of each half-waves, the direction of each peak, the width of wind direction trace before the case. All cases were assigned a sequence number and all data entered into a computer database for subsequent analysis.

Then, the following parameters were calculated for each case: the mean, maximum and minimum of the direction ranges (angular amplitudes) of the waves, the total direction range over which waves occurred, the time differences between alternate peaks and troughs, the rate of direction change of each swings (degrees / minute).

3. Results

3.1 Occurrence of meander cases

The above method was used in identifying the strip chart records of MK4 wind-vane during two years' period from 1 September 1984 to 31 August 1986, and 711 wind direction meander cases were discovered. The total time accumulated for these cases was 1274 hours, covering 8% of the hours in which wind data were identified.

According to the numbers of meander cases versus the time in a day, it is shown that about 70% of meander cases occurred during nighttime. Meanwhile, in terms of the stabilities classified by ΔT sheme, most of meander cases occurred under neutral and stable conditions (62% and 30% respectively). Table 1 gives the accumulated time of meander cases versus grades of windspeed. It is seen that most meander cases occurred under low-windspeed conditions for the site of GNPS, and that about 55% and 31% of meander cases took place at windspeeds less than 2 m / s and between 2 and 3 m / s respectively. However, as indicated by Raynor et al., the wind direction meander did not always occur under the low-windspeed conditions. For example, the time accumulated for meander cases only took up 24% of the time under the conditions with windspeed less than 2 m / s and neutral and stable stabilities.

3.2 Characteristics of meander cases

The characteristics of 711 meander cases were defined as follows:

— The average wave periods of about one half of meander cases were between 10 and 20 minutes and about one—thirds cases between 20 and 30 minutes.

— The wave numbers of meander cases varied from 2 to 20, and about one half of meander cases were found to be with 4~9 of wave numbers.

— The duration of meander cases varied over a wide range and about two—thirds of cases occurred with duration between 40 and 100 minutes.

— The mean rates of wind direction variations for most meander cases were larger than 5 degrees per minute, and those for about 47% and 27% of cases between 6 and 10 degrees per minute and between 11 and 15 degrees per minute respectively.

3.3 Effect of wind direction meander on plume dispersion

Table 2 gives the mean angular amplitudes of meander cases. It is shown that the meander cases with mean angular amplitudes between 51 and 90 degrees were relatively predominant. The mean angular amplitudes of most meander cases were several times larger than the width of wind direction trace before the corresponding case occurred, and the mean ratio was 4.6. As shown in Table 3, there were about three—fourths of meander cases with ratios between 2 and 6.

Due to the fact that the obvious variation of angular amplitudes can be explicitly reflected in values of the corresponding σ_θ (the standard deviation of horizontal wind direction fluctuation), it is expected that the horizontal plume dispersion can be significantly enhanced during the periods of meander. But, as mentioned in subsection 3.1, the wind direction meander did not always occur under the low—windspeed conditions with neutral and stable stabilities. Therefore, the use of meander factor for low—windspeed conditions, such as recommended by US NRC and IAEA, may be not adequate.

Table 4 gives the distribution of σ_θ values for the 711 meander cases. It is noticed that wind direction meander resulted in obvious increase of σ_θ values so that the horizontal plume dispersion for most cases corresponded to that under unstable conditions classified by σ_θ stability scheme. It is clear that the values of σ_θ have already included the effect of wind direction meander on plume dispersion. In other words, the σ_θ can be regarded as a good indicator of meander effect. For this reason, it is suggested that the split—sigma scheme for stability classification be used in the atmospheric dispersion calculation for nuclear power stations, i.e. the σ_θ and ΔT schemes be used for classifying stabilities in the horizontal and vertical directions respectively. In this way, it is not necessary to introduce the meander factors such as recommended by US NRC and IAEA.

4. References

1. G.S. Raynor and Janet V. Hayes, Third Conference on Meteorology of the Coastal Zone(1984), P.81—85.
2. I. Van der Hoven, Nuclear Safety, Vol.17(1976),P.223—230.
3. W.G. Snell and R.W. Jubach, NUREG / CR—2260(1981).
4. US NRC, Regulatory Guide 1.145(1982).
5. IAEA, Safety Series No. 50—SG—S3(1980).

455

Table 1 The accumulated time of meander cases versus grades of windspeed

U, m/s	U<2	2<U<3	3<U<4	4<U<6	U>6
F_1, %	55.0	31.4	9.1	3.5	1.0
t, hour	772.3	363.8	93.3	37.3	7.2
F_2, %	24.0	9.8	3.0	1.3	0.5

Note: U — windspeed;
F_1 — fraction of cases corresponding to a grade of U in the total cases;
t — accumulated time for cases corresponding to a grade of U;
F_2 — fraction of t in the time under conditions with a grade of U and neutral and stable stabilities.

Table 2 The mean angular amplitude of meander cases

| mean angular amplitude, degrees	<50	51—70	71—90	91—120	121—140	>140
fraction in 711 cases, %	13.5	31.1	22.8	19.5	6.6	4.5

Table 3 The ratios of mean angular amplitude of meander case to the width of wind direction trace before the corresponding case occurred

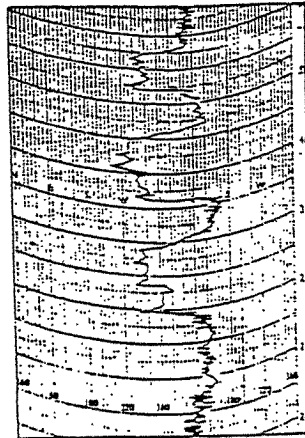| ratio, R	R<2	2<R<4	4<R<6	6<R<8	8<R<10	R>10
fraction in 711 cases, %	9.3	45.7	27.7	8.9	3.1	5.3

Table 4 The distribution of σ_θ values for 711 meander cases

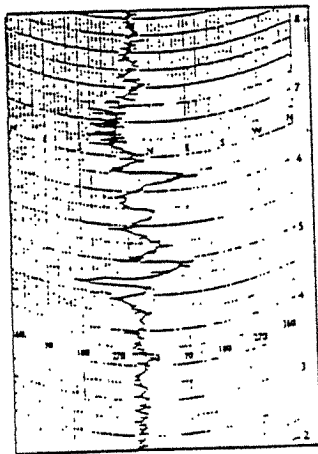| σ_θ, degree	>22.5 (A)*	17.5—22.5 (B)	12.5—17.5 (C)	7.5—12.5 (D)	3.75—7.5 (E)	<3.75 (F)
fraction in 711 cases, %	39.7	13.6	20.8	19.7	2.8	0.4

* Symbols in parentheses indicate the stabilities classified by using σ_θ scheme.
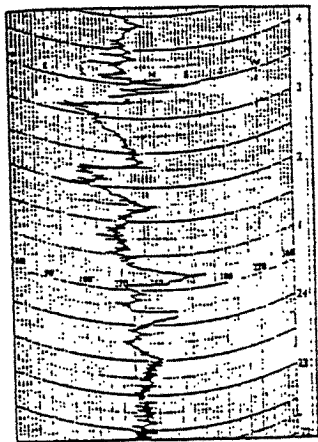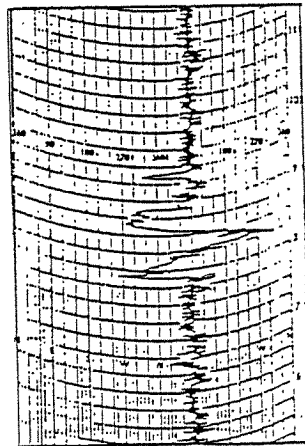
7 Feburary 1986

30 January 1986

15 August 1986

17 February 1986

Figure 1 Several typical cases of wind direction meander observed at the site of GNPS
(abscissa—the degrees of wind direction, ordinate—time in a day, in hours)
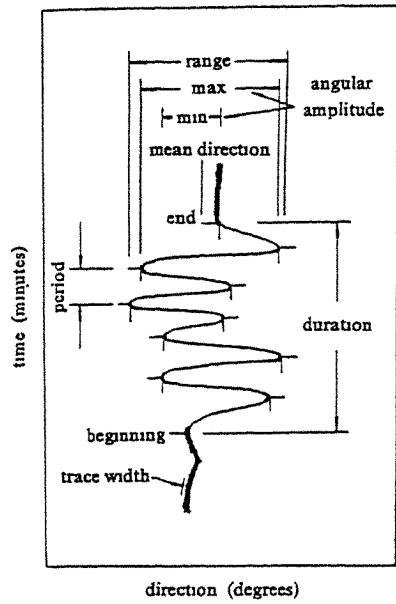
457

Figure 2 Diagram of a representative meander case illustrating the measurements taken as described in the text. Each half wave is numbered. Tick marks indicate the locations at which direction and time are read.

A study on characteristics and simulation method of pulsating wind

Y.M.Li, M.Lai and Q.Zhao

Department of Civil Engineering
Chongqing Inst. of Arch. and Engg., China

Abstract:This paper regresses the velocity power spectra of pulsating wind in mountainous areas in southern Sichuan Province in China by using a parameter identification technique. Introducing Auto—Regressive Moving Average (ARMA) Model to describe pulsating wind process, and using the Compound Form Optimization Method, the paper studies the simulation method of pulsating wind. The results can provide load inputs for random responses analysis and time—history analysis of structures under pulsating wind.

1. Introduction

Most investigations of wind disasters indicate that, wind vibration has outstanding effects on relatively high and long buildings, such as tall buildings, high—tower structures and big—span structures, etc., and sometimes it will control the design of those structures. But studing on the dynamic responses of structures under pulsating wind is not well considered. With the development of stochastic vibration theory and the improvement of computer techology, it is possible to analyze the structural dynamic responses by using the theory and time—history analysis method. So it is necessary to determine velocity power spectrum of pulsating wind and to effectively give a series of pulsating wind records which have a statistical regularity. Based on 147 sample points of power spectra, which are collected from some practical gusty wind records, the paper advances the velocity power spectra of pulsating wind in the south of Sichuan Province in China by using parameter identification technique. Furthermore, the ARMA model is used to describe pulsating wind process and the Compound Form Optimization Method is adopted to determine model parameters, and then the paper presents a method to simulate pulsating wind, and works out a computer software. Some simulation examples are given at last.

2. Regression of Horizontal Wind Velocity Spectra

Two typies of spectra are taken as mathematical models. The first is Davenport Spectrum [5] which is commonly—used in the world, and the other is China's Experiential Spectrum which agrees well with Chinese wind data. So horizontal wind velocity spectra can be regressed by using the parameter identitication method. The basic data are 147 sample points measured in the south of Sichuan Province by using Dynamic Signal Analysis Instrument 3562A and EL Contact Wind Vane and Anemograph Model. Wind velocity spectrum is obtained as

$$S_v(n) = 6.000 K \overline{V}_{10}^2 \frac{x^2}{n(0.8000 + x^2)^{1.2936}} \tag{1}$$

or

$$S_v(n) = \frac{2.3312K\overline{V}_{10}^2}{n} \exp[-\frac{(\lg x - 0.5839)^2}{0.9215}] \tag{2}$$

where, K is a coefficient of rough degree of the earth's surface, $\overline{V}_{10}$ the average wind velocity at 10–meter height, n the frequency, and $X = 1200n / \overline{V}_{10}$.

Fig.1 shows the comparasion between regressed spectra and sample points. It is thus clear that the spectrum of formula (2) agrees well with the data of the area studied.
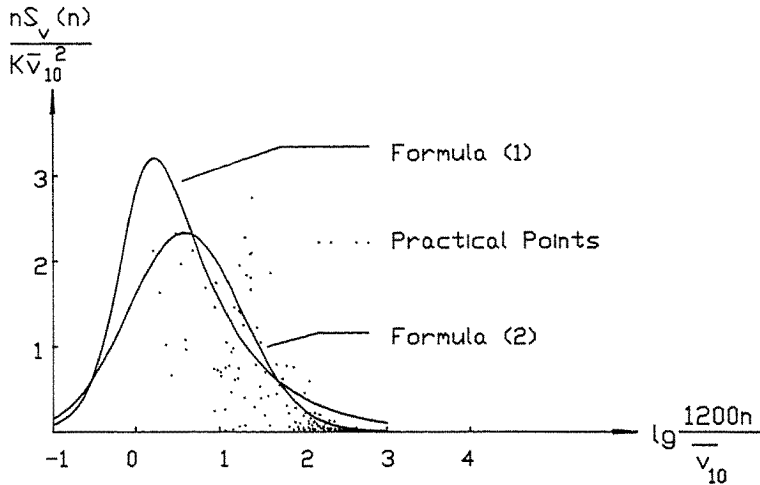

Fig.1 Comparasion between regressed spectra and sample points

3. Simulation Method of Pulsating Wind

For the reality that there are a few practical wind time–histories, it is feasible to use artificial time–histories of pulsating wind to research its characteristics and to analyse responses of structure under wind vibration. The ARMA model may be one of the best models for describing pulsating wind process.

(1) Basic Method

The ARMA model is used to describe homogeneous random process $\{X_t\}$ with a zero mean,

$$X_t + \sum_{i=1}^{m} a_i X_{t-i} = \varepsilon_t + \sum_{j=1}^{n} b_j \varepsilon_{t-j} \tag{3}$$

where, $\{\varepsilon_t\}$ is called a white noise; a_i and b_j auto–regressive coefficients and moving average coefficient respectively; m auto–regressive order and n moving average order. Formula (3) is also rewritten simply as ARMA(m,n).

460

There are many methods to model ARMA process [2], the authors have pointed out in the paper [3] that, lower−order ARMA model, such as m,n<4, may describe pulsating wind process very well. There are at least 3 obvious merits using the ARMA model to analyze time series. First, the model is so simple that it can be defined only by a_i, b_j and the square σ_ε^2 of $\{\varepsilon_t\}$. Secondly, it reflects interior regular of random data, since it transforms correlative and sequential random data into uncorrelative and sequential random variables, and it is convenient to analyze the structure and property of data. Finally, under certain conditions, its spectral characteristics only relates to the model coefficients, and it corresponds to a stationary series with rational spectrum, so it can approach the process with a continuous spectrum. Hypothesizing pulsating wind process as an ergomic process and taking wind power spectrum as the target, we can simulate pulsating wind by using the Compound Form Optimzation Method to identify the model parameters, as shown in Fig.2. The
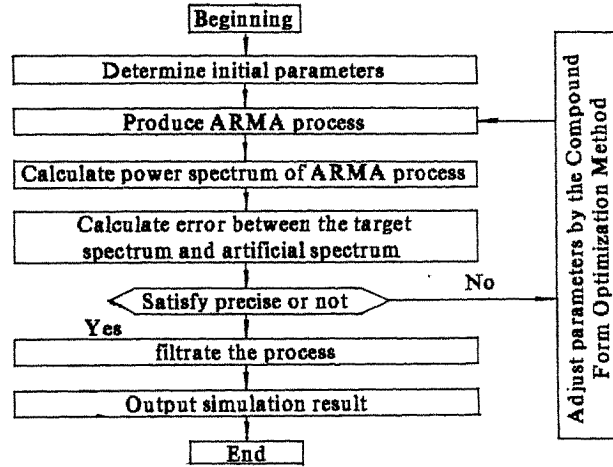

Fig.2 The basic principle of simulation method of pulsating wind

error in Fig.2 should be the sum of relative errors between the target spectrum and the simulated spectrum at some controlling points.

The principle of the Compound Form Opitimization Method is that, in a n−dimension space within nonlinear resistance, 2n vertices is used to constitute a compound form, and the error values at every vertices are compared one by one, and the worst vertex is substituted with a new vertex which can both satisfy resistant conditions and reduce the error. So much on, the most optimum vertex will be approched[4].

(2) Simulation Program and Example Analysis

With the lower−order ARMA model and the Computer Form Optimization Method, the authors have worked out a computer software PWSS to simulate pulsating wind and have analyzed a lot of examples. It is convenient to use PWSS for it doesn't need lengthy input data files and its calculating time is short. Owing to the limitation of paper space, the following only gives two artificial pulsating wind records simulating formulas (1), (2) and

461

the China's Experiential Spectrum, as shown in Fig.3 to Fig.8. According to the figures, the artificial spectra can approach the target spectra with higher precision almost at every frequency sections.
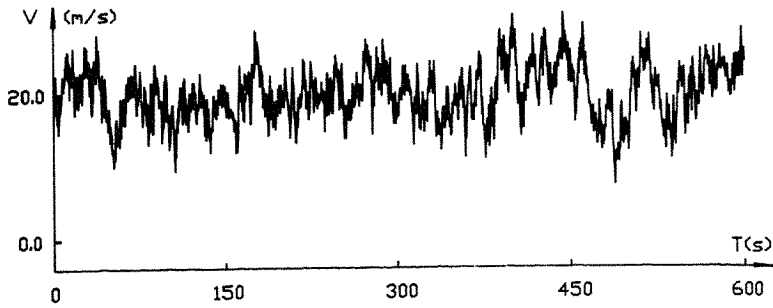

Fig.3 Artificial pulsating wind record no.1 simulating formula (1)
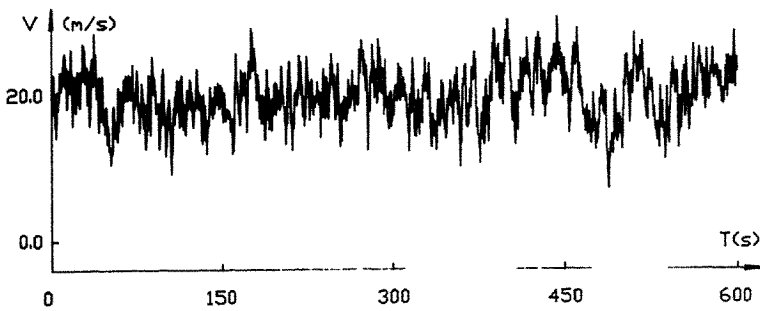

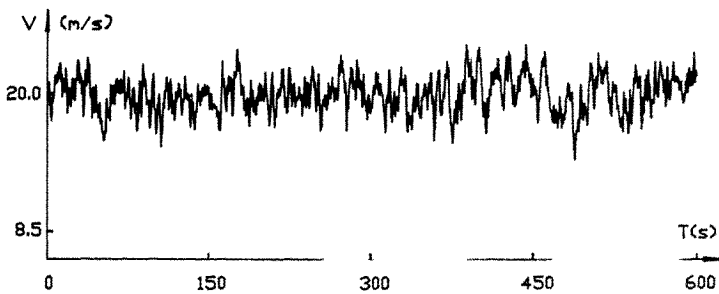Fig.4 Artificial pulsating wind record no.2 simulating formula (2)

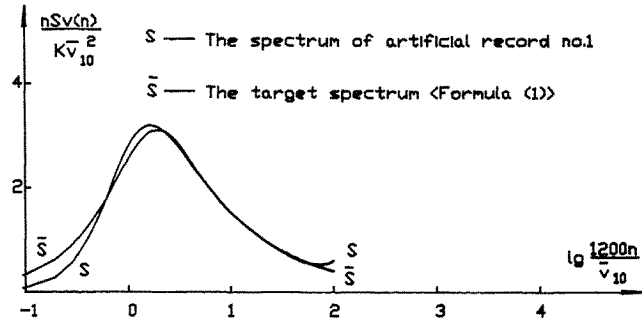Fig.5 Artificial pulsating wind record no.3 simulating the China's Experiential Spectrum
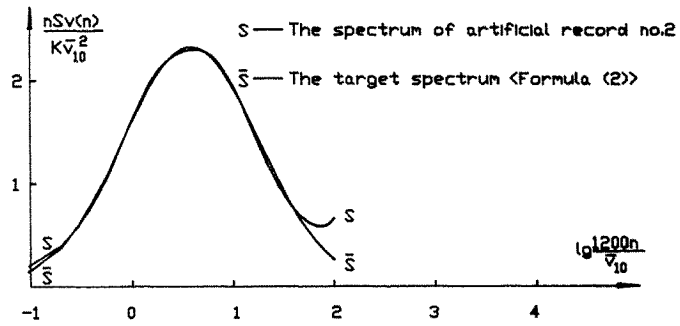
462

Fig.6 The power spectra of record no.1
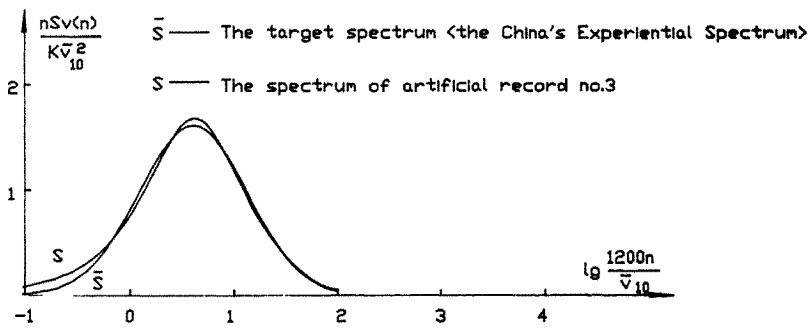

Fig.7 The power spectra of record no.2

Fig.8 The power spectra of record no.3

4. Conclusions

The following conclusions can be drawn from the paper. First, the velocity power spectrum of pulsating wind regressed from the practical data tallies better with the characteristics of pulsating wind in mountainous areas than other spectra, and it is suggested to guide the wind resistant structural design. Secondly, the ARMA model has a simple form, so it is convenient to analyze the structure and property of data for it can be determined by a few parameters, especially for its spectrum only relates to the model parameters. So the ARMA model is feasible and superior in describing pulsating wind process. Thirdly, the Compound Form Optimization Method has good stability, so the simulation method of pulsating wind can model a given time—history of wind velocity and simulate a given velocity power spetrum. Finally, the paper also gives simulation examples of the two power spectra, which indicates that the simulation method is simple, time—saving and highly precise. It can be used to analyze characteristics of pulsating wind and to analyze structural wind vibration.

References:

1. X. T. Zhang, Calculating of Wind Presure and Vibration on Structures, Publishing House of Tongji University, 1985.
2. W.Q.Yang, L.Gu, Analysis of Time Series and Modelling Dynamic Data, Publishing House of Peking University of Industry, 1987.
3. Y.M.Li, M.Lai, Applying of ARMA Model and Parameter Identification Technique in Simulation of Pulsating Wind, J. of Chongqing Inst. of Arch. Engg., (1992)17.
4. Y.Q.Wan, B.R.Liang, Programs Collection of Optimization Methods in Common Use, Publishing House of Worker, (1983) 116.
5. A.G.Davenport, The Spectrum of Horizontal Gustiness near the Ground in High Wind Quart, J. Roy. Met. Soc., 1961.

Theoretical Study on Cold-Air Damming of the Qinling Mountains

Qi Ying and Zhou Jingnan

(Institute of Mechanics,CAS,Beijing 100080,P.R.China)

ABSTRACT: In this paper,the process of the cold air invading the Qinling Mountains during January 20-22,1977 is analysed by the observations and is simulated by the mesoscale atmospheric numerical model with a higher-order turbulent closure. The simulated results are basically identical with the observed results. Furthermore, the numerical model,the dynamic mechanism of the Qinling Mountains screening the cold air from the North is systematically discussed.

1. INTRODUCTION

Qinling is a famous mountains which run from east to west in China.In winter,it has an obvious effect of screening on the cold air from the North. And in the Chinese climate, it is a famous boundary between the temperate zone and north subtropics.Therefore,studying the screen effect of the Qinling Mountains on the cold air from the North is not only an important part of the regional climate research in China but also will provide a significant scientific basis for exploiting and utilizing mountain-climate resources and wind energy.However,the dynamical mechanism of the Qinling Mountains screening northern cold air has not been studied until now.In this paper,taking the example of typical cold airflow invading the Qinling Mountains, the dynamical mechanism of Qinling screen effect on the cold air from the North is systematically analysed by the author's mesoscale numerical model with a higher-order turbulent closure(Qi,et al,1993).

2. THE MODEL

It is assumed that the model atmosphere is dry and incompressible,and satisfies hydrostatic equilibrium.The terrain coordinate transformation is

$$z^* = \bar{S} \cdot \frac{z - S_G}{\bar{S} - S_G}$$

In which S is the height of the model top,S is the terrain function,uniform in the y direction.In the terrain coordinate system,the two-dimensional momentum equations,the potential-temperature equation and the continuity equation are

$$\frac{du}{dt} = -\theta \frac{\partial \Pi}{\partial x} + fv + g \cdot \frac{z^* - \bar{S}}{\bar{S}} \cdot \frac{\partial S_G}{\partial x} + \frac{\bar{S}}{\bar{S} - S_G} \cdot \frac{\partial(-\overline{u'w'})}{\partial z^*} \tag{2 1}$$

$$\frac{dv}{dt} = fu_g - fu + \frac{\bar{S}}{\bar{S} - S_G} \cdot \frac{\partial(-\overline{v'w'})}{\partial z^*} \tag{2 2}$$

$$\frac{d\theta}{dt} = \frac{\bar{S}}{\bar{S} - S_G} \cdot \frac{\partial(-\overline{\theta'w'})}{\partial z^*} \tag{2.3}$$

$$\frac{\partial \Pi}{\partial z^*} = -\frac{\bar{S} - S_G}{\bar{S}} \cdot \frac{g}{\theta} \tag{2.4}$$

$$\frac{\partial u}{\partial x} + \frac{\partial w^*}{\partial z^*} - \frac{u}{\bar{S} - S_G} \cdot \frac{\partial S_G}{\partial x} = 0 \tag{2.5}$$

in which,

$$\Pi = C_p \left(\frac{P}{10^5} \right)^{\frac{R}{C_p}}$$

465

$$w^* = \frac{\bar{S}}{\bar{S} - S_G} \cdot w + \frac{z^* - \bar{S}}{s - S_G} \cdot u \cdot \frac{\partial S_G}{\partial x}$$

$$\frac{d}{dt} = \frac{\partial}{\partial t} + u \frac{\partial}{\partial x} + w^* \frac{\partial}{\partial z^*}$$

u is the geostrophic wind in the x direction and the variables with primes are turbulent quantities. The above equations are closed by second-order moment turbulent equations,using Mellor and Yamada's(1974) parameterization scheme.In the terrain coordinate system,the second-order moment equations are

$$\frac{d(\overline{u'_i u'_j})}{dt} = -\overline{u'_i u'_k} \frac{\partial u_j}{\partial x_k^*} - \overline{u'_j u'_k} \frac{\partial u_i}{\partial x_k^*} + \frac{g}{\theta_0}(\overline{\theta' u'_i} \delta_{j3} + \overline{\theta' u'_j} \cdot \delta_{i3}) - \frac{q}{3l_1} \cdot \frac{\alpha_0}{\alpha_{00}} (\overline{u'_i u'_j} \quad \delta_{ij}}$$

$$\cdot \frac{q^2}{3}) + \frac{\alpha_0}{\alpha_{00}} C_1 q^2 (\frac{\partial u_j}{\partial x_i^*} + \frac{\partial u_i}{\partial x_j^*}) - \frac{2}{3} \cdot \frac{q^3}{\Lambda_1} \delta_{ij} + \frac{\partial}{\partial x_k^*}$$

$$\left[q\lambda_1 \left(\frac{\partial \overline{u'_i u'_j}}{\partial x_k^*} + \frac{\partial \overline{u'_j u'_k}}{\partial x_i^*} + \frac{\partial \overline{u'_i u'_k}}{\partial x_j^*} \right) \right]. \tag{2.6}$$

$$\frac{d(\overline{\theta' u'_i})}{dt} = -\overline{u'_i u'_k} \cdot \frac{\partial \theta}{\partial x_k^*} - \overline{\theta' u'_k} \frac{\partial u_i}{\partial x_k^*} + \frac{g}{\theta_0} \overline{\theta'^2} - \frac{q}{3l_2} \overline{\theta' u_i} + \frac{\partial}{\partial x_k^*} \left[q\lambda_4 \left(\frac{\partial \overline{\theta' u'_i}}{\partial x_k^*} + \frac{\partial \overline{\theta' u'_k}}{\partial x_i^*} \right) \right] \tag{2.7}$$

$$\frac{d \overline{\theta'^2}}{dt} = -2 \overline{\theta' u'_k} \frac{\partial \theta}{\partial x_k^*} - 2 \frac{q}{\Lambda_2} \overline{\theta'^2} + \frac{\partial}{\partial x_k^*} (q\lambda_3 \frac{\partial \overline{\theta'^2}}{\partial x_k^*}) \tag{2.8}$$

in which

$$\frac{\partial}{\partial x_k^*} = (\delta_{k1} + \delta_{k2}) \frac{\partial}{\partial x_k} + \left(\frac{z^* - \bar{S}}{\bar{S} - S_G} \cdot \frac{\partial S_G}{\partial x} \cdot \delta_{k1} + \frac{\bar{S}}{\bar{S} - S_G} \cdot \delta_{k3} \right) \cdot \delta_{i} \frac{\partial}{\partial x}$$

$$q^2 = \overline{u'_1{}^2} + \overline{u'_2{}^2} + \overline{u'_3{}^2}$$

where , are respectively the potential temperature and specific volume of the atmospheric reference state, is the value of at the surface, i,j,k can be 1,2,3. $(l_1, l_1) = (A_1, A_1), (\ , \ ) = (B_1, B_1), \ = \ = \ = 0.23l, (A_1, A_2, B_1, B_2) = (0.78, 0.78,15.0,8.0)$, C = 0.056. l is mixing length:

$$l = \begin{cases} L_1 & \frac{\partial \theta}{\partial z} \leqslant 0, \\ \dfrac{L_1 \cdot L_2}{L_1 + L_2} & \frac{\partial \theta}{\partial z} > 0. \end{cases}$$

in which

$$L_1 = \frac{\dfrac{\kappa z^* \bar{S}}{\bar{S} - S_G}}{1 + \dfrac{\kappa z^* \bar{S}}{L_0 (\bar{S} - S_G)}} ,$$

$$L_0 \approx \frac{0.1 \int_0^* q z^* \left(\dfrac{S}{z - S_G} \right)^2 dz^*}{\int_0^* q \dfrac{S}{\bar{S} - S_G} dz^*}$$

$$L_2 = \frac{0.53 q}{\left(\dfrac{g}{\theta_0} \dfrac{\partial \theta}{\partial z^*} \dfrac{\bar{S} - S_G}{S} \right)^{1/2}}$$

Equations(2.1)-(2.8) are a group of closed basic equations.

3. OBSERVATIONS ANALYSIS

During the 20th-22th of January,1977, a relatively strong cold airflow invaded the Qinling Mountains.From the surface chart,850mb and 700mb charts at 08:00LST of the 20th,it is found that in the northwest to Shanxi province,there was a cold trough gradually moving to Shanxi province.At 08:00LST of the 21th,the temperatures of Xian obviously dropped in 700mb chart and relatively strong wind deflecting to north appeared in 850mb chart. It can be known from the several hour radiosonde profiles of temperatures at the observational station at the mountain north, Xian and the station of the mountain south, Ankang that on the 21th, there had been cold air invading the Qiling Mountains and the cold air flow from the upwind had crossed over the Qinling Mountains at the upper level so the atmospheric temperatures over the south and norh of the mountains were both affected at the upper level. Only the temperature drops at the south of the mounatins were less than those at the north of the mountains. The tables of daily average air-temperature variations at the observational stations in the areas of Shanbei, Guanzhong and Shannan of Shanxi province further demonstrate the following facts. At 07:00 LST of the 21th, the upper cold air from the upwind had crossed over the Qinling Mountains. But in Guanzhong area, there were not apparent decreases of the temperatures at the stations near Weihe and at the lower stations on the slope of northern valley of the Qinling Mountains on the 21th. At some stations such as Fuping and Xingping, there were temperature increases conversely. Obvious decline of temperatures mainly occurred on the 22th.In Shannan area,at the lower stations (for example, Hanyin and Xixiang), the air temperatures instead generally rised on the 21th and were basically steady on the 22th.

Table 1. Day-to-day air temperatures at various observation
stations in Shanbei on the 20th-22th of January, 1977

Station	Huangling	Fuxian	Yanchang	Yanan	Yanchuang	Wubao
Latitude	35°36'	36°00'	36°35'	36°36'	36°53'	37°31'
Longitude	109°49'	109°23'	110°04'	109°30'	110°11'	110°43'
Sea-level (m)	1081.8	920.0	804.5	957.6	803.7	752.5
20th temp. (°c)	-5.0	-6.2	-6.9	-6.7	-7.0	-5.5
21th temp. (°c)	-7.0	-9.8	-8.9	-8.6	-9.0	-8.0
22th temp. (°c)	-7.4	-6.8	-8.3	-6.0	-7.6	-7.7

Table 2. The same as in Table 1 except for in Guanzhong

Station	Taibai	Zhouzhi	Changan	Xian	Xingping	Huashan	Fuping	Dali
Latitude	34°02'	34°06'	34°09'	34°18'	34°17'	34°29'	34°47'	34°52'
Longitude	107°19'	108°12'	108°55'	108°56'	108°17'	110°05'	109°11'	109°56'
Sea-level (m)	1543.1	433.1	438.0	396.9	410.9	2064.9	470.9	367.9
20th temp. (°c)	-4.8	-1.1	-1.3	-1 7	-2.0	-5.0	-2.9	-2.2
21th temp. (°c)	-6.6	-2.0	-2.9	-3.4	-1.8	-8.1	-2.2	-2.6
22th temp. (°c)	-4.9	-4.2	-5.9	-5.1	-4.6	-4.2	-4 9	-3 7

Table 3. The same as in Table 1 except for in Shannan

Station	Zhenping	Ankang	Hanyin	Xixiang	Nanzeng	Chenggu	Yangxian	Feping
Latitude	31°57'	32°43'	38°54'	32°59'	33°00'	33°10'	33°13'	33°32'
Longitude	109°31'	109°02'	108°30'	107°43'	106°56'	107°20'	107°33'	107°59'
Sea-level (m)	995.8	290.8	413.1	446.0	536.5	486.4	468.6	1087.7
20th temp. (°c)	1.4	2.5	2.1	2.3	2.3	2.4	-1.0	-0.3
21th temp. (°c)	-0.7	3.8	3.0	3.2	2.4	2.6	-0.2	-1.2
22th temp. (°c)	0.3	2.7	3.0	3.2	1.4	1.7	-0.5	-0.5

Thus it can be seen that the upper cold air from the upwind can cross over the Qinling Mountains and affect the upper atmospheric temperatures in the south of Qinling. Only the temperature drops in the south of Qinling are less than those in the north of Qinling.However,in the northern valley of the Qinling Mountains,there firstly occurs checking the temperatures' decline induced by the cold air and even temperatures' rise appears;after that the cold air just gradually come into the

467

valley.On the south slope of the Qinling Mountains, except for at the several upper stations,the cold air not only doesn't bring the influence of decreasing but conversely the air temperatures rise.It can be seen that when a cold airflow invades the Qinling Mountains,there is not only the obstruction of Qinling Mountains to the cold airflow but also the effect of increasing temperatures at the south slope of the Qinling Mountains and the check effect of the northern valley of the Qinling Mountains on the cold airflow's invading,which results in the obvious difference of the temperatures at the south and north of Qinling Mountains.

4. NUMERICAL STUDY

Taking the average of the topographies at $107°E$, $108°20'E$ and $109°40'E$ as the model topography,the topographically thermal forcing is neglected and taking the winds and temperatures before the cold airflow's invading, that is,the average winds and temperatures in the Qinling Mountains on the 20th of January,1977 as initial fields,the initial variables are assumed to be uniform in the horizontal direction.The initial time is defined as 00:00LST, the 21th of January,1977.Cold air source is imported from the upwind lateral boundary.Comparing the simulations of the temperature profiles,at several times and at the $34°30'N$ and $32°48'N$ of the average topography, with the observations at Xian and Ankang stations,it can be known that the simulations and observations are basically identical.In addition,the simulations of the horizontal distributions' evolution of air temperatures in the Qinling Mountains are given in Fig.1.It can be known from Fig.1 that in the upwind to the northern valley of the Qinling Mountains,the temperatures gradually decline duo to the cold airflow's continual invading and become basically steady at the integral hour of 20hr. In the northern valley of the Qinling Mountains,the temperatures rise during the initial period of the cold airflow's invading and afterwards begin to decline.At the south slope of the Qinling Mountains,there occurs the temperatures' rising with the cold airflow invading and the temperatures are basically steady when the model is integrated for 20hr.The above results all tally with the observations in Table 1,2 and 3.

Fig 1
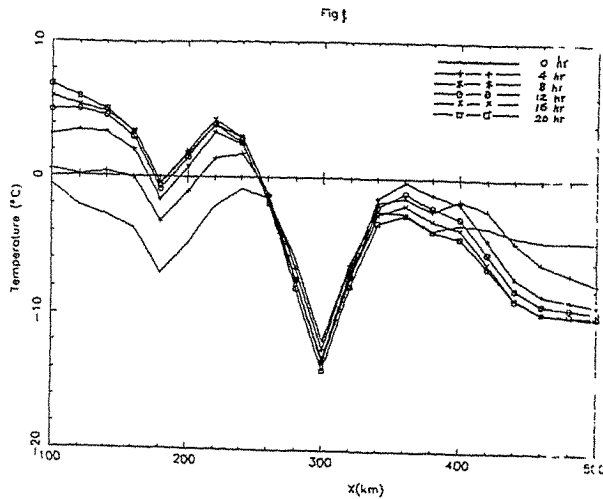
To sum up,we have successfully simulated the screen effect of the Qinling Mountains on the invading cold airflow.In order to study on the dynamical mechanism of the screen effect of the Qinling Mountains on the invading cold airflow, we will further

analyse the evolution pattern of the wind field,potential-temperature field and etc. when the cold airflow invades the Qinling Mountains.It can be known from the simulations(Only the 20hr. integral results,shown as in Fig.2, are given here due to space limit)that the cold air moves slowly after arriving at the lee slope of the northern valley and in the corresponding wind field,the strong downslope wind on the lee slope of the northern valley is almost steady and little varied.Thus it can be seen that the subsidence temperature rising induced by the downslope wind of the northern valley of the Qinling Mountains restrain the cold air from invading the whole valley in the north of the Qinling Mountains.But it can be found from the temperature fields that the cold air over the valley moves faster than that in the valley and when the cold air in the valley move near the north slope of the Qinling Mountains,it can gradually return to the inside of the valley and promote the declining of the temperatures in the valley if it meets blocking airflows.

Fig 2a. Pot_temperature(K) when the cold air passes over the Qinling mountain

MAX=318.513504   MIN=276.323006   INTER=2.812699
X(KM)   Integral hour=20 hr
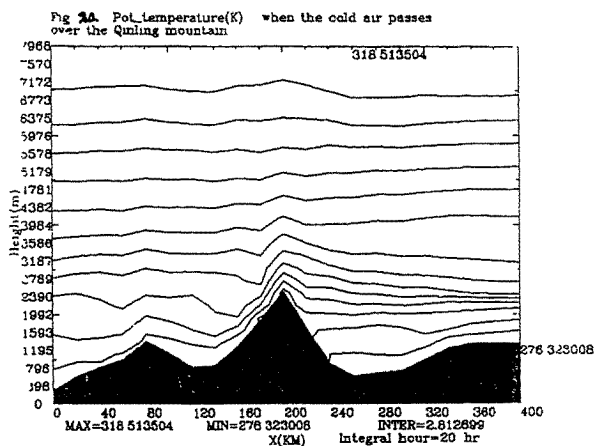
Fig.2b U-W Vector when the cold air passes over the Qinling mountain

Max=19.3   X(KM)   Integral hour= 20 hr

469
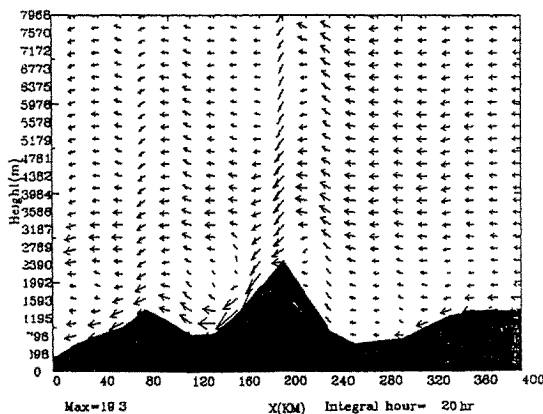
5. CONCLUSIONS

To sum up the above observational analysis and numerical study:

(1) When the cold airflow from the North invades the Qinling Mountains,the temperatures' declining in the northern valley of the Qinling Mountains has an obvious retarding effect,which is because the downslope wind on the south slope of the northern valley of the Qinling Mountains restrains the cold air from invading the inside of the valley.

(2) Besides the role of the blocking airflow at the north slope of the Qinling Mountains,obstructing cold air from invading the south of the Qinling Mountains relates to the downslope wind,on the south slope of the northern valley of the Qinling Mountains,restraining the cold air from invading the inside of the valley.

(3) The subsidence temperatures rising induced by the downslope wind on the south slope of the Qinling Mountains checks the effect of decreasing temperature brought by the invading cold air and intesifies the difference of the temperatures at the south and north slopes of the Qinling Mountains.

REFERENCES

Qi,Y. and B. Fu,Theoretical study on the interaction between airflow over a mountain and the atmospheric boundary layer. Boundary-Layer Meteorology,64,101-126,1993.

Theoretical Study on Atmospheric Boundary Layer and the Interaction with Free Atmosphere over Local Heating

Qi Ying and Zhou Jingnan

(Institute of Mechanics, CAS,Beijing 100080,P.R.China)

ABSTRACT: In this paper, by a mesoscale numerical model with a higher-order turbulent closure,the turbulent structures in the atmospheric boundary layer over a local heat source are simulated. The interactions between the atmospheric boundary layer and free atmosphere are discussed. And the phenomenon of "bore" ,which is often observed when the sea breeze disappears, can be explained.

1. INTRODUCTION

Locally thermal circulations,such as sea-land circulation, mountain-valley circulation and heat island circulation,are paid great attention to in the recent 30 years.It has been clear and definite that the turbulent transfer in the atmospheric boundary layer(ABL)plays an important role in the formation of locally thermal circulations.However,the turbulent structure in the ABL over a local heat source still needs to be further studied. In addition,in the theory of locally thermal circulation forecasting,the relationship of the interaction between ABL and free atmosphere(FA) is an open question.As a matter of fact,Giovannoni(1987) wind tunnel simulations have shown that different stratifications of environment make locally thermal circulations be of different structures.In this paper,by a atmospheric mesoscale numerical model with a higher-order turbulent closure(Qi,1992;Qi,et al 1993),the trubulent structures in the ABL over a local heat source are simulated and the interaction between the ABL and FA is discussed.

2. MODEL

It is assumed that the model atmosphere is dry and incompressible, and satisfies hydrostatic equilibrium.The underlying heat source is presumed to be uniform in the Y direction.Then the equations describing the thermal circulation forced by the heat source are

$$\frac{\partial u}{\partial t} + u\frac{\partial u}{\partial x} + w\frac{\partial u}{\partial z} = -\theta\frac{\partial \Pi}{\partial x} + fv - \frac{\partial \overline{u'w'}}{\partial z} \tag{1}$$

$$\frac{\partial v}{\partial t} + u\frac{\partial v}{\partial x} + w\frac{\partial v}{\partial z} = fu_s - fu - \frac{\partial \overline{v'w'}}{\partial z} \tag{2}$$

$$\frac{\partial \theta}{\partial t} + u\frac{\partial \theta}{\partial x} + w\frac{\partial \theta}{\partial z} = -\frac{\partial \overline{\theta'w'}}{\partial z} \tag{3}$$

$$\frac{\partial \Pi}{\partial z} = -\frac{g}{\theta} \tag{4}$$

$$\frac{\partial u}{\partial x} + \frac{\partial w}{\partial z} = 0 \tag{5}$$

in which $\Pi = C_p (\frac{p}{10^5})^{\frac{R}{C_p}}$,the variables with primes are turbulent quantities.The above equations are closed by second-order moment turbulent equations:

$$\frac{d(\overline{u'_i u'_j})}{dt} = -\overline{u'_i u'_k}\frac{\partial u_j}{\partial x_k} - \overline{u'_j u'_k}\frac{\partial u_i}{\partial x_k} + \frac{g}{\theta_0}(\overline{\theta' u'_i}\cdot\delta_{j3} + \overline{\theta' u'_j}\cdot\delta_{i3}) - \frac{q}{3l_1}\cdot\frac{\alpha_0}{\alpha_{00}}(\overline{u'_i u'_j} - \delta_{ij}$$

$$\cdot\frac{q^2}{3}) + \frac{\alpha_0}{\alpha_{00}}C_1 q^2(\frac{\partial u_j}{\partial x_i} + \frac{\partial u_i}{\partial x_j}) - \frac{2}{3}\cdot\frac{q^3}{\Lambda_1}\delta_{ij} + \frac{\partial}{\partial x_k}$$

$$\left[q\lambda_1\left(\frac{\partial \overline{u'_i u'_j}}{\partial x_k} + \frac{\partial \overline{u'_i u'_k}}{\partial x_j} + \frac{\partial \overline{u'_j u'_k}}{\partial x_i}\right)\right] \tag{6}$$

$$\frac{d(\overline{\theta' u'_i})}{dt} = -\overline{u'_i u'_k}\cdot\frac{\partial\theta}{\partial x_k} - \overline{\theta' u'_k}\frac{\partial u_i}{\partial x_k} + \frac{g}{\theta_0}\overline{\theta'^2} - \frac{q}{3l_2}\overline{\theta' u_i} + \frac{\partial}{\partial x_k}\left[q\lambda_2\left(\frac{\partial\overline{\theta' u'_i}}{\partial x_k} + \frac{\partial\overline{\theta' u'_k}}{\partial x_i}\right)\right] \tag{7}$$

$$\frac{d\overline{\theta'^2}}{dt} = -2\overline{\theta' u'_k}\frac{\partial\theta}{\partial x_k} - 2\frac{q}{\Lambda_2}\overline{\theta'^2} + \frac{\partial}{\partial x_k}(q\lambda_3\frac{\partial\overline{\theta'^2}}{\partial x_k}) \tag{8}$$

where $q^2 = \overline{u'^2_1} + \overline{u'^2_2} + \overline{u'^2_3}$, $(l_1, l_2) = (A_1 l, A_2 l)$, $(\Lambda_1, \Lambda_2) = (B_1 l, B_2 l)$, $\lambda_1 = \lambda_2 = \lambda_3$ $= 0.231$, $(A_1, A_2, B_1, B_2) = (0.78, 0.78, 15.0, 8.0)$, $C_1 = 0.056$. l is mixing length:

$$l = \begin{cases} L_1 & \frac{\partial\theta}{\partial z} \leqslant 0, \\ \dfrac{L_1\cdot L_2}{L_1 + L_2} & \frac{\partial\theta}{\partial z} > 0. \end{cases}$$

in which,

$$L_1 = \frac{\chi z}{1 + \frac{\chi z}{L_0}} \quad, \quad L_2 = \frac{0.53 q}{(\frac{q}{\theta_0}\frac{\partial\theta}{\partial z})^{\frac{1}{2}}} \quad, \quad L_0 = \frac{0.1\int_0^\infty q z\, dz}{\int_0^\infty q\, dz}$$

Equations (1)-(8) therefore make up a group of closed basic equations. They are changed into difference equations by difference and may be numerically solved with given boundary conditions.
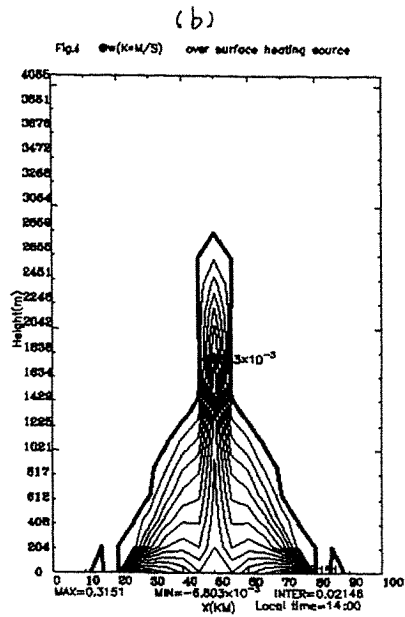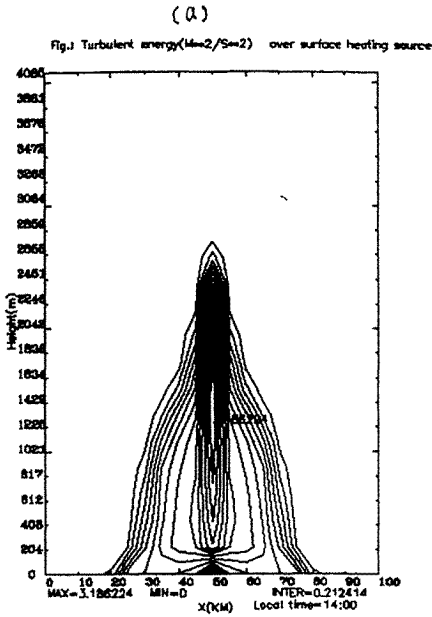
3. SIMULATIONS AND THEORETICAL ANALYSIS

Under the role of the local heat source, i.e., bottom temperature boundary condition:

$\theta = 289 + 8\sin(15t - 110) + 2.3\sin(30t + 75) + 0.3\sin(45t + 66)$ (k) (25km<x<75km)

$\theta = 289$ (k)   (x<25km or x>75km)

the locally thermal circulations are simulated by the above numerical model. During the first period of the local heat source strengthening, the ABL over the heat source uniformly develops upwards and the turbulent kinetic energy and heat fluxes are relatively uniform in the horizontal distribution. With the heat source strengthening further, the ABL over the center of the heat source rapidly develops upwards. At 14:00LST (as shown in Fig.1), the height of the ABL is up to 2.6km or so and near the height of 1.2km, there occurs a maximum value of the turbulent kinetic energy ($3.18m^2/s^2$) (Fig.1a). Correspondingly, the upward turbulent heat transfer is the strongest over the center of the heat source (Fig.1b). With the heat source weakening, the height of the ABL over the center of the heat source rapidly decline. At 18:00LST, the height of the ABL is only 400m or so, when the direction of the turbulent heat transfer has become downward. In the whole
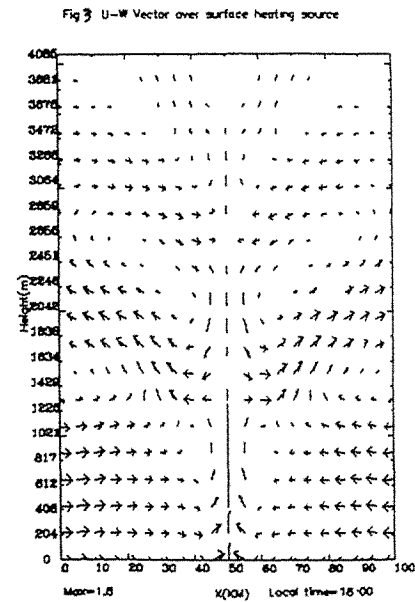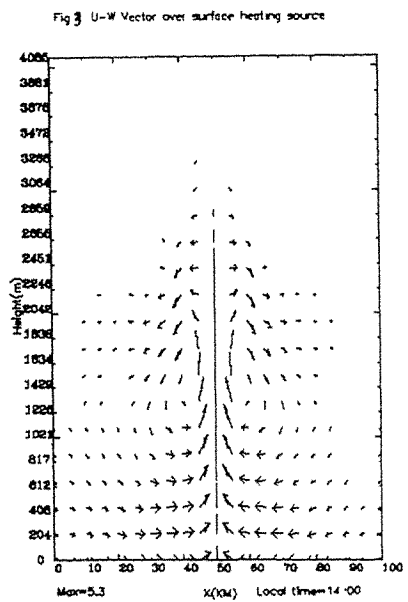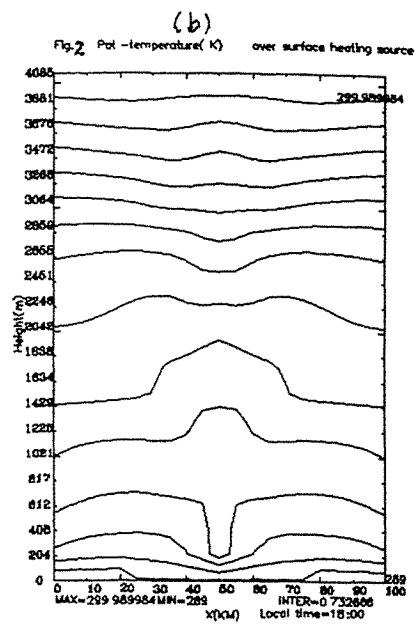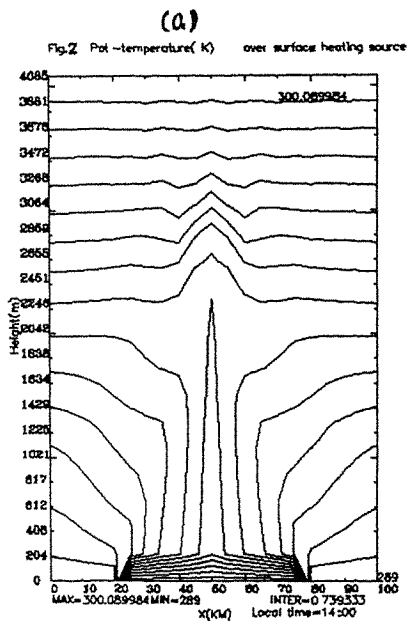
Fig.3 Turbulent energy(M=2/S=2) over surface heating source

Fig.4 ●w(K=M/S) over surface heating source

process of the local heat source evolution above,the distribution of the turbulent momentum fluxes is basically identical:In the upstream of the center of the heat source,the turbulent momentum fluxes transfer downwards in the lower part of the ABL and upwards in the middle and upper part of the ABL,while just opposite to the above in the downstream of the center of the heat source.

As we know,the height at which turbulence disappears is the height of the ABL,then we can divide the model atmosphere into the ABL with turbulence and the free atmosphere without turbulence in the vertical direction according to the distribution of turbulent energy.Thus the simulations as shown in Fig.2, Fig.3 and Fig.4 can be analysed below.

(1) The ABL within the extent of the heat source becomes the center of high temperatures due to the turbulent heat transfer(as shown in Fig.2a).However,the horizontal convergence flows corresponding to it appear only in the middle and lower part of the ABL and in the upper part of the ABL,there are opposite horizontal divergence flows(as shown in Figs.3a,4a). It can thus be seen that the thermal forcing in the ABL does not control the evolution of the flow field in the ABL completely.The reverse flows' occurrence in the ABL is enough to demonstrate that the free atmosphere has the effect of feedback on the ABL. At 18:00LST,when the local heat source is tending to disappear(see also Fig.2b),it can be known from Fig.4b that the original horizontal convergence flows in the ABL over the center of the heat source are obviously suppressed by the perturbation flows in the FA.

(2) In the FA over the heat source,the center of low temperatures

473

Fig.2 Pot -temperature(K) over surface heating source

Fig.2 Pot -temperature(K) over surface heating source

(a)

(b)

Fig 3 U-W Vector over surface heating source

Fig 3 U-W Vector over surface heating source

(a)

(b)

Fig.4, U(M/S)   over surface heating source

Fig.4, U(M/S)   over surface heating source
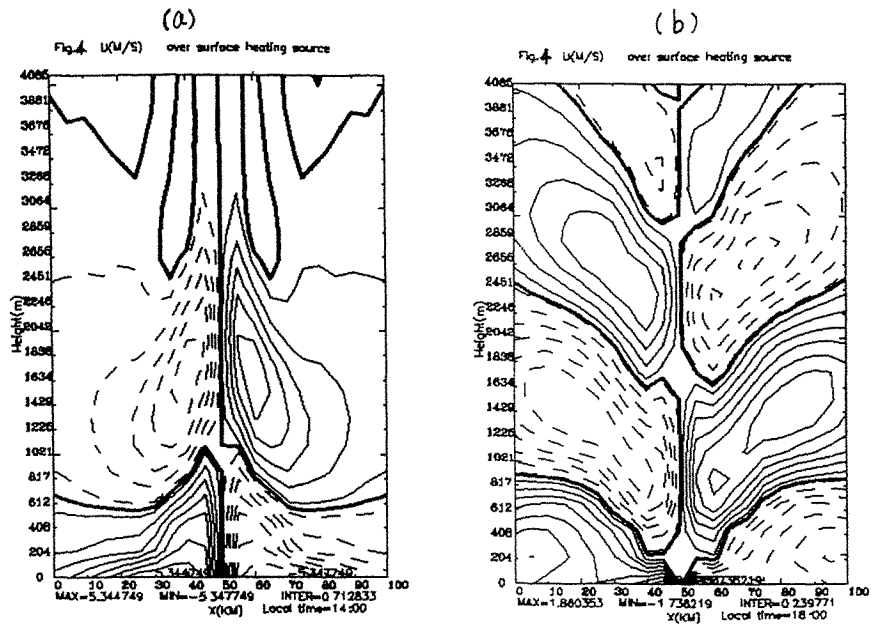
appears due to the adiabatic decreasing temperatures caused by the forced upward motion at the top of the ABL(as shown in Fig 2a) Corresponding to it,the flow field shows reverse horizontal divergence flows(as shown in Figs.3a,4a) Therefore,under the role of the local heat source forcing,the perturbation flows in the FA are principally controlled by the forced convergence flows in the ABL At 18 00LST,when the local heat source is tending to disappear,it can be easily found from Fig 2b that the center of low temperatures in the FA,caused by the forced upward motion, does not appear any more although it can be known from Fig 3b that the upward motion still exists in the ABL Reversely,there is a center of high temperatures below the height of about 600m and above the top of the ABL (400m or so) It is this center of high temperatures that is the characteristic remained after the heated ABL declines Under the trigger of the center of high temperatures,the horizontal wind field and potential-temperature field in the FA show obvious wave structures in the vertical direction(Figs 2b,4b) Therefore,when the local heat source is tending to disappear,the perturbation fields in the FA are not subjected to the forced upward motion in the ABL any more But according to the above analysis,the perturbation waves in the FA apparently suppress the convergence flows in the ABL over the center of the local heat source It can be deduced that when the local heat source is tending to disappear,such the interaction relations between the FA and ABL completely probably make the perturbation fields in the ABL also show the wave structures And the phenomenon of "bore',which is often observed when the sea breeze disappear,can be explained from this

475

4.CONCLUSIONS

In this paper,by a mesoscale numerical model with a second-order turbulent closure,the ABL and its turbulent structure in locally thermal circulations and fields of winds and temperatures in the corresponding FA are discussed.The major conclusions are as following:

(1) With the local heat source strengthening,the ABL rapidly develops upwards,especially over the center of the heat source,and at the middle of the ABL, there occurs a maximum value of turbulent kinetic energy and the upward turbulent heat transfer is the strongest.

(2) In the ABL over the local heat source, there are horizontal convergence flows at the middle and lower part and horizontal divergence flows at the upper part of the ABL.Therefore,the wind field in the ABL is apparently affected by the feedback of the FA.However,under the forcing of the local heat source,the perturbation flows in the FA are mainly controlled by the vertical motion forced at the top of the ABL.

(3) When the local heat source is tending to disappear,the perturbation fields in the FA are not controlled any more by the forced upward motion in the ABL but regulate themselves to the wave structure. Meanwhile,the convergence flows in the ABL over the center of the original local heat source are also obviously suppressed by the perturbation waves in the FA and probably make the perturbation fields in the ABL become the wave structure,too. From this,the "bore", often appearing when sea breeze disappears, can be explained.

REFERENCES

1. Y. Qi, "Theory on the Interaction between Mesoscale Terrain Flows and Atmospheric Boundary Layer and Study on the Typical Mountain Climates in China", Ph.D. thesis,Nanjing University,Nanjing,(1992) 125pp.
2. Y. Qi and B. Fu, A theoretical study on the interaction between airflow over a mountain and the atmospheric boundary layer, Boundary-Layer Meteorology , 64 (1993) 101.

Numerical Simulation of the Thermal Internal Boundary Layer in Coastal Area—Application of E-ε closure model[①]

W.G.Wang and W.M.Jiang

Department of Atmospheric Sciences,
Nanjing University,Nanjing,China

Abstract:A mesoscale PBL model with a simple turbulence closure scheme, E- ε closure scheme based on the turbulence kinetic energy(TKE) equation and the dissipation rate (ε) equation was used to simulate the wind and temperature fields,turbulence fields and the TIBL structure during the developing of the sea-breeze in the coastal area. The results obtained from this model are in concordance with that from observations and high-order closure model simulations.

1.Introduction

It is well known that the structure of thermal internal boundary layer(TIBL) in the coastal area plays an important role in the atmospheric transport and diffusion of air pollutants. Until recent years,the observation is the main method used to study TIBL. Many simple formulation cannot be agreeable completely with the results of observation at a site, and an understanding of the turbulence mechanism in the TIBL is so poorly. Numerical model with K-closure is poorly to predict the turbulence fields, and it is not available under complex conditions; High-order closure model may give the prediction of the mean fields and turbulence fields, but it is too complicated for regular application. Recently, the E- ε closure model,based on a simple closure scheme using the turbulence kinetic energy(TKE) equation and the dissipation rate (ε) equation,has been adopted in many research work. This scheme has been used mostly in field of engineering was not found in field of meteorology so far. Many studies indicate that this scheme can improve the prediction performances including the mean fields and turbulence fields significantly(Deterling and Elting,1985;Duynkerke, 1988 ;Holt and Raman,1989).

In the present study, an E-ε model has been developed and used to study the TIBL in the coastal area, results obtained from high-order closure model and observations were used to compare with that from E-ε model in this paper.

2. The model

The basic governing equations of the turbulent flow in PBL were used with the

---

assumptions of hydrostatic equilibrium and incompressibility and the turbulent kinetic energy(E) equation and the dissipation rate(ε) equation(Rodi,1985) were added as follows:

$$\frac{\partial E}{\partial t} + u\frac{\partial E}{\partial x} + w\frac{\partial E}{\partial z} = \frac{\partial}{\partial x}\frac{K_H}{\sigma_E}\frac{\partial E}{\partial x} + \frac{\partial}{\partial z}\frac{K_V}{\sigma_E}\frac{\partial E}{\partial z} +$$
$$K_V\left\{\left(\frac{\partial u}{\partial z}\right)^2 + \left(\frac{\partial v}{\partial z}\right)^2\right\} - \frac{g}{\theta}\frac{K_V}{\sigma_T}\frac{\partial\theta}{\partial z} - \varepsilon \quad (1)$$

$$\frac{\partial \varepsilon}{\partial t} + u\frac{\partial \varepsilon}{\partial x} + w\frac{\partial \varepsilon}{\partial z} = \frac{\partial}{\partial x}\frac{K_H}{\sigma_\varepsilon}\frac{\partial \varepsilon}{\partial x} + \frac{\partial}{\partial z}\frac{K_V}{\sigma_\varepsilon}\frac{\partial \varepsilon}{\partial z} +$$
$$C_{1\varepsilon}\frac{\varepsilon}{E}\left[K_V\left\{\left(\frac{\partial u}{\partial z}\right)^2 + \left(\frac{\partial v}{\partial z}\right)^2\right\} - (1-C_{3\varepsilon})\frac{g}{\theta}\frac{K_V}{\sigma_T}\frac{\partial\theta}{\partial z}\right] - C_{2\varepsilon}\frac{\varepsilon^2}{E}(2)$$

$$K_V = C_\mu\frac{E^2}{\varepsilon} \quad (3)$$

where u,w denote the velocities components in x,z directions; K_h, K_v are the eddy diffusivities in vertical and horizontal; θ is the potential temperature; σ_t is the Prandtl number, σ_k and σ_ε are the ratios of the eddy diffusivity for momentum to those for the TKE and the dissipation rate, respectively. According to the Delting and Elting's discussion(Detling and Elting,1985) and the results of the numerical experiments in this study, the parameters used in the model were as follows: $C_\mu=0.026$; $C_{1\varepsilon}=1.44$; $C_{2\varepsilon}=1.9$; $\sigma_\varepsilon=1.3$; $\sigma_E=1.0$; $\sigma_T=1.0$ and $C_{3\varepsilon}$ is equal to 1 (stable stratification) or 0 (unstable stratification).

In the 2-D model, the simulation domain was 100(Km)×4(Km), a staggered grid system was used, the number of grid points was 40×25.The similarity relationships given by Businger et.al. were used for the surface layer in the model. The bottom boundary condition of TKE and ε were: $E = 5.5u_*^2 + 0.5w_*^2$, $\varepsilon = u_*^3 / kz + g / \theta(\overline{w'\theta'})$,where u_* is friction velocity,w_* is convective velocity scale. $\overline{w'\theta'}$is the subgrid potential temperature flux. The variation of the temperature on ground surface was given by a sine distribution, but the temperature on the water surface was keep constant. At the upper boundary, variables were fixed at their appropriate values as u=v=0. At the horizontal boundaries, the derivatives with respect to x of all dependent variables were set equal to zero. Initial potential temperature was given by a vertical profile linearly-increased with height at a constant rate 5k/km.

3. Results and discussions
3.1 The simulations of fields of wind and temperature

From the analysis of the simulated wind and temperature fields,the sea-breeze circulation is oberviously found during the daytime. Since inhomogeneous heating over land and sea surface, the maximum of horizonal velocity appears at the shoreline. Because the difference between land and sea reached to its maximum at 14:00, the sea-breeze was most active for several hours after 14:00, then the speed of sea-breeze was gradually on the decrease. The convergence area on land extended to inland during the developing of sea-breeze. The

depth of unstable layer increased from shoreline to inland area, and reached to maximum depth which was the depth of inland mixing-layer.

3.2 The characters of TKE and ε in coastal area

Analyses of the TKE and the εdistributions at different times showed that there was the maximum value of TKE at 14:00,but there was no maximum of the dissipation rate ε over the land. It meant that turbulence exchange under the mixing-layer in the inland was very strong.Figure 1 presented the distributions of TKE and ε at 15:00.Due to the desease in the difference between land and water after 14:00, the peak vale of TKE was becoming weak, but the dissipation rate ε would be on the increase continuously and the turbulence exchange in the mixing-layer would be weakened. In the course of the TKE production and destruction, it was also foundthat the magnitude of the TKE and the ε was dominated by the strengh of buoyancy.Some spectial phenomenon in the coastal arae have been found from the analyses on the simulation distributions of the TKE and ε :(1) There was the greater dissipation rate on the shoreline due to stronger wind shear.(2)With the increase of the distance from shoreline to inland, the depth of layer in which the TKE greater than $0.2 \mathrm{m}^2/\mathrm{s}^2$would increase.(3) Due to the greater dissipation rate on the shoreline,decrease in the TKE would be greater than in the inland area after 14:00.
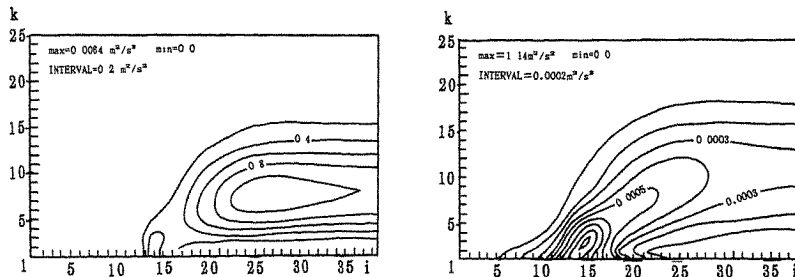
Figure 1. The contour pattern of computed TKE(a) and ε(b)

Figure 2 showed the simulated vertical profiles of terms in the TKE-equation. From the profile on shoreline at 14:00(figure 2.a),It was found that the budget of the TKE below the height of 500m was dominated by terms of buoyancy, wind shear , dissipation and vertical diffusion dominate. The effect of buoyancy decreased with the increase of height. Figure 2. b shows the profiles in the mixing-layer at 14:00. Observiously, it was found that the wind shear was very weak and the TKE-equation would be controlled by other three terms and the maximum effect of buoyancy was in the middle of mixing-layer.All of these were concordance with the thermal effect in this layer.It was supposed by some researchers that the advection term was not important to TKE budget,and the vertical advection,was connected with turbulence exchange in the boundary-layer.The profiles of the vertical advection term in the right of figure (a,b) were presented. On the whole, the main difference

479

turbulence character between the TIBL and the inland mixing-layer was : in the TIBL,the TKE's production was dominated by the wind shear and in the mixing-layer, the effect of buoyancy was very strong so that the TKE's production or destruction was controlled main-ly by the buoyancy.

3.3 Profiles of TIBL

In field of air pollution meterorology,the expermental formula, $(h_i \sim x^{1/2})$, is often used to describe the height of the TIBL.Figure 3 showed the height of the TIBL obtained from our model at the different distance from shoreline(x) and it was obviously found that the TIBL profiles was not smooth and the slope of TIBL profiles was the function of distance from shoreline. It was found that the position of the TIBL maximum height was concord-ance with the position of the centre of convergence area. This is because of local inhomogeneous of turbulence exchange of motion and heat(Deardorff and Willis,1982). It has been demostrated by the results of many observations(Stunder and Sethuraman,1985;Kerman et.al.,1982)and the numerical simulations of high- order closure model(Jiang and Wu,1992).
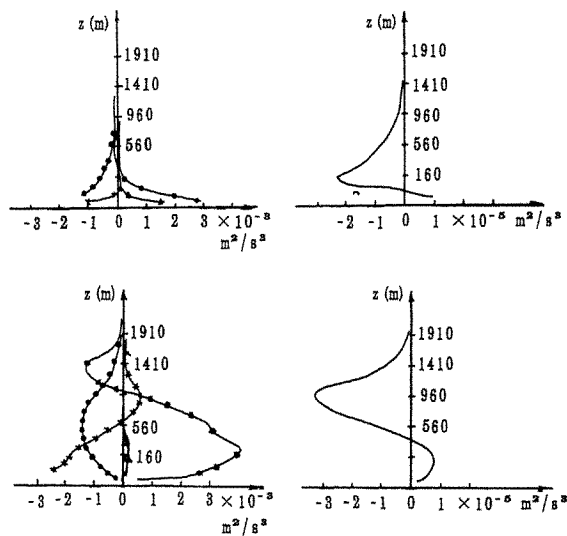
Figure 2. Vertical profiles of terms in the TKE-equation at different positions at 14:00:(a) x = 0;(b) x = 10km (the right side of (a) and (b) are profiles of vertical advection terms).Symbols in the figures denote respectively: •,dissipation term; ·,buoyancy term; ×,diffusion term; △,shear term.

Figure 4 showed the potential temperature profiles at the different distance from

shoreline at 14:00. The stable(cold) air over water was heated from surface to up after they cross shoreline. The depth of unstable layer due to heating was on the increase with the increase of distance from shoreline to inland.

4. Comparision with the results of observations or high−order closure model

The part results of simulation using E−ε model were compared with the results of observations or high−order closure model.The result on the TIBL height from the Nanticoke experiment(Kerman,1982) was used to compare with the results from the present model under the same condition.Some comparisions with high−order closure model(Jiang and Wu,1992) has also been done.It was agreeable reasonably between the results of two models,for example,the TIBL profiles and turbulence variables.
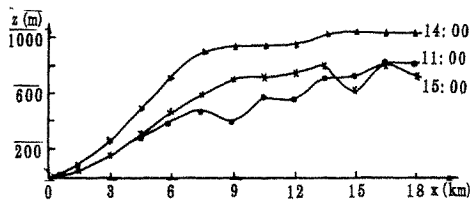
Fig. 3. Height of TIBL as funtion
of distance from shoreline,x
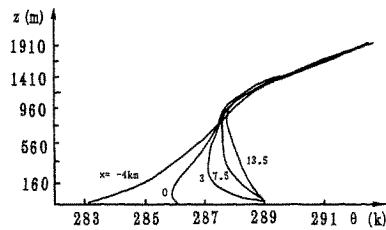
Fig. 4. Vertical profiles of the computed
potential temperature at different
position at 14:00

5.Conclusions

Based on the results obtained from analysis and comparision of the simulation results, it has been demostrated that the E−ε model might successfully simulate the mean field and the turbulence field during the course of the developing of the TIBL: (1) The obvious local sea− breeze circlation due to inhomogeneous heating on underlying surface was developed and simulated.The position of the centre of convergence area were connection with the maximum TIBL height.(2) With the distance increase from coastline, the variation of the TIBL profiles with the increasing distance from shoreline were not as smooth as $h_i \sim x^{1/2}$ monotonically . This phenomenon was agreeable with the results of many observations and modelling.(3) Wind shear was one of the major controlling factors on the budget of TKE under the TIBL,but in the mixing−layer the buoyancy term is the most important.

On the whole, the results obtained by the E−ε model set up in this paper were satisfactory. In order to improve the modelling accuracy of the model , the parameters of $\sigma_e, \sigma_E, \sigma_T$etc., shoud be obtained by means of observations or numerical simulation.

481

References:

1. H.Deterling and D.Elting,Boundary–Layer Meteorol., 33(1985)113.
2. P.G.Duynkerke,J.Atmos.Sci.,45(1988)865.
3. T.Holt and S.Raman,Reviews of Geophysics,26(1989)761.
4. W.Rodi and J.C.R.Hunt,ed.,In Turbulence and Diffusion in Stable Environments, England,Oxford University Press,(1985)111.
5. P.G.Duynkerke and G.M.Driedonks,J.Atmos.Sci.,44(1987)43.
6. J.W.Deardorff and G.E.Willis,Atmos.Environ.16(1982)1159.
7. B.R.Kerman et.al.,Atmos. Environ., 16(1982)423.
8. M.Stunder and S.Sethuraman,Boundary–Layer Meteorol.32(1985)177.
9. W.M.Jiang ,X.M.Wu et.al.,Boundary–Layer Meteorology,61(1992)301.

Experimental and numerical simulation of flow around two-dimensional hills

A.D. Ferreira, A.M.G. Lopes, D.X. Viegas and A.C.M. Sousa*

Grupo de Mecânica dos Fluidos, Universidade de Coimbra, 3000 Coimbra, Portugal
* Dept. of Mechanical Engg., University of New Brunswick, Fredericton, E3B 2E9, N.B. Canada

Abstract: The present work is devoted to the study of the turbulent isothermal flow around two-dimensional sinusoidal hills. In this work, both experimental and numerical approaches were followed. The experimental results were obtained from a simulation carried out in two wind tunnels, for a Reynolds number, based on the hill's height, ranging from 1.8×10^4 to 2.5×10^5 The results obtained experimentally comprise static wall pressure distributions, velocity profiles at strategic locations and flow visualisation. The algorithm adopted for the numerical simulation is based on a control volume approach applied to a numerically generated boundary fitted grid The transport equations are solved using the SIMPLEC formulation, and turbulence is modelled with a modified low-Reynolds number k-ε model. The comparison between numerical and experimental results show an overall good agreement.

1. Introduction

The detailed knowledge of the wind flow around hills is of great interest in many engineering applications, particularly when dealing with wind load and power mapping, pollution dispersion and agro-meteorological studies. The present work was motivated by forest fire propagation on hilly terrain, which is being currently studied by the authors.

There are many situations in nature where a two-dimensional approach can be accepted with a reasonable degree of accuracy. This is the case where there is a hill or a group of hills with a practically constant cross section and a straight crest line, with wind flowing perpendicularly to this line. In this paper a sinusoidal shaped hill is considered subjected to an incident turbulent adiabatic flow of the atmospheric type. Experimental and numerical simulations were carried out in order to determine the main properties of the average flow field around the hill, specially in the vicinity of the surface, which was always assumed to be smooth.

2. Experimental set-up

For the present work, four different hills geometries were considered, as shown in Fig. 1. The geometrical shape of the models is defined by the following equation:

$$z = \frac{H}{2}\left[1 + \sin\left(\frac{x-L}{2L} \times \pi\right)\right]$$

(1)

where H is the height of the hills, L is the length, measured in the flow directio, for z = H/2

Two different sets of experiments were conducted in two wind tunnels, which are schematically represented in Fig. 2.
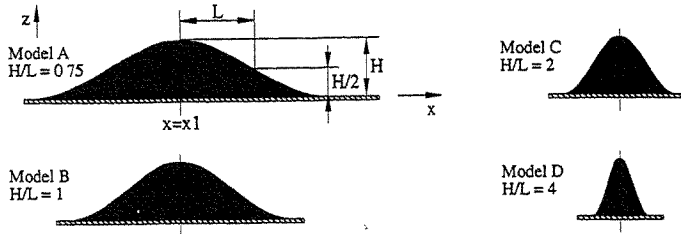
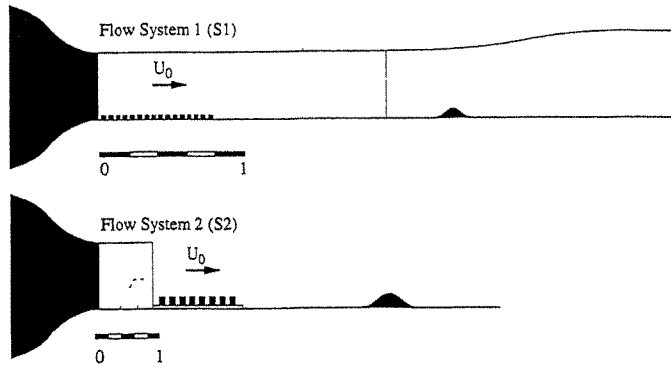Figure 1 - Definition of the geometry for the four models

Figure 2 - Schematic representation of the two wind tunnels - S_1 e S_2

It is noteworth the fact that the ceiling of the wind tunnel used in the first set of experiments could be deformed. This characteristic is justified by the need of reducing the blockage effect inherent to the closed test section, in order to achieve an approximately constant static pressure in the undisturbed flow. For a faster growth of the boundary layer, roughness elements were positioned upstream of the test section. The undisturbed velocity was set at approximately 20 m/s, and the turbulence intensity was evaluated in 5 %. The height of the four geometries studied in this wind tunnel is 6 cm, and the Reynolds number based on the height of the models was 8×10^4. The exponent of the velocity profile α ($U/U_0 = (z/\delta)^\alpha$) was evaluated in 0.16 and the depth of the boundary layer was 12 cm.

In order to achieve larger values of the Reynolds number, and also to ensure a better simulation of the atmospheric conditions, a second wind tunnel was employed. This tunnel had an open working section, and a maximum attainable velocity of 20 m/s. In this set (S_2), the experiments were conducted for various Reynolds numbers and the boundary layer profile was adjusted by placing roughness elements and vorticity generators upstream of the test section, as proposed by Counihan [1]. The geometric characteristics of the model studied in this wind tunnel are: H/L=1; H= 2m. The boundary layer profile obtained with the particular configuration had a thickness δ=.55m, and α=0.24. The turbulence intensity of the undisturbed flow was nearly 12%.

3. Numerical model

Although the present study concerns a two-dimensional situation, the numerical code was originally developed in a three-dimensional formulation. The numerical model used for the calculation of the flow field around the sinusoidal hills is based on a control volume approach. For the present case, a correct integration of the equations governing fluid behavior requires the domain to be described by means of a boundary fitted coordinate system. Grid characteristics, such as smoothness, skewness, and spatial distribution, have a decisive influence on the precision of the solution obtained, and even on the numerical stability of the iterative process. In the present work, the physical locations of each grid node were made to be solution of a set of elliptic differential equations. Grid generation using a Laplace equation was first proposed by Thompson [2], and further improved through the introduction of control functions, which allow proper adjustment of the clustering and orthogonality of grid lines near the boundaries. This method has proved to be quite robust and of easy adaptation to new geometries. A typical grid used in the present calculations may be observed in Fig 3.
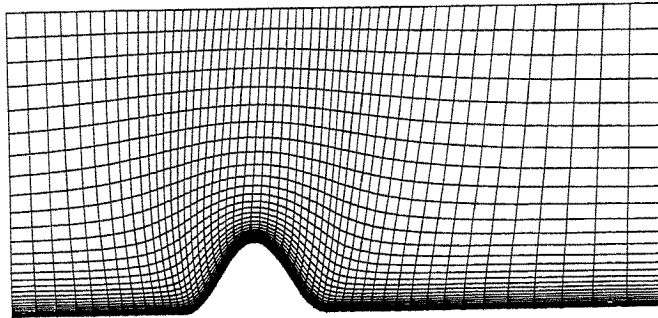
Figure 3 - Typical grid used for the present calculations

Transformation of the Navier-Stokes equations is accomplished by substituting the dependent Cartesian variables by the deformed grid variables. In the present approach, the Cartesian components of the velocity are kept as the dependent variables, since the choice of the covariant or the contravariant velocity components would lead to a much more complex set of equations. When the chain rule is applied to the original set of Navier-Stokes equations, and the terms are rearranged through the application of the metric identity, the following form results :

$$\frac{\partial}{\partial \xi_i}\left(J \rho U_i u_i\right) = -\frac{\partial \xi_i}{\partial x_i}\frac{\partial P}{\partial \xi_i} +$$
$$\frac{\partial}{\partial \xi_m}\mu_{eff}J\left[g^{mn}\frac{\partial u_i}{\partial \xi_n} + \frac{\partial \xi_m}{\partial x_j}\frac{\partial \xi_n}{\partial x_i}\frac{\partial u_j}{\partial \xi_n} - \frac{2}{3}\frac{\partial \xi_m}{\partial x_i}\frac{\partial \xi_n}{\partial x_j}\frac{\partial u_j}{\partial \xi_n}\right] - J\left[\frac{\partial \xi_j}{\partial x_i}\frac{\partial (\rho k)}{\partial \xi_i}\right] \qquad (2)$$

where u_i is a generic Cartesian velocity component, U_i represents the contravariant components of the velocity vector and J is the transformation Jacobian. The turbulent viscosity is computed with a low Reynolds number k-ε model, in a formulation similar to the one proposed by Zhang and Sousa [3], here extended to generalized coordinates. A control volume formulation [4] is employed for the

485

integration of the transport equations in each computational cell, where the variables are defined according to the staggered grid proposed by Harlow and Welch [5] Continuity and momentum equations are linked through pressure following the SIMPLEC formulation [6]. Transport equations are discretized using linear profiles for the viscous derivatives, while the convection terms are treated using a hybrid formulation [3]. These discretized equations, including the pressure correction equation, are all cast in a single general form as proposed by Patankar [4], and solved using the TDMA algorithm with sweeps in the three computational directions, except for the pressure correction equation. For this equation, due to its low rate of convergence particularly in grids with a large aspect ratio, a three level multigrid technique is used in conjunction with the TDMA algorithm As boundary conditions, the velocity and turbulence quantities are specified at the inlet of the domain. At the ground, all variables are set to zero, while the outlet boundaries are considered to be pervious to the flow. In these boundaries, the contravariant velocity components normal to the boundary are constrained by mass conservation, and for other velocity components and turbulent quantities, the second derivatives are set to zero.

4. Presentation of the results

The size of the recirculation region for S_1 was visualised by sticking wool tufts in the surface of the models, as well as in the bottom and lateral walls of the wind tunnel. The visualisation of the flow obtained for a Reynold number of $8x10^4$ is schematically represented in Fig. 4, where the lines depicted are a qualitative representation of the stream lines. The stream lines computed numerically for each hill configuration can be observed in this same figure. The values of the stream lines are not equally spaced, being selected to allow a good visualisation of the main flow characteristics. It can be observed in this figure how the size of the recirculating region is strongly dependent on the hill's shape, with a quite evident growth of the recirculation bubble size from model 2 to model 3. The comparison between the numerical and the experimental results show a good agreement, being noteworthy, nevertheless, the larger size of the predicted recirculation region. This small discrepancy may be attributed to the proximity of the tunnel outlet, relatively to the test section, in the experimental set-up.
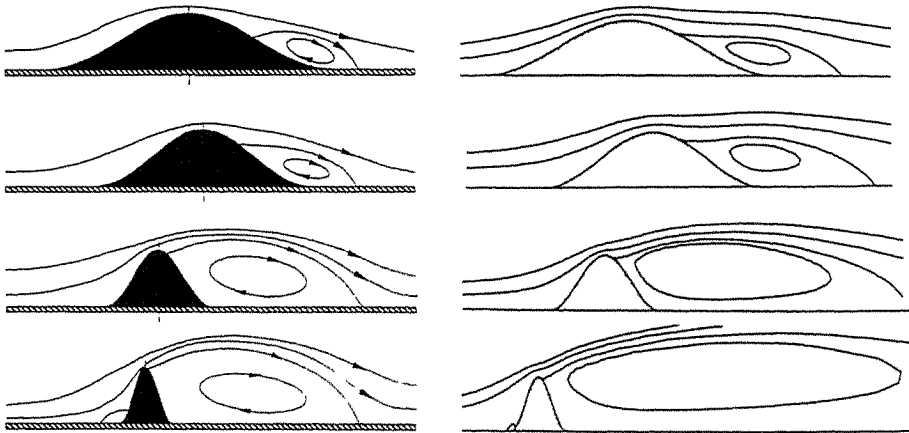

Figure 4 - Flow visualisation - experimental and numerical results - S_1 - Re=$8x10^4$

Some of the experimental and numerical results obtained in S_2 are presented in Figs 5, 6 and 7. Fig. 5(a) depicts the variation of the static wall pressure coefficient as a function of x/L, for Re=1.6x10^5. As expected, the initial Cp increase is followed by a region of low pressure, caused by the flow acceleration which maximum is situated at nearly the crest of the hill. Downstream of the crest, the energy loss due to viscosity and vorticity dissipation prevents Cp to recover the values prevailing upstream of the crest.

The velocity profile at the crest of the hill is depicted in Fig. 5(b), in terms of fractional speed-up (DS), where z' is the height above the hill's surface, at the crest of the hill (x=x_1), and ΔS is defined as $\Delta S = (U_{(x=x_1,z')} - U_{(x=-\infty,z=z')}) / U_{(x=-\infty,z=z')}$. The velocity field downstream of the hill was measured for S_2 using a 7 holes probe. This type of probe, which characteristics are described in [7], is capable of a simultaneous measurement of the velocity magnitude and its direction, for two and three-dimensional flows. The velocity vectors obtained experimentally are compared against the numerical results, in Fig. 6. Due to the fact that reverse flow could not be measured, regions with a negative component of the velocity vector are represented as dots.

(a)   (b)
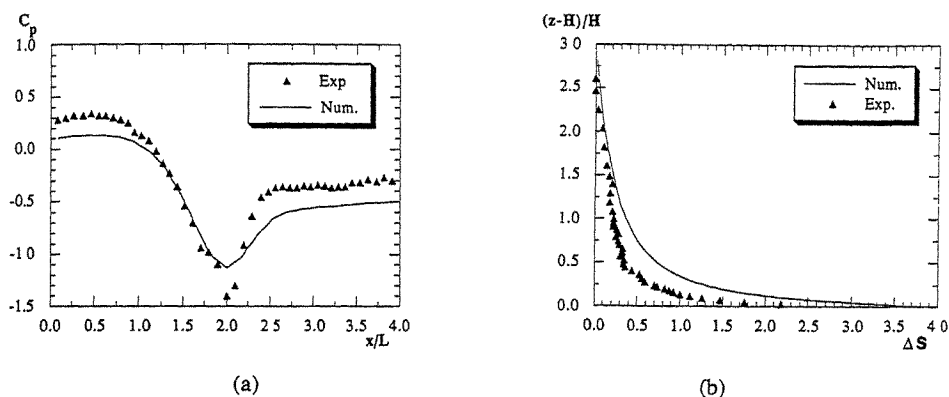
Figure 5 - Wall static pressure along the hill and velocity ratio at the hill's crest - S_2 - Re=1.6x10^5
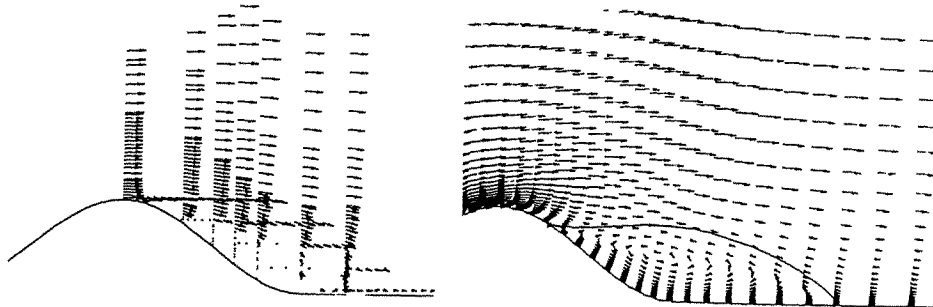
Figure 6 - Velocity vectors determined experimentally, and numerically

Figure 7 represents the variation of the drag coefficient C_d felt by the hill, as a function of the Reynolds number. In the presented results, the drag was computed uniquely from the wall static

487

pressure coefficient, which means that the contribution of the shear stresses to the total drag was not taken into account (it was evaluated, from experimental results, in 2% of the total drag [7]). It is clear, from the analysis of this figure, the existence of a transition to a supercritical regime, for a Reynolds number of, approximately, 9×10^4.
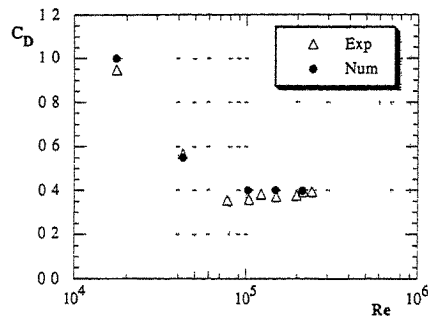
Figure 7 - Experimental and numerical results for the distribution of Cd - S_2

Conclusions

The present work describes the experimental and numerical study of the turbulent flow around two-dimensional sinusoidal hills. The results indicate that the extension of the recirculating region is strongly dependent on the hills shape. The study of the dependence of the results on the Reynolds number clearly showed the transition to a supercritical regime at $Re=9 \times 10^4$, where the non-dimensional flow characteristics is independent of the Reynolds number. Comparison between the experimental and numerical results showed a fairly good agreement.

Acknowledgements

References

[1]   J. Counihan, Atmospheric Environment, Vol. 7, pp. 673-689, 1973.
[2]   J.F. Thompson, F.C. Thames, and C.W. Mastin, J. of Comp. Ph., Vol. 15, pp. 299-319, 1974.
[3]   C. Zhang,. and A.C.M. Sousa, J. of Fluids Engineering, Vol. 112, pp.48-55, 1990.
[4]   S.V. Patankar, Numerical Heat Transfer and Fluid Flow , Hemisph. Publ. Corp, Washington, D.C., 1980.
[5]   F. H. Harlow and J.E. Welch, Physics of Fluids, Vol. 8, pp. 2182-2189, 1965
[6]   J.P. Van Doormaal, and G.D. Raithby, Numerical Heat Transfer, Vol.7, pp. 147-163, 1984.
[7]   A.D. Ferreira, Master Thesis, University of Coimbra, 1993.

488

FLOW BLOCKING ON WINDWARD SLOPE

Sang Jianguo Zhang Boyin[+] Niu Zhen nan[+]

Dept. Geophysics, Peking University

[+]Dept. Mechanics, Peking University

Abstract:A series of towing tank and numerical experiments was carried out to simulate the flow and concentration fields over a windward slope and also to seek the atmospheric conditions for airflow blocking.

I. Introduction

In the studies of the atmospheric dispersion the influences of terrain on the plume behavior and the surface concentration distribution are generally concerned[1]. In the present study the dynamic effects of the topography on the flow and concentration fields over the windward slope are to be discussed. The attention will be focused on whether the plume released from a source over the windward side can pass over the terrain; if not, where the plume will impinge on the slope surface; and whether the plume will be blocked on the windward side or it can pass around the lateral side of the terrain, and so on. The phenomena described above will influence significantly the distribution of the surface concentration. The factors dominating these phenomena are various. The important ones among them are the wind speed, the atmospheric stratification and the terrain height. They may combine a dimensionless Froude number $Fr = U/(hN)$ representing the ratio of the kinetic energy of the flow to the buoyant potential energy required to surmount the terrain.

The object of the study is the problem of the transport and diffusion in Daya Bay Nuclear Power Plant area (Fig. 1). In the normal operation the emission source with height of 80m is located at the seashore. As the prevailing southeast flow blows inland the radioactive gas released from the nuclear island passes over the reservoir and flows to the northern mountainous area. A saddle point of the topography with height of 350m is located at the northwest side of the reservoir. At the both east and west sides of the saddle the mountain tops are higher than 450m. Thus the saddle forms a narrow passageway for the on-shore airflow passing over the northen mountains.

The smoke tracer released from a 100m tower at the nuclear island in 1984—85 field experiments showed that in the morning stable on-shore flow the smoke sank to the terrain slope west of the reservoir. It indicated that the flow was blocked on the windward slope. The smoke neither passed over the saddle point nor the ridges in both sides of the saddle. It was forced to descend or to turn left to find a way out. The flow blocking may cause accumulation of the air pollutants on the windward slope. Thus the study of the atmospheric conditions inducing the blocking is essential to the safety assessment in normal operation and the emergency assessment in accident of the power plant. As the atmospheric conditions in field experiments can not be

controlled we carried out a series of physical and numerical experiments to simulate the dispersion behavior of the plume in variety of atmospheric condittions and also to seek an appropriate mathematical model to calculate the concentration distribution over this complex terrain area.

II. Towing tank experiments

The experiments were carried out in Peking University $6 \times 0.4 \times 0.6$m tank. Three types of terrain were applied; 1), plate; 2), two-dimensional ridge with height correspoding to 350m in prototype; 3), real terrain, as shown in Fig. 1, with saddle height of 350m. Three kinds of fluid stratification were taken; 1), uniform fluid, corresponding to the neutral atmosphere; 2). two-layer fluid, corresponding to an elevated inversion layer with base height of 200-300m in the real atmosphere, which forms because of the erosion of the ground inversion by surface

Fig. 1 Topography in the vicinity of Daya Bay Nuclear Power Plant. The contour interval is 50m. Rectangle enclosed by thin lines is the experimental area. The shaded area is the reservoir.

heating or because of the thermally internal boundary layer in on-shore stable air; 3), linearly continuous stratification, corresponding to the ground inversion at night or in the early morning. The towing speed was $1-2$ cm/s. Combination of terrain features, fluid stratification and towing speed may produce various expermental conditions with Froude number ranging from 0.18 to infinity. The dye tracer, emitting from a source with height corresponding to 100m in prototype, was used to simulate the plume behavior. The ratio of the emitting velocity to towing speed was $1-2$. The top view and side view photos of the dye trajectories were taken respectively by two cameras fixed with the model carriage. A television camera was simultaneously used to record the dye trajectories in order to observe the plume behavior repeatedly.

More than 30 towing experiments with combination of terrain type, stratification, towing speed and emitting velocity were conducted to simulate various dispersion states. The main results are as follws.

1), Uniform fluid with Fr infinite. The buoyant force, which exerted vertically on the fluid parcel, was zero. The dye plume, as seen from the side view photo ascended gradually with the terrain slope and finally passed over the terrain tops.

2). Stable stratification with Fr$>$1, as shown in Fig. 2. The buoyancy in the stable fluid was negative. The fluid parcel, however, had enough kinetic energy to overcome the suppress of the buoyancy and to surmount the obstacle. The dye trajectory, seen from the side view pho-

490

to, ascended with model terrain slope. But the rising was less than that in the neutral situation. The trajectory, seen from the top view photo, curved slightly as the fluid was impeded by the terrain.

3), Stable stratification with $Fr < 1$, as shown in Fig. 3. The vertical motion of the streamline passing through the source was suppressed by the stable stratification. The fluid, blocked and accumulated on the windward slope, could not pass over the terrain tops. It turned left and passed around the west end of the terrain. The streamline, seen from the side view photo, was horizontal and turned down as it touched the slope. The dye behavior was in agreement with that of the smoke tracer in the field experiments.

Fig. 2 Towing tank experiment in continuously stratified fluid with $Fr = 1.3$. Above: side view photo, below: top view photo.

II. Numerical simulation

Peking University Model of Atmospheric enviroment (PUMA) was used for numerical studies. The model includes horizontal momentum eqs., hydrostatic eq., continuity eq., thermodynamic eq. and turbulent energy eq. as well as particle random walk model. The atmospheric dynamic equations system was used to solve the flow fields in variety of atmospheric conditions. The turbulent kinetic energy calculated from the turbulent energy

Fig. 3 Same as in Fig. 2, but $Fr = 0.7$.

eq. was used to supply the turbulent diffusivities in the boundary layer parameterization and also the random fluctuation velocities in the random walk model.

According to the principle of geometry similarity and Froude number similarity a series of numerical experiments was carried out in variety of conditions corresponding to that in the towing tank experiments. The main results are as follows.

1), Neutral atmosphere. The streamlines, seen from the top view, are straight. They can pass over the terrain everywhere.

2),Stable atmosphere with potential temperature increase of 0.4K/100m and wind speed of 5m/s. Then we have $Fr = 1.3$. The simulated flow fields and the particle distribution from random walk model are shown in Fig. 4. In comparison with Fig. 3 we can see that the flow fields and dispersion state in both physical and numerical simulations are in agreement.

3), Stable atmosphere with potential temperature increase of 1.1K/100m and wind speed of 5m/s. We have $Fr = 0.75$. The flow fields and partiole distribution simulated are shown in

491

Fig. 5. The results show no difference with that of the towing tank experiments in the same Froude number (Fig. 3).

IV. Summary

In accordance with the conditions of the field experiments suitablly designed towing tank and numerical experiments can supply a large amount of information about the flow fields and dispersion state over complex terrain in variety of atmospheric conditions and may make up a deficiency of the data in field experiments.

The results show that model PUMA may properly describe the influences of the terrain on the flow and turbulence fields and simulate the dispersion state in more correct way in comparison with other models, for examples Gaussisn and its derived models.

Fig. 4 Flow field at 100m abve the ground surface and particle distribution with conditions: wind speed $v = 5m/s$ and temperature gradient $d\theta/dz = 0.34 k/100m$, i. e. $Fr = 1.3$. The contour interval is 200m.
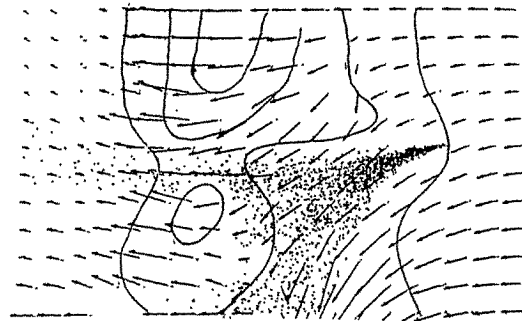
Fig. 5 Same as in Fig. 4, but $d\theta/dz = 1.27 k/100m$, i. e. $Fr = 0.7$.

References:
[1] B. A. Egan: Workshop on dispersion in complex terrain- Summary, Fourth Joint Conference on Application of Air Pollution Meteorology, 16—19 Oct. 1984, American Meteor. Society.
[2] Sang Jianguo and Wen Shigen: Numerical Calculation of Atmospheric Diffusion, Meteorological Press, 1992 (in Chinese).

Numerical Simulation of the Local Wind Field and Turbulent Characteristics for Sun-Radiation Heated, Unstable Stratified Atmospheric Boundary Layer around a Two-Dimensional hill

Du Guoliang

(Institute of Chemical Defence, China)

Abstract: In this paper the author uses three main techniques in modeling the motion of atmospheric boundary layer flowing over a two-dimensional hill: 1. Using body-fitted coordinate system with which one can exactly give the boundary conditions without interpolation in the case of complex terrain; 2. Two-equation model of turbulence (k-ε model) is employed to close the turbulent time-average equation; 3. In discretizing and solving the governing equations, SIMPLE algorithm (by Patankar) with some modifications is applied in which the power-law finite difference scheme is the essential factor for getting convergence in the iteration process. The calculated results shows that the above techniques are usable to deal with the problem in question, especially in complex terrain.

1. Introduction

The local wind field and its turbulent characteristics play a very important role in simulating atmospheric dispersion of a pollutant both experimentally and numerically. When wind flows over a hill or uneven ground surface the wind field becomes even more complicated because of the terrain complexity even not to consider the effect of radiation of the Sun. In recent years, with the development of computers and computational techniques, numerical modeling of atmospheric boundary layer in complex terrain is drawing greater and greater attention. But there are some difficulties to be overcome in order to use numerical modeling method in practice. In this paper the author suggests a new method trying to alleviate the difficulties. Three main techniques are used: The first is the use of body-fitted coordinate system (Thompson, 1974) with which the hill terrain can be transformed into a plane and the irregular physical domain into a rectangular one. So the boundary conditions can be precisely given on the ground surface without interpolation. The second is the use of the two-equation turbulent model to close the time-average N-S equations. This model is relatively simple but can result in reasonable result. In the model the buoyant effect resulting from radiation must be taken into account so as to consider the stratified atmosphere boundary layer. The last is the use of SIMPLE algorithm (Patankar & Spalding,1972) with some modifications in discretizing and solving the equations. This algorithm has overcome the difficulties in dealing with the pressure gradient term in momentum conservation equation. But the algorithm can not be directly used in body-fitted coordinate system. Some modifications must be taken to cope with the non-orthogonal curvilinear system. The suggested method is not restricted to two dimensional problems, but when three dimensional problem has to be considered, it can never be calculated on a micro-computer.

2. Coordinate Transformation

Consider a region with a two-dimensional hill in it. Let it be desired to transform it into a rectangular region with square mesh system in it as shown in Fig. 1a, and 1b.

Transformation equations are as follows:

$$\alpha x_{\xi\xi} - 2\beta x_{\xi\eta} + \gamma x_{\eta\eta} = -J^2[x_\xi P(\xi,\eta) + x_\eta Q(\xi,\eta)] \tag{1}$$

$$\alpha y_{\xi\xi} - 2\beta y_{\xi\eta} + \gamma y_{\eta\eta} = -J^2[y_\xi P(\xi,\eta) + y_\eta Q(\xi,\eta)] \tag{2}$$

Where

$$\alpha = x_\eta^2 + y_\eta^2 \qquad \beta = x_\xi x_\eta + y_\xi y_\eta \tag{3a}$$

$$\gamma = x_\xi^2 + y_\xi^2 \qquad J = x_\xi y_\eta - y_\xi x_\eta \ \text{————— Jacobian} \tag{3b}$$

$$P(\xi,\eta) = 0, \qquad Q(\xi,\eta) = -a\, e^{-b\eta} \quad (a, b > 0) \tag{3c}$$
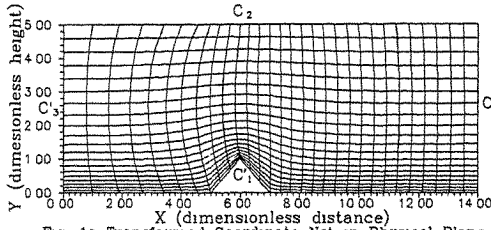
Fig 1a Transformed Coordinate Net in Physical Plane
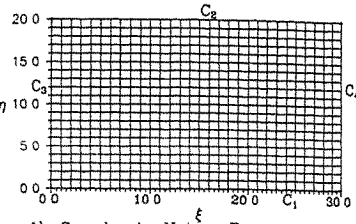
Fig 1b Coordinate Net in Transformed Plane

The mesh thickness in physical plane can be easily controlled to cope with the gradient of physical variables by varying $P(\xi,\eta)$ and $Q(\xi,\eta)$. Where the gradient of variable is greater the meshes are arranged to be thicker. Namely the nearer the points are from the ground the thicker the meshes are generated as shown in Fig 1a

The boundary conditions for Eq.(1) and (2) are listed below:

$$x = f_1(\xi, \eta_1), \qquad y = g_1(\xi, \eta_1) \qquad \text{on } C_1'$$

$$x = f_2(\xi, \eta_2), \qquad y = g_2(\xi, \eta_2) \qquad \text{on } C_2$$

where $\eta_1 = 0$, η_2 can be any integer according to how many meshes you wish to have in η direction.

$$x = f_3(\xi_1, \eta), \qquad y = g_3(\xi_1, \eta) \qquad \text{on } C_3'$$

$$x = f_4(\xi_2, \eta), \qquad y = g_4(\xi_2, \eta) \qquad \text{on } C_4'$$

$\xi_1 = 0$, ξ_2 like η_2 can be any integer according to how many meshes you wish to have in ξ direction.

Change x, y into dimensionless form (dividing by the hill height H) before transformation. Eqs. (1) and (2) can be solved by finite difference method on the ξ, η square mesh system (Fig. 1b). After solving them, the constant ξ and η line in physical plane can be obtained as shown in Fig. 1a.

3. Governing Equations and Turbulent Model

Consider mesoscale and steady state motion of the atmospheric boundary layer in which the geostrophic wind is of such a less importance that can be neglected and Boussinesq hypothesis holds. Furthermore in order to make the governing equations dimensionless, the following values should be introduced as characteristic ones: u_∞, the upper boundary undisturbed wind velocity as characteristic velocity, H, the hill height as characteristic length, $\theta_* = -q_0/\rho_0 c_p u_\infty$, where q_0 is heat flux on the ground surface, as characteristic potential temperature. Through dimension analysis, the following dimensionless variables or parameters can be obtained:

Velocity $\quad U_n = U/u_\infty$, $V_n = V/u_\infty$, Coordinate $\quad x_n = x/H$, $y_n = y/H$,

Potential temperature $\theta_n = \theta/\theta_*$, Heat flux $q_n = q/q_0$, Pressure $P_n = P/\rho_0 u_\infty^2$,

Turbulent kinetic energy $k_n = k/u_\infty^2$, Turbulent energy dissipation rate $\varepsilon_n = \varepsilon/(u_\infty^3/H)$,

Turbulent exchange coefficient $\Gamma_n = \Gamma/u_\infty H$, the values with subscript n are dimensionless.

494

For the sake of simplicity it need not to use the symbols with a subscript n to represent dimensionless variables or parameters. Instead the same symbols without a subscript are always refered to dimension-less ones unless specifying explicitly.

Let $U=uy_\eta-vx_\eta$, $V=vx_\xi-uy_\xi$ be components along constant η, ξ lines and u, v the velocity components along x, y directions.

Continuity
$$U_\xi + V_\eta = 0 \tag{4}$$

Momentum conservation :
$$(Uu)_\xi+(Vu)_\eta = [(\Gamma_u/J)(\alpha u_\xi-\beta u_\eta)]_\xi + [(\Gamma_u/J)(-\beta u_\xi+\gamma u_\eta)]_\eta + (P_\eta y_\xi-P_\xi y_\eta) \tag{5}$$
$$(Uv)_\xi+(Vv)_\eta = [(\Gamma_u/J)(\alpha v_\xi-\beta v_\eta)]_\xi + [(\Gamma_u/J)(-\beta v_\xi+\gamma v_\eta)]_\eta + (P_\xi x_\eta-P_\eta x_\xi) \tag{6}$$

Energy conservation:
$$(U\theta)_\xi+(V\theta)_\eta = [(\Gamma_u/J)(\alpha\theta_\xi-\beta\theta_\eta)]_\xi + [(\Gamma_u/J)(-\beta\theta_\xi+\gamma\theta_\eta)]_\eta + (q_{1\xi}y_\eta - q_{1\eta}y_\xi + q_{2\eta}x_\xi - q_{2\xi}x_\eta) \tag{7}$$

Turbulent model:
$$(Uk)_\xi+(Vk)_\eta = [(\Gamma_k/J)(\alpha k_\xi-\beta k_\eta)]_\xi + [(\Gamma_k/J)(-\beta k_\xi+\gamma k_\eta)]_\eta + J(G - \varepsilon) \tag{8}$$
$$(U\varepsilon)_\xi+(V\varepsilon)_\eta = [(\Gamma_\varepsilon/J)(\alpha\varepsilon_\xi-\beta\varepsilon_\eta)]_\xi + [(\Gamma_\varepsilon/J)(-\beta\varepsilon_\xi+\gamma\varepsilon_\eta)]_\eta + J(C_{\varepsilon1}G-C_{\varepsilon2}\varepsilon)\varepsilon/k \tag{9}$$

where k is turbulent kinetic energy, ε turbulent energy dissipation rate, and G its generation rate.

Auxiliary relations:
$$\Gamma_u= C_\mu k^2/\varepsilon \tag{10a}$$
$$G= (\Gamma_k/J^2)[(u_\eta x_\xi - u_\xi x_\eta + v_\xi y_\eta-v_\eta y_\xi)^2 + 2(u_\xi y_\eta -u_\eta y_\xi)^2 + 2(v_\eta x_\xi -v_\xi x_\eta)^2] - \mu q \tag{10b}$$
$$\mu = H/L_0 , \qquad L_0 = -\rho C_p u_\infty^3 T_0/gq_0 \tag{10c}$$

μ can be taken as stratification parameter of the atmosphere. $\mu \geq 0$ then atmosphere is satable while $\mu< 0$ unstable. According to semi-empirical theory

$\Gamma_k=\Gamma_u/\sigma_k$, $\Gamma_\varepsilon=\Gamma_v/\sigma_\varepsilon$, and σ_k, σ_ε are approximately constant. Table 1 lists the constant used in above equations.

Table 1. Constants Used

C_μ	$C_{\varepsilon1}$	$C_{\varepsilon2}$	σ_k	σ_ε
0.09	1.44	1.92	1.0	1.3

Equations (4) through (10) are also too complicated to be solved on a micro-computer. Some simplification should be taken. According to Laihtman's suggestion[2], in the atmosphere boundary layer, radiation effect among the earth surface, the atmosphere and the Sun can be described as an exponential function of height y. Then

$$q=\exp(-\alpha_1 y) \tag{11}$$

α_1 is so selected that makes q small enough in the upper boundary, say q=0.01 . Eq. (7) needs not to be solved.

4. Discretization of Equations and Finite Difference Scheme

Eqs. (4) through (9) form a closed set of equations and can be written in the common form:

Let $\Gamma_\phi^{(\alpha)}=\Gamma_\phi\alpha/J$, $\Gamma_\phi^{(\gamma)}=\Gamma_\phi\gamma/J$, $\Gamma_\phi^{(\beta)}=\Gamma_\phi\beta/J$, then
$$(U\phi)_\xi+(V\phi)_\eta = [\Gamma_\phi^{(\alpha)}\phi_\xi]_\xi + [\Gamma_\phi^{(\gamma)}\phi_\eta]_\eta + S_\phi \tag{12}$$

Table 2 shows the contents of S_ϕ when ϕ represents different variables.

Table 2. Contents of Source Term S_ϕ

ϕ	u	v	k	ε
S_ϕ	$P_\eta x_\xi - P_\xi y_\eta -$ $-[\Gamma_u^{(\beta)}u_\eta]_\xi-[\Gamma_u^{(\beta)}u_\xi]_\eta$	$P_\eta x_\xi - P_\xi y_\eta -$ $-[\Gamma_u^{(\beta)}v_\eta]_\xi-[\Gamma_u^{(\beta)}v_\xi]_\eta$	$-[\Gamma_k^{(\beta)}k_\eta]_\xi-[\Gamma_k^{(\beta)}k_\xi]_\eta$ $+J(G-\varepsilon)$	$-[\Gamma_\varepsilon^{(\beta)}k_\eta]_\xi-[\Gamma_\varepsilon^{(\beta)}k_\xi]_\eta$ $+J(C_{\varepsilon1}G-C_{\varepsilon2}\varepsilon)\varepsilon/k$

495

Eq. (12) can be discretized on the square mesh with side length being 1 in transformed plane. The method used was like that of algorithm (SIMPLE) used by Patankar and Spalding, But some modifications must be taken in order to cope with the special problem resulting from the use of the body-fitted system.

Fig. 2a shows part of finite difference grids and Fig. 2b one of the control volumes where the values of ϕ are assumed known at the nodes E, W, N, and S. Eq. (12) may be integrated over the square control volume (mesh) to yield:

$$A_p \phi_p = A_e \phi_E + A_w \phi_W + A_n \phi_N + A_s \phi_S + b \tag{13}$$

▦	v node
▨	u node
▢	P, k, ε nodes
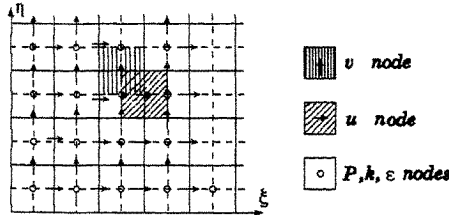
Fig. 2a Juxtaposition of grid nodes   Fig. 2b The Control Volume
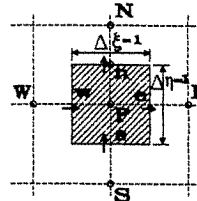
where
$$A_e = \Gamma_{\phi e}^{(\alpha)} f (U_e / \Gamma_{\phi e}^{(\alpha)}) + \langle\!\langle -U_e, 0 \rangle\!\rangle \tag{14a}$$
$$A_w = \Gamma_{\phi w}^{(\alpha)} f (U_w / \Gamma_{\phi w}^{(\alpha)}) + \langle\!\langle U_w, 0 \rangle\!\rangle \tag{14b}$$
$$A_n = \Gamma_{\phi n}^{(\gamma)} f (V_n / \Gamma_{\phi n}^{(\gamma)}) + \langle\!\langle -V_n, 0 \rangle\!\rangle \tag{14c}$$
$$A_s = \Gamma_{\phi s}^{(\gamma)} f (V_s / \Gamma_{\phi s}^{(\gamma)}) + \langle\!\langle V_s, 0 \rangle\!\rangle \tag{14d}$$

The special symbol $\langle\!\langle\ \rangle\!\rangle$ stands for the largest of quantities contained within it and $f(\ )$ is a function as shown below:

$$f(p) = \langle\!\langle 0, (1 - 0.1 |p|)^5 \rangle\!\rangle \tag{14e}$$
$$b = S_\phi \Delta\xi \Delta\eta = S_\phi \tag{14f}$$
$$A_p = A_e + A_w + A_n + A_s \tag{14g}$$

In order to get convergence in iteration, a specific juxtaposion of the velocity and pressure nodes, see Fig. 2, is required. All other equations are normally solved at the pressure nodes. if the pressure is known then Eq. (12) written for each variable at each grid mode together with the boundary conditions yield a closed set of algebraic equations.

Continuity equation (3) may be used to determine the pressure field. The finite difference equation of (3) is

$$(u\,y_\eta)_e - (v\,x_\eta)_e - (u\,y_\eta)_w + (v\,x_\eta)_w + (v\,x_\xi)_n - (u\,y_\eta)_n - (v\,x_\xi)_s + (u\,y_\xi)_s = 0 \tag{15}$$

u and v in grid nodes n and e can be written as below:

$$A_e u_e = \Sigma A_{nb} u_{nb} + b_u + (P_p - P_E) y_{\eta e} \tag{16}$$
$$A_n v_n = \Sigma A_{nb} v_{nb} + b_\nu + (P_p - P_N) x_{\xi n} \tag{17}$$

Unless the correct pressure field is employed, the resulting velocity field will not satisfy the continuity equation. Such an imperfect velocity field based on a guessed pressure field P^* will be denoted by u^*, v^*. Let us suppose that the correct pressure P, u, and v be obtained from

$$P = P^* + P', \quad u = u^* + u', \quad v = v^* + v' \tag{18}$$

Both u, u' and v, v' can be in the form of equations (16), (17). So if u^*, v^* were subtracted from (16), (17), then

$$A_e u'_e = \Sigma A_{nb} u'_{nb} + (P'_p - P'_E) y_{\eta e} \tag{19}$$
$$A_n v'_n = \Sigma A_{nb} v'_{nb} + (P'_p - P'_N) x_{\xi n} \tag{20}$$

The terms of $\Sigma A_{nb} u'_{nb}$ and $\Sigma A_{nb} v'_{nb}$ can be neglected. So

$$u'_e = (P'_p - P'_E) d_e, \qquad v'_n = (P'_p - P'_N) d_n \qquad \text{then}$$

$$u_e = u^*_e + (P'_P - P'_E) d_e , \qquad v_n = v^*_n + (P'_P - P'_N) d_n \tag{21}$$

where $d_e = y_{\eta e}/A_e$, $d_n = x_{\xi n}/A_n$ and the similar expression can be obtained for u_w and v_s.
Substitute u_e, u_w, v_n, v_s into Eq. (15) to yield

$$A_P P'_P = A_e P'_E + A_w P'_W + A_n P'_N + A_s P'_S + b \tag{22}$$

where $A_e = d_e/y_{\eta e}$, $A_w = d_w/y_{\eta w}$, $A_n = d_n/x_{\xi n}$, $A_s = d_s/x_{\xi s}$,

$$b = -(u^* y_\eta)_e + (v x_\eta)_e + (u^* y_\eta)_w - (v x_\eta)_w - (v^* x_\xi)_n + (u y_\xi)_n + (v^* x_\xi)_s - (u y_\xi)_s \tag{23}$$

If b is zero, it means that the starred velocity do satisfy the continuity equation (because after convergence of iteration, u^* will become u and v^* will become v) and no pressure correction is needed. The term b then represents a "mass source", which the pressure corrections (through their associated velocity corrections) must eliminate. Therefore b can be the criteria to determine if iteration is convergent.

5. Boundary Conditions and Solving Procedure

Where possible, we use experimental data and observation results as boundary conditions such as u, v, k, and q on the ground surface and the inlet boundary. At upper boundary we can state $u=1$, $v=0$ and $\partial k/\partial \eta$, $\partial \varepsilon/\partial \eta = 0$; at the outlet boundary, if the boundary is selected properly there is no need to give the boundary condition through letting A_e's (at the outlet) equal zero. It should be noted that the boundary conditions for pressure correction equation is very simple. We do not need to provide that condition, owing to arrangement of the grid node for P'. The meshes for P' cover entire transformed plane and the boundary coincide with the boundary control volume face, so the A_e at outlet A_n at upper boundary, A_s on the ground and A_w at the inlet can be set to zero. This is an essential measure to solve the pressure correction equation.

The solving procedure is the same as that of SIMPLE algorithm (Patankar & Spalding). The resultant set of algebraic equations can be solved by any method such as SOR or iteration line by line. The brief procedures are:
1. Guess the pressure field P^*;
2. Solve the momentum eqs. (4) and (5) to obtain u^*, and v^* ;
3. Solve the P' equation (19);
4. Calculate P from Eq. (18), by adding P' to P^*;
5. Calculate u, v, from their starred values using the velocity-correction formula (18);
6. Solve the discretization equation for other ϕ's (k, ε), according to auxiliary relation, calculating Γ_u, Γ_k, Γ_ε,
7. Treat the corrected pressure P as a new guessed one P^*, return to Step 2, and repeat the whole procedure until a converged solution is obtained (b becoming practical zero).

6. Results and Conclusion

Two shape of hills were considered, triangular and circular peek. In each case three stratifying parameters were taken into account, $\mu=-0.0001$, -0.0005, and -0.001, and $T_0= 300k$, $u_\infty= 10m/s$. H=100m. However there is no need to give the actual meteorological conditions and geometric parameters owing to using dimensionless form of equations. Fig. 3 and 4 show the calculated stream line pattern, with a recirculating region behind both shapes of the hill. The length of recirculating region is about 6-7 times of the height of the hill. This fact agrees with other author's calculation result and experimental data. Fig. 6 shows the typical turbulent exchange coefficient profile from which it can be seen that the turbulent exchange coefficient is closely related to the stratifying parameter Fig 5 shows the wind profile in different x locations and Fig. 7 the wind profile in the same location with different stratifying parameters. In Fig. 7 the vertical axis scale has been transformed into dimensionless form

497

by means of dividing it by friction velocity in order to compare it with empirical logarithmic law. At the lower part of the curves logarithmic law valid.

From discussion above, it can be concluded that the present method has been shown to produce plausible results. Before practical use of the method here further work is required to: (i) Investigate the numerical accuracy of the solutions; (ii) Test the physical realism of the solutions by making comparisons with more experimental data; (iii) Assess the effects of the locations of the boundaries on the solutions.

Fig 3 Stream Line Diagram (Circular Peak)

Fig 4 Stream Line Diagram (Triangular Peak)

Fig. 5 Velocity Profile in Different Location

Fig 6 Calculated Turbulent coeff

Fig 7 Wind Profile on the Top of Hill
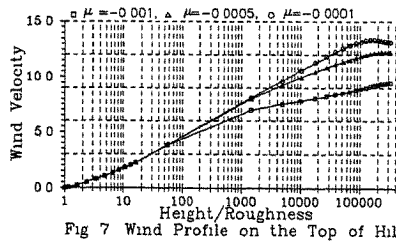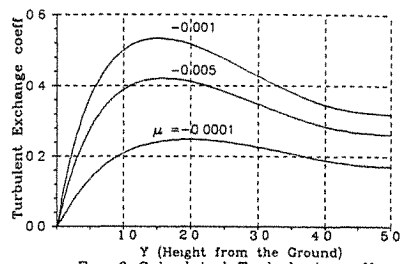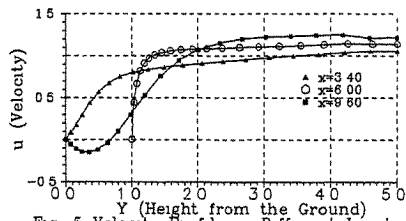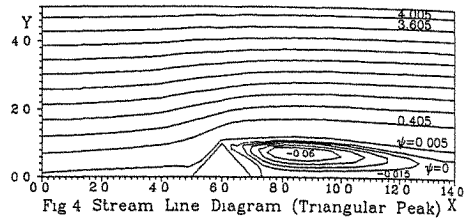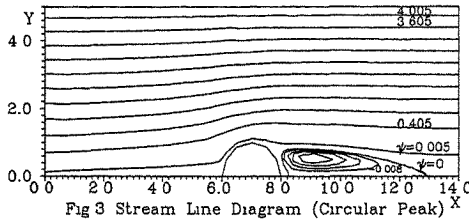
References

1. Thompson J. F., J. Computational Phys. , 15 (1974) 299.
2. Laihtman D. L., Physics if Atmospheric Boundary Layer, (Chinese version) Since Press of China (1982).
3. Du, Guoliang, Proc. the Second Asia-Pacific Symposium on Wind Engineering, Beijing, (1989) 1044.
4. Patankar S. V., Numerical Heat Transfer and Fluid Flow, Mc Gra-Hill (1980).
5. Pope S. B. and Whitelaw J. H., J. Fluid Mech., 73 (1976) 9.
6. Singhal A. K. and Spalding D. B., Computer Methods in Applied Mechanics and Engineering. 25 (1981) 365.
7. Launder B. E. and Spalding D. B., Mathematical Models of Turbulence, Academic Presss (1972)
8. Chen C. J. Turbulent Models and Finite Analytic Method , Press of Shanghai Communication University (1988).

498

Study on Turbulent Flow Over a Two-Dimensional Ridge by a Non-hydrostatic Higher-order Closure Model[1]

H.N.Liu   and   X.M.Wu

Department of atmospheric sciences, Nanjing university, Nanjing,China

Abstract: The influences of a 2-D ridge on the mean flow and turbulence structure in the neutral surface layer were numerically investigated by a non-hydrostatic higher-order turbulence closure modeldeveloped in this paper, and were simulated in an hencironmental wind tunnel . The distributions of mean wind, shear stress, turbulence energy and other quantities have been simulated. The influences of the shape of the hill, the roughness length of ridge and background wind speed on the fluctuation of flow around of the hill were discussed. Results obtained from the model compared with the date from the wind tunnel simulations.

1.Introduction

Many major sources of air pollution are located in complex terrain over which the air flow and dispersion of air pollutant are strongly controled by the terrain features. In order to understand the influence on air flow and dispersion around hopography, (1)field experiments, (2)numerical modeling (3)fluid modeling have been used.The numerical modeling have started in 1974 and 1975 with the appearance of a series of theoretical papers of Taylor and Gent(1974) and Jackson and Hunt(1975)(JH75).It was assumed in their research work that the flow was divided into the inner and the outer layer-the JH theory. The outer layer is assumed to be essentially inviscid which turbulent transfer processes are dynamically significant only within the inner layer. In order to avoid the necessity ofthe division of the flow into two layers and are not linearized, Taylor(1977)and Deaves(1976,1980) presented numerical, finite difference calculations of flow over idealized terrain features. but they use relatively simple closure hypotheses based on the use of the turbulent kinetic energy equation and the valus of turbulence are limited by the closure hypotheses. To aviod this , the higher-order closure was used in this paper. It may obtain a lot of physical information, especially the turbulence variables,which reveals the turbulence structure of 2-D terrain. Becaus the hydrostatic equation is not appropriate under the condition of small scale terrain,the model set up in this paper,was based on a non-hydrostatic equation system, and the term of the pressure perturbation was solved by means of the Poisson's equation.

2.The model

For the usual natural wind,incompressibility is a good approximation. The Coriolis and viscous term can be neglected because of small scale terrain. The equation for the Reynolds stress tensor $\overline{u'_i u'_k u'_j}$ for the two-dimensional mean flow, under neutral condition, are the following:(as space is limited, this equation in terrain-following coordinate is not given here)

$$\frac{\partial}{\partial t}\overline{u'_i u'_k} + U_j \frac{\partial}{\partial x_j}\overline{u'_i u'_k} + \overline{u'_j u'_k}\frac{\partial U_i}{\partial x_j} + \overline{u'_j u'_i}\frac{\partial U_k}{\partial x_j} =$$

$$-\frac{\partial}{\partial x_j}\overline{u'_i u'_j u'_k} - \left(\overline{u'_k \frac{\partial p}{\partial x_i}} + \overline{u'_i \frac{\partial p}{\partial x_k}}\right) - 2\overline{\varepsilon}\frac{\delta_{ik}}{3} \tag{1}$$

Where $\overline{\varepsilon}$ is the viscous dissipation rate of turbulent kinetic energy. Repeated indices indicate summation. In writing (1), it is assumed that the Reynolds number is so large that molecular diffusion terms can be neglected and locally isotropic forms can be used for the the molecular destruction terms. In quations (1), the closure approximation can be found in paper of Wyngaard et. al.(1974).

The pressure P can be solved by elliptic equation:

$$\frac{\partial^2 p}{\partial x^2} - 2A\frac{\partial^2 p}{\partial x \partial z} + (A^2 + B^2)\frac{\partial^2 p}{\partial z^2} = \frac{\rho}{\Delta t}\left(\frac{\partial u^*}{\partial x} - A\frac{\partial u^*}{\partial z} + B\frac{\partial w^*}{\partial z}\right) \tag{2}$$

where $A = \frac{S - \hat{z}}{S - z_s}\frac{\partial z_s}{\partial x}$, $B = \frac{S}{S - z_s}$, u^* and w^* is the mean velocity that pressure is neglected. z_s is the height of the ridge, S is top height of model, $\hat{z}$ is the height in terrain–following coordinate. In the model, at the top of model and the upstream boundary, all of quantities are fixed, at the downstream boundary, the derivatives with respect to x of all dependent variables are set equal to zero. The bottom boundary conditions are given by Wyngaard et. al.(1974). In present model , terrain is idealized 2–D ridge.The ridge can be characterized by its height H = 100m ,the half–height length L = 347m, and the slope is 16 ° .

3.Results and Discussions
3.1 Mean velocity

The vector of mean velocity is shown in Fig.1. The most striking features of Fig.1 are the increase in velocity at the crest and the slight deceleration at lower levels just before the hill, together with the pronounced velocity deficit in the wake. On the lee side, mean velocities are reduced considerably in the cavity region.extremely,It becomes negative near the surface. The preturbation in mean velocities caused by the ridge become insignificant beyond a distance of 16H.
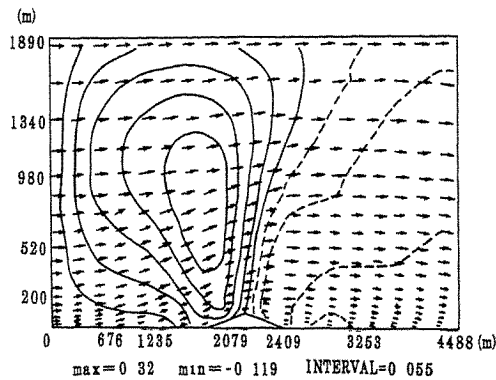
Fig.1. The Vector of mean velocity

500

In Figure 1, the contours of w are also indicated around the hill. There is a center of positive just before the top of hill and a center of negative located at the lee side. But near the surface in the cavity region, the positive of w are also found , which show the obvious reverse flow.

3.2 Turbulence moments

Figure2 presented the profile of Reynolds stress $-\overline{u'w'}$, and the $\overline{u'^2}, \overline{v'^2}$, $\overline{w'^2}$ profiles are similar and as space is limited,it is not given here.
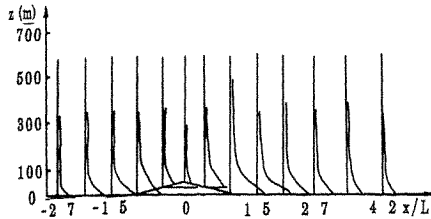
Fig.2. The profiles of Reynolds stress $-\overline{u'w'}$
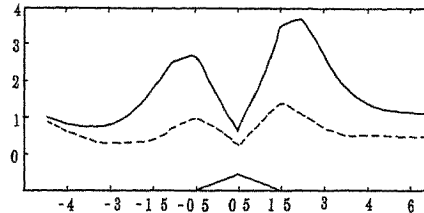
Fig.3.The distribution of $-\overline{u'w'} / u_*^2$ at $z' = 0.5$m and $z' = 50$m
(— $z' = 0.5$m,——— $z' = 50$m)

Near the surface , $-\overline{u'w'}$, $\overline{u'^2}, \overline{v'^2}$, $\overline{w'^2}$ are on the decrease in the up–slope as the top of hill is approached,and they become smallest at the top of the ridge. This can be attributed to the flow acceleration behind the hill. $-\overline{u'w'}$, $\overline{u'^2}, \overline{v'^2}$, $\overline{w'^2}$ and then show a sudden increase in their magnitudes in the cavity region, it is followed by a gradual decrease area with downwind distance.The perturbations of $-\overline{u'w'}$ are obviously confined within a layer of $z < 300$m, but for the variability of $\overline{u'^2}$, $\overline{v'^2}$, $\overline{w'^2}$ can only be seen over $z < 500$m.

The evolution of stress can be seen more clearly in Fig. 3, showing the variations of $-\overline{u'w'} / u_*^2$ at $z' = 0.5$m and $z' = 50$m respectively, where z' is the height over the local terrain. At $z' = 0.5$m, shows a increase at the foot of hill, then a strong decrease is at the hill crest and a dramatic increase is behind the ridge. The evolution of $\overline{u'^2}$, $\overline{v'^2}$ and $\overline{w'^2}$ are similar, except there are significant displacement among $\overline{u'^2}$, $\overline{v'^2}$, $\overline{w'^2}$,The peak in $\overline{w'^2}$ at downstream hillfoot occurs later than in $\overline{u'^2}$ and ahead of $\overline{v'^2}$ at the height $z < 350$m , at the upper layer ($z > 350$m), The peak in $\overline{v'^2}$ is in front of the peaks in $\overline{u'^2}$ and $\overline{w'^2}$.

3.3 The cavity region

In Figure1,there is a steady separation stream, A pronounced cavity region formed behind the hill,and it is characterized by an apparent reverse flow near the surface. The reverse flow extends to X / H = 7.6 from the foot of hill. The most important features of the cavity region are the strong deficit of mean momentum and the very active turbulent mixing. In wake region, The Reynolds stress and variance recover gradually,as the wake relaxes and expands. But the values are still bigger than those of upstream. The count of cavity and wake are defined according to the synthetic factor combined with the prominent peaks in $\overline{u'w'}$, $\overline{u'^2}$, $\overline{w'^2}$, the region of U deficit and the peaks in viscous dissipation rate. The depth of the cavity region is of order 0.5H and with horizontal region 10H. The wake region is estimated by H in

vertical and 17H in longitudinal.

In present model, the critical slope for steady separation is about 16 ° with the relative roughness $H / Z_0 = 200$. When the slope is steeper than the critical slope, a circulation will be formed in the cavity region. But the separation will also occur on hill when the slope is less than the critical slope if hill surface is rough enough .It is found that the critical slope is about 20 ° on smooth hill ($H / Z_0 = 1000$).

3.4 Effects of slope and Roughness

The features of mean flow and turbulence structure are **strongly dependent** on the shape of hill, surface roughness and background wind et. al. The distribution of $-\overline{u'w'} / u_*^2$ at $z' = 0.5$m in various slope are shown in Figure4.
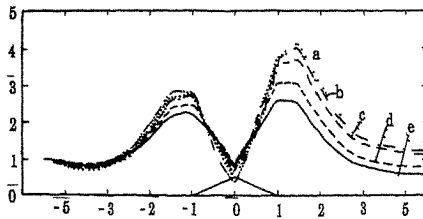
Fig.4.The distribution of
$-\overline{u'w'} / u_*^2$
(a 25°, b 20°, c 16°, d 12°, e 9.65°)
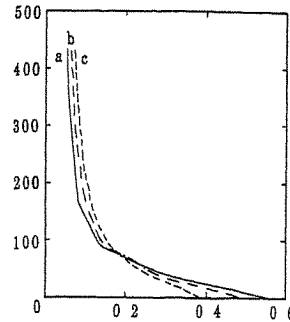
Fig.5. The profiles of turbulence energy
(a:25° ,b:16° ,c:9.65°)

It was found that the Reynolds stress $-\overline{u'w'}$, variances $\overline{u'^2}, \overline{v'^2}$ and $\overline{w'^2}$ reduce slightly at the top of steeper ridge. In the cavity region and before the hill, $-\overline{u'w'}$, $\overline{u'^2}, \overline{v'^2}$ and $\overline{w'^2}$ show a more significant increase as the slope is on the increase.

Fig.5 shows the profiles of turbulence energy in three slopes at downstream hill foot. When the hill become steeper,it is on the increase in turbulence energy in the lower layer ($Z < H$) and it is onn the decrease in upper layer ($Z > H$).

The effect of surface roughness is most significant for small values of H. Surface roughness changes the fractional speedup ratio at the crest greatly. The increase of roughness of hill leads to a strong decrease of mean velocity near the surface and a pronounced increase of $-\overline{u'w'}$, $\overline{u'^2}$, $\overline{v'^2}$ and $\overline{w'^2}$ above the ridge. It is also help to the formation of the cavity, characteried by the reverse flow. Even near the smooth surface at downstream , The mean velocities and $-\overline{u'w'} / u_*^2$, $\overline{v'^2}$ and $\overline{w'^2}$ changed also because of the variation of the roughness of hill.

3.5 Wind tunnel experiment

The experiment were performed in NJU wind tunnel . The scale of the model is 1 / 500 and slope is 16 ° . From the date of the experiments, it was found that the distributions of the mean velocity U,the turbulence intensity and the variance $\overline{u'^2}$ are concordance with the results of numerical modeling very well.

Mean velocity U is on the increase at the crest,and on the strong decrease at downwind

hill foot and just before the hill. The fractional speed—up factor ΔS is found to have maximum valus of about 0.32 at 1cm height over the crest.The distribution of the intensity of turbulence $i_x$and variance $\overline{u'^2}$ are similar to the result of numerical modeling. It also shows that there are two peaks in front of hill and at lee side respectively. When the slope become bigger, the location of the maximum deficit of U occurs later and $\overline{u'^2}$ and $i_x$are on the increase more dramatically in wake region. It is same as the results of numerical modeling. When the roughness of ridge become bigger, there is a pronounced speed deficit area near the surface and a strong increasing area of the turbulence intensity in lower leveals wih respect to the smooth ridge. Profiles of the $i_x$and u at downstream on hill foot were plotted in Figure 6 and 7, the variation of $i_x$and u are obviously confined inside the layler of $Z < 1 \sim 1.5H$.
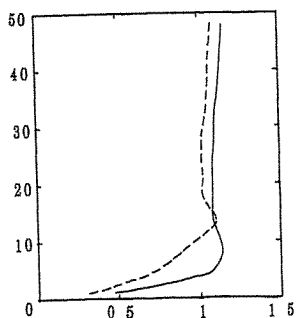
Fig.6.The profiles of mean velocity
(— smooth,——— rough)
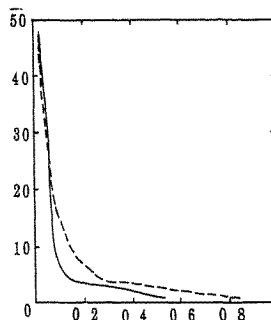
Fig.7.The profiles of turbulence intensity
(— smooth,——— rough)

4.Summary and conclusions

A non—hydrostatic higher—order turbulence closure model has been developed in this research work and the mean flow and turbulent fields around a 2— D ridge under neutral condition has been succesfully simulated. The most important feature of mean flow is that there are speed—up at the crest and the deficit in the wake region. On the contrary, The distributions of $-\overline{u'w'}, \overline{u'^2}$, $\overline{v'^2}$ and $\overline{w'^2}$are on the in the intensity at top of the hill and show that they are on the increase before the hill and in the cavity region. Many factor,such as the shape of hill,the roughness have a major influence on the distribution of these quantities. Finally, the numerical results and the date from the wind tunnel tests were compared and it was found that it was agreeable good with the data of experiment.

References:
1. D.M.Deaves, J.Wind Eng. and Indust.Aerodyn, 6 (1980) 89—111.
2. J.C.Wyngaard,K.S.Rao, O.R.and Cote, J.Atmos.Sci. 31(1974) 738—746.
3. P.S.Jackson, and J.C.R.Hunt, Quart.J.Roy.Meteorol.Soc. 101 (1975) 929—955.
4. P.A.Taylor, Boundary—layer Meteorol. 11 (1977) 439—465.
5. P.A.Taylor, and P.R.Gent, Boundary—layer Meteorol. 7 (1974) 349—362.

The Numerical Prediction of a Turbulent Flow Over a Curved Hill

Xu Cheng, Wu Xiao-song, Fa Li-xia and Wang Zhu-gao

105 Reaearch Facility
East China Institute of Technology, Nanjing, 210014, China

Abstract: The Numerical calculation for a turbulent flow over a curved "hill" is reported in the paper. A fully-elliptic numerical method has been developed to solve the Reynolds-averaged Navier-Stokes equation in curvilinear coordinate system. The k-ε turbulence model, in conjunction with wall-functions approach, is used to simulate the turbulent flow. Parts of calculation results are compared with Baskaran, Simit & Joubert exeprimental data and it is found that the computational method successfully reproduces the main feartures of the flowfield over the curved hill, including free external layer, internal layer and its developments, separation and reattachment, despite the fact that separation bubble tends to be underpredicted and boundary layer thichness be overpredicted.

1. Introduction

Many practical problems of engineering application are the complex turbulent flows with extra strain rates due to severe pressure gradients, streamline curvature, separation and reattachment. Therefore, to reveal the effects of those extra strain rates on the turblent behaviour and to predict those complex flows have been the subject of many experimental and computational investigations [1-6] . In this paper, a computer code for predicting complex flow is developed and the numerical calculation for a turbulent flow over a two-dimensional curved "hill" is carried out. The flow configurations calculated here are shown in Fig.1.
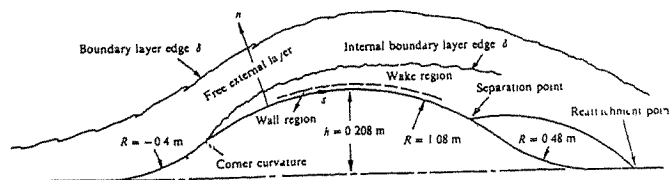
Fig.1   Flow configurations (coming from [6])

The boundary layer forms on a flat plate and then experiences a short region of concave curvature before encountering a prolonged region of convex curvature. The corresponding pressure gradient changes from adverse to favourable and back to adverse, and eventually the flow separates. The detailed experimental investigations on the flow over this geometrical model have been conducted by V Baskaran, A.J.Smits & P.N.Joubert and a set of available measurement data has been provided [5-6]. The present effort is aimed at the computation of Baskarn, Smits & Joubert's flow condition so that prediction results are examined by comparing them with experimental results.

2. The Governing Equations and Numerical Methods

The Reynolds averaged Navier—Stokes equations and the k—ε turbulence model were used to describe the turbulent flow field in this study. In a general nonorthogonal coordinate system, the Regnolds averaged form of the continuity equation for two—dimensional incompressible flow is

$$\frac{\partial \rho G_1}{\partial \xi} + \frac{\partial \rho G_2}{\partial \eta} = 0 \tag{1}$$

The momentum equations, k and ε model equations can be written as following general convection—diffusion form:

$$\frac{\partial \rho G_1 \varphi}{\partial \xi} + \frac{\partial \rho G_2 \varphi}{\partial \eta} = \frac{\partial}{\partial \xi}(\frac{\alpha}{J}\Gamma^\varphi \varphi_\xi) + \frac{\partial}{\partial \eta}(\frac{\gamma}{J}\Gamma^\varphi \varphi_\eta) + S^\beta + J S^\varphi \tag{2}$$

By integrating Eqs. (2) over an limit control volume and evaluating the variation at the surface of control volume using average variation of neighbouring cell point, the differential equations for Eqs.(2) can obtained as follows:

$$A_p \varphi_p = A_E \varphi_E + A_w \varphi_w + A_N \varphi_N + A_s \varphi_s + S_c^\varphi \Delta\xi\Delta\eta \tag{3}$$

where convetive terms and disspative terms are calculated by mixing difference method. Eqs. (3) can be solved by a under—relaxation iteration procedure.

The velocity field from Eqs (2) are substituted into the continuity equation and the concepts of pressure correction and velocity correction are adoped.

$$P = P^* + P' \qquad u = u^* + u' \qquad v = v^* + v' \tag{4}$$

where superscribe " * " denotes the solutions of momentum equation and " ' " denots correction to u,v,p. One then obtains a pressure correction equation.

$$A_p P'_p = A_E P'_E + A_w P'_w + A_N P'_N + A_s P'_s + m_p \tag{5}$$

where m_p is known as the residual mass sourse and is given by

$$m_p = [(\rho G_1^*)e - (\rho G_2^*)w]\Delta\eta + [(\rho G_2^*)n - (\rho G_2^*)s]\Delta\xi \tag{6}$$

Ordinary grid system is employed for the compulation and an additional term which is evaluated by 1—δx difference of pressure gradient minus 2—δx difference of pressure gradient is used to eliminate pressure oscillation. One example of effective form of additional term was found to be

506

$$G_{1e}^* = \overline{G_{1e}^*} + \overline{(BP_\xi^*)}e - \overline{Be(\partial P^* / \partial \zeta)}e \qquad (7)$$

The Eqs. (5) has the same format as Eqs.(3) and can also be solved by a under–relaxation iteration procedure.
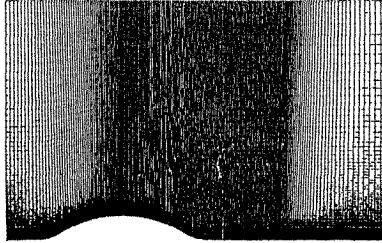
3. Results and Discussion

Fig.2　Calculation doman and grid

The calculation doman is shown in Fig.2. The top boundary is 10 curved "Hill" height. The upstream section from the front point of curved "hill" is 2 curved "hill" height and the downstream section from the rear poind of curved "hill" is 10 curved "hill" height. The computations were performal with a 200× 100 variable grid system which provides finer grid near wall (seeing Fig.2). The flow quantities at upstream section and top boundary are set and at downstream section were extrapolated from the inner solution by assuming that the first deviatives of flow properties along the ξ=const line vanish. On solid wall, the wall function method is used in present study to eliminate the large number of grid points needed to resolve the laminar sublayer.
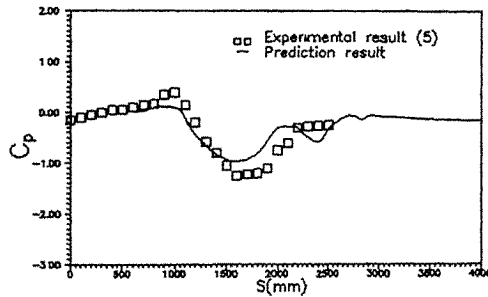
Fig.3　The wall pressure coefficient distribution

The predicted surface pressure distribution is plotted in Fig.3 and compared with the experimental data by Baskaran, Smits & Joubert [5] . The development of surface pressure

over the curved "hill" predicted here shows agreement with experimental results though the discrepancies in their magnitude are observed.
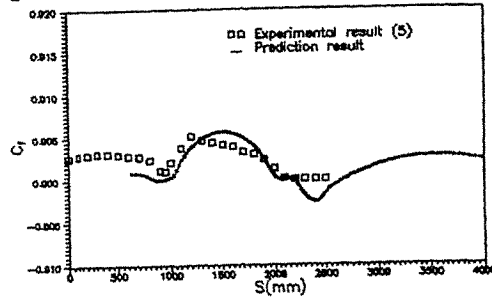
Fig.4 The skin–friction coefficient distribution

The skin–friction coefficients are shown in Fig.4. The skin friction over the leading–edge plate decreases due to the increasingly adverse pressure gradient. First turning point occurs on the concave bend, then the skin friction over the convex curvature increases . The second turing point occures in the middle region of "hill". The change trend of the skin friction follows the trend of the pressure gradients and agrees with the experimental results by Baskaran [5] et al. The discrepancy of the location of second turning point in c_f–s curve is because boundary–layer growth is not accurately predicted.
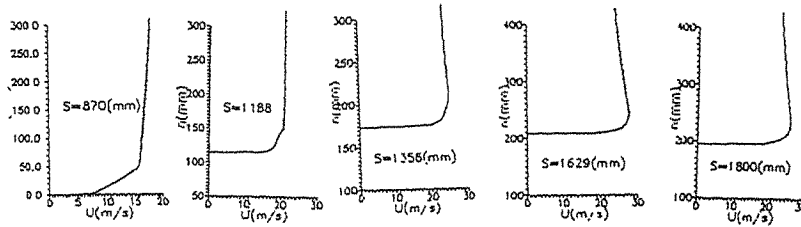
Fig.5 Mean velocity profiles, predicting results

Fig.5 shows the predicted mean velocity profiles at variable stream locations. Boundary–layer thickness increases over the leading–edge plate and decreases over former half of convex surface. It is over predicted comparing with the Baskaran's experiment. A local maximum in the mean velocity profiles forms at the crest of "hill" as expected.

508
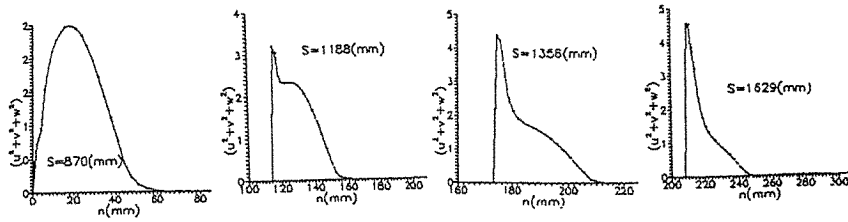
Fig.6   Turbulent kinetic energy profiles, predicting results

The characteristics of predicted k—profies (Fig.6) are similar to those reported by Baskaran el at [5] for this flow. The knee points in k—profiles forms on the convex surface and gradually propagate towards the edge of the boundary layer as the flow proceeds downstream. Below the knee points k increases with downstream distance, while outside the knee points k decreases. It is proved by Baskarn's experiment [5] that the behaviours of the knee points correspond to an internal layer forms and developments. The predicted behavour of the internal layer here is qualitatively agreement with thoes of the experiment.

The separated flow is predicted by present model and method, and the results are shown in Fig.7. The separation points ties to s=2065mm and reattachment points to s=2619mm for predicting case. The predicted reatt achment length is 554mm and is underpredicted.
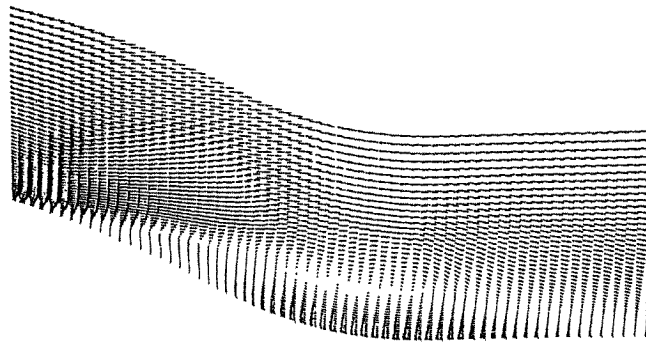
Fig.7   Velocity—vector plots for separation flowfield, predictng results

The reason for the discrepancies of this study is inadepuate turbulence modeling and wall function approach and a project of developing new turbulence modeling and method for the complex flows with separation is carrying out in East China Institute of Technology.

4. Concluding Remarks

Regnolds—averaged Navies—Stokes equations with $k-\varepsilon$ turbulent modeling in curvilinear coordinate system are solved by a finite volume method. A turbulent flow over a curved "hill" is predicted. The computation method successfully reproduces the main features of the flowfield over the curved "hill", inculding free external layer, internal layer and its developments, separation and reattachemtn. The requirement of the better turbulence modeling is indicated.

Acknowledgment

References:

[1] R.L.Simpson, AIAA Paper 85—0178
[2] P.A.Johnson, L.S. King, AIAA J., Vol.23, No.11. (1985)
[3] F.Pourahmadi and J.A.C. Humphrey, AIAA J. Vol.21 No.10, (1983)
[4] S.V.Patanker, K.C. Karki & Mongia, H.C. AIAA Paper 85—057, (1985)
[5] V.Baskaran, A.J.Smits & P.N.Joubert. J.Fluid Mech., Vol. 182 (1987)
[6] V.Baskaran, A.J.Smits & P.N. Joubert. J Fluid Mech., Vol. 237 (1991)

Extreme Wind

Analysis of peak gust vs. fastest-mile wind statistics

Richard E. Peterson, Steven D. Goldstein and K.C. Mehta[+]

Department of Geosciences
Texas Tech University, Lubbock
+Department of Civil Engineering
Texas Tech University, Lubbock

Abstract: The relationship between peak and gust wind speed and fastest one-minute wind speed occurring within the same hour has been studied for five stations in the United States. For each station at least ten years of observations were used to investigate the relationship and its variation seasonally, diurnally and with different concomitant weather events. As a result it appears that peak gust wind data could be used to estimate the fastest-one-minute wind for stations where the latter is not available.

1. Introduction

Surface weather records for stations in the United States may include several properties of the observed wind in addition to the hourly sustained value: the daily fastest-mile speed, fastest one-minute speed and/or peak gust. Many climatological studies have been based on but one of these parameters, e.g., the annual fastest-mile speed. This investigation focuses on the possible correlation between the fastest-mile wind and the peak gust for stations where both are available. Such a relationship would offer the possibility for expanding the data sources by combining information from stations where only one of the items is recorded.

2. Data Sources

Five stations were chosen for analysis (Fig.1). Amarillo (AMA) and Lubbock (LBB) are in the Texas High Plains. It would be expected that the weather phenomena responsible for extreme winds at the two sites would be similar; the relation between fastest-mile and peak gust winds might also be similar. Kansas City (MCI) and Minneapolis (MSP) are in the Central Plains but with a wider latitude separation than AMA and LBB. The characteristic weather events would be somewhat different from the High Plains sites. Syracuse (SYR) is in the Northeast with possibly a much different set of high wind generation phenomena.

The records which were examined visually were the daily surface hourly observations and the monthly station summaries (Local Climatological Data or LCD), which are assembled from the daily surface records.

The period chosen for study varied from station to station (dictated by data accessibility and homogeneity of the data collection): AMA 1980-1990; MCI 1975-1990; LBB 1980-1990; MSP 1975-1991; and SYR 1973-1990.

Fig. 1.   Station locations in this study
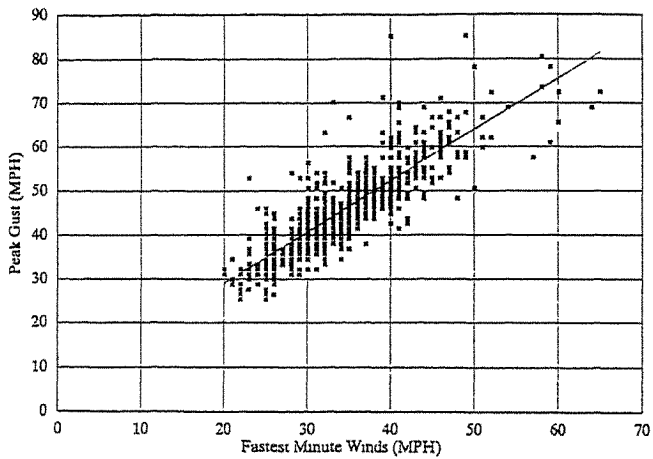
Fig. 2.   Regression analysis of peak gusts vs. fastest one minute
           winds: the total winds for all five stations.

Examination of the LCDs provided the date and speed of the fastest one-minute speed each month. Referring to the daily surface records for each date the peak gust information was extracted. If the two values fell within an hour it was assumed that the generation mechanism was common. Simultaneous weather events (e.g., blowing dust, thunderstorms, etc.) were also noted. (If the peak gust of the day did not occur within an hour of the fastest one-minute wind, the highest gust within an hour was determined; few occasions required this alternative.)

Anemometer sites in all cases are relatively smooth and open terrain, so the roughness heights should be similar. Instrument elevations differed slightly. In lieu of reducing the data to a standard height it was assumed that any relationships between the extreme wind parameters would be relatively insensitive to small variations in elevation.

3. Results

When all data for the five stations are composited (773 points), the relationship between monthly peak gust P and fastest one-minute wind speed F is given by

$$P = 5.82 + 1.16 \; F \quad \text{in mph}$$

with an $r^2 = 0.70$ (Fig.2). It may be noted that the scatter increases toward the high speeds.

Considering the data station by station (Fig.3), the r^2 values range from 0.62 (MSP) to 0.77 (LBB). In all cases the peak gust is greater than the fastest one-minute speed, but the slope of the relationship varies, 0.98 (SYR) to 1.41 (LBB).

The data, composited as well as by station, can be stratified according to various criteria; season, time of day, weather events, etc. With a smaller selection of points however, the statistical relationship becomes less clear cut. For example, for the total data set 24.6% of the events were associated with thunderstorm activity: 18% for SYR to 29% for MCI. For the total set the slope of the relationship is virtually identical to that for the total set.

With more stable conditions, winds at night are usually lighter; high wind events with abundant mechanical turbulence might be expected though to mix momentum from overhead about as well during the night as in daytime. In fact, the 34% of events that occurred at night had a slope of 1.14, only slightly different from the total.

Larger differences show up considering summer vs. winter events; the slope is 1.20 in June and 0.98 in December. Also the winds associated with blowing dust events (visibility below 7 mi.) yield a slope of 1.24; these only occur at AMA and LBB, for which the total subset slopes were 1.07 and 1.41, respectively.

4. Conclusions

On a station-by-station basis, peak gust wind data could be used to estimate the fastest one-minute wind where that information is not recorded.

515
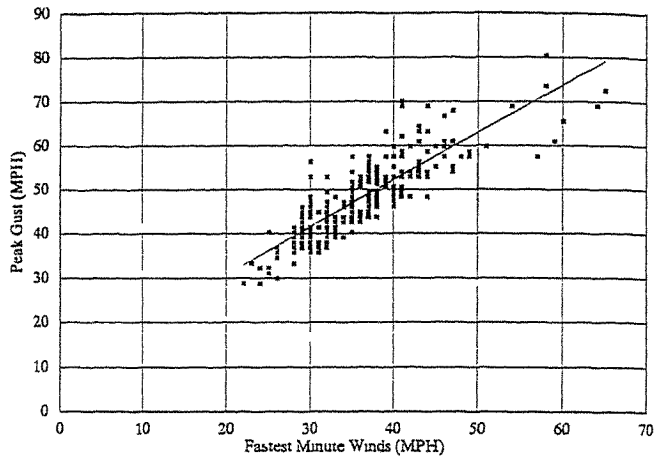
Fig. 3a. Regression analysis of peak gusts vs. fastest one minute
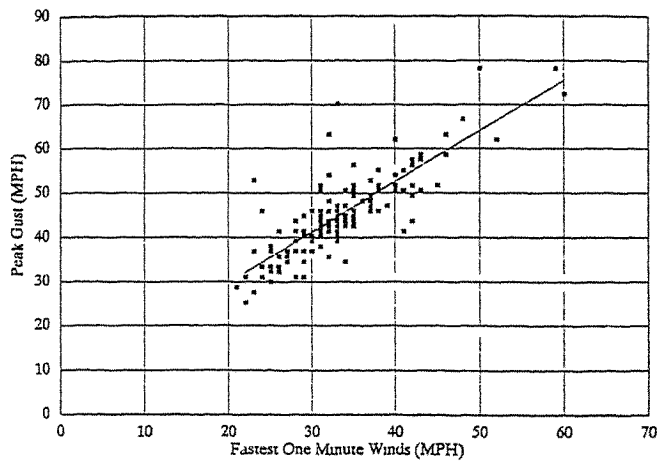winds: the total winds for Amarillo (1970-1990).

Fig. 3b. Regression analysis of peak gusts vs. fastest one minute
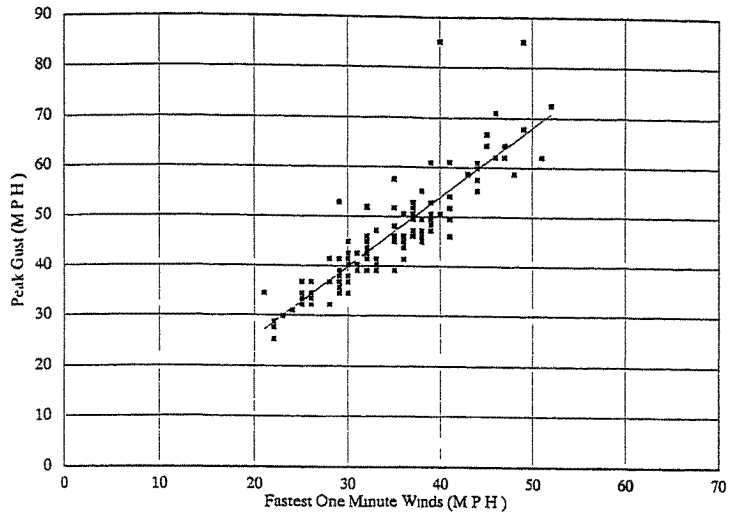winds: the total winds for Kansas City (June 1979 -
December, 1990)

516

Fig. 3c. Regression analysis of peak gusts vs. fastest one minute winds: the total winds for Lubbock (January, 1980 – December, 1988 and October, 1989-December,1990).
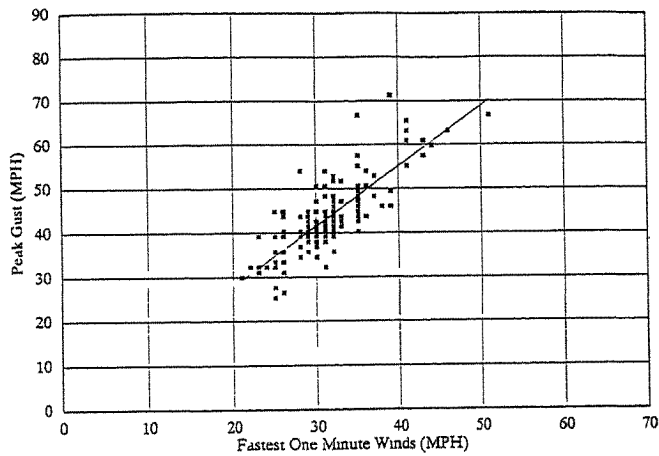

Fig. 3d. Regression analysis of peak gusts vs. fastest one minute winds: the total winds for Minneapolis (1980-1991).

517
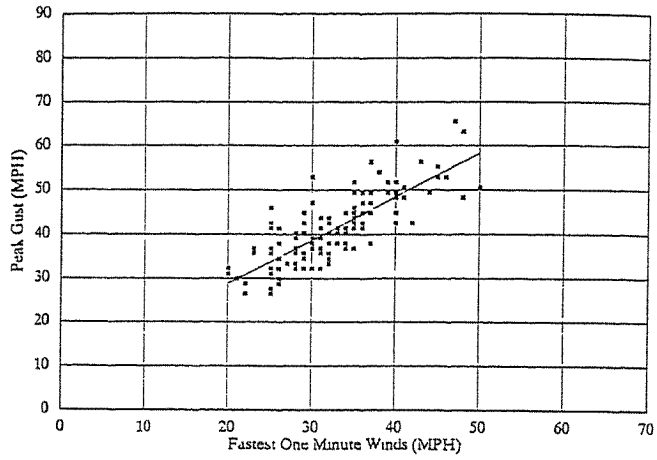
Fig. 3e. Regression analysis of peak gusts vs. fastest one minute winds: the total winds for Syracuse (1977-1987).

5. **Acknowledgment:**
   This research was sponsored by NSF Grant #BCS-8821163.

Estimating design wind speeds from short-term records

Edmond D. H. Cheng and Arthur N. L. Chiu

Department of Civil Engineering
University of Hawaii at Manoa
Honolulu, Hawaii, U.S.A.

Abstract: A method of regional analysis of short-term and fragmentary wind data from a region is developed to provide a better method of estimating extreme winds at an ungauged site. This method consists of three elements -- the basic probability functions, homogeneity tests and composite frequency functions. An application of this proposed regional analysis is demonstrated using data collected at various locations on the Island of Oahu, Hawaii.

1. Introduction

The method of combining short-term wind records within a homogeneous region is being developed. This method generally reduces the sampling error and produces extreme wind-frequency relations generally applicable within the homogeneous region. The proposed analysis of extreme winds of short-term records consists of three major elements. The first element is the development of basic probability functions for short-term records at various selected stations through current state-of-the-art techniques. The second element is the performance of a statistical homogeneity test for the selected stations so that the area or region involved may be divided into homogeneous subregions. The final element is the development of a composite extreme wind-frequency function for a homogeneous subregion. An application of this proposed method to the wind data collected on the Island of Oahu, Hawaii is demonstrated.

2. Strategy

In a region, extreme wind data obtained from locations with similar physiographic or meteorologic factors do exhibit some common characteristics. For example, if Type I distributions are assumed for the obtained extreme winds, similar slopes may be observed from the Gumbel lines. If the extreme wind speeds at these locations are reduced to dimensionless Gumbel lines, then these lines may be expected to be nearly coincident. This composite Gumbel line is then applicable throughout the entire region or in a subregion. The basic strategy of regional analysis of extreme winds in an area is to obtain a composite dimensionless extreme wind-frequency curve. The extreme wind speed for a specific return period can then be obtained from multiplying the value from this curve by a mean annual extreme wind speed at a project site. The estimation of a mean annual extreme wind speed at an ungauged project site is also addressed in this paper.

3. Analysis

In order to use available short-term wind records to full advantage, it is desirable to estimate extreme wind speeds from these short records. In the current state-of-the-art, there are four approaches for estimating extreme wind speeds from short-term records. The first approach is based on the analysis of the largest monthly wind speeds of at least three years' data [1]. This method has been well tested at 36 weather stations situated in various locations in the United States, and it has proven to be practical and adequate. The second approach is the determination of extreme wind speeds from a parent distribution [2]. Using this method, extreme wind speeds can be estimated even from records shorter than three years. The third approach [3] and the fourth approach [4] are simulation models based on short-term continuous hourly wind speed records. The selection of a proper approach is dependent upon the available data. Using that selected approach, a probability function of extreme winds at a station can thus be obtained.

4. Homogeneity test

The grouping of weather stations into regions or subregions will be guided by a sequence of homogeneity tests. For each homogeneity test, permissible ranges of variation are determined by selecting ± 1.0 standard deviation of an appropriate probability distribution. If Type I distributions are assumed for representing the annual extreme wind speeds series, the Type I cumulative distribution function (CDF) of extreme winds may be expressed in reduced variate as:

$$F(w) = e^{-e^{-w}} \tag{1}$$

with location and scale parameters equal to zero and unity, respectively. Further,

$$w = 1n \ 1n \ \frac{1}{F(w)} = -1n \ 1n \ \frac{T_r}{T_r - 1} \tag{2}$$

and the standard deviation of the reduced variate w is

$$s_w = \frac{e^w}{\sqrt{b}} \sqrt{(T_r - 1)^{-1}} = \frac{e^w}{\sqrt{b}} \sqrt{\frac{1 - F(w)}{F(w)}} \tag{3}$$

where

w	=	reduced variate of Type I distribution of extreme winds;
$F(w)$	=	CDF of w;
s_w	=	standard deviation of w;
b	=	number of years of record; and
T_r	=	recurrence interval.

520

In order to identify the inherent tendency of regional characteristics for certain weather stations, all locations with point measurements should be subjected to the initial homogeneity test. Subregions may be defined by successive homogeneity test.

5. Composite frequency function

A composite frequency function is constructed by taking mean values from site specific extreme wind-frequency functions in a homogeneous region or a subregion for the same return periods. In order to make the composite frequency curve dimensionless, the mean values are actually ratios of extreme wind speeds at various stations to the mean annual extreme winds at those respective stations.

6. Illustration

The method has been applied to wind data collected on the Island of Oahu. Since long-term annual extreme wind records exists only at the Honolulu Airport (Fig. 1), the Type I distribution function is established. However, the records collected at 14 other locations (Fig. 1) are of shorter periods or fragmented and are in wind roses format. Table 1 summarizes the wind data used in this paper.
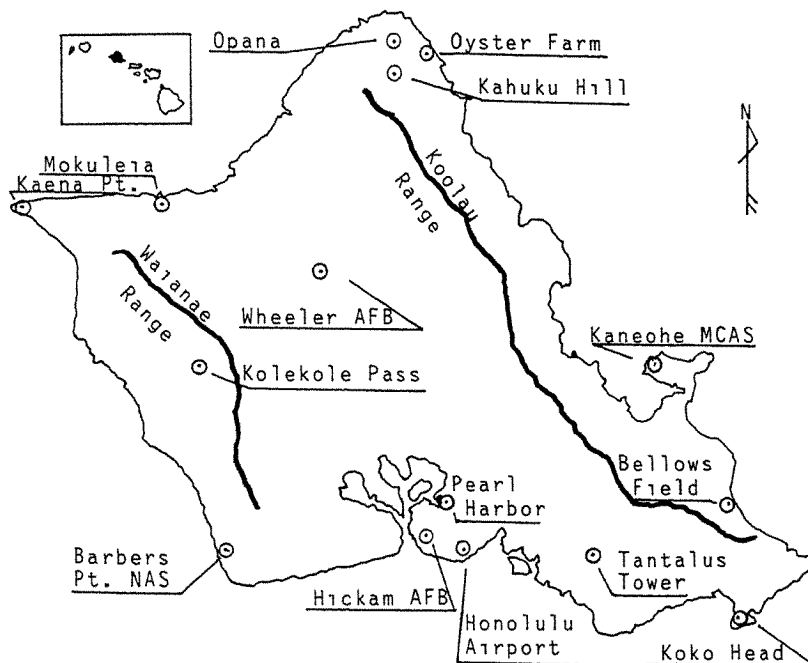
Fig. 1 Location of wind stations on Oahu, Hawaii.

521

Station	Data Period	Return Period (years)	s	V_a	V_e	$\dfrac{V_a-V_e}{s}$ (%)
(1)	(2)	(3)	(4)	(5)	(6)	(7)
Honolulu Airport	1950- 90	50	1.8	18.5	18.7	0.11
		100	2.1	20.0	19.3	0.33
Barbers Pt.NAS	1973- 77	50			21.0	
		100			21.9	
Bellows Field	1942- 45	50			22.8	
		100			23.6	
Hickam AFB	1952- 57	50			35.8	
	1966- 88	100			37.3	
Kaena Point	1975- 79	50			27.7	
		100			28.6	
Kahuku Hill	1976 -78	50			35.9	
		100			37.5	
Opana	1976- 82	50			29.4	
		100			30.4	
Kaneohe MCAS	1945- 49	50			17.8	
	1952- 65	100			18.4	
Koko Head	1977 -79	50			31.9	
		100			33.1	
Kolekole Pass	1975 -77	50			35.0	
		100			36.2	
Mokuleia	1942 -45	50			17.5	
		100			18.0	
Oyster Farm	1978- 82	50			25.4	
		100			26.4	
Pearl Harbor	1976- 78	50			18.7	
		100			19.3	
Wheeler AFB	1966- 89	50			35.5	
		100			36.8	
Tantalus Tower	1976- 79	50			34.8	
		100			36.1	

(4) s = the standard deviation of the inherent sampling error of the historical records.
(5) V_a = wind speed from the annual series.
(6) V_e = wind speed from the second approach.

Table 1. Estimated extreme winds at the 15 stations on Oahu using the annual series and the second approach (speeds in meter per second and adjusted to10 meters above ground level).

Due to the nature of the available data, the second approach was used for estimating extreme wind speeds from the wind roses at all 15 stations. In the second approach, we considered the parent distribution of the Rayleigh type. This assumption was validated by an evaluation of the shape parameter of the Rayleigh distribution for long-term annual extreme wind records at Honolulu Airport. Thus, the extreme winds derived from the second approach are, of course, Type I in nature [2].

522

In order to identify the inherent tendency of regionalization, a series of homogeneity tests are performed. In this paper, a 15-year data period was selected for calculating the values of the permissible range of variation in the homogeneity test. This was achieved by using Eqs. (1), (2) and (3) to compute the upper and lower limits for $\pm$ 1.0 s_w. All 15 sations were subjected to the initial homogeneity test and passed, which implies that the entire Island of Oahu may be considered as a homogeneous region.

To construct the dimensionless regional frequency curve for the Island of Oahu, ratios of extreme winds to the mean annual extreme winds at return periods 1.1, 1.5, 5, 15, 50 and 100 years were calculated. For Type I distributions, it can be shown that the mean annual extreme winds are wind speeds with 2.33 years of return period (Table 2 and Fig. 2).

Station	$V_{2.33}$	$\dfrac{V_{1.1}}{V_{2.33}}$	$\dfrac{V_{1.5}}{V_{2.33}}$	$\dfrac{V_{5}}{V_{2.33}}$	$\dfrac{V_{15}}{V_{2.33}}$	$\dfrac{V_{50}}{V_{2.33}}$	$\dfrac{V_{100}}{V_{2.33}}$
(1)	(2)	(3)	(4)	(5)	(6)	(7)	(8)
Honolulu Airport	15.7	0.83	0.92	1.05	1.08	1.18	1.24
Barbers Pt.NAS	16.6	0.88	0.95	1.07	1.17	1.26	1.32
Bellows Field	18.8	0.91	0.96	1.06	1.13	1.21	1.26
Hickam AFB	34.3	0.89	0.95	1.07	1.15	1.24	1.29
Kaena Point	23.2	0.92	0.96	1.05	1.15	1.19	1.23
Kahuku Hill	28.7	0.89	0.95	1.07	1.16	1.25	1.30
Opana	24.4	0.91	0.96	1.06	1.13	1.20	1.25
Kaneohe MCAS	14.9	0.91	0.96	1.06	1.13	1.20	1.24
Koko Head	26.4	0.91	0.96	1.06	1.13	1.21	1.25
Kolekole Pass	29.5	0.92	0.96	1.05	1.12	1.19	1.23
Mokuleia	12.0	0.92	0.97	1.05	1.11	1.17	1.21
Oyster Farm	20.7	0.90	0.95	1.06	1.15	1.23	1.28
Pearl Harbor	15.6	0.91	0.96	1.06	1.12	1.20	1.24
Wheeler AFB	35.2	0.91	0.96	1.06	1.13	1.20	1.24
Tantalus Tower	28.8	0.91	0.96	1.06	1.13	1.21	1.25
Mean		0.90	0.95	1.06	1.13	1.21	1.26

Table 2. Dimensionless extreme wind regional frequency curve for Oahu as a whole.
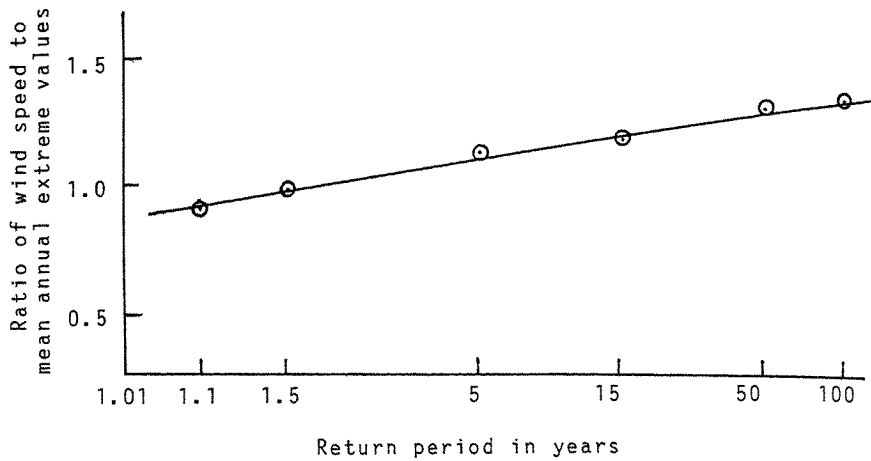
Fig. 2 Type I distribution of regional extreme wind speed frequency curve.

7. Conclusions

The preliminary results obtained from the application of this regional analysis procedure to short-term period and fragmentary wind data collected on the Island of Oahu are very encouraging. The dimensionless regional extreme wind-frequency curve serves as an effective means of estimating extreme winds for prescribed return periods at an ungauged project site.

Acknowledgment

References:

1. E. Simiu, J. J. Filliben and J. R. Shaver, "Short-term records and extreme wind speeds," J. of the Structural Div., ASCE, Vol. 108, No. ST11 (1982).
2. E. Castillo, Extreme value theory in engineering. Academic Press (1988).
3. M. Grigoriu, "Estimates of design winds from short records," J. of the Structural Div., ASCE, Vol. 198, No. ST5 (1982).
4. E. D. H. Cheng and A. N. L. Chiu, "Extreme winds simulated from short-period records," J. of Structural Engineering, ASCE, Vol. 111, No. 1 (1985).

Interannual Variability of Tropical Cyclones
Making Landfall over China

JOHNNY C.L. CHAN AND CLARENCE C.K. FONG

Department of Physics and Materials Science, City Polytechnic of Hong Kong

ABSTRACT: The interannual variability of tropical cyclones (TCs) making landfall over China is studied using the method of spectral analysis. It is found that during the period 1947-1989, a large interannual variation exists in the annual number of TCs making such landfall. Such variations have periods in both the quasi-biennial range (~2.2 years) and the El Niño/Southern Oscillation (ENSO) range (3-7 years). Further, a strong bias towards southern China exists in the latitudinal distribution of landfall location.

Cross-spectral analyses between the TC time series and those of the quasi-biennial oscillation (QBO) and the Southern Oscillation Index (SOI) indicate that (1) changes in the stratospheric QBO lead to variations in the number of landfalling TCs especially over southern China, and (2) changes in the planetary-scale circulation affects both the number of landfalling TCs and the magnitude of the SOI such that the two series are significantly correlated. The number of landfalling TCs over southern China (20-25°N) also seems to lead that over northern China (25-30°N) by approximately one year, suggesting the possibility of a long-range prediction.

1. Introduction

Since the work of Shapiro [13,14] and Gray [6,7], the interannual variability of tropical cyclone (TC) activity over each of the ocean basins has received considerable attention [10,15]. Over the western North Pacific (WNP), Chan [1] found that TC activity is very much related to the El Niño/Southern Oscillation (ENSO) phenomenon and has significant periods of 26 and 36-42 months. Dong [4] also showed that this activity is correlated with the sea-surface temperature (SST) over the eastern equatorial Pacific which can be considered to be a proxy of ENSO.

China is located in the western part of the WNP. The climatological study of Xue and Neumann [16] shows that many of TCs in the WNP landed over some part of China. Therefore, it seems reasonable to expect that the number of TCs making landfall over China should also have an interannual variation. In this study, an attempt is made to document such variations and to relate them to the ENSO and the stratospheric quasi-biennial oscillation (QBO) phenomena. The latter has been found by Gray [6] and Shapiro [15] as having significant correlation with TC activity in the North Atlantic.

The data and methodology used in this study are described in Section 2. To simplify the discussion, 'landfall' in this paper will specifically refer to that over China. The climatology of landfalling TCs is then given in Section 3. Correlations between the number of landfalling TCs and the ENSO and QBO phenomena are then presented in Section 4. These results together with possibilities of future work are discussed in Section 5.

2. Data and methodology
a. TC data

Six-hourly best-track positions of TCs over the WNP between 1947 and 1989 form the basic data for this study. To determine whether a TC during this period has made landfall over China,

the coast of China (which, for the purpose of this study, is considered to lie between 20 and 37°N) is first approximated by line segments joining the points at which the actual coastline interacts each whole degree latitude circle (Fig. 1). A TC is then considered to have made landfall over China if the line segment connecting any two consecutive 6-hourly positions of the TC intersects any line segment representing the coastline. The latitude of the intersection point is considered as the latitude of landfall for that particular TC. For a small number of TCs which re-entered the sea after landfall and landed again afterwards, only the first landfall is considered.

b. QBO and ENSO

Since the QBO does not vary much with longitude, the data with the longest record available to the author, the monthly 50hPa zonal winds at Balboa between 1951 and 1989, are used to represent the QBO. The ENSO phenomenon is represented by the difference in the monthly mean-sea-level pressures (MSLPs) between Tahiti and Darwin, commonly referred to as the Southern Oscillation Index (SOI).

Because the maximum number of TCs making landfall in a year is only 11 (see Section 3), it is not possible to correlate the monthly variations of the number of landfalling TCs with those of the QBO and ENSO. It is therefore necessary to average the monthly QBO and SOI for each calendar year. Since both of these oscillations have time scales of greater than two years, such an averaging should still retain the dominant oscillations. In fact, when a spectral analysis is applied to the annual QBO series, a dominant peak of 2.3 years occur in the power spectrum [5]. Similarly, significant peaks of the SOI

Fig. 1. Approximation of the coast of China from Leizhou Peninsula to the tip of Shandong Peninsula.

power spectrum are found at 3.6, 4.9 and 6.1 years [5]. These peaks have been previously identified as oscillations corresponding to the ENSO phenomenon (e.g. [9,12]). The annual QBO and SOI are therefore used to correlate with the annual number of landfalling TCs.

c. Methodology

The method of spectral analysis is used to identify significant periods in the annual number of landfalling TCs. Correlations between this time series and those of the annual QBO and SOI are studied using cross-spectral analyses.

Prior to each of these analyses, the following procedure is used to remove the low frequency components. The raw data are first converted into standardized variables. Each standardized series is then subjected to a low-pass Gaussian filter of 10 years. The filtered series is then subtracted from the standardized series so that only the high frequency components (< 10 years) are retained.

A Parzan window with a truncation point of 40 is used in the spectral and cross-spectral analysis, which give a 4.0 degrees of freedom [3]. Using the formula given in [11], the limiting values of the coherence square for the cross-spectral analyses at the 95% and 99% significance levels are 0.80 and 0.89 respectively.

3. Climatology of landfalling TCs

a. Number distribution

The annual number of TCs making landfall over China during the period of study is given in Fig. 2. Two series are shown : the ALL series consisting of TCs of all intensities and the TSTY (tropical storm-typhoon) series containing only those TCs which had an intensity of ≥ 17 m s^{-1} at the latest 6-hour time prior to landfall. The two series are very similar and both exhibit a large interannual variation, from a minimum of 0 and 1 (for the TSTY and ALL series respectively) in

1949 and 1955 to a maximum of 9 and 11 in 1961. Some periodicities in both series are also apparent.

The latitudinal distribution of the number of landfalling TCs shows a very distinct maximum between 21-23 °N (Fig. 3). Two other secondary peaks between 27-28°N and 31-32°N can also be identified. It is also of interest to note that no TC made landfall over China between 30-31°N during the entire period of study. It appears that north of 30°N, it is very unlikely that a TC will make landfall. An examination of the five TCs which landed between 31-32°N shows that they were all northward-moving one to two days prior to landfall and then made an abrupt turn westward.

It appears from the distribution in Fig. 3 that the data set can be divided into two sub-groups with 25°N as the cut-off point. The time series containing TCs which made landfall between 20-25°N will be labelled as TC25 (with a total of 147 out of 202) and those north of 25°N but at or south of 30°N TC30 (with a total of 47). TCs north of 30°N will be ignored in this study due to their small sample size.

b. Spectral analyses

The power spectrum of the ALL series gives significant peaks at 4.6 and 6.7 years, the latter being the dominant one (Fig. 4a). Three other smaller peaks are also apparent. However, their powers are generally close to or below that of the white-noise (defined as the average of power at all frequency ranges). The two dominant peaks are quite close to those of the annual SOI series (Section 2b). Similar results are obtained for the TSTY series (not shown).

Although the peaks at 4.7 and 6.8 years are still apparent in the TC25 series, two other maxima, one at 3.3 and the other at 2.2 years also appear and are very significant (Fig. 4b). These last two peaks may be related to the SOI and QBO, as will be discussed further in Section 4. The TC30 series shows a rather broad peak between ~4.8 and ~2.5 years with maxima at ~3.8 and 2.7 years (not shown). Note that because the sample size of this series is smaller, the truncation point for the Parzan window is set at 30. The meaning of these peaks will again be discussed in the next section.

c. Summary

The climatology of the annual number of TCs making landfall over China shows a rather large interannual variability with definite periods of oscillations which appear to be related to the QBO and SOI. Further, the latitudinal distribution of the number of landfalling TCs shows a definite bias towards the low latitudes. Stratification of these TCs based on latitude apparently provides more information on the interannual variability.

4. Cross-spectral analyses

a. With the QBO series

Since the QBO series starts only in 1951, all the TC series are truncated before the standardization and filtering procedures are carried out. The cross-spectral analysis between the
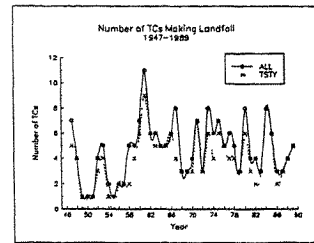
Fig. 2. Annual number of TCs making landfall over China. The ALL series contains all TCs while the TSTY series only those with tropical storm intensity or greater.
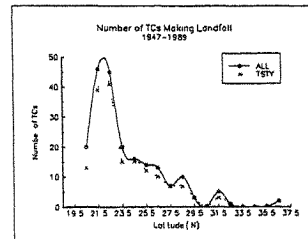
Fig. 3. Distribution of the latitude of landfall of the TCs. Mid-points of the one-degree intervals are used.

527

ALL and the QBO series does not produce any peak with a coherence square exceeding the 95% limit. However, a significant (at 95%) peak occurs in the cross-spectrum of the TSTY and QBO series (Fig. 5), with QBO leading the TSTY series by 1.6 years. More discussion of this will be given later.

(a)   (b)
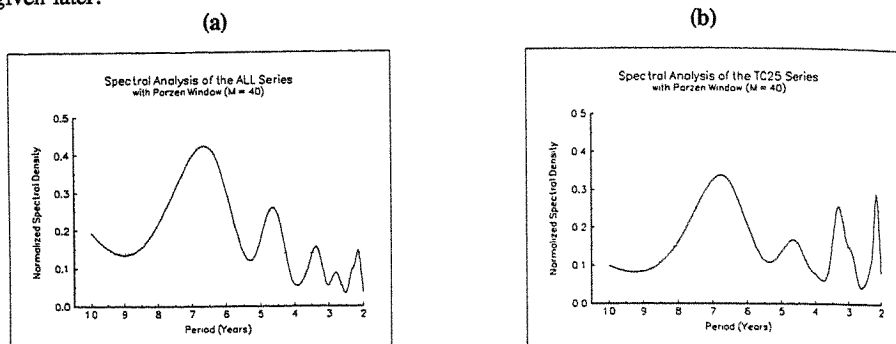
Fig. 4. Spectral analysis of (a) the ALL series and (b) the TC25 series.

The QBO-TC25 and QBO-TC30 cross-spectra also do not produce any significant peak. The different result obtained for the ALL and the TSTY series suggests that exclusion of tropical depressions (TDs) in the TC25 and TC30 series should also be considered. Indeed, when only TCs with intensities ≥ 17 m s^{-1} are included in the TC25 series, a similar peak at 2.3 years with a coherence square of 0.80 (i.e. significant at 95%) is found (not shown), with the QBO leading by 1.7 years. However, no significant peak can be identified for the QBO-TC30 cross-spectrum even if TDs are excluded.

Lau and Chan [8] hypothesized that the stratospheric QBO modifies TC activity through its coupling with the zonal winds in the tropics, which are generally easterly in the summer and westerly (but weaker than the stratospheric winds) in winter. Therefore, during the QBO-west (QBO-east) phase, conditions in the tropics will be more cyclonic (anticyclonic) and hence more (less) cyclones are likely to form. Their hypothesis appears to be consistent with the result obtained in this study.

That is, the annual number of tropical storms/typhoons making landfall over (southern) China is significantly related to the QBO, with the latter leading by ~3/4 of a cycle. As the equatorial stratospheric winds become less easterly, the number of TCs that form also begins to increase. As most of these TCs will form in the tropics, they are more likely to make landfall over southern China (south of 25°N) and hence the number of TCs making landfall will also increase. As the QBO-west phase sets in, conditions in the tropics become even more favourable for TC formation and development. Some of these TCs can become very intense or large. In this case, they will tend to track more north [2] and may interact with the mid-latitude westerlies, resulting in recurvature and no landfall over China. As a result, the increase in TC activity does not lead to further increase in the number of landfalling TCs. Therefore, it appears that the result from the cross-spectral analyses is physically reasonable. That the QBO does not correlate well with those series containing TDs may be explained by the weak intensity of these systems so that they are not strongly affected by this large-scale forcing.
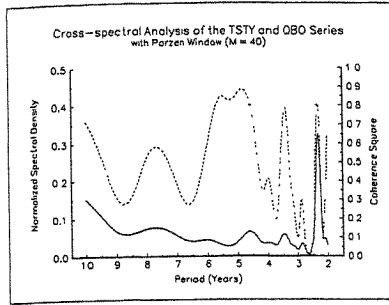
Fig. 5. Cross-spectral analysis of the TSTY and the QBO series. The solid and dashed lines represent the spectral density and the coherence square, respectively. The dotted lines are the 95 and 99% significance levels.
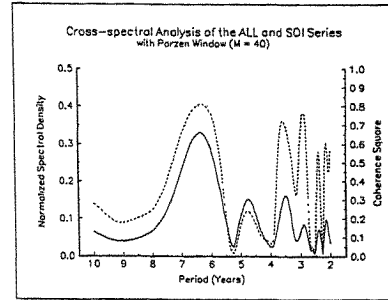
Fig. 6. As in Fig. 5, except for the ALL and the SOI series.

b. With the SOI series

The SOI-ALL and SOI-TSTY cross-spectra are quite similar, with a significant peak at 6.3 years and the SOI leading by ~4.5 years (Fig. 6, the SOI-TSTY spectrum not shown). However, when the TC series is broken down into the two latitude sub-series (TC25 and TC30), no significant correlation with the SOI series can be found. This suggests that the result with the significant correlations are probably related to a much larger scale circulation which governs the movement of TCs over the entire ocean basin.

A possible candidate is the strength of the subtropical high. If the subtropical high is very intense, it will give rise to strong easterly winds and will lead to more TCs making landfall over China. Stronger easterly winds at the surface will also lead to a piling up and subsequent warming of the waters in the equatorial west Pacific. This delayed action implies that the SOI will not increase to its maximum until sometime after the trade winds reach their maximum strength. Conversely, a weakening of the trades will lead to the opposite events happening. Thus, it is actually the TC series *leading* the SOI series by ~1.5 years, although both oscillations are results of a change in the planetary-scale circulation.

c. Between the TC25 and TC30 series

A cross-spectral analysis between the TC25 and TC30 series gives three peaks but only the one at 2.2 years is significant above the 95% level (Fig. 7) with the two series almost completely out-of-phase at this period. This implies that if more TCs make landfall over southern China in any given year, it is likely that more TCs will make landfall north of 25°N the following year.

Fig. 7. As in Fig. 5, except for the TC25 and the TC30 series.

5. Summary and conclusions

The number of TCs making landfall over China is found to have a large interannual variation with significant

529

oscillation periods at the QBO and ENSO frequencies. The latitudinal distribution of the location of landfall also shows a strong bias towards lower latitudes.

Cross-spectral analyses between the QBO and the TC series show that as the equatorial stratospheric easterly winds begin to weaken, the number of landfalling tropical storms/typhoons (especially over southern China) begins to increase. This results from an increasing number of low-latitude TCs due to an enhancement of the cyclonic condition in the tropical atmosphere. At the ENSO frequencies, the SOI and the TC series are also significantly correlated although no causality can be inferred. Instead, oscillations in both series are apparently caused by changes in the planetary-scale circulation. The number of TCs making landfall over southern China also seems to be out-of-phase with that for TCs over northern China with a period of ~2 years.

Most of the results obtained in this study appear to be physically reasonable so that they should not be due to statistical chance. However, in order to confirm the hypothesized reasoning discussed here, more detailed analyses are necessary. For example, the variations of zonal winds in the tropics need to be correlated with the frequency of landfall to establish more concrete evidence. The relationship between TC activity and QBO should also be determined, as has been done in the Atlantic by Gray (1984a,b) and Shapiro (1989). Given the QBO information, it should be possible to make predictions of the number of landfalling TCs over China. Results from these studies will be reported in future papers.

REFERENCES
1. Chan, J.C.L., *Mon. Wea. Rev.*, **113** (1985) 599-606.
2. Chan, J.C.L., and R.T. Williams, *J. Atmos. Sci.*, **44** (1987) 1257-1265.
3. Chatfield, C., *The Analysis of Time Series: An Introduction*, Chapman and Hall Ltd., (1984).
4. Dong, K., *Australian Meteor. Mag.*, **36** (1988) 219-225.
5. Fong, C.C.K. and J.C.L. Chan, *Res. Rept. AP-93-18*, Dept. of Appl. Sci., City Polytechnic of Hong Kong, (1993) 34 pp.
6. Gray, W.M., *Mon. Wea. Rev.*, **112** (1984) 1649-1668.
7. Gray, W.M., *Mon. Wea. Rev.*, **112** (1984) 1669-1683.
8. Lau, R. and M.Y. Chan, *Proc., Second Int'l Conf. E. Asia and W. Pac. Meteor. Climate*, September 7-10, (1992) Hong Kong.
9. Lau, W.K.M., *Paper presented at the IAMAP-IAHS '93 Symposium*, July 11-23, (1993) Yokohama, Japan.
10. Nicholls, N., *J. Climat.*, **4** (1984) 661-670.
11. Panofsky, H.A. and G.W. Brier, *Some Applications of Statistics to Meteorology*, Pennsylvania State University Press, (1958) 224 pp.
12. Rasmusson, E.M. and T.H. Carpenter, *Mon. Wea. Rev.*, **110**, (1982) 354-384.
13. Shapiro, L.J., *Mon. Wea. Rev.*, **110** (1982) 1007-1013.
14. Shapiro, L.J., *Mon. Wea. Rev.*, **110** (1982) 1014-1023.
15. Shapiro, L.J., *Mon. Wea. Rev.*, **117** (1989) 1545-1552.
16. Xue, Z. and C.J. Neumann, NOAA Tech Memo. NWS NHC 23, (1984) 89 pp.

The Study of Classification of Typhoon landing on China

Zhu Ruizhao   Ji Juzhi[+]   and   Ma Shuhong[++]

(Chinese Academy of Meteorological Sciences)

Abstract: The center pressure, the maximum wind speed and the number of typhoons landing on China during a period of 1949—1990 are used in conjunction with fuzzy mathematics cluster method to classify our country into three typhoon areas:ultra—strong, stronger and strong. The maximum wind speed need be transformed into 10 minutes average wind speed. The relation between the center minimum pressure and the surface maximum wind speed has been set, finally regression equations have been given by nonlinear analysis. According to the distribution function of extremes, we have computed the return period of 10 minutes maximum wind speed in 30, 50, 100 years in three areas and analyzed the feature of each area and the climatic rules of typhoons landing every year on time. It is of great scientific and practical value for typhoon climatic change, national economic program and building design etc...

1. Foreword

Every year, the coastal regions and the islands in China is destroyed by typhoons in different degree, especially in Guangdong, Hainan, Taiwan and the coastal regions of Fujian. In China, we have made deep and systematic studies on typhoon[1,2], but few studies on geographical classification for the number and the wind speed of tropical cyclone appeared. We use system cluster analysis method in fuzzy cluster quantitatively to define relation between the number, the center pressure and the maximum wind speed of tropical cyclones landing on China and have a objective classification that conform to tropical cyclone change rules in China by analogy degrees.

2. Data analysis

2.1 Data origin

Meteorological data of 42 years between 1949—1990 at 96 stations is chosen from Typhoon Year—book edited by the Chinese Meteorological Administration. We count up landing place, center pressure, maximum wind speed and storm precipitation of every tropical cyclone year by year, and finally get data of 42 years.

2.2 Data handling

2.2.1 In general, requirement of building plan is 10 minutes average wind[3] and not to be instantaneous wind speed. Because of instantaneous wind speed nearby tropical cyclone center in Typhoon Year—book, all instantaneous wind speed is transformed into 10 minutes average one.

2.2.2 Because wind force—scale has a wind speed range which the deviation between the up limit and the down one is 3—4 m / s, wind speed of landed typhoon in Typhoon Year—book is indicated with wind force—scale before 1973. In order to judge wind speed accurately, we set the relation between typhoon center maximum pressure and surface minimum wind speed by using data of 1973—1990 (see Fig.1). Then by nonlinear and regression analysis, we get formula (2.1) with function transformation method:

$$V = 6(1010 - P_0)^{0.5} \tag{2.1}$$

where V are surface maximum wind speed, P_0 is typhoon center minimum pressure. The formula (2.1) deviation between the calculation value and the observed value of below 8%.
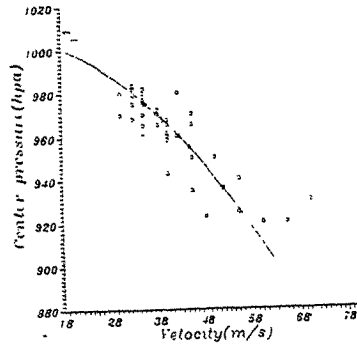
Fig.1. Typhoon center pressure and wind speed

2.2.3 Probability calculation of maximum wind speed. By using distribution function of extremes:

$$F(x) = e^{-e^{-a(x-u)}} \tag{2.2}$$

We compute return period of maximum wind speed and storm precipitation each area.

3. Classification method

Cluster analysis is a more objective method that makes numerical classification among factors quantitatively computing correlation coefficient between factors and classifying according to their correlation degrees[4].

3.1 Data standard handling

$$X'_{ik} = (X_{ik} - \bar{X}_k) / S_k \qquad (i = 1,2,...,96, k = 1,2,3) \tag{3.1}$$

where X_{ik} denotes the Kth index of the ith sample.

$$\bar{X} = 1 / n \sum_{i=1}^{n} X_{ik}; \qquad S_k = \sqrt{\frac{1}{(n-1)} \sum_{i=1}^{n} (X_{ik} - \bar{X}_k)^2} \tag{3.2}$$

Correlation coefficients between samples are computed for standard data. The larger correlation coefficient is, the more similar two sample is:

$$r'_{ij} = \frac{\sum_{k=1}^{m} (X_{ik} - \bar{X}_i)(X_{jk} - \bar{X}_j)}{\sqrt{\sum_{k=1}^{m} (X_{ik} - \bar{X}_i)^2 \sum_{k=1}^{m} (X_{ik} - \bar{X}_j)^2}} \tag{3,3}$$

3.2 Stepwise discriminatory analysis

Fuzzy correlation matrix $R = [r_{ij}]$, where $r_{ij} = 0.5 + r'_{ij} / 2$ (i,j = 1,2,...,96), is transformed into fuzzy equivalence correlation matrix R_a^* by $R^2 = R.R$, $R^4 = R^2 \cdot R^2$, $R^8 = R^4 \cdot R^4$,........ Let $S = R.R$, where $S_{ij} = \bigvee_{k=1} (r_{ik} \wedge r_{jk})$, signs $\vee$ and $\wedge$ mean as follows:

If A, B are random real numbers:

$$A \wedge B = \min(A,B)$$

532

$$A \vee B = \max(A,B)$$

When some step $k(k < \lg N / \lg 2)$ makes $R^{2^{k+1}} = R^{2^{k}}$, then $R^* = R^{2^{k}}$. R^* is a changed matrix, where element shows correlation degree each other of samples waiting for classification. Elements in R^* that are lined from large to small are regarded as specified horizontal value λ. By many times calculation classification, according to theories and experiences, the classified limit values λ are finally found. The three areas are divided by the method.

4. Typhoon classification

4.1. We have classified for many times according to method above. Let $\lambda > 0.989778$, we get aggregation samples which their instantaneous maximum wind speed is above 45m / s. Then having classified remain samples one sort which $0.963107 < \lambda < 0.989778$ and instantaneous maximum wind speeds are between 35m / s—45m / s. At last, remain samples are one. We have divided tropical cyclones landing on region in China into three areas(see Fig.2).
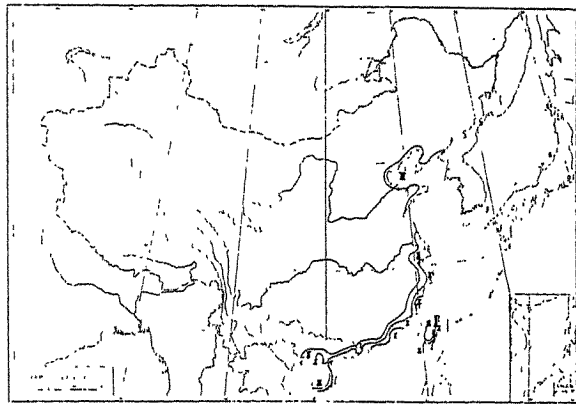
Fig. 2 classifyed map of Tropical cyclone landing on our country

Wind speed and storm precipitation of return period of each area is computed separately according to these three areas. It is also important for building, electric power, communication travel and water conservancy. Return period of each area is as table 1.

Table 1. Return periods of 10 minutes average maximum wind speed and storm precipitation

return period / area class	30 years		50 years		100 years	
	10 MAMWS (ms⁻¹)	SD (ms⁻¹)	10 MAMWS (ms⁻¹)	SP (ms⁻¹)	10 MAMWS (ms⁻¹)	SP (ms⁻¹)
I	37.3	787.5	41.0	880.0	45.6	992.9
II	31.1	744.7	33.9	826.6	37.4	926.8
III	25.6	648.9	27.8	724.2	30.4	816.0

4.2 Climatic features of each areas

I. ultra—strong areas is where the most numerous tropical and the fastest wind speed cyclones land on China. Features of this area is that coastal line is basically vertical with path of

tropical cyclone, and wind speed is highest because tropical cyclone may land directly, but owe to Taiwan's obstacle to tropical cyclone, wind speed in middle of Fujian is slower.

Taiwan is maximum wind speed area of typhoon landing on China which come up to 70—75m / s on Aug. 29th, 1959. If we compute return period only using wind speeds of Taiwan, 10 minutes average maximum in 30 years is 44.5m / s, one in 50 years is 48.5m / s, one in 100 years is 53.5m / s. Not only it is strongest in our country, but also rare in the world.

II. stronger areas distributes in the inner side of I area, which ranges from Shanghai south—east and south sea coastal to Guangxi coastal. Table 1 shows that wind speed in II area is weaker 17% than one in I area. Coastal line of this area is nearly parallel with typhoon path (see Fig.3), therefore numbers of typhoon landing directly are less than that in I area.
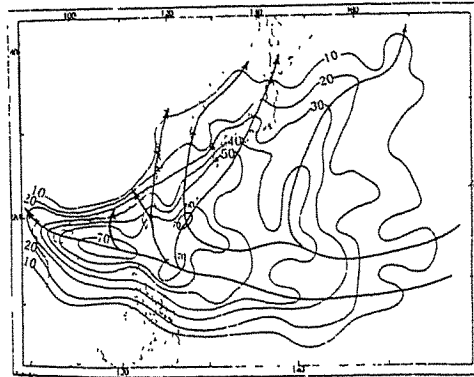
Fig.3. Typhoon landing wind speed decreas percentage

III. strong areas is in the inner of II area, north of the Yangtze River and in the range of coastal. According to previous research[3], when typhoon is landing, if coastal maximum wind speed is regarded as 100%, then maximum wind speed nearby typhoon center is 68% of coastal one at 50 km away from seashore (see Fig.4).
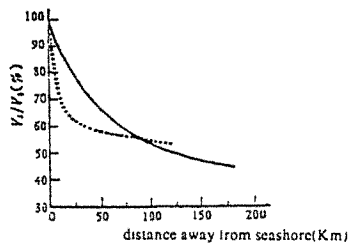
Fig.4. 5—10 months typhoon frequency map

The increase of surface roughness length mainly brings this decrease.

5. Climatic rules of typhoon landing

5.1 Numbers of typhoon landing and season change

According to statistics number of typhoon landing each year during a period of 1949—1990, We get all together 462 times and 9.3 times average year. The most times in some year can be up to 21, the least one in some year is only 6, see table 2.

Table 2. Number of typhoon landing of 1949—1990

	0	1	2	3	4	5	6	7	8	9	Total	Average
40										11	11	
50	10	6	17	12	9	7	12	7	12	9	101	10.1
60	15	21	13	12	9	14	11	16	6	6	123	12.3
70	9	18	9	12	14	11	8	10	8	6	105	10.5
80	12	14	8	7	14	13	10	8	10	11	107	10.7
90	15										15	

Typhoon landing on China may appear from May—December, but they mainly appear from July—September and is more than 75% of the whole year, see table 3.

Table 3. Number and percentage of typhoons landing on our country

month / items	5	6	7	8	9	10	11	12	Total
Total number	15	40	118	131	113	31	13	1	462
percentage	3.2	8.7	25 5	28.4	24.5	6.7	2.8	0.2	100%

5.2 Regions distribution of typhoon landing

It is mainly concentrated in Guangdong, Hainan, Taiwan and Fujian which is 84% of typhoon landing, then in Zhejiang and Guangxi, other coastal provinces and cities only take 7.2%. See table 4

Table 4. Region distribution of tropical cyclone landing on our country

province	Guangxi	Guangdong	Hainan	Taiwan	Fujian	Zhejiang	Shanghai	Jiangshu	Shandong	Liaoning	Tianjin	Total
number	16	146	91	81	69	26	5	5	12	10	1	462
percentage	3 5	31 6	20 0	17 5	14 9	5 6	1 1	1 1	2 6	2.2	0.2	

6. Conclusion

(1). Fuzzy cluster method is concluded using data of typhoon center maximum pressure, maximum wind speed and number landing divided our country into three areas: ultra—strong area (10 minutes average maximum wind speed above 45m / s), strong area (45—35m / s), stronger area (blow 35m / s). It provides scientific basis for national economy construction program and design.

(2). typhoon wind speed should be transformed into 10 minutes average wind speed. We compute return period of maximum wind speed in 30, 50, 100 years by using distribution function of extremes. Meanwhile, return period of one typhoon storm precipitation has been computed.

Reference

[1]Chen Lianshou, Di Yihi: Introduction to Typhoons in the West Pacific Ocean, Chinese Scientific Press.

[2]Science Symposium on Tropical Cyclone, Chinese Scientific Press.

[3]Zhu Ruizhao: Research on Calculation of Wind Pressure, Chinese Scientific Press.

[4]Tu Qipu, etc.: Meteorological Applied Probability statistics, Chinese Meteorological Press.

[5]Feng Peizhi, ect.: Analysis on Chinese Main Meteorological Damage(1951—1980), Chinese Meteorological Press.

PROBABILITY - BASED WIND SPEED IN INDIA
M.J. Alam and A.R. Santhakumar[+]

Research Scholar
[+]Professor, Department of Civil Engg.,
Anna University, Madras - 600 025, India.

Abstract : A probabilistic analysis of wind speeds for the annual maximum wind observed at 48 stations and extreme cyclonic wind observed at 5 coastal belts in India have been carried out. Extreme type I distribution, in general, is found to fit the data on annual maximum and extreme cyclonic wind. Based on these, equations have been obtained both for the annual maximum and extreme cyclonic speed in terms of return period, design life of the structure and optimum risk level. Using the computer program WSPEED, the characteristic design wind speeds for all the regions are calculated and compared with the relevant Indian Standards. There are considerable differences exist in certain details, especially for the cyclone prone zones and hence a cyclonic factor has been proposed for the five coastal regions. Thus the established statistics of wind speed can form a part of the calibration of partial Reliability-Based Design (RBD) codal format in India.

1. Introduction

Reliability-Based Design (RBD) codes have been developed in USA, UK, Australia and European countries to guide the selection of load and resistance factors which account for the uncertainties in the individual loads and resistances and give the overall target reliability. The statistical description of loads and resistance variables are required for the reliability analysis of structures and development of RBD Codes. In India, there is a definite need for uniform procedures and definitions across the utilities for the calculation of wind loading probabilistically which provide some quantified measure of reliability and should reflect the uncertainties in the loads that these loads will be exceeded. In this context, collection of data and establishing statistics of basic random variables (such as wind) are of prime importance. Wind speed is one of the main sources of uncertainties with random character. This paper deals with the derivation of wind speed statistics both for the annual maximum and cyclonic speed in India with the available observed wind data. Hence, the collection of data on wind speed and statistical analysis of the same are first dealt with and design wind speeds for all the regions have been calculated using the developed computer program in terms of return period, design life of the structure and optimum risk level and compared with the IS:875-1987 [1]. Keeping this view, in line with other international codes of practice and based on data collected, a cyclonic factor has been arrived at for all the coastal regions in India. The statistics of wind speed thus obtained and established can be directly applied for a probabilistic design of any structure sensitive to wind environment.

2.   Probabilistic analysis of extreme wind speeds
2.1   Analytical model

The highest annual hourly averages were made available from Indian Meteorological Department (IMD) between 1948 to 1984, for a period of over 36 years of observations. The

probability model that is generally used in India to describe the annual maximum wind speed (wind speeds less than 115 km/hr) is type I extreme (largest) distribution, called Gumbel distribution, considered for probabilistic analysis of wind speeds in all the regions. The cumulative distribution function (CDF) is given by [2]

$$F(x) = EXP[-EXP\{-\alpha(x-u)\}] \quad For \quad -\infty < x < \infty \qquad ...(1)$$

where x is the extreme wind speed, u and α are the location and scale parameters respectively which can be evaluated from the following relations: $\alpha = C1/\sigma$, $u = \bar{x} - C2/\alpha$, where C1 and C2 are functions of sample size [3], $\bar{x}$ and α are the mean and standard deviation respectively. The choice of the distribution of extreme type I is made after the investigation of fitting closeness of the data. Histograms of all these stations are drawn and mean ranking plotting are used to decide whether type I is applicable or not. The good straight line fit encourages the use of this type of distribution. The suitability of the model is arrived at after applying the chi-square test and found that type I satisfies the test at 5% level of significance for the wind speed observed at all the stations. The parameters of the distribution (u,α) are calculated using the method of moments and are tabulated alongwith the means, standard deviations and coefficients of variation of wind speed for all the regions in table 1.

2.2   Characteristic design wind speed at optimum risk level (excluding cyclonic wind speeds)

The selection of a characteristic design wind speed for a structure should be quantitatively related to the risk level which has to be taken by making a particular choice and the life of the structure. The optimum risk level of 0.64 has been selected for the design of structures against extreme winds in most of the international codes of practice [4,5,6,7]. In order to achieve the optimum risk level, the structure may be designed for a wind whose return period is equal to its life period and corresponding wind speed represents the optimum design wind speed. Thus the characteristic design wind speed at the optimum risk level for different return period and life of the structure are calculated using the computer program WSPEED and is given in Table 2. From Table 2, it can be shown that the characteristic design wind speeds for all the regions excluding coastal belt of West Bengal, Orissa, Tamilnadu, Andhra Pradesh and West Coast (Bombay) are more or less coinciding with the values specified by the IS:875-1987. So, the means standard deviations and coefficients of variation presented in Table 1 can be used to calculate the reliability index of the structures subjected to wind loading.

3.   Probabilistic analysis of cyclonic wind speed

3.1   Analytical model
The wind data of cyclones which hit the five coastal regions of India from 1891 to 1984 were collected from IMD. Histograms of the severe cyclonic wind speeds (wind speeds greater than 115 km/hr) in these coastal regions have been studied. The probability model that was used, is Gumbel type I for the five coastal regions. The CDF of the distribution is the same as mentioned in equation (1). To test the suitability of theoretical model for the observed data, Gumbel distribution type I was tried and based on the K-S goodness fit test, at 5% significance level, the distribution selected was found suitable in all the five coastal regions. The means, standard deviations and Covs were calculated and presented in Table 3 alongwith the statistical parameters (u, α) for the five coastal regions in India.

3.2 Characteristic design cyclonic wind speed at optimum risk level

The optimum risk level corresponding to the optimum cyclonic wind speed is 0.64, which is mentioned earlier and is normally specified in standard codes for well-behaved climates. Thus the characteristic design cyclonic wind speeds at optimum risk level are calculated at different return period and life of the structures for all the five coastal regions are given in Table 4. From Table 4, it can be shown that the characteristic design cyclonic wind speeds are much more higher than those recommended in the present IS:875-1987. The statistical investigation cyclonic wind speeds carried out by Venkateswarlu et al. [8] argued also the same. The present IS:875-1987 demands that the effect of cyclone in land has already been reflected in basic wind speeds and also recommends an enhancement factor of 1.15 in the absence of any definite wind data as in Australian Code of practice [4]. But according to the authors, application of this enhancement factor to basic wind speed to get cyclonic wind speed will lead to an unreliable estimate of cyclonic wind speed for the Indian coastal belt.

4.   Cyclonic factors - a proposal for IS:875-1987

The codal provisions on design wind speeds for safe and economical design of structures do not adequately take into account the effect of extreme winds during severe cyclonic storm. The above probabilistic investigation on cyclonic wind speeds, based on extreme value distribution yielded higher values than the value recommended in the IS:875-1987 for coastal regions in India. For example, the 50 Year return period cyclonic wind speed at 64% risk level based on Gumbel type I distribution for the Andhra Pradesh Coast was found to be 72 m/sec which is about 44% more than that recommended in the IS:875-1987. So the cyclonic enhancement factors for the five coastal regions are arrived at 1.44, 1.50, 1.29, 1.19 and 1.23 for Andhra Pradesh, Orissa, Tamilnadu, West Bengal and West Coast (Bombay) respectively. This would enable designers to analyse the behaviour of structures to such cyclones, in a more scientific and systematic manner.

5.   Conclusions

The probabilistic investigation on the extreme annual wind speeds and extreme cyclonic wind speeds in India are carried out and the risk-based design wind speeds, both for non-cyclonic and cyclonic zones are also established in this paper. The following conclusions can be summarized on the basis of these investigations:

(a)   As in most other countries, the Extreme type I distribution fits best to both annual maximum extreme and extreme cyclonic wind speed records in India.

(b)   The basic wind speeds recommended in the IS:875-1987 can be successfully used to design the structures for all zones except cyclone-prone zones in India and the enhancement factor 1.15 for the cyclonic zones mentioned in this practice may lead to an unreliable design.

(c)   The cyclonic enhancement factors as proposed in this paper for the five coastal regions in India can be successfully used for the calculation of design cyclonic wind speeds from the basic wind speeds as recommended in IS:875-1987.

(d) The statistical parameters as proposed in this paper both for the non-cyclonic and cyclonic zones in India can be used for the reliability (approximate) analysis of the structures and can form part of the Reliability-Based Design (RBD) Codal format in India.

References

1. IS:875, Indian Standard Code of Practice for design loadings (other than earthquake) for buildings and structures part - 3 - Wind loads (Second Revision), Indian Standards Institution, New Delhi, (1987).
2. J.R. Benjamin and C.A. Cornell, probability, Statistics and Decision for Civil Engineers, McGraw-Hill, New York, (1970).
3. E.J. Gumbel, Statistics of Extremes, Columbia University Press, New York, (1967).
4. Australian Standards, AS 1170 Part - 2, Wind forces, Standard Association of Australia, North Sydney, (1983).
5. BSI, code of basic data for the design of buildings; Chapter V loading: Part 2 Wind Loads, Fourth Edition, CP3: Chapter V: Part 2, British Standards Institution, London, (1972).
6. A58.1-1982 : American National Standard Building Requirements for minimum Design load on Buildings and other Structures, American National Standard Institute, New York, (1982).
7. NZS 4203 - 1976, New Zealand Standard Code of Practice for General Structural Design and Design loadings for buildings, Standards Association of New Zealand, Wellington, (1976).
8. B.M. Venkateswarlu et al, Risk analysis of Cyclonic Wind data, proceedings of the National seminar on Tall Reinforced concrete chimneys, New Delhi, (1985).

Station	Mean Wind Speed m/sec	Standard Deviation m/sec	COV	Location Parameter (u)	Scale Parameter(α)
Pune	22.97	4.39	0.191	21.20	0.304
Bombay	23.89	2.83	0.118	22.54	0.402
New Delhi	29.50	5.31	0.18	26.96	0.213
Calcutta	25.25	5.88	0.232	22.44	0.192
Madras	25.19	4.30	0.170	23.12	0.260
Nagpur	26.39	5.54	0.21	23.72	0.201
Bangalore	22.96	2.96	0.129	21.53	0.376
Visakapatnam	27.80	4.92	0.177	25.43	0.226
Kodaikanal	24.21	3.17	0.131	22.68	0.351

Table 1. Statistical parameters for maximum annual Wind Speed

Station	Return period (Yr) = Design life of the Structure (Years)					
	50	100	150	200	300	500
Pune	34.10	36.35	37.68	38.62	40.0	41.64
Bombay	32.27	34.0	35.0	35.72	36.73	38.0
New Delhi	45.32	48.58	50.48	51.83	53.74	56.14
Calcutta	42.81	46.42	48.54	50.03	52.15	54.80
Madras	38.16	40.83	42.40	43.50	45.06	47.02
Nagpur	43.18	46.63	48.65	50.08	52.10	54.64
Bangalore	31.93	33.78	34.86	35.62	36.70	38.06
Visakapatnam	42.74	45.81	47.60	48.87	50.67	52.93
Kodaikanal	33.82	35.80	36.96	37.78	38.93	40.39

Table 2. Optimum annual design Wind Speed (m/sec)

Region	Mean Wind Speed m/sec	Standard deviation m/sec	COV	Location Parameter (u)	Scale Parameter (α)
Orissa	49.93	10.175	0.204	45.35	0.1260
Andhra Pradesh	45.37	10.283	0.227	40.74	0.1250
Tamilnadu	41.72	8.820	0.212	37.75	0.1454
West Bengal	40.46	7.300	0.180	37.17	0.1750
West Coast (Bombay)	39.70	8.420	0.212	35.91	0.1520

Table 3. Statistical parameters for Cyclonic Wind Speed

Region	Return period (T Yrs) = Design life of the Structure (Years)					
	50	100	150	200	300	500
Orissa	76.32	81.90	85.11	87.40	90.62	94.67
Andhra Pradesh	72.0	77.58	80.83	83.12	86.37	90.46
Tamilnadu	64.58	69.42	72.21	74.19	76.98	80.50
West Bengal	59.38	63.38	65.70	67.32	69.63	72.54
West Coast (Bombay)	61.58	66.20	68.90	70.77	73.43	76.80

Table 4. Optimum Cyclonic design Wind Speed (m/sec)

STOCHASTIC MODELLING OF CYCLONES

K. Balaji Rao, K.C. Thomas, T.V.S.R. Appa Rao
Structural Engineering Research Centre, CSIR Campus, Taramani
Madras 600 113, INDIA

Abstract: The occurrences of cyclones on the east- and the west-
coasts of India are modelled using Poisson process model. The
applicability of this model in determination of reliability of the
structure and fatigue reliability of components are examined.
Bayesian theory is used to update the probability of occurrence of
cyclone of specified wind speed.

1. INTRODUCTION

    Cyclones are one of the natural hazards, which when occur cause
damage to human lives and property. To mitigate the damages due to
cyclones there is a need to understand more about the occurrences of
cyclones. Attempts have been made in the literature to fit
probability distributions for extreme wind speeds during cyclones
[1], thunder storms [2], tornadoes [3-5] etc. A brief review of
literature on probabilistic modelling of extreme wind speeds forms a
part of the report [6]. Knowing the probability distribution of the
extreme wind speed the probability of occurrence of a specified
extreme wind speed can be computed. The specified wind speed
corresponds to a particular value (known/unknown) of mean return
period on the time scale. While the probability distribution gives
the probability of occurrences, it is not possible to predict
directly the number of occurrences of wind speeds within a given
time interval (typically the life of the structure). Such
information is necessary to determine the collapse/fatigue
reliability of a structure during its life time.
    The coastal regions of India are subjected to cyclones very
frequently. To compute the reliability of structures located in the
coastal regions against the cyclonic wind loads, it is necessary to
know the number- and intensities- of cyclones to which they are
subjected to during their life time. In this paper, a time
homogeneous Poisson process model is used to describe the
occurrences of cyclones in the coastal regions of India.
    The stochastic model developed is described in Section 2. The
details of processing of the cyclonic wind speed data of the coastal
regions are presented in Section 3. The usefulness and
effectiveness of the Poisson process model developed in reliability
estimation and in decision making are shown through three examples
presented in Section 4.

2. STOCHASTIC MODEL

    Let $\{N(t), t \geq 0\}$, represent a counting process (viz. number of
cyclone occurrences in a given region). The stochastic process
$\{N(t), t \geq 0\}$ is said to be a Poisson process with a rate ν, $\nu > 0$, if
i) $N(0) = 0$
ii) The process has stationary and independent increments
iii) $P\{N(h) = 1\} = \nu h + o(h)$, and
iv) $P\{N(h) \geq 2\} = o(h)$
where h = length of time interval and $o(h)$ denotes 'order zero'.
Using this definition it can be shown that

543

$$P\{N(t) = n\} = e^{-\nu t} \, \frac{(\nu t)^n}{n!} \quad , \quad n=0,1,\ldots \tag{1}$$

The mean and the variance of the process N(t) can be shown to be νt. The justification of the use of Poisson process model for modelling the occurrences of cyclones is given in the following Section.

2.1 Justification of the use of Poisson process model:

(1) The occurrence of extreme wind speeds associated with cyclones can be assumed as occurrence of rare events as compared to the occurrences of hourly maximum wind speeds of well behaved winds.
(2) The assumption of stationary increments for N(t) is reasonable because, the distribution of the number of cyclones occurring in a given interval of time depends only on the length of the time interval. From the run- and reverse arrangement- tests [7] of cyclonic wind speeds it is found that the cyclonic wind speeds are stationary.
(3) The assumption of independent increments is reasonable since the number of cyclones of specified speed occurring in non-overlapping time intervals are independent.
(4) The conditions (iii) and (iv) state that Poisson process model can be used to model the occurrences of rare events. This indicates that the Poisson process model will perform better for higher cyclonic wind speeds (associated with higher mean return periods).

From the above discussion it is felt that the occurrences of cyclones can be modelled using Poisson process model. The Poisson process has some interesting properties some of which are used in this paper in reliability analysis of structures subjected cyclonic wind speeds.

3. PROCESSING OF CYCLONIC WIND SPEED DATA

From Eq.(1) it can be noted that Poisson process is completely defined if the value of ν, the intensity of process, is known. It can be shown that ν and the mean return period of cyclonic wind speed (T) are related by

$$\nu = \frac{1}{\bar{T}} \tag{2}$$

To compute the value of ν (or $\bar{T}$), the cyclonic wind speed data is required. Venkateswarlu et al [8] have reported the wind speeds recorded during cyclones in various states in the east- and the west- coasts of India. This information was obtained from Indian Meteorology Department and from the published records of wind speeds. These wind speeds approximately correspond to maximum wind speeds measured at a height of 10 m, in terrain category 2. The actual length of the record varied from one coastal region to the other. The various states that are affected by the cyclones on the east coast are : Andhra Pradesh, Orissa, Tamil Nadu and West Bengal. The Konkan area situated on the west coast is also affected by cyclones. The lengths of wind speed records for these states are 100 years, 41 years, 92 years, and 40 years (on the east coast), and 40 years for the Konkan area, respectively. The arrival of cyclones for different regions are shown in Fig.1, typically for three coastal areas. From Fig.1 it can be seen that in some years more than one cyclone have occurred in a year in some coastal regions. In this paper, multiple occurrences are considered as separate

544

occurrences and in the analysis entire coastal region of a given state is considered as one unit.

A small computer program is written to count the number of times a specified threshold wind speed is exceeded in the given record length (in terms of years). The mean rate of occurrence of the specified cyclone is then obtained by dividing the count value by the record length. The quantity of particular interest in the reliability estimation is the probability that a cyclone of specified intensity does not occur in a specified length of time (viz design life of the structure). This can be estimated from,

$$P \{ N \text{ (specified time)} = 0 \} = e^{-\nu(\text{specified time interval})}$$
$$P \{ N(\text{specified time}) \geq 0 \} = 1-e^{-\nu(\text{specified time interval})} \qquad (3)$$

It can be seen from the above expression that, for a given ν, the chance of occurrence of cyclone at least once in the specified time interval increases with the increase in time.

For different coastal regions considered in this paper, the intensities and mean return periods of cyclones with threshold wind speeds $\geq$ 30 knots,$\geq$ 40 knots, ..., $\geq$ 100 knots are computed. Using the values of ν, the probabilities of occurrence of each cyclone at least once in any 5yr, 10yr, 20yr, and 50yr period are calculated for a given coastal region. The exercise is repeated for five different regions considered. The values of ν and the probabilities mentioned above are presented in Table 1, typically for Andhra Pradesh coast. The results presented in this table indicate that given a cyclone of wind speed $\geq$ 80 knots has occurred now, there is a 65% chance that a cyclone with wind speed $\geq$80 knots is going to occur at least once in the next 5 years; there is 98.5% chance that the cyclone under consideration will occur in the next 20 years, and it is almost certain that the considered cyclone is going to occur in the next 50 years. Also, from this table it is seen that, for a given coastal region, the probability of occurrence of a given cyclone at least once in a specified time decreases with the increase in threshold wind speed, and the same increases with the increase in the length of the time interval.

4. APPLICATIONS OF POISSON PROCESS MODEL

Example 1
In this example the probability of failure of a structure subjected to cyclonic wind speeds is calculated based on the weakest-link hypothesis. It is assumed that the structure fails due to the failure of a critical component (such as a cladding unit) that has been designed for an extreme wind speed of V_{ex} (typically cyclonic wind speed). The mean return period of V_{ex} (estimated from the observed cyclonic wind speed data) is $\overline{T}$ years. The design life period of the structure is assumed as T years. Assuming Poisson arrival for cyclones, the probability of failure of the structure, $(P_f)_{str}$, is given by

$$(P_f)_{str} = P \{ \text{At least one cyclone with wind speeds} \geq V_{ex}$$

$$\text{occurs in } (0,T] \}$$

$$= 1 - P \{ \text{None of the cyclones occurring in } (0,T] \text{ has} \qquad (4)$$

$$\text{wind speeds} \geq V_{ex} \}$$
$$= 1 - P \{ N(T) - N(0) = 0 \} = 1-P \{ N(T) = 0 \}$$
$$(P_f)_{str} \qquad = 1 - e^{-\nu T} \qquad (5)$$

For $T = \bar{T}$, $(P_f)_{str} \approx 0.632$. On the other hand, if it is assumed that the structure fails when cyclonic wind speed exceeds V_{ex} two or more number of times during the life of the structure then, $(P_f)_{str} = 1 - e^{-\nu T}(1+\nu T)$.

Example 2
Let at any given time, the cyclones arriving at a particular location on the coastal area be classified as of Type I $(V_{ex} \geq V_1)$ with probability p or of Type II $(V_{ex} \geq V_2, V_2 > V_1)$ with probability $(1-p)$. $N(t)$ is a stochastic process which counts the total number of cyclones occurring in $(0,t]$. $N_1(t)$ and $N_2(t)$ represent the number of cyclones of Types I and II occurring in $(0,t]$, respectively. It can be seen that $N_1(t) + N_2(t) = N(t)$.

Assuming that a cladding unit fails in low cycle fatigue when m times Type I event and n times Type II event occur in interval of time $(0,T]$, the failure probability of the cladding unit, $(P_f)_{cla}$, can be determined from,

$$(P_f)_{cla} = P\{N_1(T)=m \cap N_2(T)=n\} \qquad (6)$$

It can be shown that this probability is given by

$$(P_f)_{cla} = e^{-\nu T} \frac{(\nu T)^{m+n}}{m! \; n!} p^m (1 - p)^n \qquad (7)$$

Example 3
In this example the use of Poisson process model for updation of probabilities of occurrence of cyclonic wind speeds is demonstrated. Since only a single parameter ν is required for the complete description of the process the updated probabilities of occurrence of cyclones can be determined by updating the value of ν. This can be achieved using Bayesian approach. Bayesian approach provides the formal framework for incorporating engineering judgment with observation data. Here it is assumed that the apriory distribution of ν is gamma. It can be shown that the posteriory distribution of ν is also gamma. Using this information the updated probabilities can be obtained as follows.

$$P \{ N(t)=n \} = \frac{(n+k1-1) \; (\mu 1)^{k1} \; t^n}{n! \; \Gamma(k1) \; (\mu 1 + t)^{n+k1}} \qquad (8)$$

where $\mu 1 = \mu + t_0$ and $k1 = k + n_0$, are the modified parameters of the distribution of ν. In the above formulation the

546

observation/information that n_0 cyclones of wind speed under consideration have occurred in t_0 years.

TABLE 1—The probabilities of occurrence of cyclones of various maximum wind speeds for Andhra Pradesh coast

Threshold wind speed (knots)	Mean reccurrence rate (yr^{-1})	$P\{N(5) \geq 1\}$	$P\{N(20) \geq 1\}$	$P\{N(50) \geq 1\}$
50.0	0.640	0.9592	0.9999	1.0000
60.0	0.410	0.8713	0.9997	1.0000
70.0	0.290	0.7654	0.9970	1.0000
80.0	0.210	0.6501	0.9850	1.0000
90.0	0.190	0.6133	0.9776	0.9999
100.0	0.070	0.2953	0.7534	0.9698
110.0	0.030	0.1393	0.4512	0.7769
130.0	0.020	0.0952	0.3297	0.6321
140.0	0.010	0.0488	0.1813	0.3935

Note: Record length = 100 years; Number of data points = 95
      1 Knot = 1.85 kmph

5. SUMMARY AND CONCLUSIONS

Poisson process model used in this paper is a climatological model and captures the important property that the occurrences of cyclones are rare events compared to occurrences of extreme wind speeds associated with well behaved winds. Since the model is described completely by a single parameter ν, it is simple to use. The model can be used in the estimation of time varying reliability of structures, when reliability formulations are made in the load space. The Poisson process model has been used in this paper to make probabilistic statements about the occurrences of cyclones of specified wind speeds in different coastal regions of India. Such information is needed in estimation of reliability of structures/structural components subjected to cyclonic winds. It is shown, through examples, that Poisson process model can be used in the estimation of collapse and low cycle fatigue reliability of structures/structural components (Examples 1 and 2). Poisson process model has an ideal probabilistic structure for incorporating the observed data on cyclonic wind speeds in making decisions about the future cyclone wind speed occurrences. In this paper it is shown how Bayes decision theory can be used in updating the parameter ν. By updating ν, it is possible to update the system reliability also. Thus, time varying reliability of structures located in coastal regions can be handled effectively using Poisson process model.

REFERENCES
1. Venkateswarlu, B., Arumugam, M. and Arunachalam, S., Proceedings of the National Seminar on 'Tall Reinforced Concrete Chimneys', April 1985, New Delhi, India, pp.1-24.
2. Twisdale, L.A., and Vickery,P.J., Journal of Wind Engineering, Vol.41, Nos.1-3, October 1992, pp.545-556.
3. Gomes, L. and Vickery, P.J., Jounal of Industrial Aerodynamics, Vol. 2, 1978, pp. 331-334.

4. Simiu, E and Scanlan, R.H., **Wind Effects on Structures**, Second Edition, John Wiley and Sons, New York, 1986.

5. Thom, H.C.S., Journal of Structural Division, ASCE, Vol.94, No.ST7, July 1968, pp. 1787 - 1801.

6. Balaji Rao, K., Thomas, K.C. and Appa Rao, T.V.S.R., Project Report No.STS-RR-91-2, September 1991.

7. Bendat, J.S., and Piersol, A.G., Random Data : Analysis and Measurement Procedures, Wiley-InterScience, N.Y, 1971.

8. Venkateswarlu, B., Annamalai, G., Shanmugasundaram, J., Arunachalam, S. and Arumugam, M., ` Cyclonic Wind Data for the East and West Coasts of India', Internal Report, SERC, Madras, March 1990, pp.1-8.
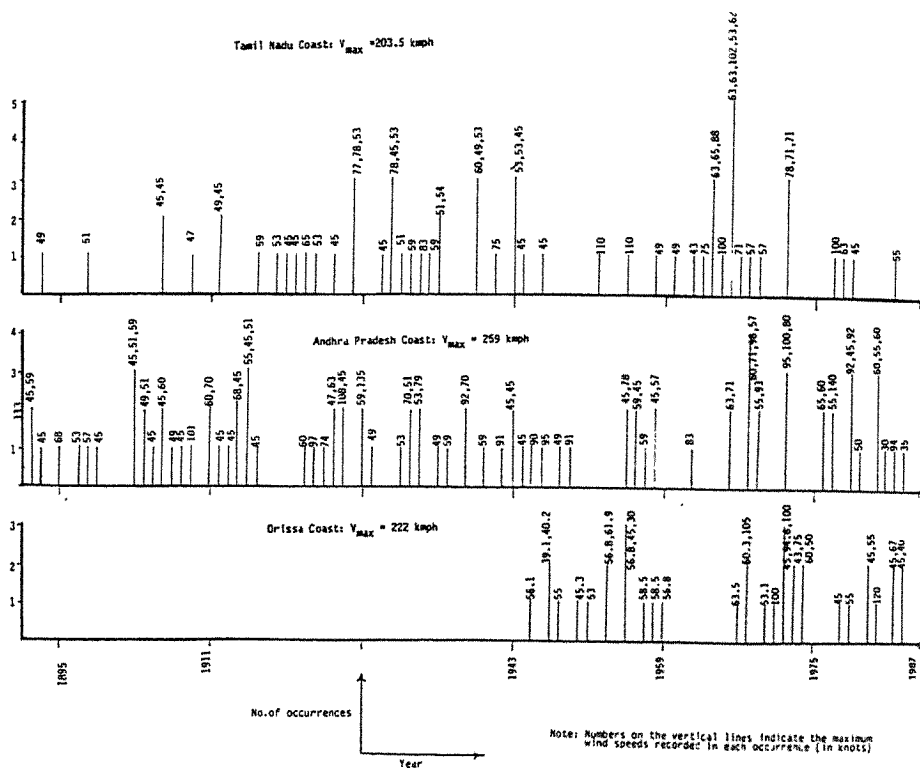
Fig.1 ARRIVAL OF CYCLONIC EVENTS

Research on The Wind Feature of Landing Typhoon on The Surface

Zheng Zhihua and Ma Wendou[+]

Kunming Institute of Technology, Kunming China

Abstract:Basing on the observation experiments on the feature of the landing typhoon on the surface, by studying and analysing the observation results, we think that landing typhoon, in surface layer, has the following features:

As the bigger u_1, the increase τ rapidly.

While typhoon landing, in same time, from 2.5m to 22m high, the wind direction difference is 25° —180°.

Wind speed pulsation difference σ increases with u_1, but turbulent intensity I reduces with u_1 increasing.

Turbulence time scale Lt, turbulence length scale Lx relate to I.

1. General Survey

According to the research plan of the program "Study of Reducing The Destructive Effect on Rubber Forest from Typhoon by Using Artificial Rubber—tea Mixed Community", supported by the National Science Foundation. We carried out the observation experiments on the wind feature of landing typhoon on the surface on Haian Island in 1990.

In accordance with the local conditions and the aim of the program, we set up a 12—meter high iron tower, on which an EL electrical anemometer was mounted   at the   height   of 2.5, 5 and 10 meters, and an EL and a DISA (Denmark DISA Hot—wire Instrument) were mounted at the height of 10 meters. At the same time, at the height of 22 meters on a nearby water tower, an EL was mounted.

After we compared the observation data obtained by DISA with those by the EL and measured the turbulence of the moderate and gentle breeze, the DISA was removed. When typhoon arrived, only the EL continued the observation.

The observation started from August 1, 1990 and lasted for 70 days till October 9, 1990.

No typhoon landed on Hainan Island in 1991. In the same year, No. 16 typhoon (August 20) and No. 19 typhoon (September 17) passed the sea surface south to Sanya city in the southern part of the Hainan Province. The two typhoons swept past our observation points,

and we got the observation record of both of them. The maximum wind power of No. 16 typhoon recorded by the EL anemometer at the 10 meters height was force 9 wind (the ten—minute average wind speed was 24. 0 m/s and the instantaneous speed was 31. 4m/s). No. 19 typhoon was force 7 wind (the ten—minute average wind speed was 13. 7 m/s and the instantaneous speed was 19. 5 m/s). Thus we got the substantial data from the observation.

In this paper, we will analyze and study the data obtained during the observation of the two typhoons.

2. The change of the landing typhoon on the surface at different altitudes

Generally, the wind—altitude gradient is expressed by the logarithm law:

$$u = \frac{u_*}{k} \text{Ln} \frac{Z}{Z_0} \qquad (1)$$

With the obtained data, the change of the values of u_* and Z_0 was calculated as shown in table 1.

date	maximum instantaneous wind speed m/s	arerage wind speed m/s	average daily wind speed m/s	values and frequency of u_* and Z_0				
				u_* $0.51<$	$\begin{matrix}0.51\\ \mid \\ 0.94\end{matrix}$	$\begin{matrix}0.94\\ \mid \\ 1.46\end{matrix}$	>1.46	other
				Z_0 $0.06<$	$\begin{matrix}0.06\\ \mid \\ 0.34\end{matrix}$	$\begin{matrix}0.34\\ \mid \\ 0.50\end{matrix}$	>0.50	other
8/28	31. 4	24. 0	18. 3	21%	25. 2%	14. 6%	2%	36.7%
9/17	19. 5	13. 7		61. 1%	19. 4%	2. 19%	0. 7%	16.7%

Table 1. The change of the values of u_* and Z_0 of the wind velocity profile about the landing typhoon on the surface.

In table 1, the values of u_* and Z_0 are from the value of the correlation coefficient which exceeds 0. 7. The column of "other" includes three conditions: First, the wind—altitude gradient doesn't follow the logarithm law, that is, the correlation coefficient is below 0. 7. Second, when the altitude changes, the wind velocity doesn't change. Third, with the altitude increasing, the wind velocity decreases.

From table 1, we can see that, when the wind velocity at 10—meter height increases, the values of u_* and Z_0 have a increase trend.

The value of u_* is related to the wind velocity gradient. Generally, if the values of u_* and Z_0 increase, the difference of the wind velocity at the different airstream layers will increase.

Thus, when the wind velocity at 10—meter height increases, the vertical air momentum exchange becomes weaker, and the difference of the wind velocity at the upper and lower layers increases. That is, the larger the landing typhoon velocity, the larger is the difference of the wind velocity at several meters height up to ten meters above ground level.

The change of the wind direction is shown as following: The typhoon we observed was a tropical low pressure anticyclone, so from the start to the finish of the typhoon, the wind directions recorded were different. At the beginning, No. 16 typhoon of August 28 was north —wind (according to the record of wind direction and velocity indicator at the 10 — meter height) then it changed into NNE, ENE, SW, the deviation range being about 180 degrees. On September 17, No. 19 typhoon, first was NNE, then changed into NE, ENE, the deviation range being about 90 degrees.

Within a certain period of typhoon, the wind direction varied at different altitudes. The changes of the wind direction of No. 16 tyhpoon from 1 o'clock to 3 o'clock (when the speed reached it's maximum) and No. 19 typhoon from 5 o'clock to 7 o'clock (which was the maximum speed) are shown in table 2.

	28th of August			17th of September		
	1 O'clock	2 O'clock	3 O'clock	4 O'clock	5 O'clock	6 O'clock
2. 5m	ENE	ENE	E	NE	ENE	NE
5. 0m	NE	NE	NE	NE	ENE	NE
10. 0m	NE	SSW	SSW	NE	NE	NE
22. 0m	SE	SSE	SSW	NE	ENE	ENE

Table 2. Changes of the wind direction with the altitude at the maximum wind speed.

3. Turbulence

Each time, the value of the wind velocity was read at five—second interval by a worker for 30 minutes from EL at 10—meter height, using the formula below, we worked out the turbulent intensity, by analyzing and calculating the obtained 23groups of ten thousand data:

$$I = \frac{\sigma_u}{u} \qquad (2)$$

The calculated results are shown in Figure 1.

The standard deviation of the wind—speeds pulsation quantity is the statistical average of the difference between the instantaneous velocity and the average wind velocity. The larger the value of I, the bigger is the extent of the wind speed pulsation to the average wind velocity. The larger the value of I, the larger is the proportion of the pulsation quantity to the aver-

age wind velocity and stronger is the atmospheric turbulence. From Figure 2, we can see that, the turbulent intensity tends to decrease (from 0.3 to 0.2) as the averge wind velocity increases, but the standard deviation of wind speed pulsation quantity tends to increase (from 1.0 m/s to 3.0 m/s) as the average wind velocity increases.
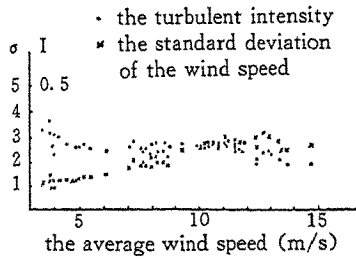
Fig. 1. the relation of the turbulence and wind velocity.

Fig. 2. The relation between the correlation coefficient and the time.

Though our observation sites are located in a terrain being relatively open, the turbulent intensity is bigger than that of the plain areas.

The relation of the turbulent intensity and wind velocity is shown in Figure 1. With the wind velocity increasing, the turbulent intensity gradually decreases. The conclusion conforms to the situaion discussed in the preceding chapter, in which the value of u. increases as the wind velocity at 10−meter height increasing. Both of them have proved that, with the wind velocity increasing, the difference of the wind velocity at several meters height up to ten meters increases, the vertical air momentum exchange becomes relatively weaker.

4. The turbulent friction stress and wind pressure

The relation between the friction velocity u. and the pulsating shear stress τ of the atmospheric turbulence is expressed by the following formula:

$$u_{\cdot} = \sqrt{\frac{\tau}{p}} \qquad (3)$$

From the formula, we have:

$$\tau = p \cdot u_{\cdot}^{2} \qquad (4)$$

552

Obviously, the atmospheric turbulent friction stress varys directly as the squre of friction velocity. Under the same condition, when the value of u. increases from 0.51 to 1.46, the value of τ is 7.2 times as much.

From table 1, we can see that, when the wind velocity at the 10—meter height above the ground level increases, the proportion of the above possibility will increaes.

5. The turbulent correlation coefficient and turbulence scale

According to statistical theory of turbulence, the correlation indicates the relevant relation of two pulsative wind speeds. The value of the turbulent stress depends on the relevant relation of the pulsative wind speeds. Using following formula, we carried out correlative analysis to the data obtained during the observation of the two typhoons.

$$R(t) = \frac{u'(t_1) \times u'(t_1 + \triangle t)}{u'(t_1)^2} \qquad (5)$$

	time scale(s)	space scale(m)
6:45	43	485
8:04	121	1303
9:00	76	728
9:40	303	1699
10:30	466	2611
11:30	86	649
12:25	149	1229
13:00	123	1015
14:20	154	1238
14:56	163	1377
15:30	107	785
16:26	43	338

Table 3. The time scale of turbulence and the space scale of turbulence.

The space scale of turbulence indicates the average dimension of the whole turbulent eddy, while the time scale of turbulence indicates the average life—span of the whole turbulent eddy. Both indicate that in the same turbulent eddy or in a single turbulent eddy, the pulsating quantities in different time—intervals are correlative before the turbulent eddy disappears,

553

they are calculated respectively by the following formulae:

The time scale of turbulence L_1:

$$L_1 = \int_0^\infty R(t)dt \qquad (6)$$

The space scale of turbulence L_2:

$$L_2 = \int_0^\infty R(x)dx \qquad (7)$$

Hence the relation between the correlation coefficient $R(L)$ and the time shown in Figure 2.

From Fig. 2 and table 3, we can see that, the time scale of turbulence of the observed typhoon is between tens and hundreds of seconds, the space scale is between 700—800 meters and 1000—2000 meters. This indicates that the turbulent stress can last for a long time.

6. Conclusions

From the above analysis, we can draw the following conclusions:

When typhoon lands on the surface, u_* and Z_0 aren't constants, they are variable in a larger range. As the wind speed at 10—meter height above ground level increases, the values of u_* and Z_0 increase and the difference between the turbulent friction stress and wind pressure at a few meters height and at ten meters or more height above ground level increase rapidly. So the dimensions and directions of force which acts on the upper and lower rubber trees are quite different, a very large monment of force is produced. This is probably one of the reasons of the breaking and even uprooting of rubber trees.

The turbulent intensity decreases with the increases of the averge wind velocity, while the standard deviation of wind speed increases with the increases of the average wind velocity, which shown that the pulsating quantity of wind force increases. This may also be one of the factors of the rubber trees breaking.

Because rubber and tea trees are mixedly cultivated and the tea trees are generally about one meter tall, the atmospheric turbulent intensity at a few meters above ground level increases and the momentum interchanging close to ground and at about ten—meter or more height increases, which makes smaller the difference of wind velocity between upper air layer and lower air layer. As a result, the possibility of the rubber trees being broken is suppressed.

Bluff Bodies - Cylinders

Mechanism of Interference Galloping of Two Identical Cylinders in Cross Flow

B. Dielen and H. Ruscheweyh

Wind Engineering,
Institute for steel structures
Technical University Aachen, Germany

Abstract:

Cylinders placed close together may be excited by a self-sustained oscillation, the so called "interference galloping". This phenonemon occurs at critical wind directions β_{crit}, when the wind speed exceeds a critical wind speed (onset velocity u_o). Large vibration amplitudes may be established and structural safety may be affected. This paper presents results of current experimental investigations of two identical cylinders placed in cross flow with small spacing ratios and low Scruton numbers. Ideas for a theoretical solution of the problem will be explained and discussed.

1. Introduction

At cylindrical structures placed close together, like chimneys in groups, parallel cables of cable-stayed bridges or transmission line systems, pipes in off-shore structures or in heat exchangers, vibrations with large amplitudes can be observed. These may be caused by vortex shedding or induced by the motion of the cylinders themselves. An aeroelastic coupling between the motion of the cylinders and the exciting forces is necessary to build up large vibration amplitudes. The phenomenon of interference galloping is observed at small Scruton numbers Sc, small spacing ratios a/d in a narrow band of wind directions.

2. The phenomenon of "interference galloping"

The phenomenon of interference galloping is characterized by the alternative changes between two basic flow pattern around the cylinders. In the first flow situation (phase I) the downstream cylinder (cylinder 2) is completely placed in the wake of the upstream cylinder (cylinder 1). Caused by small changes in wind direction or initial amplitudes the flow may switch to the other basic flow situation (phase II). It is characterized by an intense gap flow with high local wind speeds on the surface of the downstream cylinder. This causes a lift force F_y directed into the wake of the

Fig. 1: Basic flow situations during interference galloping

upstream cylinder. The downstream cylinder will move into the wake of the upstream one and the flow switches back to phase I. Because of the fact that this mechanism occurs with the frequency f_e of the cylinders (resonance), small lift forces F_y are sufficient to establish large vibration amplitudes.

Fig. 2: flow phases I and II, definition of the time lag Δt

Fig. 3: Phase lag $\Delta\varphi$ for $\hat{y}/d = 1.0$ and $\beta = 0°$

Fig. 4: Energy transfer during interference galloping

Former investigations /1,2/ have shown that the flow switching has a phase lag $\Delta\varphi$ resp. a time lag Δt relative to the lateral motion of cylinder 2.

$$\Delta\varphi = -360 \cdot \Delta t \cdot f_e \qquad (1)$$

This is shown in figure 2 in principle. The flow switching occurs after the cylinder has allready exceeded the critical position $y(\beta_{crit})$. Figure 3 shows as an example the phase lag $\Delta\varphi$ for a vibration amplitude $\hat{y}/d = 1.0$ and wind direction $\beta = 0°$ as a function of the reduced velocity

$$u_r = \frac{u}{f_e \cdot d} \qquad (2)$$

with the natural frequency f_e of the cylinder. The phase lag $\Delta\varphi$ is the basic requirement for an energy transfer from the flow into the structure. It can be seen that $\Delta\varphi$ decreases with increasing wind velocity. This is a reason for the fact that the vibration amplitudes seem to be limited, as measurements of this investigation show. Figure 4 presents the mechanism of the energy transfer in principle assuming that quasi-static force coefficients c_y are valid and the time history of c_y (full line in fig. 4b) can be shifted by Δt compared with the quasi-static value (dotted line). A force-displacement diagram (figure 4c) can be constructed from figure 4a and 4b. In case of interference galloping it has an excitation loop and a damping loop. The area of these loops are a measure of the energy dissipation (damping) and energy input (excitation) of the system. If the energy input E_i exceeds the sum of the energy dissipated by the flow $E_{d,aer}$ and dissipated by the structural damping $E_{d,s}$ the vibration amplitudes will increase, otherwise the amplitudes will decrease. If $E_i = E_{d,s} + E_{d,aer}$ a vibration with a stable amplitude is established.

The shape of the force-displacement diagrams depend on various parameters, e.g. spacing ratio a/d, vibration amplitude $\hat{y}$, mean flow direction β and lift force coefficient c_y as a function of β. Depending on the aerodynamic forces related to the motion of the cylinder, force-displacement diagrams may have the shapes presented in figure 5a to 5d. In fig. 5a the downstream cylinder is always in the wake of the upstream one (phase I, $\beta < \beta_{crit}$). Therefore the lift coefficient c_y has permanently the same value ($c_y \approx 0$). An energy input is not possible. The system is stable. In fig. 5b the mean flow direction β is beyond the critical value ($\beta > \beta_{crit}$). The lift coefficient has a value $c_y \neq 0$, but it will be approximately

constant during the whole cycle. The transfered energy (dissipation and excitation loop) will be small. The system remains stable, too.
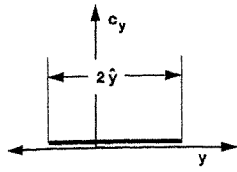
Fig. 5a: no flow switch, allways phase I
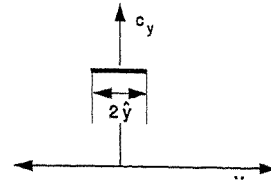
Fig. 5b: no flow switch, allways phase II
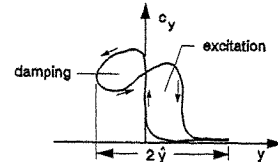
Fig. 5c: 2 switches per cycle

In fig. 5c the schematic force-displacement diagram for $ß \approx ß_{crit}$ is outlined. This is the usual situation during interference galloping. During one cycle there are big changes in the lift coefficient c_y, which cause, combined with the phase lag $\Delta\varphi$, a force-displacement diagram with a distinct damping (causing aerodynamic damping $E_{d,aer}$) and excitation loop (causing E_i). Depending on the relation between total damping ($E_{d,aer} + E_{d,s}$) and excitation (E_i) the system will be stable or not. Figure 5d shows a special case, where $ß \approx 0°$ and a big initial amplitude has established (e.g. caused by vortex shedding). In this case the curves shown in fig. 5c were passed two times per cycle (one in positive, one in negative $ß$-direction). A big amount of aerodynamic energy input E_i-$E_{d,aer}$ may be the consequence.
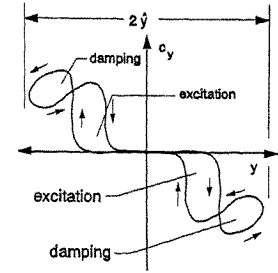
Fig. 5d: 4 switches per cycle

3. Estimation of the onset velocity u_0

The aerodynamic energy input E_i-$E_{d,aer}$ increases with increasing wind velocity (proportional to the dynamic pressure $\frac{1}{2}\rho u^2$). Therefore a critical wind velocity, called onset velocity u_0, can be expected, where interference galloping vibrations will start. Assuming that the total value of the lift force $|F_y|$ is the quasistatic value $F_{y,stat} = \frac{1}{2}\rho u^2 c_y(ß) \cdot d \cdot l$ and F_y follows the motion with a phase lag $\Delta\varphi$, a formula for the onset velocity has been developed /3/.

$$u_{0,red} = \frac{u_0}{f_e \cdot d} = 2 \cdot \sqrt{\frac{a}{d} \cdot \frac{\pi \cdot Sc}{-\sigma^* \cdot \sin(\Delta\varphi)}} \tag{3}$$

with

$$Sc = \frac{2m \cdot \delta}{\rho \cdot d^2} = \text{Scruton number} \tag{4} \qquad \sigma^* = \frac{\partial c_y}{\partial ß}\Big|_{ß_0} = \text{stability criterion} \tag{5}$$

Because of the fact that the phase lag $\Delta\varphi < 0$ instability occurs if $\sigma^* > 0$. This is the main difference to the classical galloping, where the stability criterion must be $\sigma^* < 0$ for instability. A combined stability criterion $-\sigma^* \cdot \sin(\Delta\varphi)$ may be used since the aerodynamic forces are only known for quasi-static boundary conditions and the phase lag $\Delta\varphi$ is only investigated for a few cylinder configurations and vibration amplitudes. The combined stability criterion $\sigma^* \cdot \sin(\Delta\varphi)$ can be calculated from model tests by

$$-\sigma^* \cdot \sin(\Delta\varphi) = 4 \cdot Sc \cdot \frac{\pi}{u_{0,red}^2} \cdot \frac{a}{d} \tag{6}$$

559

4. Experimental setup and model tests

In order to get more information about the dynamic behaviour of two identical neighbouring cylinders subjected to cross flow a series of model tests have been performed varying the Scruton number Sc, spacing ratio a/d, wind velocity u and direction ß. Tested parameters are Sc=3.0, 5.5, 8.5, 11.6, 14.9, a/d=1.2, 1.5, 2.0, 2.3, 3.0, 4.0, $0 < u_r < 30$ and $0 < ß < 40°$.

4.1 Experimental setup

The model tests have been performed in a small wind tunnel with a measuring cross section of 400*400 mm^2. Maximum wind speed is $u_{max} = 15$ m/s, turbulence intensity is $I_u = 2.5\%$. The diameter of the cylinders is d=5.25 cm which gives a maximum Reynoldsnumber of Re=$5.3 \cdot 10^4$ and a slenderness $\lambda = l/d = 7.6$. Each cylinder was suspended by 6 helical springs (3 à 120°at each cylinder end, see fig.6) mounted on a turnable frame. Both frames have a separate support. This reduces the mechanical interference of the two cylinders to a minimum, which is necessary to investigate small spacing ratios a/d combined with expected large vibration amplitudes. For the same reason end plates are permitted, so that inaccuracies caused by 3-D flow at the cylinder ends had to be accepted.
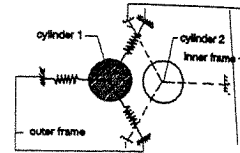
Fig. 6: 120°-suspension of the cylinders

The displacements of the two cylinders in wind direction (x-direction) and lateral direction (y-direction) have been measured by means of strain gauge measuring technique. Further informations are given in ref./4/.

4.1 Results of the measurements

The dynamic behaviour of the two cylinders can be described by elipses with a diameter $\hat{A}_i$ resp. $\hat{B}_i$ and by the direction α_i (i=1,2) in which the cylinders are vibrating (see figure 7).
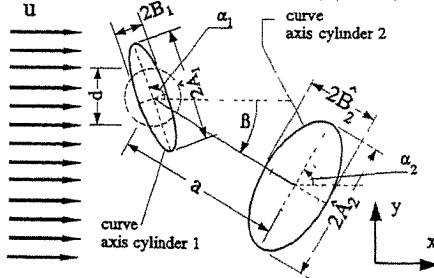
Fig. 7: Geometrical definitions

Additional the phase difference ϵ between the y-signals of both cylinders have been calculated, so that the motion of the cylinders can be discussed in relation to each other.

For each cylinder configuration (a/d, ß, Sc) a series of measurements have been made. Fig. 8 and Fig. 9 show two examples for a/d=1.5, Sc=8.5 and ß=15° resp. ß=0°, which will be used to discuss mean features of the measured results. We can see that an onset velocity $u_{0,red}$ exists ($u_{0,red} \cong 15$). The vibration amplitudes of both cylinders increase to large amplitudes. The direction of vibrations, α, differs in the first case and is relativly stable in the second case. The eliptic path of the motion, B/A, changes for ß=15° and is nearly a circle at $u_{red}=20$ (cylinder 1) while at ß=0° the elipse is constant and narrow. For the most configurations the phase difference ϵ is irregular. Only for few configruations a distinct tendency is visible.

For distance ratios a/d > 1.5 the downstream cylinder will have the larger amplitudes, for a/d=1.2 the larger amplitudes have been measured at the upstream cylinder. The amplitudes seem to have an asymptotic value if the flow velocity u_r is increased. After interference galloping has started in most cases the cylinders vibrate in nearly constant directions with increasing velocity u_r. Further it can be seen that there is a hysteresis. That means that the

560

system keeps stable for velocities beyond the onset flow velocity u_0, if there is no initial amplitude. This hysteresis has a minimum width when $\beta = \beta_{crit}$.
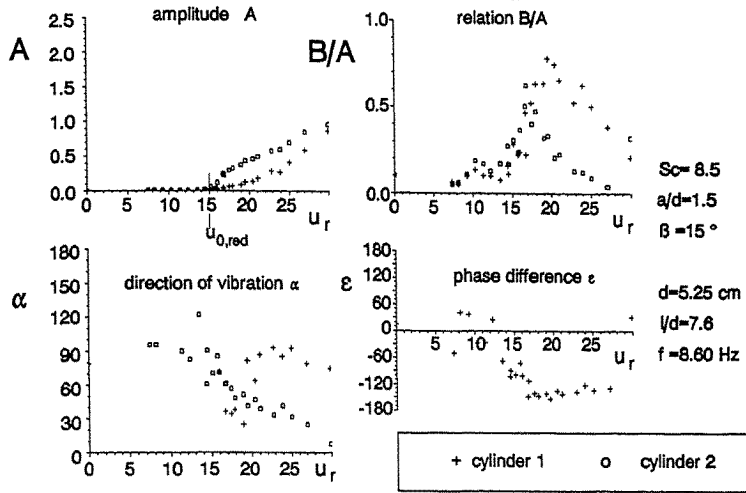
Fig. 8: Example results for $a/d = 1.5, Sc = 8.5, \beta = 15°$
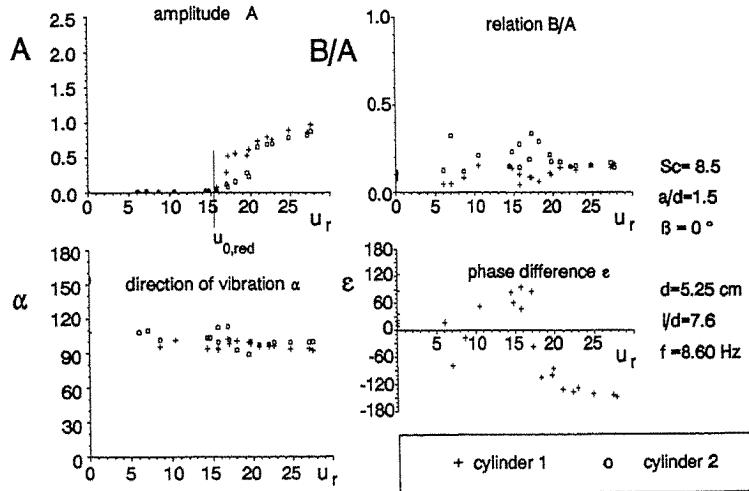
Fig. 9: Example results: $a/d = 1.5, Sc = 8.5, \beta = 0°$

From the measurements the onset velocities $u_{0,red}$ have been calculated (fig. 10). It can be seen that in general $u_{0,red}$ increases with increasing Sc number and spacing ratios a/d. In detail there are some irregularities for which no explanation could be found up to this time. For $Sc = 3.0$ no onset velocity $u_{0,red}$ can be defined, because large vibration amplitudes start from vortex shedding resonance point ($u_r \approx 5$), so that there is a mixing between vortex shedding and interference effects. Calculated values of $u_{0,red}$ based on a combined stability criterion

561

$\sigma^* \sin(\Delta\varphi) = 3.0$ are given, too. They are on the save side. A Comparison with the measured values indicate that the assumption of a constant $\sigma^* \sin(\Delta\varphi) = 3$ for all configurations is not justified.

5. Summary

Two aeroelastical cylinders with small spacing ratios and low Scruton numbers have been investigated in cross flow. Measurements of a wide variety of configurations with this 4 DOF system have shown a complicated field of response characteristics. The onset flow velocity u_0 has been measured for most of the

Fig. 10: Onset flow velocity for different Scruton numbers, Sc

cylinder configurations. A Comparison with calculated values indicates, that a simple factor for the stability criterion is not sufficient. Further work on the field of interference galloping is done.

Nomenclature:

a   - space between the cylinder axes
$\hat{A}$ - large ellipse diameter
A   - reduced ellipse diameter $A = \hat{A}/d$
$\hat{B}$ - small ellipse diameter
B   - reduced ellipse diameter $B = \hat{B}/d$
c_x, c_y - force coefficients
d   - cylinder diameter
E_i - energy input from wind
$E_{d,aer}$ - energy dissipated by aerodynamic damping
$E_{d,s}$ - energy dissipated by structural damping
f_e - cylinder frequency [Hz]
F_x, F_y - aerodynamic forces
I_u - turbulence intensity

m   - equivalent mass per length [kg/m]
Re   - Reynoldsnumber
Sc   - Scruton number
u   - flow velocity
u_0 - onset flow velocity
u_{red} - reduced flow velocity $u_{red} = u/(f_e \cdot d)$
$\hat{x}, \hat{y}$ - amplitude in x resp. y-direction
Δt - time lag
$\Delta\varphi$ - phase lag
ß   - flow direction
$ß_0$ - mean flow direction
$ß_{crit}$ - critical flow direction
δ - logarith. damping decrement
ϵ - phase difference between the vibration of the two cylinders
ρ - air density
σ^* - stability criterion

References:

1. H. Ruscheweyh; B. Dielen; Interference galloping investigations concerning the phase lag of the flow switching; Proc. 8th Int. Conf. Windengineering; 1991; London, Ontario, Canada
2. A. Dafnis; Investigations of the interference galloping effect in a water channel; unpublished report, RWTH Aachen, Germany; 1986
3. H. Ruscheweyh; Aeroelastic interference effects between slender structures; J. Wind Engineering and Industrial Aerodynamics; Vol 14; 1983; Elsevier Science Publisher B.V.; Amsterdam
4. B. Dielen; Beitrag zur Klärung des Interferenz Galloping Phänomens bei engstehenden, querangeströmten Zylindern, PhD thesis, Lehrstuhl für Stahlbau, RWTH Aachen, Germany; to be published in 1994

Numerical Study of Pressure Fluctuations
on Rectangular Cylinder in Aerodynamic Oscillation

T. Tamura, Y. Itoh, A. Wada and K. Kuwahara*

Department of Environmental Physics and Engineering,
Tokyo Institute of Technology, Japan
*The Institute of Space and Astronautical Science, Japan

Abstract: We numerically simulate unsteady flow fields around a forced-oscillating rectangular cylinder. The higher-order finite difference computation of the two-dimensional incompressible Navier-Stokes equations is applied to the dynamic interaction between the vortex motions and the torsional oscillation of a rectangular cylinder. In order to clarify the physical mechanism of the aerodynamic damping forces and the self-excited forces, we investigate the pressure fluctuations acting on the side surface. According to the computational flow visualization of the instantaneous vorticity, the vortices shed from the leading edge are controlled by the motion of a rectangular cylinder and the lock-on patterns of vortex shedding are clearly seen under the proper conditions.

1. Introduction

The unstable oscillation of rectangular cylinders occurs owing to the self-excited force mainly stemming from interactions with the separated shear flows or vortices close to the cylinder. The flow pattern with separation region around an oscillating rectangular cylinder is so complicated that the analytical theory of aeroelasticity cannot be easily applied to this bluff shape of section and the experimental approach to this problem is also difficult to comprehend the physical mechanism of the aerodynamic instability due to the separated shear flows. Thus far we have computed the incompressible flows around a square cylinder at rest and its aerodynamic characteristics have been clarified[1],[2]. We also simulated the two-dimensional unsteady flows around an oscillating rectangular cylinder in a heaving and a torsional mode[3]. Through the comparison with the experimental data, the vortex-induced instability of rectangular cylinders was investigated. Moreover we examined the necessity of the three-dimensional simulation of the aeroelastic problem[4]. On the basis of the comparison between the three-dimensional computational results of the fixed and the forced-oscillating bluff cylinders, it is confirmed that the flow structure around the cylinder becomes two-dimensionalized due to the oscillation.

Here for the understanding of fundamental aspects about the aeroelastic instability of a rectangular cylinder, we apply the direct finite difference technique[5] of the incompressible Navier-Stokes equations to the unsteady flow around a forced-oscillating rectangular cylinder in a torsional mode. With regard to the aerodynamics of an oscillating rectangular cylinders, the relation of the vortex motions and the unsteady aerodynamic forces is examined and we discuss the mechanism of the unstable oscillation and its occurrence by analyzing the pressure distribution on the side surface. The characteristics of the energy distributions are also discussed in order to investigate the vortex-induced and the self-excited instabilities of rectangular cylinders.

2. Problem Formulation

The governing equations are given by the following continuity and the Navier-Stokes equations:

$$\text{div } \mathbf{u} = 0, \tag{1}$$

$$\partial \mathbf{u}/\partial t + \mathbf{u} \cdot \text{grad } \mathbf{u} = -\text{grad } p + 1/Re\, \Delta \mathbf{u}, \tag{2}$$

where $\mathbf{u}, p, t$ and Re denote the velocity vector, pressure, time and the Reynolds number respectively, non-dimensionalized by U_0 (reference velocity), B (reference length), ρ (density) and ν (kinematic viscosity).

For the motion of a body, the moving grid system is incorporated[6]. A time-space transformation of $(t, x, y, ...)$ to $(\tau, \xi, \eta, ...)$ is imposed to the original governing equations. The acceleration term of the two-dimensional Navier-Stokes equations is represented as follows:

$$\partial_t + u\partial_x + v\partial_y =$$
$$\partial_\tau + \frac{1}{J}[(u - x_\tau)y_\eta - (v - y_\tau)x_\eta]\partial_\xi + \frac{1}{J}[-(u - x_\tau)y_\xi + (v - y_\tau)x_\xi]\partial_\eta \tag{3}$$

where J is the Jacobian. This relation means that the convection velocity in the computational domain is replaced by the relative velocity with respect to the moving coordinate. It should be noted that the grid system is moving in the physical domain, but stationary in the computational domain. The governing equations in the time-space generalized coordinate system are finally given as follows:

$$x = x(\xi, \eta, \tau)$$
$$y = y(\xi, \eta, \tau) \tag{4}$$

$$u_\tau + \frac{1}{J}[(u - x_\tau)y_\eta - (v - y_\tau)x_\eta]u_\xi + \frac{1}{J}[-(u - x_\tau)y_\xi + (v - y_\tau)x_\xi]u_\eta$$
$$= -\frac{1}{J}(y_\eta p_\xi - y_\xi p_\eta) + \frac{1}{Re}\widetilde{\Delta}u$$
$$v_\tau + \frac{1}{J}[(u - x_\tau)y_\eta - (v - y_\tau)x_\eta]v_\xi + \frac{1}{J}[-(u - x_\tau)y_\xi + (v - y_\tau)x_\xi]v_\eta$$
$$= -\frac{1}{J}(x_\xi p_\eta - x_\eta p_\xi) + \frac{1}{Re}\widetilde{\Delta}v \tag{5}$$

$$\widetilde{\Delta}A = (\alpha A_{\xi\xi} - 2\beta A_{\xi\eta} + \gamma A_{\eta\eta})/J^2$$
$$+ \{(\alpha x_{\xi\xi} - 2\beta x_{\xi\eta} + \gamma x_{\eta\eta})(y_\xi A_\eta - y_\eta A_\xi) + (\alpha y_{\xi\xi} - 2\beta y_{\xi\eta} + \gamma y_{\eta\eta})(x_\eta A_\xi - x_\xi A_\eta)\}/J^3 \tag{6}$$

$$J = x_\xi y_\eta - x_\eta y_\xi, \quad \alpha = x_\eta^2 + y_\eta^2, \quad \beta = x_\xi x_\eta + y_\xi y_\eta, \quad \gamma = x_\xi^2 + y_\xi^2 \tag{7}$$

$$\widetilde{\Delta}p =$$
$$-\{(y_\eta(u_\xi - x_{\xi\tau}) - y_\xi(u_\eta - x_{\eta\tau}))(y_\eta u_\xi - y_\xi u_\eta) + (x_\xi(u_\eta - x_{\eta\tau}) - x_\eta(u_\xi - x_{\xi\tau}))(y_\eta v_\xi - y_\xi v_\eta)$$
$$+ (x_\xi u_\eta - x_\eta u_\xi)(y_\eta(v_\xi - y_{\xi\tau}) - y_\xi(v_\eta - y_{\eta\tau})) + (x_\xi(v_\eta - y_{\eta\tau}) - x_\eta(v_\xi - y_{\xi\tau}))(x_\xi v_\eta - x_\eta v_\xi)\}/J^2$$
$$+ (y_\eta u_\xi - y_\xi u_\eta + x_\xi v_\eta - x_\eta v_\xi)/(J\Delta t) \tag{8}$$

In order to overcome the numerical instability at high Reynolds numbers, the third-order upwind scheme is employed for the nonlinear convection terms[5].

$$(u\frac{\partial u}{\partial x})_i \approx u_i\frac{-u_{i+2} + 8(u_{i+1} - u_{i-1}) + u_{i-2}}{12\delta x} + |u_i|\frac{u_{i+2} - 4u_{i+1} + 6u_i - 4u_{i-1} + u_{i-2}}{4\delta x} \tag{9}$$

where δx is the grid spacing. The numerical procedures are based on the MAC method[7]. The pressure field is determined by solving the Poisson equations and the velocity field is computed by the temporal integration of the Navier-Stokes equations.

3. Computational Model

Figure 1 shows a computational model where a rectangular cylinder with the depth-breadth ratio(D/B, D:the depth of a cylinder, B:the breadth) equal to 5.0 is placed in the computational domain

(the diameter=60*B*). The grid of 400×100=40000 points is used for the Reynolds number equal to 10^4. The approaching flow is assumed to be uniform(U_0). For the boundary condition of the pressure around the computational domain, the Dirichlet condition is imposed. On the surface of a cylinder, the velocity of moving grid at boundary is given and the Neumann condition is employed for pressure.
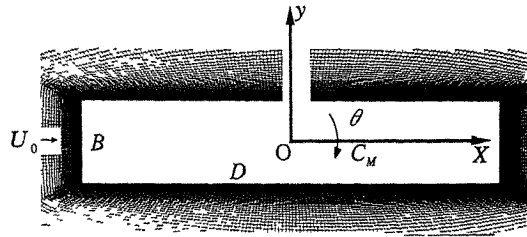
Fig. 1 Grid system for a rectangular cylincer (400×100 points).

4. Torsional Oscillation of a Rectangular Cylinder

We present the computational results of the flow around a forced-oscillating rectangular cylinder in a torsional mode(θ_0=2~10°, θ_0: the amplitude of torsional oscillation). The displacement angle θ of torsional vibration is given as follows:

$$\theta(t) = \theta_0 \sin(2\pi f_m t) \tag{10}$$

where f_m is the frequency of forced oscillation.

Figures 2 and 3 illustrate the instantaneous vorticity contours around a rectangular cylinder at rest and *Vr*=5.0, 10.0 and 30.0 ($U_0/f_m B$, the reduced velocity). In order to examine the vortex dynamics in the wake of the cylinder, the cases at $2\pi f_m t = 0$ and π(the displacement angle equals 0.) are shown. The previous experimental data[8], [9] show that the torsional response becomes larger suddenly over *Vr*=5.0 and the resonant phenomenon is observed approximately at *Vr*=5.0~8.0. The computational result indicates that the vortex pattern is symmetrically same and the vortices shed from the frontal corner are merging with the ones shed from the leeward corner at *Vr*=5.0. The process of vortex merging makes us presume that the vortex excitation appears at *Vr*=5.0. In the case at *Vr*=10.0 and 30.0, we can also see the same symmetric patterns of vortex motions. It is recognizes that the cylinder oscillation completely controls the vortex-shedding whose frequency is coincident with the torsional frequency. According to the experimental data[10], the self-excited oscillations based on the aeroelastic instability of the elongated rectangular cylinder(*D/B*=4.0) is recognized at *Vr*=30. It can be found in the computational result at *Vr*=30 that the vortices shed from the frontal corner never flow leeward constantly, but forms the bubble region close to the cylinder surface. These vortices gradually become very strong due to the concentration of vorticity.

The phase-averaged pressure distributions acting on the side surface of an oscillating cylinder at various *Vr* are shown in Fig. 4. In the case of the response phase($2\pi f_m t$) equal to 0., the effect of the torsional motion on the pressures is discussed in comparison with the case of a stationary cylinder. It is recognized in the case at *Vr*=5.0 and 10.0 that the pressure on the lower surface in the leeward region becomes positive. On the other hand, in case at *Vr*=30 the negative pressure appears in the same location, where the self-excited force is induced. The results of the different amplitude at *Vr*=30 present the almost same tendency. As the amplitude becomes larger, the pressure fluctuations also become larger.

The unsteady characteristics of the aerodynamic forces are investigated by analyzing the energy distribution on the side surface of the cylinder in Fig. 5. The total energy distribution is given as follows:

$$E_{total} = \int_0^{Tp} \left(\int_A Cp \, dA \right) r \, d\theta \tag{11}$$

where *Tp*, *A*, *Cp*, *r* are the reduced natural period, area, pressure coefficients, arm of the moment caused by each *Cp* . The energy distributions indicate the consistent result with the pressure

565

distribution on the side surface in Fig. 4. That is to say, it is recognized that the self-excited forces mainly appear in the windward region at Vr=5.0 and 10.0, and in the leeward region at Vr=30. The aerodynamic damping force is very large in the leeward region of the case at Vr=5.0 and 10.0, so finally the total torque on the rectangular cylinder becomes damping for the oscillation. With regard to the dependency of the torsional amplitude at Vr=30., the results have same tendency that two peaks appear at immediately after the frontal corner and the center of torsion. Due to these two peaks, the cases at Vr=30. become aeroelastically unstable conditions like the torsional flutter. Through the comparison with experimental data[11], the computational results are good agreement with the experimental data concerning the energy distributions based on the pressure as well as the aeroelastically unstable conditions of the oscillating cylinder.

Time variations of the torque coefficients(C_M) are given with the displacement angle of an oscillating cylinder in Fig. 6. In case of Vr=5.0, the C_M value is changing as a sinusoidal curve under vortex excitation, however at Vr=30.0 the C_M curve becomes complicated because the vortices is evolving and changing their shapes close to the side surface. The phase angle of the torque to the oscillation becomes negative at Vr=5.0 and 10.0, it shows the aeroelastically stable in this case. On the other hand, the phase becomes positive at Vr=30.0 and we can find the energy transfer of divergent oscillation. This tendency is in good agreement with the experimental data[10].

6. Conclusion

We simulate the unsteady flow around a forced-torsionally-oscillating rectangular cylinder by means of the direct finite difference technique without any turbulence model. The flow patterns around the cylinder shows the distinctive characteristics such as a vortex merging in vortex excitation or a vortex concentration in torsional flutter. The unsteady forces with regard to the aerodynamic instability are discussed, focusing on the energy distributions on the cylinder. Accordingly it is shown that the physical mechanism of unstable oscillations like a vortex-induced vibration and a torsional flutter are clarified by analyzing numerical data about the pressure distributions.

References

1. T. Tamura, E. Krause, S. Shirayama, K. Ishii and K. Kuwahara, Three-dimensional computation of unsteady flows around a square cylinder, Proc. 11th ICNMFD, Williamsburg, 1988
2. T. Tamura and K. Kuwahara, Numerical analysis on aerodynamic characteristics of an inclined square cylinder, AIAA Paper, 89-1805, 1989.
3. T. Tamura and K. Kuwahara, Numerical study on aerodynamic instability of oscillating rectangular cylinders, J. Wind Engrg. Indust. Aerodyn., Vol. 41, 1992.
4. T. Tamura, Y. Itoh, A. Wada and K. Kuwahara, Numerical Investigation on the Aerodynamic Instability of Bluff Cylinders, 1st CWE 92, J. Wind Engrg., No. 52, 1992.
5. T. Tamura, K. Tsuboi and K. Kuwahara, Numerical simulation of unsteady flow patterns around a vibrating circular cylinder, AIAA Paper, 88-0128, 1988
6. T. Kawamura and K. Kuwahara, Computation of high Reynolds number flow around a circular cylinder with surface roughness, AIAA paper, 84-0340 1984.
7. F. H. Harlow and J. E. Welch, Numerical calculation of time-dependent viscous incompressible flow of fluid with free surface, Phys. Fluids, Vol. 8, 1965.
8. Y. Nakamura, M. Nakashima and K. Watanabe, Bulletin R. I. A. M.(in Japanese), Kyushuu Univ.,No. 60, 1984
9. T. Yoshimura, A. Miyake, T. Hirayama and T. Akamatsu, Vortex excitation of elongated rectangular prism(in Japanese), Proc. Sympo. on Wind Engineering, 1986
10. H. Tomizawa, K. Washizu, A. Ohya and Y. Otsuki, Wind tunnel experiments of box-like models of buildings: Measurement of unsteady aerodynamic forces by forced oscillation method(in Japanese), Reports of the Research Laboratory of Shimizu Corporation, No. 20, 1973.
11. N. Shiraishi, M. Matsumoto, H. Shirato and T. Memita, On unsteady pressure characteristics of rectangular cylinders in flutter(in Japanese), Proc. 9th National Sympo. on WE, 1986.
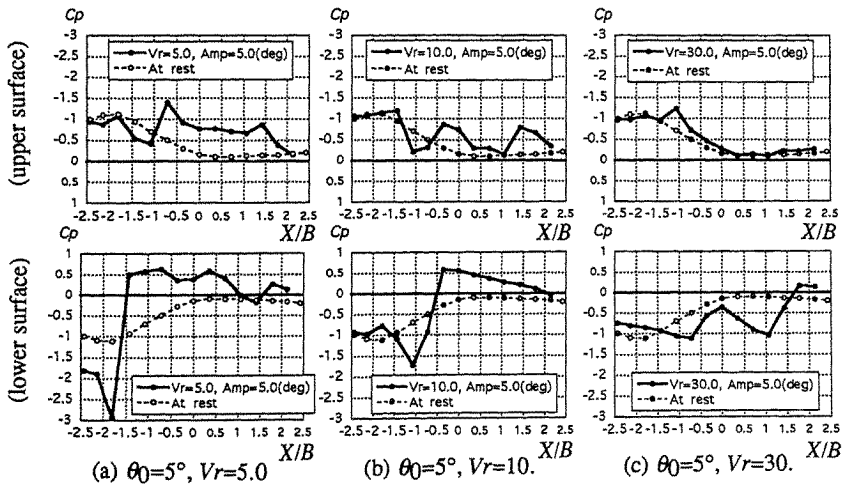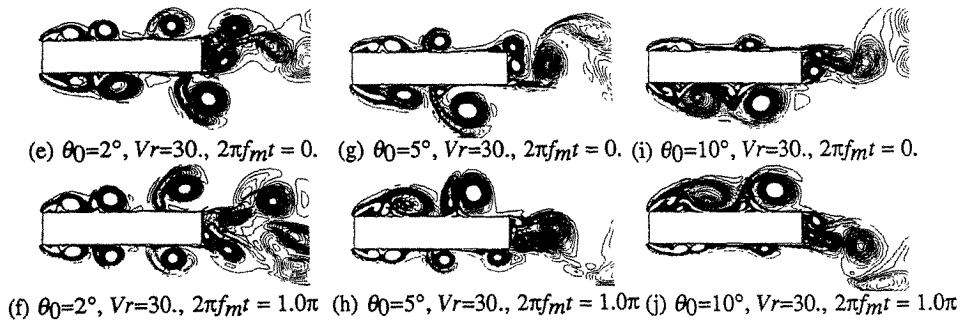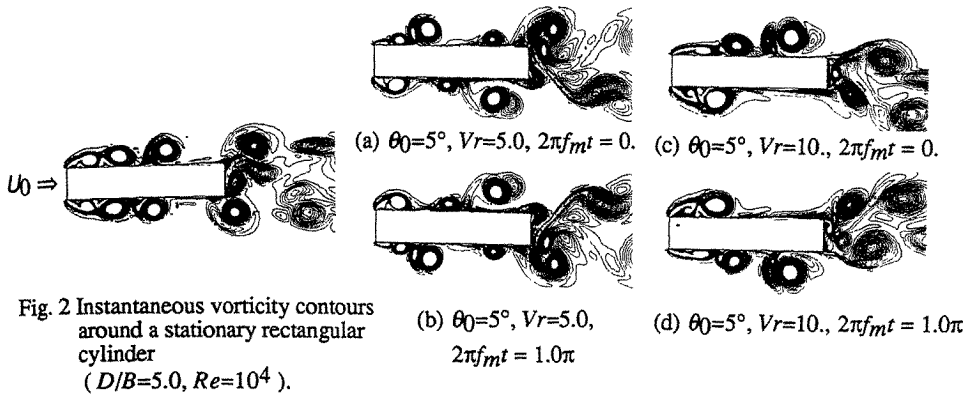
$U_0 \Rightarrow$

(a) $\theta_0=5°$, $Vr=5.0$, $2\pi f_m t = 0.$

(c) $\theta_0=5°$, $Vr=10.$, $2\pi f_m t = 0.$

Fig. 2 Instantaneous vorticity contours around a stationary rectangular cylinder ($D/B=5.0$, $Re=10^4$).

(b) $\theta_0=5°$, $Vr=5.0$, $2\pi f_m t = 1.0\pi$

(d) $\theta_0=5°$, $Vr=10.$, $2\pi f_m t = 1.0\pi$

(e) $\theta_0=2°$, $Vr=30.$, $2\pi f_m t = 0.$ (g) $\theta_0=5°$, $Vr=30.$, $2\pi f_m t = 0.$ (i) $\theta_0=10°$, $Vr=30.$, $2\pi f_m t = 0.$

(f) $\theta_0=2°$, $Vr=30.$, $2\pi f_m t = 1.0\pi$ (h) $\theta_0=5°$, $Vr=30.$, $2\pi f_m t = 1.0\pi$ (j) $\theta_0=10°$, $Vr=30.$, $2\pi f_m t = 1.0\pi$

Fig. 3 Instantaneous vorticity contours around an ocsillating rectangular cylinder in a torsional mode($D/B=5.0$, $Re=10^4$).

(a) $\theta_0=5°$, $Vr=5.0$ (b) $\theta_0=5°$, $Vr=10.$ (c) $\theta_0=5°$, $Vr=30.$

Fig. 4 Phase-averaged pressure distribution acting on the side surface of an ocsillating rectangular cylinder at $2\pi f_m t = 0.$ in a torsional mode($D/B=5.0$, $Re=10^4$).

567

(d) $\theta_0=2°$, $Vr=30$.   (e) $\theta_0=10°$, $Vr=30$.
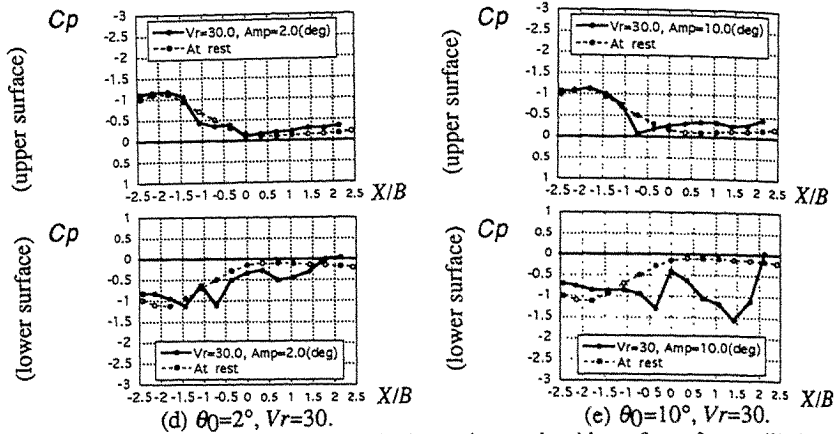
Fig. 4 Phase-averaged pressure distribution acting on the side surface of an ocsillating rectangular cylinder at $2\pi f_m t = 0$. in a torsional mode(continued).

(a) Computational results($\theta_0=5°$.)

(b) Computational results($Vr=30$.)

($\theta_0=4.46°$, $Vr=24.2$.)

(c) Experimental results by Shiraishi et al.

Fig. 5 Total Energyt distribution on side surface of an oscillating rectangular cylinder in a torsional mode($D/B=5.0$, $Re=10^4$).

(a) $Vr=5$.

(b) $Vr=10$.

(c) $Vr=30$.
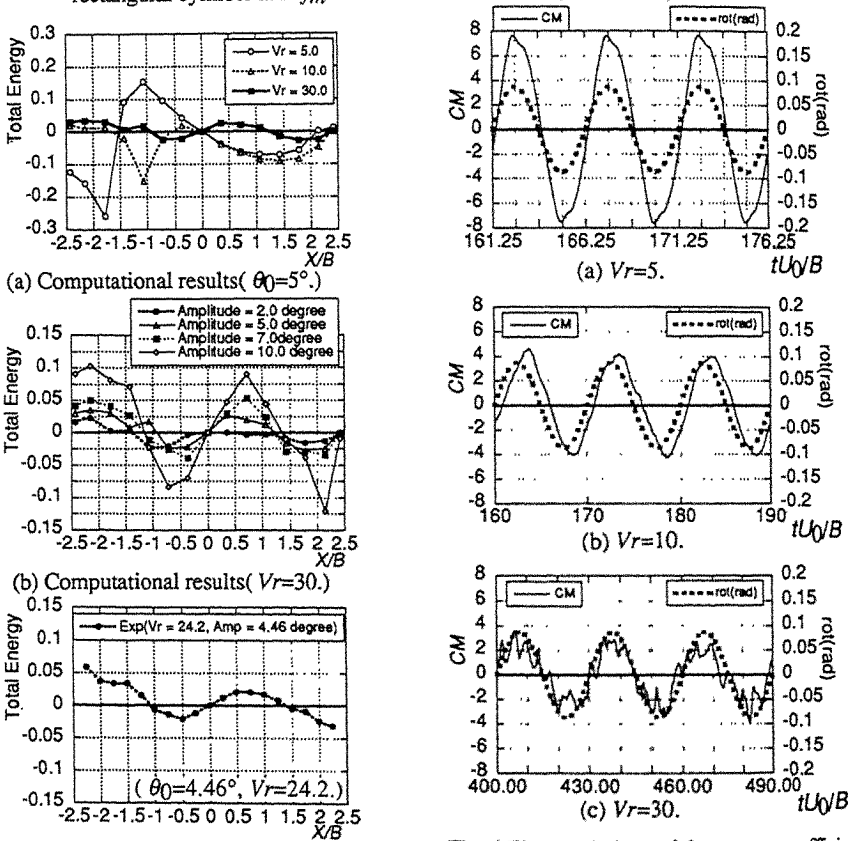
Fig. 6 Time variations of the torque coefficients (C_M) and the torsional angle($\theta_0=5°$.).

568

Numerical study of flow interaction behind two circular cylinders of equal diameters

C.W. Ng and N.W.M. Ko

Department of Mechanical Engineering
The University of Hong Kong, Hong Kong

Abstract: Impulsively started, inviscid, incompressible flows past two circular cylinders placed side by side in a uniform stream was investigated numerically by the discrete vortex model. At the bistable flow of $T/d=1.75$, where T is the transverse distance between cylinder centres, the flow development was initiated by imposing perturbation of short duration on the separated shear layers from the cylinders. An asymmetric mode of vortex shedding was observed and its possible effects on flow parameters such as Strouhal number, lift and drag are discussed.

1. Introduction

Studies of flows past bluff bodies and the wakes developed are relevant in wind engineering applications such as the effects of wind around neighbouring buildings and structures and the wind-induced vibrations. Thus, the properties of the wake and the vortex dynamics are important in the understanding of the aerodynamic sources and of their effects on the response of the building and structures.

The flow characteristics of two circular cylinders of equal diameters depend on their spacing and Reynolds number [1]. One of the features is the occurrence of bistable flow patterns at the critical spacings of $1.5 < T/d < 2.0$ where d is the diameter of the cylinder, in which the gap flow may be biased towards one of the cylinders. The switching of the biased flow occurs at irregular time intervals and depends on the Reynolds number [2].

In the present study interaction of vortices shed from two cylinders of equal diameters at $T/d=1.75$ was investigated numerically. Based on the discrete vortex method [3], the estimated flow parameters such as the Strouhal number, lift and drag will be presented.

2. Theory

For a two-dimensional, incompressible and inviscid flow, the vorticity transport equation may be written in terms of the vorticity ω and the stream function ψ as,

$$\frac{D\omega}{Dt} = \frac{\partial\omega}{\partial t} + (u \cdot \nabla)\omega = 0, \tag{1}$$

and

$$\nabla^2\psi = -\omega, \tag{2}$$

where u denotes the velocity vector. The boundary conditions to (2) are that the normal velocities on cylinder surfaces are zero and the velocity at infinity is constant at freestream mean velocity U.

3. Method

The distribution of vorticity was approximated by a set of N discrete point vortices,

$$\omega(x,t) = \sum_{n=1}^{N} \Gamma_n \delta[x - x_n(t)], \tag{3}$$

where Γ_n and $x_n(x_n, y_n)$ are respectively the circulation and vector position of the nth vortex and δ is the two-dimensional Dirac delta function. The Poisson's equation (2) was solved by the complex potential theory and the effect of the circular cylinders on ψ was determined by the method of successive images [4]. The velocity of each vortex was calculated after each time step δt and the positions of all vortices were updated according to a first-order Euler scheme. The path of a vortex near the cylinders was usually highly curved. Therefore, the vortex convection scheme was performed with a smaller time step $(0.5\delta t)$ for r less than a certain value r_c, where r is the maximum of two distances between the vortex and the two cylinder centres.

To avoid the singularity effect of a vortex, Chorin cut-off scheme and amalgamation of vortices were applied [3]. A reduction scheme on the circulation of vortices was introduced in order to allow for the three-dimensional deformation of vortex filaments [5].

The generation of vorticity near solid boundaries was approximately represented by introducing nascent vortices near laminar separation points. The laminar separation points were determined by the method of Thwaite [6]. The strength of each nascent vortex was determined from

$$\frac{\Gamma_n}{\delta t} = \frac{1}{2} U_s^2, \tag{4}$$

where U_s is the velocity of the outer flow at the separation point. Each nascent vortex was introduced at the separation point and its normal distance m from the cylinder was given by

$$\frac{2m}{d} + 1 = \frac{1 + |\Gamma_n|/\pi d U_s}{1 - |\Gamma_n|/\pi d U_s} \tag{5}$$

so that the Kutta condition is satisfied [3]. To save computational time, the total number of vortices N is limited to 2000.

The surface pressure coefficient was determined by the unsteady Bernoulli equation:

$$C_p = 1 - \frac{2}{U^2} \frac{\partial \phi}{\partial t} - \frac{q^2}{U^2}, \tag{6}$$

where q is the tangential speed on cylinder surface and ϕ the velocity potential.

The lift C_L and drag C_D coefficients were given by

$$C_D + iC_L = -\frac{1}{2} \int_0^{2\pi} C_p e^{i\theta} d\theta, \tag{7}$$

where θ is the angle of inclination to the real axis.

The numerical parameters chosen were time step $\delta t = 0.125$, cutoff radius $\sigma = 0.05$, vortex amalgamation distance $r_a = 0.05$ and $r_c = 1.3$. The first three parameters are obtained from the publications mentioned above.

4. Results and discussion

The method was first checked by computing the flow behind a single cylinder. For single cylinder flow the method of perturbation to initiate asymmetry is based on the scheme that the point vortices on one side of the wake are given small lateral displacements [3],

$$\delta x = 0.04[1 - \cos(\frac{t^* - 5}{4}\pi)], \quad \text{for } 5 < t^* < 9, \tag{8}$$

where t^* $(=2tU/d)$ is the non-dimensional time. The cylinder diameter d and the freestream velocity U are respectively the reference length and velocity. At the minimum rate of vorticity over $5 < t^* < 9$ the symmetric vortex spirals are most susceptible to small disturbances [3]. The computed vortex distribution, Strouhal number St $(=fd/U)$ and time variations of C_L and C_D for a single cylinder are in reasonable agreement with the experimental results.

For two cylinder flows four modes of perturbation, according to equation (8), were imposed on the separated shear layers from the cylinders (Table 1). The shear layers are labelled as s1 (uppermost), s2, s3 and s4 (lowest) (Fig. 1). For the mode 2 perturbation of $T/d=1.25$, $T/d=3.0$ and $T/d=3.5$, Fig. 1 shows the large scale vortex street structures, due to the phase variation of the initial shedding vortices. The flow direction is from left to right. For $T/d=1.25$, at which spacing the two cylinders are sufficiently closed to each other, a single vortex street is found (Fig. 1a). When the two cylinders are sufficiently far apart, $3.0 \leq T/d \leq 3.5$, two vortex streets are formed (Fig. 1b and 1c). Both the out-of-phase and the in-phase vortex shedding modes are possible. The wakes at the above three cases agree with the flow visualization results [7,8]. However, the evolution of a binary-vortex street due to the in-phase vortex shedding [7] is not observed in the present numerical calculation. This is probably due to the effect of Reynolds number because the flow visualization experiments were conducted at $100 < Re < 200$ [7].

For $T/d=1.75$ mode 2 perturbation was applied and vortex amalgamation is observed in which the gap vortex "2_1" from the upper cylinder comes close to the shedding vortices "3_1" and "4_1" from the lower cylinder (Fig. 2a) and they amalgamate (Fig. 2b). This process repeats for the next cycle of vortices "2_2", "3_2" and "4_2" behind the lower cylinder. However, the third vortex amalgamation ("1_3", "2_3" and "3_3") occurs behind the upper cylinder indicating bistable flows (Fig. 2c). This process of irregular time intervals had been reported previously [9]. However, the mechanism and reasons for irregular switching are still not yet known. The consequence of this process is the occurrence of two quasi-frequencies f_s and f_a due to the vortex shedding and vortex amalgamation respectively. The Strouhal number $St_s(=f_s d/U)$ due to the vortex shedding is estimated from the time variations of the front stagnation points (not shown here) to be 0.2. The wavelength of the amalgamated vortices is approximately doubled that of the vortex shedding, giving a ratio of f_s/f_a to two. This frequency ratio agrees with the experimental results of bistable flows [2,8]. The time variations of C_{pb}, C_L, and C_D of the two cylinders are shown in Fig. 3. C_L is defined as positive in the upward direction for the upper cylinder and negative for the lower one. In Fig. 3b and 3c the maximum C_L and C_D are higher than those of a single cylinder of 1 and 1.48 respectively. At time intervals t_1 and t_2 the C_{pb} of the upper cylinder (Fig. 3a) and the C_D of the lower cylinder (Fig. 3b) are higher while the opposite is true for t_3. The C_L characteristics exhibit certain phase relationship between the two cylinders, reflecting different stages of interaction at t_1, t_2 and t_3. Moreover, it is found that the time intervals t_1 and t_2 are associated with the vortex amalgamation process behind the lower cylinder while the t_3 corresponds to the one behind the upper cylinder. Therefore, evidence exists on the correlation of the vortex amalgamation and force characteristics of the two cylinders.

Numerical results with other modes of perturbation also indicate the vortex amalgamation (they are not shown here). The symmetric perturbations (modes 3 and 4) just delay the first occurrence of the vortex amalgamation process.

5. Concluding Remarks

The flows behind two circular cylinders of equal diameters placed side by side in a uniform stream have been modelled by the discrete vortex method. Four modes of perturbation were considered and they all indicate that the vortex amalgamation process is an important mechanism

for the development of the wake further downstream. The bistable flow is due to the interaction of vortices shed by the two cylinders. The maximum C_L and C_D are higher than those of a single cylinder.

6. Acknowledgment

References:
1. N.P.Cheremisinoff,Encyclopedia of Fluid Mechanics,Gulf,Houston(1989)323.
2. H.J.Kim and P.A.Durbin,J.Fluid Mech.,196(1988)431.
3. T.Sarpkaya,J.Fluids Engng.,111(1989)5.
4. C.Dalton and R.A.Helfinstine,J.Basic Engng.,Dec.(1971)636.
5. M.Kiya,K.Sasaki and M.Arie,J.Fluid Mech.,120(1982)219.
6. H.Schlichting,Boundary-Layer Theory,6th ed.,McGraw-Hill(1968)206.
7. C.H.K.Williamson,J.Fluid Mech.,159(1985)1.
8. K.Kamemoto,Bull.JSME,19(1976)283.
9. M.Hayashi,A.Sakurai and Y.Ohya,J.Fluid Mech.,164(1986)1.
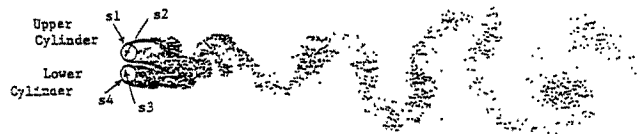
(a) $T/d = 1.25$, $tU/d = 35.1$.
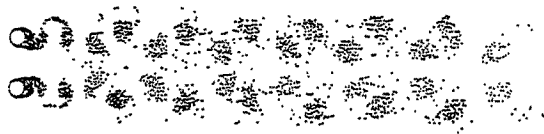
(b) $T/d = 3.0$, $tU/d = 47.3$.
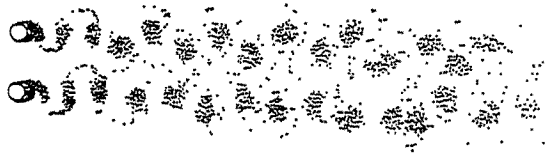
(c) $T/d = 3.5$, $tU/d = 44.5$.

Fig. 1. Distributions of vortices.

Mode	Perturbation on shear layers
1	1 and 2 (asymmetric)
2	1 and 3 (asymmetric)
3	1 and 4 (symmetric)
4	2 and 3 (symmetric)

Table 1.   Four modes of perturbation.
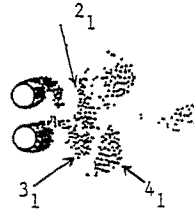
2(a) $tU/d = 7.9$.

2(b) $tU/d = 12.6$.
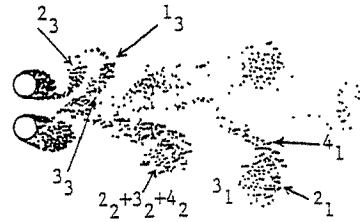
2(c) $tU/d = 15.4$.

Fig. 2.   Distributions of vortices. $T/d = 1.75$.
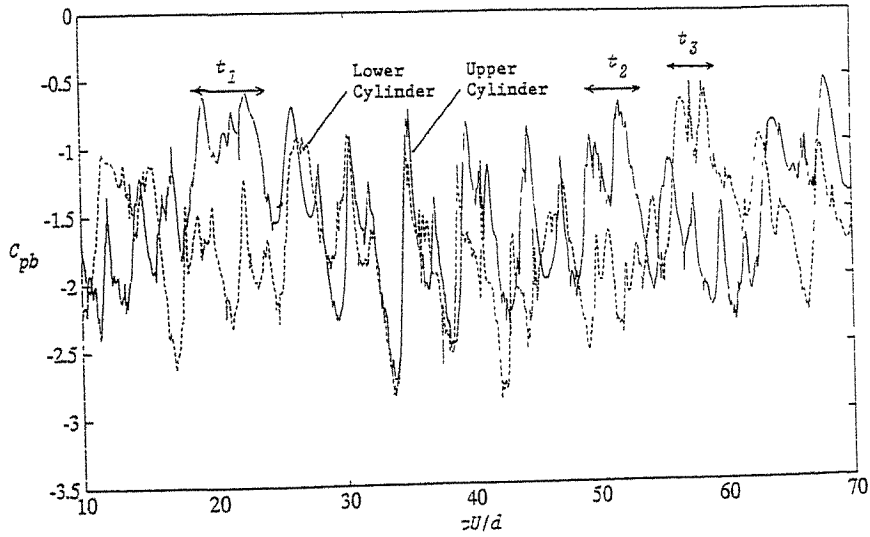
Fig. 3a.   Time variations of C_{pb}. $T/d = 1.75$.

573
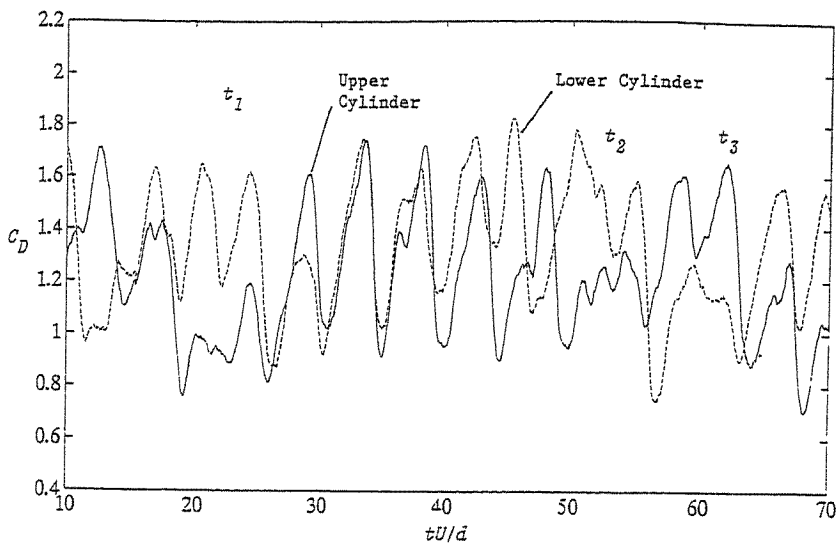
Fig. 3b. Time variations of C_D. $T/d = 1.75$.
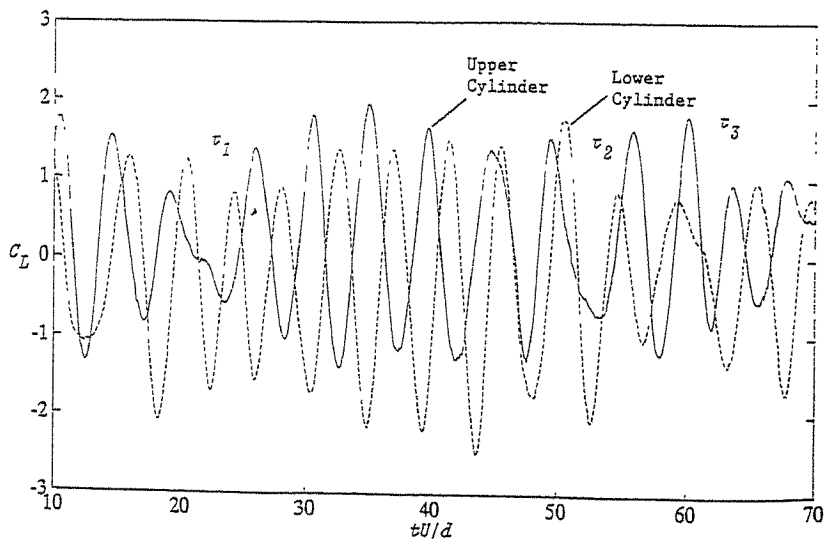
Fig. 3c. Time variations of C_L. $T/d = 1.75$.

574

Effects of turbulence characteristics on vortex-induced oscillation of two-dimensional cylinders with various structural dampings

M.Kawatani, O.Suzuki[+], H.Kim[++] and H.Kobayashi[+++]

Department of Civil Engineering
Osaka University, Japan
[+]Graduate School of Engineering
Osaka University, Japan
[++]Department of Civil Engineering
Korea Military Academy, Korea
[+++]Department of Civil Engineering
Ritsumeikan University, Japan

Abstract: This paper investigates the effects of turbulence properties on vortex-induced oscillation of two-dimensional basic rectangular cylinders with aspect ratio of 2 and 4 and those with fairings. The shape of fairings is selected taking account of an effects of turbulence that the maximum amplitude of vortex-induced oscillation is enlarged. In former study the employed structural damping has been comparatively small because of easy occurrence of aerodynamic response. So this paper also investigates the effects of structural damping. The effects of turbulence properties on vortex-induced response are evaluated in terms of the maximum amplitude in turbulent flows compared with that in a smooth flow.

1. Introduction

For investigating an aerodynamic stability of long and flexible structures, wind tunnel tests usually have been carried out in a smooth flow. However, it is well known that an aerodynamic response of structures in a smooth flow is different from that in a natural winds including turbulences. In order to assure an aerodynamic stability of structures in natural winds and to make a rational aerodynamic design, it is important to investigate the aerodynamic behavior of the structures in turbulent flows simulating natural winds in a wind tunnel.

The turbulence properties of natural winds are usually expressed in the form of a power spectrum and identified by two parameters; turbulence intensity and turbulence scale. Taking notice of vortex-induced oscillation of bluff cylinders which is strongly affected by fluctuating wind velocity, some experiments have been carried out in turbulence flows. Those results show that the fluctuation of wind velocity reduces the vortex-induced response in many cases, but enlarges the response of the rectangular cylinders with particular fairings. In those experiments, effects of turbulence intensity have been mainly emphasized, however, the effects of turbulence scale have not yet been fully examined, because a generation of turbulent flow with arbitrary scale was difficult.

This study investigates the effects of turbulence properties on vortex-induced oscillation of bluff cylinders with various structural dampings through two dimensional wind tunnel tests. The aerodynamic response of models are examined in actively controlled turbulences that was developed by authors[1-2]. Two-dimensional models are the rectangular cylinders of aspect ratio
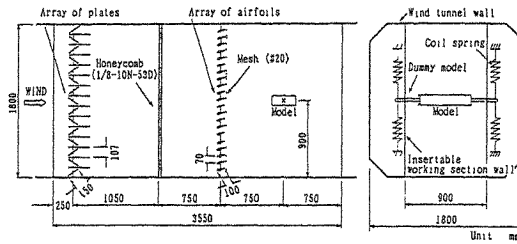
Fig.1 Active gust generator

of 2 and 4 and those with fairings. In the case of the cylinder of aspect ratio of 2 with fairings, the response in turbulence flows is larger than that in a smooth flow. In former study the employed structural damping has been comparatively small because of easy occurrence of aerodynamic response[3]. So, the effects of structural damping are also investigated. The effects of turbulence properties on vortex-induced response are evaluated in terms of the maximum amplitude in turbulent flows compared with that in a smooth flow.

2. Actively Generated Turbulence

2.1 Gust Generator

The experiments were carried out in Göttingen type wind tunnel of Osaka University whose test section was 1.8m width, 1.8m height and 9.48m length. In the test section, an active gust generator composed of two active arrays of plates and airfoils was installed as shown in Fig.1. The plates were shaken randomly to produce the horizontal fluctuation of wind velocity by changing blockage ratio of cross-section of the wind tunnel. The airfoils were also shaken randomly to produce the vertical velocity fluctuation. These arrays of plates and airfoils were driven by AC servomotors controlled by a micro computer.

To delete the undesirable vortices separated from the moving plates, a honeycomb was installed between the plate-array and airfoil-array. The screen mesh just behind the array of airfoils also reduces the size of vortices separated from airfoils. Turbulent flows were measured by hot-wire anemometer with x-type probe at the distance of 0.75m downstream from the array of airfoils.

2.2 Turbulent Properties of Actively Generated Flows

Measured spectra of horizontal and vertical velocities are shown as examples in Fig.2, together with the target one which is Kàrmàn's expression for the power spectra of natural winds. This figure shows that the measured spectra satisfactorily agree with the target ones in the wide range of frequency.

The characteristics of turbulent flows are summarized in Table 1. It is seen in this table that the intensities and scales of turbulent flows can be independently controlled by the gust generator. The turbulence intensity and scale of generated flows may cover a wide range of turbulence properties of natural winds[4]. Semi-smooth flow shown in Table 1 is produced when the arrays of plates and airfoils are at rest keeping horizontal position, and is distinguished from smooth flow obtained in the condition of removing the gust generator from the test section.

576

(a) Horizontal component　(b) Vertical component
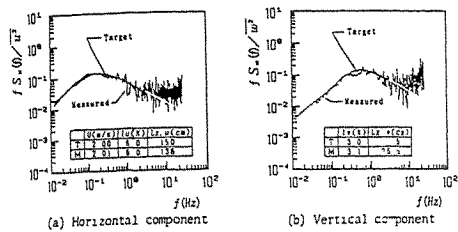
Fig.2 Power spectra of turbulent flow

Table 1 Turbulence characteristics

Turbulence No	Change of	Target				Measured			
		I_u (%)	I_w (%)	$L_{x u}$ (cm)	$L_{x w}$ (cm)	I_u (%)	I_w (%)	$L_{x u}$ (cm)	$L_{x w}$ (cm)
Semi smooth flow						1 5	1 5	3	2
TI 04	I_u & I_w	4	2			4 4	2 6	129	26 7
TI 06 *		6	3	150	37 5	5 8	3 0	154	35 1
TI 10		10	5			9 8	5 4	150	37 6
TSu 05				50		5 7	3 3	52	33 4
TSu 15 *	$L_{x u}$	6	3	150	37 5	5 8	3 0	154	35 1
TSu 35				350		6 2	3 4	310	35 8
TSw 12					12 5	6 0	3 3	134	12 3
TSw 37 *	$L_{x w}$	6	3	150	37 5	5 8	3 0	154	35 1
TSw 87					87 5	6 1	3 6	140	76 3

* TI 06 TSu 15 and TSw 37 are the same turbulences

** The mean velocity is 2m/s
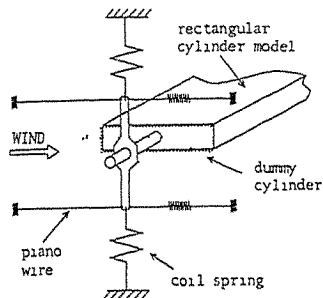
Fig.3 Supporting system

Table 2 Sectional shape and dynamic characteristics of models

Model No	Cross sectional shape Unit mm	Weight (kg・f)	Frequency (Hz)	Logarithmic decrement
A	60 ⊐ 120	1 98	5 50	0 002~0 016
AF1	60 120	2 10	5 30	0 004~0 018
D	60 210	2 19	5 00	0 004~0 015
DF1	60 240	2 32	5 00	0 009~0 020

3. Vortex–Induced Response

3.1 Experimental Method

A two dimensional cylinder is supported by coil springs such as the motion is restricted to the vertical direction as shown in Fig.3. In turbulent flows simulating natural wind, an aerodynamic behavior of the cylinders, in particular a vortex–induced vibration, was examined.

Table 2 shows the sectional and dynamic characteristics of two–dimensional cylinders employed in this study. Model A and Model D are the rectangular shapes whose vortex–induced response is strongly affected by wind velocity fluctuations. Model AF1 has regular triangular fairings with Model A, whose amplitude is increased by existence of turbulence. Model DF1 has the same fairings as Model AF1 with Model D.

3.2 Effects of Structural Damping

When the structural damping is changed, the V–A curves of the models in the semi–smooth flow are shown in Fig.4. Onset velocities of vortex–induced oscillation of all models are not affected by change of the structural damping. As the structural damping increases, the vortex–induced response decreases, and the range of velocities in which the vortex–induced oscillation occurs becomes narrow.

577
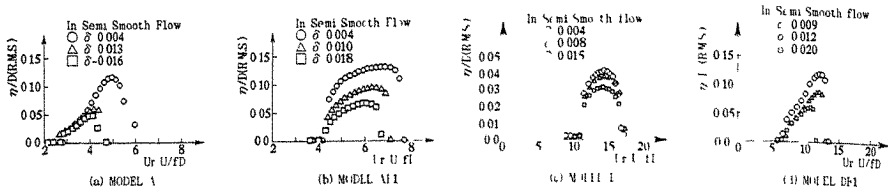
Fig 4 Response amplitude (Change of structural damping)

(a) Model A

(b) Model AF1
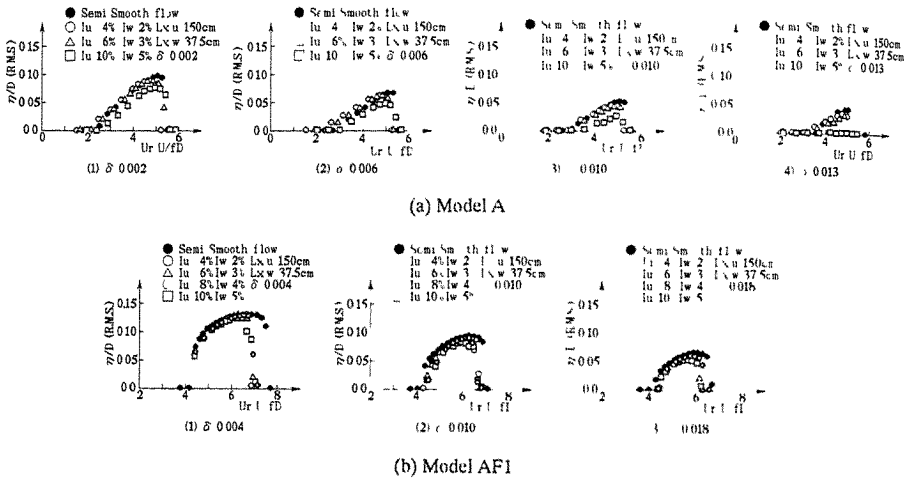
Fig.5 Response amplitude (Change of turbulence intensity)

3.3 Effects of Turbulence Intensity

When turbulence intensity is changed, the V–A curves of the models in turbulent flows and the semi–smooth flow are shown in Fig.5. In these cases, the other turbulence characteristics can be approximately kept $Lx,u=150cm$ and $Lx,w=37.5cm$ as shown in Table 1. The corresponding maximum amplitudes are also shown in Fig.6. In grid–generated flows, the amplitude of Model AF1 is increased by the existence of turbulence[3,5]. However, in actively generated turbulences, the amplitude is not almost changed by the existence of turbulence. The reason can be considered as the effects of difference of power spectra between the actively generated turbulence and the grid–generated flows. In Fig.6(a), the decrease ratio of the maximum amplitude of Model A is increased with increase of the structural damping. When a logarithmic decrement of the structural damping is 0.013 and $Iu=10\%$, the vortex–induced oscillation does not occur. Effects of turbulence intensity on vortex–induced oscillation of the other models are not affected by change of the structural dampings.

The effects of structural damping are also investigated in terms of aerodynamic damping. The aerodynamic damping of Model A and Model AF1 in turbulent flows with various turbulence intensities is measured and shown in Fig.7. Figure 7 also indicates regression lines of structural

578
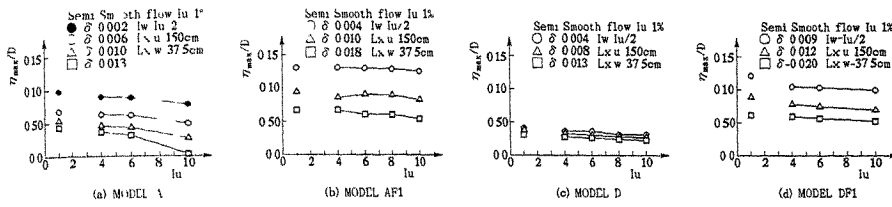
Fig 6 Maximum amplitude vs turbulence intensity

(a) Model A

(b) Model AF1
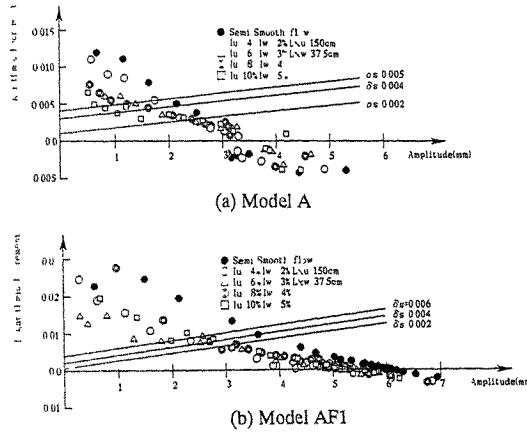
Fig 7 Aerodynamic damping (Change of turbulence intensity)
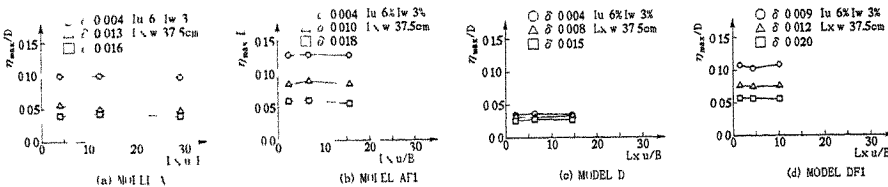
Fig 8 Maximum amplitude vs. horizontal scale

damping to amplitude. Aerodynamic damping of Model A in turbulent flows are smaller than that in smooth flow. This result is similar to that in grid-generated turbulence[6]. The aerodynamic damping of Model A is dispersed in wider range of amplitude on regression lines of structural damping compared with that of Model AF1.

3.4 Effects of Horizontal Turbulence Scale

The maximum amplitude in change of horizontal turbulence scale is shown in Fig.8. In these cases, the other turbulence characteristics are kept Iu=6% (Iw=Iu/2) and Lx,w=37.5cm. The vortex-induced responses of all models are not affected by change of horizontal turbulence scale ($5 \leqq$ Lx,u/B $\leqq 30$) with change of structural damping.

579
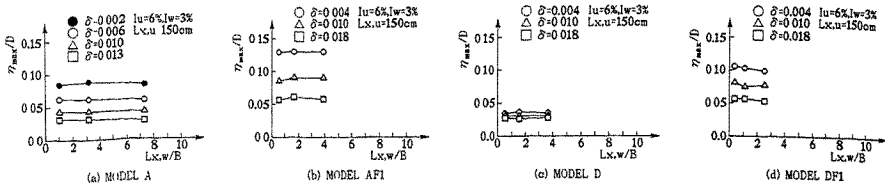
Fig.9 Maximum amplitude vs. vertical scale

3.5 Effects of Vertical Turbulence Scale

When vertical turbulence scale is changed, the maximum amplitude is shown in Fig.9. In these cases, the other turbulence characteristics are kept Iu=6% (Iw=Iu/2) and Lx,u=150cm. The change of vertical turbulence scale ($1 \leqq Lx,w/B \leqq 8$) does not affect the vortex-induced responses of all models with change of structural damping.

4. Conclusions

1) In semi-smooth flow, onset velocities of vortex-induced oscillation of all models are not affected by change of structural damping.

2) As the structural damping increase, the vortex-induced response decreases, and the range of resonant velocities of vortex-induced oscillation becomes narrow.

3) The decrease ratio of the maximum amplitude of Model A is increased with increase of the structural damping.

4) Amplitude of Model AF1 is not increased by the existence of turbulence. The reason can be considered as the effects of difference of power spectra between the actively generated turbulence and the grid-generated flows.

5) The effects of turbulence properties on vortex-induced oscillation of Model AF1, D and DF1 are not affected by change of structural damping.

6) The vortex-induced responses of all models are not affected by change of horizontal turbulence scale with change of structural damping.

7) The change of vertical turbulence scale does not affect the vortex-induced responses of all models with change of structural damping.

8) The aerodynamic damping of Model A is dispersed in wider range of amplitude on regression lines of structural damping compared with that of Model AF1.

References

1. H.Kobayashi, M.Kawatani, and O.Nakade, J of Wind Eng. and Industrial Aerodynamics, 33 (1990) 101.
2. H.Kobayashi, M.Kawatani and H.Kim, J of Wind Eng. and Industrial Aerodynamics, 41 (1992) 775.
3. M.Kawatani, H.Kim, H.Uejima and H.Kobayashi, Preprint of 2nd Int'l Colloquium on Bluff Body Aerodynamics and Applications, 1 (1992).
4. H.Kobayashi, M.Komatsu, M.Kawatani and Y.Kuroyama, Proc. of 2nd Asia-Pacific Symposium on Wind Eng., 2 (1989) 669
5. T.Suzuki and S.Hikami, Proc. 40th Annual Conf. of JSCE, (1985) I-223.
6. I.Nishio and H.Kobayashi, Proc. 42th Annual Conf. of JSCE, (1987) I-301.

Aerodynamic Behavior of Multiple Elastic Circular Cylinders with Vicinity Arrangement

Y. Kubo, T. Nakahara[+] and K. Kato

Department of Civil Engineering
Kyushu Institute of Technology, JAPAN
+Japan Bridge Co., JAPAN

Abstract: A span length of cable-stayed bridge has become longer with increment of years, which requires larger diameter, longer and heavier cables. And a heavier construction machine is required to lift the cables up to cable anchoring points on the pylon and large capacity jacking facilities are required to tensile force into the cables. From the view point of construction cost, the larger diameter and longer, heavier cables increase the construction cost. In order to reduce the construction cost or keep ordinary construction cost, what should be done is to use the smaller diameter and lighter cables and to substitute multiple small diameter cables for large diameter cables. Therefore, it is required to investigate the aerodynamic behavior of multiple cables by changing the number of cables and the spacing distance between cables by comparing the present experimental results with three-dimensional experimental results.

1. Introduction

With development of bridge engineering, cable-stayed bridges elongate the span length year by year. The cable-stayed bridges are constructed at even place where a suspension bridge is built as a optimum bridge in basis of usual design concept. Aerodynamic instabilities of cables become more serious problem with increment of the span length of cable-stayed bridges.

Considering that the long span cable-stayed bridge requires cables with the large tensile capacity,

1) large capacity lifting machines on the pylon must be installed to lift heavy cables.

2) large capacity jacking up system is required to put tensile force into large tensile capacity cable.

It enables to reduce construction cost to use the lifting machine and the jacking up system with small capacity. It is the only way to reduce the construction cost to use multiple cables with small tensile capacity in substitution of one large tensile capacity cable. The multiple cable's system has advantage for not only construction cost reduction but also replacement of damaged cables to new cables when some cables get damages by erosion at anchored portion after breaks of covering material and so on.

From above mentioned view-point, the authors have investigated the aerodynamic instabilities of multiple cables for the cable-stayed bridges. The cable-stayed bridges supported by cables at one anchorage point, generated vortex-excited vibrations and wake galloping in downstream cables and their aerodynamic vibrations have been suppressed by a method to connect cables with wires or by setting dampers at the cable end on the girders. The authors, however, have investigated the method to suppress the aerodynamic vibration by changing the space between cables and arrangement of cables. The tested cable's systems were two- to four-cable's systems as shown in Fig. 2. The focus point of the present research is to find the optimum space between cables and the optimum cable arrangement not to generate any aerodynamic vibrations.

In the present research, in order to obtain the fundamental properties of multiple cables, the experimental investigations were conducted by using circular cylinders.

2. Experimental Procedures

The aerodynamic instabilities were investigated by two and three-dimensional wind tunnel tests. The wind tunnel with test section of 1.07 x 1.07 x 8.26 m was used for two-dimensional test and the boundary-layer wind tunnel with test section of 2.4 x 1.8 x 20.0 m for three-dimensional test.

2.1 Two-dimensional test

The models were mounted as shown in Fig. 1, in order to investigate the fundamental aerodynamic behavior of multiple circular cylinders with various arrangements and spaces between circular cylinders in condition of zero angle of attack. The model was made by aluminum pipes with 25 mm diameter (D) and 2 mm thickness (t). The experimental conditions were following. The natural frequency : f = 8.3 Hz, structural damping : δs = 0.004 - 0.005, unit length weight : w = 0.813 kgf/m and length : ℓ =4.0 m.

Kinds of circular cylinder arrangement are shown in Fig. 2. (a) in the figure indicates two-circular-cylinder arrangement, (b) normal regular triangle arrangement of three circular cylinders, (c) upstream turning regular triangle arrangement of three circular cylinders, (d) downstream turning regular triangle arrangement of three circular cylinders and (e) diamond arrangement of four circular cylinders. S in the figure indicates space between circular cylinders. The Re number range of the two-dimensional test was 7.1×10^2 - 4.2×10^4.

2.2 Three-dimensional test

The three-dimensional test was planned to investigate the influence of the space and approaching flow direction to the aerodynamic vibration of circular cylinders and to confirm the results obtained in the two-dimensional test. Fig. 3 shows the model mounting for the three-dimensional test. θ in the figure indicates inclination of circular cylinder and is fixed as 30 degrees. β indicates the angle of approaching flow direction and the angle of β were changed in each testing case. The experimental conditions for the three-dimensional test were following. The model was also aluminum pipe with 25 mm diameter (D) and 1 mm thickness (t). The length: ℓ = 2.5 m, the unit length weight : w = 0.266 kgf/m, the first natural frequency : $f_1 = 0.5$ Hz, the second natural frequency : $f_2 = 39.5$ Hz, the corresponding structural dampings : δs_1 = 0.0141, δs_2 = 0.0204.

The cases tested in present research were following.
(1) Single circular cylinder ; β = 0, 30, 60, 90 degrees. (2) Two circular cylinders ; Tandem arrangement, S = 2D, 3D, 4D, β = 0, 30, 60, 90 degrees. (3) Three circular cylinders ; S = 2D, 3D, 4D, β = -90 to 90 degrees in every 30 degrees for normal regular triangle arrangement. S = 2D, 3D, 4D, β = 0 to 180 degrees in every 30 degrees for upstream turning regular triangle arrangement. The Re number range of the three-dimensional test was 5.5×10^2 - 1.7×10^4.

3. Experimental Results

The aerodynamic responses of circular cylinders were measured by laser displacement detectors. The experimental results are arranged in the figure with axes of non-dimensional double amplitude (2A/D) to reduced wind velocity (Vr = V/fD). The results and the investigations are shown in each experiments.

3.1 Two-dimensional test results
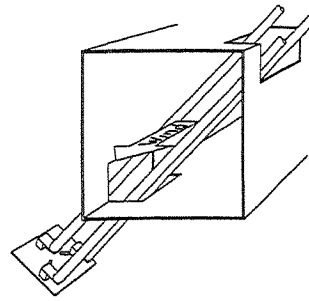
Fig.1 Model mounting system for two-dimensional test
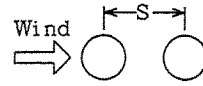
(a) Two-cables
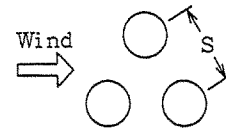
(b) Normal regular triangle
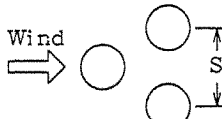
(c) Upstream regular triangle
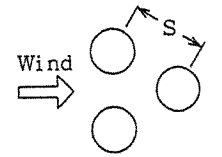
(d) Downstream regular triangle
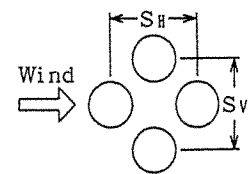
(e) Diamond

Fig.2 Kinds of circular cylinder arrangement

Fig. 4 shows the results of aerodynamic responses of two circular cylinders . (a) is the response of upstream circular cylinder and (b) is the response of downstream circular cylinder. Referring to these figures, the vortex-excited vibrations are generated at around reduced wind velocity Vr = 5 to 8 in both circular cylinders. In the downstream circular cylinder, the wake gallopings are generated at around Vr = 20 for S = 2D, Vr = 13 for 4D. The responses in the wind velocity region corresponding to the wake gallopings of downstream circular cylinder are generated by interaction at connecting point of two circular cylinders, because when the galloping of downstream circular cylinder is suppressed by a hand, the vibration of upstream circular cylinder is also suppressed. In this sense, the vibration of upstream circular cylinder at the wind velocity corresponding to the wake galloping of downstream circular cylinder is not any aerodynamic vibration but the vibration induced by the vibration due to the wake galloping of downstream circular cylinder through connecting point of both circular cylinders.

Figs. 5, 6 and 7 show the responses of three circular cylinders in regular triangle arrangement. The plots in each figure indicate the responses of a shaded circular cylinder. In the normal regular triangle arrangement, upstream and upper circular cylinders have only the vortex-excited vibrations. The downstream circular cylinder, however, generates wake galloping by the same mechanism as the wake galloping of downstream circular cylinder in two-circular-cylinder arrangement .

In turning regular triangle arrangements, as shown in Figs. 6 and 7, only vortex-excited vibrations appear except the wake galloping of one downstream circular cylinder with S = 2D. Therefore, the turning regular triangle arrangement with S = 4D is a favorable arrangement of cables for cable-stayed bridge.

For four circular cylinders, there is a possibility to arrange circular cylinders in square and diamond shape to wind directions. It is considered that the square arrangement has similar aerodynamic performances as tandem arrangement of two circular cylinders. Therefore, in the present research, the diamond arrangement was investigated. The experimental results are shown in Fig. 8. The vortex-excited vibrations are induced in upstream circular cylinder from around Vr = 5 to higher reduced wind velocity, dissimilarly to the vortex-excited vibration of a upstream circular cylinder in other arrangement of circular cylinders. The mechanism of vortex-
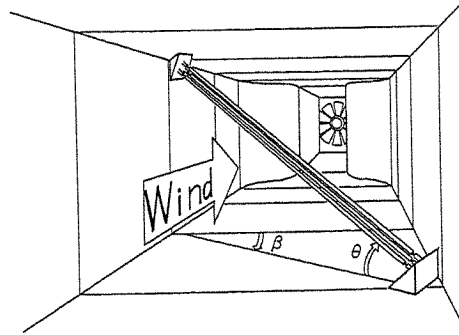
Fig.3 Model mounting system for three-dimensional test
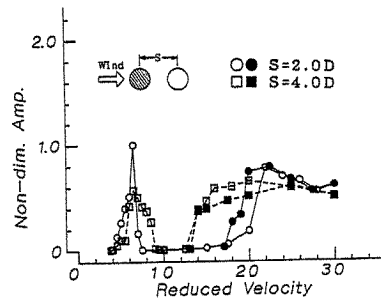
(a) Upstream circular cylinder
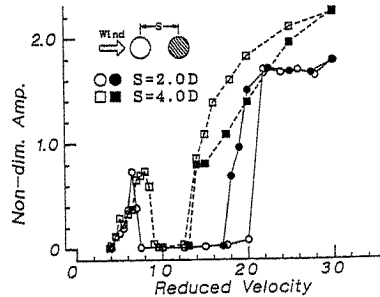
(b) Downstream circular cylinder
Fig.4 Aerodynamic responses of two-circular-cylinder system

583

(5-a)

(5-b)

(5-c)
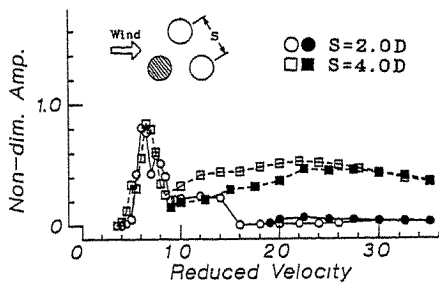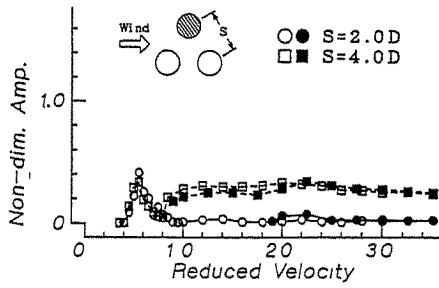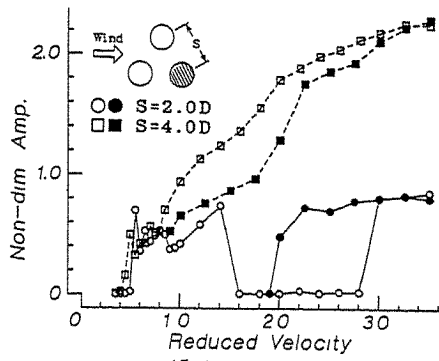
Fig.5 Aerodynamic responses of normal
regular triangle arrangement

(6-a)

(6-b)
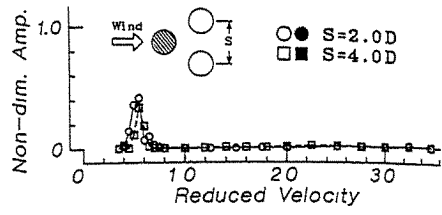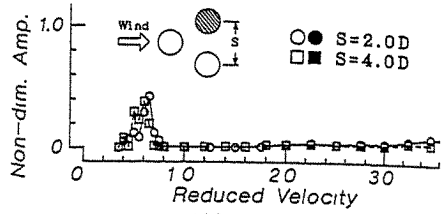
Fig.6 Aerodynamic responses of Upstream
regular triangle arrangement
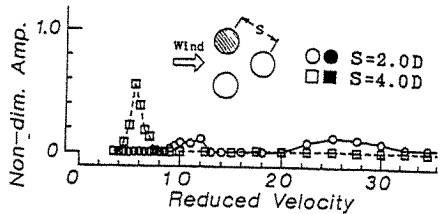
(7-a)
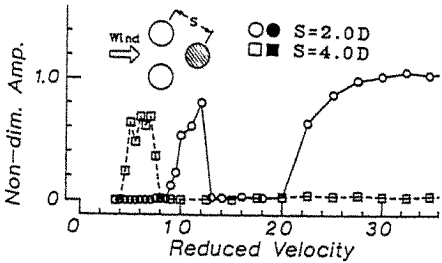
(7-b)

Fig.7 Aerodynamic responses of downstream
regular triangle arrangement

excited vibration in the upstream circular cylinder of the diamond arrangement is considered to be considerably different from normal vortex-excited vibration of a circular cylinder. The wake of upstream circular cylinder is restricted by the existence of side circular cylinders with symmetrical
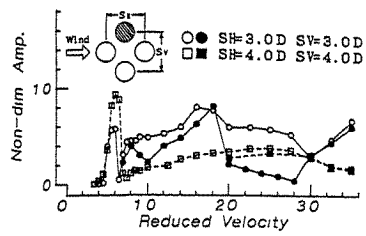
(8-a)
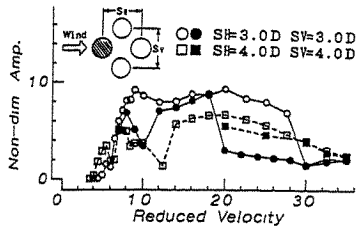
(8-b)
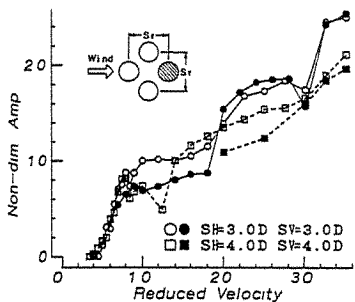
(8-c)

Fig.8 Aerodynamic responses of diamond
arrangement in two dimensional test
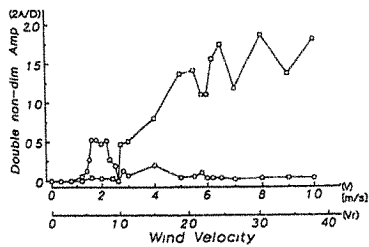
(β = 0 degrees)
Fig.9 Two tandem arrangement with 4D in
three dimensional test.
(upstream ○ — , down stream □ —)
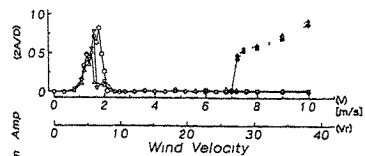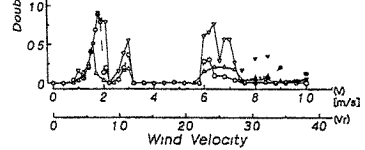
(β = 0 degrees)

(β = 30 degrees)
(a) S = 3D
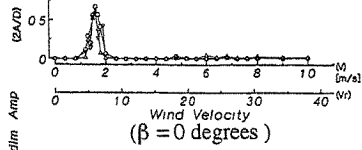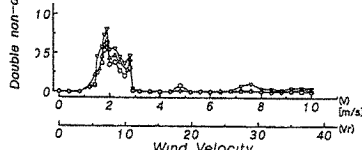
(β = 0 degrees)
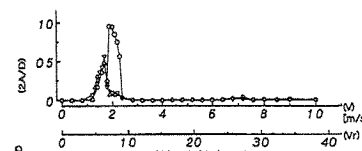
(β = 30 degrees)
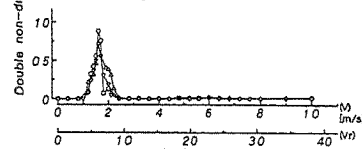
(β = 150 degrees)

(β = 180 degrees)
(b) S = 4D

Fig.10 Aerodynamic responses of turning regular
triangle arrangement in three dimensional test
(upstream ○ — , upper side △ —
lower side ▽ —)
Black marks indicate excited vibration responses

arrangement to the approaching flow and the aerodynamic responses are induced in broad wind velocity region. The aerodynamic response of side circular cylinder approaches to a similar response of single circular cylinder with increment of the space between circular cylinders. Affected by the wake of upstream circular cylinder, the downstream circular cylinder has strong wake gallopings regardless the space between circular cylinders. Therefore, the four-cable arrangement is not useful for multiple cable system of cable-stayed bridge.

3.2 Three-dimensional test results

Since the aim of three-dimensional test was to investigate the influence of the approaching flow direction to the aerodynamic performance of circular cylinders and the space is limited, only a few experimental results are shown in the present section. Fig. 9 shows the results of two-circular-cylinder arrangement with the space of 4D. Referring to the figure, the wake galloping is generated in the case of $\beta = 0$ degrees, but no wake galloping is generated in other cases of $\beta > 0$ degrees. The onset wind velocity of the galloping is similar to the two-dimensional experiment. In the cases of smaller space than 4D, the wake galloping is generated in the region $\beta <$ around 30 degrees. The aerodynamic performance of normal regular triangle arrangement is closely similar to the two-circular-cylinder arrangement.

On the other hand, as shown in Fig. 10, any wake galloping is not generated in the turning regular triangle arrangement with $S = 4D$ to any approaching flow direction. The cases with smaller space than 4D have wake galloping in the region smaller than 30 degrees.

From another investigation associated with two-circular-cylinder arrangement by authors, it is considered that the wake galloping of downstream cable has different mechanism between a region smaller space than around 3.6D and a region larger space than around 3.6D. Referring to Karman's vortex street theory, the space between vortex center is 3.6D. The downstream cable is folded in the wake of upstream cable in the case with smaller space than 3.6D and is not folded in the case with larger space than 3.6D. The experimented results show that the aerodynamic performances are different from each other between the regions smaller and larger than 3.6D.

The experimental results of the two-dimensional tests and the three-dimensional tests of $\beta = 0$ degrees show good coincidence between them. Referring to the results for the case with smaller space than 4D that the amplitude of wake galloping in the case of $\beta = 0$, is amplified in some approaching flow directions, the approaching flow direction considerably influences aerodynamic performances in the cases with smaller space than 4D.

4. Concluding Remarks

The experimental investigations were conducted to look for the optimum arrangement of multiple cables for cable-stayed bridge. The following concluding remarks are obtained.

(1) The optimum cable arrangement of multiple cable system of the cable-stayed bridges is the turning regular triangle arrangement with space of 4D as shown in Fig. 2.

(2) In the approaching flow direction of $\beta = 0$, both experimental results of two and three-dimensional tests have a good agreement. Therefore, in the cases, there is little influences of three-dimensional flow around circular cylinder based on vibration modes.

(3) It is considered that the wake galloping has different mechanisms between smaller and larger spaces than around 3.6D based on Karman's vortex street theory.

The future research concerning with the suppression of aerodynamic vibration of cables becomes more important with increment of span length of cable-stayed bridges. The authors have a plan to continue similar research by using real cables.

References:
1. M. Matsumoto, N. Shiraishi and H. shirato, Proc. Intl. Colloquium on BBAA, (Kyoto), 1988, 131.
2. Y. Kubo, K. Kato and M. Kanao, Journal of Structures and Materials in Civil Engineering, (KABSE), Vol. 4, (1989) 49.
3. Y. Kubo, T. Nakahara, K. Kato and M. Kanao, Proc. 9th Natioal Symposium on Wind Engineering, Tokyo, (1990) 275.
4. Y. Kubo, T. Nakahara and K. Kato, Proc. 10th Natioal Symposium on Wind Engineering, Tokyo, (1992) 291.

Effect of Horizontally Inclined Wind on the Vortex Induced Oscillation of a Rectangular Cylinder

H. Utsunomiya, F. Nagao, K. Asano and T. Matsumoto[+]
Department of Civil Engineering
University of Tokushima, Tokushima
[+]Nishimatsu Construction Co.Ltd., Tokyo

Abstract: The effect of horizontally inclined wind direction on the vortex induced oscillation of a rectangular cylinder (the width/depth ratio, B/D=2.5) was investigated by wind tunnel tests with scaled models, which were mounted as a two dimensional rigid model and as a three dimensional elastic model. Experimental results showed that the effect of inclined wind on the responses of the two dimensional model was relatively small but significant effect could be seen in the responses of three dimensional model. The flow visualization showed that the separated shear flow from the leading edge and the rolling–into–flow near the rear face from the upstream end had direct effects on those responses.

1. Introduction

Wind tunnel tests on bridge aerodynamics are carried out under various situations such as the construction conditions of bridges, individual local terrain, fittingly simulated natural wind [1–5] to improve the disagreement between the results of wind tunnel tests and the full scale measurements.

One reason for this difference was sometimes explained by the difference of wind direction, that was, the wind tunnel tests were carried out under the wind direction normal to the bridge axis which would bring the most conservative condition for the stability of a bridge, however the natural wind is not always blowing such a manner in real bridge.

In this paper, the effect of the horizontally inclined wind on the vortex induced oscillation of a rectangular cylinder was investigated by wind tunnel experiments. It was supposed intuitively the effect would appear as the increase of apparent width/depth ratio, B/D, which would be followed by the decrease of the response. In other case of the aerodynamic stability of inclined circular cylinders, it was said that the spanwise flow induced behind the cylinder made the amplitude of oscillation increase [6].

2. Experimental Procedures

The wind tunnel used here had a semi–closed circuit and the working section was 1.5m wide, 1.5m high and 5m long. Two dimensional rigid model (2–D model) and three dimensional elastic model (3–D model) were used in this experiment. Both models had same configurations and same dynamic properties such as the width–depth ratio B/D =2.5, the span length L=124 cm, the mass per unit length was 0.057kgf-s^2/m and the Scruton number (2mδ/ρDB) was about 30 as shown in Fig. 1. 2–D model was mounted at the center of the working section with 8 coil springs, and 3–D model was mounted directly by simple piers made of circular cylinders on the turn table of wind tunnel with the clearance of 30 cm as shown in Fig. 2. The end plates were installed at the both ends of 2–D model to protect the rolling–into–flow from the ends. The end plates were movable to the streamwise direction. On the other hand, there was no end plate for 3–D model. The

amplitude of the oscilation of the model was measured by a strain gage at the center of the span. The effect of inclined angle of wind direction, β, was examined in the range from $0°$ to $40°$ in each $10°$.

$M=0.057 \mathrm{kgf \cdot s^2/m}$
$S_c=28.3 \sim 33.1$
$f_2=10.4 \mathrm{Hz}$
$f_3=8.6 \mathrm{Hz}$

55mm

22mm
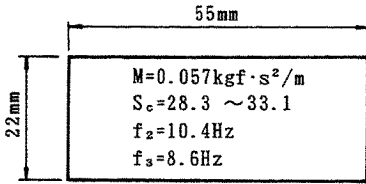
Fig. 1 Cross section and dynamic properties of models

1234mm

gap(1mm)

300mm

Turn Table

(a) 3-Dimensional elastic model

Strain Gage

Pitot tube

2-D Model

Oil damper
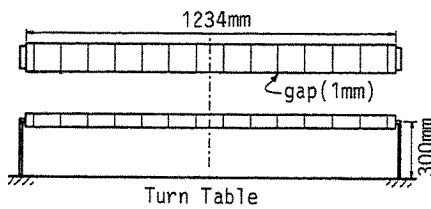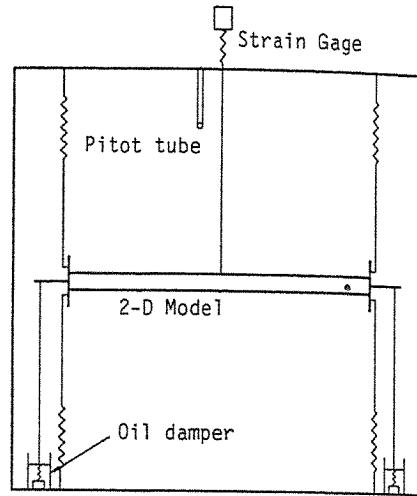
(b) 2-Dimensional rigid model

Fig. 2 General views of models mounted in wind tunnel

3. Wind Tunnel Results
3. 1 Responses of 2-D Model

Fig. 3 shows the wind velocity–amplitude curves of vortex induced oscillation of 2-D model under four different wind directions. It was seen that the resonance wind velocity regions shifted to higher wind velocity side with the increase of β. This seems to be corresponding to the increase of apparent width of the model to the wind direction with the increase of β. However, it was found that the amplitudes of responses under different wind directions were almost coincide with that for $\beta=0°$. The oscillation disappeared at $\beta=40°$ because of its large Scruton number.

Fig. 4 shows another experimental results carried out by authors [7], in which the amplitudes of vortex oscillation of 2-D model in various wind directions were compared with those of models with various cross sections of B/D corresponding to the apparent width/depth ratio in normal position, $\beta=0°$. The Scruton number of all models were held constant as Sc=9.0 smaller than those in Fig. 3. The distinct difference could be seen at $\beta=40°$ (B/D=3.3) where the amplitude of model in normal position ($\beta=0°$) became smaller considerably than that in inclined position.

3. 2 Responses of 3-D Model

Fig. 5 shows the wind velocity–amplitude curves for 3-D model. All the oscillations were the fundamental modes. The maximum amplitudes of the vortex induced oscillations were decreased
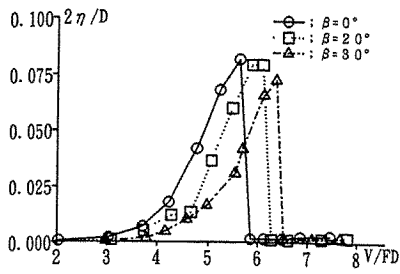
Fig. 3 V–A curves of 2–D model under various β, Sc=30.
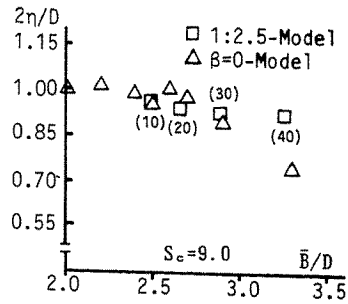
Fig. 4 Comparison the maximum amplitude of 2–D model for apparent B/D with those of 2–D in β=0°.

to the contrary with the increase in wind direction β. The resonance regions shifted to higher side and were reduced to the small area in the wind velocity field. Thus experimental results of 3–D model were very different from those of 2–D model.

The response of the 3–D model at β=0° was compared with that of 2–D model in Fig. 6, where the corrected response of 2–D model multiplied by 4/π was indicated also. It can be seen that the response curve of 3–D model almost agrees with the corrected one of 2–D model but the maximum amplitude of 3–D model is smaller than that of 2–D. This result is essential for 3–D model because the aerodynamic exciting force is depending nonlinearly on the oscillating amplitude of the model itself. The locking–in phenomenon of a vortex is broken easily near the end supports because the amplitude of oscillation is very small and the exciting force is weakened, which is followed by the decrease of the amplitude of 3–D model [7].

The decrease of amplitude of 3–D model obtained here was probably caused a sort of rolling–into–flow from both ends of the model in addition to the weakened locking–in phenomenon because the decreasing ratio was too large under inclined wind.
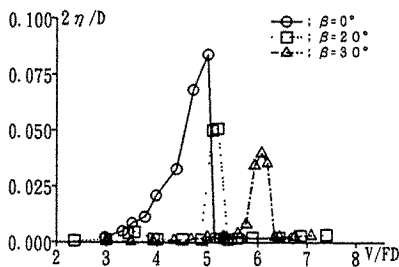
Fig. 5 V–A curves of 3–D model under various β, Sc=30.
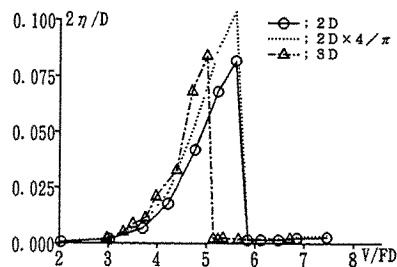
Fig. 6 Comparison the response of 3–D model with that of 2–D in β=0°.

589

4. Discussions

The flow visualization with oil mist was used to examine the reason why the constant amplitudes were held to the increase of apparent B/D in inclined conditions. Flow properties around the 2–D model at rest and in oscillating conditions were very different as shown in Fig. 7. A spanwise flow could be seen just behind the rear face at rest condition, however the flow disappeared in oscillating condition, which showed the aerodynamic exciting force was unsteady. Hence, it seems that the constant amplitudes under different wind directions were not caused by the spanwise flow as was the case of inclined circular cylinders.

Fig. 8 shows another information that the separated shear flow from the leading edge did not

Model at rest   Model in oscillation
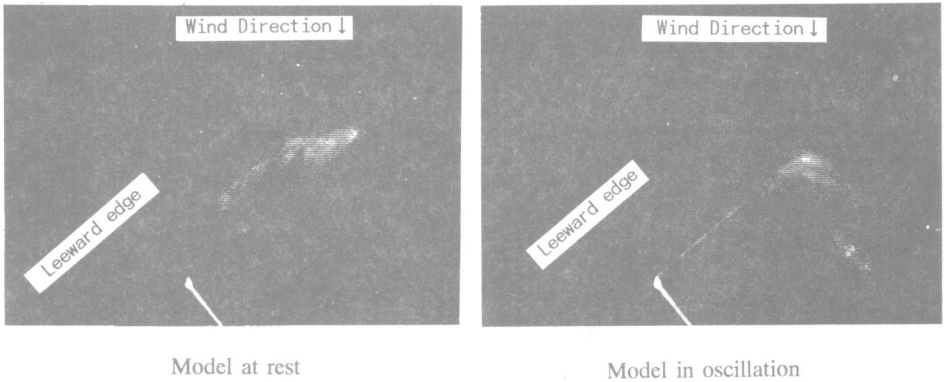
Fig. 7 Flow visualization of spanwise flow behind the rear face

Model at rest   Model in oscillation
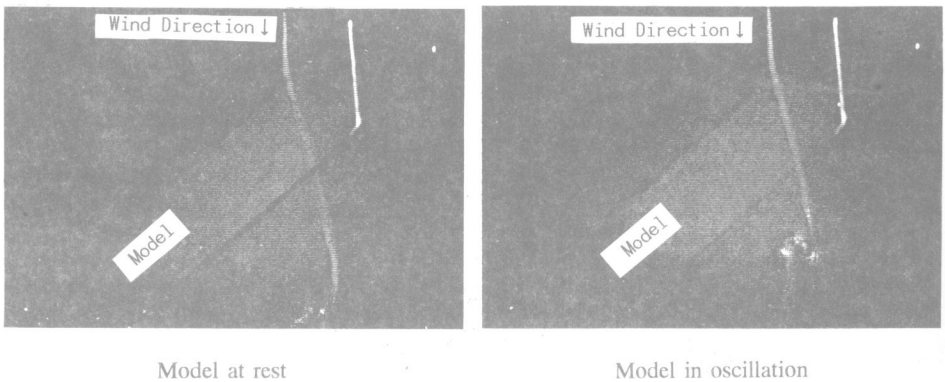
Fig. 8 Streamline passed the upper surface of model.

590

flow down along the wind direction but it was inclined toward the normal to the span axis. The separated flow in rest condition was stretching longer to downstream to make a closed wake area just behind the rear face of the model. The spanwise flow shown in Fig. 7 occurred inside of this closed wake. However, in oscillating condition,the reattachment of the separated flow near the leeward edge was accelerated and the closed wake area for the spanwise flow was not formed.

Under inclined wind directions,the increase of apparent B/D was smaller than that as expected initially. This is the main reason why the maximum amplitudes of the response of 2-D model were almost same in each wind direction.

The original 3-D model used here had no end plate at both end supports and some rolling-into-flow separated from the ends could be observed by flow visualization with oil mist. Hence the effect of this flow from ends on the response was examined by different two end conditions.

The first condition is shown in Fig. 9 where extra box sections were installed at both end supports and were extended to fix on side walls of the wind tunnel. The experimental results, which are not given here, showed that there was no significant difference in the amplitude of the model between with and without extra boxes and they did not change the end condition any more under several wind directions.

The second one was to install the movable end plates at both end supports similar to those of 2-D model. In Fig. 10, the change of oscillation amplitudes of 3-D model with end plates against the wind direction is given in comparison with those of normal 2-D and 3-D models, in which the amplitudes are normalized by η_0 at $\beta=0°$. It can be seen that the end plates were effective to reduce the rolling-into-flow in some extent and the reduction ratio of amplitude of the model with end plates to the increase of β was smaller than that without end plates. However the most of the reduction of amplitudes of 3-D model under inclined wind directions was caused by some other aerodynamic interference which was not found here.
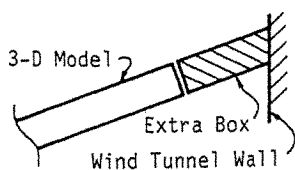
Fig. 9 Installation of extra box to
examine the rolling-into-flow.
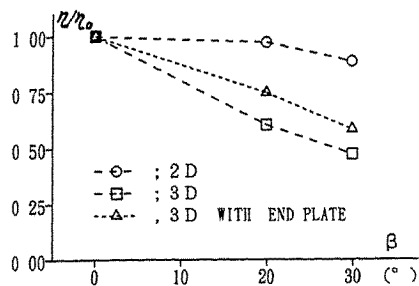
Fig. 10 Effect of end plate on the
response of 3-D model.

591

5. Concluding Remarks

Though this study has not completed up to now, especially on the response of 3–D model, some interesting results about the effects of inclined wind on the vortex induced oscillation of a rectangular cylinder were obtained as follows.

1) The effects of the horizontally inclined winds on the vertical vortex induced oscillations of 2–D model were relatively small and the responses under different wind direction, β, less than 40°, were almost coincide with that for $\beta=0°$.

2) The separated shear flow from the leading edge of 2–D model was inclined toward the normal to the span axis, and it reduced the decrease of the response although the apparent B/D was increased under inclined wind.

3) The spanwise flow just behind the rear face of 2–D model under inclined wind could be seen when the model was at rest, however it disappeared in oscillating condition. Hence this spanwise flow is not important to maintain the oscillation under inclined wind.

4) The response of 3–D model was decreased with the increase of inclined wind angle β and its reduction ratio was very large still taking into account the dependence of aerodynamic force on the amplitude of oscillation.

5) It appeared that the effect of rolling–into–flow from the model ends was relatively small through some experiments with various end conditions.

References:

1. R.L.Wardlaw and L.L.Goetteler, N.A.E.Tech.Report LTA-LA-8, (1968).
2. M.Miyazaki and M.Ito, J.Wind Engineering JAWE, No.37 (1988) 647.
3. Y.Sakai, K.Ogawa and T.Sakai, Proc.41th Annual Conference JSCE, (1986) 673 (in Japanese)
4. H.Utsunomiya, F.Nagao & Y.Yamamoto, J. Wind Engineering, No.41 (1989) 65 (in Japanese)
5. Y.Yamamoto, H.Utsunomiya & F.Nagao, J. Structural Engineering, 34A (1992) 899 (in Japanese)
6. Y.Sano, N.Shiraishi & M.Matumoto, Proc. 44th Annual Conference JSCE, (1989) (in Japanese).
7. H.Utsunomiya, F.Nagao & H.Takashima, J. Wind Engineering JAWE, No.37 (1988) 203.

Flow characteristics of two square cylinders of different size in side-by-side arrangement

P.T.Y. Wong, N.W.M. Ko and A.Y.W. Chiu

Department of Mechanical Engineering
The University of Hong Kong, Hong Kong

Abstract: This paper presents the results of the aerodynamic forces and vortex sheddings of two square cylinders in side-by-side arrangement of size ratio 2:1 at subcritical flow regime. Flow measurements were carried out at transverse spacing of $1.12 \leq T/D \leq 2.5$. The gap side shear layer of the large cylinder reattaches to its inner face for small separation, while the gap side shear layer of the small cylinder reattaches to its inner face for larger separation. The distributions of aerodynamic forces reveal an unfavourable loadings on the small cylinder at a separation of $T/D = 1.75$. Mean and fluctuating velocities were measured at the plane of $x/D = 2.0$. The results show that the flow is skewed towards the small cylinder and no bistable flow is found as in the case of equal size square cylinders.

1. Introduction

Structures, such as buildings, marine risers, bridges, cooling towers, chimneys and heat exchangers, usually appear in groups. Their aerodynamic characteristics are of great importance in the field of engineering, as they can create destructive effects to the structures. The forces acting on the structures and the vortex shedding pattern are different from those of single structure. The interaction effect of multi-structures is very complicated and different flow phenomenon may occur. In order to understand the fundamental flow mechanism involved, the simple cases of two bluff bodies were attempted[1-3]. The above reviews indicated most studies were carried out on circular cylinders of equal diameter. For the last two decades the flows over two circular cylinders of different diameters attracted attention[4-7]. Besides circular cylinder, flows over square cylinders were also investigated[8-11]. However, no work was reported on the flows over two unequal square cylinders.

The flow patterns for the equal size square cylinders in side-by-side arrangement are categoried into three regimes: single vortex street, bistable flow and two vortex streets[8]. For transverse spacing between the centres of the two cylinders, $T/D \leq 1.1$, where D is the width of the cylinder, a single vortex street is formed as in the case of a single bluff body. At the critical spacing of $1.1 < T/D < 2.5$, bistable flow is found. The flow is biased to one side and intermittently flips to the other side. The flow changes from the biased pattern to two symmetric vortex streets at $T/D \geq 2.5$ and either in-phase or anti-phase vortex streets are found.

Due to the lack of study on unequal square cylinders, this experiment attempted study with the side-by-side arrangement and the flows were within the subcritical flow regime.

2. Apparatus and Experimental Techniques

The experiments were carried out in a low speed wind tunnel of a working section of 56cm x 56cm. All the measurements were conducted at a freestream velocity U_0 of 19.8 m/s and the

inherited turbulence intensity was about 0.6 percent.

The sizes of the big D and small d square cylinders were 38.2mm and 19.1mm respectively, giving a ratio of 2:1. Their lengths were 460mm and thus their aspect ratios were 12 and 24 respectively. The blockage ratio of both cylinders was 10 percent. No blockage correction was applied. End plates were used to eliminate the effect of the tunnel boundary layers. Each square cylinder had nine 1 mm pressure tappings evenly spaced at mid-span for mean surface pressure measurements.

Mean surface pressure and hot wire measurements were taken for the transverse spacings of $1.12 \leq T/D \leq 2.5$ (Fig. 1). Data acquisition system and a 286 PC with a sampling frequency of 2 kHz per channel were used for velocities and spectral analyses.

3. Results and Discussion

For comparision the mean pressure coefficients Cp of a single square cylinder of size 38.2mm were obtained first (Fig. 2). The Reynolds numbers were Re $= 5$ x 10^4 and 2.5 x 10^4. The mean pressure coefficients at Re $= 7$ x 10^4 of Okajima et al.[8] were also included. The distributions at both Reynolds numbers are nearly the same, suggesting the flows are within the subcritical regime. However, there is slight difference in the mean base pressure coefficient between the present data and those of Okajima et al.[8].

The mean pressure coefficients of the two square cylinders at $1.12 \leq T/D \leq 2.5$ are shown in Fig. 3a to 3e. For simplicity, only the representative pressure distributions are shown here. At $T/D = 1.12$ the flow accelerates through the gap between the two cylinders, thus creating a lower Cp on the gap sides of both cylinders (Fig. 3a). The separated shear layer on the gap side of the large cylinder reattaches to its inner surface. At $T/D = 1.25$ no shear layer reattachment is found for both cylinders (Fig. 3b). At $1.375 \leq T/D \leq 2.0$ the shear layer reattachment is found only on the gap side of the small cylinder and the reattachment point moves towards the trailing corner as T/D increases (Fig. 3c - 3d). At $1.75 \leq T/D \leq 2.5$ the distributions on the gap side and outside of the large cylinder are nearly the same. At $T/D = 2.5$ the mean pressure profile of the small cylinder shows that the separated shear layer from the leading corner of the inner surface moves further downstream and does not reattach on the surface (Fig. 3e). Within the range of the present study the Cpb of the small cylinder is always lower than that of a single cylinder while the Cpb of the large cylinder is higher. For a bluff body with undisturbed wake a narrow wake corresponds to a lower Cpb and higher vortex shedding frequency[12]. Thus, the present results suggest that the small cylinder has a narrower wake than that of a single cylinder and the wake of the large cylinder is bigger. Summarizing the present results and those from the mean velocity profiles, the flow skews towards the small cylinder. This skewed flow is similar to the bistable flow of two equal square cylinders except it is stably deflected towards the small cylinder. Similar phenomenon is also found for circular cylinders of unequal diameters by Beguier et al.[13].

Fig. 4 shows the distributions of the mean base pressure coefficients Cpb of the two cylinders and their difference $| \Delta Cpb |$. The large square cylinder has a maximum Cpb of -0.71 at $T/D = 1.25$ while the minimum for the small cylinder is -1.94 at $T/D = 1.75$. At $T/D = 2.5$ the Cpb of the large and small cylinders are -1.32 and -1.54 respectively, which are close to the value of -1.55 for a single square cylinder. The maximum $| \Delta Cpb |$ is 1.13 at $T/D = 1.75$ for the present study while it is 0.89 at $T/D = 2.25$ for equal cylinders. A bluff body with lower Cpb has larger drag. Thus, the Cpb distributions in Fig. 4 are the inverse of those of C_D in Fig. 5. The small cylinder bears the largest drag force at $T/D = 1.75$ and the $| \Delta Cpb |$ also has its maximum at the same separation.

The drag coefficients C_D and the sum of the drag coefficients of both cylinders ΣC_D are

594

shown in Fig. 5. The large cylinder has a minimum C_D of 1.5 at T/D = 1.25 while the maximum of the small cylinder is 2.7 at T/D = 1.75. The C_D of large and small cylinders are 2.16 and 2.37 respectively at T/D = 2.5 while it is 2.28 for a single cylinder. Even though the large cylinder has lower C_D than that of a single cylinder and the small cylinder has higher C_D, the sum of the drag coefficients of both cylinders is less than twice that of a single square cylinder. A minimum value of ΣC_D of 3.44 is found at T/D = 1.5 for equal cylinders, but no minimum value is found for the present study.

The distributions of lift coefficients C_L in Fig. 6 show both cylinders are under attraction (Fig. 1) at $1.12 \leq$ T/D ≤ 1.375. At $1.5 \leq$ T/D ≤ 1.75 the large cylinder has a tendency to move inwards while the small cylinder outwards. For T/D ≥ 2.0 the small cylinder reverses to the attraction mode. Same phenomenon is found in the measurements of Okajima et al.[8]. For the small cylinder, the C_L has its maximum value of 0.3 at T/D = 1.75 and the coefficient of resultant force of drag and lift also has its maximum value of 2.71 at the same separation. This further concludes that the aerodynamic force exerts the largest loading on the small cylinder at a transverse separation of 1.75D.

The Strouhal numbers distributions are shown in Fig. 7. The Strouhal number St_D of the large cylinder increases at T/D ≥ 1.12. The Strouhal number St_d of the small cylinder only increases at closer spacing to a maximum of 0.21 at T/D = 1.5 and decreases at larger spacing. At T/D = 2.5 the values of St_D and St_d are 0.107 and 0.196 respectively. It appears that the shedding frequencies of the small cylinder are a multiple of those of the large cylinder. At $1.12 \leq$ T/D ≤ 2.0 St_d is twice of St_D. It drops to 1.8 only at T/D =2.5. Both the distributions of St_D and St_d are in good agreement with the results of equal cylinders[8].

Fig. 8 shows the distributions of the mean streamwise velocity U/U_o at x/D = 2.0 for different transverse spacings. The mean streamwise velocity on the outside of the large cylinder attains the freestream velocity at y/D = -1.7 at all transverse separations while on the gap side it increases steadily from $0.7U_o$ at y/D = 1.4 for T/D = 1.12 to about $1.0U_o$ at y/D = 1.7 for T/D = 2.5. The distance between the location with maximum velocity defect at y/D = 1.82 and the centre of the small cylinder at y/D = 1.12 is 0.7D for T/D = 1.12 and it decreases to 0.2D for T/D = 2.5. The profiles show that a wider wake occurs on the large cylinder side and its mean velocity gradient in the outside is larger than that on the gap side , thus justifying the assumption of the flow is skewed towards the small cylinder. This is in agreement with the findings of Beguier et al.[13] that the weaker mean velocity gradient is on the small cylinder side for unequal circular cylinders at small separation.

4. Conclusions

From the above results, the following conclusions can be made:

(a)   Skewed flow towards the small cylinder is only found in the experiment, while a bistable flow is observed in the cases of two equal size square and circular cylinders in side-by-side arrangement.

(b)   A separation of T/D = 1.75 for small cylinder is established at which the lift and drag are the largest.

References:
1.   M.M. Zdravkovich, J. Fluids Engg., 99 (1977) 618.
2.   M. Kiya, M. Arie, H. Tamura and H. Mori, J. Fluids Engg., 102 (1980) 166.

3. H.J. Kim and P.A. Durbin, J. Fluid Mech., 196 (1988) 431.

4. S.C. Luo and T.L. Gan, Aero. J., 96 (1992) 105.

5. N.W.M. Ko and P.T.Y. Wong, J. Wind Engg. and Ind. Aero., 41-44 (1992) 563.

6. A.J. Baxendale, I. Grant and F.H. Barnes, Aero. J., 89 (1985) 125.

7. C.W. Ng and N.W.M. Ko, Proc. 5th Asian Cong. Fluid Mech., Taejon, Korea, (1992) 33.

8. A. Okajima, K. Sugitani and T. Mizota, Bull. Res. Inst. for App. Mech., Kyushu University, 60 (1984) 59.

9. S.C. Luo and T.C. Teng, Aero. J., 94 (1990) 203.

10. T.A. Reinhold, H.W. Tieleman and F.J. Maher, J. Ind. Aero., 2 (1977) 223.

11. H. Haniu and H. Sakamoto, Trans. JSME, 52 (1986) 3892.

12. A. Roshko, J. Aero. Sci., 22 (1955) 124.

13. C. Beguier, F. Giralt, L. Fulachier and J.F. Keffer, Proc. Symp. on Turbulence, Berlin, (1977) 22.

14. A. Roshko, NACA TN No. 3169 (1954).
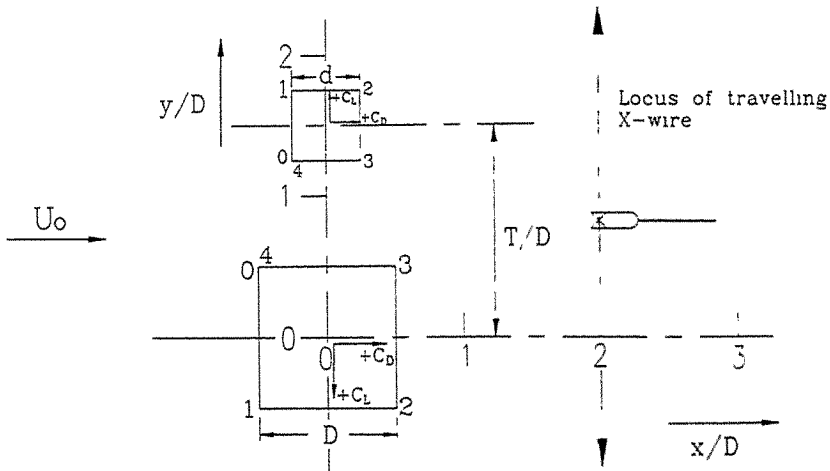
Fig. 1 Schematic diagram of square cylinders.
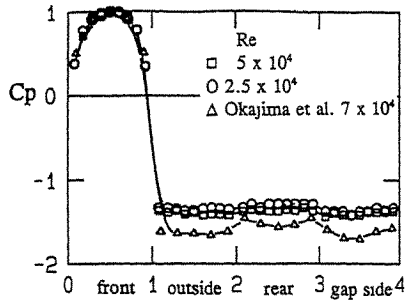
Fig. 2 Mean pressure distributions
of single square cylinder
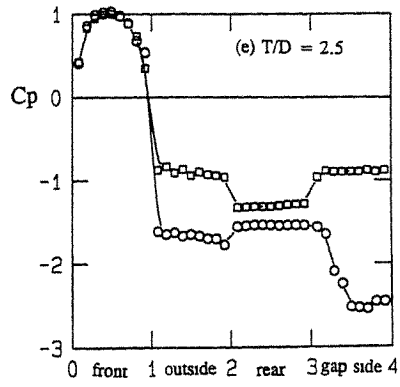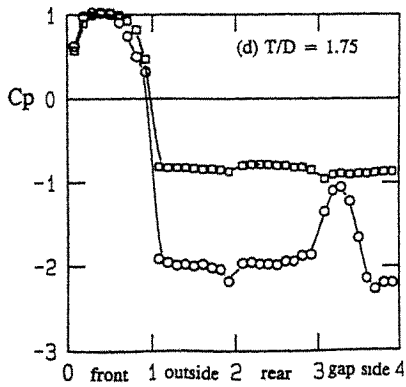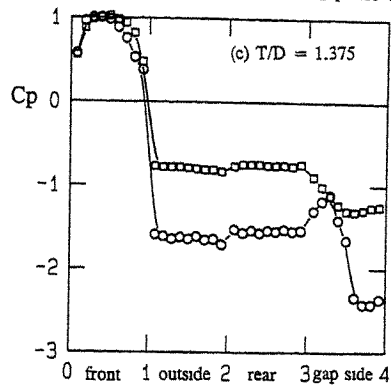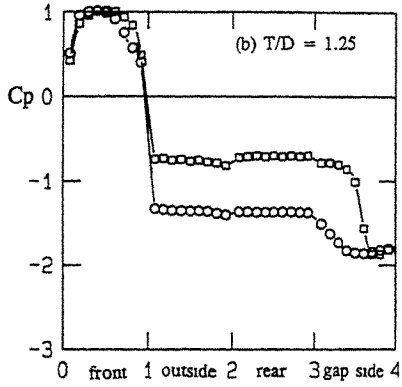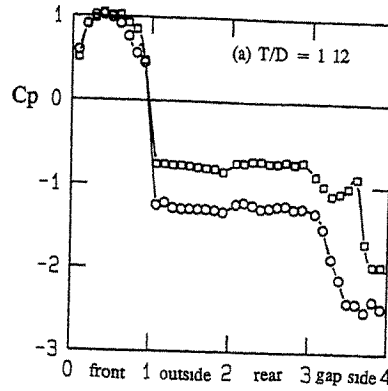
Fig. 3 Mean pressure distributions on two square cylinders
□ Large cylinder   O Small cylinder

597
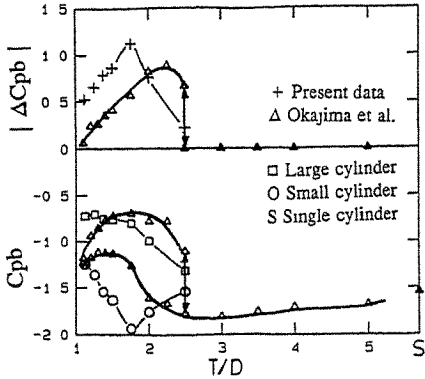
Fig. 4 Distributions of mean base pressure coefficient
and its difference
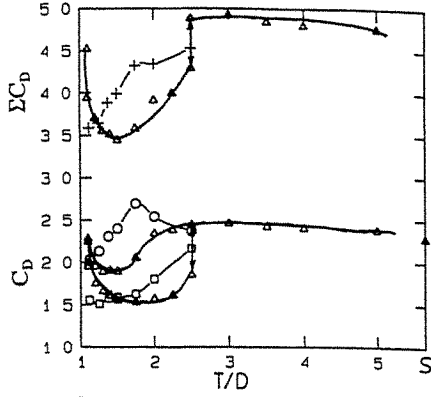
Fig 5 Distributions of drag coefficient and its
total sum   Symbols as in Fig 4
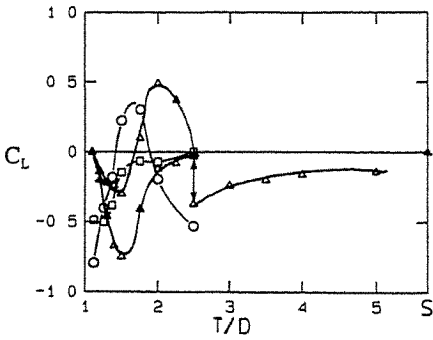
Fig. 6 Distributions of lift coefficient
Symbols as in Fig 4
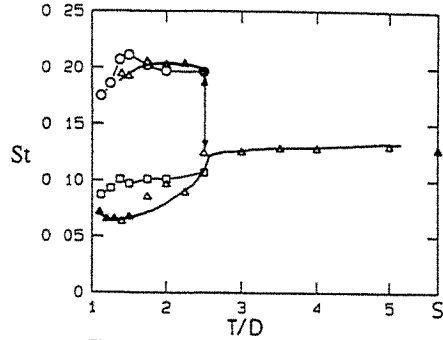
Fig 7 Distributions of Strouhal Number
Symbols as in Fig 4
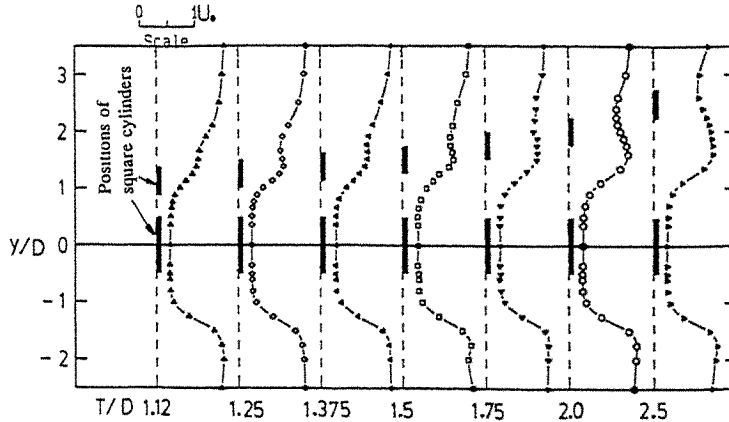
Fig 8 Mean streamwise velocity (U/U_a) profiles at x/D = 2.0 for different spacings.

598

Flow over partially grooved cylinder
with and without acoustic excitation

K.W. Lo, Y.C. Leung, C.H. Wong and N.W.M. Ko

Department of Mechanical Engineering
The University of Hong Kong, Hong Kong

Abstract: The characteristics of the flow over partially grooved circular cylinder have been investigated under different external acoustic excitation of 2.3 khz. The vortex shedding, circumferential pressures distributions and flow characteristics in the wake behind the grooved cylinder were examined. A significant change in the flow structures was found for the excited case, resulting in large drag reduction and increase in lift.

1. Introduction

Flow over grooved circular cylinders has been investigated extensively over the past decade [1,2,3]. It was found that earlier transition from subcritical to critical and from critical to supercritical flow regimes occurred at lower Reynolds number for the grooved cylinder than for the smooth cylinder. In the subcritical regime laminar separation and in the critical regime laminar separation, reattachment (separation bubble) and turbulent separation were observed. For partially grooved circular cylinder it was found that lower drag coefficient and lift could be obtained within the subcritical regime of smooth cylinder [3].

The above phenomenon was due to the perturbation of the boundary layer by the grooves [2]. Recent researches indicated that manipulation of the boundary layer can also be achieved by acoustic excitation [4,5] and there is a growing research interest in this area. It is the objective of this paper to study the effect of acoustic excitation on the boundary layer developed over a partially grooved circular cylinder.

2. Experimental Arrangement

The experiments were carried out in a wind tunnel with a test section measuring 0.56m x 0.56 m. The freestream turbulence intensity was about 0.4 percent at 22 m/s. The diameter of the cylinder d tested was 88.5 mm which corresponded to a blockage ratio of 16 percent. The effect of blockage ratio on the pressure measurement was corrected by applying the formulae of Allen and Vincenti [6]. End plates, located at 0.5d from both ends of the cylinder, were used to reduce the influence of the tunnel wall boundary layers. The Reynolds number was 1.2 x 10^5, within the subcritical Reynolds number regime of smooth cylinder.

The surface configurations studied are shown in Fig. 1. V-groove of height h of 1.22 mm and angle ϕ of 15°, giving h/d of 13.8 x 10^{-3}, was adopted. The adoption of this v-groove was due to its near lowest drag coefficient [3] and the shift to lower Reynolds number such that flow characteristics in higher flow regime could be studied. The subtend angle θ_g of the grooves was +90° beginning from the front stagnation point. The remaining part of the cylinder was smooth. Pressure tappings at 7.5° interval were located at the mid-section of the cylinder to measure the circumferential pressure distribution.

Acoustic excitation was introduced by an Altec Lansing 290-8L loudspeaker facing the grooved side of the cylinder (Fig. 1). A Bruel & Kjaer 1/8 in microphone, mounted at the center of the tunnel and 1.5 diameter upstream of the cylinder, was used to measure the sound pressure levels.

3. Results and Discussion

At constant excitation level of 120 dB Fig. 2a shows the attenuation of the power spectral level at the vortex shedding frequency of the cylinder at $x/d = 4.0$ and $y/d = 0.5$ under different acoustic excitation frequencies. Gain in the power spectral level of the vortex shedding occurs for the frequency range of 1.5 - 2 kHz and 6 - 10 kHz. For the rest of the frequency range attenuation is observed. Maximum attenuation occurs at 2.3 kHz which corresponds to 40 times of the fundamental vortex shedding frequency. It is interesting to note that despite the introduction of the acoustic wave which, as will be shown later, causes transition of the boundary layer, the fundamental vortex shedding frequency of the grooved cylinder remains unchanged at the Strouhal number of 0.23.

The attenuation at 2.3 kHz and 3.8 kHz also varies with the excitation level (Fig. 2b). In general, the attenuation level increases with higher excitation level for the sound pressure level between 100 dB and 115 dB and saturation occurs at level greater than 120 dB. Therefore, to achieve the maximum excitation effect, excitation at frequency of 2.3 kHz and 120 dB was adopted for further detailed investigation.

The circumferential pressure distributions of the grooved cylinder with and without excitation are shown in Fig. 3 and their respective pressure coefficients, wake angles, drag and lift coefficients are shown in Table 1. The distribution of the smooth cylinder [1] is also presented for comparison. As indicated by the symmetrical pressure distribution and small base pressure recovery $(C_{pb}-C_{pm})$, the flow on the smooth cylinder is within the subcritical regime . For the grooved cylinder the increase in the base pressure recovery, larger wake angles and appearance of separation bubbles at both the smooth and grooved surfaces (as indicated by the flat plateau in the curve) suggest that the flow is within the critical regime.

Under acoustic excitation a dramatic change in the pressure distribution on the smooth surface while a minor change on the grooved surface is observed. At the smooth surface, the base pressure recovery increases from 0.3 to 1.2 and the separation bubble disappears indicating transition to turbulent of the boundary layer. Further boundary layer measurements confirm that transition occurs at about 83° of the smooth surface (Fig. 4). The above results suggest that the acoustic waves excite the boundary layer on the smooth surface but have little influence on the boundary layer on the grooved surface.

The changes in the pressure distributions result in the variation of the drag and lift coefficients of the circular cylinder in the above three cases (Table 1). As compared with the smooth cylinder, the drag coefficient of the grooved cylinder is lowered by 23 percent while a slight increase in lift is observed. An additional 14 percent reduction in the drag and significant increase in lift can be observed under acoustic excitation.

Due to the transition of the boundary layer to turbulent on the smooth surface under excitation, the free shear layer separates further downstream from the front stagnation point, reducing the size of the recirculation region (Fig. 5). The unsymmetric pressure distributions on

600

the smooth and grooved surfaces cause an upward shift of the wake centre line from y/d = 0 for the case of no excitation to y/d = 0.1-0.2 for the case of excitation.

Fig. 6 shows the effect of acoustic excitation on the Reynolds stress within the wake at x/d = 3.0. Narrower wake with lower Reynolds stress is found for the case of acoustic excitation and the wake centre line is shifted to grooved side confirming the observation in Fig. 5. This phenomenon of lower Reynolds stress in the wake is due to the imposed transition of the boundary layer [1] by the acoustic excitation. Most probably, the acoustic waves at certain frequencies induce instability in the boundary layer and cause earlier boundary layer transition. However, the mechanism of the interaction between the boundary layer and acoustic waves is still unknown and requires further investigation.

4. Conclusions

The flow characteristics of the partially grooved cylinder under acoustic excitation have been studied. It is found that acoustic waves at 2.3 kHz excite the boundary layer on the smooth surface and change the flow structure significantly with attenuation in the strength of cylinder vortex shedding. The excitation results in a further reduction in drag coefficient, increase in lift coefficient and decrease in the wake size and Reynolds stress of the partially grooved cylinder.

References
1.   Y.C. Leung, Ph.D. Thesis, The University of Hong Kong, (1987).
2.   Y.C. Leung and N.W.M. Ko, Experiments in Fluids, 10(1991), 322.
3.   Y.C. Leung and N.W.M. Ko, J. of Fluids Engineering, 114(1992) 170.
4.   K.B.M.Q. Zaman and D.J. McKinzie, AIAA Journal, 29(1991) 1075.
5.   F.B. Hsiao and J.Y. Shyu, J. of Fluids and Structures 5(1991) 427.
6.   H.J. Allen and W.G. Vencenti, NACA Report 782(1944).

Table 1 Comparison of various coefficients for smooth and grooved cylinders.

Coefficient	Smooth cylinder	Grooved cylinder			
		No excitation		Acoustic excitation	
		Smooth surface	Grooved surface	Smooth surface	Grooved surface
Base pressure C_{pb}	-1.2	-1.0	-1.0	-0.8	-0.8
Minimum pressure C_{pm}	-1.2	-1.3	-1.2	-2.0	-1.3
$C_{pb}-C_{pm}$	0	0.3	0.2	1.2	0.5
Wake angle	78	111	125	119	125
Drag C_d	1.2	0.92		0.75	
Lift C_l	0	0.07		0.34	
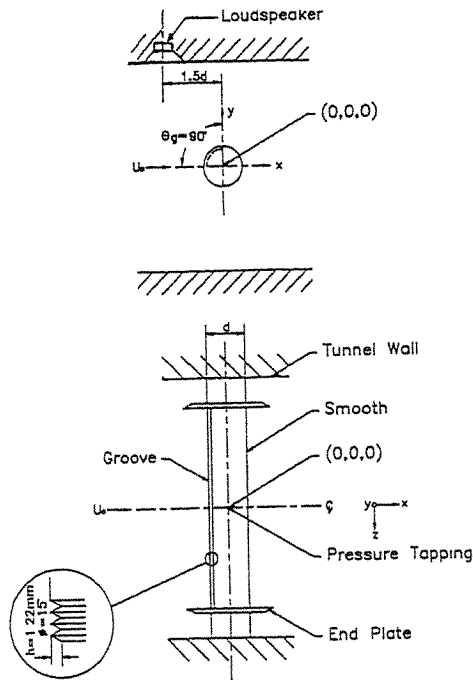
Fig. 1   Schematic diagram of experimental set up.
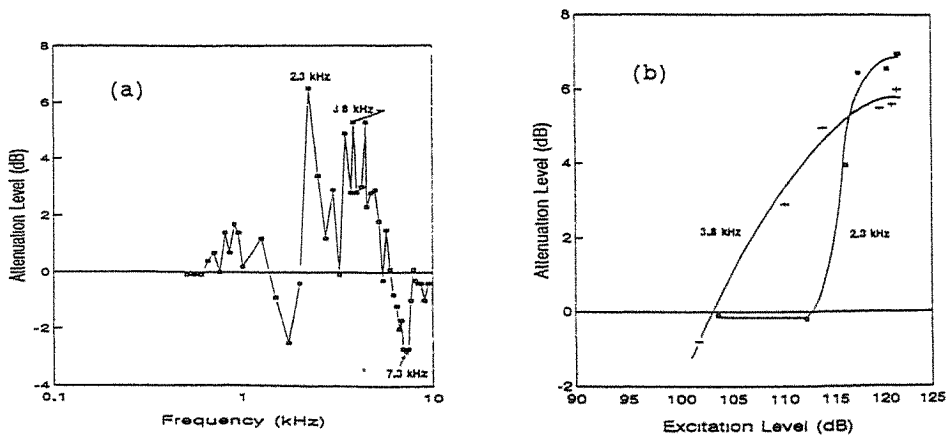
Fig. 2   Attenuation of power spectral level at vortex
shedding frequency under (a) different excitation
frequencies   (b) different excitation levels
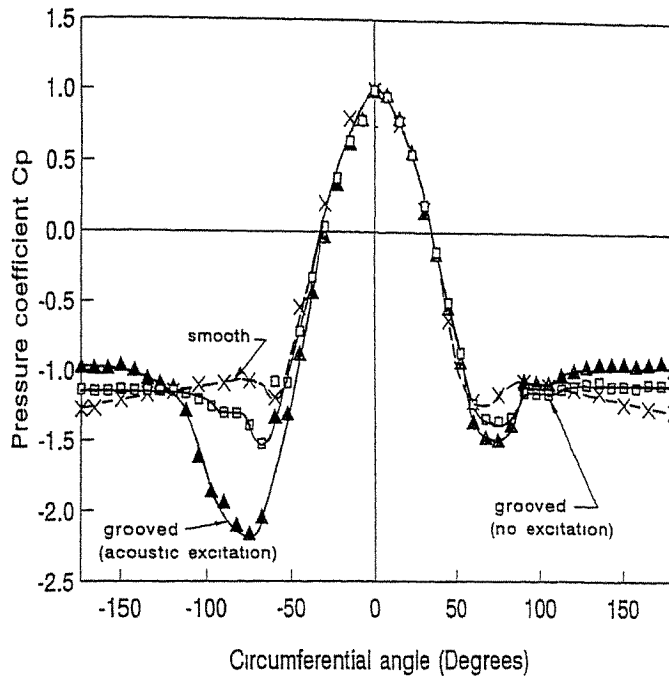
Fig. 3   Circumferential mean pressure distributions
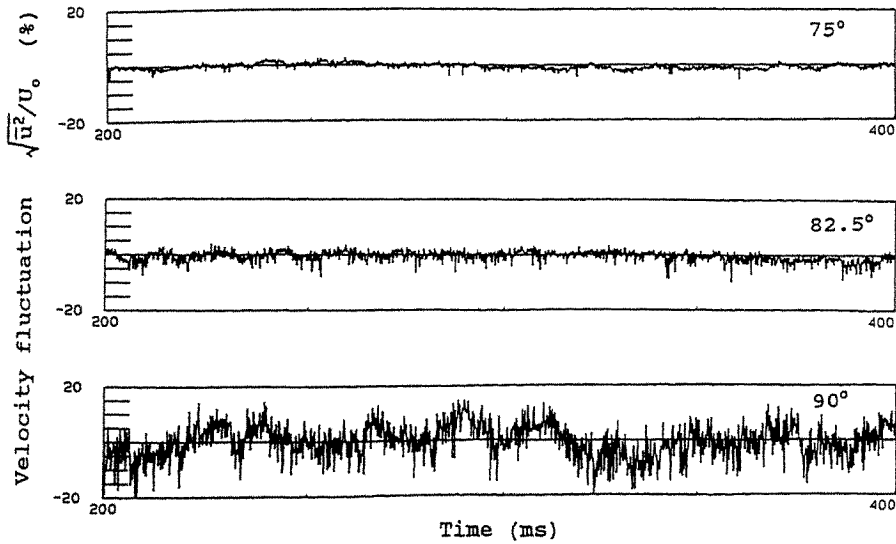
Fig. 4   Time records of velocity fluctuations at the edge
of boundary layer under acoustic excitation.

603
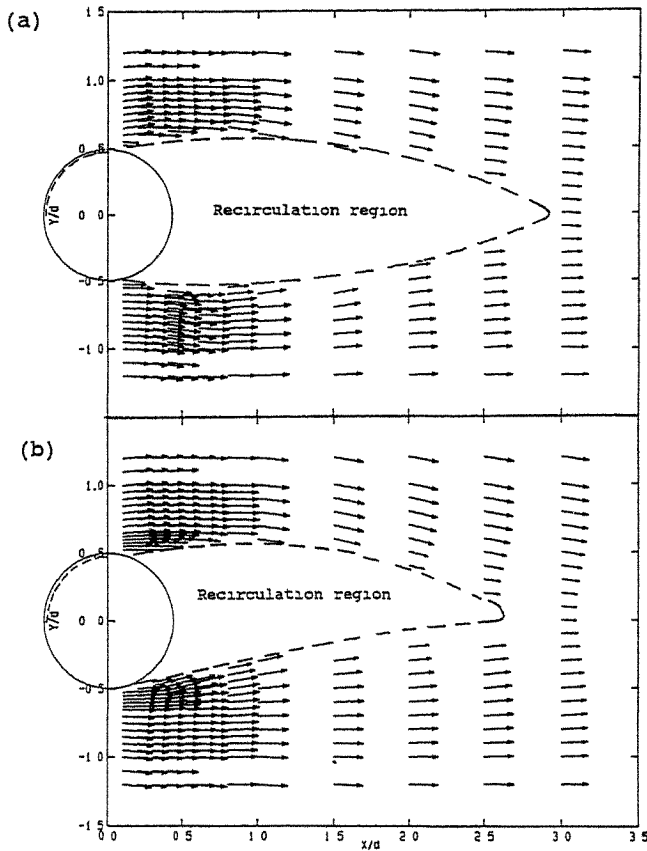
Fig. 5 Velocity vectors in the wake of the cylinder
(a) no excitation; (b) with acoustic excitation.
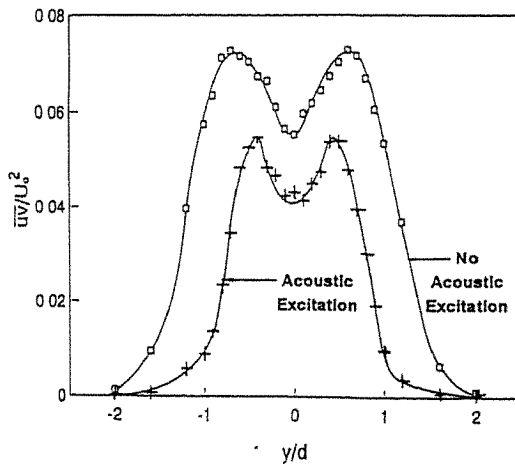
Fig. 6 Overall lateral Reynolds Stress
distributions at x/d=3.0.

604

Vibration-Induced Wind Forces on the Two Dimensional Rectangular Models

Y. Momomura, T. Ohkuma⁺, H. Marukawa⁺⁺ and T. Tsurumi⁺⁺⁺

Senior Researcher, Izumi Sohken Eng.,Co.,Ltd., Tokyo, Japan
⁺Professor Dr. Eng., Kanagawa Univ., Kanagawa, Japan
⁺⁺General Manager, Izumi Sohken Eng.,Co.,Ltd., Tokyo, Japan
⁺⁺⁺Staff, Sato Kogyo Co.,Ltd., Kanagawa, Japan

Abstract: In this paper the characteristics of a vibration-induced wind force acting on a high-rise building and the mechanism of the aeroelastic instability are studied. This was carried out on the basis of the wind pressure acting on a two dimensional rectangular section model during the forced vibration in a turbulent flow. Self-excited vibration of a completely separated flow type section model occurs due to the phenomenon so called "lock-in" except for Den Hartog's type galloping. In regard to a flow-reattachment type section model, torsional flutter is induced by the interaction between the convection velocity of the vortex and the vibration velocity in addition to the aforementioned "lock-in"

1.Introduction

Due to increases in the number of high-rise, lightly, constructed buildings with low structural damping, a study on the estimation of whether or not an aeroelastic instability will occur is becoming more and more important in the initial design stage. It has already been clarified that the galloping in an across-wind direction with a reduced wind velocity of 20 or more, can be investigated by the quasi-steady theory (for example [1]). On the other hand, both self-excited vibration induced by vortex and torsional flutter cannot be sufficiently evaluated through the application of the quasi-steady theory. It has been indicated in many studies (for example [2]~[7]) that these vibration or the characteristics of wind force during a period of vibration are influenced by the turbulence in approaching flow although the influence differs depending on a model shape. However, there are still many obscure points including the main factor regarding the occurrence of instability.

In this study, the relationship between the wind force and the mechanism of aeroelastic instability has been clarified through the measurement of the wind pressures distribution acting on a two dimensional rectangular section model during a period of forced vibration in a wind tunnel. This was done with the aim of understanding the aeroelastic mechanism of the self-excited vibration for a high-rise building.

2.Outline of the Test

The models used in the wind tunnel test were the two dimensional rectangular section with aspect ratio (D/B,D:depth, B:breadth) of 1,2 and 3 (See Fig.1). A tapping for measurement of the wind pressure was placed at the center of the span for the model. The oncoming flow was a uniform turbulent flow possessing turbulence intensity of 8%, blowing through a turbulent grid.

Vibration was forcedly input into the model through the use of a mechanical vibration system installed under the wind tunnel floor. The vibration modes were an across-wind vibration, a torsional vibration and a vibration of a coupled with these two vibrations (hereafter referred to as a coupled vibration) (See Fig.2). The mode of the coupled vibration described in this paper is assumed to be the primary mode for the frequency ratio (torsional vibration/across-wind vibration) of about 1.15~1.35 in the case of the eccentric ratio (eccentric distance/ radius of gyration of mass) of 0.1. In the test, the nondimensional vibration amplitude(A^*, θ^*) and the reduced wind velocity(U^*) were changed. $A^*(=A/B, A:$across-wind amplitude) was 0.008~0.067, $\theta^*(=\theta \cdot D/(2B))$, θ:rotated degree) was 0.003~0.03, $U^*(=U/(foB)$, fo:forced frequency) was 3~26.
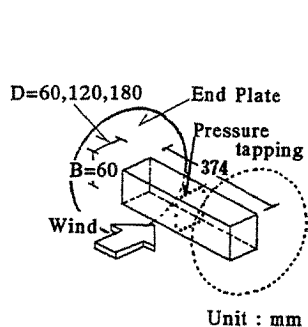
Fig.1 Model and Oncoming Wind
Direction
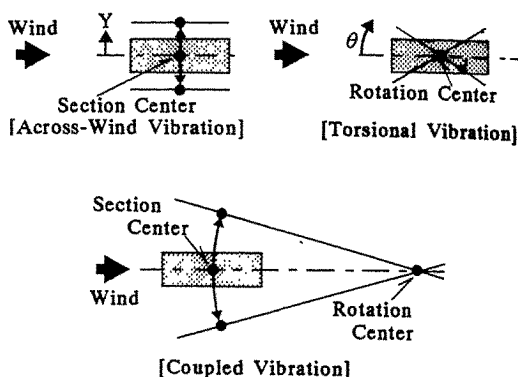
Fig.2 Mode of Forced Vibration in Test

3.Characteristics of the Wind Pressure on the Forced Vibration Models

3.1 Power Spectra and Spatial Phase Differences of Fluctuating Wind Pressure

The power spectra and the spatial phase difference in an along-wind direction, both of which are for the fluctuating wind pressure on the forced vibration models, are shown in Fig. 3 and 4, respectively. Data of the rigid models is also found in these figures. In the case of D/B≒1, regardless of the vibration mode, the characteristics of the fluctuating wind pressure acting on the forced vibration models were almost the same as those act on the rigid models. On the other hand, the fluctuating wind pressure acting on the forced vibration models in the case of D/B≧2, is more influenced by the vibration when the reduced wind velocity U^* is smaller than U^*_{sp}($U/f_{sp}, f_{sp}$:peak frequency found in the power spectra of the fluctuating wind pressure on rigid models). Furthermore, in regard to the the power spectra on the vibration model, a predominant peak is seen at the place where the frequency range corresponds to the forced frequency, and the spatial phase difference suddenly decreases at the range within the forced frequency. In the frequency range of $U^* > U^*_{sp}$, the characteristics of the fluctuating wind pressure during the forced vibration bear a close resemblance to those act on the rigid models.

(Rigid Model)　　　(D/B=1)　　　(D/B=2)
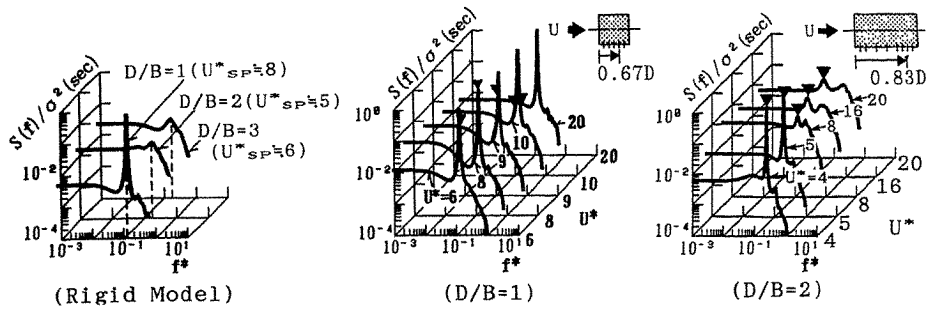
where, ▼:Forced Frequency

**Fig.3 Power Spectra of Fluctuating Wind Pressure
during Across-Wind Vibration ($A^* = 0.033$)**

(D/B=1)　　　　　(D/B=2)
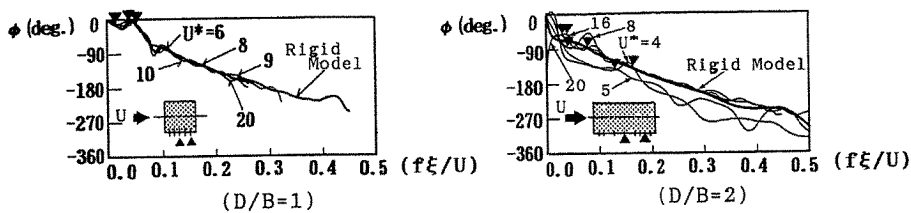
where, ▼:Forced Frequency, ξ:Two Points Distance

**Fig.4 Spatial Phase Difference of Fluctuating Wind Pressure
during Across-Wind Vibration ($A^* = 0.033$)**

3.2 Vibration-Induced Wind Pressures

As for the D/B= 1 and D/B= 2, both of which are for the vibration-induced
wind pressure coefficient acting on bottom surface of the model, are shown in
Fig.5 and 6, respectively. Both the in-phase component (C_{PR}) and the out-of-
phase component (C_{PI}) for the vibration-induced wind pressure coefficient were
obtained from Eq.(1) and Eq.(2), assuming that either an upward or a clockwise
rotation angle is positive.

$$C_{PR}= \frac{2}{T \cdot q} \int_0^T Pi(t) \cdot \frac{\zeta(t)}{\zeta_0} dt \quad (1), \qquad C_{PI}= \frac{2}{T \cdot q} \int_0^T Pi(t) \cdot \frac{\dot{\zeta}(t)}{\dot{\zeta}_0} dt \quad (2)$$

where, T:Average time, q:Velocity pressure, Pi(t): Variation of the fluctuating
　　　 wind pressure coefficient with time at i point, $\zeta(t)$:Variation of the
　　　 displacement of the vibration model or variation of the angle
　　　 displacement of one, $\dot{\zeta}(t)$:Variation of the velocity of the vibration
　　　 model or variation of the angle velocity of one, ζ_0 and $\dot{\zeta}_0$: Amplitude of
　　　 $\zeta(t)$ and $\dot{\zeta}(t)$, respectively.

607

In the case of D/B= 1, the value of the out-of-phase component is negative at each of the measuring points in the range of reduced wind velocity $U^* < U^*_{SP}$ ($\fallingdotseq 8$) and the negative value becomes smaller toward a leeward side. In $U^* \geqq U^*_{SP}$, the value is positive at all the measuring points and it also shows a large value on the windward, and become smaller toward the leeward side. The phase difference with the displacement of the vibration changes from negative to positive at all the measuring points in the vicinity of $U^* \fallingdotseq U^*_{SP}$.

In the case of D/B $\geqq 2$, the value of the out-of-phase component in the range of $U^* < U^*_{SP}$ rapidly varies from negative to positive at the position 1.0·B from the windward edge. In the range of $U^*_{SP} < U^* < 2U^*_{SP}$, due to an increase in the reduced wind velocity, an area where the value of the out-of-phase component becomes a positive moves to the leeward side and the value becomes smaller.
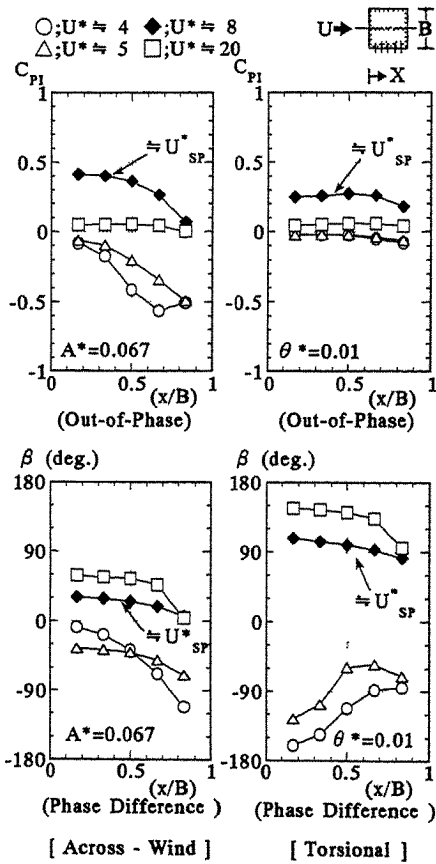
Fig.5 Vibration-Induced Wind Pressure
Coefficient for D/B= 1
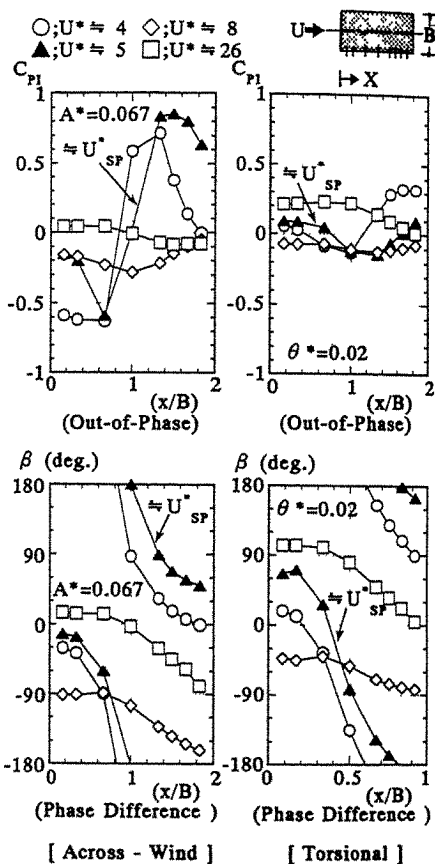
Fig.6 Vibration-Induced Wind Pressure
Coefficient for D/B= 2

608

In $U^* > 2U^*_{SP}$, with the increase in the reduced wind velocity, the value of the out-of-phase component shows a positive value on the windward and a negative value on the leeward. This negative value is found to be large during the torsional vibration rather than during the across-wind vibration. The phase difference with the vibration displacement, in $U^* < U^*_{SP}$, gently dips at the vicinity of the windward edge. The phase difference value rapidly changes approximately 180° at the vicinity of the model center and then gradually reaches 0° at the vicinity of the leeward edge. In $U^* > U^*_{SP}$, the phase difference value shows an almost constant value from the windward edge through to the position 1.0·B. In the area of leeward side more than at the position 1.0·B, it decrease in a linear with the distance from the windward edge increasing, and the spatial phase difference obtained from the gradient corresponds with one on the rigid model. Therefore, it is considered that the convection velocity of the vortex is not influenced by the vibration in $U^* > U^*_{SP}$.

4.Vibration-Induced Wind Forces

Fig.7 shows the out-of-phase component of the vibration-induced wind force coefficient which is related to a self-excited vibration. The vibration-induced wind force coefficients of lift force and torsional moment were obtained on the assumption that either an upward or a clockwise rotation angle is positive, respectively. The value for the torsional moment is that obtained for the center of the cross-section.

[During Across-Wind Vibration]   In the case of D/B= 1, the out-of-phase component of lift force rapidly changes from negative to positive in the vicinity of $U^* \doteqdot U^*_{SP}$, and exponentially damps with an increase of the reduced

Out-of-Phase Component
of Lift Force

Out-of-Phase Component
of Torsional Moment
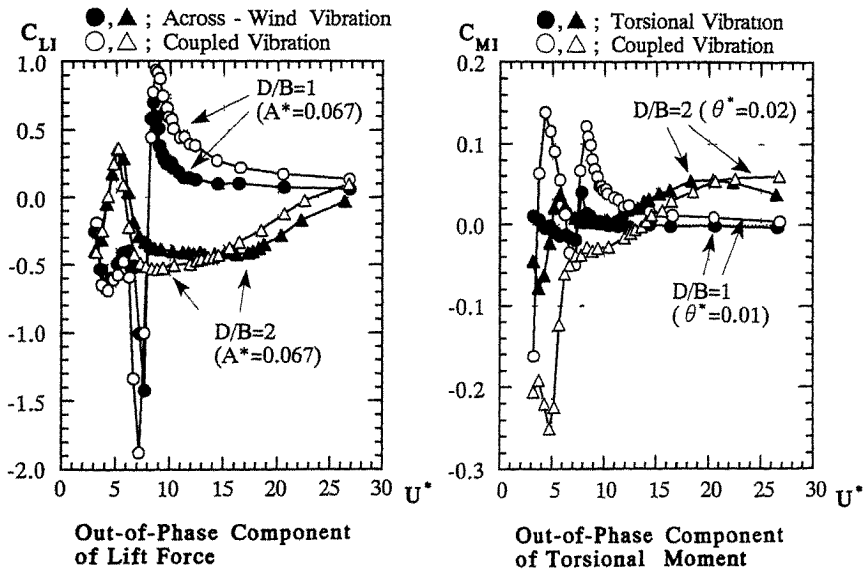
Fig.7 Vibration-Induced Wind Force Coefficient

609

wind velocity. In the case of $D/B \geqq 2$, the range in which the value for the out-of-phase component becomes positive is $0.8U^*_{SP} < U^* < 1.2U^*_{SP}$.

[During Torsional Vibration] When $D/B = 1$, the out-of-phase component of the torsional moment shows a positive value in the vicinity of $U^* \fallingdotseq 0.5U^*_{SP}$ and $U^* \fallingdotseq U^*_{SP}$. When $D/B \geqq 2$, the out-of-phase component indicates a positive value in the vicinity of $U^* \fallingdotseq U^*_{SP}$ and in the high wind velocity range of $U^* > 10$.

[During Coupled Vibration] The out-of-phase component of the lift force has a strong resemblance to the shape of that during the across-wind vibration regardless of the aspect ratio. The out-of-phase component of the torsional moment, in the case of $D/B = 1$, resembles the out-of-phase component during the torsional vibration in the qualitative tendency. However, there is a difference in which a large positive extremal value is seen in the vicinity of $U^* \fallingdotseq 0.5U^*_{SP}$ and $U^* \fallingdotseq U^*_{SP}$. In the case of $D/B \geqq 2$, the value of the out-of-phase component in the low reduced velocity range is not positive. In addition to this difference, the reduced wind velocity which change the out-of-phase component from negative to positive in high velocity range, is higher than during the torsional vibration.

5.Conclusion

In regard to the completely separated flow type section model, it is considered that the aerodynamic negative damping lift force is caused by "lock-in". The negative damping torsional moment is thought to be caused by the interaction between the convection velocity of the fluctuating wind pressure and the vibration velocity, when the reduced wind velocity U^* is less than a critical reduced velocity U^*_{SP} defined with the vortex shedding frequency.

In regard to the flow-reattachment type section model, it is considered that the aerodynamic negative damping lift force and torsional moment come about through the lock-in of the vortex shedding frequency from the separating bubble and the vibration frequency in the vicinity of $U^* \fallingdotseq U^*_{SP}$. In addition to, the negative damping torsional moment in the range of $U^* > 10$, is considered to be caused by the interaction between the convection velocity of the vortex and the vibration velocity. This wind force is important due to the fact that it has a possibility of the occurrence of torsional flutter.

Furthermore, it is clear that there is higher possibility of torsional flutter occurrence in coupled vibrating than in non-coupled vibrating for buildings with completely separated flow type section.

References:
[1]. Parkinson G.V.:Phil. Trans. Roy. Soc. Lond. A. 269, 1971, pp395-409.
[2]. H.Yamada and T.Miyata et al. :Proc. of 6th National Symposium on Wind Eng., Tokyo, November, 1980, pp185-192, in Japanese.
[3]. M.Matsumoto and N.Shiraishi et al. :Proc. of 10th National Symposium on Wind Eng., Tokyo, December, 1988, pp115-120, in Japanese.
[4]. H.Kobayashi and M.Kawatani et al. : J. of Wind Eng. (Transa. of JAWE), No.47, 1991, pp65-66, in Japanese.
[5]. Y.Taniike, Dr. thesis, Kyoto University, 1983, in Japanese.
[6]. H.Kawai:Summaries of Tech. Papers of Annual Meeting Archi. Insti. of Japan , Structures I, 1991, pp27-28, in Japanese.
[7]. Steckley A.,PhD thesis, University of Western Ontario, 1989.

.

The Vortex Shedding of a Group of
Three Equispaced circular cylinders

Xu You-Heng   Cheng Zhao
(Fudan University, Shanghai 200433)

Abstract: This experiment was carried out in a low speed wind tunnel. The vortex
shedding frequencies of each cylinder for various spacing ratios were obtained by
spectrum analysis of velocity fluctation signals measured in it's wake. It's
concluded that interference among three cylinder was related to spacing ratios
closely. When spacing ratio S/D was larger than 4.0, each cylinder behaved as a
single bluff body as far as vortex shedding frequencies were concerned. The closer
the spacing ratios were, the more serious the interference would be. When S/D was
less than 2.5, each cylinder shared a common frequency of vortex shedding at wind
direction alpha=60, meanwhile, for the other two arrangements(alpha=0 and 30), no
distinct vortex shedding from each cylinder was found in the range of S/D<2.5.

1. Introduction
    The researches on flow past a group of cylinders have been carried out widely
because their extensive background of industrial applications. The interference
between two parall circular cylinders in a free stream have been reviewed by Prof
M.M.Zdrokovich [1,2]. These two reviews are very helpful for the further
investigation.
    The vortex street will appear if flow past a single blunt body such as a circular
cylinder, and the frequency of vortex shedding from the body is mainly associated
with free stream velocity, size and shape of the body. The relationship among them
can be described with a nondimensional number: Strouhal number(St), St=FxD/V. Here F
is frequency, D is diameter of the cylinder and V is the approaching flow velocity.
    The body will be acted with the perodic forces when regular vortex shed from a
blunt body. The oscillation with large amplitude will happen and may even collapse
the structre if the frequency of vortex shedding reachs the natural frequency of the
body. The Vortex-induced oscillation is one of the most important mechanisms of
fluid-induced oscillations. Till now, the aspects of vortex shedding from single
circular cylinder are well known, and those of two circular cylinders in smooth flow
have stimulated an enormous research efforts[3,4], and also a lot of researches have
been carried out on flow past one or two rectangular cylinders[7,8,9]. But only a few
of reports on flow interference and aspects of vortex shedding of three cylinders are
presented. A.T.Sayer presented his report on aerodynamics forces of three equispaced
cylinders in various spacing ratios and several orientations relative to the
freestream in 1987[5]. In 1988, K.Lam et al. conducted their tests in a water tunnel,
they investigated vortex shedding frequencies of each cylinder by flow
visualization[6], their experiments were at Reynolds number 2.4*10^3 and 3.5*10^3.
    In the present study, the tests were conducted in a low-speed wind tunnel with a
Reynolds number of 3.7*10^4. And the frequency of vortex shedding was obtained by
spectrum analysis of velocity fluctuation measured in the wake of each cylinder.

2. Experimental Apparatus and Procedures
    The experiments were carried out in FDU-2 wind tunnel in Fudan University. A two
dimensional testing section was inserted into circular working section of the tunnel.
The dimensions of the 2-D testing section is as following: 1080mm(long), 500mm(wide),
200mm(high). The two dimensional testing section was composed with two pieces of
wooden rectangle plates(top and bottom), and it is open to air in width direction so

no attempt was made to correct for blockage effects.

Three Cylinders having diameter of 30mm were made of plexiglass rods and arranged as an equilateral triangle. The cylinders had a highly polished surface, the lengthes of them were 200mm, extended the full height of the testing section, so the end effects were avoided. One cylinder of them was fixed, when the other two cylinders rotating around this fixed cylinder, the different flow patterns with different orientations relative to the freestream were obtained. The distance between each two cylinders were varied in seven spacing ratios (1.5D, 1.75D, 2.0D, 2.5D, 3.0D, 3.5D and 4.0D) and three wind directions (alpha=0, 30 and 60 degree as shown in fig1) were used in the experiments. The velocity of freestream was 17m/sec and the Reynolds number was $3.7*10^4$ accordingly in the experiments.

Four measuring locations in the wake of each cylinder were set as fig1. Velocity measurements were made with TSI constant-temperature hot-wire anemometers, the hot-wire probe was mounted on a three-dimensional coordinate mechanism. Voltage signals from the anemometer were recorded with a TEAC R280C portable data recorder, the time interval of velocity signal at each location was taken more than 30 seconds. To play the tape back, the power spectra was got by a personal computer with A/D converter. The vortex shedding frequency could be determined by the peak frequency of the spectra. Test methods described above have been verified by experiments on flow past single cylinder and two circular cylinders respectively.

In order to determine the vortex shedding frequency of a cylinder definitely, more than one hundred of spectra were analysised for a certain location. Usually, the spectra could be catalogued into three groups. (1)Single peak spectrum, as seen in fig 2(a), it was taken from S/D=2.0, alpha=0 at the first location, the single peak was dominant in this spectrum. The amplitude at other frequencies were much lower than the peak, the regular vortex shedding was distinctly. (2)Fig 2(b) was a kind of confusion spectrum. It was taken from S/D=1.5, alpha=0 at the 12th location. There is no predominant peak existed in the spectrum. Also the spectra were different if the different initial time for doing spectrum analysis was taken. The vortex shedding could not be found in this situation. (3)Double peaks spectrum, as seen in fig 2(c)-(e), it was taken from S/D=2.5 , alpha=0 at the 12th location. It is easy to make out that the two peaks are different. but their strength varies from time to time, and which one would become the dominant peak was concerned with the initial sampling time. Nevertheless two different vortex shedding frequencies were certain at this location.

3. Results and Discussions

The Strouhal numbers varied with the spacing ratio in three wind directions were shown in Fig (3), (4) and (5).

(1): Fig (3) is for alpha=0. (Two cylinders were side by side behind front cylinder) when the distance between their centers exceeded 4.0 diameters, each cylinder in the group behaved as a single circular cylinder, they had the same Strouhal number as the single one (St=0.21 in subcritical). The Strouhal number of the upstream cylinder increased monotonicly as S/D decreasing, yet the two downstream cylinders symmetric geometrically had the vortex shedding of different frequencies which might be caused by biased gap flow. For spacing 2.5D, double-peak spectrum was got at the 12th location, they were at F1=120Hz(st=0.21) and F2=202Hz(st=0.36) respectively, in fact the latter was the vortex shedding frequency of the front cylinder. Two peaks were competing and which one would be dominant peak was varied from time to time (see fig 2(c)-(e)). The comparision between spectrums got from rear cylinder and front cylinder was made after a lot of spectra analysis with differnt initial sampling time. We suppose that: at location 12 the hot-wire detected vortex shedding signals both from upstream cylinder and downstream cylinder coincidently, and the two peaks found in spectrum were corresponding to the frequency of upstream cylinder and downstream cylinder respectively. In this case the flow about the

downstream cylinders may be markedly non-uniform because of the vortex shedding from the upstream cylinder. It was clear that the frequency of vortex shedding of the front cylinder varied from 201Hz to 202Hz. Also the range in which the frequency of the rear cylinder varied was wider than that of front cylinder, it was from 120Hz to 131Hz (St=0.21 to 0.23).

When the spacing ratio down to 2.0D, The spectra detected from location 12 were not as clear as those in range S/D>2.0, and the frequency varied in a much wider range, from 153Hz to 173Hz(St=0.27 to 0.31). Sometimes it was unable to find a dominant vortex shedding frequency. To our surprise, vortex shedding of the upstream cylinder was not suppressed.

All spectra were very confusion when S/D was less than 2.0 and no dominant peak was found. It should be attributed to serious interference among three cylinders in such a close arrangement, and perodic vortex shedding could not establish because of intensely irregular velocity fluctuation. Also the serious interference among cylinders would cause unstable gap flow which might submerge the vortex sheded from the cylinders.

(2): As seen in fig.4, the vortex shedding was detected in the whole range of spacing ratio at alpha=60 (two cylinders were side by side in front of the third one). Its strouhal number continously increased as the spacing ratio decreased from 4.0 to 3.0, and in this range strouhal number of each cylinder was close to each other. At S/D=2.5, the two upstream cylinders shared a common vortex shedding frequency, but St of the downstream cylinder decreased greatly. Bistable flow pattern was found in S/D=2.0, two front cylinders had different frequencies of vortex shedding, the two different frequencies may be correspond to a wide and a narrow wake respectively.

As far as vortex shedding frequency was concerned, three cylinders could be considered as one bluff body when S/D was less than or equal to 1.75. Because we could detect a same vortex shedding frequency at any position behind each cylinder in this range, if took the entire size of the group as "D" in formula St=F*D/U to calculate Strouhal number St, we got St=0.20--0.22, as same as that of a single circular cylinder.

(3) The Strouhal number varied with the space ratio measured at alpha=30 was shown in Fig 5 (two cylinders in tandem with a side cylinder), as in range S/D=2.5 to 4.0, there was no distinct vortex shedding from the front cylinder, which was the same as the front cylinder of only two cylinders in tandem arrangement. As in range 2.5 to 2.0 weak vortex shedding was detected now and then. As soon as S/D became 1.75 or 1.5, The distinct and perodic vortexes shedded from the front cylinder with high frequency (St=0.62 and 0.72). A dominant peak was found in spectra, this is quite different from the front cylinder of only two cylinders in tandem.

According to Fig.5, in range of S/D>2.5, the side cylinder had a Strouhal number of 0.20 which was equal to that of a single cylinder, the dominant peak in each spectrum was very clear. It meant the two cylinders in tandem had slight interference to the side one in this range of space ratio. The dominant peak could not be found when S/D<=2.0 and the spectra became more and more confusion when S/D dereased further. This indicated that the interference among three cylinders got more serious in close arrangements.

For the rear cylinder in this arrangement, distinct vortex shedding was found in range of S/D>=2.0, and confusion spectra with no dominant peak were got in its wake in range of S/D<2.0.

4. Conclusions

The frequency of vortex shedding from three equispaced circular cylinders of the same diameter has been experimentally investigated at Reynolds number of 3.7*10^4. The results may be concluded as following:
1. The interference among three cylinders was slight in range s/d>=4.0 at

alpha=0, 60 deg, and each cylinder had the same vortex shedding frequency as single cylinder. Interference occured and became serious when s/d decreased from 3.5, vortex shedding frequency varied greatly.

2. At alpha=30, the side cylinder behaved a great influence to two cylinders in tandem when S/D was less than 2.0, the front cylinder had a high vortex shedding frequency which is not found in flow past two cylinder in tandem [1].

3. At alpha=0 and 30 deg, when S/D was less than 2.0, very confusion spectra were found instead of spectra with predominant peaks, perodic vortex shedding was immersed by intensive gap flow.

4. Bistable flow patterns were found at alpha=0 and 60 deg. Owing to the lack of more spacing ratios in this study, more detailed tests should be carried out in the future to determine the bistable flow pattern.

We would like to say the interference among three circular cylinders are more complicated than that of two staggered cylinders. The results mentioned above are not unique in very close arrangements. It is very possible that different authors obtain different conclusions because a complete picture of flow pattern has not been got, for example, the unstable gap flow or bistable flow. There is still a long way to go before drawing an overall conclusion. The more extensive and advanced researches are worth conducting in this field to have a clear look in it.

We are still studying vortex shedding frequency of each cylinder simultaneously in equispaced arrangement with pressure transducers mounted inside the cylinders at present. We hope to get more information about the flow around three cylinders.

Refrence:
1. M.M.Zdravkovich, Review of flow Interference between Two Circular Cylinders in Various Arrangements, ASME Journal of Fluids Engineering, 99(1977) 618-633.
2. M.M.Zdrovkovich, Review of Interference-induced Oscillations in flow Past two Circular Cylinders in Various Arrangements, Journal of Wind Engineering and Industrial Aerodynamics, 28(1988) 183-200.
3. Kiya M. et al., Vortex shedding from Two Circular Cylinders in Staggered Arrangement, Journal of Fluids Engineering, (1980)166-173.
4. Xu You-heng, Huang Dong-qun, The unstable Flow from the Gap Between two Circular Cylinders, Journal of Hydrodynamics, Ser.b,3(1991) 110-115.
5. A.T.Sayers, Flow Interference between Three Equispaced Cylinders When Subjected to a Cross Flow, Journal of Wind Engineering and Industrial Aerodynamics, 26(1987) 1-19.
6. K.Lam and W.C. Cheng, Phenomena of Votex Shedding and Interference of Three Cylinders in Different Equilateral Arrangements, Journal of Fluid Mechanics, Vol. 196(1988) 1-26.
7 H.Sakamoto and H Haniu, Effect of Free-Stream Turbulence on Characteristics of Fluctuating Forces Acting on Two Squre Prisms in Tandem Arrangement, Journal of Fluids Engineering, Vol 140. 110 (1988)
8. F.Nagao and H.Utsunomiya, The Validity of Sectional Models on Wind Tunnel Tests for Vortex Induced Oscillation of Bridges, Journal of Wind Engineering and Industrial aerodynamics, 29(1988) 351-360.
9. H.Sakamoto, H.Haniu and Y.Obata, Fluctuating forces Acting on Two Squre Prisms in a Tandem Arrangement, Journal of Wind Engineering and Industrial Aerodynamics, 26(1987) 85-103.

Fig 1

(a)   (b)

(c)   (d)   Fig.2   (e)

615

Fig.3

Fig.5

Fig.4

616
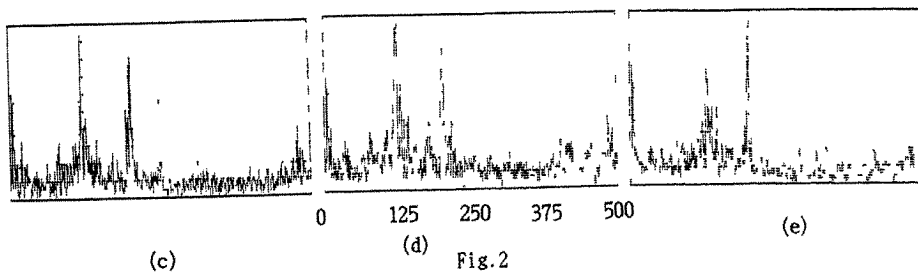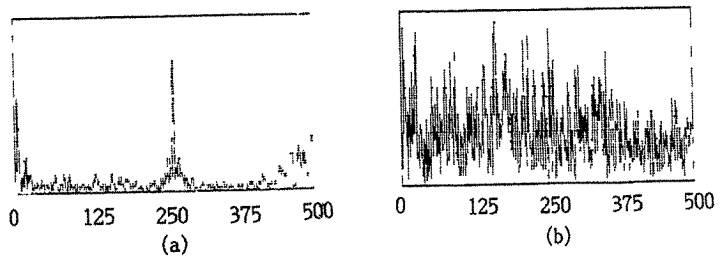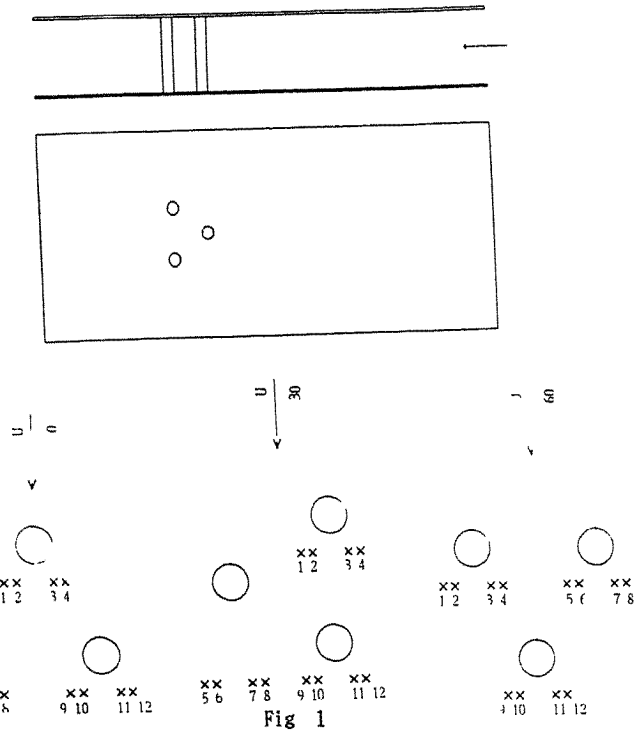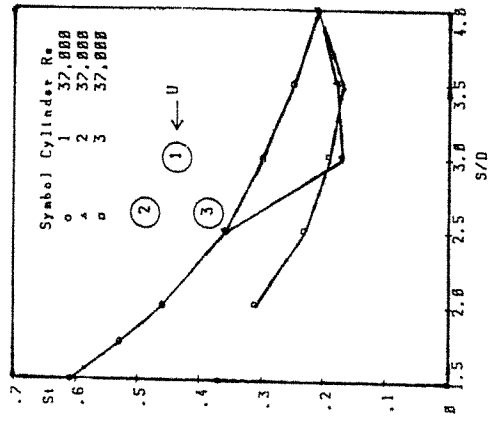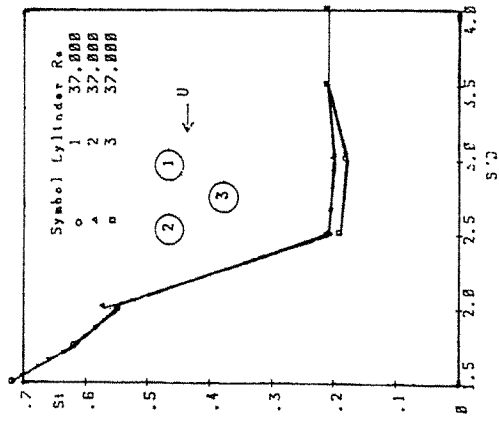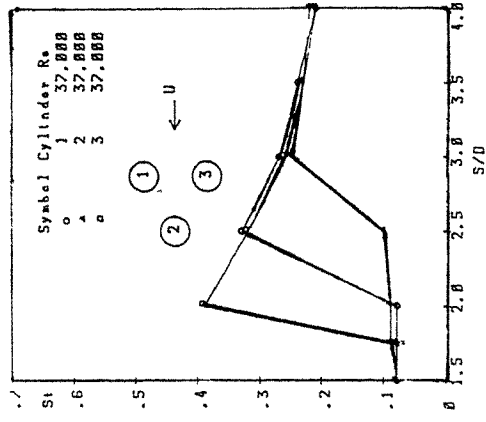
A Study of Wake Galloping of Bridge Stay-Cables

T. Yoshimura[1], M.G. Savage[2], H. Tanaka[3] and D. Urano[4]

1- Department of Civil Engineering, Kyushu Sangyo University, Higashi-Ku, Fukuoka, Japan 813
2- National Research Council Canada, Applied Aerodynamics Laboratory,
Ottawa, Ontario, Canada, K1A OR6
3- Department of Civil Engineering, University of Ottawa, Ottawa, Ontario, Canada, K1N 6N5
4- Fukuoka Branch, New Structural Engineering Inc., Hakata-Ku, Fukuoka, Japan 812

Abstract: An experimental study of the wake galloping of several configurations of parallel stay-cables for a cable-stayed bridge was conducted in two wind tunnels, one in Japan and one in Canada, to develop a method for suppressing the instability. At first, the parallel cable models were connected rigidly to each other with spacers, forming a coupled cable group whose surface-to-surface separation, or gap, could be varied from 0 to 2 cable diameters. This modification stabilized the wake galloping but it was found that a different form of instability then occurred at higher wind speeds. In this case the group of cables, rather than just the downwind cable, was unstable. With zero gap, the group was most stable, being unstable only near 5 degrees wind angle and aerodynamically stabilized otherwise. When the cable group with zero gap was twisted into a shallow helix it was found to be aerodynamically stable for all wind angles.

1. INTRODUCTION

Oscillation of parallel, smooth-surfaced stay-cables may pose serious vibration problems for cable-stayed bridges. When two stay-cables of a cable-stayed bridge are closely positioned, lateral oscillation may occur for the downwind stay in the wake of the upwind stay. This has been described as "wake galloping" (Ref. 1). Several methods of suppressing this aeroelastic instability have been demonstrated. They include the installation of end-point or inter-cable dampers and the use of cable restraints by connections between pairs of cables (Ref. 2,3). These modifications are not always effective and may not be aesthetically pleasing, both important points for the bridge designer. For example, the restraints may cure the wake galloping by increasing its critical wind speed but permit the group of cables so formed to develop new instabilities. These instabilities have several mechanisms and occur at higher wind speeds than that for wake galloping, but still at speeds below the design wind speed. Two mechanisms were identified. One occurred when a gap was present and is related to the fluid-elastic, wake-switching in heat exchangers (Ref. 4) and the other, with zero gap, was the classical galloping of a cylinder in cross flow (Ref. 8).

New methods are required to control these instabilities. Previous work at the National Research Council of Canada (NRCC) had shown that bundles of two and four power-line conductors could be stabilized by fitting spacers between them and by twisting the resulting bundle sufficiently (Ref. 5), although no studies had included the close spacing employed in stay-cables.

Wind tunnel studies of the aerodynamic instability of joined, closely-spaced stay-cables were conducted to assess the use of twist as a stabilizing method both at Kyushu-Sangyo University (KSU) and the NRCC. This paper summarizes the findings from the first study at KSU (Ref. 6) and the recent study at the NRCC (Ref. 7).

2. MODEL DETAIL AND INSTRUMENTATION

Three types of smooth-surfaced, cable models were used in the experiments at KSU and the NRCC. The smooth finish was required as a plastic cover is used for corrosion protection on the bridge stays. The

majority of the testing was conducted with pairs of cables and, in a few cases, with three cables. The first model consisted of a pair of parallel circular cables separated by a variable gap, D, that could be set at 0.0 (cables touching), 0.5, 1.0, 1.5, or 2.0 cable diameters, d. The second model consisted of a pair of cables twisted together with zero gap. Figure 1 illustrates both the twisted two-cable and three-cable models with zero gap, where the cables are twisted into a helix like a stranded rope at a pitch greater than 100 diameters of the cable. The portion of the twisted group exposed to the wind was one-half of the pitch length. These models were used for dynamic measurements when connected to a spring system and for static force measurements when connected to a balance.

The spring-mounted models had an aspect ratio of 58:1 and were mounted horizontally in the working section of the 1.5 m x 1.5 m wind tunnel at KSU. The aerodynamic damping of the models was measured for a range of wind speeds and wind angles by a free vibration method. Lift, drag, and surface pressure distributions were measured on the stationary models only.
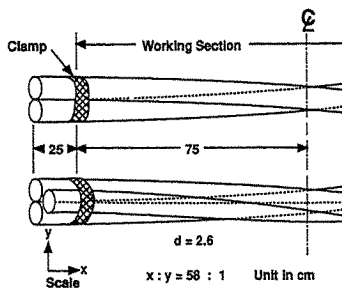
Fig. 1. Twisted stay-cable models.
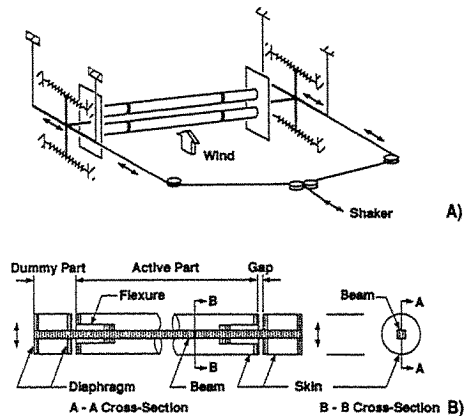
Fig. 2. Schematic of mechanism for forced oscillations (A) and dynamic balance used for the unsteady lift measurements (B) at NRCC

A third, metric dynamic force model, with an aspect ratio of 14:1, was tested in the vertical wind tunnel at the NRCC to measure the unsteady lift for the same cable geometries. The working section insert used in this wind tunnel has a 2m x 3m cross-section. The lift measurements were made by a dynamic balance module in the model using forced excitation. The model was suspended by a pair of long piano wires at each end allowing it to oscillate like a pendulum with a nearly horizontal motion. Helical springs on both sides of the model provided the required model vibration frequency and permitted free-vibration measurements. The forced-vibration measurements were made by shaking the model with an electro-magnetic shaker. Figure 2 shows a sketch of the model, the shaker system, and the dynamic balance module used for the unsteady force measurements. The balance module was suspended from the ends of the model by two pairs of strain-gauged flexures. The unsteady, total force acting on the active portion - aerodynamic plus inertial - was measured by these gauges. The inertia force was calculated from measurements of model displacement time-history, enabling the unsteady aerodynamic lift component to be extracted from the total. The aerodynamic damping was obtained from the out-of-phase component of the lift force.

Finally, flow visualization was carried out using parallel cables in the water towing tank at KSU. All the experiments were performed at sub-critical Reynolds numbers.

618

3. AERODYNAMIC DAMPING MEASUREMENTS

Parallel Cables - The aerodynamic damping measurements for the parallel cable models are presented in Fig. 3. The mass-aerodynamic-damping parameter is $M_r \delta_a = 2 M \delta_a / (\rho d^2)$, where M_r is the generalized mass, M is the mass per unit length of the model, δ_a is the aerodynamic logarithmic decrement, and ρ is the air density. The reduced wind speed is $V_r = V / (fd)$ where V is the wind speed, and f is the vibration frequency of the model in wind. The wind incidence angle is A.
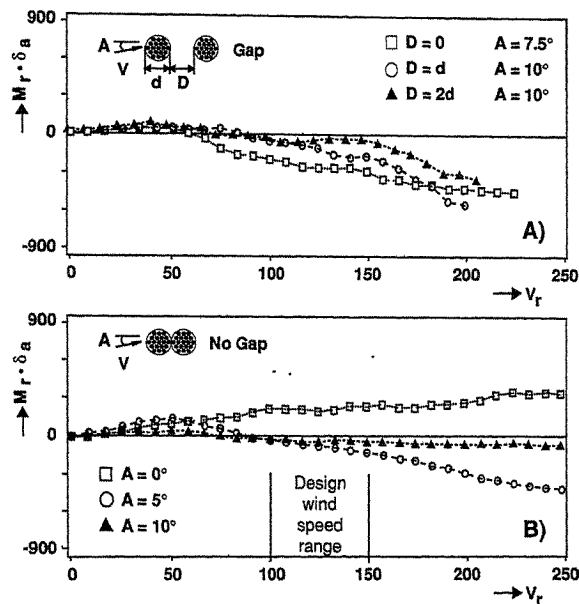
Fig. 3. Mass-aerodynamic-damping parameter vs. reduced wind speed for parallel stay-cable models for D/d = 0, 1, and 2 at several wind angles.
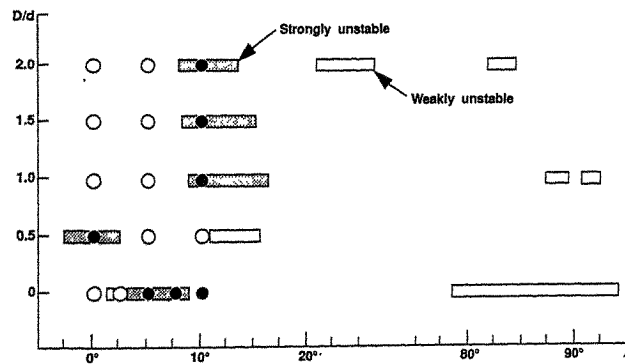
Fig. 4. Aerodynamic stability diagram for parallel stay-cable models.
● Unstable (forced vibration); ○ Stable (forced vibration); ▭ Unstable (quasi-steady theory)

619

At low wind speeds, the aerodynamic damping was positive, stabilizing the model. However, only the model with zero gap and at zero wind angle was stable over the speed range tested. For all other cases, the damping peaked when the wind speed was increased, and then reduced in magnitude, to finally become negative above a threshold wind speed. Above this wind speed, depending on structural damping, the model would be unstable. Typically, model motion was in a cross-wind direction with instability occurring at a reduced wind speed of about 60 for a one- diameter gap and 90 with zero gap.

Figure 4 summarizes the aerodynamic stability of the models. The black circles indicate the cases where instability occurred and the white circles where the model was stable. The shadowed area indicates the unstable region predicted by a quasi-steady theory (Ref. 8). "Weakly unstable" indicates that the cable is unstable for structural damping levels below that giving a logarithmic decrement of 0.005. The stability diagram predictions show that all of the models were unstable, even if only over a narrow range of wind angle. Generally, the predicted regions of strong instability correlate well with the measurements.

Figure 5 shows typical behaviour of the aerodynamic damping measured using the dynamic balance in the NRCC experiments. A comparison of the forced and free vibration measurements of aerodynamic damping for a pair of circular cables with zero gap at two wind angles shows them to be in good agreement at low wind speeds.
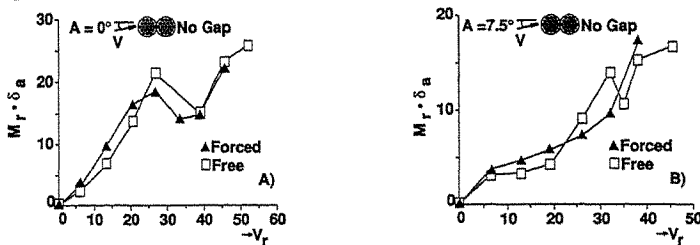
Fig. 5.   Mass-aerodynamic-damping parameter vs. reduced wind speed for parallel stay-cable models with zero gap (NRCC)

Twisted Cables - The aerodynamic damping measurements made for groups of two and three cables with zero gap are presented in Figure 6. It can be seen that both groups are now strongly stabilized by the aerodynamic forces. Effectively, only a short length of the stay-cable is exposed to unstable local wind angles and is far outweighed by the the effect of the much greater cable length of the aerodynamically stabilized portion. Because of the twist, there is now no wind angle for which instability can occur because of the continuous range of angles produced by the twist.

4. MEASUREMENTS OF MEAN LIFT AND DRAG

Figure 7 presents the mean lift and drag coefficients, C_L and C_D, measured at KSU for the parallel-cable models. The predicted unstable regions shown in Figure 4 were estimated from these measurements. The definition of the wind-axis coordinate system used is shown in the figure. The coefficients plotted are the sum of those acting on the upwind and the downwind cables. The most significant features in Figure 7, ie. those that may cause aerodynamic instability, are:

1) The sudden jump in lift that occurs near 7 degrees wind angle when a gap is present. The flow is bi-stable at this boundary and small changes in wind angle, such as those that could be caused by wind gusts or cable motion, would cause the lift coefficient to jump back and forth between zero and approximately unity. This behaviour was not observed with zero gap.

2) Regions of negative lift-curve slope, where den Hartog galloping may occur, at wind angles above 9 degrees when a gap is present and in the range of 3 to 7 deg. when the gap is zero.

620

Fig 6. Mass-aerodynamic-damping parameter vs. reduced wind speed for twisted stay-cable models.

Stranded Cable
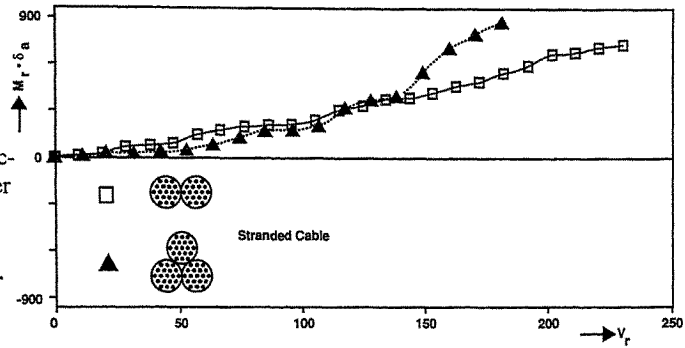
Fig 7. Typical lift and drag coefficients for parallel stay-cable models.

$$c_L = L/\tfrac{1}{2}\rho V^2 d$$
$$c_D = D/\tfrac{1}{2}\rho V^2 d$$

Wind Angle, A

$D/d = 1$

A) $\dfrac{V}{A = 15°}$ P_b

$D/d = 0$

B) $\dfrac{V}{A = 0°}$

C) $\dfrac{V}{A = 12°}$

P_b: Base Pressure
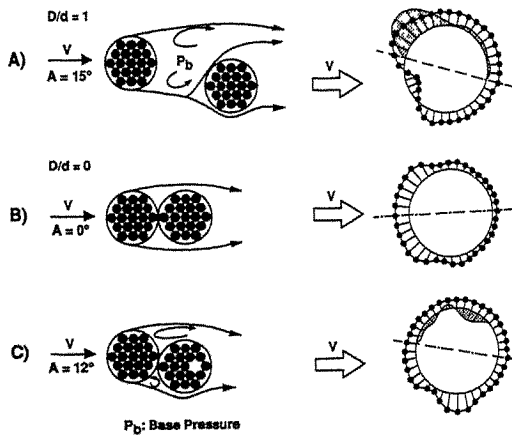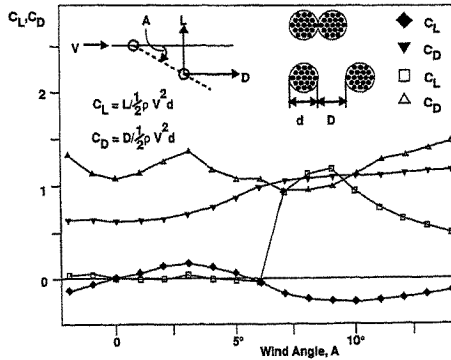
Fig. 8. Sketch of flow around a parallel stay-cable model and the accompanying surface pressure distributions on the downstream cable.

5. CHARACTERISTICS OF FLOW AND SURFACE PRESSURE ON MODEL

Because the cables are rigidly connected, the instability that results with zero gap is not due to wake galloping but is related to the jet-switching, fluid-elastic instability found in heat exchanger tubes (Ref. 4). A water tunnel investigation was performed to investigate the flow mechanism and to relate it to the pressure measurements that were made at KSU.

Figure 8 presents a set of sketches that summarize the observations made in the water tunnel and the matching pressure distributions. The upper sketch shows the flow pattern for a pair of cables with a gap of D/d=1.0 at a wind angle above the angle at which the sudden jump in lift was observed. The lower separating streamline from the upwind cable that had previously reattached to the downstream cable has now detached

621

and flows above the downwind cable. This sudden flow jump, or wake switch, occurs abruptly and produces an accelerating gap flow that causes a large lift force on the downwind cable, directed toward the centre of the wake of the upwind cable. These trends can be seen in the accompanying pressure distribution for the downstream cable (Fig. 8). The shaded area represents the difference in pressures measured at opposite locations on the upper and lower halves of the cylinder. The surface pressure distribution with a gap present, at small wind angles, would be similar to that shown in lower sketch, with signs of flow reattachment on the lower and/or the upper surfaces, and a small net pressure difference in the lift direction. Based on the large lift change, it is likely that the cable pair would tend to rotate to a smaller wind angle, causing the lift to return to zero; the cycle could then repeat, providing a partial explanation for the observed oscillation.

The lower two sketches of Figure 8 show the much different situation at A=12 degrees with zero gap. The large negative, differential pressure peak cannot form in the absence of gap flow. The unstable behaviour expected near 5 degrees wind angle is probably that due to galloping, as indicated by the negative lift-curve slope for this configuration in Figure 7.

6. CONCLUDING REMARKS

This study showed that parallel cables joined by a spacer do not exhibit wake galloping but may experience several other instabilities at higher reduced wind speeds than those associated with wake galloping. The nature of these instabilities depends on the cable separation. When a gap was present between cables, a strong form of wake-switching instability was observed and when the gap was zero, weaker galloping occurred. These phenomena were substantiated with flow visualization and surface pressure measurements. When the cable group with two or three members and zero gap was twisted with a pitch length of 100 diameters, it was stabilized. The use of contacting, twisted cables would appear to be a viable method of aerodynamically stabilizing bridge stay-cables.

7. ACKNOWLEDGEMENTS

REFERENCES:

1. K. Yokoyama, et al., "Wind-Induced Oscillation of the Cables of Large Sized Cable-Stayed Bridge and Preventive Measures ", Mitsubishi Heavy Industries Ltd., Vol.14, No. 3, 1977.
2. N.J. Gimsing, "Cable Supported Bridges— Concept and Design", John Wiley & Sons, 1983.
3. T. Yoshimura, "Aerodynamic Stability of Four Medium Span Bridges in Kyushu District", J. Wind Engineering and Industrial Aerodynamics, Vol. 42, 1992.
4. S.J. Price, and M.P. Paidoussis, "The aerodynamic forces acting on a group of two and three circular cylinders when subject to cross flow", J. Wind Eng. and Industrial Aerodynamics, 17(1984), 329-347
5. R.L. Wardlaw, K.R. Cooper, R.G. Ko and J.A. Watts, "Wind Tunnel and Analytical Investigations Into the Aeroelastic Behaviour of Bundled Conductors", IEEE PES Summer Meeting & Energy Resources Conf., Anaheim, CA., July 14-19, 1974.
6. T. Yoshimura, et al., "A Device for Suppressing Wake Galloping of Stay-Cables for Cable-Stayed Bridges", Second International Colloquium on Bluff Body Aerodynamics and Applications, Melbourne, Australia, Dec. 1992.
7. M.G. Savage and B.R. Robinson, "Unsteady Lift Measurements on a Pair of Parallel Stay-Cables for a Cable-Stayed Bridge", NRCC, to be published.
8. J.P. Den Hartog, "Mechanical Vibrations", McGraw-Hill, 1956.

Flow around and mean pressure field on a circular cylinder placed downstream of a blunt-based flat plate in staggered arrangement

H.İbrahim Keser and M.Fevzi Ünal

Istanbul Technical University
Faculty of Aeronautics and Astronautics
Maslak 80626, Istanbul-Turkey

Abstract: A study having experimental and numerical parts has been carried out into the flow around and mean pressure distributions on a circular cylinder placed in staggered arrangement with an upstream blunt-based flat plate. Attention has been given to variation with respect to transverse and longitudinal spacings between the plate and the cylinder of the drag and lift coefficients acting on the cylinder, and corresponding flow patterns and the pressure distributions calculated by means of Lagrangian discrete vortex method.

1. Introduction

Due to its practical importance in engineering applications such as group of chimney stacks, off-shore platforms, a group of bluff-bodies immersed into a fluid flow has attracted a great deal of research attention. Extensive review articles by Zdravkovich [1, 2] summarizes important research contributions into the case of group of equal-diameter circular cylinders in various arrangements, which are usually classified as tandem, side-by-side and staggered.

The staggered arrangement is likely to occur most in engineering applications, but has attracted the least research attention. Measurements of surface pressure distribution around one of the two parallel cylinders in staggered arrangement show that , there is a dominant region for the downstream cylinder associated with a negative (i.e. towards wake centerline of upstream body) lift force and decreased drag force with respect to the single cylinder value. For sufficiently large transverse separation distances, there is a small region in which the lift force is negligible and the drag force is close to that of a single cylinder, beyond which there is no interference of the wake producing bodies. Details of flow patterns corresponding to these complex variations of the forces on the downstream cylinder is not fully disclosed. However, for sufficiently close separation distances between cylinders of unequal diameters, Price [3] has found that the wake of the upstream body is displaced by the downstream cylinder, and therefore its characteristics had a negligible effect on the lift of the downstream cylinder. On the other hand, when the downstream cylinder is not in the wake of the upstream cylinder, flow rate between bodies increases due to entrainment [1].

There have been few numerical studies in the field. Recently, Slauti and Stansby [4], using an Eulerian-Lagrangian discrete vortex approximation in combination with the random-walk method to simulate the vorticity diffusion, investigated the flow around circular cylinders of equal diameters in tandem and side-by-side arrangements. Unal and Keser [5] have shown that the Lagrangian discrete vortex method successfully reproduces many experimentally-observed features of flow around a circular cylinder placed downstream of a blunt-based flat plate in tandem arrangement.

The present study concerns the case in which the downstream cylinder is in staggered

arrangement with the blunt-based plate. In the experimental part of the study, lift and drag forces acting on the cylinder were determined based on measurements of the mean pressure distributions around the downstream cylinder for a number of longitudinal and transverse spacings between the plate and the cylinder. Numerical simulation of the corresponding flow patterns and the mean pressure distributions has been done using the Lagrangian discrete vortex method.

2. Experimental Procedure

Experimental investigation has been done in an open-return wind tunnel of the I.T.U. Low Speed Aerodynamics Laboratory, which has a test section 500mm high and 500mm wide. The Reynolds number based on the plate length ($l=520$mm) is $Re_l = 6.6 \times 10^4$ and the turbulence level is 0.2%. A 400mm wide, 380mm high and 1700mm long Plexiglas false test section inserted into the main one eliminates the unfavourable effects of boundary layers developing on the tunnel walls, and allows convenience of placement of the plate and the cylinder into the stream. The leading-edge of the plate is chosen to be a semi-ellipse, length ratio of whose axes is 5 to 1 ; $H=40$mm. The circular cylinder placed downstream of the plate is made from an aluminum tube having an outer diameter $D=30$mm and a wall thickness of 6mm. The circular cylinder has eight equally-spaced pressure taps around its circumference at its mid-width. By turning the cylinder around its axis, pressure measurements have been taken at a total of 32 points. All the taps are 10mm deep and has a 0.8mm bore. Pressure measurements have been made by connecting the pressure taps directly to a electro-pneumatic micromanometer (FURNESS FC001). The connecting pipe lengths between the device and the pressure

Fig. 1. Flow configuration and various parameters of the study.

taps are 500mm. Mean pressure measurements for the above mentioned Reynolds numbers have been taken at a maximum of twelve different spacings, L/H=0.65, 1, 1.5, 2, 2.5, 2.85, 3, 4, 5, 6, 8 and 10 ; The examined-vertical distances between the centerlines of the cylinder and the plate are: E/H= 0, 0.25, 0.50 and 1.0 (Figure 1).

3. Numerical Method

Details of the numerical procedure has been given elsewhere [5], in which the case of the tandem arrangement (i.e. E/H=0) has been extensively studied. Basically, the simulation of separated flow around the blunt-based flat plate and the circular cylinder downstream is achieved by combining the vortex singularity method with the conformal mapping-image technique. First, the physical plane is mapped by means of Schwartz-Christoffel transformation to a semi-infinite plane, and the vorticity transport equation for two-dimensional inviscid flow,

$$\frac{\partial \overline{\lambda_k}(\omega)}{\partial T} = [\frac{\partial W}{\partial \lambda_k} - i\frac{\Gamma_k}{4\pi}(\frac{d^2z/d\lambda_k^2}{dz/d\lambda_k})] |\frac{d\lambda_k}{dz}|^2 \tag{1}$$

is solved in this (computation) plane. $\overline{\lambda_k}(\omega)$ is the complex conjugate of position vector having vorticity ω, and W is the complex potential. Multiplication of the complex conjugate velocity

624

($\partial \overline{W}/\partial \lambda$) by the square of the transformation modulus ($|d\lambda_z/dz|^2$) ensures that the vortices are convected correctly in the physical plane. The second term on the right hand side of the equation represents the Routh correction factor in the computation plane. By means of the complex potential,

$$W(\lambda) = -\frac{H}{\pi}\lambda^2 - \frac{i}{2\pi}\sum_{j=1}^{N_w}\Gamma_j\ln(\lambda-\lambda_j) - \frac{i}{2\pi}\sum_{k=1}^{N_f}\Gamma_k\ln(\lambda-\lambda_k)$$
$$+\frac{i}{2\pi}\sum_{j=1}^{N_w}\Gamma_j\ln(\lambda-\overline{\lambda}_j) + \frac{i}{2\pi}\sum_{k=1}^{N_f}\Gamma_k\ln(\lambda-\overline{\lambda}_k)$$

(2)

velocities at discrete vortex locations are calculated at each time step. The first term represents the potential due to the basic flow in the semi-infinite plane, whereas the second and third terms stand for N_w bound vortices representing the cylinder and an array of N_f vortices modelling the vorticity in the flow (Figure 2). Corresponding images in the lower half plane, namely the fourth and the fifth terms respectively, satisfy the boundary condition on the plate surface. The number of equally spaced control points on the cylinder surface is chosen to be 100, and the same number of bound vortices (N_w) are located at a distance $R_o = \pi D/2N_w$ from the surface. Singularity at discrete vortex locations, and therefore unrealistically high velocities in close neighbourhood of them are avoided through the use of a rigid core of constant radius $\sigma = R_o/2$.

Fig 2. Representation of cylinder
by the vortex singularities.

Knowing the induced normal velocities $\{v_n\}$ at the control points on the cylinder surface due to all causes except the bound vortices, the boundary condition there is satisfied through solution of a set of linear equations,

$$\{\Gamma\} = [A]^{-1}\{v_n\}$$

(3)

for strengths of bound vortices $\{\Gamma\}$ at each time step. [A] is the influence coefficient matrix. When solving this equation, the Kelvin's theorem, expressing the conservation of circulation,

$$\sum_{j=1}^{N_w}\Gamma_j = -\sum_{k=1}^{N_f}\Gamma_k$$

(4)

is satisfied as well, by replacing the last line of (3) (which stands for the control point at the middle of the rear surface of the cylinder) with (4). During convection of vortices emitted from the plate and the cylinder, some of them crosses the cylinder boundary and are removed from the calculation. The right hand side of (4) accounts for this lost circulation.

Discrete vortices are introduced into the flow at every other convection time step ($\delta T = 0.1$; T is the nondimensional time, i.e. $T = U\ t/H$). The introduction points for the plate are the corners of the plate, whereas for the cylinder all the bound vortices are released into the flow. From the plate, newly created vortices of strengths ($\pm\Sigma(1/2)V_s^2\delta T$) move with the velocities (V_s) at the points $z = \pm 0.6Hi$, sum is over two time steps since the last vortices are introduced. A vortex-merging procedure restricts the total number of vortices, while keeping the computation time step small enough for an accurate calculation of vortex movements [6]. The convection is done through the use of a second order scheme,

625

$$\lambda(T+\delta T)=\lambda(T)+\frac{1}{2}[3U(T)-U(T-\delta T)]\delta T \qquad (5)$$

The pressure distributions are obtained by the following formula for the pressure increment between any two consecutive points around the cylinder,

$$\Delta P_j = -\rho \Gamma_j / \Delta T \qquad (6)$$

Where, ΔT is equal to $2\delta T$, ρ is the density and Γ_j is equal to the difference between the newly created circulation at jth bound vortex location and the circulation lost by vortices crossing the jth surface segment [7]. When obtaining the pressure distribution, the pressure coefficient at the front stagnation point is set to the experimentally-determined value. Drag (C_D) and lift (C_L) coefficients are obtained by integrating the pressure distributions around the cylinder.

4. Discussion of Results

Experimentally-determined variation of normalized drag (C_D/C_{Dmax}) and lift (C_L/C_{Lmax}) coefficients of the downstream cylinder as function of the longitudinal (L/H) and the transverse (E/H) spacings are shown in Fig. 3 and 4 respectively. For all the transverse spacings, the drag coefficient increases with increasing L/H. For small transverse spacings, E/H=0 and 0.25, the rate of increase with L/H is much higher than those of the rest. Interestingly, for E/H=0 and sufficiently small longitudinal spacings (i.e. L/H≤1), the drag force acting on the cylinder is towards the plate. When E/H=0.25, C_D/C_{Dmax} indicates a variation with L/H, which is similar to that of E/H=0, except that it decreases first, making a minimum at L/H=1.5 and then increases. The variation corresponding to E/H=0.5 does not differ appreciably from the former two for L/H≥3. However, a large deviation from the cases of E/H=0 and 0.25 is observed for smaller longitudinal spacings (L/H≤3). As the cylinder is moved further towards the free-stream (E/H=1), C_D/C_{Dmax} attains its maximum values for all the longitudinal spacings (L/H).
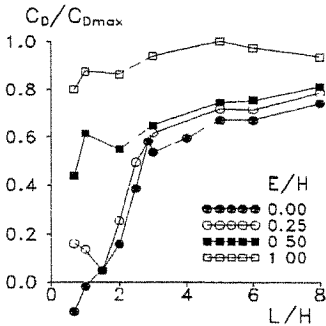
Fig. 3. Variation with respect to L/H of normalized drag coefficient (C_D/C_{Dmax}) for various E/H.
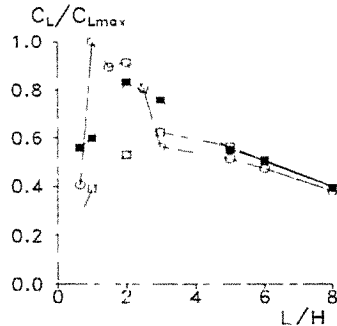
Fig. 4. Variation with respect to L/H of normalized lift coefficient (C_L/C_{Lmax}) for various E/H.

Lift force acting on the cylinder for the longitudinal and transverse spacings of this study is always directed towards the wake centerline of the plate. Corresponding to the minimum value of C_D/C_{Dmax} for E/H=0.25 at L/H=1.5, normalized lift coefficient C_L/C_{Lmax} indicates a maximum (Fig. 4). For increasing E/H, the location of the lift maximum shifts towards larger longitudinal spacings (L/H), and its rate of increase and decrease with L/H before and after the maximum

decreases. Additionally, the maximum value of the negative lift decreases with increasing transverse spacing.
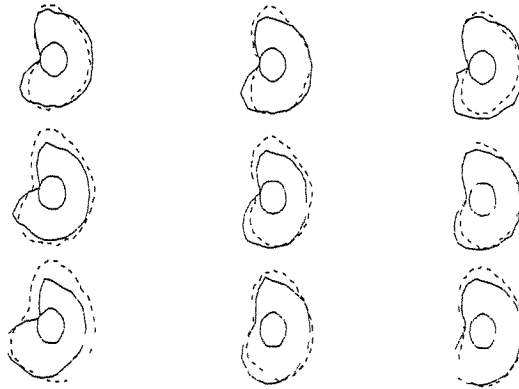
Fig. 5. Comparison of measured and calculated time-mean pressure distributions for L/H=1, 3 and 8 (from left to right) and E/H=0.25, 0.50 and 1 (from bottom to top). ------ indicates calculated distributions.
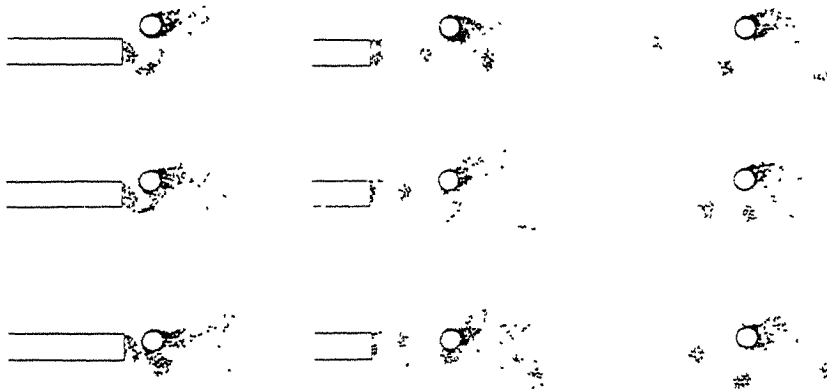
Fig. 6. Wake vortex structures for L/H=1, 3 and 8 (from left to right) and E/H=0.25, 0.50 and 1 (from bottom to top).

The polar graphs shown in Fig. 5 provide a concise representation of measured and calculated time-mean pressure distributions around the cylinder. Radial outside distance between a point on

627

the cylinder and the pressure envelope indicates suction. An important feature of the distributions is the fact that, the minimum suction position for $E/H=1$, which is normally at $\Theta=0°$ for a single cylinder (Θ is the angle measured from the front stagnation point), is rotated in the clockwise direction. As the cylinder approaches from the free stream to the wake centerline of the plate, this position rotates further round the cylinder, away from the $\Theta=0°$. For $E/H=0.25$ and $L/H=1$ the location Θ_s is close to 40°; as E/H increases, this angle decreases first to $\Theta_s \approx 30°$ for $E/H=0.5$ and to $\Theta_s \approx 10°$ for $E/H=1$. Movement of the minimum suction location indicates that the incident stream to the cylinder is tilted towards the centerline. Along with this movement, while its magnitude is increasing, the location of maximum suction pressure on the lower side of the cylinder shifts towards $\Theta=0°$. It is interesting to note that the suction on the upper surface is virtually unaffected by the presence of the upstream plate, whereas, by action of the plate-wake, the suction on the lower surface becomes larger than that at the upper side: End effect of this is the negative lift values. It seems that the above mentioned lift force variation is greatly dominated by the asymmetry of the pressure distribution at the base region. On the other hand, the drag coefficient decrease is mainly due to the increase of suction on the surface of the cylinder facing upstream. In general, the calculated pressure distributions are in agreement with the experimental ones, except for small transverse and longitudinal spacings suction pressure at the base region is predicted to be higher than that of experiment.

The discrete vortex distributions for $L/H=1$, 3 and 8 and $E/H=0.25$, .50 and 1 provide an insight into the above-mentioned variations of the drag and lift coefficients (Fig. 6). For a proper comparison, distributions correspond to non-dimensional times at which the fluctuating lift passes through a minimum. It is evident that for small spacings (e.g. $E/H=0.25$ and $L/H=1$), there is an intense gap flow between the bodies and that the wake from the plate is greatly deflected downwards. With respect to the case of single cylinder, the streamlines between the bodies (not shown here) squeeze and consequently the suction on the lower side of the cylinder which produces a downward mean-lift increases (Fig 5). For $L/H=3$, wake from the plate is not as much affected. However, interaction of the vortices emanating from the plate with surface of cylinder results in increased mean-suction on the lower side. For the largest longitudinal separation of the experiment ($L/H=8$), vortices originating from the plate travel well clear of the circular cylinder and show no indication of strong interaction with the cylinder surface.

Acknowledgments:

References:

1.   M.M. Zdravkovich, Trans. ASME, J. Fluids Engrg., 99 (1977) 618.
2.   M.M. Zdravkovich, J. Fluids and Structures, 1 (1987) 239.
3.   S.J. Price, Aeronautical Quarterly, XXVI (1976) 154.
4.   A. Slaouti and P.K. Stansby, J. Fluids and Structures, 6 (1992) 641.
5.   M.F. Unal and H.I. Keser, To appear in Proceedings of 8th International Conference on Numerical Methods in Laminar and Turbulent Flows, Swansea-U.K., July (1993).
6.   P.R. Spalart and A. Leonard, AIAA-81-1246 (1981).
7.   P.A. Smith and P.K. Stansby, J. Fluids and Structures, 5 (1991) 336.

Author Index